ASME
SETTING THE STANDARD

Journal of Engineering for Gas Turbines and Power

Published Quarterly by ASME

VOLUME 130 • NUMBER 1 • JANUARY 2008

Editor
D. R. BALLAL (2011)
Assistant to the Editor
S. D. BALLAL
Associate Editors
Gas Turbine (Review Chair)
R. BUNKER (2008)
Coal, Biomass & Alternative Fuels
K. ANNAMALAI (2010)
Combustion & Fuels
N. K. RIZK (2009)
T. SATTELMAYER (2009)
Controls, Diagnostics, & Instrumentation
A. VOLPONI (2010)
Cycle Innovation
P. PILIDIS (2010)
Electric Power
A. RAO (2010)
Structures and Dynamics
P. S. KEOGH (2010)
J. SZWEDOWICZ (2009)
D. P. WALLS (2009)
Advanced Energy Systems
J. KAPAT (2010)
Internal Combustion Engines
J. S. COWART (2008)
C. RUTLAND (2009)
T. RYAN III (2009)
M. S. WOOLDRIDGE (2008)

PUBLICATIONS COMMITTEE
Chair, B. RAVANI

OFFICERS OF THE ASME
President, S. Y. ZAMRIK
Executive Director,
V. R. CARTER
Treasurer,
T. D. PESTORIUS

PUBLISHING STAFF

Managing Director, Publishing
P. DI VIETRO
Manager, Journals
C. MCATEER
Production Coordinator
J. SIERANT

Transactions of the ASME, Journal of Engineering for Gas Turbines and Power (ISSN 0742-4795) is published bimonthly (Jan., Mar., May, July, Sep, Nov.) by The American Society of Mechanical Engineers, Three Park Avenue, New York, NY 10016. Periodicals postage paid at New York, NY and additional mailing offices.
POSTMASTER: Send address changes to Transactions of the ASME, Journal of Engineering for Gas Turbines and Power, c/o THE AMERICAN SOCIETY OF MECHANICAL ENGINEERS, 22 Law Drive, Box 2300, Fairfield, NJ 07007-2300.
CHANGES OF ADDRESS must be received at Society headquarters seven weeks before they are to be effective. Please send old label and new address.
STATEMENT from By-Laws. The Society shall not be responsible for statements or opinions advanced in papers or ... printed in its publications (B7.1, par. 3).
COPYRIGHT © 2008 by the American Society of Mechanical Engineers. For authorization to photocopy material for internal or personal use under circumstances not falling within the fair use provisions of the Copyright Act, contact the Copyright Clearance Center (CCC), 222 Rosewood Drive, Danvers, MA 01923, Tel: 978-750-8400, www.copyright.com.
Canadian Goods & Services Tax Registration #126148048

EDITORIAL

010201 Editorial
Dilip Ballal

RESEARCH PAPERS

Gas Turbines: Aircraft Engine

011201 System-Level Performance Estimation of a Pulse Detonation Based Hybrid Engine
Jeffrey Goldmeer, Venkat Tangirala, and Anthony Dean

011202 Fundamental Mechanism of Entropy Noise in Aero-Engines: Experimental Investigation
Friedrich Bake, Nancy Kings, and Ingo Roehle

Gas Turbines: Coal, Biomass, and Alternative Fuels

011401 Predicting the Performance of System for the Co-production of Fischer-Tropsch Synthetic Liquid and Power from Coal
Xun Wang, Yunhan Xiao, Song Xu, and Zhigang Guo

Gas Turbines: Combustion, Fuels, and Emissions

011501 A Novel Approach to Enhance the Hydrogen Yield of Biomass Gasification Using CO_2 Sorbent
Madhukar R. Mahishi, M. S. Sadrameli, Sanjay Vijayaraghavan, and D. Y. Goswami

011502 Flame Propagation Following the Autoignition of Axisymmetric Hydrogen, Acetylene, and Normal-Heptane Plumes in Turbulent Coflows of Hot Air
Christos N. Markides and Epaminondas Mastorakos

011503 Analysis of the Pollutant Formation in the FLOX® Combustion
H. Schütz, R. Lückerath, T. Kretschmer, B. Noll, and M. Aigner

011504 Compressor/Diffuser/Combustor Aerodynamic Interactions in Lean Module Combustors
A. Duncan Walker, Jon F. Carrotte, and James J. McGuirk

011505 FLOX® Combustion at High Pressure With Different Fuel Compositions
Rainer Lückerath, Wolfgang Meier, and Manfred Aigner

011506 Fuel Flexibility Influences on Premixed Combustor Blowout, Flashback, Autoignition, and Stability
Tim Lieuwen, Vince McDonell, Eric Petersen, and Domenic Santavicca

011507 Effects of Tailpipe Friction on the Nonlinear Dynamics of a Thermal Pulse Combustor
Achintya Mukhopadhyay, Subhashis Datta, and Dipankar Sanyal

011508 Experimental Investigation of the Stability Mechanism and Emissions of a Lifted Swirl Nonpremixed Flame
Paris A. Fokaides, Plamen Kasabov, and Nikolaos Zarzalis

011509 Impact of Ethane, Propane, and Diluent Content in Natural Gas on the Performance of a Commercial Microturbine Generator
Richard L. Hack and Vincent G. McDonell

(Contents continued on inside back cover)

This journal is printed on acid-free paper, which exceeds the ANSI Z39.48-1992 specification for permanence of paper and library materials. ♾™
♻ 85% recycled content, including 10% post-consumer fibers.

Downloaded 03 Jun 2010 to 171.66.16.160. Redistribution subject to ASME license or copyright; see http://www.asme.org/terms/Terms_Use.cfm

(Contents continued)

Journal of Engineering for Gas Turbines and Power JANUARY 2008

Volume 130, Number 1

011510 Effect of Fuel System Impedance Mismatch on Combustion Dynamics
Geo A. Richards and Edward H. Robey

Gas Turbines: Controls, Diagnostics, and Instrumentation

011601 An Optimal Orthogonal Decomposition Method for Kalman Filter-Based Turbofan Engine Thrust Estimation
Jonathan S. Litt

Gas Turbines: Cycle Innovations

011701 Design Concept for Large Output Graz Cycle Gas Turbines
H. Jericha, W. Sanz, and E. Göttlich

011702 An Iterative Method for Blade Profile Loss Model Adaptation Using Streamline Curvature
Vassilios Pachidis, Pericles Pilidis, Ioannis Templalexis, and Luca Marinai

011703 Calculations of Cooled Turbine Efficiency
J. H. Horlock and Leonardo Torbidoni

Gas Turbines: Industrial & Cogeneration

012001 Application of a Computational Code to Simulate Interstage Injection Effects on GE Frame 7EA Gas Turbine
M. Bagnoli, M. Bianchi, F. Melino, A. Peretto, P. R. Spina, S. Ingistov, and R. K. Bhargava

012002 Study and Field Tests of the Novel Low Pressure Fogger System for Industrial Gas Turbine
Y. Levy, V. Sherbaum, V. Ovcharenko, Y. Sotsenko, and I. Zlochin

012003 A Novel Free-Cooling Scheme for Combustion Turbine Inlet Air Cooling
Montaser M. Zamzam and Abdalla M. Al-Amiri

012004 Development and Validation of a Computational Code for Wet Compression Simulation of Gas Turbines
M. Bagnoli, M. Bianchi, F. Melino, and P. R. Spina

Gas Turbines: Manufacturing, Materials, and Metallurgy

012101 Comparison of Recuperator Alloy Degradation in Laboratory and Engine Testing
Bruce A. Pint, Karren L. More, Rosa Trejo, and Edgar Lara-Curzio

012102 Improved High Cycle Fatigue Damage Tolerance of Turbine-Engine Compressor Components by Low Plasticity Burnishing
Paul S. Prevéy, N. Jayaraman, Ravi A. Ravindranath, and Michael Shepard

Gas Turbines: Structures and Dynamics

012501 The Effect of Initial Injection Conditions on the Oil Droplet Motion in a Simplified Bearing Chamber
M. Farrall, S. Hibberd, and K. Simmons

012502 Numerical and Experimental Damping Assessment of a Thin-Walled Friction Damper in the Rotating Setup With High Pressure Turbine Blades
J. Szwedowicz, C. Gibert, T. P. Sommer, and R. Kellerer

012503 On Nonlinear Rotor Dynamic Effects of Aerodynamic Bearings With Simple Flexible Rotors
B. Bou-Saïd, G. Grau, and I. Iordanoff

012504 Heavily Loaded Gas Foil Bearings: A Model Anchored to Test Data
Tae Ho Kim and Luis San Andrés

012505 A Design to Improve the Effective Damping Characteristics of Hole-Pattern-Stator Annular Gas Seals
Dara W. Childs, Yoon-Shik Shin, and Brent Seifert

012506 Nonlocal Cyclic Life Prediction for Gas Turbine Components With Sharply Notched Geometries
Roland Mücke and Holger Kiewel

012507 Evaluation of Flow Behavior for Clearance Brush Seals
Yahya Dogu, Mahmut F. Aksit, Mehmet Demiroglu, and Osman Saim Dinc

012508 Neural Network Models for Usage Based Remaining Life Computation
Girija Parthasarathy, Sunil Menon, Kurt Richardson, Ahsan Jameel, Dawn McNamee, Tori Desper, Michael Gorelik, and Chris Hickenbottom

012509 Spiral Vibration of a Turbogenerator Set: Case History, Stability Analysis, Measurements and Operational Experience
Lothar Eckert and Joachim Schmied

012510 Labyrinth Seal Leakage Tests: Tooth Profile, Tooth Thickness, and Eccentricity Effects
Ahmed J. M. Gamal and John M. Vance

Internal Combustion Engines

012801 The Effect of Engine Exhaust Temperature Modulations on the Performance of Automotive Catalytic Converters
Tariq Shamim

(Contents continued on facing page)

Downloaded 03 Jun 2010 to 171.66.16.160. Redistribution subject to ASME license or copyright; see http://www.asme.org/terms/Terms_Use.cfm

Journal of Engineering for Gas Turbines and Power JANUARY 2008

Volume 130, Number 1

012802 1D Engine Simulation of a Small HSDI Diesel Engine Applying a Predictive Combustion Model
T. Cerri, A. Onorati, and E. Mattarelli

012803 Validating the Phenomenological Smoke Model at Different Operating Conditions of DI Diesel Engines
Y. V. Aghav, P. A. Lakshminarayanan, M. K. G. Babu, Azeem Uddin, and A. D. Dani

012804 Application of a Spark Ignition Engine Simulation Tool for Alternative Fuels
Nirendra N. Mustafi and Robert R. Raine

012805 Instantaneous Engine Speed Time-Frequency Analysis for Onboard Misfire Detection and Cylinder Isolation in a V12 High-Performance Engine
Fabrizio Ponti

012806 Thermomechanical Fatigue Life Prediction of Cylinder Heads in Combustion Engines
Stefan Trampert, Taner Gocmez, and Stefan Pischinger

012807 Measurement and Simulation of Instantaneous Emissions of a Heavy Truck Diesel Engine During Transients
Xavier Tauzia, Pascal Chesse, Jean-François Hetet, and Nicolas Thouvenel

DESIGN INNOVATION

015001 MotoGP 2007: Criteria for Engine Optimization
Enrico Mattarelli

The ASME Journal of Engineering for Gas Turbines and Power is abstracted and indexed in the following:

AESIS (Australia's Geoscience, Minerals, & Petroleum Database), Applied Science & Technology Index, Aquatic Sciences and Fisheries Abstracts, Civil Engineering Abstracts, Compendex (The electronic equivalent of Engineering Index), Computer & Information Systems Abstracts, Corrosion Abstracts, Current Contents, Engineered Materials Abstracts, Engineering Index, Enviroline (The electronic equivalent of Environment Abstracts), Environment Abstracts, Environmental Science and Pollution Management, Fluidex, INSPEC, Mechanical & Transportation Engineering Abstracts, Mechanical Engineering Abstracts, METADEX (The electronic equivalent of Metals Abstracts and Alloys Index), Pollution Abstracts, Referativnyi Zhurnal, Science Citation Index, SciSearch (The electronic equivalent of Science Citation Index), Shock and Vibration Digest

Downloaded 03 Jun 2010 to 171.66.16.160. Redistribution subject to ASME license or copyright; see http://www.asme.org/terms/Terms_Use.cfm

Journal of Engineering for Gas Turbines and Power

Editorial

A happy new year to all of you! As the new-year unfolds, JEGTP will make a giant leap forward with a new publications schedule, enhanced ASME Journal Tool interface, and rapid paper processing. All these changes represent a "win-win" situation for authors, readers, and subscribers. ASME has responded to the journal needs in a big way, the editorial team and ASME staff have significantly decreased the paper processing time, and the journal is publishing papers on emerging hot topics. Below is the status report.

Beginning in 2008, JEGTP will be published bimonthly (January, March, May, July, September, and November) with a total of 1,300 printed pages. JEGTP may receive a permanent additional boost of 200 pages on 1 July 2008 to equalize the inflow and outflow of papers and to prevent future paper backlog. When implemented, each issue of JEGTP will pack 250 pages of outstanding content. During the past 12 months ending in July 2007, JEGTP published 146 (vs. 105) papers and decreased the backlog from 26 to 18 months. This year, I expect to shrink the backlog to an absolute *minimum*, necessary to maintain a steady supply of papers for each journal issue.

In recent years, several professional societies and private publishers have adopted a rapid publication policy (submission to publication in 6–8 months), using a variety of schemes such as: fast track paper acceptance, rapid journal reviews, and electronic Web publishing. ASME and JEGTP must keep abreast of these changes. Accordingly, and beginning on 1 January 2008, ASME will introduce a novel **e-First**, online paper publication for most of its journals. Now, individual papers will be posted on the journal Web site within four weeks of receiving the authors' page proofs. These papers will be available immediately for citation and downloading and will be published in the next journal issue. Now, the journal statistics covering the period July 2006 through October 2007 (last quarterly issue) follows.

JEGTP published 180 papers with an acceptance rate of 24 percent. The sector mix (given in percent) was: academia (60), industry (28), and government (12) and the paper submission mix (in percent) was: North America (35), Europe (30), China & India (15), and Others (20). A total of 12 associate editors were appointed (one-third each from industry and Europe) and the cumulative paper processing time was decreased to 2 months. (Note: cumulative average time a paper remains on the journal tool awaiting the next action. For comparison, in 2005, the average *draft paper to final manuscript* approval time was 8.7 months, and in 2006 it was 5 months.) Your papers will not remain inactive on the journal tool any longer!

JEGTP covers a wide range of topics in gas turbines, power generation, nuclear engineering, internal combustion engines, and advanced energy systems. The journal has no bias, policy, or printed-page quota for a specific technical area, author affiliation (academia vs. industry), and paper origination (U.S. vs. non-U.S.). JEGTP publishes high-quality papers on a first-come, first-publish basis and the content of each issue is balanced to provide a wide flavor of technical areas. JEGTP is publishing papers on emerging hot topics. For example, JEGTP published a paper on nuclear power in the July 2007 issue and will have 11 or more papers on power engineering (including nuclear power) appear in the first three issues of 2008. JEGTP is a research journal; not a newsmagazine or a trade journal and it will not publish papers with no archival value.

JEGTP secures associate editors from diverse backgrounds, and last year six new outstanding individuals joined. They are: Coal, Biomass, and Alternative Fuels, Kalyan Annamalai (Texas A&M University); Controls, Diagnostics & Instrumentation, Allan Volponi (Pratt & Whitney); Cycle Innovation, Pericles Pilidis, (Cranfield University, U.K.); Electric Power, Ashok Rao (University of California, Irvine); Structures and Dynamics, Patrick Keogh (University of Bath, U.K.); and Advanced Energy Systems, Jayanta Kapat (University of Central Florida). My congratulations to all these individuals for their appointments and work on behalf of the journal. Also, I thank the two outgoing associate editors: Dr. Nagaraj Arakere (University of Florida, Gainesville) and Dr. K. Mark Bryden (Iowa State University, Ames) for their many years of outstanding service to the journal.

Already, the improvements made during 2007 are attracting more journal paper submissions and authors must do their part to secure a quick publication for their papers. Below are three key suggestions.

(1) Check the status of your paper regularly as it progresses through various stages of review to final (digital) manuscript submission, and electronic editing of page proofs. Please contact an associate editor if your paper continues to remain inactive on the journal tool.
(2) Submit a pdf file of your signed 1903 (copyright release) form *electronically* (do not fax) to journalcopyright@asme.org. This is more efficient, and should this form get lost or misplaced, you will have an e-mail record.
(3) Digitize your paper carefully (visit "Author Center" and read the instructions). Poor-quality graphics are unacceptable, and color figures must be checked on your black and white laser printer for adequate contrast before digitizing them. Graphics files must be labeled with Fig. or Figure.

Summarizing; in 2008, it will truly be "A New Beginning" for this journal. JEGTP remains the number one ranked journal in the world in the area of gas turbine engineering and power. Your continued support is needed to keep it there!

Dilip Ballal

Copyright © 2008 by ASME

Downloaded 02 Jun 2010 to 171.66.16.107. Redistribution subject to ASME license or copyright; see http://www.asme.org/terms/Terms_Use.cfm

System-Level Performance Estimation of a Pulse Detonation Based Hybrid Engine

Jeffrey Goldmeer
Venkat Tangirala
Anthony Dean

GE Global Research Center,
1 Research Circle,
Niskayuna, NY 12309

A key application for a Pulse detonation engine concept is envisioned as a hybrid engine, which replaces the combustor in a conventional gas turbine with a pulse detonation combustor (PDC). A limit-cycle model, based on quasi-unsteady computational fluid dynamics simulations, was developed to estimate the performance of a pressure-rise PDC in a hybrid engine to power a subsonic engine core. The parametric space considered for simulations of the PDC operation includes the mechanical compression or the flight conditions that determine the inlet pressure and the inlet temperature conditions, fill fraction, and purge fraction. The PDC cycle process time scales, including the overall operating frequency, were determined via limit-cycle simulations. The methodology for the estimation of the performance of the PDC considers the unsteady effects of PDC operation. These metrics include a ratio of time-averaged exit total pressure to inlet total pressure and a ratio of mass-averaged exit total enthalpy to inlet total enthalpy. This information can be presented as a performance map for the PDC, which was then integrated into a system-level cycle analysis model, using GATECYCLE, to estimate the propulsive performance of the hybrid engine. Three different analyses were performed. The first was a validation of the model against published data for a specific impulse. The second examined the performance of a PDC versus a traditional Brayton cycle for a fixed combustor exit temperature; the results show an increased efficiency of the PDC relative to the Brayton cycle. The third analysis performed was a detailed parametric study of varying engine conditions to examine the performance of the hybrid engine. The analysis has shown that increasing the purge fraction, which can reduce the overall PDC exit temperature, can simultaneously provide small increases in the overall system efficiency. [DOI: 10.1115/1.2771246]

Keywords: pulse detonation engine, pulse detonation combustor, hybrid engine, performance estimate

Introduction

The aviation industry recently celebrated its 100th anniversary of flight. The piston engine powered the first 50 years of aircraft propulsion. The second 50 years of propulsion have been dominated by the gas turbine, which has evolved into a very efficient, durable, versatile, and environmentally friendly power system. A renewed study of detonations and supersonic combustion phenomena in the past decade, however, may be defining the next generation of propulsion technology advancement. Not only is the combustion efficiency greater for a detonation versus the typical constant pressure process; it also contributes to pressure rise, consequent to the completion of detonative combuston in a confined chamber.

The most far-reaching application would be to merge the strengths of current gas turbines with constant volume combustion in a hybrid propulsion system. In the ultimate embodiment of this concept, the entire/partial high-pressure core of a commercial engine may be replaced by a pressure-rise combustion system, as shown in Fig. 1. The interaction of a pulsed detonation combustion (PDC) system and turbine is a matter of considerable complexity. While there is considerable experience in ensuring that the turbomachinery operates very efficiently under steady sate conditions, there is little experience base with regard to the operation of a turbine with unsteady inlet flow conditions in addition to strong wave impingement on the stator and rotor blades of the turbine. The output of the pulse detonation engine (PDE) system is a cycle consisting of fill, detonation, blowdown, purge, and refill. The turbine experiences a wide range of inlet conditions consisting of a very strong pressure pulse, a period of relatively high temperature, and a phase of low temperature and pressure corresponding to purge and refill. Turbomachinery has experienced a very significant evolution in terms of performance for steady-state conditions. Given a specific inlet condition, highly efficient turbine staging can be applied to produce good performance. For the PDE, there will be brief periods when the turbine can operate at these very high efficiencies, but this will need to be counterbalanced with the need to provide acceptable performance during nonoptimal phases of the cycle.

A classical thermodynamic analysis (thermodynamic-state approach or, more precisely, entropy method [1,2]) calculates the performance of an unsteady engine operating in a cycle from entropy increments for each process based on thermodynamic cycle alone. This method is based on the fact that for steady flows, the difference in kinetic energy between the inlet and exit planes is equal to the work done by the medium. Automotive engine cycles have successfully used this thermodynamic-state approach (pressure-volume or temperature-entropy charts) because the energy balance is greatly simplified by neglecting the kinetic energy of the working fluid, and wave dynamic/fluid mechanics considerations are not necessary to calculate the performance metrics (such as thermal efficiency and fuel-specific impulse ($I_{SP,f}$)).

Although the calculation of performance using the entropy method is thermodynamically sound, this analysis is similar to a

Contributed by the International Gas Turbine Institute of ASME for publication in the JOURNAL OF ENGINEERING FOR GAS TURBINES AND POWER. Manuscript received June 21, 2006; final manuscript received May 1, 2007; published online December 26, 2007. Review conducted by Dilip R. Ballal. Paper presented at the ASME Turbo Expo 2006: Land, Sea and Air (GT2006), Barcelona, Spain, May 8–11, 2006, Paper No. GT2006-90786.

Copyright © 2008 by ASME

Downloaded 02 Jun 2010 to 171.66.16.107. Redistribution subject to ASME license or copyright; see http://www.asme.org/terms/Terms_Use.cfm

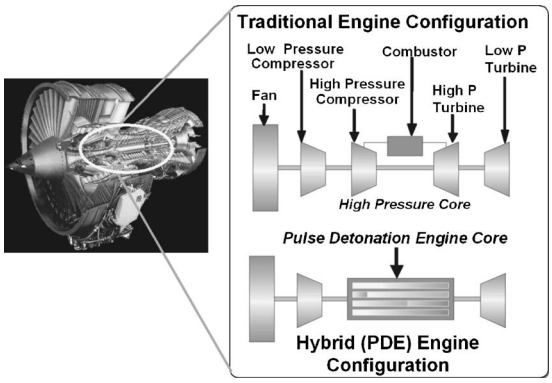

Fig. 1 Schematic of the hybrid PDE concept

steady flow analysis in that it does not involve any time derivatives, time averages, and/or unsteady terms in the balance of mass, momentum, or energy equations. Nevertheless, this approach has been used to calculate the thermodynamic performance of a PDE with the underlying assumption, due to the cyclic nature of the process, that the effect of wave interactions and unsteady flow processes can be neglected or corrected for in the thermodynamic-state representation [1–9]. Even though such analyses provide insights into thermodynamic aspects of the performance, the net effect of neglecting unsteady gas dynamic interactions in an unsteady device, such as PDE, results in large uncertainties in the performance estimates of the pulse detonation devices [3].

Many investigations of PDE performance, using analytical and/or computational methods [10–19], have focused on an ideal tube PDE, which can be described as a constant cross-sectional tube, closed at one end and open at the other end and uniformly filled with quiescent fuel-air mixtures. These investigations include multilevel, multidimensional (zero, 1D, 2D, and 2D axisymmetric) computations with and without chemical kinetics. The fuel-air systems investigated include H_2-air, $C_2H_4-O_2$, and C_2H_4-air. Real gas effects are found to have an impact on PDE cycle performance [7,8]. A recent analytical model was extensively validated for various fuel-oxidizer syatems, initial pressures, and equivalence ratios using single pulse test measurements and was proven to be a valuable tool for thrust estimations within ±15% [13]. For an ideal (single shot) tube PDE completely filled with a stoichiometric hydrogen-air mixture (at initial conditions of a pressure of 101 kPa (1 atm), a temperature of 300 K, and an equivalence ratio (Φ) of 1.0, and assuming adiabatic walls and equilibrium products), convergence of estimations for $I_{SP,f}$ at a value of 4160 s +/−5% has been reported by the computational PDE research community [10–19].

However, there is less agreement on the performance estimates for an air-breathing, hydrocarbon-fueled PDE operating in a periodic cycle because it does not easily lend itself to a classical thermodynamic cycle analysis, typical of steady state, static/in-flight operation of a conventional gas turbine cycle. There exists a need for such simplified fundamental analysis, which not only provides parametric dependence of performance on operating parameters of a PDE but also enables a quick turnaround of a multitude of performance calculations required for screening several preliminary concepts using such a device. As a PDE is essentially a nonsteady flow device, not all molecules of the working medium necessarily undergo identical processes and hence cannot be rigorously represented on a thermodynamic-state (T-s) diagram. A number of performance studies, which estimate the performance of a pure PDE operating in a periodic cycle using unsteady computational fluid dynamics (CFD) methods, were reported recently, and a PDE advantage of 19% in comparison to a ramjet operating up to a Mach number ranging from subsonic-to-supersonic conditions (0.0–3.0) and altitudes ranging from sea level to flight conditions (0–10 km) was demonstrated [20–25].

Paxson [26–28] has demonstrated that the performance of a PDC in a hybrid engine can be characterized by an averaged total pressure ratio (PR) as a unique function of the inlet temperature, the fraction of the time the inlet flow contains a reacting mixture and the stoichiometry of the mixture. A quasi-1D unsteady CFD code was used to obtain a converged limit-cycle simulation of the periodic operation of a PDC. A methodology was developed to generate a performance map and a transfer function, which can be represented on a single plot of total PR versus total enthalpy ratio (HR). Families of such curves covering the entire range of parameters can be reduced to a single transfer function on the performance map. In the present study, a similar transfer function was developed and was compared against the one developed by Paxson [26] for a hybrid engine. The advantage of such a transfer function for the performance estimation is that it can be incorporated into a system-level analysis in order to estimate hybrid engine/turbojet performance for a multitude of flight conditions. Most importantly, such a performance map for the PDC will make possible the estimation of performance using the current steady-state, cycle-deck analysis. The parametric dependence of various interfacing component parameters (interaction of the PDE with the upstream compressor and the downstream turbine components) on the performance estimates can be investigated with little or no computational expense when using the performance map for the PDC, without having to neglect the effect of unsteady fluid dynamical processes on the performance. In addition, the effect of various system-level constraints (such as the maximum allowable turbine inlet temperature, T4, based on material considerations) can be enforced while estimating the performance of the system.

To properly examine the performance of any energy or power generating system, a detailed thermodynamic analysis is required. This can be performed manually from fundamental thermodynamics or by using one of numerous commercial programs. One such program is GATECYCLE, which is a system-level cycle analysis model. GATECYCLE has been used previously for different types of power generation studies, including the use of low-heating value fuels [29], combined heat and power [30], cogeneration power plants [31], and syngas fired plants [32].

The objective of this study is to examine the benefits of a hybrid propulsion system by coupling a transfer function that models PDC performance with a commercially available system-level analysis software. This paper describes the transfer function, the system-level model, the validation of the system-level model, and the hybid engine performance study [33].

Estimation of Pulsed Detonation Combustion Performance

Problem Formulation. A pulse detonation cycle, whether it is utilized as a pressure-rise PDC or as a pure thrust producing PDE, consists of five distinct processes occurring sequentially. The processes and associated time duration are defined as (i) detonation initiation τ_{DI}, (ii) detonation propagation τ_{DP}, (iii) blowdown τ_B, (iv) purge τ_{purge}, and (v) fuel fill $\tau_{fuel\ fill}$. In a valved embodiment of a pulse detonation device (which is considered for all the computations reported here, as shown in Fig. 2(*a*)), the inlet valve separates the unsteady downstream detonation chamber region from the steady upstream inlet segment. The inlet valve is closed during the occurrence of the first of the three cycle processes and opens at the start of the purge process

A sequential schematic of a typical timing diagram of these processes in a cycle is shown in Fig. 2(*b*). A realistic detonation initiation process such as deflagration-to-detonation transition (DDT) in hydrocarbon air mixtures can take up to a few milliseconds ($\tau_{DI}+\tau_{DP}\sim 3-5$ ms) for the detonation wave to exit from the tube. The blowdown time (τ_B) is a function of the length of the

Downloaded 02 Jun 2010 to 171.66.16.107. Redistribution subject to ASME license or copyright; see http://www.asme.org/terms/Terms_Use.cfm

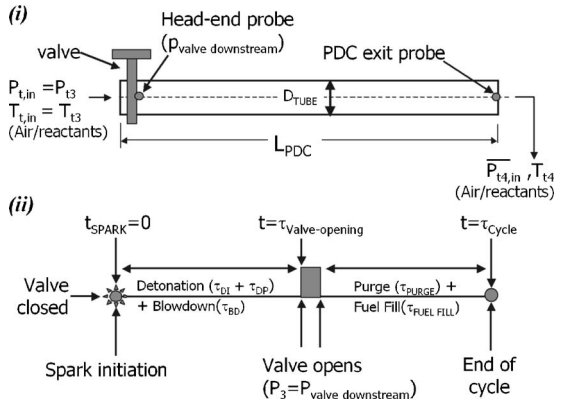

Fig. 2 A schematic of the (*a*) pulse detonation device (PDE/PDC) for performance analysis; (*b*) a representative timing diagram of the pulse detonation cycle (the overbar of a parameter *f* denotes the time average of *f*, and $\langle f \rangle$ denotes the mass)

detonation chamber and flow and mixture properties of the products of detonation. A detonation chamber can be fully purged (for a fully purged tube, only air flows into the detonation tube and is completely filled with air during the purge process) or partially purged (the detonation chamber is partially filled with air and the rest is filled with the hot combustion products from the previous cycle). Purge fraction (pf) is defined as the fraction of time when the purge air is flowing through the valve (τ_p) to the valve open time ($\tau_{VO}=\tau_p+\tau_f$, where τ_f is the fuel fill time). A higher purge fraction increases the overall cycle time and thus diminishes the thrust generated during the cycle. A minimum purge of the detonation chamber is needed to avoid preignition of the fresh reactant charge and achieve reliable and repeating operation of the pulse detonation device. In all the simulations of a repeating pulse detonation cycle reported here, a purge fraction in the range of 0.1–0.2 was specified.

Similarly, the detonation tube can be filled with fuel to its exit ($x/L=1.0$) or a fraction thereof. For specified inlet conditions of the detonation chamber, the fill fraction specifies the amount of fuel in the fuel-air mixture, entering the tube. Fill fraction can be defined as the fraction of the length of the detonation chamber (x/L, where x is the axial location up to which the tube is filled and L is the total length of the tube) filled with fresh fuel-air mixture in each cycle. Test measurements show that the fuel-specific impulse ($I_{sp,f}$) increases with decreasing fill fraction while the thrust generated by the engine decreases [29].

In summary, the parameters that define the problem include (i) inlet total pressure ($P_{t,i}$), (ii) inlet total temperature ($T_{t,in}$) (iii) exit pressure (P_e), (iv) fuel-type (C_mH_n) and equivalence ratio (Φ), (v) purge fraction, (vi) fill fraction, and (vii) detonation chamber geometry (length (L), diameter (D), and any nozzle geometry parameter if inlet/exit nozzles are considered), and they completely specify the limit-cycle problem under study. This problem specification uniquely determines the integral mass, momentum, and energy fluxes crossing the boundaries of the detonation chamber provided the accumulation terms (time dependent terms of governing equations given by Eq. (1) of Tangirala et al. [20,21]), integrated over a cycle time are negligible. In addition, the cycle process times are also determined by meeting the specification of the purge fraction and the fill fraction, which, in turn, fixes the cycle time (τ_{cycle}). However, a very robust limit-cycle algorithm is required to initiate computations from the initial steady-state conditions and to obtain a fully converged limit-cycle solution. A set of five equations (ρ, ρu, ρe, α, and β, where ρ is the density of the mixture, u is the axial velocity, e is the total internal energy, α is the reaction progress variable, and β is a conserved scalar) were solved using an unsteady, quasi-one-dimensional code for up to a finite number of cycles (~25) until limit-cycle convergence criteria were satisfied. A more complete description of the details of the numerical algorithm is presented in Tangirala et al. [20,21].

A brief summary of the strategy to obtain the limit-cycle convergence is given as follows. During the first cycle, a steady-state solution for the nonreacting flow is obtained. The detonation initiation and propagation occur only from second cycle simulation onwards. During each cycle, fuel fill time is determined using a numerical fuel probe at a location in the detonation tube corresponding to the specified fill fraction. If the specified fuel fill fraction is not met, fuel fill time is iterated, which, in turn, changes the purge time as the purge fraction is fixed. This, in turn, affects all the remaining time scales and the overall cycle time. An underrelaxation scheme was required to reduce numerical instabilities, leading to fully converged limit-cycle predictions.

Pulsed Detonation Engine Performance Metrics. Typically, the system-level performance of a turbojet/turbofan is estimated using cycle-deck analysis where thermodynamic states at various positions in the engine are well defined. In this section, the scope of the performance estimation is limited to the estimation of the performance of the PDC. Two assumptions were made in the present PDC analysis: (i) The pressure losses in the PDC are negligible, and the exit static pressure is the same as the inlet static pressure (which is valid for a straight tube PDC without any nozzle extensions); (ii) the total energy content in a given cycle is fixed (the difference between mass-averaged exit total enthalpy and the inlet total enthalpy remains constant in the limit-cycle simulations of the PDC.) Following Paxson [26,27], the performance of the pulse detonation combustor (PDC) is characterized by a performance map in a parametric space of (i) time-averaged total PR (ratio of PDC exit time-averaged total pressure to PDC inlet time-averaged total pressure) and (ii) mass-averaged total HR (ratio of PDC exit mass-averaged total enthalpy to PDC inlet mass-averaged total enthalpy). Thus, the performance over the entire operating envelope of the PDC can be represented on a single plot of total PR versus total HR. Referring to the geometry in Fig. 2(*a*), the time-averaged total PR across the PDC is defined as follows:

$$\mathrm{PR} = \frac{\bar{P}_{t,4}}{\bar{P}_{t,3}} = \frac{\bar{P}_{t,e}}{\bar{P}_{t,i}} = \frac{\int_0^{\tau_{\mathrm{cycle}}} P_{t,4}(t)\,dt}{\bar{P}_{t,i}\tau_{\mathrm{cycle}}} \tag{1}$$

In this equation, the subscripts 3 and 4 denote inlet and exit stations of the PDC. The overbar of pressure P denotes the time average of total pressure P integrated over the cycle time. The mass-averaged total HR across the PDC ($\langle H_t \rangle$ denotes the mass average of total enthalpy H_t integrated over a cycle time) is defined as follows:

$$\mathrm{HR} = \frac{\langle H_{t,4} \rangle}{H_{t,3}} = \frac{1}{H_{t,3}\tau_{\mathrm{cycle}}\dot{m}_e}\int_0^{\tau_{\mathrm{cycle}}} \dot{m}_e(t)H_{t,e}(t)\,dt \tag{2}$$

where

$$\dot{\bar{m}}_i = \dot{\bar{m}}_e = \frac{\int_0^{\tau_{\text{valve open}}} \dot{m}_i(t)\,dt}{\tau_{\text{valve open}}} = \frac{\int_0^{\tau_{\mathrm{cycle}}} \dot{m}_e(t)\,dt}{\tau_{\mathrm{cycle}}} \tag{3}$$

where $\dot{m}_i(t)$ is the instantaneous mass flow rate at the inlet of the tube, $\dot{m}_e(t)$ is the instantaneous mass flow rate at the outlet of the tube, $\dot{\bar{m}}_i$ is the time average of the inlet mass flow rate into the detonation tube, and $\dot{\bar{m}}_e$ is the time average of mass flow rate at the exit of the detonation tube.

The definition for the average total PR differs from the one given by Paxson [26]. The estimated time average of the total PR across a PDC obtained using Eq. (1) is slightly lower than the

Downloaded 02 Jun 2010 to 171.66.16.107. Redistribution subject to ASME license or copyright; see http://www.asme.org/terms/Terms_Use.cfm

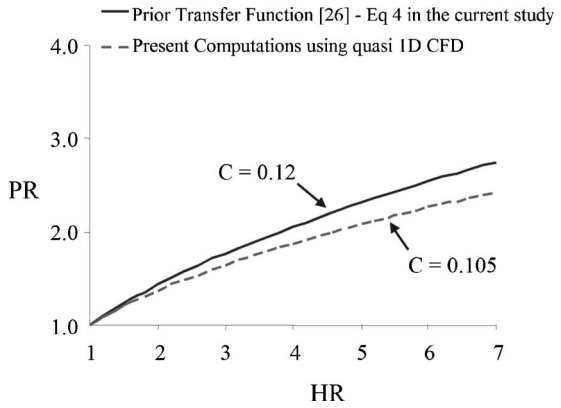

Fig. 3 Transfer functions for the total PR as a function of the total HR across a PDC

value obtained using the total PR defined by Harris et al., for all the cases presented here. The PDC performance map in the parametric space described by Eq. (1) and (2) can be used to estimate the transfer function across the PDC of the hybrid engine. This function is described in more detail in the next section.

Transfer Function for Pulsed Detonation Combustion Performance. The transfer function/curve fit for the performance of a PDC is given by Paxson [26], described as follows:

$$\mathrm{PR} = a\mathrm{HR}^{(C\gamma/\gamma-1)} \tag{4}$$

where

$$\mathrm{HR} = 1 + q_0(\gamma - 1)(1 - \mathrm{pf}) \tag{5}$$

and

$$q_0 = \frac{\Delta H_f}{(1 + \mathrm{AFR})\gamma R_g T_{t,\mathrm{in}}} \tag{6}$$

The purge fraction (pf) is defined as the ratio of the mass of air entering the detonation tube at the inlet during the purge process to the total mass of reactants (air+fuel) entering the detonation tube at the inlet during entire cycle), and AFR is the air-fuel ratio.

Figure 3 shows the transfer function given by Eq. (4), which shows the predicted total pressure rise across the PDC as a function of the total enthalpy increase (amount of chemical energy added to the PDC by the detonation process) across the PDC. Figure 3 also shows a transfer function obtained using the quasi-one-dimensional CFD computations. The predictions for pressure rise across the PDC obtained in the present study are lower by as much as 11% (maximum deviation) when compared to the estimates obtained using Eq. (4). A best curve fit of the predicted transfer function was obtained in the present study for a smaller value of $C=0.105$. The difference in the predicted transfer function is attributed to the differences in the modeling assumptions with regard to mixture properties. A constant value of $\gamma=1.3$ was used by Paxson [26], whereas a 3γ model—which more accurately captures the mixture properties (air, reactants, and burnt products)—is used in the present study. The transfer function given by Eq. (4) with a value for C of 0.105 was used in obtaining system-level performance estimations, which are presented in the following sections.

System-Level Performance Model

The system-level performance model was created in GATECYCLE, which is a commercially available PC-based program used for the design and evaluation of power generation cycles and power plants. GATECYCLE combines a graphical user interface with detailed analytical models for the thermodynamic, heat-transfer, and fluid-mechanical processes within power plants. This allows users to run design and simulation studies of any complexity. As this is a steady-state code, models run until the system reaches convergence, which typically takes 2–40 system iterations, depending on the complexity of the cycle being modeled, the convergence tolerances selected, the number and complexity of macros, and the accuracy of the initial values in the database [29]. In this model, the convergence criteria were set at 0.0001; the model will continue to iterate until the results from the last two iteration are within this relative tolerance.

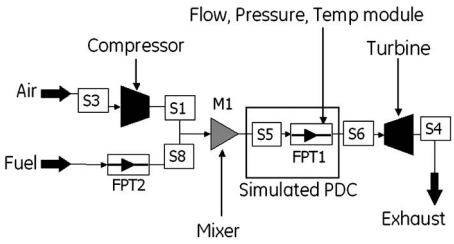

Fig. 4 Schematic of the validation model

There are four major steps in building and running a simulation model within GATECYCLE: build the model, enter any required data, run the simulation, and review the results. Once a model is built and the required inputs have been entered, dozens of simulations can be run in a few minutes. Each time a model is simulated, a sequential modular algorithm solves the energy and mass balances for the overall system as well as for each individual component, i.e., compressor, turbine, etc.

The ability to perform parametric studies of inputs and conditions can be set up using CYCLELINK, which is utility based inside GATECYCLE and allows the user full access to data within GATECYCLE from an Excel spreadsheet. CYCLELINK can be used to read any GATECYCLE data into a spreadsheet and customize your output or perform additional analysis on the output through linking the data to other cells in your spreadsheet. More importantly, CYCLELINK can be used for running case studies of GATECYCLE models. In a typical case, data input on the CYCLELINK spreadsheet is written to GATECYCLE, GATECYCLE runs, and the new output is brought into the spreadsheet.

One of the critical elements is the ability of GATECYCLE to determine the power output and efficiency of the system being evaluated. This requires the power input or output of any component in the system device to be computed and tabulated. In the case of any compressor or turbine, the system uses the isentropic efficiency as well as information on the inlet or outlet boundary conditions to determine the work done or power generated by the component and the net power generated. In order to use this tool to effectively gauge the performance of a hybrid propulsion system, a series of validation cases was examined. Theses cases and the results are presented in the next section.

Performance Model Validation

A system-level model used for the validation of the performance estimation of a pulse detonation turbine engine is presented in this section. A schematic of the GATECYCLE model is shown in Fig. 4. The model includes the following elements: compressor (C1), PDC, and a turbine or expander (EX1). The model simulates the following processes: Air enters the system and is compressed (stream S3); the air exiting the compressor (S1) enters the PDC and is mixed with fuel (M1). The fuel-air mixture then detonates and flows into the turbine via stream S6. The efficiency of the compressor is set at 90%, and the turbine is assumed to have perfect isentropic expansion.

The detonation process is modeled using a GATECYCLE element known as a flow-temperature-pressure modifier (FTPMod), as shown in Fig. 4. The module allows for increases or decreases in the flow, pressure, and energy of the flow. To simulate the pressure

Downloaded 02 Jun 2010 to 171.66.16.107. Redistribution subject to ASME license or copyright; see http://www.asme.org/terms/Terms_Use.cfm

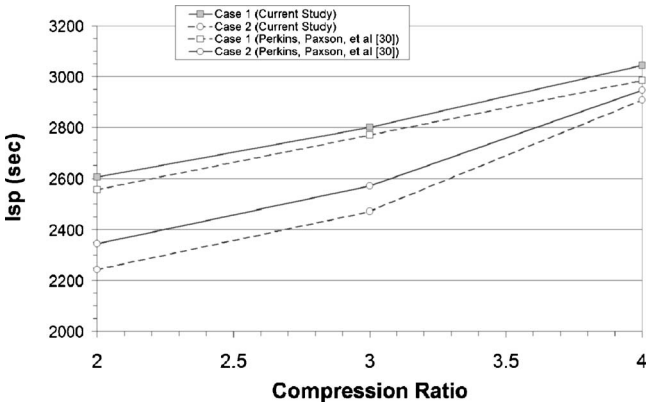

Fig. 5 Comparison of I_{sp} data for current model versus Perkins et al. [33]

increase effect of a detonation reaction, this element is used to show a fractional pressure increase in the flow, as well as an enthalpy increase due to the exothermic combustion reaction. Specifically, the transfer functions described by Eqs. (4) and (5) were included in the CYCLELINK spreadsheet and generated the PR and HR functions that determined the pressure and enthalpy rise across the FTPMod.

This model was run at a series of conditions to compare with the results published by Perkins et al. [33], in which three different hybrid gas turbines were modeled at two different conditions: Case 1, H3=474.92 kJ/kg, P3=342.6 kPa (49.7 psi (absolute)), Φ=0.498; Case 2, H3=466.55 kJ/kg, P3=355.7 kPa (51.6 psi (absolute)), Φ=0.629. The exhaust backpressure was also set to the same values as used in the reference study: Case 1, 33.9 kPa (4.92 psi (absolute)); Case 2, 30.7 kPa (4.46 psi (absolute)). The enthalpy was used to track the exact energy flows in the system. The main difference between the three configurations was the overall pressure ratio (OPR), which was set to 2, 3, and 4. The GATECYCLE model was setup to match these conditions at the combustor inlet as well as the compressor inlet conditions. Given a fixed airflow, the fuel flow was then selected to match the equivalence ratio (Φ), given the stoichiometric fuel-air ratio (FAR). The air-to-fuel ratio (AFR), which is used to determine the heat release (see Eq. (6), is also computed.

Once the inputs are set and the model is run to convergence, it returns a series of output parameters, including the power generated. The system-level efficiency is then computed as the ratio of the power generated to the energy content of the fuel in the system based on the lower heating value (LHV) and the fuel flow rate,

$$\eta_{\text{th}} = \frac{\text{Power generated}}{\dot{m}_F \text{LHV}} \tag{7}$$

The specific thrust (T_{sp}), the specific fuel consumption (S), and the specific impulse (I_{sp}) are then computed by the method described by Heiser and Pratt [2],

$$T_{\text{sp}} = \frac{1}{g_C}\sqrt{V_0^2 + 2\eta q_{\text{supp}}} - V_0 \tag{8}$$

$$S = \frac{\text{FAR}}{T_{\text{sp}}} \tag{9}$$

$$I_{\text{sp}} = \frac{g_C}{g_0 S} \tag{10}$$

Using the velocities in the reference with the computed thermal efficiency, the specific impulse of the system can be determined.

Table 1 Comparison of fuel specific impulse (s) data

Case No.	1	1	1	2	2	2
Hybrid No.	1	2	3	1	2	3
CR	2	3	4	2	3	4
Current study	2604	2800	3044	2241	2471	2909
Perkins and Paxson	2555	2770	2985	2344	2571	2947
% difference	−1.9%	−1.1%	−2.0%	4.4%	3.9%	1.3%

Performance Model Validation Results. The specific impulse results from the new calculation are compared to the results from the quasi-one-dimensional CFD code published by Perkins et al. [33], as shown in Fig. 5 and in Table 1. The current model is within 4.5% of the Perkins et al. [30] CFD results for both cases and for all three configurations, validating the current approach of using a transfer function to model the PDC performance linked with a steady-state system-level design and analysis program.

Brayton Cycle Comparison

In addition to the model validation, a simple case was performed to examine the differences between a classic Brayton cycle and a modified Brayton cycle, with a PDC instead of a deflagration-based combustor. The GATECYCLE model consisted of a compressor (C1), a combustor (or PDC), and a turbine (EX1), as shown in Fig 6. For this set of comparisons, the fuel was set as natural gas with a LHV of 4.9×10^7 J/kg (21,515 Btu/lb m). The compressor and turbine efficiencies were set at 88% and 90%, respectively. The ambient conditions were set at 101.3 kPa (14.7 psi (absolute)) and 288.7 K (60°F). In this model, the combustor (and PDC) exit temperature was kept conatant at 811 K (1000°F). In the model, the compression ratio (CR) across the compressor was varied from 1.5 to 10. The equivalence ratio (Φ) was varied to achieve the fixed combustor exit temperature of 811 K. (One of the critical impacts of fixed combustor exit temperature is that as the CR increases, T3 increases, so less fuel was required to attain the fixed T4 condition.) In the base line case, the FPT module was not active in the model; there was no pressure rise in the combustor. In the case of the PDC simulation, the PPTmod (FPT1) was used to simulate the pressure rise from a PDC.

One of the critical results of the model is the understanding that as the CR, defined as the pressure rise across C1, was increased, the amount of fuel required to achieve the desired T4 (811 K) decresed. Thus, the max Φ is equivalent to the lower CR, as shown in Fig. 7. This link between CR and Φ plays an important role on the overall efficiency of the system.

The results shown in Fig. 7 show that the power generated by the Brayton cycle increases as the equivalnce ratio increases until it peaks at an approximate equivalence ratio of 0.14. The results also illustrate that the PDC-based cycle generates more power and has a higher efficiency than the Braton cycle at any equivalence ratio. This occurs because only T4 was fixed, but since the PDC increases both the combustor exit temperature and pressure, there is a higher turbine inlet pressure for the same equivalence ratio.

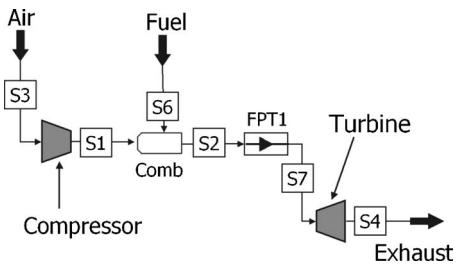

Fig. 6 Schematic of the hybrid Brayton/PDC cycle model

Downloaded 02 Jun 2010 to 171.66.16.107. Redistribution subject to ASME license or copyright; see http://www.asme.org/terms/Terms_Use.cfm

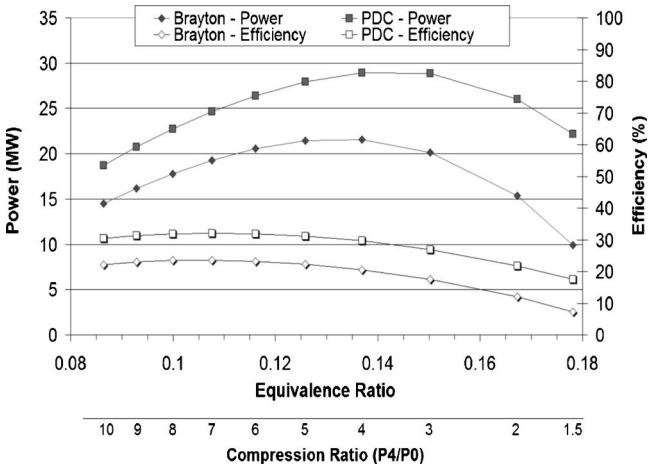

Fig. 7 Comparison of Brayton and PDC/Brayton cycle results

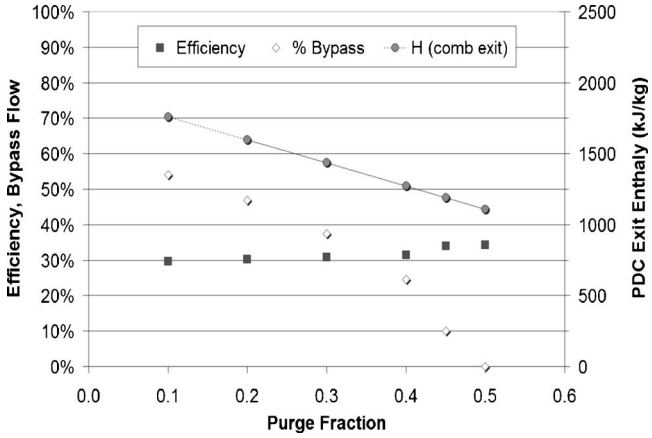

Fig. 9 Effect of purge fraction on the system performance

The figure also illustrates that increasing the compressure ratio initially increases the power and efficiency of the system, but that there is a limit to the positive effect; as the CR is increased beyond 4, the power output begins to drop and the efficiency effectively stays constant.

System-Level Performance Model

With a validated approach, a GATECYCLE model was created for evaluating a hybrid PDC-based propulsion engine cycle, as shown in Fig. 8. The model includes the following elements: fan (C2), compressor (C1), bypass loop and compressor (C3), PDC, and turbine (EX1). The model simulates the following processes: Ambient air enters the fan and is compressed. The air then enters the compressor and is further compressed to the combustor inlet (P3, H3) conditions. The air is then split at SP1 into main and bypass flows. The main flow enters the PDC and is mixed with fuel. The fuel-air mixture then detonates and is mixed with the bypass flow at M2. The combined gas then flows into the turbine. The bypass flow is used to limit the turbine inlet temperature; the pressure of this flow is boosted to match the combustor exit pressure, enabling the two flows to be mixed upstream of the turbine. The isentropic efficiency of the fan, compressor, and turbine is set to 90%.

The model is linked to a CYCLELINK Excel spreadsheet to provide inputs and outputs and to postprocess the data. The sheet includes a section for model inputs and model outputs. Using this tool, the fan outlet temperature and pressure, as well as the CR across the compressor, are model inputs set in the spreadsheet. The isentropic efficiencies of the compressors and turbine are also set as input via the spreadsheet. The airflow rate is set as a model input and the fuel flow rate is set to match an inputted FAR. The percent are bypass flow can be fixed or allowed to vary to fix the turbine inlet temperature, also known as T4. Varying the bypass to keep the turbine inlet temperature (and enthalpy) constant was accomplished using the macrofeature in GATECYCLE. The macrofeature varies the percentage of bypass flow until the enthalpy at the turbine inlet matches the desired enthalpy. The PR and HR ratios across PDC are set using the transfer functions described previously in the paper. Finally, the turbine outlet pressure is set to match the ambient pressure at the specified altitude.

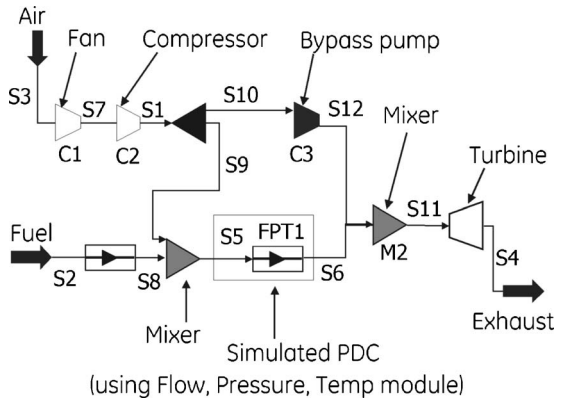

Fig. 8 Schematic of the hybrid PDC engine

The thermal efficiency of the system is determined by taking the ratio of the net energy output of the system, as determined by GATECYCLE, and the theoretical energy capability of the fuel, which is characterized by the fuel's LHV. The net energy includes the work input for the fan and compressors as well as the work extracted by the turbine.

System-Level Model Results. A series of computations were performed to examine the effects of CR, purge fraction, and turbine inlet temperature. In the first set of simulations, the turbine inlet temperature (1588 K and 1811 K) and purge fraction (0.2) were fixed, while the CR on the compressor was allowed to vary from 2 to 14. Based on an altitude of 7620 m (25,000 ft) with an ambient pressure of 37 kPa (5.4 psi (absolute)), the CR range represents an overall CR range of 8.3 to 57.9. The results, shown in Fig. 9, show the effect of purge fraction on the system and purge fraction is the portion of the PDC cycle, in which hot combustion products are exhausted out of the combustor, but during which no actual combustion occurs. As the purge fraction is increased, the PDC enthalpy decreases, so the effective PDC exit temperature decreases. This then decreases the amount of bypass flow required, which reduces the amount of air that must be pumped to the turbine inlet temperature. This has the overall effect of increasing the system efficiency.

In a second set of simulations, the compressor temperature ratio was varied. This is equivalent to an increase in the CR. The results, shown in Fig. 10, show that as the compressor temperature increases, the amount of bypass flow increases. The increased work required to pump the additional bypass flow to keep the turbine inlet temperature constant reduces the overall

Conclusions

In this paper, a transfer function model was integrated into a thermodynamics system development and analysis tool to examine the performance of a hybrid PDC system. The model was validated against published data in the literature and then com-

Downloaded 02 Jun 2010 to 171.66.16.107. Redistribution subject to ASME license or copyright; see http://www.asme.org/terms/Terms_Use.cfm

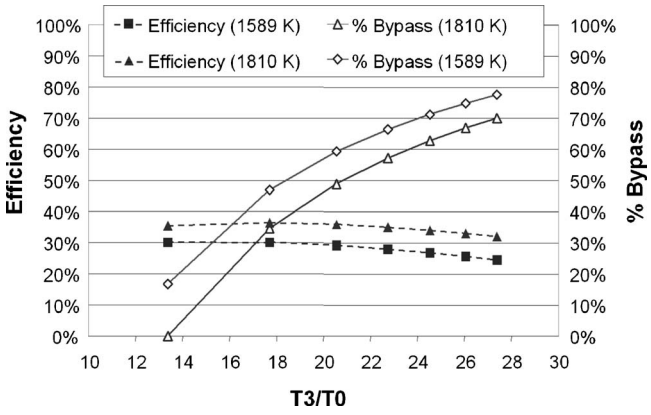

Fig. 10 Effect of temperature rise on system performance

pared against a classic Brayton cycle. The final step in the paper was to use the model to examine the performance of a hybrid PDC engine.

As shown, the model has shown that there are multiple new parameters in hybrid engine design that must be taken into account to correctly determine overall system efficiencies. Specifically, the effect and interaction of purge and bypass flows on the total system performance must be taken into account. If the cooling needs of the system could be solved without needing an additional bypass, this could create additional performance gains.

In the future, this same approach could be applied to stationary power generation. Using the same transfer functions and the same system-level model, the performance of a hybrid power generation cycle could be examined and compared to a traditional gas turbine performance.

Nomenclature

a = constant in Eq. (4)
D_{tube} = diametetr of PDC tube (m)
g_c = gravitational constant (1 kg m/N s^2)
g^0 = standard acceleration of gravity (9.81 m/s^2)
H = enthalpy (J)
HR = mass-averaged total enthalpy ratio
ΔH_f = heat of formation (J/kg of fuel)
L = length of PDC tube (m)
LHV = lower heating value (J/kg)
$\dot{m}$ = mass flow (kg/s)
pf = purge fraction of PDC cycle
P = pressure (Pa)
PR = mass-averaged total pressure ratio
q_0 = heat added (kJ/kg)
q_{supp} = total chemical energy of the fuel (kJ/kg)
R_g = gas constant (Pa m^3/kg K)
T_{sp} = specific thrust
T = temperature (K)
T = time (s)
S = specific fuel consumption (kg/N s)
I_{sp} = specific impulse (s)
V = velocity (m/s)
γ = ratio of specific heats
η = thermal efficiency
Φ = equivalence ratio
Ψ = temperature ratio
τ = time scale (s)

Subscripts

0 = ambient conditions
3 = combustor inlet plane
4 = turbine inlet plane
B = blowdown
cycle = cycle time
DI = detonation initiation
DP = detonation propagation
e = exit plane conditions
f = fuel
i = inlet plane conditions
t = time

References

[1] Foa, J. V., 1960, *Elements of Flight Propulsion*, Wiley, New York.
[2] Heiser, W. H., and Pratt, D. T., 2002, "Thermodynamic Cycle Analysis of Pulse Detonation Engines," J. Propul. Power, **18**(1), pp. 68–76.
[3] Wintenberger, E., Austin, J. M., Cooper, M., Jackson, S., and Shepherd, J. E., 2004, "Reply to Comment on Analytical Method for the Impulse of Single-Cycle Pulse Detonation Tube, D. T. Pratt," J. Propul. Power, **20**(1), pp. 189–191.
[4] Kentfield, J. A. C., 2002, "Thermodynamics of Airbreathing Pulse-Detonation Engines," J. Propul. Power, **18**(6), pp. 1075–1080.
[5] Kentfield, J. A. C., 2002, "The Idealized Performances of Pulse-Detonation Engines From an Overall Performance View Point," *38th AIAA/ASME/SAE/ASEE Joint Propulsion Conference, Indianapolis, July*, AIAA Paper Nos. 2002–3914 and 2002–3629.
[6] Hutchins, T. E., and Metghalchi, M., 2003, "Energy and Exergy Analyses of the Pulse Detonation Engine," ASME J. Eng. Gas Turbines Power, **125**, pp. 1075–1080.
[7] Povinelli, L. A., 2001, "Impact of Dissociation and Sensible Heat Release on Pulse Detonation and Gas Turbine Engine Performance," *15th International Symposium on Airbreathing Engines, Bangalore, India*, ISABE Paper No. 2001-1212.
[8] Povinelli, L. A., 2002, "Thermodynamic Cycle and CFD Analyses for Hydrogen Fueled Air-Breathing Pulse Detonation Engines," *38th AIAA/ASME/SAE/ASEE Joint Propulsion Conference, Indianapolis, July*, AIAA Paper No. 2002-3629.
[9] Dyer, R. S., and Kaemming, T. A., 2002, "The Thermodynamic Basis of Pulsed Detonation Engine Thrust Production," *38th AIAA/ASME/SAE/ASEE Joint Propulsion Conference, Indianapolis, July*, AIAA Paper No. 2002-4072.
[10] Zitoun, R., and Desbordes, D., 1999, "Propulsive Performance of Pulsed Detonations," Combust. Sci. Technol., **144**, pp. 93–114.
[11] Endo, T., and Fujiwara, T., 2002, "A Simplified Analysis on a Pulse Detonation Engine," Trans. Jpn. Soc. Aeronaut. Space Sci. **44**(146), pp. 217–222.
[12] Talley, D., and Coy, E., 2000, "The Constant Volume Limit of Pulsed Propulsion for a Constant γ Ideal Gas," *36th AIAA/ASME/SAE/ASEE Joint Propulsion Conference, Huntsville*, AIAA Paper No. 2000–3216.
[13] Wintenberger, E., Austin, J. M., Cooper, M., Jackson, S., and Shepherd, J. E., 2003, "Analytical Model for the Impulse of Single-Cycle Pulse Detonation Tube," J. Propul. Power **20**(4), pp. 765–767.
[14] Tangirala, V. E., Varatharajan, B., and Dean, A. J., 2003, "Numerical Simulations of Detonation Initiation," *41st Aerospace Sciences Meeting, Reno, NV*, AIAA Paper No. 2003–0716.
[15] Tangirala, V. E., Dean, A. J., Rasheed, A., and Chapin, D. M., 2003, "Performance Estimations of a Pulse Detonation Engine," *XVI ISOABE, Cleveland, September*, ISOABE Paper No. 2003–1215.
[16] Tangirala, V. E., Dean, A. J., Pinard, P. F., and Chapin, D. M., 2007, "Pulsed Detonation Engine Processes: Experiments And Simulations," Trans. Jpn. Soc. Aeronaut. Space Sci. vol. **176**, pp. 1779–1808.
[17] Yungster, S., 2005, "Analysis of Nozzle Effects on Pulse Detonation Engine Performance," *41st Aerospace Sciences Meeting and Exhibit, Reno*, AIAA Paper No. 2003–1316.
[18] Ebrahimi, H. B., Mohanraj, R., and Merkle, C. L., 2000, "Multi-Level Analysis of Pulsed Detonation Engines," *36th AIAA/ASME/SAE/ASEE Joint Propulsion Conference, Huntsville*, AIAA Paper No. 2000–3589.
[19] Mohanraj, R., and Merkle, C. L., 2000, "A Numerical Study of Pulse Detonation Engine Performance," *38th Aerospace Sciences Meeting, Reno*, AIAA Paper No. 2000–0325.
[20] Tangirala, V. E., Murrow, K., Fakunle, O., and Dean, A. J., 2005, "Thermodynamic and Unsteady Flow Considerations in Performance Estimation for Pulse Detonation Applications," *43rd Aerospace Sciences Meeting, Reno, NN*, AIAA Paper No. 2005–0226.
[21] Tangirala, V. E., Dean, A. J., and Harris, P., 2005, "Unsteady Flow Considerations in Performance Estimation for Pulse Detonation Applications," *19th International Symposium on Air-breathing Engines, Munich, Germany*, ISABE Paper No. 2005–1048.
[22] Harris, P. G., Guzik, S., Farinaccio, R., Stowe, R. A., Whitehouse, D., Josey, T., Hawkin, D., Ripley, R., Link, R., Higgins, A. J., and Thibault, P. A., 2002, "Comparative Evaluation of Performance Models of Pulse Detonation Engines," *38th AIAA/ASME/SAE/ASEE Joint Propulsion Conference, Indianapolis*, AIAA Paper No. 2002–3912.
[23] Harris, P. G., Guzik, S. M., and Stowe, R. S., 2004, "Design Methodology for a Pulse Detonation Engine as a Ramjet Replacement," *40th AIAA/ASME/SAE/ASEE Joint Propulsion Conference, Fort Lauderdale*, AIAA Paper No. 2004–3400.
[24] Harris, P. G., Ripley, R. C., and Guzik, S. M., 2004, "Single-Tube Two-

Downloaded 02 Jun 2010 to 171.66.16.107. Redistribution subject to ASME license or copyright; see http://www.asme.org/terms/Terms_Use.cfm

Dimensional Evaluation of a Pulse Detonation Engine as a Ramjet Replacement," *40th AIAA/ASME/SAE/ASEE Joint Propulsion Conference, Fort Lauderdale*, AIAA Paper No. 2004–3744.
[25] Ripley, R. C., Harris, P. G., and Farinaccio, R., 2004, "Multi-Tube Two-Dimensional Evaluation of a Pulse Detonation Engine as a Ramjet Replacement," *40th AIAA/ASME/SAE/ASEE Joint Propulsion Conference, Fort Lauderdale*, AIAA Paper No. 2004–3745.
[26] Paxson, D. E., 1992, "A General Numerical Model for Wave Rotor Analysis," NASA Report No. TM-105740.
[27] Paxson, D. E., 2004, "Performance Evaluation Method for Ideal Air Breathing Pulse Detonation Engines," J. Propul. Power **20**(5), pp. 945–947.
[28] Paxson, D. E., 2003, "Optimal Area Profiles for Ideal Single Nozzle Air-Breathing Pulse Detonation Engines," *39th AIAA/ASME/SAE/ASEE Joint Propulsion Conference, Huntsville*, AIAA Paper No. 2003–4512.
[29] Palmer, C. A., Erbes, M. R., and Pechtel, P. A., 1993, "Gatecycle Performance Analysis of the LM2500 Gas Turbine Utilizing Low Heating Value Fuels," *Proceedings of the seventh Congress and Exposition on Gas Turbines in Cogeneration and Utility Industrial and Independent Power Generation*, Sept. 21–23, Bournemouth, England.
[30] Marbe, A., and Harvey, S. S., 2005, "The Role of Policy Instruments for Promoting Combined Heat and Power Production With Low CO_2 Emissions in District Heating Systems," Int. J. Energy Res. **29**(6), pp. 511–537.
[31] Karvountzi, G. C., Cilfford, M., and Duby, P. F., 2004, "Effect of Fuel Cell Operation Pressure on the Optimization of A Hybrid System SOFC/Turbine for Cogeneration," *2nd International Conference on Fuel Cells Science, Engineering and Technology*, Rochester, NY, pp. 625–631.
[32] Brusca, S., and Lanzafame, R., 2003, "Analysis of Syngas Fed Gas Turbine Performance Depending on Ambient Conditions" American Society of Mechanical Engineers, International Gas Turbine Institute, Proceeding of ASME Turbo Expo, vol. 1, pp. 943–948.
[33] Perkins, H., Paxson, D., Povinelli, L., Petters, D., Thomas, S., Fittje, J., and Dyer, R., 2005, "An Assessment of Pulse Detonation Engine Performance Estimation Methods Based on Experimental Results," *41st AIAA Joint Propulsion Conference, Tuscon, AZ, July*, AIAA Paper No. 2005–3831.

Downloaded 02 Jun 2010 to 171.66.16.107. Redistribution subject to ASME license or copyright; see http://www.asme.org/terms/Terms_Use.cfm

Fundamental Mechanism of Entropy Noise in Aero-Engines: Experimental Investigation

Friedrich Bake
e-mail: friedrich.bake@dlr.de

Nancy Kings

Ingo Roehle

Department of Engine Acoustics,
Institute of Propulsion Technology,
German Aerospace Center (DLR),
Mueller-Breslau-Strasse 8,
10623 Berlin, Germany

Entropy noise caused by combustors increases rapidly with rising Mach number in the nozzle downstream of the combustion chamber. This is experimentally shown with a dedicated test facility, in which entropy waves are generated in a controlled way by unsteady electrical heating of fine platinum wires immersed in the flow. Downstream of the heating module called entropy wave generator (EWG), the pipe flow is accelerated through a convergent-divergent nozzle with a maximum Mach number of 1.2 downstream of the nozzle throat. Parameters like mass flux of the flow, nozzle Mach number, amount of heating energy, excitation mode (periodic, pulsed, or continuously), and propagation length between EWG and nozzle have been varied for the analysis of the generated entropy noise. The results are compared with the results of a one-dimensional theory found in early literature. [DOI: 10.1115/1.2749286]

Introduction

The total noise emitted by a combustion chamber consists of direct and indirect combustion noise [1]. Only the direct combustion noise is related to the combustion process. Indirect combustion noise, also called entropy noise, is related to the acceleration of gas temperature nonuniformities caused by the unsteady combustion processes (see also [2–4]). Since the nozzle guide vane of the first turbine stage is choked under almost every relevant operation condition of aero-engines, hot spots passing through the nozzle are connected with mass flow variations (monopole sound source) and also with momentum flux variations (dipole sound source). Gas temperature nonuniformities may also be the cause for broadband noise of all turbine stages, since the related density fluctuations cause pressure fluctuations on the blade and vane surfaces of each turbine stage.

Entropy noise receives increased interest by the aero-engine industry because it may have a major contribution to the total noise emission of combustion systems. With the noise reducing improvements achieved on other aero-engine components like, e.g., low noise fan design and jet noise reduction by high bypass ratios, the noise concern in aero-engine developments also includes the combustion noise issue. Especially at helicopter engines, which do almost emit no jet noise, the entropy noise seems to be of high importance.

In a review work concerning the different combustion noise sources, Strahle [5] concluded that the impact and importance of entropy noise is still controversial in the literature, which is mainly caused by the lack of comprehensive experimental investigations in this area. This deficiency of experimental entropy noise research holds, even up to now. One of the main challenges in experimentally investigating entropy noise is the separation of direct and indirect combustion noise. Muthukrishnan, Strahle, and Neale [6,7] separated direct noise sources and entropy noise in a combustor rig via coherence analysis. A comparison of sound power prediction methods including a certain modeling of entropy noise with real engine noise data (for, e.g., a Pratt and Whitney JT8D-9) by Cumpsty and Marble [8,9] and Cumpsty [10] in the late 1970s revealed a quite significant contribution of entropy noise to the total engine noise. An experimental approach with generating entropy waves by electrical heaters similar to the test rig presented here, was done by Bohn [11] and Zukoski and Auerbach [12] in the 1970s. However, the used experimental setup generated only a very low temperature modulation ($\approx$1 K) with little parameter variations and the data acquisition and processing system did not allow a high-resolution quantitative signal analysis in the time domain.

Therefore, the generation mechanisms and parameter dependencies of entropy noise are still not completely explained so far. Hence, this work within the framework of a DFG research unit on combustion noise (http://www.combustion-noise.de) presents an investigation of entropy noise phenomena on a reference test rig called entropy wave generator (EWG).

Experimental Setup

The EWG is basically an accelerated tube flow with the capability of inducing entropy waves via a heating module. The idea of this setup is to optimize and test detection methods for entropy noise and to study the parameter dependencies of the entropy noise generation mechanism. Furthermore, it allows us to validate numerical (computational fluid dynamics (CFD) and computational aeroacoustics (CAA)) studies and to confirm theoretical considerations.

A sketch of the design is shown in Fig. 1. The flow, which is supplied by a compressed air system, is calmed in a settling chamber with a honeycomb flow straightener before it enters the tube section via a bell-mouth intake. The inner diameter of the tube is 30 mm. The heating module consists of six ring sections with ten platinum wires stretched across each section. The wires have a diameter of 25 μm and a total length of about 1.2 m. In the current setup, the wires can be heated with an electrical power up to 200 W. The length of the heating module in the streamwise direction amounts to 48 mm. The tube section following the heating module is exchangeable so that three different lengths, 50, 100, and 200 mm between heating module and nozzle throat, as shown in Fig. 1, can be tested. Further downstream, the flow is accelerated through the convergent part of a convergent-divergent nozzle and then decelerated in the subsonic divergent diffuser part of the nozzle. The following 1020 mm long tube section has a diameter of 40 mm and is equipped with wall-flush mounted microphones at different axial positions for acoustic analysis. The flow leaves the test rig through an anechoic termination in order to minimize acoustic reflections into the measurement section. The maximum

Contributed by the International Gas Turbine Institute of ASME for publication in the JOURNAL OF ENGINEERING FOR GAS TURBINES AND POWER. Manuscript received May 4, 2007; final manuscript received May 7, 2007; published online January 9, 2008. Review conducted by Dilip R. Ballal. Paper presented at the ASME Turbo Expo 2007: Land, Sea and Air (GT2007), Montreal, Quebec, Canada, May 14–17, 2007. Paper No. GT2007-27300.

Copyright © 2008 by ASME

Downloaded 02 Jun 2010 to 171.66.16.107. Redistribution subject to ASME license or copyright; see http://www.asme.org/terms/Terms_Use.cfm

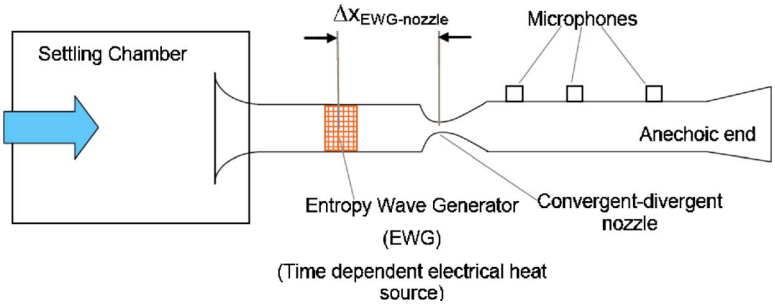

Fig. 1 Sketch of the entropy wave generator (EWG); Tube section $\Delta X_{EWG\text{-}nozzle}$ is variable, corresponding to different propagation lengths of entropy waves

mass flux is limited by the air supply to 18 g/s and the maximum Mach number in the nozzle throat amounts to Ma=1 at a mass flux of about 11 g/s and a nozzle diameter of 7.5 mm. In order to obtain information about convecting temperature fluctuations or so called entropy waves, bare wire thermocouples with a diameter of 25 μm are installed between the heating module and the nozzle. A photo of the entropy wave generator is displayed in Fig. 2.

Since the boundary conditions of this model test rig are well-defined, this setup is ideally suited for numerical simulations. Therefore, two other research groups of the Combustion Noise Initiative, funded by the German Research Foundation (DFG), are conducting numerical studies (CFD and CAA) on the generation and propagation of entropy noise, using the model test rig setup and analog parameter variations. The results of their work were published at the ASME Turbo Expo 2007 in paper No. GT2007-27173 [13].

Theoretical Aspects

One of the first analytical considerations of sound generation by accelerated or decelerated entropy waves was published in 1973 by Morfey [3]. This work was an extension of the Lighthill theory [14] for jet noise with the so called "excess jet noise" produced by density inhomogeneities in jets like, for example, in aero-engines. Following this analytical estimation by Morfey, the "excess jet noise" is scaling with the sixth power of the jet velocity. This extension of the Lighthill theory was further developed by Howe [15], describing the noise generation mechanisms in inhomogeneous and non-isentropic flows using an acoustic wave operator.

In 1975, Ffowcs Williams and Howe [16] formulated an analytical expression for the sound generation and propagation of entropy inhomogeneities called slugs or pellets convecting through a nozzle. Using the Green function, this formulation of Ffowcs Williams and Howe described the in-duct, as well as the free field radiation of entropy induced sound in the time domain, but it was restricted to low Mach number flows.

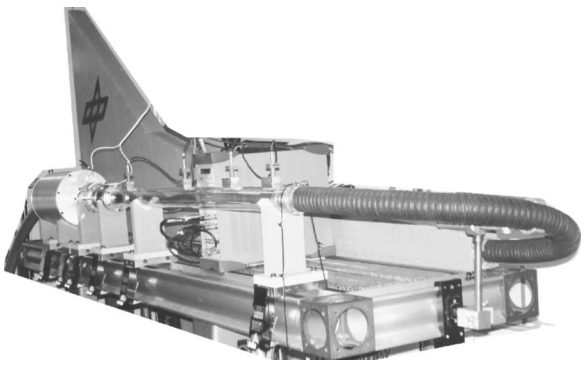

Fig. 2 Photo of the entropy wave generator (EWG)

The generation mechanism of entropy noise in one-dimensional nozzle flows is characterized by Marble and Candel [4] for compact nozzles with subsonic and supersonic flow and supersonic flow with normal shocks. Here the compactness of the nozzle stands for a very small length of the nozzle, in comparison to the wavelengths of the corresponding entropy and sound pressure waves. Marble and Candel derived expressions for the up- and downstream propagating acoustic pressure perturbations generated by both impinging entropy disturbances and impinging acoustic pressure waves. Therefore, these expressions result in the following three quasi-transfer functions for either nozzle or diffuser configurations with subcritical mean flow conditions (see also [17]):

- For a sound pressure wave caused by entropy fluctuations:

$$p'_{2+} = \frac{M_2 - M_1}{1 + M_2} \frac{\frac{1}{2} M_1}{1 + \frac{1}{2}(\kappa - 1) M_1 M_2} a_1^2 \mathrm{A} \varrho'_s \tag{1}$$

- For the transmission of an entropy wave:

$$\varrho'_{s2} = \left(\frac{1 + \frac{\kappa - 1}{\kappa} M_1^2}{1 + \frac{\kappa - 1}{\kappa} M_2^2} \right)^{\frac{1}{\kappa - 1}} \varrho'_s \tag{2}$$

- For the transmission of an acoustic pressure wave:

$$T = \frac{p'_{2+}}{p'_{1+}} = \frac{1 + M_1}{M_1 + M_2} \frac{2M_2}{1 + M_2} \frac{1 + \frac{1}{2}(\kappa - 1) M_2^2}{1 + \frac{1}{2}(\kappa - 1) M_1 M_2} \mathrm{A} \tag{3}$$

- with

$$\mathrm{A} = \left(\frac{1 + \frac{1}{2}(\kappa - 1) M_1^2}{1 + \frac{1}{2}(\kappa - 1) M_2^2} \right)^{\frac{\kappa}{\kappa - 1}} \tag{4}$$

where κ is the isentropic exponent, M_1 and M_2 the Mach numbers upstream and downstream of the nozzle or diffuser, respectively, p'_{1+} the impinging acoustic pressure wave, ϱ'_s the impinging density fluctuation corresponding to the entropy wave, ϱ'_{2s} the transmitted density fluctuation through the nozzle or diffuser, a_1 the

Downloaded 02 Jun 2010 to 171.66.16.107. Redistribution subject to ASME license or copyright; see http://www.asme.org/terms/Terms_Use.cfm

speed of sound upstream of the nozzle or diffuser, and p'_{2+} the downstream propagating acoustic pressure wave.

The results of this one-dimensional approach are compared with experimental data of this work in the Measurements and Results section.

Numerical Simulation

The corresponding numerical simulation of this setup is described in detail by Mühlbauer et al. [13]. The simulation contains a compressible URANS calculation with standard reflecting and nonreflecting boundary conditions. The partial reflection at the change of profile in the exhaust pipe shows the necessity of setting a certain reflection factor. Based on the configuration, a parametric study is carried out varying boundary conditions, amount of heating energy, and propagation length between the EWG and the nozzle, as well as tube length downstream the nozzle. The simulations of all setups show a very good agreement with the experimental data. By changing the length of the exhaust tube, the impact of the phase shift at the partly reflective boundary on the simulated noise is shown. The commercial software package ANSYS CFX is used to carry out the simulations. For the inclusion of the nonreflecting boundary conditions, a DLR (German Aerospace Center) software extension was used, relying on a formulation of nonreflecting boundary conditions for SIMPLE-like solution schemes.

Measurements and Results

The first series of measurements aims to identify and separate the entropy noise from noise related to other sources. One of the most characteristic features of entropy noise is the slow propagation velocity of entropy waves or hot spots with the flow velocity compared to acoustic waves, which propagate with the speed of sound. In the test rig, the flow velocity of the tube flow is about two orders of magnitude lower than the speed of sound.

In the second part of this section, the experimental data is compared with the results of the corresponding numerical simulation.

The third part of the measurements is a parametric study in order to evaluate the dependencies of entropy noise on the nozzle Mach number and the amplitude of the temperature or entropy perturbation.

Finally, these results are compared with the theoretically predicted values from the one-dimensional theory of Marble and Candel [4].

Entropy Noise Identification. In order to identify the generated entropy noise, the EWG response was investigated using two different excitation modes:

1. In a pulse excitation mode, microphone signals were analyzed in the time domain in a pulse excitation mode. The platinum wires of the EWG rig were heated once per second, controlled by square pulses from a function generator.
2. The cross-spectral analysis of microphone signals and excitation signals of the EWG module as a reference was evaluated while the EWG was heated periodically.

In the time domain analysis of the pulse excitation mode, a distinct propagation delay between the excitation signal and the generated acoustic pressure pulse downstream of the nozzle can be detected. This time delay results mainly from the distance between heating module and nozzle divided by the tube flow velocity upstream of the nozzle.

Figure 3 displays the convecting entropy or temperature perturbation (solid red line), measured by a fast thermocouple located 34 mm downstream of the heating module. The dotted black line indicates the heating trigger signal. The run of the solid (red) curve reveals a temperature rise from the steady flow temperature of 296 K up to 305 K, following the heating trigger with a certain propagation delay between the heater module and the temperature

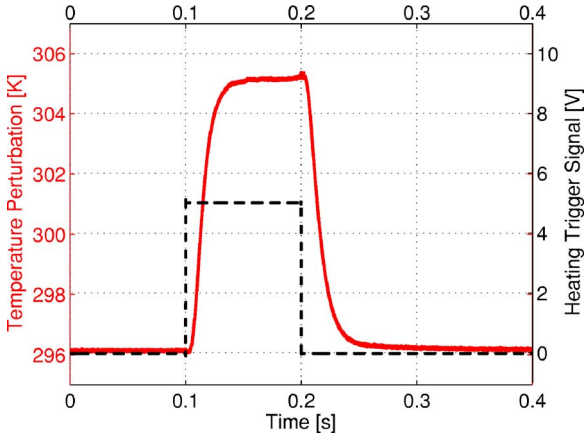

Fig. 3 Convecting entropy wave (solid red line) in terms of flow temperature perturbation measured by a fast thermocouple downstream of the heating module; the dotted black line shows the heating trigger signal

position. However, the exact edge shape of the entropy wave is not clearly determined since the temperature signal is certainly affected by the limited frequency response of the thermocouple (see also [18]).

In the first part of the parametric study this distance, as well as the flow velocity, has been varied in order to generate different propagation delays of the entropy waves. For each parameter variation, an ensemble average over 300 single pulse traces was evaluated.

Figure 4 shows the acoustic pressure pulse signals of three different measurements with different tube lengths between the heating module and the nozzle. Here, the bulk velocity in the tube section was 11.9 m/s and the Mach number in the nozzle was Ma=1. The heating current signal is also plotted in the graph as a dashed line. A positive temperature perturbation, induced by the heating of the platinum-wire module, generates a positive pressure pulse when it is accelerated through the nozzle. This pressure pulse propagates in the tube section downstream of the nozzle and is detected by the wall-flush mounted microphones. The propagation delay of the entropy noise pressure pulse is equivalent to the propagation path length between EWG and nozzle throat. With increasing tube length, the time delay of the pressure pulse increases, too. The amplitudes of the pressure pulses decrease

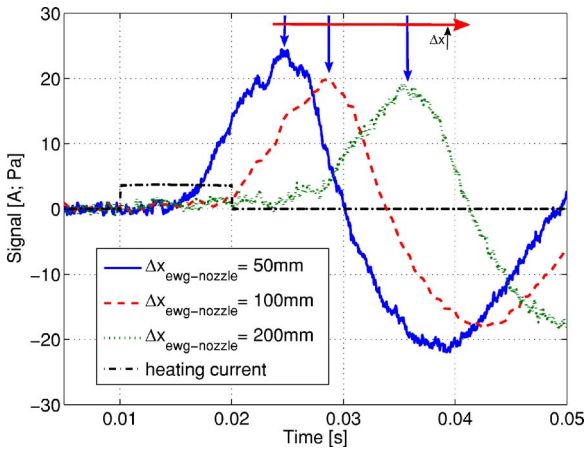

Fig. 4 Phase averaged time series of EWG microphone signals in the pulse excitation mode for different tube lengths Δx between heating module (EWG) and nozzle

Downloaded 02 Jun 2010 to 171.66.16.107. Redistribution subject to ASME license or copyright; see http://www.asme.org/terms/Terms_Use.cfm

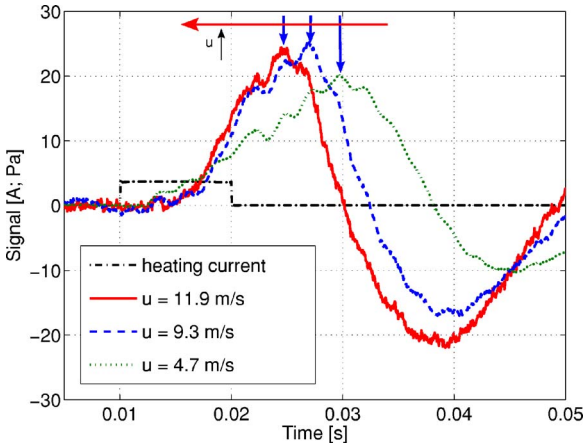

Fig. 5 Phase averaged time series of entropy-wave-generator microphone signals in the pulse excitation mode at different bulk velocities

slightly with increasing duct length, probably due to an increased dispersion of the entropy waves.

The flow velocity, and therewith the convection velocity, of the entropy waves is varied in Fig. 5. It can be seen that the increase of the bulk velocity yields a corresponding decreased time delay and an increased pressure amplitude. The maximum Mach number at this measurement series was Ma=1.

The propagation or convection time of the entropy waves can also be determined by cross-spectral analysis of microphone signals and excitation signals in the periodical (sinusoidal) forced mode. In this case, the slope of the linear phase relation in the cross spectrum is anti-proportional to the propagation speed of the entropy wave. This analysis is applied to the next part of the experimental study.

Figure 6 shows the phase plot of the cross spectra between heating current and microphone signals downstream of the nozzle for an excitation sweep from about 85 Hz to 145 Hz. The different traces correspond to different tube lengths between EWG and nozzle throat. The longest distance ($\Delta x_{\text{EWG-nozzle}}$=200 mm) results in the steepest phase line due to the same propagation velocity.

From this phase relation, the propagation velocity can be quantified, as shown in Table 1. Here, the second column displays the time delays resulting from the slope of the phase relation at different tube lengths (column one). Considering the acoustic propagation time of the generated entropy noise, the traveling speed of

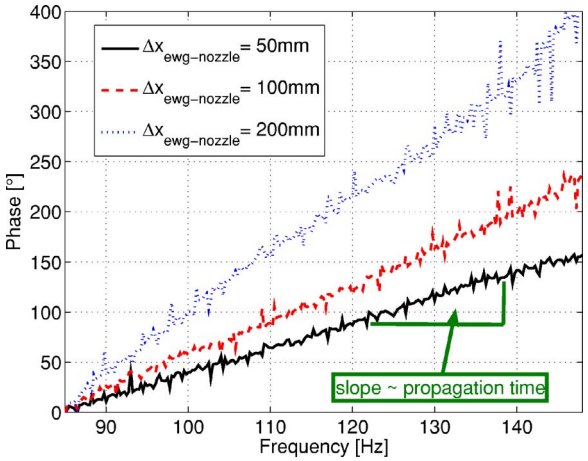

Fig. 6 Phase relation of cross spectra between heating current and microphone signals downstream of nozzle for different tube lengths between heating module (EWG) and nozzle

Table 1 Propagation velocities of entropy waves calculated from phase relation in comparison with bulk velocity of the flow for different tube lengths Δx between heating module (EWG) and nozzle

Distance $\Delta x_{\text{EWG-nozzle}}$ (mm)	Time delay (ms)	Propagation velocity (m/s)	Bulk velocity (m/s)
50	6.9	11.7	11.9
100	9.9	13.6	11.9
200	18.1	12.8	11.8

the entropy waves can be determined (column three). These phase velocities show a good agreement compared to the bulk velocity of the flow (column four). However, it has to be considered that the tube flow features a certain flow profile, where the bulk velocity, calculated from the mass flux, the tube cross section, and the mean density, is only a spatial mean value.

Comparison With Numerical Simulation. For the first comparison of the experimental data with the numerical results, a reference test case has been chosen for simulation. In this case, the test rig was fed with a mass flux of 12 g/s of air, which corresponds to a bulk velocity of 12 m/s in the tube section upstream of the nozzle and a maximum Mach number of 1.2 in the nozzle. The platinum wires were heated once per second for a duration of 0.1 s. During this heating period, a thermal power of about 100 W is transferred to the flow.

During the first part of the numerical simulation a steady state solution is determined. Figure 7 shows the Mach number distribution in the nozzle inlet flow, resulting from the steady flow field calculation. The distribution shows an acceleration up to Ma =1.2 downstream of the nozzle throat.

When the steady state solution is reached in the simulation, the flow is heated with a pulse similar to the experimental tests. The unsteady system response in this URANS is locked at several monitoring positions corresponding to the sensor positions in the experimental setup. Figure 8 shows a comparison of the acoustic pressure signal of a microphone in the tube section downstream of the nozzle with the numerical results. The two signal traces indicate a very good agreement in their unsteady behavior. When the entropy wave reaches the nozzle at $\approx t$=0.025 s, a positive pressure pulse is generated (see Fig. 8). Following this pulse, the microphones detect various reflections of this pulse from the outlet of the test rig, shown by the oscillating behavior of the signal.

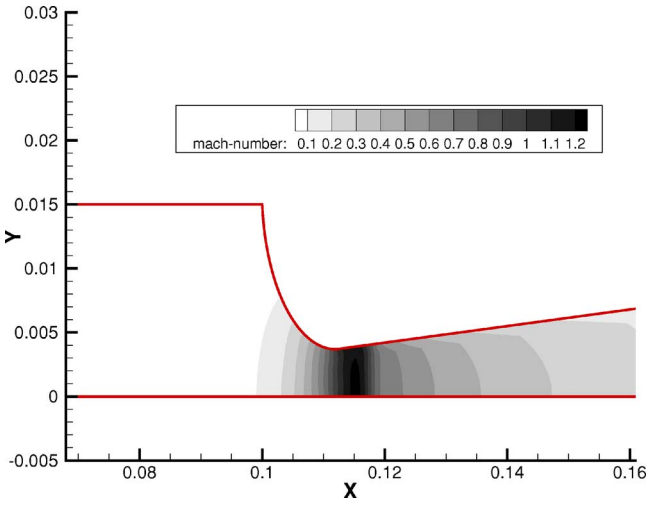

Fig. 7 Mach number distribution of the EWG nozzle flowfield; RANS simulation of reference test case

Downloaded 02 Jun 2010 to 171.66.16.107. Redistribution subject to ASME license or copyright; see http://www.asme.org/terms/Terms_Use.cfm

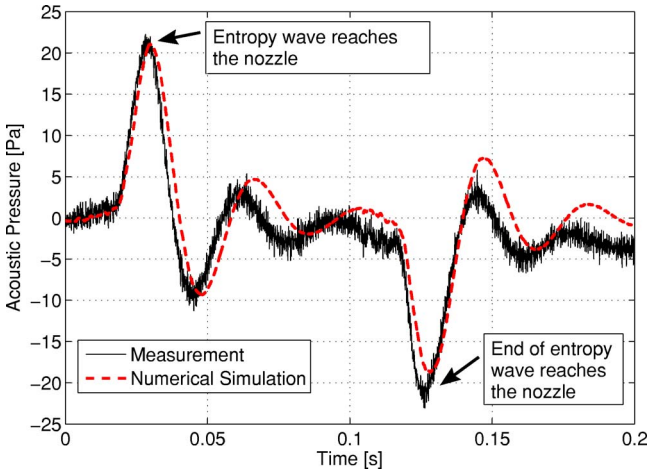

Fig. 8 Comparison of experimental data and results of the numerical simulation; acoustic pressure signal of microphone downstream of the nozzle

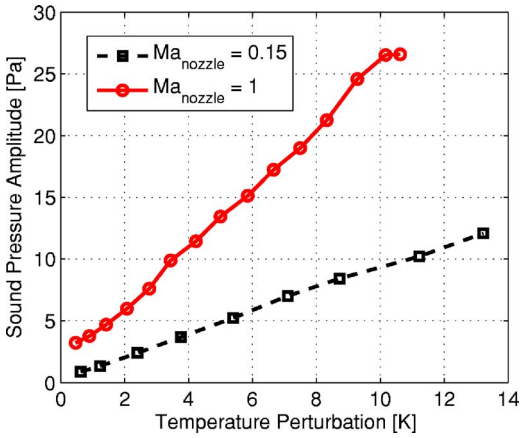

Fig. 10 Acoustic pressure pulse amplitude of generated entropy noise over accelerated temperature perturbation for two different nozzle Mach numbers $Ma_{nozzle}=0.15$ and $Ma_{nozzle}=1$

At $\approx t=0.125$ s, the trailing edge of the entropy wave enters the nozzle, and a negative pressure pulse is generated and detected by the microphones.

Study on Parameters of Entropy Noise. In order to evaluate the different parameters of entropy noise generation, a test series was conducted varying the mass flux and therewith the nozzle Mach number, as well as the amplitude of the temperature perturbation. The amplitude of the generated entropy noise was determined by extracting the acoustic pressure pulse amplitude of a microphone downstream of the nozzle. The nozzle Mach number was changed from 0.15 up to 1.0, with amplitudes of temperature fluctuations between 1 K and 13 K, measured by using a bare thermocouple with a diameter of 25 μm installed downstream of the heating module.

Figure 9 displays a contour plot of the generated entropy pressure pulse over the nozzle Mach number and the temperature fluctuation amplitude. The entropy sound pressure increases with both nozzle Mach number and accelerated temperature perturbation amplitude.

However, a deeper insight into the functional characteristics of Mach number and temperature as parameters for entropy noise is provided by Figs. 10 and 11. Figure 10 shows an almost linear relation between the temperature perturbation amplitude and the generated entropy noise amplitude for two different Mach numbers $Ma_{nozzle}=0.15$ and $Ma_{nozzle}=1$.

In contrast to the temperature, the dependency of entropy noise on the Mach number is not linear, as seen in Fig. 11, for two different temperature perturbation amplitudes 7.5 K and 9 K. For low nozzle Mach numbers up to 0.7, the entropy sound pressure amplitudes are increasing with the Mach number. Above a nozzle Mach number of $\approx$0.7, the entropy sound pressure amplitude is decreasing again. An explanation of this behavior could be the low acoustic transmission coefficient of the divergent part of the nozzle. This behavior is also prescribed by Marble and Candel [4] with the acoustical characteristics of a diffuser flow at high inlet Mach numbers.

Comparison With Theoretical Prediction. The one-dimensional theory of Marble and Candel [4] describes, in principle, only the generation of entropy noise for either a nozzle or a diffuser separately. Since, in the experimental setup, a convergent-divergent nozzle was investigated, a combination of the theoretical expressions concerning the nozzle and the diffuser part of the setup is necessary. For the comparison with the experiment, the

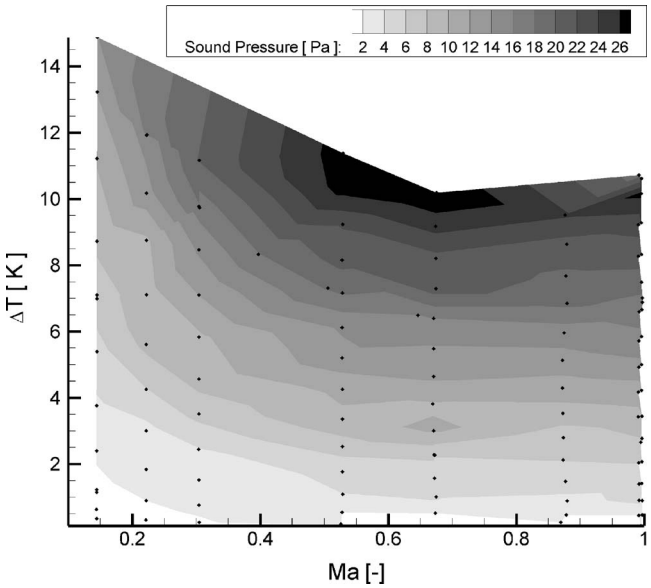

Fig. 9 Acoustic pressure pulse amplitude of generated entropy noise at different nozzle mach numbers and amplitudes of accelerated temperature or entropy perturbations

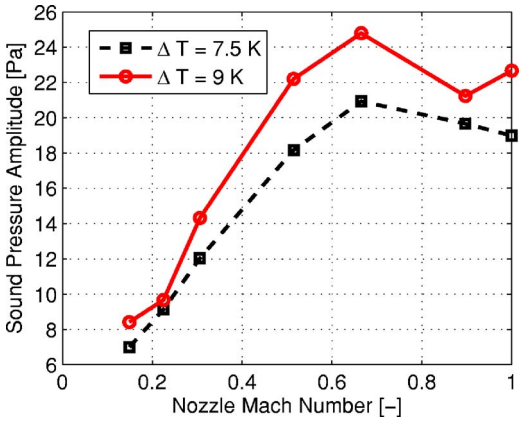

Fig. 11 Acoustic pressure pulse amplitude of generated entropy noise over nozzle Mach number for two different amplitudes of accelerated temperature perturbation

Downloaded 02 Jun 2010 to 171.66.16.107. Redistribution subject to ASME license or copyright; see http://www.asme.org/terms/Terms_Use.cfm

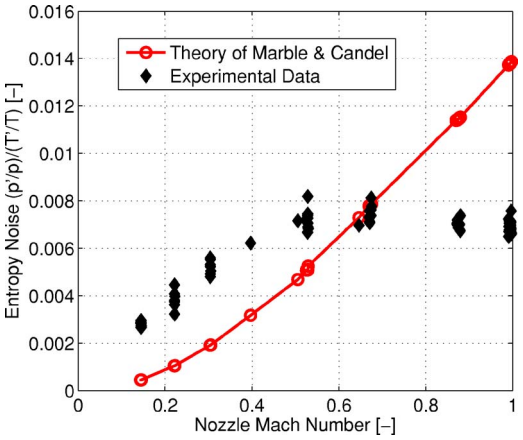

Fig. 12 Comparison of experimental data with theoretical prediction; normalized entropy sound pressure over nozzle Mach number

downstream propagating entropy pressure amplitude generated in the nozzle has to be multiplied by the transmission factor of the subsequent diffuser flow. Furthermore, the pressure wave generated by the deceleration of the entropy wave in the diffuser has to be summed up to the total downstream propagating sound pressure wave, which in the experiment is measured by the microphones in the duct section downstream of the nozzle.

Figure 12 shows the comparison of the experimental microphone data with the theory of Marble and Candel [4]. It displays the entropy sound pressure amplitude normalized by the total pressure and the relative temperature perturbation over the nozzle Mach number. For each Mach number, different temperature amplitudes have been investigated in the experiment (see Fig. 10), resulting in several black marker points for a certain Mach number in Fig. 12. For low Mach numbers, the theoretical results are lower than the acquired data, whereas for higher nozzle Mach numbers between 0.5 and 0.7, the predicted values show a good agreement with the experimental data. For a choked nozzle ($Ma_{nozzle}=1$), the measured entropy noise amplitudes are lower than the theoretical ones. The differences are not fully understood until now. Possible explanations are the compactness assumption in the theory (nozzle short in comparison with the wavelength) and the one-dimensional concept of the theory. The theory implies the nozzle length to be much smaller than the wavelength of the entropy and sound waves. Especially for the entropy wave, which has, due to the low propagation speed, a very short wavelength, this assumption may not be valid anymore. Furthermore, any radial velocity and acceleration components that are present in the experimental nozzle flow are not included in the one-dimensional theory.

Conclusion

Entropy noise was investigated in a dedicated test facility, in which entropy waves were electrically generated and accelerated through a convergent divergent nozzle. A corresponding numerical simulation, described in detail in Ref. [13], of a reference test case was introduced and a good agreement with the experimentally acquired data was presented. A parameter study on the entropy noise generation mechanism showed the expected linear dependence of the induced entropy sound pressure amplitude and the amplitude of the entropy or temperature perturbation. The correlation of the entropy noise with the nozzle Mach number indicated a strongly increasing entropy noise pressure with the Mach number for low Mach numbers, whereas for Mach numbers higher than 0.8, the entropy noise is slightly decreasing. The comparison of the measured entropy noise with the theory of Marble and Candel [4] showed quite good agreement in consideration of the one-dimensional description of the theory. In this work, the influence of the exact shape of the entropy waves with respect to the generated entropy noise level was not explicitly investigated. For future investigations, a modification of the heating control is currently under development in order to generate different edge shapes of the entropy waves.

Acknowledgment

The authors gratefully acknowledge the financial support by the German Research Foundation (DFG) through the research unit FOR 486 "Combustion Noise." We also would like to thank Dr. Ulf Michel for fruitful discussions. Thanks go to Prof. Oliver Paschereit (TU Berlin) for his contribution to this work.

References

[1] Dowling, A. P., 1996, "Acoustics of Unstable Flows," *Theoretical and Applied Mechanics*,T. Tatsumi, E. Watanabe, and T. Kambe, eds., Elsevier, Amsterdam, pp. 171–186.
[2] Kovasznay, L. S. G., 1953, "Turbulence in Supersonic Flow," J. Aeronaut. Sci., **20**(10), pp. 657–682.
[3] Morfey, C. L., 1973, "Amplification of Aerodynamic Noise by Convected Flow Inhomogeneities," J. Sound Vib., **31**(4), pp. 391–397.
[4] Marble, F. E., and Candel, S. M., 1977, "Acoustic Disturbances From Gas Non-Uniformities Convected Through a Nozzle," J. Sound Vib., **55**(2), pp. 225–243.
[5] Strahle, W. C., 1978, "Combustion Noise," Prog. Energy Combust. Sci., **4**(3), pp. 157–176.
[6] Strahle, W. C., Muthukrishnan, M., and Neale, D. H., 1977, "Experimental and Analytical Separation of Hydrodynamic, Entropy and Direct Combustion Noise in a Gas Turbine Combustor," AIAA 4th Aeroacoustic Conference, AIAA, Paper No. 77-1275.
[7] Muthukrishnan, M., Strahle, W. C., and Neale, D. H., 1978, "Separation of Hydrodynamic, Entropy, and Combustion Noise in a Gas Turbine Combustor," AIAA J., **16**(4), pp. 320–327.
[8] Cumpsty, N. A., and Marble, F. E., 1977, "Core Noise From Gas Turbine Exhausts," J. Sound Vib., **54**(2), pp. 297–309.
[9] Cumpsty, N. A., and Marble, F. E., 1977, "The Interaction of Entropy Fluctuations With Turbine Blade Rows: A Mechanism of Turbojet Engine Noise," Proc. R. Soc. London, Ser. A, **357**, pp. 323–344.
[10] Cumpsty, N. A., 1979, "Jet Engine Combustion Noise: Pressure, Entropy and Vorticity Perturbations Produced by Unsteady Combustion or Heat Addition," J. Sound Vib., **66**(4), pp. 527–544.
[11] Bohn, M. S., 1976, "Noise Produced by the Interaction of Acoustic Waves and Entropy Waves With High-Speed Nozzle Flows," Ph.D. thesis, California Institute of Technology, Pasadena, CA.
[12] Zukoski, E. E., and Auerbach, J. M., 1976, "Experiments Concerning the Response of Supersonic Nozzles to Fluctuating Inlet Conditions," ASME J. Eng. Power **98**, pp. 60–63.
[13] Mühlbauer, B., Widenhorn, A., Liu, M., Noll, B., and Aigner, M., 2007, "Fundamental Mechanism of Entropy Noise in Aero-Engines: Numerical Simulation."
[14] Lighthill, M. J., 1952, "On Sound Generated Aerodynamically," Proc. R. Soc. London, Ser. A **211**, pp. 564–587.
[15] Howe, M. S., 1975, "Contributions to the Theory of Aerodynamic Sound, With Application to Excess Jet Noise and the Theory of the Flute," J. Fluid Mech., **71**, pp. 625–673.
[16] Ffowcs Williams, J. E., and Howe, M. S., 1975, "The Generation of Sound by Density Inhomogeneities in Low Mach Number Nozzle Flows," J. Fluid Mech., **70**, pp. 605–622.
[17] Schemel, C., 2003, "Modellierung und numerische Simulation der Entstehung und Ausbreitung von Schall durch Entropiewellen in beschleunigten Rohrströmungen," diploma thesis, Technische Universität Berlin, Berlin, Germany.
[18] Strahle, W. C., and Muthukrishnan, M., 1976, "Thermocouple Time Constant Measurement by Cross Power Spectra," AIAA J., **14**(11), pp. 1642–1644.

Downloaded 02 Jun 2010 to 171.66.16.107. Redistribution subject to ASME license or copyright; see http://www.asme.org/terms/Terms_Use.cfm

Predicting the Performance of System for the Co-production of Fischer-Tropsch Synthetic Liquid and Power from Coal

Xun Wang
e-mail: xunwang@mail.etp.ac.cn

Yunhan Xiao
e-mail: xiao_yh@mail.etp.ac.cn

Song Xu
e-mail: xusong00@yahoo.com.cn

Zhigang Guo
e-mail: guozigang05@mails.gucas.ac.cn

Institute of Engineering Thermophysics,
Chinese Academy of Sciences,
P.O. Box 2706, Beijing 100080, PRC

A co-production system based on Fischer-Tropsch (FT) synthesis reactor and gas turbine was simulated and analyzed. Syngas from entrained bed coal gasification was used as feedstock of the low-temperature slurry phase Fischer-Tropsch reactor. Raw synthetic liquid produced was fractioned and upgraded to diesel, gasoline, and liquid petrol gas (LPG). Tail gas composed of unconverted syngas and FT light components was fed to the gas turbine. Supplemental fuel (NG, or refinery mine gas) might be necessary, which was dependent on gas turbine capacity, expander through flow capacity, etc. FT yield information was important to the simulation of this co-production system. A correlation model based on Mobil's two step pilot plant was applied. This model proposed triple chain-length-dependent chain growth factors and set up correlations among reaction temperatures with wax yield, methane yield, and C_2–C_{22} *paraffin and olefin yields. Oxygenates in the hydrocarbon, water, and vapor phases were also correlated with methane yield. It was suitable for syngas, iron catalyst, and slurry bed. We can show the effect of temperature on the products' selectivity and distribution. User models that can predict product yields and cooperate with other units were embedded into Aspen plus simulation. Performance prediction of syngas fired gas turbine was the other key of this system. The increase in mass flow through the turbine affects the match between compressor and turbine operating conditions. The calculation was carried out by GS software developed by Politecnico Di Milano and Princeton University. The simulated performance assumed that the expander operates under choked conditions and turbine inlet temperature equals the NG fired gas turbine. A "F" technology gas turbine was selected to generate power. Various cases were investigated to match the FT synthesis island, power island, and gasification island in co-production systems. Effects of* CO_2 *removal/LPG recovery, co-firing, and* CH_4 *content variation were studied. Simulation results indicated that more than 50% of input energy was converted to electricity and FT products. Total yield of gasoline, diesel, and LPG was* 136–155 g/N m^3 $(CO+H_2)$. *At coal feed of* 21.9 kg/s, *net electricity exported to the grid was higher than* 100 MW. *Total production of diesel and gasoline (and LPG) was* 118,000 t (134,000 t)/year. *Under the economic analysis conditions assumed in this paper, the co-production system was economically feasible. The after tax profits can research 17 million euro. Payback times ranged from 6 to 7 years.*
[DOI: 10.1115/1.2747644]

Keywords: co-production, performance prediction, FT

1 Introduction

The Fischer-Tropsch (FT) hydrocarbon synthesis is a process in which syngas reacts over a catalyst to produce hydrocarbons (principally normal paraffins and straight chain 1-olefins). If FT synthesis is integrated with IGCC, this type of system can take advantage of mass and energy integration, common operating facilities, and economy of scale in the co-production of electric power and chemicals. In view of large coal reserves in China, it is projected to play an ever increasing role in the coming decades.

The co-production of electric power and FT liquid from coal derived syngas has been known in the literature. The electric power is typically produced by a generator driven by a turbine. As previous research by Chevron [1], a portion of FT tail gas and syngas from a gasifier are combined, combusted, and utilized to generate a base load power by a steam turbine. The liquid hydrocarbons are utilized as a fuel for a gas turbine to produce supplemental power for peak load demand. The advantage is that there is little modification on the gas turbine. In a patent from APCI [2], the unreacted synthesis gas is combined with a portion of syngas from the gasifier to provide at least a portion of the fuel of the gas turbine combustor. Modifications on gas turbine combustor and through flow are necessary. Reaction heat is removed by yielding a stream of heated water. In the humidifier, dry gas contacts directly with this hot water and then is saturated. In Patent No. US20030083391A1 [3], after CO_2 removal, tail gas is sent to the gas turbine as fuel. Patent No. GB2377452 [4] also utilizes tail gas as a gas turbine fuel. Medium pressure (MP) steam produced in FT reaction is superheated by means of hot turbine flue gas and then is directed into the steam turbine. In this patent, power is generated by a gas turbine combined cycle. In Patent No. CN1786119A [5], a similar co-production system is put forward. The difference is that steam generated in the FT rector is directly expanded through a separate turbine instead of a combined cycle.

Contributed by the International Gas Turbine Institute of ASME for publication in the JOURNAL OF ENGINEERING FOR GAS TURBINES AND POWER. Manuscript received April 28, 2007; final manuscript received May 5, 2007; published online January 16, 2008. Review Conducted by Dilip R Ballal. Paper presented at the ASME Turbo Expo 2007: Land, Sea and Air (GT2007), Montreal, Quebec, Canada, May 14–17, 2007, Paper No. GT2007-27693.

Copyright © 2008 by ASME

Downloaded 02 Jun 2010 to 171.66.16.107. Redistribution subject to ASME license or copyright; see http://www.asme.org/terms/Terms_Use.cfm

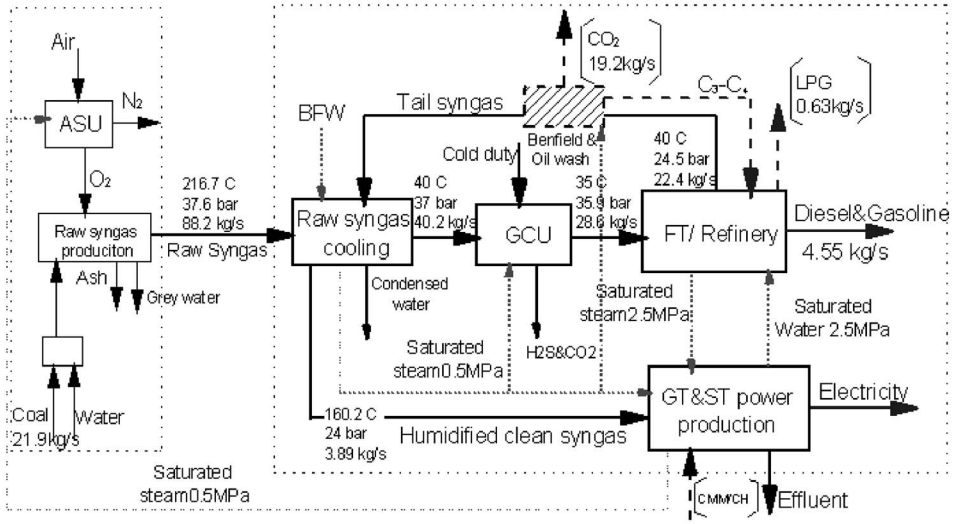

Fig. 1 Interconnecting streams of coproduction system (cases 4.1–4.3)

The US Department of Energy has supported a series of studies about FT liquid with power co-production. In a report by Bechtel Corporation et al. [6], petroleum coke and coal fueled IGCC power plants are extended to co-produce liquid transportation fuel by FT synthesis technology. The objective of this study is to reduce the cost of electricity by way of liquid co-production. The co-production system optimization focused on dividing the clean syngas between the production of FT liquids and power generation. In Ref. [7], a conceptual design and ASPEN PLUS process simulation model is developed for a Battelle FT liquefaction and combined cycle power co-production plant based on biomass gasification. Reference [8] evaluated the different options to use biomass for the production of FT liquids based on a Co catalyst and power generation with a combined cycle. It presented a broad exploration of the possibilities to produce synthetic hydrocarbons from biomass via gasification and Co catalyst based FT synthesis. A wide variety of potential conversion system configurations had been evaluated including energy efficiencies and economics. Other related researches can be found in Refs. [9–12]. These researches identified that low-temperature FT reactor technology can be used together with solid carbonaceous material gasifiers for the co-production of hydrocarbon liquids and electrical power.

Integrated IGCC with co-production is the integration of various process blocks. It is the efficiency of individual pieces and the sharing of mass and energy between different pieces that determine the overall plant performance. Because of various stream interactions between different sections in the plant, there are numerous opportunities to improve the mass and heat integration and increase the thermal efficiency. More work needs to be done based on previous research. The main objective of this paper is to set up a flexible simulation to obtain the system's detailed mass and energy information, and to assess technical and economical performance. Different techniques and various stream interactions can be obtained, analyzed, and compared. ASPEN PLUS has been chosen as the basic simulation platform. The characteristics of performance prediction in this study are as follows:

1. Gas turbine performance is predicted by "GS" [13,14]—a software developed in Politecnico di Milano and Princeton University, which was originally designed for predicting the performance of a complex gas-steam cycle. Although ASPEN PLUS is a powerful tool for chemical engineering simulation, its ability in showing the performance of a gas turbine is limited. In most of the previous co-production system studies, the gas turbine was treated as a simplified compression/expansion process with constant poly-efficiency. But to a gas fuel turbine, it is important to estimate the components characteristics and gas blade cooling information. In view of this, GS has an advantage over simplified models. It is a powerful and flexible tool that can predict the component and engine performance of a very wide variety of gas turbine with high accuracy.
2. Similar to previous studies, tail gas from FT synthesis is used as fuel for a gas turbine. But this stream directly contacts with hot water generated during raw syngas cooling and then dry gas is saturated. The low-temperature heat of syngas cooling can be utilized. NOx formation of combustion is also depressed. Heat related to syngas cooling, FT synthesis, syngas purification, sulfur recovery, H_2 production, and PSA are integrated into the steam side of the gas turbine combined cycle. The steam side can be used to export power and process heat requirements.
3. FT yield information is important to this co-production system simulation. In FT synthesis, product distributions and selectivity are influenced by many factors, including catalyst type, catalyst composition, reactor type, temperature, feed gas composition, pressure, etc. In order to illustrate the accurate products yields, a correlation model based on Mobil's two step pilot plant is used [15]. This model applies triple chain-length-dependent chain growth factors and setup correlations among reaction temperatures with wax yield, methane yield, paraffin and olefin yields. Oxygenates in the hydrocarbon phase, water phase, and vapor phase were also correlated with temperature. This model was included ASPEN PLUS. It provided the possibility to tail out the simulation completely according to the cases studied, not only for kinetics expression, but also fluid dynamic, etc.

2 System Description

2.1 Interconnection of Co-production System. Figure 1 showed the overall input streams, output streams, and integration streams between gasification block, raw syngas cooling section, gas clean up (GCU) section, the FT synthesis (reaction/refinery/hydrogen production) island, and the combined cycle.

O_2 was produced from a stand alone air separation unit (ASU) and then sent to a gasifier. A slurry of coal and water was fed to an entrained bed gasifier where it reacted with O_2 to produce syngas. Then hot syngas was quenched down to 216°C in a quench chamber and ash was removed. Raw syngas was continued to be cooled down to 40°C by steam generation and humidified water heating

Downloaded 02 Jun 2010 to 171.66.16.107. Redistribution subject to ASME license or copyright; see http://www.asme.org/terms/Terms_Use.cfm

(25.9 bar/195°C). Then this stream flowed into the GCU. In this section, H_2S, COS, and CO_2 were absorbed by solvent (refrigerated methanol). Molar fraction of H_2S+COS in clean syngas was reduced to 0.1 ppm and CO_2 molar fraction to 4.4%. The detailed acid gas removal flowsheet can be found in Ref. [16]. After acid gas removal, syngas was heated up to 235°C and fed to one through the FT reactor. The reaction temperature was 250°C, pressure 3 MPa, and CO conversion 94.3% [17]. In the FT reactor, the bulk of H_2 and CO in the syngas was converted to three streams: a vapor phase comprising light hydrocarbon products and unreacted synthesis gas, a liquid phase comprising heavier liquid hydrocarbon products, and an aqueous phase comprising water and any soluble organic compounds formed during the reaction of the synthesis gas. The distribution of the hydrocarbon was generally dependent on the type of FT catalyst used in the reactor. The vapor, the liquid, and the aqueous phase were withdrawn from the reactor. The raw oil was fed to the upgrading section. Utilities consumption of the FT products refinery can be found in Ref. [7]. After hydrocracking and thermal treating, diesel and gasoline were obtained. The vapor phase was sent directly to the humidifier and power generation section. In this paper, the syngas containing CO_2 and C_1-C_4 components was called tail gas. Alternatively, the vapor phase can be first sent to the CO_2 recovery unit (e.g., the Benfield process) and oil wash unit. C_3-C_4 components were separated and sent to the upgrading section to produce LPG. The $CO_2-C_3-C_4$ free syngas was used as a fuel of power generation (Figure 1, shade blocks). In this paper, the syngas from the oil wash process with CO_2 and C_3-C_4 removal was called CO_2 free tail gas.

In the humidifier (Fig. 5), tail gas or CO_2 free tail gas contacted directly with hot water generated in the syngas cooling section. Gas was heated and saturated to a steam content of 27% at a temperature of 160°C. This humidified syngas was a primary fuel of the gas turbine. In order to fully fire the gas turbine and avoid severe modification problem on burners and fuel manifolds, cofiring with higher heating value supplemental fuel (such as NG, or coal mine gas CMM) may be necessary (Fig. 1). Mixed fuel was combusted in pressurized air at about 1100–1400°C. Expansion of the resulting hot fuel gas generated power. Part of the power was used to drive the air compressor. Exhaust gases from the GT were routed to the HRSG and stack. The HRSG received the GT exhaust gases and generated the HP steam. Other heat in the system, including syngas cooling (5.0 bar saturated steam), FT synthesis (25.8 bar saturated steam), syngas purification, sulfur recovery, H_2 production, and PSA were integrated into the steam side of the gas turbine combined cycle. The HRSG provided superheating capability for all MP and LP saturated steam. It also provided feed water and process steam for the combined cycle, the FT synthesis facilities, the syngas cooling purification, and the sulfur recovery. Electricity was generated by a gas turbine combined cycle. This cycle can provide all mill electricity consumption. The steam turbine was a nonreheat, condensing turbine that included a HP/MP/LP section. A stream of saturated steam with 0.12 MPa was generated from a stand alone heating surface at the end of the HRSG so as to provide the heat source for the deaerator.

Table 1 Cases investigated

Case	Primary fuel	Co-firing fuel	CH_4 molar fraction in co-firing fuel (%)
1.0	Humidified tail gas	CMM	70
1.1		CH_4	99.5
3	Humidified CO_2 free tail gas	—	—
4.1		CMM	30
4.2		CMM	70
4.3		CH_4	99.5

Depending on whether or not there was syngas humidification, coal feed, LPG recovery, or co-firing, and co-firing fuel characteristics, a variety of systems can be generated. After system screening (Sec. 4.5), study in this paper was focused on four kinds of systems. Their main structures were similar. Standard cases investigated were listed in Table 1.

2.2 Basic Assumptions and Input Parameters. Table 2

2.3 Calculation of Integrated Coproduction System. After testing the capability of the software to handle each subsystem, ASPEN PLUS and GS were chosen be to the basic platform for system simulation. They were used to predict overall performances of the integrated system. Gasification, gas cooling, purification, fuel synthesis island, steam turbine, and other auxiliary sections were simulated by ASPEN PLUS. GS was specialized in the gas turbine performance prediction. The procedure was shown in Fig. 2. The detail strategy was as follows:

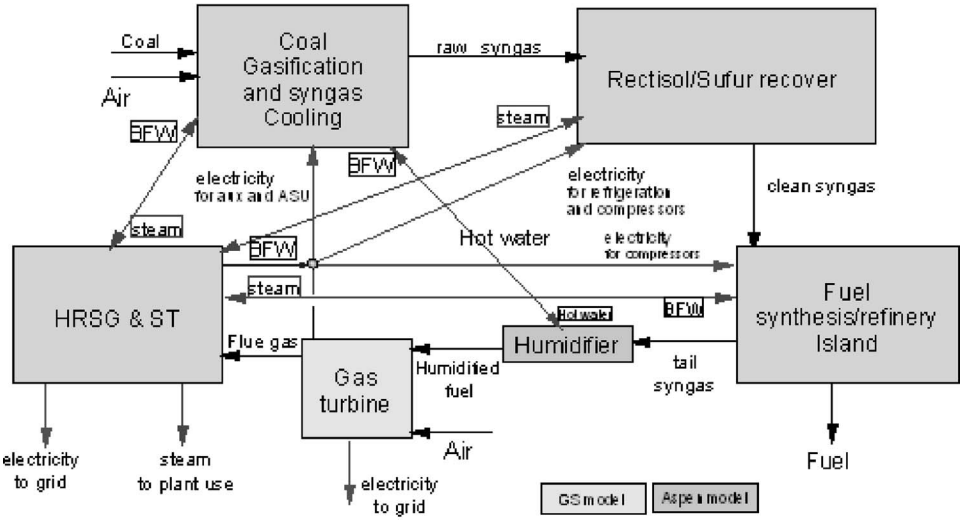

Fig. 2 Power and heat transfer

Downloaded 02 Jun 2010 to 171.66.16.107. Redistribution subject to ASME license or copyright; see http://www.asme.org/terms/Terms_Use.cfm

Table 2 Basic assumptions and input parameters

Name (main ASPEN PLUS blocks used)	
Gasifier (RGIBS)	
Coal, wet basis (kg/s) (cases 1.0–1.1, cases 4.1–4.3)	21.9
Water content in coal (wt %)	7
Slurry concentration (%)	65
Operation temperature (°C)	1350
Operation pressure (MPa)	4
Power consumption kWh/10,000 N m^3 ($CO+H_2$)	288.23
Oxidizer	
O_2 feed flow (N m^3/kg.dry coal)	0.64
O_2 purity (vol %)	99.6
ASU(Radfrac, MHEX) power consumption (kWh/N m^3 O_2)	0.55
Rectisol	
H_2S+COS molar fraction in clean syngas	0.1 ppm
CO_2 molar fraction in clean syngas (%)	4.4
Two-stage absorber (Radfrac)	Pressure drop: 0.5% Solvent/dry gas: 0.911
CO_2 removal (Flash)	Pressure 0.4 MPa
H_2S+CO_2 removal (Flash)	Pressure 0.1 MPa
Regenerator (Radfrac, noncondensor)	Pressure 0.12 MPa Reflux ratio: 0.64
Syngas cooling (MHEX,FLASH)	
Byproduct steam/water pressure (MPa)	Hot water: 2.6 LP steam pressure: 0.5
FT synthesis reactor (USER)	
Reactor type	Slurry
Catalyst type	Iron based
Fresh gas H_2/CO (molar ratio)	0.78
Syngas inlet temperature (°C)	235
Operation temperature (°C)	Isothermal, 250
Operation pressure (MPa)	3
CO conversion ratio (%)	94.3
Recycle ratio	0
By product saturated steam (MPa)	2.58
FT products fraction	see Ref. [7]
CO_2 removal process (SEP)	2433 kJ/Nm^3 CO_2
Oil wash process (SEP)	Steam (0.5 MPa): 6.7 kg/kgLPG Cold duty: 3.1 MW/kgLPG
Humidified water	Temperature 195°C Pressure 2.6 MPa
Dry gas/water (mass ratio)	0.974
Operation pressure (MPa)	2.4
Gas turbine (GS)	
Type	6FA, 60 Hz
TIT (°C)	1316
Pressure ratio	16.5
DP at compressor inlet (kPa)	1
DP at turbine outlet (kPa)	4
Steam turbine (COMPR)	
HP stage	3.43 MPa/435°C, Isentropic efficiency: 85%
MP stage	2.5 MPa/383°C, Isentropic efficiency: 80%
LP stage	0.45 MPa/202°C, Isentropic efficiency: 75%
Condenser (heater)	Pressure: 0.0042 MPa
Deaerator (mixer)	Pressure: 1.2 MPa Outlet temperature: 104°C
PSA H_2 recovery ratio (SEP)	88%

(1) The Aspen model of the coal gasification island was used to generate the raw syngas parameters (composition, temperature, pressure, and flow rate), which was used as the input of the raw syngas cooling section. The results of the syngas cooling section were taken as the input parameters for the ASPEN PLUS model of the Rectisol process.
(2) The ASPEN PLUS model of the Rectisol process was used to calculate the conditions of clean syngas and of the other flows and the values needed to calculate energy balance of the whole plant (cold, heat, and electricity duty).
(3) The ASPEN PLUS model of the fuel synthesis/refinery island was simulated with the gas composition given by Rectisol as input. The model of the synthesis island calculated the production of fuel available for export and also gave the conditions (composition, temperature, pressure, and flow rate) of the tail gas. The simulation of CO_2 removal/LPG recovery was optional depending on the case studied. By the way, the utilities consumption, by product flow, can be determined by ASPEN PLUS simulation.
(4) The GS model of gas turbine was used to predict the performances of the gas turbine, which can determine the syngas fired gas turbine power output, component performances, exhaust parameters, and cooling information. The flue gas parameters were the input of HRSG and be transferred to ASPEN PLUS simulation.
(5) The ASPEN PLUS model of HRSG and steam turbine were used to balance steam and heat of the integrated system. This final calculation took into account syngas cooling, the Rectisol process, the fuel synthesis/refinery island, the HRSG side, the sulfur recovery section, and other heat or power requirements by auxiliary systems.

3 Low-Temperature Slurry Reaction for Iron Based FT Synthesis

3.1 Characteristics and Adaptability. Fe catalysts has WGS activity, which make it possible to use low H_2/CO coal derived syngas without shift reaction. LT slurry reactors are designed for high FT wax production and low methane production. Compared to other types of reactors, it offers the advantages of better temperature control, lower catalyst loading, lower catalyst attrition rates, higher conversions to products, and lower cost. Owing to these advantages, the system studied in this paper is focused on a LT slurry reactor based on a precipitated promoted iron catalyst.

FT yield information is important to co-production system simulation. Product distributions and selectivity are influenced by catalyst type, catalyst composition, reactor type, temperature, feed gas composition, GHSV, and pressure. Various models have been proposed [15,18,19], including lump model, detail mechanism kinetics model and products distribution model.

A correlation model based on Mobil's two step pilot plant [15] is adopted. This model proposes triple chain-length-dependent chain growth factors so as to interpret the deviation from ASF law. It sets up correlations among reaction temperatures with wax yield, methane yield, and C_2-C_{22} paraffin and olefin yields. Oxygenates in hydrocarbon, water, and vapor phases are also correlated with reaction temperature. It can show the effect of temperature on products' selectivity and distribution. Because this correlation relies heavily on the Mobil bench result, it can coincide with Mobil results preciously. It is suitable for iron catalyst based slurry bed, especially under the condition $H_2/CO=0.5-2.0$, pressure=20–25 bar, and temperature=240–275°C. In original model, the ratio of olefin and paraffin, is fixed to 0.7. But in fact, this ratio will vary with carbon length. In this paper, the ratio is adjusted according to the reference data [17,20].

It should be noticed that the operation condition studied in this paper is limited to the valid range of this model. Considering FT relies heavily on catalysts and reactor, the results obtained, including liquid yield and tail gas parameters, are valid for the co-production system with the FT technique referenced by this paper.

3.2 Results Validated. Three cases (Table 3) at different operation conditions were investigated so as to compare results with that of Refs. [7,17,20]. Comparison results were shown in Figs. 3(*a*)–3(*f*). In Figs. 3(*a*)–3(*d*), the *Y* axis means actual mass flows. In Figs. 3(*e*) and 3(*f*), because of high inlet inert compositions, the *Y* axis means mass changes of each component caused by reaction. Compared with reference data, the prediction errors of C_{5+}

Downloaded 02 Jun 2010 to 171.66.16.107. Redistribution subject to ASME license or copyright; see http://www.asme.org/terms/Terms_Use.cfm

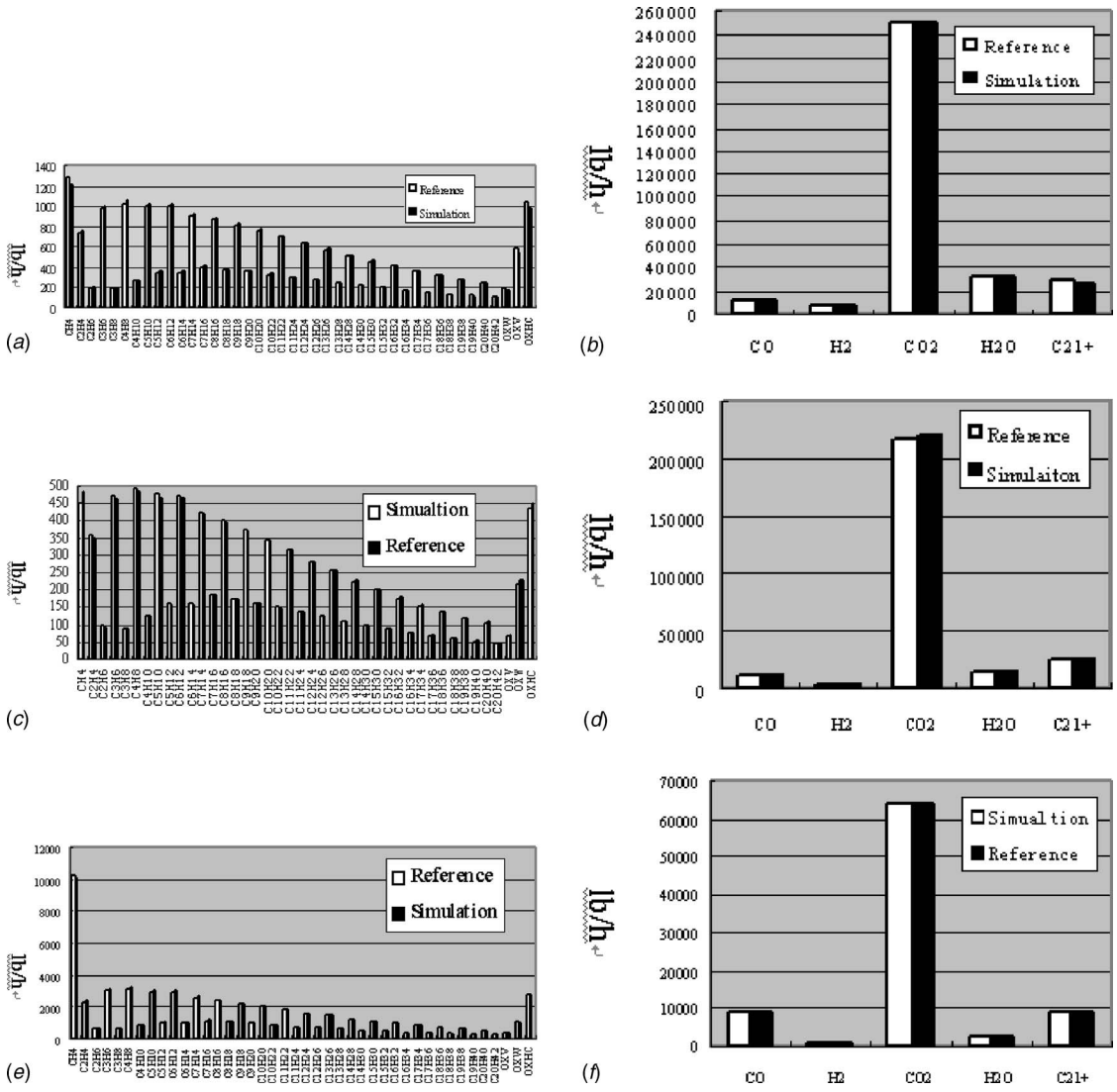

Fig. 3 (*a*) **Reactor outlet stream: (C_1-C_{20} olefin and paraffin, oxygenates (OXV,OXW,OXHC); coal derived syngas (TEXCO gasification); (*b*) Reactor outlet stream: ($CO, H_2, CO_2, H_2O, C_{21+}$); coal derived syngas (TEXCO gasification), (*c*) Reactor outlet stream: (C_1-C_{20} olefin and paraffin, oxygenates (OXV,OXW,OXHC); black liquor derived syngas; (*d*) Reactor outlet stream: ($CO, H_2, CO_2, H_2O, C_{21+}$): black liquor derived syngas; biomass derived syngas; (*e*) Reactor outlet stream: (C_1-C_{20} olefin and paraffin, oxygenates (OXV,OXW,OXHC); Biomass derived syngas (*f*) Reactor outlet stream: ($CO, H_2, CO_2, H_2O, C_{21+}$); biomass derived syngas**

Table 3 Feedstock parameters

	Temperature (°C)	Pressure (bar)	H_2/CO (Vol)
Coal derived syngas [17]	240	25	0.78
Black liquor derived syngas [20]	260	30.67	1.1
Biomass derived syngas [7]	253	20.9	0.515

	Mass flow (lb/h)						
CO	H_2	CO_2	H_2O	N_2	CH_4	C_2H_4	$C_{10}H_{20}$
184,000	10,350	87,460	9560	2706	221	0	0
280,452	22,271	80,315	1	39,955	7121	0	0
84,520	3135	17,318	6020	182	15,227	10,817	21

Downloaded 02 Jun 2010 to 171.66.16.107. Redistribution subject to ASME license or copyright; see http://www.asme.org/terms/Terms_Use.cfm

Table 4 Raw syngas (after water strip parameters)

Molar fraction (%)						
CO	H_2	CO_2	H_2O	N_2+AR	CH_4	H_2S+COS
18.7	14.5	7.1	58.9	0.245	0.0206	0.52

Table 5 Utilities consumption results

	Amount (E_{th}) (MW)	Electricity needed[a] (MW)
Heat duty	3	—
Cold duty 1	2	0.24
Cold duty 2	0.77	0.28

[a]COP is scale down by a factor of 0.7 to that of the theoretical carnot cycle.

olefin and paraffin were less than 3%. To light gas, CO, CO_2, H_2, H_2O (V), the errors were less than 2%. For coal derived syngas (entrained bed gasification), the largest prediction error was 4.5%. OXW prediction error of the black liquor case was the largest among all data, about 7.5%. Error analysis showed that this simulation can be used in system simulation and analysis.

4 Simulation Results

4.1 Raw Syngas Cooling Section (Cases 1.0–1.1, Cases 4.1–4.3). At coal feed mass flow (21.9 kg/s), the syngas from the gasification island was at a temperature of 216°C, pressure 3.76 MPa, and mass flow 88.203 kg/s (wet basis). Its other parameters were shown in Table 4.

4.2 Acid Gas Removal Section (Cases 1.0–1.1, Cases 4.1–4.3). An acid removal flowsheet can be found in Ref. [12]. Heat duties and cold duties determined by ASPEN PLUS simulation were shown in Table 5. After acid removal, the molar fraction of H_2S+COS was 0.1 ppm and the CO_2 molar fraction was 4.4%.

4.3 FT Synthesis/Refinery (Separation, Hydrocrack, Hydrotreating, Isomerization, H_2 Production). The stream connections of the FT synthesis/refinery island were shown in Fig. 4. The main results were labeled on it. Clean syngas was heated up to 235°C before entering the FT reactor. This stream passed through the reactor only one time. At 250°C/3 MPa, 94.3% of the total inlet of CO was converted [17]. Hydrocarbons with different carbon number, CO_2, and oxygenates were produced. In the hydrocarbon separation process, wax, heavy fraction synthetic oil, and light fraction synthetic oil were separated and fed to the upgrading section [7], in which final products—diesel and naphtha—were obtained. Oxygenates contained in vapor, hydrocarbon, and water were recovered or discharged. Tail gas containing unconverted gas (CO, H_2) together with CO_2, and light hydrocarbon (CH_4, C_2–C_3) were sent to the humidifier or CO_2 removal/oil wash units. Syngas was utilized to generate electricity. H_2 was needed in the raw liquid upgrading section. A small portion of clean syngas [7] was used to produce H_2. Syngas was converted to H_2 and CO_2 by way of high-temperature WGS and low temperature WGS. Then H_2 and other gases were separated by PSA. The H_2 consumption of the refinery plant was given in reference [7].

4.4 Tail Gas Humidification (Cases 1.0–1.1, Cases 2–3, 4.1–4.3). Gas Temperature=160.2°C, Gas Pressure=2.4 MPa (see Table 6).

4.5 Gas Turbine Combined Cycle. In this study, gas turbine characteristics have been modeled on the GE6FA machine, which belongs to the most advanced generation of operating machines now available on the market. The simulation is based on operating parameters and performances reported by GE. A few relevant inputs to the gas turbine model have been fine tuned to achieve the best agreement possible with the overall performance published by GE. Figure 5 showed results of Case 1.1 as an example).

In the co-production system, the gas turbine is fired by Syngas. Since Syngas usually has a lower calorific value than the natural gas or distillate fuel, a larger fuel flow rate is needed to reach a given turbine inlet temperature (TIT) than that needed with a

Table 6 Humidified gas parameters (molar fraction)

	CO	H_2	CO_2	H_2O	CH_4	C_{2+}	N_2+AR
Humidified tail gas	0.051	0.17	0.462	0.273	0.011	0.024	0.01
Humidified CO_2 free tail gas	0.149	0.498	0	0.273	0.031	0.019	0.029

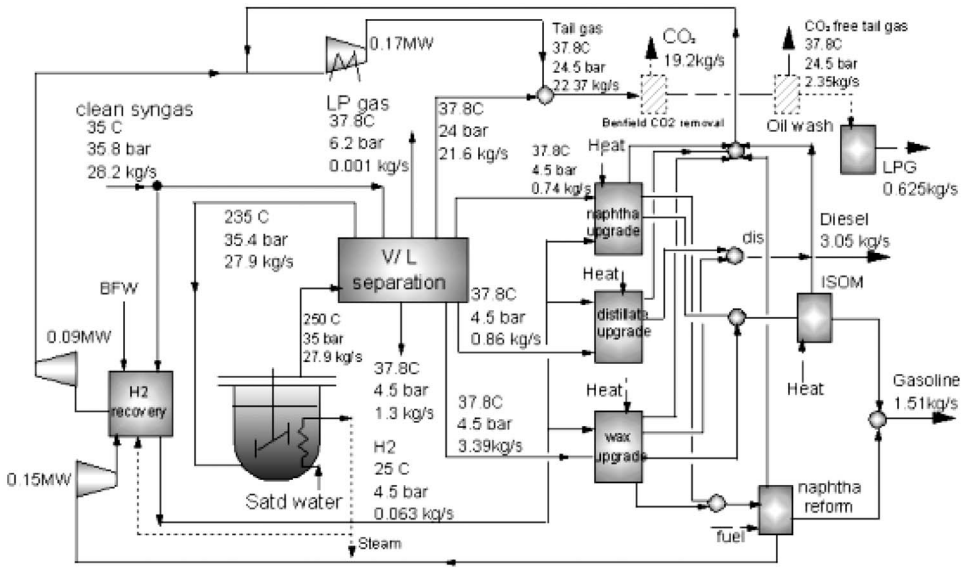

Fig. 4 FT synthesis/refinery island (cases 1.0–1.1, 4.1–4.3)

Downloaded 02 Jun 2010 to 171.66.16.107. Redistribution subject to ASME license or copyright; see http://www.asme.org/terms/Terms_Use.cfm

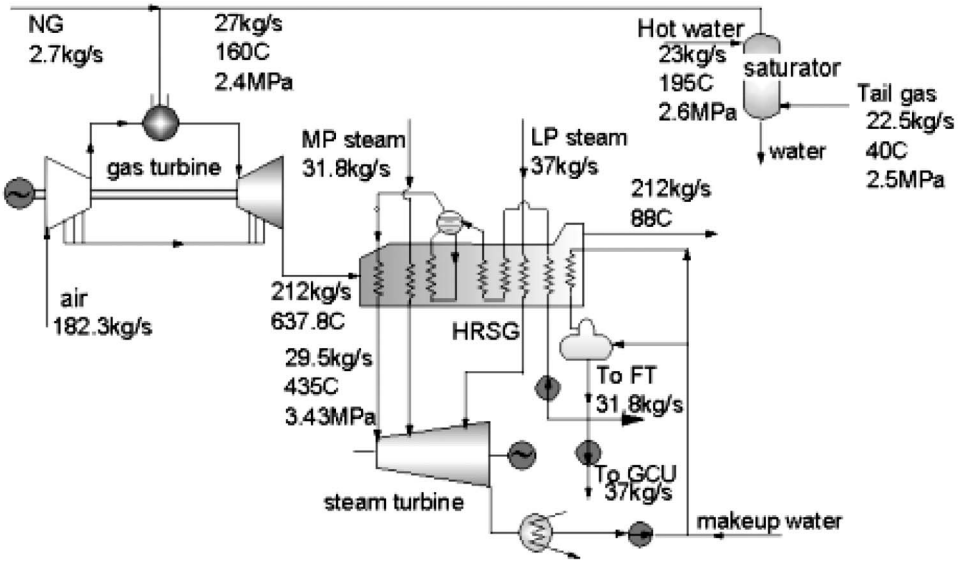

Fig. 5 Gas turbine combined cycle results (case 1.1 as example)

high-calorific-value fuel. The increase in fuel flow rate with Syngas firing, and thus the increase in mass flow through the turbine, affects the match between compressor and turbine operating conditions. Calculations carried out in GS assume [13,14] that the expander operates under aerodynamically choked conditions, i.e., the reduced mass flow of the gas turbine expander is constant. This corresponds to the operating conditions of essentially all commercial gas turbines. Then larger mass flow can be accommodated, in practice, only by increasing the pressure ahead of the turbine, i.e., to increase the gas turbine pressure ratio. Higher pressure ratios move the compressor toward the stall limit, so there is a limit to the mass flow increase that can be tolerated by the gas turbine. In this calculation it was assumed that:

- The TIT is the same as with the natural gas firing;
- The compressor can operate with a compression ratio up to 5% above its value with natural gas; and
- Further increases in fuel flow must be accommodated by reducing the air flow entering the compressor (by simulating the adjustment of inlet guide vanes).

The assumption of no change in TIT implies an increase in turbine outlet temperature (TOT) of 10–20°C and can be justified by considering that by the time the coproduction plant is commercially realized in large scale, TIT and TOT of state-of-the-art gas turbines will be significantly higher than those adopted today. The 5% increase in pressure ratio is within the range typically tolerable by the compressors of heavy-duty engines. Whether such an increase is compatible with lower air flow can only be verified by the gas turbine manufacturer (when air flow is decreased by closing the inlet guide vanes, the compressor stall margin decreases).

Another issue with using Syngas in a gas turbine is that of combustor stability and emissions. These two effects are mainly related to the Syngas chemical composition and heating value. By the way, fuel injector pressure loss characteristics may be substantially different from those realized with natural gas. This effect is related to flow rate. Based on pilot-scale experimental work and operation of gas turbines in IGCC, refineries, and steel plants, as long as the fuel calorific value is above 4–6 MJ/N m^3 combustion stability should not be a major issue. In the system considered here, the humidified fuel fed to the gas turbine has a calorific value around 6 MJ/N m^3 (CO_2 contained), so no particular flame stability problems are envisaged. The increase of pressure loss to be applied can be accommodated either by increasing the fuel pressure (which will increase fuel compression work and thus reduce overall net efficiency) or by increasing the injector cross-sectional area (which requires some extra design work and thus would increase cost). In our calculations the fuel pressure is more than 45% higher than the combustor outlet pressure.

With GS, gas turbine performances were investigated. Results of cases studies were shown in Table 7.

In Case 2, humidified tail gas is used as the fuel of the gas turbine. Due to its lower heating value (6.34 MJ/N m^3), 67.65 kg/s Syngas was needed to fully fuel the 6F gas turbine. Compared with Case 0 (NG fired), it implied evident modification on gas turbine through flow.

One way to solve this problem was to co-fuel the gas turbine by tail gas and supplemental high heating value fuel. The amount of supplemental fuel was determined by the gas turbine, Syngas flow, and composition. In Case 1.1 and Case 4.3, the gas turbine was co-fired by the FT tail gas and supplemental NG. In Case 1.1, 27.03 kg/s humidified tail gas was co-fired with 2.7 kg/s CH_4. The heating value of the mixture fed to the combustor can be increased to 10.82 MJ/N m^3. The inlet air flow of Case 1.1 would increase from 149 kg/s to 204 kg/s. The modification on the NG fired standard turbine was not very difficult. The FT reactor/refinery island and other auxiliary facilities would be 2.5 times smaller than that of Case 2. This may be of more meaning to the co-production system located in a coal mine, where usually abundant mine gas (CMM) resources exist. After the refinery, coal mine gas can be utilized as gas turbine fuel, which is also environmentally friendly.

With CO_2 removal from tail gas, Syngas heating value can be increased. This also provides an alternative way to solve the gas turbine problem. Besides, LPG extraction enhances the capability of coal to FT products. But CO_2 removal and LPG recovery lead to additional energy losses and investment costs. Its economical feasibility was discussed in Sec. 5.2. Results showed that 12.74 kg/s humidified CO_2 free tail gas was needed to fully fire gas turbines (Case 3). 2.96 kg/s CH_4 was needed to co-fire with 3.899 CO_2 free tail gas (Case 4.3).

Cases with various alternatives (humidified or dry fuel, co-firing or not, CO_2 removal or not, methane content in CMM variation) had also been investigated. Results showed that, considering the permitted mass flow and power enlargement of the gas turbine, dry tail gas containing CO_2 is difficult to fully fuel 6F or 6B engines if there is no co-firing. But humidified CO_2 free gas is possible to fully fuel 6F or 6B gas turbines without co-firing. Analysis indicated that feasible methane content ranged from 26%

Downloaded 02 Jun 2010 to 171.66.16.107. Redistribution subject to ASME license or copyright; see http://www.asme.org/terms/Terms_Use.cfm

Table 7 Gas turbine component parameters

	CASE 0 [13]	CASE 1.1	CASE 2	CASE 3	CASE 4.3
Fuel	NG	Syngas	Syngas	Syngas	Syngas
Primary fuel	NG	CH_4 humidified tail gas	humidified CO_2 free tail gas		CH_4
LHV (MJ/Nm^3) (Wet basis)	35.84	6.34	6.34	9.46	9.46
mass flow (kg/s)	4.43[a]	27.03	67.65	12.74	3.899
Temperature	15°C		160°C		
Steam (Vol %)	0		27.3		
Co-firing fuel		CH_4			CH_4
Mass flow (kg/s)		2.7025	0	0	2.9604
Temperature		15°C			15°C
Air (kg/s)	204[b]	182.3	149	199.62	207.7
GT exhaust gas mass flow (kg/s)	208.43[a]	211.82	216.65	212.36	213.9
GT exhaust gas temperature (°C)		637.7	669.7	612	607.8
GT power output (MW)	75.9[b]	90.28	104.78	85.49	80.78
Pressure ratio	15.7[b]	16.55	16.55	16.55	16.55
TIT (°C)	1315.7[a]	1315.7	1315.7	1315.7	1315.7

[a]Simulation results by GS.
[b]Given values of standard gas turbine.

to 100%.

Figure 6 showed the influence of CH_4 content in CMM on gas turbine performance. To humidified CO_2 free tail gas, it can be mixed with CMM with CH_4 contents as low as 22%. But to humidified tail gas, CH_4 content in CMM should be higher than 70%. It is clear that at given TIT, with the increase of CH_4 content, air flow and CH_4 content in mixed fuel increases, while co-firing CMM mass flow decreases. Gas turbine output decreases with CH_4 content increase. This is mainly caused by mass flow decrease. One thing to note is that co-firing CMM mass flow of CO_2 free tail gas cases were slightly larger than that of tail gas cases. This was restricted by the analysis conditions of this paper. Temperature of humidified tail gas or CO_2 free tail gas was kept at 160°C, while CMM remained at 15°C. A large amount of sensitive heat of CO_2 in tail gas makes the mixture temperature about 10°C higher than that of CO_2 free tail gas cases. Higher temperature compensated for the loss caused by dilution.

5 System Performance Summarize

5.1 Overall Mass and Energy Balance of Co-Production System. Table 8 showed the mass and energy balance of six cases. More than 50% of input energy can be converted to electricity and FT products. About 24–50% of the power generated was consumed by ASU and other auxiliary facilities. CMM or CH_4 equivalent to 0–23% of coal thermal energy was provided to the system so as to fully fire the gas turbine. Evaluated by efficiency criteria (1) and (2) defined in Table 8, CO_2 removal or co-firing with higher methane content CMM was favorable at similar production scale. With CO_2 removal, efficiency of Syngas conversion to FT was increased by about six points, but index "Effective FT efficiency" showed the negative effect of CO_2 removal.

5.2 Economic Analysis of Co-production System

Operation hours=8000 h/annual; Location factor=0.65
Interest rate=12%; project lifetime=17 years
Construction time=2 years; production time=15 years
Loan fraction=70%; interest rate on debt=6.39%
Income tax rate=33%; sales tax=5%; interest rate=12%
Depreciation time=15 years; remaining value rate=5%;
exchange rate, EURO€: RMB ¥=1:10

In order to investigate the influencing factors more deeply, an economic analysis was done. The reference capital cost estimates of major plant areas were collected from demonstration plants in

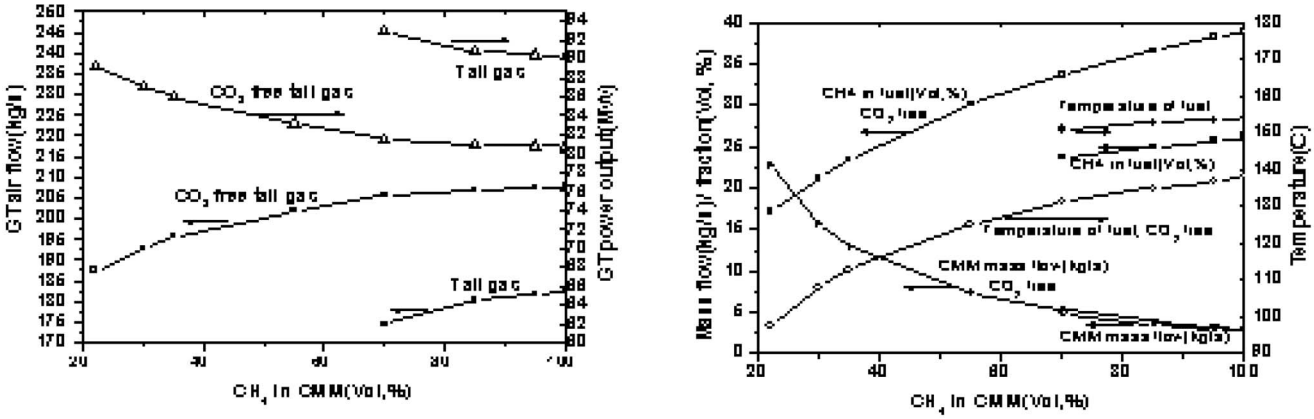

Fig. 6 Effect of CH_4 molar fraction

Downloaded 02 Jun 2010 to 171.66.16.107. Redistribution subject to ASME license or copyright; see http://www.asme.org/terms/Terms_Use.cfm

Table 8 Mass and energy balance of co-production system

	Case 1.0	Case 1.1	Case 3	Case 4.1	Case 4.2	Case 4.3
Coal feed (kg/s, wet basis)	21.91	21.91	69.30	21.91	21.91	21.91
Coal (MW, LHV)	529.34	529.34	1673.9	529.34	529.34	529.34
CMM feed (kmol/s)	0.238	0.165	0.00	0.640	0.265	0.185
CMM methane content (Vol %)	70	99.5		30	70	99.5
CMM (MW, LHV)	133.71	132.73	0.00	154.21	149.07	148.15
FT clean Syngas (MW, LHV)	393.47	393.47	1244.3	393.47	393.47	393.47
FT products (t/year)	134,726	134,726	482,974	152,726	152,726	152,726
FT products (MW, LHV)	206.85	206.85	744.58	235.45	235.45	235.45
E_{th} of diesel (MW, LHV)	133.95	133.95	423.60	133.95	133.95	133.95
E_{th} of gasoline (MW, LHV)	72.9	72.9	230.54	72.9	72.9	72.9
E_{th} of LPG (MW, LHV)	0	0	90.44	28.6	28.6	28.6
FT conversion ratio (%)	52.6	52.6	59.8	59.8	59.8	59.8
Nets sales to grid (MW)	126.26	124.93	106.93	106.59	107.35	107.80
Gas turbine (MW)	92.5	90.06	85.07	86.3	81.47	80.78
Steam turbine (MW)	74.3	74.92	129.68	68.35	68.28	68.24
Gasifier (MW)	3.485	3.485	11.021	3.485	3.485	3.485
ASU (MW)	26	26	82.221	26.	26.	26.
Rectisol (MW)	0.56	0.56	1.771	0.560	0.560	0.560
Oil wash (MW)	—	—	6.129	1.938	1.938	1.938
CMM compression (MW)	3.5	2.2	0	9.42	3.706	2.5
	Fraction of (Coal+CMM) converted to					
FT (diesel+gasoline+LPG)	0.312	0.312	0.445	0.344	0.347	0.348
Exportable electricity	0.1889	0.189	0.064	0.156	0.158	0.159
FT+exportable electricity[a]	0.5009	0.501	0.509	0.500	0.505	0.507
Marginal efficiency of CMM[b]	0.437	0.438	NA[d]	0.455	0.475	0.481
Effective FT efficiency[c]	0.560	0.557	0.522	0.540	0.549	0.552

[a]Efficiency=(FT thermal energy+net electricity output)/(coal thermal energy (MW,LHV)+CMM thermal energy).
[b]Efficiency=(net electricity of co-firing case-equivalent net electricity of non co-firing case at the same coal input)/CMM thermal energy.
[c]Efficiency=FT thermal energy/(coal thermal energy+CMM thermal energy nets electricity/0.43). Based on analysis of Sec. 4, six cases (Table 1) were chosen to analyze system performances.
[d]Na=not available.

China, manufacturers, and the literature. Table 9 listed the final economic results of six cases. Evaluated by economic criteria, these cases were all feasible. The benefit brought about by CO_2 removal and LPG recovery can overcome the drawback of investment and running cost increases. Cases with CO_2 free tail gas corresponded to higher net present values (NPVs). It was advantageous to use lower CH_4 content CMM as the co-firing fuel. Economic performance of Case 3 seemed to be the best among all cases investigated, due to its larger production capability. Its FT products were three times higher than other cases. On the other side, its gross investment was two times higher than other cases. Stable and sufficient financial support was very important to it.

6 Conclusions

(1) More than 50% of input energy can be converted to electricity and FT products. Total yield of gasoline, diesel, and LPG is 136–155 g/NM^3 ($CO+H_2$). At coal feed of 21.9 kg/s, net electricity exported to the grid is higher than 100 MW. Total production of diesel and gasoline (and LPG) is 118,000 (134,000 t)/year. The mass ratio of diesel to gasoline is 2.02. Under economic analysis conditions assumed in this paper, the after tax profits can research 17 million euro. Payback times ranged from 6 to 7 years.
(2) CO_2 removal/LPG recovery is a useful way to improve

Table 9 Economic results

	Case 1.0	Case 1.1	Case 3	Case 4.1	Case 4.2	Case 4.3
Gross Investment, €($\times 10^4$)	19,823	19,981	40,574	21,499	21,738	21,902
Fixed asset investment, €($\times 10^4$)	17,429	17,561	35,896	18,914	19,127	19,273
General cost (average per year), €($\times 10^4$)	5780	5795	1598.8	5946	5969	5985
Profit (average per year), €($\times 10^4$)	2610	2568	6805	2728	2720	2713
Return on sales (ROS) (%)	28.16	27.81	27.38	28.41	28.27	28.16
Return on investment (%)	13.16	12.85	16.77	12.69	12.51	12.39
IRR (%)	17.65	17.34	21.15	17.21	17.03	16.9
NPV, €($\times 10^4$)	8809	8493	27,271	8949	8809	8703
Payback period (year)	6.77	6.85	6.05	6.88	6.92	6.96
Capital yield (%)	16.02	13.91	20.08	15.62	15.43	15.3
Cost of oil production, €($\times 10^4$)	155.5	159.5	265.7	185.5	185.6	185.7

Downloaded 02 Jun 2010 to 171.66.16.107. Redistribution subject to ASME license or copyright; see http://www.asme.org/terms/Terms_Use.cfm

system economical and technical performances. It can help to avoid evident gas turbine modification. Furthermore, advantages brought by it can overcome the disadvantages of energy expenses and cost increase. With CO_2 removal, efficiency of Syngas conversion to FT products is increased by about six points. Cases with CO_2 free tail gas have higher NPVs. Evaluated by economic criteria NPV, co-firing with lower CH_4 content CMM is favorable. But co-firing with higher CH_4 content CMM (or NG) is an important way to fully fuel the 6F gas turbine while avoiding severe modification on the engine. Also it is better when judged by technical criteria.

(3) Considering the permitted mass flow and power enlargement of the gas turbine, dry tail gas containing CO_2 is difficult to fully fuel the 6F or 6B engine without co-firing. Humidified CO_2 free gas is possible to fully fuel the 6F or 6B gas turbine without co-firing. CMM or CH_4 equivalent to 0–23% of coal thermal energy is provided to the system so as to fully fire the 6F gas turbine. Feasible methane content in CMM ranged from 26% to 100%.

(4) Compared with reference data, the prediction errors of FT products; C_{5+} olefin and paraffin, were less than 3%. To light gases: CO, CO_2, H_2, H_2O(V), the errors were less than 2%. Error analysis showed that this simulation can be used in system simulation and analysis. FT simulation indicates that dry FT tail gas contained 30% ($CO+H_2$), 60% CO_2, and 4.2% CH_{5-} light components.

Acknowledgment

The work described in this paper has been carried out the framework of "The National High Technology Research and Development Program of China" and DOE joint project of Princeton University, Politecnico di Milano, Navigant Consulting, Inc.. The authors gratefully acknowledge the support provided through Politecnico di Milano and IET, CAS, as well as the valuable advice, software, and supporting material provided by Professor Consonni, Professor Eric Larson, Professor Sheldon Kramer, Ms. Silvia Napoletano and Dr. Haiming Jin.

Nomenclature

BFW = feed water
C_i = carbon number
DIS = diesel
E_{el} = thermal power of electricity
E_{th} = thermal power of heat
HT = high temperature
ISOM = isomerization
LT = low temperature
NAP = naphtha
OXHC = oxygenates in hydrocarbon phase
OXV = oxygenates in vapor phase
OXW = oxygenates in water phase
Satd = saturated
V/L = vapor/liquid separation
WGS = water-gas shift reaction

References

[1] Chevron, H., 1978, "Process For Base Load And Peak Load Power Generation," Patent No. US4092825.
[2] APCI, 1999, "Gasification Combined Cycle Power Generation Process With Heat Integrated Chemical Production," Patent No. US5865023.
[3] Jahnke, F. C., 2003, "Making Fischer-Tropsch Liquids And Power," Patent No. US20030083391A1.
[4] Sasol Technology Limited, 2003, "Combined Process For Producing Hydrocarbon And Power," Patent No. GB2377452.
[5] Sun, Q., 2006, "One Way To Coproduct Power And Synthetic Oil From Syngas," Patent No. CN176119A.
[6] Bechtel Corporation, Global Energy Inc and Nexant Inc., 2003, "Gasification Plant Cost And Performance Optimization," DOE Report No. DE-AC26-99FT40342: Task 2 Topical Report, Coke/Coal Gasification With Liquids Coproduction.
[7] Bechtel Corporation, 1998, "Aspen Process Flowsheet Simulation Model Of A Battelle Biomass-Based Gasification, Liquefaction and Combined-Cycle Power Plant," DOE Report No. DE-AC22-93PC91029.
[8] Michiel, J. A., and Tijmense, A., 2002, "Exploration Of The Possibilities For Production Of Fischer Tropsch Liquids And Power Via Biomass Gasification," Biomass Bioenergy, **23**, pp. 129–152.
[9] Larson, E. D., 1999, "Biomass Conversion To Fischer-Tropsch Liquids: Preliminary Energy Balances," *Proceedings of 4th Biomass Conference of The Americas*, Aug. 29–Sept. 2, Oakland, CA.
[10] Steynberg, A. P., and Nel, H., 2004, "Clean Coal Conversion Options Using Fischer-Tropsch Technology," Fuel, **83**, pp. 765–770.
[11] Bechtel Corporation, 1999, "Baseline Design/Economics For Advanced Fischer-Tropsh Technology," DOE report No. De-Aczz-91pcgo027.
[12] Botha, M. S., and Benham, C. B., 2003, "Coal-To-Liquids Via Fischer-Tropsch Synthesis," *Proceedings 244 International Technical Conference on Coal Utilization and Fuel Systems*.
[13] Consonni, S., Larson, E., Katofsky, R., 2004, "An Assessment of Black Liquor Gasification Combined Cycles Part A: Technological Issues and Performance Comparisons," Proceedings of the 49th ASME International Gas Turbine & Aeroengine Technical Congress, Exposition and Users Symposium, 14–17 June, Vienna, Austria.
[14] Consonni, S., Larson, E., Kreutz, T., and Berglin, N., 1998, "Black Liquor-Gasifier/Gas Turbine Cogeneration," J. Eng. Gas Turbines Power, **120**(3), pp. 442–449.
[15] Fox, J. M., III, and Tam, S. T., 1995, "Correlation of Slurry Reactor Fischer Tropsch Yield Data," Top. Catal., **2**, pp. 295–300.
[16] Kohl, A. I., 1997, *Gas Purification*, Gulf Publishing Company, Houston, TX.
[17] Summary Report(Coal Gasification Syngas), 2006, "Fischer-Tropsch Synthesis Reactors," personal contact.
[18] Ma, W. P., Ding, Y., 2001, "A Review And A View Of Studies On The Kinetics Of Fischer-Tropsch Synthesis," Natural Gas Chem.l Eng., **26**, pp. 42–46.
[19] Lox, E. S., et al., 1993, "Kinetics of the Fischer-Tropsch Reaction on a Precipitated Promoted Iron Catalyst," Ind. Eng. Chem. Res., **32**, pp. 71–82.
[20] Summary Report(Black Liquor Syngas), 2006, "Fischer-Tropsch Synthesis Reactors," personal contact.

Downloaded 02 Jun 2010 to 171.66.16.107. Redistribution subject to ASME license or copyright; see http://www.asme.org/terms/Terms_Use.cfm

Madhukar R. Mahishi
Mechanical & Aerospace Engineering,
University of Florida,
P.O. Box 116300,
Gainesville, FL 32611-6300
e-mail: mahishi@ufl.edu

M. S. Sadrameli[1]
Department of Chemical Engineering,
University of North Dakota,
Grand Forks, ND 58202
e-mail: ameli@und.edu

Sanjay Vijayaraghavan
Mechanical and Aerospace Engineering,
University of Florida,
P.O. Box 116300,
Gainesville, FL 32611-6300
e-mail: sanv@ufl.edu

D. Y. Goswami
Clean Energy Research Center,
University of South Florida,
4202 E Fowler Avenue,
Tampa, FL 33620
e-mail: goswami@eng.usf.edu

A Novel Approach to Enhance the Hydrogen Yield of Biomass Gasification Using CO_2 Sorbent

Hydrogen yield of conventional biomass gasification is limited by chemical equilibrium constraints. A novel technique that has the potential to enhance the hydrogen yield by integrating the gasification and absorption reactions has been suggested. The method involves gasification of biomass in presence of a CO_2 *sorbent. Ethanol was used as the model biomass compound and CaO was the representative sorbent. Equilibrium modeling was used to determine the product gas composition and hydrogen yield. The analysis was done using ASPEN PLUS software (version 12.1) and the Gibbs energy minimization approach was followed. The effects of temperature, pressure, steam/ethanol ratio, and CaO/ethanol ratio on product yield were investigated. Three case studies were conducted to understand the effect of sorbent addition on the hydrogen yield. Thermodynamic studies showed that the use of sorbents has the potential to enhance the equilibrium hydrogen yield of conventional gasification by* $\sim$19% *and reduce the equilibrium* CO_2 *content of product gas by 50.2%. It was also found that the thermodynamic efficiency of sorbent-enhanced gasification (72.1%) was higher than conventional gasification (62.9%). Sorbent-enhanced gasification is a promising technology with a potential to improve the yield and lower the cost of hydrogen production.* [DOI: 10.1115/1.2747252]

Keywords: biomass, hydrogen, gasification, thermodynamics, sorbent

1 Introduction

In the next decade or two, hydrogen is expected to become a prominent energy carrier for stationary and mobile power generation applications [1,2]. The chemical energy stored in hydrogen can be converted to mechanical energy by combusting in an internal combustion (IC) engine or it can be directly converted into electricity by fuel cells without any carbon emissions and with minimal emission of other polluting gases. At present, the main process for hydrogen production is by catalytic steam reforming of methane [3]. Hydrogen produced from fossil fuel sources significantly contributes to the greenhouse gas emissions and environmental pollution. In order to have environment-friendly hydrogen, it must be produced from renewable resources. A number of different ways of producing renewable hydrogen are being investigated [4]. Of all the resources, biomass holds the greatest promise in the near future [4,5]. Thermochemical biomass gasification has been identified as a potential method for producing renewable hydrogen [6–8].

The authors carried out a basic thermodynamic analysis of biomass gasification in a previous study [9]. In that study, the favorable operating conditions for hydrogen production at thermodynamic equilibrium obtained by gasifying biomass were determined. The gasifier temperature, gasifier pressure, steam-to-biomass ratio (moles of steam per mole of biomass), and equivalence ratio (a measure of air supplied in biomass gasification) were varied over certain ranges and the product gas yield was found by the Gibbs energy minimization approach. It was concluded in the earlier study that steam biomass gasification produces a gas mixture rich in H_2, containing other gases such as CO, CO_2, CH_4, and small amounts of higher hydrocarbons. The highest hydrogen yield occurred at a gasification temperature of 1050 K. Lower temperature caused incomplete gasification thereby producing more hydrocarbons and less hydrogen. Higher temperature reduced the hydrogen yield due to reverse water gas shift reaction. Hence, the highest hydrogen yield has a temperature constraint. The optimum pressure was found to be atmospheric; higher pressures reduced the hydrogen yield while lower pressures did not offer any substantial increase in hydrogen. Hence, pressure too, imposes a constraint on the maximum hydrogen that can be produced from biomass. It was found that the steam-to-biomass ratio can be increased to give higher hydrogen yield, but this was at the cost of supplying extra steam. It was also observed that beyond a certain steam-to-biomass ratio, the hydrogen yield increased only marginally with most of the supplied steam going unreacted. Hence, in order to enhance the hydrogen yield of conventional biomass gasification, it was necessary to find new or improved techniques, which are simple, energy efficient, and inexpensive. The product gas coming out of the gasifier consists of gases other than hydrogen, such as CO, CO_2, and CH_4, and these need to be separated. Hence, the problem of gas separation also needs to be addressed.

In recent years, sorbents (such as calcium oxide) have been proposed to separate CO_2 and thereby increase the hydrogen yield of conventional steam methane reforming (SMR) and coal gasification processes. Hydrogen yield of more than 95% (dry molar basis) has been obtained experimentally in laboratory-scale steam methane reforming process [10]. Apart from high hydrogen yield, sorbent addition also offers other advantages, such as low reaction temperature, easy CO_2 separation, and a potential to lower the capital cost. In theory, the concept of using sorbents can be applied to any carbonaceous fuel, such as coal, heavy oils, biomass, or organic waste.

2 Sorbent-Enhanced Reforming

The concept of producing hydrogen by reforming hydrocarbons in the presence of a sorbent dates back to as early as 1868 [11]. In 1967, Curran et al. separated CO_2 at high temperature using cal-

[1]On sabbatical from Tarbiat Modarres University, Tehran, Iran.

Submitted to ASME for publication in the JOURNAL OF ENGINEERING FOR GAS TURBINES AND POWER. Manuscript received September 5, 2005; final manuscript received December 23, 2006; published online November 2, 2007. Review conducted by Frank Morton. Paper presented at the 2005 ASME International Mechanical Engineering Congress (IMECE2005), November 5–11, 2005, Orlando, FL.

Copyright © 2008 by ASME

Downloaded 02 Jun 2010 to 171.66.16.107. Redistribution subject to ASME license or copyright; see http://www.asme.org/terms/Terms_Use.cfm

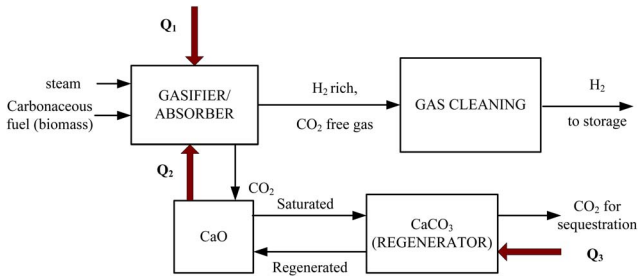

Fig. 1 Concept of sorbent-enhanced biomass gasification

cined dolomite [12]. More recently Balasubramanian et al. [10], Ortiz and Harrison [13] and Peng [14] have experimentally shown a novel method of improving hydrogen yield of conventional SMR and effectively separating CO_2. Lin et al. have proposed an innovative HyPr-RING (hydrogen production by reaction interaction novel gasification) technique that uses sorbents for producing hydrogen by gasification of coal [15–17]. The underlying concept of sorbent enhanced gasification is shown in Fig. 1. There are two main reactors in the process; first is the gasifier/absorber. Here, any carbonaceous fuel (in this case biomass) is supplied to the reactor to which steam is also being fed. The fuel reacts with steam to produce a gas mixture containing hydrogen, carbon monoxide, carbon dioxide, and some hydrocarbons (mainly methane). The carbon monoxide reacts with steam to produce additional hydrogen and CO_2 as per the water gas shift (WGS) reaction

$$CO + H_2O \rightarrow CO_2 + H_2 \quad \Delta H_R = -41.2 \text{ kJ/mol} \tag{1}$$

The calcium oxide sorbent, which is present in the gasifier, absorbs the carbon dioxide produced by the reforming reaction and gets converted to calcium carbonate as per the following reaction:

$$CaO + CO_2 \rightarrow CaCO_3 \quad \Delta H_R = -178.3 \text{ kJ/mol} \tag{2}$$

Heat released during the exothermic CO_2 absorption process is supplied to the endothermic steam gasification of biomass, thereby reducing the net external heat supplied to the gasifier. After some time, all the CaO gets converted to $CaCO_3$. The CaO is then regenerated by heating it in a regenerator (which is the other main reactor used in the process, refer to Fig. 2). The thermal energy for regeneration is supplied either by burning supplemental fuel or burning uncombusted char that remains in the calcium carbonate residue. The hydrogen produced may also have small amounts of impurities, such as carbon monoxide, methane, and tars. Hence, it is passed through a gas cleaning system (consisting of cyclones, filters, and possibly a hydrocarbon reforming catalyst bed) so as to obtain a clean gas that is rich in H_2. Through simultaneous gasification and CO_2 absorption, the equilibrium of the water gas shift reaction is shifted toward H_2. A typical woody

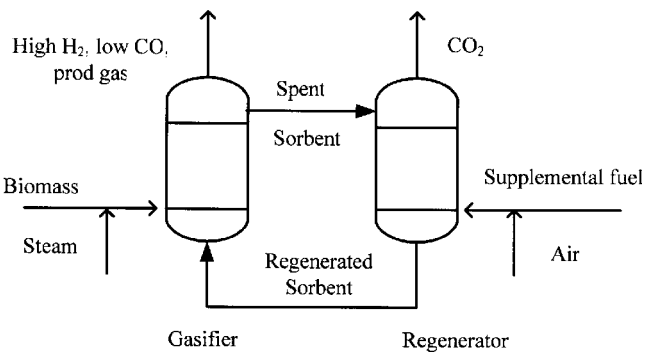

Fig. 2 Schematic of sorbent-enhanced gasification

biomass fuel can be represented as $CH_{1.5}O_{0.7}$ [6]. The reactions taking place in sorbent enhanced gasification for such a fuel can be written as follows:

$$CH_{1.5}O_{0.7} + 0.3H_2O \rightarrow CO + 1.05H_2 \quad \Delta H_R = +74.4 \text{ kJ/mol} \tag{3}$$

$$CO + H_2O \rightarrow CO_2 + H_2 \quad \Delta H_R = -41.2 \text{ kJ/mol} \tag{4}$$

$$CaO + CO_2 \rightarrow CaCO_3 \quad \Delta H_R = -178.3 \text{ kJ/mol} \tag{5}$$

The overall reaction is given by Eq. (6), which represents the idealized sum reaction for sorbent enhanced gasification. Here, the formation of secondary products (methane, coke, and tar) is neglected. The regeneration of spent sorbent is given Eq. (7).

$$CH_{1.5}O_{0.7} + 1.3H_2O + CaO \rightarrow CaCO_3 + 2.05H_2 \quad \Delta H_R = -145.1 \text{ kJ/mol} \tag{6}$$

$$CaCO_3 \rightarrow CaO + CO_2 \quad \Delta H_R = +178.3 \text{ kJ/mol} \tag{7}$$

3 Simulation and Results

Sensitivity studies have been carried out in order to determine the effect of process variables on the equilibrium hydrogen yield. Ethanol was used as the model biomass compound and ASPEN PLUS software was used to model the process flow [18]. The motivation for using ethanol was based on the fact that the physical, thermodynamic, and transport properties for this biomass compound are well documented and are already built into ASPEN database. This makes it convenient to carry out the process simulations. The choice of ethanol as a model compound does not necessarily imply the biomass-ethanol-hydrogen route for producing hydrogen. Ethanol can be produced from renewable resources, such as corn, starch, sugarcane, cellulose, and waste materials from agro industry, using biological or other methods, and this is a subject matter of another study. A unique feature of using ethanol is that the biomass-ethanol-hydrogen systems are nearly CO_2 neutral. However, the availability of data and convenience of modeling a known process feed were the major factors behind choosing ethanol as the model biomass compound.

Broadly, three cases were analyzed as under:

- base case (no sorbent)
- reforming with sorbent in the reformer
- reforming with sorbent in the water gas shift (WGS) reactor

The process variables studied were temperature, pressure, steam/ethanol ratio, and CaO/ethanol ratio.

3.1 Case I: Ethanol Reforming (Base Case). The general reforming reaction between ethanol and steam can be written as

$$C_2H_5OH + H_2O \rightarrow \text{Products} \tag{8}$$

According to the thermodynamic considerations and experimental testing of ethanol steam reforming over Cu/Ni catalyst at temperatures above 600°C, the main products evolved are CH_4, H_2O, CO_2, CO, H_2, and solid carbon, C [19]. There are also trace amounts of ethylene and acetaldehyde. However, in the simulations, the concentration of products with two carbon atoms is found to be negligible compared to other products.

Referring to the simulation flow sheet in Fig. 3, ethanol and water are mixed (in MIXER) and heated (in HEATER) to a temperature of 700°C. The products are then sent to a Gibbs reactor (REFORMER), which is at the same temperature as HEATER and is maintained at atmospheric pressure. The reformation reaction yields a mixture of gases that flow into a cooling heat exchanger (COOLER), which is used to recover the waste heat from product

Downloaded 02 Jun 2010 to 171.66.16.107. Redistribution subject to ASME license or copyright; see http://www.asme.org/terms/Terms_Use.cfm

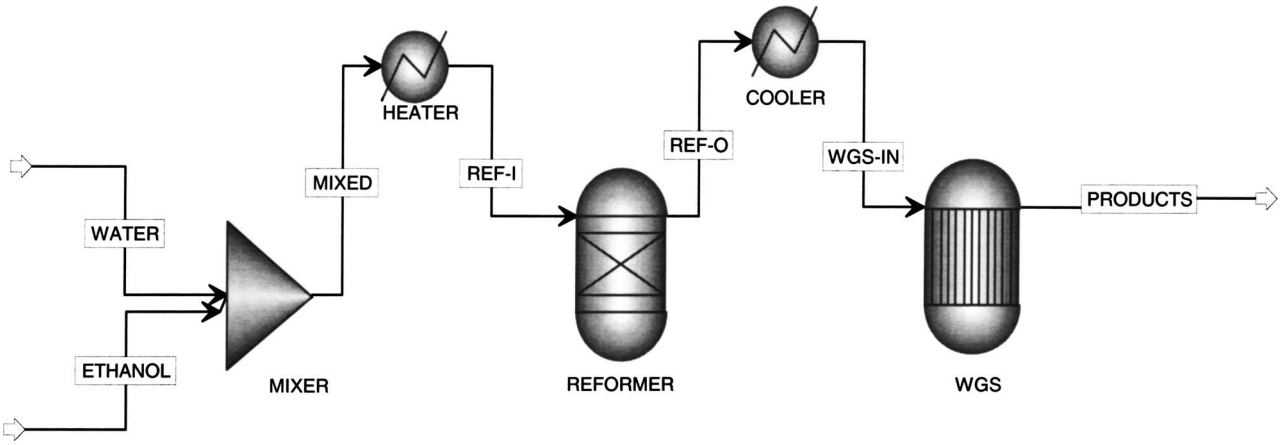

Fig. 3 Simulation flow sheet of conventional ethanol steam reforming (no sorbent) (case I)

gases. The gases then enter the second Gibbs reactor (WGS) in which water gas shift reaction takes place at 300°C to produce more hydrogen as per the following reaction:

$$CO + H_2O \rightarrow CO_2 + H_2 \quad \Delta H_R = -41.2 \text{ kJ/mol} \tag{9}$$

The results of the simulation are given in Table 1. All the gas yields for this case and the next two cases are given in kmols. The ethanol feed is kept fixed at 1 kmol. As shown in the results, the hydrogen yield by reforming is 4.69 kmol/kmol of ethanol feed. The hydrogen yield increases to 4.79 kmol/kmol of ethanol after the water gas shift reaction (WGS outlet). A sensitivity analysis was later carried out.

The steam-to-ethanol molar feed ratio was varied from 3 to 8, the temperature was varied from 500°C to 900°C, and the pressure was varied from 1 atm to 24 atm. The results of the sensitivity analysis are shown in Figs. 4–6. Figure 4 illustrates the effect of temperature on the product yield. The temperature has a significant effect on the equilibrium concentration of the products. As the reaction temperature increases, the hydrogen molar flow rate increases and reaches a maximum at 725°C. At the same temperature, methane yield reduces to a very small value. The increase of hydrogen yield is due to the reaction of ethanol with steam. As temperature increases the hydrocarbons (methane and higher) are reformed and converted to hydrogen. At still higher temperatures (more than 800°C), the water-gas shift reaction starts occurring in the reverse direction. This consumes the hydrogen and CO_2, and hence, the hydrogen yield starts reducing. Figure 5 shows the effect of varying reactor pressure on the product gas composition. It is seen that the steam reforming of ethanol is best done at atmospheric pressure. The effect of steam to ethanol molar ratio is shown in Fig. 6 for a reforming temperature of 700°C. The addition of steam increases the hydrogen yield while reducing the methane and CO yields. Although high steam-to-ethanol ratio is favorable from hydrogen production point of view, it will be limited by the energy cost of the system.

3.2 Case II: Ethanol Reforming With Sorbent in Reforming Reactor. In this case, we analyze the addition of CaO to the steam ethanol reforming process. It is seen in Fig. 7, that CaO is an input to the REFORMER in addition to the ethanol and steam mixture. The following reaction takes place during the reforming process:

$$CaO(s) + CO_2(g) \rightarrow CaCO_3(s) \quad \Delta H_R = -178.3 \text{ kJ/mol} \tag{10}$$

The separation of CO_2 from the gaseous phase will displace the equilibrium of the gas mixture to a higher hydrogen yield and a lower CO concentration. The products from the reformer are the same as case I, in addition CaO and $CaCO_3$ are present. The flow sheet of the simulation is shown in Fig. 7. The reformer products are sent to the separator (SEP) for separation of gases from solids. The gases, which include H_2, CO, CO_2, CH_4, and steam, are cooled to 300°C in the heat recovery exchanger (COOLER) and then enter the WGS reactor. The solids are sent to the regenerator (REGEN) in which $CaCO_3$ is thermally dissociated to CaO and CO_2 at 850°C. The results of the simulation in this case are shown in Table 2. The hydrogen yield in this case is higher than the base case. The total amount of hydrogen produced per kilomole of ethanol feed after the shift reactor is 5.7 kmols, which is almost 19% more than the no sorbent case (case I). The amount of

Table 1 Simulation results for case I

	ETOH	WAT	MIX	REF-I	REF-O	WGS-IN	PROD
Temperature (°C)	25	25	25	700	700	300	300
Pressure (atm)	1	1	1	1	1	1	1
Vapor fraction (-)	0	0	0	1	1	1	1
Molar flow (kmol/h)	1	4	5	5	8.89	8.89	8.44
Mass flow (kg/h)	46.07	72.06	118.13	118.13	118.13	118.13	118.13
Enthalpy (kJ/h)	−292.6	−1129	−1421	−1045	−794.2	−920	−961
H_2 (kmol)					4.69	4.69	4.79
CO (kmol)					1.10	1.10	0.10
CO_2 (kmol)					0.84	0.84	1.53
Ethanol (kmol)	1		1	1	0.00	0.00	0.00
H_2O (kmol)		4	4	4	2.21	2.21	1.84
CH_4 (kmol)					0.05	0.05	0
C_2H_4 (kmol)					0	0	0.19
CH_3CHO (kmol)					0	0	0.00

Downloaded 02 Jun 2010 to 171.66.16.107. Redistribution subject to ASME license or copyright; see http://www.asme.org/terms/Terms_Use.cfm

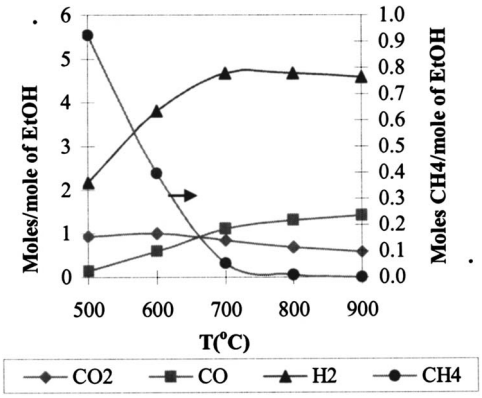

Fig. 4 Effect of reformer temperature on the product yield (steam/EtOH ratio=4, *P*=1 atm, no sorbent)

CO_2 in product gas is reduced from 1.53 kmol to 0.76 kmol due to the absorption by calcium oxide. A sensitivity analysis was later conducted. The temperature, pressure, and steam/ethanol ratio were varied over a wide range, and the product yield was determined as in case I.

The effect of temperature on the product yield is shown in Fig. 8. At temperatures lower than 750°C, the hydrogen production is greatly enhanced by the separation of CO_2; above this temperature the molar flows are similar to the previous case, meaning that the CO_2 separation reaction is no longer effective. Because of the exothermic nature of CO_2 separation reaction, it is favorable to operate at lower temperature. Hydrogen production is maximum at 650°C, which is approximately 100°C lower than the base case.

The effect of pressure on the product yield is shown in Fig. 9. Similar to the base case, operating the reactor at high pressure is not desirable due to the decrease in hydrogen yield. The steam/ethanol ratio is varied from 3 to 8. This ratio greatly enhances the steam reforming of ethanol in the presence of CaO. Figure 10 shows the results of varying this ratio at 700°C and atmospheric pressure.

The results are similar to the base case with higher amounts of hydrogen (~10%). Finally, the effect of varying the amount of sorbent on the product yield is shown in Fig. 11. The CaO/ethanol ratio of zero corresponds to the base case (no sorbent). As the amount of CaO is increased, it absorbs the carbon dioxide and is converted to $CaCO_3$. The carbon dioxide continues to be absorbed as it is produced until only a small amount (corresponding to equilibrium) remains. Beyond a certain CaO/ethanol ratio, the absorption is not effective. The amount of hydrogen produced increases up to the point where the CO_2 absorption is effective. Beyond that point the increase in hydrogen yield is not significant.

Adding excess CaO is energy inefficient because it simply gets heated and cooled and does not help in CO_2 removal. Hence, it is essential to add only an optimum amount of CaO, as much as needed for removing all or most of the CO_2 from the product gas.

3.3 Case III—Ethanol Reforming With Sorbent in WGS Reactor. This is a variation of case II. Here the sorbent is placed in the WGS reactor, and hence, the water gas shift and CO_2 absorption reactions (both exothermic) take place in the same reactor (Fig. 12). The advantage of having CaO in the WGS reactor instead of REFORMER is that all the carbon oxides get absorbed, and therefore, we get pure hydrogen with only trace amounts of CO and CO_2 in the product gas. The gas may be used in a fuel cell or any other suitable application with minimal cleaning. Table 3 shows the simulation results for this case. It was observed from the results that the hydrogen yield for this case is much less than the hydrogen yield for case II (by almost 13%). It was also observed that the amount of heat energy to be supplied in this case is higher than the base case with only a marginal improvement (3.3%) in the hydrogen yield over the base case.

Although the WGS reactor rejects a large amount of heat, the temperature at which this heat is available is very low (300°C) and, thus, the quality of waste heat is poor. Hence, on the basis of no substantial increase in H_2 yield and much larger energy input than conventional gasification (heat is also supplied for regeneration of spent sorbent), this case was not analyzed further.

4 Energy Studies

An energy analysis was carried out to study the effect of sorbent addition on the hydrogen yield of cases I and II. In order to have a common base for comparison, the process conditions for both cases were kept the same and are given as follows:

Ethanol flow rate	1 kmol/h
Steam flow rate	4 kmol/h
Process pressure	1 atm
Reformer temperature	700°C
WGS reactor temperature	300°C
Regenerator temperature	850°C
CaO flow rate	3 kmol/h

A steam-to-ethanol molar ratio of four was chosen for the analysis. This is the stoichiometric amount of steam required per unit mole of ethanol feed. Higher steam-to-ethanol ratios will give higher hydrogen, but this will be at the cost of additional steam that needs to be supplied to the reformer. A lower steam-to-ethanol ratio would consume less energy, but at the same time, it produces less hydrogen. Hence, the stoichiometric amount was chosen for the analysis to get an idea of the efficiency of ethanol reforming for

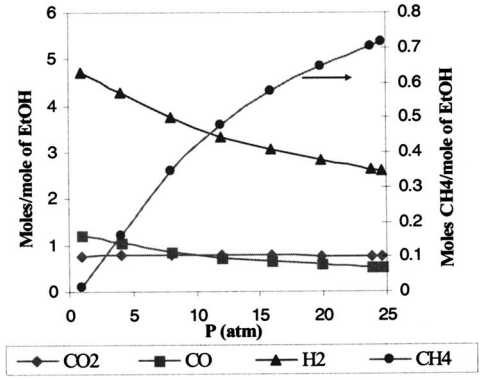

Fig. 5 Effect of reactor pressure on the product yield (steam/EtOH ratio=4, *T*=700°C, no sorbent)

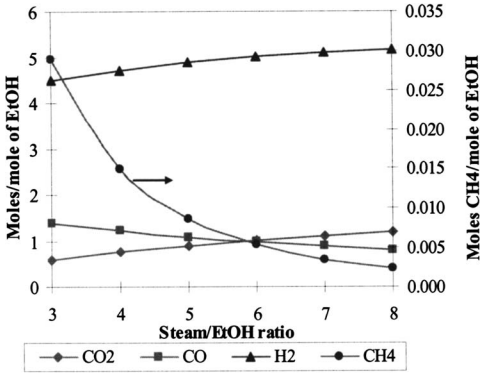

Fig. 6 Effect of steam/EtOH ratio on product yield (*T*=700°C, *P*=1 atm, no sorbent)

Downloaded 02 Jun 2010 to 171.66.16.107. Redistribution subject to ASME license or copyright; see http://www.asme.org/terms/Terms_Use.cfm

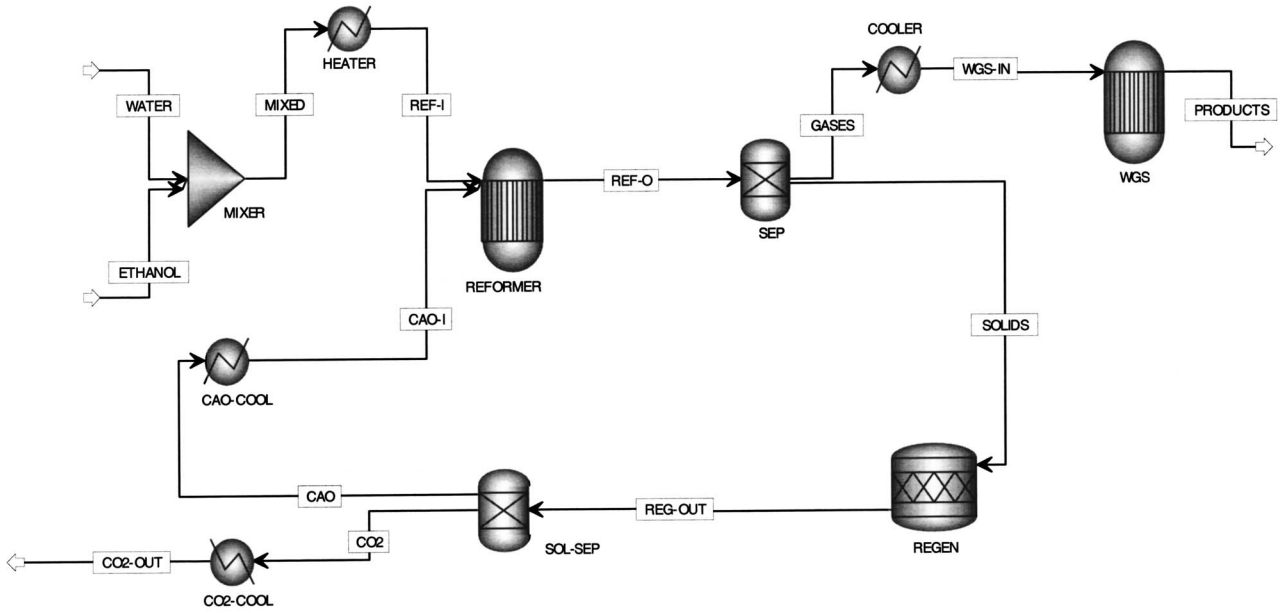

Fig. 7 Simulation flow sheet of ethanol steam reforming with CaO sorbent (sorbent placed in reformer) (case II)

hydrogen production for the two cases. The enthalpy of the various streams was calculated. The first law of thermodynamics was applied to all the reactors and heat exchangers, and the heat duty was then calculated. The product gas composition and the heat duties of the different reactors for the two cases are given in Table 4. The thermodynamic efficiency is then calculated as per the following definition:

$$\eta = \frac{\text{Energy Output}}{\text{Energy Supplied}} \tag{11}$$

$$\eta = \frac{\text{Lower Heating Value of Product gas}}{\text{LHV of biomass} + \text{External heat supplied}} \tag{12}$$

Here, the external heat supplied includes the following:

- heat input to the HEATER (used to produce steam-ethanol vapor mixture)
- heat input to the REFORMER
- heat input to the regenerator (REGEN) (applicable to sorbent case only)

The lower heating value of product gas is calculated as follows:

$$\text{LHV of gas} = n_{H_2} * \text{LHV}_{H_2} + n_{CO} * \text{LHV}_{CO} + n_{CH_4} * \text{LHV}_{CH_4} \tag{13}$$

Table 4 gives the product yield and heat duty of the different reactors. Table 5 gives the values of the input and output energies and the thermodynamic efficiency for the two cases. From Table 4, we observe that using sorbents increases the equilibrium H_2 yield of conventional gasification by about ~19% and reduces the equilibrium CO_2 content of product gas by 50.2%. It is also observed that the heat duty of the REFORMER is reduced by 42% as compared to conventional gasification.

5 Discussion of Results and Practical Considerations

The three case studies compared the effect of conventional ethanol reforming (case I) to sorbent-enhanced steam ethanol reforming when the sorbent was placed in the REFORMER (case II) and when it was placed in the WGS reactor (case III). The sensitivity studies showed that the hydrogen yield for case II is higher than case I for all temperatures in the range of 500–700°C. The CO_2 absorption reaction is exothermic, and if this reaction takes place in the reformer, it can supply heat in situ to the endothermic

Table 2 Simulation results for case II

	CAO-1	EtOH	GAS	MIX	PROD	REF-I	REF-O	SOL	WAT	WGS-I
Temperature (°C)	25	25	700	25	300	700	700	700	25	300
Pressure (atm)	1	1	1	1	1	1	1	1	1	1
Vapor fraction (-)	0	0	1	0	1	1	1	0	0	1
Mole flow (kmol/h)	3	1	7.83	5	7.80	5	10.83	3	4	7.83
Mass flow (kg/h)	168.2	46.1	69.9	118.1	69.9	118.1	286.4	216.5	72.1	69.9
Enthalpy (kJ/h)	−2006.4	−292.6	−418	−1421	−543	−1045	−2842	−2466	−1129	−502
H_2 (kmol)			5.28		5.70		5.28			5.28
CO (kmol)			0.58		0.09		0.58			0.58
CO_2 (kmol)			0.29		0.76		0.29			0.29
Ethanol (kmol)		1	0	1	0	1	0			0
H_2O (kmol)			1.65	4	1.19	4	1.65		4	1.65
CH_4 (kmol)			0.04		0.05		0.04			0.04
C_2H_4 (kmol)			0		0		0			0
CH_3CHO (kmol)			0		0		0			0
CaO (kmol)	3		0		0		1.90	1.90		0
$CaCO_3$ (kmol)			0		0		1.10	1.10		0

Downloaded 02 Jun 2010 to 171.66.16.107. Redistribution subject to ASME license or copyright; see http://www.asme.org/terms/Terms_Use.cfm

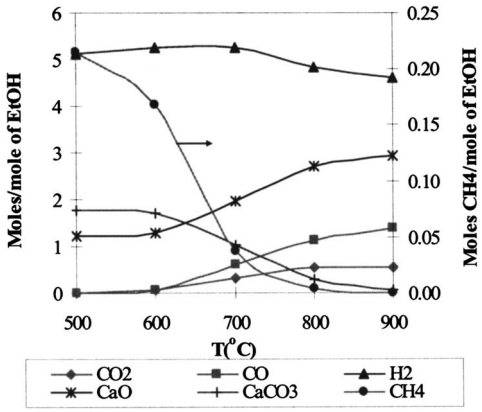

Fig. 8 Effect of reformer temperature on product yield (steam/EtOH=4, P=1 atm, CaO/EtOH=3)

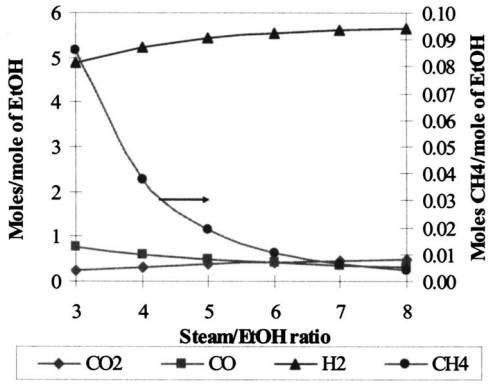

Fig. 10 Effect of steam/EtOH ratio on the product yield (T =700°C, P=1 atm, CaO/EtOH=3)

ethanol reformation process. Hence, the net external heat required by the reformer is reduced. We saw in the energy and efficiency calculations that the reformer heat duty was reduced by 42% for case II as compared to case I. The reduced heat duty implies a compact reformer, and this would mean a reduction in the capital cost. If the exothermicity of the CO_2 absorption matches the endothermicity of ethanol reforming, the reformation step can become adiabatic. It was also observed in the sensitivity studies that the product gas has less CO and CO_2 in case II as compared to the conventional reforming of case I. If the sorbent can absorb all the CO (through water gas shift reaction) and CO_2, and reform the hydrocarbons in the product gas, many expensive downstream equipment, such as a WGS reactor and pressure swing adsorption unit, may not be needed (this is possible if all the CO first gets converted into CO_2 by the shift reaction, and later, all CO_2 is absorbed by the CaO sorbent). These would be replaced by a single reactor (regenerator) and less expensive gas cleaning equipment, such as cyclones, filters, and electrostatic precipitators for removing the residual impurities. Therefore, there is a potential to reduce the capital cost of hydrogen production by using sorbents. Hence, considering the improvement in hydrogen yield, in situ heat transfer in the reformer, and the possibility of reducing the capital costs, case II is better than case I.

In case III, the sorbent is placed in the WGS reactor, which is operated at 300°C. It is observed, in this case, that the product gas is rich in hydrogen without any CO or CO_2. This happens due to the sorbent, which is now placed in the WGS reactor, and it absorbs all the carbon oxides. In actual practice, however, it is observed that the kinetics of the CO_2 absorption reaction is very slow at temperatures below 500°C [20]. The kinetics of the reaction is most favorable in the temperature range 550–700°C. Although the case is theoretically attractive, from a practical standpoint there would be lot of carbon oxides in the product gas with either the same or marginal improvement in hydrogen yield as compared to case I. In case III, the heat released during the exothermic CO_2 absorption is available at a much lower temperature (300°C) than case II (700°C). This waste heat is of minimal utility as most other processes in the system operate at more than 300°C. Hence, based on the practical considerations and marginal improvement in hydrogen yield, case III was not considered for further study.

Sorbent enhanced biomass gasification has the potential to produce a hydrogen-rich gas stream that is depleted of carbon oxides. However, there are many concerns that need to be addressed for the process to have practical utility and one of them is the sulfur content in biomass feedstocks. Many biomass resources contain small amount of sulfur, which combines with oxygen to produce sulfur dioxide. The sulfur dioxide can further combine with calcium oxide to produce calcium sulfate as per the following reaction:

$$CaO + SO_2 + 0.5O_2 \rightarrow CaSO_4 \quad (14)$$

Hence, in every cycle there will be loss of sorbent. This has to be compensated by make-up sorbent and separation of calcium sulfate from the residue. Tar formation during biomass gasification is another area of concern that needs to be addressed [7,21]. Tars are typically formed at low temperatures (below 400°C) and tend to settle on the catalyst bed typically during reactor startup.

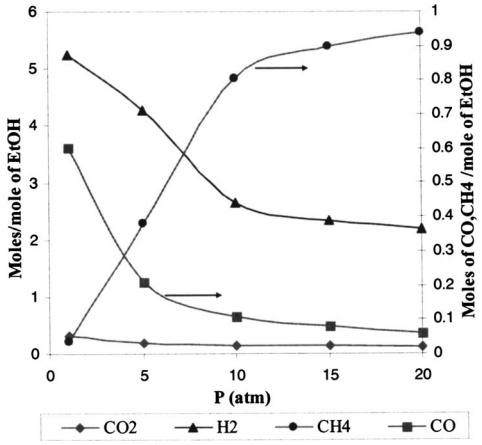

Fig. 9 Effect of pressure on product yield (steam/EtOH=4, T =700°C, CaO/EtOH=3)

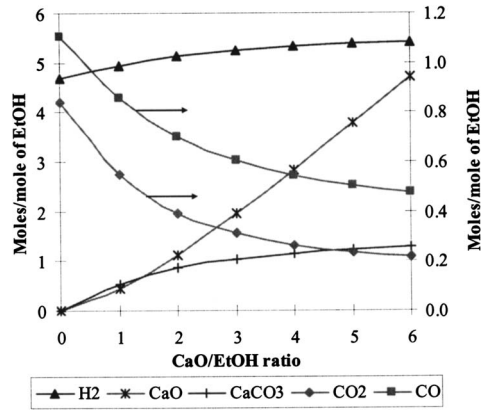

Fig. 11 Effect of CaO/EtOH ratio on product yield (steam/EtOH ratio=4, T=700°C, P=1 atm)

Downloaded 02 Jun 2010 to 171.66.16.107. Redistribution subject to ASME license or copyright; see http://www.asme.org/terms/Terms_Use.cfm

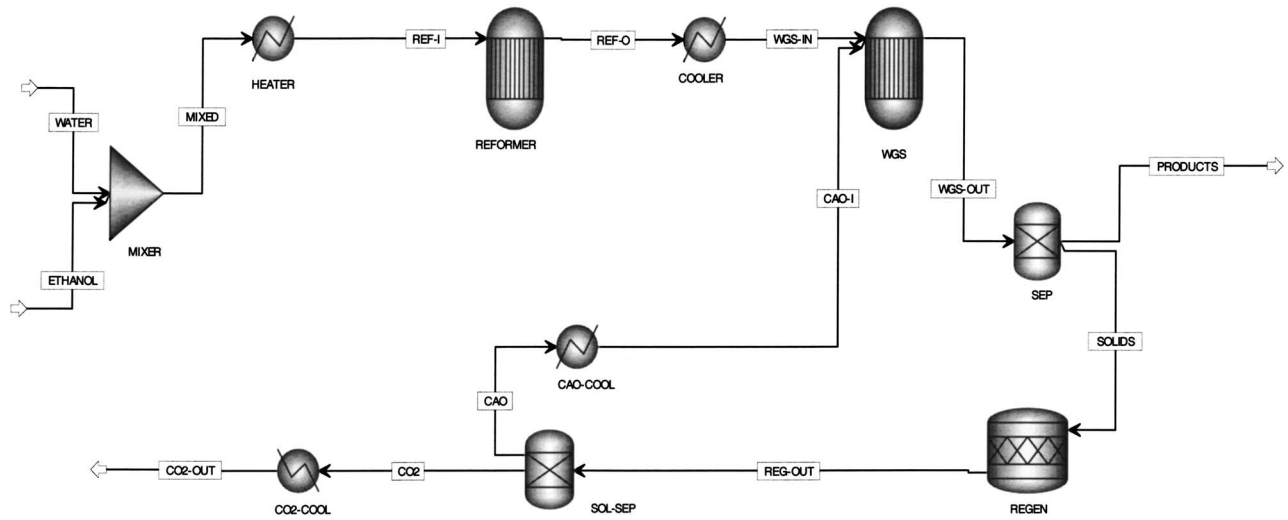

Fig. 12 Simulation of ethanol steam reforming including CaO sorbent (sorbent placed in WGS reactor) (case III)

There is also a possibility of tar deposition on the calcium oxide bed. In the past, some studies on the use of dolomites (calcium and magnesium salts) have shown that they have tar-reforming capability [22]. Calcium oxide is produced from dolomites by calcination followed by removal of magnesium compounds. It is expected that calcium oxide, like dolomites, also has some tar-reforming abilities. However, this needs to be ascertained by actual experimental studies.

In actual biomass gasification systems, the biomass would most likely be in solid fibrous form, such as wood pellets or peanut shells. This has to be mixed with the calcium oxide sorbent. The sorbent may be in the form pellets or in powder form. Powdered sorbent provides more surface area but is prone to attrition and carry over by flow of flue gases. Pelletized sorbent has the advantage of being less prone to carry over; however, it provides less surface area than powdered sorbents. The choice of the physical form of sorbent would also affect the product gas composition and the quantity of make-up sorbent that needs to be added for losses due to attrition and carry over.

The objective of the present work was to conduct a theoretical study on the use of sorbents for hydrogen production from biomass. However, as we have seen above, there are many practical considerations that must be addressed in order to make the sorbent enhanced biomass gasification process a mature technology that is commercially attractive.

6 Summary and Conclusions

Sorbent-enhanced gasification is a novel concept for producing a hydrogen-rich gas from carbonaceous fuels. It has already been demonstrated at the laboratory scale for producing hydrogen by steam methane reforming. In principle, the concept can be applied to any carbon-containing fuel including biomass. The potential advantages of SEG are as follows:

- higher hydrogen yield
- lower operating temperature as compared to conventional gasification
- reduced CO_2 in product gas
- less equipment needed and, thus, reduced capital costs (It is hypothesized that sorbent-enhanced gasification or reforming will require less equipment, due to combination of reactions, than conventional, and hence, there is a possibility of reducing the capital cost.)

Table 3 Simulation results of case III

	CAO-1	EtOH	MIX	PROD	REF-I	REF-O	SOL	WAT	WGS-I	WGS-O
Temperature (°C)	25	25	25.00	300	700	700	300	25	300	300
Pressure (atm)	1	1	1	1	1	1	1	1	1	1
Vapor fraction (-)	0	0	0	1	1	1	0	0	1	1
Mole flow (kmol/h)	3	1	5	6.74	5	8.89	3	4	8.89	6.74
Mass flow (kg/h)	168.2	46.1	118.1	41.7	118.1	118.1	244.7	72.1	118.1	41.7
Enthalpy (kJ/h)	−1881	−292.6	−1421	−251	−1045	−794	−2717	−1129	−920	−334
Mole flow (kmol/h)										
C_2H_4				0		0			0	0
H_2 (kmol)				4.95		4.68			4.68	4.95
CO (kmol)				0		1.10			1.10	0
CO_2 (kmol)				0		0.84			0.84	0
Ethanol (kmol)		1	1	0	1	0			0	0
H_2O (kmol)			4	1.52	4	2.21		4	2.21	1.52
CH_4 (kmol)				0.26		0.05			0.05	0.26
C_2H_4 (kmol)										
CH_3CHO (kmol)										
CaO (kmol)	3			0		0	1.26		0	0
$CaCO_3$ (kmol)				0		0	1.74		0	0

Downloaded 02 Jun 2010 to 171.66.16.107. Redistribution subject to ASME license or copyright; see http://www.asme.org/terms/Terms_Use.cfm

Table 4 Comparison of energy consumption in biomass gasification with and without sorbent

	Case I	Case II
Output yield	(kmol/kmol of ethanol)	
H_2	4.79	5.70
CO	0.1	0.09
CO_2	1.53	0.762
CH_4	0.00	0.05
H_2O	1.84	1.19
Heat Duty	(kW)	
HEATER	+108.6	+108.6
REFORMER	+65.9	+38
COOLER	−33.9	−27.9
WGS	−15.8	−6.7
REGEN	NA	+61.2
CO_2-COOL	NA	−12.4
CAO-COOL	NA	−34.9

Table 5 Thermodynamic efficiency and Heat input

	Case I	Case II
LHV of product gas (kJ/h)	1176.3×10^3	1435.9×10^3
LHV of biomass (kJ/h)	1242×10^3	1242×10^3
Total heat supplied (kJ/h)	628.1×10^3	748.2×10^3
Thermodynamic efficiency	62.9%	72.1%

This paper reports a theoretical study of hydrogen production by steam reforming of ethanol. It was observed that the hydrogen yield substantially improves if the reformation is carried out in presence of a sorbent. This happens due to the equilibrium shifting in favor of hydrogen. Based on the encouraging results obtained from theoretical studies, the authors are conducting an experimental investigation of the process. However, there are some important areas that need to be addressed, chief among them are the following:

- form of sorbent (powder or pellet) and how it is mixed with the biomass feedstock
- sorbent loss due to formation of calcium sulfate
- tar-reforming ability of calcium oxide sorbent
- energy consumed during regeneration
- kinetics of the CO_2 absorption and desorption processes

Acknowledgment

The authors wish to acknowledge that this work was carried out under US DOE Grant No. DE-FG36-04GO14224.

Nomenclature and Abbreviations

EtOH = ethanol/ethanol process stream in ASPEN flow sheet
GAS = "gases" stream in ASPEN flow sheet
LHV_x = lower heating value of species x (kJ/mol)
MIX = "mixed" stream in ASPEN flow sheet
P = pressure (atm)
T = temperature (K)
PROD = "product" stream in ASPEN flow sheet
PSA = pressure swing adsorption
SEG = sorbent-enhanced gasification
SMR = steam methane reforming
SOL = "solids" stream in ASPEN flow sheet
WAT = "water" stream in ASPEN flow sheet
WGS = water gas shift (-)
WGS-I = WGS reactor inlet stream in ASPEN flow sheet
WGS-O = WGS reactor outlet stream in ASPEN flow sheet
WGS = water gas shift (−)
n = number of moles (mol)

Greek

ΔH_R = heat of reaction (kJ/mol)
η = thermodynamic efficiency (%)

References

[1] Larson, E. D., and Katofsky, R. E., 1994, *Advances in Thermochemical Biomass Conversion*, Elsevier, London, pp. 495–498.
[2] Cox, J. L., Tonkovich, A. Y., Elliott, D. C., Baker, E. G., and Hoffman, E. J., 1995, "Hydrogen From Biomass: A Fresh Approach," *Proc. of 2nd Biomass Conference of the Americas*, Portland, OR, National Renewable Energy Laboratory, Golden CO, NREL/CP-200–8098, CONF-9508104, pp. 657–675.
[3] Pena, M. A., Gomez, J. P., and Pierro, J. L. G., 1996, "New Catalytic Routes for Syngas and Hydrogen Production," Appl. Catal., A, **144**, pp. 7–57.
[4] U.S. DOE, "Multiyear Research Development and Demonstration Plan: Planned Program Activities for 2003–2010," U.S. Department of Energy, Office of Energy Efficiency and Renewable Energy, Hydrogen, Fuel Cells and Infrastructure Technologies Program (HFCIT), pp. 1–34, http://www.eere.energy.gov/hydrogenandfuelcells/mypp/pdfs/production.pdf
[5] Bridgwater, A. V., 2003, "Renewable Fuels and Chemicals by Thermal Processing of Biomass," Chem. Eng. J., **91**, pp. 87–102.
[6] Turn, S., Kinoshita, C., Zhang, Z., Ishimura, D., and Zhou, J., 1998, "An Experimental Investigation of Hydrogen Production From Biomass Gasification," Int. J. Hydrogen Energy, **23**(8), pp. 641–648.
[7] Asadullah, M., Ito, S., Kunimori, K., Yamada, M., and Tomishige, K., 2002, "Biomass Gasification to Hydrogen and Syngas at Low Temperature: Novel Catalytic System Using Fluidized Bed Reactor," J. Catal., **208**, pp. 255–259.
[8] Franco, C., Pinto, F., Gulyurtlu, I., and Cabrita, I., 2003, "The Study of Reactions Influencing Biomass Steam Gasification Process," Fuel, **82**, pp. 835–842.
[9] Mahishi, M., Vijayaraghavan, S., Deshpande, D., and Goswami, D. Y., 2005, "A Thermodynamic Analysis of Hydrogen Production by Gasification of Biomass,"*Proc. of ISES 2005 Solar World Congress*, Aug. 6–12, Orlando, American Solar Energy Society, Boulder, CO, Paper No. 1670.
[10] Balasubramanian, B., Ortiz, A. L., Kaytakoglu, S., and Harrison, D. P., 1999, "Hydrogen From Methane in a Single-Step Process," Chem. Eng. Sci., **54**, pp.3543–3552.
[11] Adris, A. M., Pruden, B. B., Lim, C. J., and Grace, J. R., 1996, "On the Reported Attempts to Radically Improve the Performance of the Steam Methane Reforming Reactor,"Can. J. Chem. Eng., **74**, pp. 177–186.
[12] Curran, G. P., Fink, C. E., and Gorin, E., 1967, "CO_2 Acceptor Gasification Process: Studies of Acceptor Properties," *Fuel Gasification*, F. C. Schorda, ed., Advances in Chemistry, Vol. 69, American Chemical Society, Washington, pp. 141–165.
[13] Ortiz, A. L., and Harrison, D. P., 2001, "Hydrogen Production Using Sorption-Enhanced Reaction," Ind. Eng. Chem. Res., **40**(23), pp. 5102–5109.
[14] Harrison, D. P., and Peng, Z., 2003, "Low Carbon Monoxide Hydrogen by Sorption-enhanced Reaction," Int. J. Chem. React. Eng., **1**, Article No. A37.
[15] Lin, S. Y., Suzuki, Y., Hatano, H., and Harada, M., 2002, "Developing an Innovative Method HyPr-RING to Produce Hydrogen From Hydrocarbons," Energy Convers. Manage., **43**, pp. 1283–1290.
[16] Lin, S., Harada, M., Suzuki, Y., and Hatano, H., 2005, "Process Analysis for Hydrogen Production by Reaction Integrated Novel Gasification (HyPr-RING)," Energy Convers. Manage., **46**, pp. 869–880.
[17] Lin, S., Harada, M., Suzuki, Y., and Hatano, H., 2002, "Hydrogen Production From Coal by Separating Carbon Dioxide During Gasification," Fuel, **81**, pp.2079–2085.
[18] Aspentech Inc., 2004, Aspen Plus, version 12.1, User Guide manual, Cambridge, MA.
[19] Cavallaro, S., and Freni, S., 1996, "Ethanol Steam Reforming in a Molten Carbonate Fuel Cell: A Preliminary Kinetic Investigation," Int. J. Hydrogen Energy, **21**(6), pp. 465–469.
[20] Silaban, A., and Harrison, D. P., 1995, "High Temperature Capture of Carbon-Dioxide: Characteristics of the Reversible Reaction Between CaO(s) and CO_2," Chem. Eng. Commun., **137**, pp. 177–190.
[21] Sutton, D., Kelleher, B., and Ross, J. R. H., 2001, "Review of literature on Catalysts for Biomass Gasification," Fuel Process. Technol., **73**, pp. 155–173.
[22] Olivares, A., Aznar, M. P., Cabarello, M. A., Gil, J., Frances, E., and Corella, J., 1997, "Biomass Gasification Product Gas Upgrading by In-Bed Use of Dolomite," Ind. Eng. Chem. Res., **36**, pp. 5220–5226

Downloaded 02 Jun 2010 to 171.66.16.107. Redistribution subject to ASME license or copyright; see http://www.asme.org/terms/Terms_Use.cfm

Flame Propagation Following the Autoignition of Axisymmetric Hydrogen, Acetylene, and Normal-Heptane Plumes in Turbulent Coflows of Hot Air

Christos N. Markides

Epaminondas Mastorakos

Hopkinson Laboratory,
Department of Engineering,
University of Cambridge,
Trumpington Street,
Cambridge, Cambridgeshire CB2 1PZ, UK

Axisymmetric plumes of hydrogen, acetylene, or n-heptane were formed by the continuous injection of (pure or nitrogen-diluted) fuel into confined turbulent coflows of hot air. Autoignition and subsequent flame propagation was visualized with an intensified high-speed camera. The resulting phenomena that were observed include the statistically steady "random spots" regime and the "flashback" regime. It was found that with higher velocities and smaller injector diameters, the boundary between random spots and flashback shifted to higher air temperatures. In the random spots regime the autoignition regions moved closer to the injector with increasing air temperature and/or decreasing air velocity. After a localized explosive autoignition event, flames propagated into the unburnt mixture in all directions and eventually extinguished, giving rise to autoignition spots of mean radii of 2–5 mm *for hydrogen and* 6–10 mm *for the hydrocarbons. The average flame propagation velocity in both the axial and radial directions varied between 0.5 and 1.2 times the laminar burning speed of the stoichiometric mixture, increasing as the autoigniting regions shifted upstream.* [DOI: 10.1115/1.2771245]

Keywords: kernel growth, flame propagation, flame velocity, autoignition, flashback

Introduction

Recently, the inhomogeneous (nonpremixed) autoignition of axisymmetric nitrogen-diluted hydrogen [1,2], acetylene [2] and normal (n)-heptane [2,3] plumes in confined turbulent coflows of hot air has been studied experimentally. Observations and measurements have shown that the emergence of autoignition leads inevitably toward either a full flame establishment or a short-lived flame. The autoignition and postignition combustion phenomena consisted of the following three stages, as illustrated in Fig. 1 with a photomultiplier tube (PMT) trace of global chemiluminescence emission from the hydroxyl radical (OH^*) and simultaneous direct high-speed OH^* images. Initially, an explosive autoignition event (or autoignition kernel) appeared at a well-defined but random location and instant.

Following this, unsteady flamelets propagated into the surrounding high-temperature, unburnt inhomogeneous mixture, whose composition can be characterized by the mixture fraction (ξ) or equivalence ratio (φ). The postignition flames either gradually extinguished in relative proximity to the original point of autoignition ("random spots" regime), or propagated upstream to give rise to a normal fully-fledged nonpremixed flame stabilized on the injector rim if the injection velocities were low enough ("flashback" regime) or to a lifted flame if the velocities were high enough ("lifted flame" regime) [1,2]. It is interesting to explore these phenomena further, particularly the flame propagation phase following localized autoignition since this constitutes a dangerous situation in the premix ducts of lean-premixed gas turbines and may also be relevant in homogeneous charge compression ignition (HCCI) and diesel engines.

Flame propagation in homogeneous mixtures has been investigated extensively in both continuous flow configurations [4] and combustion vessels [5]. In the case of successful forced (spark) ignition of inhomogeneous mixtures, the flame front propagates upstream along the stoichiometric mixture fraction (ξ_{ST}) isosurface as a triple or edge flame depending on the local strain rate, with a speed two to five times the laminar burning velocity of a stoichiometric mixture (S_L) [6,7]. In the case of flame initiation due to autoignition, as in the experiments described here, the initial explosive appearance of the flame, although randomly located in space, occurs at a well-defined (and a priori easily estimated) instantaneous ξ termed the "most reactive" mixture fraction (ξ_{MR}) [8]. As the flame travels, it progresses through regions of inhomogeneous mixture that is chemically "close to autoignition," meaning that it has been reacting in the hot environment and has an evolved radical pool relative to cold/frozen conditions. This may be expected to have an impact in the overall flame speed, and so the edge flame speed in inhomogeneous mixtures following autoignition, as in diesel engines, may be expected to be different from the edge flame speed in spark-ignition situations, as in the ignition of nonpremixed flames in various combustors.

The autoignition of transient diesel sprays in engine combustion chambers has been visualized with high-speed photography [9,10], as has HCCI combustion [11]. In contrast, images of autoignition and subsequent postignition flame propagation of gaseous fuel plumes in any continuous flow apparatus are almost nonexistent. Direct numerical simulations (DNSs) of flame propagation following autoignition in turbulent mixing layers have shown that, following localized autoignition at ξ_{MR}, the flame propagates across the layer with a velocity of the order of (or even slightly less than) S_L [8]. Given the fact that in the simulations the

Contributed by the International Gas Turbine Institute of ASME for publication in the JOURNAL OF ENGINEERING FOR GAS TURBINES AND POWER. Manuscript received June 15, 2006; final manuscript received March 5, 2007; published online December 13, 2007. Review conducted by Dilip R. Ballal. Paper presented at the ASME Turbo Expo 2006: Land, Sea and Air (GT2006), Barcelona, Spain, May 8–11, 2006, Paper No. GT2006-91157.

Copyright © 2008 by ASME

Downloaded 02 Jun 2010 to 171.66.16.107. Redistribution subject to ASME license or copyright; see http://www.asme.org/terms/Terms_Use.cfm

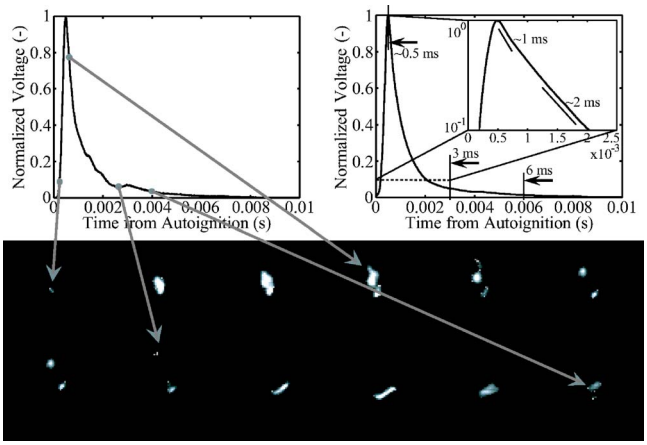

Fig. 1 Top left: Typical instantaneous PMT (with OH* filter) voltage profile of single acetylene autoignition spot. Top right: Average PMT OH* profile (over many as shown on the left). Bottom: Fast OH* image sequence (left to right and top to bottom) taken simultaneously with the PMT measurement shown on the top left at 10 kHz. Flow direction upwards. Reproduced from Markides [2].

mixture surrounding the autoignition kernel is itself chemically evolved, this speed is considered relatively low. More measurements are necessary to improve our understanding of the flame propagation processes in this "premixed phase" of diesel engine combustion.

This work aims to describe the observed operating regimes, to quantify the conditions demarking the onset of flashback, to provide high spatial and temporal resolution images of the flame fronts, and to supply data on the velocity of the flame originating from the autoignition spots. To this end, we have measured the propagation velocities of flamelets following localized autoignition in the case of nitrogen-diluted hydrogen, acetylene, and *n*-heptane plumes injected concentrically into confined turbulent coflows of hot air, with high-speed OH^* imaging.

Experimental Methods

Apparatus. Figure 2 shows the apparatus, which has previously been used to study mixing [12] and autoignition [1–3] in axisymmetric coflows. A detailed description can be found in Markides [2], but in this section we provide a summary of the most relevant points to the aims of this paper.

Compressed laboratory air at a regulated backpressure of 10.0 ± 0.5 bar[1] was filtered, dried, and fed to a Bronkhorst High-Tech digital thermal mass flow controller (MFC). The air MFC has the following technical specifications: an accuracy of ±0.5% of reading plus ±0.1% of full scale and a reproducibility of 0.1% of full scale. The resulting indeterminate (random) uncertainty in the measurement of the air mass flow (m_{air}) is not more than ±1%. Further downstream the air was heated by four low-cost high-temperature inline electrical resistance heaters that were developed in-house. Measurements of the air temperature at the exit of the heaters were employed as negative feedback inputs into proportional-integral-derivative (PID) temperature controllers that were manually pretuned and used to control the voltage supplies to the heaters to minimize temperature gradients and drifts. During the measurements, with a constant preset reference temperature and steady flow of air, the instantaneous deviation of the measured air temperature from the reference never exceeded 1 °C

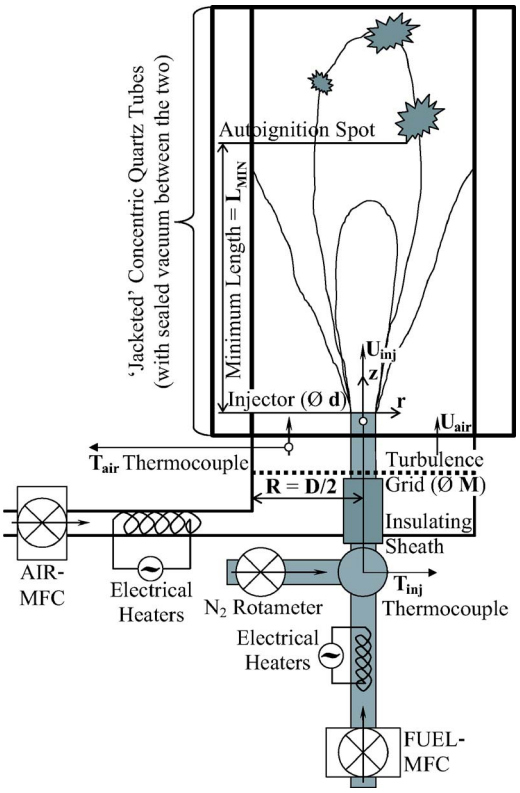

Fig. 2 Apparatus sketch

(obtained with a 0.20 mm diameter, R-type thermocouple wire with a response time constant of ≈0.3 s). After the heaters, a perforated plate of 44% solidity with circular 3.0 mm diameter (*M*) holes was used for turbulence generation, followed by a final section consisting of a 35.0 mm contraction length, designed to inhibit boundary layer growth, promote uniform velocity and temperature conditions, and minimize flow separation and unsteadiness leading into the test section. The main experiment flow section consisted of a vertically orientated 0.50 m long cylindrical quartz tube with inner diameter (*D*) of 25.00±0.03 mm (and inner radius *R*), open to atmosphere. The "jacketed" (two sealed concentric) quartz tube configuration incorporated a preevacuated annular volume to reduce heat losses and maintain uniform temperature conditions in the flow, while providing full optical access and requiring no additional insulation. The complete assembly (excluding the quartz tube) was heavily insulated with a 150 mm thick lagging layer of nonrefractory ceramic blankets along its whole length.

At the inlet of the quartz tube, which was 26 mm upstream of the injector nozzle exit, a twin-bore ceramic-sheathed 0.2 mm diameter bare-wire butt-welded R-type thermocouple was embedded in the wall and protruded by 9±1 mm into the flow, with a horizontal orientation. This was used to measure the bulk air temperature at the inlet (T_{air}). The raw T_{air} reading was corrected for both radiative and conductive heat losses. Typically, the heat loss correction can be broken down into radiative heat losses of 0.2% at low temperatures (≈800 K), increasing to 0.4–0.5% at high temperatures (≈1100 K), and conductive losses of 0.2% at low flow velocities (<20 m/s), increasing to 0.4–0.5% at high flow velocities (>20 m/s). After correction, the reported T_{air} is associated with an indeterminate (systematic) uncertainty of ±0.3% and a determinate uncertainty of ±0.6%. Air with T_{air} up to 1200 K has been utilized for the experiments mentioned in this paper.

Two gaseous fuels were used: hydrogen (99.999% v/v purity) and acetylene (99.6% v/v purity), supplied from compressed cyl-

[1]Quantities are reported to the least significant figure allowed by the uncertainty. Uncertainties are relative and are reported at one significant figure and 95% confidence level (or a confidence interval of two standard deviations (s.d.)).

Downloaded 02 Jun 2010 to 171.66.16.107. Redistribution subject to ASME license or copyright; see http://www.asme.org/terms/Terms_Use.cfm

inders. Their mass flow rates were set and measured with a second Bronkhorst High-Tech digital fuel MFC. The measurement of the fuel mass flow rate (m_{fuel}) has a 1% determinate and (systematic) ±0.8–3% indeterminate uncertainty, the latter decreasing at higher m_{fuel}. In addition to these fuels, *n*-heptane was also used, which is a liquid at room temperature and pressure and was thus prevaporized. A precalibrated positive displacement peristaltic pump and small electric heater were used for this purpose. The capability of the pump to set the mass flow of *n*-heptane is associated with a worst-case error of ±6% for the lowest flow rates, improving to ±4% for the highest.

Nitrogen was supplied from a compressed cylinder (99.9995% v/v purity). Flow rate adjustment and measurement was achieved with a pair of suitably ranged coarse/fine precalibrated rotameters, equipped with pressure gauges at their exits. The pressure and ambient temperature variations were taken into account (by means of their effect on the density) for corrections to the raw indicated flow rates. The total indeterminate uncertainty in the measurement of the mass flow rate of nitrogen (m_{N_2}) is ±6–10%. In the *n*-heptane experiments the fuel MFC was used instead of the rotameters, improving the nitrogen mass flow indeterminate uncertainty to ±3–6%. Intense mixing promoted the thorough dilution of the pure fuel with nitrogen, resulting in diluted-nitrogen fuel mixtures that will be referred to as "diluted-fuel" or "injected stream." The total injected stream mass flow rate (m_{inj}) was equal to the pure fuel plus nitrogen mass flow rates, $m_{inj}=m_{fuel}+m_{N_2}$. In addition, the injected stream dilution will be described by the mass fraction of fuel in the diluted-fuel mixture (Y_{fuel}). The total uncertainty in Y_{fuel} is up to ±5–7% for hydrogen and acetylene, improving to ±3% for *n*-heptane.

The pure or nitrogen-diluted fuel was injected into the quartz tube axially and continuously through a 2.24±0.03 mm inner (d) and 2.96±0.02 mm outer (d_o) diameter stainless steel thin-walled hypodermic tube injector at ambient pressure. The injector was positioned at the centerline of the quartz tube, with the nozzle exit 63 mm downstream of the perforated plate in order to allow the turbulence to develop. For most of its length the injector tube was encased in a 2.0 mm thick-walled ceramic sheath to insulate the fuel from the hot air, keep it at a cooler temperature, and inhibit fuel decomposition prior to injection. A 500 mm long and 0.25 mm diameter stainless-steel-sheathed mineral-insulated K-type thermocouple was placed through the injector all the way to the injection location and allowed for areal time measurement of the fuel stream injection temperature (T_{inj}). It is noted that, in general, T_{inj} in these experiments depended on forced convective heat transfer from the hot coflow air, through the stainless steel injector tube walls, to the fuel flowing inside the injector and ranged from about 600 K to 1100 K, with a ±0.8% uncertainty.

Flow Condition Characterization. Let r denote the radial distance from the centerline of the tube and z the axial distance from the injector. The inlet bulk air velocity (U_{air}) is defined as the cross-sectional volumetric averaged velocity based on m_{air}, the density of air at inlet conditions (T_{air} and ambient pressure), and the annular area defined by the outer injector wall and the inner quartz tube extent ($d_o/2<r<R$), i.e., $\pi/4(D^2-d_o^2)$. To describe the dynamic condition of the air stream at the inlet of the quartz tube we define a turbulent Reynolds number, $\mathrm{Re}_{turb}=u'_{air}L_{turb}/\nu_{air}$. Here, u'_{air} is the root mean square (rms) of the turbulent fluctuations of the axial velocity, L_{turb} the integral turbulent lengthscale, and ν_{air} the kinematic viscosity of air, all at the quartz tube inlet. In the experiments presented in this paper, U_{air} ranged between 10 m/s and 35 m/s (with a total uncertainty of 1.5%) and Re_{turb} between 40 and 200. The injected diluted-fuel stream velocity (U_{inj}) is based on m_{inj}, the flow area of the injector $\pi d^2/4$, and the diluted-fuel stream density at T_{inj} and ambient pressure. The uncertainty in the measurement (and, consequently, setting) of U_{inj} was within ±4% for acetylene and ±6% for *n*-heptane. In this paper, we concentrate on experiments in which U_{inj} was adjusted to attain "equal velocity" flow and mixing conditions. For this requirement, the normalized injection velocity (υ_{inj}), defined as $\upsilon_{inj}=U_{inj}/U_{air}$, was set to be nearly equal to unity, with worst-case deviations of 20%, or $\upsilon_{inj}=1.00\pm0.20$. It is important to note that the injected flow is not a jet, but rather a low momentum release into the coflow. Consequently, the flow field, as well as the resulting plumes, will be momentum-dominated by the background turbulence in the coflow [12].

In this paper, we correlate measurements of the flame propagation phenomena with the reported inlet conditions. This is done based on the understanding that the complete flow field (velocities, temperatures, and scalar mixing) conditions inside the tube during autoignition and combustion can be fully and uniquely described by the aforementioned reported inlet measurements (T_{air}, T_{inj}, U_{air}, υ_{inj}, and Y_{fuel}). To assist future modeling attempts of these phenomena and to inspect the full conditions inside the tube and their relation to the reported inlet variables, we performed cold and hot flow characterization experiments, described collectively by the lack of autoignition/combustion in the tube.

A Dantec constant temperature anemometer system with a 1.25 mm long, 5 μm diameter hot wire was used to measure axial velocities, with and without injected flow, at cold (room) conditions. Aiming to replicate the autoignition conditions as closely as possible, the cold flows were set to exhibit Reynolds number similarity with the hot (autoignition) flows. The injection velocity was then set to achieve equal velocity. Measurements of the local mean axial velocity U showed that the ratio U/U_{air} was about 1.15 in the region away from the injector and quartz tube wall boundary layers ($0.08<r/D<0.42$, $z=0$). From the rms of the fluctuation of the local axial velocity (u'), $u=\langle u'^2\rangle^{1/2}$, the normalized rms intensity u/U at ($r/D\approx0.25$, $z=0$) was 0.14–0.15, decaying to 0.10 by 42 mm downstream. The integral length scale L_{turb} was obtained by integrating over the normalized autocorrelation function of u' and the use of Taylor's hypothesis. At ($r/D\approx0.25$, $z=0$), it was found to be 3–4 mm, i.e., of the order of the grid hole size, increasing by 1 mm in the first 42 mm downstream. Power spectra and probability density functions (pdfs) showed that the coflow was turbulent and near homogeneous, as expected. Radial profiles of U were also taken at representative autoignition temperatures with a high-temperature Pitot tube and thermocouple used in close proximity, the latter to measure the local temperature and hence evaluate the local air density. At these elevated temperatures, the presence of the temperature boundary layer and the finite heat losses to the wall caused the velocity boundary layer to thicken, reducing the region of uniformity to $r/R=0.10$–0.65. Finally, a high-temperature hot wire was employed at a single hot condition ($T_{air}=800$ K and $U_{air}=20.6$ m/s) and single location in the flow ($r/R=0.5, z=0$) to obtain u/U that was found to be between 0.05–0.10.

The local absolute temperature T was measured with a fine 76 μm diameter K-type thermocouple wire (≈0.04 s time constant). In addition, the fluctuations T' were obtained after compensation for the finite time constant of the wire in the frequency domain [2]. The thermocouple measurements have shown that the (local) mean temperature into the tube $\langle T\rangle$ was uniform for $r/R=0.15$–0.60, down to $z=80$ mm. Axially, $\langle T\rangle$ dropped linearly by 10 K in the first 100 mm due to heat losses. The rms of the temperature fluctuations, $\langle T'^2\rangle^{1/2}$, were found to be small relative to $\langle T\rangle$, with values of $\langle T'^2\rangle^{1/2}/\langle T\rangle$ in the range 0.05–0.25%, affirmed both by a high-temperature hot wire and a compensated fine thermocouple. This corresponds to about 0.5–2.5 K. Finally, the normalized cross-correlations of velocity and temperature fluctuations, $\langle u'T'\rangle/U\langle T\rangle$, were small with an indicative value of 5×10^{-6}. The temperature fluctuations were well described by a normal (Gaussian) process.

To simulate and understand the axisymmetric mixing field formed by the continuous, concentric injection of fuel from the

Downloaded 02 Jun 2010 to 171.66.16.107. Redistribution subject to ASME license or copyright; see http://www.asme.org/terms/Terms_Use.cfm

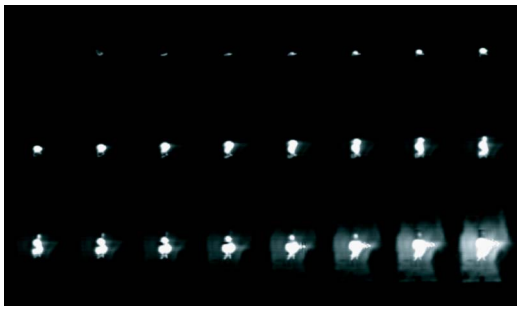

Fig. 3 Acetylene autoignition and flashback. Fast image sequence (left to right, top to bottom) at 13.5 kHz. Conditions T_{air}=809 K, U_{air}=10.4 m/s, υ_{inj}=0.93, $Y_{C_2H_2}$=0.75. Flow direction upwards.

finite-sized nozzle into the confined turbulent air coflows, high-resolution two-dimensional acetone planar laser-induced fluorescence (PLIF) measurements of the conserved scalar ξ were performed at low temperatures (T_{air}=473 K). For an extensive description of these experiments and data on the mixing field in this configuration, see Markides and Mastorakos [12]. Briefly, measurements of the local concentration of the injected fuel were suitably normalized to obtain the ξ field from the relatively close lengths to the source to a downstream distance of about 60–70 mm, or 30d. The two-dimensional scalar dissipation rate χ_{2D} was calculated from the sum of the axial and radial gradients of the measured planar ξ. Measurements of the mean $\langle\xi\rangle$ were consistent with the Gaussian plume equation, with the resulting plumes having Gaussian radial profiles and axial decay in the far field as expected from previous studies. The plumes were initially relatively thin and short, with the $\langle\xi\rangle$=0.1 isocontour occupying radial lengths of $r/d<1.5$ or $r/R<0.15$ and axial lengths along the centerline up to 8d, or 20 mm. The variance $\langle\xi'^2\rangle$ increased to a maximum and then decayed downstream. The rms $\langle\xi'^2\rangle^{1/2}$ normalized by the mean, $\langle\xi'^2\rangle^{1/2}/\langle\xi\rangle$, increased from zero close to the source to a value of about 4 downstream for these equal velocity flows. The above allow one to reason that, initially, the mixing will occur in regions of relatively uniform velocity, but also that downstream the plume will quickly diffuse into the tube. The full, mean three-dimensional $\langle\chi_{3D}\rangle$ was estimated by symmetry, in the mean, along the centerline. This was adequately described by the time scale ratio model, with C_D=2 for axial distances corresponding to a residence time greater than 0.1–0.2 k/ε turbulent time scales and radial distances $r/d<1$, where k is the turbulence kinetic energy and ε its mean dissipation.

Autoignition Achievement. Approximately 1–2 h were required for the heat-up process, during which the apparatus temperature was gradually increased until it reached the desired temperature necessary for autoignition. Steady operation was allowed for about 1 h at the elevated temperature for the apparatus to reach thermal equilibrium. At this stage, fuel flow would be allowed. The fuel and nitrogen flow rates were adjusted to get the desired diluted-fuel composition. With continuous injection of the correct diluted fuel, autoignition would be detected in the tube. However, autoignition was allowed to continue for 1–2 min before any measurement was taken to permit final adjustments and to ensure that transients had decayed and drifts had been minimized. At this point, the raw T_{air}, T_{inj}, and the flow rates of the air, fuel, and nitrogen were recorded.

As previously mentioned, it was found that depending on the conditions, various regimes of operation were possible, including such behavior as random spots and flashback, with the latter being dominant at higher T_{air} and lower U_{air}. The transient, short-lived autoignition-propagation-extinction of a spot, such as the one in

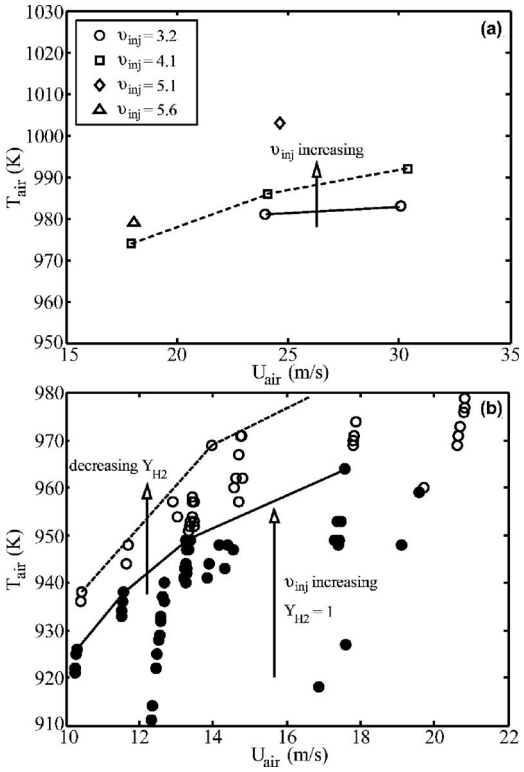

Fig. 4 Temperature-velocity operation envelope limits for hydrogen. (*a*) Y_{H_2} fixed to 0.15. Data points signify transition limit to flashback. (*b*) Filled data points are for Y_{H_2}=1.00, υ_{inj}=3.2–5.6. Empty data points for Y_{H_2}=0.05–0.40, υ_{inj}=0.35–12.6. Data points signify stable random spots behavior. Lines signify a transition limit to Flashback.

Fig. 1, whereby each autoignition event was associated with flamelets that extinguished in relative proximity to the original autoignition site, was only possible in the random spots regime. In contrast, in the flashback regime the flame did not extinguish and propagated upstream with increasing size and intensity. The first appearance of autoignition was quickly followed by the establishment of a fully fledged, large-scale diffusion flame on the injector. Figure 3 shows a typical flashback sequence.

It is interesting to examine the exact conditions for which such behavior is possible. The hydrogen flashback transition is presented in Fig. 4. In Fig. 4(*a*) the data points and lines mark the boundaries of the lowest T_{air} necessary at a particular U_{air} to cause the first instance of flashback (lower bound). Data are shown for four different values of υ_{inj}, as indicated in the legend. For a given dilution then, in this case Y_{H_2}=0.15, the T_{air} necessary for flashback increases with increasing U_{air} and υ_{inj}. In Fig. 4(*b*) below, all the data points indicate the possibility of random spots behavior. For a given U_{air}, increasing T_{air} beyond the limit noted by the solid (for Y_{H_2}=1) or dashed (for Y_{H_2}=0.05–0.40) resulted in flashback. With all else being fixed, the effect of increased dilution is to increase considerably the T_{air} necessary for flashback. Finally, experiments with the smaller injector,[2] d=1.03 mm (not shown), revealed that the possibility of flashback was greatly reduced.

Therefore, in summary, the onset of flashback shifted to higher T_{air} with higher U_{air}, higher υ_{inj}, and smaller d. We now turn our attention to the velocity of propagation of the autoignition spots in the random spots regime. Here, autoignition occurs repeatedly and flamelets exist and propagate, but on a local scale only and in

[2]Recall that the default injector had d=2.24 mm.

Downloaded 02 Jun 2010 to 171.66.16.107. Redistribution subject to ASME license or copyright; see http://www.asme.org/terms/Terms_Use.cfm

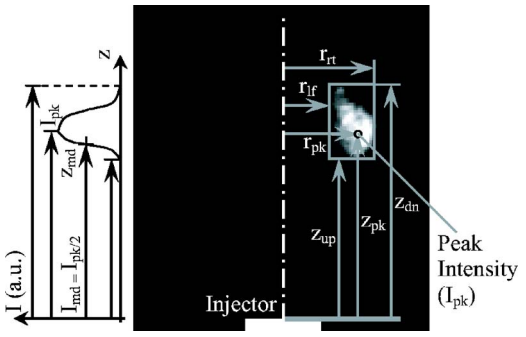

Fig. 5 "Autoignition spot" definitions. Flow upwards. Vectors showing a positive displacement.

close proximity to the original autoignition sites. The short-lived nature of each flamelet due to extinction minimizes the contamination of its observations by other postignition flames.

Measurement, Processing, Analysis, and Calculations. A custom intensified complementary metal oxide semiconductor (CMOS) system, capable of high-speed UV-sensitive imaging, was used to provide fast OH^* chemiluminescence image sequences showing both the process of the explosive emergence of autoignition and of the subsequent unsteady postignition flamelet propagation. It consisted of a 10-bit Phantom v.4.2 CMOS camera and a C9546-04MP46 Hamamatsu intensifier. As with most CMOS cameras, the image size is linked to the potential framing rate. Typically, in this work, 500×100 pixel imaging areas were utilized, allowing frame rates of up to 12 kHz. The intensified CMOS was used with a UV lens and a further OH^* optical filter, band centered at 307 ± 1 nm. The Nikkor lens has a nominal focal length of 105 mm and a maximum aperture of $f/4.5$. It was operated fully open to capture the weak chemiluminescence signals.

Each of the near-instantaneous fast images was examined for the axial and radial locations and extents of the autoignition spots and the "thickness" of the flame fronts. These direct measurements were then used to calculate the absolute postignition velocities of: (i) the longitudinal advection of the spots, (ii) the longitudinal propagation of the upstream flame fronts, and (iii) the transverse propagation of the radial (left and right) flame fronts, originating at the autoignition sites, as described in this section (below). In turn, the absolute velocities were used to estimate the velocities with which the flames propagated upstream relative to the oncoming unburnt flow, which were then compared with the laminar premixed flame speeds at representative conditions and mixture compositions.

At this stage it is useful to define the displacement and velocity variables used in this paper. Figure 5 shows an instantaneous autoignition spot and demonstrates the various lengths based on displacement distances relative to the injector and centerline.

The longitudinal half-size of the spot can be obtained from the difference between the downstream and upstream extents of the spot, $Z_{spot}=(z_{dn}-z_{up})/2$. Similarly, the transverse half-size of the spot is $R_{spot}=(r_{rt}-r_{lt})/2$. The geometric centerline of the spot $(s_{rad}=r_{lf}+R_{spot}, s_{ax}=z_{up}+Z_{spot})$ does not necessarily coincide with the point of peak intensity (I_{pk}), which we denote by (r_{pk},z_{pk}). Nevertheless, we do not expect these two points to be far from each other and, in fact, measurements have shown that in the mean, the point of peak intensity was closer to the injector than the geometric center by less than $0.05\langle Z_{spot}\rangle$. Additionally, we define a measure of the "steepness" of the spot upstream (earliest) flame front intensity or, equivalently, a spot upstream flame thickness, $\Delta=z_{md}-z_{up}$, as the distance between z_{up} and the minimum axial length z_{md} from the injector at which the intensity of the spot reaches half the peak value, $I_{md}=I_{pk}/2$. Absolute longitudinal velocities are defined based on these displacements. The absolute upstream flame front velocity is $U_{up}=dz_{up}/dt$, while the longitudinal advection velocity of the spot can be either $U_{spot}=ds_{ax}/dt$ or $U_{spot}=dz_{pk}/dt$ since s_{ax} and z_{pk} are similar. Here, we choose the latter for reasons that are explained in the "Flame Front and A/Ignition Spot Advection Velocities" section. Relative longitudinal velocities that are used include the velocity of the upstream flame front relative to the oncoming flow, $S_T=U_{up}-U_{air}$. Finally, the (absolute and relative) transverse flame velocity is $V_{spot}=dR_{spot}/dt$.

From separate photomultiplier tube (PMT) measurements, but also directly from the fast image sequences, we know that the standard deviation of the upstream flame front propagation velocity normalized by its mean, lies between 0.2 and 0.6, with 0.4 as a more representative median value. Hence, in order to provide a converged measurement of the mean velocity during a single run of given conditions, to within (say) 10% statistical uncertainty and 95% confidence level, it would be necessary to make measurements from about 70 flames. Furthermore, from the same measurements, it was found that the propagation velocities were a function of the time from explosive autoignition (see Fig. 1, and also Fig. 13). In order to overcome this problem and report on a single value of velocity for each flame we define any propagation velocity as the average distance traveled from the moment of explosive autoignition, i.e., corresponding to the maximum in Fig. 1, to the time the chemiluminescence intensity reaches 5% of its maximum value. Then, to achieve a respectable temporal resolution, we required (on average) at least 20 images per flame. This, together with the condition for converged statistics, translate into a requirement for the evaluation of at least 1400 instantaneous images for a single flame velocity measurement. Clearly, it is difficult to achieve this goal with a manual investigation of the fast image sequences. Here, these actions were performed by an automated process.

A flame tracking script was used to examine the axial and radial flame fronts, as defined in Fig. 5. In the measurements presented here 10,000 images were recorded on average per run (set of conditions). Collectively, for the three fuels tested in this way, about 50 conditions were tested, resulting in $1/2\times10^6$ images that had to be processed for the four distinct longitudinal and three transverse definitions of the flame location. The indeterminate uncertainty in locating the flame front in any image is 5%, corresponding to a velocity of 0.6 m/s. The worst-case determinate uncertainty arising from the arbitrary thresholding applied to differentiate between different spots in the same image, and hence the correct tracking of the same spot throughout its "lifetime," is 2%.

Finally, the measured relative longitudinal and transverse velocities were compared with S_L. The laminar flame speeds of hydrogen, acetylene, and *n*-heptane were obtained with RUN1DL [13], a premixed laminar flame solver with detailed molecular transport, at the supplied conditions and nitrogen dilution, but for stoichiometric air-fuel balance. Detailed chemical schemes were used for all fuels [14–16]. The premixed flame equations in RUN1DL return S_L as a solution to a problem that has a boundary condition of zero reaction rate at the unreacted/cold boundary. This is not strictly so since the high temperatures employed here cause finite reaction rates even before the flame zone and, hence, in the calculations S_L is in principle a function of the location of the flame from the cold boundary. However, a sensitivity analysis showed that S_L did not vary by more than $\pm3-5\%$ due to the location of the flame from the cold boundary.

All data are presented as a function of the minimum autoignition length L_{min}. As demonstrated in Fig. 2 L_{min} is defined as the minimum axial distance from the injector at which autoignition was observed during a run and can be related to other measures of autoignition length [1–3].

Downloaded 02 Jun 2010 to 171.66.16.107. Redistribution subject to ASME license or copyright; see http://www.asme.org/terms/Terms_Use.cfm

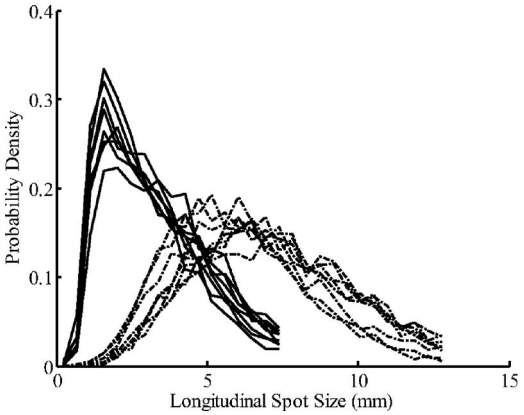

Fig. 6 Pdfs of upstream flame front thickness (solid) and autoignition spot half-size (dash-dot) for *n*-heptane with T_{air} =1100–1140 K, U_{air}=14 m/s, 18 m/s, Y_{fuel}=0.95, and υ_{inj} =1.0–1.2

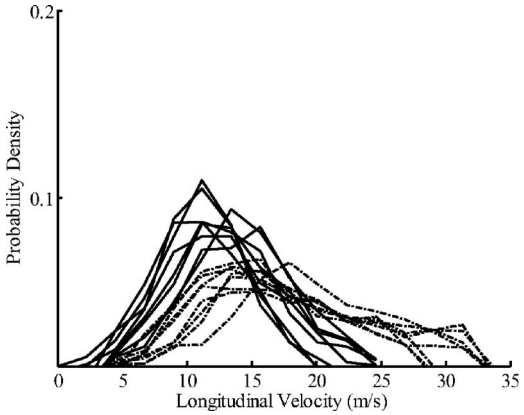

Fig. 8 Pdfs of upstream flame front (solid) and autoignition spot center advection (dash-dot) velocity for *n*-heptane. Conditions as in Fig. 6.

Results and Discussion

Flame Front Thickness and A/Ignition Spot Size. To assess the quality of the measurements we first probe the results for the lengths in Fig. 5, from which the velocities were calculated. pdfs of the longitudinal upstream flame front thickness Δ (solid) and spot half-size Z_{spot} (dash-dot) for *n*-heptane are shown in Fig. 6.

All pdfs are negatively skewed, biased toward the injector, but especially the thickness pdfs. This agrees with the independent finding that the spots occur in bursts [2], such that isolated, independent events of a nominal size are succeeded intermittently by a sequence of spots that propagate and give rise to secondary spots away from the initial point of (primary) explosion. Generally, it is difficult to distinguish (even by eye) between primary and secondary events, and so the effective thickness and spot size increase. The probability of Z_{spot} being larger than $D/2$ (=R=12.5 mm) is about 3–15% of its maximum. Given the (on average) ellipsoid ($\langle Z_{spot}\rangle/\langle R_{spot}\rangle=1.1\pm0.1$) appearance of the spots, this suggests that the spot flame fronts are correctly captured to within 10% by the flame tracking script, as we anticipate the spot to quench at the tube inner wall, thus limiting its maximum radial size to $R_{spot}<D/2$. Consider now the mean longitudinal autoignition spot half-size $\langle Z_{spot}\rangle$ (empty symbols) and upstream flame front thickness $\langle\Delta\rangle$ (filled symbols) for *n*-heptane, as shown in Fig. 7.

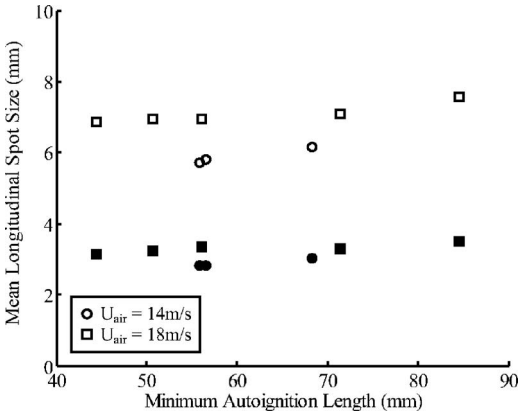

Fig. 7 Mean upstream flame front thickness (filled) and autoignition spot longitudinal half-size (empty) as a function of L_{min} for *n*-heptane with T_{air}=1100–1120 K, U_{air}=14 m/s, Y_{fuel}=0.95, and υ_{inj}=1.0 (circles) and T_{air}=1100–1140 K, U_{air}=18 m/s, Y_{fuel} =0.95, and υ_{inj}=1.0–1.2 (squares)

The mean front thickness is little affected by the conditions and L_{min}, remaining in the range 3.0–3.5 mm. However, the spot size $\langle Z_{spot}\rangle$ increases slightly with L_{min} for the same U_{air} and with U_{air} for the same L_{min}, going from 5.5 mm to 7.5 mm. In fact, it increases almost linearly with increasing L_{min}, perhaps suggesting a link with the mean plume width (perhaps of the lean flammability limit composition) at the axial length where autoignition occurs, which also increases linearly with z. At long L_{min}, we expect $\langle Z_{spot}\rangle$ to be largest because the plume is widest, and an adequate mixing has introduced a finite flammable mixture across a greater extent of the tube. Indeed, at the limit of autoignition at $L_{min}\approx85$ mm $\langle Z_{spot}\rangle$ is at its largest (about 7.5 mm). The mean composition at the longest L_{min} will be nearest to φ_{PM}. The premixed equivalence ratio φ_{PM} is defined as the equivalence ratio after a complete mixing between the air and nitrogen-diluted *n*-heptane. For these experiments φ_{PM}=0.4–0.5, near the lean flammability limit, φ_{LFL}, of 0.53 [17]. In addition, from 0D conditional moment closure (CMC) [2], ξ_{MR}=0.09–0.14, corresponding to φ_{MR} =1.4–2.3.

Similar results were obtained for acetylene, with $\langle Z_{spot}\rangle$ between 8 mm and 10 mm. Hydrogen spots and upstream reaction zones were found to be smaller and thinner respectively, agreeing with Markides [2] who noted that the two-dimensional pfds of autoignition (contaminated by postignition combustion of the spots) were much thinner in their radial extent for this fuel. The mean flame front thickness was found to be 1–3 mm, while $\langle Z_{spot}\rangle$ was between 2 mm and 5 mm. These values should be compared with equivalent results for the hydrocarbon fuels. Clearly, the hydrogen reaction zones extinguish much closer to the original explosions than what was measured for the hydrocarbons. Possibly, this can be explained in terms of ξ_{MR} for hydrogen, which, at 0.007–0.035 (or an equivalence ratio of 0.2–0.3), was leaner by an order of magnitude than that of *n*-heptane and φ_{PM} for hydrogen, which in these experiments was about 0.015–0.021. In addition, the lean flammability limit for hydrogen is φ_{LFL} =0.10 [17]. Consequently, the initial appearance of the flame will be situated farther away from the stoichiometric contour, and the bulk of the mixture into which the flame will be propagating will be well beyond the flammability limits that would allow the flames to propagate. Recall that for *n*-heptane unlike hydrogen, φ_{PM}(=0.4–0.5) was close to φ_{LFL}(=0.53).

Flame Front and A/Ignition Spot Advection Velocities. Figure 8 shows pdfs of the absolute (relative to the injector and tube) velocities obtained from the data of Fig. 6, namely, the propagation velocities of the upstream flame fronts and those of the (geometrical center of the) spots.

Downloaded 02 Jun 2010 to 171.66.16.107. Redistribution subject to ASME license or copyright; see http://www.asme.org/terms/Terms_Use.cfm

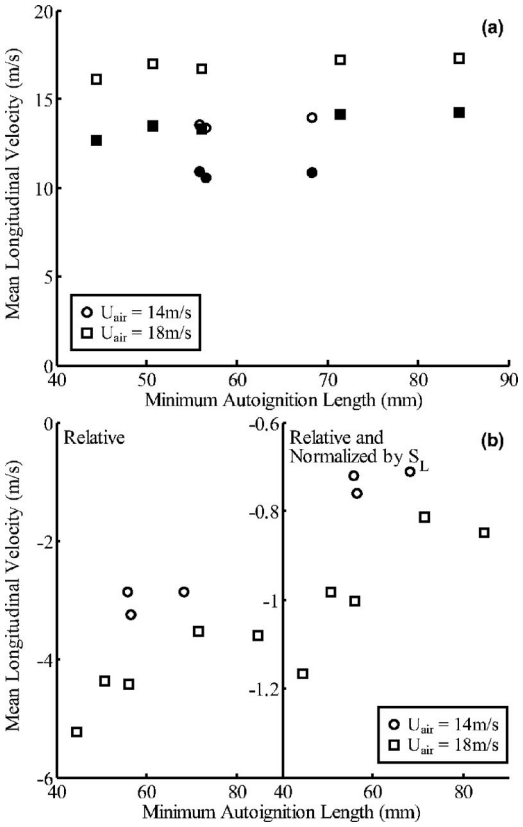

Fig. 9 Mean velocities as a function of L_{min} for *n*-heptane with conditions as in Fig. 6. (*a*) Absolute longitudinal upstream flame front (solid) and autoignition spot advection (empty) velocities. (*b*) Upstream longitudinal flame front velocity.

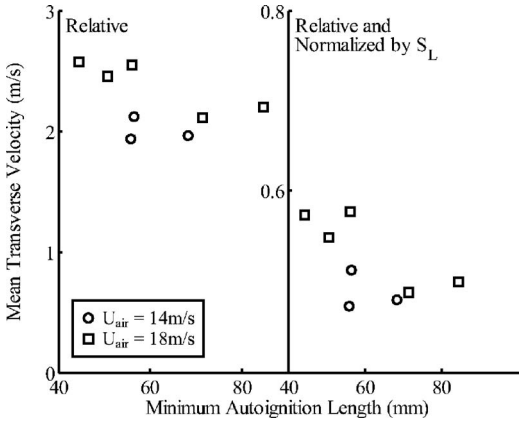

Fig. 10 Mean transverse velocity of left and right flame fronts for *n*-heptane with conditions as in Fig. 6

It is important to note that the velocities are both positive. All reaction zones (including the upstream ones) move downstream and away from the injector. This is important because it suggests that within any instantaneous image, limited information of the downstream extent of the spot (z_{dn}) might be lost due to the finite exposure time, but not so for the upstream extent (z_{up}). Based on the pdfs in Fig. 8 we calculated the mean absolute longitudinal velocities that are plotted against L_{min} in Fig. 9(*a*). The mean spot velocity $\langle U_{spot} \rangle$ (empty symbols), both for the U_{air}=14 m/s (circles) and 18 m/s (squares) data, was found to be within $0.90-1.05U_{air}$, leading one to remark that the spots must be advected by the mean flow. In addition, this was checked for the case of the point of peak intensity as well, and it was found that $\langle U_{pk} \rangle / U_{air}$=0.95–1.10. As an aside, the longitudinal velocities of the fronts downstream of the geometric center were greater than the corresponding upstream ones, or $U_{up} < U_{spot} < U_{dn}$. In fact, the longitudinal velocity of the upstream flame fronts was found to be about 70–75% of that of the point of peak intensity and about 60–80% of that of the downstream flame fronts. Moreover, the velocity of the point of peak intensity $\langle U_{pk} \rangle$ was about 10% higher than that of the geometric center of the spot, $\langle U_{spot} \rangle$. The above findings imply that $U_{up} < U_{pk} \approx U_{spot} \approx U_{air} < U_{dn}$, meaning that S_T ($=\langle U_{up} \rangle - U_{air}$) is negative. Recognizing that the general trend is for $|S_T|$ to decrease with L_{min} (explained below), the fact that $U_{up} < U_{dn}$ implies that $\langle U_{dn} \rangle$ is affected by density (product gas expansion) effects. For this reason, we use the velocity of the point of peak intensity $\langle U_{spot} \rangle = d\langle z_{pk} \rangle / dt$ as the best spot "advection" velocity and consider only the propagation of the upstream flame fronts for the estimation of S_T, $S_T = U_{up} - U_{air}$.

Figure 9(*b*) contains the same data as in 9(*a*), but relative to the oncoming flow, with S_T (left) and S_T normalized by the laminar flame speed for those conditions (right). The upstream fronts of the spots move against the flow at a speed of the order of S_L, even though their resultant motion is still downstream. We predict then that when $S_L > U_{air}$, flashback will ensue. Yet, the relative speed of the upstream fronts decrease with increasing L_{min}, more than what can be accounted for by the change in S_L in the domain. This is an interesting finding and can be explained in terms of the decrease in χ at longer z (and hence L_{min}), augmented by the decrease in pdf(ξ) at the compositions close to ξ_{ST} associated with higher flame speeds.

In the radial direction (Fig. 10) $\langle V_{spot} \rangle$ was between 2–3 m/s, about $0.6-0.7\langle U_{spot} \rangle$ or $0.5-0.6S_L$, also decreasing with increasing L_{min}. This finding is consistent with the previously stated result of spots slightly elongated in the axial direction by up to 20%. Since the propagation in the radial direction is, on average, unaffected by the bulk motion of the flow, the fact that the trend of $\langle V_{spot} \rangle$ in Fig. 10 and the magnitude of $\langle V_{spot} \rangle / S_L$ closely resemble the longitudinal data (trends and magnitude of S_T) gives credence to our previous estimates for S_T.

Having considered the case of *n*-heptane so far, we turn our attention to acetylene and hydrogen. Figure 11 shows longitudinal upstream flame front velocities, both absolute, relative (left), and relative to U_{air} and normalized by the laminar flame speed (right). The absolute flame velocities varied from 15 m/s to 26 m/s for acetylene and from 6.5 m/s to 8.5 m/s for hydrogen. Yet, we note that the relative propagation of these flame fronts is once again near the laminar flame speed, but also that the S_T decreases as autoignition/propagation occurs at longer L_{min}.

To summarize briefly, we have used three different fuels (and hence ξ_{ST}, ξ_{MR}, φ_{PM}), a wide range of nitrogen dilutions, temperatures, and velocities, obtaining flame velocity data at ultimately different autoignition lengths in a fixed geometry. For all tested fuels a consistent result emerges concerning the upstream flame front velocity, S_T. Firstly, its direction is positive, but relative to U_{air} this becomes negative. In other words, the upstream flame fronts in the autoignition spots travel downstream in an absolute sense, but upstream relative to the oncoming flow. Secondly, the magnitude of the upstream flame front velocity or flame speed, $|S_T|$, remains of the order of the laminar flame speed, S_L, as found by Mastorakos et al. [8], with a slight trend for $|S_T|$ to decrease with increasing L_{min}, dropping below S_L at long L_{min}, and to increase even at the same L_{min} at higher U_{air}. Despite the fact that the flow is turbulent and the mixture is not frozen, the flamelet propagation speed seems to be of the order of the laminar burning velocity. This may be because following autoignition at ξ_{MR}, the flamelet propagates in mixtures with composition far from stoichiometry.

Downloaded 02 Jun 2010 to 171.66.16.107. Redistribution subject to ASME license or copyright; see http://www.asme.org/terms/Terms_Use.cfm

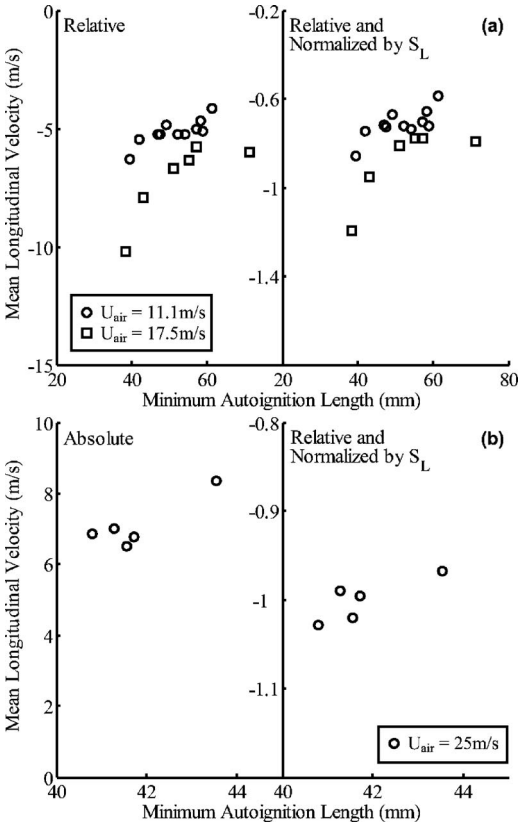

Fig. 11 Mean longitudinal upstream flame front velocities as a function of L_{min}. (*a*) Acetylene with U_{air}=11.1 m/s, T_{air} =806–824 K, Y_{fuel}=0.6, and v_{inj}=1.0 (circles) and U_{air} =17.5 m/s, T_{air}=850–879 K, Y_{fuel}=0.6, and v_{inj}=1.0 (squares). (*b*) Hydrogen with T_{air}=950 K, U_{air}=25 m/s, Y_{fuel}=0.2–1.0, and v_{inj}=0.9–1.0.

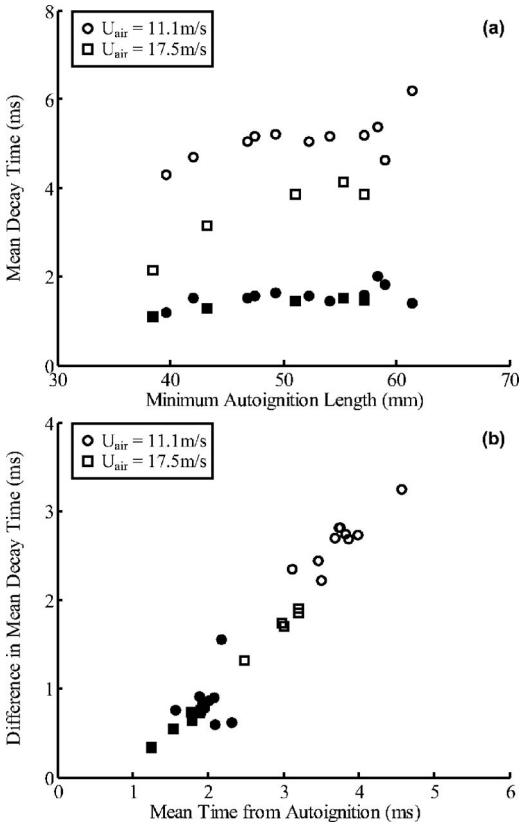

Fig. 13 (*a*) Mean acetylene decay time from the instant of autoignition to 10% (solid) and 1% (empty) decay thresholds as a function of L_{min}. Conditions as in Fig. 11(*a*). (*b*) Difference in mean decay time as a function of the time from autoignition from 10% to 5% (solid) and from 5% to 1% (empty) decay thresholds. Calculated based on data in (*a*).

Evolution of the Propagation Velocities. It is common for the extinction process to appear as one in which the overall size of the spot diminishes. It has been previously stated that the propagation velocities were a function of the time from explosive autoignition (see Fig. 1) and that the reported value of velocity of each flame front was defined as the average distance traveled from the moment of explosive autoignition to the time the chemiluminescence intensity reached 5% of its maximum value. This was chosen to correspond approximately to the condition for the growth of a spot, i.e., $dZ_{spot}/dt>0$ or $dR_{spot}/dt>0$, as demonstrated in Fig. 12.

In this section we quantify the temporal evolution of the propagation velocities with acetylene data. Figure 13(*a*) shows the mean time taken for the intensity of the spots to decay to three different fractions of their maximum value. The maximum value is attained about 0.5 ms after the explosive emergence of autoignition. The mean decay time increases with increasing L_{min} for all thresholds, reflecting the fact that as autoignition occurs farther downstream the propagation velocity decreases, consistent with the direct velocity results. Note that the time to decay to 10% of the maximum, unlike the decay to 1%, is only dependent on L_{min} and not affected by U_{air} for the same L_{min}. This might suggest that the former is mostly dependent on the flow geometry in that the spot intensity will reach this level when it has reached a certain (such as φ_{PM} or φ_{LFL}) extent of the plume. We may also speculate that the latter depends additionally, perhaps, on the local micromixing (including the pdf(ξ) and the conditional $\chi|\xi$) at the regions where the propagation is taking place.

Going a step further, Fig. 13(*b*) shows a clear positive correlation between the rate of decay of the spot intensity and the mean time from autoignition at which the rate is evaluated. This would have been expected, for example, by considering the decreasing modulus of the gradient in the profile in Fig. 1. Physically, this represents the extinction process of the spots as the flame fronts propagate from ξ_{MR} toward leaner and richer mixtures that tend to decrease the flame speed. In addition, the data points from the higher velocity case (squares) have a higher rate of decay (lower difference in decay time), perhaps corresponding to the known higher χ at those locations [2,12].

Fig. 12 Evolution of spot flame fronts at 13.5 kHz. Flow direction shown and scale given. Reproduced from Ref. [1].

Conclusions

The autoignition of axisymmetric plumes of pure or nitrogen-diluted hydrogen, acetylene, and *n*-heptane, injected continuously into confined turbulent hot coflows of hot air, has been visualized with an intensified high-speed camera. Localized autoignition and postignition flame phenomena have been observed, including the statistically steady random spots and the flashback behaviors. The boundary between these regimes of operation has been explored. It was found that the onset of flashback shifted to higher air temperatures with higher velocities and smaller injector diameters.

Downloaded 02 Jun 2010 to 171.66.16.107. Redistribution subject to ASME license or copyright; see http://www.asme.org/terms/Terms_Use.cfm

In the random spots regime, as the air temperature increased and/or air velocity decreased, the autoignition regions moved (upstream) toward the injector. After a localized explosive autoignition event, flames propagated in all directions into the unburnt mixture and eventually (after a few milliseconds) extinguished, giving rise to autoignition spots of mean radii 2–5 mm for hydrogen and 6–10 mm for the hydrocarbons. The average flame propagation velocities varied from $0.5S_L$ to $1.2S_L$, where S_L is the laminar burning speed of the stoichiometric mixture. This was not expected, especially given the turbulent nature of the flow and the chemically evolved state at the locations of autoignition, but is consistent with previous DNS results [8] and can be attributed to the fact that most of this propagation occurs through mixtures very different from stoichiometric ones. The propagation velocities were found to increase as the autoigniting regions shifted upstream, perhaps due to the mixture composition and/or the increase in the scalar dissipation rate in those regions of the flow. Further experiments in different flow geometries, such as with a smaller injector or a modified turbulence grid, can help to clarify some of these results. In the future, it is also important to verify these findings with detailed planar optical measurements.

Acknowledgment

We thank Dr. Ivor Day for lending us his Dantec Constant Temperature Anemometer unit, Ed Richardson for undertaking the premixed laminar flame speed calculations, and Giorgio De Paola for the 0D CMC calculations. Figure 1 has been reprinted from Markides [2]. Figure 12 has been reprinted from Markides and Mastorakos [1] with permission from Elsevier. This work has been funded by the EPSRC.

References

[1] Markides, C. N., and Mastorakos, E., 2005, "An Experimental Study of Hydrogen Autoignition in a Turbulent Co-Flow of Heated Air," Proc. Combust. Inst., **30**, pp. 883–891.
[2] Markides, C. N., 2005, "Autoignition in Turbulent Flows," Ph.D. thesis, University of Cambridge, Cambridge, U.K.
[3] Markides, C. N., De Paola, G., and Mastorakos, E., 2007, "Measurements and Simulations of Mixing and Autoignition of an N-Heptane Plume in a Turbulent Flow of Heated Air," Exp. Therm. Fluid Sci., **31**, pp. 393–401.
[4] Ballal, D. R., and Lefebvre, A. H., 1979, "Ignition and Flame Quenching of Flowing Heterogeneous Fuel-Air Mixtures," Combust. Flame, **35**, pp. 155–168.
[5] Kaminski, C. F., Hult, J., Aldén, M., Lindenmaier, S., Dreizler, A., Mass, U., and Baum, M., 2000, "Spark Ignition of Turbulent Methane/Air Mixtures Revealed by Time-Resolved Planar Laser-Induced Fluorescence and Direct Numerical Simulations," Proc. Combust. Inst., **28**, pp. 399–405.
[6] Ko, Y. S., and Chung, S. H., 1999, "Propagation of Unsteady Tribrachial Flames in Laminar Non-premixed Jets," Combust. Flame, **118**, pp. 151–163.
[7] Ahmed, S. F., and Mastorakos, E., 2006, "Spark Ignition of Lifted Turbulent Jet Flames," Combust. Flame, **146**, pp. 215–231.
[8] Mastorakos, E., Baritaud, T. B., and Poinsot, T. J., 1997, "Numerical Simulations of Autoignition in Turbulent Mixing Flows," Combust. Flame, **109**, pp. 198–223.
[9] Edwards, C. F., Siebers, D. L., and Hoskin, D. H., 1992, "A Study of the Autoignition Process of a Diesel Spray Via High Speed Visualization," SAE Tech. Pap. Ser., **920108**, pp. 1–18.
[10] Arnold, A., Dinkelacker, F., Heitzmann, T., Monkhouse, P., Schäfer, M., Sick, V., Wolfrum, J., Hentschel, W., and Schindler, K.-P., 1992, "Di Diesel Engine Combustion Visualized by Combined Laser Techniques," Sym. (Int.) Combust., [Proc.], **24**, pp. 1605–1612.
[11] Murase, E., Hanada, K., Miyaura, T., and Ikeda, J., 2005, "Photographic Observation and Emission Spectral Analysis of Homogeneous Charge Compression Ignition Combustion," Combust. Sci. Technol., **177**, pp. 1699–1723.
[12] Markides, C. N., and Mastorakos, E., 2006, "Measurements of Scalar Dissipation in a Turbulent Plume With Planar Laser-Induced Fluorescence of Acetone," Chem. Eng. Sci., **61**, pp. 2835–2842.
[13] ROTEXO GmbH & Co. KG, 2005, COSILAB: The Combustion Simulation Laboratory-Version 1.2.3, Haan, Germany, http://www.SoftPredict.com
[14] Connaire, M. O., Curran, H. J., Simmie, J. M., Pitz, W. J., and Westbrook, C. K., 2004, "A Comprehensive Modeling Study of Hydrogen Oxidation," Int. J. Chem. Kinet., **36**, pp. 603–622.
[15] Held, T. J., Marchese, A. J., and Dryer, F. L., 1997, "A Semi-Empirical Reaction Mechanism for N-Heptane Oxidation and Pyrolysis," Combust. Sci. Technol., **123**, pp. 107–146.
[16] Laskin, A., and Wang, H., 1999, "On Initiation Reactions of Acetylene Oxidation in Shock Tubes. A Quantum Mechanical and Kinetic Modeling Study," Chem. Phys. Lett., **303**, pp. 43–49.
[17] Glassman, I., 1996, *Combustion*, Academic, San Diego, pp. 163 and 581–587.

Downloaded 02 Jun 2010 to 171.66.16.107. Redistribution subject to ASME license or copyright; see http://www.asme.org/terms/Terms_Use.cfm

H. Schütz
DLR-German Aerospace Center,
Institute of Combustion Technology,
Linder Höhe,
51147 Cologne, Germany
e-mail: harald.schuetz@dlr.de

R. Lückerath
DLR-German Aerospace Center,
Institute of Combustion Technology,
Pfaffenwaldring 38-40,
70569 Stuttgart, Germany
e-mail: rainer.lueckerath@dlr.de

T. Kretschmer
DLR-German Aerospace Center,
Institute of Combustion Technology,
Linder Höhe,
51147 Cologne, Germany

B. Noll

M. Aigner

DLR-German Aerospace Center,
Institute of Combustion Technology,
Pfaffenwaldring 38-40,
70569 Stuttgart, Germany

Analysis of the Pollutant Formation in the FLOX® Combustion

FLOX®, or flameless combustion is characterized by ultralow NO_x *emissions. Therefore the potential for its implementation in gas turbine combustors is investigated in recent research activities. The major concern of the present paper is the numerical simulation of flow and combustion in a FLOX®-combustor [Wünning, J. A., and Wünning, J. G., 1997, "Progress in Energy and Combustion Science," **23**, pp. 81–94; Patent EP 0463218] at high pressure operating conditions with emphasis on the pollutant formation. FLOX®-combustion is a highly turbulent and high-velocity combustion process, which is strongly dominated by turbulent mixing and chemical nonequilibrium effects. By this means the thermal nitric oxide formation is reduced to a minimum, because even in the nonpremixed case the maximum combustion temperature does not or rather slightly exceeds the adiabatic flame temperature of the global mixture due to almost perfectly mixed reactants prior to combustion. In a turbulent flow, the key aspects of a combustion model are twofold: (i) chemistry and (ii) turbulence/chemistry interaction. In the FLOX®-combustion we find that both physical mechanisms are of equal importance. Throughout our simulations we use the complex finite rate chemistry scheme GRI3.0 for methane and a simple partially stirred reactor (PaSR) model to account for the turbulence effect on the combustion. The computational results agree well with experimental data obtained in DLR test facilities. For a pressure level of 20 bar, a burner load of 417 kW and an air to fuel ratio of* $\lambda = 2.16$ *computational results are presented and compared with experimental data.* [DOI: 10.1115/1.2747266]

Keywords: FLOX®-combustion, numerical simulation, complex finite rate chemistry, PaSR model

Introduction of the Flox Principle

FLOX® is a registered trademark of WS Wärmeprozesstechnik [1]. The combustor design was supplied by this company and the manufacturing, particularly with regard to the specific demands of the high pressure operation, was accomplished by DLR. The term FLOX® is an acronym for "flameless oxidation," which actually means that no distinct flame is visible. The way in which this is performed and what follows as a consequence thereof, will be pointed out in the following. The fuel used in the experiments and the simulations is natural gas and its composition is depicted in Table 1.

In order to give a first impression of the FLOX® principle a longitudinal slice through combustor axis and two subtending nozzles is displayed in Fig. 1. The streamlines represent the flow and we recognize an outer and a stronger inner recirculating vortex that stabilizes the flame. In view of the pollutant formation the molar fraction distribution of CO and NO is shown on the upper and lower half of Fig. 1, respectively. At first glance we observe that the reaction zone is far detached from the nozzle exit.

In principle, FLOX® is a technique employed to reduce nitric-oxide (NO) emission to a minimum within the combustion process. The relevant NO-formation mechanisms during methane combustion are: (i) Zeldovich (thermal NO), (ii) Fenimore (prompt NO), and (iii) N_2O–NO. It is generally accepted that with increasing combustion temperature the thermal NO-formation becomes absolutely dominant over the other mechanisms. Therefore, low NO-emission values may be attained if the combustion is controlled in a manner in which the temperature does not exceed the adiabatic flame temperature of the global mixture.

Equilibrium computations reveal that increasing adiabatic flame temperature correlates with increasing preheating temperature and with decreasing air to fuel ratio λ. In order to maintain high operational efficiency, the preheating temperature has to be as high as possible. Consequently, adiabatic flame temperatures below 1800 K imply an air to fuel ratio λ in the range of $2 < \lambda < 3$.

If reaction occurs before the mixture is globally mixed on the molecular level, the local flame temperature is higher than the adiabatic flame temperature of the global mixture due to regimes of lower air to fuel ratio which are closer to stoichiometry than the global mixture. This should be avoided, in particular, flashback into the nozzle is absolutely prohibitive.

As is seen in Fig. 2, the mixing of fuel and oxidizer taking place in the burner is not complete; indeed, there is a slight nonconcentric distribution of methane on the nozzle exit cross section with a maximum concentration of 17.7% near the nozzle axis and a minimum concentration of 0.3% at the nozzle walls. Details of the nozzle design are not shown here.

It will be seen in the computational results that this incomplete mixing in the burner is of less relevance in the FLOX®-combustion. The key is that mixing proceeds at extremely high flow velocity. The consequence is that on the one hand turbulent mixing is highly improved in the shear layer around the impinging jet and on the other hand that chemical reactions are strongly delayed by reason of nonequilibrium effects, even for high preheating temperatures. This is also the reason why simulations using combustion models on the basis of equilibrium or near-

Contributed by the International Gas Turbine Institute of ASME for publication in the JOURNAL OF ENGINEERING FOR GAS TURBINES AND POWER. Manuscript received January 4, 2007; final manuscript received January 29, 2007, published online January 9, 2008. Review conducted by Dilip R. Ballal. Paper presented at the ASME Turbo Expo 2006: Land, Sea and Air (GT2006), May 8–11, 2006, Barcelona, Spain, Paper No. GT2006-91041.

Copyright © 2008 by ASME

Downloaded 02 Jun 2010 to 171.66.16.107. Redistribution subject to ASME license or copyright; see http://www.asme.org/terms/Terms_Use.cfm

Table 1 Operational conditions. The air to fuel ratio is defined as $\lambda=(n_{Air}/n_{Fuel})/(n_{Air}/n_{Fuel})_{stoic}$, where n is the respective number of moles and the subscript stoic denotes stoichlometry

Air to fuel ratio λ of the global mixture	(1)	2.16
Pressure	(bar)	20
Air temperature	(K)	721
Fuel temperature	(K)	352
Air mass flow	(g/s)	302
Fuel mass flow	(g/s)	8.33
Specific heat density	(MW/m^3/bar)	12.3
Burner load	(kW)	417
Fuel composition	(mole %) CH_4	97.88
	C_2H_6	0.76
	C_3H_8	0.37
	CO_2	0.06
	N_2	0.93

equilibrium chemistry (e.g., presumed pdf using flamelets) completely fail, as they predict combustion in the nozzle [2].

The incompletely mixed fuel/air jet perpendicularly enters the combustion chamber with high, nonswirled velocity, forming a recirculating annulus around the jet due to mass continuity (see Fig. 1). After a certain penetration depth the jet expands, leading to a strong reduction of the velocity magnitude. Prior to the onset of the chemical reactions at appropriate flow velocity values, mixing is further improved on-the-fly by turbulence. Simultaneously, the jet is further preheated by the recirculating hot flue gases. This process is also supported by the hot combustor walls, as is found by *Vaz* [2]. The influence of the entrainment of the flue gases in the jet is not quantified here.

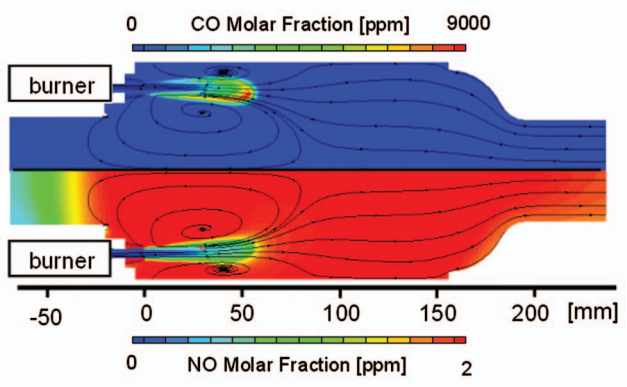

Fig. 1 CO and NO molar fraction distribution and streamline representation of the flow on longitudinal slice through nozzle and combustor axis for λ=2.16. Note: the molar fraction is related to dry gas and 15% O_2 concentration at the combustor exit (see Table 2).

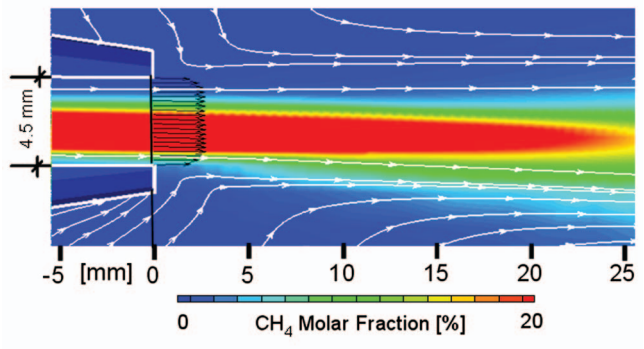

Fig. 2 Inhomogeneous methane distribution at burner nozzle exit, CH_{4min}=0.3%, CH_{4max}=17.7% -turbulent velocity profile at the nozzle exit, $v_{max}\approx$187 m/s, $v_{mean}\approx$173 m/s. Note: Maximum speed of $v\approx$197 m/s is reached about 3.7 mm downstream of the nozzle exit-streamlines indicating recirculation around the jet.

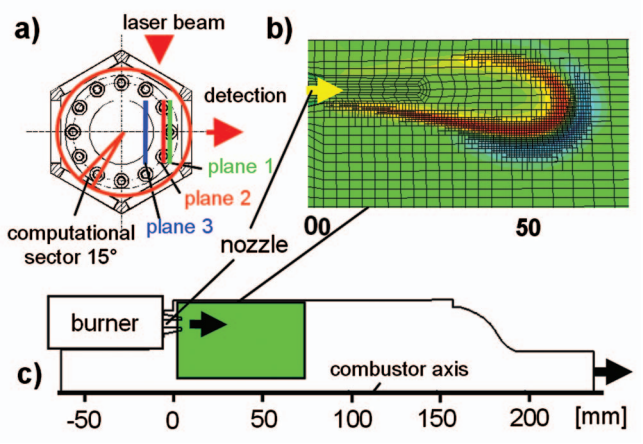

Fig. 3 Schematic of the experimental/computational setup

Due to nonequilibrium chemistry effects the formation of a flame is spatially delayed up to a volumetric heat release at mean temperatures in the range of or even below the adiabatic flame temperature. Accordingly a distinct flame is no more visible. At that temperature the NO-formation is very low (1–10 ppm); far below the equilibrium values which indicates that this process is very slow. In contrast, the CO formation and consumption is very fast, and we may expect exhaust values in the range of the equilibrium data.

Computational and Experimental Setup

The computational domain is derived from the combustor, which was experimentally investigated at the DLR test facility. Combustor length and diameter are 200 and 100 mm, respectively. From Fig. 3(*a*) we see that on the combustor head twelve nozzles (inner Ø 4.5 mm) are equidistantly arranged along a circle (Ø 80 mm) centered about the combustor axis. For a better optical access, the cross section of the combustion chamber on the test rig is of hexagonal shape. However, in the simulations a cylindrical geometry with a combustor diameter of 106 mm is assumed in order to reduce the computational cost. Hence, the computational domain may be limited to a 15 deg sector as indicated in Fig. 3(*a*). The axial extent of the domain is displayed in Fig. 3(*c*). Scalability issues of the investigated FLOX® combustor had not been addressed in the present paper as it was our primary goal to develop and validate our combustion code. However, this topic will be investigated in future work.

For the flow simulation we use the commercial code Fluent 6.1. applying the realizable k-ε model with standard wall functions and the segregated solver. Chemistry and turbulence/chemistry interaction are computed using the DLR combustion code *IGNIS*, which supplies the Fluent code with the source terms for the composition and internal energy transport equations. These transport equations are then solved in Fluent. Based on our experience, the best results concerning performance, stability and accuracy are achieved by performing unsteady computations. Coupling Fluent and *IGNIS* in a steady mode does not converge or is highly inefficient due to the need for very small relaxation factors.

In order to lower computational cost, we use the Fluent code capability to dynamically adapt the computational mesh to the physical solution. Precisely, we start the computation with a very coarse mesh of about 8000 cells. A steady state solution is finally obtained on an adapted mesh of about 80,000 cells. As the adap-

Downloaded 02 Jun 2010 to 171.66.16.107. Redistribution subject to ASME license or copyright; see http://www.asme.org/terms/Terms_Use.cfm

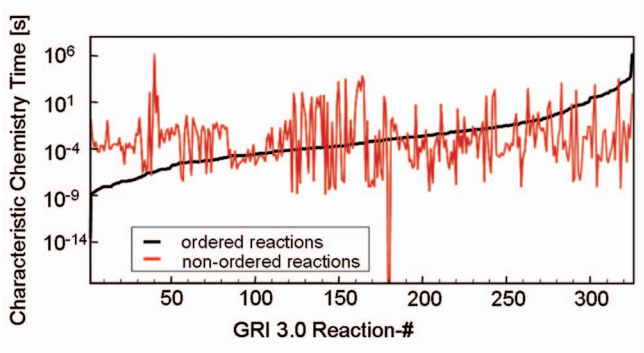

Fig. 4 Characteristic chemistry time over the elementary reactions of the GRI3.0 reaction scheme. Red colored line: nonordered; black colored line: ordered chemical reactions.

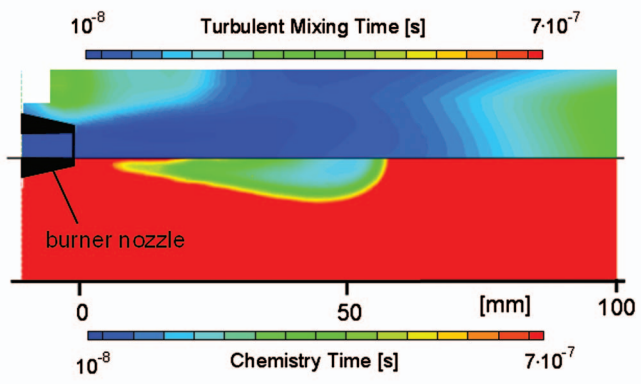

Fig. 5 Characteristic chemistry time (lower half) and turbulent mixing time (upper half) in the combustion zone on a longitudinal slice through the burner nozzle and combustor axis

tation criteria we use the global reaction rate and the production rates for CO and OH. For example a mesh cutout after a mesh-refinement procedure based on the CO production rate is shown in Fig. 3(*b*). Computations are performed for the operational conditions summarized in Table 1.

The Combustion Model

The IGNIS code is a powerful chemistry simulation package incorporating different turbulent combustion models. IGNIS may be coupled with any arbitrary CFD-code via user-defined functions supplying the internal energy and species densities transport equations with the appropriate source terms. The code kernel is a highly optimized routine solving complex chemical systems of elementary reactions applying the "Reference Species Technique" [3] (see Appendix A). This technique is a semi-implicit solution procedure where the individual reaction equations are sequentially solved by linearization in the respective reference species. In this regard we found it crucial for the quality of the solution to rearrange and solve the elementary reactions in the order of increasing characteristic chemistry times. Within the global time step τ the characteristic chemistry time τ_{chem} is then used as the time step in a subcycled explicit solution process of each reaction equation. Thus, the solution of a fast reaction is introduced into the solution process of the next slower reaction, and so on. As an example, the reordering of the reactions in the computational cell of greatest heat release is shown in Fig. 4. While the original order reveals a strongly fluctuating behavior the rearranged order is represented by a smooth curve revealing that the characteristic chemistry times of the fastest and the slowest reaction ranging from 10^{-9} to 10^{6} s, respectively. Unfortunately this order is different for each cell and each time level and has to be computed separately.

With our focus on the pollutant emission we decided to use the GRI3.0 [4] reaction mechanism comprised of 325 elementary reactions and 53 species to investigate the relative importance of the different NO-formation mechanisms. In practice, solution of a very complex chemistry system is prohibitive for the concurrent use of an elaborate turbulence/chemistry interaction model (for example, the presumed pdf approach) by reason of the computational cost. Therefore the simple "Partially Stirred Reactor Model" [5,6] (see Appendix B) is applied in the present computations. This model suffers from the fact that all the turbulent structures in a computational cell have the same mean composition and that there is only one integral turbulent mixing time involved. On this account the model has to be calibrated by adjusting the model constant C_{mix} in Eq. (B5) of Appendix B by comparison with experimental data. For the FLOX®-combustion we found an appropriate value of $C_{\text{mix}}=0.002$. The justification for this will be given later.

In order to evaluate the combustion model it is useful to compute the local turbulent Damköhler number which may be interpreted as a measure of the relative importance of turbulence and chemistry in the combustion zone. From the results of the simulation used below for the code and model validation we first compute the characteristic chemistry time as defined in Eq. (A9) of Appendix A. The distribution of the chemistry time and the characteristic turbulent mixing time is plotted on the lower and upper half of Fig. 5, respectively. Figure 5, as well as subsequent figures, represents a cutout of the reaction zone behind the burner nozzle on a longitudinal slice through burner nozzle and combustor axis.

At first glance we see that the chemistry time is almost one order of magnitude higher than the turbulence mixing time indicating that the FLOX® combustion is notably dominated by finite rate chemistry effects. Both characteristic times are combined to form the Damköhler number defined through Eq. (B10). For comparison the distribution of the heat release rate and the Damköhler number is plotted on the upper and lower half of Fig. 6, respectively.

We observe that heat of combustion is released on an envelope around the impinging fuel/air jet with a maximum of 10^{10} W/m^3 located about 55 mm downstream behind the nozzle exit. We further observe that the Damköhler number strongly correlates with the heat release rate, however, the maximum value of $\text{Da}_T \cong 0.4$ is located slightly upstream of the point of maximum heat release. This fact is also reflected in Fig. 5 by an absolute minimum in the chemistry time.

If the computed Damköhler number is located in the Borghi-

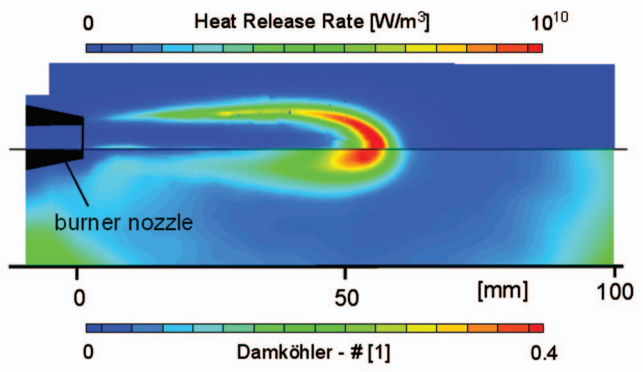

Fig. 6 Damköhler-# (lower half) and heat release rate (upper half) in the combustion zone on a longitudinal slice through the burner nozzle and combustor axis

Downloaded 02 Jun 2010 to 171.66.16.107. Redistribution subject to ASME license or copyright; see http://www.asme.org/terms/Terms_Use.cfm

Table 2 Comparison of computational and experimental results

Air to fuel ratio λ			2.16		
Max. nozzle velocity (m/s)			195		
Adiabatic temperature (K)			1749		
Equil. CO molar fraction (ppm)			3.8/2.8[a]		
Equil. NO molar fraction (ppm)			2587		
Combustion model	Simulation GRI3.0 quasilaminar		Simulation GRI3.0 PaSR		Experiment
Max. mean temperature (K)	1755		1750		1719[c]
Exhaust temperature (K)	1743		1742		1267[b,d]
Max. CO molar fraction (ppm)	6668		9084		···
Exhaust CO molar fraction (ppm)	3.6	2.3[a]	3.6	2.3[a]	<1.0[a,b]
Max. NO_x molar fraction (ppm)	3.2		3.0		···
Exhaust NO_x molar fraction (ppm)	2.5	1.8[a]	2.3	1.6[a]	6.2[a,b]

[a]Concentration for dry exhaust gas related to 15% O_2 concentration.
[b]Suction thermocouple probing 65 mm behind the combustor exit.
[c]Measured on an area as indicated-in Fig. 9.
[d]Temperature decreased due to undefined amount of cooling air, uncorrected thermocouple.

diagram [7] we find that the FLOX® combustion is characterized by the conditions prevailing in a more or less well stirred reactor.

From the above considerations we may conclude that our choice to use a complex finite rate chemistry scheme along with the partially stirred reactor model is justified in the FLOX® application.

Results

Code and Model Validation. For the validation of the combustion models and the evaluation of the computational results OH-LIF measurement data are available from DLR-experiments relating to the relative amount of OH-radicals and the temperature [8]. Details of the experimental theory are not presented here but may be found in [9]. The species concentrations of CO and NO were detected by suction probing 65 mm downstream of the combustor exit (Ø 50 mm). The outer diameter of the probe is 5 mm and we may assume that the probe does not interfere with the combustor flow. The exhaust temperature was measured with an uncorrected thermocouple. All these values are resumed in Table 2 and used as validation data for the simulations. The measured pressure drop across the combustor of about 5% is coincident with the computational result.

OH. OH is involved in almost all elementary reactions and consequently has an important influence on the accurate prediction of the pollutant formation. In Figs. 7 and 8 the results of the simulations without (quasilaminar) and with application of the PaSR-model are qualitatively compared with the LIF-measured OH-concentration on slice plane 2, as indicated in Fig. 3(*a*).

In the simulations the onset of the OH-formation is rather abrupt with a steep gradient in the reaction zone. In contrast, there is a smooth transition of OH from the zero value in the center of the jets to the surroundings. This is certainly due to a strong turbulent exchange or entrainment across the shear layer between the jets and the recirculating hot flue gases. This physical process is only deficiently described by the k-ε turbulence model. Obviously, this is not only a problem of the combustion model but rather of the turbulence model in the flow simulation code.

The results of the quasilaminar approach presented in Fig. 7 clarifies the pure chemistry aspect of the combustion assuming that the composition at the beginning of each time step is perfectly mixed on the molecular level. This is the limit of infinitely fast turbulent mixing or $\tau_{mix}=0$. Although the flame front is strongly delayed behind the nozzle exit due to finite rate chemistry effects, comparison with the experimental data shows that the reaction is still to fast. This shows that we have to account for the incomplete mixing in the computational cells by application of the PaSR turbulence/chemistry interaction model. As mentioned above the PaSR-model has to be calibrated by adjusting the model parameter C_{mix} in Eq. (B8). For this purpose we used the OH-LIF measurement data to determine a value of $C_{mix}=0.002$ by tuning the conformity of the computational and experimental OH-distribution pattern. The result is shown in Fig. 8.

With the C_{mix} parameter fixed, we further compare computational and experimental results for the temperature and the global emission values at the combustor exit. These values are summarized in Table 2 with reference to the corresponding equilibrium data.

Temperature. Figure 9 shows the temperature distribution on plane 3 of Fig. 3(*a*) related to a color map ranging from 1200 K up to 2000 K. The result of the simulation is displayed on the upper half of the figure while the data from the LIF experiment is shown on a rectangular cutout near the combustor center on the lower half. Comparing both data on the corresponding rectangular areas as outlined in Fig. 9 we find that the computational distribution is almost homogeneous with the average value of 1750 K

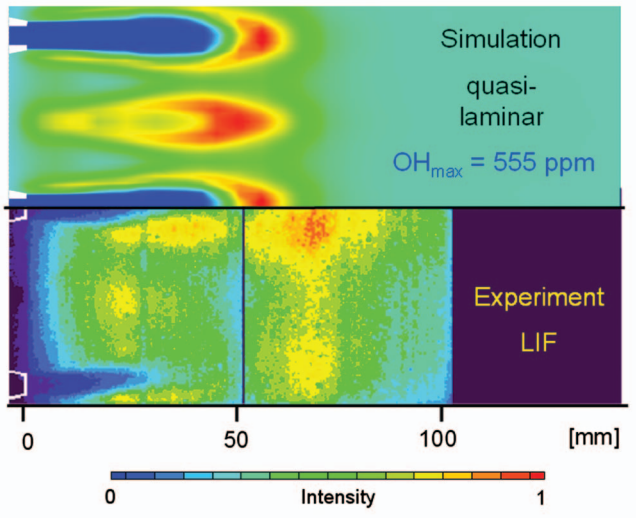

Fig. 7 OH molar fraction distribution on slice plane 2 (see Fig. 3(*a*)) for λ=2.16. Comparison-Simulation: GRI3.0 quasilaminar/ Experiment: LIF.

Downloaded 02 Jun 2010 to 171.66.16.107. Redistribution subject to ASME license or copyright; see http://www.asme.org/terms/Terms_Use.cfm

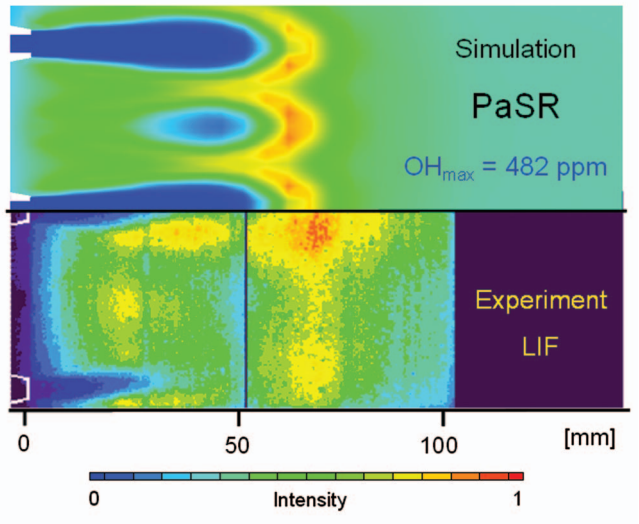

Fig. 8 OH molar fraction distribution on slice plane 2 (see Fig. 3(*a*)) for λ=2.16. Comparison-Simulation: GRI3.0+PaSR-model (C_{mix}=0.002)/Experiment: LIF.

being very close to the adiabatic flame temperature of the global mixture. Against this the experimental data are very inhomogeneous in the range of 1498–1983 K indicating turbulent effects. The averaged value is 1719 K and is about 30 K lower than the computational result. As already discussed above with respect to the OH distribution the computational code is not able to correctly predict this inhomogeneity. The consequence thereof in terms of the NO formation will be discussed below.

Due to some heat loss across the combustor wall the computed exhaust temperature is about 10 K lower than the maximum temperature. This value does not match the experimental value which is almost 475 K lower. However, it has to be noted that in the experiment the exhaust flow is diluted by an unspecified amount of cooling air and that there is no radiative correction of the thermocouple.

CO and NO at the Combustor Exit. The maximum value of the CO molar fraction in the reaction zone is far beyond the equilibrium value of 2.8 ppm. We also find that this value is essentially higher with application of the PaSR model (≈9000 ppm) than with the quasilaminar approach (≈6600 ppm). This tendency is in the opposite direction of the OH formation (see Figs. 7 and 8) which will be investigated in more detail in the next section. However, in both combustion models CO is reduced in the remainder of the combustor and approaches a value of 2.3 ppm related to 15% O_2 at the combustor exit, which is slightly lower than the equilibrium data. The respective experimental value is less than 1.0 ppm.

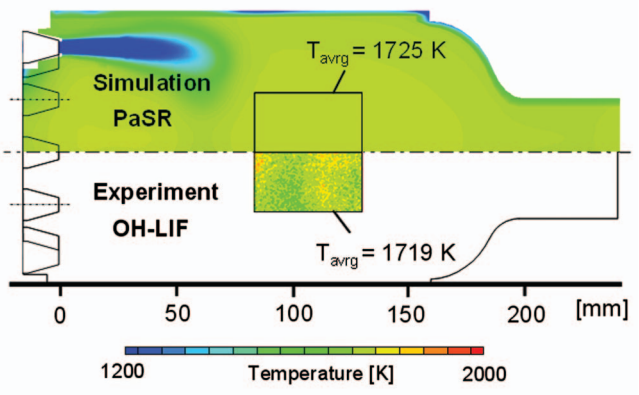

Fig. 9 Temperature distribution on slice plane 3 (see Fig. 3(*a*)) for λ=2.16-Comparison-Simulation: GRI3.0+PaSR/Experiment: OH-LIF

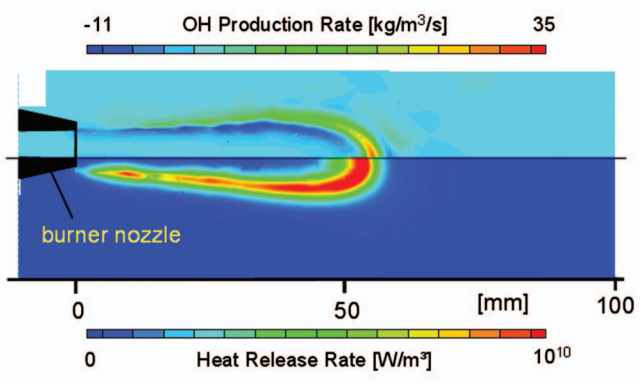

Fig. 10 OH (upper half) production rate and heat release rate (lower half) in the combustion zone on a longitudinal slice through the burner nozzle and combustor axis

Concerning the NO_x formation the computational result at the combustor exit is 1.8 ppm for the quasilaminar model and 1.6 ppm for the PaSR model, respectively. The experimental value is 6.2 ppm. For almost perfectly premixed combustion Leonard and Stegmaier [10] found an NO_x emission value of less than 2 ppm for a combustion temperature of 1750 K. They further found that this is independent of pressure level, preheating temperature, and residence time. Even though mixing on-the-fly prior to combustion—as it is characteristic for the FLOX® combustion—is efficient, we conclude from the work of Leonard and Stegmaier that in the present application the mixing is not yet perfect. One indication of this is given by the measured temperature distribution displayed in Fig. 9 where hot spots of up to 2000 K may be found. The fact is that turbulent structures may contain near-stoichiometric mixture locally resulting in temperature values essentially higher than the cell mean temperature. Accordingly the thermal NO formation in the experiment is higher than the value computed from the mean cell temperature. The reason is, as explained before, that first the k-ε model in the RANS approach has a strong smoothing behavior and second that the PaSR model does not account for different composition in the turbulent substructures of the computational cells. Both deficiencies will be addressed in future works.

In contrast to the decrease of CO, the NO concentration slowly increases towards the combustor exit. Consequently there must be an optimal combustor length with an acceptable level of the CO and NO emission values, as well. The process of CO and NO formation will be considered in more detail in the next section.

Analysis of CO and NO Formation. As mentioned before, OH plays an important role in the formation and consumption of CO as well as NO. Therefore the production rate of OH is incipiently compared with the heat release rate as shown on the upper and lower half of Fig. 10, respectively.

Identifying the layer of maximum heat release with the flame front we observe that the OH production rate increases in the streamwise direction on a cross section through the flame front. Roughly speaking, OH is consumed in front of the flame front and attains its absolute maximum immediately behind the flame front. The formation process of OH is far to complex to be displayed here rather its influence on the pollutant formation is discussed below.

CO Formation. From Fig. 11 we find that the CO formation inversely correlates with the OH formation. For a better under-

Downloaded 02 Jun 2010 to 171.66.16.107. Redistribution subject to ASME license or copyright; see http://www.asme.org/terms/Terms_Use.cfm

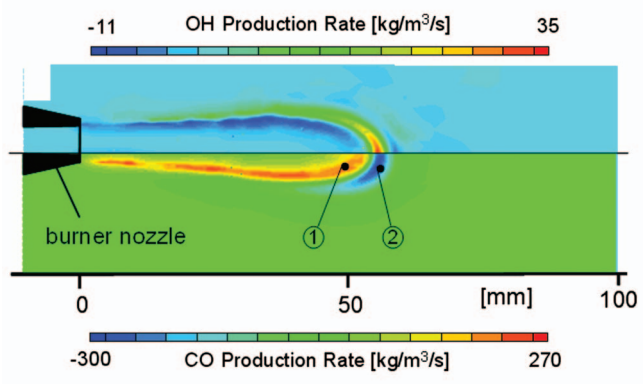

Fig. 11 OH (upper half) and CO (lower half) production rate in the combustion zone on a longitudinal slice through the burner nozzle and combustor axis. 1, 2 analysis points.

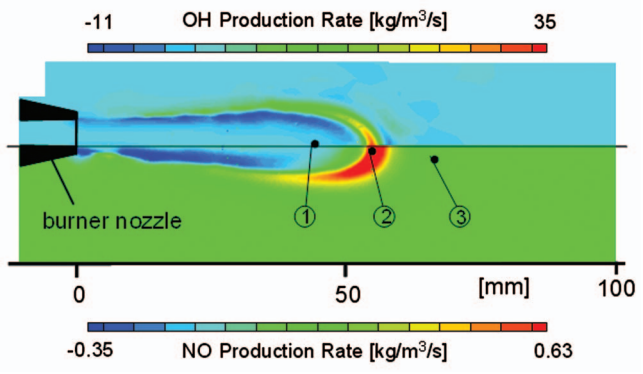

Fig. 13 OH (upper half) and NO (lower half) production rate in the combustion zone on a longitudinal slice through burner nozzle and combustor axis. 1, 2, 3 analysis points.

standing of this fact the GRI3.0 reaction mechanism is analyzed with respect to the CO formation at the two characteristic points of highest production and consumption, as indicated in Fig. 11. The result is depicted in Fig. 12 where the relative amount of the CO production is plotted over the individual equations of the GRI3.0 reaction scheme. The red bars in the charts signify the elementary reactions that produce CO primarily from HCO, viz., $HCO+H_2O \Leftrightarrow CO+H+H_2O$, $HCO+O_2 \Leftrightarrow CO+HO_2$, and $HCO \Leftrightarrow CO+H$. In the blue colored reactions, CO is consumed. We observe that at both analysis points the same elementary reactions are involved. While the CO formation process is comprised of several reactions with several intermediate species involved (see legend in Fig. 11), the CO consumption is primarily described by a single one reaction, viz., $CO+OH \Leftrightarrow CO_2+H$.

At the analysis point 2 where OH is at its maximum this reaction is absolutely predominant over the formation reactions resulting in an almost complete consumption of CO. Against this the CO consumption at the analysis point 1 is essentially diminished for lack of OH radicals. Also the formation reactions are stronger leading to a net production and also to an absolute maximum of CO of about 9000 ppm at this point (see Fig. 1).

NO Formation. In analogy to CO the distribution of the NO formation is compared with the OH formation in Fig. 13. However, in contrast to CO the NO formation directly correlates with the OH formation. Clearly, the production of NO begins with the advent of the OH formation.

Here we analyze the NO formation at the three points indicated in Fig. 13 with the results for the first and second analysis point shown in Fig. 14. The first analysis point is located in front of the reaction zone where we find a weak consumption of NO. The respective analysis of the reaction mechanism shown in Fig. 14 reveals that this primarily results from two competing reactions describing an exchange between NO and NO_2. Of course, this is not really a reduction of the pollutant emission since NO_2 is also a harmful chemical. Additionally there is also a minor amount of NO consumption attributed to Fenimore reactions that are associated with the CH species (see Fig. 14).

The second analysis point is located at the maximum of the NO formation. The respective analysis in Fig. 14 reveals that compared to the first analysis point a lot more reactions are involved. In particular, the number of Fenimore reactions is numerous. These are the blue colored reactions in Fig. 14 and are those reactions that are associated with the CH species (see legend of Fig. 14). In addition we also find a contribution of the three Zeldovich reactions (red) and two reactions describing the NO formation from N_2O (green). The analysis at the third point is similar to that at the second point and is not plotted here.

Recapitulating, the relative amount attributed to the different NO formation mechanisms at the three analysis points and integrated over the whole computational domain is shown in Table 3.

In the reaction zone (point 2) the amount of Fenimore-NO is almost 70% and the amount of NO produced from the Zeldovich, N_2O and NO_2 reactions is approximately in equal measure of

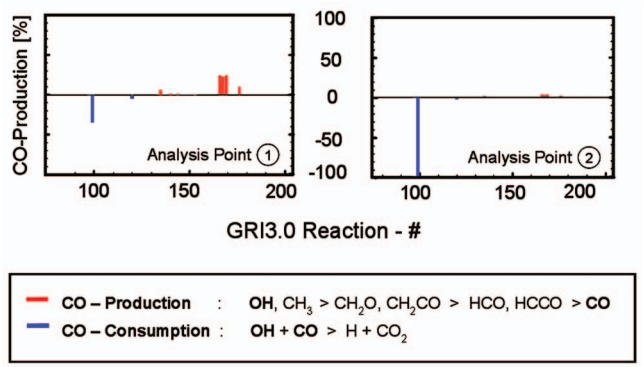

Fig. 12 Relative amount of CO production plotted over the elementary reactions of the GRI3.0 mechanism at analysis point 1 (left) and analysis point 2 (right)

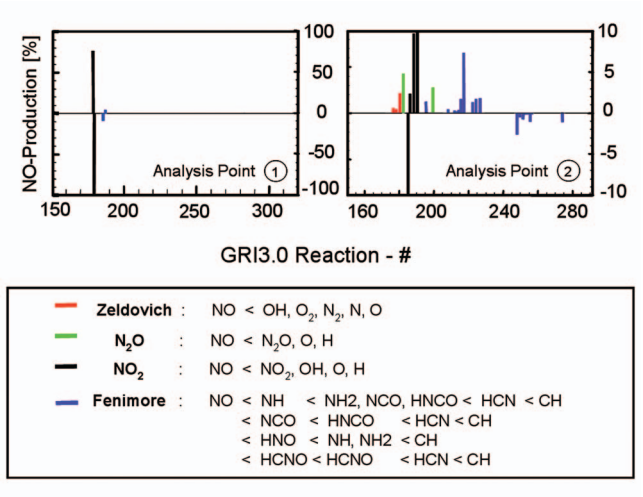

Fig. 14 Relative amount of NO production plotted over the elementary reactions of the GRI3.0 mechanism at analysis point 1 and 2. Red: Zeldovich, Green: N_2O, Black: NO_2, Blue: Fenimore.

Downloaded 02 Jun 2010 to 171.66.16.107. Redistribution subject to ASME license or copyright; see http://www.asme.org/terms/Terms_Use.cfm

Table 3 Relative amount of the NO formation mechanisms at the three analysis points indicated in Fig. 13 and Integrated over all computational cells (global)

	Point 1	Point 2	Point 3	Global
Zeldovich	0.0%	7.8%	30.5%	40.7%
Fenimore (prompt)	−9.8%	67.3%	33.5%	26.6%
N_2O	0.1%	10.1%	34.2%	31.7%
NO_2	−90.1%	14.8%	−1.8%	−1.0%

about 10%. Beyond the reaction zone at analysis point 3 the Fenimore-NO decreases and simultaneously the relative importance of Zeldovich- and N_2O-NO is increased. NO and NO_2 are almost counterbalanced in the respective reactions. The percentage values at point 3 seem to be representative for the remainder of the combustion chamber. This is evident from the comparison of the global integrated values with the results of point 3. As mentioned above Zeldovich- or thermal NO becomes dominant in the case of high temperatures. Obviously the FLOX®-combustion is characterized by a temperature level where NO produced from the Zeldovich-, Fenimore-, and N_2O-mechanisms is of the same order of magnitude.

Conclusions

In the present paper results of the numerical simulation of the FLOX®-combustion at 20 bar and $\lambda=2.16$ were presented and validated using experimental data from the DLR test facility. For this purpose the highly optimized DLR-combustion code IGNIS was presented and used throughout the computations in a coupled unsteady mode with the commercial code Fluent. The computational results are in good agreement with the experimental data.

In the reaction zone the turbulent Damköhler number is in the range of unity indicating equal importance of the finite rate chemistry and the turbulence/chemistry interaction model. In this regard we successfully applied the GRI3.0 reaction mechanism in combination with the PaSR model. With respect to the NO formation we found that the contribution from the three NO formation mechanisms: Zeldovich, Fenimore, and N_2O is approximately of equal measure. However, in the case of incomplete mixing the PaSR model has to be improved with respect to the inhomogeneous composition in the turbulent substructures within the computational cells. Furthermore it was found, that the turbulent mixing process between the high-velocity fuel/air jet and the recirculating hot flue gases is deficiently described by the k-e turbulence model leaving some potential for further improvement.

Acknowledgment

This work presented was financially supported in part by the European Community within the Project New Combustion Systems for Gas Turbines (NGT) under Contract No. ENK5-CT-2001-00564.

Nomenclature

a_{ir} = stoichiometric coefficients of educt species in reaction r
b_{ir} = stoichiometric coefficients of product species in reaction r
c_i = molar concentration of species i
c_i^r = molar concentration of species i in reaction r
$\underline{c}_i$ = mean concentration of species i in the cell
C_{mix} = PaSR model constant
Da_T = turbulent Damköhler number
Da_T^r = turbulent Damköhler number defined for reaction r
F_i^r = reaction rate of species i in reaction r
k = turbulent kinetic energy
k_{fr} = Arrhenius coefficients for forward reactions
k_{br} = Arrhenius coefficients for backward reactions
Q = the internal energy
Re_T = turbulent Reynolds number

Greek

ε = dissipation rate of k
Δh_i^0 = heat of formation of species i at absolute zero
κ = reactive volume fraction of the computational cell
ν = kinematic viscosity
τ = infinitesimal time step
τ_{chem}^r = characteristic chemistry time of reaction r
τ_{chem} = integral characteristic chemistry time
τ_{mix} = integral characteristic turbulent mixing time
τ_K = Kolmogorov time scale
τ_T = Taylor time scale

Subscripts

i = species counter
r = elementary reaction counter
K = indicates reference species

Superscripts

r = elementary reaction counter
N = indicates quantity in nonreacting volume fraction of the cell also indicates preceding time level
R = indicates quantity in the reacting volume fraction of the cell

Appendix A: Reference Species Technique

Each combustion process is described by the solution of a system of elementary chemical reactions of the form

$$\frac{dc_i}{dt}=\sum_r \frac{dc_i^r}{dt}=\sum_r F_i^r(c_j) \tag{A1}$$

where c_i is the molar concentration of species i and F_i^r is the rth reaction rate defined as

$$F_i^r(c_j)=(b_{ir}-a_{ir})[\Omega_{\mathrm{fr}}-\Omega_{\mathrm{br}}] \tag{A2}$$

with

$$\Omega_{\mathrm{fr}} := k_{\mathrm{fr}}\prod_j c_j^{a_{jr}} \quad \text{and} \quad \Omega_{\mathrm{br}} := k_{\mathrm{br}}\prod_j c_j^{b_{jr}} \tag{A3}$$

.

In Eqs. (A2) and (A3), a_{ir} and b_{ir} are the stoichiometric coefficients and k_{fr} and b_{fr} are the Arrhenius-type reaction coefficients for forward and backward reactions, respectively. Equation (A1) is a strongly nonlinear system of equations whose fully implicit solution, applying the Newton linearization is very tedious. In contrast, although the explicit solution is very simple it is time step dependent and frequently leads to an unphysical composition (negative species densities).

In the IGNIS code, a semi-implicit solution procedure according to the so-called "reference species technique" [3] is applied, which displays a very fast and stable solution behavior. The basic idea is to linearize Eq. (A1) with respect to the species K which for each reaction r is in greatest danger of being driven negative. This species is defined to be the reference species c_K^r following from the condition

$$c_K^r=\left\{ c_i^r \left| \frac{\dfrac{dc_i^r}{dt}}{c_i^r}=\text{minimum } \mathbf{i} \right. \right\} \tag{A4}$$

Performing Taylor series expansion of F_i^r around $(F_i^r)^N$ (the upper index N denotes the preceding time level) and neglecting all

Downloaded 02 Jun 2010 to 171.66.16.107. Redistribution subject to ASME license or copyright; see http://www.asme.org/terms/Terms_Use.cfm

derivatives in the Jacobian matrix except those with respect to the reference species c_K^r leads to the following semi-implicit form of Eq. (A1)

$$\frac{dc_i}{dt} = \sum_r \frac{dc_i^r}{dt} \cong \sum_r (b_{ir} - a_{ir})\dot{\omega}_r^* \tag{A5}$$

with

$$\dot{\omega}_r^* = \frac{\Omega_{\mathrm{fr}}^N - \Omega_{\mathrm{br}}^N}{1 + \dfrac{\tau}{\tau_{\mathrm{chem}}^r}} \tag{A6}$$

where τ_{chem}^r is the characteristic chemistry time for each elementary reaction, viz.,

$$\tau_{\mathrm{chem}}^r := \frac{c_K^{rN}}{(a_{Kr} - b_{Kr})(a_{Kr}\Omega_{\mathrm{fr}}^N - b_{Kr}\Omega_{\mathrm{br}}^N)} \tag{A7}$$

and τ is an infinitesimal time step used to approximate the temporal derivative of the reference species.

In analogy to Eq. (A5) the source term in the internal energy equation reads

$$\frac{dQ}{dt} = -\sum_r \sum_i (b_{ir} - a_{ir})\Delta h_i^0 \dot{\omega}_r^* \tag{A8}$$

where Q is the internal energy and Δh_i^0 is the heat of formation of species i at absolute zero.

In order to specify an expression for a characteristic chemistry time τ_{chem} representative for all elementary reactions in a computational cell we found it reasonable to derive this from Eq. (A8) as a heat release weighted average of the form

$$\tau_{\mathrm{chem}} = \frac{\displaystyle\sum_r Q_r \frac{\tau_{\mathrm{chem}}^r}{\tau + \tau_{\mathrm{chem}}^r}}{\displaystyle\sum_r Q_r \frac{1}{\tau + \tau_{\mathrm{chem}}^r}} \tag{A9}$$

with

$$Q_r := \sum_i (b_{ir} - a_{ir})\Delta h_i^0 (\Omega_{\mathrm{fr}}^N - \Omega_{\mathrm{br}}^N) \tag{A10}$$

Appendix B: Partially Stirred Reactor Model (PaSR)

This model is based upon the fundamental assumption that within a computational cell chemical reaction may occur only in the volume fraction κ of the cell where reactants are mixed on a molecular level. The mean concentration $\overline{c_i}$ of each involved species in the considered cell is then given by the simple linear relation

$$\overline{c_i} = (1 - \kappa)c_i^N + \kappa c_i^R; \quad \kappa \in [0,1] \tag{B1}$$

Here the upper indices R and N denote the reactive and nonreactive part of the cell, respectively. Equation (B1) may be interpreted as a temporal process where c_i^N is the initial concentration and $\overline{c_i}$ is the mean concentration after the lapse of an infinitesimal time τ.

In a turbulent flow, the reactive composition is generated by turbulent dispersion and molecular diffusion. The turbulent dispersion is a very complex process proceeding simultaneously on all turbulent length scales with an inherent spectrum of characteristic mixing times.

In the present model the temporal decay of turbulent eddies up to the Kolmogorov-scale is described by a single integral mixing time τ_{mix} which will be explained later. It is evident that κ is proportional to τ (molecular diffusion) and also proportional to $1 - \tau_{\mathrm{mix}}$ (turbulent dispersion). Assuming equal proportionality Eq. (B1) may be written in the form

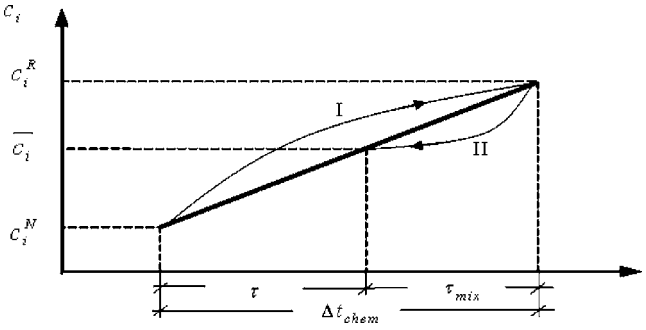

Fig. 15 Graphical representation of Eq. (12)

$$\frac{\overline{c_i} - c_i^N}{\tau} = \frac{c_i^R - \overline{c_i}}{\tau_{\mathrm{mix}}} \equiv F_i^R \tag{B2}$$

Equation (B2) is graphically displayed in Fig. 15 where it is further assumed that the slope of the curve is equal to the reaction rate F_i^R in the reactive part κ of the cell. In Fig. 15 we distinguish two parallel processes I and II:

(I) During reaction time $\Delta t_{\mathrm{chem}} = \tau + \tau_{\mathrm{mix}}$ the initial molar concentration in the reactive fraction κ changes from c_i^N to c_i^R;
(II) The reactive fraction is mixed by turbulence with the nonreactive fraction resulting in the averaged concentration $\overline{c_i}$.

Equation (B2) written for the reference species K of reaction r and Taylor-series expansion of $(F_K^r)^R$ around $\overline{(F_K^r)}$ leads to the implicit form

$$\frac{\overline{(c_K^r)} - (c_K^r)^N}{\tau} = \kappa_r \overline{(F_K^r)} \tag{B3}$$

with

$$\kappa_r := \frac{1}{1 + \mathrm{Da}_T^r} \quad \text{and} \quad \mathrm{Da}_T^r := \frac{\tau_{\mathrm{mix}}}{\tau_{\mathrm{chem}}^r} \tag{B4}$$

In Eq. (B4) a turbulent Damköhler number Da_T^r for reaction r was introduced as the ratio of a characteristic turbulent mixing time related to a characteristic chemistry time.

Semi-implicit formulation of Eq. (B3) using the reference species technique and summing up over all elementary reaction finally yields

$$\frac{d\overline{c_i}}{dt} \cong \frac{\overline{c_i} - c_i^N}{\tau} = \sum_r \kappa_r (b_{ir} - a_{ir})\dot{\omega}_r^* \tag{B5}$$

with

$$\dot{\omega}_r^* = \frac{\Omega_{\mathrm{fr}}^N - \Omega_{\mathrm{br}}^N}{1 + \kappa_r \dfrac{\tau}{\tau_{\mathrm{chem}}^r}} \tag{B6}$$

Comparing Eqs. (B5) and (B6) with Eqs. (A5) and (A6) reveals that the turbulence/chemistry interaction is accounted for through the term κ_r, which depends on the turbulent Damköhler number as specified in Eq. (B4). τ_{chem}^r is given by Eq. (A7) and with definition of the Kolmogorov time scale $\tau_K \sim \sqrt{\nu/\varepsilon}$, the Taylor time scale $\tau_T \sim k/\varepsilon$, and the turbulent Reynolds number $\mathrm{Re}_T := k^2/\upsilon\varepsilon = (\tau_T/\tau_K)^2$ the following expressions for τ_{mix} are found in the literature.

According to the model of Byggstøyl and Magnussen [11]

Downloaded 02 Jun 2010 to 171.66.16.107. Redistribution subject to ASME license or copyright; see http://www.asme.org/terms/Terms_Use.cfm

$$\tau_{\text{mix}} = \frac{1}{23.6}\left(\frac{k^2}{\upsilon\varepsilon}\right)^{1/4}\frac{k}{\varepsilon} = \frac{1}{23.6}(\text{Re}_T)^{1/4}\tau_T \tag{B7}$$

τ_{mix} increases with increasing turbulent Reynolds number which results in the unphysical fact that the amount of the reactive volume fraction κ decreases.

An alternative approach is given by Karlsson and Chomiak [12] as the geometrical mean of the Kolmogorov and the Taylor time scales, viz.,

$$\tau_{\text{mix}} = C_{\text{mix}}\sqrt{\tau_T\tau_K} = C_{\text{mix}}(\text{Re}_T)^{-(1/4)}\tau_T \tag{B8}$$

Kjäldman [12] reported that best results were obtained by simply using the Taylor time scale

$$\tau_{\text{mix}} = C_{\text{mix}}\tau_T \tag{B9}$$

C_{mix} is a model constant which lies in the range of $C_{\text{mix}}=0.001-0.3$ depending on the flow considered.

For a better interpretation of the computational results it is useful to define global expressions for the fine structure volume fraction κ and the turbulent Damköhler number representative for all reactions in each computational cell. Using Eq. (A9) we may define analogously to Eq. (B4),

$$\text{Da}_T := \frac{\tau_{\text{mix}}}{\tau_{\text{chem}}} \tag{B10}$$

and

$$\kappa := \frac{1}{1+\text{Da}_T} \quad \text{or} \quad \text{Da}_T := \frac{1-\kappa}{\kappa} \tag{B11}$$

Finally, we recognize from Eq. (B11) that within the PaSR-model the Damköhler number may be interpreted as the ratio of the nonreacting, coarse-structured volume fraction related to the reacting, fine-structured volume fraction of each computational cell.

References

[1] Wünning, J. A., Patent EP 0463218.

[2] Vaz, D. C., Borges, A. R. J., van Buijtenen, J. P., and Spliethoff, H., 2004, "On the Stability Range of a Cylindrical Combustor in the Flameless Oxidation Regime," GT2004–53790, Proceedings of the ASME Turbo Expo 2004, June 14–17, Vienna, Austria.

[3] Amsden, A. A., O'Rourke, P. J., and Butler, T. D., 1989, KIVA-II: A computer Program for Chemically Reactive Flows with Sprays. LA-11560-MS.

[4] Smith, G. P., Golden, D. M., Frenklach, M., Moriarty, N. W., Eiteneer, B., Goldenberg, M., Bowman, C. T., Hanson, R. K., Song, S., Gardiner, W. C. Jr., Lissianski, V. V., and Qin, Z., 1999, "GRI3.0 mechanism version 3.07/30/99," see http://www.me.berkley.edu/gri_mech.

[5] Nordin, P. A. N., 1995, "Complex Chemistry Modelling of Diesel Sprays," Ph.D. thesis, Chalmers University of Technology, Göteborg.

[6] Karlsson, J. A. J., 1995, "Modelling Auto-Ignition, Flame Propagation and Combustion in Non-Stationary Turbulent Sprays," Ph.D. thesis, Chalmers University of Technology, Göteborg.

[7] Warnatz, J., Maas, U., and Dibble, R. W., 1997, *Verbrennung*, Springer-Verlag, Berlin Heidelberg, 2. Auflage.

[8] Lückerath, R., Schütz, H., Noll, B., and Aigner, M., 2005, "Experimental Investigations of FLOX®-Combustion at High Pressure," Flameless Combustion Workshop, Lund, Sweden, June 19–21.

[9] Meier, U. E., Wolff-Gaßmann, D., and Stricker, W., 2000, "LIF Imaging and 2D Temperature Mapping in a Model Combustor at Elevated Pressure," Aerosp. Sci. Technol., **4**, pp. 403–414.

[10] Leonard, G., and Stegmaier, J., 1993, "Development of an Aeroderivative Gas Turbine Dry Low Emission Combustion System," ASME Paper No. 93-GT-288.

[11] Byggstøyl, S., and Magnussen, B. F., 1985, "A Model for Flame Extinction in Turbulent Flow," 4th Symposium on Turbulent Shear Flows, pp. 381–395.

[12] Karlsson, J. A. J., and Chomiak, J., 1995, "Physical and Chemical Effects in Diesel Spray Ignition," 21st Congress of CIMAC, Interlaken Switzerland, May 15–18.

Downloaded 02 Jun 2010 to 171.66.16.107. Redistribution subject to ASME license or copyright; see http://www.asme.org/terms/Terms_Use.cfm

Compressor/Diffuser/Combustor Aerodynamic Interactions in Lean Module Combustors

A. Duncan Walker

Jon F. Carrotte

James J. McGuirk
e-mail: j.j.mcguirk@lboro.ac.uk

Department of Aeronautical and Automotive Engineering,
Loughborough University,
Loughborough LE11 3TU, UK

The paper reports an experimental investigation into the possibility of increased interactions between combustor external aerodynamics and upstream components, e.g., prediffuser, compressor outlet guide vane (OGV), and even the compressor rotor, caused by the trend in lean module fuel injectors to larger mass flows entering the combustor cowl. To explore these component interaction effects, measurements were made on a fully annular rig comprising a single stage compressor, an advanced integrated OGV/prediffuser, followed by a dump diffuser and a generic combustor flametube with metered cowl and inner/outer annulus flows. The flow split entering the cowl was increased from 30% to 70%. The results demonstrate that, with fixed geometry, as the injector flow increases, the performance of the prediffuser and feed annuli suffer. Prediffuser losses increase and at high injector flow rates, the diffuser moves close to separation. The substantial circumferential variation in cowl flow can feed upstream and cause rotor forcing. Notable differences in performance were observed inline and between injectors at the OGV exit, suggesting that geometry changes such as an increased dump gap or nonaxisymmetric prediffuser designs may be beneficial. [DOI: 10.1115/1.2747646]

Introduction

In future aeroengine gas turbine combustor designs, lean module combustion will be essential in order to achieve required NO_x targets. Consequently, up to 70% of the flow issuing from the compressor may be required to enter the flametube through the fuel injectors, compared with (typically) 30% in current combustor designs. To accommodate this increased mass flow requirement while maintaining an acceptable pressure drop, lean module fuel injectors will be significantly larger than their conventional air-spray counterparts. This will necessitate geometry changes to the combustor external aerodynamic layout such as a deeper flametube, potentially increasing the aerodynamic loss due to increased turning within the dump region. In addition to affecting the turning losses incurred by the residual airflow entering the feed annuli surrounding the flametube, these geometry and flow split changes and the strongly 3D (circumferential) distribution of the flow into the combustor head compared to current practice are likely to increase the coupling or interaction between the combustor external aerodynamics and upstream components such as the compressor outlet guide vane (OGV)/prediffuser combination and possibly even lead to forcing of the final compressor rotor stage.

Upstream modification of turbomachinery flow due to the potential field introduced by downstream components is by no means a new phenomenon. It has led, for example, to work on optimization of the aerodynamic interaction between the fan and by-pass OGVs (Shahpar et al. [1]). Equally, the two-way interaction between the prediffuser, upstream OGV, and downstream combustor is well known. The impact of OGV wakes on the performance of a downstream located prediffuser has been fully documented (Stevens et al. [2], Barker and Carrotte [3,4]), as has the beneficial effect of the blockage caused by the downstream combustor cowl stabilizing the prediffuser flow (Klein [5]). Recent works by Barker et al. [6] and Walker et al. [7] have shown how, by adopting an integrated approach whereby the design of the OGV and prediffuser are considered simultaneously, the OGV wake flows can be manipulated to advantage in achieving improved prediffuser performance. Finally, computational fluid dynamics (CFD) simulations have also recently addressed the topic of interaction between closely coupled components such as compressor and combustor (Schlueter et al. [8]). In this work, the main effort was placed on identification of appropriate techniques for coupling the unsteady Reynolds-averaged Navier-Stokes prediction of the compressor flow with the large-eddy simulation prediction of the prediffuser/combustor combination. It seems that the coupling was essentially one way (downstream in the engine), so that although combustor cowl/fuel injector pressure and flow characteristics could influence the prediffuser, it was assumed that these did not penetrate further upstream and influence the compressor calculation. While this is certainly the design intent, and is a good assumption for present designs, the present paper is aimed at addressing the question as to how strong this upstream effect might be for lean module type geometries and injector flow splits.

The present investigation extends the study of Walker et al. [7] to consideration of combustor cowl (fuel injector) flow in addition to the compressor/prediffuser components. An experimental investigation has been undertaken to characterize the extent that the component interactions described above are modified when increasing the injector airflow from conventional levels to those expected in lean module combustors, using a combustion system layout typical of current design practice. The experimental study utilizes the same rig as used by Walker et al. [7]. This comprises a fully annular generic lean module combustor downstream of a single stage axial compressor. The OGV/prediffuser coupling is effected via an advanced integrated OGV/prediffuser geometry [4,5]. Several traverse planes are used to gather five-hole probe data that allow the flow structure to be examined through the rotor, OGV, prediffuser, and in the inner/outer annulus supply ducts, quantifying the extent of the component interactions and associated system performance. Several configurations are investigated where the injector mass flow has been increased systematically from 30% to 50% and finally 70%.

Contributed by the International Gas Turbine Institute of ASME for publication in the JOURNAL OF ENGINEERING FOR GAS TURBINES AND POWER. Manuscript received May 1, 2007; final manuscript received May 4, 2007; published online January 9, 2008. Review conducted by Dilip R Ballal. Paper presented at the ASME Turbo Expo 2007: Land, Sea, and Air (GT2007), Montreal, Quebec, Canada, May 14–17, 2007. Paper No. GT2007-27872.

Copyright © 2008 by ASME

Downloaded 02 Jun 2010 to 171.66.16.107. Redistribution subject to ASME license or copyright; see http://www.asme.org/terms/Terms_Use.cfm

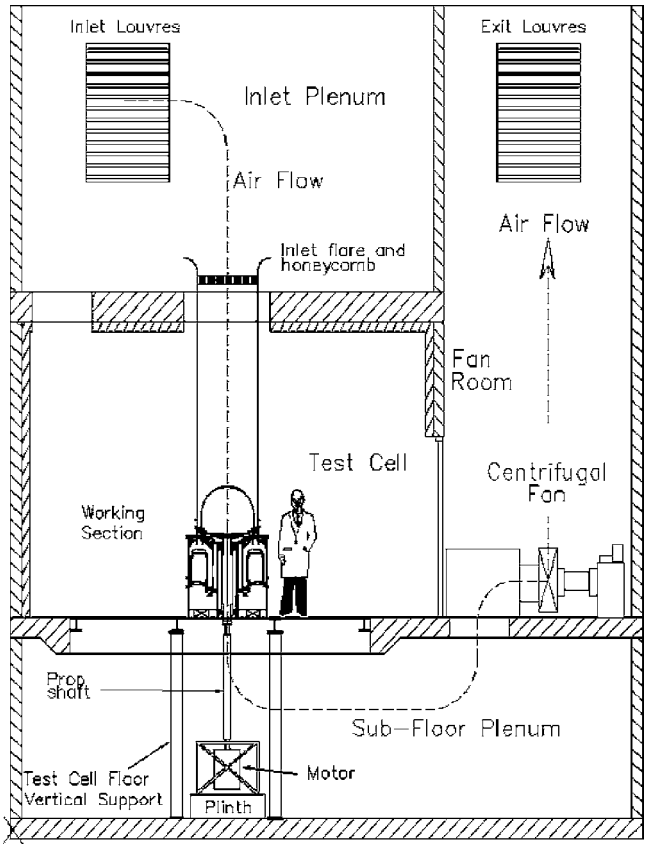

Fig. 1 Test facility

Experimental Facility

During this project, all experimental data were obtained on a low speed isothermal test facility operating at nominally atmospheric conditions. Figure 1 provides an illustrative sketch, and full details are provided in [7]. During the present study, an additional centrifugal fan was added, in series, to the system. This gave a greater flexibility in control and provided the extra drive required to overcome the increased rig pressure drop incurred by forcing a higher proportion of air through the combustor cowl.

The working section (Fig. 2) is comprised of a single stage axial compressor, an OGV prediffuser assembly, and a representation of a downstream combustion system. Geometric details on integrated guide vane (IGV), rotor, and OGV rows are given in [7]. The rotor is operated at a fixed nondimensional mass flow ($\dot{m}\sqrt{(RT)}/AP$), and speed ($N\pi D/\sqrt{(\gamma RT)}$) corresponding to a flow coefficient (V_a/U) of $\phi=0.403$ and a mass flow of approximately 4 kg s^{-1}. This results in an axial velocity through the blade rows of approximately 40 ms^{-1}(Mach number 0.12) and an OGV Reynolds number of approximately 1.6×10^5. The downstream flow distribution to the feed annuli and combustor cowl is controlled by a system of throttles; the centrifugal fan is utilized as a further throttle to ensure that the axial compressor maintains the desired operating condition.

Test Geometry

Integrated OGV/Prediffuser. The OGV row has 160 vanes whose geometry includes specific lean, sweep, and camber characteristics that were determined in [6] by a process of manual CFD optimization. This achieves a spanwise blade loading variation that creates secondary flows to transport higher momentum towards the walls, thus offloading the end wall boundary layers within the prediffuser. Hence, as reported in [7], this integrated OGV (IOGV) design was able to achieve a prediffuser area ratio of 1.8 without separation. At the same nondimensional length of 2.23, this would have resulted in separation according to the standard Howard et al. [9] design chart.

Generic Flame Tube Cowl and "Fuel Injectors." The same simple flametube geometry as used previously [7] was retained in the present work. This presents the IOGV/prediffuser with a representative downstream blockage. Lean module combustors may not feature air admission ports in the annuli, hence no dilution holes were included in the flametube liner walls. The resultant generic flametube, illustrated in Fig. 3, has 20 "fuel injectors" represented by 20 simple holes, with the area of these set initially (Test 1) to match the effective area of an injector sized to take 30% of compressor discharge flow. As the mass flow through "injectors" and hence the cowl was increased, the ratio of mass flow to "injector" area was maintained by increasing the size of the holes. This meant that as the mass flow increased, the relative acceleration of the dump flow into the cowl did not change. The final configurations tested are detailed in Table 1.

Instrumentation

Probes. Aerodynamic performance was assessed using suitably calibrated miniature five-hole probes as described by Wray and Carrotte [10] and employed in non-nulled mode to determine the local flow vector and total and static pressures. As indicated in Fig. 2, five-hole probe area traverses were conducted at rig inlet (X1), rotor exit (X2), OGV exit (X3), prediffuser exit (X4), within the inner (X5i), and outer (X5o) feed annuli and just upstream of the dummy injector (XI). The probes were traversed in the radial direction using a stepper motor powered linear guide attached to the external casings of the test section. Circumferential traversing was achieved by rotation of the casing or rotation of the IGV, OGV, and flametube.

Data Reduction and Errors. Overall aerodynamic performance is quantified in terms of total pressure loss and static pressure recovery coefficients derived from the five-hole probe area traverses data, corrected to the International Civil Aviation Organisation (ICAO) standard day conditions. Thus, at any measurement plane, the mass flow rate and bulk average velocity are defined:

$$\dot{m} = \int \rho U dA = \rho \bar{U} A \tag{1}$$

The mass flow balance on area traverse planes was within ±1% of the rig mass flow entering the test facility measured via a five-hole probe traverse at plane (X1). Spatially averaged values of total and static pressure at each plane were derived using the mass-weighted technique described by Klein [5], e.g.,

$$\tilde{P} = \frac{1}{\dot{m}} \int P d\dot{m} = \frac{1}{\rho \bar{U} A} \int P \rho U dA \tag{2}$$

The mass-weighted total pressure loss (λ) and static pressure rise (C_p) coefficients are then defined as

$$\lambda_{1-2} = \frac{\tilde{P}_1 - \tilde{P}_2}{\tilde{P}_1 - \tilde{p}_1} \quad C_{p_{1-2}} = \frac{\tilde{p}_2 - \tilde{p}_1}{\tilde{P}_1 - \tilde{p}_1} \tag{3}$$

The mass-weighted total pressures were repeatable to within ±1 mm H_2O, which amounts to less than ±0.5% of the dynamic pressure at OGV exit. Thus, the repeatability of the derived total pressure loss and static pressure rise coefficients was better than ±0.005 of the values presented.

Results and Discussion

Cowl Flow Variation. As an indication of the strength of the variation in cowl inlet flow conditions induced by the flow split

Downloaded 02 Jun 2010 to 171.66.16.107. Redistribution subject to ASME license or copyright; see http://www.asme.org/terms/Terms_Use.cfm

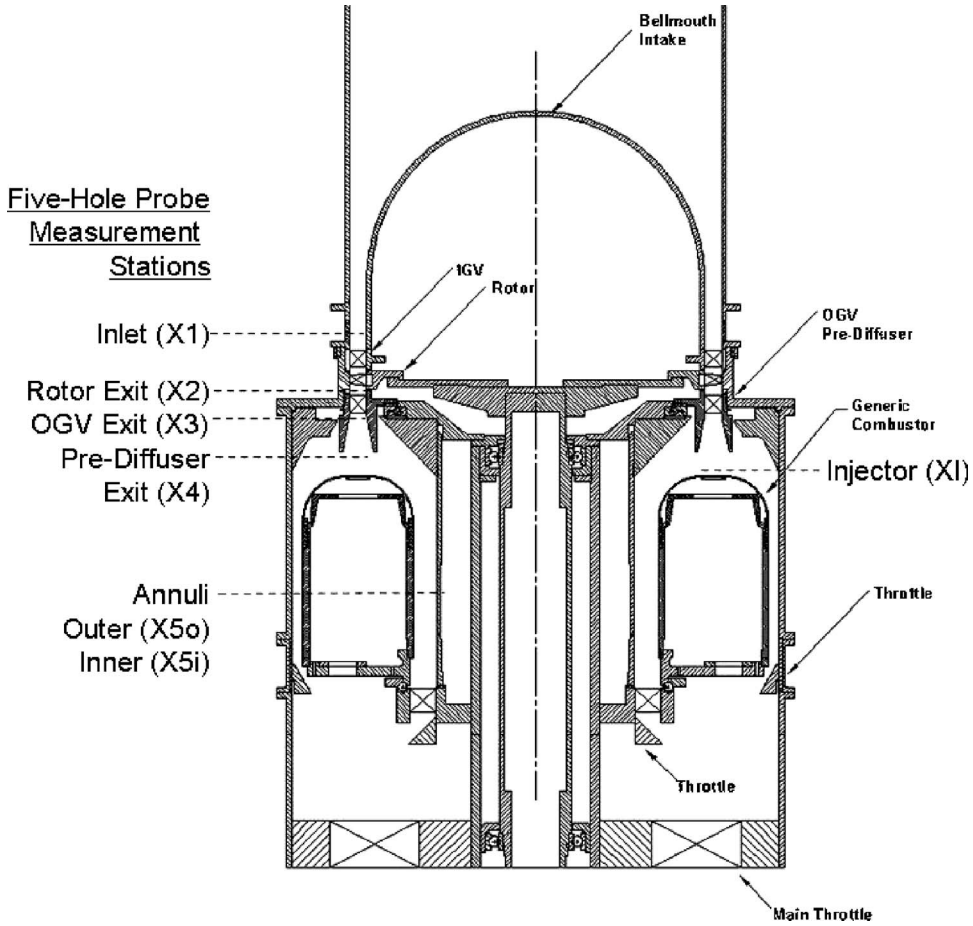

Fig. 2 Measurement planes

changes, Fig. 4 shows measured values of the total pressure field just upstream (13 mm) of the hole in the combustor cowl for the two higher mass flows (50% and 70%) (expressed as a loss coefficient with respect to the rotor exit plane (X2)). One particular point to notice is the increase in nonuniformity of the total pressure feed to the injector implied at the high flow (70%) condition. Since lean module fuel injectors may need high levels of flow uniformity to achieve lean emissions performance, it is clear that extra efforts to ensure this by suitable tailoring of the combustor external aerodynamics are likely to be needed. To increase injector flow while keeping prediffuser/dump diffuser geometry the same is unlikely to be acceptable. As the porosity of the cowl increases, and the dump gap remains the same, the downstream static pressure field as seen by the prediffuser exit changes from one that is effectively uniform circumferentially at low cowl flows—varying from a higher level in between injectors where flow impingement occurs to a slightly lower level in line with the "sink" flow areas of the cowl that feed the fuel injectors—to a larger amplitude variation in static pressure at increased cowl flow from the highs in between injector locations, to significant lows inline with injectors. At the very least, this is likely to disturb the beneficial blockage effect on the prediffuser expected at an unchanged dump gap. Whether the effect penetrates even further upstream is now addressed.

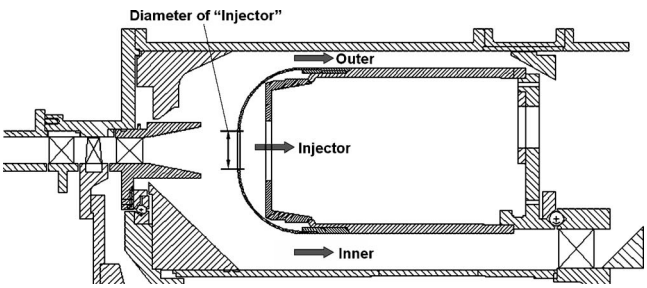

Fig. 3 Cowl details

Rig Inlet (X1) and Rotor Exit (X2). Figure 5 presents the nondimensional axial velocity profiles at rig inlet (X1) for the various cowl flow splits; the different development lengths on the inner/outer annulus walls in the rig entry section explain the different inner/outer boundary layer shapes seen at station X1. Figure 5 shows that upstream of the IGV, the inlet profile remains constant for all conditions; the IGV is too far upstream even at the highest cowl flow rate to sense the downstream change in flow split. This is, however, not the case for the rotor exit (X2) profiles, as can be seen in Fig. 6, which contains normalized and pitch-averaged axial velocity, yaw angle, and total pressure profiles; these have been averaged over a single IGV sector (i.e., two OGV sectors given the blade numbers), and the bulk Mach number at station X3 is 0.12. Cleary, for 30% and 50% cowl flow, the rotor

Table 1 Summary of test configurations

Test No.	"Injector" diameter (mm)	Mass flow split, % (inner/cowl/outer)
1	40.0	35/30/35
2	52.5	25/50/25
3	61.5	15/70/15

Downloaded 02 Jun 2010 to 171.66.16.107. Redistribution subject to ASME license or copyright; see http://www.asme.org/terms/Terms_Use.cfm

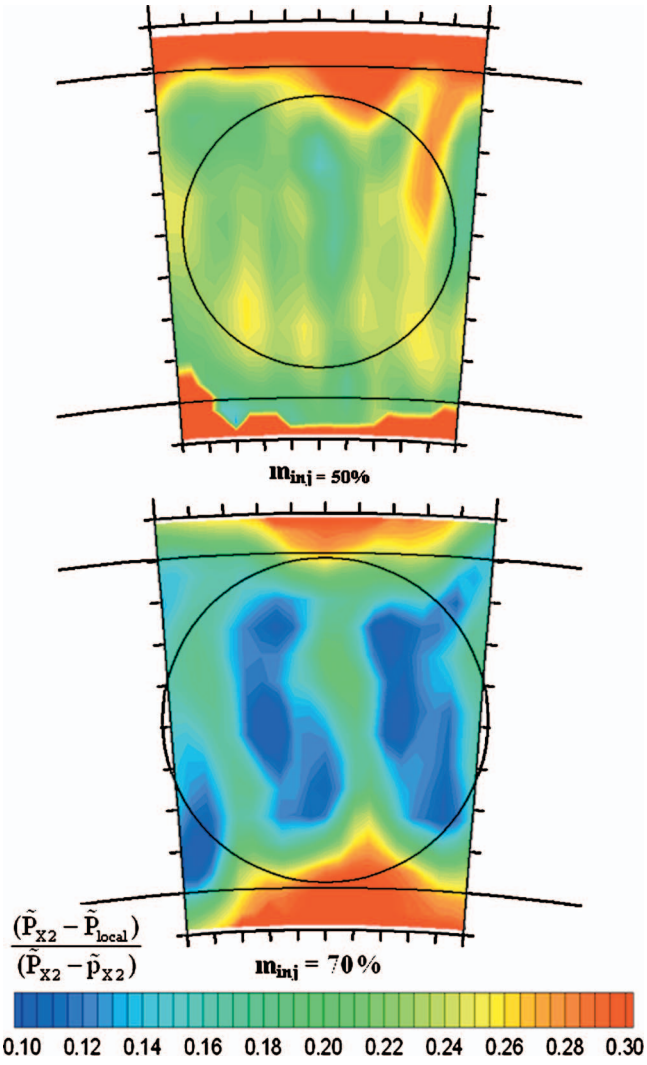

Fig. 4 Cowl inlet data: m_{inj}=50% (top), m_{inj}=70% (bottom) (height=80 mm, sector angle $\Delta\theta$=9 deg (4-OGV passages))

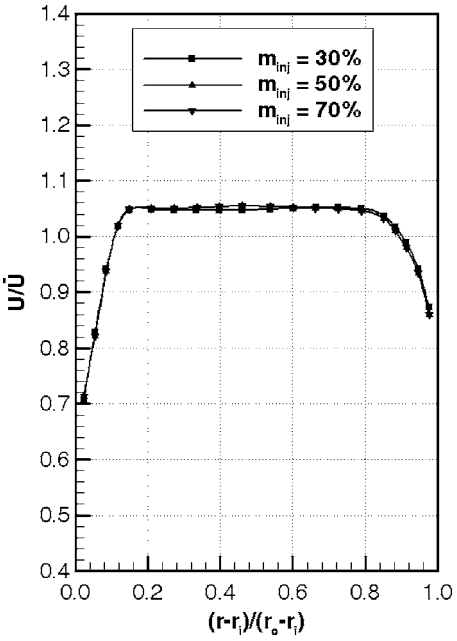

Fig. 5 Rig inlet axial velocity profile (X1)

exit conditions only change marginally. However, for 70% of the prediffuser efflux passing through the cowl, the rotor exit flow field is clearly altered. The velocity profiles show a flow deficit at the tip of the rotor—a feature also reflected in the pressure and yaw angle profiles. The change in the combustor flow split to 70% cowl flow has created a strong enough variation in the downstream static pressure field to feed upstream and force the compressor rotor. Note that the left hand pressure profiles in Fig. 6 are plotted as two sets for the 70% case. One set represents a two OGV pitch average taken inline with injectors and one is taken in between injectors. Although some difference is seen, the nondimensionalizing dynamic head is taken relative to the local OGV sector and hence circumferential variations in flow strength are not seen. The right-hand pressure plot in Fig. 6 shows an average taken over a whole injector sector (eight OGV passages, again, one sector is in between and one inline with the injector location. Now a clear difference is seen in the total pressure level in the core passage between sectors, indicating that as the rotor passes through the circumferentially varying static pressure field, it is forced to move around on its characteristic.

Figure 7 quantifies the magnitude of the varying static pressure seen by the rotor at both 50% and 70% conditions from measurements of a fixed wall static at rotor exit (X2) as the combustor was rotated though two sectors. At 50% cowl flow, there are only slight variations in the measured pressure circumferentially, probably due to the potential field of the OGV, but only just within measurement accuracy. The static pressure for the 70% case, however, can be seen to vary significantly from inline to in between injectors, showing a low pressure inline. The circumferential resolution in the data is again just sufficient to pick up the changes in static pressure caused by the potential field of the downstream OGVs. However, this is small compared to the variation caused by the cowl flow suction field, which is equivalent to approximately 5% of the rotor total pressure rise. This is certainly enough to force the rotor to move locally up or down its characteristic. The fact that the changes in downstream flow split can penetrate as far upstream as the rotor and can affect its operation is significant, and shows that dump gap design rules to achieve optimum stability for prediffusers will clearly not be transferable between conventional and lean module combustors.

OGV Exit (X3). Final confirmation of the change in upstream interaction between 50% and 70% flow split is provided in Fig. 8. This shows the circumferential variation of a single OGV exit (X3) total pressure measurement located at midannulus height between two OGVs as the combustor is rotated through one injector sector. At 30–50% cowl flow, the pressure is constant to within measurement accuracy. Caution must be exercised here in that this measurement is only at midblade passage, midannulus height, so it cannot be unequivocally concluded that the OGV row does not see the variation in circumferential blockage provided by the combustor (see below). However, at 70%, the measured pressure at OGV exit varies significantly and periodically with the injector location. The magnitude of this variation is relatively large at 7% of the local dynamic pressure. Velocity data averaged over respective sectors shows that with respect to the rig overall mass flow rate, the indicated mass flow per sector varies from inline to in between injectors by ±5%. It is clear, therefore, that at 70%, the downstream pressure field has propagated upstream and beyond the OGV to influence the rotor. The OGV performance is also affected by this interaction. Figure 9 plots axial velocity contours for two 2-OGV sectors in between and inline with injectors. Adjacent OGV wakes differ because there is one IGV per two OGVs and the IGV wake persists through the rotor, deepening the left-hand OGV wake. For 70% cowl flow, there appears to be a reduction in the bulk velocity. Table 2 details the total pressure loss and static pressure recovery across the OGV. For the two lower flow

Downloaded 02 Jun 2010 to 171.66.16.107. Redistribution subject to ASME license or copyright; see http://www.asme.org/terms/Terms_Use.cfm

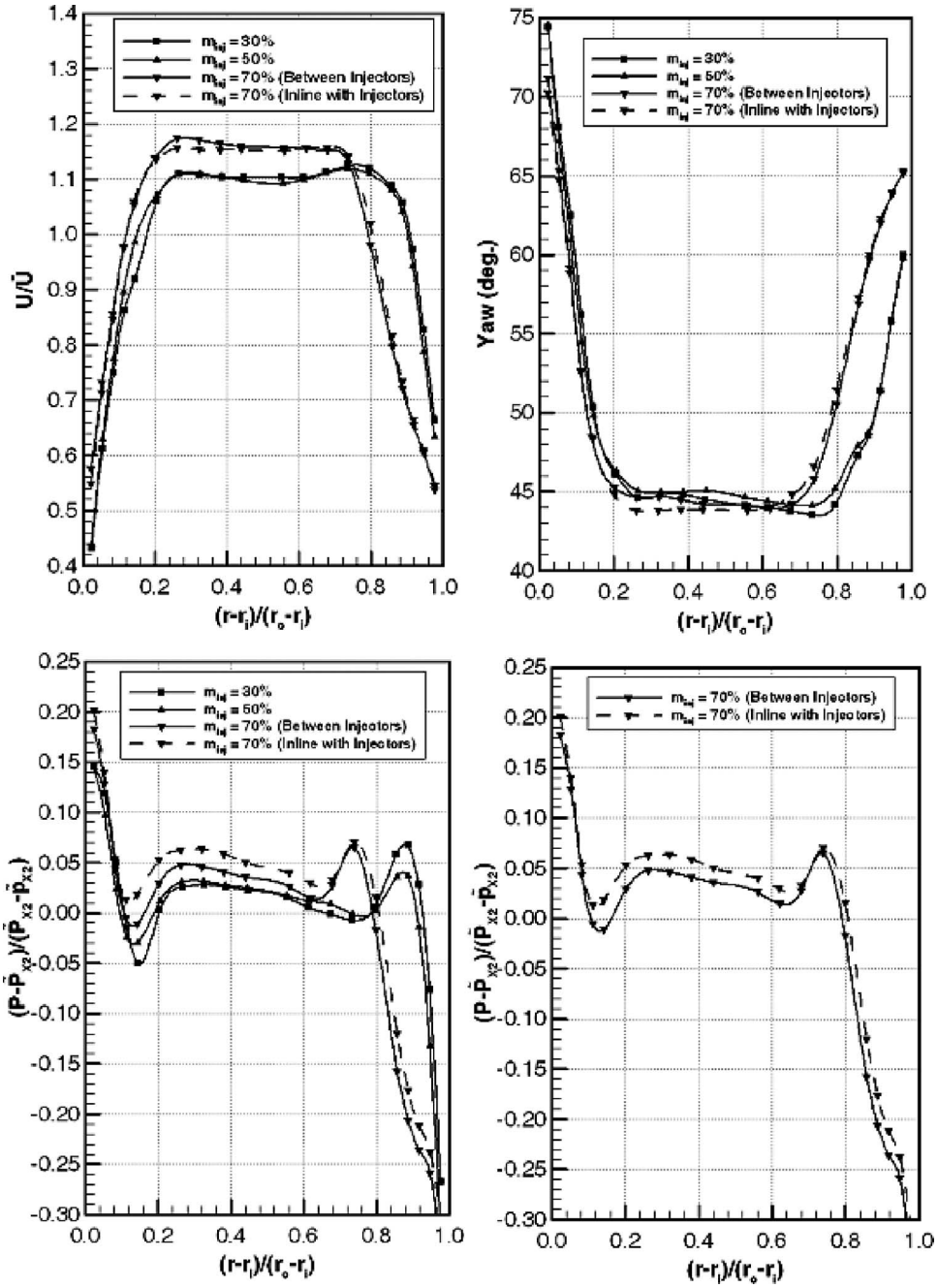

Fig. 6 Pitch averaged profiles at rotor exit (X2)

splits, performance is maintained. Over a whole injector sector it would appear that 70% cowl flow produces a similar level of OGV performance. However, if separate 2-OGV sectors are considered, this is not the case. Between injectors, where there is a flow deficit, λ increases from 0.13 to 0.15, whereas inline with injectors, where there is increased flow, λ falls to 0.1.

Prediffuser Exit (X4). Given that, for Test 3, the rotor and OGV are affected by the circumferential variation in blockage presented by the combustor, it would be logical to expect this to be reproduced at prediffuser exit. Additionally, it would also be reasonable to assume that variations of prediffuser exit flow should be observed as the airflow through the cowl increases. Figure 10 indicates that this is indeed the case. Normalized axial velocity contours were gathered over a full injector sector (the bulk average Mach number at station X4 is 0.07). Clearly, as the combustor mass flow is redistributed, the flowfield and OGV wake structure also change. Increasing the injector flow from 30% to 50% alters the OGV wake development, with the flow taking on an inboard bias. The most likely explanation for this is that at 50% flow, although the upstream interaction has not reached the rotor, it has reached the OGV and the total pressure profile at OGV exit has been modified. This change is then amplified by the prediffuser to produce the inboard bias shown. At 70% cowl flow, the flow structure at prediffuser exit changes again, exhibiting low velocity regions suggesting the inner wall boundary layer in particular is under duress. The residual swirl level at prediffuser exit also changes with test condition. At 30% cowl flow, the pitch-averaged residual yaw angle is ~−4 deg over the central 60% of the passage height, rising to ~3 deg near the diffuser end walls. At 50% flow, this changes to ~4 deg in the core flow and as much

Downloaded 02 Jun 2010 to 171.66.16.107. Redistribution subject to ASME license or copyright; see http://www.asme.org/terms/Terms_Use.cfm

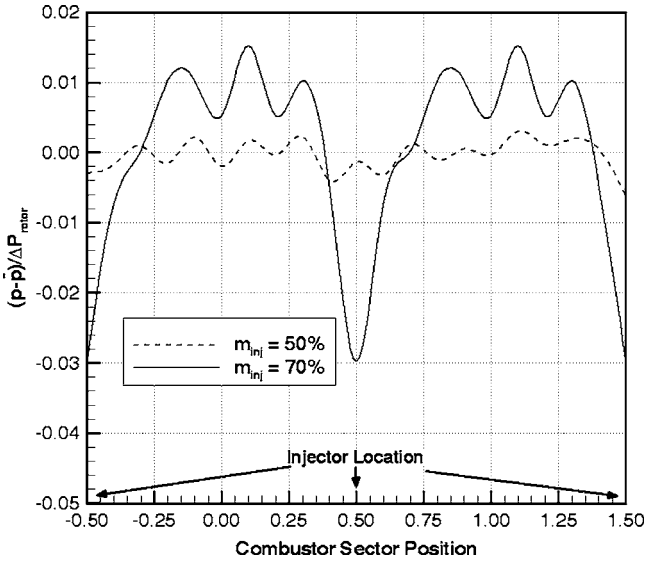

Fig. 7 Rotor exit (X2) static pressure

as 20 deg in the wall regions. At 70% cowl flow, since the rotor exit condition has now changed appreciably, the core swirl angle is ~−2 deg over most of the passage height, rising to ~5 deg near the outer wall.

Overall System Performance. Measurements in both feed annuli allow the overall system performance to be established. Table 3 gives the mass-weighted total pressure loss and static pressure recovery coefficients for the inner annulus (X5i) quoted with respect to both rotor exit (X2) and OGV exit (X3). As the injector mass flow is increased from conventional air-spray levels (30%), to levels more typical of lean module designs (50–70%), the total pressure loss increases. The system loss from rotor exit is 22% of rotor exit dynamic for 30% cowl flow and this rises to 23% for 50% and 26% for 70%. The overall system static pressure rise is not significantly affected, but both λ and C_p values from OGV exit to annulus show a large increase in loss and deterioration in feed quality as the injector mass flow increases. The data for the outer annulus indicate similar trends and are not repeated here.

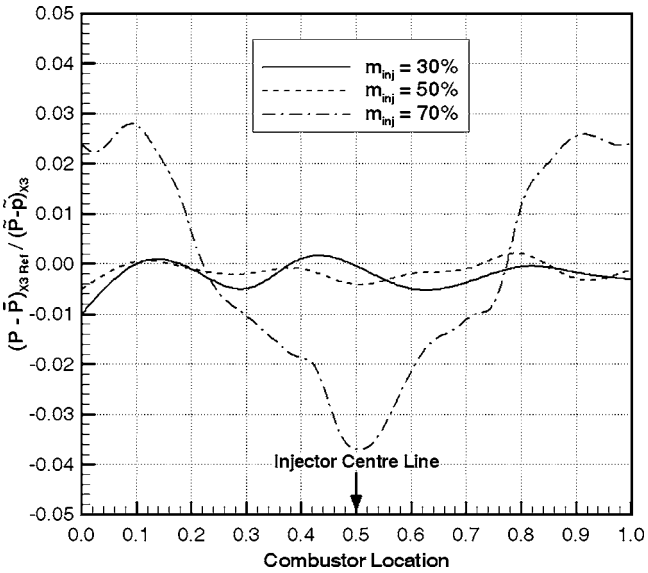

Fig. 8 OGV exit (reference) total pressure

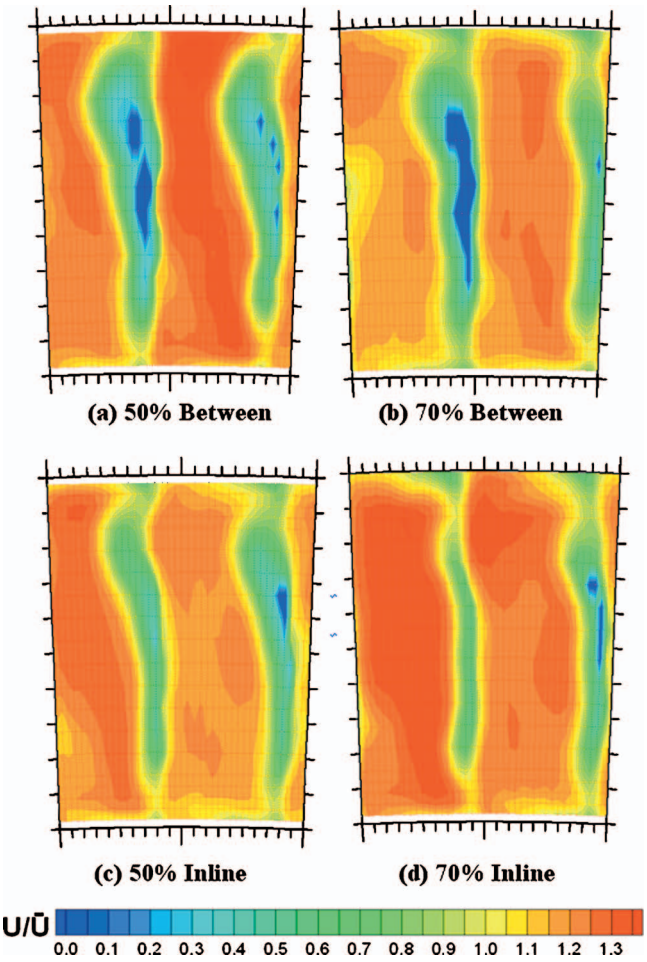

Fig. 9 Axial velocity contours at OGV exit (X3): (*a*) 50% between, (*b*) 70% between, (*c*) 50% inline, (*d*) 70% inline (height =36.6 mm, sector angle Δθ=4.5 deg (2-OGV passages))

Conclusions

The effect on combustion system external aerodynamics of increasing the injector flow split from air-spray levels to those typical of lean module injectors has been studied. In order to do this, three combustor flow configurations were tested each utilizing the same inlet section, IGV, rotor, and integrated OGV/prediffuser. The flow fraction of compressor efflux entering the cowl was systematically increased from 30% to 50% and 70% while increasing the effective area of cowl to maintain a constant mass flow per unit area. From the results presented here, the following conclusions can be made:

- For all flow splits, rig inlet conditions remained constant.
- At rotor exit, there was no change in the flowfield as the cowl mass flow increased from 30% to 50%. At 70%, a notable circumferential variation in the static pressure field

Table 2 OGV performance data

Test No.	λ_{X2-X3}	Cp_{X2-X3}
1	0.132	0.38
2	0.128	0.38
3 (Burner sector)	0.129	0.38
3 (2-OGV sector between)	0.153	0.36
3 (2-OGV sector inline)	0.097	0.39

Downloaded 02 Jun 2010 to 171.66.16.107. Redistribution subject to ASME license or copyright; see http://www.asme.org/terms/Terms_Use.cfm

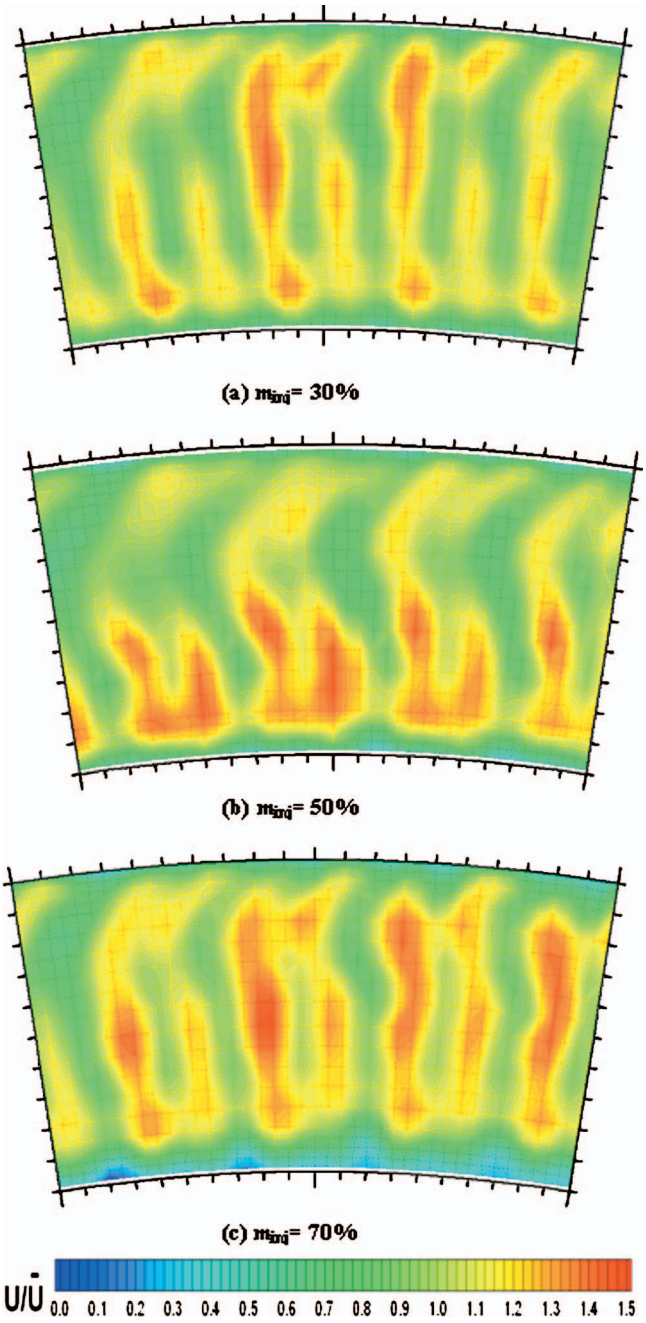

Fig. 10 Axial velocity contours at prediffuser exit (X4): (*a*) m_{inj}=30%, (*b*) m_{inj}=50%, (*c*) m_{inj}=70% (height=65.9 mm, sector angle $\Delta\theta$=18 deg (8-OGV passages))

was observed. This resulted in a degradation of the outboard, tip flow as the rotor was forced locally to move up/down its characteristic.

- Similarly for 30% to 50% cowl flow, the performance of the OGV row did not change, but at 70%, a circumferential redistribution of mass flow was observed, increasing by ~5% in line with the injectors and decreasing by the same amount in between. Consequently, the OGV total pressure loss coefficient varied from 0.097 in line to 0.153 between injectors with an overall sector average of 0.129.
- As the cowl mass flow increased from 30% to 50% and 70%, the prediffuser flow quality worsened, particularly near the inner wall, where at 70% the prediffuser was close to separation.
- System performance from rotor through to feed annuli is a direct function of the condition of the prediffuser exit flow field, particularly the boundary layer flow. As the injector air flow was increased and the prediffuser performance decreased, the annulus flow incurred higher losses and became less uniform. For both annuli the loss coefficient increased, suggesting an increase in system loss of almost 20% at the higher injector flow.
- An estimate of injector feed suggested that at the higher flow rate, the total pressure was nonuniform.

Table 3 Inner annulus performance data

Test No.	λ_{X2-X5I}	λ_{X3-X5I}	$C_{P_{X2-X5I}}$	$C_{P_{X3-X5I}}$
1	0.224	0.159	0.71	0.71
2	0.232	0.204	0.72	0.69
3	0.262	0.284	0.71	0.65

Acknowledgment

The financial support of the European Union under contract No. F-AST3-CT-2003-502961 (INTELLECT_DM) is gratefully acknowledged. The authors would also like to express their appreciation to L. Monk, W. Niven, and A. Fardoe for their help in the construction of the test facility. The helpful comments and technical support provided by A. Barker are gratefully acknowledged.

Nomenclature

A = passage area
AR = area ratio
c = outlet guide vane chord
C_p = static pressure rise coefficient
h = annulus passage height
L = diffuser length
$\dot{m}$ = mass flow rate
N = rotor speed
P, p = local total or static pressure
R = gas constant (perfect gas law)
R_n = nondimensional radius $((r-r_i)/(r_o-r_i))$
r = radius relative to rig centerline
r_i, r_o = inner casing, outer casing radius
s = blade pitch
T, t = total or static temperature
U = rotor midpassage blade speed
V_a = midpassage axial velocity
x = axial distance
α = kinetic energy flux coefficient
ϕ = flow coefficient (V_a/U)
ρ = density
λ = total pressure loss coefficient

Subscripts

X1 = rotor inlet traverse plane
X2 = rotor exit/OGV inlet traverse plane
X3 = OGV exit traverse plane
X4 = prediffuser exit traverse plane
X5*i* = inner annulus traverse plane
X5*o* = outer annulus traverse plane

Superscripts

– = area weighted spatially averaged mean value
~ = mass weighted spatially averaged mean value

References

[1] Shahpar, S., Giacche, D., and Lapworth, L., 2003, "Multi-Objective Design and Optimisation of Bypass Outlet Guide Vanes," ASME Paper GT2003-38698.

Downloaded 02 Jun 2010 to 171.66.16.107. Redistribution subject to ASME license or copyright; see http://www.asme.org/terms/Terms_Use.cfm

[2] Stevens, S. J., Harasgama, S. P., and Wray, A. P., 1984, "The Influence of Blade Wakes on Combustor Shortened Prediffusers," J. Aircr., **21**(9), pp. 641–648.
[3] Barker, A. G., and Carrotte, J. F., 2001, "Influence of Compressor Exit Conditions on Combustor Annular Diffusers, Part 1: Diffuser Performance," J. Propul. Power, **17**(3), pp. 678–686.
[4] Barker, A. G., and Carrotte, J. F., 2001, "Influence of Compressor Exit Conditions on Combustor Annular Diffusers, Part 2: Flow Redistribution," J. Propul. Power, **17**(3), pp. 687–694.
[5] Klein, A., 1995. "Characteristics of Combustor Diffusers," Prog. Aerosp. Sci., **31**(3), pp. 171–271.
[6] Barker, A. G., Carrotte, J. F., Luff, J., and McGuirk, J. J., 2003, "D1.1 Design of an Integrated OGV/Diffuser System," Loughborough Univ, UK, Dept. of Aero. & Auto. Eng. Report No. TT03R01.
[7] Walker, A. D., Carrotte, J. F., and McGuirk, J. J., 2006, "Enhanced External Aerodynamic Performance of a Generic Combustor Using an Integrated OGV/Prediffuser Design Technique," ASME Paper No. GT2006-90184.
[8] Schlueter, J., Wu, X., Pitsch, H., Kim, S., and Alonso, J., 2005. "Integrated Simulations of a Compressor/Combustor Assembly of a Gas Turbine Engine," ASME Paper No. GT2005-68204.
[9] Howard, J. H. G., Henseler, H. J., and Thornton-Trump, A. B., 1967. "Performance and Flow Regimes for Annular Diffusers," ASME Paper No. 67-WA/FE-2.
[10] Wray, A. P., and Carrotte, J. F., 1993, "The Development of a Large Annular Facility for Testing Gas Turbine Combustor Diffuser Systems," Paper No. AIAA-93-2546.

Downloaded 02 Jun 2010 to 171.66.16.107. Redistribution subject to ASME license or copyright; see http://www.asme.org/terms/Terms_Use.cfm

FLOX® Combustion at High Pressure With Different Fuel Compositions

Rainer Lückerath

Wolfgang Meier

Manfred Aigner
e-mail: Rainer.Lueckerath@DLR.de

Institute of Combustion Technology,
German Aerospace Center (DLR),
Pfaffenwaldring 38-40,
D-70569 Stuttgart, Germany

In flameless oxidation (FLOX®) *the combustion is distributed over a large volume by a high internal flue gas recirculation. This technology has been successfully used for many years in technical furnaces under atmospheric conditions with very low* NO_x *emissions. In the work presented here,* FLOX® *combustion was for the first time investigated at high pressure in order to assess its applicability for gas turbine combustors. A* FLOX® *burner was equipped with a combustion chamber with quartz windows and installed into a high pressure test rig with optical access. The burner was operated under typical gas turbine conditions at a pressure of* 20 bar *with thermal powers up to* 475 kW. *Natural gas, as well as mixtures of natural gas and* H_2 *were used as fuel. The* NO_x *and* CO *emissions were recorded for the different operating conditions.* OH^* *chemiluminescence imaging and planar laser-induced fluorescence of* OH *were applied in order to characterize the flame zone and the relative temperature distributions. The combustion behavior was investigated as a function of equivalence ratio and fuel composition, and the influence of the gas inlet velocity on mixing and emissions was studied. For various operating conditions, the lean extinction limits were determined.* [DOI: 10.1115/1.2749280]

Keywords: FLOX®, flameless combustion, gas turbine combustion

Introduction

The widely applied concept of lean premixed combustion in stationary gas turbines (GTs) has led to a significant reduction of NO_x emissions in comparison to non-premixed GT combustion [1,2]. However, its susceptibility to thermoacoustic instabilities, the risk of flashback, and its sensitivity with respect to changes of the fuel composition are limitations for a safe and reliable operation [3–6]. Therefore, alternative concepts are still desirable and are an area of research and development. Here, the flameless oxidation (FLOX® [7]) combustion technology, also termed flameless, volume, or mild combustion [8–10], presents an attractive alternative for low-emission combustors. Due to a high dilution of the reactants by inert gases such as N_2, CO_2, or H_2O, flame reactions are delayed and combustion does not take place in thin reaction zones but is rather distributed over a larger volume. Thereby, peak temperatures and high NO_x production rates are avoided. A flameless oxidation process developed and patented by WS Wärmeprozesstechnik GmbH is based on a high internal flue gas recirculation that is driven by the high momentum of the air and fuel jets entering the combustion chamber. With this technique, stable lean combustion was achieved without oscillations and flashback. A range of low NO_x and CO emissions was quantified. This technology has been successfully applied for many years to industrial furnaces at atmospheric pressure [8,9]. However, it has not been employed for practical combustors at high pressure so far.

In this paper, we report about investigations of flameless oxidation for gas turbine applications. Within the framework of the European Commission funded project *New Combustion Systems for Gas Turbines* [11], this combustion concept was investigated and tested under typical gas turbine conditions with natural gas as fuel [12]. In the German project COOREFF-T [13], the fuel flexibility of this burner has been studied by using different mixtures of natural gas and hydrogen. For the experiments, a FLOX® burner was installed into a high-pressure test rig at DLR in Stuttgart and operated at pressures up to 30 bar. A combustion chamber with quartz windows and large optical ports in the test rig allowed the application of optical and laser measuring techniques. Here, OH^* chemiluminescence imaging and planar laser induced fluorescence (PLIF) of OH radicals were applied. The high intensity of the OH^* chemiluminescence indicates the regions of the flame zone and the integrated intensity is a measure for the heat release rate. PLIF of OH identifies regions of high temperatures ($T \gtrsim 1400$ K) and its intensity distribution reflects the relative temperature distribution. In addition, the exhaust gas emissions were monitored by chemical analytical methods.

The main goals of the investigations were a characterization of the FLOX® combustion process at high pressure, the identification of ranges of stable low-emission operation, the study of the influence of H_2 admixture to natural gas on the combustion behavior, and the generation of an experimental data base that can be used for the validation of numerical simulations [14,15].

Experimental Set Up

The main components of the experiment were a FLOX® burner with 12 nozzles developed by WS Wärmeprozesstechnik GmbH by the optical combustion chamber and the high-pressure test rig for PLIF of OH and chemiluminescence, and the chemical analytics. These components are described in more detail below.

Burner and Combustion Chamber. The 12 single nozzles of the FLOX® burner were positioned on a reference circle with a diameter of 80 mm (see Fig. 1). Each single nozzle comprised a fuel nozzle with a diameter of 1 mm surrounded by an air nozzle with a diameter of 4.5 mm (or alternatively 6 mm, but not treated in this paper). The fuel nozzle was positioned upstream of the air nozzle so that the fuel entered the air nozzle in the center of the air stream (compare Figs. 1 and 2). The flames were ignited by a pilot

Contributed by the International Gas Turbine Institute of ASME for publication in the JOURNAL OF ENGINEERING FOR GAS TURBINES AND POWER. Manuscript received May 3, 2007; final manuscript received May 9, 2007; published online January 9, 2008. Review conducted by Dilip R. Ballal. Paper presented at the ASME Turbo Expo 2007: Land, Sea and Air (GT2007), Montreal, Quebec, Canada, May 14–17, 2007, Paper No. GT2007-27337.

Copyright © 2008 by ASME

Downloaded 02 Jun 2010 to 171.66.16.107. Redistribution subject to ASME license or copyright; see http://www.asme.org/terms/Terms_Use.cfm

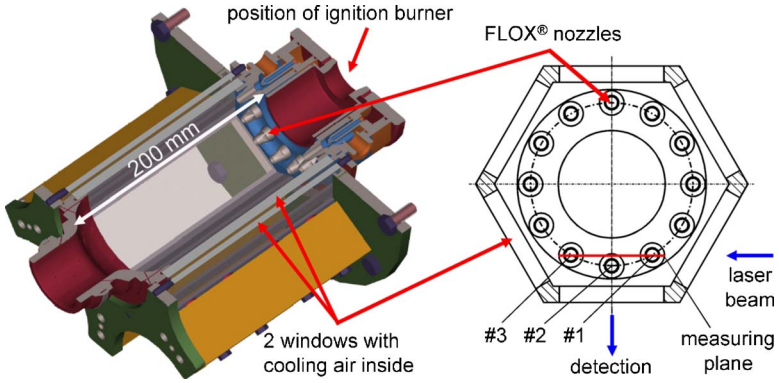

Fig. 1 The hexagonal combustion chamber: longitudinal section (left) and cross section with a view of the FLOX® burner with 12 single nozzles (right). The measuring plane of the PLIF experiment is indicated. The three nozzles visible through the window on the detection side are labeled #1 to #3.

burner that was located in the center of the nozzle arrangement.

Originally, the combustion chamber had a cylindrical shape, but for the application of laser diagnostic methods, plane windows are preferred. Therefore, a hexagonal cross section of the combustion chamber was chosen as indicated in Fig. 1. Compared to an often used square cross section, this geometry exhibits a smaller deviation from the axial symmetry of the flow field. The length of the combustion chamber was 200 mm and the inner diameter of the hexagon was 100 mm. On each of the six sides of the combustion chamber, two quartz plates were mounted with a slit between them for guiding cooling air. The plates were pressed onto the sealings by the metal blocks seen in Fig. 1 that were tensed by springs. The quartz windows yielded access to a length of 160 mm of the combustion chamber. The exit of the combustion chamber had a diameter of 50 mm.

The nozzles were supplied with air at $T=600-735$ K and fuel at room temperature. The mean velocity at the exit of the nozzles was in the range of $v_{\text{nozzle}}=40-160$ m/s. The burner was operated at a pressure of $p=20$ bar with a maximum thermal power of $P_{\text{therm}}=475$ kW.

High Pressure Test Rig. The burner with the hexagonal combustion chamber was horizontally mounted in the pressure vessel of the high pressure test rig. Through large windows in the pressure vessel, a good optical access to the combustion chamber was achieved. The air was supplied by a compressor and electrically heated to gas turbine relevant temperatures. The air entered the test rig downstream of the combustion chamber and was then guided as a cooling film through the slits between the quartz plates of the combustion chamber before it reached the nozzles of the burner. The mass flow rate of the air entering the burner was determined from the pressure drop at the burner inlet ports. Under ideal conditions, an accuracy on the order of 1% can be achieved with orifice flow meters. However, when the velocity profile upstream of an orifice deviates from a fully developed turbulent pipe flow or other installation effects decrease the accuracy, the error can be up to ≈10% in an extreme case [16]. For the current

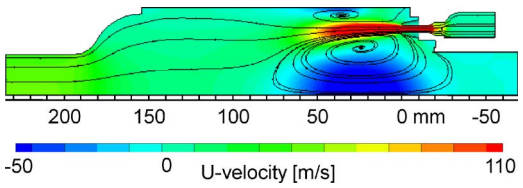

Fig. 2 Calculated axial velocity and streamline representation of the flow on longitudinal slice through nozzle and combustor axis

experiment, the error was estimated to be about 5–7%. The natural gas used as fuel had a typical composition of 94% CH_4, 2.5% C_2H_6, 0.4% C_3H_8, 2.3% N_2, 0.7% CO_2, and 0.1% higher hydrocarbons. The mass flow rate was measured by a Coriolis flow meter with an accuracy of about 1%. Several pressure transducers recorded the pressure in the combustion chamber and the pressure drop at the burner. A suction probe behind the combustion chamber enabled the measurement of the concentrations of NO, NO_2, CO, and O_2 and the exhaust temperature was measured at the same location with a thermocouple. The data logging system of the test facility recorded every 5 s values of the concentrations and all relevant information about the operation of the burner, such as mass flows, temperatures, and pressures.

Measuring Techniques. For PLIF of OH, the frequency-doubled output of a Nd:YAG-pumped dye laser (10 Hz repetition rate, 5–10 ns pulse duration) was formed into a light sheet with a height of $h\approx 58$ mm and a thickness of $d\approx 0.4$ mm. The light sheet was aligned vertically through the horizontal combustion chamber. Pulse energies ranged from 3 mJ to 4 mJ. The wavelength was tuned to the $Q_1(4)$ line of the $A^2\Sigma^+-X^2\Pi$ $(v'=1,v''=0)$ transition of OH at $\lambda\approx 282.5$ nm. The excited fluorescence was collected at 90 deg by an intensified CCD camera fitted with an achromatic 100 mm UV lens ($f/2$, Halle Nachf.) and a UV ($\lambda\approx 312\pm 20$ nm) interference filter. The single-pulse images were corrected with regard to the intensity distribution of the light sheet. This distribution was measured by reflecting a portion of the light sheet into a quartz cell filled with dye solution and detecting the fluorescence from the dye with a second CCD camera. Due to the excitation with a laser light sheet, the PLIF signal originated from a well-defined vertical plane. The measured PLIF images shown in this paper were recorded from a plane intersecting the axes of two nozzles (nozzles #1 and #3; see Fig. 1). In the FLOX® combustion, the expected temperatures are quite low. Therefore, the relatively strong $Q_1(4)$ line of the Q-branch of the OH radical was chosen for the PLIF excitation.

Under the given experimental conditions, the OH PLIF signal is approximately proportional to the OH number density, because variations in fluorescence quenching and Boltzmann fraction are small [17]. Furthermore, at the high pressures prevailing in the combustion chamber, the OH concentrations are close to chemical equilibrium, i.e., the concentration increases exponentially with temperature [18]. Therefore, the OH PLIF distribution also reflects a relative temperature distribution.

For the measurement of the OH^* chemiluminescence (CL), the same intensified CCD camera as for the PLIF measurements was used. The signal intensity of the OH^* chemiluminescence depends on the concentration of the electronically excited OH^* radicals,

Downloaded 02 Jun 2010 to 171.66.16.107. Redistribution subject to ASME license or copyright; see http://www.asme.org/terms/Terms_Use.cfm

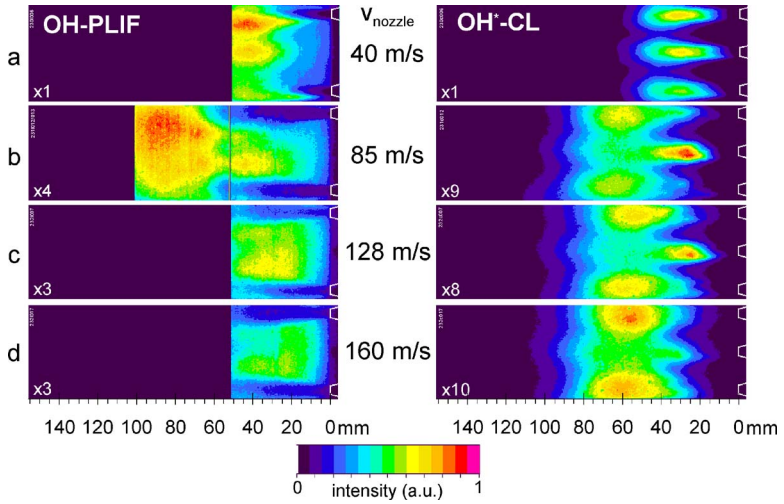

Fig. 3 Averaged OH PLIF and OH* chemiluminescence images for different inlet velocities. The positions of the nozzles are indicated on the right side of each image. In the PLIF images, only the nozzles #1 and #3 in the measuring plane are shown. Operating conditions for image pairs a/b/c/d: 91/167/235/300 g/s air (T_{air}=588/669/706/714 K), 2.6/4.4/6.2/7.7 g/s natural gas, λ=2.0/2.2/2.2/2.3, T_{ad}=1698/1695/1712/1700 K, P_{therm}=132/222/308/385 kW, 50/1.6/1.7/1.4 ppm NO_x, 2.2/<1/<1/<1 ppm CO.

which are formed by chemical reactions, predominantly via $CH+O_2 \rightarrow CO+OH^*$ [19]. Due to the short lifetime of OH^*, the chemiluminescence originates only from the reaction zone. Therefore, this technique yields information about the size and position of the flame zone [20]. The signal was detected with a gate time of 40 μs. Because the signal from the entire combustion chamber was collected by the camera, the signals were spatially integrated in the depth.

The view of the camera was through one side window with the nozzles on the right side (Fig. 1). The images of the CCD camera covered the complete 160 mm long window section so that the main part of the combustion chamber is seen. The height of the image is about 50 mm and limited by the window. The PLIF signal is excited by a laser light sheet with a width of approximately 58 mm. The light sheet was aligned for most of the experiments in front of the nozzles, and in some cases, additionally 50 mm further downstream. For all CL and PLIF experiments, 200 single instantaneous images were recorded and averaged.

The NO_x concentration in the exhaust gas was determined by means of UV absorption (ABB Limas 11), the CO concentration by IR absorption (ABB URAS 14), and the O_2 concentration by paramagnetism (ABB Magnos 16). All concentrations of NO_x (NO, NO_2) and CO were normalized to 15% O_2.

Measuring Procedure and Classification of Results. More than 90 different operating conditions were investigated at a pressure of 20 bar. During a measurement series, the air equivalence ratio λ, i.e., the reciprocal of the equivalence ratio Φ, was increased in several steps by decreasing the mass flow of the fuel until the flame extinguished. At most of the settings of λ, optical measurements were performed. These measurement series were repeated with different mean velocities in the inlet nozzles in the range of $40\ \mathrm{m/s} \leq v_{nozzle} \leq 160\ \mathrm{m/s}$, and with different thermal powers of 100–475 kW. The resulting specific power density for these conditions was between 3 and 14 MW/(m^3 bar). The inlet velocity was increased (i) by increasing the total mass flows, i.e., the thermal power or (ii) by reducing the diameter of the nozzles from 6.0 mm to 4.5 mm. From the calibrated pressure drop at the entrance of the burner, the air mass flow into the burner was calculated for each experiment. Together with the mass flow of the fuel, the overall air equivalence ratio λ was determined. The pressure drop at the nozzles was less than 2% except for the experiments with inlet velocities of 128 m/s (3.2%) and 160 m/s (5.3%).

For the characterization of the operating range with low NO_x emissions, which depend strongly on temperature, both λ and the air preheat temperature T_{air} have to be considered. Unfortunately, T_{air} could not be held constant during a variation of λ. Because the air was used for cooling the combustion chamber prior to combustion, the air preheat temperature T_{air} at the burner depended on the temperature loss due to cooling and, thus, on the thermal power of the flames. Therefore, experiments at different λ were also performed at different T_{air}. In order to combine both parameters λ and T_{air} to one quantity reflecting the effective temperature dependence, the adiabatic flame temperature T_{ad} was chosen. In the data logging system, the information about T_{air} as well as about λ (calculated from the mass flows of air and fuel) are available. Therefore, T_{ad} could be determined from an equilibrium calculation that accounts for both T_{air} and λ. The uncertainty of λ stems mainly from the uncertainty of the air mass flow and was on the order of ±5–7% (see above). This corresponds to an uncertainty of about ±40–70 K for T_{ad}.

Results and Discussion

Overall Flow Field. In order to yield an impression of the overall flow field, Fig. 2 shows a calculated axial velocity distribution in a plane containing the burner axis and a nozzle [21]. The nozzle exit is defined as axial position $z=0$ mm. It is seen that a large central and a smaller outer recirculation zone are established that extend in the example displayed up to $z \approx 90$ mm. However, the size and velocities change with operating conditions and this example shall merely serve as an illustration of the general flow characteristics.

Influence of Inlet Velocity. The penetration depth of the injected jets of fresh gas, the mixing, and the flue gas recirculation depend, of course, on the inlet velocity of the fuel/air mixtures. Therefore, this is an important parameter for the performance of the combustor. In Fig. 3, the OH PLIF and chemiluminescence

Downloaded 02 Jun 2010 to 171.66.16.107. Redistribution subject to ASME license or copyright; see http://www.asme.org/terms/Terms_Use.cfm

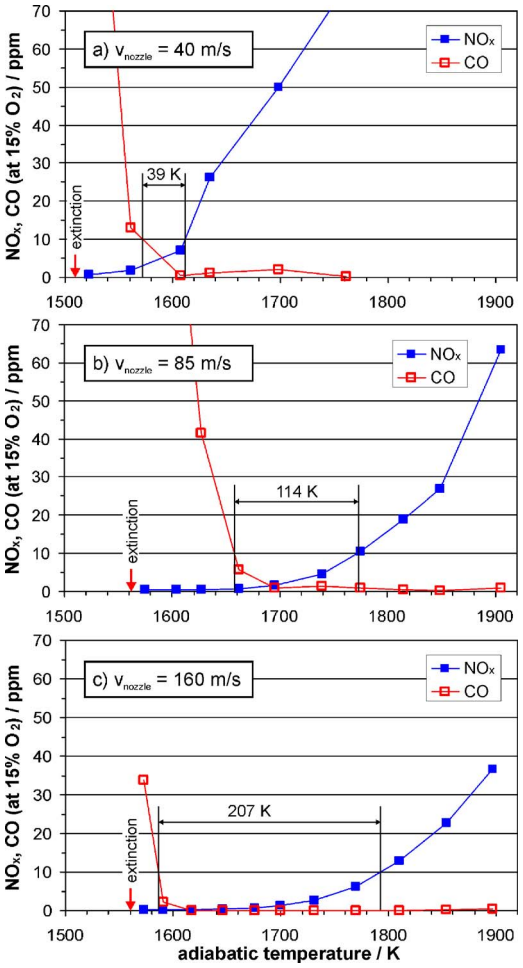

Fig. 4 NO_x and CO emissions versus T_{ad} for different jet velocities v_{nozzle}. Operating conditions (a/b/c): v_{nozzle} =40/85/160 m/s, 91–300 g/s air (T_{air}=563–733 K), 2.0–9.5 g/s natural gas, P_{therm}=101–475 kW.

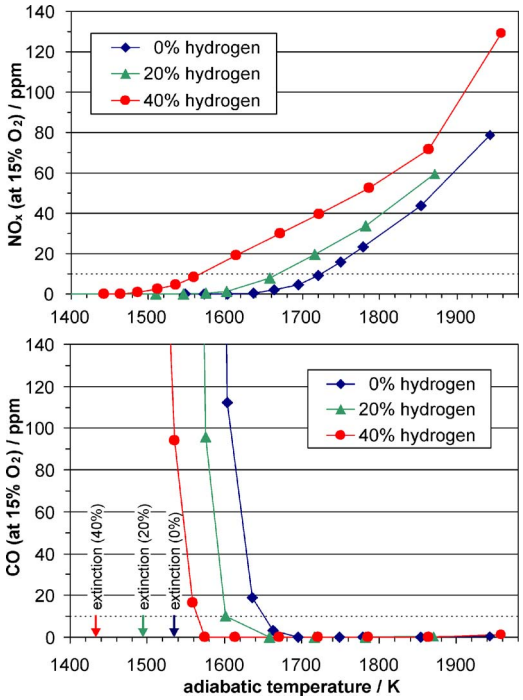

Fig. 5 NO_x and CO emissions versus T_{ad} for different fuel mixtures of natural gas with hydrogen. Operating conditions: v_{nozzle}=86 m/s, 169–192 g/s air (T_{air}=669–700 K), 2.8–6.0 g/s natural gas, 0.0–5.1 g/s H_2, P_{therm}=168–306 kW.

distributions are displayed for the inlet velocities v_{nozzle}=40, 85, 128, and 160 m/s for an almost constant T_{ad} of 1700 K. In the PLIF images, the positions of the nozzles #1 and #3 whose axes are intersected by the laser sheet are indicated on the right side. In the chemiluminescence images, also the nozzle #2 (out of the laser sheet plane) is indicated. In the PLIF measurements, the laser sheet position covers the first 52 mm downstream from the nozzles and only for v_{nozzle}=85 m/s, a second sheet position was used. Because the signal intensities varied drastically with v_{nozzle}, the images are displayed with different scaling factors. A scaling factor of, e.g., "×4" given in the PLIF and CL images indicates that the signal intensity was multiplied by a factor of 4. This means that a larger scaling factor is used for a weaker signal. Considering that low OH PLIF signals reflect cold regions, it can be seen that the penetration depth of the relatively cold jets in front of the nozzles varies with v_{nozzle} from ~25 mm at 40 m/s to more than 55 mm at higher velocities. Accordingly, the positions of the flame zones, characterized by high OH^* chemiluminescence intensities, move downstream with increasing v_{nozzle}. At 160 m/s, the flame zone covers almost homogeneously the downstream region $z \approx 30-90$ mm and combustion is finished at $z \approx 100-110$ mm. In the OH PLIF images, the relatively high intensities between the jets reflect a high temperature level. This region is, thus, quite homogeneously filled with hot recirculated flue gas.

Figure 4 shows the NO_x and CO emissions as a function of T_{ad} for the inlet velocities 40, 85, and 160 m/s. As stated before, the fuel flow rate was gradually reduced in these measurements until extinction occurred. The NO_x concentration increases with T_{ad}, as expected from the Zeldovich mechanism [22]. However, with increasing v_{nozzle}, a shift of the NO_x curves to higher T_{ad} (or lower NO_x) is observed. This might be caused by the shorter residence times of the gases within the combustion chamber at higher flow rates and by a more homogeneous temperature distribution due to more intense mixing prior to combustion resulting in lower peak temperatures. The CO concentrations are low at high T_{ad} and increase as the extinction limit is approached, because combustion becomes unstable and incomplete prior to blowout. The increase of the CO concentration for the velocities of 40 m/s and 160 m/s is approximately at the same adiabatic temperature, but for the velocity of 85 m/s it is about 70 K higher. At 85 m/s, the temperature gap between the increase of CO emissions and extinction is also considerably larger than for the other velocities displayed. This behavior is surprising and, up to now, the reason is unclear.

In order to compare different operating conditions quantitatively, we define the low emission operating range as the range where NO_x and CO emissions were less than 10 ppm. As indicated in Fig. 4, the low emission operating range increases with v_{nozzle} from ΔT_{ad}=39 K at 40 m/s to ΔT_{ad}=207 K at 160 m/s.

Influence of Hydrogen Admixture. The influence of hydrogen as admixture to natural gas on the emission characteristic is displayed in Fig. 5 for 0%, 20%, and 40% H_2 (by volume with equal total thermal power). From the NO_x curves, it is seen that with increasing H_2 admixture, the NO_x concentration rises at lower T_{ad}. This might be explained by the higher reactivity of H_2, which reduces the chemical time scale in comparison to the time scale of the mixing and can, thus, lead to combustion under locally smaller λ values than λ_{global}. In this way, regions with relatively high temperatures could occur that would promote the NO_x production [22]. With respect to the CO emissions, the measurements show the expected trend that with increasing H_2 fraction, the extinction limit moves to lower T_{ad} and that CO concentrations decrease.

Downloaded 02 Jun 2010 to 171.66.16.107. Redistribution subject to ASME license or copyright; see http://www.asme.org/terms/Terms_Use.cfm

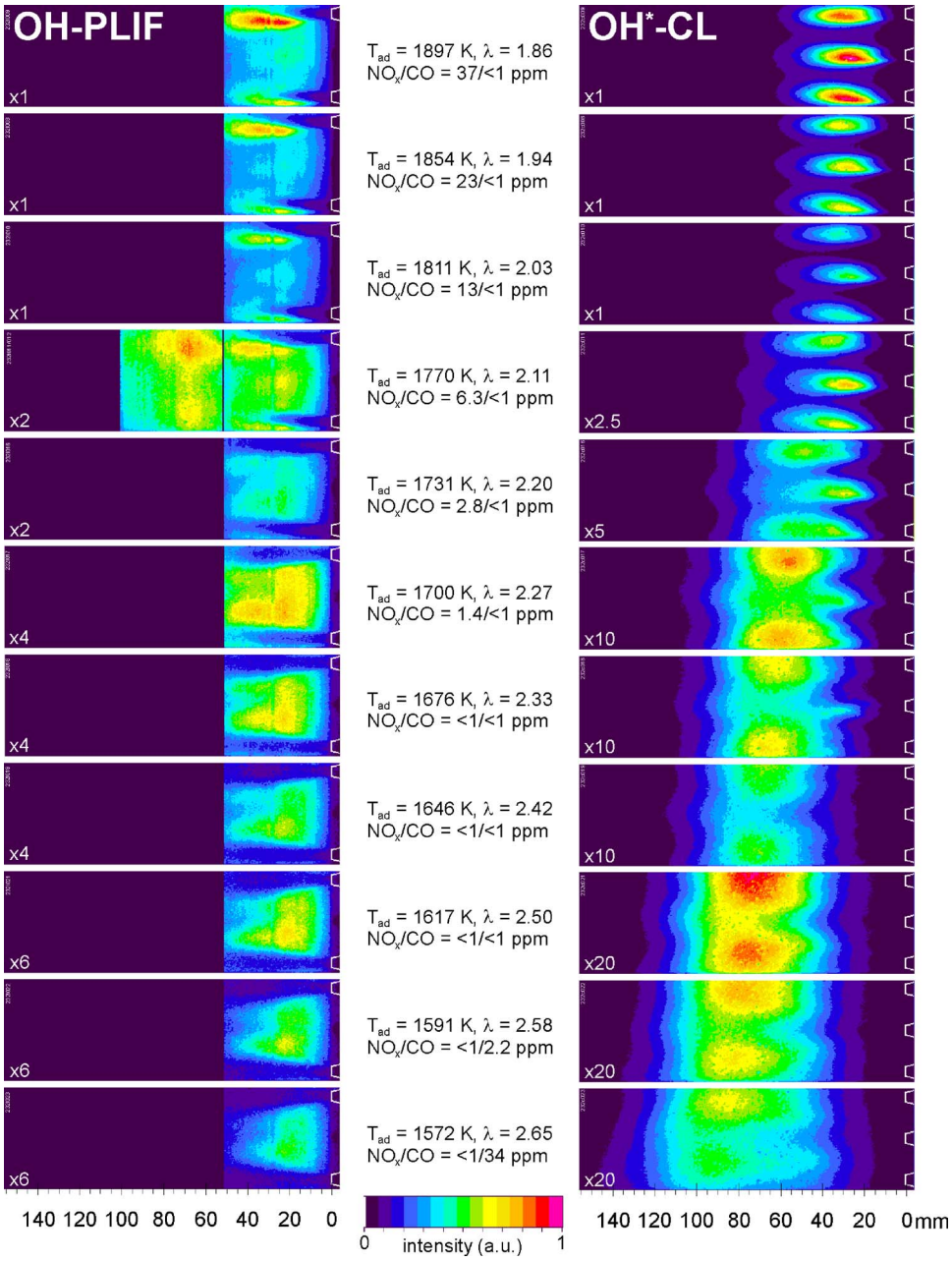

Fig. 6 Averaged images of OH PLIF and OH* chemiluminescence for different air equivalence ratios λ. T_{ad}, λ, and the NO_x and CO emission values are given for each pair of images. The positions of the nozzles are indicated on the right side of each image. Operating conditions: v_{nozzle}=160 m/s, 300 g/s air (T_{air}=705–733 K), 6.5–9.5 g/s natural gas, P_{therm}=323–475 kW.

The shorter ignition delay time of the hydrogen compared to the natural gas led to an earlier reaction and, therefore, to a reduced distance of the flame zone from the nozzles. This behavior was observed but is not shown here.

Variation of Equivalence Ratio. In order to characterize the changes of the flame zone and the OH distribution for the transition from lean to ultra-lean conditions, the air equivalence ratio λ was gradually increased from λ=1.86 to 2.65 for a velocity of v_{nozzle}=160 m/s and natural gas as fuel. Figure 6 shows the mean OH PLIF distributions and the OH^* chemiluminescence images obtained from this measurement. In addition, T_{ad} and the NO_x and CO emissions are given for each λ. The chemiluminescence distributions show that for λ=1.86, individual flame zones are established in front of each nozzle with a size of roughly 40 mm in length and 12 mm in diameter. With increasing λ, the flame zones become larger and finally merge to one large flame zone while the local intensities decrease by more than a factor of 20 (see scaling factor in images). At λ=2.65, the region with OH^* chemiluminescence spreads from $z \approx 25$ mm to 140 mm. The corresponding OH PLIF images exhibit significant intensity variations over the imaged region for low values of λ. For example, the high intensity region in the upper end of the image at λ=1.86 is evidence of a high temperature zone. With increasing λ, the distributions become more homogeneous in accordance with the chemiluminescence images. The strong decrease of the concentration of the OH radical of more than a factor of 10 is explained by the decrease of

Downloaded 02 Jun 2010 to 171.66.16.107. Redistribution subject to ASME license or copyright; see http://www.asme.org/terms/Terms_Use.cfm

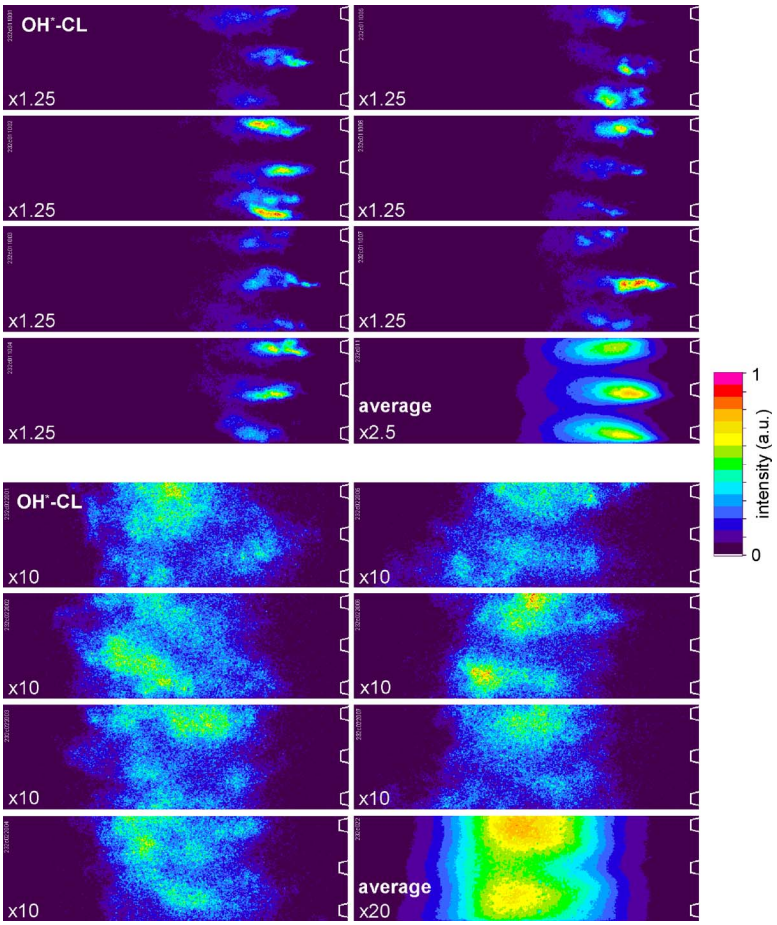

Fig. 7 Instantaneous images and corresponding averaged image of the OH* chemiluminescence for λ=2.1 (upper images) and λ=2.6 (lower images). Operating conditions: v_{nozzle}=160 m/s, 300 g/s air (T_{air}=720/705 K), 8.3/6.7 g/s natural gas, λ=2.1/2.6, T_{ad}=1770/1591 K, P_{therm}=417/333 kW, 6.3/<1 ppm NO_x, <1/2.2 ppm CO.

flame temperature. In this measurement series, the NO_x concentrations drop from 37 ppm at λ=1.86 to 1.4 ppm at λ=2.27 and stay below 1 ppm for the fuel-leaner conditions. At λ=2.58, the CO concentrations begin to rise, and at λ≈2.7, the flame extinguished.

Instantaneous Chemiluminescence Images. Examples of instantaneous chemiluminescence images with an exposure time of 40 μs are displayed in Fig. 7, together with the averaged distributions for λ=2.1 and 2.6 for v_{nozzle}=160 m/s. At λ=2.1, individual flame zones can be observed that exhibit significant shot-to-shot variations in size, position, and intensity. With an exposure time of 40 μs, a slight blurring of the structures might be possible due to the motion of the flow (for example, for a flow velocity of 25 m/s, the flame zone would move 1 mm during 40 μs). The images suggest that each individual flame zone forms a connected region, and that flame extinction and re-ignition does not occur. At λ=2.6, the images exhibit only little structure. Individual flame zones are not present and the shot-to-shot variations are much smaller than at λ=2.1.

Summary and Conclusions

A FLOX® burner was equipped with an optical combustion chamber and installed into the high pressure test rig at DLR in Stuttgart. The burner was operated with preheated air and natural gas with and without hydrogen admixtures at a pressure of 20 bar. The main goal of the investigation was an assessment of the applicability of the FLOX® combustion scheme for gas turbine combustors.

A successful operation of the FLOX® combustor with low emissions could be demonstrated for the first time at high pressure. It was shown that the jet exit velocity v_{nozzle} of the fuel/air mixtures had a strong influence on the mixing process within the combustion chamber, and that the low emission operating range increased with v_{nozzle}. The structures and size of the flame zones were characterized by OH* chemiluminescence imaging, and PLIF of OH was used to image the relative temperature distributions. For air preheat temperatures of T_{air}≈700 K and an inlet velocity of v_{nozzle}=160 m/s, low NO_x emissions (<10 ppm) were achieved for air equivalence ratios λ>2.1 when the flame zones were distributed relatively homogeneously over a large volume. For these conditions, the temperature distributions were also quite homogeneous. CO emissions were low until the lean extinction limit of the flames was approached at λ≈2.7. For natural gas and high values of v_{nozzle}, a stable low-emission operating range of up to Δλ=0.5, or expressed in adiabatic temperature ΔT_{ad}=207 K, could be demonstrated. With admixtures of H_2 to the natural gas, the range of stable operation could be extended; however, the NO_x emissions increased probably due to inhomogeneities in the temperature distribution.

Downloaded 02 Jun 2010 to 171.66.16.107. Redistribution subject to ASME license or copyright; see http://www.asme.org/terms/Terms_Use.cfm

In conclusion, it can be stated that the results support the suitability of the FLOX® combustion scheme for gas turbine applications at high pressure.

Acknowledgment

This work has been funded by the European Commission within the project *New Combustion Systems for Gas Turbines* under Contract No. ENK5-CT-2001-00564, and by the German Federal Ministry for Economy and Labour under Contract No. 0327710L within the AG TURBO collaborative programme "COOREFF-T," Project No. 2.1.3. The content is within the responsibility of the authors. The authors would like to acknowledge the support of O. Lammel, B. Noll, H. Schütz, and C. Wahl.

References

[1] Correa, S. M., 1992, "A Review of NO_x Formation Under Gas-Turbine Combustion Conditions," Combust. Sci. Technol. **87**, pp. 329–362.
[2] Lefebvre, A. H., 1999, *Gas Turbine Combustion*, Taylor & Francis, Philadelphia.
[3] Dowling, A. P., and Hubbard, S., 2000, "Instability in Lean Premixed Combustors," Proc. Inst. Mech. Eng., Part A **214**, pp. 317–332.
[4] Candel, S., 2002, "Combustion Dynamics and Control: Progress and Challenges," Proc. Combust. Inst. **29**, pp. 1–28.
[5] Kröner, M., Fritz, J., and Sattelmayer, T., 2002, "Flashback Limits for Combustion Induced Vortex Breakdown in a Swirl Burner," ASME Paper No. GT-2002-30075.
[6] Lieuwen, T., 2003, "Combustion Driven Oscillations in Gas Turbines," Turbomachinery Internat. **44**, pp. 16–19.
[7] FLOX® is a registered trademark of WS Wärmeprozesstechnik GmbH, Renningen, Germany.
[8] Wünning, J. A., and Wünning, J. G., 1992, "Burners for Flameless Oxidation With Low NO_x Formation Even at Maximum Air Preheat," Gaswärme International **41**(10), pp. 438–444.
[9] Wünning, J. A., and Wünning, J. G., 1997, "Flameless Oxidation to Reduce Thermal NO-Formation," Prog. Energy Combust. Sci. **23**, pp. 81–94.
[10] Cavaliere, A., and Joannon, M., 2004, "Mild Combustion," Prog. Energy Combust. Sci. **30**, pp. 329–366.
[11] Project of the European Commission "New Combustion Systems for Gas Turbines" (NGT), Contract No. ENK5-CT-2001-00564.
[12] Flamme, M., Al-Halbouni, A., Wünning, J. G., Scherer, V., Schlieper, M., Aigner, M., Lückerath, R., Noll, B., Stöhr, R., and Binninger, B., 2003, "Low Emission Gas Turbine Combustors Based on Flameless Combustion," *Proc. European Combustion Meeting*, Orléans, France, October 25–28.
[13] Project of the German Federal Ministry for Economy and Labour "Brennstoffflexibler, schadstoffarmer, zuverlässiger Gasturbinenbrenner," Contract No. 0327710L within the AG TURBO collaborative programme COOREFF-T, Project No. 2.1.3.
[14] Schütz, H., Lückerath, R., Kretschmer, T., Noll, B., and Aigner, M., 2005, "Complex Chemistry Simulation of FLOX®—'Flameless Oxidation'—Combustion," *Proc. Eighth International Conference on Energy for a Clean Environment, Clean Air*, Lisbon, Portugal, June 27–30.
[15] Schütz, H., Lückerath, R., Kretschmer, T., Noll, B., and Aigner, M., 2006, "Analysis of the Pollutant Formation in the FLOX® Combustion," ASME J. Eng. Gas Turbines Power (to be published).
[16] Morrison, G. L., DeOtte, R. E., and Beam, E. J., 1992, "Installation Effects Upon Orifice Flowmeters," Flow Meas. Instrum. **3**, pp. 89–93.
[17] Letzgus, M., Brockhinke, A., and Kohse-Höinghaus, K., "LASKIN—A Simulation Program for Time-Resolved LIF-Spectra," University of Bielefeld, Faculty of Chemistry, Physical Chemistry I, http://pc1.uni-bielefeld.de/~laskin.
[18] http://gaseq.co.uk
[19] Dandy, D. S., and Vosen, S. R., 1992, "Numerical and Experimental Studies of Hydroxyl Radical Chemoluminescence in Methane-Air Flames," Combust. Sci. Technol. **82**, pp. 131–150.
[20] Lee, J. G., and Santavicca, D. A., 2003, "Experimental Diagnostics for the Study of Combustion Instabilities in Lean Premixed Combustors," J. Propul. Power **19**, pp. 735–750.
[21] Schütz, H., DLR, private communication.
[22] Turns, S. R., 2000, *An Introduction to Combustion*, McGraw Hill, New York.

Downloaded 02 Jun 2010 to 171.66.16.107. Redistribution subject to ASME license or copyright; see http://www.asme.org/terms/Terms_Use.cfm

Tim Lieuwen
School of Aerospace Engineering,
Georgia Institute of Technology,
Atlanta, GA 30318

Vince McDonell
UCI Combustion Laboratory,
University of California,
Irvine, CA 92697-3550

Eric Petersen
Mechanical, Materials & Aerospace Engineering,
University of Central Florida,
Orlando, FL 32816

Domenic Santavicca
Department of Mechanical and Nuclear Engineering,
The Pennsylvania State University,
University Park, PA 16802

Fuel Flexibility Influences on Premixed Combustor Blowout, Flashback, Autoignition, and Stability

This paper addresses the impact of fuel composition on the operability of lean premixed gas turbine combustors. This is an issue of current importance due to variability in the composition of natural gas fuel supplies and interest in the use of syngas fuels. This paper reviews available results and current understanding of the effects of fuel composition on combustor blowout, flashback, dynamic stability, and autoignition. It summarizes the underlying processes that must be considered when evaluating how a given combustor's operability will be affected as fuel composition is varied.
[DOI: 10.1115/1.2771243]

Introduction

This work is motivated by interest in developing fuel-flexible combustors capable of operating with highly variable and potentially low quality fuels, while producing minimal air pollutants. Development of gas turbines capable of fuel-flexible operation raises a variety of issues. For example, there is a potential reduction in compressor stall margin due to the higher mass flow rate of gas through the turbine than the compressor for diluted fuels. Pollutant emissions may also be impacted, as the variation in oxidation chemistry can have important influences on NOx and CO emissions. Also significant are durability issues, particularly for the turbine section, as opportunity fuels often contain a variety of corrosive or otherwise damaging compounds. Combustor operability issues are also significant and form the focus of this paper. In particular, operability issues in lean premixed combustion systems are emphasized.

Current dry low emission technology primarily focuses on burning natural gas, a fuel that is mainly composed of methane. However, interest in utilizing other energy resources as well as concern about energy security have motivated interest in utilizing coal-derived syngas or fuels from other sources, such as biomass, landfill gas, or process gas [1]. Technologies such as integrated gasification combined cycle (IGCC) plants enable the combustion of coal and other solid or liquid fuels, while still meeting aggressive emission targets and achieving high efficiency.

A simplified schematic illustrating the basic approach for lean premixed systems is shown in Fig. 1. Within the mixing length, fuel, and high pressure, hot air from the compressor mix but must not react until they reach the combustion chamber. While premixing the fuel and air has allowed impressive emission reduction, it creates operability issues that are strongly exacerbated by variability in fuel composition.

Combustor operability issues of interest include those related to operating the combustor in a safe, efficient, and reliable manner. This includes having the combustor reliably hold the flame so that it neither flashes back nor blows out, and burn the fuel in a "quiet," steady fashion.

Fuel variability has profound influences upon four combustor operability issues: blowout, flashback, combustion instability, and autoignition.

Blowout refers to when the flame becomes detached from the location where it is anchored and is physically "blown out" of the combustor. Blowout is often referred to as the "static stability" limit of the combustor. Blowout occurs when the time required for chemical reaction becomes longer than the combustion zone residence time. It is an issue because the chemical kinetic rates and flame propagation speeds vary widely with fuel composition. For example, many candidate fuels have similar heating values but also have chemical kinetic times that vary by an order of magnitude.

The opposite problem is *flashback*, where the flame physically propagates upstream of the region where it is supposed to anchor and into premixing passages that are not designed for high temperatures. Similar to blowout, flashback is an issue because of the widely varying flame speeds of candidate fuels. Again, fuels with similar heating values but with flame speeds that vary by factors of 5 or more are common.

Combustion instability refers to damaging pressure oscillations associated with oscillations in the combustion heat release rate. These oscillations cause wear and damage to combustor components and, in extreme cases, can cause liberation of pieces into the hot gas path, damaging downstream turbine components. Combustion instability issues are highlighted here because the conditions under which they occur can be strongly influenced by the fuel composition.

Autoignition refers to the homogeneous ignition of the reactive mixture upstream of the combustion chamber. Similar to flashback, it results in chemical reactions and hot gases in premixing sections, but its physical origins are quite different from those of flashback. Rather than the flame propagating upstream into the premixing section, autoignition involves spontaneous ignition of the mixture in the premixing section. Autoignition is an important issue because the conditions under which it occurs are not only a function of pressure and temperature, but also fuel composition.

The objective of this paper is to compile known results and discuss their implications on each of the operability issues discussed above. This is intended to provide the reader with an un-

Contributed by the International Gas Turbine Institute of ASME for publication in the JOURNAL OF ENGINEERING FOR GAS TURBINES AND POWER. Manuscript received June 13, 2006; final manuscript received July 4, 2006; published online January 11, 2008. Review conducted by Dilip R. Ballal. Paper presented at the ASME Turbo Expo 2006: Land, Sea and Air (GT2006), 2006, Barcelona, Spain, May 8–11, 2006, Paper No. GT2006-90770.

Copyright © 2008 by ASME

Downloaded 02 Jun 2010 to 171.66.16.107. Redistribution subject to ASME license or copyright; see http://www.asme.org/terms/Terms_Use.cfm

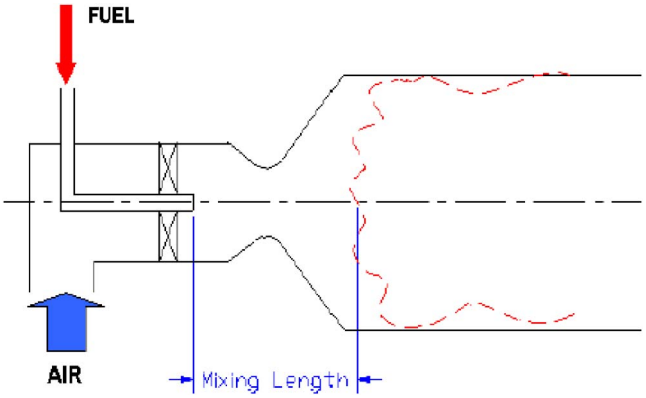

Fig. 1 Sketch of basic approach for lean premixed combustion

derstanding of the underlying processes that must be considered when evaluating how a given combustor's operability will be affected as fuel composition is varied.

These issues are of considerable relevance in both the United States and the European Union because of interest in the use of regasified liquefied natural gas (LNG) and the use of coal-derived and bioderived syngas fuels.

At present, the parameter used to characterize gas composition is Wobbe index, which offers a measure of heating value, and perhaps more importantly, an index against which the ability of the overall fuel handling and injection system to accommodate the fuel composition can be judged. If the Wobbe Index varies too far from the design value, changes are needed in the entire fuel system.

However, from a combustion specialist's point of view, the Wobbe index does not capture the effects of other fuel properties, such as flame speed or combustion chemistry, that affect the operability of lean premixed combustor systems. As such, this paper aims to provide a better understanding of the parameters that do characterize the influence of fuel composition upon critical operability issues.

Overview of Fuels and Their Properties

Imported LNG, while being predominantly composed of methane, generally contains significantly higher levels of higher hydrocarbons, such as ethane, propane, and butane, than domestic supplies [2]. Syngas fuels are typically composed primarily of H_2, CO, and N_2, and may also contain smaller amounts of CH_4, O_2, CO_2, and other higher order hydrocarbons [3]. Depending upon the source and particular processing technique, these fuels can have significant ranges in relative composition of these constituents. To illustrate, Moliere [4] compares the composition of several syngas fuels, showing that the volumetric H_2/CO ratio varies from a low of 0.33 to a high of 40, the percentage of diluent gases (e.g., N_2, CO_2, Ar) 4–51%, and the percentage of water 0–40%.

Landfill gas constituents are typically CH_4 and CO_2 [5]. In landfills, typical CO_2 to CH_4 concentration ratios range from 35%/60% to 55%/35% with balance N_2 [6]. Gases from anaerobic digestion of sewage, used commonly in wastewater treatment plants, typically have 65–75% CH_4 with the balance N_2 [6].

While a significant amount of fundamental understanding of flame propagation and the stability characteristics of lean, premixed systems has been gained in conventionally fueled, natural gas-air systems [7], little is known about these issues for alternate gaseous fuels. Furthermore, the majority of the fundamental investigations of the combustion characteristics of these synthetic gases are for nonpremixed flame configurations [8–12].

It is useful to summarize some of the basic properties of the constituents of these fuels and the interactions that occur when these constituents are blended to form the candidate fuels of interest. Consider syngas fuels, which are composed primarily of H_2 and CO. Both H_2 and CO act as fuels when oxidized. Individually, they produce higher adiabatic flame temperatures (at stoichiometric conditions in air) than CH_4, i.e., 2383 K and 2385 K, as compared to 2220 K. H_2 and CO also have lower flammability limits (ϕ=0.14 and 0.34, respectively) than CH_4 (ϕ=0.46), and higher maximum adiabatic laminar flame speeds (320 cm/s and 55 cm/s versus 40 cm/s for methane) [13].

This comparison of pure fuels does not, however, give a complete picture, since the performance of mixtures cannot be inferred from knowledge of the global performance of the constituents. This is a critical point that is emphasized in the detailed discussion that follows. As an example, CO and H_2 have *significantly* different transport properties and flame speeds. CO, which has a higher specific heat release than H_2, has chemistry that is coupled to H_2 oxidation through the reaction $CO+OH \rightarrow CO_2+H$, which dominates CO oxidation (at least) at atmospheric pressure.

The coupling is also important in that, together, CO and H_2 oxidation can cover a wide range of time scales that may bridge the relevant fluid dynamic, turbulent time scales. The chemical time scales of CO/H_2 mixtures are quite different from methane, and given the large spectrum of turbulent time scales in practical combustors, the combustion processes can cover several orders of magnitude of Damköhler number. For example, interactions between turbulent mixing processes and, say, H_2 oxidation may occur in the "flamelet" regime, those associated with CO oxidation in a "torn flamelets" regime, and OH recombination (which plays a key role in CO oxidation) in the distributed reaction regime.

The addition of methane, of interest because syngas fueled plants may cofire with a certain fraction of natural gas, introduces other interactions, particularly with H_2/CH_4 mixtures. Several recent studies have focused on H_2/CH_4 flames and shown that small additions of H_2 substantially enhance the mixture's resistance to extinction or blowout [14–17]. For example, fundamental studies show that the extinction strain rate of methane flames is doubled with the addition of 10% H_2 [18,19]. Similarly, CO/CH_4 flames also have coupled chemistry [20].

Final words on diluents in the fuel and their impact on combustion are as follows. The most common diluents are N_2, H_2O, and CO_2. Diluents in the fuel impact the flame in at least three ways, through changes in (1) mixture specific heat and adiabatic flame temperature, (2) chemical kinetic rates, and (3) radiative heat transfer. The addition of N_2 apparently has straightforward effects, as it is only manifested through the first item above, an influence that can be easily quantified with standard equilibrium calculations. H_2O and CO_2 additions, however, exert additional subtle effects through the latter two items. As noted by the second point, CO_2 and H_2O do not act as passive diluents in the fuel but interact kinetically [21]. For example, computational studies have shown that the flame speeds of mixtures with CO_2 dilution are lower than those of mixtures diluted with a fictitious chemically inert species with the same specific heat as CO_2 [16].

The third effect of CO_2 and H_2O dilution is through enhanced levels of radiative absorption and emission, as these species are far more effective absorbers and emitters than oxygen or nitrogen. For example, CO_2 dilution can result in lower flame temperatures and lower laminar flame speeds (compared to air dilution) due to radiative losses from the flame, which can also impact emissions [14,22,23].

Fuel Composition Influences on Basic Combustion Properties

The objective of this section is to provide an overview of the influence of fuel composition on several basic combustion properties that, in turn, have important impacts on the operability issues highlighted in this paper. Many of these results are based upon calculations which, unless otherwise indicated, were ob-

Downloaded 02 Jun 2010 to 171.66.16.107. Redistribution subject to ASME license or copyright; see http://www.asme.org/terms/Terms_Use.cfm

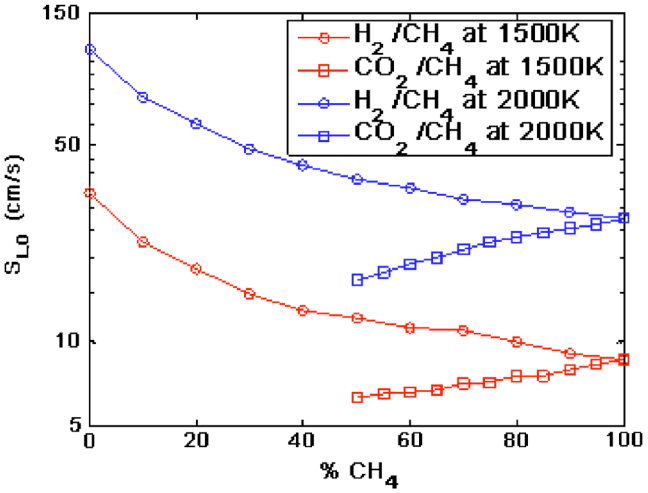

Fig. 2 Predicted dependence of laminar flame speed upon CH_4 concentration (by volume) for CH_4/H_2 and CH_4/CO_2 mixtures. Adiabatic flame temperature fixed at indicated value. Pressure=1 atm, reactant temperature=300 K.

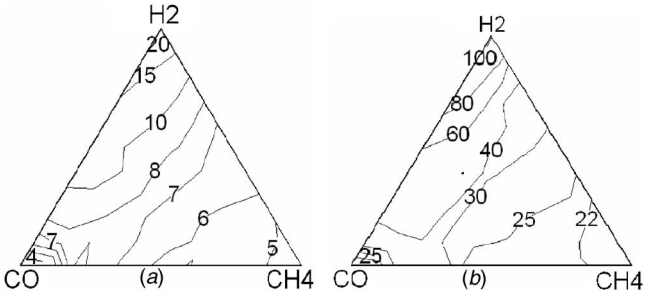

Fig. 3 Dependence of laminar flame speed (cm/s) upon fuel composition at fixed 1500 K (left) and 1900 K (right) adiabatic flame temperatures at 4.4 atm with 460 K reactants temperature

tained with CHEMKIN and its application programs, using the GRI 3.0 mechanism [24]. While this mechanism was primarily optimized for methane/air mixtures, good comparisons between its predictions and measurements have been obtained for a range of H_2/CO mixtures as well [21].

Laminar Flame Speed. Consider first the laminar flame speed S_L. The basic flame speed properties of CH_4, CO, and H_2 are discussed at length in a variety of sources [13]; so we focus upon their mixtures. A key point here is that the flame speed does not vary linearly between the respective pure values of the mixture constituents; i.e., $S_{L,\text{mix}} \neq X_1 S_{L,1} + X_2 S_{L,2}$, where X denotes either mole or mass fraction of each species. This is illustrated in Fig. 2, which plots the dependence of the flame speed (note that the y axis is a log scale) of H_2/CH_4 and CH_4/CO_2 mixtures upon mixture composition. Note that the mixture fuel/air ratio is adjusted at each point such that its adiabatic flame temperature remains constant at the indicated value. This method of plotting the data eliminates the dependence of flame speed on flame temperature and thereby reveals the dependence on fuel composition. Note that the addition of H_2 to CH_4 does not have a significant impact upon the flame speed until H_2 is the dominant constituent of the mixture. This behavior is to be contrasted with the effect of H_2 addition upon, for example, the extinction strain rate where a small addition of H_2 produces a very large effect.

This plot also shows the impact of CO_2 addition, where even if the mixture equivalence ratio is augmented to maintain a constant flame temperature, the flame speed is still lower than the nondiluted mixtures, a point that follows the earlier discussion on diluent effects.

Insight into the flame speed characteristics of CO/H_2 syngas mixtures with varying degrees of methane cofiring can be obtained from Fig. 3, which plots the dependence of the flame speed upon fuel composition at two fixed adiabatic flame temperatures, 1500 K and 1900 K. The fuel composition by volume is given by the location within the triangle, where the three vertices denote pure CO, H_2, or CH_4. At each point, the mixture equivalence ratio is adjusted such that the mixture has the given flame temperature. As expected, the high H_2 mixtures have the highest flame speeds.

Turbulent Flame Speed. Correlations of the turbulent flame speed of the form $S_T = S_L f(u')$, where u' denotes turbulence intensity, have been obtained from numerous studies [13]. Although there are quantitative differences between the predictions of the various correlations, which are primarily the result of geometric differences in the experimental configurations, they also share a number of common characteristics. In particular, they show that as the turbulence intensity increases, the turbulent flame speed initially increases, then asymptotes to a constant value, and then at very high turbulence intensities begins to decrease. The most obvious effect of fuel properties on the turbulent flame speed is through the laminar flame speed. For example, for a given turbulence intensity and a given burner, fuels with higher laminar flame speeds should have higher turbulent flame speeds.

However, turbulence intensity and laminar flame speed alone do not capture many important characteristics of the turbulent flame speed, such as the effects of flame instabilities and flame stretch. These effects are strongly dependent on "preferential diffusion," where differences in the relative rates of mass diffusion (of the deficient species) and/or thermal diffusion, usually expressed in terms of the Lewis number[1] affect the local laminar flame speed and the tendency of the flame to become spontaneously wrinkled (even in the absence of turbulent fluctuations). This latter effect is particularly important in the case of syngas fuels because of the large differences in diffusivity of the various fuel components. Therefore, two different fuel mixtures having the same laminar flame speed, turbulence intensity, and burner can have *appreciably* different turbulent flame speeds.

To illustrate, Fig. 4 is reproduced from Kido et al. [25] and plots the dependence of the turbulent flame speed for a variety of H_2, CH_4, and C_3H_8 mixtures. These mixtures were carefully chosen to have identical laminar flame speeds, as indicated by the S_T curves converging at $u'=0$. Note, however, that *the curves widely diverge as* u' increases from zero. In particular, note the substantially higher turbulent flame speed of the H07-15N mixture, which is a hydrogen blend, relative to the methane fuels (MO7-15N, M09-15N, MO98-15N). This graph clearly indicates that fuels with the same laminar flame speed can easily have variations in turbulent flame speed that approach an order of magnitude.

The variation of S_T with fuel composition for the physically interesting cases where the upstream turbulence intensity and flame temperature are held constant is nontrivial. This is due to the competition of two effects. First, experimental data indicate that the augmentation of the turbulent flame speed by flow turbulence, $d(S_T/S_L)/d(u'/S_L)$, increases with the percentage of H_2 in the fuel (or, more generally, with decreases in Lewis number). Thus, as shown in Fig. 4, S_T is much larger for the lean H_2 than the CH_4 mixture. However, in this case S_L remains constant.

If flame temperature and u' are held constant, S_L increases and, therefore, u'/S_L decreases with increases in H_2 concentration. Thus, there is a competition between two factors as H_2 levels increase: the increase of $d(S_T/S_L)/d(u'/S_L)$ and the decrease in u'/S_L. We have attempted to quantify these effects using the semiempirical model developed by Kido et al. [26], which has been

[1]The Lewis number, Le, is the ratio of the thermal to mass diffusivity.

Downloaded 02 Jun 2010 to 171.66.16.107. Redistribution subject to ASME license or copyright; see http://www.asme.org/terms/Terms_Use.cfm

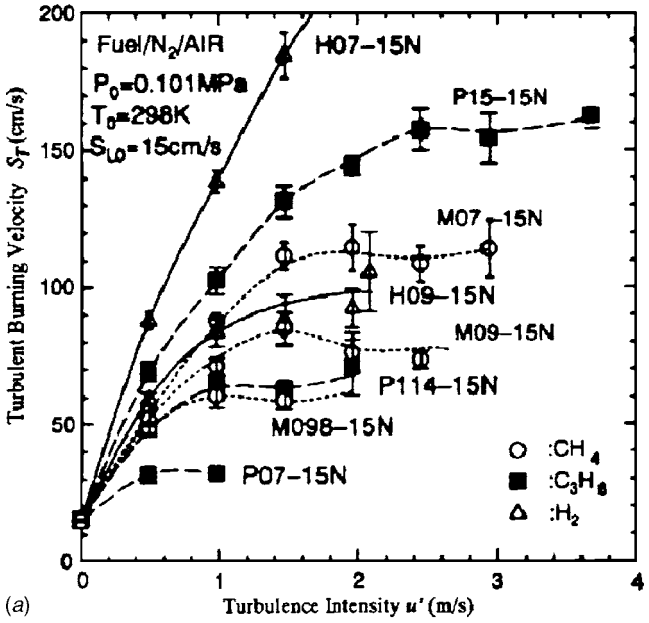

(*a*)

Mixture	Molar Fraction Fuel	O_2	N_2	ϕ	S_{L0} (cm/s)
H07-15N	H_2	0.71	7.14	0.7	15.26
H09-15N	H_2	0.56	6.94	0.9	15.88
M07-15N	CH_4	2.86	11.17	0.7	15.10
M09-15N	CH_4	2.22	10.82	0.9	14.91
M098-15N	CH_4	2.04	10.51	0.98	14.84
P07-15N	C_3H_8	7.14	29.05	0.7	14.94
P114-15N	C_3H_8	4.39	23.82	1.14	15.34
P15-15N	C_3H_8	3.33	13.70	1.5	14.99

(*b*)

Fig. 4 Dependence of turbulent flame speed upon turbulence intensity for several fuel blends with the same laminar flame speed (reproduced from Kido et al. [25])

benchmarked on CH_4/H_2 flames, as shown in Fig. 5.

Figure 5 shows that the ratio S_T/S_L can increase, decrease, or remain approximately constant as the relative CH_4/H_2 concentrations change. We can understand these trends from the above discussion and reference to Fig. 2. For example, in the $u'=4$ m/s, $T_{ad}=1500$ K case, S_T/S_L increases as the CH_4 levels increase from approximately 10–50%. This is due to the corresponding increase in $d(S_T/S_L)/d(u'/S_L)$ and the relatively constant value of S_L and, therefore, u'/S_L. At higher H_2 concentration levels, however, the flame speed begins to pick up dramatically, decreasing u'/S_L and, therefore, S_T/S_L.

Autoignition and Chemical Kinetic Time Scales. Fuel flexibility directly affects the chemical kinetics of the mixture and its autoignition characteristics. As a first step, the combustion designer may look at tabulated "autoignition temperatures," such as those shown in Table 1. This tabulated value refers to the temperature above which the mixture will spontaneously ignite, if given sufficient time. While these values are useful to some extent, the complex nature of ignition, coupled to the lack of information on fuel mixtures, warrants a more detailed treatment. In particular, these values must be placed in the context of time scales relevant to the gas turbine premixer. As a result, ignition delay time (the time required for a mixture to spontaneously ignite at some given condition) is of greater direct value to the combustion specialist.

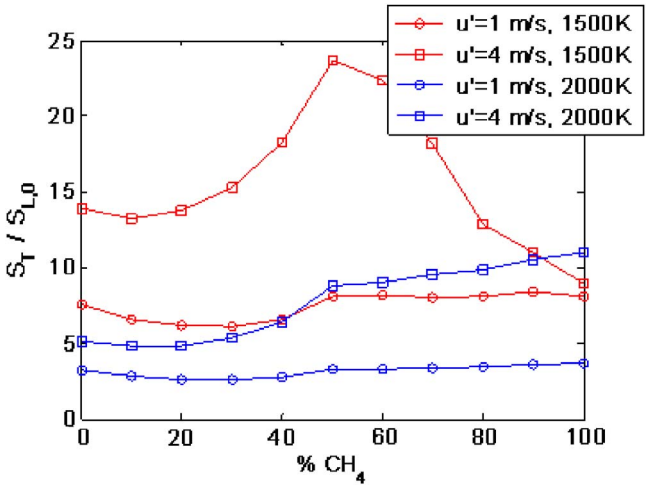

Fig. 5 Predicted dependence of S_T/S_L for CH_4/H_2 mixtures upon CH_4 concentration at fixed adiabatic flame temperatures of 1500 K and 2000 K, integral length scale=5.1 cm. Results obtained from application of model developed by Kido et al. [25].

Ignition delay time is important because it is (1) a direct indication of potential autoignition and (2) a useful parameter that defines the chemical kinetic time scale at any temperature, such as in the main burner.

In the present context, ignition delay time is defined as the time it takes a certain mixture of fuel and oxidizer at an initial temperature and pressure to begin reacting, where reaction is marked by the rapid depletion of the reactants and the formation of transient intermediate species such as OH, CH_3, and HO_2. The rapid buildup of such intermediate species becomes a useful parameter on which to base an ignition delay time. Excited-state species such as OH^* and CH^* are for similar reasons useful indicators of reaction [27].

Several studies focused on natural gas have been performed over the years and are summarized by Spadaccini and Colket [28]. Methane ignition data at high pressures are also available [29–32], though few data exist for most other fuels at pressures above 1 atm. For fuel blends of methane with H_2 and other hydrocarbons, recent experiments are available from Petersen et al. [33] at temperatures between 1100 K and 1800 K and pressures up to 30 atm, but are otherwise scarce. A kinetics model for ignition of CH_4 and CH_4/H_2 blends was demonstrated over the conditions of the recent study [33,34], based on the GRI-MECH 3.0 mechanism and others available in the literature [35–37].

Likewise, few ignition data existed for CO/H_2 blends at elevated pressures and real fuel-air mixtures prior to the recent studies of Kalitan and Petersen [38,39]. It is shown in these works that the recent CO/H_2 oxidation model of Davis et al. [40] does a fair job at reproducing the trends seen in the CO/H_2 ignition data, although some improvements at higher pressures and lower temperatures are still needed.

Figure 6 presents the predicted dependence of ignition delay

Table 1 Autoignition temperatures [13]

Species	Temperature[a] (K)
Butane	678–703
Carbon monoxide	882–924
Diesel	498–506
Ethane	745–788
Hydrogen	752–1072
Methane	800–905

[a]Generally at 1 atm.

Downloaded 02 Jun 2010 to 171.66.16.107. Redistribution subject to ASME license or copyright; see http://www.asme.org/terms/Terms_Use.cfm

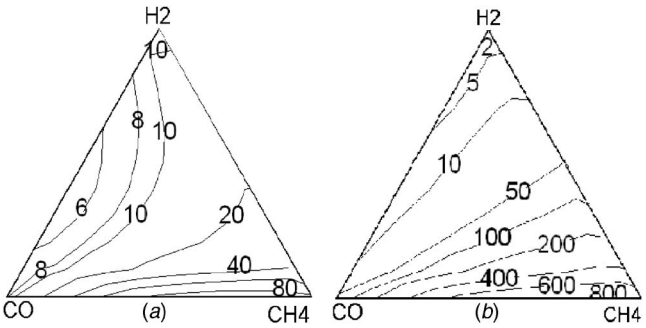

Fig. 6 Dependence of characteristic kinetic time scales upon fuel composition at mixture temperatures of 1000 K (left, in ms) and 1400 K (right, in μs). Compositions are based on those that will produce an adiabatic flame temperature of 1500 K at 4.4 atm with a 460 K reactant temperature.

time on fuel composition for mixtures of CH_4, H_2, and CO at two representative conditions. As in the above calculations, the mixtures in Fig. 6 are based on fuel-air combinations corresponding to an adiabatic flame temperature of 1500 K at 4.4 atm and a reactant temperature of 460 K. The ignition delay times are based on the rapid rise of OH as predicted by the kinetics model developed in Petersen et al. [33,41] and Hall et al. [34]. Two extremes in ignition temperature are presented for the mixtures in Fig. 6: one at 1000 K representing intermediate temperatures and one at 1400 K representing higher temperatures.

For the 1000 K ignition times (given in milliseconds), the longest times (and hence slower chemical kinetics) are attributed to the mixtures containing mostly methane. In general, the characteristic kinetic times decrease with the addition of hydrogen, with the lowest times (and hence faster chemical kinetics) corresponding to mixtures of CO and H_2. Similar conclusions can be drawn for the higher-temperature (1400 K) conditions, although the times shown are in microseconds. For example, CH_4-only mixtures ignite at approximately 800 μs at 1400 K, while most H_2- and CO-based mixtures ignite in less than 10 μs.

However, the subtleties of mixture composition, temperature, and pressure can become complicated in the $CH_4/H_2/CO$ system, due mainly to the second explosion limit behavior[2] of hydrogen oxidation at higher pressures and lower temperatures. Such behavior is attributed to the well-known depletion of the OH radical pool in favor of less-reactive HO_2 radicals [42].

Figure 7 presents ignition-time plots for a range of mixtures at a pressure of 15 atm and for $\phi=0.4$ (corresponding approximately to an adiabatic flame temperature of 1500 K). Methane/hydrogen blends are shown in Fig. 7(*a*). As expected, the ignition delay time decreases with the addition of H_2; this ignition-promoting effect of hydrogen is most pronounced at higher temperatures. At lower temperatures, the effect of hydrogen addition diminishes.

Figure 7(*b*) presents the ignition delay times for a range of CO/H_2 mixtures at 15 atm, calculated using the mechanism of Davis et al. [40]. The ignition of such mixtures tends to be dominated by the hydrogen oxidation kinetics [38,39]. As shown in Fig. 7(*a*), little difference between the ignition times for blends ranging from 20% to 100% hydrogen is observed. The hydrogen oxidation kinetics at higher pressures and lower temperatures therefore play a critical role in CO/H_2 mixtures, and further improvement is needed in this regard, particularly the effect of collision partners on the HO_2-formation reaction $H+O_2+M=HO_2+M$.

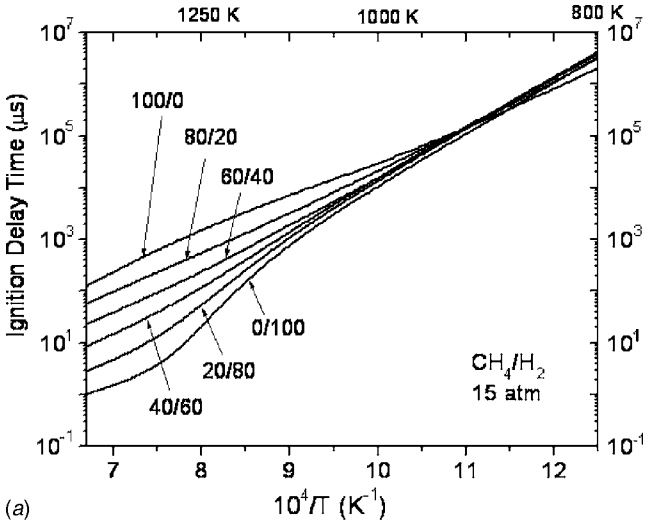

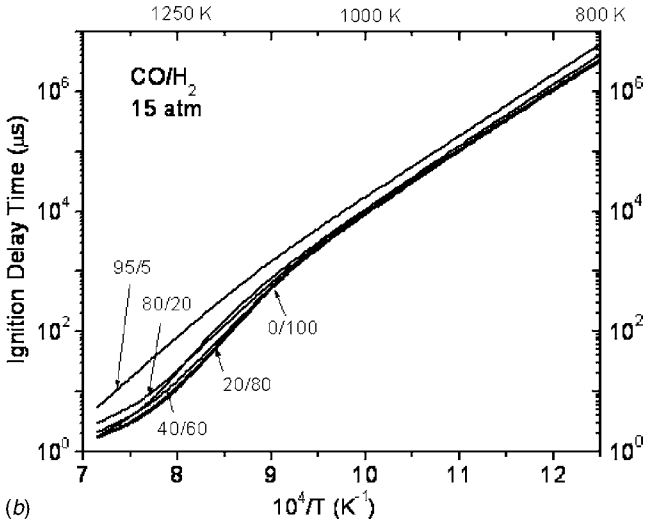

Fig. 7 Effect of mixture composition of CH_4/H_2 (left) and CO/H_2 (right) blends on ignition delay times at 15 atm and $\phi=0.4$

Pressure effects can be displayed in a similar fashion by plotting ignition-time curves for a single mixture over a range of pressures from 1 atm to 30 atm.

Figure 8(*a*) presents such a plot for a 60/40 CH_4/H_2 blend ($\phi=0.4$). Although one might expect that increasing pressure would automatically lead to a faster reaction time, this is not always the case. For example, near 1000 K, the 1 atm ignition times are nearly the same as the ignition times for the 15 and 30 atm cases. The transition from the first to the second explosion limit behavior is evident by the curvature of the 1 atm curve around 1000 K.

The varied effect of pressure on a typical CO/H_2 mixture is even more pronounced, as seen in Fig. 8(*b*) for a 60/40 blend ($\phi=0.4$). In the temperature region between about 1200 K and 900 K, the 1 atm ignition times are predicted to be shorter than the 15 and 30 atm times. At higher temperatures, the 15 atm times are shorter than the 30 atm ones. Similar trends are seen in other CO/H_2 blends at lean conditions.

Because of the lack of experimental data at practical conditions, the calculations in Figs. 6–8 are based on chemical kinetics

[2]In the H_2/O_2 system, there are two pathways through which the $H+O_2$ reaction proceeds: $H+O_2=OH+O$, a chain-branching pathway, and $H+O_2+M=HO_2+M$, a chain-terminating pathway. The classical second explosion limit refers to the region of temperature and pressure where the chain termination reaction becomes important, hence slowing down the ignition process. This second limit generally occurs at higher pressures and lower temperatures. The first limit favors the chain-branching reaction and occurs at higher temperatures and lower pressures.

Downloaded 02 Jun 2010 to 171.66.16.107. Redistribution subject to ASME license or copyright; see http://www.asme.org/terms/Terms_Use.cfm

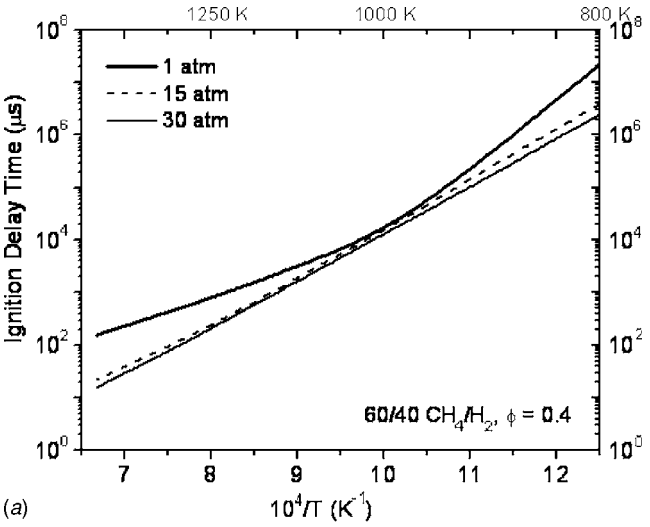

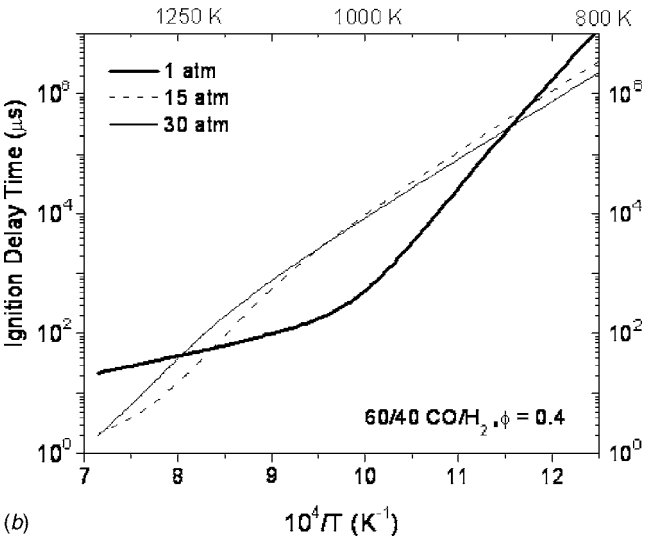

Fig. 8 Effect of pressure on ignition delay times for 60/40 blends of CH_4 or CO with H_2 at ϕ=0.4 (left, CH_4/H_2 blend; right, CO/H_2 blend)

mechanisms that are still in need of refinement. From recent studies in the authors' laboratories, the general trend is for existing kinetics models to overpredict ignition times of methane- and CO-based fuel blends at elevated pressures. The general ignition trends presented herein, however, should still hold even if their absolute magnitudes are incorrect.

Combustor Operability Issues

The phenomena discussed above can be placed in the context of a "stability loop" as illustrated in Fig. 9. As shown, maintaining stable burning while avoiding static and dynamic instabilities and flashback requires careful consideration. Furthermore, these stability maps are dependent not only on engine temperature and pressure but also on fuel composition. Note that autoignition is not reflected in Fig. 9 because it is an issue primarily associated with the fuel preparation.

Blowout. Insight into the sensitivity of a combustor's blowout characteristics to fuel composition can be gained from available quasiempirical correlations and physical correlations. Methods for developing blowout correlations in the latter case have been studied extensively [13,43–46], with essentially the same form of correlation that relates the blowout limits to a ratio of a *chemical*

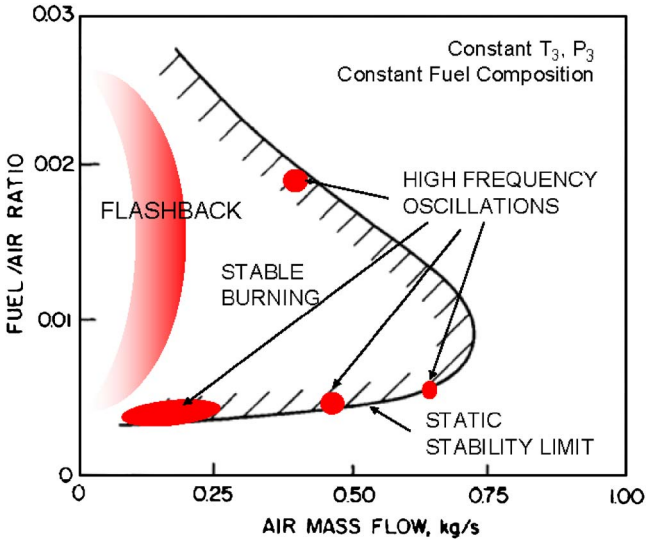

Fig. 9 Representation of combustion phenomena relative to stability loop

kinetic time and residence time, τ_{chem}/τ_{res}. In well stirred reactor theory, this ratio is often referred to as a combustor loading parameter. While this model certainly has limitations, it nonetheless provides some insight into the variation of blowout limits with fuel composition.

When applied to blowout limits of premixed flames, this chemical time can be estimated as

$$\tau_{chem} = \alpha/S_L^2 \tag{1}$$

where S_L and α denote the laminar flame speed and thermal diffusivity, respectively [47,48]. Alternative chemical times, such as the blowout residence time of a well stirred reactor model, give comparable results. Note that this is a different chemical time scale than the autoignition time discussed earlier, which is controlled by different chemical reactions. The residence time is generally scaled as d/U_{ref}, where d and U_{ref} denote a characteristic length scale (e.g., a recirculation zone length) and velocity scale, respectively. Putting this together, the reactor based theory predicts that blowout limits should scale with the Damköhler number:

$$\mathrm{Da} = \frac{\tau_{res}}{\tau_{chem}} = \frac{S_L^2 d}{\alpha U_{ref}} \tag{2}$$

While clearly there are important issues such as appropriate choice of length and velocity scale, Damköhler number scalings have been found to capture blowout trends across a wide range of fuel compositions, as illustrated by Fig. 10. These data consist of a number of permutations of $CO/H_2/CH_4$ fuel blends, ranging from pure fuels to various combinations [49].

While scatter is present in the data, the results show that blowout occurs at a roughly constant value of the Damkohler number, in this case, at 0.6. More importantly, it shows that the impact of fuel composition on blowout trends of a system can be captured by considering the chemical kinetic times of the mixture. To illustrate, we calculated the predicted blowout equivalence ratio of each of these mixtures assuming blowout at Da=0.6. In almost all cases, the difference between the predicted blowout equivalence ratio and its actual measured value was less than 0.03.

Given, therefore, the significance of the chemical time in determining blowout conditions, it is useful to quantify its values for a range of fuel compositions of interest. Figure 11 plots the dependence of the calculated chemical time, $\tau_{chem}=\alpha/S_L^2$, upon fuel

Downloaded 02 Jun 2010 to 171.66.16.107. Redistribution subject to ASME license or copyright; see http://www.asme.org/terms/Terms_Use.cfm

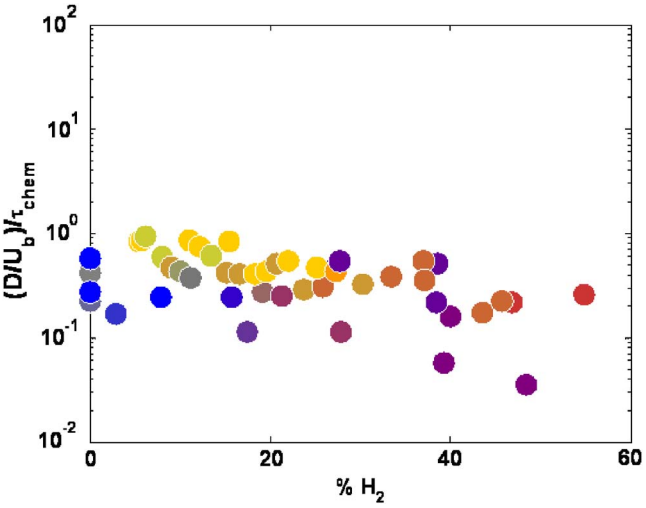

Fig. 10 Ratios between residence time and chemical time at constant premixer exit velocity of 60 m/s, combustor pressure of 1.7 atm, and 300 K reactant temperature

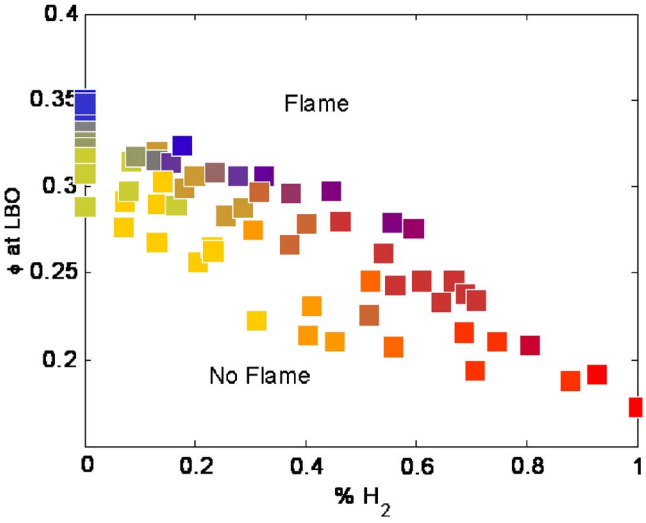

Fig. 12 Dependence of LBO equivalence ratio upon H_2 mole fraction at constant premixer exit velocity of 60 m/s and 4.4 atm combustor pressures, 460 K inlet temperature

composition of $H_2/CO/CH_4$ mixtures at two fixed flame temperatures, 1500 K and 1900 K. Note the order of magnitude variation in chemical time from the fast H_2 mixtures to the slow CO mixtures.

One implication of this result is that higher hydrogen mixtures will blow out at leaner equivalence ratios, as can be seen by replotting similar data to that shown in Fig. 10 but replacing the y axis with the equivalence ratio at blowout. These results are shown in Fig. 12.

Similar considerations can be used to determine how a given system's blowout tendencies will be affected by changes in fuel composition.

Flashback. Flashback occurs when the turbulent flame speed exceeds the flow velocity along some streamline, allowing the flame to propagate upstream into the premixing section. Flashback often occurs in the flow boundary layer, since this is the point of lowest flow velocity. As such, the effect of fuel composition variations upon flashback depends on the corresponding change in turbulent flame speed S_T. As alluded to in an earlier section, the substantial variations in S_T that exist with variations in fuel composition are only beginning to be fully appreciated, while this point appears to be well established, no comprehensive data sets or validated models currently exist. As the characteristics of S_T have been discussed in an earlier section, they will not be repeated here.

Boundary layer flashback characteristics have been extensively characterized. However, in swirling flows, flashback can potentially occur by other mechanisms as well, whose dynamics are not wholly captured by the parameter S_T. Kroner et al. [50] and Umemura and Tomita [51] have suggested the phenomenon of "combustion induced vortex breakdown." The basic idea is that the flame contributes to vortex breakdown, and therefore a low or negative flow region ahead of it. The flame advances forward, causing the vortex location breakdown region to advance farther upstream. This process continues as the flame proceeds farther and farther upstream. In this case, flashback can occur even if S_T is everywhere less than the flow velocity. However, we can make the tentative conclusion that the key fuel related parameter that will influence the occurrence of combustion induced vortex breakdown is the temperature ratio across the flame[3] [52], not the chemical kinetic characteristics of the mixture. For fixed flame temperatures, as considered in many of the above results, variations in fuel composition should, therefore, not change the characteristics of this process.

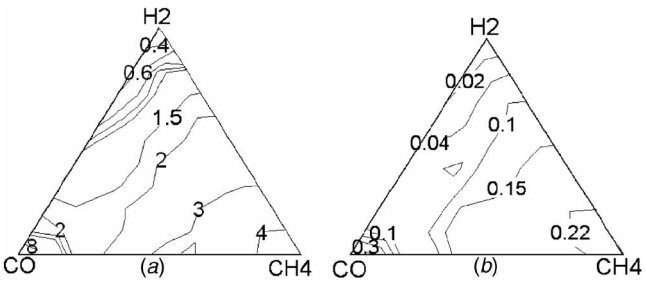

Fig. 11 Dependence of chemical time (ms) on fuel composition at fixed adiabatic flame temperature, 1500 K (left) and 1900 K (right), at 4.4 atm with 460 K reactant temperature

Combustion Instability. Combustion instabilities are characterized by large amplitude pressure oscillations that are driven by unsteady heat release. A necessary, but not sufficient, condition for an instability to occur is that the unsteady pressure and heat release oscillations must be in phase (or, more precisely, that their phase difference is less than 90 °C). Fuel composition variations affect combustion instabilities by altering this phase angle.

In order to understand how variations in fuel composition affect the phase difference between pressure and heat release fluctuations, it is necessary to consider the specific mechanism responsible for the instability. Two mechanisms are known to be particularly significant in premixed systems: these are fuel/air ratio oscillations and vortex shedding. In the former mechanism, acoustic oscillations in the premixer section cause fluctuations in the fuel and/or air supply rates, thus producing a reactive mixture whose equivalence ratio varies periodically in time. The resulting mixture fluctuation is convected to the flame where it produces

[3]We can obtain insight into the effect of fuel composition on this phenomenon by considering the mechanism responsible for vortex breakdown. While there are undoubtedly a variety of mechanisms for the instabilities leading to breakdown, one likely candidate is an axisymmetric, inviscid mechanism discussed by Brown and Lopez [52]. For this mechanism, the breakdown point will favor regions of adverse pressure gradient, or equivalently, flow divergence. Flame fronts that are inclined to the flow induce a radial component in the approach flow velocity because of the gas expansion process and deflection of streamlines across the flame. The magnitude of this induced flowfield is a function of the density ratio across the flame and the flame's inclination angle with respect to the flow.

Downloaded 02 Jun 2010 to 171.66.16.107. Redistribution subject to ASME license or copyright; see http://www.asme.org/terms/Terms_Use.cfm

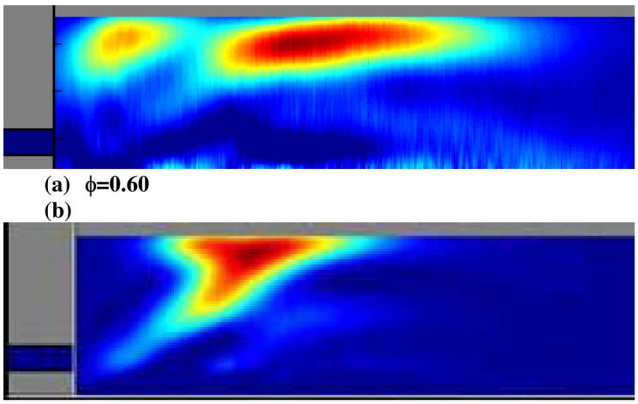

Fig. 13 Two-dimensional chemiluminescence flame images showing the effect of equivalence ratio on the distance to the flame "center of mass" for a fixed inlet velocity of 72 m/s and inlet temperature of 200°C

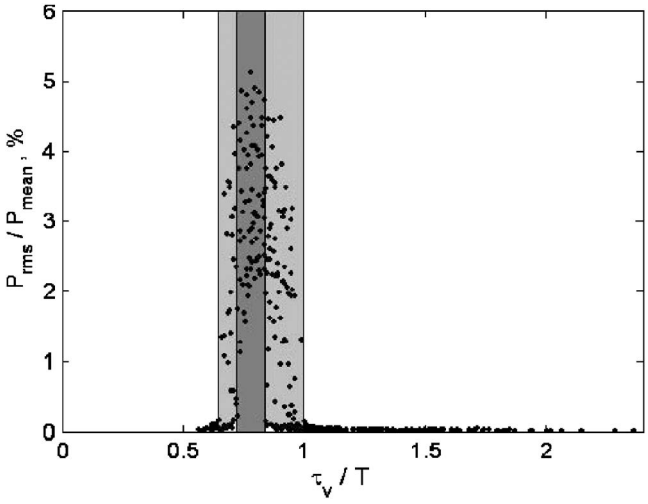

Fig. 14 Normalized rms pressure fluctuation in the combustor versus the vortex convection time ($\tau_V = \tau_{conv}$) divided by the acoustic period, *T*

heat release oscillations that drive the instability. The coupling of the premixer acoustics with the fuel system is affected by the pressure drop across the fuel injector.

The vortex shedding mechanism, as its name suggests, is due to large scale, coherent vortical structures. These structures are the result of flow separation from flameholders and rapid expansions, as well as vortex breakdown in swirling flows. They are convected by the flow to the flame where they distort the flame front and thereby cause the rate of heat release to oscillate.

Fuel/air ratio oscillations and vortex shedding become important when the resulting heat release perturbation is in phase with the pressure fluctuation. This can be expressed by the following relationship:

$$\tau_{conv} + \tau_{chem} = kT \tag{3}$$

where τ_{conv} refers to the time required for either the equivalence ratio perturbation or the vortex to convect from its point of formation to the "center of mass" of the flame, τ_{chem} refers to the chemical delay time, T refers to the acoustic period, and k is an integer constant whose value depends upon the combustion chamber acoustics [53,54].

Variations in fuel composition impact the phase relationship expressed by Eq. (3) by affecting both the convective and chemical times. The effect of fuel composition on the chemical time is clear. The effect on the convective time can be better understood from the following equation which expresses the convective time as the sum of the convective time in the premixer (τ_{pm}) and the convective time in the combustor (τ_{comb}):

$$\tau_{conv} = \tau_{pm} + \tau_{comb}$$

$$\tau_{conv} = [L_{pm}/u_{pm}] + [L_f/(\alpha u_{comb})] \tag{4}$$

where L_{pm} refers to the distance from the point of origin of the disturbance to the entrance to the combustor, u_{pm} refers to the mean convective velocity in the premixer, L_f refers to the distance the perturbation travels from the combustor entrance to the center of mass of the flame, and u_{comb} refers to the mean convective velocity in the combustor, which can be expressed as a fraction α of the velocity in the premixer.

The effect of variations in fuel composition on the convective time is primarily the result of the effect of flame speed on the location of the flame center of mass. For example, increasing the percentage of hydrogen in a syngas fuel will increase the flame speed and therefore change the location of the flame center of mass. This is illustrated by the two-dimensional chemiluminescence flame structure images shown in Fig. 13 [54,55]. (Note that only the upper half of the combustor is shown and the flow is from left to right.) In this case, the flame speed is changed by adjusting the equivalence ratio, while the inlet velocity and temperature are constant. These results show that as the flame speed increases, as a result of increasing the equivalence ratio, the distance to the flame center of mass decreases, which corresponds to a shorter convection time in the combustor. As discussed below, such a change can cause a stable combustor to go unstable or an unstable combustor to go stable.

The effect of variations in the flame center of mass on the stability characteristics of a lean premixed combustor in the situation where vortex shedding is the dominant driving mechanism is shown in Fig. 14 [34]. This figure is a plot of the normalized rms pressure fluctuation in the combustor versus the vortex convective time ($\tau_V = \tau_{conv}$) divided by the acoustic period, T. Each data point on this figure represents a different combination of equivalence ratio, inlet velocity, and combustor length. The combustor length was varied to vary the acoustic frequency ($f = 1/T$). This result shows that instabilities are only observed when the pressure fluctuation and the vortex driven heat release fluctuation are in phase, i.e., when $\frac{1}{2} < \tau_V/T < 1$. Note that within the light gray shaded regions, there are both stable and unstable conditions. As noted previously, not only must the heat release and pressure fluctuation be in phase but the gain must be greater than the damping for the combustor to go unstable.

Autoignition. Designing the premixer to preclude autoigntion requires knowledge of the ignition delay time for the fuel being used and the local conditions relative to a time scale associated with the premixing. As illustrated in Fig. 1, a long mixing length is desired to achieve sufficient premixing. However, the complex aerodynamics associated with swirl, separation, and strong gradients can make it difficult to assign a single time scale to represent the physical premixing time in a given system. In general, a poor aerodynamic design will result in high pressure loss and will be much more prone to flashback, so design strategies for precluding these phenomena will also help mitigate the possibility of autoignition. The time scale associated with physical mixing in current low emission combustors is on the order of 1–5 ms based on bulk velocities and premixer volumes.

The key question then is whether the ignition delay time of the fuel being used at the local premixer conditions is longer, shorter, or about the same as the premixing time scale. If the ignition delay time is much longer than several milliseconds, concerns about autoignition may be allayed to some degree. Of course all

Downloaded 02 Jun 2010 to 171.66.16.107. Redistribution subject to ASME license or copyright; see http://www.asme.org/terms/Terms_Use.cfm

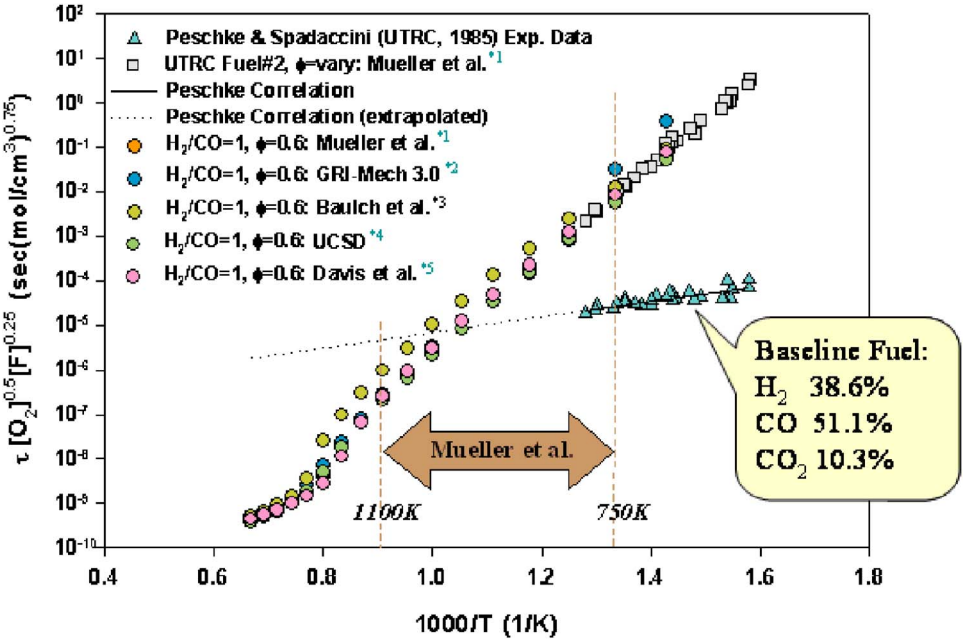

Fig. 15 Comparison of flow reactor data with kinetic modeling using different detailed mechanisms [35,40,56–59]

aspects of the operation must be considered, including start up, load shedding, and so on, when considering the implications. Given the tremendous amount of experience and anecdotal data on natural gas fired industrial gas turbines using lean premixed combustion strategies, a useful way to view the question is to compare how the ignition delay time for the fuel of interest compares with natural gas. Figure 7(*a*) illustrates an example of such a comparison for mixtures of hydrogen and methane at 15 atm pressure. While the presence of hydrogen greatly reduces the ignition delay time at high temperatures, for gas turbine combustor inlet temperatures (more typically 600–1000 K), the difference between methane and hydrogen is fairly small. Temperatures above 750 K reflect high pressure ratio machines and/or recuperated cycles. Furthermore, the ignition delay times suggested by Figs. 7 and 8 are 10–100 ms at typical gas turbine combustor inlet temperatures, which should be sufficient to preclude ignition delay in an aerodynamically well designed premixer. As a case in point, Fig. 7 illustrates an example for pure hydrogen and suggests, perhaps counterintuitively, that hydrogen is relatively safe to work with relative to autoignition for gas turbine premixer conditions. Indeed, if the spontaneous ignition temperature of hydrogen is comparable to methane and other fuels (e.g., Table 1), it is might be concluded that higher hydrocarbons or backup fuels such as diesel will be more prone to autoignition than hydrogen containing fuels. However, since typical tabulated data do not include pressure and fuel mixture effects, this conclusion is still somewhat speculative.

Because pressure effects and actual delay times are important in gas turbine applications and because of nonlinear behavior exhibited for some species such as hydrogen, as shown in Fig. 8, considerable interest in further verifying the answers to the key question about the ignition delay time exists. While shock tubes are commonly used for such measurements [28,30,31], flow reactors have also been used, but on a much more limited basis. These two approaches tend to favor high temperature and low temperature, respectively. The flow reactor is more representative of the actual gas turbine type conditions and features some aspects not possible in the shock tube, such as radiation from hot walls. Limited studies have been done at gas turbine conditions with flow reactors. A comparison of shock tube based kinetic calculations with flow reactor data is shown in Fig. 15. These results suggest two "schools of thought" depending on the type of test rig used and indicate a need for further work in this area to validate the low temperature (i.e., combustor inlet conditions) behavior.

Concluding Remarks

The observations and analyses presented here illustrate a number of subtle details that give rise to nonintuitive and nonlinear behavior with mixtures. A key take-away point is that behavior of fuel mixtures can be markedly different than that of the individual constituents. As a result, behaviors such as turbulent flame speed or ignition delay time may behave in a highly nonlinear manner as fuel mixtures change. It is also clear that hydrogen, when present in these fuels, provides many unique impacts on the behavior. This is due to its significantly different transport properties and flame speed compared with other gases. Because of these complex mixture effects, it is important to gain more understanding of the relationship between fuel mixture composition and properties such as flame speed and ignition and chemical delay times. Finally, it is apparent that traditional engineering design parameters such as Wobbe Index, heating value, and autoignition temperature are insufficient to capture the potential impact of future fuels on combustion system operability.

Acknowledgment

The authors of this paper are participants in the University Turbine Systems Research (UTSR) program, a DOE-sponsored program that is investigating fundamental problems that are of interest to the gas turbine community, with particular focus upon coal-derived fuels. This publication was prepared with the support of the U.S. Department of Energy, Office of Fossil Energy, National Energy Technology Laboratory, under Contract Nos. 03-01-SR95, 03-01-SR109, 03-01-SR111, and 04-01-SR114 (Dr. Richard Wenglarz, contract monitor). In addition, the assistance of Q. Zhang in performing chemical kinetic calculations and of Dr. J. G. Lee and E. Gonzalez in performing the flame structure and instability measurements is gratefully acknowledged.

References

[1] Richards, G. A., McMillian, M. M., Gemmen, R. S., Rogers, W. A., and Cully, S. R., 2001, "Issues for Low-Emission, Fuel-Flexible Power System," Prog.

Downloaded 02 Jun 2010 to 171.66.16.107. Redistribution subject to ASME license or copyright; see http://www.asme.org/terms/Terms_Use.cfm

Energy Combust. Sci., **27**, pp. 141–169.
[2] Flores, R. M., McDonell, V. G., and Samuelsen, G. S., 2003, "Impact Of Ethane & Propane Variation In Natural Gas On The Performance Of A Model Gas Turbine Combustor," ASME J. Eng. Gas Turbines Power, **125**(3), pp. 701–708.
[3] Klimstra, Jacob, 1986, "Interchangeability of Gaseous Fuels—The Importance of the Wobbe Index," SAE Paper No. 861578.
[4] Moliere, M., 2002, "Benefiting from the Wide Fuel Capability of Gas Turbines: A Review of Application Opportunities," ASME Paper No. GT-2002-30017.
[5] King, S., 1992, "The Impact of Natural Gas Composition on Fuel Metering and Engine Operating Characteristics," SAE, Paper No. 920593.
[6] Tillman, D. A., and Harding, N. S., 2004, *Fuels of Opportunity: Characteristics and Uses in Combustion Systems*, Elsevier, New York, pp. 273–287.
[7] Durbin, M., and Ballal, D., 1996, "Studies of Lean Blowout in a Step Swirl Combustor," ASME J. Eng. Gas Turbines Power, **118**.
[8] Barlow, R. S., Fiechtner, G. J., Carter, C. D., and Chen, J. Y., 2000, "Experiments on the Scalar Structure of Turbulent $CO/H_2/N2$ Jet Flames," Combust. Flame, **120**, pp. 549–569.
[9] Correa, S. M., and Gulati, A., 1998, "Non-Premixed Turbulent CO/H2 Flames at Local Extinction Conditions," Proc. Combust. Inst., **22**, pp. 599–606.
[10] Drake, M. C., 1986, "Stretched Laminar Flamelet Analysis of Turbulent H2 and $CO/H_2/N_2$ Diffusion Flames," Proc. Combust. Inst., **21**, pp. 1579–1589.
[11] Correa, S. M., Gulati, A., and Pope, S. B., 1988, "Assessment of a Partial Equilibrium/Monte Carlo Model for Turbulent Syngas Flames," Combust. Flame, **72**, pp. 159–173.
[12] Masri, A. R., and Dibble, R. W., 1988, "Spontaneous Raman Measurements in Turbulent CO/H2/N2 Flames Near Extinction," Proc. Combust. Inst., **22**, pp. 607–618.
[13] Glassman, I., 1996, *Combustion*, Academic, New York.
[14] Maloney, D., 2002, "The Simulation Validation Project at NETL," DOE Report.
[15] Schefer, R. W., 2003, "Hydrogen Enrichment for Improved Lean Flame Stability," Int. J. Hydrogen Energy, **28**, pp. 1131–1141.
[16] Wicksall, D., and Agrawal, A., 2001, "Effects of Fuel Composition on Flammability Limit of a Lean, Premixed Combustor," ASME Paper No. 2001-GT-0007.
[17] Yoshimura, T., McDonell, V. G., and Samuelsen, G. S., 2005, "Evaluation of Hydrogen Addition to Natural Gas on the Stability and Emissions Behavior of a Model Gas Turbine Combustor," ASME Paper No. GT2005-68785.
[18] Sankaran, Ramanan, Im, and Hong, G., 2002, "Dynamic Flammability Limits of Methane/Air Premixed Flames With Mixture Composition Fluctuations," Proc. Combust. Inst., **29**, pp. 77–84.
[19] Jackson, G. S., Sai, R., Plaia, J. M., Boggs, C. M., and Kiger, K. T., 2003, "Influence of H_2 on the Response of Lean Premixed CH_4 Flames to High Strained Flows," Combust. Flame, **132**, pp. 503–511.
[20] Vagelopoulos, C. M., and Egolfopoulos, F. N., 1994, "Laminar Flame Speeds and Extinction Strains Rates of Mixtures of Carbon Monoxide With Hydrogen, Methane, and Air," Proc. Combust. Inst., **25**, pp. 1317–1341.
[21] Natarajan, J., Nandula, S., Lieuwen, T., and Seitzman, J., 2005, "Laminar Flame Speeds of Synthetic Gas Fuel Mixtures," ASME Paper No. GT2005-68917.
[22] Effinger, M. W., Mauzey, J. L., and McDonell, V. G., "Characterization and Reduction of Pollutant Emissions From a Landfill and Digester Fired Microturbine Generator," ASME Paper No. GT2005-68520.
[23] McDonell, V. G., Effinger, M. W., and Mauzey, J. L., "Correlation of Landfill and Digester Gas Composition With Gas Turbine Pollutant Emissions," ASME Paper No. GT2006-90727.
[24] Kee, R. J., Rupley, F. M., Miller, J. A., Coltrin, M. E., Grcar, J. F., Meeks, E., Moffat, H. K., Lutz, A. E., Dixon-Lewis, G., Smooke, M. D., Warnatz, J., Evans, G. H., Larson, R. S., Mitchell, R. E., Petzold, L. R., Reynolds, W. C., Caracotsios, M., Stewart, W. E., Glarborg, P., Wang, C., and Adigun, O., 2000, CHEMKIN collection, Release 3.6, Reaction Design, Inc., San Diego, CA.
[25] Kido, H., Nakahara, M., Nakashima, K., and Hashimoto, J., 2002, "Influence of Local Flame Displacement Velocity on Turbulent Burning Velocity," Proc. Combust. Inst., **29**, pp. 1855–1861.
[26] Kido, H., Nakahara, M., Hashimoto, J., and Barat, D., 2002, "Turbulent Burning Velocity of Two Component Fuel Mixtures of Methane, Propane and Hydrogen," Jpn. Soc. Mech. Eng. Int. J., **45**, pp. 355–362.
[27] Hall, J. M., Rickard, M. J. A., and Petersen, E. L., 2005, "Comparison of Characteristic Time Diagnostics for Ignition and Oxidation of Fuel/Oxidizer Mixtures Behind Reflected Shock Waves," Combust. Sci. Technol., **177**, pp. 455–483.
[28] Spadaccini, L. J., and Colket, M. B. III, 1994, "Ignition Delay Characteristics of Methane Fuels," Prog. Energy Combust. Sci., **20**, pp. 431–460.
[29] Petersen, E. L., Röhrig, M., Davidson, D. F., Hanson, R. K., and Bowman, C. T., 1996, "High-Pressure Methane Oxidation Behind Reflected Shock Waves," Proc. Combust. Inst., **26**, pp. 799–806.
[30] Petersen, E. L., Davidson, D. F., and Hanson, R. K., 1999, "Ignition Delay Times of Ram Accelerator CH_4/O_2/Diluent Mixtures," J. Propul. Power, **15**, pp. 82–91.
[31] Huang, J., Hill, P. G., Bushe, W. K., and Munshi, S. R., 2004, "Shock-Tube Study of Methane Ignition Under Engine-Relevant Conditions: Experiments and Modeling," Combust. Flame, **136**, pp. 25–42.
[32] Zhukov, V. P., Sechenov, V. A., and Starikovskii, A. Yu., 2003, "Spontaneous Ignition of Methane-Air Mixtures in a Wide Range of Pressures," Combust., Explos. Shock Waves, **30**, pp. 487–495.
[33] Petersen, E. L., Hall, J. M., Smith, S. D., de Vries, J., Amadio, A., and Crofton, M. W., 2005, "Ignition of Fuel-Lean Natural Gas Blends at Gas Turbine Pressures," *ASME Turbo EXPO 2005*, Reno, Jun., Paper No. GT2005-68517.
[34] Hall, J. M., and Petersen, E. L., 2005, "Development of a Chemical Kinetics Mechanism for CH_4/H_2/Air Ignition at Elevated Pressures," AIAA Paper No. 2005-3768.
[35] Smith, G. P., Golden, D. M., Frenklach, M., Moriarty, N. W., Eiteneer, B., Goldenberg, M., Bowman, C. T., Hanson, R. K., Song, S., Gardiner, W. C., Lissianski, V. V., and Qin, Z., GRI-MECH 3.0, http://www.me.berkeley.edu/gri-mech/.
[36] Hunter, T. B., Wang, H., Litzinger, T. A., and Frenklach, M., 1994, "The Oxidation of Methane at Elevated Pressures: Experiments and Modeling," Combust. Flame, **97**, pp. 201–224.
[37] Wang, H., and Laskin, A., 1999, "On Initiation Reactions of Acetylene Oxidation in Shock Tubes A Quantum Mechanical and Kinetic Modeling Study," Chem. Phys. Lett., **303**, pp. 43–49.
[38] Kalitan, D. M., Petersen, E. L., Mertens, J. D., and Crofton, M. W., 2005, "Ignition and Oxidation of Lean CO/H_2 Fuel Blends in Air," AIAA Paper No. 2005-3767.
[39] Kalitan, D. M., and Petersen, E. L., 2006, "Ignition of Lean CO/H/Air Mixtures at Elevated Pressures—Part II," ASME Paper No. GT2006-90488.
[40] Davis, S. G., Joshi, A. V., Wang, H., and Egolfopoulos, F., 2005, "An Optimized Kinetic Model of H_2/CO Combustion," Proc. Combust. Inst., **30**, pp. 1283–1292.
[41] Petersen, E. L., Davidson, D. F., and Hanson, R. K., 1999, "Kinetics Modeling of Shock-Induced Ignition in Low-Dilution CH_4/O_2 Mixtures at High Pressures and Intermediate Temperatures," Combust. Flame, **117**, pp. 272–290.
[42] Skinner, G. B., and Ringrose, G. H., 1965, "Ignition Delays of a Hydrogen-Oxygen-Argon Mixture at Relatively Low Temperatures," J. Chem. Phys., **42**, pp. 2190–2192.
[43] Zukoski, E. E., 1997, "Afterburners," in *Aerothermodynamics of Gas Turbine and Rocket Propulsion*, G. Oates, ed., Dover, New York.
[44] Spaulding, D., 1955, *Some Fundamentals of Combustion*, Butterworth, London, Chap. 5.
[45] Longwell, J., Frost, E., Weiss, M., 1953, "Flame Stability in Bluff-Body Recirculation Zones," Ind. Eng. Chem., **45**(8), pp. 1629–1633.
[46] Putnam, A. A., and Jensen, R. A., 1949, "Appplication of Dimensionless Numbers to Flash-back and Other Combustion Phenomena," Proc. Combust. Inst., **125**, pp. 89–98.
[47] Plee, S. L., and Mellor, A. M., 1979, "Characteristic Time Correlation for Lean Blowoff of Bluff Body Stabilized Flames," Combust. Flame, **35**, pp. 61–80.
[48] Radhakrishnan, K., Heywood, J., and Tabaczynski, R., 1981, "Premixed Turbulent Flame Blowoff Velocity Correlation Based on Coherent Structures in Turbulent Flows," Combust. Flame, **42**, pp. 19–33.
[49] Noble, D., Zhang, Q., Shareef, A., Tootle, J., Meyers, A., and Lieuwen, T., 2006, "Syngas Mixture Composition Effects Upon Flashback and Blowout," ASME Paper No. 2006-90470.
[50] Kroner, M., Fritz, J., and Sattelmayer, T., 2002, "Flashback Limits for Combustion Induced Vortex Breakdown in a Swirl Burner," ASME Paper No. GT-2002-30075.
[51] Umemura, A., and Tomita, K., 2001, "Rapid Flame Propagation in a Vortex Tube in Perspective of Vortex Breakdown Phenomenon," Combust. Flame, **125**, pp. 820–838.
[52] Brown, G., and Lopez, J., 1990, "Axisymmetric Vortex Breakdown Part 2: Physical Mechanisms," J. Fluid Mech., **221**, pp. 553–576.
[53] Lieuwen, T., Torres, H., Johnson, C., and Zinn, B. T., 2001, "A Mechanism for Combustion Instabilities in Premixed Gas Turbine Combustors," ASME J. Eng. Gas Turbines Power, **123**(1), pp. 182–190.
[54] Gonzalez-Juez, E., Lee, J. G., and Santavicca, D. A., "A Study of Combustion Instabilities Driven by Flame-Vortex Interactions," AIAA Paper No. 2005-4330.
[55] Lee, J. G., and Santavicca, D. A., 2003, "Experimental Diagnostics for the Study of Combustion Instabilities in Lean Premixed Combustors," J. Propul. Power, **19**(5), pp. 735–750.
[56] Mueller, M. A., Kim, T. J., Yetter, R. A., and Dryer, F. L., 1999, "Flow Reactor Studies and Kinetic Modeling of the H2/O2 Reaction," Int. J. Chem. Kinet., **31**, pp. 113–125.
[57] Baulch, D. L., Cobos, C. J., Cox, R. A., Frank, P., Hayman, G., Just, Th., Kerr, J. A., Murrells, T., Pilling, M. J., Troe, J., Walker, R. W., and Warnatz, J., 1994, "Summary Table of Evaluated Kinetic Data for Combustion Modeling: Supplement 1," Combust. Flame, **98**, pp. 59–79.
[58] Williams, F. A. et al., http://maeweb.ucsd.edu/combustion/cermech/
[59] Peschke, W. T., and Spadaccini, L. J., "Determination of Autoignition and Flame Speed Characteristics of Coal Gases Having Medium Heating Values," Final Report for AP-4291 Research Project 2357-1.

Downloaded 02 Jun 2010 to 171.66.16.107. Redistribution subject to ASME license or copyright; see http://www.asme.org/terms/Terms_Use.cfm

Effects of Tailpipe Friction on the Nonlinear Dynamics of a Thermal Pulse Combustor

Achintya Mukhopadhyay[1]
e-mail: amukhopadhyay@mech.jdvu.ac.in

Subhashis Datta[2]

Dipankar Sanyal

Department of Mechanical Engineering,
Jadavpur University,
Kolkata 700 032, India

The effect of tailpipe friction on the combustion dynamics inside a thermal pulse combustor has been investigated using a nonlinear model consisting of four coupled first order ordinary differential equations. The dynamics of the system is represented through time series plots, time-delay phase plots, and Poincaré maps. The results indicate that as the tailpipe friction factor is lowered, the system undergoes a transition from steady combustion through oscillating combustion to an intermittent combustion with chaotic characteristics before extinction. The time series data are shown to be useful indicator for early detection of extinction. In one approach (thresholding), the occurrence of local peak pressures below a predefined threshold value is identified as an event and the number of events (event count) and largest number of successive cycles with such events (event duration) are recorded as the friction factor is lowered. In another approach, the statistical moments (kurtosis) of the data are used. Number of kurtosis peaks above a prescribed value and variance of the kurtosis values are recorded for decreasing values of friction factor. All these numbers sharply increase as the system approaches extinction. [DOI: 10.1115/1.2771252]

Introduction

Pulse combustors are known to have high thermal efficiencies, high heat transfer rates, and lower pollutant emission than steady flow combustors. Typically, the most crucial components of a pulse combustor are the combustion chamber and a tailpipe attached at the end of the combustion chamber. The operations of pulse combustors are characterized by self-sustained oscillations that have their origin in the strong coupling between the combustor dynamics and the flow in the tailpipe. The operation and emission characteristics of the combustor are extremely sensitive to the design details and operating conditions of the combustor. The first known application of pulse combustors was in V-1 "buzz-bomb" rockets used by the Germans during World War II [1]. The next major application of pulse combustors occurred in late 20th century when domestic heat pumps, based on pulse combustors, were developed to improve their efficiencies [2]. The pulsating action of these combustors makes these systems attractive for a variety of domestic, industrial, and even propulsion applications. However, additional complexities in designing and commissioning of the combustors and lack of proper understanding of these combustors have severely limited their acceptability.

Several investigators have looked into different aspects of pulse combustion with a view to understanding the underlying physical mechanisms behind low emission, high efficiency, and high heat transfer. Keller and Hongo [3] discussed the mechanisms of NO_x production in pulse combustors. They concluded that several complementary mechanisms are responsible for the low NO_x production. Due to the pulsating flows, rates of heat transfer in pulse combustors are higher. This leads to lower temperature of the combustion products. The rapid mixing of the cooler combustion chamber gases and the hot combustion products create a short residence time at high temperatures, leading to reduction in thermal NO_x formation. Keller et al. [4] examined the emission of CO and NO_x from a lean premixed pulse combustor and concluded that the flame temperature, chemical kinetics, and residence time at high temperature were best controlled through equivalence ratio and macroscopic mixing. Thus, the dynamics of the pulse combustor strongly influences the emission and performance of the combustor. Margolis [5] investigated the nonlinear dynamics of a pulse combustor.

Conventionally, pulse combustors involve mechanical valves to regulate the inlet air and fuel flow depending on the combustion chamber pressure. However, Richards et al. [6] developed a pulse combustor that did not require any mechanical actuation for pulsating action. The pulsations were achieved through self-sustained oscillations, even with steady mass flow rates at the inlet. They modeled the combustor as a well-stirred reactor with a tailpipe attached to it. The flow through the tailpipe was modeled as a slug flow. Daw et al. [7] demonstrated the existence of a bifurcation that ultimately leads to chaos through investigations with a laboratory-scale pulse combustor and a model combustor, using the model of Ref. [6]. The work used residence time as the bifurcation parameter. Rhode et al. [8] used the model of Richards et al. [6] to demonstrate that the flammable range of flow time can be extended by controlling the chaos using friction factor as the control variable. In et al. [9], on the other hand, extended the flammable regime of a pulse combustor by maintaining (anticontrol) chaos in the system that prevented the system from a transition to flame extinction. In their numerical experiment, the only parameter varied was the residence time, which was used both as the bifurcating parameter and the control parameter.

The works of both Richards et al. [6] and Rhode et al. [8] both illustrate that tailpipe friction plays a crucial role in the operation of a pulse combustor. However, the dynamic characterization of the combustor due to changes in tailpipe friction has not been studied in detail. Since self-sustained oscillations can be maintained only for limited ranges of parameters, changes in tailpipe friction from the nominal value can alter the combustion characteristics. The changes may take place due to both wall corrosion and temperature fluctuations. Tailpipe friction can also be manipulated through various active control means like injection of transient air jets into the tailpipe, acoustic oscillations, or mechanical vibrations as suggested by Rhode et al. [8]. The objective of this paper is to investigate the changes in dynamic characteristics of

[1]Corresponding author.
[2]Also at the University Institute of Technology, The University of Burdwan, Burdwan, West Bengal, India.

Submitted to ASME for publication in the JOURNAL OF ENGINEERING FOR GAS TURBINES AND POWER. Manuscript received July 26, 2006; final manuscript received April 17, 2007; published online January 11, 2008. Review conducted by Thomas Sattelmayer.

Copyright © 2008 by ASME

Downloaded 02 Jun 2010 to 171.66.16.107. Redistribution subject to ASME license or copyright; see http://www.asme.org/terms/Terms_Use.cfm

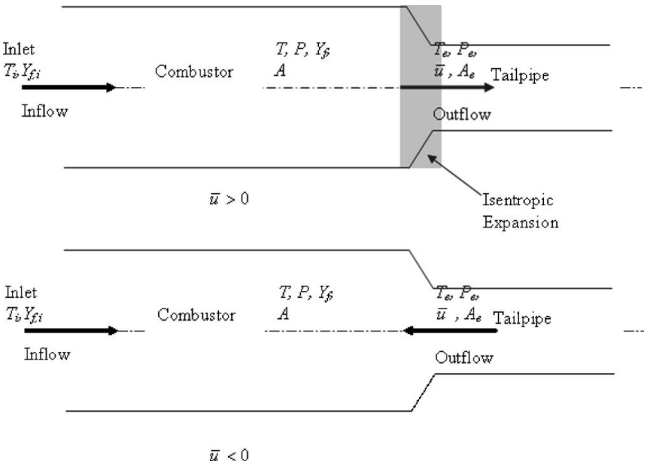

Fig. 1 Schematic of a thermal pulse combustor

the pulse combustor due to small changes in friction factor. The paper also explores the feasibility of using these dynamic characteristics for prediction of combustor performance.

Problem Formulation

The present model is identical to that of Richards et al. [6]. However, in Ref. [6], only self-sustained oscillations are considered. The present work, additionally, admits the presence of sinusoidal pulsations in mass flow rate at the inlet. Similar flow pulsations have been considered by Marsano et al. [10]. However, that work considers large amplitude and near resonant pulsations. The present work, on the other hand, focuses on the effects of pulsations of low amplitude and low frequency. The effects of such pulsations are expected to significantly differ from that of Marsano et al. [10]. The major assumptions of the model are (1) perfectly stirred reactor (PSR) for the combustor, (2) slug flow in the tailpipe, (3) constant specific heat and ideal gas model for the reactant and product gases, (4) single-step Arrhenius model for chemical kinetics, and (5) convective heat loss to the wall. The model is described in terms of four ordinary differential equations, which are derived as follows. The first equation is derived from a lumped model of conservation of energy within the reactor as

$$\frac{d\bar{T}}{dt} = \frac{\gamma\bar{T}}{\bar{P}}\left(\frac{\bar{Z}_i}{\tau_f} + \frac{1}{\tau_h} + \frac{1}{\tau_c}\right) - \frac{\bar{T}^2}{\bar{P}}\left[\frac{\bar{Z}_i}{\tau_f} + (\gamma - 1)\frac{Z_e}{\rho_0} + \frac{\gamma}{\bar{T}_w \tau_h}\right] \quad (1)$$

Combining Eq. (1) with conservation of mass gives the equation for pressure as

$$\frac{d\bar{P}}{dt} = \gamma\left(\frac{\bar{Z}_i}{\tau_f} + \frac{1}{\tau_h} + \frac{1}{\tau_c}\right) - \gamma\bar{T}\left[\frac{Z_e}{\rho_0} + \frac{1}{\bar{T}_w \tau_h}\right] \quad (2)$$

Conservation of fuel mass yields the equation for fuel mass fraction as

Table 1 List of model parameters used

A	0.0167 m^2	L_{TP}	0.61 m
V	0.0001985 m^3	p_0	1×10^5 Pa
B'	3.85×10^8 s^{-1}	T_a	50
C_p	1200 J/kg K	T_0	300 K
D_{TP}	0.0178 m	T_w	1000 K
f	Variable	$Y_{f,i}$	0.06
h	120 W/m^2 K	γ	1.27
$L_{c,1}$	0.0119 m	ρ_0	1.12 kg/m^3
$L_{c,2}$	0.7434 m	τ_f	0.027 s

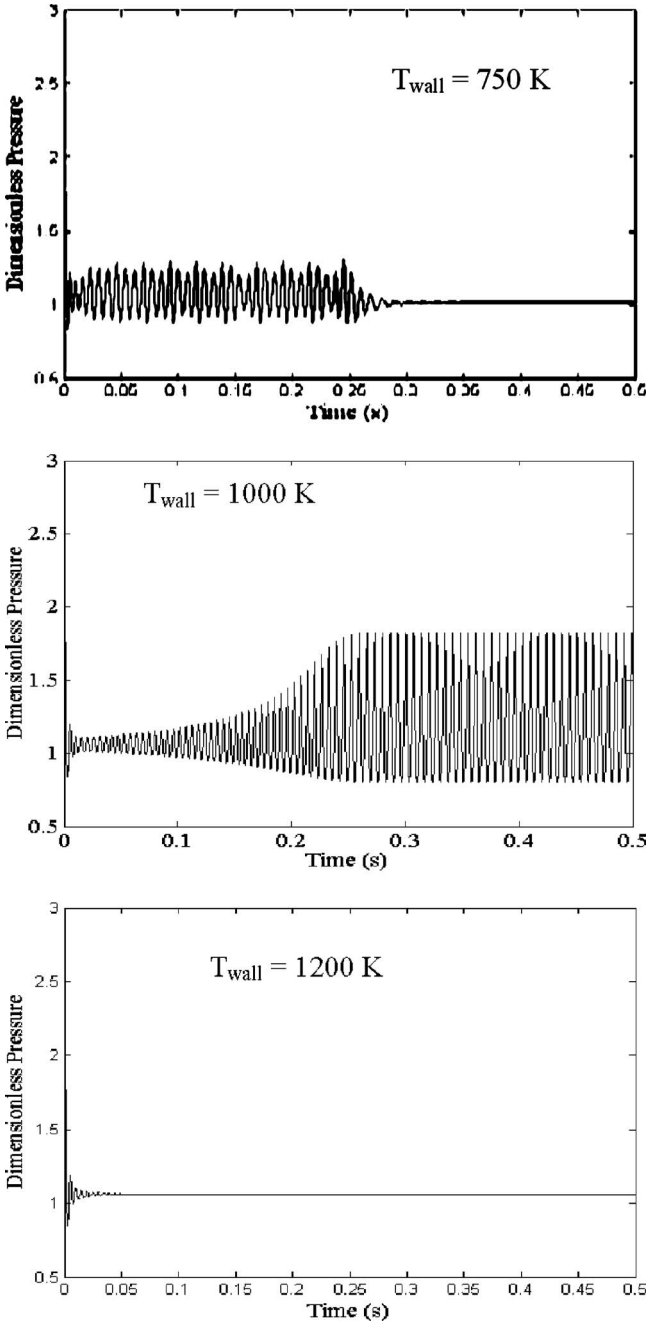

Fig. 2 Comparative study with the results of Richards et al. [6]

$$\frac{dy_f}{dt} = \frac{\bar{Z}_i \bar{T}}{\bar{P}}\frac{1}{\tau_f}(y_{f,i} - y_f) - \frac{C_p T_0}{\Delta h_c}\frac{\bar{T}}{\bar{P}}\frac{1}{\tau_c} \quad (3)$$

Finally, momentum balance in the tailpipe gives the equation for gas velocity in the tailpipe as

$$\frac{d\bar{u}}{dt} = \frac{RT_0\tau_f}{L_{c,2}L_{\mathrm{TP}}}\frac{\bar{T}_e}{\bar{P}_e}(\bar{P}_e - 1) - \frac{f}{2}\frac{\bar{u}^3}{|\bar{u}|}\frac{1}{D_{\mathrm{TP}}}\frac{L_{c,2}}{\tau_f} \quad (4)$$

In the above equations, the dimensionless characteristic times are defined as

$$\tau_f = \frac{\rho_0}{Z_i} \quad (5a)$$

Downloaded 02 Jun 2010 to 171.66.16.107. Redistribution subject to ASME license or copyright; see http://www.asme.org/terms/Terms_Use.cfm

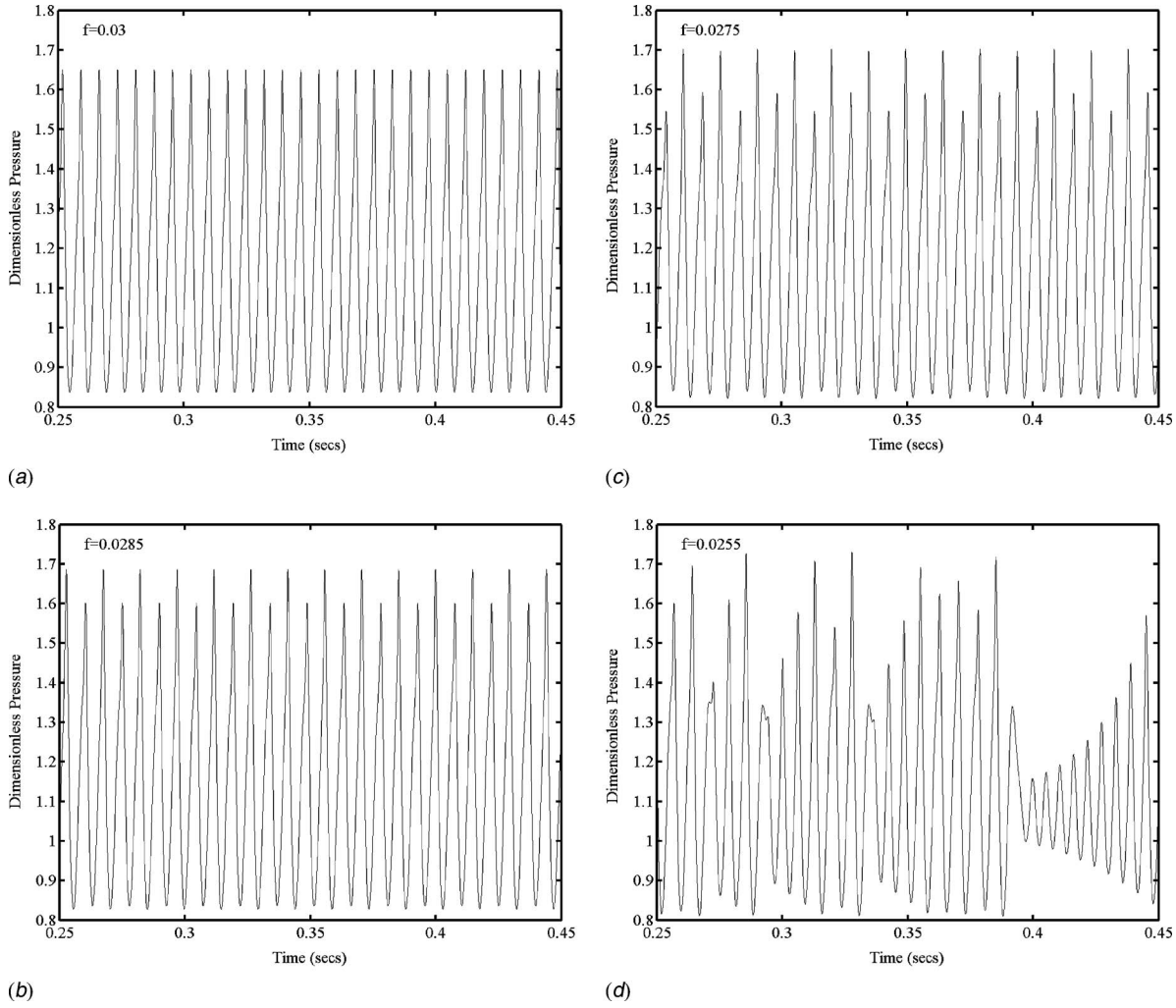

Fig. 3 Time series data for pressure at (*a*) *f*=0.03, (*b*) *f*=0.0285, (*c*) *f*=0.0275, and (*d*) *f*=0.0255

$$\tau_h = \frac{L_{c_1}\rho_0 C_p T_0}{hT_w} \tag{5b}$$

$$\tau_c = \left[\frac{B'\Delta h_c}{C_p T_0}\frac{P^2}{T^{3/2}} y_F^2 \exp\left(-\frac{T_a}{T}\right)\right]^{-1} \tag{5c}$$

The chemical time scale, defined in Eq. (5*c*), is based on a single-step global Arrhenius kinetics of the form

$$\omega_f = -A' T^{1/2}\rho^2 y_F y_O \exp\left(-\frac{T_a}{T}\right) \tag{6a}$$

For stoichiometric mixtures, using the relation that $y_O = \nu_O y_F$ at all times, the above equation reduces to

$$\omega_f = -A' \nu_O T^{1/2}\rho^2 y_F^2 \exp\left(-\frac{T_a}{T}\right) \tag{6b}$$

The above simplification enables us to eliminate the conservation equation for the oxidizer separately.

An expression for Z_e needed to close the system is obtained from conservation of mass within the tailpipe as

$$Z_e = \frac{\bar{u}}{\tau_f}\frac{\bar{p}_e}{\bar{T}_e} \tag{7}$$

Finally, the flow through the nozzle connecting the combustor and the tailpipe is assumed isentropic owing to the short length of the section, although irreversibilities are present in both the combustor and the tailpipe. The pressure and temperature in the tailpipe are related to the combustor variables through isentropic relations as

$$\bar{T}_e = \bar{T} - \frac{\bar{u}^2 L_{c_2}^2}{2C_p T_0 \tau_f^2} \tag{8a}$$

and

$$\bar{p}_e = \bar{p}\left(\frac{\bar{T}_e}{\bar{T}}\right)^{\gamma/(\gamma-1)} \tag{8b}$$

For investigating forced oscillations, the mass flow rate is perturbed sinusoidally as

$$\bar{Z}_i = 1 + \sin \omega t \tag{9}$$

The governing equations are solved as a system of coupled nonlinear ordinary differential equations using the library function ODE45 of commercial package, MATLAB. This function uses a fourth order Runge-Kutta method. The time steps are selected adaptively by the integrator. In the present case, the upper bound of the time step was set at 10^{-5} s. However, the actual time step used is much finer ($\sim 2.5\times 10^{-6}$ s). This gives a data sampling rate of around 40,000 Hz.

Downloaded 02 Jun 2010 to 171.66.16.107. Redistribution subject to ASME license or copyright; see http://www.asme.org/terms/Terms_Use.cfm

Results and Discussions

A model pulse combustor of specified geometry was investigated for dynamic response (Fig. 1). The values of $L_{c,1}$ and $L_{c,2}$ were fixed at 0.0119 m and 0.7434 m, respectively. Propane was used as the fuel and only stoichiometric mixtures of fuel and air were considered. The geometric and kinetic parameters were adopted from Ref. 6 and are given in Table 1. The flow time was fixed at 0.027 s. The choice of flow time is consistent with the range of flow times for which self-sustained oscillations were obtained at the nominal value of friction factor by earlier researchers [6,8]. To initiate the reaction, the initial temperature was raised to five times the ambient temperature. The choice of the initial time step affected only the initial transience ($t<0.1$ s), which has not been considered for the analysis presented here ($t>0.25$ s). The parameter varied in the current investigation is friction factor.

Direct validation of the predictions of the model presented here with experimental results is difficult to achieve as explained by previous workers [6,7,11,12]. On one hand, the experiments were mostly done with lean fuel-air mixtures to prevent overheating of the combustor. On the other hand, the simplified model, developed by Richards et al. [6], uses chemical kinetic parameters that are tuned for near-stoichiometric mixtures, which precludes its use for lean mixtures. However, this model has been extensively used in literature and has been shown to capture the essential features of the nonlinear dynamics of the system. Figure 2 shows the results for three wall temperatures. The time series data show that the combustor pressure oscillations get damped both at high and low wall temperatures while approach a limit cycle at intermediate temperatures. At low temperature, the oscillation dies down due to extinction of the flame. At intermediate temperatures, the reaction rate is such that the fuel inflow rate is higher than the consumption rate leading to accumulation of fuel in the combustor. This is also accompanied by a rise in temperature caused by mixing of fresh reactants with hot exhaust gases and compression of gas during flow reversal in the tailpipe. This increases the reaction rate until the fuel consumption exceeds the fuel supply rate and the trend is reversed. This gives rise to the oscillatory behavior. On the other hand, at high temperatures, the reaction rate is so high that the fuel accumulation does not take place and so the oscillations are not observed. These results are in agreement with those of Richards et al. [6], where this behavior is explained in detail. The experimental results of Richards et al. [6] show that as the equivalence ratio approaches stoichiometric conditions, the frequency of oscillation for the limit cycle behavior increases. The frequency corresponding to the highest equivalence ratio of 0.85 in the experiments is 167 Hz. For identical geometry and flow time, the simulation gives a frequency of 185 Hz for stoichiometric mixture, which is, thus, consistent with the experimental results.

Time Series Data. Friction factor in the tailpipe strongly influences the flow oscillations of the exhaust gas and, in turn, the combustion characteristics in the combustor. Friction factor in the tailpipe can undergo small changes due to both wall corrosion and changes caused due to temperature fluctuations. The system of equations presented above gives the temporal variations for the state variables. The dynamic characteristics of all the state variables are similar. However, for experimental determination of time series, the instruments used need to have very small response times. This makes temperature and fuel mass fraction difficult for analysis as the corresponding sensors generally have large response times. Considering the feasibility of possible future experimental investigations, simulation results are presented for pressure only.

From Eq. (4), it is evident that the role of friction factor is to retard the flow in the tailpipe in both forward and reverse directions. At high friction factors ($f>0.035$) (not shown for brevity), the friction slows down the gas flow and essentially damps out the oscillations. This reduces the temperature and hence pressure amplitude, ultimately leading to steady combustion [6]. As the friction factor is lowered at $f=0.03$, sustained oscillations are observed. Since oscillatory combustion is the desired state in pulse combustors, this state is identified as the nominal state. On further

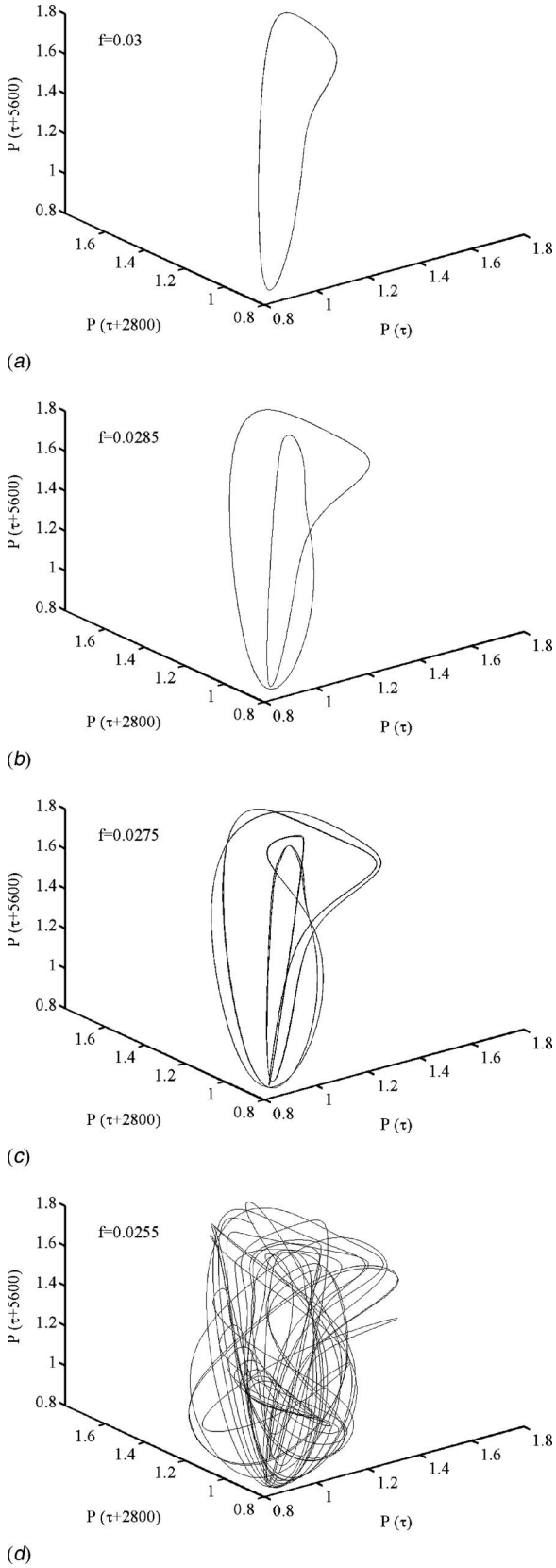

Fig. 4 Three-dimensional time-delay phase plots at (*a*) $f=0.03$, (*b*) $f=0.0285$, (*c*) $f=0.0275$, and (*d*) $f=0.0255$

Downloaded 02 Jun 2010 to 171.66.16.107. Redistribution subject to ASME license or copyright; see http://www.asme.org/terms/Terms_Use.cfm

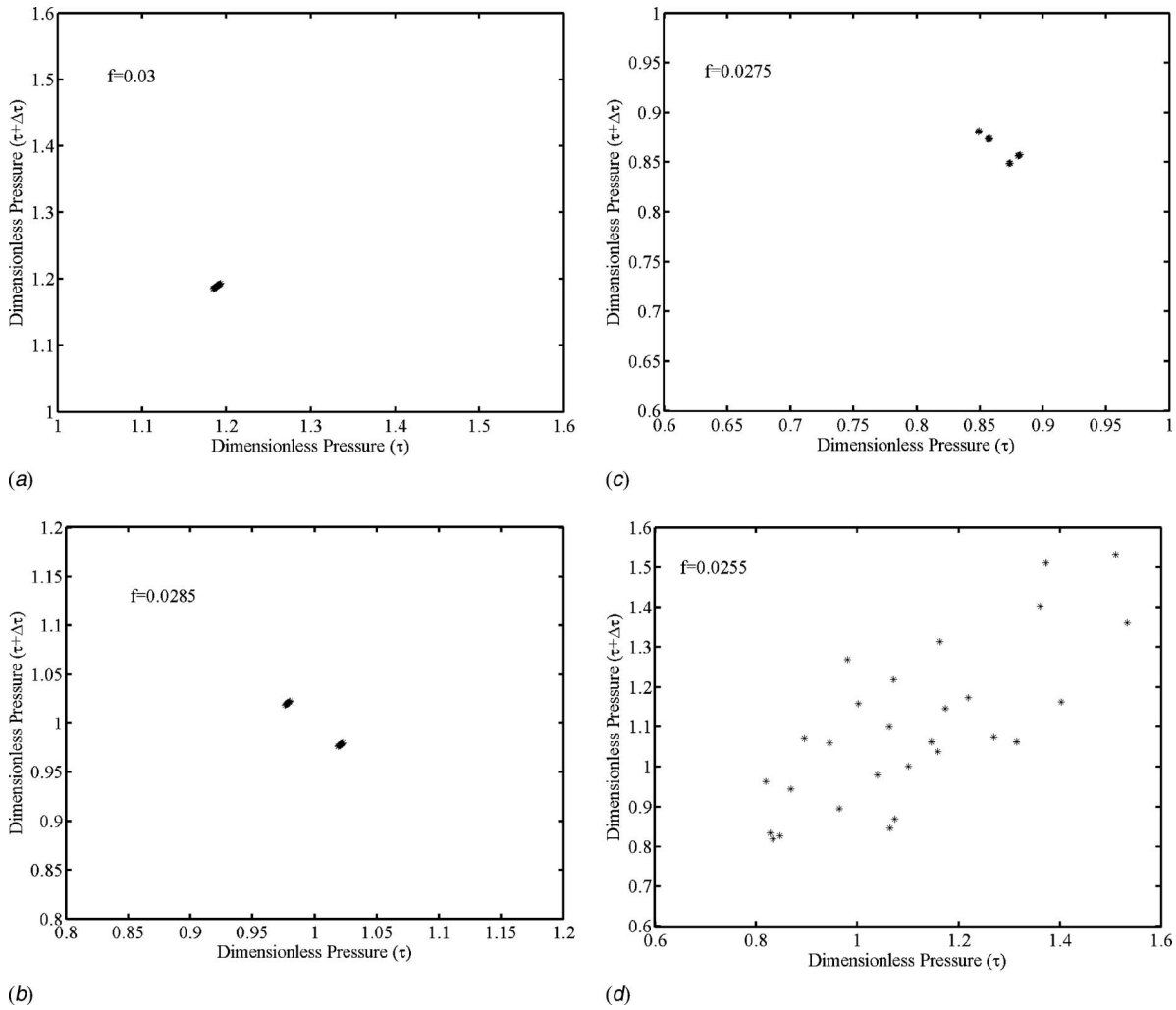

Fig. 5 Poincaré maps for pressure at (*a*) $f=0.03$, (*b*) $f=0.0285$, (*c*) $f=0.0275$, and (*d*) $f=0.0255$

reduction of friction factor, during forward flow, the efflux of hot gases from combustion chamber increases. This leads to an inadequate mixing of hot gases with fresh reactants. This lowers the combustor temperature, which weakens and extinguishes the flame. After the pressure drops below atmospheric ($\tilde{P}<1$), the flow is reversed and the incoming hot gas reignites the flame. Reduction in friction factor implies lower retardation and hence delayed flow reversal. Thus, at sufficiently low values of friction factor, the returning gases do not enter the combustion chamber soon enough to reignite the fresh charge.

Figure 3 presents the results for the dynamic characteristics of the combustor pressure for different friction factors. The results are presented for the period following the initial transience, such that the results are not affected by the choice of the initial condition. At a friction factor of around 0.035 (not presented here for brevity), the system pressure becomes steady following the initial transience. As the friction factor decreases, low amplitude pressure oscillations are observed, which gets quickly damped. At $f=0.03$, steady undamped oscillations are observed. Since these self-sustained oscillations give higher rates of heat transfer and lower pollutant emission compared to steady combustion, this friction factor is considered as the design operating condition in this work. From Fig. 3, it is apparent that at this friction factor, the peaks of the same value appear at identical intervals, thus indicating a unique frequency of oscillation. As the friction factor is lowered, at $f=0.0285$, alternate pulses appear with lower peaks, thus effectively reducing the frequency to half the original value. This phenomenon, known as period doubling, is one of the possible routes to chaos [13]. Such period-doubling bifurcation in thermal pulse combustors has also been reported by Daw et al. [7] and In et al. [9], who used flow time as the bifurcation parameter. As the friction factor is lowered to 0.0275, further bifurcation occurs. At this frequency, pulses with three different amplitudes appear, which lowers the frequency to one-fourth of the original value. Further bifurcations continue as the friction factor is lowered, until the combustion becomes irregular with the appearance of oscillations of varying amplitudes. The time series at $f=0.0255$ indicates intermittent combustion, characterized by extinction and reignition events. Below this value of the friction factor, the flame is extinguished.

Time-Delay Phase Plots. Phase-space representations, generated by plotting dependent variables against one another, provide a convenient way of distinguishing between periodic and chaotic phenomena. The distinctive features of the geometry of the phase plot can be used to characterize the dynamics of the system. However, generating phase plots with different state variables require recording of several sensor data with comparable sampling rates, which is often not feasible. A strategy commonly adopted in dynamic analysis to overcome this difficulty involves use of Takens embedding theorem [14]. The basic premise of this theorem is that the dynamics of a multidimensional system can be reconstructed from the time series data of a single variable. In this method, the time series data for pressure $p(t)$ are used to form a vector with d

Downloaded 02 Jun 2010 to 171.66.16.107. Redistribution subject to ASME license or copyright; see http://www.asme.org/terms/Terms_Use.cfm

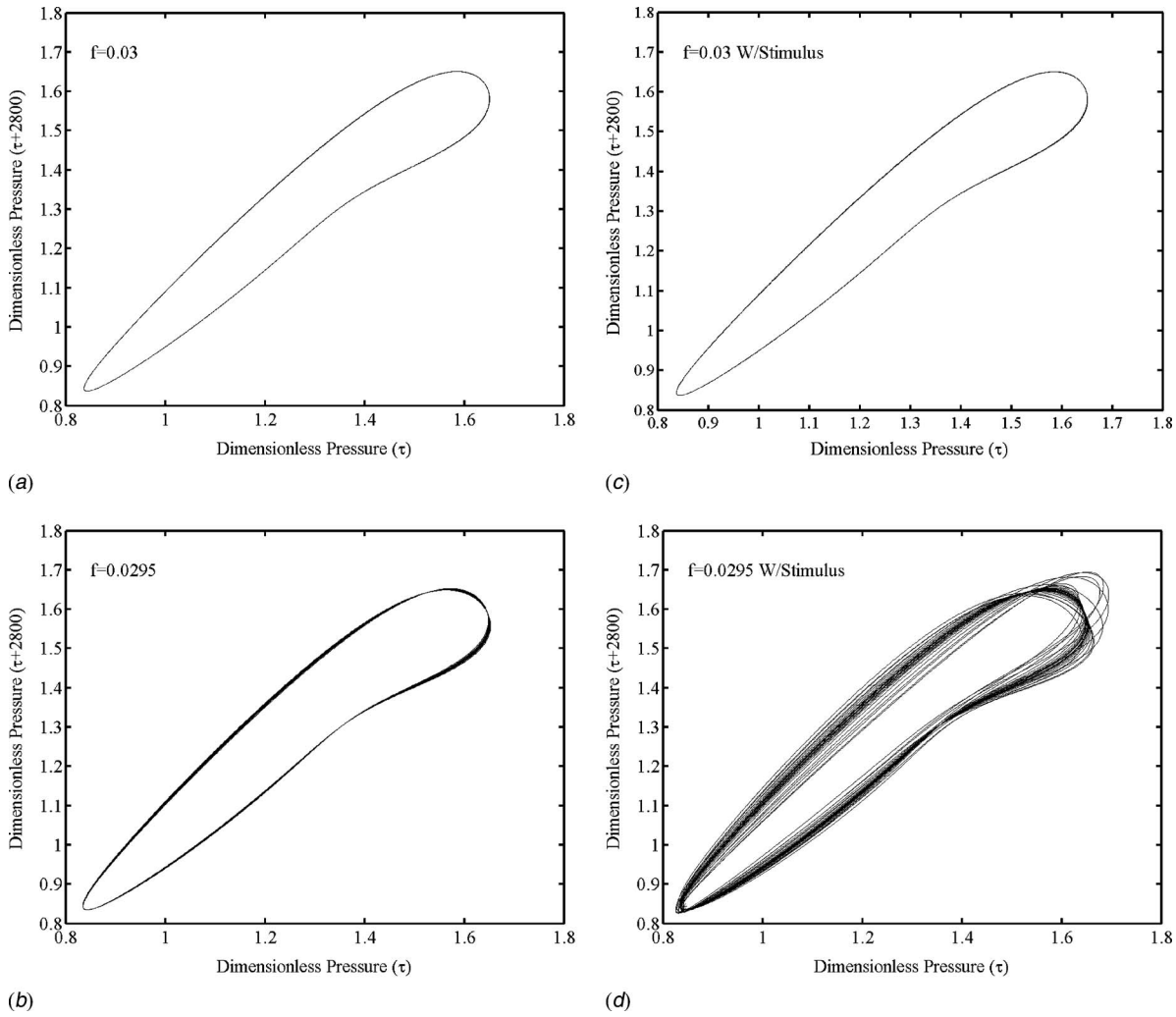

Fig. 6 Time-delay phase plots for pressure under self-sustained oscillation (*a*) and (*b*) and forced oscillation (*c*) and (*d*)

components $\{p(t), p(t+t_L), \ldots p(t+(d-1)t_L)\}$. Two crucial parameters in this reconstruction are the time delay t_L between successive components of the vector and the dimension of the vector, d. Thus, a d-dimensional space is reconstructed from the scalar data. The dimension d, known as embedding dimension, is related to the dimension of the attractor n as $d \geq (2n+1)$ [14]. The time delay t_L is adopted as an integral multiple of the sampling time t_S [13]. Extensive tests with different delay times reveal that the geometric characteristics of the attractor are best revealed with $t_L = 2800 t_S$. Since, in this study, the time steps are of the order of 2.5×10^{-6} s, the delay time corresponds to a time of about 7×10^{-3} s, which is close to the time period of oscillation for $f = 0.03$. Results computed with $d=2$ and $d=3$ reveal similar information regarding evolution of the dynamic characteristics of the system as f is lowered. Hence, results are presented only for the three-dimensional reconstruction.

Figure 4 presents the results for a three-dimensional time-delay phase plot for the different friction factors considered in Fig. 3. The plots are generated by plotting $p(t)$, $p(t+t_L)$, and $p(t+2t_L)$. At $f=0.03$, the phase plot is a limit cycle, confirming the periodic nature of the temporal variation observed in Fig. 3. At $f=0.0285$, the attractor gets distorted into a complicated geometry. The appearance of the attractor as a superposition of two limit cycles is a consequence of the appearance of a lower frequency in the time series data, corresponding to the first period-doubling bifurcation. On further reduction of f to 0.0275, the attractor becomes further distorted and several complex structures appear. The corresponding time series data indicate a second period-doubling bifurcation at this stage. As the friction factor is further lowered to 0.0255, the phase plot becomes completely disorganized and fills up the entire space. Such geometry is indicative of a transition to chaos. The phase plots are nonintersecting curves. The apparent intersection of the phase plots on a three-dimensional projection, shown here, implies that the dimension of the attractors exceeds 3.

Poincaré Maps. For high dimensional systems, phase-space diagrams of dimensions higher than 3 are required. A geometrically simpler representation is obtained with the help of Poincaré sections. Poincaré section is a plane set up across the paths of the trajectory [15]. Every time the trajectory comes back to intersect the plane, a point is obtained on the plane. Each point stands for a return visit by the trajectory. For periodic attractors, the time to return to the Poincaré plane is approximately equal to the period of the attractor. In such cases, a Poincaré map is obtained by stroboscopically sampling the time series data. Thus, the state vectors $\{p(t_S), p(t_S+\Delta t)\}$ are generated similar to the generation of time-delay phase construction. The only difference is in the choice of sampling time. With the above state vectors, the pseudophase space is constructed with the variables $\{p(t_S), p(t_S+\Delta t), t_S\}$. The Poincaré section is obtained by sampling the data at equal inter-

Downloaded 02 Jun 2010 to 171.66.16.107. Redistribution subject to ASME license or copyright; see http://www.asme.org/terms/Terms_Use.cfm

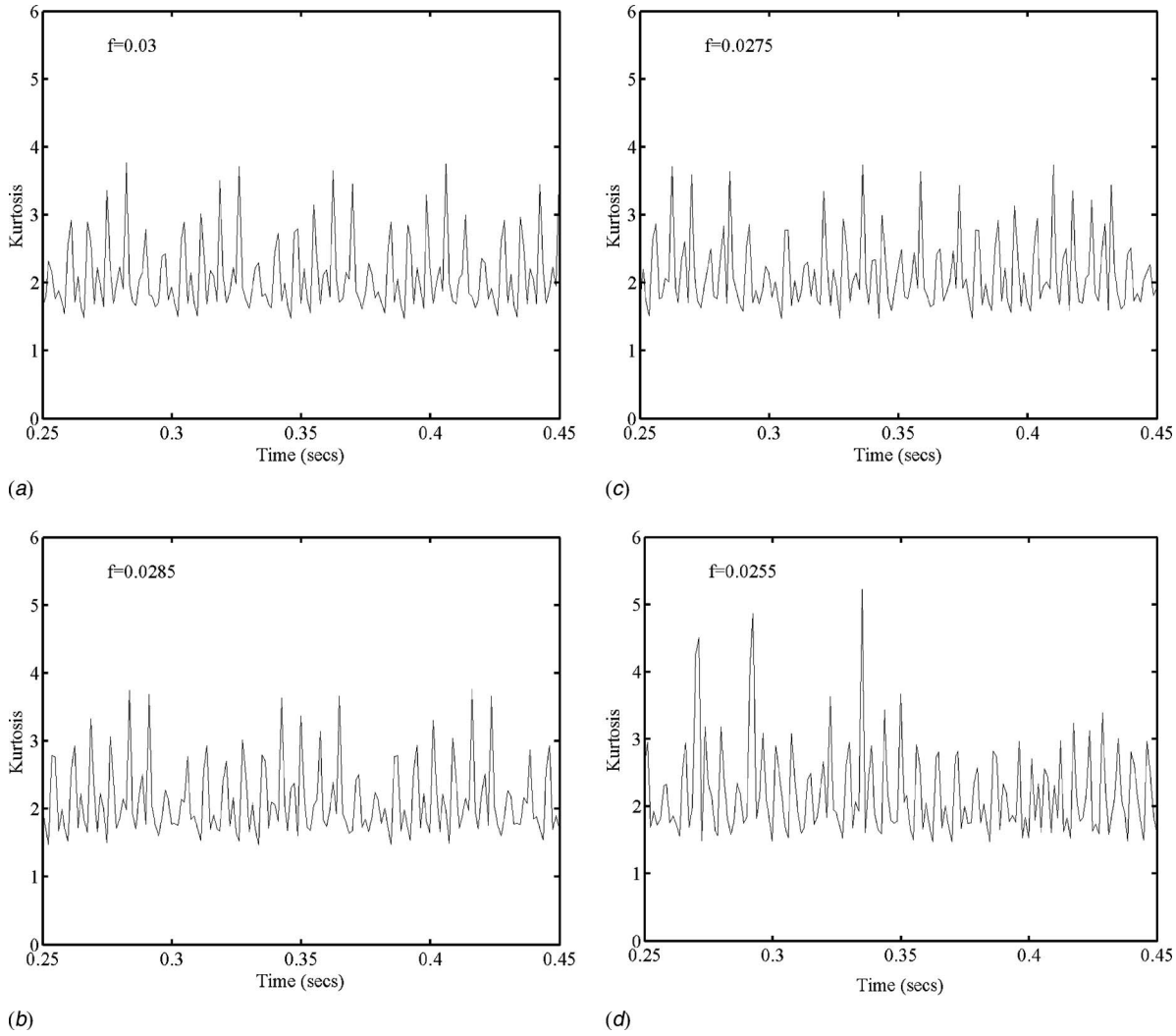

Fig. 7 Kurtosis of pressure data at (*a*) *f*=0.03, (*b*) *f*=0.0285, (*c*) *f*=0.0275, and (*d*) *f*=0.0255

vals of time t_S. This sampling time and the time delay Δt are taken equal to the period of oscillation for the system [16]. The time period corresponds to the frequency of the steadily oscillating case ($f=0.03$).

Figure 5 presents the Poincaré maps for the cases illustrated in Figs. 2 and 3. For $f=0.03$, the Poincaré map appears as a single point on the plane. The slight broadening is possibly due to numerical noise generated. Such a map confirms the periodic nature of the attractor. At $f=0.0285$, the Poincaré map represents the system as two points on the state diagram, as is expected for Period-2 orbits. The map for $f=0.0275$ similarly shows four distinct state points. This representation clearly confirms the second period-doubling bifurcation, leading to a Period-4 attractor. As the friction factor decreases to 0.0255, the periodic structure is completely lost and this leads to a Poincaré map that is densely populated over the entire domain. Such a phase representation also points to a strange attractor.

Forced Oscillation. The results presented so far correspond to self-sustained oscillations. However, pulsations may also be obtained by perturbing the incoming flow. Figure 6 presents results due to self-sustained oscillations and forced oscillations. The forced oscillations are obtained by imposing a sinusoidal perturbation in the mass flow rate at the inlet. The amplitude and frequency of the oscillation are 2% of the mean flow rate and 10 Hz, respectively. The motivation for selecting these values is to investigate the effect of low amplitude perturbations at frequencies far removed from the fundamental natural frequency of the system, which decreases from ~185 Hz at $f=0.0325$ to ~140 Hz at $f=0.030$. From the figure, it is observed that at $f=0.030$, the phase plots are practically identical for self-sustained and forced oscillations. However, as the friction factor changes slightly to 0.0295, distinct changes are observed in the dynamic characteristics. These results are distinctly different from those of Marsano et al. [10], which considers the effects of large amplitude oscillations at frequencies of the order of the natural frequency of the system. This result has important implications for detecting small changes in operating parameters. The earlier results showed that a decrease in friction factor implies a transition toward extinction. This result shows that with appropriate external stimuli, even small changes in friction factor can be identified that cannot be inferred from dynamic data of self-sustained oscillations. As demonstrated by Mukhopadhyay et al. [17], such external stimuli can be used for detection of anomaly in pulse combustor behavior. The choice of the external stimulus should be strong enough to cause identifiable changes in dynamic characteristics but sufficiently weak so as not to extinguish the flame.

Statistical Analysis. The kurtosis or fourth statistical moment of the dynamic pressure data was computed because of its sensitivity to intermittent events. The kurtosis is defined as

Downloaded 02 Jun 2010 to 171.66.16.107. Redistribution subject to ASME license or copyright; see http://www.asme.org/terms/Terms_Use.cfm

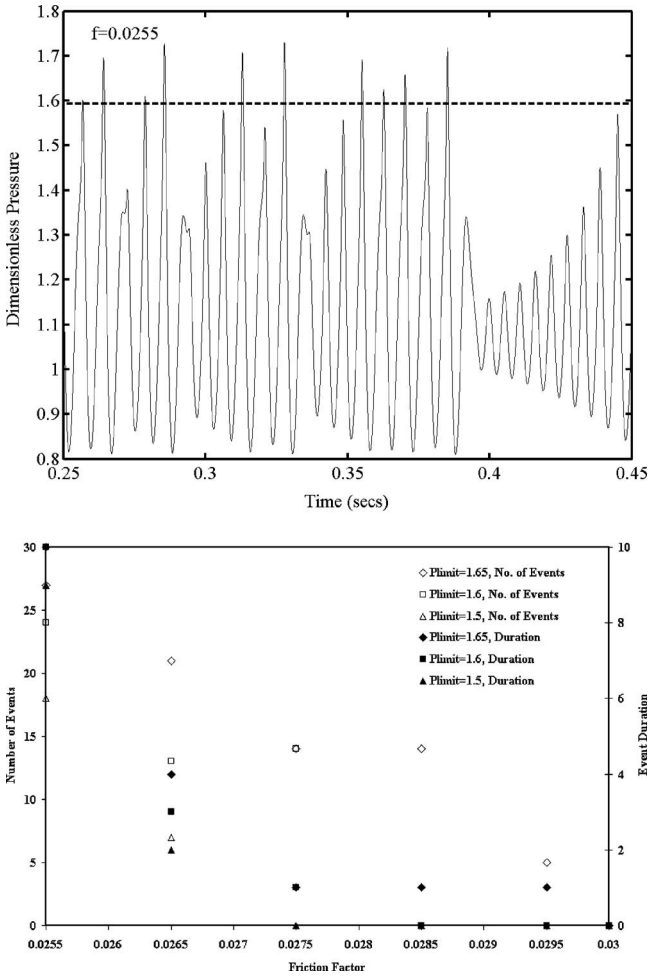

Fig. 8 Variation in number and duration of events based on peak threshold with friction factor

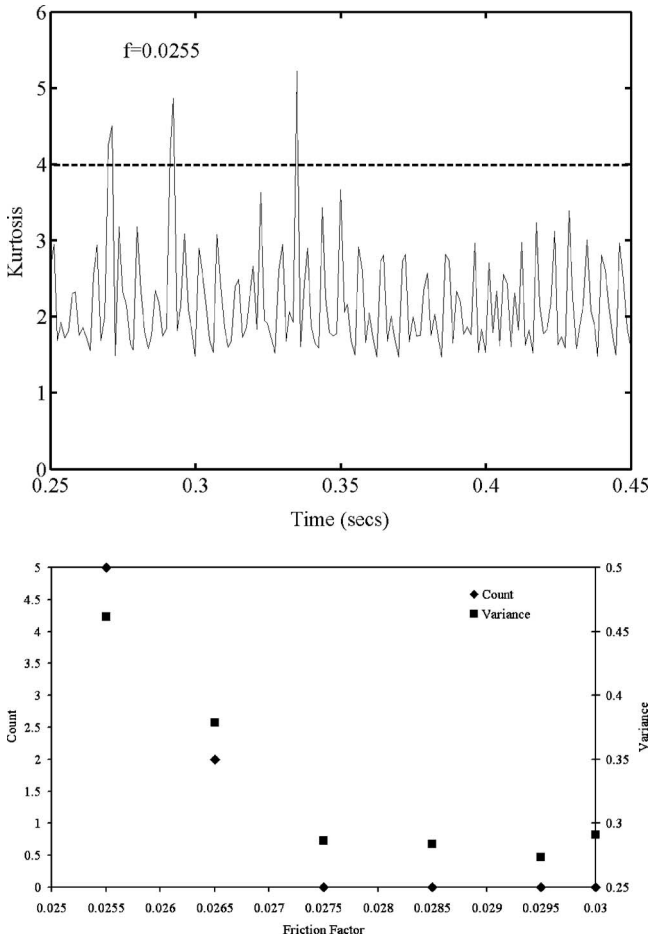

Fig. 9 Variation in number of events and variance based on kurtosis with friction factor

$$k = \frac{\sum_{i=1}^{N} [p(t_i) - \mu]^4}{\sigma} \tag{10}$$

In the above equation, $p(t_i)$, μ, and σ denote the instantaneous pressure data, its mean, and its variance, respectively. Due to the oscillating nature of the data, even at design conditions, a moving average kurtosis is computed considering 1000 data at a time. Figure 7 shows the kurtosis of the data at various friction factors as the system dynamics changes from regular oscillatory to chaotic. From the figure, it is observed that close to extinction (f =0.0255), a large number of peaks appear, indicative of the intermittent nature of the combustion.

Anomaly Detection. A major motivation of investigating the dynamic characteristics of combustion systems is to develop techniques of predicting development of system anomalies like blowout and extinction, from the dynamic data. Nair and Lieuwen [18] discussed different postprocessing techniques of dynamic pressure data for early prediction of blowout of premixed flames in different types of burners. Along similar lines, we examine the utility of dynamic pressure data for online detection of imminent extinction using two approaches. In the first approach, the dynamic data are used directly while in the second, a moving average kurtosis of the data is used.

In Fig. 7, a thresholding approach [18] is used for signal analysis as follows. A threshold pressure, P_{limit}, is selcted. An "event" is identified whenever the peak pressure falls below the threshold value. In a specified time interval, the number of such events is counted and identified as "event count." In addition, the number of successive peaks that fall below the threshold limit is also computed. The largest number of such successive peaks below the threshold pressure in a given time interval is designated as "event duration." Obviously, the efficacy of the method for early detection of anomalies is sensitive to the choice of the threshold value. If the threshold pressure is too low, events will be detected only when the system is very close to extinction. On the other hand, too high a value will make the technique oversensitive and lead to "false alarms."

Figure 8 presents the results for three threshold limits, P_{limit} =1.5, 1.6, and 1.65. From the results, we observe that as the friction factor decreases from 0.03 to 0.0255, the number and duration of events sharply increase for all pressure levels. However, for P_{limit}=1.65, the events start occurring very early and their number and duration show significant values even at conditions far from extinction (f=0.0295) while for P_{limit}=1.5, the events start occurring very late (f=0.0265), when the system is already close to the extinction. On the other hand, at a trigger pressure of 1.6, the number and duration of the events show a marked increase from f=0.0275, which is optimally placed from the perspective of early detection of extinction.

Figure 9 illustrates the role of kurtosis of the time series data on the early detection of extinction. Two approaches are used. In the first approach, a threshold value of the moving average kurtosis is used. An event is identified, when the kurtosis exceeds a preset value (4 in Fig. 9). The number of events sharply increases as the system moves toward extinction. In the second approach, the vari-

Downloaded 02 Jun 2010 to 171.66.16.107. Redistribution subject to ASME license or copyright; see http://www.asme.org/terms/Terms_Use.cfm

ance of the local kurtosis is computed. The variance also shows a dramatic increase as the friction factor decreases. These results, therefore, establish the use of kurtosis in early prediction of imminent extinction.

Conclusions

A lumped nonlinear dynamic model of thermal pulse combustor has been developed. The model consists of four coupled nonlinear ordinary differential equations. Chemical reactions are represented through a single-step global Arrhenius chemistry. The heat loss to the walls is represented through a predefined constant convective heat transfer coefficient. Similarly, the friction in the tailpipe is expressed in terms of a friction factor.

The results indicate that at a friction factor of 0.03, the system undergoes steady oscillations. As the friction factor is reduced, the system undergoes a period-doubling bifurcation to extinction. The dynamic characteristics of the system are more sensitive to changes in friction factor under the influence of low amplitude, low frequency disturbances.

Finally, several techniques have been identified for early detection of flame extinction. In one approach, the time series data for combustor pressure data are directly used while in the other one, the statistical moments (kurtosis) of the data are used.

Nomenclature

A = combustor surface area (m^2)
A_e = combustor cross-sectional area (m^2)
B' = preexponential factor (s^{-1})
C_p = specific heat at constant pressure (J/kg K)
D_{TP} = diameter of tailpipe (m)
f = friction factor (dimensionless)
h = convective heat transfer coefficient (W/m^2 K)
h_{eff} = effective heat transfer coefficient (W/m^2 K)
$L_{c,1}$ = first characteristic length (V/A) (m)
$L_{c,2}$ = second characteristic length (V/A_e) (m)
L_{TP} = length of tailpipe (m)
$\dot{m}_i$ = mass flow rate at combustor inlet (kg/s)
$\dot{m}_e$ = mass flow rate at combustor exit (kg/s)
p = pressure (Pa)
p_0 = ambient pressure (Pa)
$\bar{P}$ = p/p_0 (dimensionless)
p_e = pressure in tailpipe (Pa)
$\bar{P}_e$ = p_e/p_0 (dimensionless)
T = temperature (K)
T_a = activation temperature (K)
T_0 = ambient temperature (K)
$\bar{T}$ = T/T_0 (dimensionless)
T_e = temperature in tailpipe (K)
$\bar{T}_e$ = T_e/T_0 (dimensionless)
T_w = wall temperature (K)
$\bar{T}_w$ = T_w/T_0 (dimensionless)
u = gas velocity in tailpipe (m/s)
$\bar{u}$ = $u/(L_{c,2}/\tau_f)$ (dimensionless)
V = combustor volume (m^3)
y_f = fuel mass fraction (dimensionless)
Z_i = $\dot{m}_i/V$ (kg/m^3 s)
Z_{i_0} = mean value of Z_i (kg/m^3 s)
$\bar{Z}_i$ = Z_i/Z_{i_0} (dimensionless)
Z_e = $\dot{m}_e/V$ (kg/m^3 s)
ε = amplitude of mass flow rate oscillation (dimensionless)
γ = ratio of specific heats (dimensionless)
ρ_0 = ambient density (kg/m^3)
τ_c = characteristic flow time (s)
τ_f = characteristic heat transfer time (s)
τ_h = characteristic chemical reaction time (s)
ω = angular frequency (rad/s)
ω_f = fuel consumption rate (kg/m^3 s)

References

[1] Foa, J. V., 1960, *Elements of Flight Propulsion*, Wiley, New York.
[2] Zinn, B. T., 1986, *Advanced Combustion Methods*, Academic, New York, Chap. 2.
[3] Keller, J. O., and Hongo, I., 1990, "Pulse Combustion: The Mechanism of NO_x Production," Combust. Flame, **80**, pp. 219–237.
[4] Keller, J. O., Bramlette, T. T., Barr, P. K., and Alvarez, J. R., 1994, "NO_x and CO Emissions from a Pulse Combustor Operating in a Lean Premixed Mode," Combust. Flame, **99**, pp. 460–466.
[5] Margolis, S. B., 1994, "The Nonlinear Dynamics of Intrinsic Acoustic Oscillations in a Model Pulse Combustor," Combust. Flame, **99**, pp. 311–322.
[6] Richards, G. A., Morris, G. J., Shaw, D. W., Kelley, S. A., and Welter, M. J., 1993, "Thermal Pulse Combustion," Combust. Sci. Technol., **94**, pp. 57–85.
[7] Daw, C. S., Thomas, J. F., Richards, G. A., and Narayanaswamy, L. L., 1995, "Chaos in Thermal Pulse Combustion," Chaos, **5**, pp. 662–670.
[8] Rhode, M. A., Rollins, R. W., Markworth, A. J., Edwards, K. D., Nguyen, K., Daw, C. S., and Thomas, J. F., 1995, "Controlling Chaos in a Model of Thermal Pulse Combustion," J. Appl. Phys., **78**, pp. 2224–2232.
[9] In, V., Spano, M. L., Neff, J. D., Ditto, W. L., Daw, C. S., Edwards, K. D., and Nguyen, K., 1997, "Maintenance of Chaos in a Computational Model of Thermal Pulse Combustor," Chaos, **7**, pp. 605–613.
[10] Marsano, S., Bowen, P. J., and O'Doherty, T., 1998, "Cyclic Modulation Characteristics of Pulse Combustors," Sym. (Int.) Combust., [Proc.], **27**, pp. 3155–3162.
[11] Narayanaswamy, L., and Richards, G. A., 1996, "Pressure-Gain Combustion: Part I—Model Development," Trans. ASME: J. Eng. Gas Turbines Power, **118**, pp. 461–468.
[12] Richards, G. A., and Gemmen, R. S., 1996, "Pressure-Gain Combustion: Part II—Experimental and Model Results," Trans. ASME: J. Eng. Gas Turbines Power, **118**, pp. 469–473.
[13] Hilborn, R. C., 2000, *Chaos and Nonlinear Dynamics*, 2nd ed., Oxford University Press, New York.
[14] Takens, F., 1981, *Dynamical Systems and Turbulence* (Lecture Notes in Mathematics), D. A. Rand and L. S. Young, eds., Springer-Verlag, Berlin, Vol. 898.
[15] Williams, G. P., 1997, *Chaos Theory Tamed*, Taylor & Francis, London.
[16] Berge, P., Pomeau, Y., and Vidal, C., 1986, *Order Within Chaos*, Wiley, New York.
[17] Mukhopadhyay, A., Datta, S., Gupta, S., Ray, A., and Yang, V., 2003, "Anomaly Detection in a Generic Thermal Pulse Combustor," 2003 Fall Technical Meeting of the Eastern States Section of the Combustion Institute, Oct. 2003.
[18] Nair, S., and Lieuwen, T., 2005, "Acoustic Detection of Blowout in Premixed Systems," J. Propul. Power, **21**, pp. 32–39.

Downloaded 02 Jun 2010 to 171.66.16.107. Redistribution subject to ASME license or copyright; see http://www.asme.org/terms/Terms_Use.cfm

Experimental Investigation of the Stability Mechanism and Emissions of a Lifted Swirl Nonpremixed Flame

Paris A. Fokaides
Chair of Combustion Technology
e-mail: Paris.Fokaides@vbt.uni-karlsruhe.de

Plamen Kasabov

Nikolaos Zarzalis

Engler-Bunte-Institute,
University of Karlsruhe (TH),
Kaiserstrasse 12,
76128 Karlsruhe, Germany

We report on the experimental investigation of a confined lifted swirl nonpremixed flame by applying a novel Airblast nozzle (Zarzalis, N., et al., 2005, Fuel Injection Apparatus, Patent No. DE 10 2005 022 772.4, EP 06 009 563.5). 3D-laser doppler anemometry, a nonintrusive, laser-based measurement technique, is adapted for the measurement of all three mean velocity components and of the six Reynolds stress components. The determination of the temperature and mixture field occurs by employing in-flame measurement techniques. Valuable information concerning the mixing procedure, the temperature distribution, the turbulence level, and the velocity field of the flame is provided. The results demonstrate that there is sufficient residence time in the precombustion area of the lifted flame in order to achieve spatial and temporal uniformity of the mixture, leading to a quasi-premixed state. It was also found that hot reaction products, carried upstream by an annular zone of reverse flow, react with fresh unburnt mixture in a re-ignition process. The determination of the flow pattern revealed the presence of an inner weak recirculation zone in the nozzle vicinity and a dominant external recirculation zone. The examination of the probability density function of the velocity measurements was also found to be a very useful tool in terms of the analysis of the turbulence structure of the flow. The bimodal distribution in the shear layer between the downstream flow and the recirculated gases yields the existence of large scale eddies. Finally, the significant reduced NO_x emissions in the lean area were also shown by means of emission measurements for elevated pressure conditions. [DOI: 10.1115/1.2749279]

Introduction

Partially premixed flames represent a class of hybrid flames established when a quantity of oxidizer is molecularly mixed with the fuel stream before entering the reaction zone, where additional oxidizer is available for complete combustion. This model of combustion can be used to exploit the advantages of both nonpremixed and premixed flames regarding operational safety, lower pollutant emissions, and flame stability. Lifted swirl flames are a representative application of partially premixed combustion, and are considered to be the breakthrough that should enable high-level reduction in NO_x emissions. Despite their importance, many aspects of lifted swirl flames have not been adequately investigated and consequently are not clearly understood. The present work is motivated by the aspects of this promising art of combustion, and it is designed to increase knowledge of the fundamental factors governing the stability of the confined lifted swirl nonpremixed flame.

Experimental Setup

The studied atomizer is an assembly based on the Airblast concept (Figs. 1) [1,2]. The applied configuration is of the prefilming type, in which the liquid is first spread out in a thin, continuous sheet by means of an annular gap (1) and then subjected to the atomizing action. Two separate concentric swirled airflows (2,3) that flow through a number of equispaced tangential ports (4,5), allow the atomizing air to impact on both sides of the fuel sheet, and ensure the thorough mixing of air and fuel. In case gaseous fuels are applied, the atomizer lip is slightly modified, in order to enable the feed of the gas through an annular gap within the primary air flow. Three different atomizers were tested for the purpose of this investigation: one for the atmospheric experiments and two for the elevated pressure experiments. The configuration for the atmospheric experiments resulted out of the experimental work of the authors within previous research projects [3]. The high swirl number of the primary swirl body (4) results in the breakdown of the vortex, whereas the construction of the secondary radial swirler (5) encounters the displacement of the flame further downstream and thus its lift-off. A very detailed description of this specific construction and the physics behind its configuration is provided in [1]. The theoretical swirl numbers of the inner as well as the outer airflow resulted according to Leuckel [4] only from the geometry data of the swirl generators, as the ratio of the angular to the axial flux momentum divided by the narrowest radius of each inner and outer channel:

$$S_{o,\mathrm{th}} = \frac{\dot{D}_o}{\dot{I}_o R} \tag{1}$$

The swirl numbers, as well as the effective areas of the nozzles, are provided to the readers in Table 1.

For the investigation under elevated pressure conditions, two similar nozzles were used, both scaled down by a geometry factor of 2. The first one was identical to the described atomizer, and the other one had a modified secondary swirl body, producing an attached swirl diffusion flame.

Two test facilities were utilized within the scope of this study: one operating under atmospheric pressure conditions and an elevated pressure combustion rig. A schematic of the atmospheric

Contributed by the International Gas Turbine Institute of ASME for publication in the JOURNAL OF ENGINEERING FOR GAS TURBINES AND POWER. Manuscript received May 2, 2007; final manuscript received May 8, 2007; published online January 11, 2008. Review conducted by Dilip R. Ballal. Paper presented at the ASME Turbo Expo 2007: Land, Sea and Air (GT2007), Montreal, Quebec, Canada, May 14–17, 2007, Paper No. GT2007-27126.

Copyright © 2008 by ASME

Downloaded 02 Jun 2010 to 171.66.16.107. Redistribution subject to ASME license or copyright; see http://www.asme.org/terms/Terms_Use.cfm

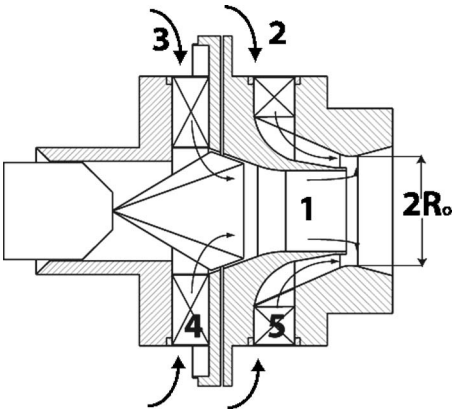

Fig. 1 Investigated Airblast atomizer [1]

test facility is seen in Fig. 2. This test stand consists of two basic segments: the nozzle holder in which the mounting and positioning of the studied nozzle occurs, and an optic accessible combustion chamber where the measurement techniques are carried out.

In order to enable the performance of field measurements, the nozzle holder can be moved axially inside the combustion chamber. Its concept allows the independent adjustment of the mass flow rate and the preheat temperature of the primary and the secondary flow. The supply of the test facility with combustion air is realized with a side channel compressor that can provide $\dot{M}$ =0.05 kg/s of air with 550 mbar overpressure. The mass flow of the air is measured by variable area flow meters and the air is preheated by means of electric air preheaters. Within the nozzle holder, the pipe that delivers the fuel to the nozzle atomizer is water cooled in order to prevent fuel vaporization caused by the preheated air in the case in which liquid fuel is combusted.

Table 1 Investigated Airblast nozzle

	$S_{o,\text{th}}$	A_{eff}, mm^2	$\frac{M_i}{M_T}$
Inner	0.76	115	
Outer	≈0	225	≈0.34
Total	≈0.3	340	

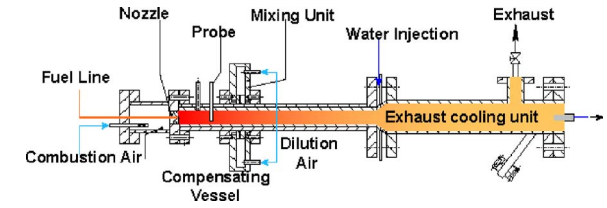

Fig. 3 Schematic setup of the pressurized combustion rig

The combustion chamber is isolated and water cooled in order to ensure the performance of reproducible measurements under adiabatic conditions. Its diameter D_{CC} is four times the throat diameter of the nozzle diffuser D_O, and its length L_{CC} was limited by an annular ring outlet at four-and-a-half times its diameter D_{CC}. This outlet geometry was chosen in order to ensure that no backflow through the exit section occurs [5]. Two properly aligned silica-glass windows enable the optical access to the combustion chamber so that the application of the LDA measurement technique could be applied. Visualization of the flame spontaneous emission by means of a CCD camera could be performed by the use of a silica glass tube chamber, whereas in this case the process is far away from the adiabatic operation point due to significant radiation heat losses (Fig. 12).

A combustion pressurized rig was applied for the measurement of the combustion emissions under elevated pressure conditions [6]. The construction of the combustor allows the realization of the RQL concept, whereas in terms of this study, this option was not utilized. The test bench is designed to host experiments up to 20 bar. It consists of five adiabatic elements, namely, the compensating vessel, the rich stage chamber, the air diluter, the lean stage chamber, and the exhaust cooling unit, all depicted in Fig. 3. Compared to the atmospheric combustor, the pressurized combustion unit is scaled down by a factor of 2. Two three-speed piston compressors are employed to provide air with a maximum mass flow rate $\dot{M}$=0.125 kg/s. Fluctuations that may occur are compensated by means of a pressurized storage vessel of 1000 l. The

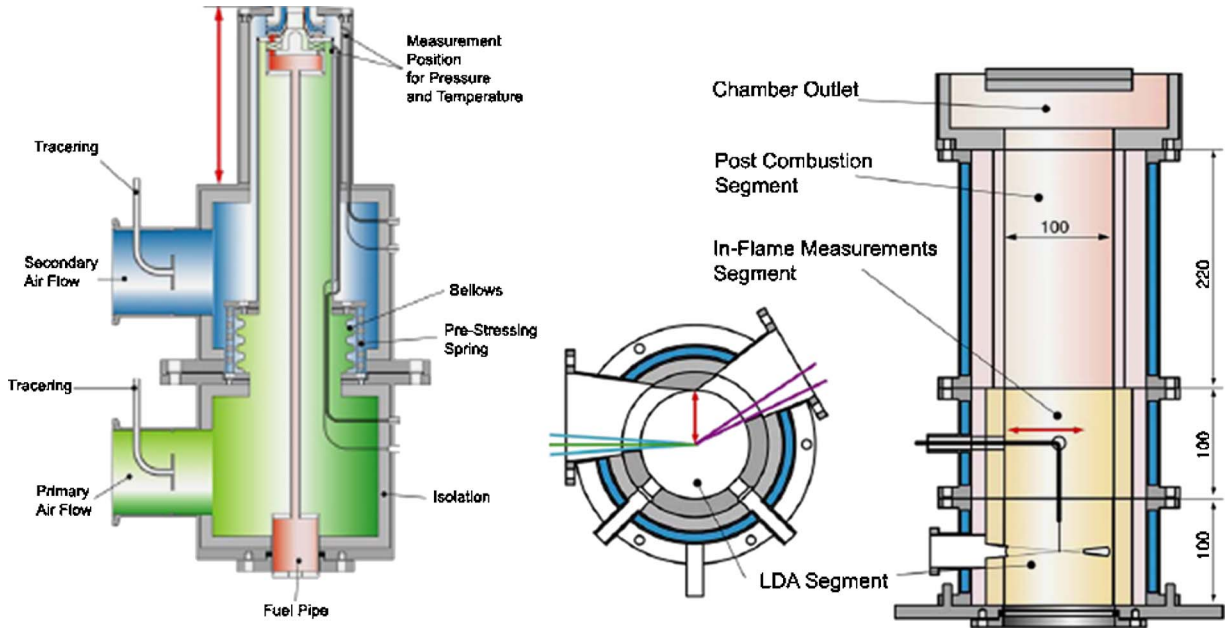

Fig. 2 Schematic setup of the atmospheric combustion chamber

Downloaded 02 Jun 2010 to 171.66.16.107. Redistribution subject to ASME license or copyright; see http://www.asme.org/terms/Terms_Use.cfm

Table 2 Operating conditions for selected test cases

Atmospheric pressure experiments (methane)		
	Isothermal lifted	Reactive lifted
$T_{PR,A}$, K	323	373
P_A, bar	1	1
$\dot{M}_A$, kg/s	0.02	0.0185
U_o, m/s	42	40
Re	55,000	45,000
ΔP, %	2	2
Φ	-	0.65
Elevated pressure experiments (Jet-A1)		
	Reactive attached	Reactive lifted
$T_{PR,A}$, K	573	573
P_A, bar	7; 9	7; 9
$\dot{M}_A$, kg/s	0.02; 0.025	0.025; 0.031
U_o, m/s	45	65
Re	55,000; 70,000	85,000; 115,000
ΔP, %	3	3
Φ	0.5–1.2	0.5–1.2

air is preheated by a pressurized electrical preheater, and its mass flow is adjusted with an orifice flow meter. The mass flow of the liquid fuel (Jet-A1), supplied by a diaphragm metering pump with a vibration damper, is adjusted by a Coriolis flow meter.

The operating conditions of the performed measurements study are summarized in Table 2.

As denoted in Table 2, methane was applied for the atmospheric pressure investigation, whereas the high pressure tests were run with liquid Jet-A1 fuel, the real design for this application. The choice of the gaseous fuel under atmospheric conditions was made in order to enable the detailed investigation of the flame, by neglecting secondary parameters that could have an impact on the process and should have also been investigated, such as, for example, the two-phase flow within the flow pattern. The liquid fuel, on the other hand, does not affect the measurement techniques applied for the combustion emissions under elevated pressure conditions, and therefore was preferred in this case. Compared to the methane lifted flame, the lean blow-out limits of the Jet-A1 flame are shifted to slightly lower equivalence ratios Φ (Fig. 4), whereas the structure of the flame and its lift-off height remain similar [3].

Results and Discussion

Flow Pattern. A measurement campaign employing a commercial 3D-DANTEC LDA was conducted for the time-resolved determination of all three velocity components. The applied configu-

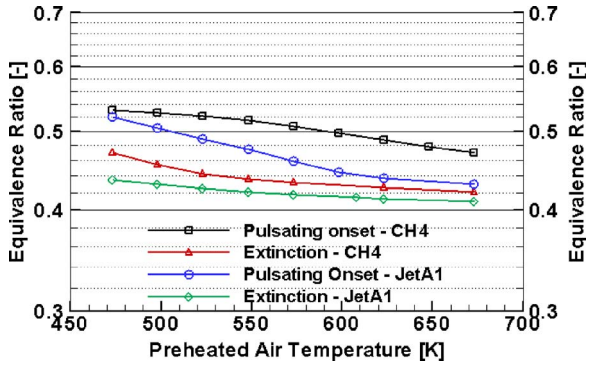

Fig. 4 Lean blow-out limits against temperature of preheated air under atmospheric conditions for methane and Jet-A1 [3]

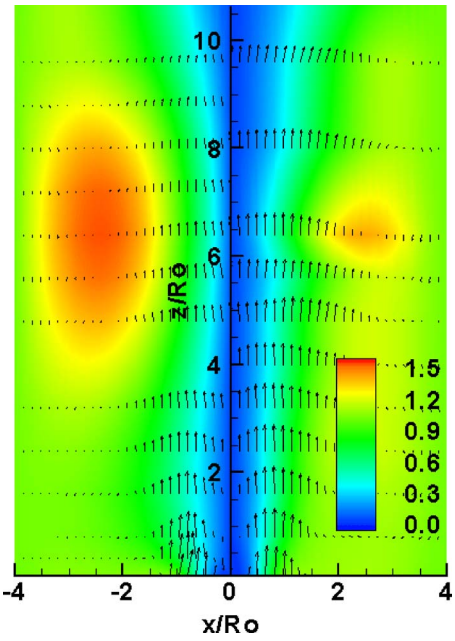

Fig. 5 Reactive (right) and isothermal flow (left): mass flow stream function Ψ and UV vector plot

ration was chosen at 30 deg off-axis forward scattering, in order to ensure a high signal-to-noise ratio and support the performance of high data rate measurements. The calculation of all three mean velocity components and of the six Reynolds stress components resulted from 20,000 to 50,000 samples measured at each grid location. As light source, a multi-line argon ion laser (COHERENT - INNOVA 90) was used at a typical operating output power of around 0.5 W. Magnesia oxide particles with diameter less than 1.2 μm, brushed off from a massive cylinder, served as tracer material for the combustion gas and air, in both air flows. Nondimensional coordinating of the system was performed based on the throat radius R_o of the diffuser. Velocities are normalized by the throat radius velocity U_O. Reynolds stresses are normalized by U_O^2 and the turbulent kinetic energy k by $\frac{1}{2}U_{O^2}$.

Figure 5 shows the mass flow stream function Ψ contours for the isothermal and the reactive flow. In both cases, the presence of an inner weak recirculation zone in the nozzle vicinity and a dominant outer recirculation zone along the confinement is revealed. The size and the intensity of the outer recirculation zone vary in terms of the density and thus of the temperature field. According to Thring and Newby [7], the entrained air in a turbulent jet depends on the density ratio of the downstream propagating unburnt mixture to the surrounding burnout fluid. In the case of the reactive flow, the increase of this ratio results in the weakening of the outer recirculation zone.

As far as the turbulent kinetic energy k is concerned, Fig. 6 illustrates its contour for the isothermal and the reactive case. The turbulent kinetic energy per unit mass can be expressed as

$$k = \frac{1}{2}(\overline{u'^2} + \overline{v'^2} + \overline{w'^2}) \tag{2}$$

As expected, the elevated temperature dampens the turbulent mixing and thus postpones the completion of the procedure. Elevated turbulence levels are observed further downstream, signifying the shear layer between the upstream propagating jet and the downstream propagating hot gases. Compared to similar measurements performed with the same infrastructure and similar boundary conditions concerning an attached diffusion swirl flame [5], the reached levels of k seem to be much lower. This indicates the impact of the lower swirl number S in the case of the lifted flame.

Downloaded 02 Jun 2010 to 171.66.16.107. Redistribution subject to ASME license or copyright; see http://www.asme.org/terms/Terms_Use.cfm

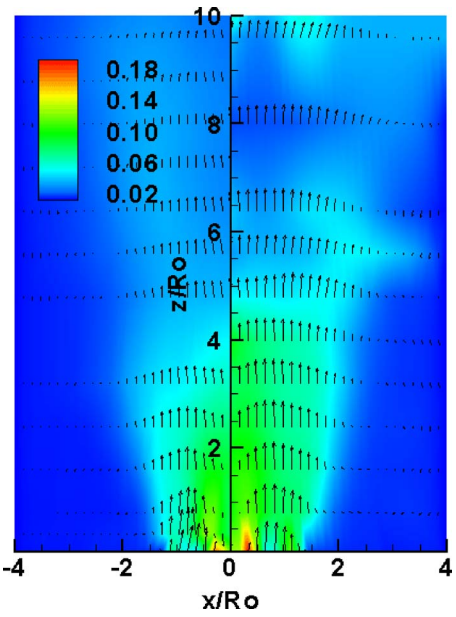

Fig. 6 Reactive (up) and isothermal flow (down): turbulent kinetic energy *k* and UV vector plot

Figure 7 compares the evolution of the mean axial velocity U under isothermal and reactive conditions. In the nozzle vicinity, negative velocities were measured on the axis in both cases, indicating the existence of a weak inner recirculation zone, which supports the mixing procedure in the precombustion zone, but does not participate in the flame stabilization process. As expected, in the reactive case, higher axial velocities are measured, whereas this difference becomes greater near and in the combustion zone. A better understanding of the impact of the combustion on the axial momentum is provided by the evolution of the local density of the axial momentum flux $\rho U^2/I_o$ (Fig. 8). A moderate increase of the axial momentum flux is observed within the first measurement planes; this effect becomes much more pronounced further downstream of the nozzle exit.

The reduced turbulence exchange in the case of the lifted flame is also confirmed from the measured turbulent shear stresses. In Fig. 9, the measured correlation $\overline{U'V'}$ for the lifted flame measurements is depicted. As expected, no deviation occurs concerning the turbulent transport across the axis, since the boundary condition of rotationally symmetric flows and thus $\overline{U'V'}(r=0)=0$ is satisfied. A quantitative comparison of $\overline{U'V'}$ for an attached and a lifted flame [5] reveals weaker turbulent exchange of axial momentum flux in radial direction in the case of the lifted flame.

The examination of the probability density function of the velocity measurements can be a very useful tool in terms of the analysis of the turbulence structure of the flow. Within the boundary layer, bimodality of the axial velocity PDFs was revealed. A bimodal distribution implies the existence, at different times, of two dominant gas directions whose temperatures and velocities vary widely and are centered at either one of the contiguous peaks. Bimodal distributions are usually located in shear layers created by mixing interfaces of fresh pockets of reactants with external recirculated hot gases. The interaction results in large

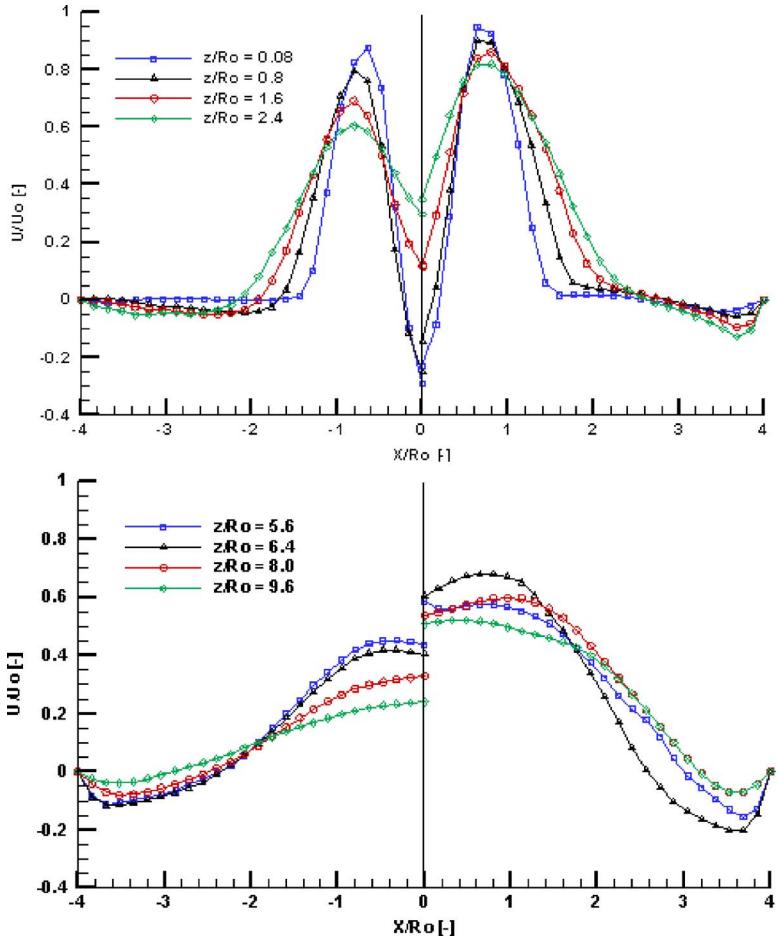

Fig. 7 Isothermal (left) and reactive flow (right): mean axial velocity $\bar{U}/U_o$

Downloaded 02 Jun 2010 to 171.66.16.107. Redistribution subject to ASME license or copyright; see http://www.asme.org/terms/Terms_Use.cfm

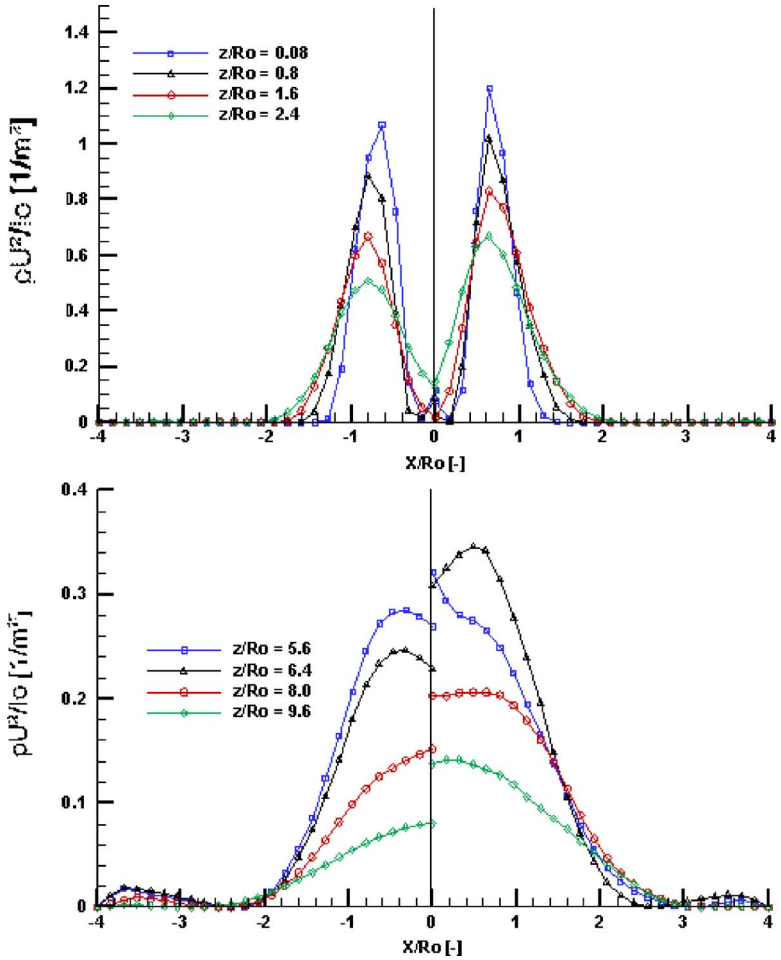

Fig. 8 Isothermal (left) and reactive flow (right): local density of axial momentum $\rho U^2/IO$

eddies of hot and cold gases existing at different times at the same location [8,9]. Figure 10 presents the evolution of the statistical distribution of the axial velocity as one moves from inside the vortex, through the shear zone into the surrounding outside gases for $z/R_o=5.6$. The distribution becomes distorted, and thus bimodal as the LDA diagnostic volume straddles the shear zone ($U=0$ m/s). This is a very interesting finding of this study, yielding the existence of large scaled eddies in the shear layer between the upstream flow and the recirculated hot gases.

Mixture Field. Measurements of multi-species concentrations in the field have been conducted in order to allow a better under-

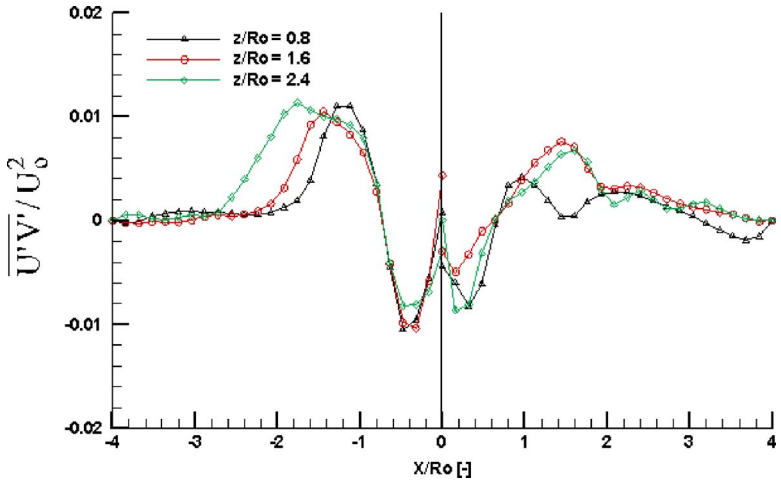

Fig. 9 Isothermal (left) and reactive flow (right): shear stress $\overline{U'V'}/U_o^2$ in nozzle vicinity

Downloaded 02 Jun 2010 to 171.66.16.107. Redistribution subject to ASME license or copyright; see http://www.asme.org/terms/Terms_Use.cfm

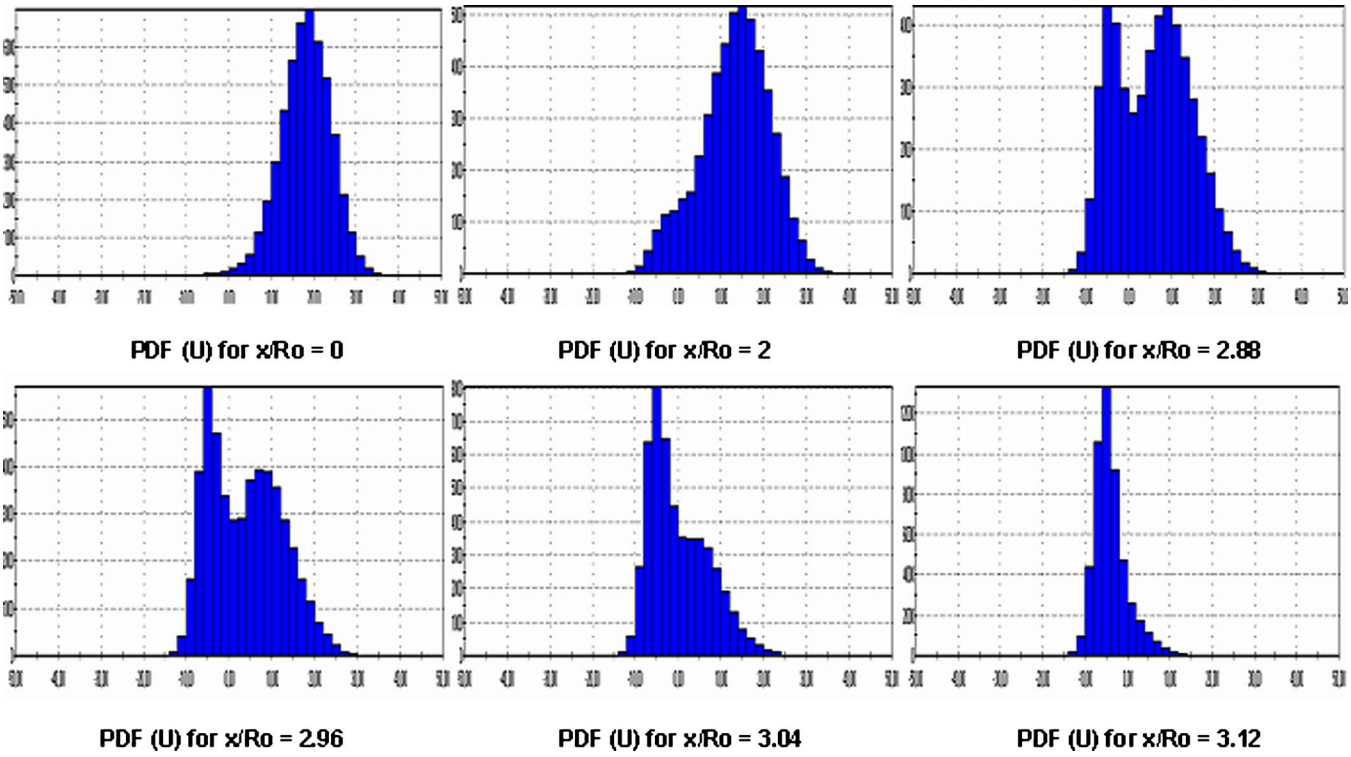

Fig. 10 Reactive flow: PDF evolution of axial velocity through shear layer for z/R_o=5.6

standing of the complex turbulence-chemistry interactions. The local concentration was subsequently analyzed by means of conventional gas analysis, based on molecular excitation processes, due to modulated infrared absorption. Two commercial analyzers (Hartmann and Braun Model URAS 14 and Magnos 14) [10] and a suction probe of 1 mm were applied.

Figure 11 presents the local equivalence ratio of the reactive field obtained by analyzed gas samples as well as the flame front, as it was detected by the carbon monoxide measurements (Fig. 15), as well as by the spontaneous emission of the flame (Fig. 12). The calculation of the local equivalence ratio from measurements of carbon monoxide, carbon dioxide, hydrocarbons, and the oxides of nitrogen uses a matrix solution of a set of ten simultaneous equations based on the combustion chemical equation of hydrocarbon fuel [11]. As this measurement yields, there is sufficient residence time below the flame base to achieve spatial and temporal uniformity of the mixture, leading to a quasi-premixed state. The results appear to be in line with previous work concerning lifted diffusion jet flames [12,13], proposing that fuel and air are fully premixed at the base of a lifted flame.

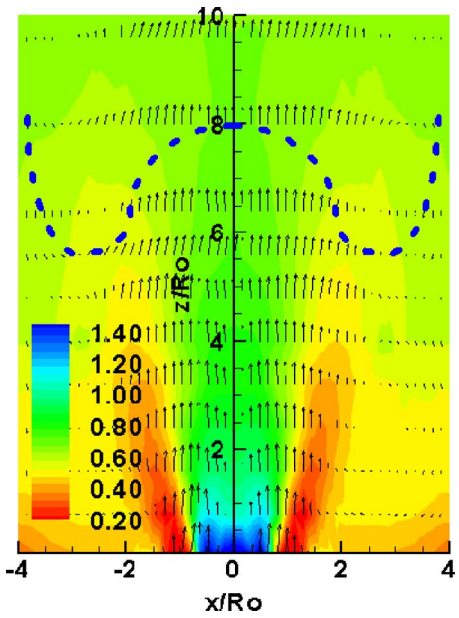

Fig. 11 Reactive flow: local equivalence ratio with flame front and UV vector plot

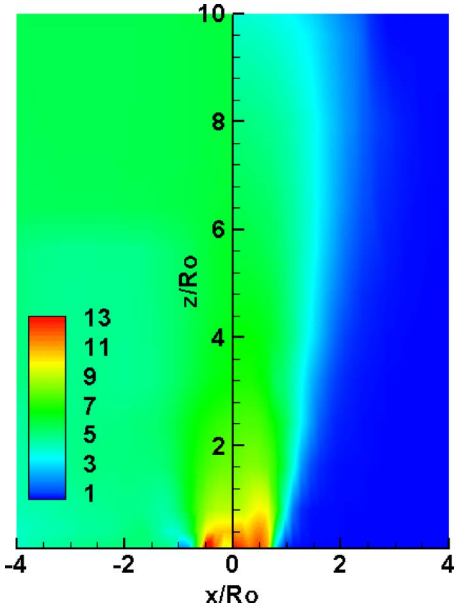

Fig. 12 Flame illumination for the investigated conditions (aperture *f*/5.6 exposure time 1/30 s)

Downloaded 02 Jun 2010 to 171.66.16.107. Redistribution subject to ASME license or copyright; see http://www.asme.org/terms/Terms_Use.cfm

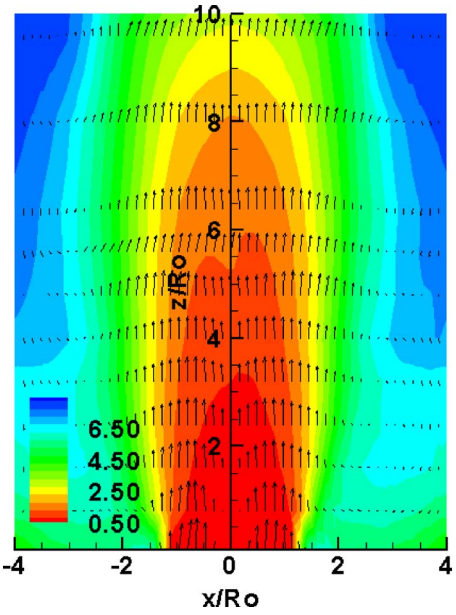

Fig. 13 Isothermal (left) and reactive flow (right): methane concentration, % vol.

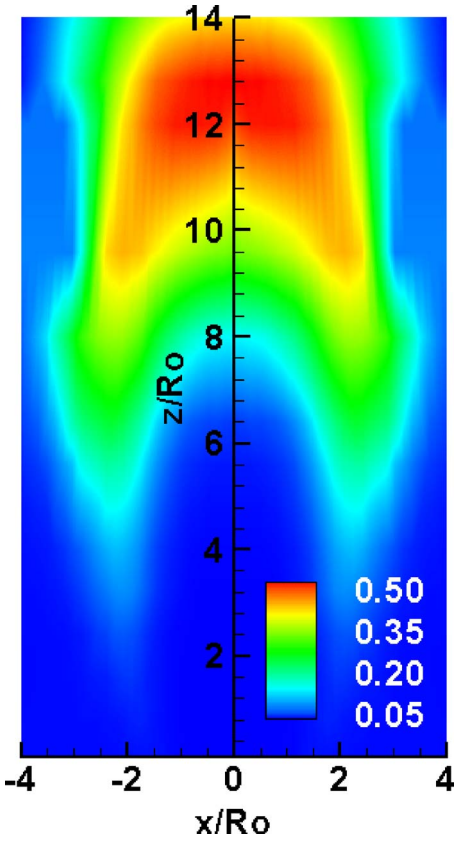

Fig. 14 Reactive flow: carbon dioxide concentration, % vol.

Compared to the isothermal conditions, the macromixing of air and fuel in the reactive case is slightly dampened. This probably occurs due to the impact of the temperature and thus of the kinematic viscosity on the diffusive mass transport. In the isothermal case, quantities of methane responding to the global adjustment of the mixture were also measured in the surrounding area of the jet, upstream from the nozzle exit, whereas in the reactive field, fuel was fully oxidized in its downstream path (Fig. 13). Due to the confinement of the flow, the evolution of an external recirculation zone resulting in the horizontal transport of methane from the upper layers to the jet's base, is to be assumed [14].

The dominance of the large recirculation zone moving the hot products upstream and parallel to the jet's boundary layer can also be confirmed from the examination of the carbon dioxide concentration in the flame. These concentration levels were found to be significant across the stabilization area, whereas in the jet core they were negligible (Fig. 14). This evidences that in the case of a confined lifted flame, hot reaction products, carried to the edges of the jet, react with fresh unburnt mixture in a re-ignition process supporting the stability of the combustion [15].

The carbon monoxide concentration is in very good agreement with the spontaneous emission captures locating the main reaction zone of the flame. The widespread region in which carbon monoxide is measured (Fig. 15) is probably a result of the effective restriction of its oxidation due to the presence of hydrocarbon species [16]. The anchor-shaped form of the reaction zone of the lifted flame in this case is very similar to the characteristic structure of the tribranchial flame [17]. However, the suspicion raised by this observation for the existence of a stabilization mechanism similar to that of the triple flame, is not supported either from the velocity field or from the local equivalence ratio.

Temperature Field. High frequency temperature measurements were performed by means of an S type (Pt/Pt-10% Rh) compensated microthermocouple probe, with wire diameter of 100 μm [18]. The raw temperature data were corrected for radiative losses in terms of a heat transfer coefficient determined from the frequency response of the compensated signal according to a function proposed by Sato and Kumura [19].

The contours of mean and rms temperatures are shown in Fig. 16. The combination of mean and fluctuating temperatures allows the location of the combustion area as well as the regions of boundary layers. The low mean temperatures near the nozzle vicinity in the jet signify that even though the mixture at this location is highly turbulent, no combustion occurs. This also occurs

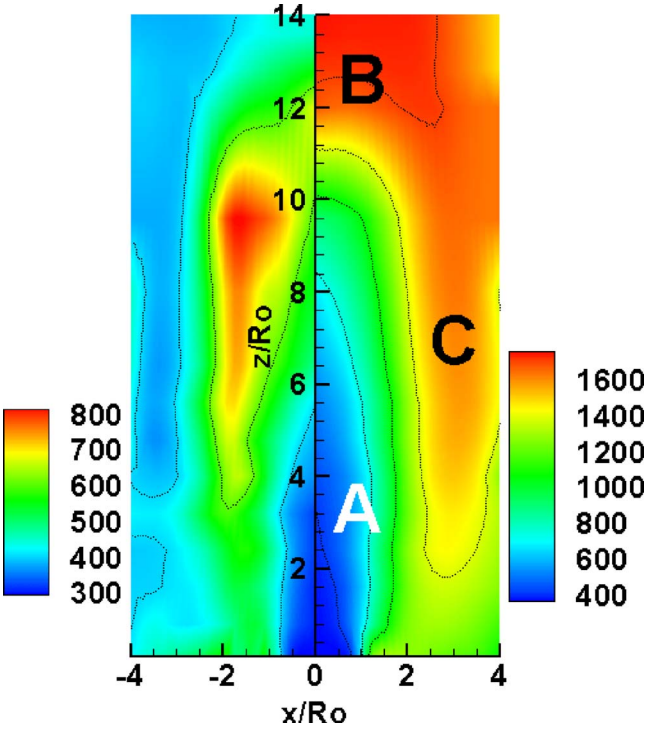

Fig. 15 Reactive flow: carbon monoxide concentration, % vol.

Downloaded 02 Jun 2010 to 171.66.16.107. Redistribution subject to ASME license or copyright; see http://www.asme.org/terms/Terms_Use.cfm

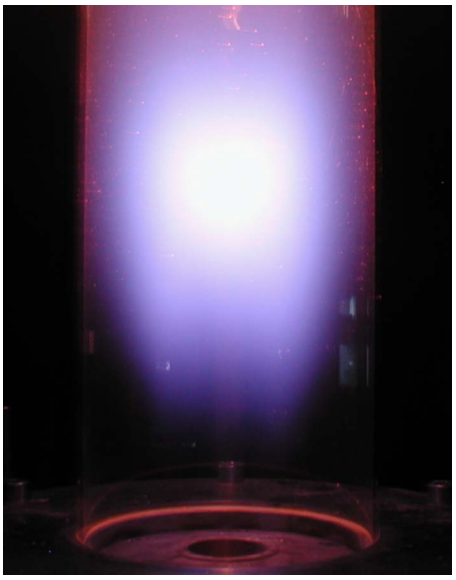

Fig. 16 Reactive flow: mean temperature (right) Trms (left) (in K) and combustion regimes (A,B,C)

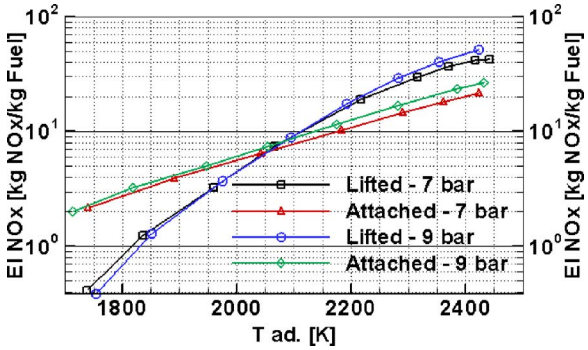

Fig. 17 EINO$_x$ emissions (kg NO$_x$/kg fuel) for lifted and attached flame against adiabatic flame

due to the high axial velocities located at this regime. As the unburnt mixture approaches the combustion area, the temperature grows progressively reaching ignitable levels at $z/R_o=8$. Areas of high temperature fluctuations between the jet and the recirculated gases outside the combustion zone are due to intermittency effects caused by the fluctuating boundary layer between the unburnt jet and the combustion products.

The reaction zone is devoid of steep temperature gradients, confirming that a dominant inner recirculation zone does not exist. Temperature peaks, which usually result from the nonhomogeneous character of a diffusive flame, were also found to be avoided; i.e., quasi-premixed conditions are apparently accomplished. The highest temperatures in the field reach 80% of the adiabatic combustion temperature responding to the global stoichiometry, indicating heat losses of the system. The hottest regions themselves show only moderate levels of fluctuating temperatures, apparently due to the mixture homogeneity [20].

Another important observation concerns the spatial structure of the reaction zone in terms of an arrow-shaped front propagating upstream and parallel to the jet shear layer towards its edge. This procedure is apparently potentiated by entrainment phenomena [7], already described in this paper in terms of a dominant outer recirculation zone. The elevated temperature conditions located at the jet base are expected to have a major impact on the increase of the local laminar burning velocity and, thus, on the local turbulent burning velocity. The flammability limits of the mixture at this position are also expected to rise significantly. Acting on the assumption of the Vanquickenborne model [12], the combustion should be possible in higher flow velocities and, thus, in a lower equivalence ratio. This indicates that extended lean blow-out limits are expected to be achieved in the case of the confined swirled lifted nonpremixed flame, enabling the progress towards lean combustion.

Flame Topology. A brief recapitulation can be summed up out of the findings of this study, concerning the topology of a lifted confined swirl nonpremixed flame, in terms of the mixing procedure, the temperature distribution, the turbulence levels, and the velocity distribution within the flame. Four regions can be identified, with the precombustion area being the most important of them, concerning the conditions that have to be fulfilled in order to achieve the stabilization of the lifted flame (Fig. 16):

(a) **Precombustion area:** A weak inner recirculation zone accelerates the mixing procedure. The flow is highly turbulent and the macromixing is achieved. The temperature gradually rises from the preheating temperature of the mixture to ignitable levels. There is also an influence of the temperature field on the flux of the axial momentum.

(b) **Combustion zone:** The temperature reaches progressively its maximum levels, corresponding to 80% of the adiabatic combustion temperature. No recirculation zone is observed within the combustion region, and the reaction is devoid of temperature peaks. CO emission indicates the combustion zone, which has an arrow-shaped form. Large scale eddies exist in the shear layer between the upstream flow and the recirculated gases.

(c) **Outer recirculation area:** Part of the combusted products performs an upstream recirculation next to the downstream propagating unburnt mixture, and thus these hot reaction products react with fresh unburnt mixture in a re-ignition process, supporting the stability of the combustion. This procedure is of great importance for the maintenance and stabilization of the lifted combustion, since efforts to ignite the lifted flame in a nonconfined environment failed. Areas of high temperature fluctuations between the jet and the recirculated gases outside the combustion zone occur due to intermittency effects.

(d) **Postflame region:** The reactive species are fully oxidized resulting in the existence within the mixture of the expected combustion products of the global mixture adjustment (not labeled in Fig. 16). The temperature approaches constant levels and equals the adiabatic combustion temperature, devoid of the heat losses due to radiation and heat transfer to the chamber walls due to heat conduction and convection.

NO$_x$ Emissions. In order to approve its operability, the lifted swirl nonpremixed flame was also tested under high pressure conditions in the pressurized rig described in the experimental setup section. Within the scope of these experiments, the applied nozzle was scaled down by a factor of 0.5 and was compared to a similar Airblast configuration producing an attached swirl flame. The experiments were carried out with Jet-A1 fuel, in order to achieve near service conditions. Gas analysis was performed by means of Fourier transform infrared spectroscopy, focusing on the emissions of nitric oxide (NO$_x$).

The production of NO$_x$ depends on a variety of parameters, such as the local temperature, the local mixing rates, the global flame residence time, and the radiative heat losses [21]. According to the main chemical pathway responsible for NO$_x$ formation in combustion (the thermal NO pathway postulated by Zeldovich), temperatures above 1700 K are required in order to significantly activate the NO production [22].

NO$_x$ emissions for the described nozzles plotted against the adiabatic flame temperature are depicted in Fig. 17. The experi-

Downloaded 02 Jun 2010 to 171.66.16.107. Redistribution subject to ASME license or copyright; see http://www.asme.org/terms/Terms_Use.cfm

ments were performed for preheating temperatures of 573 K, pressures of 7 and 9 bar, and an equivalent ratio Φ range from 0.5 to 1.2. The results demonstrate that the lifted flame achieves, as expected, the required objective, namely, the reduction of the NO_x emissions in the lean area, and thus in adiabatic combustion temperatures below 2000 K. This occurs due to the premixed character of the lifted flame. The absence of an inner recirculation zone in the flame also results in a lower residence time within the hot regime of the flame and thus in lower NO_x emissions [23].

Conclusions

This study aimed to investigate a confined lifted swirl nonpremixed flame. The results demonstrated that, for the investigated flame, a significant amount of the total fuel flow was already mixed at a macrolevel upstream of the flame stabilization zone. Temperature peaks, resulting from nonhomogeneity, were found to be avoided and hence combustion with low production of the pollutant NO_x was accomplished. The combination of velocity and temperature maps correlated to the mixture field made it possible to locate the stabilization area, the recirculation zones, as well as the postflame region. The results showed a flow field devoid of a large dominant inner recirculation zone. A significant amount of exhaust gases was found upstream from the reaction zone and perimetrical from the downstream jet, forming an outer recirculation zone that apparently dominated the stabilization of the lifted swirl nonpremixed flame. This procedure is of vital importance for the maintenance and stabilization of the lifted combustion, since efforts to ignite the lifted flame in a nonconfined environment failed. The lifted swirl nonpremixed flame was also found to have significant reduced NO_x emissions and elevated pressure conditions at the lean area under, compared to a similar Airblast configuration producing an attached swirl flame.

Acknowledgment

We kindly acknowledge financial support by the European Commission through project TLC (Contract No. AST4-CT-2005-012326).

Nomenclature

D = diameter, m
D = angular momentum, kg m^2/s
I = axial momentum, kg m/s
L = length, m
$\dot{M}$ = mass flux, kg/s
P = power, W
R = radius, m
Re = Reynolds number
S = swirl number
T = temperature, K
U = axial velocity component, m/s
V = radial velocity component, m/s
K = turbulence kinetic energy, m^2/s^2
P = pressure, bar
X = radial coordinate, m
Z = axial coordinate, m

Greek Symbols

Δ = finite difference
Ψ = mass flow stream function
P = density, kg/m^3
Φ = equivalence ratio

Subscripts

A = air
AD = adiabatic
CC = combustion chamber
O = referencing nozzle throat
PR = preheating

Operators

$-$ = time averaged
$'$ = fluctuation

Abbreviations

CCD = charge coupled device
$EINO_x$ = emission index of nitric oxides
LDA = laser Doppler anemometry
PDF = probability density function
rms = root mean square
RQL = rich quench lean

References

[1] Zarzalis, N., Fokaides, P. A., and Merkle, K., 2005, Fuel Injection Apparatus, Patent No. DE 10 2005 022 772.4, EP 06 009 563.5.
[2] Lefebvre, A., 1989, *Atomisation and Sprays*, Hemisphere Publishing Corporation, Washington, DC.
[3] Fokaides, P., and Zarzalis, N., 2006, Report on Stability and Flow Characterisation at Atmospheric Pressure Conditions," Deliverable D.2.3.3.a. for the European project "Towards Lean Combustion" (Contract No. AST4-CT-2005-012326).
[4] Leuckel, W., 1967, "Swirl Intensities, Swirl Types and Energy Loss of Different Swirl Generating Devices," IFRF-Doc. No. G 02/a/16.
[5] Merkle, K., Haessler, H., Buechner, H., and Zarzalis, N., 2003, "Effect of Co- and Counter-Swirl on the Isothermal Flow- and Mixture-Field of an Airblast Atomizer Nozzle," Int. J. Heat Fluid Flow, **24**, pp. 529–537.
[6] Ricken, V., 2006, "Untersuchungen zur Stickoxidemission von Gasturbinenbrennkammern mit luftgestufter Verbrennungsführung," Ph.D. thesis, TU Karlsruhe, Germany (in German).
[7] Thring, M. W., and Newby, M. P., 1953, "Combustion Length of Enclosed Turbulent Jet Flames," *4th International Symposium on Combustion*, Baltimore, MD, pp. 789–796.
[8] Flores, D., 2003, "Analysis of Lean Premixed Turbulent Combustion Using Coherent Anti-Stokes Raman Spectroscopy Temperature Measurements," Ph.D. thesis, Brigham Young University, Provo, UT.
[9] Vanoverberghie, K., Van Den Bulck, E., and Tummers, M., 2004, Flow Structure of Lifted Swirling Jet Flames," Flow, Turbul. Combust., **73**, pp. 25–47.
[10] *Analysentechnik, Advance Optima, Modulares Prozessanalysensystem*, 42/24-10-3 DE, Hartmann & Braun, Belgium.
[11] SAE, 1994, "Procedure for the Calculation of Gaseous Emissions From Aircraft Turbine Engines," SAE Paper No. APR1533.
[12] Vanquickenborne, L., and van Tiggelen, A., 1966, "The Stabilization of Mechanism of Lifted Diffusion Flames," Combust. Flame, **10**, pp. 59–69.
[13] Eickhoff, H., Lenze, B., and Leuckel, W., 1984, "Experimental Investigation on the Stabilization Mechanism of Jet Diffusion Flames," *20th Symposium (International) on Combustion*, The Combustion Institute, pp. 311–318.
[14] Craya, A., and Curtet, R., 1955, "On the Spreading of a Confined Jet," Acad. Sci., Paris, C. R., **241**(1), pp. 621–622.
[15] Broadwell, J., Dahm, W., and Mungal, M., 1984, "Blowout of Turbulent Diffusion Flames," *Twentieth Symposium (International) on Combustion*, The Combustion Institute, pp. 303–310.
[16] Smooke, M. D., Mitchell, R. E., and Keyes, D. E., 1989, "Numerical Solution of Two-Dimensional Axisymmetric Laminar Diffusion Flames," Combust. Sci. Technol., **67** pp. 85–122.
[17] Domingo, P., and Vervisch, L., 1996, "Triple Flames and Partially Premixed Combustion in Autoignition of Non-Premixed Turbulent Mixtures," *Twenty-Sixth Symposium (International) on Combustion*, The Combustion Institute, pp. 233–240.
[18] Kunugi, M., and Jinno, H., 1959, "Measurements of Fluctuating Flame Temperature," *7th International Symposium on Combustion*, pp. 942–948.
[19] Sato, A., and Kumura, J., 1975, "A Correctional Calculation Method for Thermocouple Measurement of Temperature in Flames," Combust. Flame, **24**, pp. 34–41.
[20] Gupt, K. A., Lewis, M. J., and Daurer, M., 2001, "Swirl Effects on Combustion Characteristics of Premixed Flames," J. Eng. Gas Turbines Power, **123**, pp. 619–626.
[21] Warnatz, J., Maas, U., and Dibble, R. W., 2001, *Combustion, Physical and Chemical Fundamentals, Modeling and Simulation, Experiments, Pollutant Formation*, 3rd ed., Springer, New York.
[22] Zeldovich, Y. B., 1946. "The Oxidation of Nitrogen in Combustion and Explosions," Acta Physicochim. URSS, **21**.
[23] Schmitel, P., Günter, B., Lenze, B., Leuckel, W., and Bockhorn, H., "Turbulent Swirling Flames: Experimental Investigation of the Flow Field and Formation of Nitrogen Oxide," *28th Combustion Symposium (International)*, pp. 303–309.

Downloaded 02 Jun 2010 to 171.66.16.107. Redistribution subject to ASME license or copyright; see http://www.asme.org/terms/Terms_Use.cfm

Impact of Ethane, Propane, and Diluent Content in Natural Gas on the Performance of a Commercial Microturbine Generator

Richard L. Hack

Vincent G. McDonell

UCI Combustion Laboratory,
University of California,
Irvine, CA 92697-3550

The impact of fuel composition on the performance of power generation devices is gaining interest as the desire to diversify fuel supplies increases. In the present study, measurements of combustion performance were conducted on a commercial natural gas-fired 60 kW *gas turbine as a function of fuel composition. A statistically designed experiment was carried out and exhaust emissions were obtained for significant amounts of ethane and propane. In addition, a limited study of the effect of inerts was conducted. The results show that emissions of NO_x, CO, and NO_x/NO are not well correlated with common descriptions of the fuel, such as higher heating value or methane number. The results and trends indicate that the presence of higher hydrocarbons in the fuel leads to appreciably higher NO_x emissions for both test devices operating under similar lean conditions, while having less impact on CO emissions.* [DOI: 10.1115/1.2770493]

Introduction

Gas turbines have traditionally been able to operate on a wide variety of fuels (e.g., Meier et al. [1]). Currently, designers and operators of advanced natural gas-fired gas turbine systems are using lean-premixed strategies to meet current and future emissions regulations. The principal rationale behind lean operation stems from the desire to reduce the emissions of oxides of nitrogen (NO_x). However, lean operation can lead to increased emission of carbon monoxide (CO) and unburned hydrocarbons (UHCs), both of which impact the combustion efficiency (η_C) of the system. As a result, a relatively narrow operating region exists where emission of all three pollutants are minimized, which is usually found near the lean flammability limit of the combustion system. An additional complication is that, to be successful, lean burn strategies must not only be overall lean but they must also narrow the overall *range* of equivalence ratios throughout the combustion zone. As a result, the success of the lean-premixed system relies on careful mixing of the fuel and air.

As a consequence, advanced gas turbine combustion systems must operate within narrow margins in order to meet regulated emission targets. As a result, these systems are susceptible to instabilities, eliminating much of the "tolerance" to system and operational variation that have been positive attributes of conventional combustion systems in the past. Because of reduced tolerance to operational factors, interest in the effect that fuel variability has on the operation and performance of a gas turbine combustor is increasing. Natural gas composition varies around the United States (see Table 1), and even more so around the world. Furthermore, the variability in natural gas composition is increasing as producers relax their control on the amount of inert gases (such as CO_2) and high-molecular fuel species (such as hexane) in the natural gas supply. The potential for significant amounts of imported LNG into the United States creates yet additional possible variation, as shown in Table 2.

Due to the reduced tolerances of advanced lean-premixed, natural gas-fired combustion systems, the sensitivity of combustor operation to this variability needs to be ascertained (e.g., Richards et al. [4]). The presence of higher hydrocarbons in natural gas, for instance, may lead to shortened ignition delay times and possible reduced autoignition temperatures. The kinetic reaction rates for the various fuel compositions will also differ, causing changes in the flame speed and location of the lean stability limit. Moreover, reaction flashback has a greater opportunity to occur under some circumstances.

A number of characteristics are commonly used to describe the fuel. One characteristic is the heating value, which is generally reported as the energy contained per unit volume of fuel. In the case of higher hydrocarbons, for example, propane will have nearly three times the energy per unit volume as methane.

Another characteristic is "methane number" (MN), which describes "knock resistance" in an internal combustion engine environment. The MN is therefore somewhat related to the combustion properties of the fuel such as reaction rate. It is analogous to the "motor octane number" (MON) defined for gasoline. While defined in the context of internal combustion engines for transportation, MN may also impact performance of power generation devices located in the same distribution region.

The MON equivalent for natural gas is also related to the reactive hydrogen to carbon ratio (H/C) of the fuel as follows[1]:

$$\mathrm{MON} = -406.14 + 508.04\left(\frac{\mathrm{H}}{\mathrm{C}}\right) - 173.55\left(\frac{\mathrm{H}}{\mathrm{C}}\right)^2 + 20.17\left(\frac{\mathrm{H}}{\mathrm{C}}\right)^3 \tag{1}$$

Further, empirical correlations are available to relate MN to a MON "equivalent" of the gas as a measure of knock resistance according to:

$$\mathrm{MN} = 1.624\mathrm{MON} - 119.1 \tag{2}$$

Another fuel characteristic is the Wobbe index, which is an expression of the fuel energy content per relative density. It is commonly used to determine compatibility of fuel systems with fuel type. For example, for a given injector hole diameter, the energy content of the fuel can pass for a given pressure drop that is

Contributed by the International Gas Turbine Institute of ASME for publication in the JOURNAL OF ENGINEERING FOR GAS TURBINES AND POWER. Manuscript received March 29, 2006; final manuscript received October 4, 2006; published online January 16, 2008. Review conducted by Geoff Myers. Paper presented at the ASME Turbo Expo 2005: Land, Sea and Air (GT2005), Reno, NV, June 6–9, 2005, Paper No. GT2005-68777.

[1]California Air Resources Board, "Proposed Amendments to the California Alternative Fuels for Motor Vehicles Regulations," Appendix D.

Copyright © 2008 by ASME

Downloaded 02 Jun 2010 to 171.66.16.107. Redistribution subject to ASME license or copyright; see http://www.asme.org/terms/Terms_Use.cfm

Table 1 Typical concentrations of fuel constituents for natural gas sources in the U.S. (Liss, 1992)

Constituent	Mean	Min	Max
Methane (%vol)	93.9	74.5	98.1
Ethane	3.2	0.5	13.3
Propane			
Without C_3 peak shaving	0.7	0	2.6
With C_3 peak shaving	0.1	0	23.7
Hexanes +	0.1	0	0.4
Inerts (contract specs)			
CO_2		0	3
H_2O (ppm)		0.05	0.2

related to the Wobbe index. The higher hydrocarbons will provide more energy for a given pressure drop and therefore less mass flow is needed to achieve a given temperature rise. This strategy is helpful for "peak shaving" to reduce the demands on the natural gas supply. A "modified" Wobbe index is also used, which accounts for fuel temperature variation (and therefore temperature based density changes). In the present study, the fuel is not subject to significant heating due to the design of the engine used.

It is clear that any one of the above indices is insufficient to fully describe the impact of the fuel composition on the combustion system. The present study focuses on the effect of fuel composition on the emissions of effluents and general operational issues for gas turbine type combustion systems.

Experiment

Microturbine Generator. For the present study, tests were conducted on the device illustrated in Fig. 1, which is a commercial 60 kW natural gas-fired microturbine generator (MTG). A Capstone C-60 MTG was utilized. This 60 kW MTG features a single stage compressor and single stage turbine on a common shaft as well as an annular combustor configuration. The Capstone combustor incorporates a globally swirl stabilized combustion process with fuel injectors that are canted slightly from purely radial orientation. The overall strategy results in "diluted combustion" (e.g., Milani and Saponaro [5]) in which the reactants are partially mixed with products before they react. The pressure ratio is nominally 4:1 and recuperation of the exhaust gas for preheating the incoming combustion air is incorporated to increase the overall efficiency. The recuperator provides preheated air to the combustor at a temperature of $1050 \pm 25°F$, regardless of the turbine load and/or the ambient temperature.

A fuel staged lean-premixed strategy is utilized for the combustion system that results in low emissions over much of the operating range. The fuel/air premixing occurs within the six individual fuel injectors with a fraction of the total combustion air. Previous measurements have shown little variation in the level of mixedness over a wide range of fuel flows (e.g., Phi et al. [6]). This premixing strategy, while successful at mitigating emission, also raised some concerns for tolerance to fuel composition since the higher flame speeds and reaction rates associated with ethane and propane compared to natural gas could result in flashback into the premixer, which would result in diffusion reactions that would generate significantly higher levels of NO_x and/or hardware damage.

Table 2 Typical LNG composition comprehensive data on LNG composition was not identified; these examples provide a representative range from worldwide sources, (CFI, [2]; SEU, [3])

Constituent	Min	Max
Methane (%vol)	83.2	99.7
Ethane	0.1	2.3
Propane	0	5.0

Fig. 1 C-60 MTG

An important feature of the C-60 MTG that affects the potential impact of fuel composition on emission performance is the control system. The system allows a user defined power output setpoint to be entered and then regulates fuel flow to maintain this setting. The control system is constrained by two engine characteristics: (1) the engine speed must remain below 96,000 rpm and (2) the turbine exhaust temperature (TET) target is 635°C. In the present study, the majority of the tests were carried out at a 60 kW setting, 96,000 rpm, and a measured TET of 635°C.

Since for a given requested power setting the turbine exit temperature remains constant, it can be expected that the global reaction temperature would remain constant regardless of the incoming fuel heat content. This control strategy is important relative to the mechanism by which fuel composition may impact NO_x emissions. It has been shown that NO_x is sensitive to fuel composition for the situation where the combustion temperature is held at a fixed level below the point where thermal NO_x is predominant. This has been attributed to the coupling between composition and the "prompt" and "N_2O" NO_x formation mechanisms at both a fundamental (e.g., Steele et al. [7]) and a practical level of combustion (Flores et al. [8]). Hence, for the C-60 MTG, composition effects on the overall firing temperature are minimized due to the system control strategy, which implies that only localized effects of fuel composition (e.g., temperature changes at the reaction front, composition based effects on prompt and N_2O mechanisms) play a role in NO_x emissions.

Gas Blending. Operation on the desired gas compositions for sustained periods of time required a precise metering system to be utilized. To accomplish this, a pair of needle valve downstream of a pair of Coriolis effect mass flow meters (Emerson/Micromotions, Boulder, CO) was utilized to meter and monitor the flow of ethane and propane. The Coriolis meters are true mass

Downloaded 02 Jun 2010 to 171.66.16.107. Redistribution subject to ASME license or copyright; see http://www.asme.org/terms/Terms_Use.cfm

Table 3 Typical natural gas composition

n	Consistent	MF (%)
1	Methane CH_4	96.975
2	Ethane C_2H_6	0.982
3	Propane C_3H_8	0.109
4	iso-Butane C_4H_{10}	0.014
5	n-Butane C_4H_{10}	0.015
6	iso-Pentane C_5H_{12}	0.004
7	n-Pentane C_5H_{12}	0.004
8	C6	0.004
9	C7	0.001
10	C8	0.000
11	CO_2	1.574
12	O_2	0.000
13	N_2	0.322

Table 4 Calibration gas composition for on-line GC

Component	Concentration (%)
C_1	89.59
C_2	5.00
C_3	1.02
Iso–C_4	0.299
Normal C_4	0.299
Neo–C_5	0.10
Iso–C_5	0.10
Normal C_5	0.10
C_6	0.03
CO_2	1.00
N_2	2.46

flow meters and are seemingly immune to the variations in temperature and phase of the flowing media. At UCI, the natural gas supply is pressurized to ~120 psi (gauge). The injection of higher gaseous hydrocarbons (ethane and propane) into a high pressure stream is complicated by the relatively low vapor pressure and the Joule–Thomson cooling effects of both of the gases causing phase and temperature variations that vex the utilization of more conventional thermal based mass flow meters.

The control of the gas flow was accomplished via manual needle valves. For propane, the tank was heated to increase the vapor pressure to approximately 150 psi (gauge). The Coriolis meter operated at the supply pressure; the final pressure drop from the supply to the natural gas mixing point occurred across the needle valve downstream of the Coriolis meter, displacing any cooling effects far away from the metering system. For ethane, the supply pressure was reduced at the tank from a supply pressure of ~500 psi (gauge) to 150 psi (gauge). The refrigeration properties of ethane are not as pronounced as propane and visible frosting of the regulator only occurred at high flow rates. As with propane, the metering valve was located downstream of the flow metering device.

Initial flow rates for the propane and ethane were calculated based upon approximate heat rate of the turbine and the expectation that the microturbine would regulate flow to maintain a constant heat input rate. Utilizing the on-line gas chromatograph (described below), the composition was measured and the flows adjusted to meet the desired composition.

An ABB "Total-flow™" on-line gas chromatograph (GC) was utilized for analysis of the fuel streams. The analyzer monitors three gas streams: (1) the line natural gas as delivered, (2) after the gas compressor, and (3) the blended gas stream. For this program, the analyzer was called upon to provide both the "as delivered" natural gas composition shown in Table 3 (from which the various compositions were derived) and to provide analysis of the blended gas as provided to the MTG as a quality check. The analyzer works in a "batch" mode (rather than continuous) analyzing a new gas sample at a maximum rate of once every 3 min. Owing to the transit time for the sample to be delivered to the GC, delay times of approximately 10 min between composition change and detection on the GC were normal.

The Total-Flow™ analyzer is designed for remote "pipeline" monitoring and has a self-calibration feature. The calibration gas utilized is based upon an industry standard nominal gas composition (Table 4) and is not specific to either the actual line gas or blended compositions utilized in this project. Hence, the blended gas composition measured, especially the ethane and propane components, should be considered representative and indicative of the composition rather than quantitatively precise. Also, as a result of its role as a "utility" pipeline GC, its analysis utilizes protocols common to the gas delivery industry that do not readily fit other laboratory analysis. This is particularly true in the calculation of the heating value, reported as the "dry" heating value in the analysis. In particular, the GC utilizes calculation protocol GPA-2172-86. The GC calculated higher heating value (HHV) is 2–3% higher than calculated using the heats of combustion of the various hydrocarbon components.

A Horiba PG250 was utilized to measure the emission levels in the MTG exhaust stream. The PG250 measures NO_x (NO and NO_2) using EPA Method 7E, CO using EPA Method 10, and CO_2 and O_2 using EPA Method 3A. For the present study, NO_x and NO were individually quantified. The NO_x converter efficiency was measured (~94% for the study) and used to correct the results.

Accurate emission measurements require proper care in assembling the sample train and in calibrating the system on a regular interval. In the present case, the sample train consists of a $\frac{1}{4}$ in. diameter stainless steel probe, Teflon sample lines, refrigerated sample cooler with water dropout, vacuum pump, and particulate filter. The sample train utilized is consistent with California Air Resources Board requirements (CARB Method 100).

Test Matrix

Two types of test matrices were utilized for the tests. In the first, a statistically designed matrix was utilized to explore the role of higher hydrocarbons on the MTG performance. This matrix was based on methane concentrations from 78% to 100%, ethane concentrations of 0–17%, and propane concentrations from 0% to 22%. Due to the gas blending process, the exact target values called for by the mixture design were not achieved. As a result, the actual values recorded during the testing were used for the analysis. The matrix (actual values run) is shown in the Appendix.

The second test utilized specific target concentrations to help assess the impact of diluent content on the performance. For tests on the MTG, four specific gas blends were defined for testing with properties described in Table 5.

1. Pipeline natural gas with a MN > 88
2. natural gas with MN = 80 ± 0.5

Table 5 Fuels utilized for specific MN tests

	Natural Gas	CH_4–MN 80	CH_4–MN 73	CH_4–MN 73 w/inerts
Higher Heating Value (btu/scf)	1018	1104	1141	1080
F-Factor, 60F (dscf/mmbtu)	8443	8460	8468	8516
H/C ratio	3.94	3.75	3.68	3.68
Calculated MN*	101	79.5	73.3	73.2
MON**	135	121	118	118
% inerts, vol	1.76	1.60	1.55	6.82

Downloaded 02 Jun 2010 to 171.66.16.107. Redistribution subject to ASME license or copyright; see http://www.asme.org/terms/Terms_Use.cfm

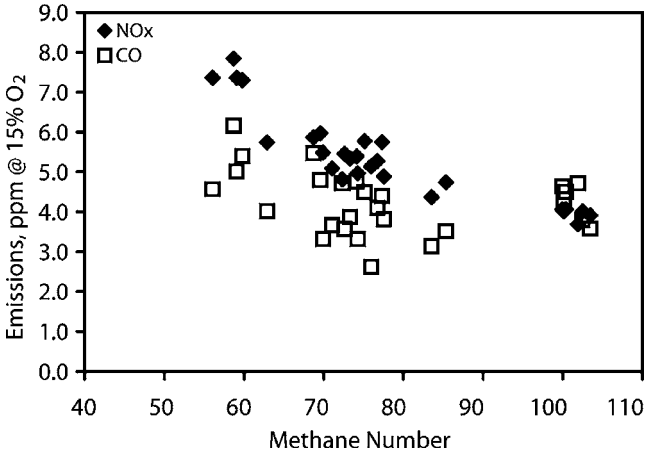

Fig. 2 Emissions as a function of MN (constant turbine exit temperature)

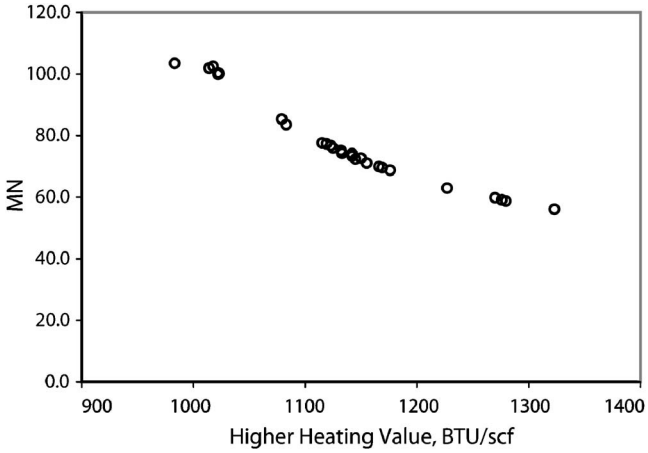

Fig. 4 MN as function of HHV

3. natural gas with MN=73±0.5
4. Natural gas with MN=73±0.5 and with a final inert content of 5.9±0.1 vol %

Results

Results from the two types of tests are presented in this section. It is noted that the two test series were obtained months apart and done on two physically different MTGs.

Mixture Model Tests. The results for the mixture model tests shown in Appendix are presented in this section. All the results for the mixture model tests were obtained at full load (60 kW) with the measured TET a constant 635°C and an engine speed of 96,000 rpm. As mentioned above, this implies that the global reaction zone temperatures are essentially independent of the fuel composition.

Before presenting the results of the analysis of variance (ANOVA) of the measurements, some general behavior can be determined from conventional *X-Y* plots. Figure 2 presents the NO_x and CO emission levels as a function of the MN. The results for NO_x exhibit some correlation with MN despite the constant turbine exit temperature. This suggests that the presence of the higher hydrocarbons (which reduces MN) leads to the formation of higher levels of NO_x. The results for CO do not exhibit as strong a trend with MN.

Figure 3 presents the emissions results as a function of HHV. The results exhibit similar trends as for MN. If the MN is plotted versus HHV (Fig. 4), the reason for the similarity is apparent, since these two values are correlated. It is noted that the presence of inerts can give rise to significantly different HHV for a given MN, as illustrated in Table 5. This is discussed in more detail in the section on the specific MN test results.

Figures 2–4 summarize the global behavior of the emissions performance. In order to provide additional strength to the observations, an ANOVA was carried out for NO_x, CO, and NO_x/NO ratio as a function of the fuel composition.

The results showed that, for the fuel compositions shown in Appendix, CO and NO_x/NO ratio had no statistically significant dependency on fuel composition at full load. However, the ANOVA did indicate that NO_x levels were correlated with fuel composition. The results are shown graphically in Fig. 5. The results illustrate that, for the range of compositions run, the NO_x values depend on each fuel component, with high levels of C1 leading to the lowest levels of NO_x (near 4 ppm) and the highest levels of C3 (~22%) leading to the highest NO_x levels (near 7.5 ppm). The "dots" on the triangle plot represent the compositions for which measurements were made corresponding to the

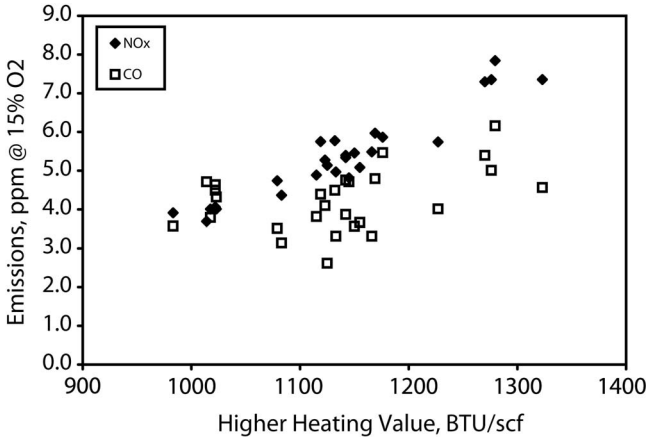

Fig. 3 Emission as a function of HHV (constant turbine exit temperature)

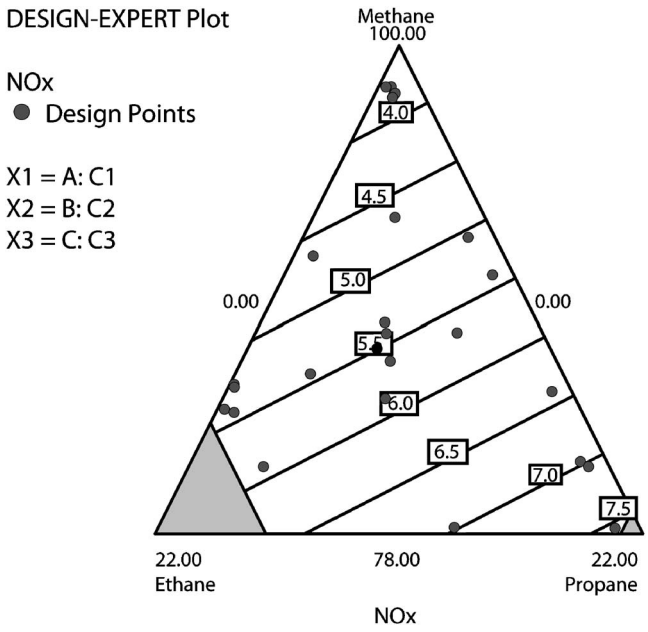

Fig. 5 NO_x (ppm at 15% O2) dependency on fuel composition (% by volume)

Downloaded 02 Jun 2010 to 171.66.16.107. Redistribution subject to ASME license or copyright; see http://www.asme.org/terms/Terms_Use.cfm

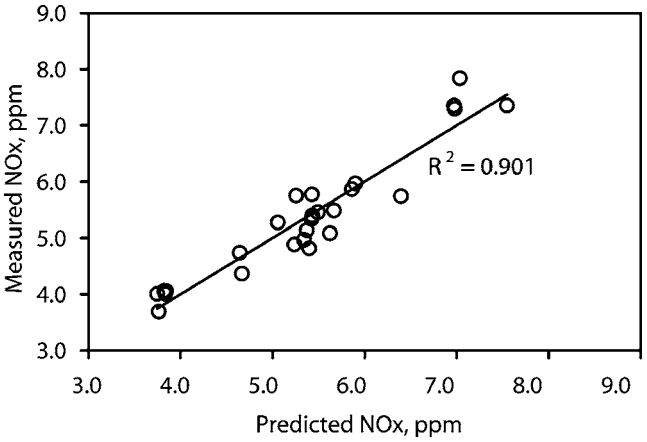

Fig. 6 Measured versus predicted (Eq. (3)) NO_x levels

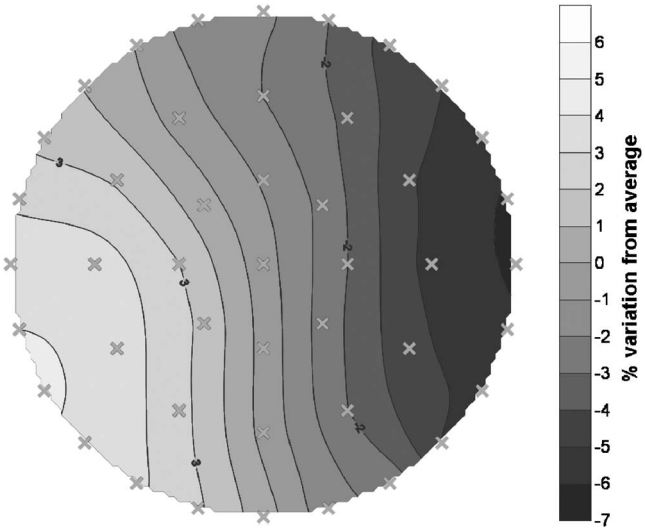

Fig. 7 Measured MTG injector exit plane fuel distribution (natural gas)

conditions shown in Appendix.

An expression for NO_x dependency on fuel composition was determined from the ANOVA and a linear model was identified as providing the best level of correlation. This result is shown as Eq. (3), which expresses the NO_x as a function of the % volume of each component.

$$NO_x \text{ (ppm at 15 \% O2)} = 0.035104C1(\%) + 0.14719C2(\%) + 0.22470C3(\%) \quad (3)$$

Normalized analysis of the coefficients can be used to determine the relative impact of each fuel component. In the current case, the relative impact of C1, C2, and C3 on NO_x are 3.51, 5.98, and 7.68, respectively. Since the range of values for each component varies by about 20% in the present case, this indicates that changing the C3 concentration has about three times (7.68/2.51) the impact on the NO_x emissions in ppm than does changing C1. As a result, it can be concluded that presence of higher hydrocarbons increases the NO_x produced in a statistically significant way as compared to methane. The comparison of the measured and predicted NO_x levels is shown in Fig. 6.

A comparison of the relative importance of the C1–C3 components can be made with results from a model combustor obtained at atmospheric conditions with a inlet temperature of 660 K (Flores et al. [8]). In that study, the relative importance went as 2.93, 3.37, and 4.58 for C1–C3, respectively. In the model combustor study, changing C3 had about 1.5 times the impact of changing C1 versus C3 found in the present study, but the trends are quite similar. It is noted that, for the study of Flores et al. [8], the level of mixing was also studied.

In the present case, the level of premixing is believed to be quite good accoriding to measured mixing levels for this same MTG fuel injector operated on natural gas. These results are illustrated in Fig. 7 and indicate that, on average, the variation is less than 4% over the plane. Additional details are available elsewhere (e.g., Phi et al. [6]).

The specific role of the added ethane and propane on the injector mixing performance has not been quantified, but because the levels added are significant, it is possible the mixing could be affected. This is important to quantify, because, if the mixing is the same for each fuel composition, and the overall bulk firing temperature is the same (as it needs to be for the turbine exit temperature to remain constant), then the reason for the differences in NO_x as a function of fuel composition must be associated with either (1) local differences in reaction temperatures, which may give rise to different thermal NO_x levels, or (2) facilitation of additional NO_x formation pathways due to the presence of the higher hydrocarbons (e.g., Steele et al. [7]). The second possibility was found to be the likely cause of the NO_x increases found with higher hydrocarbons in the model combustor study through sensitivity analysis (Flores et al. [8]).

That CO is not statistically affected by fuel composition as full load suggests that the overall temperatures and residence times are sufficient for oxidation of CO regardless of the fuel composition. Unfortunately, this does not provide any additional insight into the NO_x behavior.

Specific Methane Number Tests. Results from the tests conducted as illustrated in Table 5 are presented in this section. It is again noted that these tests were conducted during a time when the ambient temperature was considerably higher than it was during the mixture model testing. The specific MN tests were conducted at both full load and 50% load.

The results for NO_x are shown graphically in Fig. 8. The two runs reflect testing done on two different days that had significant ambient temperature differences. While it is understood that variations in ambient temperature can and do result in variations in the NO_x emissions as is specifically demonstrated by the Run 1-Run 2 differences on natural gas, the goal of presenting the results in as shown is to illustrate the effect of the MN variation regardless of ambient temperature. This form of the test was designed to allow

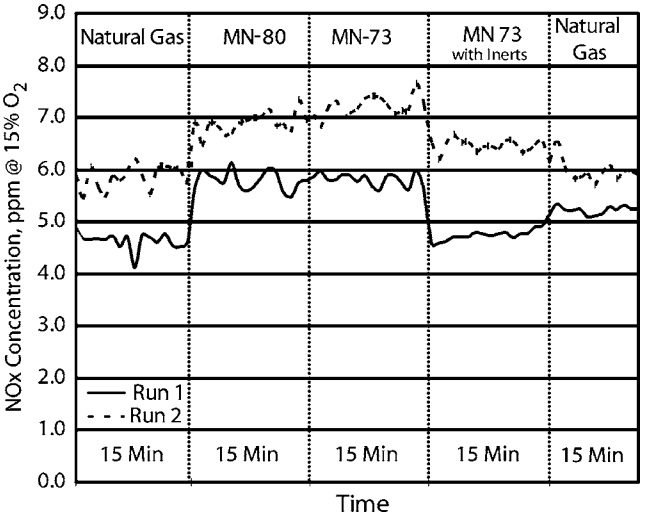

Fig. 8 NO_x levels versus time for specific MN tests (see Table 5)

Downloaded 02 Jun 2010 to 171.66.16.107. Redistribution subject to ASME license or copyright; see http://www.asme.org/terms/Terms_Use.cfm

Table 6 MN specific test NO_x results at full load

MN	Avg	Stdev
103	5.49	0.25
79	6.65	0.05
72	6.78	0.25
73 (with inerts)	5.83	0.65
103	5.88	0.09

"real time" changes in emissions levels to be observed. The MTG was operated on base line natural gas and then, after 15 min, was subjected to the MN of 80 fuel mix and the emissions were monitored for 15 min. Then the MN-73 mix was set and the MTG run for 15 min. This was followed by the operation on MN-73 with inerts for 15 min, and then finally, the MTG was operated again on the base line natural gas. The results show several interesting trends. First, the lower MN fuels without inerts result in a step increase in NO_x. When the inerts are added (with same MN of 73), the NO_x levels are reduced. Finally, the variation from day to day appears to be around 1 ppm. It is noted that the mixture model testing was conducted over several days and several repeat points were included on each day in order to specifically allow an evaluation of the statistical significance of the fuel composition effects in the presence of ambient condition variations.

A summary of the actual results is shown in Table 6. The results show that adding inerts to the MN 73 case leads to a reduction in NO_x as indicated in Fig. 8.

Because the results from the MN specific tests were conducted on a different engine and were obtained months earlier than the mixture model testing, it is useful to compare the measurements with those done during the mixture model test matrix presented previously. The results are shown in Fig. 9. The results show the same trends for two test series, but with the MN specific test NO_x levels ranging to levels that are systematically 1–2 ppm higher compared to the mixture model test series. Considering that the tests were done on two different MTGs with different sampling equipments and done so at two times during the year with greatly different ambient temperatures, the results are considered quite similar.

The mixture model results presented previously indicated that CO had no statistically significant dependency on fuel composition. The explanation was that, for the full load condition, sufficient time and temperature were available to completely oxidize the CO. Since the specific MN tests were conducted at 50% load, where overall temperatures will be cooler, the CO results are revisited.

Figure 10 presents these results in a format similar to Fig. 8. In this case, the CO levels appear to be dramatically influenced by the fuel composition. At the part load condition, the presence of the higher hydrocarbons greatly reduces the amount of CO. Further, when inerts make up the MN73 fuel, the CO levels jump again. At 50% load, the same turbine exit temperature setpoint is maintained—again suggesting that the "global" thermal environment (i.e., the combustor exhaust temperature) is similar for each fuel blend. Hence, the results shown in Fig. 10 suggest that localized effects are playing a role in the CO oxidation.

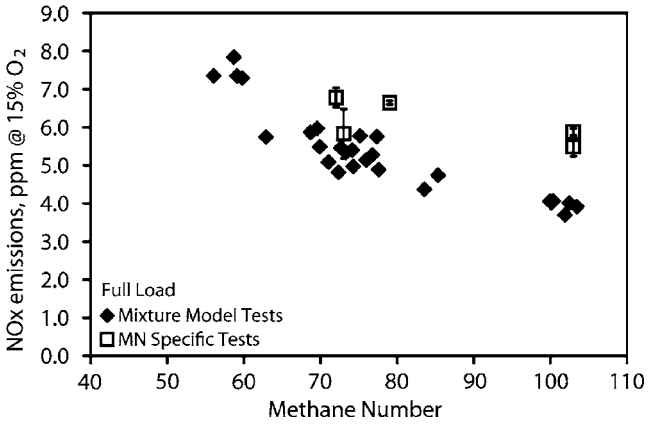

Fig. 9 Comparison of NO_x measurements for two test series

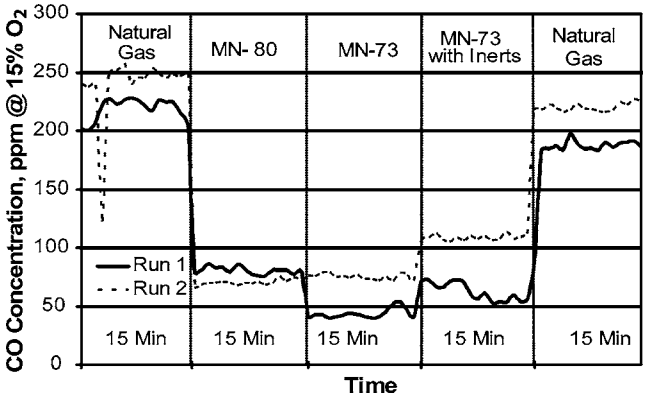

Fig. 10 Corrected CO emission levels for 50% load

Summary and Conclusions

Testing was conducted on a commercial MTG operated on different gaseous fuels that were characterized by their MN. The fuels comprised natural gas with the presence of ethane, propane, and, in some cases, inert gases. A statistically designed experiment was carried out at full load and shows that the presence of higher hydrocarbons leads to elevated NO_x levels when compared to 100% methane. The CO levels do not depend on fuel composition at full load. However, the CO levels are strongly dependent on fuel composition for the part load tests. The results do show that MN affects NO_x emissions. The lower MN fuels give rise to higher NO_x values, even with similar firing temperatures which suggests that either NO_x formation mechanisms enabled by the presence of higher hydrocarbons are playing a role in the generation of NO_x from these very lean systems or that localized temperature effects are impacting the NO_x behavior. These explanations assume that the fuel/air mixing is independent of fuel composition.

Further, the results show the challenge associated with classifying the fuel with a specific characterization such as MN or HHV. While some of the combustion performance seems to be correlated with these values, the examples showing how inerts impact the emissions levels with a constant MN illustrates the risk of using a single index to infer combustion performance behavior.

Acknowledgment

The support of the South Coast Air Quality Management District in the MN specific tests is gratefully acknowledged. The assistance of Mark Effinger in the the running of the mixed gas experiments associated with the MTG tests is greatly appreciated. Funding from the California Energy Commission supported the Mixture Model MTG testing.

Downloaded 02 Jun 2010 to 171.66.16.107. Redistribution subject to ASME license or copyright; see http://www.asme.org/terms/Terms_Use.cfm

Appendix: Test Matrix and Measured Results

					Results HHV (BTU/scf)				Emission at 15% O2			
Case	C1	C2	C3	CO2	HHV	Wobbe index (MJ/m^3)	H/C	MN	NO	NO_x	CO	NO_x/NO
1	85.80	3.80	8.96	1.48	1166	50.30	3.64	69.89	4.22	5.49	3.32	1.30
2	82.00	15.75	0.32	1.44	1125	49.52	3.71	75.94	4.15	5.14	2.62	1.24
3	82.80	0.88	14.41	1.48	1227	51.11	3.54	62.89	4.59	5.74	4.01	1.25
4	90.38	3.98	3.62	1.64	1083	48.60	3.79	83.53	3.42	4.37	3.14	1.28
5	85.84	6.75	5.49	1.54	1133	49.57	3.69	74.25	3.89	4.97	3.32	1.28
6	87.85	0.94	9.20	1.62	1145	49.66	3.67	72.33	3.68	4.82	4.71	1.31
7	84.15	7.37	6.58	1.56	1155	49.97	3.65	71.04	3.86	5.08	3.67	1.32
8	96.00	1.26	0.56	1.81	1014	47.29	3.95	101.90	2.97	3.69	4.71	1.24
9	83.20	14.79	0.20	1.49	1115	49.40	3.73	77.57	3.85	4.89	3.82	1.27
10	96.30	1.50	0.33	1.41	1018	47.42	3.96	102.47	2.98	4.01	3.79	1.35
11	84.60	11.30	3.38	1.16	1142	50.26	3.69	74.11	4.28	5.40	4.76	1.26
12	84.95	7.70	5.73	1.13	1150	49.92	3.67	72.62	4.08	5.46	3.57	1.34
13	79.92	1.17	17.27	1.19	1276	52.05	3.47	59.08	5.71	7.35	5.01	1.29
14	77.00	1.11	20.30	1.09	1323	52.88	3.40	56.04	5.63	7.36	4.57	1.31
15	95.90	1.23	0.88	1.44	1022	47.47	3.94	100.36	3.24	4.06	4.50	1.25
16	89.70	1.19	7.31	1.32	1123	49.29	3.72	76.73	4.10	5.28	4.10	1.29
17	83.15	14.85	0.27	1.35	1119	49.47	3.69	77.32	4.39	5.75	4.39	1.31
18	82.67	8.43	7.21	1.27	1176	50.40	3.27	68.71	4.54	5.87	5.47	1.29
19	95.84	1.38	0.85	1.42	1023	47.51	2.99	100.14	3.25	4.01	4.32	1.23
20	77.83	8.32	13.27	1.16	1270	52.55	3.19	59.79	5.73	7.30	5.40	1.27
21	88.85	8.45	0.87	1.43	1079	48.62	3.48	85.32	3.74	4.74	3.51	1.27
22	82.07	15.43	0.82	1.33	1132	49.73	3.67	75.12	4.42	5.78	4.50	1.31
23	95.75	1.44	0.86	1.59	1022	47.51	2.98	99.94	3.21	4.06	4.64	1.26
24	79.60	0.92	17.72	1.36	1280	52.08	2.99	58.69	5.97	7.84	6.16	1.31
25	79.63	15.33	3.32	1.40	1169	50.37	3.53	69.57	4.81	5.97	4.79	1.24
26	85.43	6.93	5.81	1.50	1142	49.73	3.24	73.29	4.24	5.34	3.87	1.26

References

[1] Meier, J. G., Hung, W. S. Y., and Sood, V. M., 1986, "Development and Application of Industrial Gas Turbines for Medium-BTU Gaseous Fuels," ASME J. Eng. Gas Turbines Power, **108**, pp. 182–190.

[2] Cryogenic Fuels, Inc., 1991, "Liquid Methane Fuel Characterization and Safety Assessment Report," Report No. CFI-1600.

[3] Shea, K., 2005, Sempra Energy Utilities, private communication.

[4] Richards, G. A., McMillian, M. M., Gemmen, R. S., Rogers, W. A., and Cully, S. R., 2001, "Issues For Low-Emission, Fuel-Flexible Power Systems," Prog. Energy Combust. Sci., **27**, pp. 141–169.

[5] Milani, A., and Saponaro, A., 2001, "Diluted Combustion Technologies," IFRF Combustion Journal.

[6] Phi, V. M., Mauzey, J. L., McDonell, V. G., and Samuelsen, G. S., 2004, "Fuel Injector and Emissions Characteristics of a Commercial Microturbine Generator," presented at *Turbo Expo 2004*, Vienna, Austria, Jun., Paper GT-2004-54039.

[7] Steele, R. C., Tonouchi, J. H., Nicol, D. G., Horning, D. C., Malte, P. C., and Pratt, D. T., 1998, "Characterization of NO_X, N_2O, and CO for Lean-Premixed Combustion in a High-Pressure Jet-Stirred Reactor," ASME J. Eng. Gas Turbines Power, **120**, pp. 303–310.

[8] Flores, R. M., McDonell, V. G., and Samuelsen, G. S., 2003, "Impact of Ethane and Propane Variation in Natural Gas on the Performance of a Model Gas Turbine Combustor," ASME J. Eng. Gas Turbines Power, **125**, pp. 701–708.

Downloaded 02 Jun 2010 to 171.66.16.107. Redistribution subject to ASME license or copyright; see http://www.asme.org/terms/Terms_Use.cfm

Effect of Fuel System Impedance Mismatch on Combustion Dynamics

Geo A. Richards
National Energy Technology Laboratory,
U.S. Department of Energy,
PO Box 880,
Morgantown, WV 26505
e-mail: gricha@netl.doe.gov

Edward H. Robey
National Energy Technology Laboratory,
Parsons,
PO Box 880,
Morgantown, WV 26505
e-mail: eroby@netl.doe.gov

Combustion dynamics are a challenging problem in the design and operation of premixed gas turbine combustors. In premixed combustors, pressure oscillations created by the flame dynamic response can lead to damage. These dynamics are typically controlled by designing the combustor to achieve a stable operation for planned conditions, but dynamics may still occur with minor changes in ambient operating conditions or fuel composition. In these situations, pilot flames or adjustment to fuel flow splits can be used to stabilize the combustor, but often with a compromise in emission performance. As an alternative to purely passive design changes, prior studies have demonstrated that adjustment to the fuel system impedance can be used to stabilize combustion. Prior studies have considered just the response of an individual fuel injector and combustor. However, in practical combustion systems, multiple fuel injectors are used. In this situation, individual injector impedance can be modified to produce a different dynamic response from individual flames. The resulting impedance mismatch prevents all injectors from strongly coupling to the same acoustic mode. In principle, this mismatch should reduce the amplitude of dynamics and may expand the operating margin for stable combustion conditions. In this paper, a 30 kW *laboratory combustor with two premixed fuel injectors is used to study the effect of impedance mismatch on combustion stability. The two fuel injectors are equipped with variable geometry resonators that allow a survey of dynamic stability while changing the impedance of the individual fuel systems. Results demonstrate that a wide variation in dynamic response can be achieved by combining different impedance fuel injectors. A base line 7% rms pressure oscillation was reduced to less than 3% by mismatching the fuel impedance.*
[DOI: 10.1115/1.2771249]

1 Introduction

Methods to control combustion dynamics are an important consideration in the design and operation of low-emission gas turbine combustors. Numerous papers in recent years have considered both passive [1–4] and active methods [5–9] to reduce unwanted pressure oscillations that typically accompany lean-premixed combustion. Through a variety of mechanisms, lean-premixed combustion is particularly prone to dynamic oscillations. Pressure fluctuations p' can easily produce heat release perturbations q', providing additional energy to drive the oscillation in a feedback loop between p' and q'. Many passive and active techniques seek to change the phase angle in the feedback between p' and q'. For example, changes to the convective time lag are a well-understood method to change the phase angle and can produce stability in some engines [4]. In a similar manner, the phase angle can be modified by changing the fuel system impedance. The fuel system impedance controls both the magnitude and phase of fuel pulses produced by pressure perturbations in the premixer and can be selected to enhance stability during the combustor development [10].

Fixed adjustments to the phase angle can successfully control oscillations if no other parameters in the feedback loop change. However, in practical applications, engines must operate at different fuel/air ratio and different ambient conditions, with modest changes in fuel composition. Depending on the engine, the effect of these variables has been shown to modify the combustion stability [11], as observed in rig tests [12]. Because these effects cannot be counteracted by a fixed adjustment to phase angle, it has been suggested that variable adjustment to the fuel system impedance may offer a practical method to "tune" the combustor dynamics, allowing operation over a wider range of ambient conditions and fuel composition [13,14]. In an earlier paper [13], the present authors studied a variable geometry resonator attached to the fuel supplying the premixer. Without adjusting the resonator, the combustor oscillated over a wide range of operating conditions. By adjusting the resonant properties of the fuel system, oscillations were attenuated over a significant portion of the operating map. Changes to the fuel system impedance were shown to change the phase angle of fuel/air perturbations by 60 degs. Images of the flame were used to show that regions of damping were produced in the flame as a consequence of changing the fuel system impedance. While these results are encouraging, changes to the phase angle through adjustments in the fuel system impedance have definite limitations. Combustors with closely spaced natural acoustic frequencies can simply oscillate at a new frequency in response to changes in the phase angle [15]. In other words, retuning the fuel system can simply tune the combustor to oscillations at a different frequency.

Recognizing the limits to adjusting the phase angle, it is possible to exploit the fact that practical engine applications use multiple fuel injectors. The idea is to produce a different dynamic response on individual fuel injectors, insuring that no single injector can strongly couple to a given acoustic mode. Berenbrink and Hoffmann [16] have shown that multiple premix injectors can be fitted with different length extension tubes, producing different convective time lags. This modification allowed a gas turbine engine to operate at conditions that had otherwise been dynamically unstable. Lovett and Uznanski [17] used multiple fuel paths to

Contributed by the International Gas Turbine Institute of ASME for publication in the JOURNAL OF ENGINEERING FOR GAS TURBINES AND POWER. Manuscript received June 30, 2006; final manuscript received July 21, 2006; published online January 16, 2008. Review conducted by Lee Langston. Paper presented at the ASME Turbo Expo 2005: Land, Sea and Air (GT2005), Reno, NV, June 6–9, 2005, Paper No. GT2005-68386.

Copyright © 2008 by ASME

Downloaded 02 Jun 2010 to 171.66.16.107. Redistribution subject to ASME license or copyright; see http://www.asme.org/terms/Terms_Use.cfm

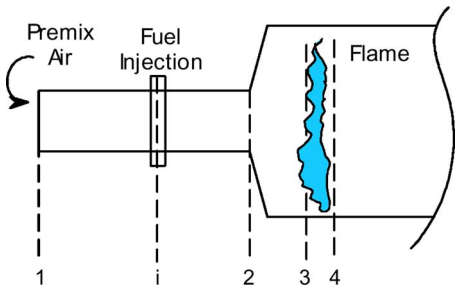

Fig. 1 Geometry of combustor model, showing the nomenclature for a single fuel injector. Multiple fuel injectors are analyzed in the same manner.

produce different dynamic responses in two different fuel paths, again minimizing the dynamic response to any single acoustic frequency. This approach reduced the dynamics for select values of the flow rate in the secondary fuel path.

This paper also considers the effects of fuel system impedance on dynamics. Unlike prior studies, this paper considers multiple injectors, adjusted to give different dynamic responses. As outlined above, this approach has the potential advantage of avoiding the problem associated with impedance adjustment, i.e., retuning the dynamics to a new combustor frequency. Because the individual injectors can be dynamically mismatched, it is possible to enhance stability because the injectors are not strongly coupled to any given frequency. The success of the technique obviously depends on the extent of the imposed injector impedance adjustment.

To assess the potential of this concept, Sec. 2 presents a model of the dynamic response for two fuel injectors with variable impedance fuel supply. This model shows that impedance tuning on two injectors can produce a significant difference between them and may enhance combustion stability. This expectation is tested experimentally on a laboratory combustor using two fuel injectors, which is described in Sec. 3, with the results presented in Sec. 4. The focus of this paper is gaseous-fueled premix injectors. Similar concepts would be difficult to apply to liquid-fueled injectors. Liquid fuels are nearly incompressible, thereby having limited dynamic responses at frequencies of interest.

2 Model of Two-Injector Dynamics

The response of an individual fuel injector has been fully analyzed in prior publications [13,22], and will only be briefly reviewed here. The nomenclature is shown in Fig. 1. Air entering at the left (station 1) is mixed with fuel at station i before proceeding to the dump plane (station 2) and then being consumed in an assumed disk-shaped flame between stations 3 and 4. More realistic flame geometries can also be considered, but the intent here is to develop a model describing the response of the fuel and air injection. The instantaneous heat release of the flame is then the product of the mass flow entering the flame and the heat of reaction,

$$Q = \rho_3 U_3 A_{\mathrm{fl}} Y_{\mathrm{f3}} \Delta H_f \tag{1}$$

Writing the variables as the sum of average and fluctuating components (e.g., $U = U_{\mathrm{av}} + u'$, etc.), the perturbation quantities are to the first order,

$$\frac{q'}{Q_{\mathrm{av}}} = \frac{\rho'_3}{\rho_{\mathrm{av}}} + \frac{Y'_{\mathrm{f3}}}{Y_{\mathrm{f3.av}}} + \frac{u'_3}{U_{\mathrm{3.av}}} + \frac{A'_{\mathrm{fl}}}{A_{\mathrm{fl.av}}} \tag{2}$$

The terms on the right represent the heat release fluctuation due to the following physical processes (left to right): (1) compression of the mixture due to pressure perturbations, (2) variation in the mass fraction of fuel arriving at the flame, (3) variation in the rate of mixture entering a fixed position flame front, and (4) fluctuations in the area of the flame. Converting to a frequency domain analysis, an acoustic model of the premixer is used to express the first three terms as a function of the pressure perturbation in the combustor and the impedance of various components. Pockets of rich or lean mixture are convected with a time lag τ from station i to the flame at station 3. The resulting equation for the heat release perturbation is as follows:

$$\frac{q'}{Q} = \left[\frac{1}{\gamma} + \frac{P_{3.\mathrm{av}}}{m_{3.\mathrm{av}}} \left(\frac{1}{q_{\mathrm{st}} \phi Z_{\mathrm{fi}}} - \frac{1}{Z_{\mathrm{ai}}} \right) \right] \left(\Psi_{0.0} + \Psi_{0.1} \frac{1}{Z_3} \right) e^{-j\omega\tau} + \frac{P_{3.\mathrm{av}}}{Z_3 m_{3.\mathrm{av}}} \left] \frac{p'_3}{P_{3.\mathrm{av}}} + \frac{A'_{\mathrm{fl}}}{A_{\mathrm{fl.av}}} \right. \tag{3}$$

The Ψ terms are the elements of an acoustic transfer matrix [18] and are defined by the acoustic geometry between station i and station 3. Three terms inside the square brackets are analogous to the first three terms in Eq. (1). The reciprocal of the specific heat represents the change in reaction rate that accompanies the increasing density produced by pressure perturbations. The term multiplied by $e^{-j\omega\tau}$ represent the production and transport of fuel/air ratio perturbations. Note that this term is an effective difference between the (reciprocal) air and fuel impedance at station i. If the impedance of these terms is large, the response is small, meaning that the fuel/air perturbations are small. For example, choking both the fuel and the air supply would correspond to large impedance, such that pressure perturbations could not modulate the flow of fuel or air. Note that practical injectors cannot use a choked supply of air, so that the air flow will typically be modulated in accordance with Z_{ai}. The concept of tuning the fuel system impedance enters through the term Z_{fi}, which is controlled by the geometry of the fuel system. It is necessary to design a nominal value of $q_{\mathrm{st}} \phi Z_{\mathrm{fi}}$ to be comparable to Z_{ai} so that adjustments to Z_{fi} can have an impact on the overall dynamics [13].

The last term inside the square brackets in Eq. (3), $P_{3.\mathrm{av}}/Z_3 m_{3.\mathrm{av}}$, represents the variation of flow entering a (assumed) fixed flame position. The mass flow of fuel/air entering the flame is inversely proportional to the impedance at station 3. If the impedance at this position is low, small pressure perturbations will produce relatively large acoustic velocity perturbations. It is likely that this term would need to be modified to account for translation or distortion of the flame in the oscillating flow [19]. Direct translation of the flame would reduce the magnitude of this term, while distortion could be accounted for in the flame area term $A'_{\mathrm{fl}}/A_{\mathrm{fl.av}}$. The size of these terms is difficult to quantify in practical applications, and they may play an appreciable role in the overall combustion response, particularly where injectors can interact [20]. While the exact contribution of these terms is difficult to quantify, it has been shown that adjustments to the fuel impedance [13,14] or fuel time lag [4] play a significant role in stabilizing the flame. For this reason, in the present analysis, it is most useful to consider just the *change* in the term multiplying $e^{-j\omega\tau}$ as the fuel system impedance is modified. These terms are subsequently referred to as the convective terms. Where convection of fuel perturbations are known to contribute significantly to dynamics, adjusting the convective terms will be useful to modify the dynamics.

The preceding discussion has focused on the response of an individual fuel injector, and was presented with more details in an earlier paper [13]. The analysis is now extended to consider multiple fuel injectors, particularly two injectors supplying a premixed flame in a common combustor. For acoustic frequencies typical of gas turbine dynamics ($<\sim 1000$ Hz), the acoustic wavelength is long enough so that adjacent flames experience approximately the same acoustic pressure. Thus, from the standpoint of linear acoustics, the heat release from each flame contributes in an additive fashion to the acoustic energy. Equation (3) is written for each injector, and the respective heat release from each injector is added to produce a net heat release perturbation in response

Downloaded 02 Jun 2010 to 171.66.16.107. Redistribution subject to ASME license or copyright; see http://www.asme.org/terms/Terms_Use.cfm

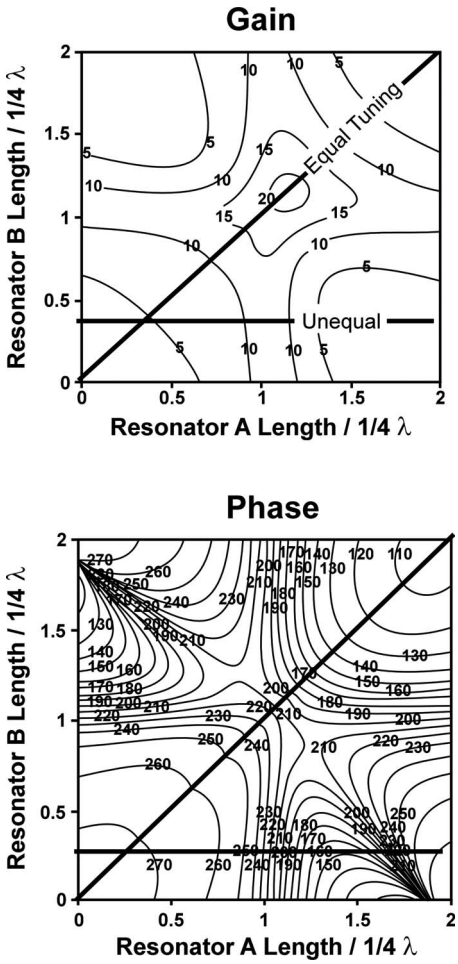

Fig. 2 Gain and phase of transfer function for two fuel injectors showing the effects of resonator tuning. Diagonal and horizontal lines show equal tuning and one unequal situation.

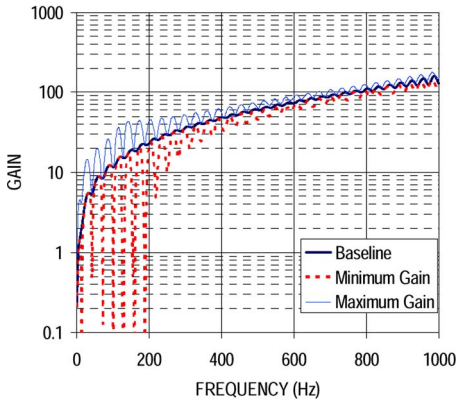

Fig. 3 Plot of calculated transfer function gain for various resonator length combinations. Base line compared to observed minimum and maximum gain.

to a common pressure p'_3. Excluding the uncertain contribution of the flame area term $A'_{fl}/A_{fl.av}$, and denoting the two injectors as A and B, the resulting response is

$$\frac{q'}{Q_{av}} = \{[\cdots A \cdots] + [\cdots B \cdots]\}\frac{p'_3}{P_{av}} \tag{4}$$

The terms $[\cdots A \cdots]$ and $[\cdots B \cdots]$ represent the evaluation of the terms in square brackets from Eq. (3) for each individual injector A and B. The sum of the A and B terms define the transfer function between p_3'/P_{av} and q'/Q_{av}. As defined above, the convective terms (multiplying $e^{-j\omega\tau}$) in Eq. (4) were evaluated numerically for the fuel injector/combustor geometry that is described in Sec. 3. The results for a 210 Hz excitation and a representative flow rate (20 m/s bulk premixer velocity, $\phi=0.8$) are presented in Fig. 2. The gain and phase of the convective term is plotted against the resonator lengths for injectors A and B. These curves were generated by evaluating Eq. (4) with a standard mathematical software (MATHCAD) and then by plotting the results.

The resonator lengths are normalized by the quarter wavelength at 210 Hz. The diagonal and horizontal lines have been added for reference, with the diagonal line corresponding to equally adjusted fuel impedance. This is analogous to adjusting the impedance on one injector, having twice the size. Following the diagonal, the gain rises appreciably to a maximum of more than 20. The phase changes from 270 deg to 110 deg along the diagonal but is accompanied by large values of gain in the middle of the phase change. Large values of gain produce large fluctuation in fuel/air ratio, which are destabilizing unless they have the correct phase. Thus, equal tuning of the resonators provides a limited choice for combnations of gain and phase.

Considering next the situation where the resonators are tuned differently (the horizontal line), note that appreciable phase changes can also be achieved, but with lower gain. Following the horizontal line, representing normalized resonator lengths $1.5 < L_A < 2$, the phase can be adjusted from 150 deg to 250 deg while the gain is less than 5. Thus, compared to equal tuning, it is possible to produce a wide variation in phase at a relatively constant or small gain. These results suggest some advantage to mistuning the fuel system impedance compared to adjusting all the resonators equally.

Figure 2 corresponds to a single oscillating frequency. An important consideration is that actual combustors may operate at different frequencies and that the benefits of mistuning will be different at different operating frequencies. For this reason, an algorithm was developed to evaluate a combination of resonator lengths over a range of frequencies. Again, neglecting the term $A'_{fl}/A_{fl.av}$, the transfer function (Eq. (4)) was calculated for variable lengths L_A and L_B over a range of frequencies up to 1000 Hz. The lengths were varied in 1 cm increments from 0 m to 1 m. At each length combination, the gain was calculated, and in this manner it was possible to find the maximum and minimum gain that was possible for resonator tuning combinations at any frequency. This corresponds to physically tuning the resonators at arbitrary lengths until the greatest and lowest responses are achieved. The results of this calculation are shown in Fig. 3 and demonstrate that at most frequencies, it was possible to produce a gain that was significantly larger than the base line, i.e., zero-length resonators.

This should be expected—it is possible to set up a resonance in the fuel system that contributes to the gain. However, it was also possible at most frequencies to locate a resonator tuning combination that produced a gain equal or less than the base line. Lower gains are generally advantageous; however, stability depends on the phase of the response, as well as the actual combustion and acoustic feedback. Given the uncertain nature of the combustion response, it is not possible to interpret Fig. 3 as a guarantee for improved combustion stability, but in combination with Fig. 2, these results show that resonator mistuning merits the experimental evaluation described next.

3 Experimental Description

The experimental setup, shown in Fig. 4, is similar to that described in an earlier paper [13]. The significant difference in this work is that two fuel premixers are located side by side in a common combustor tube, compared to the earlier setup, which used a single fuel injector. Air enters the annulus (dimensions

Downloaded 02 Jun 2010 to 171.66.16.107. Redistribution subject to ASME license or copyright; see http://www.asme.org/terms/Terms_Use.cfm

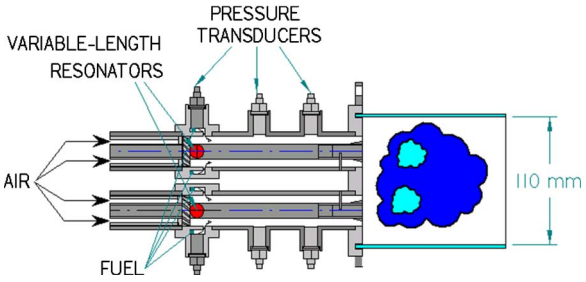

Fig. 4 Layout of combustor using two premix fuel injectors

12.7×26.6 mm) of both premixers through a sintered metal plate that serves as the acoustic boundary for the premixer that chokes the flow. Downstream of the choke plate, the air is swirled by a slotted disk that is 6.4 mm thick along the flow axis. Fourteen slots, with a kerf width of 1.37 mm, are cut at 45 deg to the flow axis to generate swirling flow. Fuel is injected from 15 holes with 1.2 mm diameters. These holes were sized to allow jet penetration and mixing before the premix fuel enters the combustor. The downstream end of the premix center body is terminated with a conical expansion made from a commercial compression fitting ferrule. The ferrule axial length is 7.3 mm with a larger outside diameter of 17.3 mm and serves to provide a flow acceleration at the tip of the premixing annulus, which prevents flame anchoring inside the premixer passage. This insures consistent flame anchoring at the step expansion and has been shown to improve data repeatability. The combustor is a quartz tube (11 cm inside diameter×0.6 m long) that exits to a 36 cm diameter housing, which ducts both the exhaust products and acoustic noise out of the laboratory building.

As shown in Fig. 4, both of the individual fuel injectors are outfitted with three pressure transducers, Kistler Model 206. Two of the transducers are located in the barrel of the premixer annulus. These transducers can be used in a two-microphone method to calculate the acoustic pressure and velocity at any point along the axis of the premixer. These calculations are subject to the limits of one-dimensional acoustics and have been verified for nonreacting cases by directly measuring the pressure at a third position in a similar setup as the premixer. In Fig. 4 a third transducer is located in the plenum that supplies fuel to the 15 holes that inject fuel into the annulus. This transducer can be used to directly measure the pressure supplying the fuel and record changes as the resonator length is changed. In Fig. 4, the variable length resonators are attached to the plenum supplying the fuel injection holes and would extend out of the plane of the figure.

The fuel injection and resonator details are shown in Fig. 5. Fuel enters a plenum region that is sized to distribute the fuel evenly to 15 holes with 1.2 mm diameters into the air premixing passage. Using the jet penetration expressions from Lefebvre [21], the fuel jets are designed to penetrate into the middle of the annular premix region and should be well mixed before entering the combustion zone. A quarter-wave resonator, with variable length (0–0.8 m) and a diameter of 10.6 mm, is attached to the plenum

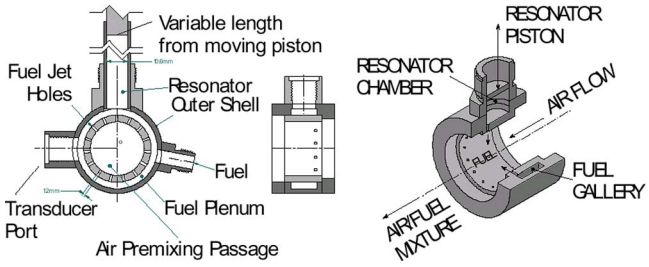

Fig. 5 Details of fuel premixer, with variable length resonator

region. Changing the length of this resonator by moving the position of the piston will modify both the magnitude and phase of fuel perturbations. The significant difference between the fuel injector shown in Fig. 5 and the prior work reported in Richards et al. [22] is the much lower acoustic resistance of the fuel jets. More jets, resulting in a lower pressure drop, are used in this design to counteract the large air response. It is emphasized that the choice of jet pressure drop is a tradeoff with both premixing requirements and the air response magnitude. The specific choice of jet diameter, resonator diameter, and fuel plenum size are made by comparing the size of terms in Eq. (3) and then selecting the parameters accordingly to achieve control and still produce an acceptable premixing. Based on jet penetration correlations, the fuel jets used here were designed to produce a spatial mass-fraction variation of 10% across the jet at the end of the premixer barrel.

Careful attention was given to producing an identical arrangement in both fuel injector assemblies. The flow split on the air side was controlled with metered orifices upstream of the fuel injectors. To insure that the fuel flow split to each nozzle was identical to the others, precision machined orifices were honed until the fuel flow matched to within 1%. In spite of these precautions, it was not possible to insure an exact symmetry between the injector dynamic response. The fuel modules themselves were tested for dynamic response by exciting the premixing air in a cold-flow test and measuring the pressure produced in the "galley," which supplies the holes (Richards et al.[22]). The result of these tests showed that the measured response of the fuel injector ports differed slightly; for example, the respective steady-state discharge coefficients were 0.49 and 0.46. As shown by Laudien et al.[23], the difference between square and rounded corners on an acoustic orifice can produce a significant change in the acoustic loss, making it very difficult to produce identical acoustic responses from the fuel injectors using 15 orifices. Recognizing that these limits would exist in any practical application of this concept, tests are described below with the recognition that an exact symmetry in the response is not likely or needed. The intent of the resonator tuning is to create dynamically different responses among injectors. However, for research purposes, it was desirable to produce an identical response to simplify data interpretation.

For practical application of the tuning concept, it would be ideal to simply add a resonator as a branch to an existing fuel system, thereby locating the resonator outside of the engine casing. Whether this could be achieved or not requires a detailed analysis of the fuel system of interest. Calculations not reported here show that some practical fuel injector geometries may allow this option, but must consider the combined response of the added resonator and existing fuel system.

Since testing was performed at an atmospheric pressure, without air preheating, it was expected that emission levels would not be representative of a genuine gas turbine application: thus, no attempt was made to record emissions. Instead, the focus of these tests was to demonstrate the benefit of impedance tuning on dynamics so that subsequent testing could be developed on a high-pressure gas turbine application. Calculations were carried out to evaluate the behavior of resonator tuning on a high-pressure fuel injector. These calculations suggest that no fundamental barriers exist to applying the same concepts to fuel injectors operating at gas turbine pressure and temperature conditions.

4 Experimental Results

The resonator position will be referenced by indicating the length of the quarter-wave tube resonators ($L_A.L_B$). The combustor was operated initially with the resonators in the (0,0) position. An operating map was recorded over the range of equivalence ratio and bulk nozzle velocities shown in Fig. 6. Because the fuel was supplied through choked orifices, with a limited supply pressure, it was not possible to cover an arbitrary range of bulk velocity and equivalence ratio. Thus, the higher velocity cases were

Downloaded 02 Jun 2010 to 171.66.16.107. Redistribution subject to ASME license or copyright; see http://www.asme.org/terms/Terms_Use.cfm

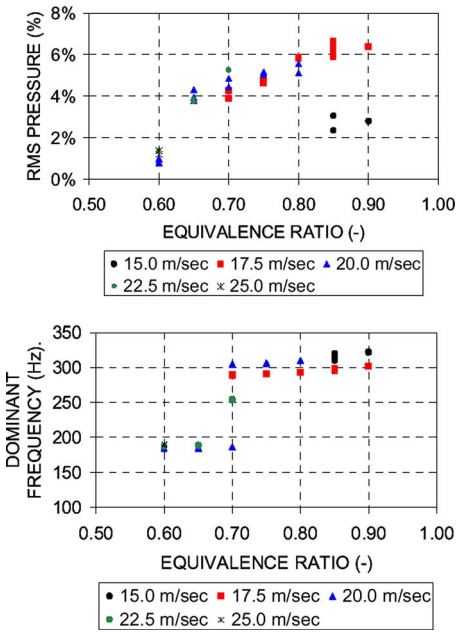

Fig. 6 Observed combustor rms pressure and oscillating frequency versus equivalence ratio at various bulk velocities. Resonator position (0,0).

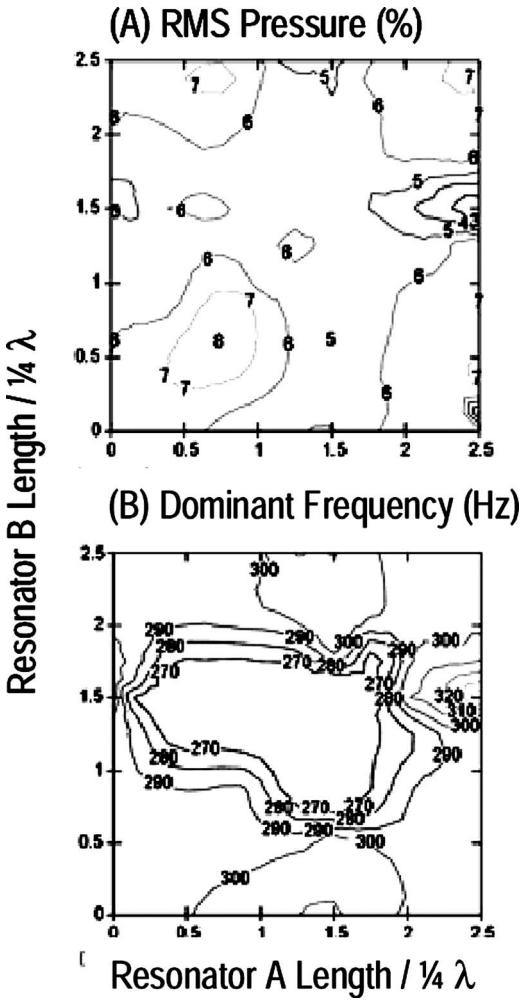

Fig. 7 Contour plots of the rms pressure (*a*) and oscillating frequency (*b*) as a function of the resonator lengths. The resonator length is normalized by the 1/4 wavelength at 300 Hz (0.371 m).

limited to lower equivalence ratios. The plot shows that the combustor was unstable over much of the operating range, with a rms pressure ranging from 1% to 7% of the ambient pressure. The corresponding frequencies ranged from 200 Hz to 300 Hz, changing with the operating conditions. To provide an especially challenging test of the concept of adjusting the resonators, the operating condition with the highest rms was selected for further study. As shown in the graph, this condition corresponds to a bulk velocity of 17.5 m/s and an equivalence ratio of 0.85, and will be referred to as the base line operating condition.

A parametric study of the effect of the resonator mismatch was carried out at the base line operating condition. The contour plots of Fig. 7 show the rms pressure and dominant frequency as the resonator lengths are varied. Data were collected over a matrix of resonator lengths, with the observed rms and frequency recorded in three replicate tests. The results were averaged at each combination of resonator lengths, and the contour plots were produced using standard plotting routines. For convenience, the resonator lengths are normalized by the quarter wavelength of the sound in the fuel at 300 Hz (0.366 m). The actual operating frequency ranges from 270 Hz to 340 Hz, so this normalization is only an approximate guide to the structure of the wave in each resonator. Normalized in this manner, the resonator length=1 should produce a quarter-wave response in the resonator at 300 Hz.

The most important feature of the graph in Fig. 7(*a*) is that the rms pressure can be significantly reduced compared to the base line. Note that the (0,0) position is characterized by a rms pressure of 7%, but at the (2.5, 1.5) position, a region exists where the rms pressure is reduced to less than 3% by the impedance mismatch. Again, this result was achieved at the equivalence ratio/flow rate where the strongest base line oscillation was observed (Fig. 6). These results demonstrate the potential of impedance mismatch to reduce oscillating pressures. Equal tuning at this condition did not reduce dynamics and, in fact, led to a modest increase at (0.75, 0.75) up to 8% rms.

From theoretical considerations, it should be expected that Fig. 7(*a*) is symmetric about a line where both resonator lengths are equal (refer to the discussion of Fig. 2). However, the experimental data are only approximately symmetric. Note that the contours form islands that are centered on the symmetry line for lengths less than (1.5, 1.5). Also note that the highest rms occurs on the symmetry line, as expected. At this condition, both resonators are working together to augment the dynamics. For lengths longer than (1.5, 1.5), the symmetry is not as good. The dramatic reduction at (2.5, 1.5) is not as pronounced across the symmetry line, but it is still observed; see (1.5, 2.5). The precise reasons for the lack of symmetry may be related to the slight difference in the acoustic response of individual fuel modules, which could not be avoided in manufacturing (see Sec. 3). Visual images of the flames, viewed at a right angle to the flow axis, appeared to be symmetric. Future studies will include time-resolved images of the flame at these two conditions to determine why the response is not completely symmetric.

The observed oscillating frequencies (Fig. 7(*b*)) are also an important consideration. As shown in Fig. 3, the transfer function of the fuel injection process can be optimized with resonator tuning at any given frequency. However, the stability of the closed-loop combustion system must consider the acoustic feedback at all frequencies, simultaneously. Optimal resonator tuning can produce a very low net response at a particular frequency, but neighboring frequencies may not be attenuated as well. Because the combustor acoustics can provide feedback over a range of frequencies, specific resonator tuning arrangements may lead to shifts in the oscillating frequency, as observed experimentally in Fig. 7. Frequencies range from 270 Hz to 310 Hz as the resonator tuning is

Downloaded 02 Jun 2010 to 171.66.16.107. Redistribution subject to ASME license or copyright; see http://www.asme.org/terms/Terms_Use.cfm

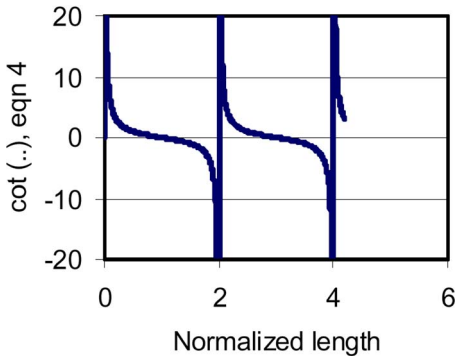

Fig. 8 Plot of the cotangent term in Eq. (5) showing the repeating impedance value for normalized lengths greater than 2

changed. A subtle point to consider is what happens when either (normalized) resonator length equals 2. When the resonator length equals 2, the resonator will behave like a quarter-wave tube excited at twice the quarter-wave frequency, producing very high impedance at the mouth of the resonator. It might be expected that the combustor should behave in the same manner as when the length is zero, which also produces high (infinite) impedance at the resonator mouth (it is a hard boundary). The impedance of an idealized quarter-wave tube can be calculated as in standard acoustic textbooks [24] as

$$Z_{\text{res}} = -j\frac{\cot(\omega L_{\text{res}}/c)}{\rho A_{\text{res}}} \tag{5}$$

Figure 8 shows just the cotangent term in Eq. (5) at 300 Hz excitation. The data is plotted as a function of the resonator length L_{res}, again normalized by the quarter wavelength at 300 Hz. Note that the impedance is large at the zero length, as expected, and repeats beyond length equal to 2. Although the ideal resonator impedance repeats beyond 2, lengths 0 and 2 are fundamentally different in terms of the combustion response. When the resonator length is 0, the impedance is infinite at all frequencies because the resonator mouth is a hard boundary. When the resonator length is 2, the impedance is large only at the normalizing frequency of 300 Hz.[1] Because the combustor can oscillate at other frequencies, the resonator impedance will not necessarily mimic the hard boundary, which exists for all frequencies when the resonator length is zero. Furthermore, for a single frequency, it can be shown analytically that the net response of the fuel module (i.e., the resonator, the fuel galley, and the holes that inject the fuel) versus resonator length repeats with period 2, but is shifted from 0 due to the nonzero impedance of the fuel galley and holes.

The preceding discussion explains why both the frequency and rsm pressure data in Fig. 7 do not simply repeat the pattern from lengths $0<L<2$ and $L>2$. Note that in these data, the lowest rms pressure was observed for resonator lengths, which might not have been studied if it was assumed that the resonance would be similar for lengths greater than two quarter waves. Investigations of resonator tuning should therefore carefully consider the nature of acoustic resonance and the potential difference in combustion response at otherwise similar single-frequency resonator settings.

5 Summary and Conclusions

This paper reports the effect of mismatching the fuel system impedance on combustion dynamics. A theoretical analysis of the fuel injector response, without combustor feedback, shows that the net production of fuel/air perturbations can be significantly modified in both phase and gain by mistuning the individual fuel injectors. This was examined experimentally by operating a 30 kW atmospheric pressure combustor with two premix fuel injectors. Each injector was fitted with a variable geometry fuel resonator, allowing a study of the dynamics while resonator tuning was adjusted. A base line survey of equivalence ratio and velocity, with resonator volume equal to zero, was used to identify the strongest amplitude oscillation. This base line condition produced an oscillation of 7% at approximately 290 Hz. The base line operating condition was then used for a survey of resonator mistuning. It was found that selected combinations of resonator tuning could reduce the base line oscillation to less than 3% of ambient. An analysis of the data showed that the resonator tuning was only approximately symmetric with respect to the two injectors, and this is attributed to the difficulty of producing identical acoustic orifices in both premixers. The operating data also show that the oscillating combustion frequency changes with resonator tuning, and emphasize the need to consider the acoustic feedback of the combustor when planning resonator settings. In particular, it was shown that expected high-impedance resonator settings can be confounded by the complete fuel injector response (not just the resonator response) and frequency shifts to lower impedance values or vice versa.

Future work will evaluate how the combustion response changes on the individual injectors, using phase-resolved flame images to identify where combustion damping is produced. Combined with a model for acoustic feedback, these results should identify criteria needed for enhancing stability on arbitrary combustor applications.

Acknowledgment

This work was supported by the U.S. Department of Energy Turbine Program through Richard Dennis, Technology Manager. Expert experimental testing and setup was provided by Rick Addis

Nomenclature

A_{fl} = instantaneous flame area (m^2)
A'_{fl} = unsteady (time varying) component of flame area (m^2)
$A_{\text{fl.av}}$ = time averaged flame area (m^2)
A_{res} = area of the resonator mouth, Eq. (5) (m^2)
c = speed of sound (m/s)
f = frequency (Hz)
j = imaginary number suffix, square root of −1
L_A, L_B = length of resonators A and B, normalized as indicated in the text (-)
L_{res} = length of resonator ideal quarter-wave resonator, Eq. (5) (m)
m_{ai} = instantaneous air mass flow (kg/s) at the fuel injection station
m_{fi} = instantaneous fuel mass flow (kg/s) at the fuel injection station
$m_{i.\text{av}}$ = time averaged total mass flow (kg/s) at the fuel injection station
$m_{3.\text{av}}$ = time averaged total mass flow (kg/s) at the flame
$P_{3.\text{av}}$ = time averaged pressure (Pa) at the flame front
$p(t)$ = combustion chamber pressure (Pa) as a function of time
p' = unsteady (time varying) component of pressure (Pa)
p'_i = unsteady (time varying) component of pressure (Pa) at the fuel injection station
p'_3 = unsteady (time varying) component of pressure (Pa) at the flame front
Q = instantaneous heat release rate (W)

[1]Recall that the resonator lengths were normalized by the quarter wavelength at 300 Hz. Thus, the resonator mouth has very high impedance at length 2 only at 300 Hz. This corresponds to exciting a quarter-wave tube at twice its natural frequency.

Downloaded 02 Jun 2010 to 171.66.16.107. Redistribution subject to ASME license or copyright; see http://www.asme.org/terms/Terms_Use.cfm

Q_{av} = time averaged heat release rate (W)
q' = perturbation component of heat release rate (W)
q_{st} = stiochiometric fuel/air mass ratio (-)
t = time (s)
U_3 = instantaneous bulk gas velocity (m/s) at the flame front
$U_{3.av}$ = time averaged bulk gas velocity (m/s) at the flame front
u'_3 = unsteady (time varying) component of bulk gas velocity (m/s) at the flame front
Y_{f3} = instantaneous fuel mass fraction (-) at the flame front
Y'_{f3} = unsteady (time varying) component of fuel mass fraction (-) at the flame front
$Y_{f3.av}$ = time averaged fuel mass fraction (-) at the flame front
Z_{ai} = acoustic impedance (1/m s) of the premixer passage at the fuel injection station
Z_{fi} = acoustic impedance (1/m s) of the fuel injection port, at the premixer duct wall
Z_3 = acoustic impedance (1/m sec) of the combustion chamber at the flame front
ΔH_f = heat of reaction of the fuel (J/kg)
ϕ = equivalence ratio (-)
γ = ratio of specific heats (-)
ρ_3 = instantaneous gas density (kg/m^3) at the flame front
ρ'_3 = unsteady (time varying) component of gas density (kg/m^3) at the flame front
ρ_{av} = time averaged gas density (kg/m^3) at the flame front
τ = transport time (s) from fuel injection station to flame front
ω = circular frequency (radians), $2\pi f$
$\boldsymbol{\psi}$ = acoustic transfer matrix and associated elements

References

[1] Paschereit, C. O., and Gutmark, E., 2004, "The Effectiveness of Passive Combustion Control Methods," ASME Paper No. GT2004-53587.
[2] Scarinci, T., Freeman, D., and Day, I., 2004, "Passive Control of Combustion Instability in a Low Emission Aeroderivative Gas Turbine," ASME Paper No. GT2004-53767.
[3] Mongia, H. C., Held, T. J., Hsiao, G. C., and Pandalai, R. P., 2003, "Challenges and Progress in Controlling Dynamics in Gas Turbine Combustors," J. Propul. Power, **19**(5), pp. 822–829.
[4] Steele, R. C., Cowell, L. H., Cannon, S. M., and Smith, C. E., 2000, "Passive Control of Combustion Instability in Lean Premixed Combustors," ASME J. Eng. Gas Turbines Power, **122**(3), pp. 412–419.
[5] Seume, J. R., Vortmeyer, N., Krause, W., Hermann, J., Hantschk, C.-C., Zangl, P., Gleis, S., Vortmeyer, D., and Orthmann, A., 1998, "Application of Active Combustion Instability Control to a Heavy Duty Gas Turbine," ASME J. Eng. Gas Turbines Power, **120**(4), pp. 721–726.
[6] Jones, C. M., Lee, J. G., and Santavicca, D. A., 1999, "Closed-Loop Active Control of Combustion Instabilities Using Subharmonic Secondary Fuel Injection," J. Propul. Power, **15**(2), pp. 1–7.
[7] Cohen, J. H., Rey, N. M., Jacobson, C. A., and Anderson, T. J., 1999, "Active Control of Combustion Instabilities in a Liquid-Fueled Low-NO_x Combustor," ASME J. Eng. Gas Turbines Power, **121**(2), pp. 281–284.
[8] Shcherbik, D., Neumeier, Y., Lubarsky, E., Zinn, B. T., McManus, K., Fric, T. F., and Srinivasan, S., 2003, "Suppression of Instabilities in Gaseous Fuel High-Pressure Combustor Using Non-Coherent Oscillatory Fuel Injection," ASME Paper No. GT2003-38103.
[9] Richards, G. A., Thornton, J. D., Robey, E. A., and Arellano, L., 2004, "Open Loop Active Control of Combustion Dynamics on a Gas Turbine Engine," ASME Paper No. IMECE2004-59702.
[10] Black, S. H., 1993, "Apparatus for Reducing Fuel/Air Concentration Oscillations in Gas Turbine Combustors," U. S. Patent No. 5,211,004.
[11] Nerd, L. O., and Andersen, H. G., 2004, "A Study of Parameters Affecting the Combustion Stability and Emissions Behavior of Alstom Heavy-Duty Gas Turbines," ASME Paper No. GT2004-53228.
[12] Janus, M. C., Richards, G. A., Yip, M. J., and Robey, E. H., 1997, "Effects of Ambient Conditions and Fuel Composition on Combustion Stability," ASME Paper No. 97-GT-266.
[13] Richards, G. A., Straub, D. L., and Robey, E. H., 2003, "Control of Combustion Dynamics Using Fuel System Impedance," ASME Paper No. 2003-38521.
[14] Lee, J. G., Kim, K., and Santavicca, D. A., 2002, "A Study of the Role of Equivalence Ratio Fluctuations During Unstable Combustion in a Lean Premixed Combustor," AIAA Paper No. 2002-4015.
[15] Richards, G. A., Straub, D. L., and Robey, E. H., 2003, "Passive Control of Combustion Dynamics in Stationary Gas Turbine Combustors," J. Propul. Power, **19**(5), pp. 795–810.
[16] Berenbrink, P., and Hoffmann, S., 2000, "Suppression of Dynamics Combustion Instabilities by Passive and Active Means," ASME Paper No. 2000-GT-0079.
[17] Lovett, J. A., and Uznanski, K. T., 2002, "Prediction of Combustion Dynamics in a Staged Premixed Combustor," ASME Paper No. GT-2002-30646.
[18] Munjal, M. L., 1987, *Acoustics of Ducts and Mufflers*, Wiley, New York.
[19] Scheurmans, B. H., Polifke, W., and Paschereit, C. O., 1999, "Modeling Transfer Matrices of Premixed Flames and Comparison with Experimental Results," ASME Paper No. 99-GT-132.
[20] Kunze, K., Hirsch, C., and Sattelmayer, T., 2004, "Transfer Function Measurements on a Swirl Stabilized Premix Burner in an Annular Combustion Chamber," ASME Paper No. GT2004-53106.
[21] Lefebvre, A. H., 1999, *Gas Turbine Combustion*, Taylor & Francis, Philadelphia, PA.
[22] Richards, G. A., Straub, D. L., and Robey, E. H., 2001, "Dynamic Response of a Premix Fuel Injector," ASME Paper No. 2001-GT-0036.
[23] Laudien, E., Pongratz, R., Pierro, R., and Preclik, C., 1995, "Experimental Procedures Aiding the Design of Acoustic Cavities," *Liquid Rocket Engine Combustion Instability*, V. Yang and W. Anderson, eds. AIAA, Washington, DC, pp. 377–399.
[24] Kinsler, L. E., Frey, A. R., Coppens, A. B., and Sanders, J. V., 1982, *Fundamentals of Acoustics*, Wiley, New York.

Downloaded 02 Jun 2010 to 171.66.16.107. Redistribution subject to ASME license or copyright; see http://www.asme.org/terms/Terms_Use.cfm

An Optimal Orthogonal Decomposition Method for Kalman Filter-Based Turbofan Engine Thrust Estimation

Jonathan S. Litt
US Army Research Laboratory,
Glenn Research Center,
21000 Brookpark Road, MS 77-1,
Cleveland, OH 44135

A new linear point design technique is presented for the determination of tuning parameters that enable the optimal estimation of unmeasured engine outputs, such as thrust. The engine's performance is affected by its level of degradation, generally described in terms of unmeasurable health parameters related to each major engine component. Accurate thrust reconstruction depends on knowledge of these health parameters, but there are usually too few sensors to be able to estimate their values. In this new technique, a set of tuning parameters is determined that accounts for degradation by representing the overall effect of the larger set of health parameters as closely as possible in a least-squares sense. The technique takes advantage of the properties of the singular value decomposition of a matrix to generate a tuning parameter vector of low enough dimension that it can be estimated by a Kalman filter. A concise design procedure to generate a tuning vector that specifically takes into account the variables of interest is presented. An example demonstrates the tuning parameters' ability to facilitate matching of both measured and unmeasured engine outputs, as well as state variables. Additional properties of the formulation are shown to lend themselves well to diagnostics.
[DOI: 10.1115/1.2747254]

Introduction

In-flight estimation of unmeasurable turbofan engine outputs, such as thrust, is difficult because the values depend on the degradation level of the engine, which is often not known accurately. Degradation is generally defined in terms of off-nominal values of health parameters, such as efficiency and flow capacity, related to each major engine component. It is possible to estimate these health parameter deviations, given that there are at least as many sensors as parameters to be estimated. In standard engine installations, however, there are typically fewer sensors than health parameters, making accurate estimation impossible. An approach used in this situation is to select a subset of health parameters to estimate, assuming the others remain unchanged. If any of the unaccounted-for health parameters deviate from nominal, their effect will be captured to some extent in the estimated subset. As a result, the estimated values will no longer represent the true health parameter deviations. There are examples in the literature of a subset of health parameter "tuners" being used to reconstruct performance variables such as thrust [1–3], but this approach of health parameter subset selection is much better established as a diagnostic tool for gas path analysis [4–6], where studies have determined which health parameters give good indications of certain faults for particular types of turbine engines [7–9].

When a Kalman filter is used to estimate the subset of health parameters, the estimates of measured outputs will usually be good, i.e., the sensed outputs and the recreated values obtained using the health parameter estimates will match, even if the health parameter estimates themselves are inaccurate. However, good estimation of sensed outputs does not guarantee that the estimation of unmeasured outputs will be accurate. Since thrust is affected by the level of degradation, poor health parameter estimation can result in poor thrust reconstruction. It might be possible to determine a subset of health parameters that produces good thrust reconstruction even when all health parameters deviate, but this is a time-consuming, empirical, trial-and-error process that gives no guarantee about the optimality of the result given the potential range of health parameter deviations and operating conditions.

The main issue that affects the estimation accuracy is that the total influence of the health parameters needs to be approximated using fewer variables. The selection of a subset of health parameters is not a general approach to solving this problem as long as all health parameters may deviate. We would like to derive a set of tuning parameters (not necessarily a subset of health parameters) that is smaller in dimension than the set of health parameters, but retains as much information as possible from that original set.

The following sections of this paper describe and formulate the thrust estimation problem mathematically, and then outline a new approach to the solution using singular value decomposition to obtain an optimal set of tuners. Following that, a concise design process is described that generates a set of optimal tuners at each operating (linearization) point, explicitly including all variables of interest; these tuners are incorporated into the Kalman filter to provide the optimal estimates. The technique is then demonstrated through an example. After the example, there is general discussion about the technique that covers other applications, such as its use as a diagnostic tool. Finally, conclusions are presented.

Contributed by the International Gas Turbine Institute of ASME for publication in the JOURNAL OF ENGINEERING FOR GAS TURBINES AND POWER. Manuscript received January 23, 2006; final manuscript received March 2, 2007; published online December 26, 2007. Review conducted by Dilip R. Ballal. Paper presented at the ASME Turbo Expo 2005; Land, Sea and Air (GT2005), June 6–9, 2005, Reno, NV Paper No. GT2005-68808.

Problem Development

For a linear point design or a piecewise linear state variable model, the equations of interest are

Copyright © 2008 by ASME

Downloaded 02 Jun 2010 to 171.66.16.107. Redistribution subject to ASME license or copyright; see http://www.asme.org/terms/Terms_Use.cfm

$$\dot{\boldsymbol{x}} = A\boldsymbol{x} + B\boldsymbol{u} + L\boldsymbol{p} + \boldsymbol{e}$$

$$\boldsymbol{y} = C\boldsymbol{x} + D\boldsymbol{u} + M\boldsymbol{p} + \boldsymbol{w}$$

$$\boldsymbol{z} = E\boldsymbol{x} + F\boldsymbol{u} + N\boldsymbol{p} \tag{1}$$

where $\boldsymbol{x}$ is the vector of state variables, $\boldsymbol{u}$ is the vector of control inputs, $\boldsymbol{y}$ is the vector of measured outputs, and $\boldsymbol{z}$ is the vector of auxiliary (unmeasurable or at least unmeasured) model-based outputs. The vector $\boldsymbol{p}$ represents the engine health parameters, which induce shifts in other variables as the health parameters move away from their nominal values. The vector $\boldsymbol{e}$ represents white process noise with covariance Q, and $\boldsymbol{w}$ represents white measurement noise with covariance R. The matrices A, B, C, D, E, F, L, M, and N are of appropriate dimension.

As the health parameter vector $\boldsymbol{p}$ is an unknown input to the system, we would like to be able to estimate it since it affects unmeasurable parameters such as thrust. The health parameters may be treated as a set of biases, and thus are modeled without dynamics. With this interpretation, we can represent Eq. (1) as

$$\begin{bmatrix} \dot{\boldsymbol{x}} \\ \dot{\boldsymbol{p}} \end{bmatrix} = \begin{bmatrix} A & L \\ 0 & 0 \end{bmatrix} \begin{bmatrix} \boldsymbol{x} \\ \boldsymbol{p} \end{bmatrix} + \begin{bmatrix} B \\ 0 \end{bmatrix} \boldsymbol{u} + \boldsymbol{e} = A_{\text{aug}}\boldsymbol{x}_{\text{aug}} + B_{\text{aug}}\boldsymbol{u} + \boldsymbol{e}$$

$$\boldsymbol{y} = [C\ M] \begin{bmatrix} \boldsymbol{x} \\ \boldsymbol{p} \end{bmatrix} + D\boldsymbol{u} + \boldsymbol{w} = C_{\text{aug}}\boldsymbol{x}_{\text{aug}} + D\boldsymbol{u} + \boldsymbol{w}$$

$$\boldsymbol{z} = [E\ N] \begin{bmatrix} \boldsymbol{x} \\ \boldsymbol{p} \end{bmatrix} + F\boldsymbol{u} = E_{\text{aug}}\boldsymbol{x}_{\text{aug}} + F\boldsymbol{u} \tag{2}$$

This new system has at least as many eigenvalues at the origin as there are elements of $\boldsymbol{p}$ (the eigenvalues of A_{aug} are the eigenvalues of A plus an additional $\dim(\boldsymbol{p})$ zeros due to the augmentation). Once the $\boldsymbol{p}$ vector is appended to the state vector, it may be directly estimated, provided that the realization in Eq. (2) is observable.

Using this formulation, the number of health parameters that can be estimated is limited to the number of sensors, the dimension of $\boldsymbol{y}$ [10]. This is easily seen by examining the observability criterion [11], which states that for observability, the matrix $[(\lambda I - A_{\text{aug}})^T C_{\text{aug}}^T]^T$ must be full rank for each eigenvalue λ of A_{aug}, i.e.,

$$\forall \lambda \in \{\text{eig}(A_{\text{aug}})\}, \text{rank}\left(\begin{bmatrix} \lambda I - A_{\text{aug}} \\ C_{\text{aug}} \end{bmatrix} \right) = \dim(\boldsymbol{x}_{\text{aug}})$$

Since the matrix A_{aug} in Eq. (2) clearly has at least as many zero eigenvalues as there are health parameters, the observability criterion matrix reduces to $[-A_{\text{aug}}^T\ C_{\text{aug}}^T]^T$ for each zero eigenvalue, implying that for observability, C_{aug} must have at least as many rows (i.e., there must be at least as many sensors) as A_{aug} has rows of zeros.

Since there are usually fewer sensors than health parameters, the problem becomes one of choosing the best set of tuners for the application. This is addressed next.

Problem Formulation. In this work, the objective is to determine a tuning vector of low enough dimension to be estimated, that represents as much of the health parameter information as possible in a known way. This tuning vector should permit shifts in the variables of interest, caused by health parameter deviations, to be represented as closely as possible in a least-squares sense.

We may define $\boldsymbol{\delta}$ as the vector of shifts due to the health parameters,

$$\boldsymbol{\delta} = \begin{bmatrix} L \\ M \\ N \end{bmatrix} \boldsymbol{p} = G\boldsymbol{p} \tag{3}$$

Given that the number of elements in the tuning vector (tuners) is less than the number of health parameters, we know that, except for specific cases, the estimated tuners will not represent true health parameter values. Therefore, there is no reason to model the tuning vector as a subset of existing health parameters and, in fact, $\boldsymbol{\delta}$ can be matched more closely without this constraint. The key is to find a matrix U^* and tuning vector $\boldsymbol{q}$ that correspond to G and $\boldsymbol{p}$ in Eq. (3), of small enough dimension that the tuning vector can be estimated, and the product approximates $\boldsymbol{\delta}$ in a least-squares sense. That is, $\boldsymbol{\delta} = G\boldsymbol{p} \approx \hat{\boldsymbol{\delta}} = U^*\boldsymbol{q}$, $\boldsymbol{p} \in \mathbb{R}^n$, $\boldsymbol{q} \in \mathbb{R}^k$, $k < n$, and

$$J = (\boldsymbol{\delta} - \hat{\boldsymbol{\delta}})^T (\boldsymbol{\delta} - \hat{\boldsymbol{\delta}}) = \tilde{\boldsymbol{\delta}}^T \tilde{\boldsymbol{\delta}} \tag{4}$$

is minimized.

For the tuning vector $\boldsymbol{q}$ to contain as much of the information contained in $\boldsymbol{p}$ as possible, $\boldsymbol{p}$ is mapped into $\boldsymbol{q}$ through a transformation V^* such that $\boldsymbol{q} = V^*\boldsymbol{p}$ where V^* is full rank. Thus Eq. (4) becomes

$$\begin{aligned} J &= (\boldsymbol{\delta} - \hat{\boldsymbol{\delta}})^T (\boldsymbol{\delta} - \hat{\boldsymbol{\delta}}) = (G\boldsymbol{p} - U^*\boldsymbol{q})^T (G\boldsymbol{p} - U^*\boldsymbol{q}) \\ &= \boldsymbol{p}^T (G - U^*V^*)^T (G - U^*V^*)\boldsymbol{p} \end{aligned} \tag{5}$$

Since G may have rank as large as n (full rank) and the inner dimension of U^*V^* is only k, U^*V^* will not be full rank. Thus, Eq. (5) may be rewritten in vector 2-norm notation,

$$J = \min_{\text{rank}(U^*V^*)=k} \|\boldsymbol{\delta} - U^*V^*\boldsymbol{p}\|_2^2 \tag{6}$$

Another interpretation of Eq. (5) is that we want to approximate G by a lower rank matrix through the minimization of the Frobenius norm (the square root of the sum of the squares of each matrix element), i.e.,

$$J = \min_{\text{rank}(U^*V^*)=k} \|G - U^*V^*\|_F$$

The solution to both of these minimization problems is obtained using singular value decomposition (SVD) [12], and we shall show that SVD leads to an optimal solution of the form U^*V^*.

Singular Value Decomposition. The singular value decomposition of any $m \times n$ matrix G, with $m \geq n$, may be defined as

$$G = U\Sigma V^T \tag{7}$$

where U and V^T are orthonormal square matrices, $U \in \mathbb{R}^{m \times m}$, $V \in \mathbb{R}^{n \times n}$, and Σ is a matrix of the same dimensions as G, with the upper portion a diagonal matrix of the singular values of G and the lower portion all zeros. That is,

$$\Sigma = \begin{bmatrix} \sigma_1 & 0 & \cdots & 0 \\ 0 & \sigma_2 & & \vdots \\ \vdots & & \ddots & 0 \\ 0 & \cdots & 0 & \sigma_n \\ 0 & \cdots & 0 & 0 \end{bmatrix}$$

where $\sigma_1 \geq \sigma_2 \geq \cdots \geq \sigma_n \geq 0$, $UU^T = I_m$, and $VV^T = I_n$.

Some algebraic manipulation shows that Eq. (7) is equivalent to

$$G = \sum_{i=1}^{n} \sigma_i \boldsymbol{u}_i \boldsymbol{v}_i^T \tag{8}$$

where $\boldsymbol{u}_i$ is the ith column of U and $\boldsymbol{v}_i$ is the ith column of V ($\boldsymbol{v}_i^T$ the ith row of V^T). Equation (8) is called the rank one decomposition of G because G is represented by the sum of rank one matrices.

If the rank of an $m \times n$ matrix H is $k < n$, its SVD is

Downloaded 02 Jun 2010 to 171.66.16.107. Redistribution subject to ASME license or copyright; see http://www.asme.org/terms/Terms_Use.cfm

$$H = [\underbrace{\boldsymbol{u}_1 \cdots \boldsymbol{u}_k}_{U_k} \boldsymbol{u}_{k+1} \cdots u_m] \begin{bmatrix} \Sigma_k & 0 \\ 0 & 0 \end{bmatrix} [\underbrace{\boldsymbol{v}_1 \ldots \boldsymbol{v}_k}_{V_k} \boldsymbol{v}_{k+1} \cdots \boldsymbol{v}_n]^T$$

$$= [U_k \boldsymbol{u}_{k+1} \cdots \boldsymbol{u}_m] \begin{bmatrix} \Sigma_k & 0 \\ 0 & 0 \end{bmatrix} [V_k \boldsymbol{v}_{k+1} \cdots \boldsymbol{v}_n]^T = U_k \Sigma_k V_k^T \quad (9)$$

where U_k consists of the first k columns of U, V_k consists of the first k columns of V, and Σ_k is the upper left diagonal $k \times k$ block of Σ containing the nonzero singular values.

The linear least-squares problem

$$\min_{\text{rank}(H)=k} \|\boldsymbol{\delta} - H\boldsymbol{p}\|_2^2$$

can be solved using Eq. (9) as

$$\boldsymbol{p}_{LS} = H^{\dagger}\boldsymbol{\delta} = [V_k \boldsymbol{v}_{k+1} \cdots \boldsymbol{v}_m] \begin{bmatrix} \Sigma_k^{-1} & 0 \\ 0 & 0 \end{bmatrix} [U_k \boldsymbol{u}_{k+1} \cdots \boldsymbol{u}_n]^T \boldsymbol{\delta}$$

$$= V_k \Sigma_k^{-1} U_k^T \boldsymbol{\delta} \quad (10)$$

where the pseudoinverse of the nonsquare, non-full rank, block diagonal singular value matrix Σ in Eq. (9) is that matrix's transpose with the nonzero block inverted.

Additionally, any full rank $m \times n$ matrix G, with $m \geq n$, is most closely approximated in the Frobenius norm sense by a matrix H of rank $k < n$, i.e.,

$$\|G - H\|_F = \min_{\text{rank}(H)=k} \|G - H\|_F$$

when H is given by

$$H = \sum_{i=1}^{k} \sigma_i \boldsymbol{u}_i \boldsymbol{v}_i^T = U_k \Sigma_k V_k^T \quad (11)$$

the first k terms of Eq. (8).

The Frobenius norm is equal to the square root of the sum of the squares of the singular values of the matrix (which is equal to the square root of the sum of the squares of each matrix element), thus $\|G-H\|_F = \sqrt{\sigma_{k+1}^2 + \cdots + \sigma_n^2}$ is minimal since the singular values are ordered from largest to smallest and the difference consists of only the smallest ones.

Thus, Eqs. (9) and (11) are the same, and both imply Eq. (10). Moreover, the solution has the structure of the original U^*V^* formulation proposed in Eq. (5), even though this structure was not assumed in the derivation of these results, it simply falls out as a consequence of the SVD approach (see [12] or a similar text for derivations, proofs, definitions of norms, etc.).

This demonstrates that using the SVD to obtain the U^*V^* formulation will indeed give the optimal approximation to $\boldsymbol{\delta}$ in a least-squares sense. The procedure for coming up with the optimal matrices and their use will be described next.

Design Procedure. The design procedure follows directly from the above derivation.

1. For each linearization point, create G by stacking L, M, and N as in Eq. (3). The L and M matrices must be included for the accuracy of the Kalman filter estimates, the variables used to create N are left to the user's discretion.
2. Compute the magnitude of each row $\boldsymbol{g}_i$ of G as $\boldsymbol{g}_i \boldsymbol{g}_i^T$ for scaling. Premultiply G by

$$W = \begin{bmatrix} \sqrt{\boldsymbol{g}_1 \boldsymbol{g}_1^T} & 0 & 0 \\ 0 & \ddots & 0 \\ 0 & 0 & \sqrt{\boldsymbol{g}_m \boldsymbol{g}_m^T} \end{bmatrix}^{-1}$$

   This is important because there may be several orders of magnitude difference between the values in different rows of G, and since the SVD minimizes the difference between the elements of G and U^*V^* in a least-squares sense (Frobenius norm), all rows should be about the same magnitude to prevent the large matrix elements from dominating. Recognizing, however, that some variables need to be estimated more accurately than others, additional weights can be incorporated into the diagonal elements of W to account for this relative importance. This is all done after any other scaling or balancing used to develop the initial realization (Eq. (1)).
3. Compute the SVD as in Eq. (7) from the scaled G, $WG = (WU)\Sigma V^T$.
4. Unscale WU by premultiplying by W^{-1}. This brings the magnitude of each row back to its appropriate level and makes it compatible with the rest of the realization.
5. Generate U^* and V^* by selecting only the k most significant terms of Eq. (8). At most, k will equal the number of sensors less the number of zero eigenvalues in the original A matrix. Incorporate the $k \times k$ singular value matrix into U^* such that $U^* = U_k \Sigma_k$ and $V^* = V_k^T$. Thus,

$$G = \begin{bmatrix} L \\ M \\ N \end{bmatrix} \approx \hat{G} = (U_k \Sigma_k) V_k^T = U^* V^* = \begin{bmatrix} U_L^* \\ U_M^* \\ U_N^* \end{bmatrix} V^* = \begin{bmatrix} \hat{L} \\ \hat{M} \\ \hat{N} \end{bmatrix}$$

   where $U_L^* V^* = \hat{L} \approx L$, $U_m^* V^* = \hat{M} \approx M$, and $U_N^* V^* = \hat{N} \approx N$. Thus, we have generated a common right factor for the approximation of all three matrices L, M, and N.
6. Using the rows of U^* that correspond to the original L, M, and N, set up the Kalman filter using the new augmented system equations

$$\begin{bmatrix} \dot{\boldsymbol{x}} \\ \dot{\boldsymbol{q}} \end{bmatrix} = \begin{bmatrix} A & U_L^* \\ 0 & 0 \end{bmatrix} \begin{bmatrix} \boldsymbol{x} \\ \boldsymbol{q} \end{bmatrix} + \begin{bmatrix} B \\ 0 \end{bmatrix} \boldsymbol{u} + \boldsymbol{e}$$

$$\boldsymbol{y} = [C \; U_M^*] \begin{bmatrix} \boldsymbol{x} \\ \boldsymbol{q} \end{bmatrix} + D\boldsymbol{u} + \boldsymbol{w}$$

$$\boldsymbol{z} = [E \; U_N^*] \begin{bmatrix} \boldsymbol{x} \\ \boldsymbol{q} \end{bmatrix} + F\boldsymbol{u} \quad (12)$$

   This system will generally be observable if $\boldsymbol{q}$ is of small enough dimension.

Table 1 State variables, health parameters, and actuators

State variables	Health parameters	Actuators
XN12	FAN efficiency[b]	WF36
XN25	FAN flow capacity[a–c]	VBV
TMHS23	LPC efficiency[a,b]	VSV
TMHS3	LPC flow capacity[b,c]	
TMBRNL	HPC efficiency[a,b]	
TMBRNC	HPC flow capacity[a–c]	
TMHS41	HPT efficiency[a–c]	
TMHS42	HPT flow capacity[a–c]	
TMHS5	LPT efficiency	
	LPT flow capacity[a,c]	

[a]Health parameters estimated in seven sensor case.
[b]Health parameters estimated in eight sensor case.
[c]Health parameters estimated in six sensor case.

Turbofan Engine Example

A large commercial turbofan engine model linearized at a cruise operating point is used to evaluate the concept. The model has nine state variables, ten health parameters, three control inputs, all shown in Table 1, and seven sensors, shown in Table 2. The auxiliary outputs of interest are shown in Table 3. The linear model is used as the "truth" model for this example. It must be noted that for this work, the P25 measurement in the conventional sensor suite is replaced by P17. Without this substitution, thrust estimation is poor. This indicates that the ability to estimate unmeasured

Downloaded 02 Jun 2010 to 171.66.16.107. Redistribution subject to ASME license or copyright; see http://www.asme.org/terms/Terms_Use.cfm

Table 2 Sensor sets and sensor standard deviation (std. dev. as percent of steady-state values at full power)

Conventional sensor set	New sensor set	Standard deviation (%)
XN12	XN12	0.25
XN25	XN25	0.25
—	P17	0.50
P25	—	0.50
T25	T25	0.75
PS3	PS3	0.50
T3	T3	0.75
T49	T49	0.75

outputs is strongly influenced by sensor location. The weights on net and gross thrust (step 2 in the design procedure) are doubled because of the relative importance of these auxiliary variables. The model is run open loop, so all control inputs remain at 0, i.e., they do not deviate from the trim value for the linear model and no actuator bias is present. All ten health parameters are shifted randomly up to 3% in the direction of degradation, and these shifts result in shifts in the measured variables. The linear truth model and Kalman filter estimator use the same A, B, C, and D matrices, but the truth model has all ten health parameters entering through the L, M, and N matrices. The Kalman filter is set up using the system in Eq. (12) with a seven-element $\boldsymbol{q}$ vector.

To demonstrate the optimality of the SVD-based tuner approach, it was compared to the Kalman filter approach that uses health parameter-based tuners. To make the comparison as meaningful as possible, the health parameter tuners were chosen specifically to be compatible with the metric used by the SVD approach (Eq. (4)). Structurally, the Kalman filter is designed to estimate seven selected health parameter tuners (while assuming the others remain constant) and the corresponding columns of L, M, and N are retained. An optimal selection process based on orthogonal least squares (OLS) [13,14] is used to determine which health parameters to estimate. Briefly, the scaled G matrix (from step 2 in the design procedure, the same one as used for the SVD-based tuners) is multiplied by a random health parameter vector $\boldsymbol{p}$ whose ten elements take on values from 0% to 3% in the appropriate direction (positive for the HPT and LPT flow capacities, negative for all others). OLS is used to choose the seven columns of G that best align with the shift vector $\boldsymbol{\delta}=G\boldsymbol{p}$. This is repeated thousands of times for different random $\boldsymbol{p}$ vectors and the results are tallied. The individual columns that are selected most often determine the health parameters that on average best capture the degradation-induced shifts. The most often selected columns are indicated in Table 1. Of the 120 (10 choose 7) possible sets of columns, this exact set was selected ~9% of the time.

Results

To demonstrate the ability of the optimal tuners to approximate a variety of health parameter-induced shifts well, all ten health parameters are shifted randomly. The results shown are for a representative random sequence, many simultaneous random shifts were performed at this operating point with similar results. Figure 1 shows the state variable estimation over a time sequence containing ten such sets of random shifts. Generally, the variables are reconstructed accurately with the exception of TMBRNC, combustor case metal temperature, which does not seem to have much of an effect on any other variables.

Table 3 Auxiliary outputs to be estimated in flight

Auxiliary outputs
WR2A
FN
FG
SMW12
SMW2
SMW25

Figure 2 shows the output variables for the same sequence of health parameter shifts. These also demonstrate good matching, which is to be expected when using a Kalman filter.

Figure 3 shows the auxiliary parameters. For all cases of health parameter shifts, both estimators performed well. Because of the large gains on some of the auxiliary variables, the estimates needed to be low-pass filtered to attenuate the magnified noise level. The estimation performance on net and gross thrust and two of the three stall margins, as well as total fan corrected flow, was consistently accurate. The only auxiliary parameter whose estimate was consistently poor is LPC stall margin, SMW2. Adjustment of the weighting matrix W in step 2 of the design procedure made little difference in the results.

In an effort to obtain a better LPC stall margin estimate, new U^* and V^* were determined, this time using SMW2 as the only auxiliary parameter, i.e., N in Eq. (3) has only one row. If SMW2 requires different information than the other variables for accurate estimation, generating a new G matrix would result in a different SVD (the SVD of a matrix is unique) possibly prioritizing the tuners such that SMW2 could be reconstructed. Even with the new G matrix though, the estimation of SMW2 is poor. This may be due to the L and M matrices dominating the generation of the U^* and V^* matrices, but it is more likely a sensor placement issue (in fact, replacing P17 with P25 greatly improves the estimation of SMW2, even without additional weighting).

Likewise, a slight improvement in net and gross thrust estimation was achieved by the SVD-based tuners when the auxiliary parameters consisted of only those two variables.

In order to compare the performance of the tuners statistically, runs containing a sequence of 400 simultaneous random shifts of all ten health parameters were performed. After each set of shifts, the engine simulation was allowed to reach steady state and data from each variable were gathered and averaged. This information was used to compute an average percent error for each variable in steady state over the entire sequence. The quantity was computed as

$$\%\,\text{error} = \frac{100}{400}\sum_{i=1}^{400}\left|\frac{\text{actual deviation}_i - \text{estimated deviation}_i}{\text{trim value}_i}\right|$$

$$\approx \frac{100}{400}\sum_{i=1}^{400}\left|\frac{\text{actual}_i - \text{estimate}_i}{\text{actual}_i}\right|$$

The comparison of the percent estimation error of the state variables, outputs, and auxiliary outputs based on this run for the two sets of tuners are presented in Tables 4–6, respectively. It can be seen that both sets of tuners produce similar results in most cases, but where the error is relatively large (TMBNC in Table 4, and SMW2 and SMW25 in Table 6), the SVD-based tuners are significantly better. Results for the estimated degradation-induced shifts in each variable, $\boldsymbol{\delta}=G\boldsymbol{p}$ (Eq. (3)), were similar. The value of the metric (Eq. (4)) for the scaled shifts in the two cases was 2.187 for the SVD-based tuners and 6.016 for the health parameter-based tuners. It must be noted that minimization of the metric does not in itself guarantee minimization of the total least squares error without appropriate weighting in step 2 of the design procedure. In this example, the SVD-based tuners give a value of 42.6865 for the sum of the squared percent estimation error of the variables in Tables 4–6, compared to 95.4661 for the health parameter-based tuners.

Additionally, estimation performance was evaluated for comparable sequences of 400 random simultaneous shifts in all ten health parameters with six sensors and with eight sensors. For the eight-sensor case, P25 was added to the "new sensor set" of seven shown in Table 2. The tuners used were the first eight health

Downloaded 02 Jun 2010 to 171.66.16.107. Redistribution subject to ASME license or copyright; see http://www.asme.org/terms/Terms_Use.cfm

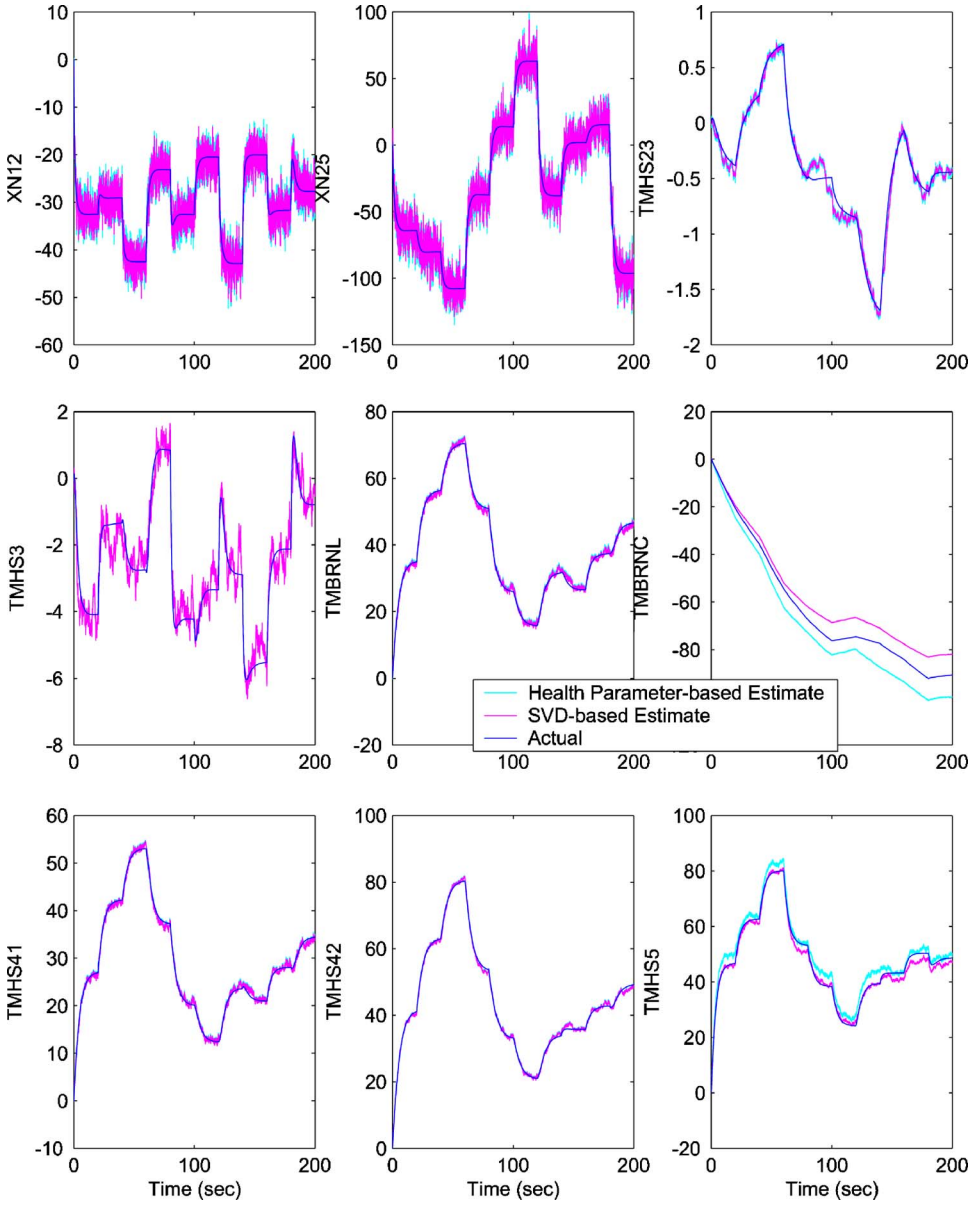

Fig. 1 State variables, scaled actual and estimates

parameters indicated in Table 1 (LPT efficiency and flow capacity were not used), selected using OLS. As expected, the estimate of SMW2, which was poor with only seven sensors, was much more accurate, as was the estimate of TMBRNC. For eight sensors, the value of the metric for the SVD-based tuners was 2.0883 and 6.5243 for the health parameter-based tuners; this is essentially the same as for the seven sensor case, with the difference being attributed to the random factors of sensor noise and the health parameter shifts. The sum of the squared percent estimation error for the SVD-based tuners was 6.0438 compared to 7.1943 for the health parameter-based tuners. For the six sensor case, the T3 sensor was removed from the "new sensor set" shown in Table 2. The tuners used were the flow capacities of each component plus HPT efficiency, indicated in Table 1, which were selected using engineering judgment. It was possible to get reasonably good matching of the auxiliary outputs with this set of tuners, but no set investigated produced accurate reconstruction of the state variables. The value of the metric for the SVD-based tuners in the six-sensor case was 9.4068 and 12.4667 for the health parameter-based tuners. The big increase in the metric values over the cases with more sensors indicates that significant information has been lost by approximating the G matrix by a rank six matrix. The relative size of the dropped singular values gives an indication of this. In this case, the sum of the squared percent estimation error for the SVD-based tuners was 53.8702 compared to 78.1314 for the health parameter-based tuners.

Further Application of Tuners

The example shows that the optimal tuner selection method obtained using SVD provides accurate estimates of most variables of interest, including auxiliary parameters such as thrust. The SVD formulation has several attractive properties that make its use in this application highly desirable beyond what has already been discussed. In addition to providing the least-squares solution to the approximation of the shift vector $\boldsymbol{\delta}$, other features include (i) the approximation error to the matrix G is known; (ii) fault detection is possible through the tuners' ability to capture sudden shifts, even if the tuners do not correspond to individual health parameters; and (iii) the orthogonality of the V matrix suggests a way to isolate a component fault, while at the same time some of

Downloaded 02 Jun 2010 to 171.66.16.107. Redistribution subject to ASME license or copyright; see http://www.asme.org/terms/Terms_Use.cfm

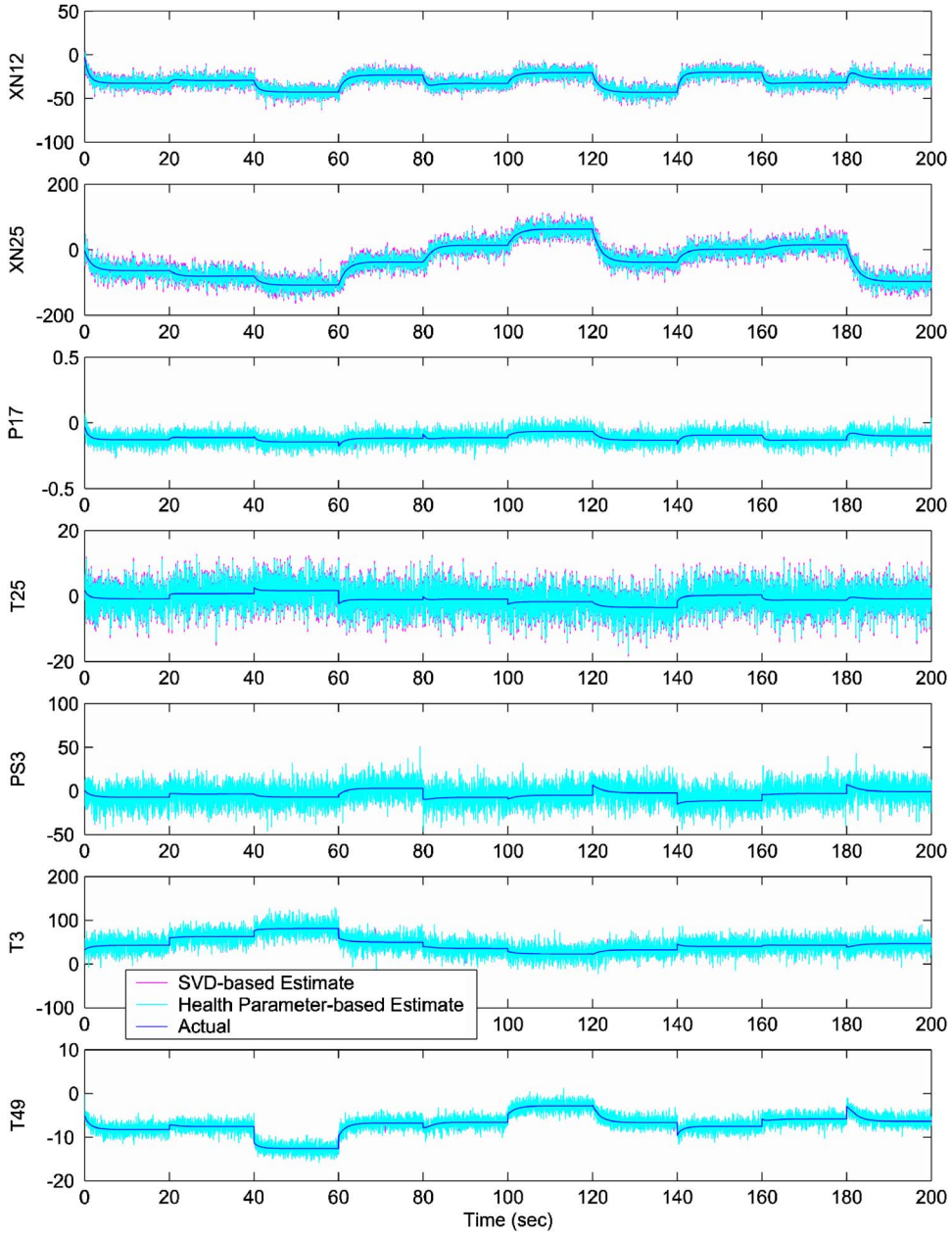

Fig. 2 Output parameters, scaled actual and estimates

the true health parameter shifts may be able to be reconstructed accurately, in some cases. The following sections provide more detail on each of these topics.

Approximation Error of *G*. Since

$$G = \sum_{i=1}^{n} \sigma_i \boldsymbol{u}_i \boldsymbol{v}_i^T = \sum_{i=1}^{k} \sigma_i \boldsymbol{u}_i \boldsymbol{v}_i^T + \sum_{i=k+1}^{n} \sigma_i \boldsymbol{u}_i \boldsymbol{v}_i^T = \hat{G} + \sum_{i=k+1}^{n} \sigma_i \boldsymbol{u}_i \boldsymbol{v}_i^T \tag{13}$$

the approximation error of G is the last term of Eq. (13), namely,

$$\tilde{G} = G - \hat{G} = \sum_{i=k+1}^{n} \sigma_i \boldsymbol{u}_i \boldsymbol{v}_i^T$$

The error in the approximation of G depends on both the number of terms dropped in the approximation and on the size of the singular value in each dropped term. (Singular values give an indication of the linear independence of the columns of G. Thus, if the singular values in the dropped terms are very small, not much information is lost, but on the other hand, if the columns of G are not linearly independent, the accurate estimation of the health parameters is impossible, regardless of the number of sensors.) The fact that the error is known allows, for instance, the calculation of accuracy bounds on the health parameter-induced shifts, $\boldsymbol{\delta}$, and on the estimated variables themselves.

The error introduced into the system equations (Eq. (12)) through the approximation of G represents modeling error. The process noise term $\boldsymbol{e}$ in the state equation is used at least partially to represent model uncertainty, so a level can be established by multiplying the known approximation error $\tilde{G}$ by a range of degradation values $\boldsymbol{p}$. Since the level of degradation is unknown a priori, it can be considered a random variable and, thus, so can

Downloaded 02 Jun 2010 to 171.66.16.107. Redistribution subject to ASME license or copyright; see http://www.asme.org/terms/Terms_Use.cfm

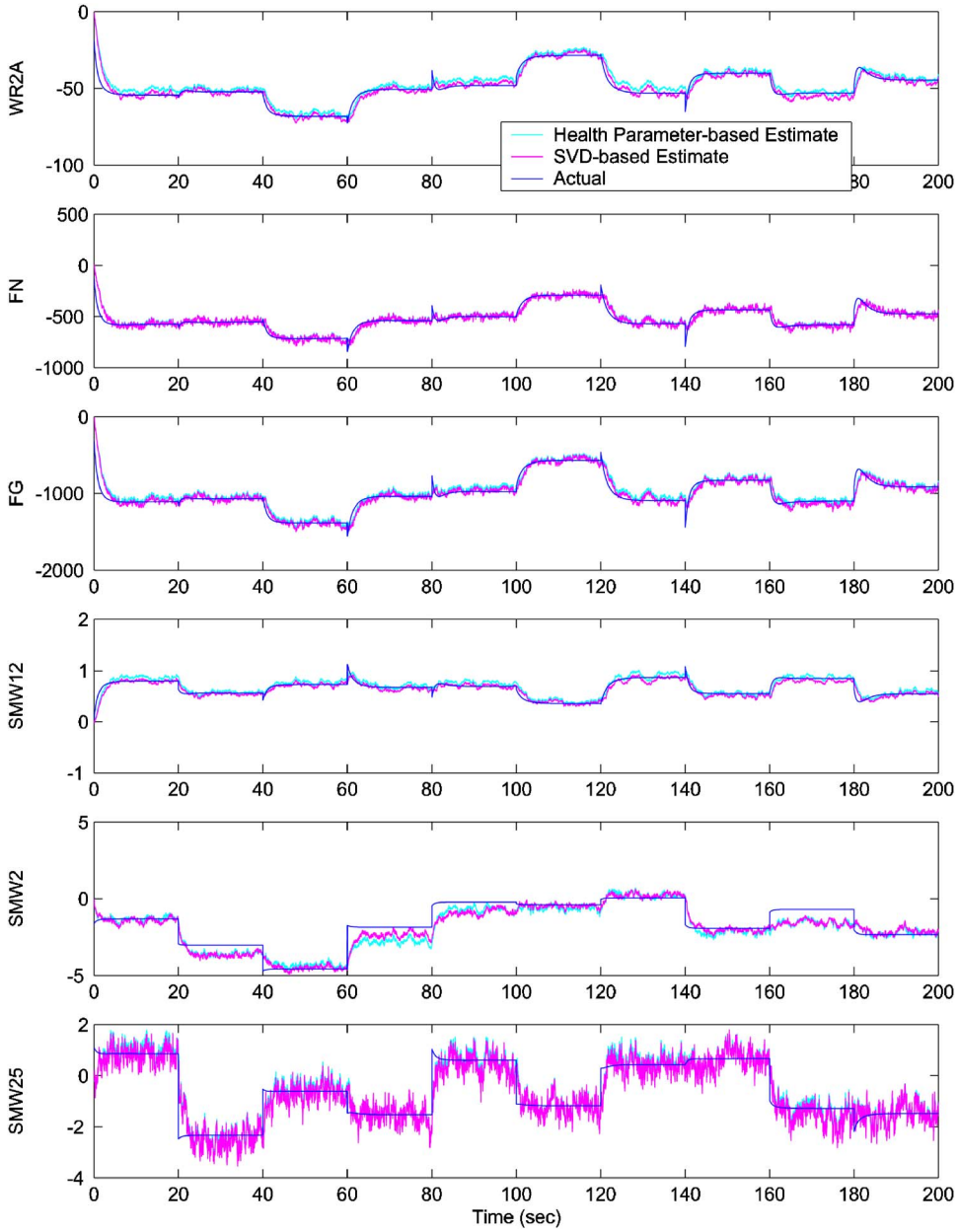

Fig. 3 Auxiliary parameters, scaled actual and filtered estimates

$\tilde{G}\boldsymbol{p}$. The covariance of this product could be used to help determine the process noise covariance matrix Q for the Kalman filter, which is often considered a design parameter.

Table 4 Percent error of state variable estimates

State variables	SVD-based tuners	Health parameter-based tuners
XN12	0.0318	0.0317
XN25	0.0269	0.0267
TMHS23	0.0129	0.0130
TMHS3	0.0363	0.0363
TMBRNL	0.0278	0.0306
TMBRNC	0.4083	1.1256
TMHS41	0.0300	0.0313
TMHS42	0.0267	0.0274
TMHS5	0.3208	0.1942

Fault Detection. Even though the tuners do not represent individual health parameters, component faults can be detected by sudden shifts. The objective of fault detection in this context is to be able to distinguish an abrupt shift representing a fault, from the general "background level" of degradation caused by use and

Table 5 Percent error of output estimates

Outputs	SVD-based tuners	Health parameter-based tuners
XN12	0.0317	0.0318
XN25	0.0286	0.0285
P17	0.0634	0.0633
T25	0.0859	0.0857
PS3	0.1027	0.1027
T3	0.0990	0.0990
T49	0.0748	0.0748

Downloaded 02 Jun 2010 to 171.66.16.107. Redistribution subject to ASME license or copyright; see http://www.asme.org/terms/Terms_Use.cfm

Table 6 Percent error of auxiliary output estimates

Auxiliary outputs	SVD-based tuners	Health parameter-based tuners
WR2A	0.1081	0.0787
FN	0.2704	0.2745
FG	0.1225	0.1169
SMW12	0.4348	0.3469
SMW2	6.1605	9.3142
SMW25	2.0326	2.6733

wear, represented by slowly varying $\boldsymbol{q}$ during normal operation. Since $\boldsymbol{q}=V^*\boldsymbol{p}$, the shifts are mapped into $\boldsymbol{q}$ as long as they are not limited to the null space of V^*, that is, as long as they do not lie completely within the span of $[\boldsymbol{v}_{k+1}\ldots\boldsymbol{v}_n]^T$. However, since this space contains the least significant directions of possible shift (since only the smallest singular values are dropped) and the tuners will, in general, cut across rather than align with the influence of each health parameter, additional shifts due to faults $\Delta\boldsymbol{q}=V^*\Delta\boldsymbol{p}$ will very likely be nonzero for any significant shift in an element of $\boldsymbol{p}$.

To demonstrate this, component faults of 3% magnitude were injected, sustained for 20 s, and removed, in succession through each of the ten health parameters (efficiency then flow capacity for each component in the order shown in Table 1), as shown in Table 7. Figure 4 shows the estimated tuners during this sequence of shifts. As the health parameters shift, the tuners generally shift as well, so changes can be determined and thus faults can be detected. The fan efficiency fault is hard to determine as the tuner shifts that correspond to it are small, but several tuners clearly shift in response to a fault in fan flow capacity. When looking at all tuners together, it is reasonably clear in most cases when a fault has occurred. Different sets of tuners result from different weightings of the G matrix (step 2 of the design procedure), and it is possible to have at least one of the SVD-based tuners align well with an actual health parameter.

One thing that is clear from Fig. 4 is that, in this example, the elements of $\boldsymbol{q}$ are tracked accurately, and this is a consequence of the procedure used to select them. This is not the case in general when the tuners are modeled as actual health parameters. Figure 5 shows the Kalman filter estimates of the health parameter-based tuners with the same input sequence as in Fig. 4. In Fig. 5, the tuners clearly indicate abrupt shifts due to faults, but often do not match the health parameters they represent because of the influence of unmodeled health parameters. Techniques exist to select the health parameters for estimation that are least affected by the umodeled health parameters and sensor uncertainty [15–18]. From a diagnostics point of view, this is fine, but there is no guarantee that those health parameters will facilitate good reconstruction of auxiliary parameters such as thrust.

The ability to estimate the state and auxiliary variables in the presence of actuator bias is not addressed here. From Eq. (1), it is clear that the effect of actuator bias is no different from that of health parameter shifts. Thus, as long as the tuners can capture this effect, the results should not deteriorate significantly. As with component degradation and faults, constant actuator biases should be generally represented by the elements of $\boldsymbol{q}$, and any sudden actuator shifts due to bias should be captured as shifts in the elements of $\boldsymbol{q}$.

Table 7 Health parameter shifts representing component faults

Time (s)	Health parameters	Shift
0–20	FAN efficiency	−3%
20–40	FAN flow capacity	−3%
40–60	LPC efficiency	−3%
60–80	LPC flow capacity	−3%
80–100	HPC efficiency	−3%
100–120	HPC flow capacity	−3%
120–140	HPT efficiency	−3%
140–160	HPT flow capacity	3%
160–180	LPT efficiency	−3%
180–200	LPT flow capacity	3%

Fault Isolation. By construction, the vector of estimated tuners $\hat{\boldsymbol{q}}\approx V^*\boldsymbol{p}$ (since G is not perfectly recreated by U^*V^*, the estimated $\boldsymbol{q}$ will not exactly equal $V^*\boldsymbol{p}$, even in a noise-free environment) and the columns of V are orthonormal. Of course, V is a square $n\times n$ matrix and V^* is $k\times n$, but if k is close to n, in some cases $V^{*T}V^*\approx I_n$. The implication of this is that $V^{*T}\hat{\boldsymbol{q}}\approx\boldsymbol{p}$. Thus, even if the magnitude of the shift is not determined accurately, the shift might be able to be isolated to the affected health parameters (or at least the affected component) by identifying those elements of the $V^{*T}\hat{\boldsymbol{q}}$ vector with the largest shifts. Analysis of the V^* matrix will determine the feasibility of the approach on a case by case basis.

It is interesting to note that the $V^{*T}\hat{\boldsymbol{q}}\approx\boldsymbol{p}$ approximation is actually the least squares estimate of $\boldsymbol{p}$ from Eq. (3). This is clear from the fact that

$$\hat{\boldsymbol{\delta}}=U^*\hat{\boldsymbol{q}}=U_k\Sigma_k\hat{\boldsymbol{q}}\approx G\boldsymbol{p}=U\Sigma V^T\boldsymbol{p}$$
$$\Rightarrow\boldsymbol{p}_{LS}=V\Sigma^{\dagger}U^{-1}U_k\Sigma_k\hat{\boldsymbol{q}}=V_k\hat{\boldsymbol{q}}=V^{*T}\hat{\boldsymbol{q}} \tag{14}$$

where $\Sigma^{\dagger}$ is the transpose of Σ with the square singular value block inverted. Note that once U is unscaled in step 4 of the design procedure it is no longer orthonormal; thus, U^{-1} rather than U^T is used in Eq. (14).

Figure 6 shows the recreated set of health parameters using $\hat{\boldsymbol{p}}\approx V^{*T}\hat{\boldsymbol{q}}$. It is clear that shifts in certain variables are easily isolated while others are mapped back as shifts smeared across more than one health parameter. For this example, it seems that health parameter shifts in the high-pressure shaft components (HPC and HPT) are easier to isolate than those on the low-pressure shaft. For instance, the plots for FAN efficiency and LPT efficiency are very similar, meaning that it would be hard for a diagnostic system to distinguish between them. Efficiency and flow capacity of the LPC are clearly interrelated, with one being nearly the opposite of the other; for cases such as this, one might constrain the problem by assuming that efficiency and flow capacity corresponding to a single component shift together, somewhat simplifying the isolation logic. The issue always exists of simultaneous shifts in the health parameters of multiple components confounding the problem.

It is interesting to compare the results in Fig. 6 to those in Fig. 5, which shows the Kalman filter estimates of seven health parameter-based tuners. The quality of the reconstruction is similar in that the same three parameters (FAN flow capacity, HPC efficiency, and HPT flow capacity) were estimated accurately in both cases and those estimates corrupted by unmodeled shifts in health parameters were the same in both cases, but the approach demonstrated in Fig. 6 has the benefit that the remaining three health parameters are reconstructed as well, albeit corrupted by shifts in other variables. One observation is that the reconstruction of each of these remaining health parameters (FAN efficiency, LPC flow capacity, and LPT efficiency) is strongly related to the reconstruction of some other health parameter, underscoring the lack of observability. Still, a diagnostic system might be able to use this information to isolate faults.

If actuator bias $\boldsymbol{u}_{\text{bias}}$ were to be added on top of the health parameter deviations, it would certainly make the fault isolation task more challenging. An approach to address this is to define G such that

Downloaded 02 Jun 2010 to 171.66.16.107. Redistribution subject to ASME license or copyright; see http://www.asme.org/terms/Terms_Use.cfm

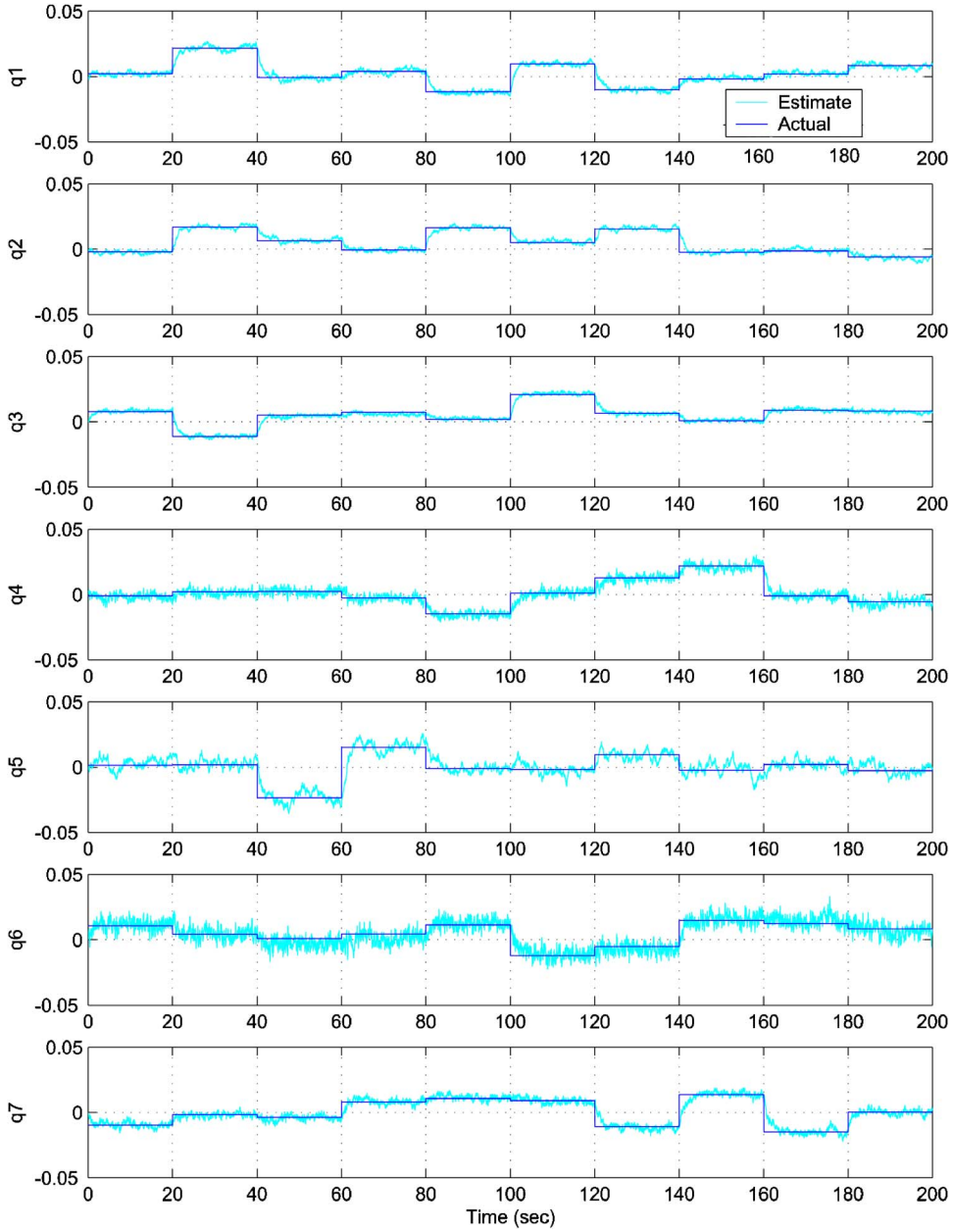

Fig. 4 Estimated q signals and V^*p, demonstrating fault detection

$$\delta = \begin{bmatrix} L & B \\ M & D \\ N & F \end{bmatrix} \begin{bmatrix} p \\ u_{\text{bias}} \end{bmatrix} = G \begin{bmatrix} p \\ u_{\text{bias}} \end{bmatrix}$$

This explicitly accounts for actuator bias, but the increase in the number of columns of G means that the U^*V^* approximation will be less accurate, since the size of q is fixed. A consequence of this is that $V^{*T}V^*$ is further from I_n (in the sense of the Frobenius norm) and thus the $[p^T \; u_{\text{bias}}^T]^T \approx V^{*T}q$ approximation is not as good as when fewer faults are accounted for.

Conclusions

A new optimal linear point design approach to determine engine deterioration tuning parameters that enables the accurate reconstruction of unmeasured engine outputs was presented. It was designed specifically for the case where there are too few sensors to estimate the true engine health parameters. The tuning parameters are determined using singular value decomposition, which was shown to generate the best approximation to the influence of the full set of health parameters in a least-squares sense, using a set small enough to be estimated. A concise design procedure to generate the tuners was described. An example demonstrated that the method worked well in reconstructing the unmeasured parameters of interest. It was shown to perform better against its metric than a health parameter-based Kalman filter specifically designed for the metric used, and it will generally result in a smaller total squared estimation error with appropriate weighting incorporated into the metric. This highlights the freedom inherent in the SVD-based approach as a result of the weighting, while the selection of possible subsets of health parameters for tuners is limited. Still, the choice of weights in the SVD approach is not arbitrary since the variables interact, and allowing poor state estimation, for instance, will ultimately hurt the accuracy of the auxiliary variables. It was also shown that the ability to estimate well is sensitive to sensor placement. As a side benefit of the estimator formulation process, the tuners have desirable properties for diagnostics be-

Downloaded 02 Jun 2010 to 171.66.16.107. Redistribution subject to ASME license or copyright; see http://www.asme.org/terms/Terms_Use.cfm

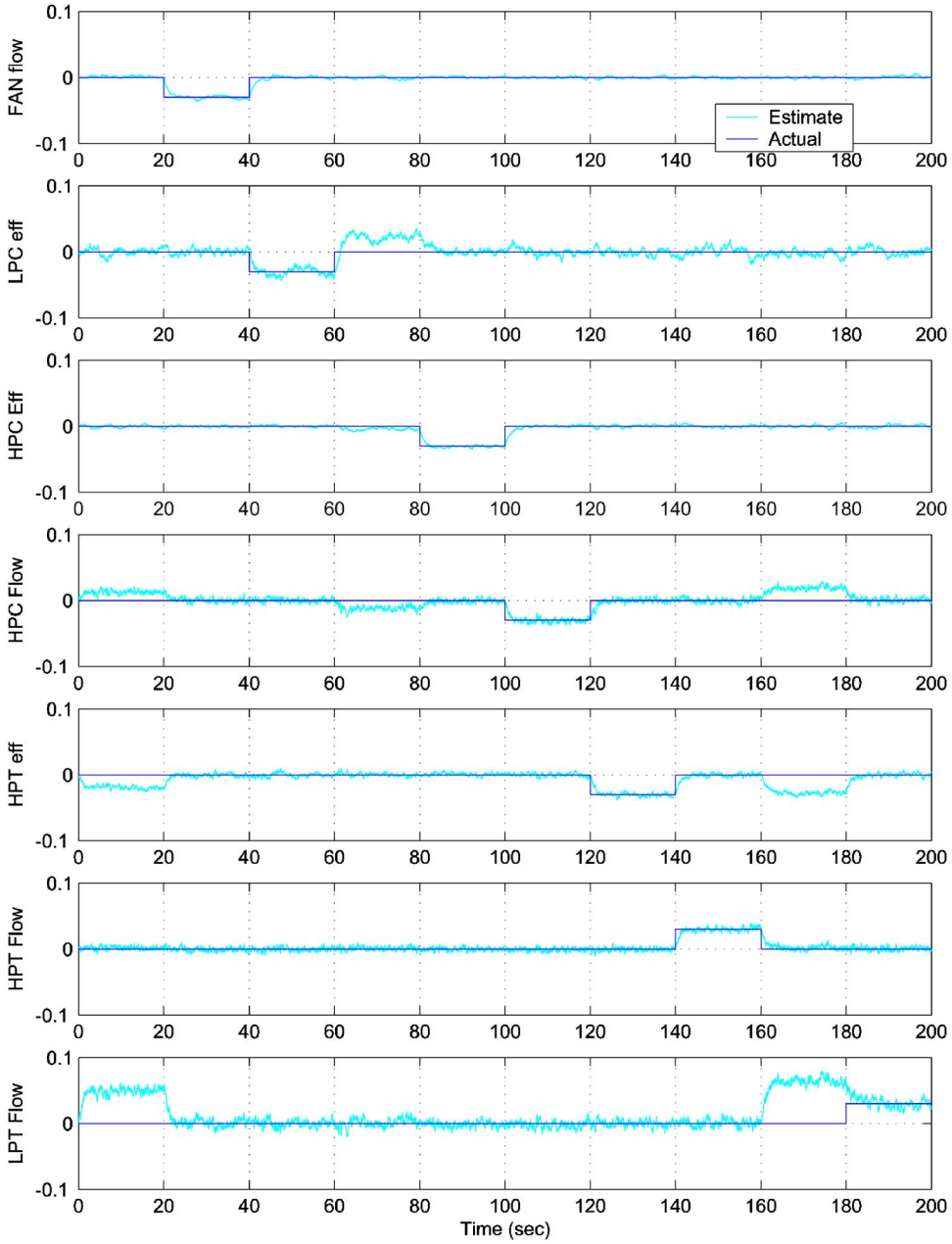

Fig. 5 Estimated health parameter-based tuners

cause of the orthogonal decomposition. In particular, the reconstruction of the complete set of health parameters compares favorably to the estimation of only a subset by a health parameter-based Kalman filter. The effect of actuator bias was not investigated with respect to the optimal tuners determined for health parameter degradation; however, a consistent approach to account for it explicitly was proposed.

Areas of future research involve the generation of bounds on the accuracy of the low rank matrix approximation and their effect on estimation, the continuity of the SVD for piecewise linear implementations, and further investigation into the fault detection and isolation properties of the SVD formulation.

Acknowledgment

The author wishes to thank Tak Kobayashi for his inspirational discussions and insights that led to the development of this work.

Nomenclature

$A, A_{aug}, B, B_{aug}, C, C_{aug}, D, E, E_{aug}, F, G, L, M, N$ = system matrices
$\boldsymbol{e}, \boldsymbol{w}$ = noise vectors
FAN = fan
FG = gross thrust
FN = net thrust
HPC = high-pressure compressor
HPT = high-pressure turbine
LPC = low-pressure compressor
LPT = low-pressure turbine
LS = least-squares (subscript)
$\boldsymbol{p}$ = vector of health parameters
P17 = bypass discharge pressure
P25 = HPC inlet pressure

Downloaded 02 Jun 2010 to 171.66.16.107. Redistribution subject to ASME license or copyright; see http://www.asme.org/terms/Terms_Use.cfm

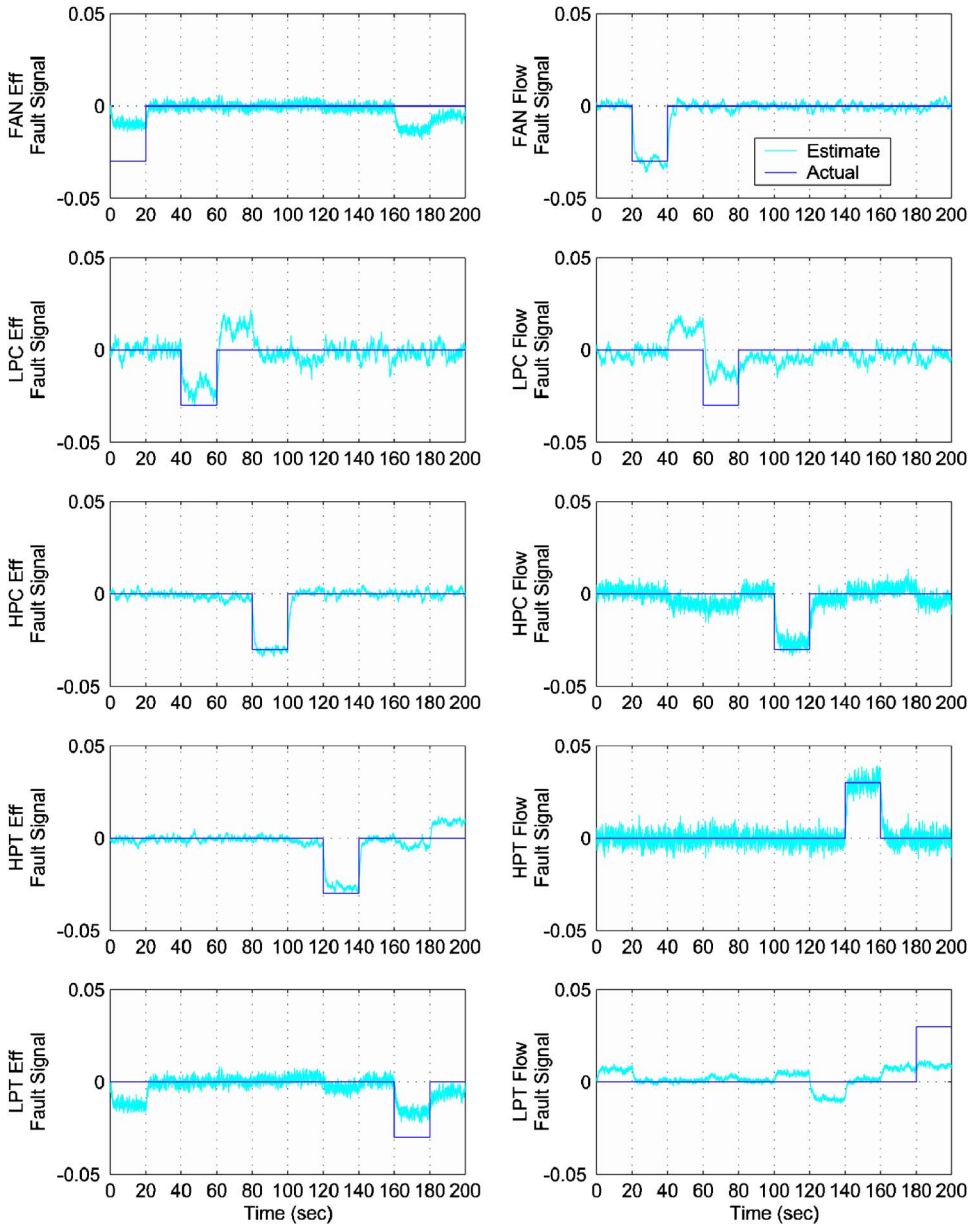

Fig. 6 Fault signal $\hat{p} \approx V^{*T}\hat{q}$ and actual health parameter shift, demonstrating fault isolation

PS3 = combustor inlet static pressure
Q, R = noise covariance matrices
$\boldsymbol{q}$ = vector of optimal tuners
SMW12 = fan stall margin
SMW2 = LPC stall margin
SMW25 = HPC stall margin
T25 = HPC inlet temperature
T3 = combustor inlet temperature
T49 = LPT inlet temperature
TMHS23 = LPC metal temperature
TMHS3 = HPC metal temperature
TMHS41 = HPT nozzle metal temperature
TMHS42 = HPT metal temperature
TMHS5 = LPT metal temperature
TMBRNC = combustor case metal temperature
TMBRNL = combustor liner metal temperature
U = orthogonal matrix obtained using SVD
U^* = optimal transformation matrix
$\boldsymbol{u}$ = vector of control inputs
$\boldsymbol{u}_i$ = ith column of U
V = orthogonal matrix obtained using SVD
V^* = optimal transformation matrix
$\boldsymbol{v}_i$ = ith column of V
VBV = variable bleed valve
VSV = variable stator vane
WF36 = fuel flow
WR2A = total FAN corrected flow
$\boldsymbol{x}$ = state vector
$\boldsymbol{x}_{\text{aug}}$ = augmented state vector
XN12 = low-pressure spool speed
XN25 = high-pressure spool speed
$\boldsymbol{z}$ = vector of auxiliary outputs
$\boldsymbol{\delta}$ = vector of health parameter-induced shifts
Σ = singular value matrix obtained using SVD
σ_i = ith singular value

Downloaded 02 Jun 2010 to 171.66.16.107. Redistribution subject to ASME license or copyright; see http://www.asme.org/terms/Terms_Use.cfm

References

[1] Luppold, R. H., Gallops, G. W., Kerr, L. J., and Roman, J. R., 1989, "Estimating In-Flight Engine Performance Variations Using Kalman Filter Concepts," AIAA-89-2584.

[2] Turevskiy, A., Meisner, R., Luppold, R. H., Kern, R. A., and Fuller, J. W., 2002, "A Model-Based Controller for Commercial Aero Gas Turbines," ASME Paper No. GT2002-30041.

[3] Kobayashi, T., Simon, D. L., and Litt, J. S., 2005, "Application of a Constant Gain Extended Kalman Filter for In-Flight Estimation of Aircraft Engine Performance Parameters," ASME Paper No. GT2005-68494.

[4] Brotherton, T., Volponi, A., Luppold, R., and Simon, D. L., 2003, "eSTORM: Enhanced Self Tuning On-Board Real-Time Engine Model," *Proc. of 2003 IEEE Aerospace Conference*, IEEE, New York, pp. 3075–3086.

[5] Kobayashi, T., and Simon, D. L., 2003, "Application of a Bank of Kalman Filters for Aircraft Engine Fault Diagnostics," ASME Paper No. GT2003-38550.

[6] Kobayashi, T., and Simon, D. L., 2004, "Evaluation of an Enhanced Bank of Kalman Filters for In-Flight Aircraft Engine Sensor Fault Diagnostics," ASME Paper No. GT2004-53640.

[7] Stamatis, A., Mathioudakis, K., and Papailiou, K. D., 1990, "Adaptive Simulation of Gas Turbine Performance," ASME J. Eng. Gas Turbines Power, **112**, pp. 168–175.

[8] Tsalavoutas, A., Mathioudakis, K., Stamatis, A., and Smith, M., 2001, "Identifying Faults in the Variable Geometry System of a Gas Turbine Compressor," ASME J. Turbomach., **123**, pp. 33–39.

[9] Ogaji, S. O. T., Sampath, S., Singh, R., and Probert, S. D., 2002, "Parameter Selection for Diagnosing a Gas-Turbine's Performance-Deterioration," Appl. Energy, **73**, pp. 25–46.

[10] España, M. D., 1994, "Sensor Biases Effect on the Estimation Algorithm for Performance-Seeking Controllers," J. Propul. Power, **10**, pp. 527–532.

[11] Callier, F. M., and Desoer, C. A., 1991, *Linear Systems Theory*, Springer-Verlag, Berlin, p. 240.

[12] Stewart, G. W., 1973, *Introduction to Matrix Computations*, Academic Press, New York, pp. 322–324.

[13] Chen, S., Billings, S. A., and Luo, W., 1989, "Orthogonal Least Squares Methods and Their Application to Non-Linear System Identification," Int. J. Control, **50**, pp. 1873–1896.

[14] Chen, S., Cowan, C. F. N., and Grant, P. M., 1991, "Orthogonal Least Squares Learning Algorithm for Radial Basis Function Networks," IEEE Trans. Neural Netw., **2**, pp. 302–309.

[15] Stamatis, A., Mathioudakis, K., and Papailiou, K. D., 1992, "Optimal Measurement and Health Index Selection for Gas Turbine Performance Status and Fault Diagnosis," ASME J. Eng. Gas Turbines Power, **114**, pp. 209–216.

[16] Grönstedt, T. U. J., 2002, "Identifiability in Multi-Point Gas Turbine Parameter Estimation Problems," ASME Paper No. GT2002-30020.

[17] Pinelli, M., and Spina, P. R., 2002, "Gas Turbine Field Performance Determination: Sources of Uncertainties," ASME J. Eng. Gas Turbines Power, **124**, pp. 155–160.

[18] Mathioudakis, K., and Kamboukos, Ph., 2004, "Assessment of the Effectiveness of Gas Path Diagnostic Schemes," ASME Paper No. GT2004-53862.

Downloaded 02 Jun 2010 to 171.66.16.107. Redistribution subject to ASME license or copyright; see http://www.asme.org/terms/Terms_Use.cfm

Design Concept for Large Output Graz Cycle Gas Turbines

H. Jericha

W. Sanz
e-mail: wolfgang.sanz@tugraz.at

E. Göttlich

Institute for Thermal Turbomachinery
and Machine Dynamics,
Graz University of Technology,
Graz, Austria

The introduction of closed cycle gas turbines with their capability of retaining combustion generated CO_2 can offer a valuable contribution to the Kyoto goal and to future power generation. Therefore research and development work at the Graz University of Technology since the 1990s has led to the Graz Cycle, a zero emission power cycle of highest efficiency. It burns fossil fuels with pure oxygen which enables the cost-effective separation of the combustion CO_2 by condensation. The efforts for the oxygen supply in an air separation plant are partly compensated by cycle efficiencies far higher than for modern combined cycle plants. Upon the basis of the previous work, the authors present the design concept for a large power plant of 400 MW net power output making use of the latest developments in gas turbine technology. The Graz Cycle configuration is changed, insofar as condensation and separation of combustion generated CO_2 takes place at the 1 bar range in order to avoid the problems of condensation of water out of a mixture of steam and incondensable gases at very low pressure. A final economic analysis shows promising CO_2 mitigation costs in the range of \$20–30/ton CO_2 avoided. The authors believe that they present here a partial solution regarding thermal power production for the most urgent problem of saving our climate. [DOI: 10.1115/1.2747260]

Introduction

In the last 100 years the concentration of some greenhouse gases in the atmosphere has markedly increased. There is a wide consensus in the scientific community that this seems to influence the Earth's surface temperature and thus the world climate.

Therefore, in 1997 the Kyoto Conference has defined the goal of global greenhouse gas emission reduction to about 5% in the next years compared to the 1990 emission level. CO_2 is the main greenhouse gas due to the very high overall amount emitted by human activities. About one third of the overall human CO_2 emissions are produced by the power generation sector. In the EU there is strong pressure on utilities and industry to reduce the CO_2 emissions from power generation. So, there is a strong driving force to develop commercial solutions for the capture of CO_2 from power plants.

The authors believe that oxy-fuel cycles with internal combustion of fossil fuels with pure oxygen are a very promising technology and that their Graz Cycle can be the most economic solution for CO_2 capture from fossil power generation once the development of the new turbomachinery components needed is done. Oxygen is needed in large quantities for this kind of cycle and can be generated by air separation plants which are in use worldwide with great outputs in the steel making industry and even in enhanced oil recovery (EOR) [1].

The basic principle of the so-called Graz Cycle has been developed by Jericha in 1985 [2] for solar generated oxygen-hydrogen fuel, and in 1995 changed to fossil fuels [3,4]. This was the first proposal for gas turbine oxy-fuel CO_2 capture. Improvements and further developments since then were presented at several conferences [5–9]. Any fossil fuel gas (preferably with low nitrogen content) is proposed to be combusted with oxygen and by neglecting small impurities only the two combustion products, CO_2 and H_2O, are generated. The cycle medium of CO_2 and H_2O allows an easy and cost-effective CO_2 separation by condensation. Furthermore, the oxygen combustion enables a power cycle with a thermal efficiency among the very best ever proposed, thus largely compensating for the additional efforts of oxygen production.

At the ASME IGTI Conference 2004 in Vienna a Graz Cycle power plant (High Steam Content Graz Cycle, S-Graz Cycle) was presented with a thermal cycle efficiency of nearly 70% (excluding work for oxygen supply and CO_2 compression) based on syngas firing, and relatively low CO_2 retention costs [10].

The very promising data aroused interest in several institutions in Europe, among them the Norwegian oil and gas company Statoil ASA. In cooperation with Statoil the S-Graz Cycle was reevaluated and optimized with assumptions on component losses and efficiencies which Statoil and Graz University of Technology had agreed on. At the ASME IGTI conference 2005 [11] the results were presented with a net cycle efficiency of 52.7% for methane firing, if the efforts of oxygen supply and compression of captured CO_2 for liquefaction are considered. The CO_2 mitigation costs were evaluated to \$20.7/ton CO_2 avoided.

These investigations also formed the basis of a techno-economic evaluation study by the two most important and most successful gas turbine companies in Europe. The feasibility of the S-Graz Cycle was accepted and the cost structure discussed in detail. The result was on one side that the cryogenic air separation unit ASU appears to have too high investment costs. On the other side the condensation of water out of a mixture of steam and incondensable gases, a thermodynamic technical problem not yet solved in European science, has to be more clearly investigated.

Therefore the object of this paper is to present the authors' work on the following subjects:

- Modification of the S-Graz Cycle configuration to condensation in the range of 1 bar providing combustion generated CO_2 for separation. By slight recompression, evaporation of pure steam at reasonably high pressure and efficient expansion in a large output steam turbine is made possible.
- Increase of net plant output to 400 MW providing for the additional tasks of oxygen production, CO_2 capture, and delivery for pipeline use or liquefaction. The power effort is included in the overall efficiency raising the shaft output design value to 490 MW.
- Two-shaft design of the turbo set with a fast running shaft comprising the main compressors C1 and C2 and the com-

Contributed by the International Gas Turbine Institute of ASME for publication in the JOURNAL OF ENGINEERING FOR GAS TURBINES AND POWER. Manuscript received June 12, 2006; final manuscript received February 14, 2007; published online December 26, 2007. Review conducted by Dilip R Ballal. Paper presented at the ASME Turbo Expo 2006: Power for Land, Sea and Air, Barcelona, Spain, May 8–11, 2006, Paper No. GT2006-90032.

Copyright © 2008 by ASME

Downloaded 02 Jun 2010 to 171.66.16.107. Redistribution subject to ASME license or copyright; see http://www.asme.org/terms/Terms_Use.cfm

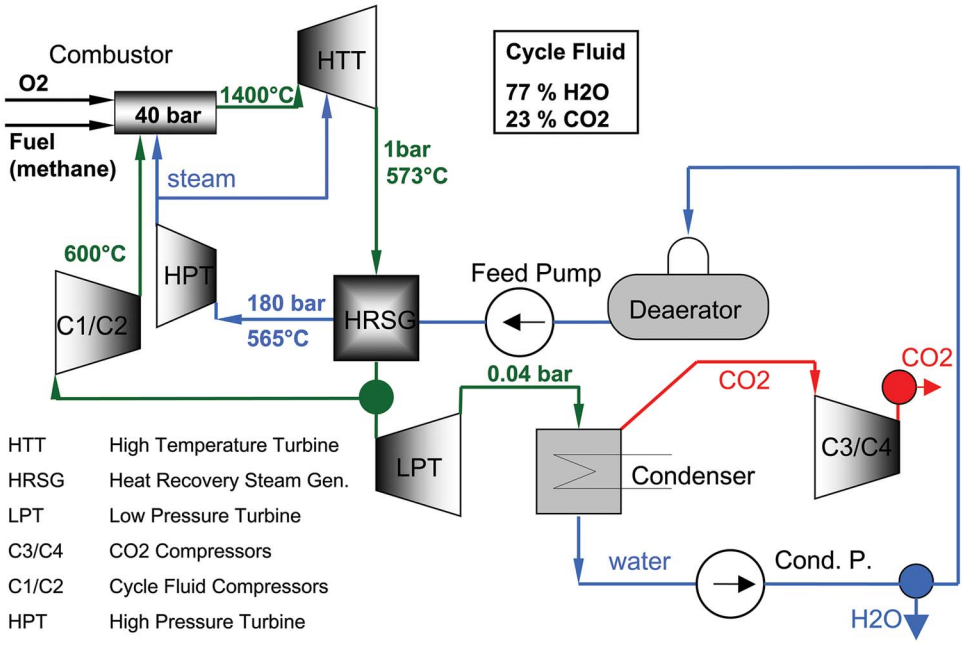

Fig. 1 Principle flow scheme of the basic Graz Cycle power plant

pressor turbine and with a power shaft connected to the generator.

- Incorporation of advanced flow and cooling development throughout the gas turbine components for smaller size and cost, and reduction of high temperature material by rotor steam cooling on all accessible surfaces.

Deliberations on part load and cold start for the situation of the novel cycle medium are also presented.

In this work the nomination "Graz Cycle" means "S-Graz Cycle," which is the more efficient variant and will be presented in the future.

Graz Cycle Basic Configuration

The Graz Cycle is suited for all kinds of fossil fuels. The best results regarding net cycle efficiency and mitigation costs can be obtained for syngas firing from coal gasification, if the syngas production effort is not considered in the thermodynamic balance (but only in the economic balance by elevated fuel costs). The higher net cycle efficiency results from the lower oxygen demand of syngas per heat input reducing the effort of oxygen supply considerably. And finally, the higher carbon content results in more favorable mitigation costs per ton CO_2 avoided. But, in this work thermodynamic data presented are for a cycle fired with methane, because it is the most likely fuel to be used in a first demonstration plant.

Figure 1 shows the principle flow scheme of the S-Graz Cycle with the main cycle data as published in [11].

Basically the Graz Cycle consists of a high temperature Brayton cycle (compressors C1 and C2, combustion chamber and high temperature turbine (HTT), and a low temperature Rankine cycle (low pressure turbine (LPT), condenser, heat recovery steam generator (HRSG), and high pressure turbine (HPT)). The fuel together with the nearly stoichiometric mass flow of oxygen is fed to the combustion chamber, which is operated at a pressure of 40 bar. Steam as well as a CO_2/H_2O mixture is supplied to cool the burners and the liner.

A mixture of about 74% steam, 25.3% CO_2, 0.5% O_2, and 0.2% N_2 (mass fractions) leaves the combustion chamber at a mean temperature of 1400°C, a value achieved by G and H class turbines nowadays. The fluid is expanded to a pressure of 1.053 bar and 579°C in the HTT. Cooling is performed with steam coming from the HPT at about 330°C (13.7% of the HTT inlet mass flow), increasing the steam content to 77% at the HTT exit. It is quite clear that a further expansion down to the condenser pressure would not end at a reasonable condensation point for the water component, so that the hot exhaust gas is cooled in the following HRSG to vaporize and superheat steam for the HPT; the pinch point of the HRSG is 25°C at the superheater exit. After the HRSG only 45% of the cycle mass flow are further expanded in the LPT. For a cooling water temperature of 8°C the LPT exit and thus condenser pressure is 0.041 bar.

Gaseous and liquid phase are separated in the condenser. From there on the gaseous mass flow, which contains the combustion CO_2 and half of the combustion water, is compressed to atmosphere by C3 and C4 with intercooling and further extraction of condensed combustion water, and supplied for further use or storage. At atmosphere the CO_2 purity is 96%; further water extraction is done during further compression for liquefaction.

After segregating the remaining combustion H_2O, the water from the condenser is preheated, vaporized, and superheated in the HRSG. The steam is then delivered to the HPT at 180 bar and 549°C. After the expansion it is used to cool the burners and the HTT stages.

The major part of the cycle medium—the return flow after the HRSG—is compressed using the main cycle compressors C1 and C2 with intercooler and is fed to the combustion chamber with a maximum temperature of 600°C.

The cycle arrangement of the Graz Cycle offers several advantages: On the one hand, it allows heat input at very high temperature, whereas on the other hand expansion takes place down to vacuum conditions, so that a high thermal efficiency according to Carnot can be achieved. But only less than half of the steam in the cycle releases its heat of vaporization by condensation. The major part is compressed in the gaseous phase and so takes its high heat content back to the combustion chamber.

Large Power Graz Cycle With Working Fluid Condensation/Evaporation in the 1 bar Range

In the basic S-Graz Cycle configuration the authors proposed an expansion of the portion of the working fluid which has to be

Downloaded 02 Jun 2010 to 171.66.16.107. Redistribution subject to ASME license or copyright; see http://www.asme.org/terms/Terms_Use.cfm

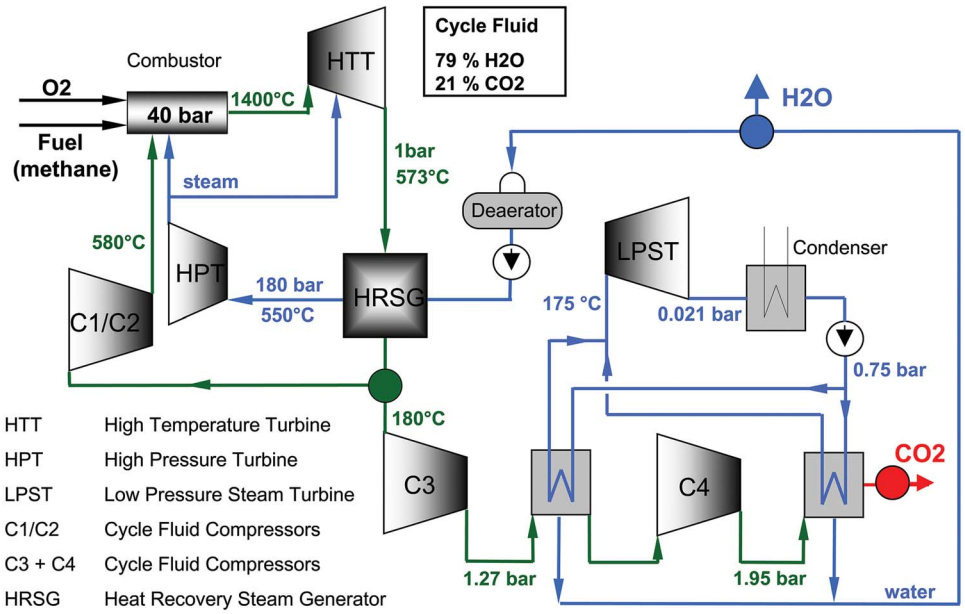

Fig. 2 Principle flow scheme of modified Graz Cycle power plant with condensation/evaporation in the 1 bar range

segregated from the circulating flow to be expanded down to vacuum pressure. This flow contains the captured CO_2 and steam from the combustion as well as the cooling steam flow. Recent research [12] shows that difficulties in condensation arise in the formation of water films on the cooling tubes and in concentration of CO_2 forming a heat transfer hindering layer so that only a low heat transfer coefficient in condensation will be achieved. This results in excessively large condenser heat transfer surface and related high costs.

Therefore, it was suggested in the Austrian patent of the Graz Cycle [13] to condense this mass flow at atmosphere, separate the combustion CO_2, and revaporize the water at a reduced pressure level using the condensation heat. The pure steam is then fed to a low pressure steam turbine (LPST), where it can be expanded to a condenser pressure lower than that for the working fluid mixture.

Thermodynamic investigations presented at the ASME 2005 Conference [11] showed that best results can be obtained for a dual pressure evaporation at 0.55 and 0.3 bar. But for these low evaporation pressures, large volume flows arise and the losses of live steam pipes and valves counteract the gains of this process.

Therefore a novel configuration is proposed in this work which allows single-pressure evaporation at a reasonable pressure level. The process is now split into the high-temperature cycle and a separate low-temperature condensation process as shown in the simplified scheme of Fig. 2. The high-temperature part consists of HTT, HRSG, C1/C2 compressors, and HPT. Again condensation of the working fluid in the 1 bar range is proposed in order to avoid the problems of a working fluid condenser at vacuum conditions as described above. The heat content in the flow segregated after the HRSG for condensation is still quite high so re-evaporation and expansion in a bottoming cycle is mandatory. The detailed flow sheet used for the thermodynamic simulation can be found in [14] and gives mass flow, pressure, temperature, and enthalpy of all streams.

The bottoming cycle operates with pure steam with extensively cleaned feed water, and together with the very low cooling water temperatures of northern Europe, allows to attain condenser pressures down to 0.02 bar.

For proper re-evaporation, two sections of working fluid condensation are provided, each following a compressor stage with a reasonable increase of flow pressure resulting in a higher partial condensation pressure of the water content. The two compressor stages can be regarded as prerunners of the CO_2 delivery compressor and will be helpful in cleaning the turbomachinery, piping, and HRSG interior from air in preparation of a cold start. The heat exchangers are well developed modern boiler elements providing steam just below 1 bar for the condensing steam turbine.

At the first pressure level of 1.27 bar about 63% of the water content can be segregated, so that the power demand of the second compression stage is considerably reduced. It compresses up to 1.95 bar, which allows the segregation of an additional 25% of the contained water. Further cooling of the working fluid, also for water preheating, leads to the separation of an additional 11%, so that the water content of the CO_2 stream supplied at 1.9 bar for further compression is below 1%. After segregation of the water stemming from the combustion process, the water flow is degassed in the deaerator with steam extracted after the HPT and fed to the HRSG for vaporization and superheating.

This two-step precompressed condensation counteracts the effect of sinking H_2O partial pressure due to condensed water extraction from working fluid and thus allows a reasonably high constant re-evaporation pressure of 0.75 bar for the bottoming steam cycle. Figure 3 shows the heat-temperature diagram for this condensation/evaporation process. After the start of water condensation, the working fluid temperature decreases only slightly, leading to relatively small mean temperature differences of 8 K in the first evaporator and 12 K in the second evaporator. After having condensed and separated most of the water content, the temperature of the working fluid decreases strongly in the water preheaters of the bottoming cycle.

About three quarters of the condensation cycle mass flow is evaporated and superheated in the first condenser. It is mixed with the steam of the second condenser/evaporator unit providing steam of 0.75 bar and 175°C at the LPST inlet. Expanding the steam to a condensation pressure of 0.021 bar for a cooling water temperature of 8°C provides about 72 MW power output. A four-flow design is necessary to handle the high volume flow for a 400 MW Graz Cycle.

Steam is extracted at a pressure of 0.12 bar from the LPST and fed to the deaerator. The expansion line is to the major part in the dry steam region and crosses the Wilson line only before the last

Downloaded 02 Jun 2010 to 171.66.16.107. Redistribution subject to ASME license or copyright; see http://www.asme.org/terms/Terms_Use.cfm

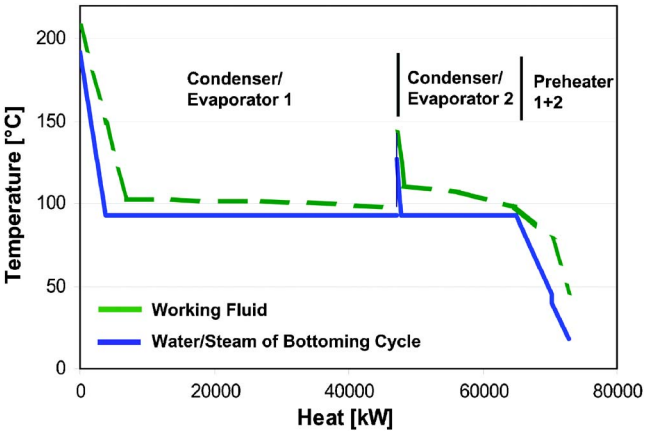

Fig. 3 Heat-temperature diagram of the condensation/ evaporation process

stage, so that only very fine droplets in the outer last stage sections are formed. A very high expansion efficiency hardly hindered by formation of humidity is to be expected.

Table 1 gives the power balance of the modified Graz Cycle plant of 400 MW net power output in comparison with the scaled-up basic configuration published in [11]. The heat input is the same for both cycles allowing a better comparison of the turbomachinery sizes. The C3 and C4 compressors have different tasks in both cycles. In the basic cycle they recompress the separated CO_2 flow to 1 bar, whereas in the modified cycle they increase the working fluid pressure for a more favorable condensation/evaporation condition as described above. The modified Graz Cycle works with a smaller mass flow of the working fluid, so that both turbine and compressor total power decrease, whereas the net power output remains nearly the same. This leads to a similar thermal efficiency of about 66.5% or an electrical net efficiency of about 64.65%.

By considering the efforts for oxygen production and compression as well as the efforts of CO_2 compression to 100 bar for liquefaction, the net efficiency further reduces to 52.72% for the basic cycle and 53.12% for the modified cycle. This higher efficiency stems from a reduced CO_2 compression effort due to the higher supply pressure of 1.9 bar in the modified cycle. Thus the specific energy consumption is reduced from 350 kJ/kg to 300 kJ/kg CO_2. The net efficiency of 53.12% is higher than that of most other CO_2 capture technologies if evaluated under the same conditions, so that this new concept is worth a further feasibility investigation.

Table 1 Graz Cycle power balance

	Basic layout	New layout
HTT power (MW)	634.7	617.9
HPT power (MW)	48.0	49.9
LPT/LPST power (MW)	70.5	71.6
Total turbine power (MW)	753.2	739.4
C1 power (MW)	137.2	131.1
C2 power (MW)	90.2	82.6
C3 power (MW)	11.5	8.9
C4 power (MW)	4.8	6.6
Pump power (MW)	5.3	5.5
Total compression power (MW)	249.0	234.7
Net shaft power (MW) without mechanical losses	504.2	504.7
Total heat input Q_{zu} (MW)	758.6	758.6
Thermal cycle efficiency (%)	**66.47**	**66.52**
Electrical power output (MW) including mechanical, electrical, and auxiliary loss	490.3	490.7
Net electrical cycle efficiency (%)	**64.63**	**64.68**
O_2 generation and compression (MW)	74.7	74.7
Efficiency considering O_2 supply (%)	**54.78**	**54.83**
CO_2 compression to 100 bar (MW)	15.6	13.0
Net power output (MW)	**400.0**	**403.0**
Net efficiency η_{net} (%)	**52.72**	**53.12**

Design Concept for a Very Large Graz Cycle Plant of 400 MW Net Output

In this work the design concept for a Graz Cycle power plant of 400 MW electrical net output is presented. This power is derived from a 490 MW turbo shaft configuration. The difference is caused by the power demand of the ASU and by the driving power for the oxygen compressor in order to deliver oxygen to the combustor at 42 bar and by the CO_2 compressor which has to deliver the captured CO_2 at a pipeline pressure of over 100 bar.

Gas turbines, compressors, and combustor require the best flow development achieved up to now in gas turbine technology. In the course of this project our institute has found novel solutions for blade cooling, steam cooled combustor burner design, and optimal rotor construction and rotor dynamics. The innovative burner design helps to achieve the mentioned very high thermal efficiency (see [6] for details of the burner design), further improved by the positive change on the lower temperature end of the power cycle flow scheme as described above.

In this design proposal intensive use of steam cooling is made not only for blades, but for all rotors in the high-speed high-temperature region. In that manner a solid and simple rotor design forged from one piece or welded from separate disks can be used with no internal friction between rotor disks as might be possible in a rotor assembled from separate disks. This type of rotor design provides for high blade load carrying capability with acceptable radial stress. The newly developed high-chromium ferritic steels will be applied making use of their superior heat conduction and low thermal expansion properties. The relatively high speed selected provides for long blades in the last stages with high flow efficiency and low tip clearance loss.

The one-shaft system as in air-breathing gas turbines is not applicable since in the Graz Cycle system the compressor flow volume is smaller and the number of stages required considerably higher. Therefore a much higher compressor speed as power turbine speed is an effective solution.

The main gas turbine components are arranged on two shafts, the compression shaft and the power shaft (see Fig. 4). The compression shaft consists of the cycle compressors C1 and C2, which are driven by the first part of the high temperature turbine (HTT), the compressor turbine HTTC. It runs free on its optimal speed of 8500 rpm. This relatively high speed is selected for reason of obtaining sufficient blade length at the outlet of C2 and to reduce the number of stages in both compressors. The second part of the HTT, the power turbine HTTP, delivers the main output to the generator. A further elongation of the shaft is done by coupling the four-flow LPST at the opposite side of the generator. The HPT can be coupled to the far end of the LPST or can drive a separate generator. The two shafts are based on the same spring foundation. The intercooler between C1 and C2 is located on the fixed foundation.

C1/C2 Compressor Design With Intercooler. The working fluid compressor C1 is driven by the HTTC at 8500 rpm. The high speed poses a special problem for the first stage of C1 which has yet been solved by flow research and is now applied in many aircraft jet engines and also stationary compressor designs [15,16]. The high tip Mach number on the first stage should not exceed the value of 1.4 for reasons of shock formation. With the help of a slight positive inlet swirl an inlet Mach number of 1.3 is designed.

Compression at C1 starts at 106°C and reaches 442°C at the outlet to the intercooler. For reasons of rotor dynamics the shafts

Downloaded 02 Jun 2010 to 171.66.16.107. Redistribution subject to ASME license or copyright; see http://www.asme.org/terms/Terms_Use.cfm

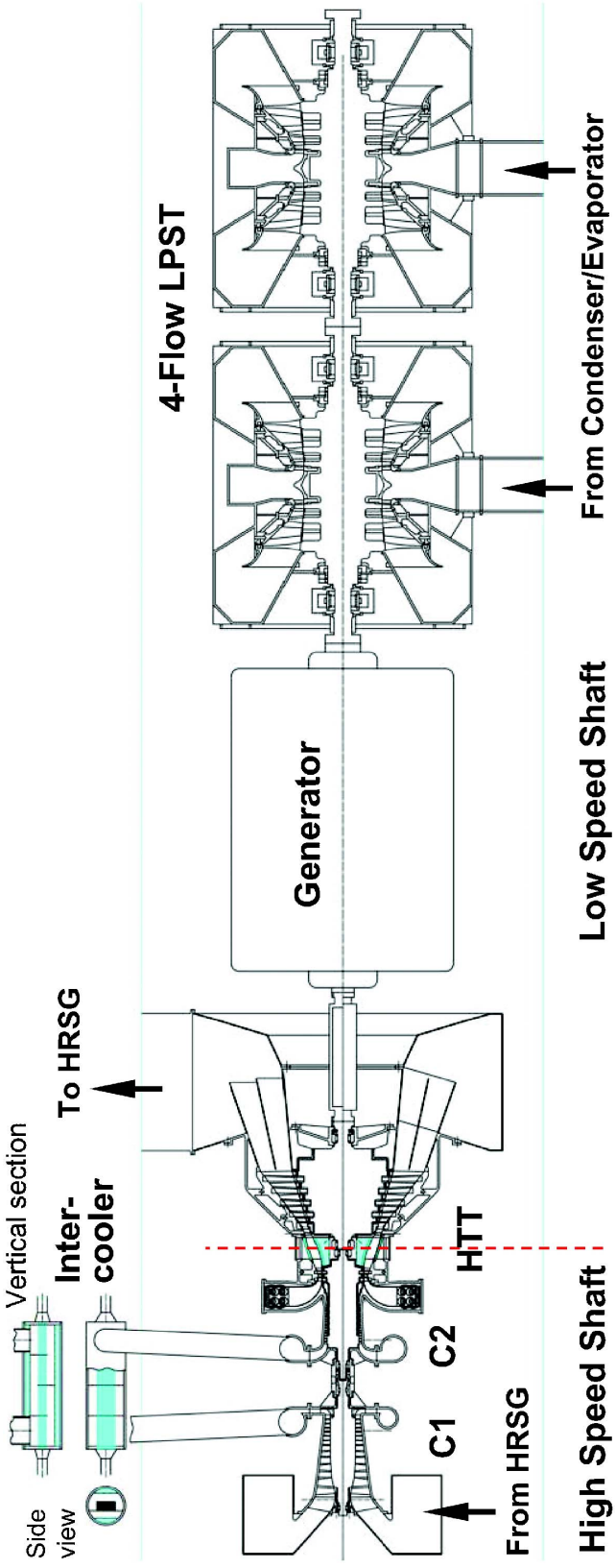

Fig. 4 Arrangement of the main turbomachinery for a 400 MW Graz Cycle plant

of C1 and C2 are separated with intermediate bearings and a solid coupling. This makes the transfer of cooling flow difficult, so that cooling of the drum rotor of C1 will not be applied. This is possible by a combination of rotor materials.

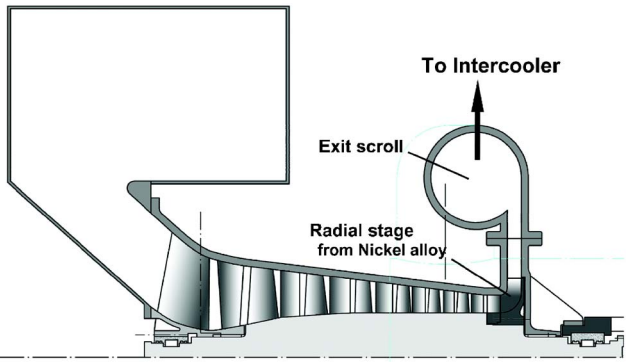

Fig. 5 C1 design with an uncooled drum rotor and an additional radial stage from nickel alloy, with radial diffuser and exit scroll to the intercooler

The first part with seven axial stages is a ferritic steel drum, which reaches only 390°C. This material can be highly stressed without creep at temperatures below 400°C. By the application of a final radial wheel which has to be milled separately from nickel alloy and which is mounted to the main drum by elastic centering the rotor construction of C1 is completed, as shown in Fig. 5. The radial wheel with a wide vaneless diffuser and scroll improves the flow transfer to the intercooler.

The inlet temperature to C2 is somewhat lowered by the intercooler but still reaches 380°C. During the course of compression the working fluid reaches an outlet temperature of 580°C, so that from the second stage onwards cooling has to be applied on the rotor surface of the bladed annular flow channel. Seven axial stages with a stepwise decrease of blade length from 90 to 40 mm are supported on a drum rotor with disk extensions of constant diameter. Figure 6 shows the C2 rotor with the counter flow of cooling steam on the drum surface. It is guided by means of openings under the bladed disk extensions and is prevented from flowing into the main flow by sealing strips. These strips are carried on both sides of the stationary blades. By proper selection of the feed pressure this flow can be optimized at a small penalty of dilution of the main flow.

Excellent flow properties of this compressor can be expected due to its blade mounting on a stiff rotor with very small radial tip clearances and flow losses together with an aspect ratio of outer to inner flow radius of 440/400 mm at the last stage.

The intercooler requires some development work. The fluids on both sides are unconventional insofar as the working fluid on one side is to be cooled by high pressure steam on the other side. Heat transfer from compression work to steam superheat is thus achieved. The authors can point at previous development work at their institute in a similar problem, i.e., the design of an 850°C steam plant in double loop configuration as published by Perz et al. [17], where many boiler heat transfer problems were treated.

In the case given, the intercooler is thermodynamically part of the HRSG superheater and is thus arranged close to the HRSG. Its cooling flow is steam of 196 bar pressure. It is designed as a solid tube which should be supported on solid ground foundation. The heat transfer surface is realized by 180 tubes of 3.1 m length held in support plates which guide the working gas flow from the C1 outlet to the C2 inlet. The outer shell of the intercooler is internally insulated and is connected to both compressors by ample flow areas in flexible scroll and tube arrangements (see Fig. 4).

HTT Compressor Turbine (HTTC). The same drum rotor either forged in one piece or welded up from separated disks carries not only the C2 but also the compressor turbine HTTC. The flow design of the HTTC will be a two-stage reaction turbine with 50% reaction at the mean section of both blade rows. The high rotor

Downloaded 02 Jun 2010 to 171.66.16.107. Redistribution subject to ASME license or copyright; see http://www.asme.org/terms/Terms_Use.cfm

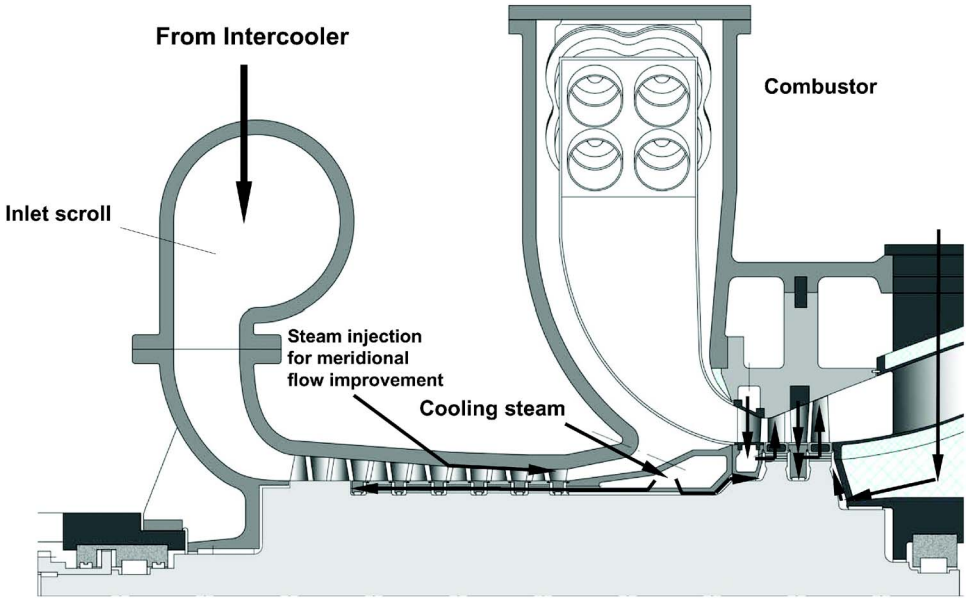

Fig. 6 Design of C2 drum rotor with cooling steam flow arrangement, combuster, and HTTC

speed of 8500 rpm as mentioned before provides for long blade lengths, i.e., a first stage blade of 100 mm and a second stage blade of 164 mm with an inner radius of 533 mm (see Fig. 7). This results in excellent flow properties in subsonic condition and together with the high reaction of the blade on all radii (50% at the mean section and at least 25% at the hub) a high blade flow efficiency is expected. Low tip clearances are applied, also contributing to this goal and can be achieved by the excellent rotor dynamics of the stiff drum rotor and very careful blade cooling.

The high speed and power of this turbine is made possible by ample steam cooling. Nozzles and blades are cooled in conventional serpentine passage design with holes as shown in the cooling arrangement of Fig. 7. Rotor cooling steam is supplied along the whole drum surface. It is fed into a labyrinth seal in the inner range of the combustion chamber allowing the steam to flow to both sides. One flow is directed backwards under the dump diffuser into the outer surface of the C2 providing cooling steam as described above. The main amount of cooling steam flows along the rotor drum at the inner radius of the combustor casing towards the first disk of the HTTC.

The first nozzles are hollow with proper cooling passages and are cooled by steam fed from the casing outside in the radial inward direction. The steam is collected in a chamber of the diaphragm just opposite the first blade root. Via nozzles, blowing in the direction of rotor speed, the cooling steam is then fed to the lower part of the blade fir-tree root. From there it flows along the serpentine passages under pumping action of the rotor wheel and is delivered to the blade surface via laser drilled holes to form the conventional cooling films at the appropriate locations of the blade. The second guide vanes are supplied with cooling steam which is fed into the outer rim of the diaphragm. There it flows radially inwards also to supply the rotor surface in-between stages and the inlet to the second stage blades which are also built with serpentine passages and the appropriate cooling holes. In principle, this design was applied for the well-known gas turbine model GT10, originally designed by Zerlauth [18].

The drum rotor of C2 and HTTC will be designed for the high stress considering the effect of steam cooling on all surfaces. In

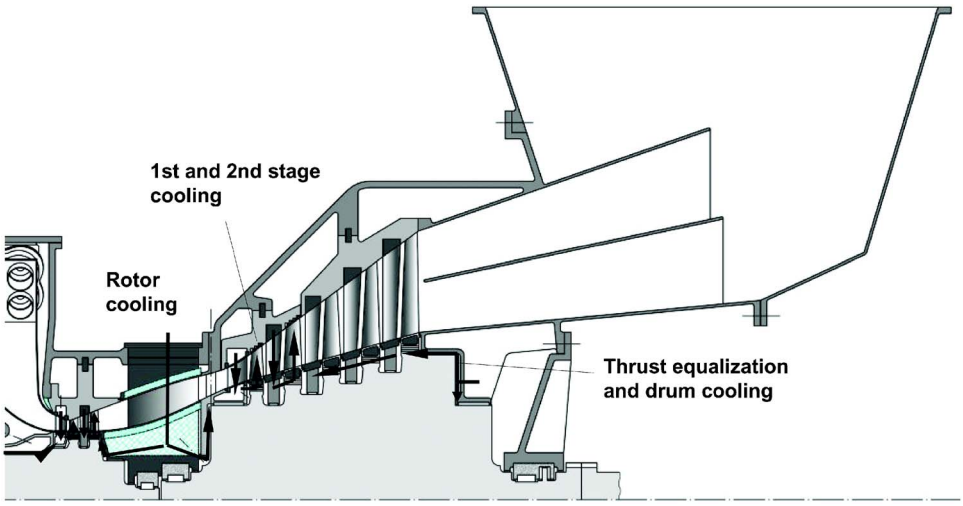

Fig. 7 Design of two-stage HTTC and 50 Hz HTTP

Downloaded 02 Jun 2010 to 171.66.16.107. Redistribution subject to ASME license or copyright; see http://www.asme.org/terms/Terms_Use.cfm

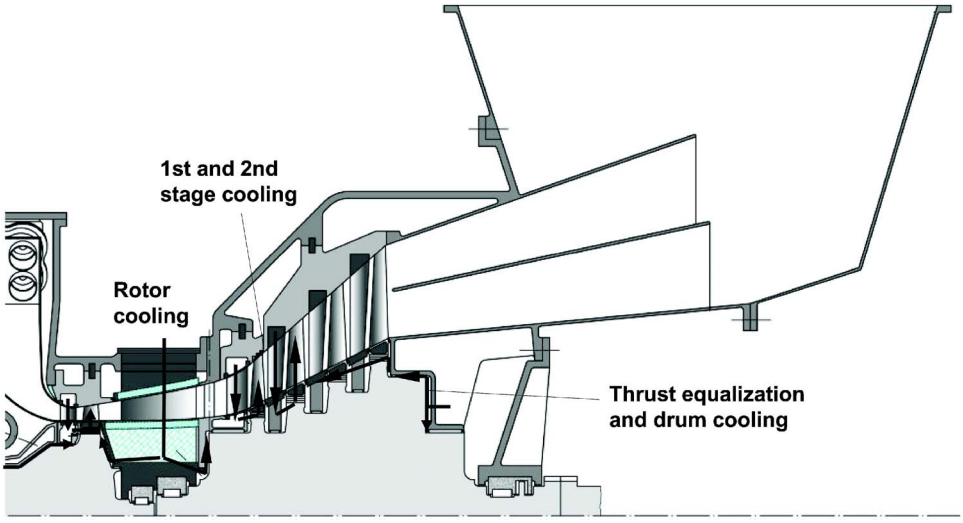

Fig. 8 Design of transonic one-stage HTTC and 60 Hz HTTP

terms of rotor dynamics, stiff bearing shaft extensions and solid double-lobe oil bearings provide for high shaft and high bearing stiffness in order to have all critical speeds sufficiently high.

HTTC Alternative Transonic Stage Design. The authors' institute has done extensive development work for the design of transonic turbine stages. Not only several computer programs have been developed for investigating three-dimensional transonic flow, but a unique test installation for transonic stages was built where many effects of unsteady viscous transonic flow were investigated (e.g., [19]). The test installation has aided the development of industrial gas turbines and is now in use for several EU projects.

A novel innovative cooling system has also been developed and could be applied here in order to save cooling medium, high temperature material, and cost of manufacture and at the same time providing most effective blade cooling at the blade leading edge in transonic flow [20,21]. The design could follow the development path of General Electric in providing thermal barrier coating on the rotating blades since these blades are free of the multitude of cooling holes and are supplied only by a low number of slots creating cooling steam films covering the whole surface.

Therefore, alternatively the HTTC expansion could also be done with one transonic stage as shown in Fig. 8. This can be achieved by a higher radius and stage loading at a somewhat reduced degree of reaction. Such a stage would sit on the same rotor as described before and it would have a mean radius of 750 mm at a blade length of 120 mm. A further advantage of a transonic stage would be the much smaller radius difference from compressor turbine outlet to power turbine inlet, depending also on the speed of the power turbine for which design proposals for 50 and 60 Hz are presented here.

HTT Power Turbine (HTTP). A gas turbine system with two shafts at highly different speeds as it has to be built here requires an intermediate bearing to be arranged right between the stages of the compressor turbine outlet and power turbine inlet. The flow of gas transmitted is at very high velocity, at temperatures of 1075 °C and at a pressure of 14 bar. A conventional design would provide an outlet diffuser, an outlet casing, a transition duct, and an inlet casing in-between these gas turbine parts. Frictional loss and heat loss, even with internal and external insulation, would be unavoidable. In previous design solutions for industrial-size turbines with almost the same cycle conditions the authors have proposed a single overhung disk with a transonic stage for the compressor turbine and one or two overhung disks for the power turbine directly opposite to take over the gas flow in a common casing [10]. This solution requires a high speed power turbine which can only be built relying on gears of high speed and high power. The power output of 92 MW in that case made it possible since gas turbines transferring around 100 MW from gas turbine speeds of 5400 rpm to 3000 rpm are in use in industry.

The large power output in the case presented here forbids the use of gears for such high-speed power transfer. Therefore the possible electrical frequencies of 50 Hz in Europe and 60 Hz in the USA and the western hemisphere were investigated. The power turbine is proposed with a strong change of inner radius on a solid shaft. Five stages are necessary for the 50 Hz design of Fig. 7 and four stages for the 60 Hz design of Fig. 8. The axial outlet speed should be kept at medium value in order to reduce the exhaust loss, to reduce axial diffuser exit length, and to facilitate the flow transfer to the HRSG inlet.

The design proposed provides the last blade lengths of 750 mm at 50 Hz and of 600 mm at 60 Hz, both at 1300 mm inner radius. At the inlet the inner radius at 50 Hz is somewhat larger than the HTTC outlet, but at 60 Hz, together with a transonic HTTC, there is a flow path at almost the same radius as shown in Fig. 8.

The intermediate bearing casing in its hot environment has to be insulated on its outer surface in a mode of insulation withstanding the friction of the hot outer flow. The same holds true for the three supporting ribs, which have to provide ample inner space for transfer of oil and cooling air and for leakage steam outlet from labyrinths on both shaft sides as well as for monitoring equipment. At the same time the bearing should be as short as possible and the ribs should provide only a minimum of flow resistance. Certainly this is an object that deserves intensive flow, stress, and heat transfer deliberations.

The thrust equalization of both types of power turbines cannot be made in the conventional manner of steam turbines. A balance piston requires a diameter of about the mean blade mean diameter to give proper balance of axial forces. In this case such a design would require an unacceptable flow turn and deviation of the hot gas flow at inlet. (In a one-shaft gas turbine the problem does not exist, since compressor thrust and turbine thrust balance each other.) On the other hand, to carry the axial thrust of a large power turbine especially in the conical form is impossible for oil thrust bearings. Size and oil friction power loss would be too high. Therefore a stepped labyrinth on the exhaust side of the rotor drum is proposed as shown in Figs. 7 and 8, which is supplied with internal steam pressure to provide for the necessary thrust equalization. The steam supply also feeds the cooling flow which is led along the rotor drum surface under the root sealing plates of the last and the penultimate stage, whereas cooling flow to the first

Downloaded 02 Jun 2010 to 171.66.16.107. Redistribution subject to ASME license or copyright; see http://www.asme.org/terms/Terms_Use.cfm

and second stages is supplied via the hollow nozzle blades to an inner diaphragm cavity from which the inflow to the hollow rotor blades is effected. Power turbine thrust bearing is arranged outboard of the casing in the vicinity of the steam operated balance piston (see Figs. 7 and 8).

Low Pressure Steam Turbine (LPST). The LPST is fed with steam of 0.75 bar and 175°C. Expanding the steam to a condensation pressure of 0.021 bar leads to a high volume flow. At 50 Hz a four-flow design with three stages as shown in Fig. 4 is able to handle the high steam flow with excellent efficiency. The last stage is transonic with a blade length of 970 mm. In the shaft arrangement this steam turbine is coupled to the far side of the main generator.

HPT. The HPT is a standard high-speed back-pressure steam turbine of 50 MW power output for which many designs are in the market. A geared type seems to be a superior solution since better flow efficiency and operability due to nozzle boxes and low number of stages with long blades and low leakage loss can be achieved. It can be coupled to the far end of the LPST or can be used to drive a separate smaller electric generator.

Compressors C3 and C4. The delivery compressors C3 and C4, which increase the pressure of the working fluid prior to condensation in order to obtain better evaporation conditions for the bottoming steam cycle, are also needed to vent the internal volume before start up. They are driven by two separate speed-controlled motors.

Combustion. The combustion chamber and burner design proposed has been thoroughly tested in the science of combustion. Research partners have run CH_4/oxygen burners in a steam environment successfully [22,23]. The authors' proposal [7] of setting a separate oxygen and fuel inlet in the center of a strong steam vortex in a large number of separate burners within the combustion chamber provides for easy control of amount and ratio of oxygen and fuel together with ignition and flame observation. The steam vortex keeps together both reactants. The independent supply of both reactants together with the high flame speed caused by pure oxygen lets expect improvements compared to the otherwise acoustic vibration prone conventional low-NOx combustion chamber flows.

Part Load and Start-Up. In part load the maximum gas turbine temperature can be lowered by reduction of heat input. With the free-running compressor shaft adjustment of flow and temperature can be effected precisely in operating IGVs and turbine valves accordingly.

To keep the working fluid and the CO_2 delivery line free of nitrogen at each cold start, careful scavenging of all internal volumes in turbomachinery, HRSG, and piping has to be done. Fuel and oxygen input can be governed for each burner so that ignition and safe operation of flames is secured.

Economic Evaluation

Despite the high efficiency and the positive impact on the environment by a Graz Cycle power plant, a future application of this technology and an erection of a power plant mainly depend on the economic balance. The main indicator characterizing the economic performance of a power plant for CO_2 capture are the mitigation costs. They represent the increased capital and operational costs incurred by new and additional equipment and lower cycle efficiencies in relation to the CO_2 mass flow avoided. The CO_2 captured has an economic value of about \$10/ton, if it can be used for enhanced oil recovery (EOR) or of about \$30/ton in the future CO_2 emission trading scenario. These prices show the current threshold for the economic operation of zero emission power plants.

In order to estimate the mitigation costs for a Graz Cycle plant, an economic comparison with a state-of-the-art combined cycle power plant of 58% efficiency is performed. The economic balance is based on the following assumptions: (1) the yearly operating hours are assumed at 8500 h/yr; (2) the capital charge rate is 12%/yr, which corresponds to an interest rate of 8% over a depreciation period of 15 years; (3) methane fuel costs are 1.3¢/kWh$_{th}$; (4) the investment costs per kW are the same for the reference plant of about 400 MW net power output and the Graz Cycle plant (see below); (5) additional investment costs are assumed for the air separation unit (ASU), for additional equipment and CO_2 compression to 100 bar (see Table 2 [24]); and (6) the costs of CO_2 transport and storage are not considered because they depend largely on the site of a power plant.

Table 2 Estimated investment costs

Component	Scale parameter		Specific costs
Reference plant			
Investment costs	Electric power	\$/kW$_{el}$	414
Graz Cycle plant			
Plant investment costs	Electric power	\$/kW$_{el}$	414
Air separation unit[a]	O_2 mass flow	\$/(kg O_2/s)	1,500,000
Other costs (piping, CO_2-recirc.)[a]	CO_2 mass flow	\$/(kg CO_2/s)	100,000
CO_2-compression system[a]	CO_2 mass flow	\$/(kg CO_2/s)	450,000

[a]Reference 24.

The assumption of similar investment costs for a conventional and a Graz Cycle power plant is based on a comparison with typical turbomachinery sizes for a 400 MW combined cycle plant as given in Table 3. It shows that the turbine and HRSG power are of similar size, whereas the compressor power is remarkably smaller. On the other hand the Graz Cycle needs a larger generator due to the additional power consumption for ASU and CO_2 compression. Development efforts needed especially for HTT and combustor are not considered in the investment costs.

Table 4 shows the result of the economic evaluation. Compared to the reference plant, the capital costs are about 70% higher only by considering the additional components for O_2 supply and CO_2 compression, so that they contribute mostly to the difference in

Table 3 Comparison of equipment size for a 400 MW plant in terms of power

	Conventional CC plant	Graz Cycle plant
Turbine of "gas turbine"/HTT	667 MW	618 MW
compressor of "gas turbine"/ C1+C2+C3+C4	400 MW	232 MW
Steam turbine/HPT+LSPT	133 MW	120 MW
HRSG	380 MW	360 MW
Generator	400 MW	490 MW

Table 4 Economic data for a 400 MW Graz Cycle plant

	Reference plant	Graz Cycle plant
Plant capital costs (\$/kW$_{el}$)	414	414
Additional capital costs (\$/kW$_{el}$)		288
CO_2 emitted (kg/kWh$_{el}$)	0.342	0.0
Net plant efficiency (%)	58.0	53.1
COE for plant amort. (¢/kWh$_{el}$)	0.58	0.99
COE due to fuel (¢/kWh$_{el}$)	2.24	2.45
COE due to O&M (¢/kWh$_{el}$)	0.7	0.8
Total COE (¢/kWh$_{el}$)	**3.52**	**4.24**
Differential COE (¢/kWh$_{el}$)		0.72
Mitigation costs (\$/ton CO_2 avoided)		21.0

Downloaded 02 Jun 2010 to 171.66.16.107. Redistribution subject to ASME license or copyright; see http://www.asme.org/terms/Terms_Use.cfm

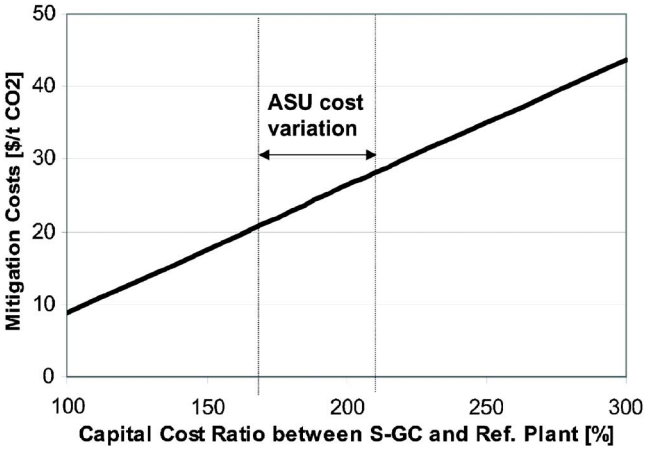

Fig. 9 Influence of capital costs on the mitigation costs (CO_2 provided at 100 bar)

cost of electricity (COE). The fuel costs have the major influence on the COE, especially for syngas firing, but they do not differ largely between reference and Graz Cycle plant. The O&M costs are assumed to be 15% higher for a Graz Cycle plant due to the operation of additional equipment.

Based on these assumptions, the COE of a methane fired Graz Cycle plant of 53.1% net efficiency is 0.72 ¢/kWh_{el} higher than for the reference plant. Thus the mitigation costs are \$21.0/ton of CO_2 avoided, if CO_2 liquefaction is considered. This value is clearly below the threshold value of \$30/ton showing the economic potential of the Graz Cycle.

The results of the economic study depend mainly on the assumptions about investment costs, fuel costs, and capital charge rate. A cost sensitivity analysis performed in [11] showed that a variation of the capital costs has the main influence on the economics, since they contribute most to the mitigation costs. Unfortunately, there is a large uncertainty of these costs. A survey of the ASU costs vary in the range of \$230–400/kW_{el} (the same price as for a complete power plant). These costs are for a cryogenic ASU as used, e.g., in the steel industry for half a century. There is certainly a potential for effectivity increase. Oxygen from membranes which are under intensive development now is not yet available for plants of the output under discussion, so the ASU appears to be a decisive cost factor. Only considering its cost variation, the mitigation costs vary between \$21.0 and \$27.9/ton CO_2 for the methane fired plant (see Fig. 9).

This high sensitivity to the capital costs shows the dilemma in performing an exact economic evaluation, since their estimation for a Graz Cycle power plant is very difficult because of the new turbomachinery components. The authors claim that their design of high-speed transonic stages with innovative steam cooling allows a cost-effective manufacture. In these considerations about the height of additional investment costs, a further advantage of the Graz Cycle, the almost NO*x*-free power generation was not evaluated. According to [25] exhaust flow NO*x* and CO catalytic reduction to achieve single-digit emissions (in strict attainment areas) can increase gas turbine genset plant costs by 40–50%.

Conclusions

The Graz Cycle is an oxy-fuel power cycle with the capability of retaining all the combustion generated CO_2 for further use. In order to avoid the difficulties of condensation of water out of a mixture of steam and incondensable gases at very low pressures, a modified cycle configuration was presented with condensation in the range of 1 bar. It allows a separate bottoming steam cycle with reasonably high pressures and efficiencies, so that a high net cycle efficiency above 53% can be expected.

The output of the Graz Cycle plant is raised from industrial size to 400 MW net output. A design concept for this size is presented with two shafts. A fast-running compression shaft is driven by the compressor turbine HTTC, whereas the power shaft comprises the power turbine HPT and the LPST.

In an economic analysis the Graz Cycle power plant is compared with a reference plant. The resulting mitigation costs are in the range of \$20–30/ton CO_2 avoided depending on the costs of the ASU and thus are below a threshold value of \$30/ton CO_2 (assumed for future CO_2 emission trading).

The authors have thus presented a design solution for an oxy-fuel CO_2 retaining gas turbine system which can by acceptance of the international gas turbine industry be put into operation within a few years. The authors believe that this system is equal in thermodynamic performance to any other proposal in the field of CO_2 reduction, and is superior in applying gas turbine experience and research accumulated to this day.

References

[1] Gas Turbine World, 1998, *Pemex Injection for Cantarell Field EOR*, Pequot Publishing Inc.

[2] Jericha, H., 1985, "Efficient Steam Cycles With Internal Combustion of Hydrogen and Stoichiometric Oxygen for Turbines and Piston Engines," CIMAC Conference Paper No. T13, Oslo, Norway.

[3] Jericha, H., Sanz, W., Woisetschläger, J., and Fesharaki, M., 1995, "CO_2-Retention Capability of CH_4/O_2-Fired Graz Cycle," CIMAC Conference Paper, Interlaken, Switzerland.

[4] Jericha, H., and Fesharaki, M., 1995, "The Graz Cycle—1500°C Max Temperature Potential H_2-O_2 Fired CO_2 Capture With CH_4-O_2 Firing," ASME Paper No. 95-CTP-79.

[5] Jericha, H., Lukasser, A., and Gatterbauer, W., 2000, "Der Graz Cycle für Industriekraftwerke gefeuert mit Brenngasen aus Kohle- und Schwerölvergasung" (in German), VDI Berichte 1566, VDI Conference Essen, Germany.

[6] Jericha, H., and Göttlich, E., 2002, "Conceptual Design for an Industrial Prototype Graz Cycle Power Plant," ASME Paper No. 2002-GT-30118.

[7] Jericha, H., Göttlich, E., Sanz, W., and Heitmeir, F., 2004, "Design Optimisation of the Graz Cycle Prototype Plant," ASME J. Eng. Gas Turbines Power, **126**, pp. 733–740.

[8] Heitmeir, F., Sanz, W., Göttlich, E., and Jericha, H., 2003, "The Graz Cycle—A Zero Emission Power Plant of Highest Efficiency," XXXV Kraftwerkstechnisches Kolloquium, Dresden, Germany.

[9] Jericha, H., Sanz, W., Pieringer, P., Göttlich, E., and Erroi, P., 2004, "Konstruktion der ersten Stufe der HTT-Gasturbine für den Graz Cycle" (in German), VDI Berichte 1857, VDI Tagung "Stationäre Gasturbinen: Fortschritte und Betriebserfahrungen," Leverkusen, Germany.

[10] Sanz, W., Jericha, H., Moser, M., and Heitmeir, F., 2005, "Thermodynamic and Economic Investigation of an Improved Graz Cycle Power Plant for CO_2 Capture," ASME J. Eng. Gas Turbines Power, **127**, pp. 765–772.

[11] Sanz, W., Jericha, H., Luckel, F., and Heitmeir, F., 2005, "A Further Step Towards a Graz Cycle Power Plant for CO_2 Capture," ASME Paper No. GT2005–68456.

[12] Karl, J., and Hein, D., 1999, "Effect of Spontaneous Condensation on Condensation Heat Transfer in the Presence of Non Condensable Gases," *Proceedings of the 5th ASME/JSME Joint Thermal Engineering Conference*, San Diege, CA.

[13] Jericha, H., and Sanz, W., 2001, "Wärmekraftanlagen mit Verbrennung von Kohlenwasserstoffen mit reinem Sauerstoff zur Stromerzeugung bei Rückhaltung von Kohlendioxyd" (in German), Austrian Patent No. AT 409 162 B.

[14] Jericha, H., Sanz, W., and Göttlich, E., 2006, "Design Concept for Large Output Graz Cycle Gas Turbines," ASME Paper No. GT2006-90032.

[15] Benvenuti, E., 1997, "Design and Test of a New Axial Compresssor for the Nuovo Pignone Heavy-Duty Gas Turbine," ASME J. Eng. Gas Turbines Power, **119**, pp. 633–639.

[16] Hennecke, D. K., 1997, *Transsonik-Verdichter-Technologien für stationäre Gasturbinen und Flugtriebwerke* (in German), Festschrift zum Jubiläum 100 Jahre Turbomaschinen TU-Darmstadt, TU-Darmstadt, Darmstadt, Germany.

[17] Perz, E., Gasteiger, G., Steinrück, P., Mader, O., and Jericha, H., 1988, "Design of a 50 MW Pilot Plant for a High Efficiency Steam Cycle," ASME Paper No. 88-GT-154.

[18] Zerlauth, F., 1986, "Sulzer Gasturbinen-Konstruktionen" (in German), Conference on Turbomachinery Developments, Graz University of Technology, Graz, Austria.

[19] Göttlich, E., Neumayer, F., Pieringer, P., Woisetschläger, J., Sanz, W., and Heitmeir, F., 2004, "Investigation of Stator-Rotor Interaction in a Transonic Turbine Stage Using Laser-Doppler-Velocimetry and Pneumatic Probes," ASME J. Turbomach., **126**, pp. 297–305.

[20] Göttlich, E., Lang, H., Sanz, W., and Woisetschläger, J., 2002, "Experimental Investigation of an Innovative Cooling System (ICS) for High Temperature Transonic Turbine Stages," ASME Paper No. 2002-GT-30341.

Downloaded 02 Jun 2010 to 171.66.16.107. Redistribution subject to ASME license or copyright; see http://www.asme.org/terms/Terms_Use.cfm

[21] Göttlich, E., Innocenti, L., Vacca, A., Sanz, W., Woisetschläger, J., Facchini, B., Jericha, H., and Rossi, E., 2004, "Measurement and Simulation of a Transonic Innovative Cooling System (ICS) for High-Temperature Transonic Gas Turbine Stages," ASME Paper No. GT2004-53712.
[22] Chorpening, B. T., Casleton, K. H., and Richards, G. A., 2003, "Stoichiometric Oxy-Fuel Combustion for Power Cycles With CO_2 Sequestration," Proceedings of the Third Joint Meeting of the U.S. Sections of The Combustion Institute, Chicago, IL.
[23] Inoue, H., Kobayashi, N., and Koganezawa, T., 2001, *Research and Development of Methane-Oxygen Combustor for Carbon Dioxide Recovery Closed-Cycle Gas Turbine*, CIMAC Conference Paper, Hamburg, Germany.
[24] Göttlicher, G., 1999, "Energetik der Kohlendioxidrückhaltung in Kraftwerken," (in German), VDI Fortschritt-Berichte , VDI Verlag, Düsseldorf, Reihe 6, Energietechnik, No. 421.
[25] Gas Turbine World, 2003, *2003 Handbook for Project Planning, Design and Construction*, Pequot Publishing Inc.

Downloaded 02 Jun 2010 to 171.66.16.107. Redistribution subject to ASME license or copyright; see http://www.asme.org/terms/Terms_Use.cfm

An Iterative Method for Blade Profile Loss Model Adaptation Using Streamline Curvature

Vassilios Pachidis
e-mail: v.pachidis@cranfield.ac.uk

Pericles Pilidis
e-mail: p.pilidis@cranfield.ac.uk

Department of Power and Propulsion,
School of Engineering,
Gas Turbine Engineering Group,
Cranfield University,
Cranfield, Bedfordshire, MK43 0AL, UK

Ioannis Templalexis
Section of Thermodynamics, Power and Propulsion,
Hellenic Air Force Academy,
Dekeleia Air Base, Greece
e-mail: templalexis@hafa.gr

Luca Marinai
Department of Power and Propulsion, School of Engineering,
Gas Turbine Engineering Group,
Cranfield University,
Cranfield, Bedfordshire, MK43 0AL, UK
e-mail: l.marinai@cranfield.ac.uk

The various incidence, deviation, and loss models used in through-flow analysis methods, such as streamline curvature, are nothing more than statistical curve fits. A closer look at public domain data reveals that these statistical correlations and curve fits are usually based on experimental cascade data that actually display a fairly large scatter, resulting in a relatively high degree of uncertainty. This usually leads to substantial differences between the calculated and actual performances of a given gas turbine engine component. Typically, matching calculated results from a through-flow analysis against experimental data requires the combination of various correlations available in the public domain, through a very tedious, complex, and time consuming "trial and error" process. This particular study supports the view that it might actually be much more time effective to "adopt" a given loss model against experimental data through an iterative, physics-based approach, rather than try to identify the best combination of available correlations. For example, the well-established "Swan's model" for calculating the blade profile loss factor in subsonic and transonic axial flow compressors depends strongly on approximate correlations for calculating the blade wake momentum thickness, and therefore represents such a case. This study demonstrates this by looking into an iterative approach to blade profile loss model adaptation that can provide a relatively simple and quick, but also physics-based way of "calibrating" profile loss models against available experimental data for subsonic applications. This paper presents in detail all the analysis necessary to support the above concept and discusses Swan's model in particular as an example. Finally, the paper discusses the performance comparison of a two-dimensional, streamline curvature compressor model against experimental data before and after the adaptation of that particular loss model. This analysis proves the potential of the simulation strategy presented in this paper to "adopt" a given loss model against experimental data through an iterative, physics-based approach. [DOI: 10.1115/1.2747643]

Keywords: streamline curvature, compressor, performance, simulation, loss model, wake momentum thickness, adaptation

1 Introduction

The scope of this section is to provide a synopsis of the past and more recent development of streamline curvature (SLC) through-flow analysis methods, provide the reader with a brief description of the theoretical background, and also describe briefly how blade row pressure losses are typically taken into account in SLC calculations.

1.1 Development of SLC. The compressor flow field is highly three dimensional, turbulent, and viscous. An inviscid through-flow analysis method, however, in which viscosity effects are taken into account by means of empirical models and correlations, can offer sufficient accuracy. SLC methods have therefore continued to receive refinements over the years and are still considered by industry and academia as "state of the art software" capable of providing an accurate, quick, and inexpensive solution compared to the full, three-dimensional, CFD methods.

Although Wu [1] provided the basis for a hub-to-shroud flow field calculation, the term "streamline curvature" became generally associated with through-flow analysis in 1967 following the work of Novak [2], and Jansen and Moffatt [3]. Between the 1960s and the 1990s a substantial number of computer codes for axial-flow turbomachine flow field analysis were developed using streamline curvature methods such as Denton [4], Jennions and Stow [5,6], and Barbosa [7].

Although streamline curvature methods have been around since the early 1950s, they have been mainly focused on simulating the flow field inside isolated components. More recently, these same authors in Templalexis et al. [8] and Pachidis et al. [9] published several zooming research efforts using 2D SLC component models. These analyses looked into the integration of streamline curvature component models with zero-dimensional cycle analysis, for high-fidelity studies in the context of the whole engine performance.

1.2 SLC Theoretical Background. The SLC method basically solves the discrete equations of continuity, motion, energy, and state in a form that incorporates the full three-dimensional compressor geometry and on a computational grid which is constructed in the meridional direction.

Computation nodes are defined at the intersections of the streamlines and the blade edges (Fig. 1). The flow within the compressor is considered as axi-symmetric, compressible, and inviscid. For this specific type of flow the law of conservation of angular momentum has the following form in vector quantities. Where F are blade forces which are neglected in this case

$$-\frac{1}{\rho}\vec{\nabla}P=\frac{D\vec{W}}{Dt}+\vec{\omega}\times\vec{\omega}\times\vec{r}+2\vec{\omega}\times\vec{W}+\vec{F} \tag{1}$$

Contributed by the International Gas Turbine Institute of ASME for publication in the JOURNAL OF ENGINEERING FOR GAS TURBINES AND POWER. Manuscript received April 27, 2007; final manuscript received April 30, 2007; published online December 26, 2007. Review conducted by Dilip R Ballal. Paper presented at the ASME Turbo Expo 2007: Land, Sea and Air (GT2007), Montreal, Quebec, Canada, May 14–17, 2007, Paper No. GT2007-27402.

Copyright © 2008 by ASME

Downloaded 02 Jun 2010 to 171.66.16.107. Redistribution subject to ASME license or copyright; see http://www.asme.org/terms/Terms_Use.cfm

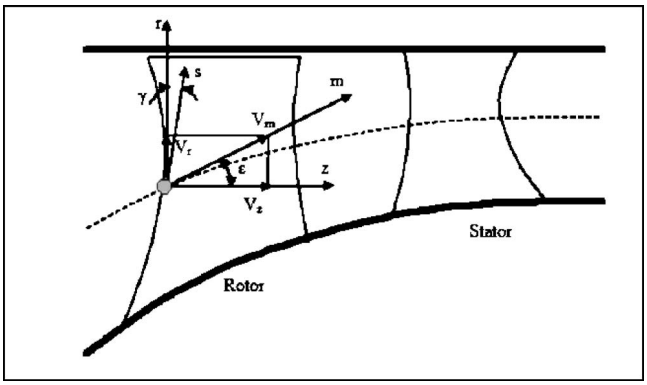

Fig. 1 Coordinate system

Resolving each term of the above equation into cylindrical coordinates (z, r, w–axial, radial, tangential), the following four expressions are derived:

(i) The pressure forces

$$-\frac{1}{\rho}\vec{\nabla}P=\left(-\frac{1}{\rho}\frac{\partial P}{\partial r}\right)\vec{e}_r+\left(-\frac{1}{r\rho}\frac{\partial P}{\partial w}\right)\vec{e}_w+\left(-\frac{1}{\rho}\frac{\partial P}{\partial z}\right)\vec{e}_z \tag{2}$$

(ii) The material derivative of the relative velocity in steady state conditions ($\partial\vec{W}/\partial t\approx 0$)

$$\frac{D\vec{W}}{Dt}=(\vec{W}\cdot\vec{\nabla})\cdot\vec{W}+\frac{\partial\vec{W}}{\partial t}\Leftrightarrow\frac{D\vec{W}}{Dt}$$
$$=\left(W_r\frac{\partial\vec{W}}{\partial r}\right)\cdot\vec{e}_r+\left(\frac{W_w}{r}\frac{\partial\vec{W}}{\partial w}\right)\cdot\vec{e}_w+\left(W_z\frac{\partial\vec{W}}{\partial z}\right)\cdot\vec{e}_z$$
$$\Leftrightarrow\begin{cases}\dfrac{DW_r}{Dt}=W_r\dfrac{\partial W_r}{\partial r}+\dfrac{W_w}{r}\dfrac{\partial W_r}{\partial w}+W_z\dfrac{\partial W_r}{\partial z}\\ \dfrac{DW_w}{Dt}=W_r\dfrac{\partial W_w}{\partial r}+\dfrac{W_w}{r}\dfrac{\partial W_w}{\partial w}+W_z\dfrac{\partial W_w}{\partial z}\\ \dfrac{DW_z}{Dt}=W_r\dfrac{\partial W_z}{\partial r}+\dfrac{W_w}{r}\dfrac{\partial W_z}{\partial w}+W_z\dfrac{\partial W_z}{\partial z}\end{cases} \tag{3}$$

(iii) The centripetal acceleration

$$\vec{\omega}\times\vec{\omega}\times\vec{r}=(\vec{\omega}\cdot\vec{r})\cdot\vec{\omega}-(\vec{\omega}\cdot\vec{\omega})\cdot\vec{r}=-(\omega^2 r)\vec{e}_r+\vec{e}_w+\vec{e}_z \tag{4}$$

where the terms $\vec{e}_w$ and $\vec{e}_z$ are neglected (≈ 0).

(iv) The coriollis acceleration

$$2\vec{\omega}\times\vec{W}=(-2\omega W_w)\vec{e}_r+(2\omega W_r)\vec{e}_w+\vec{e}_z \tag{5}$$

where the term $\vec{e}_z$ is neglected (≈ 0).

After the transformation of the discrete equations and the solution of a system of equations, the result is a nonlinear partial differential equation of the following form

$$\frac{\partial V_m^2}{\partial s}=V_m^2 2\cos^2\alpha\left(\frac{\cos(\varepsilon+\gamma)}{R_c}-\frac{\tan\alpha\dfrac{\partial\alpha}{\partial s}}{\cos^2\alpha}+\sin(\varepsilon+\gamma)\right.$$
$$\left.\times\left(-\frac{1}{\cos(\varepsilon+\gamma)}\frac{\partial\varepsilon}{\partial s}+\frac{\tan(\varepsilon+\gamma)}{R_c}-\frac{\partial(\ln(r\rho))}{\partial m}\right)\right)$$
$$+2\cos^2\alpha\left(\frac{\partial I}{\partial s}-2\cos\gamma\omega(V_w-U)-T\frac{\partial S}{\partial s}\right) \tag{6}$$

The above equation, known as the "full radial equilibrium equation" represents the gradient of the meridional velocity in the s direction and is solved by a finite difference approximation via an iterative approach. At the beginning, node coordinates are unknown since the streamline positions have not been determined yet. An initial guess of the streamline positions is made and calculations are carried out until new positions for the nodes are determined.

At every iteration the grid changes and an assessment of the streamline positions is made based on the previous guess. The iterative procedure is carried out so that the streamlines are repositioned until, eventually, their position remains constant and all the flow field properties are established.

1.3 Blade Row Pressure Loss Calculation. What basically determines the overall pressure ratio and isentropic efficiency of a compressor is the pressure loss across its blade rows. The total pressure across blade rows is not constant due to the presence of losses. For a rotating blade row, the relative total pressure is slightly reduced, whereas for a stationary blade row this is sensed by the reduction in absolute total pressure.

Calculating blade losses in compressors is an extremely difficult task due to the complex, three-dimensional nature of the flow field. There are several factors that contribute to the generation of losses in a compressor. It would be fair to say that although consensus exists on the end result, which is an increase in entropy and reduction in total pressure, the exact mechanisms through which losses are generated and their complicated interactions have not been completely understood yet.

The standard approach that has been adopted over the years by several researchers in the field, such as Miller et al. [10], Creveling and Carmody [11], and Barbosa [7], is based on the assumption that different types of cascade loss are independently generated and can be analytically related to the resulting deficit in total pressure. To a good estimation, the total loss in a compressor blade row is typically established by properly adding together, and correcting for three-dimensional effects, different loss factors. In other words, it is assumed that the total pressure loss of the blade row is the result of the interaction of different loss components, i.e., profile losses, secondary losses, and shock losses, which are considered to act through independent mechanisms. More analytically, the blade mass flow-averaged total loss factor is typically calculated for the rotor from

$$\bar{\omega}'_{\text{tot}}=\bar{\omega}'_{\text{prof}}\,f_{\text{Re}}+\bar{\omega}'_{\text{sh}}+\bar{\omega}'_{\text{sec}} \tag{7}$$

where $\bar{\omega}_{\text{prof}}$ is the blade profile loss factor; $\bar{\omega}_{\text{sh}}$ is the blade shock wave loss factor; $\bar{\omega}_{\text{sec}}$ is the secondary loss factor; and f_{Re} is a correction due to the Reynolds effects.

Knowing the total loss factor, which is established iteratively during the calculation of the radial equilibrium equation, and the total and static pressures at the blade row inlet, the total pressure at the blade row outlet can easily be determined from [12]

$$\bar{\omega}'_{\text{tot}}=\frac{(P'_{o,2})_{\text{ideal}}-P'_{o,2}}{P'_{o,1}-P_1}$$
$$=\left(\frac{P'_{o,2}}{P'_{o,1}}\right)_{\text{ideal}}\left(\frac{1-\dfrac{\left(\dfrac{P'_{o,2}}{P'_{o,1}}\right)}{\left(\dfrac{P'_{o,2}}{P'_{o,1}}\right)_{\text{ideal}}}}{1-\left[\dfrac{1}{1+\dfrac{\bar{\gamma}-1}{2}(M'_1)^2}\right]^{(\bar{\gamma}/\bar{\gamma}-1)}}\right) \tag{8}$$

The ideal relative pressure ratio is given by

$$\left(\frac{P'_{o,2}}{P'_{o,1}}\right)_{\text{ideal}}=\left\{1+\frac{\bar{\gamma}-1}{2}\frac{(\omega r_2)^2}{\bar{\gamma}RT'_{o,1}}\left[1-\left(\frac{r_1}{r_2}\right)^2\right]\right\}^{(\bar{\gamma}/\bar{\gamma}-1)} \tag{9}$$

Downloaded 02 Jun 2010 to 171.66.16.107. Redistribution subject to ASME license or copyright; see http://www.asme.org/terms/Terms_Use.cfm

The last expression, given for the relative frame of reference, takes into account the magnitude of the inlet relative Mach number and the change in radius, from blade row inlet to blade row outlet, of any given streamline. Where ω is the spool angular speed, r_1/r_2 is the streamline inlet over outlet r coordinate ratio, and $\bar{\gamma}$ is the average ratio of specific heats between blade row inlet and outlet.

For the calculation of the various loss components (or factors), several researchers have incorporated their expertise and experimental findings into correlations of parameters which describe the various flow features in blade passages. Such correlations usually attempt to synthesize the results of many tests into simpler formulae or sets of curves. They are generally averages of test results or their statistical curve fits. The main limitation of this approach is that the various empirical correlations cannot be expected to represent accurately every individual compressor design. A generic model for all compressors is rather unrealistic and the success or failure of this approach really depends on in-house expertise which allows for the incorporation of suitable correction factors that can bring a particular model closer to reality.

This study looked into a physics-based, iterative approach to blade profile loss model adaptation that can provide a relatively simple and quick way of "calibrating" loss models against available experimental data. From Eq. (7) it quickly becomes evident that when the flow in the compressor is subsonic or transonic as in many cases, and when severe shock wave losses are absent, the factor that contributes the most to the blade row total pressure loss, efficiency loss, and hence overall compressor performance, is the blade profile loss factor $\bar{\omega}_{\text{prof}}$. The "Swan's model" was adopted in this case and is discussed analytically in the following sections as a good example.

2 Calculation of Blade Profile Loss

This section explains how blade profile losses are typically calculated in SLC software with focus on the well-established "Swan's model" This section also means to provide the reader with a brief overview of the development of the various blade profile loss models that eventually led to Swan's.

Blades are known to operate with a separated region toward the trailing edge. Profile losses are associated with the development of the boundary layers on the blade surfaces, and the generated wake behind them, and make up only a small percentage of the total loss in a stage. Concerning the profile loss associated with the blade wetted surface, it is related to the blade-to-blade boundary layer momentum thickness and usually it is a small percentage of the overall profile loss, accounted for as blade friction loss. The wake mixing process downstream of the blade trailing edge is considered to be the greatest contributor to profile losses, especially under extreme incidence angles.

Lieblein and Roudebush [13] experimenting with low-speed, two-dimensional compressor blade cascades, showed that the blade profile loss can be expressed in terms of the blade wake momentum thickness. They used a power law profile to represent the wake and were then able to correlate the profile loss in terms of the wake momentum thickness and shape factor H, defined as the ratio of the displacement to the momentum thickness. The loss in stagnation pressure is not constant downstream of the blades but increases as the wakes mix out. Lieblein and Roudebush used the definition of the shape factor H as a measure of the degree to which the wake has mixed out and to quantify the entropy generation process. They also showed that mixing was almost completed approximately within 33% of a chord downstream of the blade trailing edge, at an average shape factor value between 1.1 and 1.2, provided that the boundary layer remained attached to the blade surfaces. Much later on, Koch and Smith [14] verified Lieblein's and Roudebush's method by looking into several different sources of loss based on a boundary layer calculation method that could take into account compressibility effects, Reynolds effects, surface roughness, and streamline movement.

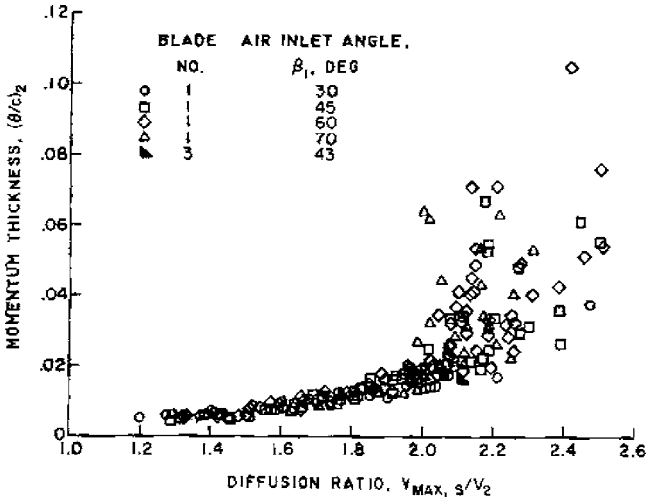

Fig. 2 Experimental variation of wake momentum thickness with suction-surface diffusion ratio [16]

Lieblein [15,16], continuing the analysis of low-speed, 10% thick compressor cascade sections, tried to relate the blade wake momentum thickness to velocity diffusion and blade loading. Through experiments he concluded that blade surface velocity distributions that result in large amounts of diffusion tend to produce relatively thick boundary layers on the blade surfaces that subsequently merge forming strong wakes. By analyzing a wide range of blade sections at various angles of attack he eventually established universal correlations between the wake momentum thickness and blade loading parameters such as the diffusion factor D and the equivalent diffusion factor D_{eq} (Figs. 2 and 3).

Although Lieblein's approach was restricted to low-speed, two-dimensional cascade flow, his equivalent diffusion factor in particular, appeared to describe satisfactorily the relationship between blades and profile losses over a wide range of flow conditions. Based on Lieblein's work, Swan [17] introduced a more practical method of predicting blade profile losses in transonic compressors. According to Swan's model, the equivalent diffusion factor D_{eq} and minimum loss equivalent diffusion factor D^*_{eq} can be established as per Lieblein. From the minimum loss equivalent diffusion factor the minimum loss wake momentum thickness can be established through a statistical curve fit. At off-design, the wake momentum thickness can be calculated from tabulations relating the wake momentum thickness and minimum-loss wake momentum thickness to D^*_{eq} and D_{eq} (Figs. 4 and 5). Having established the wake momentum thickness, the blade profile loss can be calculated as per Lieblein.

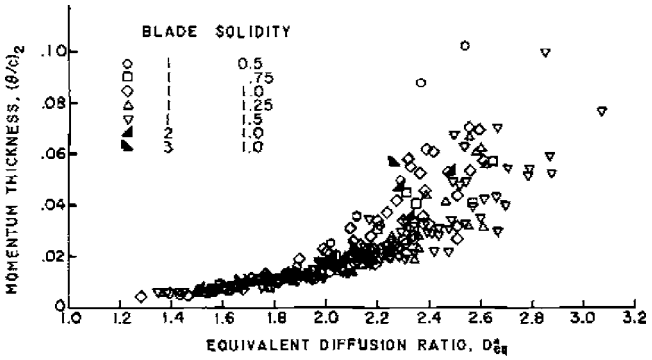

Fig. 3 Wake momentum thickness variation with equivalent diffusion ratio for data points at angles of attack greater than minimum loss [16]

Downloaded 02 Jun 2010 to 171.66.16.107. Redistribution subject to ASME license or copyright; see http://www.asme.org/terms/Terms_Use.cfm

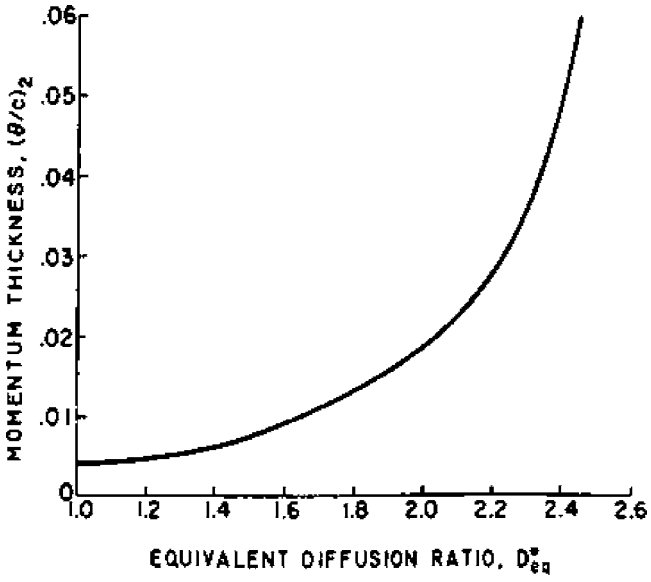

Fig. 4 Representative variation of wake momentum thickness with equivalent diffusion ratio at minimum-loss angle of attack used in calculations of cascade loss variations [16]

2.1 Swan's Blade Profile Loss Model. From the previous section and from Figs. 2–5 it becomes clear that Swan's model is strongly based on Lieblein's experimental cascade data that actually display a fairly large scatter, resulting in a relatively high degree of uncertainty. The exact model developed by Swan for the calculation of the blade profile loss, is described here in more detail, for the relative frame of reference.

In order to address the problem of the three-dimensional nature of the flow in real compressor blade rows, Swan extended Lieblein's [15] basic correlation of the minimum-loss equivalent diffusion factor for two-dimensional cascades given by

$$D^*_{eq} = \frac{\cos\beta_2}{\cos\beta_1}\left[k_1 + k_4\frac{\cos^2\beta_1}{\sigma}(\tan\beta_1 - \tan\beta_2)\right] \tag{10}$$

to

$$D^*_{eq} = \left[k_1 + k_4\frac{\sin^2\beta_1}{\sigma}\left(\cot\beta_1 - \frac{r_2 V_{m,2}}{r_1 V_{m,1}}\cot\beta_2 - \frac{r_1}{V_{m,1}}\left(1 - \frac{r_2^2}{r_1^2}\right)\right)\right]\frac{\sin\beta_2}{\sin\beta_1}\frac{V_{m,1}}{V_{m,2}} \tag{11}$$

The minimum-loss wake momentum thickness parameter can be established from the minimum-loss equivalent diffusion factor through the experimental-statistical curve fits. At off-design con-

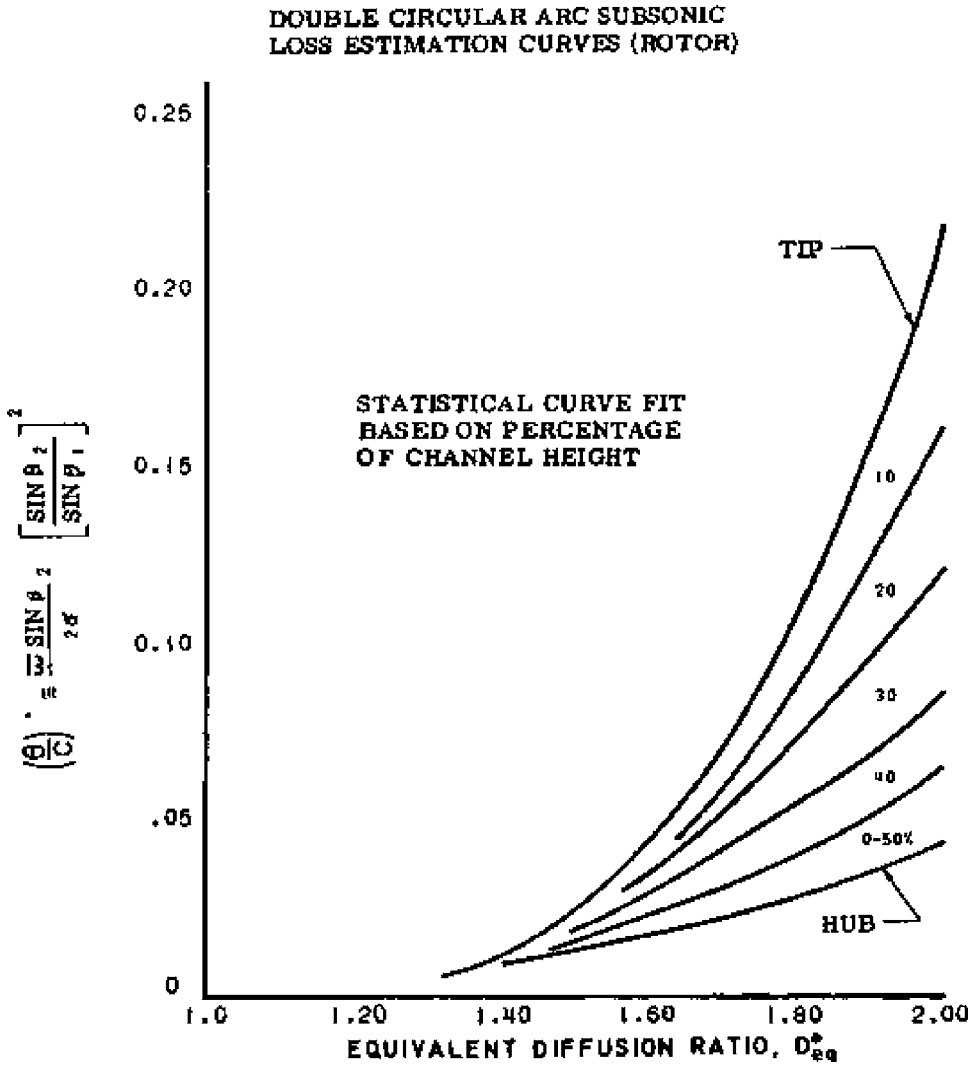

Fig. 5 Estimated variation of wake momentum thickness with minimum-loss equivalent diffusion ratio [17]

Downloaded 02 Jun 2010 to 171.66.16.107. Redistribution subject to ASME license or copyright; see http://www.asme.org/terms/Terms_Use.cfm

ditions, Swan derived the following correlation for the equivalent diffusion factor that takes into account changes in incidence

$$D_{\text{eq}} = \left[k_1 + k_2(i - i^*)^{k_3} + k_4 \frac{\sin^2 \beta_1}{\sigma} \left(\cot \beta_1 - \frac{r_2 V_{m,2}}{r_1 V_{m,1}} \cot \beta_2 - \frac{r_1}{V_{m,1}} \left(1 - \frac{r_2^2}{r_1^2} \right) \right) \right] \frac{\sin \beta_2}{\sin \beta_1} \frac{V_{m,1}}{V_{m,2}} \tag{12}$$

The above expression is again an extension to Lieblein's more fundamental definition of equivalent diffusion factor for two-dimensional cascades given by

$$D_{\text{eq}} = \frac{\cos \beta_2}{\cos \beta_1} \left[k_1 + k_2(i - i^*)^{k_3} + k_4 \frac{\cos^2 \beta_1}{\sigma} (\tan \beta_1 - \tan \beta_2) \right] \tag{13}$$

where the constants k_i are determined from tests and depend on the particular blade profile and thickness distribution selected. For example, k_1 is equal to 1.12, k_2 equals 0.0117 for NACA 65 series blades, and 0.007 for the C4 circular-arc blades, k_3 is equal to 1.43, and k_4 was found to be equal to 0.61.

Having established the minimum-loss wake momentum thickness parameter, minimum-loss equivalent diffusion factor, and equivalent diffusion factor, the wake momentum parameter can be established from experimental curve fits correlated by Swan as shown below.

For $D_{\text{eq}} > D^*_{\text{eq}}$

$$\frac{\theta}{c_{\text{aero}}} - \left(\frac{\theta}{c_{\text{aero}}} \right)^* = (0.827 M_1' - 2.692 M_1'^2 + 2.675 M_1'^3)(D_{\text{eq}} - D^*_{\text{eq}})^2 \tag{14}$$

and for $D_{\text{eq}} < D^*_{\text{eq}}$

$$\frac{\theta}{c_{\text{aero}}} - \left(\frac{\theta}{c_{\text{aero}}} \right)^* = (2.80 M_1' - 8.71 M_1'^2 + 9.36 M_1'^3)(D_{\text{eq}} - D^*_{\text{eq}})^2 \tag{15}$$

As mentioned before, Lieblein established a relationship between the blade profile loss and wake momentum thickness through the shape factor H. For incompressible two-dimensional cascade flow, the wake momentum thickness can be theoretically established from the following correlation

$$\frac{\theta}{c_{\text{aero}}} = \frac{\bar{\omega}'_{\text{prof}}}{2\sigma} \frac{\cos^3 \beta_2}{\cos^2 \beta_1} \left\{ \frac{3H - 1}{2H} \left[1 - \left(\frac{\theta}{c_{\text{aero}}} \right) \frac{H\sigma}{\cos \beta_2} \right]^3 \right\} \tag{16}$$

Experiments showed that at conventional cascade measuring stations, H actually varied very little with different blade profiles and incidence angles. In other words, the wake momentum thickness was found to vary over most of the typical diffusion range primarily with the terms before the brackets in the last equation. Therefore, the last equation can be safely reduced to the following for a more straightforward calculation of the blade profile loss factor (see also Fig. 6)

$$\frac{\theta}{c_{\text{aero}}} = \frac{\bar{\omega}'_{\text{prof}}}{2\sigma} \frac{\cos^3 \beta_2}{\cos^2 \beta_1} \tag{17}$$

It must be stated that Swan's model for calculating the blade profile loss factor does not include any contribution from shock losses. These are accounted for by different loss models as described before.

3 2D Fan Model Performance Simulation and Discussion of Results

For the purposes of this analysis, a 2D model of a two-stage fan was constructed utilizing Cranfield's 2D SLC COMPRESSOR software. This software has been specifically developed at Cranfield University in the United Kingdom for the modeling of the flow field in multistage, axial-flow compressors. The internal workings of the 2D SLC COMPRESSOR software have been reported in detail by Templalexis et al. [8], Pachidis, et al. [9], and also Pachidis [18]. It is therefore inappropriate to repeat here the description of the various loss and deviation models used in the code. The interested reader should refer to the above publications. The basic capability however that the 2D SLC COMPRESSOR software was initially developed to handle is outlined below:

- facilitate steady-state, multistage compressor performance analysis in 2D, at both subsonic and transonic regimes;
- handle any type of standard or user-defined blade profile and compressor geometry;
- handle standard and user-defined models for secondary losses, shock losses, Reynolds number effects, deviation, incidence, boundary layer blockage, tip clearance losses, etc.;
- identify conditions for surge and choking and handle non-uniform inlet flow conditions; and
- calculate the overall compressor map and provide a converged solution at any given operating point within minutes

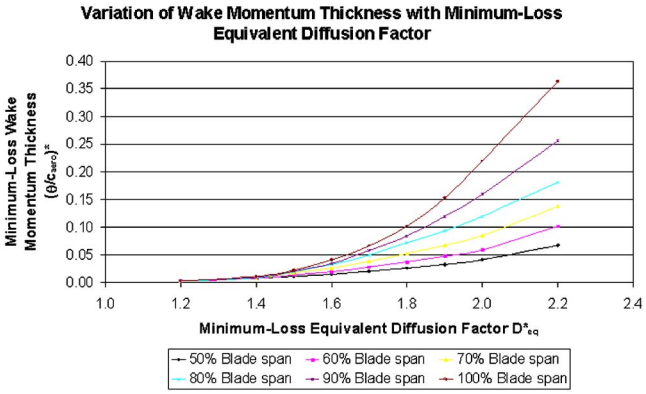

Fig. 6 Estimated variation of wake momentum thickness with minimum-loss equivalent diffusion factor for DCA subsonic rotors

The 2D SLC COMPRESSOR software incorporates several loss and deviation models in order to provide the user with extra flexibility when experimenting with different loss models. For the calculation of the blade profile loss Swan's model has been incorporated among others and was used in this case. As explained before, the minimum loss wake momentum thickness was graphically obtained from the minimum loss equivalent diffusion factor according to Swan's model and the following graph stored in the software as a tabulation.

3.1 Initial Comparison Against Experimental Data. The two-stage 2D fan model was constructed according to the detailed geometric data published in NASA Technical Paper No. 1493 by Urasek et al. [19]. The performance of the SLC two-stage compressor model under uniform inlet conditions was compared against the measured performance data provided in the aforementioned report. The overall design performance of the two-stage compressor is given in Table 1.

Table 1 Two-stage compressor design overall parameters

Pressure ratio	2.399
Temperature ratio	1.334
Isentropic efficiency	0.849
Corrected mass flow (kg/s)	33.248
rpm	16,042.800
Inlet hub to tip ratio	0.375
First rotor tip speed (m/s)	428.896
Second rotor tip speed (m/s)	405.341

Downloaded 02 Jun 2010 to 171.66.16.107. Redistribution subject to ASME license or copyright; see http://www.asme.org/terms/Terms_Use.cfm

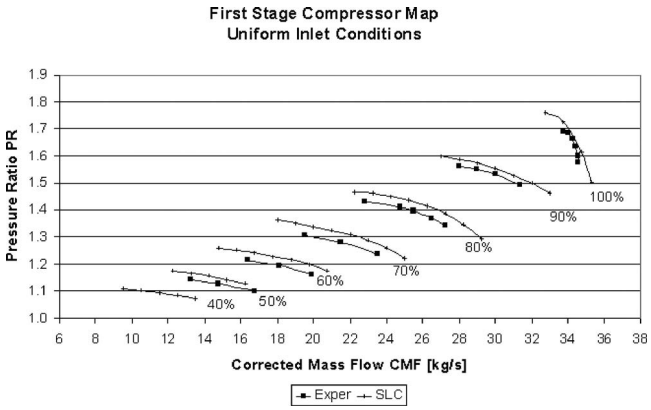

Fig. 7 Initial comparison with experimental results for the first stage—pressure ratio versus corrected mass flow

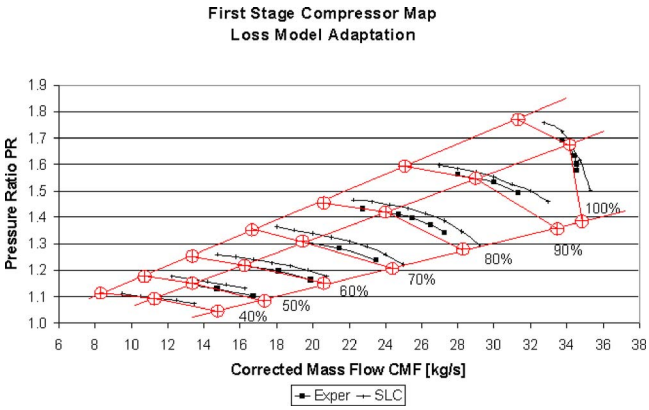

Fig. 9 Adaptation with experimental results—blade wake momentum thickness scaling factor matrix

In order to allow the comparison to take place, two-dimensional profiles of flow properties at the outlet of the compressor were averaged along the blade span, from hub to casing, back into nondimensional values using a standard area-weighting rule. Figures 7 and 8 present the initial comparison between the measured and simulated compressor performance for the first stage.

The initial comparison revealed a good overall qualitative agreement between the experimental and calculated compressor performance. All pressure ratio versus corrected mass flow speed lines followed the overall shape of the experimental speed lines and were in a good qualitative and quantitative agreement with experimental data close to design point conditions. Away from design point conditions, the SLC software predicted slightly higher pressure ratios than the experimental readings. The observed difference in the calculated pressure ratio was slightly less than 1%, in the best case, and slightly greater than 4% in the worst case. Similarly, isentropic efficiency curves appeared to follow the experimental trends close to design point conditions, however, away from the design point, the SLC prediction of isentropic efficiency appeared overestimated, resulting in a higher pressure ratio observed at almost all relative nondimensional rotational speeds.

The results presented above were the direct outcome of a given combination of loss models, including Swan's model for the determination of the blade profile loss. As mentioned before, when the flow in the compressor is subsonic as in this case, and when severe shock wave losses are absent, the factor that contributes the most to the blade row total pressure loss, efficiency loss, and hence overall compressor performance, is the blade profile loss factor $\bar{\omega}_{\text{prof}}$. Clearly, the initial comparison against experimental data indicated that pressure losses were underpredicted in this particular case. In other words, the differences between the SLC calculated compressor characteristics and the experimental ones mainly arose from the inability of the selected loss model to calculate the blade wake momentum thickness accurately (with other factors contributing as well, but of smaller significance such as incidence model, secondary loss model, etc).

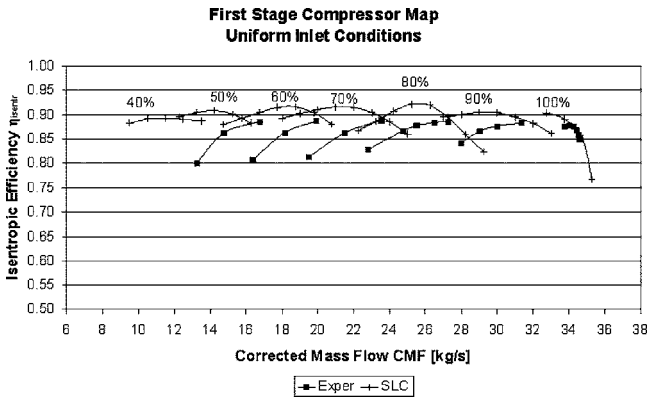

Fig. 8 Initial comparison with experimental results for the first stage—isentropic efficiency versus corrected mass flow

3.2 Loss Model Calibration. Using a different loss model combination would have resulted in different results, either better or worse. Given that experimental data were available in this case, and that trying to find the best combination of loss models would have taken quite a lot of time, a different approach was followed in order to improve the agreement between the SLC software predictions and the experimental results. This approach demanded the iterative execution of the 2D SLC model, for the creation of a "database" of scalars, employing a Newton–Raphson convergence procedure. These scalars were subsequently applied to the loss model's predictions in order to improve accuracy.

More analytically, running the 2D SLC model several times and iteratively, for a fixed compressor rotational speed and mass flow, established a scalar for the blade wake momentum thickness. In other words, different scalars were iteratively applied to Swan's loss model predictions for the blade wake momentum thickness until the SLC results (with respect to compressor pressure ratio and efficiency) matched the experimental data at that particular operating point. This procedure was repeated several times, for different compressor rotational speeds and mass flows, establishing a complete database of scalars for the whole range of compressor operating conditions.

The shape of the characteristic nondimensional speed lines in this case allowed the database of scalars to be established as a function of corrected mass flow and speed, at the extreme points of every speed line including an intermediate station, as shown in Fig. 9. Alternatively, the data base of scalars could have been established as a function of pressure ratio and relative nondimensional rotational speed or even as a function of beta-line and nondimensional speed.

During program execution and according to the calculated compressor operating point, intermediate scalars were established through linear interpolation, for operating points inbetween the various speed lines, and through cubic spline interpolation, for points falling onto "calculated" speed lines.

Although scalars could have been established for more than three points per speed line, this approach proved to work well in this particular case, providing a physics-based, simple, and quick way of "calibrating" the SLC model against the available experimental data. Obviously, for compressor characteristics exhibiting stronger curvatures, more points would probably need to be established depending on the accuracy required.

The method was attempted with the focus on matching the ex-

Downloaded 02 Jun 2010 to 171.66.16.107. Redistribution subject to ASME license or copyright; see http://www.asme.org/terms/Terms_Use.cfm

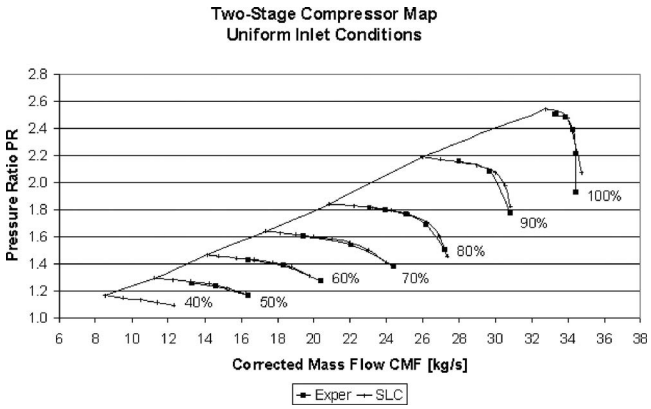

Fig. 10 Final comparison with experimental results for both stages—pressure ratio versus corrected mass flow

act shape of pressure ratio versus corrected mass flow speed lines rather than the shape of efficiency lines, as Figs. 10 and 11 reveal, although the opposite could have been achieved as well. The database of blade wake momentum thickness scalars was programmed in the original loss model itself as a look-up table and was subsequently used in any following analyses.

The loss model adaptation resulted in a very good qualitative and quantitative agreement between the simulated and experimental data for uniform inlet conditions, especially in the case of the pressure ratio versus corrected mass flow speed lines for obvious reasons. Isentropic efficiency versus corrected mass flow speed lines were in a much better qualitative and quantitative agreement than before, although the overall shape of the lines did not exactly match the experimental readings, especially toward operating conditions far away from the design point. It must be stated again that no particular effort was made to achieve an even better agreement between simulated and experimental data by trying different combinations of the loss models available in the 2D COMPRESSOR SLC software.

The physics-based calibration of the 2D SLC compressor model as described above, not only brought its overall performance closer to the experimental results under uniform inlet conditions, but also facilitated the successful validation of its performance under distorted inlet conditions.

For the model's validation under distorted conditions, NASA Technical Paper No. 1294 [20] was used as a reference. This paper discusses in detail the performance of a single-stage fan with and without inlet radial distortion. The design overall parameters of the single-stage fan discussed in NASA TP No. 1294 are very similar to the first stage of the NASA TP No. 1493 two-stage compressor.

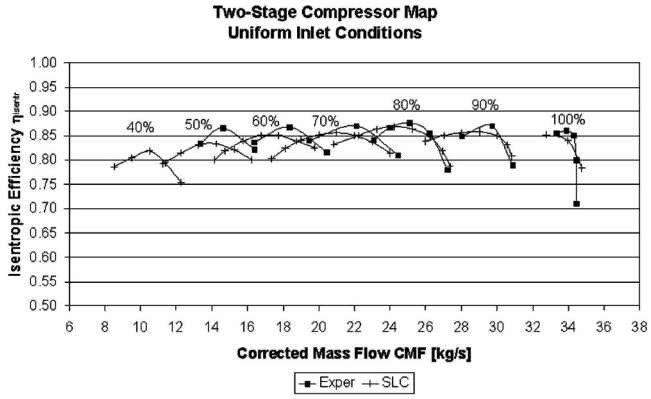

Fig. 11 Final comparison with experimental results for both stages—isentropic efficiency versus corrected mass flow

The details of this validation process under distorted inlet conditions have already been reported in Pachidis et al. [9] and the interested reader should refer to this publication. Generally speaking the analysis showed similar qualitative and quantitative trends for the same kind and extent of radial pressure distortion which proved the versatility and generality of the adaptation approach adopted by this study.

4 Discussion and Conclusions

It is the author's view that there is no loss model without limitations or at least without a given restricted range of applicability. For example, Lieblein's correlations were derived from low-speed, two-dimensional cascade experiments. One needs to keep in mind that the losses of blades operating inside a compressor behave quite differently from that in cascades. Also the approximation of the blade profile loss coefficient being equal to twice the wake momentum thickness in Eqs. (16) and (17) is only valid in the case of a fully attached flow.

Empirical correlations are very dependent on the experiment's conditions. As it was demonstrated in this case, one should be very cautious when applying these correlations to different geometries. If the wake momentum thickness correlation comes from experimental data of a single rotor, or a stationary single row cascade, when applied to a multistage compressor in order to calculate the loss coefficient, the results would be different. That would happen because the wake would be truncated by the downstream rotor and the wake mixing process would not have enough space to be completed.

Swan's correlations address the problem of the three dimensionality of the flow field but still the flow needs to be kept subsonic for a reasonable control on data scatter to be maintained. Swan's loss model also assumes that losses increase continuously from hub to tip which is a rather crude approximation.

It is always an advantage for through-flow analysis software, such as the 2D SLC COMPRESSOR software available at Cranfield, to provide the user with several alternative correlations, which could then be combined and compared against experimental data (if available) to find the most successful combination, given the application. Perhaps combining different loss models together would be sufficient to predict the flow field reasonably accurately. However, this approach needs to be thoroughly experimentally tested before being put into practical use and usually results in a rather complex and tedious task.

This particular study demonstrated that especially in subsonic or transonic applications it is actually much more straightforward and time effective to calibrate a given loss model against experimental data through an iterative, physics-based approach, rather than try to identify the best combination of available correlations.

The well-established "Swan's model" for calculating the blade profile loss factor in subsonic and transonic axial flow compressors depends strongly on approximate correlations for calculating the blade wake momentum thickness, and was therefore used in this case as a good example.

This paper presented in detail all the supporting analysis and finally discussed the performance comparison of a 2D SLC compressor model against experimental data before and after the adaptation of that particular loss model.

Under uniform inlet conditions, the adaptation managed to achieve a much better agreement with the available experimental data than initially obtained, within a realistic amount of time and through a relatively straightforward iterative process.

More importantly, the successful validation of the performance of the 2D SLC model under distorted inlet conditions proved the versatility and generality of the adaptation approach adopted by this study.

Downloaded 02 Jun 2010 to 171.66.16.107. Redistribution subject to ASME license or copyright; see http://www.asme.org/terms/Terms_Use.cfm

Nomenclature

Abbreviations

SLC = streamline curvature
SFC = specific fuel consumption
TET = turbine entry temperature

Latin Symbols

c = blade chord
D = diffusion ratio
f = correction factor
H = shape factor
i = incidence angle
j = number of node or streamline
k = blade angle, constant
M = mach number
P = pressure
r = radius
R_c = streamline curvature
Re = Reynolds number
S = entropy
T = temperature
t = blade thickness
U = blade speed
W = relative velocity, mass flow
V = absolute velocity

Greek Symbols

α = absolute air angle
β = relative air angle
γ = ratio of specific heats, sweep angle
δ = deviation angle, displacement thickness
ε = deflection angle, streamline slope
ζ = stagger angle
θ = camber angle, momentum thickness
ρ = density
σ = solidity
ω = loss coefficient, rotational speed

Subscripts

1 = inlet plane
2 = outlet plane
0 = zero camber conditions/total conditions
aero = aerodynamic
Eq = equivalent
geom = geometrical
m = meridional
prof = profile
r = radial
Re = Reynolds
sec = secondary
sh = shock, shape
tot = total
z = axial

Superscripts

* = minimum loss conditions
$\bar{}$ = mean value
$'$ = relative frame of reference

References

[1] Wu, C. H., 1952, "A General Through-Flow Theory of Three-Dimensioanl Flow in Subsonic and Supersonic Turbomachines of Axial-, Radial-, and Mixed-Flow Types," NASA Paper No. TN2604.
[2] Novak, R. A., 1967, "Streamline Curvature Computing Procedures for Fluid-Flow Problems," J. Eng. Power, **89**, pp. 478–490.
[3] Jansen, W., and Moffatt, W. C., 1967, "The Off-Design Analysis of Axial Flow Compressors," J. Eng. Power, **89**, pp. 453–462.
[4] Denton, J. D., 1978, "Throughflow Calculations for Transonic Axial Flow Turbines," J. Eng. Power, **100**, pp. 212–218.
[5] Jennions, I. K., and Stow, P., 1985, "The Quazi-Three-Dimensional Turbomachinery Blade Design System, Part I: Throughflow Analysis, Part II: Computerized System," Trans. ASME: J. Eng. Gas Turbines Power, **107**, pp. 308–316.
[6] Jennions, I. K., and Stow, P., 1986, "The Importance of Circumferential Non-uniformities in a Passage Averaged Quasi-Three-Dimensional Turbomachinery Design System," Trans. ASME: J. Eng. Gas Turbines Power, **108**, pp. 240–245.
[7] Barbosa, J. R., 1987, "A Streamline Curvature Computer Program for Axial Compressor Performance Prediction," Ph.D thesis, Vol. 1, Cranfield Institute of Technology, School of Mechanical Engineering.
[8] Templalexis, I., Pilidis, P., Pachidis, V., and Kotsiopoulos, P., 2006, "Development of a 2D Compressor Streamline Curvature Code," *Proceedings ASME Turbo Expo, Power For Land, Sea and Air*, Barcelona, Spain, May, Paper No. GT2006–90867.
[9] Pachidis, V., Pilidis, P., Templalexis, I., Alexander, T., and Kotsiopoulos, P., 2006, "Prediction of Engine Performance under Compressor Inlet Flow Distortion using Streamline Curvature," *Proceedings ASME Turbo Expo, Power For Land, Sea and Air*, Barcelona, Spain, May, Paper No. GT2006–90806.
[10] Miller, G. R., Lewis, G. W., and Hartmann, M. J., 1961, "Shock Losses in Transonic Rotor Rows," J. Eng. Power, **83**, pp. 235–242.
[11] Creveling, H. F., and Carmody, R. H., 1968 "Axial Flow Compressor Computer Program for Calculating Off-Design Performance (Program IV)," Prepared for NASA, Report No. CR-72427, General Motors, Allison Division, Indianapolis, IN.
[12] Bullock, R. O., and Johnsen, I. A., 1965, "Chapter III—Compressor Design System, NASA SP 36—Aerodynamic Design of Axial Flow Compressors," Scientific and Technical Information Division, National Aeronautics and Space Administration, Washington DC.
[13] Lieblein, S., and Roudebush, W. H., 1956, "Theoretical Loss Relations for Low-Speed Two-Dimensional-Cascade Flow," Technical Note, No. NACA TN 3662, National Advisory Committee for Aeronautics, Washington, DC.
[14] Koch, C. C., and Smith, L. H., 1976, "Loss Sources and Magnitudes in Axial-Flow Compressors," J. Eng. Power, **98**, pp. 411–424.
[15] Lieblein, S., 1957, "Analysis of Experimental Low-Speed Loss and Stall Characteristics of Two-Dimensional Compressor Blade Cascades," Research Memorandum No. NACA RM E57A28, National Advisory Committee for Aeronautics, Washington, DC.
[16] Lieblein, S., 1959, "Loss and Stall Analysis of Compressor Cascades," J. Basic Eng., **81**, pp. 387–400.
[17] Swan, W. C., 1961, "A Practical Method of Predicting Transonic Compressor Performance," J. Eng. Power, **86**, pp. 322–330.
[18] Pachidis, V., 2006, "Gas Turbine Advanced Performance Simulation," Ph.D thesis, Cranfield University, School of Engineering, Bedfordshire, UK.
[19] Urasek, D. C. Gorell, W. T., and Cunnan, W. S., 1979, "Performance of Two-Stage Fan Having Low-Aspect-Ratio, First Stage Rotor Blading," NASA Technical Paper No. 1493.
[20] Schmidt, J. F., and Ruggeri, R. S., 1978, "Performance With and Without Inlet Radial Distortion of a Transonic Fan Stage Designed for Reduced Loading in the Tip Region," NASA Technical Paper No. 1294.

Downloaded 02 Jun 2010 to 171.66.16.107. Redistribution subject to ASME license or copyright; see http://www.asme.org/terms/Terms_Use.cfm

Calculations of Cooled Turbine Efficiency

J. H. Horlock
Whittle Laboratory,
University of Cambridge,
Cambridge, CB3 0DY, UK

Leonardo Torbidoni
Ansaldo Energia,
16152 Genoa, Italy
e-mail: leonardo.torbidoni@aen.ansaldo.it

The efficiency of a cooled turbine stage has been discussed in the literature. All proposed definitions compare the actual power output with an ideal output, which has to be determined; but usually, one of two definitions has been used by turbine designers. In the first, the so-called Hartsel efficiency, the mainstream gas flow, and the various coolant flows to rotor and stator are assumed to expand separately and isentropically to the backpressure. In the second, it is assumed that these flows mix at constant (mainstream) gas pressure before expanding isentropically (sometimes, the rotor coolant flow is ignored in this definition). More recently, it has been suggested that a thermodynamically sounder definition is one in which the gas and coolant flows mix reversibly and adiabatically before isentropic expansion to the backpressure. In the current paper, these three efficiencies are compared, for a typical stage—the first cooled stage of a multistage industrial gas turbine. It is shown that all the efficiencies fall more or less linearly with increase of the fractional (total) coolant flow. It is also shown that the new definition of efficiency gives values considerably lower than the other two efficiencies, which are more widely used at present. Finally, the various irreversibilities associated with the flow through a cooled turbine are calculated. Although all these irreversibilities increase with the fractional coolant flow, it is shown that the "thermal" irreversibility associated with film cooling is higher than the other irreversibilities at large fractional coolant flow.
[DOI: 10.1115/1.2771250]

1 Introduction

In an earlier paper [1], various ways for defining the thermodynamic efficiency of a cooled turbine were discussed; in all the definitions, the actual power output is compared with an ideal power output, and it is that ideal power that is the main subject of discussion.

Most turbine designers usually use one of two definitions. In the first (the so-called Hartsel efficiency η_{Hart}), the mainstream gas flow and the various coolant flows to rotor and stator are assumed to expand separately and isentropically to the backpressure, giving the ideal power output. In the second (sometimes called the mainstream pressure mixed efficiency $\eta_{\text{mp-mix}}$), it is assumed here that the gas and coolant flows mix at constant (mainstream) gas pressure before expanding isentropically to the backpressure, giving a different ideal power output (but note that sometimes only the nozzle coolant is assumed to be mixed with the mainstream gas, it being implied that the rotor coolant does not contribute to the work output, actual or ideal). These two definitions, η_{Hart} and $\eta_{\text{mp-mix}}$, are well documented in the literature and do not require further discussion here.

But, Young and Horlock [1] recommended that a new form of efficiency should be used, the so-called "fully reversible mixed" efficiency $\eta_{\text{fr-mix}}$. In this form, the ideal power output is assumed to be obtained in a fully reversible adiabatic process between a reversibly mixed entry state (of the same stagnation enthalpy and entropy as the entering hot gas and coolant streams) and an exit state at the backpressure (the stagnation pressure at exit from the actual turbine). We discuss this new definition further in the next section.

The parameters K_{ext}, K_{int} appear in complex equations and are defined in the Appendix.

Contributed by the International Gas Turbine Institute of ASME for publication in the JOURNAL OF ENGINEERING FOR GAS TURBINES AND POWER. Manuscript received July 5, 2006; final manuscript received August 9, 2006; published online January 11, 2008. Review conducted by Dilip R. Ballal. Paper presented at the ASME Turbo Expo 2006: Land, Sea and Air (GT2006), Barcelona, Spain, May 8–11, 2006, Paper No. GT2006-90424.

2 Fully Reversible Mixed Efficiency

The mass flows of the entry gas and cooling streams are taken as m_g and Σm_{ci}, with $(m_g+\Sigma m_{ci})=1$, and their corresponding entry states expressed in terms of stagnation conditions as (p_{01g}, h_{01g}) and (p_{01ci}, h_{01ci}). The actual exit state (unit mass flow, fully mixed) is (p_{03}, h_{03}). If the entering streams were initially mixed reversibly and adiabatically, then the resulting state of the mixed stream (of unit mass) would be state 01, with the specific (stagnation) enthalpy given by

$$h_{01} = m_g h_{01g} + \Sigma m_{ci} h_{01ci} \tag{1}$$

and the specific entropy by

$$s_{01} = m_g s_{01g} + \Sigma m_{ci} s_{01ci}$$

After an isentropic expansion to the common backpressure p_{03}, the state (h_{03ss}, s_{03ss}) would be reached, where $s_{03ss}=s_{01}$.

The fully reversible mixed efficiency definition is then

$$\eta_{\text{fr-mix}} = \frac{h_{01} - h_{03}}{h_{01} - h_{03ss}}$$

From the steady flow energy equation for adiabatic flow through the turbine, the numerator is the actual power output P, since

$$P = (m_g h_{01g} + \Sigma m_{ci} h_{01ci}) - h_{03} = h_{01} - h_{03}$$

the leaving flow being fully mixed (and of unit mass flow) and having stagnation enthalpy h_{03}.

In practice, this actual power output will usually be obtained from experimental measurement, either of the power output P directly, via torque and rotational speed, or of the enthalpy fluxes $h_{01}=m_g h_{01g}+\Sigma m_{ci} h_{01ci}$ and h_{03}. The latter give the numerator of the efficiency expression (we neglect both the disk coolant flows and the windage here). Alternatively, a full computational fluid dynamics (CFD) method may be used to calculate the power output.

The denominator can then be obtained in one of two ways.

(a) In the first, the hypothetical state (h_{01}, s_{01}) is first deter-

Copyright © 2008 by ASME

Downloaded 02 Jun 2010 to 171.66.16.107. Redistribution subject to ASME license or copyright; see http://www.asme.org/terms/Terms_Use.cfm

mined, and a mixed flow isentropic expansion, from the resulting pressure p_{01} to the backpressure p_{03}, is calculated to give the state (h_{03ss}, s_{03}), with $s_{03}=s_{01}$. The ideal work is then $(h_{01}-h_{03ss})$.

(b) In the second, the various entropy increases in the actual process may be calculated as $s_{03}-s_{01}=\Sigma m\Delta s=\Delta\Sigma$. The enthalpy h_{03ss} can then be obtained from

$$h_{03ss} = h_{03} - \int_{03ss}^{03} Tds = h_{03} - \bar{T}(s_{03} - s_{03ss})$$

where

$$\bar{T} = \frac{\int_{03ss}^{03} Tds}{s_{03} - s_{03ss}} \cong \frac{T_{03} + T_{03ss}}{2} \tag{2}$$

We may note that if a full calculation method has been used to obtain the actual work output, the entropy increase

$$s_{03} - s_{03ss} = s_{03} - s_{01} = \Sigma m\Delta s = \Delta\Sigma$$

will have been obtained in the course of that calculation.

The two methods ((a) and (b)) would give identical results if it were not for the approximation involved in Eq. (2).

As was pointed out in Ref. [1], method (b) for calculating obtaining the fr-mix efficiency is analogous to modifying the classical rational efficiency, which is of the form

$$\eta_R = \frac{h_{01} - h_{03}}{b_{01} - b_{03}} = \frac{1}{1 + (T_{ds}\Sigma m\Delta s)/P} \tag{3}$$

where b is the steady flow availability and T_{ds} is the so-called dead state temperature, but in method (b), T_{ds} is replaced by the temperature $\bar{T}$ and $\eta_{fr\text{-}mix}$ results.

An alternative way of writing Eq. (3) is

$$\eta_R = 1 - \frac{T_{ds}\Sigma m\Delta s}{P + T_{ds}\Sigma m\Delta s} = 1 - \mu$$

where

$$\mu = \frac{T_{ds}\Sigma m\Delta s}{(h_{01} - h_{03}) + T_{ds}\Sigma m\Delta s} \tag{4}$$

and we shall use this nondimensional form for the losses in turbine efficiency later, in examining the various components of those losses (e.g., due to heat transfer, friction, mixing, etc.).

3 Calculations

In this paper, we illustrate how the fully reversible mixed efficiency $\eta_{fr\text{-}mix}$ will vary with cooling flow quantity through a number of calculations based on method (b). Some of these calculations have also been spot checked for accuracy against method (a) and the two methods were found to be virtually identical numerically.

It should be noted that in earlier calculations of the performance of a cooled turbine stage, Torbidoni and Horlock [2] also made an estimate of various cooled turbine efficiencies for a single operating condition of their particular turbine design, with a specified allowable blade temperature. It was based on a complex "stepped" calculation through the stage. Here, we use a simpler calculation code in order to show how the efficiencies change with a very wide cooling flow range. The approach is essentially similar to that of Torbidoni and Horlock, but it is quicker although probably not as accurate.

The first stage of a modern high temperature gas turbine is specified, the major design parameters of which are given in Table 1, together with assumptions about the turbine entry conditions.

Table 1 Stage design data

Polytropic efficiency	0.9
Inlet pressure	35 bars
Inlet temperature	1800 K
Stage loading coefficient	1.0
Pressure ratio	2.25
Coolant inlet pressure	36.5 bars (nozzle); 24.3 bars (rotor)
Coolant inlet temperature	885 K (nozzle); 787 K (rotor)
Maximum blade metal temperature	1100–1300 K
Internal cooling efficiency	0.7
Film cooling effectiveness	0.4
Metal Biot number	0.15
TBC Biot number	0.3 (nozzle); 0.2 (rotor)

We first calculate how the required cooling flow quantity varies with the maximum allowable metal temperature $T_{b,max}$ (this is a practical approach in which we assume a current value of $T_{b,max}$ and then allow a hypothetical improvement in materials, which enables that value to be increased and the required cooling flow reduced). The thermodynamic effect of decreasing the required cooling flow is to reduce the magnitude of the various cooling irreversibilities and increase the fr-mix efficiency toward the uncooled turbine efficiency η_U. The gas and coolant entry conditions and the specified turbine stage aerodynamic design parameters are held constant in these calculations.

We compare such calculations of $\eta_{fr\text{-}mix}$ with the more commonly used Hartsel efficiency η_{Hart} [3] and the mainstream pressure mixed efficiency $\eta_{mp\text{-}mix}$ [4].

The stage calculations were carried out using the code developed by Young and Wilcock [5,6], which used equations for the properties of real gases. It was employed in cycle calculations of gas turbine plants with cooled turbines reported by Wilcock et al. [7]. From these calculations for overall plants, the detailed performance of the first cooled turbine was abstracted. Within the code, the cooling flows required for the rotor and stator of this stage are estimated using the methods described initially by Horlock et al. [8] and in fuller detail by Young and Wilcock [6]. The analyses developed by the latter authors for the various irreversibilities associated with cooling are also calculated within the code.

With the cooling flows known, a stage calculation then proceeds as follows.

(i) The entry pressures and temperatures for gas and coolant are assumed, together with the stage pressure ratio, so the exit pressure is known but not the enthalpy.
(ii) A value of exit stagnation temperature (and enthalpy) is guessed. A convenient first guess is the temperature at exit for the uncooled turbine using the prescribed pressure ratio and the prescribed basic uncooled free stream loss stage (i.e., associated with the uncooled polytropic efficiency).
(iii) The corresponding value of the relative total enthalpy at rotor inlet is obtained from the reaction, which is known from the specified stage loading and nozzle exit swirl.
(iv) With the given maximum metal temperature, coolant entry temperatures, and assumed empirical heat transfer data, the blade cooling effectiveness is found (for stator and rotor separately), together with the required coolant flows, the heat quantities convectively transferred (Q_s and Q_r), and the various temperatures within each row (i.e., $T_{b,ext}$, T_w, etc.).
(v) The various entropy increases are obtained from the Young and Wilcock expressions [6], as listed in the Appendix. Additional empirical constants are required. These various entropy increases are summed and then added to the entering entropy flux to give the exit entropy for the (unit) mixed outflow.
(vi) From the exit entropy, the exit stagnation pressure, and the

Downloaded 02 Jun 2010 to 171.66.16.107. Redistribution subject to ASME license or copyright; see http://www.asme.org/terms/Terms_Use.cfm

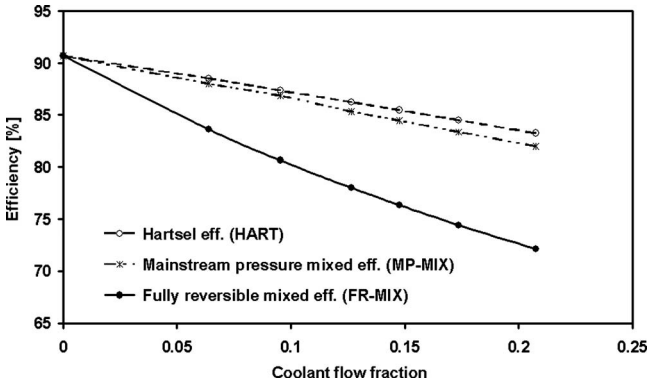

Fig. 1 fr-mix, Hartsel, and mp-mix efficiencies compared for varying coolant flow fractions

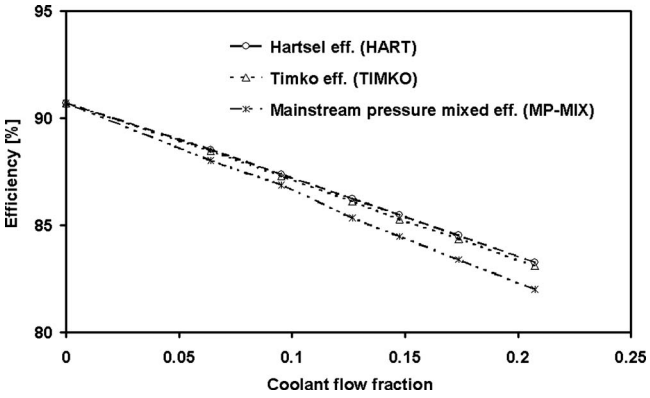

Fig. 2 Timko efficiency compared with Hartsel and mp-mix efficiencies for varying coolant flow fractions

gas constituents, the exit stagnation temperature is obtained from the gas equations.

(vii) This temperature is compared with guessed exit temperature.

(viii) The calculation is iterated until the exit temperature converges.

(ix) The exit stagnation enthalpy h_{03} is then known.

With the overall performance of the first turbine stage thus calculated, the fr-mix efficiency can then be obtained using method (b) described above. The code gives the entry stagnation enthalpy h_{01}, using Eq. (1), the actual work output $(h_{01}-h_{03})$, the exit stagnation temperature T_{03}, and the irreversibilities $(\Sigma m\Delta s=\Delta\Sigma)$. The enthalpy h_{03ss} attained in a hypothetical isentropic expansion is then obtained as described in the preceding section, and the fr-mix cooled turbine efficiency $\eta_{\text{fr-mix}}$ can be estimated. The Hartsel and mp-mix efficiencies are more straightforward to calculate once the nozzle and rotor cooling flows are known.

The cooled turbine efficiencies were obtained in this way over a range of cooling flows. These were varied by specifying a succession of blade metal temperatures, while holding all the other parameters constant (e.g., gas entry temperature and pressure, coolant temperature and pressure). The uncooled polytropic efficiency was also held constant at 0.9 (i.e., the value used by Wilcock et al. [7]).

The efficiencies $\eta_{\text{fr-mix}}$, η_{Hart}, and $\eta_{\text{mp-mix}}$ are compared in Fig. 1. It is seen that the fr-mix efficiency is much lower than the other two, more conventional, efficiencies.

An interesting "hybrid" efficiency, η_{Timko}, was proposed by Timko [9]. He derived the ideal power by assuming that only the nozzle coolant mixed with the mainstream gas flow (at constant mainstream pressure) before expanding to the backpressure p_{03} and that the rotor coolant expanded separately and isentropically to p_{03}. The ideal power result is thus intermediate between those for the Hartsel and mp-mix efficiencies. The calculated hybrid efficiency η_{Timko} is compared with these two efficiencies in Fig. 2.

Finally, Fig. 3 shows how the various irreversibilities associated with cooling, in the nondimensional form of Eq. (4), change with the magnitude of the blade metal temperature and hence with the cooling flow fraction.

4 Discussion and Conclusions

The calculations of Fig. 1, relating to the three efficiencies, merit careful consideration. It might initially have been expected that the fr-mix and Hartsel efficiencies would be identical since the reference denominators in both the efficiency expressions are for adiabatic and fully reversible expansions. But, on further consideration, it should be appreciated that the exit conditions are not the same; although both are at the pressure p_{03}, the mainstream gas, nozzle, and rotor coolants are separate for Hartsel but are fully mixed for the fr-mix efficiency.

For "real" gas flows of semiperfect gases, with $c_p(T)$ and $R \cong$ const, the difference in the enthalpy drops between mixed and unmixed expansions can be quite significant if the initial temperatures are radically different, $T_{01ci} \neq T_{01g}$. In gas turbines, c_p for the combustion products is greater than that of the coolant streams although the specific gas constants are almost the same. Young and Wilcock [5] have shown that under these conditions, the enthalpy drops in an isentropic expansion of mixed gases from a given stagnation pressure and through the same pressure ratio may be greater than when they are unmixed. This means that the Hartsel efficiency may be expected to be greater than the fr-mix efficiency and the calculations of Fig. 1 show that this is the case. Indeed, it is theoretically possible for Hartsel efficiency to be greater than unity, for very high polytropic efficiencies, which is unsatisfactory, as pointed out by Young and Horlock [1].

Another critical issue discussed in Ref. [1] is whether the rotor coolant should enter into the efficiency calculation. The authors argued that it certainly should, since it has the potential to do work, no matter whether it actually does work on the rotor and contributes to the shaft power. The magnitude of the actual rotor coolant work depends on the amount of preswirl imparted to the rotor coolant before it enters the rotor cooling passages and the tangential velocity with which it leaves (usually assumed to be the same as that of the mainstream gas flow). This rotor coolant work was found to be significant in the calculations presented here and it has been included in the estimates of the power output and hence the efficiencies.

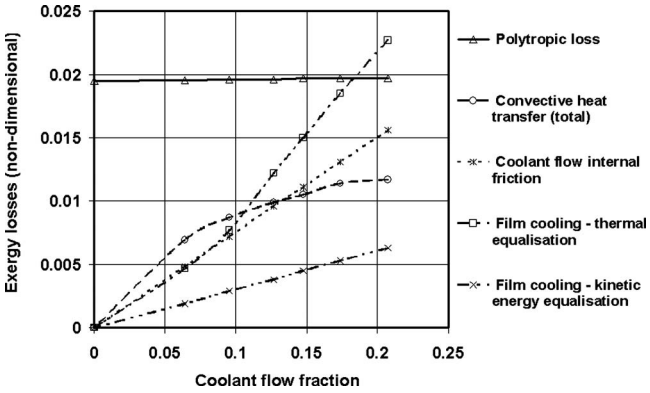

Fig. 3 Energy losses (nondimensional form) for the complete stage (stator plus rotor) and for varying coolant flow fractions. All these losses are included within the fr-mix efficiency

Downloaded 02 Jun 2010 to 171.66.16.107. Redistribution subject to ASME license or copyright; see http://www.asme.org/terms/Terms_Use.cfm

Figure 1 also shows that the fr-mix efficiency is much less than the mainstream pressure fully mixed efficiency $\eta_{\text{mp-mix}}$. Indeed, the latter is not much less than the Hartsel efficiency. This is also illustrated in Fig. 2, which shows the Timko efficiency. As to be expected, this hybrid efficiency falls between the Hartsel efficiency and the somewhat lower fully mixed efficiency:

$$\eta_{\text{Hart}} \geqslant \eta_{\text{Timko}} \geqslant \eta_{\text{mp-mix}}$$

Figure 3 illustrates how the several losses arising in a cooled turbine vary with the coolant fraction. It should be remembered that the coolant fraction was varied by changing the allowable blade metal temperature with all other parameters held constant, i.e., assuming that improved materials had become available and less cooling air was required. In presenting these calculations, the separate entropy changes for heat transfer across the main stream to the thermal barrier, across that barrier to the external metal, across the blade metal, and from the blade metal to the internal coolant were summed to give an overall convective heat transfer loss. The other losses shown in Fig. 3 are the basic uncooled free stream loss, the internal coolant frictional loss, and the two losses in film cooling—that due to equalization of the mainstream and coolant temperatures and that due to the equalization of the velocities of the two streams.

The basic uncooled free stream loss remains substantially constant because the polytropic efficiency (uncooled) is held constant, although the gas constituents are varying with the cooling fraction. However, all the coolant losses increase more or less linearly with the coolant fraction, including the sum of the convective heat transfer loss and that due to thermal equalization in film cooling. However, at high coolant flow rates, the latter increases even more quickly and the former tends to flatten off. This is because at large coolant flows, the film cooling discharge temperature is at its lowest and the difference from the free stream temperature is highest. The thermal equalization loss becomes the largest loss, whereas the kinetic energy loss due to mixing in film cooling is the lowest of the losses.

The magnitude of all these losses, as listed in Refs. [5,6], is of course dependent on the various assumptions in the calculations made from the expressions listed in the Appendix. Nevertheless, it would appear that given those assumptions, which roughly accord with practice, the losses due to thermal equalization due to film cooling and to internal coolant friction produce the highest penalty in reducing the cooled turbine efficiency below that of the uncooled turbine.

Acknowledgment

The authors are grateful to Professor John Young and Dr. Roger Wilcock for the use of their comprehensive code in obtaining the results described in this paper.

Nomenclature

b = steady flow availability (specific)
c_p = specific heat at constant pressure
h = specific enthalpy
M = Mach number
m = mass flow rate
P = power output
p = pressure
Q = heat quantity
R = specific gas constant
s = specific entropy
T = temperature
V = velocity

Greek

γ = ratio between the constant pressure and the constant volume specific heats
$\Delta\Sigma$ = rate of entropy creation by irreversible processes
η = efficiency
μ = function defined in Eq. (4)
ϕ = angle between the injected coolant flow and the mainstream gas

Subscripts

0 = total (as opposed to static) quantities
1, 2, 3, 4 = stator inlet, stator outlet/rotor inlet, rotor outlet, stage outlet
b = blade metal
basic = referring to basic losses
c = coolant
conv = referring to convective heat transfer losses
ds = dead state
ext = external, gas side
fr-mix = fully reversible mixed (efficiency)
g = mainstream gas
Hart = Hartsel (efficiency)
i = coolant condition at inlet to blade passages, ith coolant stream
int, F = referring to internal friction losses
k = coolant condition at compressor bleed point
max = maximum (referring to blade metal temperature)
mix, KE = referring to film cooling kinetic energy equalization losses
mix, Q = referring to film cooling thermal equalisation losses
mp-mix = mainstream pressure mixed (efficiency)
R = rational
r = rotor
s = stator
ss = isentropic
Timko = Timko (efficiency)
U = uncooled (efficiency)
w = blade wall, external blade surface
x = coolant condition at exit from blade (before mixing), or injection point

Superscript

$-$ = mean or average (gas properties, etc.)

Appendix

Application of the analysis of Young and Wilcock [6] to each of the two rows of the cooled stage yields the following expressions for the various losses (relative conditions and velocities apply for the rotor).

Basic uncooled free stream loss,

$$\Delta\Sigma_{\text{basic}} = m_{g,1} R_g (1 - \eta_{\text{basic}}) \ell n \left(\frac{p_{0g,1}}{p_{0g,4}} \right)$$

Convective heat transfer loss,

$$\Delta\Sigma_{\text{conv}} \cong m_c c_{pc} \left[K_{\text{int}} \ell n \left(\frac{T_{0c,x}}{T_{0c,i}} \right) - K_{\text{ext}} \left(\frac{T_{0c,x} - T_{0c,i}}{T_{0g}} \right) \right]$$

where

$$K_{\text{int}} = 1 + \frac{\gamma_c - 1}{2} M_c^2$$

$$K_{\text{ext}} = 1 + \frac{\gamma_g - 1}{2} M_g^2$$

Internal friction loss,

$$\Delta\Sigma_{\text{int},F} = m_c c_{pc} \left[\ell n \left(\frac{T_{0c,x}}{T_{0c,k}} \right) - K_{\text{int}} \ell n \left(\frac{T_{0c,x}}{T_{0c,i}} \right) \right] - m_c R_c \ell n \left(\frac{p_{0c,x}}{p_{0c,k}} \right)$$

Film cooling thermal equalization loss,

Downloaded 02 Jun 2010 to 171.66.16.107. Redistribution subject to ASME license or copyright; see http://www.asme.org/terms/Terms_Use.cfm

$$\Delta\Sigma_{\mathrm{mix},Q} \cong m_c c_{pc}\left[\ell n\left(\frac{T_{g,x}}{T_{c,x}}\right) - \left(1 - \frac{T_{c,x}}{T_{g,x}}\right)\right]$$

Film cooling kinetic energy equalization loss,

$$\Delta\Sigma_{\mathrm{mix,KE}} = m_c\left[\frac{(V_{g,x} - V_{c,x}\cos\phi)^2}{2T_{g,x}} + \frac{(V_{c,x}\sin\phi)^2}{2T_{g,x}}\right]$$

References

[1] Young, J. B., and Horlock, J. H., 2006, "Defining the Efficiency of a Cooled Turbine," ASME J. Turbomach., **128**, pp. 658–667.

[2] Torbidoni, L., and Horlock, J. H., 2006, "Calculation of the Expansion Through a Cooled Gas Turbine," ASME J. Turbomach., **128**, pp. 555–563.

[3] Hartsel, J. E., 1972, "Prediction of Effects of Mass-Transfer Cooling on the Blade-Row Efficiency of Turbine Airfoils," *AIAA Tenth Aerospace Sciences Meeting*, San Diego, Paper AIAA-72–11.

[4] Kurzke, J., 2002, "Performance Modelling Methodology: Efficiency Definitions for Cooled Single and Multistage Turbines," ASME Paper No. 2002-GT-30497.

[5] Young, J. B., and Wilcock, R. C., 2002a, "Modelling the Air-Cooled Gas Turbine—Part 1: General Thermodynamics," ASME J. Turbomach., **124**, pp. 207–213.

[6] Young, J. B., and Wilcock, R. C., 2002b, "Modelling the Air-Cooled Gas Turbine—Part 2: Coolant Flows and Losses," ASME J. Turbomach., **124**, pp. 214–221.

[7] Wilcock, R. C., Young, J. B., and Horlock, J. H., 2005, "The Effect of Turbine Blade Cooling on the Cycle Efficiency of Gas Turbine Power Plants," ASME J. Eng. Gas Turbines Power, **127**, pp. 109–120.

[8] Horlock, J. H., Watson, D. T., and Jones, T. V., 2001, "Limitations on Gas Turbine Performance Imposed by Large Turbine Cooling Flows," ASME J. Eng. Gas Turbines Power, **123**, pp. 487–494.

[9] Timko, L. P., 1980, "Energy Efficient Engine: High Pressure Turbine Component Test Perfomance Report," NASA Report No. CR-168289.

Downloaded 02 Jun 2010 to 171.66.16.107. Redistribution subject to ASME license or copyright; see http://www.asme.org/terms/Terms_Use.cfm

M. Bagnoli

M. Bianchi

F. Melino

A. Peretto

DIEM University of Bologna,
Viale Risorgimento,
2-40136 Bologna, Italy

P. R. Spina
ENDIF,
University of Ferrara,
Via Saragat,
44100 Ferrara, Italy

S. Ingistov
WCC/BP

R. K. Bhargava
Foster Wheeler USA Corp.,
2020 Dairy Ashford Road,
Houston, TX 77077

Application of a Computational Code to Simulate Interstage Injection Effects on GE Frame 7EA Gas Turbine

This paper investigates effects of interstage water injection on the performance of a GE Frame 7EA gas turbine using aerothermodynamic modeling. To accomplish this objective, a computational code, written in FORTRAN 90 language and developed by DIEM University of Bologna, has been used. The calculation procedure considers effects of evaporation of injected water within the compressor including droplets dynamics, which are necessary in order to fully evaluate effects of wet compression on the gas turbine performance. The robustness of the computational code is demonstrated by evaluating stage-by-stage compressor performance and the overall gas turbine performance in the presence of inlet evaporative fogging, overspray fogging, and interstage water injection. The presented results show that water injection location influences compressor stage loading redistribution differently. The plausible explanations to the observed trends of various performance parameters are presented in this paper. [DOI: 10.1115/1.2771247]

Introduction

In recent years, high pressure fogging approach for gas turbine power augmentation has become a widely investigated topic [1–12] due to many advantages it offers to gas turbine users. The various intake air direct cooling techniques, such as inlet fogging, fog overspray (wet compression), and interstage water mist injection, have been implemented on gas turbines in simple and combined cycle applications. Both wet compression and interstage injection involve multiphase flow and water evaporation during the compression process. The phenomenon of two phase flow compression in axial compressor is not yet fully understood and is a subject to further field testing and investigation.

In recent years, concerted efforts have been made in understanding effects of overspray fogging on the compressor performance using numerical analyses with different degrees of simplifications and assumptions [1,2,6,7]. Whereas Zheng et al. [3] presented a detailed thermodynamic analysis providing a good insight on the overall compressor performance in the presence of overspray fogging. A comparison of experimental and analytical studies showing effects of overspray fogging on the compressor was presented by Utamura et al. [1]. Their study clearly showed impact of droplet size on the evaporation of water inside the compressor stages.

On the contrary, the effects of interstage injection on compressor performance have not been fully explored. The first analytical and experimental study, in current authors' opinion, was presented by Arsen'ev and Berkovich [13]. In spite of the fact that details on the analytical work presented by Arsen'ev and Berkovich were limited, their study showed increased net power output and efficiency with interstage injection compared to the case when water was injected upstream of the compressor. Furthermore, their study suggested an optimum compressor stage after which the gas turbine performance started to decrease. Recently, implementation of interstage injection in a heavy-duty industrial gas turbine has been reported by Ingistov [14,15]. It must be noted that in the field implementation of interstage injection approach, water was injected simultaneously upstream of three stages. Therefore, one must be cautious in comparing field results with the results of analytical study.

The first attempt to analytically simulate stage-by-stage compressor performance including the overall gas turbine performance in the presence of the interstage injection was reported by Bagnoli et al. [8]. Their study was conducted using a commercial program [16] combined with the approach of performance prediction using generalized performance curves of compressor and turbine developed by Spina [17]. A comprehensive review of the current understanding of various fogging technologies was recently presented by Bhargava et al. [10–12].

In the present paper, a detailed study on the effects of interstage injection is carried out for a heavy-duty industrial gas turbine (GE Frame 7EA). The analysis has been carried out using a new computational code, named IN. FO. G. T. E. [18], fully developed by the energy systems research team of DIEM University of Bologna and is briefly described below.

IN.FO. G.T.E. Software

Up to now, to evaluate the performance change using fogging systems on gas turbine, commercial energy systems simulation software has been adopted. These commercial codes have many advantages, such as a good user interface, low learning time, and user friendly features. As a result, the available commercial programs are widely used by plant engineers, engineering companies, consultants, academia, and others either to evaluate performance

Contributed by the International Gas Turbine Institute of ASME for publication in the JOURNAL OF ENGINEERING FOR GAS TURBINES AND POWER. Manuscript received June 28, 2006; final manuscript received October 17, 2006; published online December 17, 2007. Review conducted by Dilip R. Ballal. Paper presented at the 2006 ASME Turbo Expo 2006: Land, Sea and Air (GT2006), Barcelona, Spain, May 8-11, 2006, Paper No. GT2006-90343.

Copyright © 2008 by ASME

Downloaded 02 Jun 2010 to 171.66.16.107. Redistribution subject to ASME license or copyright; see http://www.asme.org/terms/Terms_Use.cfm

of an existing energy system or to design a new system [16,19]. On the other hand, usually, the commercial codes are not intended to conduct a detailed turbomachinery design such as stage-by-stage performance analysis of an axial compressor with complicated operating condition, namely, interstage injection in authors' previous work [8], where a commercial software [16] was used to investigate the performance change due to interstage injection effects, it was found difficult, if not impossible, to evaluate in detail effects of wet compression. In fact, as demonstrated by the work of Bagnoli et al. [8], an additional analysis was required to obtain stage-by-stage compressor performance using the methodology presented in Ref. [17].

To overcome above described limitations of the commercially available programs, a new physical-mathematical gas turbine model was set up. This new calculation code, details of which are discussed by Bagnoli et al. [18], is able to realize a stage-by-stage analysis of any gas turbine in the presence of interstage water injection, including inlet evaporative fogging and overspray fogging. In particular, the new computational code has the following capabilities:

- consider the interstage injection of water
- take into account thermodynamic properties of air (such as total pressure, relative humidity, and temperature) and physical and thermodynamic characteristics of water droplet (such as property of the liquid phase, droplet volume, and temperature) in order to evaluate the dynamic process that involves heat and mass transfer between humid air and liquid water during evaporation
- take into account the influence of injected water temperature on gas turbine performance
- evaluate the pressure and temperature of the air stage-by-stage along the compressor and the presence of liquid water (so it supplies where the injected water completely evaporates among the compressor)
- analyze the change in compressor working point due to the water injection in reference to the surge limit

Because of the code's capability to evaluate stage-by-stage compressor performance analysis, the user also has estimation of the amount of water evaporated and complete flow properties of the fluid at the exit of each compressor stage.

The large amount of parameters and input data required by the program, because of complex and detailed analysis capabilities of the code, allows it to reproduce the operating condition of any gas turbine and to evaluate in detail performance changes in the case of water injection.

To validate the wet compression model and other calculation procedures implemented in the IN.FO.G.T.E. code, results obtained from the developed code were compared with the results from other investigators [1,7]. A comparison of normalized flow coefficient for a generic 12 stage compressor with the work of White and Meacock [7] shows that results from two models are quite compatible, as is evident from Fig. 1. It may be noted that at different flow conditions, root mean square error values between the results of two studies are about 0.03. A more detailed discussion on the validation of the new code is provided by Bagnoli et al. [18].

Gas Turbine Modeling. The IN. FO. G.T. E. program was adapted and tuned in order to study the performances of an existing GE Frame 7EA gas turbine in the presence of interstage injection.

This gas turbine, a midsize heavy-duty industrial gas turbine developed for 60 Hz applications, consists of a 17 stage axial compressor and a 3 stage axial turbine with a produced power output of about 84 MW and an electrical efficiency of about 32.2%.

A scheme of the GE Frame 7EA gas turbine, highlighting the various water injection points examined in the following study and the turbine cooling air streams (CASs) is shown in Fig. 2. In

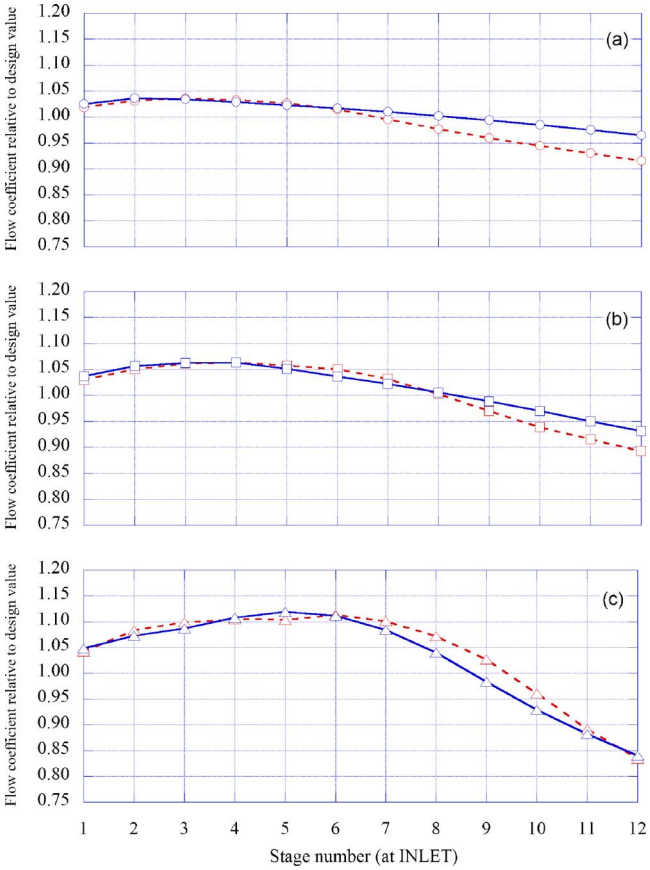

Fig. 1 Normalized flow coefficient change at the stage inlet as calculated by White and Meacock [7] (red dotted lines) and by the developed calculation code [18] (blue continuous lines) versus stage number and water to air ratio: 1% (*a*), 2% (*b*), and 5% (*c*) Reference: 15°C, 1.013 bars, 100% of RH, droplets diameter equal to 5 μm

the simulations, two compressor air bleed ports (downstream from 5th and 17th stages) for turbine cooling and the possibility of high pressure fogging, overspray, and water interstage injection in four different locations were considered. In particular, high pressure fogging (FOG, in Fig. 2) and overspray (WIP1, in Fig. 2) are realized by placing two nozzles grids, respectively, in the compressor inlet duct and immediately upstream of the compressor inlet section. The other injection points (from WIP2 to WIP5 in Fig. 2) are placed upstream from second to fifth stage to realize the interstage injection.

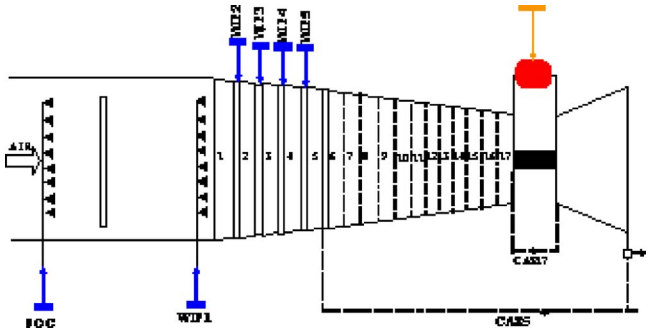

Fig. 2 GE Fr7EA simulation model

Downloaded 02 Jun 2010 to 171.66.16.107. Redistribution subject to ASME license or copyright; see http://www.asme.org/terms/Terms_Use.cfm

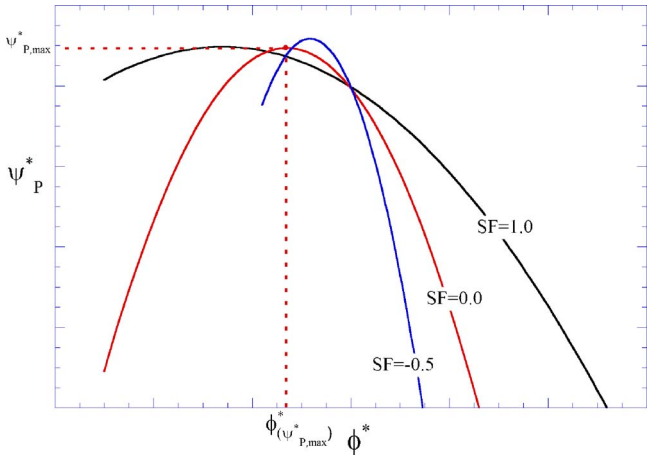

Fig. 3 Generalized compressor stage characteristics $\psi_p^* = F_\psi(\phi^*, \mathrm{SF})$

Calculation Code Tuning on GE Frame 7EA

As a first step, the program has been tuned (i.e., all the configuration parameters required as input by the code have been determined) to reproduce the performance of the machine at different ambient and load conditions in "dry conditions" (without water injection). In particular, the tuning was carried out with reference to 12 operating points corresponding to four values of ambient temperature (5°C, 15°C, 30°C, and 40°C) and three values of turbine inlet temperature (1113°C, 986°C, and 856°C). The selected values of turbine inlet temperature correspond to machine loads at ISO conditions equal to 100%, 80%, and 60%, respectively. All the calculations consider inlet guide vanes (IGVs) fully opened and no pressure losses at the compressor inlet and at the turbine outlet.

In order to simulate compressor stage performance in off-design conditions, generalized relationships between pressure coefficient, stage isentropic efficiency, and flow coefficient normalized to the design values were used [17,18]. These relationships allow the complete evaluation of stage characteristics once the stage design point $((\psi_p)_{\mathrm{des}}, (\eta)_{\mathrm{des}}, (\phi)_{\mathrm{des}})$ is known. In Figs. 3 and 4, the generalized stage characteristics $\psi_p^* = F_\psi(\phi^*, \mathrm{SF})$ and the generalized stage efficiency curve are shown. In particular, a parameter called shape factor (SF) was introduced in order to account for different stage characteristics based on different stage type and this allows the obtainment of a number of generalized

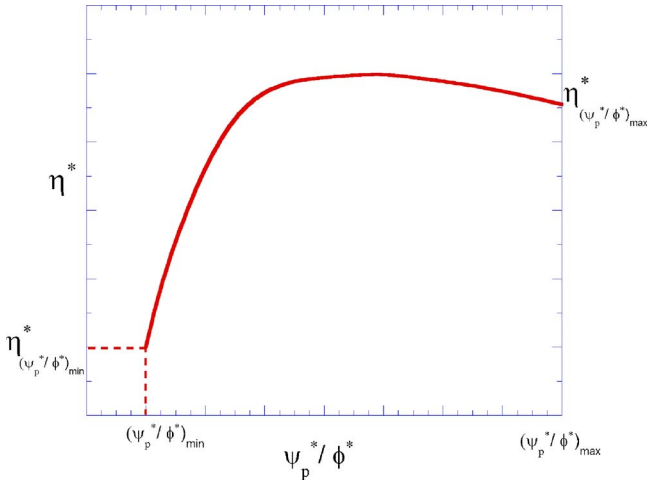

Fig. 4 Generalized compressor stage efficiency curve

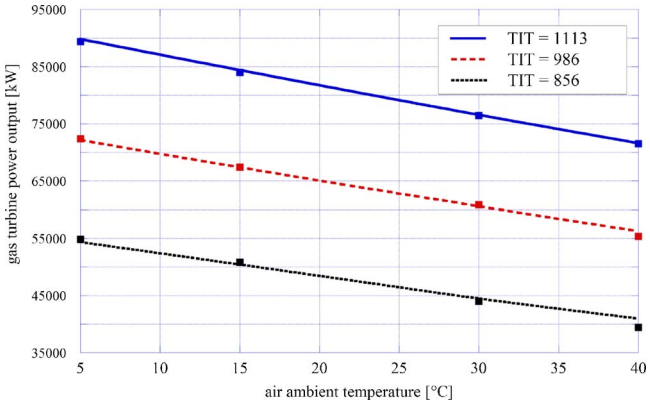

Fig. 5 Frame 7EA power output evaluated by GTPRO (continuous lines) and by the code (square markers) as function of ambient temperature and load

$\psi^* = F_\psi(\phi^*, \mathrm{SF})$ curves covering all experimental data points reported by Muir et al. [20]. In this manner, the above mentioned $\psi_p^* = F_\psi(\phi^*, \mathrm{SF})$ equation becomes [17]

$$\psi_p^* = \psi_{p,\max}^* - \frac{\psi_{p,\max}^* - 1}{[\phi_{\psi_{p,\max}}^* + \mathrm{SF}(\phi_{\psi_{p,\max}}^* - 1) - 1]^2}[\phi_{\psi_{p,\max}}^* + \mathrm{SF}(\phi_{\psi_{p,\max}}^* - 1) - \phi^*]^2$$

Moreover, the definition of some geometrical parameters of the compressor is required by the IN. FO. G. T. E. code: So the values of the mean radii of the 17 compressor stages, the tip and root radii, and the axial length of the stages have been supplied as input to the calculation code.

Finally, the position of the air bleed ports, placed at the fifth and at the last stage, and their design air mass flow rate were defined.

The pressure losses through the combustor are assumed equal to the 4% of the pressure at its inlet, while no pressure losses at the compressor inlet and at the turbine outlet were considered.

For the turbine, a map characterized by a constant value of the flow function was chosen. This choice for the gas turbine performance map and the use of compressor stage performance maps characterized by a SF equal to −0.5 allow to reproduce with an acceptable accuracy the performance of the Frame 7EA as it will be shown below.

According to the previous assumptions, in Figs. 5–7, the comparison between the main performance parameters of the Frame 7EA evaluated by the computational code (square markers) and the values of GTPRO gas turbine library [16], which reproduces the

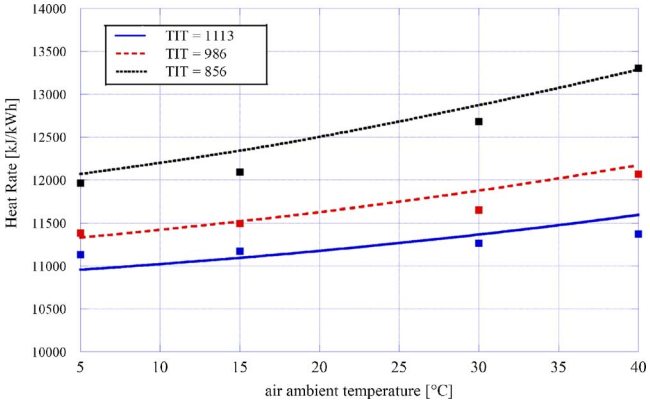

Fig. 6 Frame 7EA Heat Rate evaluated by GTPRO (continuous lines) and by the code (square markers) as function of ambient temperature and load

Downloaded 02 Jun 2010 to 171.66.16.107. Redistribution subject to ASME license or copyright; see http://www.asme.org/terms/Terms_Use.cfm

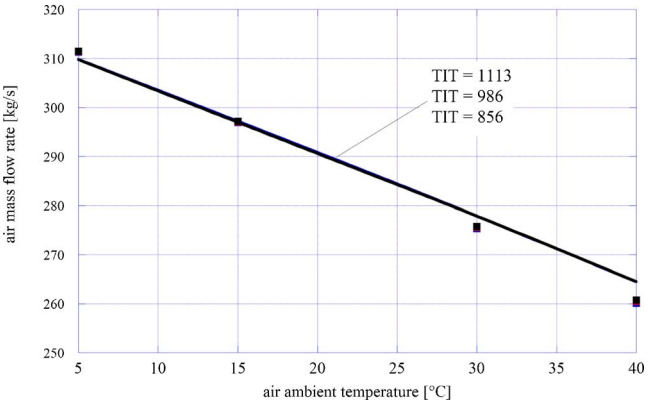

Fig. 7 Frame 7EA air mass flow rate evaluated by GTPRO (continuous lines) and by the code (square markers) as function of ambient temperature and load

performance of the machine, (continuous lines) for three loads (equal to 100%, 80%, and 60%) as function of ambient temperature are presented.

From these figures, it could be observed that the IN.FO.G.T.E. program reproduces the performance of the real machine with an acceptable accuracy. The greatest differences between the calculation code and GTPRO results occur at low gas turbine load at high temperatures. In operation at full load (turbine inlet temperature equal to 1113°C), the percentage difference between the program and GTPRO results is always less than the 2%, while at a load of 60% (turbine inlet temperature equal to 856°C) the maximum difference is of about the 4.5%.

Ge Frame 7EA Gas Turbine Performance With Water Injection

To examine effects of interstage injection on gas turbine performance parameters, the following two ambient conditions are considered: ISO case (ambient temperature of 15°C, pressure of 1.013 bars, and relative humidity of 60%) and HOT case (40°C, 1.013 bars, and 40% RH). The HOT case is considered as the base case to evaluate effects of interstage injection because power enhancement techniques such as high pressure fogging and interstage injection are considered more effective at high ambient temperature and low relative humidity.

The performance analysis was carried out taking into account the following assumptions:

- IGVs are maintained fully open;
- gas turbine is regulated at constant TIT;
- inlet and exhaust pressure losses are neglected;
- the temperature of the injected water has been assumed always equal to 15°C;
- the diameter of the injected water droplet has been assumed equal to 10 μm; and
- effects of droplet dynamics have been considered taking into account heat and mass exchange between air and water during the compression process.

The results obtained for the two climatic conditions, without the effects of interstage injection, are summarized in Table 1.

The analysis carried out on GE Frame 7EA gas turbine, equipped with injection systems such as fogging and interstage water injection, was developed referring to the already defined two ambient conditions of ISO and HOT cases. The water injection was realized according to the schemes previously described and presented in Fig. 2.

Considering the above mentioned assumptions, the simulations carried out by using IN.FO. G. T. E. software have supplied the results reported in Figs. 8–12 with dotted and continuous lines for ISO and HOT conditions, respectively.

Table 1 Comparison of performance and thermodynamic parameters of GE Frame 7EA at ISO and HOT conditions

	ISO case 15°C, 60%HR	HOT case 40°C, 40%HR	Diff.
Power output (kW)	84001	71383	−15%
Heat rate (kJ/kW h)	11174	11357	+2%
Air mass flow rate (kg/s)	296.96	262.13	−12%
Pressure ratio	12.60	11.16	−11%
Compressor outlet temperature (°C)	366	392	+26°C
Exhaust temperature (°C)	536	547	+11°C

Figure 8 shows the power boost trend as a function of injected water, expressed as a percentage of inlet air flow rate, for different locations of water injection. In the graph the results as calculated value of power output with water injection (P_{out}) normalized with the power output corresponding to the dry ISO case ($P_{out,ISO}$) are shown. In Fig. 8 and Table 1, it should be noted that the gas turbine lost approximately 15% power output due to high ambient temperature (HOT case) compared to the ISO case. In the above mentioned figure, for example, it must be noted how approximately 1.6% of water injection at stator of the compressor stage 2 (WIP2) allows to recover the lost power for the HOT case. The results obtained from simulations and plotted in figure supply the amount of required injected water to recover the power loss due to high ambient temperature, in the case of variable injection points.

It should be further observed that, both in ISO and HOT cases, water consumption increases in order to obtain the same increase in power output, as the injection point moves from fogging to upstream of the fifth stage. This observation implies that, for a given amount of injected water mass flow rate, the power boost per unit of water injection ($PB=(P_{out}-P_{out,ISO})/\dot{m}_{inj}$) decreases as the injection point moves from the first to the fifth stage. The higher amount of power boost, for a given amount of injected water to air flow ratio, for the case identified as FOG is mainly attributed to the evaporation efficiency or the droplet residence time, which is maximum if water is injected at a location close to the inlet filter. Furthermore, the droplet residence time decreases as the injection point moves closer to the compressor inlet.

In Fig. 9, the variation of normalized heat rate as a function of injected water mass flow rate and the locations of injection is shown and, in particular, it should be noted that gas turbine cycle efficiency improves with various water injection locations for both ISO and HOT ambient conditions. For the ISO case, it is further noted that the heat rate value in the case of water injection is always lower than heat rate evaluated in dry case. In particular, the heat rate value increases as the injection point moves downstream in the compressor. For both the ISO and HOT cases, for a given water and air mass flow ratio, the maximum improvement in gas turbine efficiency is noted with water injected upstream the compressor (FOG). It is very important to highlight that in the HOT case for an injection in the inlet duct, the design value of HR can be reached for a water to air ratio equal to about 1%, while, in the case of injection upstream in the fifth stage, the design value of HR is reached for a water to air ratio equal to about 2.2%. These values are greater than those required to recover the loss in power output due to high ambient temperature (1.4% of water to air ratio in FOG case and 1.9% in WIP5 case, Fig. 8). These results suggest that the interstage injection technology is more effective to gain power than the gas turbine efficiency even if also in this aspect good results could be obtained. The observed improvement in the values of HR with interstage water injection can be attributed to the performance enhancement in the compressor section (decrease in compressor specific work), as shown in Fig. 12.

Downloaded 02 Jun 2010 to 171.66.16.107. Redistribution subject to ASME license or copyright; see http://www.asme.org/terms/Terms_Use.cfm

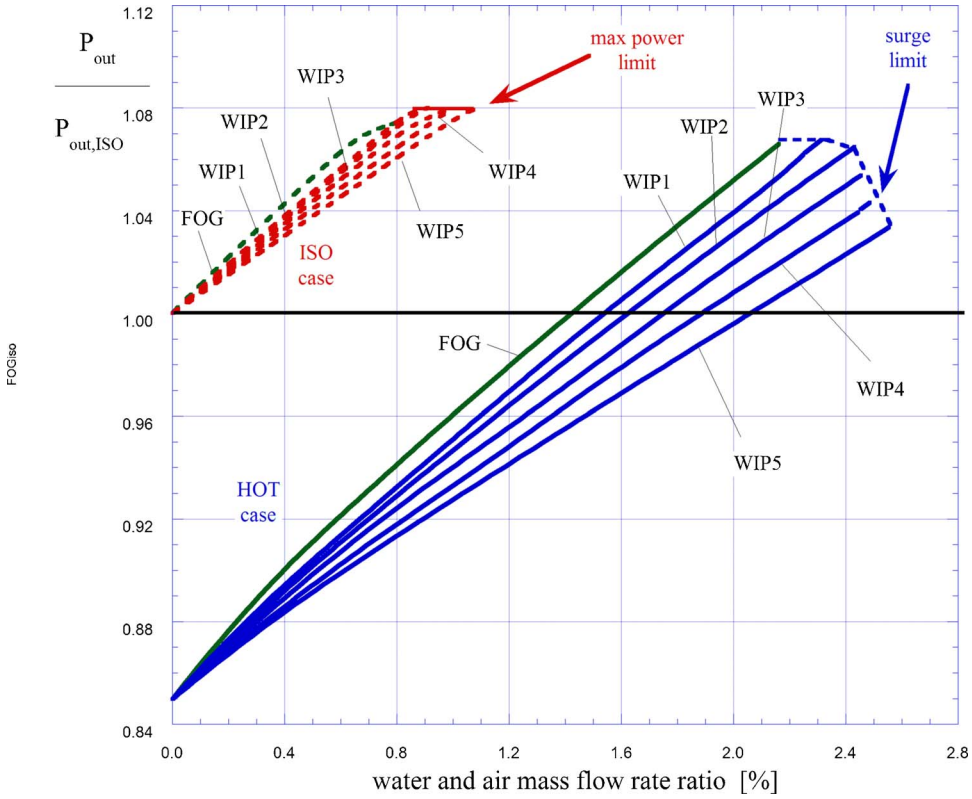

Fig. 8 Gas turbine power output change as function of injected water and air mass flow rate ratio and injection point

In Figs. 10 and 11, the increases of overall compressor pressure ratio and of the total air mass flow rate at the gas turbine inlet due to water injection are shown. These results regarding gas turbine behavior are mainly due to the cooling effects inside the compressor. Furthermore, in both ISO and HOT cases, the maximum increase of the compressor pressure ratio is observed as injection is performed upstream the first stage (WIP1), whereas maximum value of air mass flow rate is obtained with injection in the inlet duct (FOG) and the highest water injection mass flow rate.

As previously mentioned, fogging or interstage water injection influences performance characteristics of the compressor. This aspect is clearly shown in Fig. 12 in which the reduction in compression work caused by cooling effects within the compressor is presented. The maximum reduction in compressor specific work (that reach values of about 97% of the specific work in ISO dry case) is achieved in the case of water injection taking place in the inlet duct and the highest water injection mass flow rate at HOT conditions.

Based on the review of performance results, presented in Figs. 8–12, it is quite evident the performance improvements from interstage injection are comparatively lower than conventional fogging (inlet evaporative and overspray). It is important to mention that the interstage injection technique was implemented in the field to keep compressor clean (reduce fouling effects) rather than gain power boost. The interstage injection did help in keeping the compressor clean as the off-line wash cycle duration was almost doubled, as reported by Ingistov [14].

It should be noted in Figs. 8–12 that the maximum acceptable gas turbine power output and the surge limit in the compressor

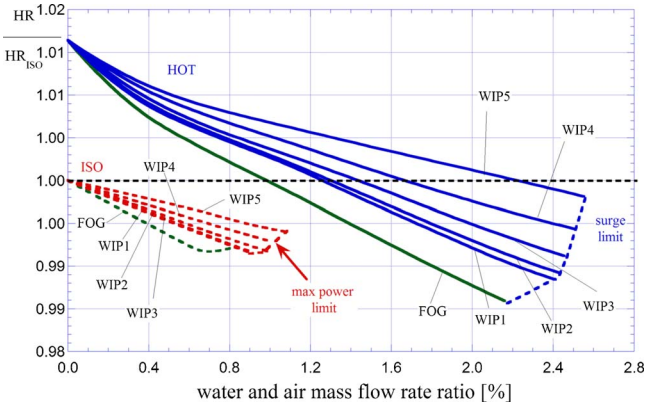

Fig. 9 Gas turbine heat rate change as function of injected water and air mass flow rate ratio and injection point

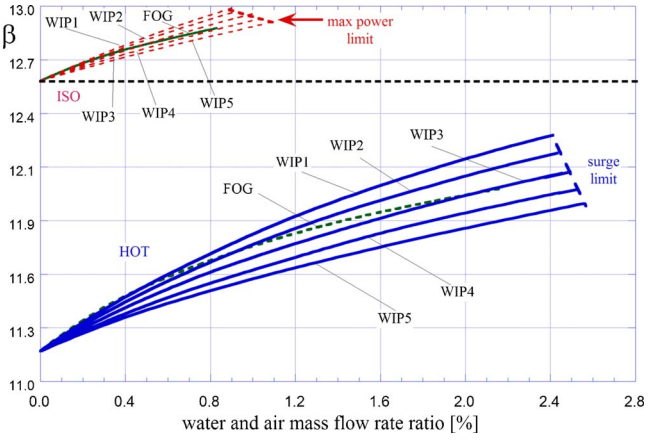

Fig. 10 Compressor pressure ratio as function of injected water and air mass flow rate ratio and injection point

Downloaded 02 Jun 2010 to 171.66.16.107. Redistribution subject to ASME license or copyright; see http://www.asme.org/terms/Terms_Use.cfm

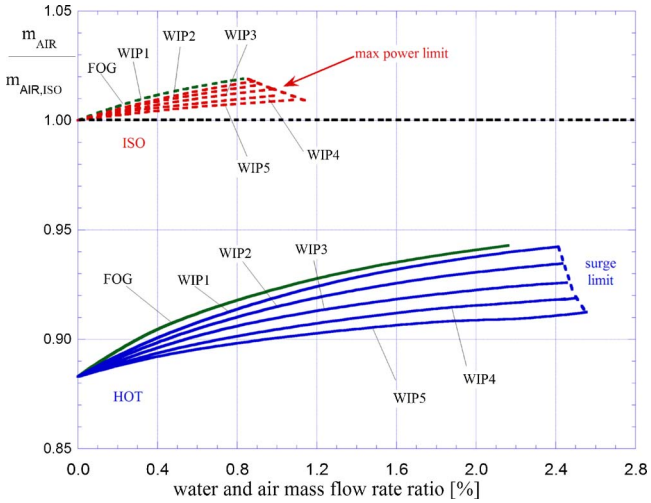

Fig. 11 Air mass flow rate at compressor inlet as function of injected water and air mass flow rate ratio and injection point

limit the total amount of water that is possible to inject into the compressor. In particular, it should be noted that the maximum acceptable gas turbine power output is associated with the gas turbine mechanical integrity and the electric generator capacity: In this study, the $P_{out}/P_{out,ISO}$ maximum value is assumed equal to 1.08. On the other hand, the surge limit in the compressor limits $P_{out}/P_{out,ISO}$ to different values dependent on injected water mass flow rate and water injection location.

In addition to the above discussed overall gas turbine performance, it is important to examine effects of injection points and injected water amount on the compressor stage performance map. In Figs. 13(*a*)–13(*d*), the performance characteristics of the first and the last compressor stage, 1st and 17th stages, are shown for different amounts of water injected at three different locations (WIP1, WIP2 and WIP5) for the ISO ((*a*) and (*b*)) and HOT ((*c*) and (*d*)) cases. For the first stage in the case of using overspray fogging water injection, an increase in normalized stage flow coefficient occurs because of inlet cooling effect for the ISO case (Fig. 13(*a*)). Moreover, as expected, an extra increase in injected water flow brings a decrease in pressure coefficient and stage pressure ratio. Due to the reasons just given, for the ISO case, unloading in the first stage occurs regardless of location of the injection and the amount of injected water.

Considering the 17th stage, at ISO conditions, the normalized pressure coefficient increases and the stage flow coefficient decreases for each injection point because of a decrease in the air temperature as a result of continuous evaporative cooling in various compressor stages. A decrease in stage flow coefficient brings an increase of stage loading also clear in Fig. 14(*a*).

The compressor behaviour in the case of interstage injection, and more in particular the trend of flow coefficient is clearly noted in Figs. 14(*a*) and 14(*b*). In these figures, a redistribution of the stage loading (unloading of the first few stages and increased loading of later stages of the compressor) is quite evident for the three injection locations and the amount of injected water.

It is evident from Figs. 13(*c*) and 13(*d*) that the effects of interstage injection on compressor stage performance for the HOT case are similar to that observed for the ISO case. It should be observed that at HOT conditions, because of high ambient temperature, if no injection is performed, the "A" operating point has reduced value of stage flow coefficient compared to the design case, as shown in Fig. 13(*c*). If the HOT case is compared to the ISO case, it is evident that a larger amount of injected water is required to achieve stage flow coefficients higher than the compressor design values in the first stage, as can be seen by comparing Fig. 14(*a*) and 15(*a*).

In conclusion, as an example, in Figs. 16 and 17, the temperature and the pressure profiles across the compressor with reference to 40°C of air ambient temperature and 40% of relative humidity without water injection and with 6.8 kg/s of water injected upstream of the third stage (WIP3), are presented.

In particular, in Fig. 16, the heavy modification to the temperature profile due to the evaporation of the injected water (from the exit of the third stage to the exit of the sixth stage) can be observed.

Moreover, in Fig. 17, which highlights the increase of compressor pressure ratio due to water injection, it could be observed that the pressure across the compressor is lower in the case with water injection with respect to the dry compression until the 15th stage is reached. This evidence is coherent with Figs. 13(*a*)–13(*d*) because the water injection allows the unloading of the first stages and the overloading of the last stages.

Finally, the evaporation ratio, defined as the percentage of evaporated water to the total injected amount as function of the compressor stages with reference to 40°C of air ambient temperature and 40% of relative humidity without water injection and

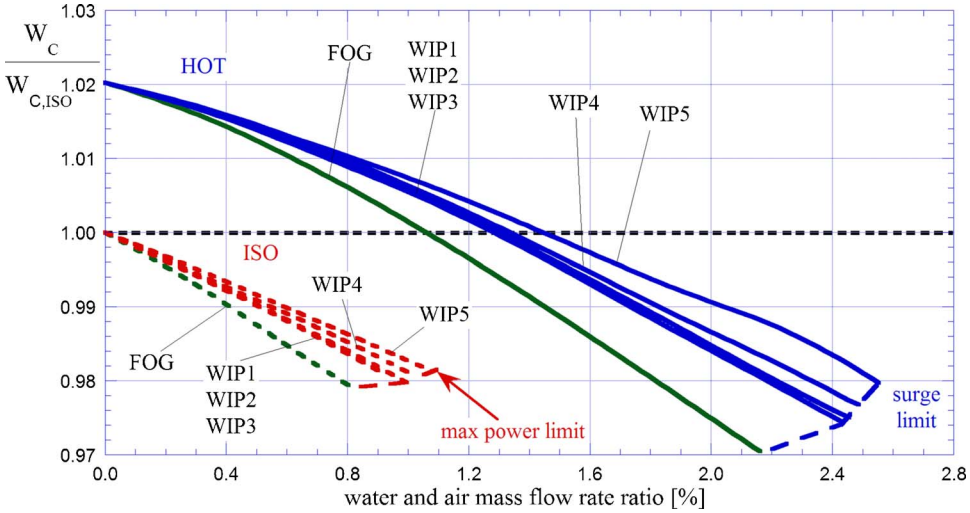

Fig. 12 Compressor specific work change as function of injected water and air mass flow rate ratio and injection point

Downloaded 02 Jun 2010 to 171.66.16.107. Redistribution subject to ASME license or copyright; see http://www.asme.org/terms/Terms_Use.cfm

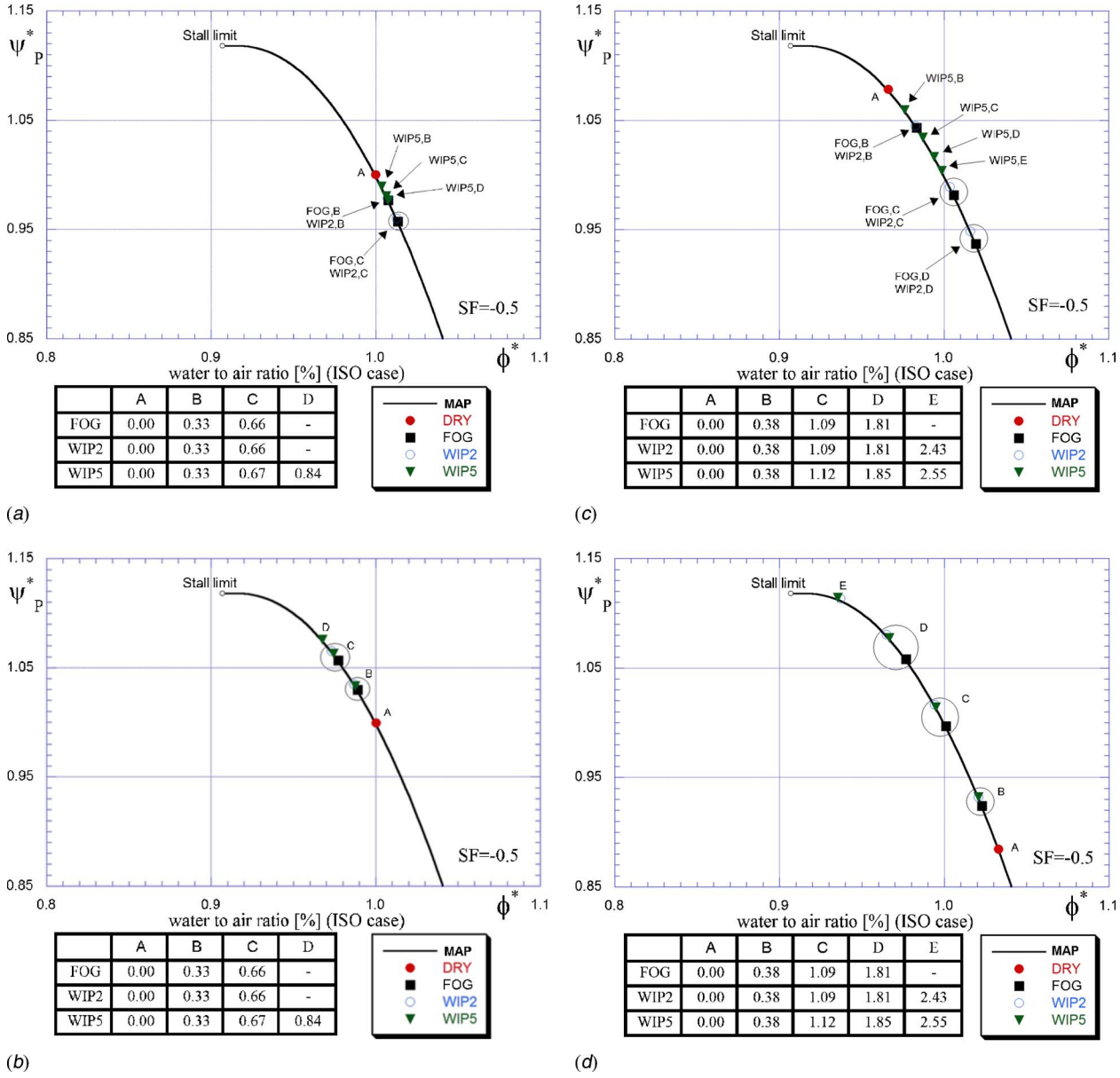

	A	B	C	D
FOG	0.00	0.33	0.66	-
WIP2	0.00	0.33	0.66	-
WIP5	0.00	0.33	0.67	0.84

	A	B	C	D	E
FOG	0.00	0.38	1.09	1.81	-
WIP2	0.00	0.38	1.09	1.81	2.43
WIP5	0.00	0.38	1.12	1.85	2.55

Fig. 13 (a) First stage performance maps and operating points with water injection (Reference: ISO case). (b) 17th stage performance maps and operating points with water injection (Reference: ISO case). (c) First stage performance maps and operating points with water injection (Reference: HOT case). (d) 17th stage performance maps and operating points with water injection (Reference: HOT case).

with 6.8 kg/s of water injected upstream of the third stage (WIP3), is presented in Fig. 18. From this figure, it could be observed that the evaporation of water ends into the sixth stage, as also evident from the Fig. 16.

Concluding Remarks

In the present paper, an investigation on the effects of interstage injection on GE Frame 7EA gas turbine performance has been carried out using an energy system simulation code (IN. FO. G. T. E.) developed by DIEM University of Bologna. In particular, simulation code has been set up on experimental data and then a stage-by-stage analysis of the compressor and an overall gas turbine performance investigation have been performed. These parameters have been evaluated considering different injection points (from FOG to WIP5), water mass flow rates and climatic conditions (ISO and HOT cases). The results obtained by the simulation study allow the authors to make the following concluding remarks:

- A careful examination of the 1st and 17th stage performance characteristics shows an unloading of the first stage and an increase in loading of the 17th stage for every case of injection point and ambient condition investigated. Increasing the amount of water injected causes 17th stage operating point to move closer to the surge line suggesting that one has to be cautious in selecting the water amount to inject inside the compressor.
- The maximum power boost is obtained if the water injection is realized upstream of the compressor in the inlet duct both for the ISO and HOT cases.
- The total water amount that is possible to inject into the compressor is limited by ambient conditions, maximum allowable gas turbine power output (due to mechanical

Downloaded 02 Jun 2010 to 171.66.16.107. Redistribution subject to ASME license or copyright; see http://www.asme.org/terms/Terms_Use.cfm

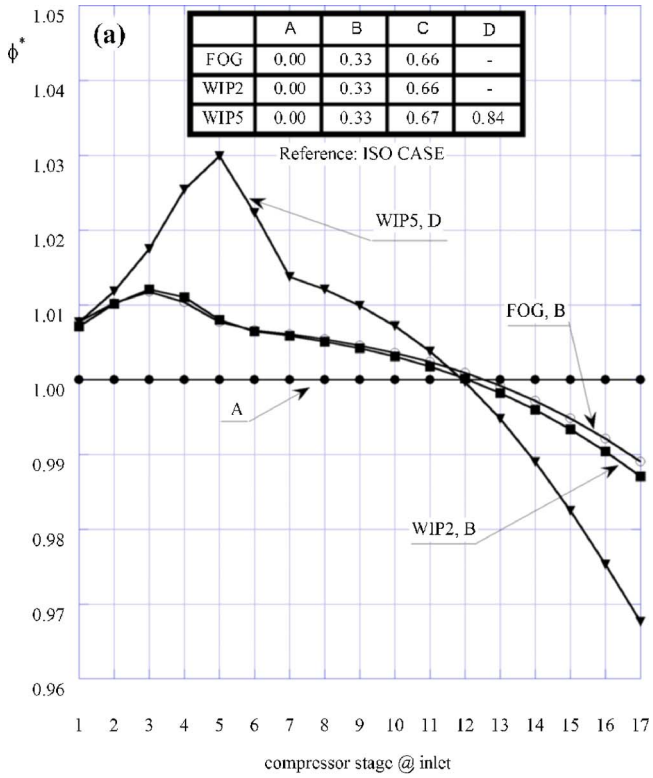

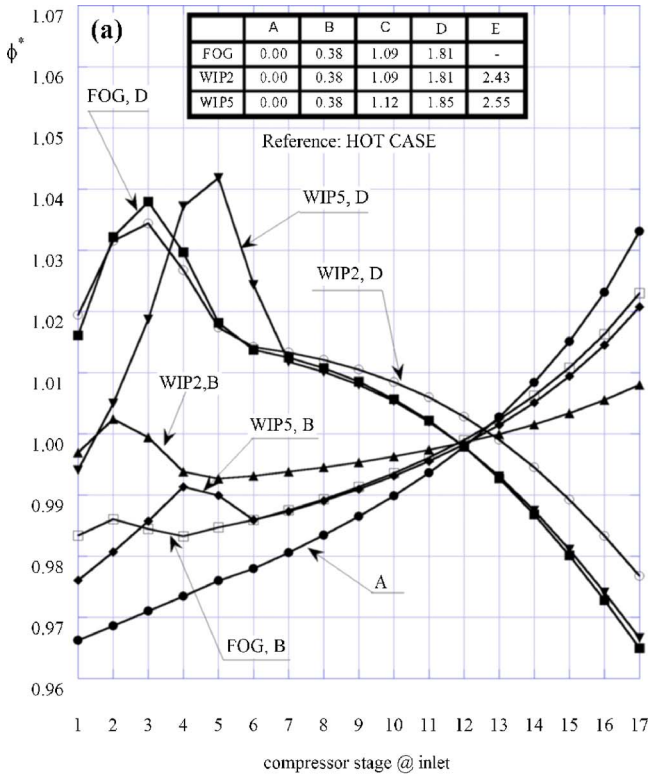

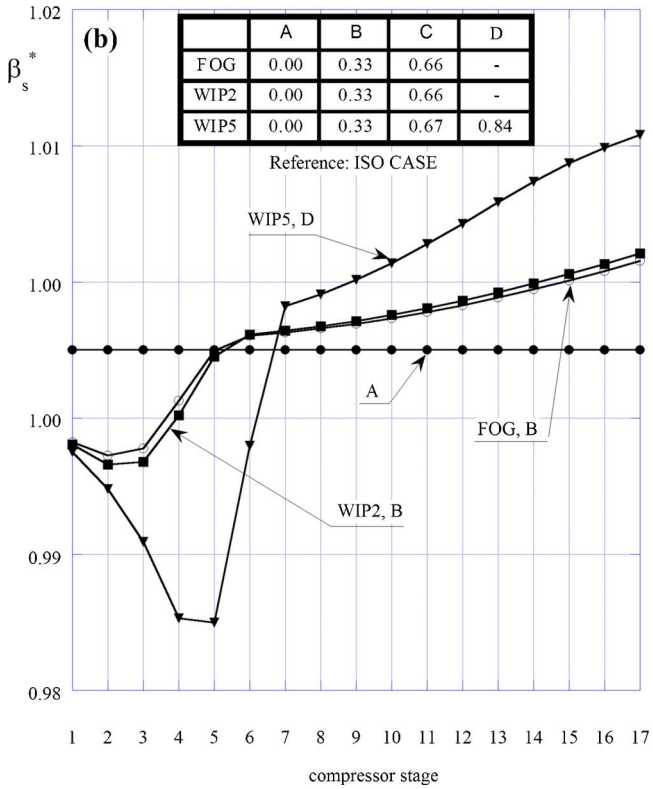

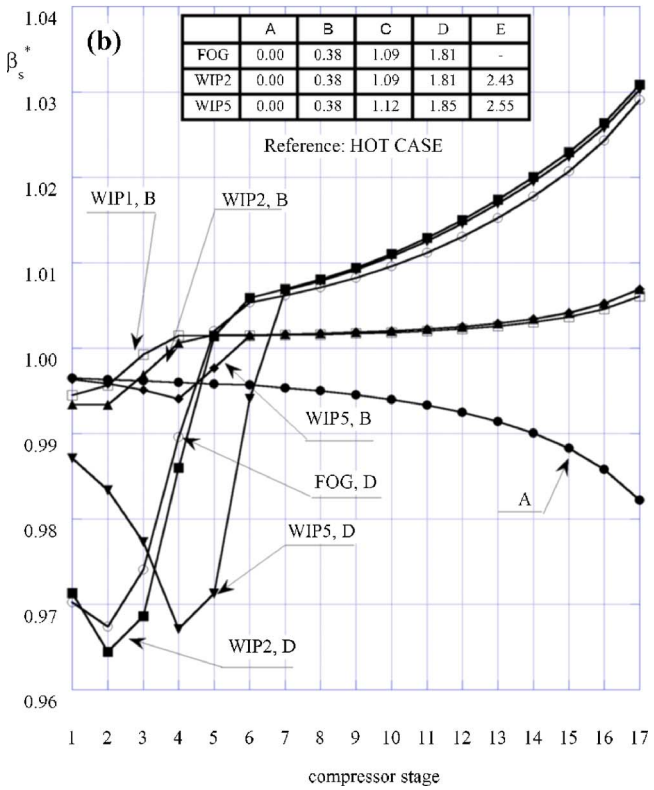

Fig. 14 (*a*) Normalized flow coefficient trend at the inlet of each stage as function of injection point and water amount (ISO case). (*b*) Normalized stage pressure ratio as function of injection point and water amount (ISO case).

Fig. 15 (*a*) Normalized flow coefficient trend at the inlet of each stage as function of injection point and water amount (HOT case). (*b*) Normalized stage pressure ratio as function of injection point and water amount (HOT case).

strength of the shaft and electric generator capacity), and the compressor surge limit.

The validity of the developed program has been demonstrated by comparing the results with the results published in the literature. Furthermore, its robustness has been demonstrated by applying the code in evaluating detailed gas turbine performance under different fogging conditions (inlet evaporative, overspray, and in-

Downloaded 02 Jun 2010 to 171.66.16.107. Redistribution subject to ASME license or copyright; see http://www.asme.org/terms/Terms_Use.cfm

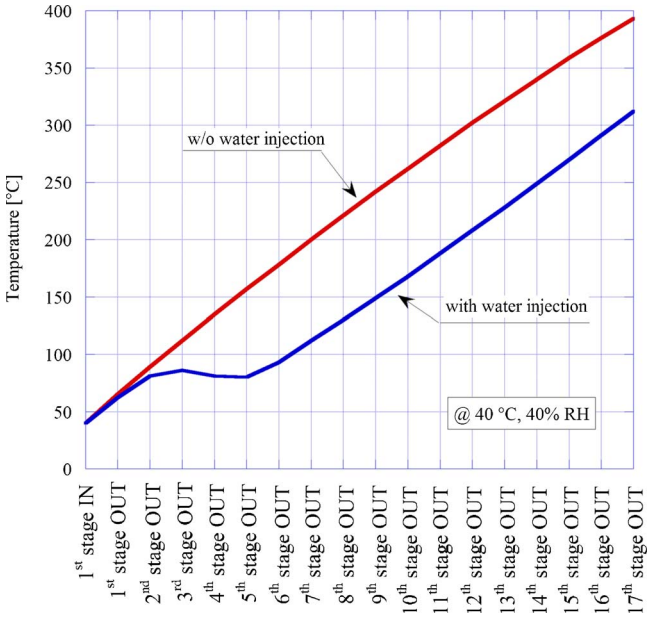

Fig. 16 Temperature profile across the compressor, with reference to 40°C of air temperature and 40% of relative humidity, in case of no water injection and with 6.8 kg/s of water injected upstream of third stage (WIP3)

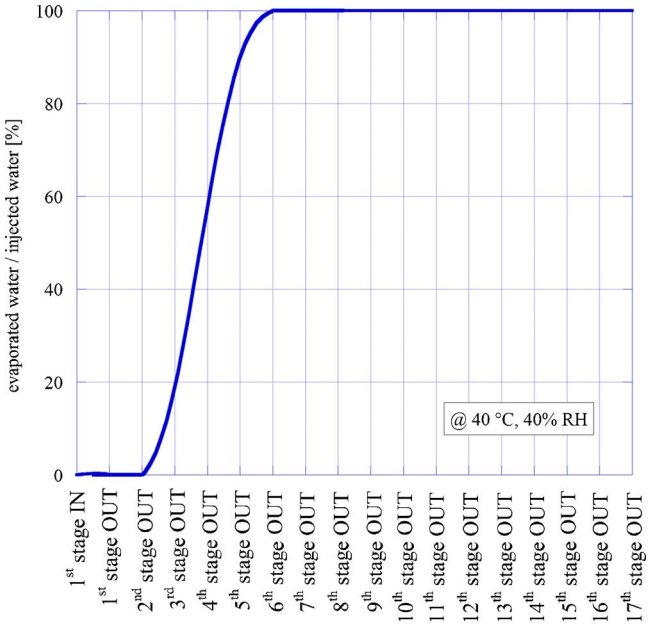

Fig. 18 Evaporated water to injected water ratio across the compressor, with reference to 40°C of air temperature and 40% of relative humidity, in the case of 6.8 kg/s of water injected upstream of third stage (WIP3)

terstage injection). To improve reliability of the code, more rigorous testing of the program against the field data are required.

Acknowledgment

Authors wish to thank Professor Giorgio Negri di Montenegro for his support and suggestions during the realization of the present paper.

Nomenclature

HR = heat rate

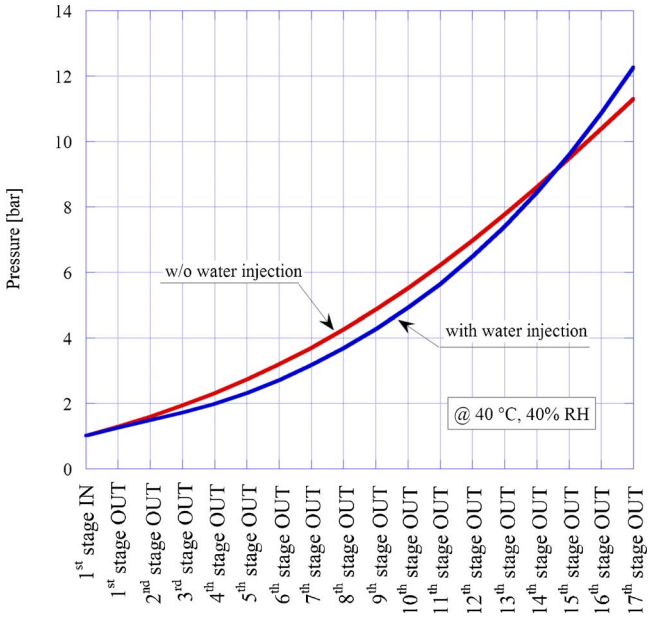

Fig. 17 Pressure profile across the compressor, with reference to 40°C of air temperature and 40% of relative humidity, in case of no water injection and with 6.8 kg/s of water injected upstream of third stage (WIP3)

$\dot{m}$ = mass flow rate
P_{out} = gas turbine power output
p = pressure
PB = power boost
RH = relative humidity
SF = shape factor
T = temperature
TIT = turbine inlet temperature
W = specific work
β = pressure ratio
η = total to total isentropic efficiency
ϕ = flow coefficient
Ψ_P = pressure coefficient

Subscripts and Superscripts

* = normalized to the design value
C = compressor
des = design
is = isentropic
ISO = relative to the ISO values
max = maximum
min = minimum
S = compressor stage
T = turbine

Acronyms

CAS = cooling air stream
IGVs = inlet guide vanes
IN.FO. G.T.E. = interstage fogging gas turbine evaluation
rpm = revolutions per minute
WIP = water injection point

References

[1] Utamura, M., Kuwahara, T., Murata, H., and Horii, N., 1999, "Effects of Intensive Evaporative Cooling on Performance Characteristics of Land-Based Gas Turbine," *Joint Power Generation Conference*, p. 34.
[2] Horlock, J. H., 2001, "Compressor Performance with Water Injection," ASME Paper No. 2001-GT-0343.
[3] Zheng, Q., Sun, Y., Li, S., and Wang, Y., 2002, "Thermodynamic Analysis of Wet Compression Process in the Compressor of Gas Turbine," ASME Paper No. GT-2002–30590.

Downloaded 02 Jun 2010 to 171.66.16.107. Redistribution subject to ASME license or copyright; see http://www.asme.org/terms/Terms_Use.cfm

[4] Chaker, M., Meher-Homji, C. B., and Mee, T. R., III, 2002, "Inlet Fogging of Gas Turbine Engines—Part A: Fog Droplet Thermodynamics, Heat Transfer and Practical Considerations," ASME Paper No. GT-2002-30562.
[5] Chaker, M., Meher-Homji, C. B., and Mee, T. R., III, 2002, "Inlet Fogging of Gas Turbine Engines—Part B: Fog Droplet Sizing Analysis, Nozzle Type, Measurement And Testing," ASME Paper No. GT-2002-30563.
[6] Haertel, C., and Pfeiffer, P., 2003, "Model Analysis of High-Fogging Effects on the Work of Compression," ASME Paper No. GT-2003-38117.
[7] White, A. J., and Meacock, A. J., 2003, "An Evaluation of the Effects of Water Injection on Compressor Performance," ASME Paper No. GT-2003-38237.
[8] Bagnoli, M., Bianchi, M., Melino, F., Peretto, A., Spina, P., R., Bhargava, R., and Ingistov, S., 2004, "A Parametric Study Of Interstage Injection on GE Frame 7 EA Gas Turbine," ASME Paper No. GT2004-53042.
[9] Cataldi, G., Gunter, H., Matz, C., McKay, T., Hoffman, J., Nemet, A., Lecheler, S., and Braun, J., 2004, "Influence of High Fogging Systems on Gas Turbine Engine Operation and Performance," ASME Paper No. GT2004-53788.
[10] Bhargava, R. K., Meher-Homji, C. B., Chaker, M. A., Bianchi, M., Melino, F., Peretto, A., and Ingistov, S., 2005 "Gas Turbine Fogging Technology: A State-of-the-Art Review, Part I: Inlet and Evaporative Fogging-Analytical and Experimental Aspects," ASME Paper No. GT2005-68336.
[11] Bhargava, R. K., Meher-Homji, C. B., Chaker, M. A., Bianchi, M., Melino, F., Peretto, A., and Ingistov, S., 2005 "Gas Turbine Fogging Technology: A State-of-the-Art Review, Part II: Overspray Fogging-Analytical and Experimental Aspects," ASME Paper No. GT2005-68337.
[12] Bhargava, R. K., Meher-Homji, C. B., Chaker, M. A., Bianchi, M., Melino, F., Peretto, A., and Ingistov, S., 2005 "Gas Turbine Fogging Technology: A State-of-the-Art Review, Part III: Practical Considerations And Operational Experience," ASME Paper No. GT2005-69144.
[13] Arsen'ev, L. V., and Berkovich, A. L., 1996, "The Parameters of Gas Turbine Units with Water Injected into the Compressor," Therm. Eng., **43**6, pp. 461–465.
[14] Ingistov, S., 2001, "Interstage Injection System for Heavy Duty Industrial Gas Turbine Model 7EA," ASME Paper No. 2001-GT-0407.
[15] Ingistov, S., 2002, "Interstage Injection Into Axial Compressor, Gas Turbine Model 7EA, Part 2," ASME Paper No. GT-2002-30656.
[16] THERMOFLOW 15, Release 1, Thermoflow Inc. Sudbury, MA.
[17] Spina, P. R., 2002, "Gas Turbine Performance Prediction by Using Generalized Performance Curves of Compressor and Turbine Stages," ASME Paper No. GT-2002-30275.
[18] Bagnoli, M., Bianchi, M., Melino, F., and Spina, P. R., 2005, "Development and Validation of a Computational Code for Wet Compression Simulation of Gas Turbines," ASME Paper No. GT2006-90342.
[19] GATECYCLE, Release 5.22, Enter Software Inc. Menlo Park, CA.
[20] Muir, D. E., Saravanamuttoo, H. I. H., and Marshall, D. J., 1989, "Health Monitoring of Variable Geometry Gas Turbines for the Canadian Navy," ASME J. Eng. Gas Turbines Power, **111**, pp. 244–250.

Downloaded 02 Jun 2010 to 171.66.16.107. Redistribution subject to ASME license or copyright; see http://www.asme.org/terms/Terms_Use.cfm

Y. Levy
e-mail: levyy@aerodyne.technion.ac.il

V. Sherbaum

V. Ovcharenko

Israel Institute of Technology,
Haifa 32000, Israel

Y. Sotsenko
Israel Electric Company,
Haifa 31000, Israel

I. Zlochin
Optiguide Ltd.,
Yokneam 29062, Israel

Study and Field Tests of the Novel Low Pressure Fogger System for Industrial Gas Turbine

Based on three patented innovations (air-assist atomizer, wetness sensor, and closed loop programmable logic controller (PLC)), a new low-pressure power gas turbine augmentation system was developed. Two modifications of air-assist atomizer were tested in the Jet Engine Laboratory of the Technion. The tests were performed to investigate influence of thermodynamic parameters on spray characteristics, as droplet size and velocity distribution of the spray. The system as a whole has passed field test in a gas turbine of a power station. Droplet characteristics, conceptual design aspects, and test results are described. It was found that the droplet sauter mean diameter was 20 μm. *The field tests demonstrated that the power augmentation system operates safely and reliably. Wetness sensors and closed loop PLC proved to be a safe method for power augmentation, which prevents droplet penetration into the compressor inlet.* [DOI: 10.1115/1.2770487]

Keywords: fogging, air-assist atomizer, droplet size

1 Introduction

Site Climatic Conditions. Gas turbines ingest a constant volume of air regardless of the ambient air temperature. When the ambient temperature increases, the power output decreases. There are several proven methods to cool inlet air and to increase its density including evaporation, fogging, and using refrigerated packaged chiller systems. Different types of cooling technology are described and compared by Cortes and Willems [1] and Loria and Degon [2]. Currently, the fogging technology is the most-used one for power augmentation of gas turbines.

A power plant of Israel Electric Corporation (IEC) that incorporates a GE gas turbine (PG541B) was selected to test the new power augmentation system. It is located in the South of Israel near the town Eilat, on the shore of the Red Sea. The unit is used as a spine reserve and the annual power factor is about 20%.

To evaluate the benefits of inlet fogging system for Eilat climatic conditions, the site climatic characteristics were analyzed in terms of cooling potential (the difference between dry and wet bulb temperatures). It is assumed that the operating range of power augmentation system is limited by the minimum ambient temperature of 10 °C and minimum cooling potential of 3 °C. According to the climatic data, the annual cooling potential is around 62,157 cooling (°C) hours (CDH). Taking into account the power factor, the potential annual added power for the PG6541B gas turbine is estimated to be as high as 4400 MW h. The water consumption for this purpose is about 4500 tons.

Atomizers for Fogging Systems. The most commonly used types of atomizers are the jet impinging and air-assist ones. The main drawbacks of the jet impinging atomizers are the requirement for high water pressure drop (hundreds of bars) as is widely applied, for example, by the Mee fogger systems. In addition, Lefebvre [3] pointed out that impinging atomizers have high sensitivity to geometric properties; hence, they require high machining quality. In addition, as such atomizers may suffer from erosion, they require regular inspection to monitor their atomization quality under operating conditions. These problems may be overcome by using air to augment the atomization process at lower water injection pressures, i.e., using air-assist atomizers for the fogging. Their description can be found in Refs. [4–7]. A distinguished feature of the air-assist atomizer is that even though it includes three orifices, it is less sensitive to erosion. Due to the low liquid velocities, such atomizers have relative large liquid orifice diameter and therefore they are less liable to blockages from particles and impurities in the water. Consequently, less effort is needed for inspection as compared to jet impinging atomizers.

A widely used type of air-assist nozzle is manufactured by the Delavan Company [3]. Air is introduced tangentially into the nozzle chamber to create primary atomization. As liquid leaves the orifice, it impinges against deflector ring. This serves a dual purpose: accurate control of spray angle and breakup of the spray into smaller drops.

A comparison between air-assisted and single-fluid pressure atomizers was carried out by Hoffman et al. [8]. Their results indicate substantial differences in the distribution of the droplet diameter and mass flux for both injection systems. For example, the pressure atomizer at high mass delivery rates produced a spray that collapsed into a dispersed cylindrical shape, while at low rates, a hollow cone structure was generated. In addition, the air-assist device discharges 87% of its injected volume within the first of three poppet oscillations while producing a wide hollow cone structure. The air-assist atomizers require a small quantity of high-pressure air while air blast atomizers require low pressure air at high flow rate. Wigg [9] investigated the mechanism of atomization and highlighted the importance of the kinetic energy of atomizing air. To his opinion, the energy difference between inlet air and emerging spray is the dominant factor affecting the mean drop size. He obtained the following dimensionless expression for mass medium diameter of droplets:

$$dv50 = 20\nu_L^{0.5}\dot{m}_L^{0.1}(1+\dot{m}_L/\dot{m}_A)h^{0.1}\sigma^{0.2}\rho_A^{-0.3}U_R^{-1.0} \quad (1)$$

Nukiyama and Tanasawa [10] and Mayer [11] received poor correlation with Eq. (1). To take into account the effect of drop coalescence in the spray, Eq. (1) was modified as follows:

$$dv50 = 20\nu_L^{0.5}\dot{m}_L^{0.1}(1+\dot{m}_L/\dot{m}_A)h^{0.1}\sigma^{0.2}\rho_A^{-0.3}U_R^{-1.0}[1 + 5.0(\dot{m}_L/\dot{m}_A)^{0.6}\dot{m}_L^{0.1}] \quad (2)$$

Contributed by the International Gas Turbine Institute of ASME for publication in the JOURNAL OF ENGINEERING FOR GAS TURBINES AND POWER. Manuscript received February 7, 2006; final manuscript received May 20, 2007; published online January 9, 2008. Review conducted by Alcides Codeceira Neto. Paper presented at the ASME Turbo Expo 2005: Land, Sea and Air (GT2005), June 6–9, 2005, Reno, NV, Paper No. GT2005-68320.

Copyright © 2008 by ASME

Downloaded 02 Jun 2010 to 171.66.16.107. Redistribution subject to ASME license or copyright; see http://www.asme.org/terms/Terms_Use.cfm

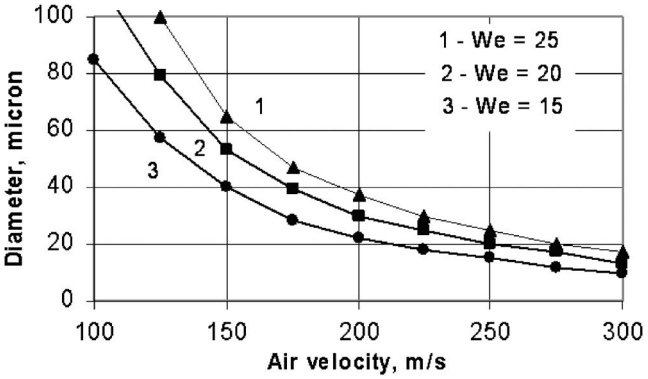

Fig. 1 Effect of air velocity on maximum droplet diameter for different critical Weber numbers

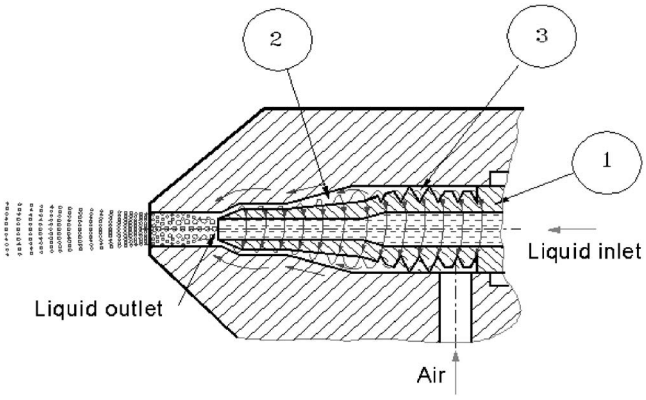

Fig. 2 Schematic drawing of tested atomizer: (1) narrow tube, (2) acceleration chamber, and (3) helical channel

Inamura and Nagai [12], investigating internal-mixing nozzles, observed disturbances of large wavelength in the liquid flowing along the wall, causing the liquid film to break down into drops through formation of unstable ligaments at the end of the wall. They called this process "atomization by ligament formation." If air velocity increases, the wavelength of the disturbances diminishes and drop size decreases. Elkotb et al. [13] received the following equation for Sauter mean diameter (SMD) calculation:

$$\mathrm{SMD} = 51 d_0\, \mathrm{Re}^{-0.39}\, \mathrm{We}^{-0.18} (\dot{m}_L/\dot{m}_A)^{0.29} \tag{3}$$

where $\mathrm{Re} = \rho_L U_R d_0/\mu_L$ and $We = \rho_L d_0 U_R^2/\sigma$.

The equation for internal and external mixing nozzles was received by Simmons [14]:

$$\mathrm{SMD} = C(\rho_L^{0.25}\mu_L^{0.06}\sigma^{0.375}/\rho_A^{0.375})[\dot{m}_L/(m_L U_L + m_A U_A)]^{0.55} \tag{4}$$

where empirical coefficient C depends on the atomizer design. Glathe et al. [15] studied the eccentricity influence on the performance of air-assist atomizer and they received a slight effect of this parameter on atomizer performances. Advanced modeling of droplet breakup in two-phase flows was carried out by Schmehl et al. [16]. Atomization mechanism and droplet spectrum were studied by Sattelmayer and Wittig [17]. The objective of the present work is to analyze the performance of the novel air-assist atomizer and to test it within a novel fogger system. It is known that the high gas velocity is able to break down large droplet Weber number, We_{cr}, which represents the criterion for deformations that leads to disintegration of the liquid drop. The maximum diameter of single liquid droplet can be expressed by the relationship

$$D_{\max} = \sigma \mathrm{We}_{cr}/\rho_a U_a^2 \tag{5}$$

where critical Weber number varies between 13 and 22 [3].

Figure 1 shows that aerodynamic forces enable to receive fine spray, less than in the most existing air-assist atomizers. The reason that actual sprays have droplets more size is that the difference between air and liquid velocities quickly decreases. So, droplets disintegrate mainly due to the turbulent velocity fluctuations of the air flow. We try to avoid this phenomenon in our design by special design use [18].

Air-Assist Atomizer Tests

The present chapter provides atomization performances of the novel air-assist atomizer for gas turbine cooling system.

Atomizer Parameters. Detailed description of the atomizer design is presented by Tavor [18]. Its schematic concept is shown in Fig. 2.

Liquid flows through a successively narrowing tube (1), see Fig. 2, that extends from the liquid inlet to a liquid outlet. Acceleration chamber (2) creates an airflow pattern reaching very high speeds. Air is supplied through a helical channel (3). This results in swirling the air flow and high relative velocities between air and water. The airflow vortex sucks in water from a Venturi column. The impact between the air flow and water produces microdroplets. The low liquid velocity at the outlet of the liquid tube enables using a significantly large orifice (typically 1.38 mm or 2.7 mm in diameter). This large orifice prevents clogging, thus making the fogger system a highly reliable one. Even when water quality is poor or when special crop treatment agents are used, annual inspection and cleaning are all that is needed. Two atomizers with different water consumptions were studied and their principal data are shown in Table 1.

Dependence of water capacity on water pressure for an air pressure of 6 bars for atomizer No. 1 is shown in Fig. 3.

Experimental Setup. The experimental setup (Fig. 4) consists of water pump, compressor with air supply line, manometers, valves, and tested atomizers. The photographs were taken by the HP-618 digital camera with an exposure time of 1/75 s. Droplet diameter was measured by phase-Doppler particle analyzer/laser Doppler velocimeter system (PDPA) of the TSI Inc.

The system recorded the droplet size distribution, droplet velocity distribution, and concentration (number/cm^3). The allowable range of measured droplet diameter was 1–200 μm. Processing a minimum number of 5000 measurements enabled plotting the droplets' SMD and velocity histograms. The measurements of the droplet size distribution were carried out at 100 mm and 300 mm downstream of the atomizer tip. Air pressure was changed from 6 bars to 8 bars.

Experimental Results. Droplet diameter distributions along the spray for various values of the air pressure for atomizer No. 1 are shown in Fig. 5. One can see that the change of the air pressure drop in the range from 6 bars to 8 bars has insignificant ef-

Table 1 Principal data of tested atomizers

	Atomizer No. 1	Atomizer No. 2
Fogger orifice diameter (mm)	2.42	4.8
Water outlet orifice diameter (mm)	1.38	2.7
Water consumption at atmospheric pressure (norm. l/h)	6	20
Air consumption (norm. l/min)	55	230
Standard working air pressure (bars) (gage)	6	6

Downloaded 02 Jun 2010 to 171.66.16.107. Redistribution subject to ASME license or copyright; see http://www.asme.org/terms/Terms_Use.cfm

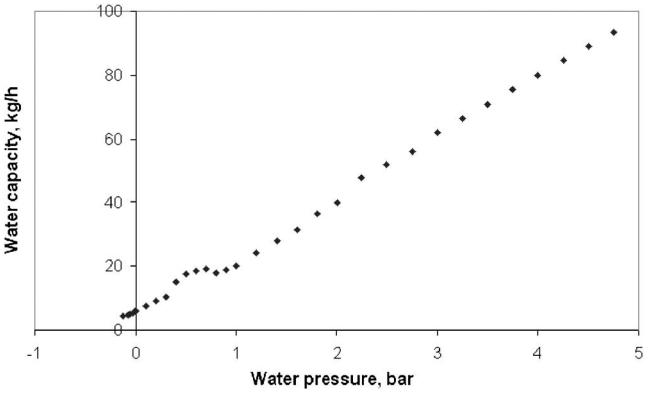

Fig. 3 Dependence of water capacity on input water pressure at an input air pressure of 6 bars (gauge)

fect on the droplet size. Therefore, further measurements were carried out only for a nominal pressure drop equal to 6 bars. The effect of the distance from the exit nozzle is shown in Fig. 6. It is evident that the droplet diameter becomes larger with increase in the distance. This can be explained by the evaporation of the small droplets. The axial velocity distribution of the droplets is depicted in Fig. 7. The velocities drop with distance, as typical in free jet flow.

Similar data for atomizer No. 2 are shown in Figs. 8 and 9. One can see that the droplet diameter enhances with distance from the nozzle.

Comparison of the volume flux of two atomizers for distance from the nozzle equal to 100 mm is depicted in Fig. 10. The distribution is similar for both atomizers. The maximum value is at the half of the spray width.

The comparison of axial velocities for two atomizers (Fig. 11) shows that the spray formed after atomizer No. 2 has higher velocity and less spray angle due to larger air to liquid flow rate ratio.

In spite of almost uniform droplet size distribution along the

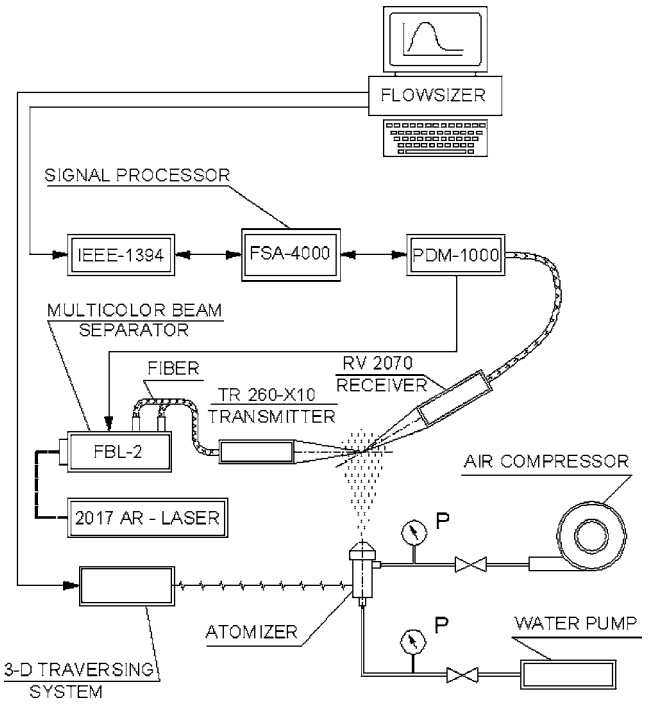

Fig. 4 Experimental setup

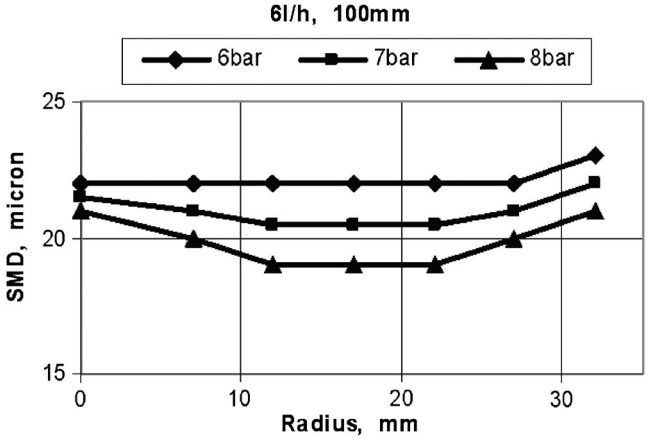

Fig. 5 Droplet size distribution along spray radius for various pressure drop values, atomizer No. 1

radius, the concentration distribution has a strong nonuniformity due to the air channel design that provides air swirl flow at the nozzle exit. It levels off when the distance from the atomizer outlet increases. It is important to note that both atomizers have close droplet diameter values (slightly lower for atomizer No. 2) and similar concentration distribution. It means that the main effect on the droplet size is due to change in the air/liquid ratio and relative air/water velocity that are close for two atomizers, whereas the air and liquid nozzle diameters were significantly different (Table 1). The spray velocities and air/liquid ratio, at identical pressure conditions, were higher for atomizer No. 2. The reason is probably the lower pressure drop at the air helical channel due to the larger flow passages. The higher velocities also result in some decrease of the droplet size. Comparison between the experimental data and the empiric relationships obtained by

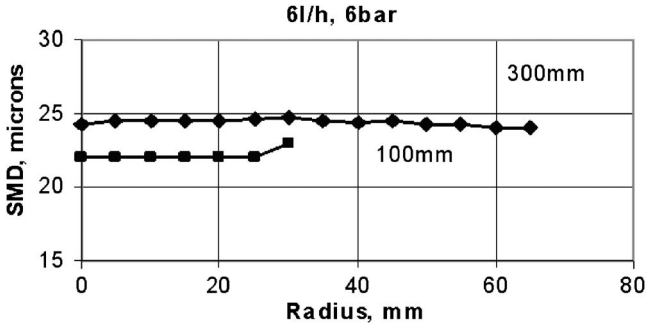

Fig. 6 Droplet size distribution along spray radius, distance from nozzle exit 100 mm and 300 mm, atomizer No. 1

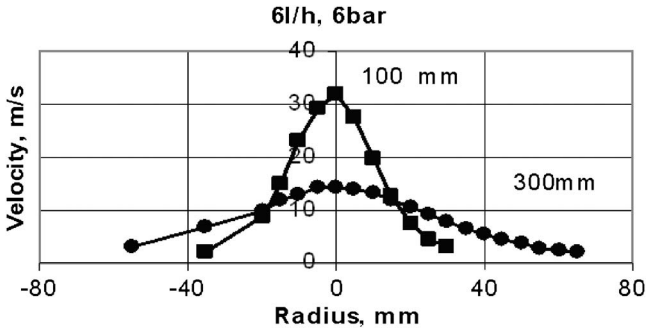

Fig. 7 Droplet axis velocity distribution along spray radius, atomizer No. 1

Downloaded 02 Jun 2010 to 171.66.16.107. Redistribution subject to ASME license or copyright; see http://www.asme.org/terms/Terms_Use.cfm

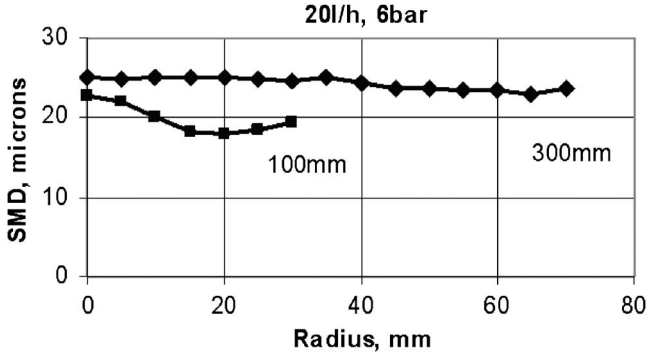

Fig. 8 Droplet size distribution along spray radius, distance from nozzle exit 100 mm and 300 mm, atomizer No. 2

other authors (Eqs. (1)–(3)) is shown in Table 2.

One can see from this table that empirical relationships derived by Elkotb et al. [13] and Simmons [14] correlate well with our results; however, Wigg's equation give higher values for droplet size (it should be noted that this equation was destined for internal-mixing atomizers). As may be inferred from Eqs. (2) and (3), the droplet size depends in inverse proportion on relative air-liquid velocity in power 0.5–1. Equation (1) shows stronger dependence on this value (power of 2). As to the effect of the liquid nozzle diameter on the droplet size, we have not observed its influence. Such result corresponds better to Eq. (4), where this parameter is absent.

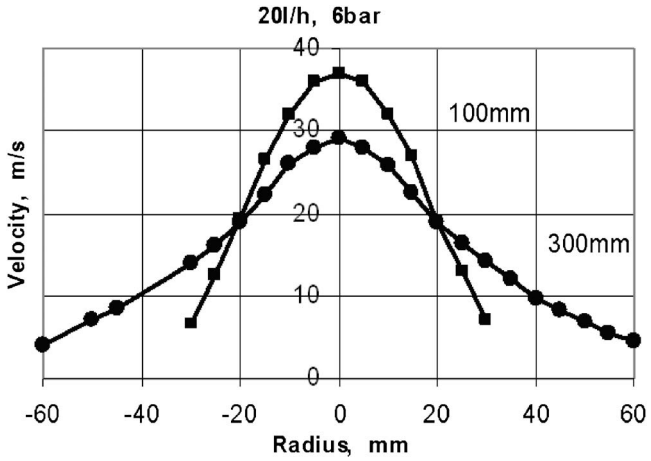

Fig. 9 Droplet axis velocity distribution along spray radius, distance from nozzle exit 100 mm and 300 mm, atomizer No. 2

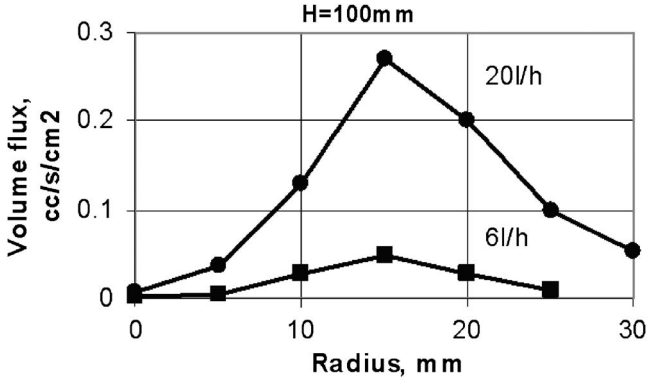

Fig. 10 Radial volume flux distribution, distance from nozzle exit 100 mm

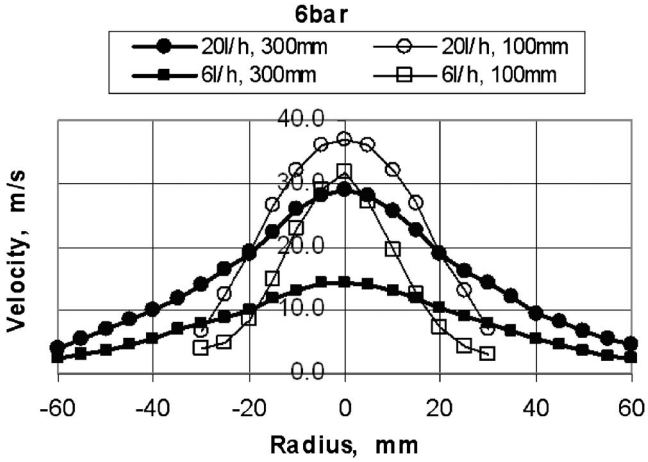

Fig. 11 Comparison of velocity values and velocity distribution along spray radius for atomizer Nos. 1 and 2

Atomization spray cone is shown in Fig. 12. The other important result is that for a given system, there is a lower limit of the droplet diameter that depends on the difference between air and liquid velocities (Fig. 1) and air/fuel ratio. Comparison of SMD values for 100 mm and 300 mm distances (Figs. 6 and 8) shows that the droplet diameter enhances. Two possible mechanisms are small droplet evaporation and droplet coalescence [19].

A small cone spray angle (about 24 deg for all pressure drops) is important to prevent interaction between adjacent sprays (when several atomizers are mounted at the same cross section in a form of a matrix). A small cone angle is also important to minimize droplet coalescence. The correlation between liquid velocity and droplet size at the maximum liquid concentration point (for a given distance from the atomizer exit) is shown in Fig. 13. The measurements demonstrate that anywhere in the spray, droplet velocity is almost independent of the droplet size; hence, coalescence must be insignificant. This is also confirmed by the results presented above (Figs. 6 and 8).The droplet SMDs for both tested atomizers were about 20 μm. A comparison with available literature data shows better performance of the investigated atomizers, as their droplet size is smaller than reported by other authors. This can be explained by the strong swirl and shear force of the high-speed air at the atomizer exit. Consequently, the liquid jet disintegrates by the corresponding aerodynamic forces, thus making such process more effective.

Field Tests

The considered fogging cooling system is a pilot system. In order to minimize risk of possible erosion of compressor blades, compressor case distortion, etc., it was decided that during the

Table 2 Comparison between experimental data and empiric relationships obtained by other authors (Eqs. (1)–(3))

Equation No.	Atomizer No. 1 droplet size (μm)	Atomizer No. 2 droplet size (μm)	Remarks
(1)	59	82	
(2)	29	37	
(3)	25	33	Same coefficient C
Test data	22	20	SMD
	22	22	vd50

Downloaded 02 Jun 2010 to 171.66.16.107. Redistribution subject to ASME license or copyright; see http://www.asme.org/terms/Terms_Use.cfm

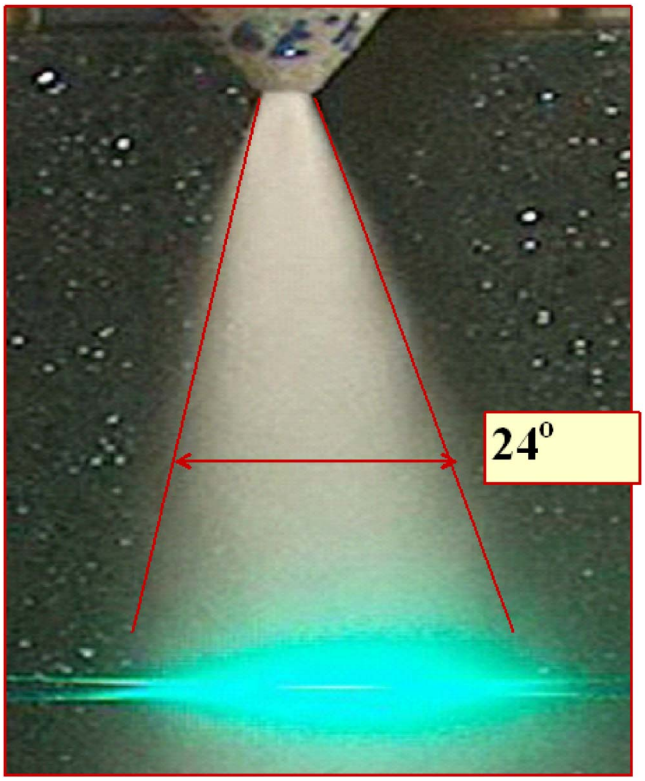

Fig. 12 Spray geometry at atomizer No. 1 exit. Input air pressure is equal to 6 bars (gauge).

first phase of the tests, the fogger system should be installed upstream of the air filters. It was realized that such arrangement decreases global efficiency and capability of the system to augment the gas turbine (GT) power. However, the task of the present work was only to verify the reliability of the atomizers, the wetness sensor developed by Zlochin [20], and the closed loop programmable logic controller (PLC) developed by Zlochin and Moria [21].

Description of Low-Pressure Fog-Cooling System. The system consists of an array of fog nozzle manifolds. Water flow rate was controlled by a PLC according to ambient conditions and the wetness sensor readings. The required media are water at ambient

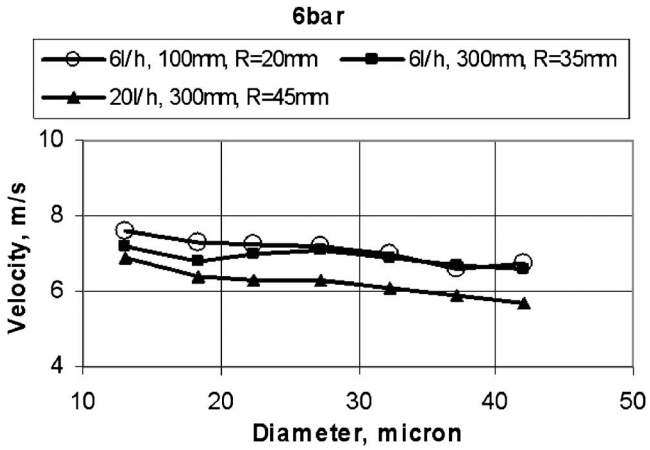

Fig. 13 Dependence of droplet velocity (along spray axis) on SMD at the maximal concentration point for atomizer Nos. 1 and 2

Table 3 Auxiliary energy demand for high- and low-pressure (with and without external air compressor) fogging systems

GT	Frame 6E	Frame 9E
Increased GT power output (kW)	35997	115823
Fogging water flow (kg/s)	0.82	2.44
Injected air flow (low-pressure augmentation system) (kg/s)	0.53	1.576
Power of water pump (high-pressure augmentation system) (kW)	19.705	58.636
Power loss (%) of GT output (high-pressure augmentation system)	0.05	0.05
Power of external air compressor (low-pressure augmentation system) (kW)	134.1	398.8
Power loss, % of GT output (low pressure augmentation system, external air compressor)	0.37	0.34
Power reduction due to compressor discharge air bleeding (low-pressure augmentation system) (kW)	292	877
Power loss (%) of GT output (low-pressure augmentation system, discharge air bleeding)	0.81	0.76

pressure and air at a pressure of 6–7 bars. The compressed air required for the system operation can be supplied from the compressor of the GT itself. Water consumption at atmospheric pressure is 6 l/h. Low-pressure water system (water is sucked by the air jet) does not require pump use. The large size of the orifice prevents clogging, ensures stable quality of atomizing process during lifetime, minimizes the impact of manufacturing deviations, and reduces operating and maintenance costs.

The patented wetness sensor is an on-line monitoring one, which can detect free water in the air upstream of the compressor inlet to prevent any possible damage from power augmentation system. This capacitive sensor comprises an internal electrode plate and isolated plate. A layer of free water captured from the air stream forms the second electrode on the outer surface of the isolated plate, which is electronically connected to the electronic circuit. The thickness and the area of the water film vary in accordance to the free water amount in the air, and so does the capacitance. The capacitance is measured and is converted by the controller to the wetness index (WIDX). Wetting takes place when air in the inlet duct is fully saturated or if there are relatively large water droplets, caused by condensation and fog coalescence on the inlet structures. The PLC controls the fog. It reads the wetness sensor's levels and adjusts the water flow by using proportional valves and thus turning on and off the fog generators' stages, according to the required set point.

Thermodynamic Aspects. The required air can be received from external compressor (instrument or service air) or from the GT compressor air bleeding system. No pressure source is required for water. The comparison of auxiliary energy demand of high- and low-pressure augmentation systems for GT frames 6E and 9E is presented in Table 3. The following conditions are considered: ambient temperature of 40°C, relative humidity of 40%, and efficiency of evaporation of 85%.

One can see that the low-pressure fogger system consumes more energy but it has high reliability, it is convenient in service, and does not require any significant auxiliary equipment. Hence, the increase in energy consumption can be considered as an acceptable trade-off for these benefits. Field tests during longer pe-

Downloaded 02 Jun 2010 to 171.66.16.107. Redistribution subject to ASME license or copyright; see http://www.asme.org/terms/Terms_Use.cfm

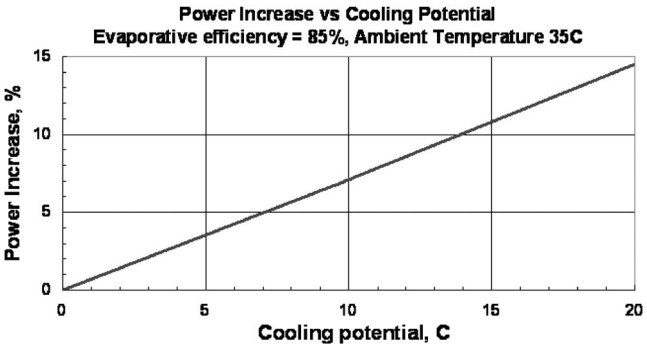

Fig. 14 Recovery of GT power out on hot day as function of cooling potential

riod will enable comparing its economic validity with other fogging systems. For the typical value of cooling potential (14–15°C), bleeding does not exceed 0.4% of compressor inlet air flow. The net power and efficiency increase on a hot day is shown in Figs. 14 and 15.

Field Test Results. In August 2001, the fogger system was installed and tested at Unit 2 (PG6541B) of Eilat Power Station. The system was installed upstream of the filters at four levels with three manifolds at each level (12 manifolds) and 25 nozzles at each manifold (a total of 300 nozzles), Fig. 16. The compressed air required for the operation of the system was supplied from self-cleaning air filter system of the GT. During the tests that lasted 1.5 h on August 27 and 2 h on August 28, no variations in the filter pressure drop or in the color of cylindrical and conical filter cartridges were observed. Results of visual inspection were as follows:

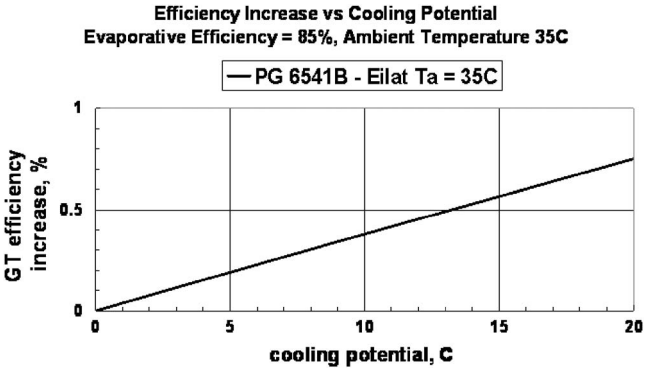

Fig. 15 Recovery of GT efficiency on hot day as function of cooling potential

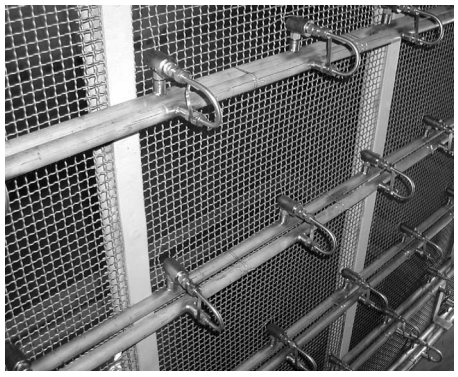

Fig. 16 Installed nozzles

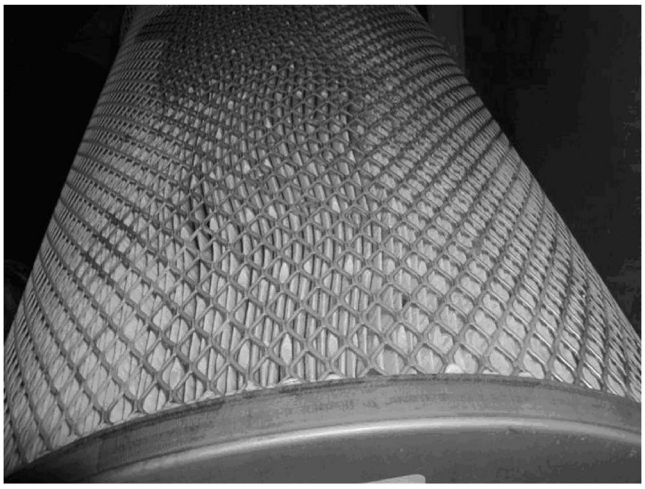

Fig. 17 Distorted filter cartridge ribs

- Upper part of cylindrical filter cartridge was full of water.
- Water passed through a cartridge.
- Shape of filter cartridge ribs changed (from straight to wavy, Fig. 17).
- Water traces in compressor inlet plenum were not detected.

Based on the assumption that the change in the cartridge rib shape has adverse effect on filter performance, at the end of the test, the air filter cartridges were dismantled at the end of the test and sent to manufacturers (Donaldson and Airguard) for inspection. Results of the inspection for both cylindrical and conical filters did not show any signs of damage or aging. The tested filters remained as good as new and were not damaged by the fog.

After the first phase of field test, the power augmentation system was modified and arranged as two-stage system. The first comprised 12 lines (20 nozzles in each line) in front of filters (240 nozzles) and the second stage, 8 lines (12 nozzles in each line) behind the silencer in the inlet plenum. Two main reasons for such configuration were to decrease the impact of augmentation system upon the air filters and to increase the cooling effect without compressor blade damage. A polycarbonate manhole was installed for visual inspection during the test (on-line control).

The goals of the second phase of field test were optimization of water distribution between the first and the second stages of augmentation system in terms of maximum power increase and safe operation of main GT equipment (without water droplets at the inlet of compressor) and evaluation and optimization of the PLC closed loop operation mode and location of wetness sensors.

As mentioned above, on-line visual control was carried out through the manhole (specially made from polycarbonate). Additional visual inspection of inlet plenum and compressor blades took place before and immediately after the test. No damage of GT equipment was detected. The increase of the specific output shows the efficiency of the augmentation process, i.e., increase in addition to power output per 1 l of injected water under the same climatic conditions. The comparison between one- and two-stage power augmentations demonstrated that the two-stage system is 20% more effective than the single-stage one in terms of net power increase.

The location of the second stage (before the trash screen, where the inlet air velocity is high and the distance from compressor intake is short) limits the cooling capability of the augmentation system. The wetness sensor reduces water consumption of the second stage to prevent droplet entrance into compressor, in accordance with climatic conditions. Figure 18 shows the measured and approximated performance data of the two-stage system in Eilat.

Downloaded 02 Jun 2010 to 171.66.16.107. Redistribution subject to ASME license or copyright; see http://www.asme.org/terms/Terms_Use.cfm

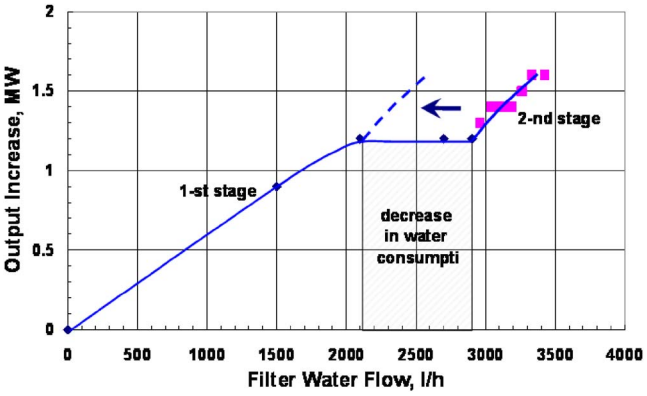

Fig. 18 Performance of two-stage power augmentation system

The performance of the first stage (lower left curve) has a long flat section where increase in water flow does not have an impact on power output. The second stage was turned on when the water flow rate at the first stage reached 2900 l/h. The reason is that the first stage is arranged before the inlet air filter. The average distance between the atomizers and the filter covers is about 2 m and it is not sufficient for complete evaporation at high water flow rate. After reaching a certain value, further increase in water consumption does not result in cooling the inlet air but rather intensifies fog condensation at the air filter covers and nearby structures (it looks like rain). This phenomenon indicates that the evaporation capability of the first stage reaches the maximum in spite of the fact that the relative humidity is below 100%. Consequently, it is believed that the earlier incorporation of the second stage (the upper and right part of the performance curve) will reduce water consumption for the same power increase and thus improve the efficiency of the system. Effectively, it will shift the performance curve to the left (in the direction of the arrow, Fig. 18). Such a study is a subject of a future project at Eilat Power Station.

Conclusion

During the field tests and two years of operation, the power augmentation system operated safely and reliably. The two-stage power augmentation system is 20% more effective than one-stage system with foggers' location upstream of inlet air filters. Wetness sensors and closed loop PLC proved to be a safe method for power augmentation, which prevents droplet penetration into the compressor inlet. The droplet SMD for both tested atomizers was about 20 μm. The droplet size increases with distance due to droplet evaporation or/and droplet coalescence. The spray cone angle was 24 deg. Such an angle can be useful to prevent droplet coalescence where atomizers are mounted close to one another in the same cross section.

Nomenclature

GT = gas turbine
PLC = programmable logic controller
CDH = cooling degree (°C) hours
Ta = ambient temperature
RH = relative humidity
C = empirical coefficient, dimensionless
d_0 = nozzle diameter, m
h = height of air annulus, m
SMD = Sauter mean diameter, m
$\dot{m}$ = mass flow rate, kg/s
U = velocity, m/s
μ = dynamic viscosity, kg/(m s)
ν = kinematic viscosity, m^2/s
ρ = density, kg/m^3
σ = surface tension, N/m

Subscripts

A = air
cr = critical
L = liquid
R = air relative to liquid

References

[1] Cortes, C., and Willems, D., 2003, "Gas Turbine Air Cooling Techniques: An Overview of Current Technologies," *SIEMENS—WESTINGHOUSE, Power-GEN 2003*, Las Vegas, NV, December 9–11, pp. 7–19.
[2] Loria, D., and Degon, A., 2003, "Increase the Value of Your Power Plant," *Power Augmentation Technologies for Existing Simple-Cycle and Combined-Cycle Power Plants*, pp. 1–9.
[3] Lefebvre, A. H., 1989, *Atomization and Sprays*, Hemisphere, New York.
[4] Romp, H. A., 1937, *Oil Burning*, Stechert and Company, New York.
[5] Mullinger, P. J., and Chieger, N. A., 1974, "The Design and Performance of Internal Mixing Multi-Jet Twin-Fluid Atomizers," J. Inst. Fuel, **47**, pp. 251–261.
[6] Sargeant, M., 1982, "Blast Atomizer Developments in the Central Electricity Generating Board," *Proceeding of the Second International Conference on Liquid Atomization and Spray Systems*, Madison, WI, pp. 131–135.
[7] Hurly, J. F., and Doyle, B. W., 1985, "Design of Two-Phase Atomizers for Use in Combustion Furnaces," *Proceeding of the Third International Conference on Liquid Atomization and Spray Systems*, London, pp. 1–13.
[8] Hoffman, J. A., Eberhard, E., and Martin, J. K., 1997, "Comparison Between Air-Assisted and Single-Fluid Pressure Atomizers for Direct-Injection SI Engines via Spatial and Temporal Mass Flux Measurements," University of Wisconsin, Report No. A477423.
[9] Wigg, L. D., 1964, "Drop Size Prediction for Twin Fluid Atomizers," J. Inst. Fuel, **27**, pp. 500–505.
[10] Nukiyama, S., and Tanasawa, Y., 1939, "Experiments on the Atomization of Liquids in an Airstream," Trans. Jpn. Soc. Mech. Eng., **5**, pp. 68–75.
[11] Mayer, E., 1961, "Theory of Liquid Atomization in High Velocity Gas Stream," America Rocket Soc. J., **31**, pp. 1783–1785.
[12] Inamura, T., and Nagai, N., 1985, "The Relative Performance of Externally and Internally Mixed Twin-Fluid Atomizers," *Proceeding of the Third International Conference on Liquid Atomization and Spray Systems*, London, pp. IIC/2/1–IIC/2/11.
[13] Elkotb, M. M., Mahdy, M. A., and Montaser, M. E., 1982, "Investigation of External Mixing Airblast Atomizers," *Proceeding of the Second International Conference on Liquid Atomization and Spray Systems*, Madison, WI, pp. 105–115.
[14] Simmons, H. C., 1979, "The Prediction of Sauter Mean Diameter for Gas Turbine Fuel Nozzles of Different Types," ASME Paper No. 79-WA/GT-5.
[15] Glathe, A., Wozmiak, G., and Richter, T., 2001, "The Influence of the Eccentricity on the Performance of a Coaxial Prefilming Air-Assist Atomizer," Atomization Sprays, **11**, pp. 21–33.
[16] Schmehl, R., Klose, G., Maier, G., and Wittig, S., 1998, "Efficient Numerical Calculation of Evaporating Sprays in Combustion Chamber Flows," *92nd Symposium on Gas Turbine Combustion, Emissions and Alternative Fuels*, Lisbon, Portugal, pp. 51-1–51-11.
[17] Sattelmayer, Th., and Wittig, S., 1986, "Internal Flow Effects in Prefilming Airblast Atomizers: Mechanisms of Atomization and Droplet Spectra," ASME J. Eng. Gas Turbines Power, **108**, pp. 465–472.
[18] Tavor, E., "Atomizer," U.S. Patent No. 5,513,798.
[19] Valencia-Bejarano, M., and Langrish, T. A. G., 2004, "Experimental Investigation of Droplet Coalescence in a Full-Cone Spray From a Two-Fluid Nozzle Using Laser Diffraction Measurements," Atomization Sprays, **14**, pp. 355–374.
[20] Zlochin, I., "Wetness Sensor," U.S. Patent No. 6,575,621.
[21] Zlochin, I., and Moria, G., 2004, "A Gas Turbine Fogging System and Methods for Its Control and Trouble Detection," U.S. Patent Application No. WO 2004/025102 A1.

Downloaded 02 Jun 2010 to 171.66.16.107. Redistribution subject to ASME license or copyright; see http://www.asme.org/terms/Terms_Use.cfm

A Novel Free-Cooling Scheme for Combustion Turbine Inlet Air Cooling

Montaser M. Zamzam
Senior Mechanical Engineer
Abu Dhabi Company for Onshore
Oil Operations (ADCO),
P.O. Box 270,
Abu Dhabi, UAE
e-mail: mzamzam@adco.ae

Abdalla M. Al-Amiri
Associate Professor
Mechanical Engineering Department,
United Arab Emirates University,
P.O. Box 17555,
Al-Ain, UAE
e-mail: alamiri@uaeu.ac.ae

Free cooling is a well-known concept in the HVAC industry in which the cold water produced by a cooling tower is used directly to satisfy the requirement of the cooling load without assistance by the chiller; this concept, however, is not reported in the turbine inlet air-cooling applications. Free cooling works well as long as the ambient wet bulb temperature (WBT) is sufficiently low to produce cold water at the required temperature, but once WBT reaches its threshold value (hence, free-cooling mode is ceased) and the chiller kicks off working under its normal mode of operation, i.e., free cooling is either enabled or disabled. The proposed system in this paper provides, in addition to the above modes of operation, a novel mode that utilizes the cooling tower as a primary source of cooling simultaneously with the chiller that serves as a secondary source at elevated WBT. This new feature significantly reduces the yearly operating hours of the chiller and possibly its size, depending on the desired inlet air temperature, actual weather conditions, and design WBT. Chiller size can vary between 0% and 100% as compared to a similar classical chiller system with significant reduction in the operating hours. The proposed system consists basically of chiller, cooling tower, cooling coils, interconnecting piping, and controls. The arrangement of the system equipment changes with the operation modes in two configurations: dual water circulation loops and single water circulation loop. In the dual-loop configuration, the system has two separate loops such that the evaporator and the cooling coils are tied in one loop, while the cooling tower and condenser in the other loop; whereas in the single-loop configuration, all equipment is connected in series in one water circulation loop. This paper presents the major equipment and characteristics of the novel chiller scheme. In addition, the study outlines the potential reduction in the chiller load, size, and operating hours under a generalized weather envelope. The paper portrays the feasibility of using the proposed cooling scheme for turbine inlet air cooling. [DOI: 10.1115/1.2749287]

Keywords: free cooling, cooling tower, combustion turbine inlet air cooling

1 Introduction

The performance of a combustion turbine is inherently tied to ambient air conditions. Gas turbine output suffers significantly at increased temperature levels due to the reduced available combustion air mass flow rate. On the contrary, cooled denser air gives the system a higher mass flow rate and pressure ratio, resulting in an increase in combustion turbine output. Usually this is accompanied by an overall increase in the system efficiency due to the suppression in its heat rate. Recently, combustion turbine inlet air cooling systems have received considerable attention as a viable design option in increasing power output. Such cooling systems bring the combustion turbine units to operate close to the manufacturer's design condition, and in some cases, independently of climatic conditions [1]. Typically, the turbine power output (kW) increases around 0.387% for every 1°F drop in the inlet air dry bulb temperature (DBT), meanwhile, the heat rate (Btu/kW) reduces approximately 0.166% for DBT above 60°F (15.6°C) [2].

The available inlet air-cooling techniques are classified under either evaporative or refrigerative type systems. The aforementioned include water-through-media and fogging [3] options, while the latter include continuous cooling, direct expansion, and liquid chillers [4]. In comparison with evaporative techniques, refrigeration systems are more complex and require much higher capital investment and operation and maintenance cost and consume high parasitic power. On the other side, their applications are not constrained by the wet bulb temperature value and, thus, higher power augmentation can be achieved.

Among the above, refrigerative systems that utilize water chiller provide greater flexibility in terms of expandability, standby, location, chilled water distribution, and much more. Air-cooled chillers have a relatively low coefficient of performance (COP), which is reflected in higher parasitic power and energy consumption that may equate 30% of the power increased in the turbine as a result of inlet air cooling. Water-cooled chillers, though, have almost double the value of COP as that of air cooled chillers, yet the parasitic power and energy consumption constitute major negative elements in the techno-economic study of the refrigerative cooling systems.

In general, the classical chilled water system for combustion turbine inlet air cooling (CTIAC) consists of chiller, inlet air cooling coil, cooling tower, pumps, interconnection piping, and control systems. The captured heat from the inlet air cooling coil is rejected along with the energy added to the cycle from the compressor through the condenser by means of the cooling tower. Such an additional energy arriving from the compressor requires the tower to dissipate more load than that actually imposed by the cooling process. The classical water-cooled chiller system is characterized with two separate water loops. One loop comes in direct contact with the atmospheric air via the cooling tower to reject heat from the condenser, while the second loop links the cooling coil and the chiller evaporator.

Contributed by the International Gas Turbine Institute of ASME for publication in the JOURNAL OF ENGINEERING FOR GAS TURBINES AND POWER. Manuscript received May 5, 2007; final manuscript received May 5, 2007; published online January 9, 2008. Review conducted by Dilip R. Ballal. Paper presented at the ASME Turbo Expo 2007: Land, Sea and Air (GT2007), Montreal, Quebec, Canada, May 14–17, 2007, Paper No. GT2007-27621.

Copyright © 2008 by ASME

Downloaded 02 Jun 2010 to 171.66.16.107. Redistribution subject to ASME license or copyright; see http://www.asme.org/terms/Terms_Use.cfm

Free cooling, as known in the HVAC industry, is employed to reduce the energy consumption of the chiller. Free cooling comes in different arrangements based on the operational characteristics desired, but all share the same concept that the load will be met by the cooling tower without chiller operations. Free-cooling opportunities diminish at elevated ambient wet bulb temperature as the tower becomes incapacitated, forcing the cooling system to activate the chiller. Thus, the conventional free-cooling concept is employed by either utilizing the tower cold water only when possible, or otherwise the chiller cold water, but not both at once. Free-cooling theory and classifications are beyond the scope of this work and the reader is advised to refer, for instance, to ASHRAE [5] and Marley [6,7] for further information.

From a water circulation standpoint, a free-cooling scheme can be either direct or indirect. In the direct scheme, a cooling tower picks the entire cooling load through a bypass arrangement when the tower cold water temperature dips below the required temperature for the inlet air coil. In such a case, a single water loop is maintained between the load and cooling tower. Despite its simplicity, the direct free cooling is not typically recommended due to the possibility of contamination into the clean chilled water loop [6]. On the contrary, the indirect free-cooling scheme employs a heat exchanger to alter the risk associated with possible contamination. This is achieved by physically segregating the water loops of the cooling tower and water chiller. A flat plate heat exchanger is typically installed owing to the moderate range of operating temperature and pressure it requires and its possible low temperature approach that may go as low as 2°F (1.1°C) [8].

2 Proposed Cooling Scheme

LOTOCH [9] is an acronym used for the proposed cooling scheme that is a combination of load-tower-chiller. LOTOCH can also be seen as a combination of indirect evaporative (cooling tower) and mechanical (chiller) cooling systems. In principle, the LOTOCH system has the capability to work under two distinct operational configurations. The first is typical of the classical chilled water system, where the system has two separate water circulation loops such that the evaporator and the cooling coils are tied in one loop, while the cooling tower and condenser are in the other loop. This system will be referred to as the "dual-loop arrangement" as illustrated in Fig. 1. Furthermore, the second operational configuration of the proposed system becomes applicable when all system components are connected in a series arrangement, which permits the same water to circulate throughout all equipment as one loop. This system will be referred to as the "single-loop arrangement," as demonstrated in Fig. 2. In the series arrangement, the tower as a prime source of cooling may be able, under certain load and ambient conditions, to solely achieve the load temperature similar to the conventional free cooling schemes or otherwise through the assistance offered by the chiller. The chiller will only be brought up to assist the tower when the latter is not able to meet the load. Hence, cooling will be utilized from the tower even when the chiller is running, which is considered a unique feature of the LOTOCH system. This particular arrangement can be considered as an energy saving mode of operation.

As earlier stated, the classical chiller system operates in a dual-loop arrangement in which the chiller is solely responsible to achieve the load temperature whenever the tower is ineffective in achieving that temperature, owing to the increase in ambient WBT. It should be emphasized again that the system components of a classical water chiller are retained in the proposed system; however, the size of equipment, their capacities, arrangement, and operation philosophy are different, also, the interconnecting piping is configured to alternate between both arrangements. For the sake of further explanation, it should always be noted that the single-loop arrangement (one loop) is the basic operation mode of the LOTOCH system, while the dual-loop arrangement (two loops) is a special mode under certain operating conditions. It should be reiterated that in the single-loop arrangement, the chiller is always the prime source of cooling, and assistance from the chiller will be provided only as and when required.

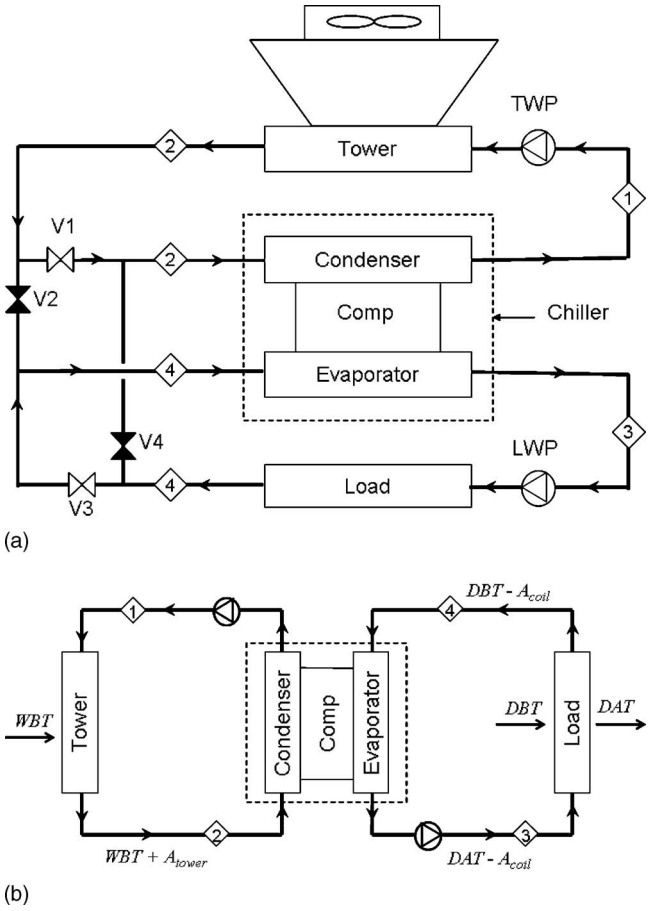

Fig. 1 Dual-loop arrangement of the proposed LOTOCH system (conventional cooling operation): (*a*) interconnecting piping arrangement; (*b*) flow schematic diagram

3 Operating Boundaries and Limitations

The system operates within an external envelope of conditions that represent the extremes of the surrounding weather conditions; these are maximum WBT/ DBT/RH and minimum DBT/RH. Another set of internal boundary limits can be identified based on the equipment characteristics and the desired inlet air temperature (DAT) setting, as shown schematically in Fig. 3 on the psychrometric chart, as follows.

3.1 No Cooling Line (DAT Line). The recorded DBT values below the desired DAT setting will not incur any cooling demand. Any ambient condition with DBT value matching the DAT setting will be graphically represented by a vertical line at DBT=DAT and will be referred to as the G-M-K line.

3.2 Shut-Off Line (H-L Line). This line distinguishes two zones of ambient conditions: one in which the cooling system is considered working idle, and another in which the cooling system is fully shut down. This is graphically represented by a vertical line drawn parallel to the "no cooling" line for DBT values lower than DAT setting with a preset value (e.g., 2–3°F, 1.1–1.7°C), depending on the fluctuation frequency of the ambient DBT value. The system may also be requested to change from idle to off position if the idle situation continues for more than a prespecified time interval (e.g., 1 h).

Downloaded 02 Jun 2010 to 171.66.16.107. Redistribution subject to ASME license or copyright; see http://www.asme.org/terms/Terms_Use.cfm

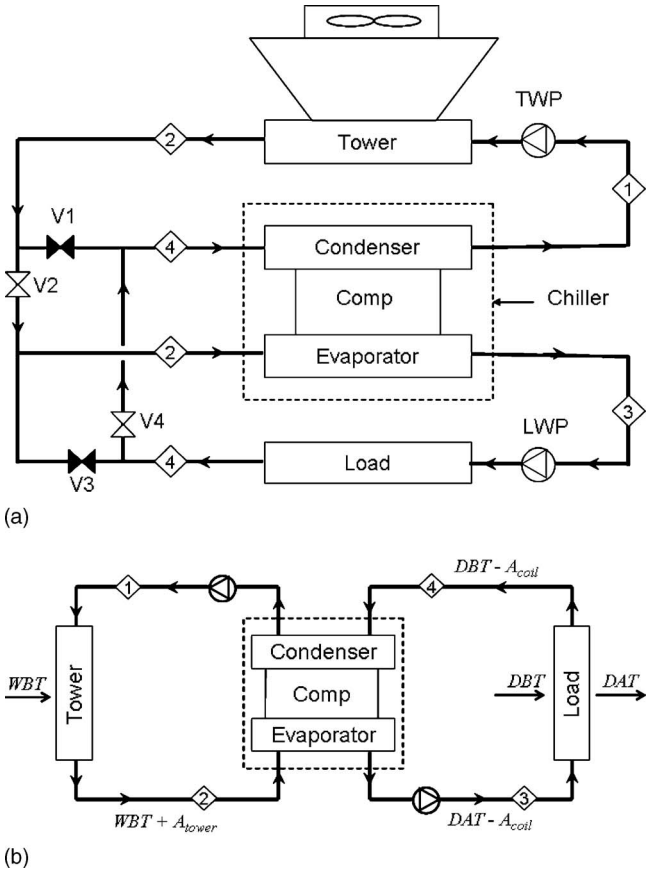

Fig. 2 Single-loop arrangement of the proposed LOTOCH system (novel scheme operation): (*a*) interconnecting piping arrangement; (*b*) flow schematic diagram

3.3 Mixed Cooling Line (M-J Line). This line distinguishes two zones of ambient conditions: one in which the load can be totally met by the cooling tower and another that requires operating both the tower and chiller with the tower serving as the primary cooling source. This line is drawn as a straight line parallel to WBT lines and mathematically expressed as WBT=DAT $-(A_{\text{tower}}+A_{\text{coil}})A_{\text{tower}}$, which is the cooling tower approach and defined as the difference between the cold water temperature and the ambient or inlet wet-bulb temperature in °F, whereas A_{coil} is the cooling coil approach and defined as the difference between the supply water temperature to the coil and the desired air temperature in °F.

3.4 Tower Cap Line (F-M Line). This line defines the range of ambient temperature values in which the return water delivered from the cooling tower is not cold enough to remove any heat from the cooling coil. It can be seen from Fig. 4 that this curved line is maintained parallel to the saturation line and is held underneath it by a quantity equivalent to the summation of A_{tower} and A_{coil}. This line can be mathematically expressed as DBT=WBT $+(A_{\text{tower}}+A_{\text{coil}})$.

3.5 Multimode Point (*M*). It is defined as the point where different internal boundary limiting lines intersect and the LOTOCH system can possibly undergo any operation mode as explained in the subsequent sections.

4 Operation Modes of the System

The operation modes of the LOTOCH system can be classified based on its arrangement into the following categories:

4.1. Single-loop arrangement operation modes

4.1.1. Tower and chiller cooling (TAC) mode
4.1.2. All-tower (ALT) cooling mode
4.1.3. No cooling (NOC) mode

4.2. Dual-loop arrangement operation modes

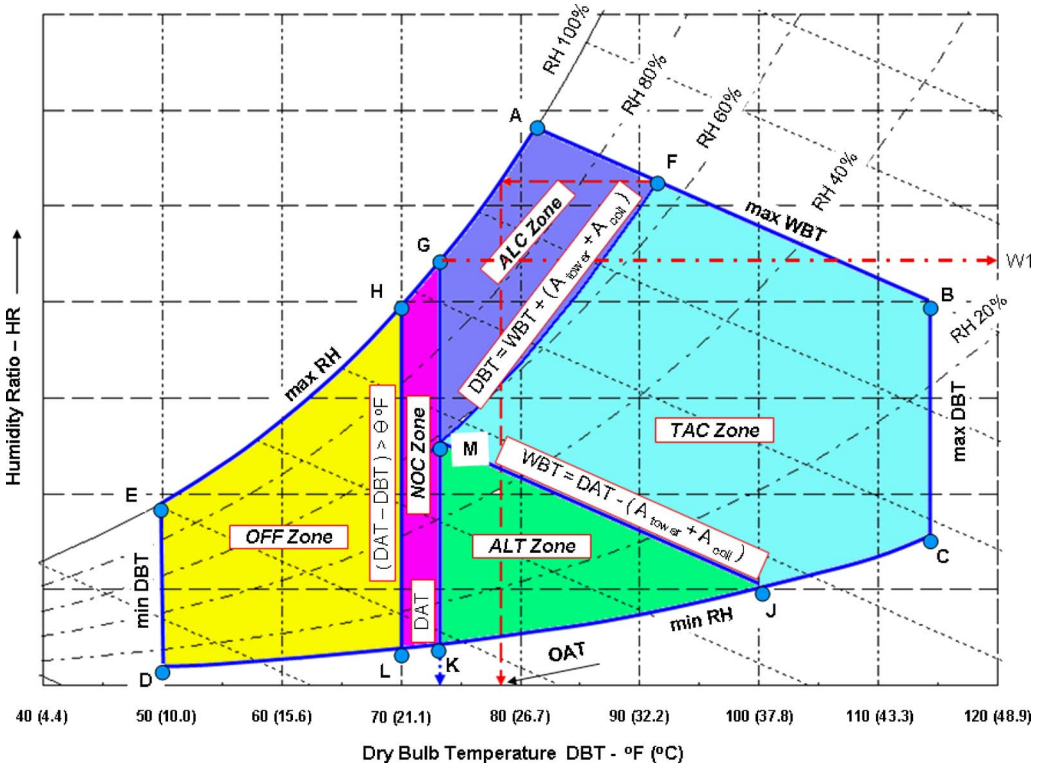

Fig. 3 The weather envelope and operating boundaries mapped onto the psychrometric chart

Downloaded 02 Jun 2010 to 171.66.16.107. Redistribution subject to ASME license or copyright; see http://www.asme.org/terms/Terms_Use.cfm

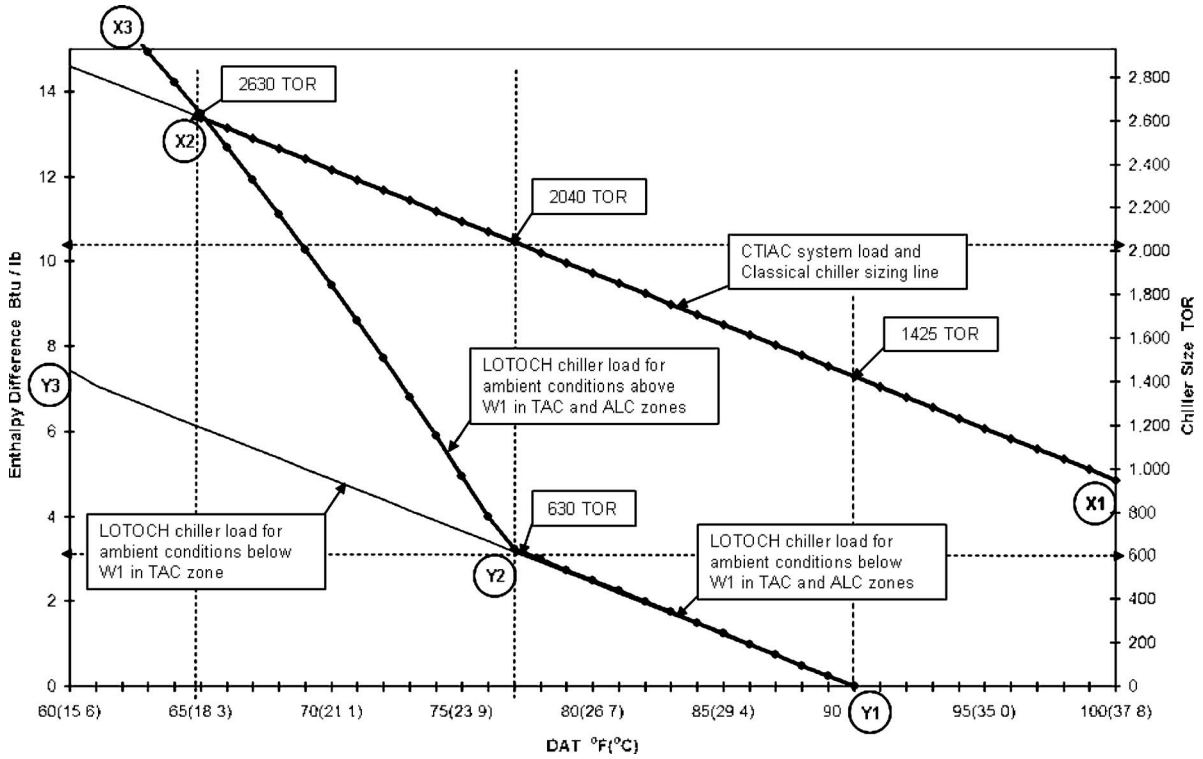

Fig. 4 Chiller loading and capacity of LOTOCH system versus classical chiller system at different DAT

4.2.1. All-chiller (ALC) cooling mode
4.2.2. No cooling (NOC) mode

4.3. Shutdown arrangement
4.3.1 Shutoff (OFF) mode

Based on the defined operating weather envelope and the distinguished dividing lines highlighted above, various operation modes are manifested from the proposed system. Ideally, the system logic will examine the DAT setting against the recorded ambient DBT to decide on the most appropriate mode of operation as follows.

4.1 Single-Loop Arrangement Operation Modes

4.1.1 Tower and Chiller (TAC) Cooling Mode. This mode takes place when ambient DBT falls between the mixed cooling line and the tower cap line. As stated earlier, this is considered a unique feature of this system since it utilizes free cooling from the tower while the chiller is running in a manner in which a considerable part of the cooling load is primarily met by the tower, while the rest is met by the chiller.

4.1.2 All-Tower (ALT) Cooling Mode. In dry weather when ambient WBT dips below the mixed cooling (M-J) line, the tower supply water will be cold enough to solely remove the required amount of heat without running the chiller similar to the conventional free-cooling scheme.

4.1.3 No Cooling (NOC) Mode. Whenever the ambient DBT is between the shut-off line and the DAT line, the system will work idle for some time as "hot standby" without any cooling requirements ready to move to any other operation mode.

4.2 Dual-Arrangement Operation Modes

4.2.1 All-Chiller (ALC) Cooling Mode. When the ambient condition lies above the DAT line and tower cap line, the system will operate in "all-chiller" mode. This mode is similar to the classical chiller arrangement in which the cooling tower will not be effective in removing any heat, load-free cooling will be ceased.

4.2.2 No Cooling (NOC) Mode. As explained in 4.1.3, when the ambient condition is above the tower cap line or its extrapolated extension into the NOC zone, then the system logic will assume the dual-loop arrangement so that it is ready to operate in all-chiller (ALC) mode.

4.3 Shutdown Arrangement

4.3.1 Shut-Off (OFF) Mode. The system is expected to be off when the ambient DBT is lower than the shut-off line such as during night periods or on cold days.

5 System Performance

Based on the established operating boundary limits, bearing in mind the prescribed tower approach (A_{tower}) and cooling coil approach (A_{coil}) and in order to satisfy the heat transfer requirements irrespective of the amount of heat loss or gain, the following limiting operating relations, as displayed in Figs. 1–3, can be established:

- Minimum cold water temperature obtained from the tower:

$$T_{\text{tower,out}} = \text{WBT} + A_{\text{tower}} \tag{1}$$

- Maximum cold water temperature needed to maintain DAT:

$$T_{\text{load,in}} = \text{DAT} - A_{\text{coil}} \tag{2}$$

- Minimum hot water temperature exits from the load (for a cross-flow cooling coil):

$$T_{\text{load,out}} = \text{DBT} - A_{\text{coil}} \tag{3}$$

Downloaded 02 Jun 2010 to 171.66.16.107. Redistribution subject to ASME license or copyright; see http://www.asme.org/terms/Terms_Use.cfm

Under the series arrangement of the LOTOCH system, the same amount of water circulates throughout the load, condenser, tower, and evaporator. As such, heat gain or loss in each component is directly proportional to the water temperature difference across it. Considering steady state operation conditions, the cooling load can consequently be calculated in proportion to the temperature difference as follows:

- Total cooling load (across the cooling coil):

$$\Delta T_{\text{load}} = T_{\text{load,out}} - T_{\text{load,in}} = (\text{DBT} - A_{\text{coil}}) - (\text{DAT} - A_{\text{coil}}) = \text{DBT} - \text{DAT} \quad (4)$$

- Cooling load exerted by the evaporator:

$$\Delta T_{\text{evap}} = T_{\text{tower,out}} - T_{\text{load,in}} = (\text{WBT} + A_{\text{tower}}) - (\text{DAT} - A_{\text{coil}}) = (\text{WBT} - \text{DAT}) + (A_{\text{tower}} + A_{\text{coil}}) \quad (5)$$

Several mathematical expressions can be derived from Eq. (5) for the following scenarios:

- $\Delta T_{\text{evap}} = (A_{\text{tower}} + A_{\text{coil}})$ when WBT=DAT. This conclusion confirms that the maximum ΔT_{evap} that is required to be removed by the chiller is equivalent to $(A_{\text{tower}} + A_{\text{coil}})$ and is anticipated at WBT_{max}.
- $\Delta T_{\text{evap}} \leq 0$ when $\text{DAT} \leq \text{WBT} + (A_{\text{tower}} + A_{\text{coil}})$. This means that the cooling load exerted by the chiller is equal to zero for any ambient condition on or below the "mixed cooling line," and the heat load will be fully met by the cooling tower.
- $\Delta T_{\text{evap}} = \text{DBT} - \text{DAT}$ when $\text{DBT} = \text{WBT} + (A_{\text{tower}} + A_{\text{coil}})$. This expression represents the "tower cap" line, which means that the evaporator will remove the entire load for any ambient condition on this line.
- $\Delta T_{\text{evap}} > (\text{DBT} - \text{DAT})$ when $\text{DBT} < \text{WBT} + (A_{\text{tower}} + A_{\text{coil}})$. This expression indicates that the evaporator will provide more cooling than what is required by the cooling load. This obviously makes the proposed system not feasible under this condition and the system will accordingly be requested to switch to the classical chiller system. It is interesting to note that under this condition, the exiting water from the cooling coil will ultimately be colder than the cold water stream from the tower. This scenario holds true when the ambient condition falls on or above the "tower cap" line.

A good indicator on the utilization of the chiller as compared to the total load met by the system can be established through the definition of the chiller-load ratio (CLR). The CLR can be expressed as the ratio of the evaporator load to the total load. For the same ambient condition and water flow rate in all components, CLR can be mathematically expressed as:

$$\text{CLR} = \Delta T_{\text{evap}} / \Delta T_{\text{load}} = [\text{WBT} - \text{DAT} + (A_{\text{tower}} + A_{\text{coil}})] / (\text{DBT} - \text{DAT}) \quad (6)$$

This relation is valid for any ambient condition bounded by the mixed cooling line and the tower cap line. Furthermore, the following conclusions can be deduced from Eq. (6) and the above mathematical expressions:

- CLR=1 for any ambient condition on the tower cap line;
- CLR=0 for any ambient condition on the mixed cooling line;
- $0 < \text{CLR} < 1$ for any ambient condition within the TAC zone.

Al-Amiri and Zamzam [10] explored the factors affecting the performance and feasibility of CTIAC applications using conventional refrigerative and evaporative cooling systems. The factors included ambient temperature distribution, design DBT and WBT, DAT, AFTOR, and COP of the cooling system. Similarly, this study explores LOTOCH performance at different DAT and weather conditions. A base load, simple-cycle industrial frame turbine with technical specifications and performance characteristics as identified in the comparative assessment report [2] is chosen to work under a specific weather regime. Al-Ain City's weather regime that has been identified as a typical pattern for the aired weather in the Arabian Gulf Region [10], is used for the analysis. The following design criteria are assumed: DBT 120°F (48.9°C), WBT 80°F (26.7°C), turbine output 100 MW, inlet air flow rate 2,342,346 Ib/h (295 kg/s), coil approach 5°F (2.8°C), and tower approach 5°F (2.8°C).

The three lines shown in Fig. 4 represent the chiller loading and capacity of LOTOCH system versus classical chiller system at different DAT. Line X1-X2-X3 represents the cooling load required for inlet air cooling at different DAT. In the case of using a classical refrigerative system, the same line will also represent the required chiller size. Chiller in LOTOCH system has two different loading scenarios represented by line Y1-Y2-Y3 and the bended line Y1-Y2-X3. The first scenario takes place when the ambient air condition lies below line W1 within the TAC or ALC zones, as indicated in Fig. 3, where W1 is the humidity ratio corresponding to the dew point temperature of the DAT. In such situations, inlet air will be sensibly cooled without latent heat removal and the cooling load will be presented by a straight line Y1-Y2-Y3. The second scenario is when the ambient air condition is above W1, for which sensible and latent heat removal will be required. Cooling load will follow the previous pattern in the sensible cooling process Y1-Y2, then ramps up once air reaches its dew point and humidity removal has started, line Y2-X2-X3 represents this part of the process. Because ambient air conditions cover both above and below W1, then the chiller capacity must be able to remove latent heat when required. It is worth noticing from Fig. 4 that the required chiller load to cool inlet air from DBT 120°F (48.9°C) to 77°F (25.0°C) is only 630 TOR in LOTOCH system as compared to 2040 TOR required from the classical refrigerative chiller. Inlet air temperature given in this example (77°F (25.0°C)) represents the optimum cooling temperature in terms of required chiller TOR per ΔT cooling; chiller capacity ramps up more rapidly for cooling below this temperature. The ratio of chiller loading under the LOTOCH system compared to that under the classical system (630/2040) can also be obtained from Eq. (6) for any ambient condition within the TAC zone. Whenever DAT is below the DPT of the design ambient condition (120/80°F in this example), LOTOCH operates exclusively in ALC mode and performs typically like the classical system, as demonstrated by line X2-X3. The LOTOCH size will be the same as the classical system, however, LOTOCH performance will continue enjoying the advantage of energy reduction throughout the free-cooling hours.

Obviously, LOTOCH significantly reduces the chiller load and consequently, its size, depending on the DAT and the design weather condition. The chiller size may vary between 0% and 100% as compared to a similar classical chiller system. In essence, the chiller load will be effectively 0% when the ambient condition is in the ALT cooling zone, while the chiller load shall be equal to its maximum designed capacity, i.e., 100%, when the ambient condition is in the ALC cooling zone. The chiller load varies between 0% and 100% when the ambient condition varies between the aforementioned limits within the TAC cooling zone.

6 System Feasibility

The LOTOCH system does not only reduce the size of the chiller as explained above, but also its operation hours. The prespecified weather regime of Al-Ain City is used to explore the feasibility of LOTOCH as a CTIAC system. The actual hourly temperature record of a six-month summer season (May–October) is used to predict the operation hours of each equipment based on

Downloaded 02 Jun 2010 to 171.66.16.107. Redistribution subject to ASME license or copyright; see http://www.asme.org/terms/Terms_Use.cfm

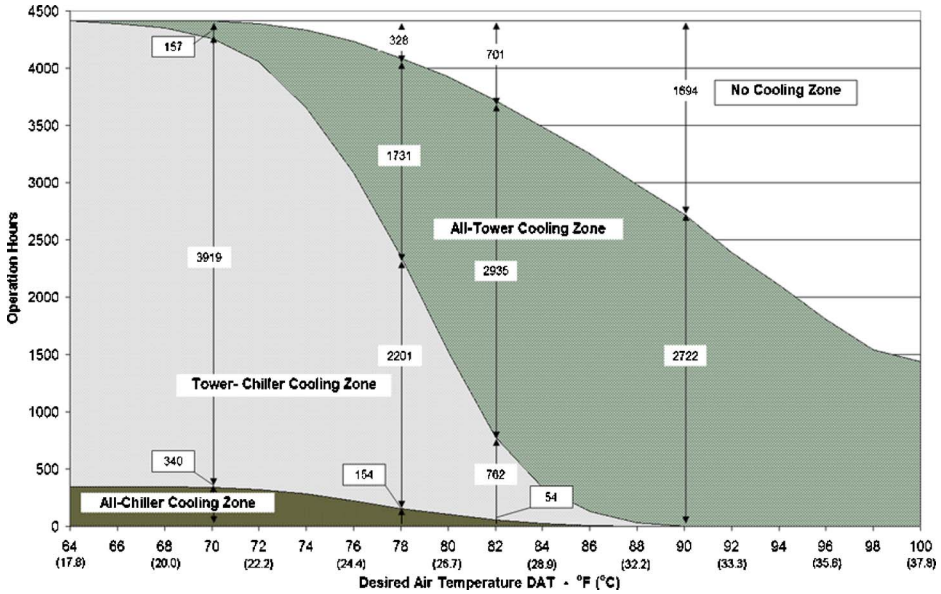

Fig. 5 Distribution of the operation hours of LOTOCH system equipment around the summer season under a chosen weather pattern at different DAT

the conclusions derived in the above section. Figure 5 portrays the distribution of the operation hours of each operation mode at different DAT for Al-Ain City over a typical summer season. Figure 5 shows that when DAT is at 90°F or above, cooling is not required for 1694 h and obtained for 2722 h by the tower solely while the chiller is always off. Chiller starts operations when DAT goes below 90°F, either as a primary cooler or secondary to assist the tower. For instance, if DAT is equal to 78°F, chiller handles the load fully in ALC mode for 154 h and assists the tower in TAC mode for 2201 h while it is off when the load is met by the tower only for 1731 h in the ALT mode or when cooling is not required for 328 h (NOC mode).

It is obvious that the majority of the operation hours lie in ALT and TAC zones while only a few hours come under ALC zone. The conventional free-cooling scheme can only cool air at conditions within ALT zones but not within TAC zones which is a unique feature of the LOTOCH system. For most weather scenarios, the number of hours in TAC zone is by far much more than that in ALT zone. In such cases, the LOTOCH scheme will dramatically increase the free-cooling hours, making it a superior energy saving system.

In summary, a LOTOCH system working at the optimum temperature 77°F (25.0°C) in Al-Ain City will provide 43°F cooling to a turbine inlet air resulting in a 15% net increase in the turbine output (i.e., 15 MW). The system capacity will be about 630 TOR and will cost \$550–\$650 K, i.e., 35–45 \$/kW power increment. This is very cost effective as compared to the conventional cooling systems or installing new turbines, which may cost 90–115 \$/kW and 500–800 \$/kW, respectively. The capital cost of both the LOTOCH and conventional cooling systems gets closer as DAT approaches the DPT, at which both systems will have the same cooling capacity and investment cost.

7 System Components

The principal features and functions of each component in the LOTOCH system are briefly summarized here.

7.1 Inlet Air Cooling Coil. A fin and tube heat exchanger is proposed to be installed in the path of the turbine inlet air, such that the chilled water flows inside the tubes while the air passes over the fins. The cooling coil will primarily work on the incoming cold water from the cooling tower, which often has high temperature in close proximity to the incoming or desired air temperature. Therefore, the cooling coil will require special design attention to operate at a relatively tight approach, high temperature level, and low temperature range. The heat transfer area must be significantly increased by increasing either or both the coil surface area and its depth. Furthermore, increased coil depth may become a concern due to the space or pressure drop limitations. Finally, the coil will experience an increase in weight that will require special construction attention. In the event that the DAT value is set below the ambient DPT, latent heat will be removed, adding risk of moisture carryover into the compressor. Installing a moisture eliminator and/or reducing coil face velocity are possible solutions to mitigate this risk.

7.2 Closed-Loop Cooling Tower. A cooling tower is the primary source of cooling in the LOTOCH scheme. Two important parameters significantly quantify the tower size; namely, the tower range (defined as the temperature difference between the water entering and leaving the tower) and the tower approach (defined as the temperature difference between the leaving water and the ambient WBT). The ambient WBT has a significant impact on the thermal performance of a cooling tower. In order to increase free cooling opportunity, the tower approach must be kept as low as practically possible (preferably not more than 5°F (2.8°C)). The cooling tower may also receive water temperature as high as 125°F (51.7°C) or higher from the condenser. Although such a high temperature level is beyond the CTI Certification, some tower manufacturers guarantee tower performance under these conditions with special design features.

7.3 Water-Cooled Chiller. As demonstrated in Fig. 4, the chiller operates in the series arrangement for DAT between the ambient air design WBT and its corresponding DPT. As such, the required evaporator water temperature varies from a few degrees above ambient air WBT to a few degrees below DPT to offset the approach of the tower and cooling coil, respectively. For instance, when the ambient design condition of the surrounding weather is (DBT/ WBT: 120°F (48.9°C)/ 80°F (26.7°C)), then the recommended range of evaporator cold water is 85°F (29.4°C) to 59°F (15.0°C). Such high evaporator temperature ultimately renders a higher chiller COP as compared to 55°F (12.8°C) to 45°F (7.2°C) in the classical chiller application. On the other hand, the condenser will also see higher water temperature that—in contrast to

Downloaded 02 Jun 2010 to 171.66.16.107. Redistribution subject to ASME license or copyright; see http://www.asme.org/terms/Terms_Use.cfm

the evaporator—reversely affects the COP. Condenser outlet temperature may go as high as 125°F (51.7°C), depending on the weather condition. Chiller manufacturer must be consulted in the performance and operation limitations at such high condenser water temperature level.

8 Conclusion and Recommendations

The current study presents a novel water chiller system that effectively utilizes the free-cooling concept to enhance the performance of combustion turbine. The system consists of the same components as a typical chilled water system, i.e., chiller, cooling tower, inlet air cooling coils, etc. Different operating modes were identified and discussed after establishing the operating envelope for the proposed system. The system has the capability to work under two distinct operational configurations. One is typical to the classical chilled water system, where the system has two separate water circulation loops such that the evaporator and the cooling coils are tied in one loop, while the cooling tower and condenser in the other loop. Furthermore, the second operational configuration of the proposed system calls for utilizing free cooling from the cooling tower even when the chiller is running, which is a unique feature of the system. Such a configuration can be furnished when all system components are connected in a series arrangement, i.e., the cooling tower followed by the evaporator, then the cooling coil, and finally the condenser. This particular arrangement can be considered as an energy saving mode of operation. Overall, the proposed system has two chief advantages:

- reducing the chiller load and consequently its size
- increasing the free cooling duration.

Nomenclature

A_{coil} = cooling coil approach
A_{tower} = cooling tower approach
ALC = all-chiller cooling
ALT = all-tower cooling
AFTOR = air flow to output ratio
CLR = chiller-load ratio
COP = coefficient of performance
CTI = Cooling Technology Institute
CTIAC = combustion turbine inlet air cooling
DAT = desired air temperature
DBT = ambient dry bulb temperature
DPT = ambient dew point temperature
ΔT = temperature difference
Ib/h = pound mass per hour
LOTOCH = load-tower-chiller system
LWP = load water pump
NOC = no cooling
RH = relative humidity
TAC = tower and chiller cooling
TOR = ton of refrigeration
TWP = tower water pump
WBT = ambient wet bulb temperature
M = multimode point
OFF = shut-off mode

References

[1] Stewart, W. E., 1999, *Design Guide: Combustion Turbine Inlet Air Cooling System*, ASHRAE, Atlanta, GA, Technical Report No. 902, pp. 165–173.
[2] Brown, D. R., Katipamula, S., and Koynenbelt, J. H., 1996, "A Comparative Assessment of Alternative Combustion Turbine Inlet Air Cooling Systems," Pacific Northwest National Lab., Richland, WA, Technical Report No. PNNL-10966.
[3] Chaker, M., Meher-Homji, C. B., Mee, T., III, and Nicholson, A., 2003, "Inlet Fogging of Gas Turbine Engines Detailed Climatic Analysis of Gas Turbine Evaporation Cooling Potential in the USA," ASME J. Eng. Gas Turbines Power, **125**(1), pp. 300–309.
[4] Jolly, S., Nitzken, J., and Shepherd, D., 1998, "Evaluation of Combustion Turbine Inlet Air Cooling Systems," presented at the Power-Gen Asia, New Delhi, India.
[5] *ASHRAE Handbook: Fundamentals*, 2000, American Society of Heating, Refrigeration and Air-Conditioning Engineers, Inc., Atlanta, GA, Chap. 50.
[6] "The Application of Cooling Towers for Free Cooling," 1982, Marley Cooling Technologies, Inc., Overland Park, KS, Technical Report No. H-002.
[7] "External Influences on Cooling Tower Performance," 1983, Marley Cooling Technologies, Inc., Overland Park, KS, Technical Report No. H-004.
[8] Cooling Towers Certification STD-201, 2002, Cooling Towers Institute, Houston, TX.
[9] Zamzam, M., and Al-Amiri, A., 2006, "Free Cooling Scheme for Process Cooling and Air Conditioning Applications," Patent Cooperation Treaty, International Application No. PCT/EG2006/000027.
[10] Al-Amiri, A., and Zamzam, M., 2005, "Systematic Assessment of Combustion Turbine Inlet Air Cooling Techniques," ASME J. Eng. Gas Turbines Power, **127**, pp. 159–169.

Downloaded 02 Jun 2010 to 171.66.16.107. Redistribution subject to ASME license or copyright; see http://www.asme.org/terms/Terms_Use.cfm

M. Bagnoli
M. Bianchi
F. Melino

DIEM,
University of Bologna,
Viale del Risorgimento 2,
40136 Bologna, Italy

P. R. Spina
ENDIF,
University of Ferrara,
Via Saragat,
44100 Ferrara, Italy

Development and Validation of a Computational Code for Wet Compression Simulation of Gas Turbines

In this paper, a calculation code, developed in house by the authors, able to evaluate the performance of a gas turbine with all possible fogging strategies (high pressure fogging, overspray, and interstage injection) is presented and discussed. The code has a flexible structure and can be applied to evaluate the performance of every commercial gas turbine model. The aim of the calculation code is to overcome the limits of the most widespread commercial software, especially with regard to the two phase flow compression process simulation. The calculation code was validated on results available in the literature showing a good agreement with experimental and theoretical results.
[DOI: 10.1115/1.2771563]

Introduction

In recent years there has been increasing attention to the fogging approach, among all available inlet air cooling techniques for gas turbine power enhancement, thanks to its simplicity, effectiveness, and comparatively low initial investment cost and less installation downtime [1].

The various fogging strategies and, in particular, high-pressure fogging and overspray, have been implemented in simple and combined cycle applications and, today they can be considered consolidated technologies. In fact, it is estimated that there are over 1000 gas turbines that use high-pressure fogging or overspray worldwide [2].

Overspray, as opposed to high-pressure fogging, involves the study of multiphase flow and water evaporation during the compression process (wet compression). The concept of wet compression is not a new idea in gas turbine applications for power augmentation. In fact, one of the early studies on this topic comes from the late 1940s by Klienschmidt [3]. The first systematic analysis of power augmentation by water ingestion at the compressor inlet in the case of the turbojet engine was developed by Wilcox and Trout [4] while Hill [5] discussed the effects of inlet cooling on load redistribution in the stages of an axial compressor. In the past few years a large number of studies were developed to better understand the effect of wet compression [6–11]. The use of wet compression allows one to decrease the compressor specific work and discharge temperature, depending on its polytropic efficiency, and to increase the compressor pressure ratio and mass flow rate [7,9,10]. These benefits are influenced by various parameters such as the injected water droplets diameter, the evaporation rate, and injected water mass flow rate [6,8]. Moreover, it can be observed that the water evaporation through the compressor changes its working point on the performance maps, with a redistribution of load among the different compressor stages [10–12].

The interstage injection, also called interstage fogging, is a strategy for compressor performance increase which consists of a liquid water injection directly into the compressor stages, between stator blades all around the perimeter, either at one stage or simultaneously at different stages. The use of this technique in conjunction with the other inlet cooling methods (such as high-pressure fogging, overspray fogging, or traditional evaporative cooling) allows the obtainment of an additional power boost.

The injection of water within the compressor is expected to increase the compression performance for two main reasons: the first is the cooling effect due to water evaporation (such as the traditional wet compression); and the second important aspect is the compressor on-line washing realized by the liquid water before its evaporation.

Unlike traditional fogging, the use of interstage injection requires modification of the gas turbine compressor as discussed by Ingistov [13,14].

To the author's knowledge, the interstage injection approach to improve gas turbine performance has not yet been fully studied and investigated in the literature. The main aspects of interstage water injection that need to be understood are the influence of factors such as the water injection point along the compressor, injected water temperature, and mass flow rate and droplets diameter on the compressor performance and on the overall power output and efficiency of the gas turbine. Moreover, the change of working point in compressor performance maps due to water injection needs to be investigated.

A parametric study of the effects of interstage injection on gas turbine performance was carried out in one of the an author's previous works [12] by using a commercial software for energy systems simulation. Although the results of this analysis were relevant to better understand the effects of interstage injection (in particular for what concerns the compressor stages load redistribution and the reduction of surge margin), they are influenced by the hypothesis assumed in [12], mainly due to the rigid structure of the commercial software. In particular among the other limitations, by using the commercial software it was not possible to evaluate the influence of droplets diameter, pressure, and temperature on the evaporation process, and also to consider the evaporation process of water droplets during the compression process as a dynamic phenomenon, since the water that can evaporate is estimated only as a function of the saturation capacity of the air.

To overcome these limitations, a calculation code in Fortran 90 language, named interstage fogging gas turbine evaluation (IN.FO.G.T.E.) was developed in house by the authors, in order to analyze the gas turbine behavior in the presence of any fogging strategy (high-pressure fogging, overspray, and interstage water injection). The code has a flexible structure and can be applied to

Contributed by the International Gas Turbine Institute of ASME for publication in the JOURNAL OF ENGINEERING FOR GAS TURBINES AND POWER. Manuscript received October 16, 2006; final manuscript received October 17, 2006; published online January 11, 2008. Review conducted by Dilip R. Ballal. Paper presented at the ASME Turbo Expo 2006: Land, Sea and Air (GT2006), Barcelona, Spain, May 8–11, 2006, Paper No. GT2006-90342.

Copyright © 2008 by ASME

Downloaded 02 Jun 2010 to 171.66.16.107. Redistribution subject to ASME license or copyright; see http://www.asme.org/terms/Terms_Use.cfm

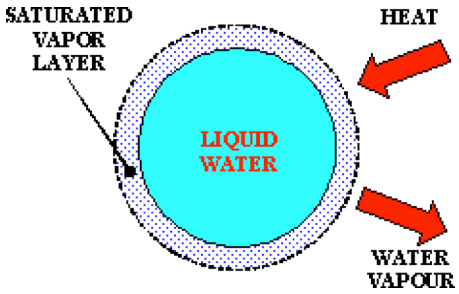

Fig. 1 Scheme of a water droplet exchanging heat and mass with the surrounding air

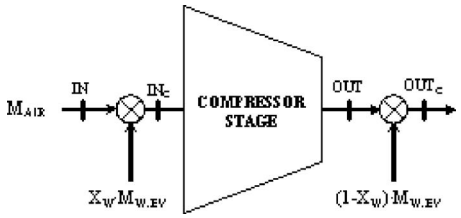

Fig. 2 Model adopted for compressor stage wet compression calculation

evaluate the performance of every commercial gas turbine model.

Wet Compression Calculation Model

The heat and mass transfer between humid air and liquid water is influenced by many factors which can be divided into two main categories:

- thermodynamic characteristics of the air (relative humidity, total pressure, and temperature); and
- geometrical and thermodynamic characteristics of water droplet (droplet volume, characteristics of the liquid phase, droplet temperature).

With reference to Fig. 1, regarding the evaporation of a water droplet in air, it can be usually assumed that [9]:

- the water droplet is a perfect sphere;
- the physical properties of air and liquid water are homogeneous in each phase considered;
- an infinitesimal volume of vapor saturated at the droplet surface surrounds the water droplet until complete water evaporation occurs;
- the temperature inside the droplet and on its surface is uniform; and
- the air is not soluble into the liquid water.

Applying the energy and mass balance to the system presented in Fig. 1, the following differential equations, able to estimate the variation of droplet surface temperature (T_L) and diameter (D_D), can be obtained [9]

$$\frac{dT_L}{dt} = \frac{6 \cdot \mathrm{Nu} \cdot \lambda_{\mathrm{REF}}}{\rho_L \cdot D_D^2 \cdot c_L}(T_G - T_L) + \frac{3 \cdot \Delta h_{\mathrm{LAT}}}{D_D \cdot c_L} \cdot \frac{dD_D}{dt} \tag{1}$$

$$\frac{dD_D}{dt} = \frac{4 \cdot \rho_{\mathrm{REF}} \cdot D_V}{\rho_L \cdot D_D} \cdot \ln\left(\frac{1+\omega}{1+\omega_L}\right) \tag{2}$$

Equations (1) and (2) estimate the surface temperature variation (dT_L/dt) and the diameter reduction (dD_D/dt) of a water droplet in an air stream as a function (among others parameters) of the thermodynamic conditions of the air. In the case of wet compression the temperature and pressure of air rapidly change due to the compression. This evidence, together with the interaction between air and liquid droplets, makes the analytical integration of Eqs. (1) and (2) difficult. In fact, the increase in air temperature due to the compression process is contrasted by the cooling effect of water droplets evaporation. Moreover, the change of the thermodynamic conditions of air through the compressor influences the thermal exchange with the water droplets. In particular, the increase of temperature and pressure influences the saturation capacity of the air and then the droplets evaporation process. This phenomenon is a continuous process which occurs along the whole compressor until the complete evaporation of water.

To overcome the difficulties regarding the analytical integration of Eqs. (1) and (2) along a compressor stage and to simulate the compression in the presence of liquid water which evaporates as an adiabatic process with a constant mass flow (so that standard compressor stage performance maps can be used), the exchanges of latent heat and of sensible heat between liquid water and air were modeled as two separate phenomena. In particular, the exchange of latent heat was concentrated at the inlet and outlet of the stage, while the exchange of sensible heat was assumed to occur at constant temperature and pressure at the middle of the stage. In more detail, the "wet" compression process was modeled as sketched in Fig. 2.

In fact, because $M_{W,\mathrm{EV}}$ is the total mass of liquid water that can evaporates during the whole stage compression process, the corresponding total cooling $\Delta T = f(M_{W,\mathrm{EV}})$ was divided into two fractions

$$\Delta T_1 = f[X_W \cdot M_{W,\mathrm{EV}}]$$

$$\Delta T_2 = f[(1 - X_W) \cdot M_{W,\mathrm{EV}}]$$

whose effects were considered concentrated at the inlet (ΔT_1) and at the outlet (ΔT_2) of the stage by using a tuning parameter $X_W \in [0,1]$, as in Fig. 2.

The physical state of the air at the exit of the compressor stage is represented by the point OUT_C in Fig. 2, but the specific stage of the compression work is assumed to be the enthalpy difference between the point OUT and the point IN_C of the adiabatic compression.

As mentioned above, the exchange of sensible heat was modeled as a process that occurs separately from the exchange of latent heat and at constant temperature and pressure. This assumption is reasonable considering the small temperature increase of the air during the compression in a single compressor stage (usually 20–25 °C).

By the use of these hypotheses Eq. (1) reduces as follows

$$\frac{dT_L}{dt} = \frac{6 \cdot \mathrm{Nu} \cdot \lambda_{\mathrm{REF}}}{\rho_L \cdot D_D^2 \cdot c_L}(T_G - T_L) \tag{3}$$

According to the previous assumptions, the analytical integration of Eqs. (2) and (3) with respect to the radius (from R_{D1} to $R_{D2} \leq R_{D1}$), droplet surface temperature (from T_{L1} to T_{L2}), and time (from 0 to $\Delta t = \Delta x / V_X$, where Δx is the stage length and V_X is the axial flow velocity of air across the compressor stage) leads to

$$T_{L2} = T_G + (T_{L1} - T_G) \cdot \exp\left(-\frac{6 \cdot \mathrm{Nu} \cdot \lambda_{\mathrm{REF}}}{\rho_L \cdot D_D^2 \cdot c_L}\frac{\Delta x}{V_X}\right) \tag{4}$$

$$R_{D2}^2 = R_{D1}^2 + 2 \cdot \frac{\rho_{\mathrm{REF}}}{\rho_L} \cdot D_v \cdot \ln\left(\frac{1+\omega}{1+\omega_L}\right) \cdot \frac{\Delta x}{V_x} \tag{5}$$

By considering a monodisperse spray,[1] the total mass of water that evaporates can be written as a function of the radius reduction and of the number of droplets (n_D) as follows

[1]It should be observed that, considering a spray, the injected droplets are characterized by a certain diameters distribution. In order to represent this distribution some parameters, such as Sautern mean diameter (SMD) (defined as the ratio of total injected droplets volume to surface area), mean diameter, etc., can be used.

Downloaded 02 Jun 2010 to 171.66.16.107. Redistribution subject to ASME license or copyright; see http://www.asme.org/terms/Terms_Use.cfm

$$M_{W,\mathrm{EV}} = n_D \cdot \rho_L \cdot \frac{4}{3}\pi \cdot (R_{D1}^3 - R_{D2}^3) \tag{6}$$

By matching Eqs. (5) and (6), it follows that

$$M_{W,\mathrm{EV}}(i) = \frac{4}{3}\pi \cdot n_D \cdot \rho_L \cdot \left[R_{D1}^3 - \left(R_{D1}^2 + 2 \cdot \frac{\rho_{\mathrm{REF}}}{\rho_L} \cdot D_v \cdot \ln\left(\frac{1+\omega}{1+\omega_L} \right) \cdot \frac{\Delta x}{V_x} \right)^{3/2} \right] \tag{7}$$

The reference point with respect to which ρ_{REF}, λ_{REF}, ω_L, and D_V in Eqs. (4)–(7) are evaluated, was assumed as the one corresponding to the average values of temperature and pressure across the stage. In more detail, for each stage the average values of temperature (T_G) and pressure (p_G) were estimated, as follows:

- T_G is the average value between the inlet and the outlet state of the compressor stage; with reference to Fig. 2, it was evaluated as

$$T_G = \left(\frac{T_{IN} + T_{\mathrm{OUT}_C}}{2} \right)$$

- p_G was evaluated as the isobar which passes through the point resulting from the intersection between the isothermal T_G and the polytropic compression from IN_C to OUT (Fig. 2).

The temperature of the vaporlayer which surround the water droplet (T_{REF}) is evaluated by the aid of the so called 1/3 rule applied to T_L and T_G [15], as

$$T_{\mathrm{REF}} = T_L + \gamma \cdot (T_G - T_L) \tag{8}$$

in which $0.3 \leqslant \gamma \leqslant 0.4$. For the calculations presented in this paper a value of γ equal to 0.4 was used.

Finally the values of the density for the saturated air (ρ_{REF}), diffusion coefficient (D_V), and maximum specific humidity (ω_L), which is the humidity in saturated conditions, were evaluated with reference to the total pressure p_G and to the temperature T_{REF}.

Regarding the diffusion coefficient, among the expressions available in the literature, the one proposed by Fuller [16] was chosen

$$D_V = 10^8 \frac{0.00143 \cdot T^{1.75}}{p \cdot W_{\mathrm{AB}}^{1/2} \cdot [(\Sigma_V)_A^{1/3} + (\Sigma_V)_B^{1/3}]^2} \quad (\mu\mathrm{m}^2/\mathrm{s})$$

in which

$$W_{\mathrm{AB}} = \frac{2}{\frac{1}{W_A} + \frac{1}{W_B}} = \frac{2}{\frac{1}{28.970} + \frac{1}{18.016}} = 22.216 \quad (\mathrm{g/mole})$$

and Σ_V can be evaluated as the sum of the diffusion volumes of the simple molecules which interact during the evaporation process. In particular, Σ_V is equal to 19.7 and 13.1 ($\mathrm{cm}^3 \cdot \mathrm{mol}$) for air and water, respectively [16].

The use of the evaporation model previously described (Eqs. (4)–(7)) allows us to evaluate the mass of liquid water that evaporates as a function of the droplet diameter ($2 \cdot R_{D1}$), surface temperature (T_L), residence time through the compressor stage ($\Delta x / V_X$), and of the temperature difference between the exit and the inlet of the stage ($T_{\mathrm{OUT}_C} - T_{\mathrm{IN}}$) (see Fig. 2).

On the basis of the previous considerations, an iterative calculation procedure was developed and introduced in the IN.FO.G.T.E program which was able to evaluate the performance of a compressor stage in the presence of liquid water at the inlet.

In more detail, the first step of this procedure is the evaluation of the compressor stage performance assuming no liquid water at its inlet ("dry" compression). On the basis of the values of inlet and outlet temperature and pressure corresponding to the "dry" compression, the average temperature ($T_G(i)$) and pressure ($p_G(i)$) are estimated. By means of these values, a first value of the droplet surface temperature change across the stage (Eq. (4)) and then the temperature of the vaporlayer which surrounds the water droplet (Eq. (8)) are evaluated. By introducing these parameters in Eq. (7) the mass of liquid water ($M_{W,\mathrm{EV}}(i)$) able to evaporate through the compressor stage is estimated. According to the values of the parameter X_W and $M_{W,\mathrm{EV}}$ (i) the value of $\Delta T_1(i)$ is calculated and then $\mathrm{IN}_C(i)$ is estimated; the point $\mathrm{OUT}_{(i)}$ is estimated from compressor stage performance maps and then, from the value of $\Delta T_2(i)$, the point $\mathrm{OUT}_{C(i)}$ is calculated. From the points IN and $\mathrm{OUT}_{C(i)}$ a new mass of evaporable liquid water ($M_{W,\mathrm{EV}}(i+1)$) is then evaluated. The procedure stops when the difference between the masses of liquid water which evaporates across the stage calculated in two successive steps is lower than an imposed tolerance.

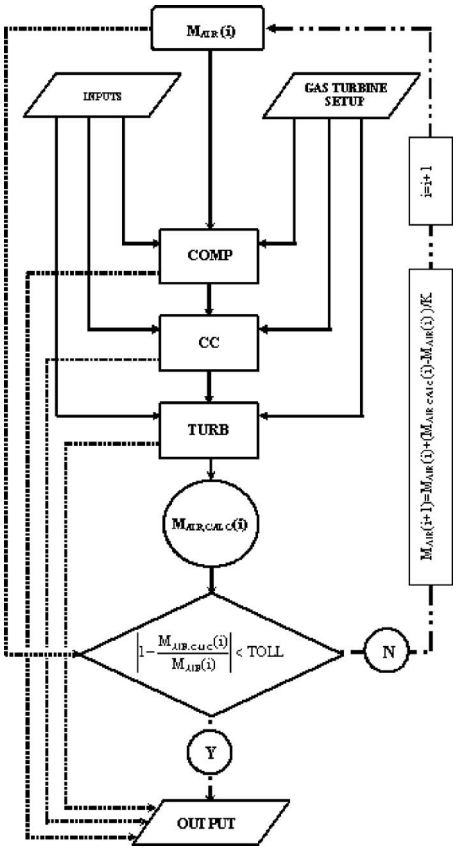

Fig. 3 Main program (*MAIN*) flow chart

Once the performances of a single compressor stage are evaluated, the calculation proceeds with the following compressor stage, so that the performances of the overall multistage compressor are obtained by a "stage-stacking" procedure.

IN.FO.G.T.E. Calculation Code Main Aspects

The calculation code is able to evaluate the performance of a gas turbine in the presence of every fogging strategy, such as inlet fogging, overspray, and in particular interstage water injection.

The main structure of the calculation code is presented in Fig. 3. Three calculation modules: COMP, CC, and TURB, are highlighted; they contain the physical-mathematical models used to evaluate the performance of compressor, combustor, and turbine, respectively. These modules consist of a wide number of internal calculation routines.

The management of COMP, CC, and TURB modules, of code internal logic, and of all iterative calculation processes is realized by

Downloaded 02 Jun 2010 to 171.66.16.107. Redistribution subject to ASME license or copyright; see http://www.asme.org/terms/Terms_Use.cfm

the "main program" (MAIN). In the flow chart of the main program (Fig. 3) the flows of data (both input and output) between the various calculation modules are also highlighted. The main program supplies the necessary input data (INPUTS and GAS TURBINE SETUP arrays in Fig. 3) to the three modules and reads the outputs of their internal calculation process. It should be observed that the data in the INPUTS array must be defined by the program User while the GAS TURBINE SETUP array contains all the parameters that characterize the machine.

In particular the data in the INPUTS array are as follows:

- ambient conditions (site temperature, pressure, and relative humidity);
- injection point(s) location(s) and/or presence of high-pressure fogging system;
- temperature(s) (T_W), pressure(s) (p_W), mass flow rate(s) (M_W) of injected water, and droplet diameter(s) (D_D);
- gas turbine control logic (constant turbine inlet temperature, constant turbine outlet temperature, etc.);
- fuel composition, pressure (p_{FUEL}) and temperature (T_{FUEL}); and
- mass flow rate(s) (M_{WSCC}), pressure(s) (p_{WSCC}), and temperature(s) (T_{WSCC}) of injected water and/or steam in the combustion chamber.

The data in the GAS TURBINE SETUP array are as follows:

- gas turbine performance and thermodynamic parameters at ISO conditions;
- number of compressor stages;
- geometrical data of the compressor stages;
- compressor stage performance maps;
- compressor air bleed ports;
- turbine performance maps;
- inlet fogging (if present) efficiency;
- pressure losses at compressor inlet, through the combustion chamber and at the turbine outlet;
- mathematical models tuning parameters;
- compressor and turbine mechanical efficiency; and
- generator efficiency.

The parameters calculated by the different modules of the code are collected by the main program and written in the OUTPUT array. In particular the data in the OUTPUT array are as follows:

- gas turbine power output and heat rate;
- pressure, temperature, and air (and liquid water, if present) mass flow rate at the exit of each compressor stage;
- compressor pressure ratio;
- pressure, temperature. and mass flow rate of gasses at the combustion chamber exit;
- pressure, temperature, and mass flow rate of gasses at the turbine exit; and
- turbine expansion ratio.

Compressor Stage Performance Maps. In order to simulate compressor stage performance in off-design conditions, generalized relationships between pressure coefficient $\psi_p^* = \psi_p/(\psi_p)_{\mathrm{DES}}$, stage isentropic efficiency $\eta^* = \eta/(\eta)_{\mathrm{DES}}$, and flow coefficient $\phi^* = \phi/(\phi)_{\mathrm{DES}}$ (all normalized to the design values) were used [17]. These relationships allow the complete evaluation of stage characteristics once the stage design point ($(\psi_p)_{\mathrm{DES}}$, $(\eta)_{\mathrm{DES}}$, $(\phi)_{\mathrm{DES}}$) is known.

The first generalized relationship, $\psi_p^* = F_\psi(\phi^*)$, was set up based on the work of Muir et al. [18], who obtained a generalized curve by fitting experimental data points of a number of compressor stages. First, the curve was approximated using the following relationship

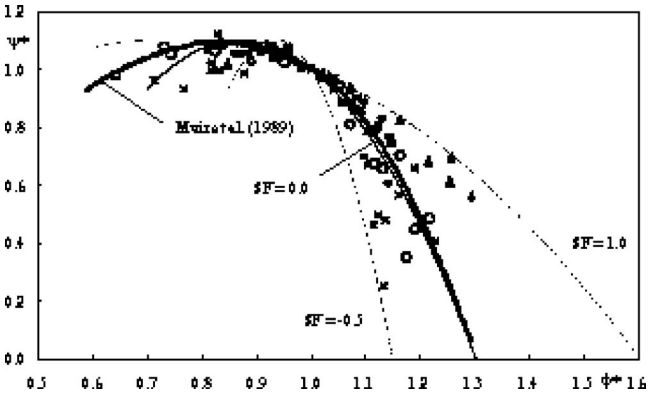

Fig. 4 Generalized stage characteristics $\psi_p^* = F_\psi(\phi^*, \mathrm{SF})$ and experimental data points [17]

$$\psi_p^* = \psi_{p,\max}^* - \frac{\psi_{p,\max}^* - 1}{(\phi_{\psi_{p,\max}}^* - 1)^2} \cdot (\phi_{\psi_{p,\max}}^* - \phi^*)^2$$

Second, in order to account for different stage characteristics based on different stage types, the shape factor (SF) was introduced to obtain a number of generalized $\psi^* = F_\psi(\phi^*, \mathrm{SF})$ curves covering all experimental data points reported by Muir et al. [18]. In this manner, the equation of generalized curves becomes [17]

$$\psi_p^* = \psi_{p,\max}^* - \frac{\psi_{p,\max}^* - 1}{[\phi_{\psi_{p,\max}}^* + \mathrm{SF} \cdot (\phi_{\psi_{p,\max}}^* - 1) - 1]^2} \cdot [\phi_{\psi_{p,\max}}^* + \mathrm{SF} \cdot (\phi_{\psi_{p,\max}}^* - 1) - \phi^*]^2 \quad (9)$$

In Fig. 4 three curves $\psi_p^* = F_\psi(\phi^*, \mathrm{SF})$ obtained by using $\mathrm{SF} \in [-0.5, 1]$ are shown.

The second generalized relationship, $\eta^* = F_\eta(\psi_p^*/\phi^*)$, was obtained from the generalized stage efficiency curve proposed by Howell and Bonham [19]

$$\eta^* = 1 - \frac{1 - \eta_{(\psi_p/\phi)_{\min}}^*}{\left[1 - \left(\frac{\psi_p^*}{\phi^*}\right)_{\min}\right]^{3.5}} \left(1 - \frac{\psi_p^*}{\phi^*}\right)^{3.5}, \frac{\psi_p^*}{\phi^*} \in \left[\left(\frac{\psi_p^*}{\phi^*}\right)_{\min}, 1\right] \quad (10)$$

$$\eta^* = 1 - \frac{1 - \eta_{(\psi_p/\phi)_{\max}}^*}{\left[\left(\frac{\psi_p^*}{\phi^*}\right)_{\max} - 1\right]^2} \left(\frac{\psi_p^*}{\phi^*} - 1\right)^2, \frac{\psi_p^*}{\phi^*} \in \left[1, \left(\frac{\psi_p^*}{\phi^*}\right)_{\max}\right] \quad (11)$$

In Fig. 5 the generalized stage efficiency curve obtained by using Eqs. (10) and (11) is reported, together with data obtained from the curve proposed by Howell and Bonham [19].

The relationships $\psi_p^* = F_\psi(\phi^*, \mathrm{SF})$ and $\eta^* = F_\eta(\psi_p^*/\phi^*)$ can be, in particular, considered independent from the gas composition (and so from the water amount into the air), since it was experimentally verified that these relationships do not modify significantly for values of k from 1.1 to 1.4 [20].

Air Extraction. The evaluation of the air extracted from the compressor was carried out by considering that the flow function (FF) [21] of the extracted air remains constant and equal to its design value ($\mathrm{FF}_{\mathrm{DES}}$). This means that each air mass flow rate extracted along the compressor (M_{EX}) was evaluated as

Downloaded 02 Jun 2010 to 171.66.16.107. Redistribution subject to ASME license or copyright; see http://www.asme.org/terms/Terms_Use.cfm

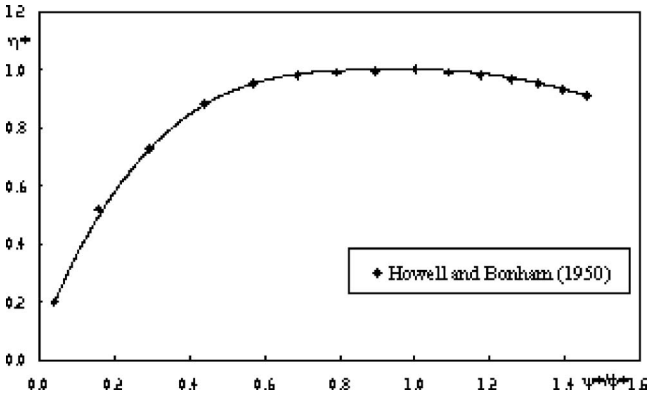

Fig. 5 Generalized stage efficiency curve [17]

$$M_{EX} = \frac{FF_{DES}}{\frac{\sqrt{T_{EX}}}{p_{EX}} \cdot \sqrt{R \Big/ \left[k \cdot \left(\frac{2}{k+1} \right)^{(k+1)/(k-1)} \right]}} \tag{12}$$

The value of M_{EX} calculated through Eq. (12) was divided into two terms by using a tuning parameter $X_{EX} \in [0,1]$ to take into account the fraction of extracted air used for the turbine cooling (M_{COOL}) and the remain on a mass flow (M_{LA}) which is assumed to be lost (bearing cooling or other). It results as follows

$$M_{COOL} = X_{EX} \cdot M_{EX}, \quad M_{LA} = (1 - X_{EX}) \cdot M_{EX}$$

Turbine Performance Evaluation. Turbine performances were evaluated by considering the turbine in choking conditions, which means a constant value of flow function (FF) at the turbine inlet. The flow function is defined by the following relation [21]

$$FF = \frac{M_{IT}\sqrt{T_{IT}}}{p_{IT}} \cdot \sqrt{R \Big/ \left[k \cdot \left(\frac{2}{k+1} \right)^{(k+1)/(k-1)} \right]}$$

The effect of turbine blade cooling on the expansion process was taken into account by assuming that the total turbine cooling air mass flow rate is mixed part upstream and part downstream of the turbine [21–23].

Wet Compression Model Validation

The wet compression model used in the IN.FO.G.T.E. program was validated by comparison with data available in the literature on this topic [6,10]. In particular the experimental results presented by Utamura et al. [6] were used as a test case.

To achieve this goal, the calculation code was tuned to simulate the behavior of a GE F9E gas turbine in dry conditions.

The simulation of wet compression on this machine was carried out with the code by considering the same ambient conditions, injected water amount, and droplets diameter described in the experimental test presented by Utamura et al. [6].

In Fig. 6 the power relative variation versus injected water to air ratio is reported with reference to the tests ambient conditions, which are 29.7°C of ambient temperature and 70% of relative humidity, and considering an injected droplet diameter equal to 10 μm. In particular, in this figure the experimental values (circle markers) are compared to the results obtained by the IN.FO.G.T.E calculation code (continuous line) and the ones estimated by Utamura et al. [6]. It should be noted that the calculation code estimates with a good accuracy the experimental data points; in particular the root mean square error between the experimental data and the calculated ones is equal to about 0.07.

In Fig. 7 the change in gas turbine efficiency due to water injection is presented. In this case, the calculation code developed also reproduced with an acceptable accuracy the available experimental values.

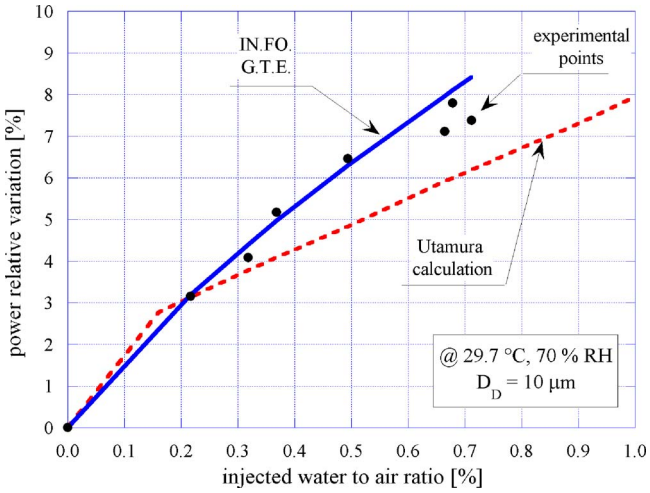

Fig. 6 Power relative variation versus injected water to air ratio: experimental data (circle marker), Utamura et al. [6] calculation (red dotted line), and IN.FO.G.T.E. code calculation (blue continuous line)

In Fig. 8 the evaporation rate (defined as the ratio between the evaporated water and the total injected water) as calculated by Utamura et al. [6] and by using the calculation, code developed is presented versus compressor length (including the compressor inlet duct) and injected droplet diameter (equal to 10 μm, 20 μm, and 30 μm). From the figure it can be observed that the two models estimate an evaporation rate quite different. This difference grows up as the droplet diameter increases. In particular the evaporation rate evaluated by the IN.FO.G.T.E. shows an exponential trend mainly due to Eq. (4), which estimates the droplet surface temperature change across the compressor. In the authors' opinion this evidence is coherent to the dynamics of the droplet evaporation. In fact, as the water droplets move ahead along the compressor, the diameters decrease, and the air pressure and temperature increase; this fact speeds up the water evaporation as shown in Fig. 8.

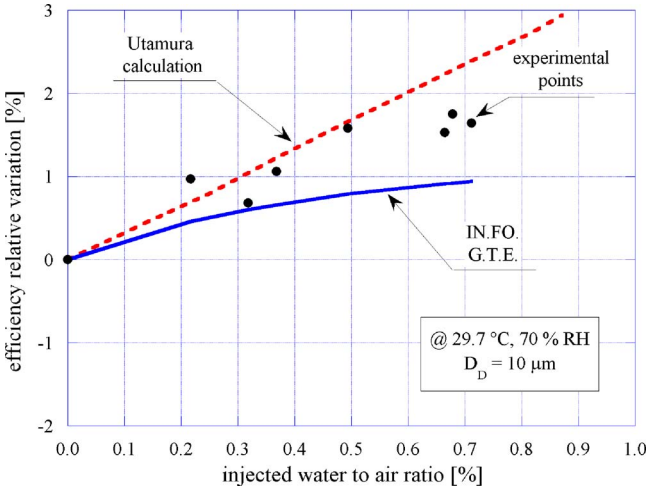

Fig. 7 Efficiency relative variation versus injected water to air ratio: experimental data (circle marker), Utamura et al. [6] calculation (red dotted line), and IN.FO.G.T.E. code calculation (blue continuous line)

Downloaded 02 Jun 2010 to 171.66.16.107. Redistribution subject to ASME license or copyright; see http://www.asme.org/terms/Terms_Use.cfm

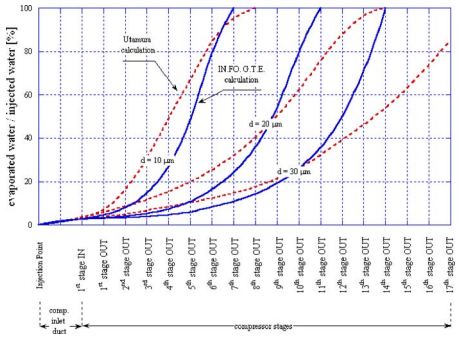

Fig. 8 Evaporated water to injected water ratio through the compressor for a GE F9E gas turbine: Utamura et al. [6] calculation (red dotted line) and IN.FO.G.T.E. code calculation (blue continuous line)

A last comparison for the calculation code validation was carried out by considering the results obtained by White and Meacock [10]. In particular, the analysis of wet compression was realized by considering the same generic 12 stage compressor (whose characteristics are reported in the Appendix) coupled with a turbine in the choking condition with constant inlet temperature and constant rotational speed.

The results obtained by the calculation code developed were compared to the ones presented by White and Meacock [10]. In

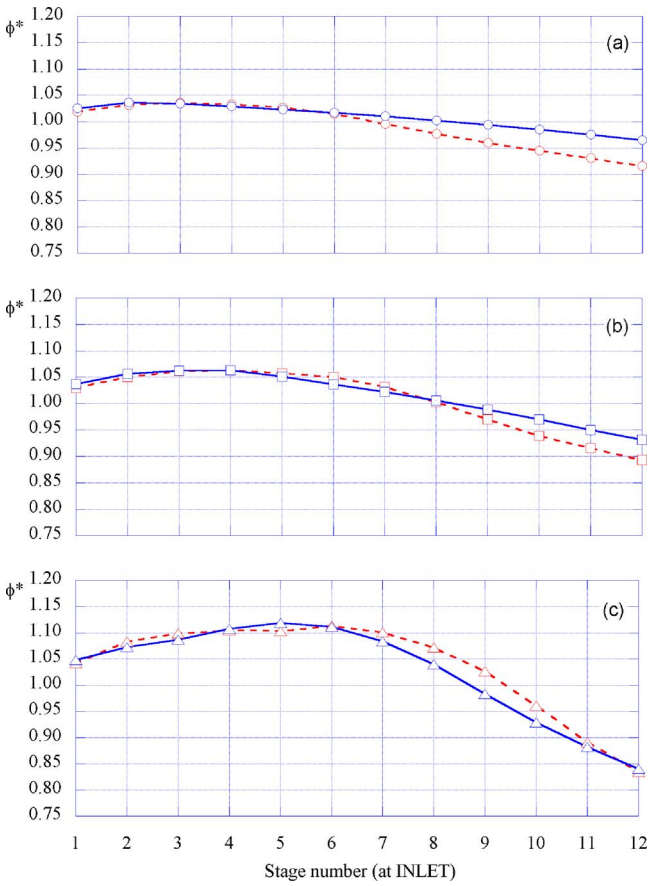

Fig. 9 Normalized flow coefficient change at the stage inlet as calculated by White and Meacock [10] (red dotted lines) and by IN.FO.G.T.E. code (blue continuous lines) versus stage number and water to air ratio: 1% (*a*), 2% (*b*), and 5% (*c*)—Reference: 15°C, 1.013 bar, 100% RH, D_D=5 μm

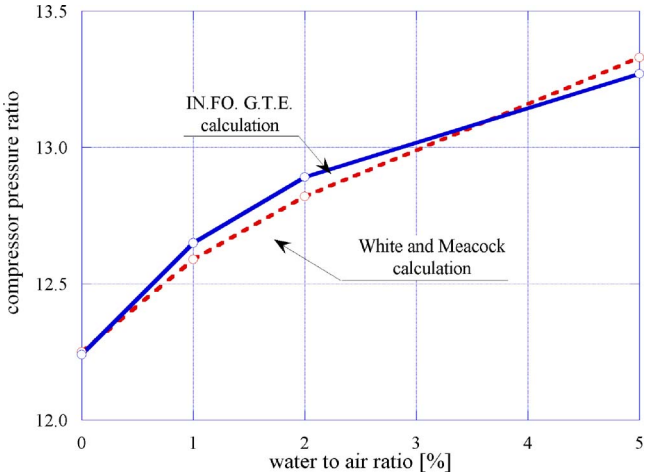

Fig. 10 Compressor pressure ratio change as calculated by White and Meacock [10] (red dotted line) and by the developed calculation code (blue continuous line) versus water to air ratio

Figs. 9(*a*)–9(*c*) the ratio between the flow coefficient with water injection (realized upstream of the compressor inlet) and its design value versus compressor stage number and injected water to air ratio (from 1% to 5%) is presented with reference to 15°C of air temperature, 1.013 bar of ambient pressure, and 100% of relative humidity, by considering a droplet diameter of injected water equal to 5 μm. It can be observed that there is good agreement between the results obtained by White and Meacock [10] and the calculation code. In particular, the root mean square error between the two series of data is equal to about 0.03.

Finally, in Fig. 10 the comparison between the increase in compressor pressure ratio due to water injection as evaluated by White and Meacock [10] and by the calculation code is presented. This figure also shows good agreement between results of White and Meacock [10] and the one obtained by the IN.FO.G.T.E. code.

Concluding Remarks

In the present paper a calculation code, developed in house by the authors, is presented and discussed. The code simulates the performance of a gas turbine with every fogging strategy (including the interstage injection).

The calculation code is able to estimates the evaporation of water during a compression process by solving the thermal exchange equations (taking into account both latent and sensible heat) between water droplets and air.

The code was validated on results available in the literature and in particular with the ones presented by Utamura et al. [6] and White and Meacock [10], showing a good agreement with experimental and theoretical results.

Acknowledgment

The authors wish to thank Professor Giorgio Negri di Montenegro and Professor Antonio Peretto for their support and suggestions during the realization of the present paper.

Downloaded 02 Jun 2010 to 171.66.16.107. Redistribution subject to ASME license or copyright; see http://www.asme.org/terms/Terms_Use.cfm

Nomenclature

c_L = liquid water specific heat
c_p = specific heat at constant pressure
D = diameter
D_V = diffusion coefficient
FF = flow function
h = enthalpy
k = specific heat ratio
M = mass flow rate
n_D = number of droplets
Nu = Nusselt number
p = pressure
R = gas constant, radius
SF = shape factor
t = time
T = temperature
V_X = axial flow velocity
W = molecular weight
X_{EX} = tuning parameter regarding the compressor air extraction
X_W = tuning parameter regarding the water evaporation
Δ = difference, variation
Δx = stage length
ϕ = flow coefficient
γ = 1/3 rule constant
η = efficiency
λ = thermal conductivity
ρ = density
ω = specific humidity
ω_L = specific humidity in saturated conditions
ψ_P = pressure coefficient

Subscripts and Superscripts

* = normalized value with respect to design value
AIR = air
COOL = cooling
D = water droplet
DES = design
EV = evaporated
EX = extracted
FUEL = fuel
IT = turbine inlet section
G = gas
L = relative to liquid water
LA = leakage
LAT = latent heat of evaporation
REF = reference state
S = saturation, steam
SMD = Sautern mean diameter
W = water

Acronyms

CALC = calculated
CC = combustion chamber
COMP = compressor
IN = stage inlet
IN_C = stage inlet downstream from the cooling fraction
OUT = stage outlet
OUT_C = stage outlet downstream from the cooling fraction
RH = relative humidity
TOLL = tolerance value
TURB = turbine

Appendix: Compressor Main Data

Table 1 Compressor geometry main data

Number of stages	12
Design pressure ratio	12.25
Rotational speed	5000 rpm
Design mass flow	156.75 kg/s
Mean blade radius	0.5 m
IGV exit angle	15.0 deg
Stator inlet angles	42.2 deg (stages 1, 12), 46.0 deg (stages 1–11)
Stator exit angles	15 deg
Rotor inlet angles	55.9 deg
Rotor exit angles	40.0 deg (stages 1, 12), 35.4 deg (stages 1–11)
Axial chord	40% blade height
Axial blade gaps	25% axial chord

Table 2 Compressor area schedule

Stage	Inlet area (m^2)
1	0.947
2	0.821
3	0.675
4	0.564
5	0.478
6	0.410
7	0.355
8	0.310
9	0.273
10	0.243
11	0.217
12	0.194

References

[1] Tawney, R., Pearson, C., and Brown, M., 2001, "Options to Maximize Power Output for Merchant Plants in Combined Cycle Applications," ASME Paper No. 2001-GT-0409.
[2] Bianchi, M., Melino, F., Peretto, A., Bhargava, R. K., Chaker, M. C., Ingistov, S., and Meher-Homji, C. B., 2005, "Gas Turbine Fogging Technology: A State of the Art Review, Part I: Inlet and Evaporative Fogging—Analytical and Experimental Aspects," ASME Paper No. GT2005-68336.
[3] Kleinschmidt, R. V., 1947, "Value of Wet Compression in Gas-Turbine Cycles," Mech. Eng. (Am. Soc. Mech. Eng.), **69**(2), pp. 115–116.
[4] Wilcox, E. C., and Trout, A. M., 1951, "Analysis of Thrust Augmentation of Turbojet Engines by Water Injection at Compressor Inlet Including Charts for Calculating Compression Process with Water Injection," NACA Report No. 1006.
[5] Hill, P. G., 1963, "Aerodynamic and Thermodynamic Effects of Coolant Injection on Axial Compressors," Aeronaut. Q., **1**, pp. 331–348.
[6] Utamura, M., Kuwahara, T., Murata, H., and Horii, N., 1999, "Effects of Intensive Evaporative Cooling on Performance Characteristics of Land-Based Gas Turbine," *Proceedings Joint Power Generation Conference*, p. 34.
[7] Horlock, J. H., 2001, "Compressor Performance with Water Injection," ASME Paper No. 2001-GT-0343.
[8] Zheng, Q., Sun, Y., Li, S., and Wang, Y., 2002, "Thermodynamic Analysis of Wet Compression Process in the Compressor of Gas Turbine," ASME Paper No. GT-2002-30590.
[9] Hartel, C., and Pfeiffer, P., 2003, "Model Analysis of High-Fogging Effects on the Work of Compression," ASME Paper No. GT-2003-38117.
[10] White, A. J., and Meacock, A. J., 2003, "An Evaluation of the Effects of Water Injection on Compressor Performance," ASME Paper No. GT-2003-38237.
[11] Cataldi, G., Gunter, H., Matz, C., McKay, T., Hoffman, J., Nemet, A., Lecheler, S., and Braun, J., 2004, "Influence of High Fogging Systems on Gas Turbine Engine Operation and Performance," ASME Paper No. GT2004-53788.
[12] Bagnoli, M., Bianchi, M., Melino, F., Peretto, A., Spina, P. R., Bhargava, R., and Ingistov, S., 2004, "A Parametric Study of Interstage Injection on GE Frame 7 EA Gas Turbine," ASME Paper No. GT-2004-53042.
[13] Ingistov, S., 2001, "Interstage Injection System for Heavy Duty Industrial Gas Turbine Model 7EA," ASME Paper No. 2001-GT-407.
[14] Ingistov, S., 2002, "Interstage Injection into Axial Compressor, Gas Turbine Model 7EA," ASME Paper No. GT-2002-30656.
[15] Sparrow, E. M., and Gregg, J. L., 1958, "The Variable Fluid Property Problem in Free Convection," Trans. ASME, **80**, 879–886.

Downloaded 02 Jun 2010 to 171.66.16.107. Redistribution subject to ASME license or copyright; see http://www.asme.org/terms/Terms_Use.cfm

[16] Eckert, E. R. G., and Drake, R. M., Jr., 1959, *Heat and Mass Transfer*, 2nd ed., McGraw-Hill, New York.
[17] Spina, P. R., 2002, "Gas Turbine Performance Prediction by Using Generalized Performance Curves of Compressor and Turbine Stages," ASME Paper No. GT-2002-30275.
[18] Muir, D. E., Saravanamuttoo, H. I. H., and Marshall, D. J., 1989, "Health Monitoring of Variable Geometry Gas Turbines for the Canadian Navy," ASME J. Eng. Gas Turbines Power, **111**, pp. 244–250.
[19] Howell, A. R., and Bonham, R. P., 1950, "Overall and Stage Characteristics of Axial Flow Compressors," Proc. Inst. Mech. Eng., **163**, pp. 235–248.
[20] Csanady, G. T., 1964, *Theory of Turbomachines*, McGraw-Hill, New York.
[21] *Thermoflow 15, release 1*, 2005, Thermoflow Inc., Sudbury, MA.
[22] Benvenuti, E., Bettocchi, R., Cantore, G., Negri di Montenegro, G., and Spina, P. R., 1993, "Gas Turbine Cycle Modeling Oriented to Component Performance Evaluation from Limited Design or Test Data," *Proceedings 7th ASME COGEN—TURBO*, Bournemouth, UK, IGTI, Vol. 8, pp. 327–337.
[23] Bettocchi, R., and Spina, P. R., 1997, "Influence of the Control Logic on Gas Turbine Operation," ASME Paper No. 97-AA-127.

Downloaded 02 Jun 2010 to 171.66.16.107. Redistribution subject to ASME license or copyright; see http://www.asme.org/terms/Terms_Use.cfm

Comparison of Recuperator Alloy Degradation in Laboratory and Engine Testing

Bruce A. Pint
e-mail: pintba@ornl.gov

Karren L. More

Rosa Trejo

Edgar Lara-Curzio

Materials Science and Technology Division,
Oak Ridge National Laboratory,
Oak Ridge, TN 37831-6156

In order to increase the efficiency of advanced microturbines, durable alloy foils are needed for their recuperators to operate at 650–700°C. Prior work has demonstrated that water vapor in the exhaust gas causes more rapid consumption of Cr from austenitic alloys, leading to a reduction in lifetime for the thin-walled components in this application. New commercial alloy foils are being tested in both laboratory tests in humid air and in the exhaust gas of a modified 60 kW microturbine. Initial results are presented for a commercial batch of 80 μm alloy 120 foil. The Cr consumption rates in laboratory testing were similar to those observed in previous testing. The initial results from the microturbine indicate a faster Cr consumption rate compared to the laboratory test, but longer term results are needed to quantify the difference. These results will help to verify a Cr consumption model for predicting lifetimes in this environment based on classical gas transport theory. [DOI: 10.1115/1.2436565]

Introduction

Distributed generation is an attractive solution both for energy security and energy efficiency demands. In cases of transmission line failure, natural disaster, or terrorist events, the capability for on-site power generation can maintain a variety of critical services, including communications and medical care. Although reciprocating engines have long met this need, small (25–300 kW) gas turbines or microturbines [1,2] offer an additional potential advantages due to their fuel flexibility, lower emissions, and use of waste heat (i.e., combined heat and power [3,4]), which greatly increases their overall efficiency.

Two problems limiting marketplace acceptance of microturbines are cost and electrical efficiency (currently, <30%), especially in the current environment of increasing fuel costs. Because of the relatively small size and single-shaft design of most microturbines, there are not many opportunities for improving their efficiency except by increasing the recuperator (i.e., heat exchanger) efficiency or by increasing the turbine inlet temperature, which also increases the recuperator operating temperature [5].

There are a number of different recuperator designs, but most employ thin-walled components in order to maximize specific heat transfer [5–7]. The most widely used material has been type 347 stainless steel foil (~100 μm thick, composition in Table 1) because of its excellent combination of creep and corrosion resistance. However, over the past decade it has become clear that, for recuperator temperatures above ~590°C (1100°F), serious durability problems have been encountered for type 347 foils [8–10]. It is now widely recognized that this accelerated degradation in exhaust gas is due to the presence of water vapor and that all chromia-forming alloys exhibit greater degradation in the presence of water vapor due to the volatilization of the oxy-hydroxide, $CrO_2(OH)_2$ [11,12].

In the past few years, a number of replacement materials have been investigated and implemented. For example, alloy 625 is being used in the recuperator of a 4 MW engine [13] and alloy 120 is being studied for use in a 60 kW microturbine [14]. A less expensive alternative material is Nb-modified Fe-20Cr-25Ni, which had been developed in the 1950s by the British nuclear materials program and was subsequently developed as a tube alloy, 709 [15]. This material is now commercially available in foil form [16]. However, it was recently demonstrated that all of these advanced alloys lose Cr at approximately the same rate during laboratory exposures in humid air at 650–700°C, seemingly independent of Cr, Ni, or Mn content [17]. Furthermore, even with their high Cr and Ni contents, the Fe-base alloys in foil form, 120 and 709, formed Fe-rich oxide nodules at 650°C. The reason for the nodule formation was that the near-surface region, and, particularly, the alloy grain boundaries, became depleted in Cr because of evaporation of the reaction product and the diffusion of Cr in the alloy at that temperature is not fast enough to resupply the surface. Extrapolation of the Cr loss rates measured after 10,000 hr exposures to the desired 40,000 hr minimum service life indicated potential problems for all of these alloys. However, there is no correlation data available between laboratory and actual recuperator exposures. This paper reports the initial comparison results of Cr depletion from commercial 80 μm foil alloy 120 exposed in laboratory testing and in the exhaust gas of a modified 60 kW microturbine [18]. Because of the short duration of the microturbine exposure (1000 hr), it is difficult to quantify the difference between the two tests. Qualitatively, it appears that the depletion is much more significant in the exhaust gas compared to the laboratory test.

Experimental Procedure

The material tested in this study was commercially fabricated 80 μm alloy 120 foil with an average grain size of 23 μm (Fig. 1). Chemical composition from a piece of bulk alloy 120 material is provided in Table 1. For comparison, results from other commercial foils also are included.

For the laboratory test, specimens (~12×18 mm) were tested in the as-rolled condition and were cleaned in acetone and methanol prior to oxidation. Mass changes were measured using a Mettler-Toledo model AG245 balance. Exposures were 100 hr cycles at 650°C, 700°C, or 800°C. Oxidation exposures in humid air were conducted by flowing the gas at 850 cc/min through an alumina tube that was inside a resistively heated tube furnace. Distilled water was atomized into the flowing gas stream above its condensation temperature and heated to the reaction temperature within the alumina tube. The amount of water flowing through the

Contributed by the International Gas Turbine Institute (IGTI) of ASME for publication in the JOURNAL OF ENGINEERING FOR GAS TURBINES AND POWER. Manuscript received June 20, 2006; final manuscript received July 3, 2006; published online December 13, 2007. Review conducted by Dilip R. Ballal. Paper presented at the ASME Turbo Expo 2006: Land, Sea and Air (GT2006), May 8–11, 2006, Barcelona, Spain. Paper No. GT2006-90194.

Copyright © 2008 by ASME

Downloaded 02 Jun 2010 to 171.66.16.107. Redistribution subject to ASME license or copyright; see http://www.asme.org/terms/Terms_Use.cfm

Table 1 Alloy chemical compositions (weight percent) and average grain sizes (micrometers) of the foil and sheet materials

	Cr	Ni	Mn	Si	Nb	Mo	Other	Grain size (μm)
Type 347	17.8	9.9	1.6	0.5	0.5			5
709	20.3	24.7	1.0	0.4	0.2	1.5		16
20/25+Nb	20.3	25.4	1.1	0.3	0.4	1.5		10
120	24.7	37.6	0.7	0.2	0.6	0.3		23
625	23.1	63.8	0.04	0.2	4	8.9	3Fe	12

tube was measured to calculate its concentration and calibrate the amount of injected water. A water content of 10 ± 1 vol % was used for these experiments. Up to 40 specimens were positioned in alumina boats in the furnace hot zone so as to expose the specimen faces to the flowing gas. For testing in air, the alumina furnace tubes were not sealed.

The engine exposures were conducted in a modified 60 kW Capstone Turbine Corp. microturbine located at ORNL. The turbine was modified to allow higher turbine exit temperatures and placement of six ports at the entrance to the recuperator where specimen holders can be inserted. Details of the port locations and specimen holder are provided elsewhere [18,19]. Foil specimens were formed with a 23.1 mm dia and were laser welded onto four locations on the holder with one thermocouple at each location. The temperature along the holder varied from 720°C to 600°C. The foils were internally pressurized at 0.4 MPa (60 psi) resulting in a ~50 MPa stress in the foil. This reproduces the stress state in a primary surface recuperator during typical operation, where the foil has compressed inlet air on one side and exhaust gas at near ambient pressure on the other side.

After oxidation, specimens were Cu plated or mounted directly in epoxy and sectioned for metallographic analysis and electron probe microanalysis (EPMA) to determine Cr depletion. In general, three composition profiles across the foil thickness were performed with a 1 μm step size and summed to determine the residual Cr content in the specimen.

Results

Laboratory Testing in Humid Air. Specimens of two commercial foils, alloys 120 and 20/25+Nb, are being tested under the same conditions as prior work [10,17] at 650°C, 700°C, and 800°C. An example of the mass gain data is shown in Fig. 2. For comparison, the mass gain for commercial type 347 foil is shown where an accelerated mass gain was observed after <2000 hr of testing at 650°C. The new batches of commercially rolled material are showing similar mass gain behavior as the previous laboratory rolled foils with similar compositions (Table 1). However, the information that can be learned from the specimen mass gain data is limited because it is the summation of several mechanisms, including oxide scale growth, evaporation, and spallation of the scale,

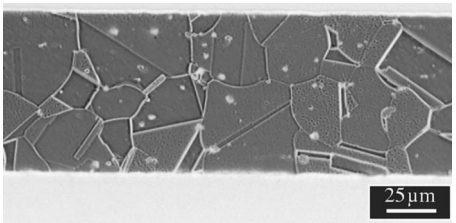

Fig. 1 Light microscopy of polished cross sections of as-received 80 μm alloy 120 foil

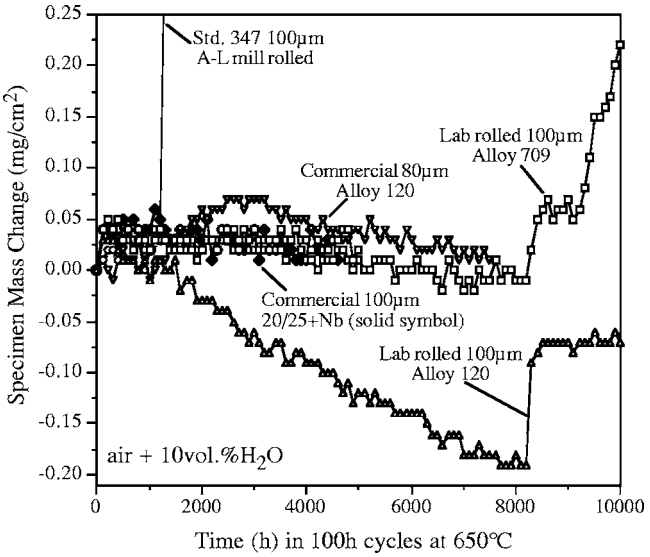

Fig. 2 Specimen mass gains for various foil materials during 100 hr cycles in humid air at 650°C

$$\Delta M_{\text{specimen}} = \Delta M_{\text{oxide growth}} - \Delta M_{\text{evap.}} - \Delta M_{\text{spall}}$$

In this work, there was no evidence of scale spallation; thus, oxide growth and oxy-hydroxide evaporation are summed in the data. In general, the mass gain can be used to identify the onset of accelerated attack but is not very useful in quantifying the amount of Cr lost because of these competing factors.

Individual specimens of 80 μm alloy 120 foil were stopped after 1000 hr and 5000 hr for characterization. Figure 3 shows polished cross sections of these specimens. In general, the oxide increased in thickness with time and temperature. However, the oxide appeared slightly thinner at 700°C compared to 650°C (Figs. 3(*a*) and 3(*c*)). At all conditions, internal penetrations were observed. At 650°C, a few small Fe-rich oxide nodules had begun to form (Figs. 3(*a*) and 3(*b*)).

To illustrate the effect of water vapor on the oxidation of this material, Fig. 4 shows a comparison after 10,000 hr exposures at 700°C for 90 μm commercial alloy 120 foil. The specimen exposed in laboratory air (Fig. 4(*b*)) had a much thinner oxide scale than the specimen exposed in humid air (Fig. 4(*a*)). However, occasional penetrations and small nodules were observed.

Microturbine Exposures. A set of alloy 120 foil specimens were removed from the microturbine specimen holder after 1000 hr. Figure 5 shows polished cross sections for the specimens exposed at the four specimen holder locations with temperatures of 720°C, 690°C, 670°C, and 600°C. As with the laboratory exposures, internal penetrations were observed at each temperature. Nodule formation was observed at the higher temperatures. A very thin reaction product was observed at the two lower temperatures. Although these temperatures were not exactly the same as those in the laboratory test, comparing Figs. 3(*a*), 3(*c*), and 5, the scale thicknesses in the two tests after 1000 hr do not correlate particularly well with temperature.

Characterization by EPMA. To quantify the relative Cr depletion in the two tests, composition profiles were measured using EPMA. Figure 6 gives example profiles for some of the foils shown in Fig. 3. (The EPMA profiles are in atomic percent so the Cr contents are higher than the weight percent in Table 1.) Chromium depletion was concentrated near the specimen surface with the Cr composition at the center of the foil remaining relatively unchanged. Occasional peaks in the profiles are attributed to Cr-rich carbides [20]. As with the oxide thickness, the amount of Cr depletion did not increase with temperature between 650°C and

Downloaded 02 Jun 2010 to 171.66.16.107. Redistribution subject to ASME license or copyright; see http://www.asme.org/terms/Terms_Use.cfm

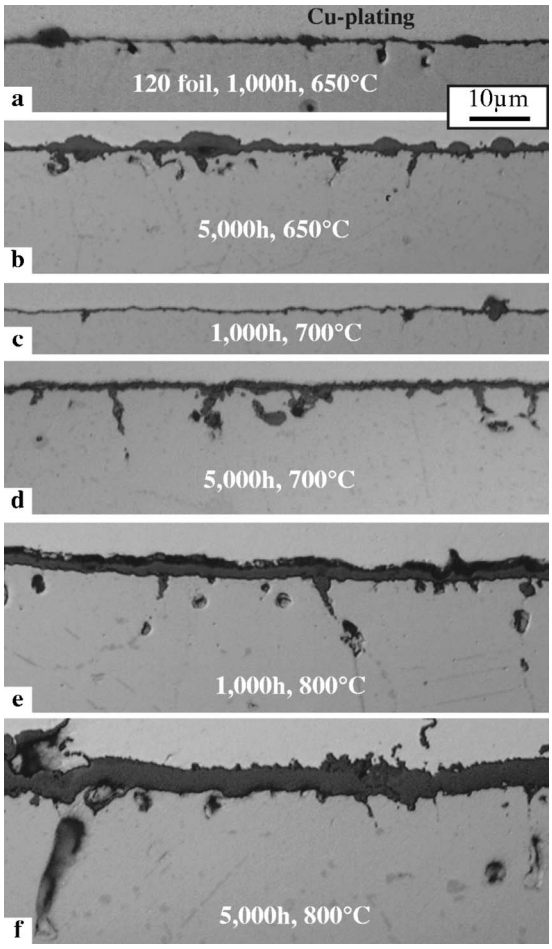

Fig. 3 Light microscopy of polished cross sections of 80 μm alloy 120 foil oxidized in humid air for (a) 1000 hr at 650°C, (b) 5000 hr at 650°C, (c) 1000 hr at 700°C, (d) 5000 hr at 700°C, (e) 1000 hr at 800°C, and (f) 5000 hr at 800°C

700°C. The depletion after exposure for 5000 hr at 650°C (Fig. 6(*a*)) was much more distinct than that observed after 5000 hr at 700°C. At 800°C, a large amount of depletion was observed after only 1000 hr (Fig. 6(*d*)). The depletion in each case was fairly uniform on both sides of the specimen.

For the specimens exposed to the microturbine, the profiles were less pronounced due to the relatively short exposure. Figure 7 shows profiles from the highest temperature, 720°C, after 1000 hr. Only one side of the specimen was exposed to the exhaust gas, and as expected, this side showed more Cr depletion.

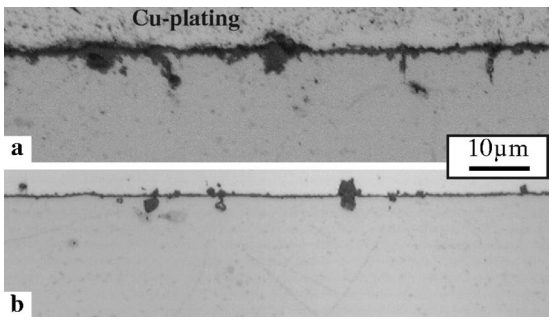

Fig. 4 Light microscopy of polished cross sections of 90 μm alloy 120 foil oxidized for 10,000 hr at 700°C in (a) humid air and (b) laboratory air

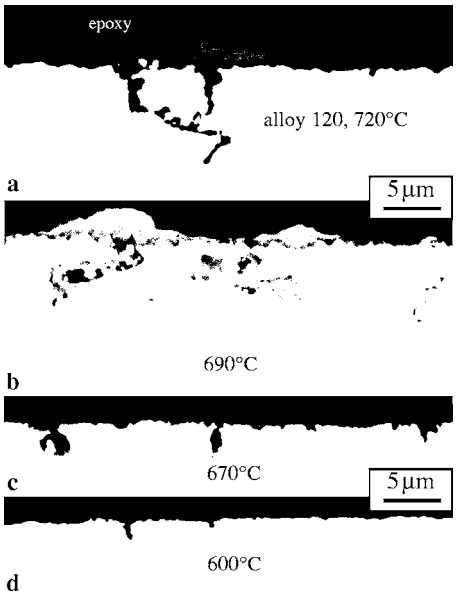

Fig. 5 Secondary electron images of polished cross sections of alloy 120 foil exposed for 1000 in the exhaust gas of a 60 kW microturbine. The specimens were exposed at (a) 720°C, (b) 690°C, (c) 670°C, and (d) 600°C.

One of the profiles showed more depletion than the other (arrow in Fig. 7) due to intersection with one of the alloy grain boundaries. As shown previously [17], at 650–700°C, the Cr depletion is higher on alloy grain boundaries near the surface due to increased Cr diffusion along these boundaries. To illustrate this, Fig. 8 shows EPMA Cr and O maps from three of the microturbine exposures. The Cr maps show the surface oxide scale on both sides is enriched in Cr as are the alloy grain boundaries due to carbide formation. However, near the surface exposed to exhaust gas (top of each map), the alloy grain boundaries go from enriched (bright) to depleted (dark). In several cases, oxide has penetrated down the grain boundaries and Fe-rich oxide nodules (arrows in O maps) tend to nucleate above depleted alloy grain boundaries. On the side not exposed to the exhaust gas, no nodules or penetrations were observed. These depletion observations are very similar to those reported previously for foils of alloys 709, 120, and 625 [17]. Thus, the less-depleted profile in Fig. 7 was not near an alloy grain boundary, while the other was on a boundary.

To quantify the Cr depletion, the profiles were used to determine the remaining metal thickness and the Cr content at each 1 μm increment was summed and compared to profiles from the starting thickness and Cr content to determine the amount of Cr lost. Table 2 summarizes some previously obtained results after 10,000 hr laboratory exposures in humid air where the depletion layer was very distinct. After 10,000 hr, the Cr depletion in alloy 120 specimens increased with temperature from 650–800°C.

In the shorter term exposures in this study, the summation did not yield a statistically significant depletion after many of the 1000 hr exposures. Even the 5000 hr exposure at 700°C only showed a small depletion. Figure 9 summarizes the depletions that were measurable and their standard deviations. These points are plotted along with the previous 10,000 hr data points for alloy 120 foils, and the lines fit the data at each condition. For the laboratory exposures, substantial depletion was observed after 5000 hr at 650°C, where more distinct depletion profiles were evident (Fig. 6(*a*)) and for 1000 hr and 5000 hr exposures at 800°C. For comparison to the data in humid air, an alloy 120 foil specimen exposed for 5000 hr in laboratory air showed 1/3 less Cr depletion without water vapor.

Downloaded 02 Jun 2010 to 171.66.16.107. Redistribution subject to ASME license or copyright; see http://www.asme.org/terms/Terms_Use.cfm

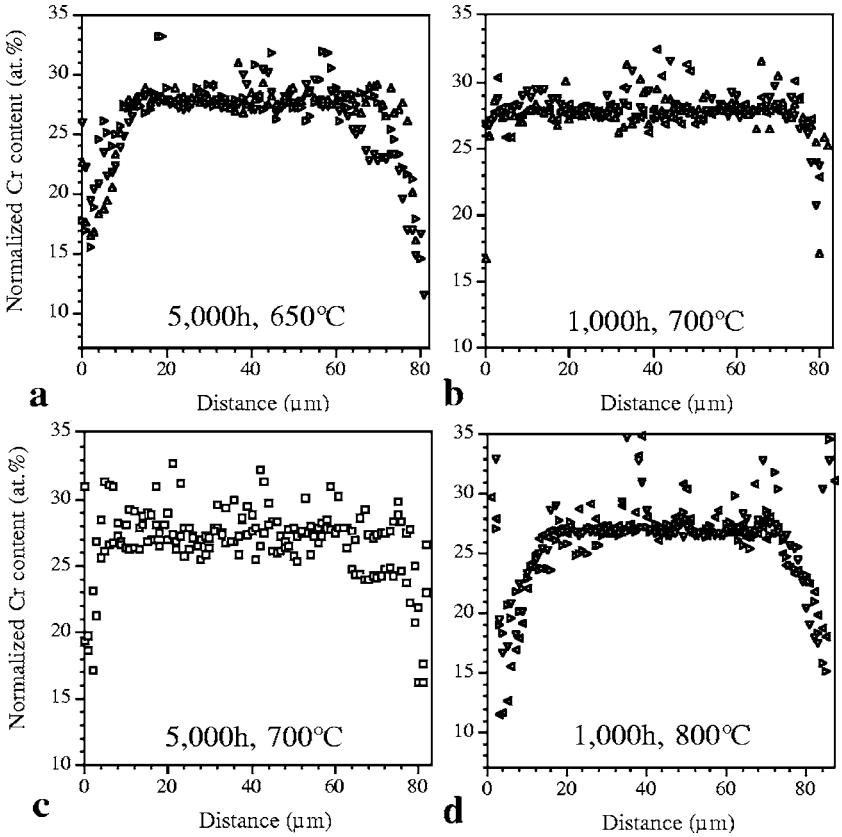

Fig. 6 EPMA Cr profiles from three scans across the cross section of alloy 120 foils after laboratory exposures in humid air for (a) 5000 hr at 650°C, (b) 1000 hr at 700°C, (c) 5000 hr at 700°C, and (d) 1000 hr at 800°C

The foil exposed to exhaust gas for 1000 hr at 720°C was the only specimen from the microturbine to show a significant depletion. The exposures at lower temperatures did not show distinct profiles like this specimen (Fig. 7). However, because the two profiles were so different, a very high standard deviation was obtained. Additional profiles need to be measured to obtain a more accurate assessment of the Cr depletion in this specimen.

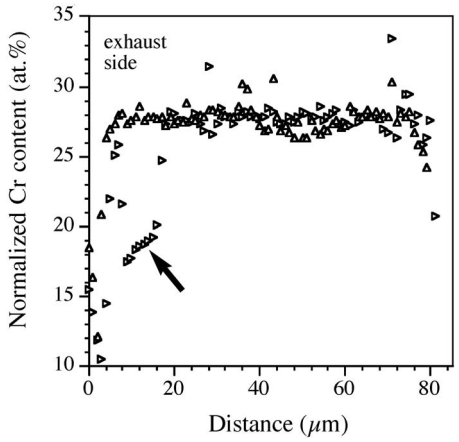

Fig. 7 EPMA Cr profiles from two scans across the cross section of alloy 120 foil after exposures in a microturbine recuperator for 1000 hr at 720°C. The side exposed to the exhaust gas is marked.

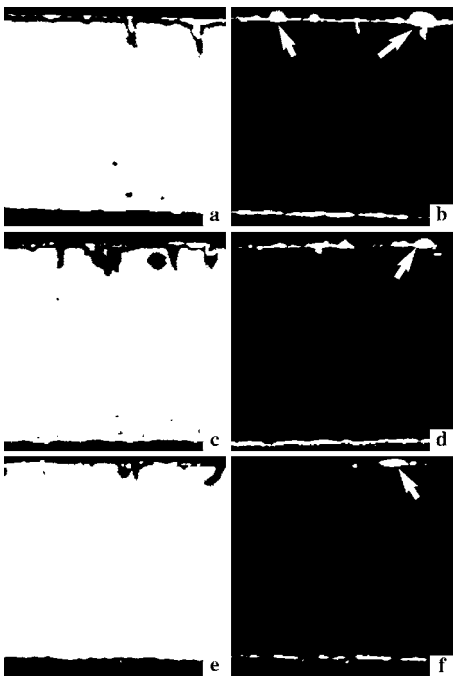

Fig. 8 EPMA Cr (a,c,e) and O (b,d,f) maps of 80 μm alloy 120 foil after 1000 hr exposures in exhaust gas at (a,b) 720°C, (c,d) 690°C, and (e,f) 670°C. The exhaust gas side is up in these images.

Downloaded 02 Jun 2010 to 171.66.16.107. Redistribution subject to ASME license or copyright; see http://www.asme.org/terms/Terms_Use.cfm

Table 2 Amount of Cr consumed (weight percent) for various foil materials oxidized in humid air for 10,000 hr (except where noted). The standard deviation for three EPMA profiles is shown.

Alloy	650°C	700°C	800°C
709	−1.7±1.0%	−2.2±0.8%	−10.2±0.5%[a]
120 (ORNL roll)	−2.0±0.3%	−2.7±0.6%	
120 (Commercial)		−2.5±0.9%	−12.2±0.3%

[a]after 6000 hr.

Model Development. The first step in the development of a lifetime model was completed by applying classical gas transport theory to the Cr evaporation assuming the evaporation of $CrO_2(OH)_2$ occurs by the reaction,

$$\frac{1}{2}Cr_2O_3(s) + \frac{3}{4}O_2(g) + H_2O(g) = CrO_2(OH)_2(g) \quad (1)$$

Details of this analysis are available elsewhere [21]. The experimental Cr depletion results for alloy 709 foil specimens [17] were compared to calculations based on recent $CrO_2(OH)_2$ thermodynamic data from E. Opila at NASA Glenn Research Center. By using the experimental gas composition, specimen length l and velocity v, a good match was obtained between the calculation and the experimental results (Fig. 10). Thus, it is reasonable to assume that this evaporation mechanism is responsible for the Cr loss and the accelerated corrosion observed in the recuperator.

The next step in the model development was to perform the same calculations based on the recuperator conditions. One of the most important variables for this calculation was the v/l ratio and its effect on the Cr loss flux, J_{Cr}, at several temperatures, as shown in Fig. 11. The expected v/l ratio in the recuperator is marked as well as the conditions for the laboratory test in Fig. 11. The other differences between the two conditions are the water vapor content (10% in the laboratory test is nominally twice that expected in the engine exhaust) and that only one side of the foil is exposed to the exhaust gas in the recuperator. The net is an expected factor of 2 increase in Cr loss in the recuperator compared to the laboratory test. Unfortunately, the depletion from the current specimens are not significant enough to reliably quantify using the current EPMA technique to verify the difference between these conditions.

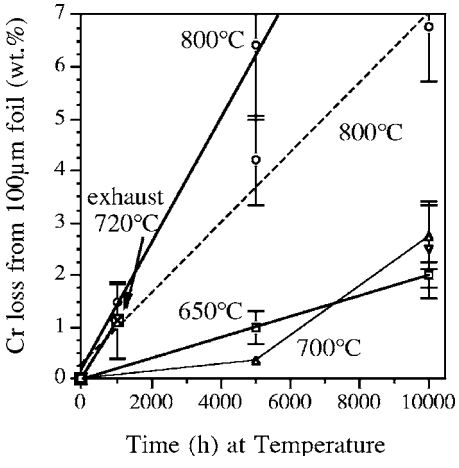

Fig. 9 Chromium mass losses from alloy 120 foil specimens as a function of time after exposures to air+10%H_2O (solid lines) at 650–800°C and exhaust gas at 720°C. Values for 800°C exposures in laboratory air (dashed line) are shown for comparison.

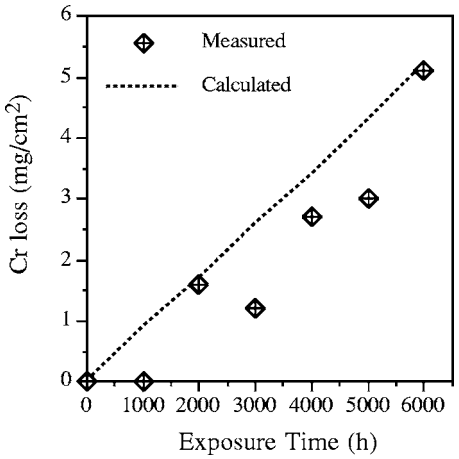

Fig. 10 Comparison of the calculated and measured Cr loss from alloy 709 foils exposed to humid air at 800°C

Discussion

A correlation between laboratory and engine testing is one of the final unresolved issues remaining in quantifying the degradation of austenitic steels in the recuperator environment. The present mechanistic model suggests that Cr is being lost at a linear rate due to the formation of $CrO_2(OH)_2$. Once the alloy is depleted in Cr, an accelerated attack occurs, resulting in FeO_x nodule formation and rapid loss of metal, which cannot be tolerated in a thin-walled recuperator. The linear kinetics of this mechanism allow the 10,000 hr laboratory data to be easily extrapolated to a 40,000 hr or longer exposure. However, the conditions in the recuperator are significantly different from those in the laboratory test and Cr depletion rates are needed as a function of temperature to predict lifetimes in the recuperator application.

Because of the much higher gas velocity in the recuperator, it is anticipated that Cr evaporation will be faster in that environment. Because of the difference in v/l, the calculation predicted a factor of 8 higher [21]. However, the 10% water vapor in the laboratory test was approximately twice that in exhaust gas. Based on Eq. (1), with a constant oxygen partial pressure, the partial pressure of $CrO_2(OH)_2$ should be proportional to the H_2O pressure and thus be reduced by a factor of 2. Also, the laboratory test exposed both sides of the specimen to humid air, whereas only one side is exposed in the recuperator. Thus, a net-factor-of-2 higher rate in

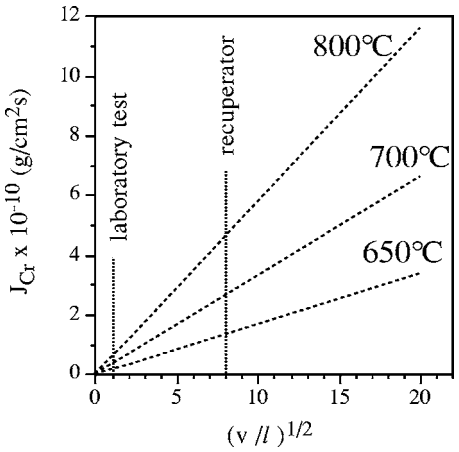

Fig. 11 Calculated Cr loss fluxes as a function of $(v/l)^{1/2}$ for air+5%H_2O at 650–800°C. Vertical dashed lines mark conditions in the laboratory test compared to the approximate conditions in a recuperator.

Downloaded 02 Jun 2010 to 171.66.16.107. Redistribution subject to ASME license or copyright; see http://www.asme.org/terms/Terms_Use.cfm

the recuperator was predicted [21]. Comparing the depletion profiles in Fig. 7 for the recuperator at 720°C to those in Fig. 6(*b*) for the 700°C laboratory test qualitatively confirms that the depletion in exhaust gas was faster than in the laboratory test. The loss in the recuperator at 720°C was similar to the laboratory test at 800°C (Fig. 9). However, the standard deviations were very different. Additional profiles need to be measured for the former specimen to obtain a more reliable Cr depletion. However, longer exposures in the microturbine with higher Cr depletion levels will make it much easier to measure the depletion and provide the needed effect of temperature on the rate.

The effect of temperature does not appear as straightforward in the laboratory test as in the microturbine results. In the laboratory tests, the oxide scale and Cr depletion were noticeably higher at 650°C compared to 700°C. This difference may be due to the formation of a higher Cr content oxide at the higher temperature. In general, it would be expected that better selective oxidation of Cr would occur at higher temperature (due to faster Cr diffusion in the alloy), possibly changing the scale from a faster-growing Fe-Cr spinel to a slower-growing chromia. Characterization of the scale on long-term exposures of a FeCr alloy showed this change with temperature [22], as did short term exposures of NiCr alloys [23]. Thus, a slower-growing oxide may have formed at the higher temperature, resulting in a thinner oxide and less alloy depletion.

The effect of temperature on the evaporation rate also may play a role. Because of the combination of scale growth and evaporation, paralinear kinetics have been observed and should result in a steady-state scale thickness [24]. A typical paralinear reaction is

$$\frac{dX}{dt} = \frac{k_p}{t} - k_{ev}\frac{dX}{dt} \tag{2}$$

where X is the scale thickness, t is time, k_p is the parabolic rate constant for diffusion-controlled scale growth, and k_{ev} represents the vaporization loss rate. Once the scale reaches this steady-state thickness X_{ss}, when $dX/dt=0$, continued exposure should result in temperature-dependent evaporation controlling further Cr depletion

$$\Delta M_{\mathrm{Cr}} = k_{ev}t + X_{ss}N_{\mathrm{Cr}} \tag{3}$$

where ΔM_{Cr} is the cumulative mass loss of Cr and N_{Cr} is the concentration of Cr in the scale of thickness X_{ss}. Thus, at long times (e.g., <2000 hr at 650°C), where changes in ΔM_{Cr} are dominated by k_{ev} and the specimen mass begins to decrease with time (Fig. 2), the effect of temperature on the evaporation rate will eventually become clear. Comparing the Cr depletion levels at 650°C and 700°C, the measured depletion was initially lower at 700°C (Fig. 9). However, after 10,000 hr, the amount of Cr loss was higher at 700°C than at 650°C, indicating an increase in k_{ev} with temperature.

For the exposures in the microturbine, it was not possible to quantify the exact depletion at the lower temperatures. However, the Cr maps in Fig. 8 qualitatively indicate more degradation and associated depletion at 720°C than at the lower temperatures, where the depth of grain boundary depletion was lower and fewer and smaller oxide penetrations and nodules formed.

The exact mechanism by which water vapor (or perhaps H_2) increases the scale growth rate (e.g., Fig. 4) or causes nodule formation on the Cr-depleted substrate has not been determined. However, these mechanisms do not appear to be critical to quantifying the degradation rate. Comparing Figs. 3(*d*) and 4(*a*) the Cr-rich oxide scale does not appear to increase in thickness much between 5000 hr and 10,000 hr at 700°C in the laboratory test. Thus, most of the Cr being lost from the foil substrate in this time period is likely due to the evaporation mechanism.

The specimens in the exhaust gas exposure also were subject to a hoop stress of ~50 MPa. The effect of stress on degradation in this environment has not been well studied. The penetrations observed for these samples in Fig. 5 may lead to the assumption that this resulted from the applied stress. However, the same penetrations were observed in the unstressed laboratory specimens (Fig. 4). Another assumption is that the applied stress will have a negative effect on performance. In the literature, applied stress has been observed to both increase and decrease the oxidation rate of chromia-forming alloys [25,26]. Where stress resulted in a thinner, more Cr-rich oxidation product, the result was attributed to increased Cr diffusion in the alloy. Enhanced diffusion could be critical in this application where the relatively slow diffusion of Cr in the alloy at 650°C results in the high Cr depletion rates at the foil surface. Thus, this issue needs to be carefully examined to determine the role of stress in this system.

There also is a possibility that other reaction products in the gas stream or impurities affect the rate of corrosion in the microturbine. Species such as CO or CO_2 have been shown to internally carburize austenitic steels at these temperatures [27]. Longer-term exposures may provide more insight into a potential carburization mechanism. However, higher Cr contents tended to reduce the extent of internal carburization [27]. Regarding fuel impurities or ingested dust, there was no evidence in the current specimens of any surface deposits that may have accelerated the corrosion rate.

If the present model were correct and the Cr depletion rate is twice that of the laboratory test, then the depletions in Table 2 extrapolate to very high Cr depletions after 40,000 hr. These results suggest that alloy 120 would lose 50% of its Cr content at 650°C after 40,000 hr. However, the deviations on these measured values are quite large resulting in an unreliable prediction.

Another factor that needs to be further considered is the eventual formation of a thick Fe-rich oxide layer on almost any austenitic alloy in this application. Based on the nodule formation observed in both experiments, a layer will likely form at some point in service. It is not certain if a continuous Fe-rich oxide layer on the surface could reduce the Cr depletion rate by inhibiting the evaporation of the oxy-hydroxide. However, this layer needs to be considered in modeling recuperator performance in terms of heat transfer. A thick surface oxide may significantly reduce the effectiveness of the recuperator during long-term service.

Summary

Initial results were presented comparing specimens of commercial 80 μm alloy 120 foil exposed in humid air in a low-velocity laboratory test to specimens exposed in the exhaust gas of a 60 kW microturbine. After 1000 hr in the microturbine exhaust, Cr depletion is clearly evident at the highest exposure temperature. However, the quantification error is sufficiently large that it is difficult to extrapolate the data to longer times or compare it to results for the laboratory test. The same material has been exposed for 5000 hr in laboratory testing. Qualitatively, the Cr depletion was higher in the microturbine exposures. However, longer-term exposures will make it easier to quantify this difference and provide more information on the effect of temperature on the depletion rate.

Acknowledgment

The author would like to thank J. L. Moser, G. W. Garner, H. Longmire, and L. R. Walker at ORNL for assistance with the experimental work, D. J. Young, University New South Wales, for developing the model as a visiting scientist at ORNL, and D. J. Young, P. J. Maziasz, S. Dryepondt, and P. F. Tortorelli for comments on the paper. This research was sponsored by the U.S. Department of Energy, Distributed Energy and Electrical Reliability Program under Contract No. DE-AC05-00OR22725 with UT-Battelle, LLC.

References

[1] Watts, J. H., 1999, "Microturbines: A New Class of Gas Turbine Engine," Global Gas Turbine News, **39**(1), pp. 4–8.
[2] Hamilton, S. L., 2003, *The Handbook of Microturbine Generators*, PennWell Corp., Tulsa.

Downloaded 02 Jun 2010 to 171.66.16.107. Redistribution subject to ASME license or copyright; see http://www.asme.org/terms/Terms_Use.cfm

[3] Maidment, G. G., and Tozer, R. M., 2002, "Combined Cooling Heat and Power in Supermarkets," Appl. Therm. Eng., **22**, pp. 653–665.
[4] Pilavachi, P. A., 2002, "Mini- and Micro-Gas Turbines for Combined Heat and Power," Appl. Therm. Eng., **22**, pp. 2003–2014.
[5] McDonald, C. F., 2003, "Recuperator Considerations for Future Higher Efficiency Microturbines," Appl. Therm. Eng., **23**, pp. 1463–1487.
[6] Omatete, O., Maziasz, P. J., Pint, B. A., and Stinton, D. P., 2000, "Recuperators for Advanced Microturbines," Report No. ORNL/TM-2000/304, Oak Ridge National Laboratory, Oak Ridge, TN.
[7] Kesseli, J., Wolf, T., Nash, J., and Freedman, S., 2003, "Micro, Industrial, and Advanced Gas Turbines Employing Recuperators," International Gas Turbine & Aeroengine Congress & Exhibition, Atlanta, June 2–5, ASME Paper No. GT2003-38938.
[8] Pint, B. A., and Rakowski, J. M., 2000, "Effect of Water Vapor on the Oxidation Resistance of Stainless Steels," Houston, NACE Corrosion 2000, Orlando, March, NACE Paper No. 00-259.
[9] Rakowski, J. M., 2001, "The Oxidation of Austenitic Stainless Steel Foils in Humidified Air," International Gas Turbine & Aeroengine Congress & Exhibition, Amsterdam, June 3–6, ASME Paper No. 2001-GT-360.
[10] Pint, B. A., 2006, "Stainless Steels With Improved Oxidation Resistance for Recuperators," ASME J. Eng. Gas Turbines Power, **128**, pp. 370–376.
[11] Asteman, H., Svensson, J.-E., Norell, M., and Johansson, L.-G., 2000, "Influence of Water Vapor and Flow Rate on the High-Temperature Oxidation of 304L: Effect of Chromium Oxide Hydroxide Evaporation," Oxid. Met., **54**, pp. 11–26.5.
[12] Opila, E. J., 2004, "Volatility of Common Protective Oxides in High-Temperature Water Vapor: Current Understanding and Unanswered Questions," Mater. Sci. Forum, **461–464**, pp. 765–774.
[13] Stambler, I., 2004, "Mercury 50 Rated at 4600 kW and 38.5% Efficiency With 5 ppm NO_x," Gas Turbine World, Feb–Mar, pp. 12–16.
[14] Matthews, W. J., Bartel, T., Klarstrom, D. L., and Walker, L. R., 2005, "Engine Testing of an Advanced Alloy for Microturbine Primary Surface Recuperators," International Gas Turbine & Aeroengine Congress & Exhibition, Reno-Tahoe, June 6–9, ASME Paper No. GT2005-68781.
[15] Kikuchi, M., Sakakibara, M., Otoguro, Y., Mimura, H., Araki, S., and Fujita, T., 1985, "An Austenitic Heat Resisting Steel Tube Developed for Advanced Fossil-Fired Steam Plants," *High Temperature Alloys, Their Exploitable Potential*, J. B. Marriott, M. Merz, J. Nihoul, and J. Ward, eds., Elsevier, London, pp. 267–276.
[16] Rakowski, J. M., Stinner, C. P., Lipschutz, M., and Montague, J. P., 2004, "The Use and Performance of Oxidation and Creep-Resistant Stainless Steels in an Exhaust Gas Primary Surface Recuperator Application," International Gas Turbine & Aeroengine Congress & Exhibition, Vienna, June 14–17, ASME Paper No. GT2004-53917.
[17] Pint, B. A., 2005, "The Effect of Water Vapor on Cr Depletion in Advanced Recuperator Alloys," International Gas Turbine & Aeroengine Congress & Exhibition, Reno-Tahoe, June 6–9, ASME Paper No. GT2005-68495.
[18] Lara-Curzio, E., Maziasz, P. J., Pint, B. A., Stewart, M., Hamrin, D., Lipovich, N., and DeMore, D., 2002, "Test Facility for Screening and Evaluating Candidate Materials for Advanced Microturbine Recuperators," International Gas Turbine & Aeroengine Congress & Exhibition, Amsterdam, Netherlands, June 3–6, ASME Paper No. 2002-GT-30581.
[19] Lara-Curzio, E., Trejo, R., More, K. L., Maziasz, P. J., and Pint, B. A., 2005, "Evaluation and Characterization of Iron- and Nickel-Based Alloys for Microturbine Recuperators," International Gas Turbine & Aeroengine Congress & Exhibition, Reno-Tahoe, June 6–9, ASME Paper No. GT2005-68630.
[20] Maziasz, P. J., Swindeman, R. W., Shingledecker, J. P., More, K. L., Pint, B. A., Lara-Curzio, E., and Evans, N. D., 2003, "Improving High-Temperature Performance of Austenitic Stainless Steels for Advanced Microturbine Recuperators," *Engineering Issues in Turbine Machinery, Power Plant and Renewables, Maney*, Parsons, London, pp. 1057–1073.
[21] Young, D. J., and Pint, B. A., 2006, "Chromium Volatilization Rates From Cr_2O_3 Scales Into Flowing Gases Containing Water Vapor," Oxid. Met., **66**, pp. 137–153.
[22] Hoelzer, D. T., Pint, B. A., and Wright, I. G., 2000, "A Microstructural Study of the Oxide Scale Formation on an ODS Fe-13Cr Alloy," J. Nucl. Mater., **283–287**, pp. 1306–1310.
[23] Kumar, L., Venkataramani, R., Sundararaman, M., Mukhopadhyay, P., and Garg, S. P., 1996, "Studies on the Oxidation Behavior of Inconel 625 Between 873 and 1523 K," Oxid. Met., **45**, pp. 221–244.
[24] Tedmon, C. S., 1966, "The Effect of Oxide Volatilization on the Oxidation Kinetics of Cr and Fe-Cr Alloys," J. Electrochem. Soc., **113**, pp. 766–768.
[25] Calvarin-Amiri, G., Molins, R., and Huntz, A. M., 2001, "Coupling Between Oxidation and Mechanical Stresses: Application to the Oxidation of Ni-20Cr Foils," Mater. Sci. Forum, **369–372**, pp. 467–474.
[26] Schmitt, J. F., Pacia, N., Pigeat, P., and Weber, B., 1995, "Study of the Initial Oxidation of a Ni-20Cr Alloy in the Temperature-Range 550–830°C – Influence of Mechanical Deformation," Oxid. Met., **44**, pp. 429–452.
[27] McCoy, H. E., 1965, "Type 304 Stainless Steel vs. Flowing CO_2 at Atmospheric Pressure and 1100–1800°F," Corrosion (Houston), **21**, pp. 84–94.

Downloaded 02 Jun 2010 to 171.66.16.107. Redistribution subject to ASME license or copyright; see http://www.asme.org/terms/Terms_Use.cfm

Improved High Cycle Fatigue Damage Tolerance of Turbine-Engine Compressor Components by Low Plasticity Burnishing

Paul S. Prevéy
e-mail: pprevey@lambdatechs.com

N. Jayaraman
e-mail: njayaraman@lambdatechs.com

Lambda Technologies,
3929 Virginia Avenue,
Cincinnati, OH 45227

Ravi A. Ravindranath
NAVAIR Propulsion and Power,
22195 Elmer Road,
Patuxent River, MD 20670-1534
e-mail: ravi.ravindranath@navy.mil

Michael Shepard
Ph.D.
WPAFB AFRL/MLLMN,
2230 10th Street,
WPAFB, OH 45433-7817
e-mail: michael.shepard@wpafb.af.mil

Significant progress has been made in the application of low plasticity burnishing (LPB) technology to military engine components, leading to orders of magnitude improvement in damage tolerance. Improved damage tolerance can facilitate inspection, reduce inspection frequency, and improve engine operating margins, all leading to improved military readiness at significantly reduced total costs. Basic understanding of the effects of the different LPB process parameters has evolved, and finite element based compressive residual stress distribution design methodologies have been developed. By incorporating accurate measurement of residual stresses to verify and validate processing, this combined technology leads to a total solution approach to solve damage problems in engine components. An example of the total solution approach to develop LPB processing of a first stage Ti-6Al-4V compressor vane to improve the foreign object damage tolerance from 0.002 in. to 0.025 in. is presented. The LPB process, tooling, and control systems are described, including recent developments in real-time process monitoring for quality control. Performed on computer numerical control (CNC) machine tools, LPB processing is easily adapted to overhaul and manufacturing shop operations with quality assurance procedures meeting military and industry standards, facilitating transition to military depots and manufacturing facilities. [DOI: 10.1115/1.2771244]

Keywords: low plasticity burnishing, residual stress, damage tolerance, foreign object damage, FOD, compressor components, fatigue design diagram, FDD, high cycle fatigue, fatigue cracking, mitigation of damage, surface treatment

Introduction

Turbine-engine compressor components such as blades, vanes, integrally bladed rotors (IBRs), or bladed disks (blisks) are prone to high cycle fatigue (HCF) and foreign object damage (FOD) at critical locations on the leading and trailing edges. Some fan and compressor components have a FOD tolerance of less than 0.005 in., and consequently require extensive inspection, rework, and replacement. Dovetail regions of the compressor blades and dovetail posts of the compressor rotors are also prone to fretting induced microcracking. Inspections of such microcracks are very cumbersome and difficult, and often involve very complex and expensive instruments and highly trained personnel. Typically, compressor vanes and blades cost several thousand dollars each and rotors cost several tens of thousands of dollars. Costs of an IBR or blisk could run into hundreds of thousands of dollars. HCF accounts for 56% of major aircraft engine failures, and ultimately limits the service life of most critical components [1]. An estimated $400 million is expended annually for HCF-related inspection and maintenance, greatly increasing the total ownership cost of military aircraft. The associated reduction in time on wing increasingly impacts military readiness. Considering all these factors, increased damage tolerance for these critical components will lead to substantially reduced early retirement of components, ease of inspection, less frequent and less expensive inspection and maintenance, and therefore significantly improved military readiness.

The deep stable layer of compressive residual stress produced by low plasticity burnishing (LPB) [2–4] has been demonstrated to produce remarkable improvement in damage tolerance, corrosion fatigue, and fretting in a variety of materials. Damage tolerance in IN718 [5], Ti-6Al-4V [6,7], Ti-6-2-4-6 [8], 17-4PH [9], and Custom 450 [10] have been studied extensively in laboratory coupons. Mitigation of corrosion pitting damage in aluminum [11] and steel [12] and active corrosion in aluminum [13] have been reported. Application of LPB to produce through-thickness compression in the leading edge of a rotating engine component, Ti-6Al-4V first stage fan blade, produced an order of magnitude improvement in damage tolerance [14]. These developmental test programs have led to the compilation of a large database on many different alloy systems supporting the application of LPB induced compression to combat a variety of damage conditions in turbine-engine components.

By means of theoretical modeling [15,16], a clear understanding of the magnitude and depth of compressive residual stresses required to mitigate damage while addressing other design-related issues such as part distortion has been developed. Tool design and real-time process quality assurance (QA) have been fully ad-

Contributed by the International Gas Turbine Institute of ASME for publication in the JOURNAL OF ENGINEERING FOR GAS TURBINES AND POWER. Manuscript received June 14, 2006; final manuscript received July 21, 2006; published online January 11, 2008. Review conducted by Dilip R. Ballal. Paper presented at the ASME Turbo Expo 2006: Land, Sea and Air (GT2006), Barcelona, Spain, May 8–11, 2006, Paper No. GT2006-90894.

Copyright © 2008 by ASME

Downloaded 02 Jun 2010 to 171.66.16.107. Redistribution subject to ASME license or copyright; see http://www.asme.org/terms/Terms_Use.cfm

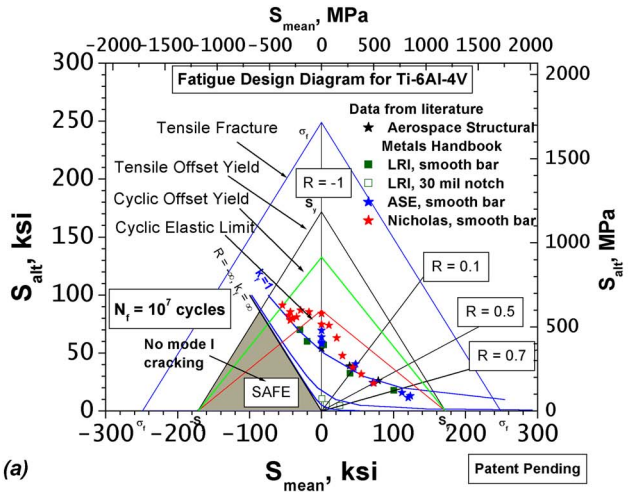

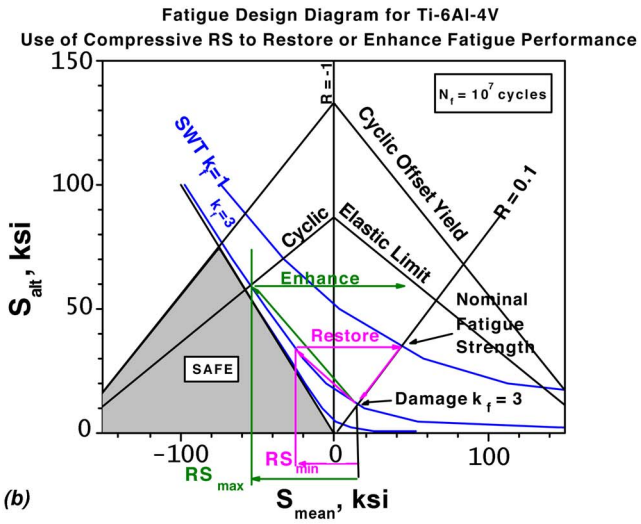

Fig. 1 (*a*) FDD for Ti-6Al-4V and (*b*) demonstration of the use of FDD

dressed. Through these efforts, a simple new philosophy for turbine-engine life extension and life management has emerged. The traditional approach to mitigate damage and improve HCF performance of a turbine-engine component is to either change the design or the material, both very time-consuming and expensive undertakings. The new fatigue enhancement design approach is to introduce appropriate compressive residual distributions at critical locations to cancel applied tension and mitigate damage mechanisms. This design approach is based on the use of fatigue design diagram (FDD) to determine the optimum level of compression needed for mitigating the amount of damage quantified by the

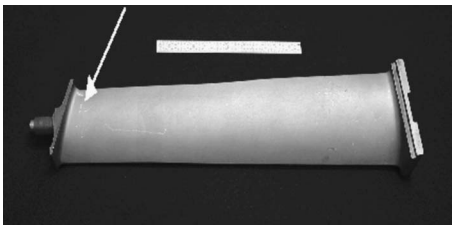

Fig. 2 The Ti-6Al-4V compressor vane with FOD limited trailing edge. The arrow indicates the region sensitive to foreign object damage (FOD).

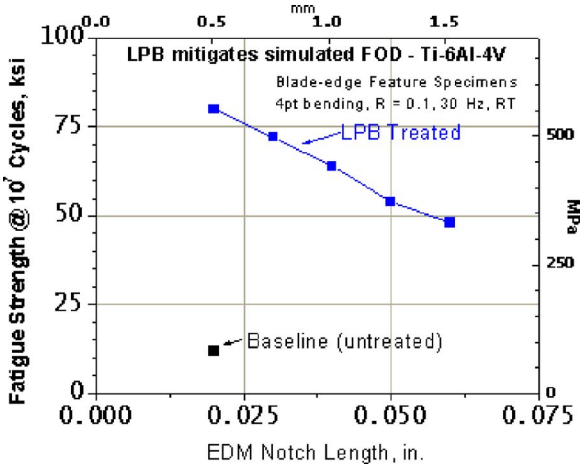

Fig. 3 Effect of simulated FOD on the fatigue strength of feature specimens of Ti-6Al-4V compressor vane

effective fatigue stress concentration factor, k_f. Using the optimum residual stress as the target, LPB processing parameters and CNC control code are developed, and the resulting residual stress distribution is measured on actual components using X-ray diffraction ($\sin^2 \Psi$ method). The measured residual stresses are then input into a finite element model (FEM) of the component to determine the net distribution of residual and applied stresses. Finite element analysis (FEA) is used during design of the residual stress distribution to determine the distribution of compensatory tension and to limit the distortion to the design tolerances. Once the desired residual stress distribution is achieved, components are LPB treated for fatigue testing. Processing QA is implemented by real-time monitoring, recording, and controlling of the LPB process parameters. In this paper, a brief description of the FDD is presented in the next section, followed by the application of the total solution methodology to improve the FOD tolerance of a first stage compressor vane from <0.002 in. to 0.025 in. using LPB.

Fatigue Design Diagram

Following Lambda's LPB Development Protocol, the failure analysis and material characterization were completed followed by the design of a specific compressive residual stress distribution for the component. The compressive distribution is designed using the FDD [17]. The FDD is a novel extension of the Haigh (or Goodman) diagram to include the region of compressive mean stresses. Unlike the Goodman line, the Smith-Watson-Topper (SWT) model is used to account for the variation in the fatigue strengths at various mean stresses for a given fatigue life, say, 10^7 cycles. When damage is accounted for by Neuber-type stress concentration factor (k_t) or more appropriately, k_f, the fatigue stress concentration factor, a series of SWT lines can be drawn in the modified Haigh diagram or FDD. This FDD can then be used for predicting fatigue behavior incorporating the residual stress states existing in the component. The FDD predicts a safe region in which Mode I cracking is not possible. When operating in this region, damage conditions such as FOD, fretting-induced shear microcracks, corrosion pits, etc., will not transition into propagating fatigue cracks. This allows the design of compressive residual stress distributions to mitigate specific damage conditions for a given component and applied stress field. For example, Fig. 1(*a*) shows the fully constructed FDD for Ti-6Al-4V with confirming fatigue data. Figure 1(*b*) demonstrates the use of FDD to design the correct magnitude of compressive residual stresses for fully restoring and enhancing the fatigue performance of a damaged part operating at $R=0.1$ with damage producing a $k_f=3$. Residual stress distributions for the part geometry, critical location, and

Downloaded 02 Jun 2010 to 171.66.16.107. Redistribution subject to ASME license or copyright; see http://www.asme.org/terms/Terms_Use.cfm

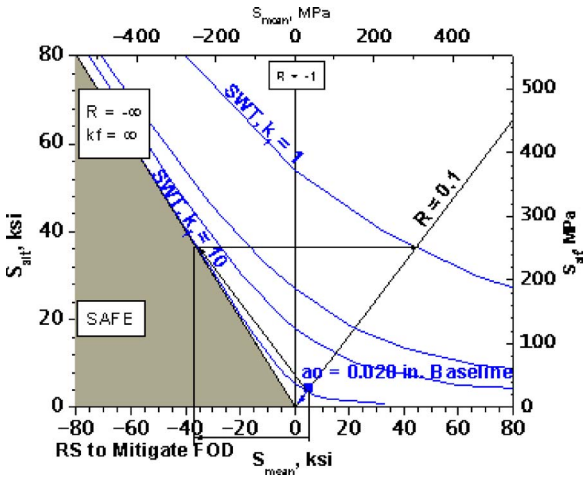

Fig. 4 A magnified version of the Ti-6Al-4V FDD for simulated FOD of 0.020 in. in blade-edge specimens

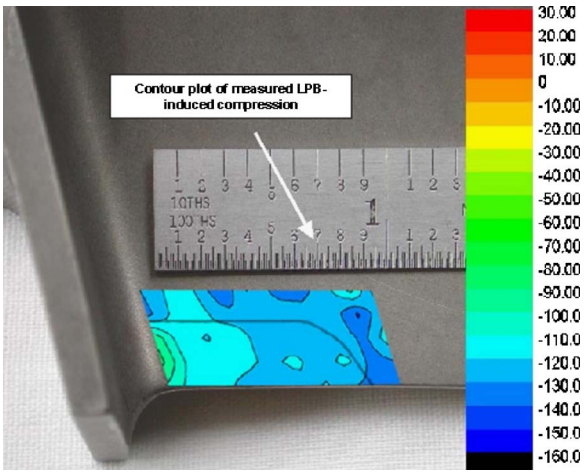

Fig. 5 LPB-induced compressive residual stress distribution of the TE of Ti-6Al-4V compressor vane shown in the form of a contour plot

damage conditions were then designed using the FDD for Ti-6Al-4V. The designed residual stresses were then incorporated into FEMs of the part to determine the magnitude and locations of compensatory tension and the distortion caused by introducing the compression.

Design Process

Figure 2 shows a photograph of the Ti-6Al-4V first stage compressor vane, with an arrow indicating the affected region. The vane is prone to cracking at the high stress location on the trailing edge (TE) near the platform, and is FOD limited in service to no more than 0.002 in. at the critical location.

Quantitative measure of damage is possible by empirically determining the fatigue stress concentration factor (k_f) associated with each damage condition. In Fig. 3, the fatigue strengths for 10^7 cycles are plotted to estimate k_f as the ratio of the fatigue strength of the smooth bar (undamaged state) over the damaged state. In the example shown here, the damage was simulated using electrical discharge machining (EDM) notches in Ti-6Al-4V blade-edge specimens simulating the features of the TE of the first stage compressor vane. EDM notches, with a cracked recast layer in residual tension at the bottom of the notch, were chosen as a worst-case condition for simulated FOD. EDM notches ranging in size from 0.020 in. to 0.060 in. were used. The EDM notch of

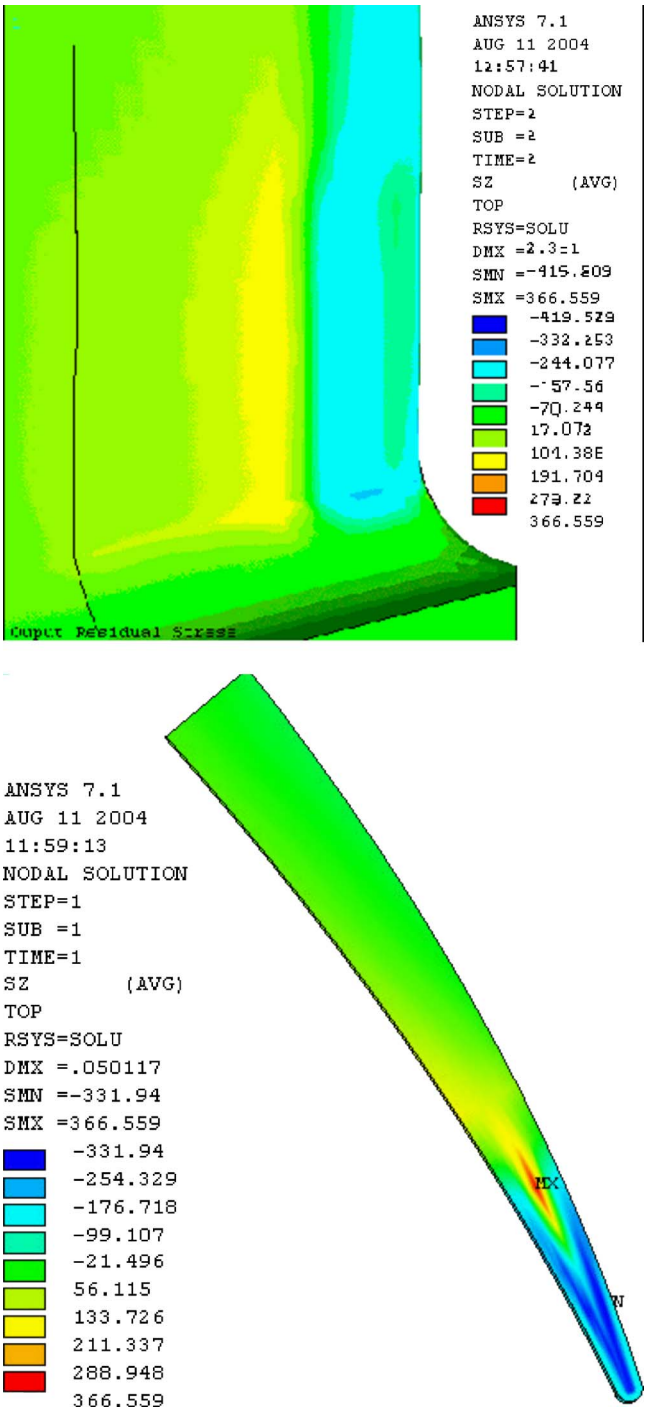

Fig. 6 Stress contours showing the location and magnitude of compensatory tension due to LPB-induced compression on the TE of Ti-6Al-4V vane

0.020 in. corresponds to a k_f of nominally 10. Note that the effect of introducing residual compression, shown by the LPB treated blade-edge feature specimen in Fig. 3, provides tolerance of even a 0.060 in. notch that is much better than the base line (untreated) specimen with only a 0.020 in. notch.

The stress state at the crack tip is represented in a FDD in Fig. 4: an optimum design compression of about −45 ksi (kips per square inch) at the weakest point in the component is predicted. That is, compressive residual stresses of this magnitude at the

Downloaded 02 Jun 2010 to 171.66.16.107. Redistribution subject to ASME license or copyright; see http://www.asme.org/terms/Terms_Use.cfm

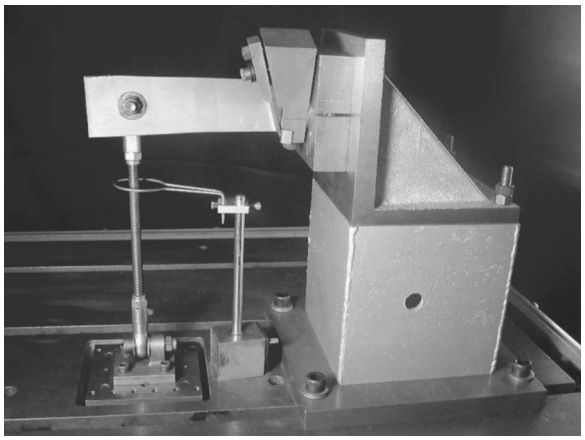

Fig. 7 Photograph showing the fatigue test setup for Ti-6Al-4V compressor vane TE in a Sonntag SFF-1U fatigue machine in cantilever loading

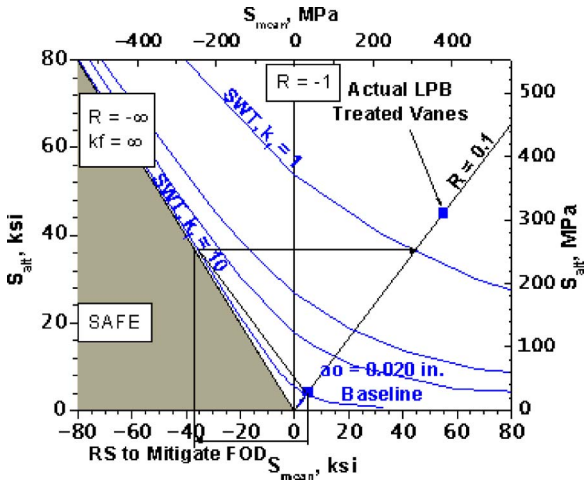

Fig. 9 FDD for the Ti-6Al-4V vane with the test result of the LPB treated vane plotted

bottom of the FOD in the midthickness point of the vane will fully mitigate the effects of 0.020 in. FOD, restoring the allowed alternating stress.

Using the design, LPB processing parameters and CNC code were developed, and vanes were LPB processed to produce the designed residual stress field. Figure 5 shows the measured residual stress distribution in the form of a stress contour map superimposed upon the outline of the LPB zone. The compressive residual stress field was then input into a FEM and analyzed to determine the location and magnitude of compensatory tensile stresses.

The vane was meshed in ANSYS using parabolic hexahedral (20 node brick) elements. Eight elements were used to model through the thickness of the TE in the LPB region and beyond, including into the inner platform blend. The remaining areas of the vane were meshed using parabolic (ten noded) tetrahedral elements. ANSYS has pyramid elements to transition between hexahedrons and tetrahedrons. Critical areas, such as the platform blend, were premeshed with surface elements to control the mesh spacing and force the underlying solid elements to conform to the surface geometry. The surface premesh elements were deleted before solution. The model consisted of a total of 150,272 nodes with 450,816 degrees of freedom. A linear elastic material model was used.

The results from FEA are shown in the form of stress contours in Fig. 6. In this figure, the LPB-induced residual stresses and the compensatory tensile stresses are shown. The tensile stresses are designed to be located at regions that see very little service stresses and are remote from FOD. FEA also helped determine the inevitable distortion due to the introduction of the compressive zones, and to adjust the design to keep the distortion within design tolerances.

After confirming that the optimum LPB condition had been achieved by residual stress measurement, additional vanes were LPB treated and fatigue tested. For this purpose, fielded and retired vanes with unknown service history were available for testing. Randomly selected vanes were LPB treated and fatigue tested in a Sonntag SF-1U machine. The test setup is shown in Fig. 7 with the truncated vane loaded in cantilever bending mode. All the vanes were tested at a stress ratio R of 0.1, frequency of 30 Hz at room temperature. A group of base line and LPB treated specimens with 0.020 in. deep EDM notch to simulate FOD conditions were also tested.

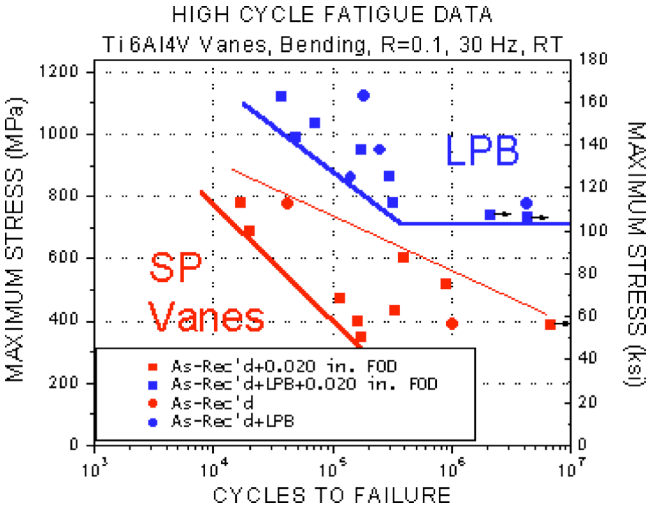

Fig. 8 Fatigue test results for Ti-6Al-4V compressor vane comparing LPB processed and shot peened (SP) vanes taken from service. Scatter in the SP vane is attributed to widely distributed field generated FOD.

Fig. 10 Photograph showing the LPB process setup in a five-axis CNC milling machine with a caliper tool set ready for LPB processing of the TE of a Ti-6Al-4V compressor vane

Downloaded 02 Jun 2010 to 171.66.16.107. Redistribution subject to ASME license or copyright; see http://www.asme.org/terms/Terms_Use.cfm

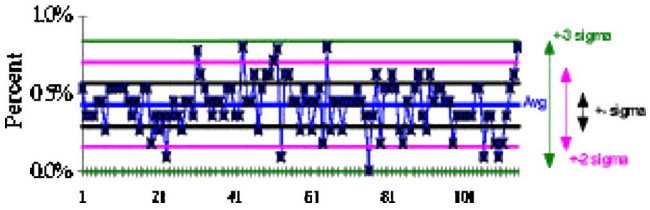

Fig. 11 Typical plot of the variation of every step of the vane LPB processing showing a range within 1% for processing window of ±16%

The HCF results from the vane tests are shown in Fig. 8. The benefits of LPB are evident. LPB processed vanes, either with or without 0.020 in. FOD, showed 10^7 cycles fatigue strength of over 100 ksi at $R=0.1$. Subsequent engine tests conducted by the original equipment manufacturer (OEM) on vanes with ballistic FOD have further confirmed these results. Figure 9 shows the FDD with the test result from Fig. 8 plotted.

Processing of Components and Quality Assurance

Based on the determination of optimal compressive residual stress distribution, production LPB processing tooling and shop routing for serviceable vanes were develop for a five-axis CNC milling machine. The fixture and the caliper tool developed are shown in Fig. 10. The primary process variables are dynamically controlled, monitored, and recorded in computer files for QA purposes and statistical process control (SPC). The closed-loop control assures that the operation parameters are kept within the specified window, and if rare deviations beyond the specified window occur, the exact location and magnitude of deviation are marked and the component is tagged for further investigation and appropriate corrective actions. Figure 11 shows that the typical variations seen in the process parameters are well within 1% of the set point, while the QA window processing window of 16% is allowed, providing a robust and real-time monitored process.

Summary and Conclusions

A comprehensive design methodology, based on the FDD for designing optimal compressive residual stress distributions for the critical regions of turbine-engine compressor components, has been presented. This methodology integrates the FDD approach with FEA to design complex compressive residual stress fields for turbine-engine components. When combined with the capabilities for accurate measurement of residual stresses for process verification and fatigue testing for validation, the proposed design method provides an attractive approach to solve fatigue damage problems in engine components. The method has been successfully applied to improve the FOD tolerance of a Ti-6Al-4V compressor vane from 0.002 in. to 0.025 in. using LPB processing to introduce through-thickness compression in the region of high applied stress on the TE of the vane.

References

[1] Propulsion Directorate, 2000, "High Cycle Fatigue (HCF) Program 1999 Annual Report," Paper No. AFRL-PR-WP-TR-2000-2004.

[2] Gabb, T., Telesman, J., Kantos, P., and Prevey, P., 2002, "Surface Enhancement of Metallic Materials," *Advanced Materials and Processes*, Peg Hunt, ed., ASM, Materials Park, OH, pp. 69–72.

[3] "Longer Life With Low Plasticity Burnishing," 2001, *Manufacturing Engineering*, B. Hogan, ed., SME, pp. 34–38.

[4] 1998, U.S. Patent No. 5,826,453; 2002, U.S. Patent No. 6,415,486.

[5] Prevéy, P. S. P., Telesman, J., Gabb, T., and Kantzos, P., 2000, "FOD Resistance and Fatigue Crack Arrest in Low Plasticity Burnished IN718," *Proceedings of the Fifth National High Cycle Fatigue Conference*, Paper No. IN718.

[6] Prevéy, P., Shepard, M., and Smith, P., 2001, "The Effect of Low Plasticity Burnishing (LPB) on the HCF Performance and FOD Resistance of Ti-6Al-4V," *Proceedings of the Sixth National Turbine Engine High Cycle Fatigue (HCF) Conference*, Jacksonville, FL, Mar. 5–8.

[7] Shepard, M. S., Prevéy, P. P., and Jayaraman, N. J., 2003, "Effect of Surface Treatments on Fretting Fatigue Performance of Ti-6Al-4V," *Proceedings of the Eigth National Turbine Engine HCF Conference*, Monterey, CA, Apr. 14–16.

[8] Prevéy, P. P., Jayaraman, N. J., and Shepard, M. S., 2004, "Improved HCF Performance and FOD Tolerance of Surface Treated Ti-6-2-4–6 Compressor Blades," *Proceedings of the Ninth National HCF Conference*, Pinehurst, NC, Mar. 16–19.

[9] Prevéy, P. P., Jayaraman, N. J., and Ravindranath, R. R., 2003, "Low Plasticity Burnishing (LPB) Treatment to Mitigate FOD and Corrosion Fatigue Damage in 17-4 PH Stainless Steel," *Proceedings of the Tri-Service Corrosion Conference*, Las Vegas, NV, Nov. 17–21.

[10] Jayaraman, N. J., and Prevéy, P. P., 2003, "Application of Low Plasticity Burnishing (LPB) to Improve the Corrosion Fatigue Performance and FOD Tolerance of Alloy 450 Stainless Steel," *Proceedings of the Tri-Service Corrosion Conference*, Las Vegas, NV, Nov. 17–21.

[11] Prevéy, P. P., and Cammett, J. C., 2002, "The Influence of Surface Enhancement by Low Plasticity Burnishing on the Corrosion Fatigue Performance of AA7075-T6," *Proceedings of the Fifth International Aircraft Corrosion Workshop*, Solomons, MD, Aug. 20–23.

[12] Prevéy, P. P., Jayaraman, N. J., Ontko, N. O., Shepard, M. S., Ware, R. W., and Coate, J. C., 2004, "Mechanical Suppression of SCC and Corrosion Fatigue Failures in 300M Steel Landing Gear," *Proceedings of ASIP 2004*, Memphis, TN, Nov. 29–Dec. 2.

[13] Prevéy, P. P., and Cammett, J. C., 2002, "Restoring Fatigue Performance of Corrosion Damaged AA7075-T6 and Fretting in 4340 Steel With Low Plasticity Burnishing," *Proceedings of the Sixth Joint FAA/DoD/NASA Aging Aircraft Conference*, San Francisco, CA, Sept. 16–19.

[14] Prevéy, P. P., Hornbach, D. H., Cammett, J. C., and Ravindranath, R. R., 2002, "Damage Tolerance Improvement of Ti-6-4 Fan Blades With Low Plasticity Burnishing," *Proceedings of the Sixth Joint FAA/DoD/NASA Aging Aircraft Conference*, San Francisco, CA, Sept. 16–19.

[15] Prevéy, P. P., Jayaraman, N. J., and Ravindranath, R. R., 2004, "Incorporation of Residual Stresses in the Fatigue Performance Design of Ti-6Al-4V," *Proceedings of the International Conference on Fatigue Damage of Structural Materials V*, Hyannis, MA, Sept. 19–24.

[16] Prevéy, P. P., Jayaraman, N. J., and Ravindranath, R. R., 2005, "Use of Residual Compression in Design to Improve Damage Tolerance in Ti-6Al-4V Aero Engine Blade Dovetails," *Proceedings of the Tenth Nat, HCF Conference*, New Orleans, LA, Mar. 8–11.

[17] Prevéy, P. P., Jayaraman, N. J., and Ravindranath, R. R., 2004, "Introduction of Residual Stress to Enhance Fatigue Performance in the Initial Design," *Proceedings, Turbo Expo 2004*, Vienna, Austria, Jun. 14–17.

Downloaded 02 Jun 2010 to 171.66.16.107. Redistribution subject to ASME license or copyright; see http://www.asme.org/terms/Terms_Use.cfm

The Effect of Initial Injection Conditions on the Oil Droplet Motion in a Simplified Bearing Chamber

M. Farrall

S. Hibberd[1]
e-mail: stephen.hibberd@nottingham.ac.uk

K. Simmons
e-mail: eazksim@gwmail.nottingham.ac.uk

University Technology Centre in Transmission Systems,
School of Mechanical, Materials and Manufacturing Engineering,
University of Nottingham,
Nottingham NG7 2RD, United Kingdom

Increasing demands on aeroengines to operate at higher shaft speeds and temperatures require an understanding and optimization of the integral systems. The ability to model movement of oil around bearing chambers in the form of droplets and films is a current area of interest. This paper presents a two-phase numerical modeling approach developed for predicting air, oil droplet, and oil film behavior within an aeroengine bearing chamber including the significant droplet/film interactions. In-house code is linked to the commercial CFD package CFX4.3 and a predictive algorithm for determining the outcome of droplet impact with a wall film and the associated transfer of oil mass and momentum is developed. The method is used to simulate the motion of oil droplets shed from a roller bearing in a simplified aeroengine bearing chamber geometry and through a parametric study shows that initial droplet size distribution parameters (mean diameter and spread) have a significant effect on oil deposition location. In contrast, the Sauter mean diameter of droplets within the chamber showed little sensitivity to initial injection parameters. The behavior of oil within a bearing chamber is strongly influenced by the conditions with which it leaves the bearing. There is potential for performance improvement if bearing shed can be controlled or if chamber design can be modified such that oil behavior is insensitive to initial shed conditions. [DOI: 10.1115/1.2770480]

Keywords: bearing chambers, two-phase, droplets, Lagrangian, droplet impact

1 Introduction

Increasing demands on aeroengines to operate at higher shafts speeds and temperatures require an understanding and optimization of the integral systems. This especially applies to bearing chambers, which contain a complex two-phase flow formed by the interaction of the sealing airflow and lubrication oil. A typical bearing chamber is formed by a combination of rotating components, a typical shaft speed being 7000 rpm, and stationary walls, inducing a strong azimuthal component of flow. This flow is modified by the presence of flow inlets (bearings and seals), and flow outlets (vent and scavenge ports). Oil is supplied to the bearings for lubrication and as a result discrete oil droplets are ejected into the rotating airflow. Because angular momentum is transferred to the droplets from the bearing and associated bearing cage, the droplets ultimately impinge on the outer chamber housing. The impingement may result in immediate deposition, in which case a wall film is formed that migrates around the chamber. Alternatively, droplets may break up on impact with smaller droplets being ejected back into the airflow and further impingement may occur. Figure 1 illustrates schematically the important physical phenomena occurring in such bearing chambers.

The heat transfer through the chamber housing will be affected by the local film thickness, the distribution of which depends on the input of mass and momentum from the impinging droplets. These source terms ultimately come from the initial conditions given to the released oil droplets. It is therefore crucial when modeling such systems to either have accurate data regarding the droplets initial conditions or knowledge of the solution sensitivity to key parameters.

Investigations into bearing chamber flows are limited with work focusing on the heat transfer through the chamber housing [1–4] and characterization of oil film flows [1,3,5–9]. An initial numerical investigation into the oil droplet motion in bearing chambers was conducted by Glahn et al. [10]. Experimental data regarding the diameters and velocities of oil droplets generated by a roller bearing and associated cage were used as initial conditions in a Lagrangian calculation of the droplet motion. Due to the absence of a wall impact model, the droplets were only tracked to the point of impingement on the chamber housing. Farrall et al. [7–9] developed in-house models to account for droplet impacts and the subsequent film motion in bearing chambers. The models were validated by simulating the flow in a test facility at the *Institut fur Thermische Stroumngsmachinen* [9]. To apply the model to other geometries, data regarding the initial distribution of droplet diameters and velocities are required. Currently, no experimental correlations that can account for the change in key parameters, such as the mean diameter, with shaft speed and oil flow rate exist, and thus it is crucial to understand the potential impact of the assumed initial conditions for the shed droplets.

This paper presents the 2D version of the model used by Farrall et al. [9] to compute the air and oil droplet motion in a bearing chamber. The model is used to calculate the deposition of oil on the chamber housing as a result of droplet impingement, as well as the change in the Sauter mean diameter (SMD) around the chamber for a single set of operating conditions. The sensitivity of these results to changes in the ejected droplet initial conditions is then investigated.

[1]Corresponding author.

Submitted to ASME for publication in the ASME JOURNAL OF ENGINEERING FOR GAS TURBINES AND POWER. Manuscript received December 13, 2004; final manuscript received October 9, 2005; published online December 13, 2007. Review conducted by Nagaraj Arakere.

Copyright © 2008 by ASME

Downloaded 02 Jun 2010 to 171.66.16.107. Redistribution subject to ASME license or copyright; see http://www.asme.org/terms/Terms_Use.cfm

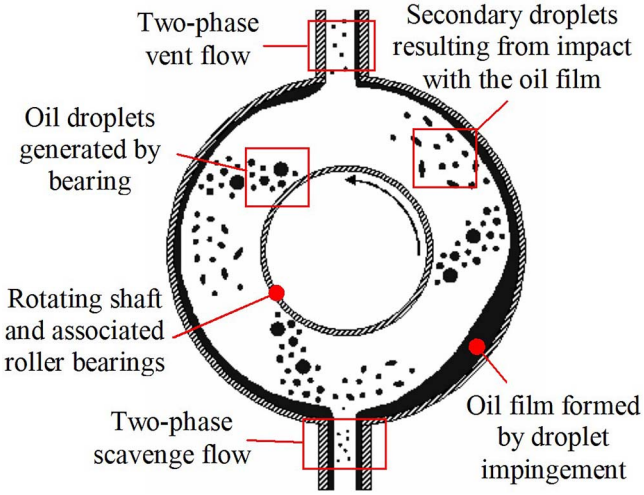

Fig. 1 Physical phenomena occurring in a bearing chamber

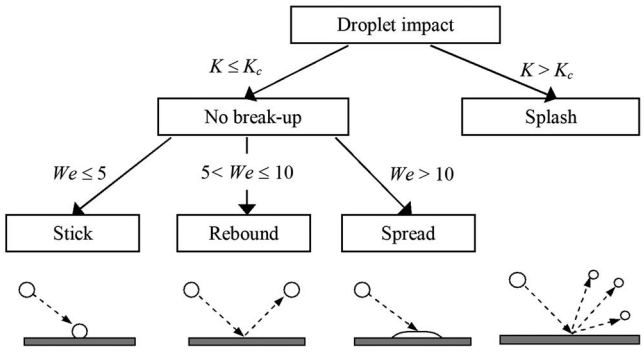

Fig. 2 Schematic showing the structure of droplet/film interaction model and the transition criteria for the various outcomes

2 Computational Model

The simulation involves the implementation of successive stages. Firstly, the airflow in the chamber is calculated using the commercial CFD package CFX-4.3. Oil droplets are then released and tracked through the chamber, employing the droplet impact model where necessary. The model provides a boundary condition for the Lagrangian particle tracking routine in CFX-4.3, taking information regarding the droplet impingement and determining the outcome of the impact. Appropriate post-impingement characteristics are then calculated and new droplets sourced where necessary. Details of the model components are now presented.

2.1 Airflow in the Chamber. The 2D continuity and momentum equations are solved for an incompressible, isothermal flow with turbulence accounted for using the k-ε model. The modeling of an oil film on the chamber housing is omitted in the present study and thus no-slip boundary conditions are applied at the shaft and outer wall. The equations are discretized using the higher-order upwind differencing scheme and solved using the SIMPLE pressure-correction algorithm of Patankar and Spalding [11] as incorporated in CFX-4.3.

2.2 Oil Droplet Motion. Droplet parcels are tracked through the domain using a Lagrangian model [12] taking aerodynamic drag as the dominant force on the droplet. The relative importance of gravity on the droplet motion in such flows has been shown to be negligible [10,13] and is thus omitted. The droplets are modeled as rigid spheres assuming a low droplet loading in the chamber. Collisions between droplets and the modification of the airflow by the oil droplets' momentum are therefore omitted. In addition to this, the effect of turbulent dispersion has been omitted as previous studies have shown that its influence is relatively small for droplet diameters considered [10].

2.3 Droplet Impacts. Impacts with the chamber housing are accounted for using an in-house submodel based on experimental data and correlations obtained for de-ionized (DI) diesel engines. These data are used as it currently forms the most comprehensive set available. The model classifies each impact with the chamber housing primarily on whether the droplet breaks up. This is achieved through the evaluation of the splashing parameter $K(=\mathrm{We}_d^{0.5}\mathrm{Re}_d^{0.25})$. If the droplet does not *splash*, the impact is further classified into the regimes of *stick*, *rebound*, and *spread*. The structure of the model is shown schematically in Fig. 2 together with the associated parameter values for each regime. The critical value of the impact parameter K_c, termed the splashing threshold, above which breakup occurs is determined from the experimental correlation proposed by Cossali et al. [14],

$$K_c = 649 + 3.76/(R_{\mathrm{nd}})^{0.63} \tag{1}$$

as a function of the surface roughness parameter, $R_{\mathrm{nd}}(=R_a/d_l)$. In the following sections, the post-impingement characteristics and criterion for which they are valid are discussed in more detail. It should be noted that the model has been developed for investigating the motion of oil films and thus, while the presence of an oil film is omitted in the present analysis, the correlations used are valid for droplet impacts with thin liquid layers.

2.4 Impacts With $K \leqslant K_c$. The Weber number of the incident droplet is calculated to determine whether the impact results in stick, rebound, or spread. Based on experimental data for droplets impinging on a liquid layer [15], the criteria given in Table 1 are used to decide on the outcome of the impact.

Computationally, the regimes of stick and spread are treated identically, with the droplet's velocity vanishing on impact. If droplets rebound from the film, the tangential velocity U_{ta}, and normal velocity U_{na}, after impact are calculated in terms of the velocities U_{tb} and U_{nb} before impact using

$$U_{\mathrm{ta}} = \frac{5}{7} U_{\mathrm{tb}} \tag{2}$$

$$U_{\mathrm{na}} = -eU_{\mathrm{nb}} \tag{3}$$

valid for small particles bouncing on a wetted surface [15,16]. The coefficient of restitution e in Eq. (3) is determined from the correlation presented by Bai and Gosman [16] as

$$e = 0.993 - 1.76\theta_I + 1.56\theta_I^2 - 0.49\theta_I^3 \tag{4}$$

where θ_I denotes the angle that the impacting droplet makes with the film surface.

2.5 Impacts With $K > K_c$. Impacts for which $K > K_c$ result in breakup of the incident droplets. In this case, a number of postimpingement characteristics, such as secondary droplet diameters and velocities, must be determined. These are discussed in more detail in the following sections. The model presented is

Table 1 Criteria for impacts with no breakup

Impact regime	Criteria
Stick	$\mathrm{We} \leqslant 5$
Rebound	$5 < \mathrm{We} \leqslant 10$
Spread	$\mathrm{We} > 10$ and $K \leqslant K_c$

Downloaded 02 Jun 2010 to 171.66.16.107. Redistribution subject to ASME license or copyright; see http://www.asme.org/terms/Terms_Use.cfm

based on the work of Stanton and Rutland [15] and Bai and Gosman [16], taking into account the experimental results of Mundo et al. [17,18] and Sammenfink et al. [19].

2.5.1 Secondary Droplet Diameters. Before calculating the representative diameters, characterizing the splashed droplets, the total mass fraction of the incident droplet ejected in the form of secondary droplets, η, is determined. This is calculated using the correlation of Mundo et al. [20], modified by the inclusion of an upper limit suggested by the experimental data of Stow and Stainer [21] to prevent non-physical results for values of K above 200, as

$$\eta = \begin{cases} 8.03 \times 10^{-11} K^{4.1718} & K \leqslant 200 \\ 0.9 - 5.792 e^{-1.15 \times 10^{-2} K} & K > 200 \end{cases}, \tag{5}$$

With knowledge of the ejected mass fraction, secondary droplet diameters and corresponding numbers can be determined. The secondary diameters are assumed to satisfy a log-normal probability density function [19–21],

$$\mathrm{pdf}(x) = \frac{1}{x\sigma\sqrt{2\pi}} \exp\left[- \frac{\ln(x/\bar{x})^2}{2\sigma^2} \right], \tag{6}$$

in which x corresponds to the diameter of the secondary droplet, normalized with the impinging droplet diameter. The mean $\bar{x}$ and standard deviation σ are given by

$$\bar{x} = 0.114 K^{-0.0701},$$

$$\sigma = 0.1486 K^{0.187},$$

as suggested from the correlations presented by Stow and Stainer [21]. For practical calculations, it is convenient to divide the diameters of the splashed droplets into three groups, based on the impinging droplet diameter, corresponding to small ($0.0 < d \leqslant 0.1 d_I$), medium ($0.1 d_I < d \leqslant 0.2 d_I$), and large ($d > 0.2 d_I$) droplets. The representative diameter for each group is taken to be the mean diameter in that range. The corresponding number of secondary droplets N_i is then obtained by imposing conservation of mass given by

$$N_i d_i^3 = \eta \left[\int_{x_0}^{x_1} \mathrm{pdf}(x) dx \right] d_I^3. \tag{7}$$

As N_i is an integer, the value obtained using Eq. (7) is rounded to the nearest integer and the diameter adjusted accordingly. For small values of η, it is possible that a significant portion of the splashed material lies within the medium and large diameter ranges, but insufficient for a droplet to be formed. To account for this, a condition given by Eq. (8), which determines the droplet diameter assuming only one droplet is formed from the splashed material and compares it to the minimum diameter in the medium range,

$$\left[\eta \int_{0.1}^{1} \mathrm{pdf}(x) dx \right]^{1/3} d_I > 0.1, \tag{8}$$

has been built into the model. If Eq. (8) does not hold, then the splashed droplets are assumed to be of one size corresponding to that of the smallest diameter range with the appropriate number of ejected droplets being determined.

2.5.2 Secondary Droplet Velocities. Performing an energy balance on the splashing process yields

$$\frac{\rho}{12} \sum_{i=1}^{3} N_i d_i^3 U_i^2 + \sigma \sum_{i=1}^{3} N_i d_i^2 = \frac{\rho}{12} d_I^3 U_I^2 + \sigma d_I^2 - E_s, \tag{9}$$

where N_i denotes the number of daughter droplets of diameter d_i, resulting from the impact of a droplet of diameter d_I. The term E_s denotes the energy required to promote splashing and is written in terms of the critical value of We [15,16], obtained from the splashing threshold, as

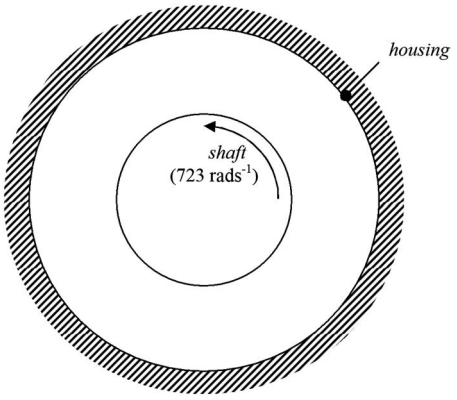

Fig. 3 Schematic of representative 2D chamber geometry

$$E_s = \frac{\mathrm{We}_c \pi \sigma}{12} \left(\frac{d_I}{\cos \theta_I} \right)^2. \tag{10}$$

It has been found in the present study that the velocity predicted for ejected droplets can be five to six times that of the impinging droplet when a low mass fraction is ejected. This non-physical behavior occurs if no account is taken of the loss of energy that results from the deposition of material. To account for this additional energy loss, a multiplication factor, equal to the ratio of the predicted value of the splashed mass fraction to the upper limit (Eq. (5)), has been added to the right hand side of Eq. (9) yielding

$$\frac{\rho}{12} \sum_{i=1}^{3} N_i d_i^3 U_i^2 + \sigma \sum_{i=1}^{3} N_i d_i^2 = \frac{\eta}{\eta_{\max}} \left[\frac{\rho}{12} d_I^3 U_I^2 + \sigma d_I^2 \left(1.0 - \frac{\mathrm{We}_c}{12.0 \cos^2 \theta_I} \right) \right]. \tag{11}$$

Additional equations are required in order to determine the representative speeds of ejection of droplets in each interval, U_i. These are formed on the basis of the model presented by Bai and Gosman [16] who used an experimental correlation in order to relate the velocities of the secondary droplets to their respective diameters. The ejection velocity, U_i, is given by

$$\left(\frac{U_i}{U*} \right) = \ln\left(\frac{d_i}{d_I} \right) / \ln\left(\frac{d*}{d_I} \right) \quad i = 1,2. \tag{12}$$

In the above, $d*$ and $U*$ denote the maximum droplet diameter ejected as a result of the impact and its corresponding velocity. Substitution of Eq. (12) into Eq. (11) yields an explicit equation for the determination $U*$ and hence the secondary velocities of the splashed droplets.

2.5.3 Droplet Ejection Angle. In the model, all secondary droplets are ejected forward of the point of impingement at the same angle, specified using the experimental correlation of Mundo et al. [20] as

$$\theta_{ej} = \frac{\pi}{180} \left[30.631 - 0.0804 \left(90 - \frac{180}{\pi} \theta_I \right) \right], \tag{13}$$

where θ_{ej} and θ_I denote the angles of reflection and impingement, respectively, measured from the tangent to the film surface.

3 Representative Two Dimensional Chamber

The model is used to investigate the oil droplet motion and subsequent impingement in a representative 2D aeroengine bearing chamber, shown schematically in Fig. 3. The geometry comprises two concentric, circular cylinders of radii 93 mm and

Downloaded 02 Jun 2010 to 171.66.16.107. Redistribution subject to ASME license or copyright; see http://www.asme.org/terms/Terms_Use.cfm

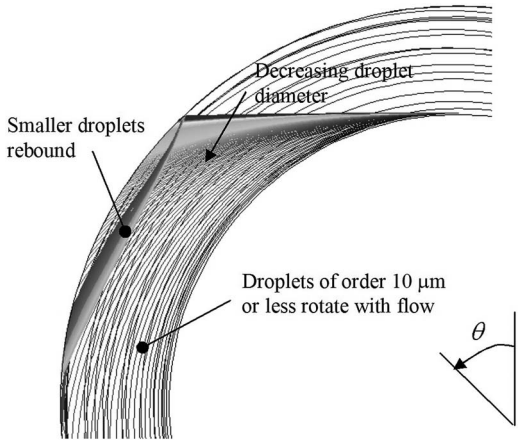

Fig. 4 Trajectories of oil droplets shed from the inner shaft

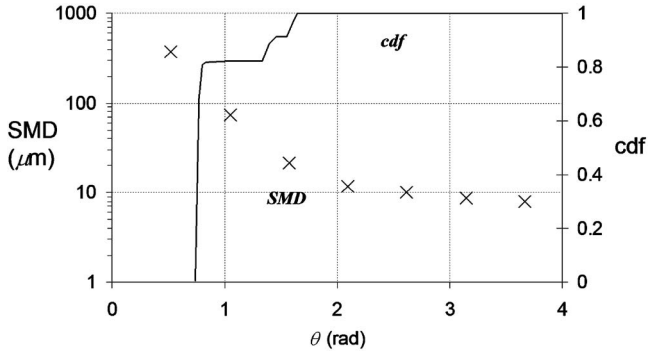

Fig. 5 Plots showing the variation with angular location of (*a*) the cdf for the oil deposited on the chamber housing (cdf) and (*b*) the SMD

128 mm. The inner cylinder (*shaft*) rotates with a typical angular velocity of 723 rad s^{-1} (7000 rpm), while the outer cylinder (*housing*) is stationary. The air in the chamber is taken as having a density and dynamic viscosity of 1.225 kg m^{-3} and 1.7894×10^{-5} kg m^{-1} s^{-1}, respectively, and is solved on a computational grid comprising 16 cells, two way biased in the radial direction, and 120 cells, uniformly spaced in the circumferential direction. Oil droplets, having a density and dynamic viscosity of 954 kg m^{-3} and 9.5×10^{-3} kg m^{-1} s^{-1}, in the range of 1–800 μm are released from a single angular location on the shaft with initial radial and azimuthal velocities of 0 and $0.5 r_i \omega_i$, respectively. In light of the diameter distributions found in previous studies [9,10], the droplet diameters initially satisfy a Rossin–Rammler distribution with a mean diameter of 300 μm and a spread parameter of 5. The presence of a wall film is neglected in the present study with the surface of the housing taken as being hydraulically smooth. This results in the splashing threshold, K_c, in Eq. (1) taking the limiting value of 649.

A parametric analysis is carried out to ascertain the sensitivity of the solution to changes in the droplets initial conditions. In particular, the effect of the assumed mean diameter and spread parameter in the initial droplet diameter distribution as well as the initial radial velocity is investigated. Results for the oil droplet motion are analyzed using two plots.

1. Cumulative distribution function (cdf). This is defined as the amount of oil deposited on the chamber housing between the initial injection point and the angle θ given by

$$\text{cdf} = \frac{1}{M_{\text{inj}}} \left(\int_0^{\theta} m d\theta \right)$$

2. Sauter mean diameter (SMD). This gives the average droplet diameter in the core flow along a given radial line, calculated using

$$\text{SMD} = \frac{\sum_{i=1}^{n} N_i d_i^3}{\sum_{i=1}^{n} N_i d_i^2}$$

4 Prediction of Oil Droplet Motion

From the calculation of the droplet trajectories, a critical diameter of 200 μm is found, above which the droplets travel in a straight line to the chamber housing. This can be observed in Fig. 4, which shows the trajectories of released droplets. The droplets have sufficient energy on impact to promote splashing, releasing secondary droplets back into the core flow. These secondary droplets remain in the outer half of the chamber impacting on the housing at some point further around the chamber.

The influence of the aerodynamic drag, deflecting the droplet trajectory from a straight path, becomes increasingly evident for those released droplets having a diameter less than 200 μm. The deflection of the droplet results in a decreased impact angle on the chamber housing, and hence normal impact velocity. This, along with the smaller droplet diameter, results in the droplets having insufficient energy to promote splashing. Instead, the oil is deposited on the chamber housing.

The effect of splashing and the subsequent cumulative deposition (cdf) and the predicted SMD are observed in Fig. 5. The angle θ is measured from the point of release in an anticlockwise manner as indicated in Fig. 4. It is observed from the cdf that just over 80% of the oil released is deposited at the location of the first impact, $\theta \approx 0.8$. As the released distribution is biased toward the larger diameter droplets, the motion and impingement of these droplets will determine the deposition characteristics. This is reflected in Fig. 5 by the negligible change in the cdf between $\theta = 0.8$ and $\theta = 1.4$ even though there are droplets adhering to the wall in this region (see Fig. 4). A second angular region where oil is deposited exists between $\theta = 1.4$ and $\theta = 1.6$, resulting from the impingement of the splashed droplets. It is further observed that for the conditions studied, 100% of the oil is deposited on the chamber housing, indicating that those droplets held in the core flow (see Fig. 4) account for a negligible proportion of the mass injected into the chamber.

The results for the predicted SMD with angular location are plotted using a log scale. It is observed that the SMD decreases from around 300 μm to around 80 μm as a result of the first impact with the chamber housing. The SMD then decreases further as more of the droplets deposit on the chamber housing with the value asymptoting to 8 μm for $\theta > 3$. This final value relates to the droplets suspended in the core flow in the chamber.

5 Sensitivity of Droplet Motion to Initial Injection Conditions

Having obtained base line results for the deposited mass and associated SMD, consideration is now given to the effect of the initial conditions imposed for the droplets release.

5.1 Effect of Mean Diameter. The sensitivity of the results to the assumed value of $\bar{d}$ has been studied for mean diameters of 100 μm, 200 μm, 300 μm, and 400 μm. With values of $\bar{d}$ of 200 μm or less, the released oil is carried by droplets that adhere to the chamber housing on impact. This is reflected in Fig. 6, which shows profiles of the cdf, by the almost steplike increase in the deposited oil from 0 to 1. For values of $\bar{d}$ of 300 μm and

Downloaded 02 Jun 2010 to 171.66.16.107. Redistribution subject to ASME license or copyright; see http://www.asme.org/terms/Terms_Use.cfm

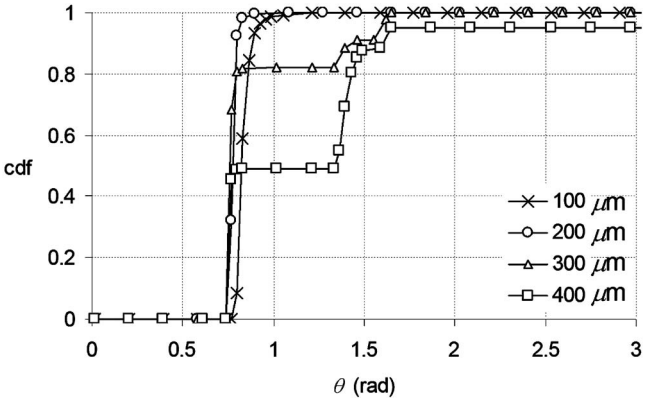

Fig. 6 Profiles of the cdf with angular location for different values of *d*

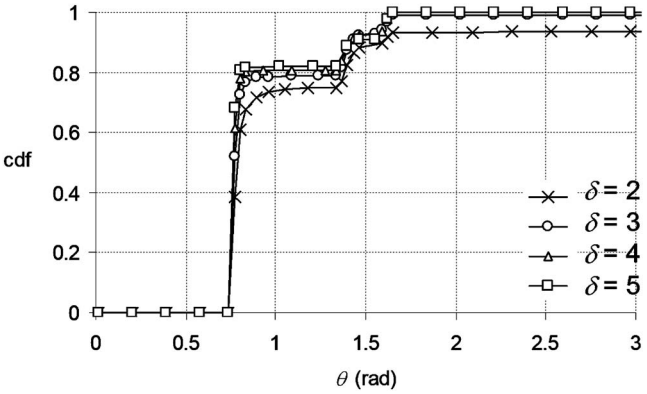

Fig. 8 Profiles of the cdf with angular location for different values of δ

above, the oil is carried by droplets that splash on impact with the chamber housing. This results in a portion of total oil released being splashed back into the core flow as secondary droplets and deposited further round the chamber. It is further noted that as $\bar{d}$ increases, the amount of oil deposited at the primary impact location decreases. The greater the amount of oil ejected in the form of secondary droplets, the greater the amount carried by droplets with diameters small enough to follow the airflow. This effect becomes apparent when $\bar{d}$ takes a value of 400 μm with 5% of the released oil remaining in the core flow.

Figure 7 shows the calculated SMD with angular location for the core flow, from which it is noticed that the effect of $\bar{d}$ is insignificant for values above 100 μm. When $\bar{d}$ takes a value of 100 μm, there is a significant weighting given to the smaller droplets. This decreases the predicted SMD for $\theta < 2$. After the first impingement location, $\theta \approx 0.8$, the oil phase comprises splashed droplets and those that are carried around by the airflow. Splashing typically results in a daughter droplet of around 30% the original diameter and thus, for all values of $\bar{d}$ studied, the splashed droplet diameters will be the same magnitude as those affected by the airflow. This results in no significant effect on the predicted SMD.

5.2 Effect of Variance. The mean diameter is held constant at a value of 300 μm and computations carried out to establish the sensitivity of the solution to the assumed spread δ of the initial distribution of droplets released. It is observed that from Fig. 8 that the cdf for the deposited oil is relatively insensitive for values of $\delta \geq 3$. With a spread parameter of 2, the distribution of diameters encompasses those droplets that remain suspended in the core flow. This results in less oil being deposited, indicated by the cdf curve being shifted down relative to the other curves. In terms of the SMD, it was found that the spread assumed for the initial droplet diameter distribution had an insignificant effect on the predicted values.

5.3 Effect of Radial Velocity. The final parameter studied is the initial radial velocity of the released droplets. The diameter distribution is now fixed with a mean diameter and spread parameter of 300 μm and 5, respectively. Simulations of the droplet's motion have been carried out with the initial radial velocity of the released droplets taking a value between 0% and 30% that of the azimuthal component. Increasing the initial radial velocity of the droplet increases the impact speed and angle, thus lowering the critical diameter for which splashing occurs. In addition, the change in the initial release angle will cause the droplets to impact on the chamber housing at smaller values of θ. This is shown in Fig. 9 by the shift in the cdf curves. In general, it is found that as the radial component of velocity is increased, the amount of oil deposited through primary impact decreases. However, the deposition at subsequent impacts increases such that all of the oil released is eventually deposited on the chamber housing. Again, no significant effect is observed on the predicted SMD around the chamber.

6 Discussion

In optimizing aeroengine bearing chamber designs, it is vital that the supplied oil performs its purpose and is then removed from the chamber efficiently. Oil remaining in the chamber either as small droplets in the form of a two-phase core flow or in the

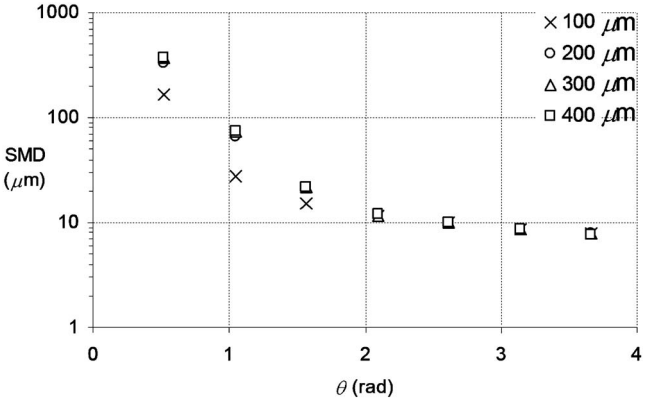

Fig. 7 The change of SMD with angular location for different values of *d*

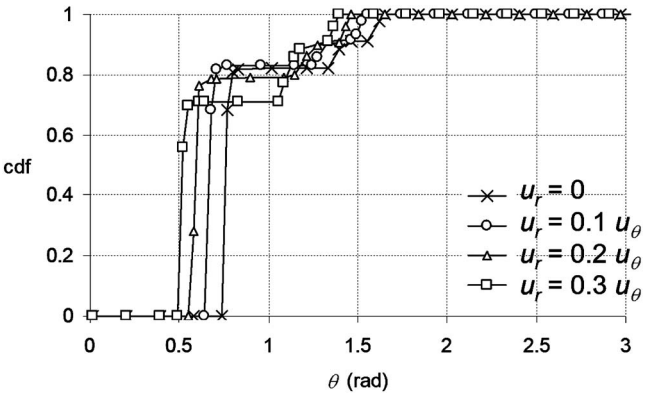

Fig. 9 Profiles of the cdf with angular location for different values of *ur*

Downloaded 02 Jun 2010 to 171.66.16.107. Redistribution subject to ASME license or copyright; see http://www.asme.org/terms/Terms_Use.cfm

film as a result of a badly designed scavenge can lead to serious heat to oil problems. The focus of the study has been to understand how key parameters, such as the mean diameter and spread of the distribution of the released droplets, affect the droplet dynamics and related deposition. The study showed that the predicted change in SMD with angular location is relatively insensitive to changes in the initial conditions. This was attributed primarily to the splashing significantly decreasing the maximum droplet diameter after the primary impact. In terms of the oil deposited on the chamber housing, it was found that the mean diameter assumed in the initial droplet distribution is the key parameter. A small mean diameter results in 100% of the released oil being deposited at the primary impact location. As the mean diameter is increased, the amount splashed back in the form of secondary droplets increases. As a result, some of the oil is carried further round the chamber before being deposited. More importantly, a proportion of the oil remains in the core flow, thus increasing the residence time of the oil in the chamber. This oil can then pick up a greater amount of heat, which leads in many industrial applications to a faster degradation of the oil. Moreover, to ensure enough oil adheres to the housing so that sufficient heat is removed, a greater amount of oil needs to be supplied to the chamber.

Viewing the results from the design perspective, the study suggests that to maximize the deposition on the chamber housing the oil exiting the bearing should satisfy a diameter distribution with a mean diameter less than 300 μm and a spread parameter greater than 3. Better chamber designs, in terms of the oil flow, might thus be bought about by focusing attention to controlling the shed from the bearings.

7 Conclusions

A 2D model of the two-phase air/oil flow has been presented and used to investigate the oil droplet motion and impingement relevant to an aeroengine bearing chamber. Results regarding the change in droplet diameter with angular location and the deposition of oil on the chamber housing have been used to assess the impact of key parameters on the oil droplet dynamics. It was found that while the SMD is relatively insensitive to changes in the mean diameter and spread of the initial droplet distribution, the deposition characteristics are more sensitive. A small mean droplet diameter results in complete deposition at the primary impact location, whereas a larger mean droplet diameter results in a portion of the oil that is splashed back into the core flow and transported further round the chamber.

Acknowledgment

The authors would like to thank Rolls-Royce plc for their financial support of this work.

Nomenclature

d = droplet diameter (m)
e = coefficient of restitution
E = energy (J)
k = turbulent kinetic energy ($m^2\ s^{-2}$)
K = impact parameter, $K=We^{1/2}Re^{1/4}$
m = mass deposited on housing ($kg\ s^{-1}$)
M = mass ($kg\ s^{-1}$)
N = number of droplets
r = radial distance (m)
R_a = surface roughness (m)
R_{nd} = nondimensional surface roughness, $R_{nd}=R_a/d_I$
Re = Reynolds number, $Re=\rho d_I U_I/\mu$
SMD = Sauter mean diameter (m)
U = velocity ($m\ s^{-1}$)
We = Weber number, $We=\rho d_I U_I^2/\sigma$
$\bar{x}$ = mean value of x

Greek Symbols

ε = turbulent dissipation energy ($m^2\ s^{-3}$)
η = splashed mass fraction
μ = dynamic viscosity ($kg\ m^{-2}\ s$)
θ = angle (rad)
ρ = density ($kg\ m^{-3}$)
σ = surface tension/distribution parameter (Nm^{-1})
ω = angular velocity ($rad\ s^{-1}$)

Subscripts

a = after impact
b = before impact
c = critical
d = dissipated
i = inner cylinder/ith droplet
inj = injected
I = incident droplet
k = kinetic
n = normal component
s = surface
t = tangential component

References

[1] Wittig, S., Glahn, A., and Himmelsbach, J., 1994, "Influence of High Rotational Speeds on Heat Transfer and Oil Film Thickness in Aero Engine Bearing Chambers," ASME J. Eng. Gas Turbines Power, **116**, pp. 395–401.

[2] Glahn, A., Busam, S., and Wittig, S., 1997, "Local and Mean Heat Transfer Coefficients Along the Internal Housing Walls of Aero Engine Bearing Chambers," ASME Paper No. 97-GT-261.

[3] Glahn, A., and Wittig, S., 1999, "Two-Phase Air/Oil Flow in Aero-Engine Bearing Chambers-Assessment of an Analytical Method for the Internal Wall Heat Transfer," Int. J. Rotating Mach., **5**(3), pp. 155–165.

[4] Busam, S., Glahn, A., and Wittig, S., 2000, "Internal Bearing Chamber Wall Heat Transfer as a Function of Operating Conditions and Chamber Geometry," ASME J. Eng. Gas Turbines Power, **122**, pp. 314–320.

[5] Glahn, A., and Wittig, S., 1996, "Two-Phase Air/Oil Flow in Aero Engine Bearing Chambers: Characterization of the Oil Film Flow," ASME J. Eng. Gas Turbines Power, **118**(3), pp. 578–583.

[6] Chew, J. W., 1996, "Analysis of the Oil Film on the Inside Surface of an Aero-Engine Bearing Chamber Housing," ASME Paper No. 95-GT-300.

[7] Farrall, M. B., Hibberd, S., and Simmons, K., 2000, "Computational Modelling of Air/Oil Flow in an Aero-Engine Bearing Chamber," *Proceedings of ASME 2000 Fluid Engineering Division Summer Meeting*, Boston, MA, June 11–15, ASME, New York, pp. 1–8.

[8] Farrall, M., Hibberd, S., and Simmons, K., 2003, "Modelling Oil Droplet/Film Interaction in an Aero-Engine Bearing Chamber," *Proceedings of ICLASS 2003*, Sorento, Italy, July 13–18, CD (8 pp.).

[9] Farrall, M., Simmons, K., Hibberd, S., and Gorse, P., 2004, "A Numerical Model For Oil Film Flow in an Aero-Engine Bearing Chamber and Comparison with Experimental Data," ASME Paper No. GT-53698.

[10] Glahn, A., Kurreck, M., Willmann, M., and Wittig, S., 1995, "Feasibility Study on Oil Droplet Flow Investigations Inside Aero Engine Bearing Chambers-PDPA Techniques in Combination With Numerical Approaches," *Proceedings of International Gas Turbine and Aeroengine Congress and Exposition*, Houston, TX, June 5–8, ASME, New York, pp. 1–9.

[11] Patankar, S. V., and Spalding, D. B., 1972, "A Calculation Procedure for the Heat, Mass and Momentum Transfer in Three-Dimensional Parabolic Flows," Int. J. Heat Mass Transfer, **15**, pp. 1787–1806.

[12] CFX, CFX-4.2 Solver Manual, CFX International, 8.19 Harwell, Didcot, Oxfordshire X11 0RA, UK, 1997.

[13] Farrall, M., 2000, "Numerical Modelling of Two-Phase Flow in a Simplified Bearing Chamber," Ph.D. thesis, University of Nottingham.

[14] Cossali, G. E., Coghe, A., and Marengo, M., 1997, "The Impact of a Single Drop on a Wetted Solid Surface," Exp. Fluids, **22**, pp. 463–472.

[15] Stanton, D. W., and Rutland, R. J., 1996, "Modeling Fuel Film Formation and Wall Interaction in Diesel Engines," SAE Paper No. 960628.

[16] Bai, C., and Gosman, A. D., 1995, "Development of Methodology for Spray Impingement Simulation," SAE Paper No. 950283.

Downloaded 02 Jun 2010 to 171.66.16.107. Redistribution subject to ASME license or copyright; see http://www.asme.org/terms/Terms_Use.cfm

[17] Mundo, Ch., Sommerfeld, M., and Tropea, C., 1997, "Numerical and Experimental Investigation of Spray Characteristics in the Vicinity of a Rigid Wall," Exp. Therm. Fluid Sci., **15**(3), pp. 228–237.
[18] Mundo, Ch., Sommerfeld, M., and Tropea, C. 1995, "Droplet-Wall Collisions: Experimental Studies of the Development and Breakup Process," Int. J. Multiphase Flow, **21**(2), pp. 151–173.
[19] Samenfink, W., Elsaber, A., Dullenkopf, K., and Wittig, S., 1998, "Droplet Interaction With Shear-Driven Liquid Films: Analysis of the Secondary Droplet Characteristics," *Proceedings of ILASS-Europe*, Manchester, Jul. 6–8, pp. 128–134.
[20] Mundo, Ch., Sommerfeld, M., and Tropea, C., 1994, "Experimental Studies of the Deposition and Splashing of Small Liquid Droplets Impinging on a Flat Surface," *Proceedings of ICLASS-94*, Rouen, France, Jul., pp. 134–141.
[21] Stow, C. D., and Stainer, R. D., 1977, "The Physical Products of a Splashing Water Drop," J. Meteorol. Soc. Jpn., **55**(5), pp. 518–532.

Downloaded 02 Jun 2010 to 171.66.16.107. Redistribution subject to ASME license or copyright; see http://www.asme.org/terms/Terms_Use.cfm

Numerical and Experimental Damping Assessment of a Thin-Walled Friction Damper in the Rotating Setup With High Pressure Turbine Blades

J. Szwedowicz
ABB Turbo Systems Ltd.,
Bruggerstreet 71a,
CH-5401 Baden, Switzerland
e-mail: jaroslaw.szwedowicz@ch.abb.com

C. Gibert
Ecole Centrale de Lyon,
CNRS/LTDS UMR 5513,
36 Avenue Guy de Collongue,
F-69134 Ecully Cedex, France
e-mail: claude.gibert@ec-lyon.fr

T. P. Sommer
ALSTOM (Switzerland) Ltd.,
Power Turbo-Systems,
Brown Boveri Street 7,
CH-5401 Baden, Switzerland
e-mail: thomas.sommer@power.alstom.com

R. Kellerer
ALSTOM (Switzerland) Ltd.,
Power Turbo-Systems,
Brown Boveri Street 7,
CH-5401 Baden, Switzerland
e-mail: rudolf.kellerer@power.alstom.com

Underplatform friction dampers are possible solutions for minimizing vibrations of rotating turbine blades. Solid dampers, characterized by their compact dimensions, are frequently used in real applications and often appear in patents in different forms. A different type of the friction damper is a thin-walled structure, which has larger dimensions and smaller contact stresses on a wider contact area in relation to the solid damper. The damping performance of a thin-walled damper, mounted under the platforms of two rotating, freestanding high pressure turbine blades, is investigated numerically and experimentally in this paper. The tangential and normal contact stiffness that are crucial parameters in optimal design of any friction damper are determined from three-dimensional finite element computations of the contact behavior of the damper on the platform including friction and centrifugal effects. The computed contact stiffness values are applied to nonlinear dynamic simulations of the analyzed blades coupled by the friction damper of a specified mass. These numerical analyses are performed in the modal frequency domain, which is based on the harmonic balance method for the complex linearization of friction forces. The numerical dynamic results are in good agreement with the measured data of the real mistuned system. In the analyzed excitation range, the numerical performance curve of the thin-walled damper is obtained within the scatter band of the experimental results. For the known friction coefficients and available finite element and harmonic balance tools, the described numerical process confirms its usability in the design process of turbine blades with underplatform dampers.
[DOI: 10.1115/1.2771240]

Introduction

Friction dampers are in widespread use in the turbomachinery industry to control vibration amplitudes of rotating blades. Several designs, such as dog bone, pin type, or wedge elements, are employed both as dampers and/or seals. Efficient design methods are of crucial importance to allow damper designs to perform in optimized, but robust manner.

One of the first attempts to model the dynamics of blades with underplatform dampers was made by Griffin [1], who identified the damper stiffness as a key parameter in damper optimization. During the past 25 years, various numerical techniques have been developed and applied to the design of solid dampers of diverse shapes and assembly manners. Most of these methods employ reduced order models and harmonic balance methods to decrease the time needed for the solution of the nonlinear algebraic equations describing the blade dynamics including friction effects.

A large number of papers on the numerical modeling of the frictional dissipation between shrouds and on underplatform friction dampers can be found in literature. Cameron et al. [2], Griffin [1], Wang et al. [3–6], Popp [29], Yang and Menq [7], Sextro et al. [8], Csaba [9], Gaul and Nitsche [30], Sanliturk et al. [10], Sextro [31], Petrov and Ewins [11] provide thorough reviews of the available literature and methods solving nonlinear vibrations of mechanical systems with friction. Petrov's interface element [11,12] describes analytically the nonlinear contact behavior at specified contact point. These elements reduce to a minimum the computational effort required for the analysis of the nonlinear damper-blade dynamics approximated with more complex Fourier coefficients [12]. His method allows efficient modeling of mistuning effects caused by manufacturing tolerances of blades as well as by variation in damper contacts within a blade-disk assembly [11]. A mistuned disk assembly is modeled using mode shapes from a cyclically symmetric finite element (FE) model of the tuned blade assembly as input (Feiner and Griffin [32], Petrov [12]). A different approach for the dynamic analysis of the mistuned blades including the variation in damper configuration is based on a sensitivity analysis and the assumption of a Weibull distribution. This procedure is validated experimentally and numerically with Monte Carlo simulations by Goetting et al. [13].

All these papers deal with typical industrial applications of underplatform dampers consisting of solid dampers of very compact dimensions and various shapes. Alternatively, thin-walled structures (Fig. 1) that generate smaller contact stresses on a wider contact area in comparison with a solid damper can be used. By cutting down the height of the thin-walled damper, its mass can effectively be tuned for needs of different blades without changing its contact stiffness properties from a practical point of view. Investigations into the damping characteristics of such thin-walled dampers are not reported in literature.

The elaborated mathematical models for simulations of the blades with solid dampers are sufficiently mature for performing sensitivity analyses of nonlinear forced vibrations (Petrov [12] or

Contributed by the International Gas Turbine Institute for publication in the JOURNAL OF ENGINEERING FOR GAS TURBINES AND POWER. Manuscript received June 6, 2006; final manuscript received May 29, 2007; published online December 18, 2007. Review conducted by Dilip R. Ballal. Paper presented at the Turbo Expo 2006: Land, Sea and Air (GT2006), Barcelona, Spain, May 8–11, 2006, Paper No. GT2006-90951.

Copyright © 2008 by ASME

Downloaded 02 Jun 2010 to 171.66.16.107. Redistribution subject to ASME license or copyright; see http://www.asme.org/terms/Terms_Use.cfm

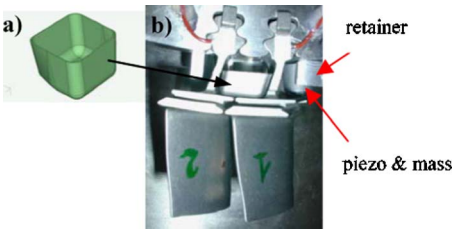

Fig. 1 Thin-walled damper assembly, (*a*) thin-walled damper, (*b*) assembled blade damper system

Panning et al. [14]). However, the reliability of these investigations depends very strongly on the correct assessment of friction coefficients as well as the contact stiffness. These properties have been measured using a range of different experimental setups. Griffin [1] has probably done the first experimental assessment of the damper properties. In general, the friction coefficient is evaluated from the measured hysteresis loop, as explained in detail by Koh et al. [15]. They applied Mindlin's theory [16] to the analytical assessment of the stiffness properties between the sphere and flat contact.

In order to include blade vibrations in the experimental investigation of the damper behavior, nonrotating test rigs of two to three beamlike blade models have been used where dampers are loaded by static gravity force to represent the centrifugal force acting on the damper (e.g., Balmer [17], Sanliturk et al. [18], Yang and Menq [19], Szwedowicz et al. [20]). To get more realistic conditions, rotating rigs are used with bladed disks that run in vacuum conditions. The beamlike blade models are reported by Stanbridge et al. [21] and Goetting et al. [13].

The scarceness of data taken in rotating rigs and the interest in the behavior of thin-walled dampers were motivation to carry out the present work as part of the Research Programme ADTurBII (Elliott et al. [22]). Reflecting the collaborative approach taken in the project, the current paper presents an experimental and numerical study of a thin-walled damper in a rotating rig. First, the test rig and experimental results are described. Then the numerical method is outlined with particular emphasis on the prediction of the contact stiffness. Finally, the numerical results for the damper performance are compared to the rig data. It will be shown that the computed results are in good agreement with the test data.

Test Rig Description and Experimental Results

An experimental rig for different types and shapes of friction dampers assembled into real rotating turbine blades was designed and built at the Ecole Centrale de Lyon (ECL). This rig (Fig. 2) consists of a rotating disk running in an evacuated chamber. Two

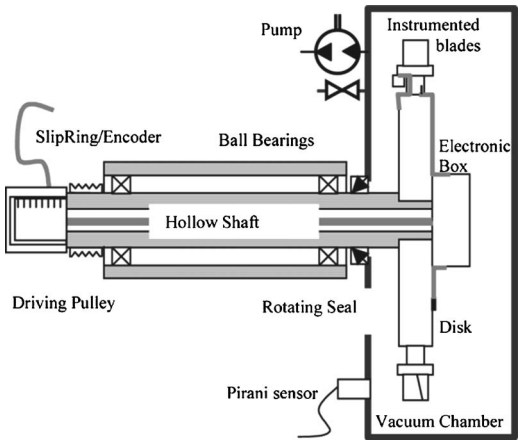

Fig. 2 Rotating blade setup in vacuum conditions

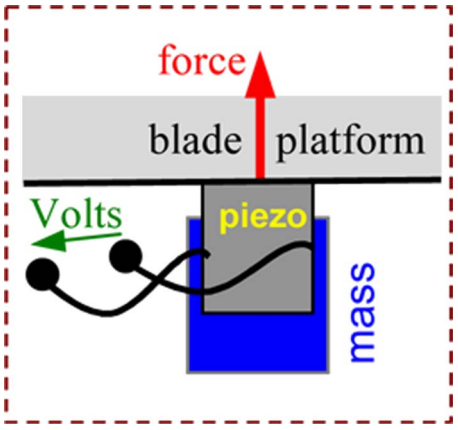

Fig. 3 Schematic of the piezoelectric shaker

pairs of turbine blades, symmetrically mounted on the disk, are equipped with "on-board" piezoelectric shakers. The turbine blades can be fitted with different types of underplatform dampers.

The excitation provided by the piezoelectric shakers can be chosen independently from the rotating speed by variation of the voltage at the piezoelement. Rotational speeds up to 5000 rpm can be achieved and the minimum pressure is about 1 mbar. The rig has four measurement channels on the rotating part, two channels for piezoelectric excitations (maximum 100 V), two for accelerometers, and two for temperatures on bearing supports. An endshaft slip ring/encoder is used for carrying electrical power and measurement signals between fixed and rotating parts and for shaft velocity measurement.

Excitation of the Blades. Piezoelectric actuators have been widely used in rotating blade applications, typically using piezoelectric patches working in d_{31} mode bonded to the airfoil (Kielb and Abhari [23], Charleux et al. [24]). Due to the particular geometry and dimensions of the turbine blades used here, special piezoelectric shakers have been assembled consisting of a tungsten carbide (CW) seismic mass and a small LVPZT stack translator mounted under the blade platform (Fig. 3). The elongation of the translator working in d_{33} mode, essentially proportional to the tension provided by a power amplifier, generates inertial reaction forces proportional to the square of the frequency that are transmitted to the blade. The translator is driven with a direct component of $+50\ V_{dc}$ superimposed with an alternating component ($\pm 50\ V_{ac}$) in order to operate within the specified 0–100 V range without any risk of degradation for the remnant polarization.

The slip ring electrical capacities, the power consumption increasing linearly with frequency, and actuator capacitance take part in the overall shaker performance and full range limitations. The weight of the attached mass finds some obvious limits due to available space and to centrifugal force, which has to remain below the push capacity of the actuator to avoid depolarization or damage caused to the ceramic. For the high stiffness of the ceramic, the resulting resonance frequency of the oscillator constituted by the translator associated with its mass is several thousands of hertz above the application frequency range. In addition, a shaker has an influence of approximately 2% on the first frequency of the original blade, whose dynamic behavior is still representative. Also, the static deformation of blades under centrifugal load is slightly affected by the shaker.

Two shakers, identically mounted to two blades, are driven independently by means of two different power amplifiers (Fig. 4). The phase between two alternating components can be chosen with either 0 deg or 180 deg relative phase using a voltage inverter circuit. This gives the opportunity to provide excitation pre-

Downloaded 02 Jun 2010 to 171.66.16.107. Redistribution subject to ASME license or copyright; see http://www.asme.org/terms/Terms_Use.cfm

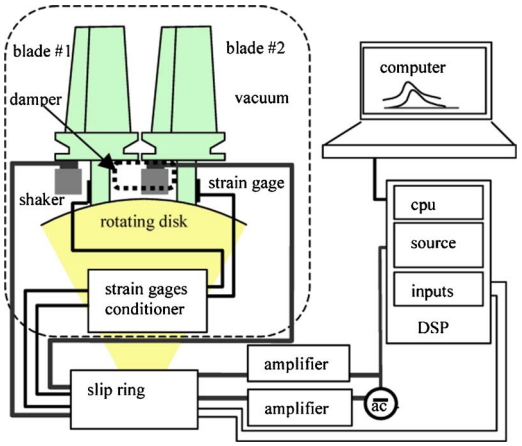

Fig. 4 Instrumentation of the rotating test rig for blades with friction dampers

dominantly on in-phase (IP) or out-of-phase (OOP) mode shapes of two analyzed blades. The OOP mode shape is more sensitive to the presence of the damper between vibrating blades.

As the piezoelectric actuator is used in an open-loop mode, there remains about 15% hysteresis between input tension and actual elongation only resulting in a quasiconstant phase lag of about 5 deg between these latter quantities within the frequency range used here. Also, acceptable deviations of less than 10% of the nominal translator gain (0.06 μm/V) due to the piezoelectric nonlinear behavior were found. Note that possible use of available open-loop control systems would require additional channels on the slip ring.

The chosen excitation method also requires particular care in dealing with the risk of loss of the mass attached to the piezoelectric stack. An inboard retainer device was designed and mounted on the disk in order to prevent ejection of the shaker mass in the case of failure of the ceramic attachment (Fig. 1). Within the assumptions explained above, the driving voltage provided to the ceramics that essentially determines the stroke of the piezoelectric stacks will be considered to be the known input of the dynamical system.

Instrumentation and Experimental Conditions. The response of the two blades is measured using strain gauges attached to the shank of each blade (Fig. 4). Two additional strain gauges are applied on the disk to measure its response. Strain signals are locally conditioned by means of on-board cards including signal conditioners installed in the electronic box. The gauge signals are converted to current before sending them to the slip ring along the hollow shaft through shielded wires. Conventional temperature and accelerometer sensors are used for machine monitoring and balancing of the rotor.

The pressure level inside the chamber is monitored by means of a Pirani sensor and is held to a prescribed value of ~20 mbars by using a two-stage rotary vane pump. Sealing is mainly achieved by means of static O-ring joints and a mechanical rotating seal. The lowest achievable pressure of about 1 mbar cannot be used because of the corona effect for the piezoelectric material in vacuum. The air insulation properties are a function of pressure and are greatly degraded in the range from 100 mbars to 0.1 mbar.

Fluctuations of the shaft speed were less than 2% and the resonance frequencies of the blades that strongly depend on the shaft speed could be repeated within less than 1% scatter between runs.

Swept Sine Measurements: Data Reduction. The response of the blades is obtained by means of a swept sine measurement technique performed in the vicinity of a given resonance. Series of measurements are made at different frequencies to provide frequency response functions (FRFs). The nonlinear behavior of the vibrating blades is characterized by measuring the FRFs with sweeps run at different constant voltage levels.

The sweep rate has to be chosen carefully depending, in particular, on the damping ratio. Too high sweep rate may induce artificial distortions in the FRFs, if insufficient time is available to reach the steady state vibration. Rules established for linear oscillators may be used for initial trials (Ewins [25], Lalanne [26]). Sweeping of frequencies up and down also helps to select the sweep rate. Ultimately, due to nonlinearity, swept sine parameters had to be adjusted in an iterative manner for a given set of test parameters (i.e., shaft velocity and voltage level). Although this kind of test has been shown to be slow, it provides a good signal to noise ratio, a way of directly exhibiting nonlinearities and data that can be easily compared with numerical results from hot-based multicast (HBM) solutions.

Experimental Results. The experimental configuration has been firstly tested without damper in order to establish a reference configuration. The damping is then supposed to be induced mainly by friction in fir trees. Samples of responses obtained for increasing voltage levels from 1 V to ~35 V, on the first flexural OOP mode of vibration, are shown in Fig. 5 for a given speed. The level of strain reaches about 120 microstrain for the maximum excitation level. Neglecting the nonlinearities, the corresponding damping ratio has been roughly estimated to be ~0.2% using the half-power technique. The frequency shift due to shaker excitation is less than −0.4% of the mean frequency and was observed to decrease with increasing speed. The frequencies of the first flexural IP and OOP modes of the blade have a similar sensitivity of nearly +0.01 Hz/rpm with respect to shaft speed. Depending on the speed and the excitation level, damping ratios were found between typical values of 0.01–0.3% in that so called "undamped case."

Tests performed with the dampers have revealed a significant effect on the frequency of the first OOP resonance that could be shifted up to nearly +50% in the experiment compared to the undamped case at the same speed. In contrast, the IP resonance is affected less than one could expect, with shifts only on the order of +1%. The nonlinear behavior of the damped blades was exhibited during measurements by typical downward sliding resonances while increasing the level (Fig. 6). Frequency shifts of about −10% from a resonance measured at a low level for a given speed were obtained by means of the used excitation device. For "equivalent" excitation conditions (frequency level), the magnitude of the measured strains is reduced by a factor of 10–50 and damping ratios are found on the order of ~1% to ~10% on the damped OOP resonance.

Numerical Analyses of the Measured Blades With Damper

Standard finite element codes solve the blade dynamic problem with friction by using time-marching methods. Due to the low material and aerodynamic damping ratio, often below 0.3% for freestanding turbine blades, the time integration of the nonlinear dynamic equations requires large amount of computational time for a typical FE model to be spent for each excitation frequency of interest. Therefore, this kind of method is suitable for verification of a damper design under particular operating conditions, but not for the design and optimization of damper systems.

Assuming periodic vibrations of the blades with the dampers, this nonlinear dynamic problem can be simulated effectively by using the HBM, based on a complex Fourier decomposition of the nonlinear friction forces. In general, each contact point is then represented linearly in the modal domain by a set of spring and dashpot elements. Therefore, contact stiffness is a key input to these methods.

Downloaded 02 Jun 2010 to 171.66.16.107. Redistribution subject to ASME license or copyright; see http://www.asme.org/terms/Terms_Use.cfm

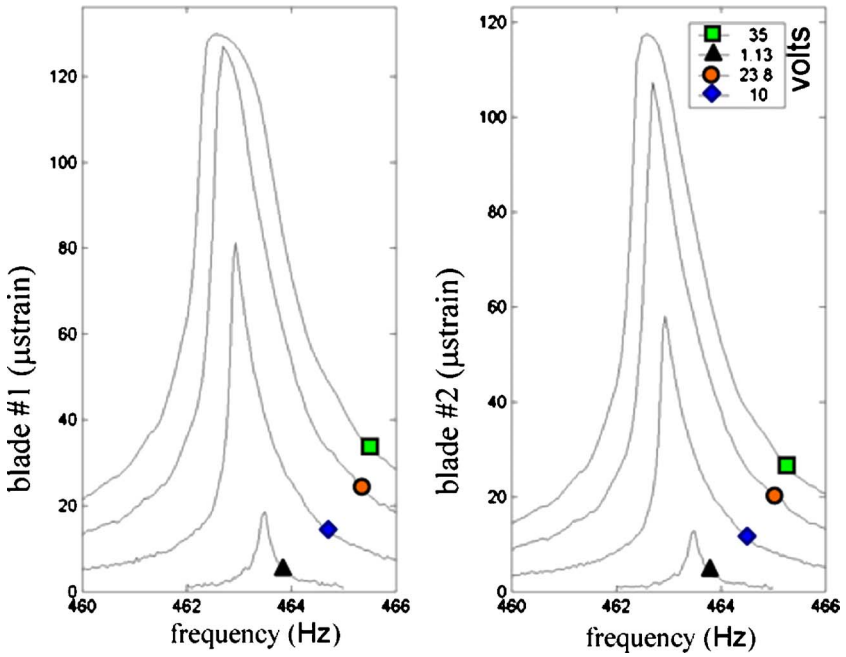

Fig. 5 Experimental undamped responses of OOP first flexural mode for excitation levels of 1 V, 10 V, 24 V, and 35 V at speed n_o

Finite Element Determination of the Stiffness Properties. To reduce experimental costs, various 2D FE procedures were elaborated through simulations of benchmark experiments (e.g., Szwedowicz et al. [20]).

For smooth contact with a dry friction model and constant friction coefficient, the 2D FE calculations yield a higher contact stiffness compared to the measured data, as shown in Fig. 7. However, the FE procedure still delivers the best overview of contact stiffness variations according to the design requirements. By including roughness in the FE procedure, the numerical results will better match the measured data.

However, a 2D model is insufficient for simulations of notch stresses at the damper ends, for the assessment of the asymmetrical tangential contact properties as well as for the thin-walled damper under investigation here. A 3D finite element model is required for such calculations. From a 3D FE analysis of two blades under centrifugal load, rigidly clamped at their fir trees and with a defined flat contact including friction on the damper with free-free boundary condition (Fig. 8), the strip contact area is

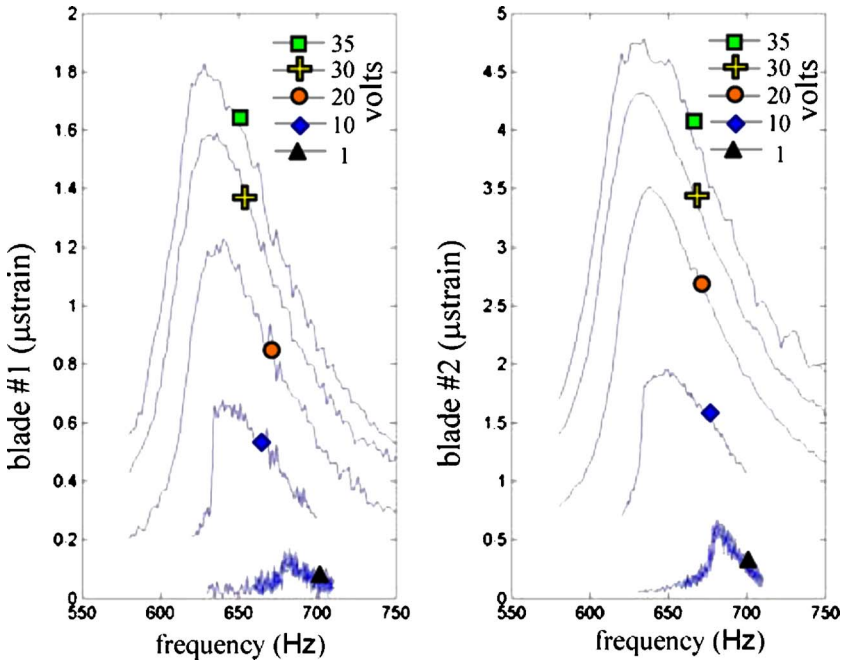

Fig. 6 Experimental damped responses of OOP first flexural mode for excitation levels of 1 V 10 V, 20 V, 30 V, and 35 V at speed n_o, where response differences between blades 1 and 2 are due to the asymmetrical contact conditions (Fig. 8)

Downloaded 02 Jun 2010 to 171.66.16.107. Redistribution subject to ASME license or copyright; see http://www.asme.org/terms/Terms_Use.cfm

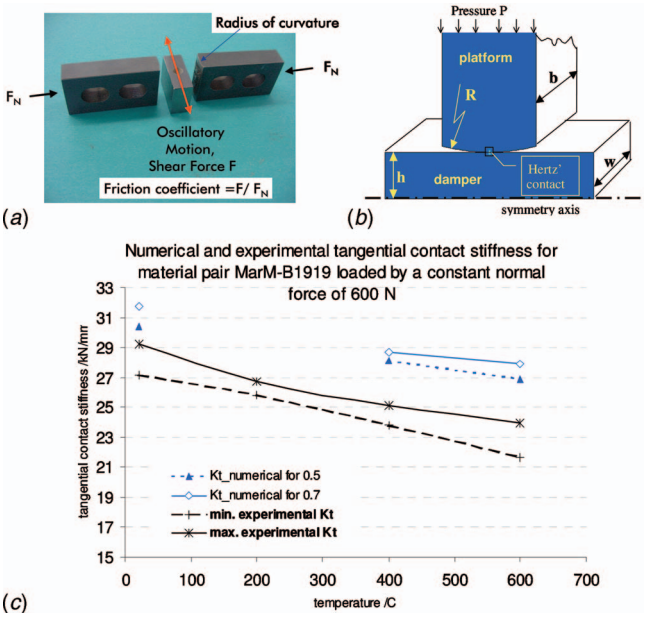

Fig. 7 Specimen (*a*), 2D FE model (*b*) and the comparison of the calculated contact stiffness for friction coefficients of 0.5 and 0.7 with the experimental data (*c*) measured at the ALSTOM setup for quasistatic tests

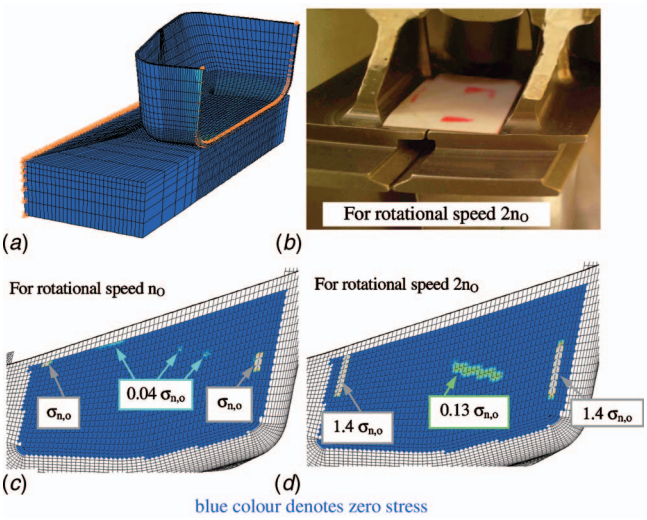

Fig. 9 (*a*) A 3D parabolic FE model exploiting the symmetry of the damper configuration and (*b*) the measured contact area compared to ((*c*) and (*d*)) the FE contact normal pressure, where $\sigma_{n,O}$ and n_O are normalized normal contact stress and rotational speed, respectively

identified on the damper. The highest contact normal stresses are located on 2 and 1 contact spots, respectively, on both opposite contact sides of the damper.

The resolution of the full 3D model is, however, not sufficient to yield reliable results for the contact stiffness. To improve the reliability of the FE contact results (see, e.g., Sinclair et al. [27]), a 3D parabolic FE model for the damper and platform only (Fig. 9) is used, exploiting the symmetry of the damper configuration, which is simplification of the real asymmetrical contact conditions [Fig. 9(*b*)]. In order to allow an assessment of the normal contact stiffness, three rows of parabolic finite elements are applied across the damper wall thickness. Neglecting the contact roughness, the contact surface is represented by regular elements of a size of 0.24×0.24 mm^2. The contact stresses under centrifugal load and a prescribed vibration amplitude were calculated for different rotational speeds, as shown in Fig. 9, where n_O and $\sigma_{n,O}$ denote the normalized speed and normal stress, respectively. Due to the elastic deformations of the thin-walled damper, the principle contact strips are located close to the walls of the damper. For the maximum rotational speed of $2n_O$, the third contact area appears in the middle region on the damper contact area with the contact pressure of 13% of the normalized contact pressure $\sigma_{n,O}$. In this damper region, the microslip friction dissipation can occur even for small excitation. For higher excitation, the entire damper can be in the macromotion. The increase of the rotational speed by 100% significantly changes the contact stress inside the contact area, but the contact stresses on the contact contour vary about 40%. The numerical contact area corresponds well to the measured contact pattern, as illustrated in Fig. 9. In the measurement, the three spot contacts are caused mainly by the asymmetrical position of the damper on the blades. On the other hand, to apply the entire FE model of the damper, the computer capacity was not enough for getting the numerical results in the reasonable computational time.

For a solid damper, due to its compact dimensions, usually determining its contact stiffness is sufficient and the solid damper is considered to be a rigid body in the dynamic simulation. The stiffness of the thin-walled damper depends on local contact deformations as well as on large scale deflections of the damper structure that both vary with the magnitude of the centrifugal load.

To determine the stiffness properties of the thin-walled damper, firstly the centrifugal load is applied to the damper and the platform to find the contact area for the specified friction coefficient. The platform deformation and bending effect are negligible in comparison with the damper behavior. For the calculated deformed state, a small virtual acceleration G_n in the normal direction n is firstly applied incrementally to the damper (Fig. 10). By increasing the acceleration, at each numerical increment i corresponding to the increase of the acting load, the normal reaction

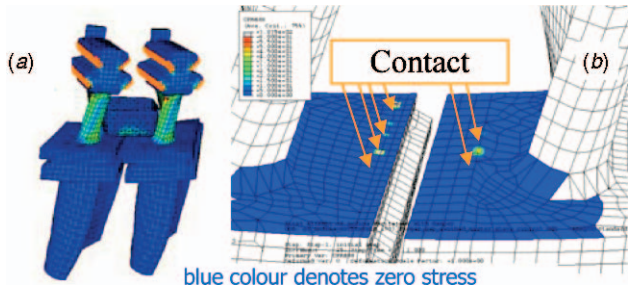

Fig. 8 von Mises centrifugal stress (*a*) and the contact normal stress (*b*) computed with the coarse parabolic FE model of two blades with the damper

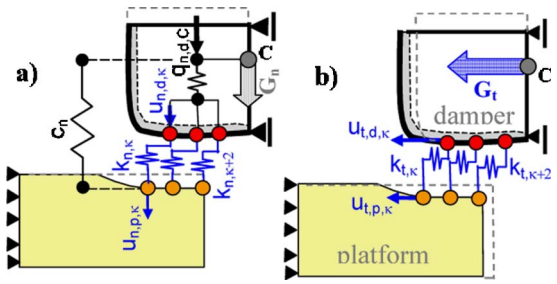

Fig. 10 Scheme of the virtual accelerations acting on the damper for its stiffness assessment in the normal *n* (*a*) and tangential *t* (*b*) direction, where *C* is the center gravity of the damper and *k* means the node in contact

Downloaded 02 Jun 2010 to 171.66.16.107. Redistribution subject to ASME license or copyright; see http://www.asme.org/terms/Terms_Use.cfm

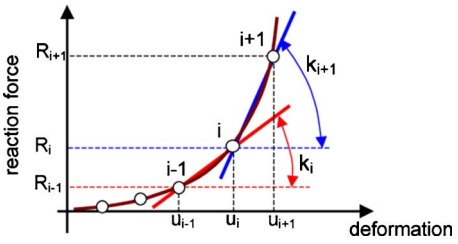

Fig. 11 The determination of the linearized stiffness k_i from the nodal deformation u_i and reaction force R_i at node in contact for different increments i of the nonlinear FE solution of the contact problem

force $R_{n,\kappa,i}$ and normal contact deformation $u_{n,\kappa,i}$ are obtained at each node κ, which is in contact with the platform. At the numerical increment i, the nodal contact stiffness $k_{n,\kappa,i}$ at node κ in the sticking contact is determined from (Fig. 11)

$$k_{n,\kappa,i} = (R_{n,\kappa,i} - R_{n,\kappa,i-1})/(u_{n,\kappa,i} - u_{n,\kappa,i-1}) \tag{1}$$

In addition, the global stiffness c_n in the normal direction of the entire thin-walled damper is needed for proper simulations of bending vibrations of the analyzed blades with the damper. For the calculated deformation of the center of the damper gravity $q_{n,C}$ (Fig. 10), the global normal stiffness of the damper c_n is determined at each numerical increment i from

$$c_{n,i} = \frac{m \cdot G_{n,i} - \sum_{\kappa=1}^{K} R_{n,\kappa,i}}{q_{n,i} - \sum_{\kappa=1}^{K} u_{n,\kappa,i}} \tag{2}$$

where m denotes the damper mass. The global normal stiffness c_n varies from 1.0 kN/mm up to 3.2 kN/mm by an increase of 250% of the normalized normal load, as presented in Fig. 12.

By applying a virtual acceleration G_t in tangential direction t to the damper (Fig. 9), very small tangential deformations of the damper in contact with the platform are induced for an assumed friction coefficient of 0.4. For the tangential reaction force $R_{t,\kappa,i}$ and tangential contact deformation $u_{t,\kappa,i}$, the tangential contact stiffness $k_{t,\kappa,i}$ at node κ in contact is determined in the same manner as the normal contact stiffness $k_{n,\kappa,i}$ (see Eq. (1)) from

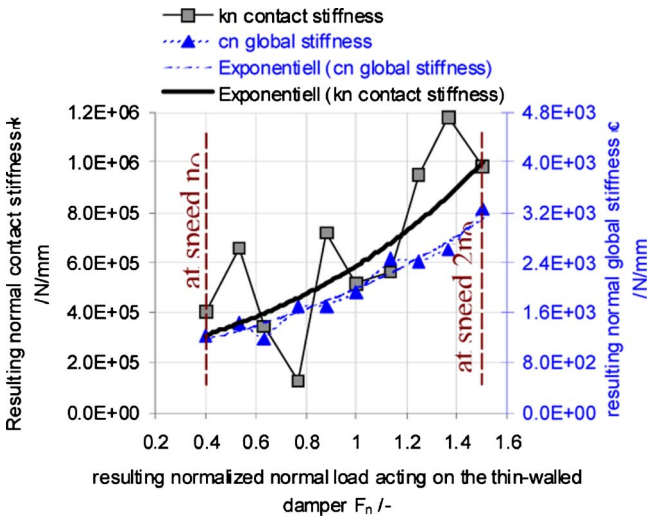

Fig. 12 The resulting normal contact stiffness k_n and global normal stiffness c_n of the thin-walled damper in terms of the centrifugal load F_n

Table 1 The tangential and normal contact stiffness as well as the global normal stiffness of the thin-walled damper determined from the FE results for a friction coefficient of 0.4 at 20°C

Rotational speed	Tangential contact stiffness k_t (MN/m)	Normal contact stiffness k_n (MN/m)	Global normal stiffness c_n (MN/m)
n_o	5.7	310.0	1.0
$2n_o$	28.4	1040.0	3.2

$$k_{t,\kappa,i} = (R_{t,\kappa,i} - R_{t,\kappa,i-1})/(u_{t,\kappa,i} - u_{t,\kappa,i-1}) \tag{3}$$

where i denotes a numerical increment of the nonlinear FE solution of the contact problem.

The obtained nodal tangential springs at all nodes K in contact (Fig. 10) are in serial configuration and the total tangential contact stiffness $k_{n,i}$ is found at each FE increment i as

$$\frac{1}{k_{t,i}} = \sum_{\kappa=1}^{K} \frac{1}{k_{t,\kappa,i}} \tag{4}$$

For the symmetrical FE model of the damper, it is not possible to determine the reliable global tangential stiffness c_t, and this analysis is not performed in this paper. For speeds $2n_O$ and n_O, the tangential k_t and normal contact stiffness k_n and c_n calculated are shown in Table 1 for a friction coefficient of 0.4 and ambient temperature. These stiffness values are treated as reference values for dynamic simulations with different friction coefficients from 0.05 to 0.8.

Linear Dynamics of the Blades at the Rotating Setup. Besides the stiffness and inertia properties of the damper, natural frequencies and mode shapes of the freestanding blade are needed in the nonlinear forced response analysis. A free vibration FE analysis of the rotating setup shown in Fig. 13 shows that the

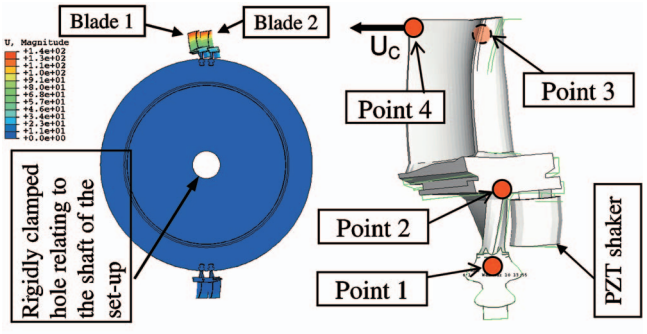

Fig. 13 The FE fundamental bending mode shape of interest of the blades with shaker in the rotating setup, where green color denotes blade at standstill

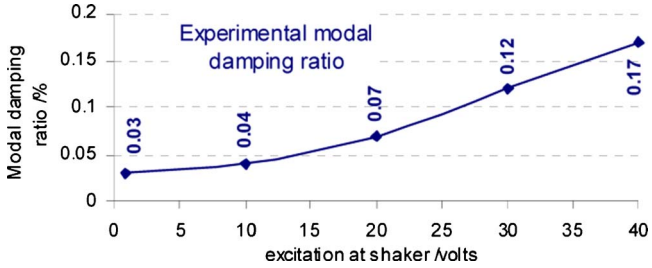

Fig. 14 The experimental damping ratio of the blade in the vacuum condition with the PZT shaker and without damper at 20°C and constant speed n_O

Downloaded 02 Jun 2010 to 171.66.16.107. Redistribution subject to ASME license or copyright; see http://www.asme.org/terms/Terms_Use.cfm

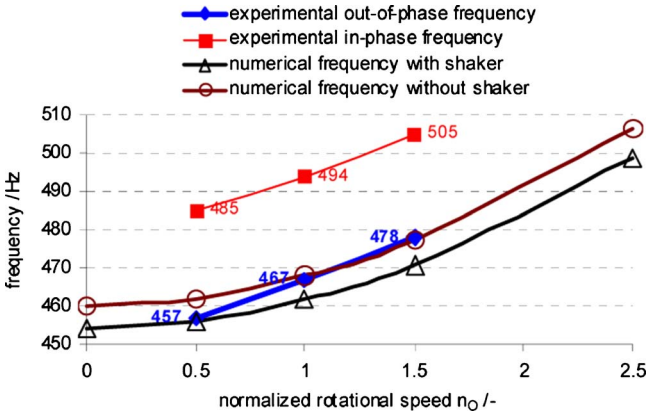

Fig. 15 The numerical eigenfrequencies of the rigidly clamped blade and the measured resonance frequencies of pair blades coupled weakly by the disk

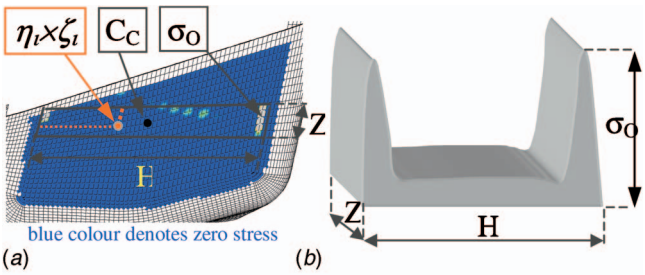

Fig. 17 (*a*) FE contact normal stresses on the damper whose the contact area is represented in the nonlinear analysis by a finite number $\eta \times \zeta$ of contact points on the rectangular area $H \times Z$ considering (*b*) the technical pressure distribution

lowest blade bending mode shape of interest here is well decoupled from vibrations of the disk. For this mode shape, the vibration ratio of the blade tip amplitude to the platform amplitude is equal to 2.7, confirming the suitability of the blade for successful application of an underplatform damper.

Modal damping ratios of the rotating blade including the shaker determined experimentally from the measured resonance response functions by using the half-power method are shown in Fig. 14.

The forced responses of the tested blades are computed in the modal domain by applying the method and computational code of Goetting [28], which approximates the friction forces using a first order HBM. The vibration of the tuned blade is characterized by the displacement from ten FE mode shapes of the rigidly clamped airfoil evaluated at four points shown in Fig. 13. The computed eigenfrequencies of the rigidly clamped, uncoupled airfoil correspond reasonably well with the experimental resonance frequencies of the OOP mode, i.e., the mode of interest for the damping investigation, of the two measured blades (Fig. 15).

Resonance responses at the blade tip (point 4 in Fig. 13) of the tuned blades are calculated for the full range of excitation levels tested in the rig, applying constant damping ratios for all ten mode shapes. In order to compare the computational results to the experiments, the calculated response of the blade tip is recast into strains at the gauge location on the shank by using a transmission factor known from the linear FE free vibration analysis and cross-checked with bench tests of the real hardware. As shown in Fig. 16, the numerical resonance amplitudes of the tuned blade model without damper correspond very well to the experimental results. The discrepancy between the two measured blades is mainly due to different locations of the strain gauge.

Nonlinear Dynamics of the Blades at the Setup. The same numerical process, which was applied to the linear dynamics analysis, is repeated for two tuned blades with the thin-walled damper that is in contact under the platforms under centrifugal load. The contact area and normal forces are obtained from the static centrifugal FE analysis and are input parameters into the nonlinear dynamic simulation. A rectangular contact area $H \times Z$ is discretized by a finite number $\eta \times \zeta$ of contact points (Fig. 17). By applying multipoint constraints, the local contact stiffness and contact forces at each ιth contact point $\eta_\iota \times \zeta_\iota$ are obtained from the damper stiffness (k_n and k_t) and FE resulting normal force. Using the kinematic constraints, the initial spatial motion of each contact point ι is determined from the oscillations of the resulting contact point C_C (Fig. 17) known from the FE free vibration calculation. For free-free boundary conditions imposed on the damper, the inertia moments are obtained from the FE calculation.

For very small excitations, the two blades are coupled elastically by the underplatform damper and the resonance frequency of the coupled system is obtained from the computation. Using the normal and tangential stiffness from Table 1, the eigenfrequencies of the two tuned blades with the underplatform damper are computed and compared to the OOP experimental resonance frequency of 683 Hz at speed n_O in Fig. 18. By applying the numerical global normal stiffness c_n of 1.0 MN/m and the tangential contact stiffness k_t of 5.7 MN/m (Table 1) calculated eigenfrequency of 560 Hz is obtained, which is significantly lower than the measured one (683 Hz). By applying a normal contact stiffness k_n of 1040 MN/m, the computed blade response become

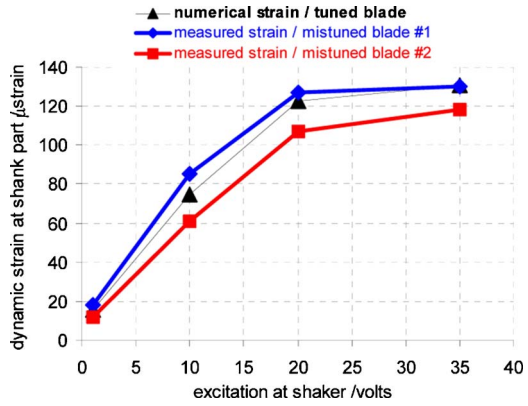

Fig. 16 The numerical resonance amplitudes of the tuned blade and experimental resonance amplitudes of two mistuned blades without damper measured at the ECL setup in the vacuum condition at 20°C and speed n_O

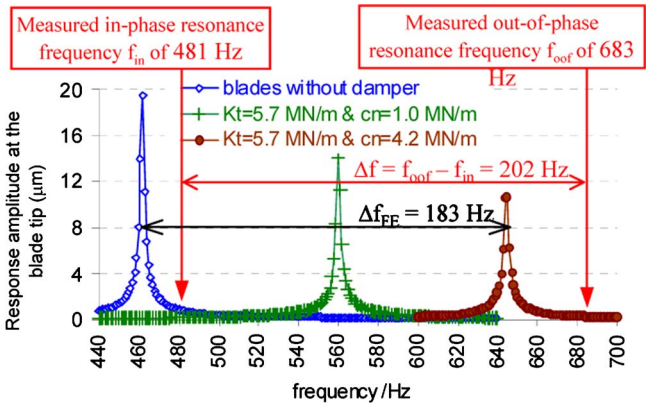

Fig. 18 Numerical eigenfrequencies of two tuned blades with sticking underplatform damper for the validation of the damper stiffness properties with respect to the measured resonance frequencies with very low excitation at speed n_O and 20°C

Downloaded 02 Jun 2010 to 171.66.16.107. Redistribution subject to ASME license or copyright; see http://www.asme.org/terms/Terms_Use.cfm

Table 2 Comparison of the numerical and experimental results of two measured blades with sticking damper at rotational speed n_o and 20°C

Results	In-phase frequency f_{in} (Hz)	Out-of-phase frequency f_{eef} (Hz)	Frequency coupling effect $\Delta f = f_{oof} - f_{in}$ (Hz)
Expt.	481	683	202
Numerical	462	645	183
Relative error (%)	4.0	5.6	9.4

unstable due to chattering effects and finally lost contact caused by a too stiff damper. Arguing that the real normal stiffness of the thin-walled damper is likely to be between the FE stiffness c_n and k_n due to insufficient FE refinement of the damper wall, the normal stiffness c_n is increased to tune the numerical eigenfrequency to the measured OOP resonance of 683 Hz. Finally, for the updated normal stiffness of 4.2 MN/m, an OOP eigenfrequency of 645 Hz is obtained numerically, which compares well to the measured resonance frequency (Fig. 18). For getting better frequency agreement, a further increase of the normal contact stiffness induces numerical instabilities. The determined frequency coupling effect Δf_{FE} of 183 Hz of the rigidly clamped blades corresponds well to the measured frequency difference of 202 Hz between the OOP and IP resonance frequencies of the measured blades (Fig. 18). An additional uncertainty was possible contact of damper's walls with the blade shank part, which was not proved numerically and experimentally. This effect might increase the eigenfrequency of the blades coupled by the damper, too.

As shown in Table 2, the obtained relative errors to the measured data are below 6% of the numerical results. For the further simulations, these errors obtained with the relatively simple contact model are considered to be sufficiently small considering the geometrical complexity of the thin-walled damper (Fig. 1) and its real contact with the mistuned blades.

Friction coefficients were not measured as part of this study. For the small contact normal stress σ_O in the present configuration, friction coefficients of 0.1 and 0.2 for the applied material pairs are considered to be realistic for use in the numerical analysis of the OOP blade resonance. For the different excitation levels, the computed resonance response functions correspond well with the asymmetrical experimental RRFs caused by slipping-sticking damper considering also their crumple forms in Fig. 19. The experimental resonance response functions of the blades without the damper are fairly symmetrical as it is presented in Fig. 5.

The numerical response amplitudes of the tuned blades are either too high or too small for friction coefficients of 0.1 and 0.2, respectively, in relation to the measured strain amplitudes of the mistuned blades 1 and 2. However, the measured responses of both blades differ by more than 100%. By including the underplatform damper, the resonance frequencies do not vary between both blades (Fig. 19). However, their response amplitudes alter significantly. An explanation for this effect can be found from the asymmetrical contact described by the three contact spots shown in Fig. 8. Then, blade 1 is damped more than blade 2. In the numerical simulation, which was done before the measurements, a symmetrical contact configuration (Fig. 16) on both tuned blades is assumed and the effect of the strong amplitude difference of the measured blade cannot be calculated.

By increasing the excitation from 1 V up to 34 V at PZT shaker, the known effect of resonance shift is measured for both blades, whose resonance frequencies decrease from 670 Hz to 631 Hz by 39 Hz (Fig. 19). The calculated shift of about 27 Hz of the resonance frequencies is smaller, which might be caused by the symmetrical contact configuration and the constant contact stiffness c_n and k_t in the model. In reality, the contact stiffness can vary in terms of sticking and slipping motions on the different regions of the contact area depending on the excitation magnitude and the spatial elastic deformation of the thin-walled damper.

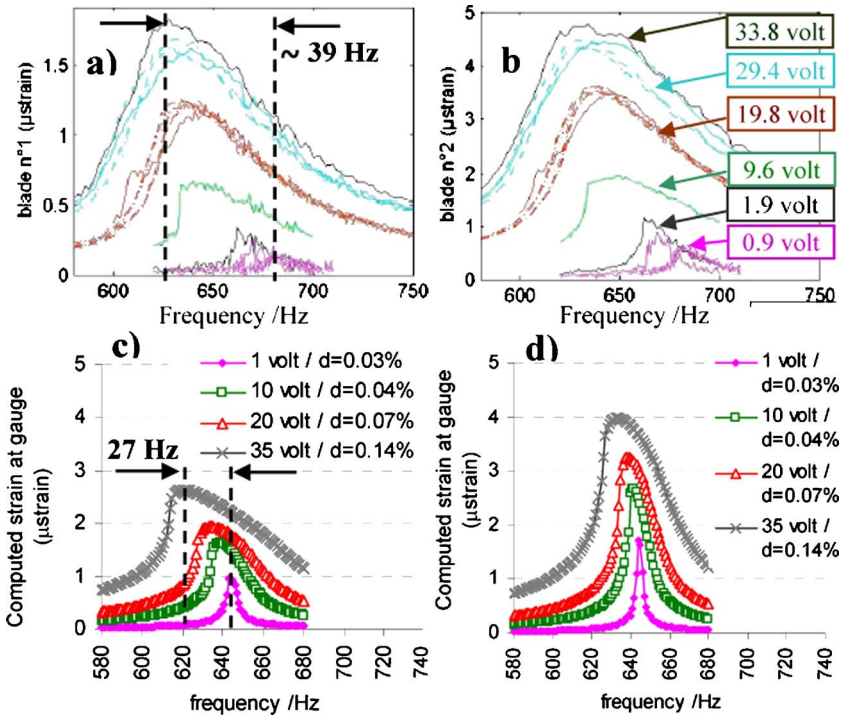

Fig. 19 The measured resonance response functions of the mistuned two blades ((*a*) and (*b*)) with the damper compared to the numerical results of the two tuned blades with damper for μ=0.1 (*c*) and μ=0.2 (*d*), where *d* means the experimental damping ratio of the blades without damper

Downloaded 02 Jun 2010 to 171.66.16.107. Redistribution subject to ASME license or copyright; see http://www.asme.org/terms/Terms_Use.cfm

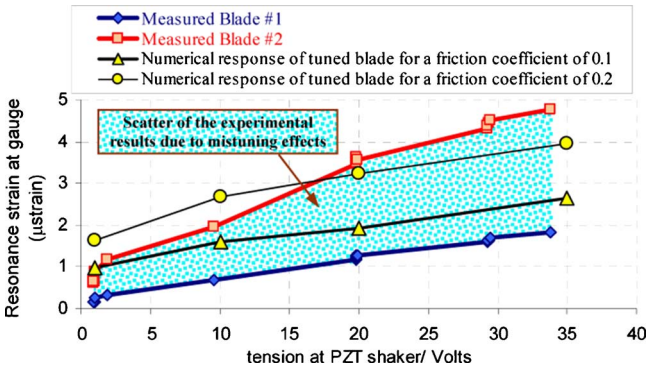

Fig. 20 The experimental performance curves of the two mistuned blades with the thin-walled damper compared to the numerical ones of the tuned blades obtained for friction coefficients μ of 0.1 and 0.2

Extracting the resonance amplitudes from the resonance response functions (Fig. 19), the experimental and numerical performance curves are compared in Fig. 20. The numerical results for both friction coefficients of 0.1 and 0.2 overestimate the resonance amplitude compared to the experimental data for the lowest excitation of 1 V. For the rest of the excitation range, the numerical results essentially lie within the band described by the experimental results of blades 1 and 2. For a friction coefficient of 0.1, the numerical results correspond well to the experimental data especially for the excitation above 20 V, where the numerical and experimental performance curves of blade 1 are parallel to each other. The observed discrepancy between the calculated and measured performance curves might confirm changeability of the friction coefficient for the small normal contact stresses generated by the thin-walled damper. Furthermore, the roughness, which was not included in the numerical analysis, would influence the dynamic behavior of both blades with the damper.

In general, the thin-walled damper delivers effective dissipation capability for the vibrating blades, as presented in Fig. 21. For low friction coefficient, the calculated resonance amplitudes of the blade with damper are significantly smaller than the resonance response of the freestanding blade. Moreover, small contact stresses generated on the damper would prevent wear problems.

Conclusions

In an attempt to evaluate the potentiality of models to be used for predicting damper efficiency in limiting vibration amplitudes of turbine blades, a dual experimental and computational approach has been established.

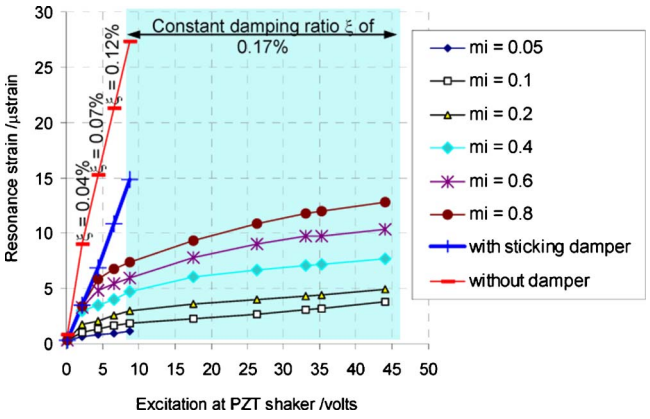

Fig. 21 Illustration of the damping capabilities of the thin-walled damper for the analyzed blades, where "mi" denotes friction coefficient

Dynamic tests with the underplatform thin-walled damper have been performed in vacuum condition at a temperature of 20°C. The experimental conditions have been simplified in order to focus on structural effects brought by the coupling of two blades by the thin-walled damper. For the real turbine blades and dampers, consistent and repeatable results have been obtained with different excitation levels. The nonlinear behavior of rotating and vibrating blades due to friction has been characterized experimentally and confirmed numerically. Because of the presence of the damper, a remarkable reduction of amplitudes is obtained, but also significant shift of the OOP resonance frequency is measured with respect to the blade frequencies without dampers.

For the thin-walled damper, the HBM has been tested successfully as an effective tool, which is less time consuming in relation to the FE time-marching approach. For the specified friction coefficient, the presence of the damper in the blade dynamics is simplified to its mass and inertia moments, and, in particular, to the normal and tangential resulting springs attached from the damper center of gravity to the central point of the contact area. In the nonlinear dynamic analysis, the contact area is represented by a finite number of contact points to simulate the microslip effects.

The contact stiffness parameters are calculated by means of FE modeling of the actual geometry of the blade platform and the damper. The FE process of the stiffness determination is well validated with the experimental results of solid dampers at various temperatures. By using the similar FE refinement on the contact like for the solid damper, the normal and tangential stiffness properties of the thin-walled damper are obtained numerically. These data are then used to perform a dynamic simulation of turbine blades with the sticking thin-walled damper. The computed resonance frequencies of the blade with damper are in an agreement with the experimental results for the tangential FE contact stiffness and the adjusted normal global stiffness of the damper. The adjusted normal stiffness of the thin-walled damper is four times higher than the FE value and confirms that the applied FE refinement for the normal deformation of the thin-walled damper was not enough fine. Instead of the symmetrical FE model, the thin-walled damper should be represented as the entire model with very fine mesh, both on the contact and away from the contact zone, which was beyond computer capacity during the realization of this work.

For an assumed friction coefficient of 0.1 with respect to the applied material pair, the calculated resonance amplitudes of the tuned blades with the thin-walled damper are in the scatter band of the measured results of the mistuned blades. Some obtained discrepancies between the measured friction test and the calculated results especially for the low excitation need further investigations. In further numerical investigations, the mistuned blades and asymmetrical contact configuration on the damper have to be taken into account to obtain fully reliable numerical results.

As far as prediction of the amplitudes is of importance, the present results are considered to be of sufficient quality for a preliminary design of damper close to optimum damper weight.

Acknowledgment

The work described is part of the Research Programme ADTurBII (Aeroelastic Design of Turbine Blades II), a project funded by the European Community under the "Competitive and Sustainable Growth" Programme (1998–2002), Contract No. G4RD-CT-2000-00189. Funding support for the Swiss project partners was provided by the Swiss Federal Office for Education and Science. The authors want to thank the European Community, the Swiss authorities and all other members of the Consortium for their financial support and for their overall contributions to the project. Details of the members of the consortium may be found on the project website[1].

[1]www.energy.kth.se/adturb2.

Downloaded 02 Jun 2010 to 171.66.16.107. Redistribution subject to ASME license or copyright; see http://www.asme.org/terms/Terms_Use.cfm

References

[1] Griffin, J. H., 1980, "Friction Damping of Resonant Stresses in Gas Turbine Airfoils," ASME J. Eng. Power, **102**(2), pp. 329–333.

[2] Cameron, T. M., Griffin, J. H., Kielb, R. E., and Hossac, T. M., 1987, "An Integrated Approach for Friction Damper Design," ASME Booklet DE, Vol. 5, pp. 205–211.

[3] Wang, J. H., and Yau, H. Y., 1990, "Design of Shroud Interface-Angle to Minimize the Forced Vibration of Blades," ASME Gas Turbine and Aeroengine Congress and Exhibition, Brussels, ASME Paper No. 90-GT-247.

[4] Wang, J. H., and Yau, H. Y., 1990, "Design of Blade-Shroud to Minimize the Sensitivity of Response to Preload Mistuning," *Proceedings of the Third International Conference on Rotordynamics*, Lyon, France, Sept. 9–12, pp. 341–350.

[5] Wang, J. H., and Shieh, W. L., 1991, "The Influence of Variable Friction Coefficient on the Dynamic Behaviours of Blade With Friction Damper," J. Sound Vib., **149**, pp. 137–145.

[6] Wang, J. H., and Chen, W. K., 1993, "Investigation of a Blade With a Friction Damper by HBM," Trans. ASME: J. Eng. Gas Turbines Power, **115**, pp. 294–299.

[7] Yang, B. D., and Menq, C.-H., 1998, "Characterization of Contact Kinematics and Application to the Design of Wedge Dampers in Turbomachinery Blading, Part I: Stick-Slip Contact Kinematics," ASME J. Eng. Gas Turbines Power, **120**(2), pp. 410–417.

[8] Sextro, W., Popp, K., and Wolter, I., 1997, "Improved Reliability of Bladed Disks due to Friction Dampers," ASME Paper No. 97-GT-189.

[9] Csaba, G., 1999, "Modelling of a Microslip Friction Damper Subjected to Translation and Rotation," ASME Paper No. 99-GT-149.

[10] Sanliturk, K. Y., Ewins, D. J., and Stanbridge, A. B., 2001, "Underplatform Dampers for Turbine Blades: Theoretical Modelling, Analysis and Comparison With Experimental Data," ASME J. Eng. Gas Turbines Power, **123**, pp. 919–929.

[11] Petrov, E. P., and Ewins, D. J., 2003, "Analytical Formulation of Friction Interface Elements for Analysis of Nonlinear Multi-harmonic Vibrations of Bladed Discs," ASME J. Turbomach., **125**, pp. 364–371.

[12] Petrov, E. P., 2005, "Sensitivity Analysis of Nonlinear Forced Response for Bladed Discs With Friction Contact Interfaces," ASME Paper No. GT2005-68935.

[13] Goetting, F., Sextro, W., Panning, L., and Popp, K., 2004, "Systematic Mistuning of Bladed Disk Assemblies With Friction Contacts," ASME Paper No. GT2004-53310.

[14] Panning, L., Popp, K., Sextro, W., Goetting, F., Kayser, A., and Wolter, I., 2004, "Asymmetrical Underplatform Dampers in Gas Turbine Bladings: Theory and Application," ASME Paper No. GT2004-53316.

[15] Koh, K.-H., Griffin, J. H., Filippi, S., and Akay, A., 2004, "Characterization of Turbine Blade Friction Dampers," ASME Paper No. GT2004-53278.

[16] Mindlin, R. D., 1949, "Compliance of Elastic Bodies in Contact," ASME J. Appl. Mech., **16**, pp. 259–268.

[17] Balmer, B., 1992, "Erhoehung der Daempfung von Turbinenschaufeln durch Reibelement (Damping Increase of Turbine Blades Through Friction Damper)," Fortschr.-Ber. VDI-Reihe 11, No. 197, VDI-Verlag GmbH, Duesseldorf, Germany.

[18] Sanliturk, K. Y., Stanbridge, A. B., and Ewins, D. J., 1995, "Friction Dampers: Measurements, Modelling and Application to Blade Vibration Control," *Proceeding of Design Engineering Technology Conferences*, ASME Paper No. De-Vol. 84-2, Vol. 3 Pt. B, pp. 1377–1382.

[19] Yang, B. D., and Menq, C.-H., 1998, "Characterization of Contact Kinematics and Application to the Design of Wedge Dampers in Turbomachinery Blading—Part I: Stick-Slip Contact Kinematics," ASME J. Eng. Gas Turbines Power, **120**(2), pp. 410–417; Yang, B. D., and Menq, C.-H., 1998, "Characterization of Contact Kinematics and Application to the Design of Wedge Dampers in Turbomachinery Blading—Part II: Prediction of Forced Response and Experimental Verification," ASME J. Eng. Gas Turbines Power, **120**(2), pp. 418–423.

[20] Szwedowicz, J., Kissel, M., Ravindra, B., and Keller, R., 2001, "Estimation of Contact Stiffness and its Role in the Design of a Friction Damper," ASME Paper No. 2001-GT-0290.

[21] Stanbridge, A. B., Sever, I. A., and Ewins, D. J., 2002, "Vibration Measurements in a Rotating Blisk Test Rig Using an LDV," *Fifth International Conference on Vibration Measurements by Laser Techniques*, Ancona, Jun. 18–21.

[22] Elliott, R., Green, J. S., and Seinturier, E., 2005, "Aeroelastic Design of Turbine Blades—ADTurBII Overview," *Sixth European Conference on Turbomachinery Fluid Dynamics and Heat Transfer*, Lille, France, Mar. 7–11.

[23] Kielb, J. J., and Abhari, R. S., 2003, "Experimental Study of Aerodynamic and Structural Damping in a Full-Scale Rotating Turbine," ASME J. Eng. Gas Turbines Power, **125**, pp. 102–112.

[24] Charleux, D., Gibert, C., Thouverez, F., Lombard, J. P., and Dupeux, J., 2005, "Analysis of a Bladed Disk With Friction in Blade Attachments," *XXIII IMAC*, Orlando, FL, Jan. 27–30.

[25] Ewins, D. J., 2003, *Modal Testing: Theory, Practice and Application*, Baldock: Research Studies Press, ISBN 0863802184.

[26] Lalanne, C., 1999, *Vibrations et chocs mécaniques, Tome 1: Vibrations sinusoidales*, Hermès, Paris.

[27] Sinclair, G. B., Comier, N. G., Griffin, J. H., and Meda, G., 1999, "Contact Stresses in Dovetail Attachments: Finite Element Modelling," ASME Paper No. 99-GT-387.

[28] Goetting, F., 2002, "Analyse des Schwingungsverhaltens von verstimmten Beschaufelungen mit Reibelementen (Analysis of Vibration Behaviour of Mistuned Bladed Discs With Friction Dampers)," Fortschr.-Ber. VDI-Reihe 11, No. 327, VDI-Verlag GmbH, Duesseldorf, Germany.

[29] Popp, K., 1994, "Nichtlineare Schwingungen Mechanischer Strukturen mit Fuge-oder Kontakt-stellen (Non-Linear Vibration of Mechanical Structures with Grooves of Contacts)," ZAMM, **74**, pp. 147–165.

[30] Gaul, L. , and Nitsche, R., 2000, "Dynamics of Structures With Joint Connections in Structural Dynamics—Part II: Current States and Future Directions," D. J. Ewins and D. J. Inman, eds., Research Studies Press Limited (RSP).

[31] Sextro, W., 2002, "Dynamical Contact Problems With Friction: Models, Methods, Experiments and Applications," Lecture Notes in Applied Mech., Vol. 3, Springer-Verlag, Berlin.

[32] Feiner, D. M., and Griffin, H. H., 2002, "A Fundamental Model of Mistuning for a Single Family of Modes," ASME Paper No. GT-2002-30425.

Downloaded 02 Jun 2010 to 171.66.16.107. Redistribution subject to ASME license or copyright; see http://www.asme.org/terms/Terms_Use.cfm

On Nonlinear Rotor Dynamic Effects of Aerodynamic Bearings With Simple Flexible Rotors

B. Bou-Saïd[1]
Laboratoire de Mécanique des Contacts et des Solides,
Bâtiment Jean D'Alembert 20 Rue des Sciences INSA,
20 Avenue A. Einstein 69 621,
Villeurbanne Cedex, France
e-mail: benyebka.bou-said@insa-lyon.fr

G. Grau
Microturbo 8 Chemin du Pont de Rupé BP 2089,
Toulouse Cedex 2, 31 019 France

I. Iordanoff
ENSAM-33405,
Talence Cedex, France

The last decades have experienced a growing enhancement of aeronautical oil free turbomachinery. The classical linear approach of rotor dynamics commonly uses stiffness and damping coefficients to model journal bearings. In the present study, a nonlinear time dependant calculation is used for the dynamic simulation of a rotor mounted with aerodynamic (gas) bearings. A comparison between the two approaches indicates that the dynamic behavior of such bearings can be nonlinear in operating ranges where the rotor eccentricity reaches high values. In that case, the linear approach may lead to incorrect results and the nonlinear approach should be performed for better rotor dynamic prediction. A numerical procedure which analyzes the dynamic behavior of simple flexible rotors taking into account the nonlinear (transient regime) characteristics of aerodynamic bearings is presented. A simple example highlights the needs of nonlinear simulations in order to predict dynamic performance in oil-free turbomachinery.
[DOI: 10.1115/1.2747262]

Keywords: foil bearings, rotor dynamics, stability, gas lubrication

Introduction

The designers of turbine engines have always had to deal with very severe restrictions concerning weight. Consequently, these designers focused on an increase in the specific power involving a reduction in the size of the machines, and an increase in rotating speed. In ranges of 30,000 to more than 100,000 rpm, an aerodynamic (gas bearing) approach seems well adapted compared to the traditional technological elements which cannot meet certain requirements, e.g., those concerning adequate lifetime. Thus air bearings have received considerable attention in these last decades and find increasing applications whenever elevated speeds, low loads, and a high degree of accuracy are necessary.

There are two operating conditions for aerodynamic bearings which are quite distinct: a dry contact-mixed lubrication mode, and an aerodynamic lubrication mode. The first condition corresponds to the transient mode and specifically the start-stop phases. This study deals with the latter behavior, when a complete film of air separating the rotating member from the static member is created. The determination of the pressure field in the bearings from the solution of the Reynolds equation in the case of compressible fluids, in particular with perfect gases, has been intensively investigated [1–3]. Air bearing static behavior has been previously treated by several authors [3–11].

Once static properties are known, designers must investigate the dynamic properties of the system consisting of the shaft and the bearings. In this paper, we will first treat the dynamic behavior of a rigid shaft mounted symmetrically on two aerodynamic bearings. Two methods of calculation, linear and nonlinear, are presented and compared in this simple case. This comparison reveals differences in results according to the loading, particularly in terms of speed instability and response to an unbalance excitation force. This portion of the study will lead us to suspect that the linear approach may be inadequate in some range of operating conditions compared to the nonlinear approach. Next, an improvement taking into account damping within the deformable structure of the bearings is highlighted. The last part of this study enables us to improve our understanding of the dynamic behavior of a deformable shaft by including nonlinear aspects of the problem.

A first model is based on a simplified approach to the problem. The step by step calculation is validated by comparison with the traditional linear rotor dynamics analysis. An improvement of this model is then made possible using the Rayleigh-Ritz method based on three elementary vibration modes taken for the shaft. Thus, we can evaluate the influence of the flexibility of the rotor on its critical engine failure speeds, and also on the level of stability of the system. The encouraging results of this modeling lead us to a more complicated finite element method approach. In our conclusions we will point out the principal results and place the present contribution in context. Finally, some directions of future research will be proposed.

Bump Foil Bearing

Many numerical and experimental studies have been concerned with the static and dynamic characteristics of so-called bump foil bearings. These works are generally concerned with two separate issues:

- Tribological phenomena related to the stop/start phases. Dry friction occurring during these phases is the main cause of deterioration of the bearings. The texture and shape of the surfaces and the materials in contact play a major role in these phenomena [12–15];
- Development of models to predict aerodynamic bearing performance in terms of carrying capacity, power loss and dynamic behavior [3,7,16,17].

This work is a contribution to the second research area. The bump foil technology allows us to take a very simple structural approach to the analysis. The upper foil ensures the continuity of the profile. The geometry of the bearing and the structural behavior are governed by the springs on which the upper foil is pressed, see Fig. 1.

Architecture and Geometry. Bump foil bearings present several alternatives. Indeed, the number of lobes and foils (for which

[1]Corresponding author.

Submitted to ASME for publication in the JOURNAL OF ENGINEERING FOR GAS TURBINES AND POWER. Manuscript received July 7, 2006; final manuscript received March 27, 2007; published online December 26, 2007. Review conducted by Nagaraj Arakere. Paper presented at the 2002 ASME Wind Energy Symposium (WIND2002), January 14–17, 2002, Reno, NV.

Copyright © 2008 by ASME

Downloaded 02 Jun 2010 to 171.66.16.107. Redistribution subject to ASME license or copyright; see http://www.asme.org/terms/Terms_Use.cfm

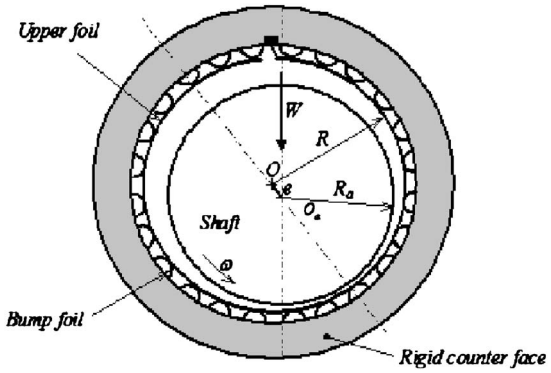

Fig. 1 Bump foil bearing description

the stiffness varies) can be adapted according to the desired performance. The first bearing developed with this technology consisted of a rigid sleeve onto which a corrugated foil and an upper foil are welded extending along all the bearing circumference. This foil assembly determines the general profile of the bearing film and its deformability (Fig. 1).

A correct implementation of the fixed deformable structure of the bearing foil must consider a variation of its structural stiffness with the angular position of the considered point [18]. The characteristics of this type of bearing are very close to its rigid counterpart (a smooth journal bearing) and this allows the bearing to support high loads,[9,19].

Aerodynamic Performance. The literature is replete with numerical and experimental work presenting the static and dynamic performance of foil bearings [19–30]. The description of their behavior follows the same format as for hydrodynamic bearings. However, in addition, one has to take into account the effect of compressibility of the fluid coupled with the structural deformation, i.e., an aero-elastic coupling.

The analysis of the foil bearing dynamic behavior can be carried out according to two different methods. In the linear method, the dynamic coefficients (stiffness and damping matrices) of the bearing are first calculated. Reynolds equation is solved for small increments of relative journal and bearing displacement and velocity, enabling evaluation of these coefficients. These matrices are then used to study the rotor dynamics. [31–34]. With the nonlinear method, the rotor dynamic movements are calculated in a step by step fashion based on the coupled resolution of Reynolds equation. This process gives the forces due to the bearings, and the equations of rotor dynamics [35–38].

The assumption of small displacements of the shaft center inside the bearing causes the linear analysis to have certain limitations. The method assumes that the variation of aerodynamic force with respect to its equilibrium position is nearly linear. A nonlinear analysis calculates the bearing forces at each time step to study the rotor dynamic behavior. No assumptions are needed for the bearing force evolution [30,39,40]. This type of study is rarely presented in the literature of foil bearings because of large computer demands in terms of time and memory [41,42]. On the other hand, similar work with incompressible fluids [35,31,43], confirms the importance of considering this type of analysis in certain operating conditions.

Indeed, some isolated works highlight interesting phenomena on the specifics of the linear and nonlinear approaches [44–46]. According to these works, the linear approach presents a restricted field of validity. It is thus important to investigate this point in order to avoid erroneous results.

Bearing Damping. The phenomena related to damping within the bearing structure are the subject of many numerical and experimental studies. One of the assumptions used in the past to explain the higher damping of the foil bearings is based on the presence of internal friction inside the deformable structure. Consequently, to add damping, some researchers assumed it was sufficient to increase the friction coefficient between the foils by using various types of coatings. Peng and Carpino [47] presented an analytical study in which they showed that damping in air bearings increases when the air film stiffens. As the eccentricity or the load increases the air film becomes stiffer and thus activate the dry friction between the bump and the housing. This phenomenon induces additional damping. They noticed that when the air film is flexible, i.e., when the load is light or the rotational speed is relatively low, ball bearings offer more damping than foil bearings. On the other hand, for higher load and speed, when the film of air is stiff, foil bearings provide more damping than their rigid counterparts due to the damping generated by friction between the foils of the deformable structure [48–50]. Damping can be considered using a viscous model when the load is small and the temperature high. Apparently, the addition of internal friction does not have any notable influence [28].

Table 1 Data input for the lobed bearing

L/D	0.75, 1, 1.25
D	50 mm
Number of pad	3
Pad angle, deg	110
Radial clearance, μm	50

Rotor Model. Classical theoretical studies have been interested in the dynamic characteristics considering the simplified case of a rigid rotor supported symmetrically by two identical bearings. The modeling of the dynamic action of the bearings is performed using the linear approach. Few authors considered the nonsymmetrical problem with a deformable rotor, and no existing study presents the direct coupling (with nonlinear analysis of the bearings) between the dynamic analysis of the rotor and its interaction with the foil bearings.

Comparison Between Linear and Nonlinear Methods

It is interesting to compare the linear and nonlinear methods to determine the range of validity. To this end, results in terms of stability level and unbalance response are given. For simplification, a rigid rotor symmetrically mounted on two identical three lobes rigid bearing is considered. The geometry of the lobes is circular and no geometrical preload is applied. The main characteristics are given in Table 1. The load on the bearing is only that of the rotor mass. For the stability study (Fig. 2), the critical speed is investigated for different rotor mass values. For the unbalance study (Fig. 3), the rotor mass is fixed at 2.25 kg and the mass unbalance is fixed at 1 g mm.

The results presented in Figs. 2 and 3, thus confirm the nonlinear dynamic behavior of the air bearings according to the operating range. Concerning stability, at high loads (corresponding to high eccentricity) the stability threshold given by the linear approach differs from that given by a nonlinear approach. Concerning response to a mass unbalance, there is a transition between the ranges where the two methods are in agreement and where they present strong differences. At high velocity (low values of eccentricity), the two methods give identical results, but they present dramatically different results at low velocity (high values of eccentricity).

However, the differences in phenomena observed concerning the domains of validity of the two approaches remain to be clarified. The definition of the limits of validity of the linear theory is thus a relevant direction of study for aerodynamic bearings. The comparison of the results given by linear and nonlinear approaches, Figs. 2 and 3, highlights the differences between these two methods. The curves obtained are very distinct. These differ-

Downloaded 02 Jun 2010 to 171.66.16.107. Redistribution subject to ASME license or copyright; see http://www.asme.org/terms/Terms_Use.cfm

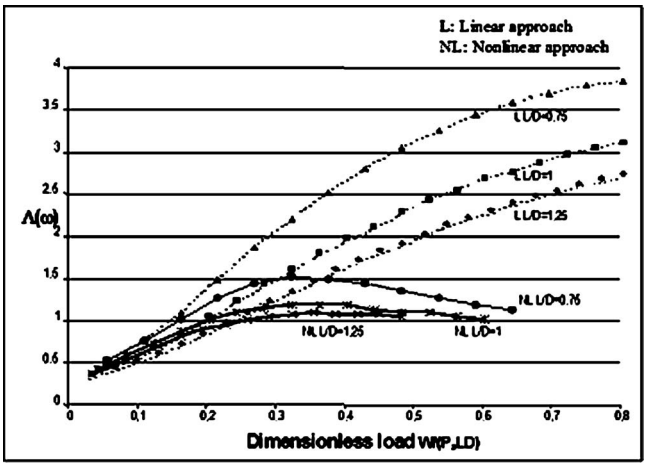

Fig. 2 Evolution of critical speed value against the dimensionless static load

ences occur both in term of stability threshold and response to unbalance. When aerodynamic bearings are highly loaded, it seems to be more accurate to use the nonlinear analysis.

Accounting for Structural Damping

Following the conclusion of the study where we compared the linear and nonlinear approaches, we set up a model taking into account a structural damping similar to that presented for the linear analysis in [51] and [33], but adapted to nonlinear calculation [26].

Modeling. This model has been detailed in [52]. The main idea here consists in rewriting the balance equations for deformable bearings taking into account the speed of deformation. The compressive forces generated in the air film are balanced by forces due to the bearing stiffness (or the compliance S_c) and due to its damping (viscous damping coefficient per unit of area noted C_e), Fig. 4.

Starting from the balance forces on the upper foil the expression of the variation of the pressure field between t and $t+dt$ can be written as

$$(P^{t+dt} - P^t) = \frac{1}{S_c}(H^{t+dt} - H^t) + \mathrm{C_e}\left(\left.\frac{dH}{dt}\right|_{t\to t+dt} - \left.\frac{dH}{dt}\right|_{t-dt\to t} \right) \tag{1}$$

Expressions of the terms dH/dt described previously are as follows:

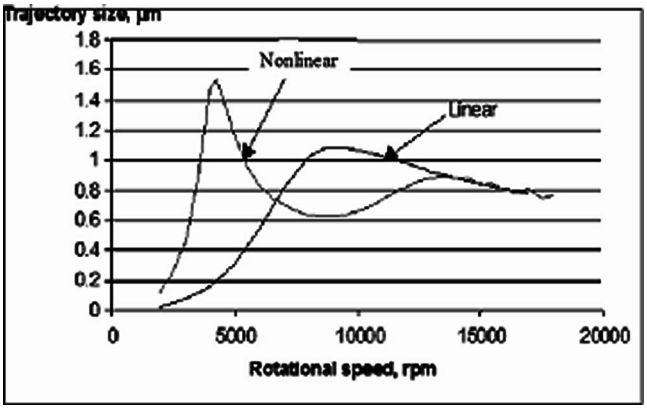

Fig. 3 Comparison of linear and nonlinear approaches

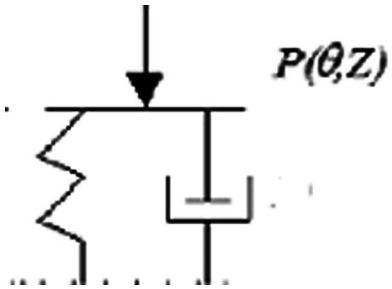

Fig. 4 Sketch of the model

$$\left.\frac{dH}{dt}\right|_{t\to t+dt} = \frac{H^{t+dt} - H^{t+dt}_{\mathrm{save}}}{\Delta t} \quad \text{and} \quad \left.\frac{dH}{dt}\right|_{t-dt\to t} = \frac{H^t - H^t_{\mathrm{save}}}{\Delta t} \tag{2}$$

where H^t_{save} is the film thickness at time t before deformation, H^t is the film thickness at time t after deformation, $H^{t+dt}_{\mathrm{save}} = H^t$ + displacement of the shaft between t and $t+dt$ (the film thickness at time $t+dt$ before deformation), and H^{t+dt} is the film thickness at time $t+dt$ after deformation. From the above, (1) can be expressed in the following form:

$$(P^{t+dt} - P^t) = \frac{1}{S_c}(H^{t+dt} - H^t) + \mathrm{C_e}\left(\frac{H^{t+dt} - H^{t+dt}_{\mathrm{save}}}{\Delta t} - \frac{H^t - H^t_{\mathrm{save}}}{\Delta t} \right) \tag{3}$$

Therefore, the relation giving the film thickness can be obtained as

$$H^{t+dt} = H^t + \frac{S\,.\,\Delta t}{\Delta t + S_c\,.\,\mathrm{C_e}}\left(P^{t+dt} - P^t + \frac{\mathrm{C_e}}{\Delta t}(H^{t+dt}_{\mathrm{save}} - H^t_{\mathrm{save}}) \right) \tag{4}$$

This film thickness is then introduced in the Reynolds equation in order to obtain the pressure field at each time step,

$$\frac{\partial}{\partial\theta}\left[PH^3\frac{\partial P}{\partial\theta} \right]^{t+\Delta t} + \frac{\partial}{\partial Z}\left[PH^3\frac{\partial P}{\partial Z} \right]^{t+\Delta t} = \Lambda\left(\frac{\partial PH}{\partial\theta} \right)^{t+\Delta t} + 2\Lambda\left(\frac{P^{t+\Delta t} - P^t}{\Delta t}H^{t+\Delta t} + P^{t+\Delta t}\frac{H^{t+\Delta t} - H^t}{\Delta t} \right) \tag{5}$$

Influence of Damping on the Threshold of Stability. The structural damping coefficient influence on the stability threshold is then studied using the set up model. The viscous damping coefficient used in the model can be replaced, in an equivalent way, by the damping coefficient used classically in rotor dynamics [53,54],

$$\alpha = \frac{C_e}{2\sqrt{KM}}$$

where: C replaces the viscous damping coefficient C_e, K replaces the reverse of the compliance coefficient S_c, and M represents the mass of the rotor assigned to the bearing.

All the studied profiles of the bearings are with three deformable smooth lobes (Fig. 5) and all the grooves are identical and have an extent of 10 deg (Table 2). We thus have represented the critical engine failure speed diagram for various values of α associated with this profile, Fig. 6. For comparison, we include the curve corresponding to the rigid profile.

It appears clearly that the addition of damping within the deformable structure, brings about a striking increase of the stability level for a compliant bearing (as for the low values of α). As could be expected, the higher the damping coefficient, the higher the critical speed. Furthermore, the critical speed does not decrease further with load increase. The relation between the critical

Downloaded 02 Jun 2010 to 171.66.16.107. Redistribution subject to ASME license or copyright; see http://www.asme.org/terms/Terms_Use.cfm

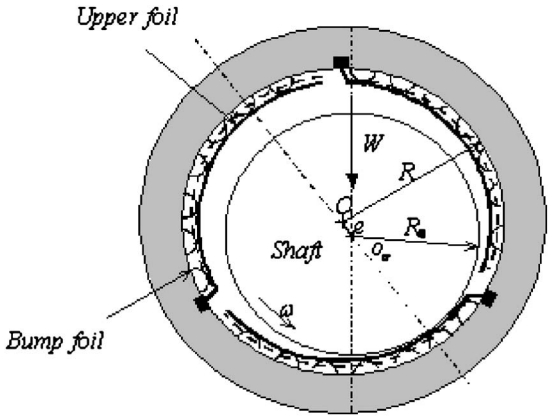

Fig. 5 Schematic of three lobed deformable bearing

engine failure speed and the static load seems to deviate from linear behavior and attain increasing polynomial nature.

Comments. In standard approaches the dynamic behavior of a deformable shaft supported by hydrodynamic bearings or ball bearings, is evaluated with the assumption that the bearing action is linear. The stiffness and damping matrix of the bearings are calculated and then introduced into a rotor dynamic computer code. This type of coupling is described as "weak." In the case of the aerodynamic bearings, we have been able to demonstrate that a linear dynamic analysis can lead to erroneous results according to the considered operation range.

The nonlinear character of a journal aerodynamic bearing is thus a significant fact to be considered in order to carry out an analysis of the rotor dynamic behavior. Therefore, we propose a "strong" coupling whereby the interaction of the bearings with the shaft is performed directly, step by step in time, in only one mode of the total calculation. In this first part the rotor was rigid and

Table 2 Main calculation characteristics for damping study

L/D	0.667
Number of pad	3
Pad angle, deg	110
Radial clearance, μm	50
Dimensionless compliance	0.2
$\alpha = \frac{C_c}{2\sqrt{KM}}$	0, 0.05, 0.1

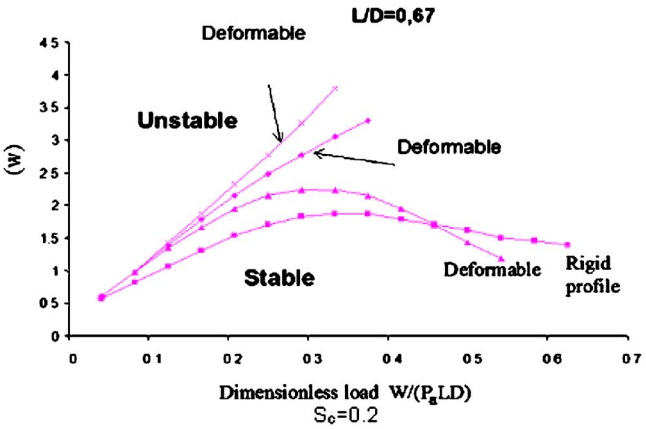

Fig. 6 Critical engine failure speed diagram for various values of α

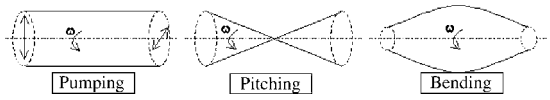

Fig. 7 Schematic representation of the considered vibration modes

symmetrically supported by two identical aerodynamic bearings.

It is now interesting to study the behavior of a more realistic case where the rotor is deformable and the bearings are not symmetrically mounted on the rotor. Because the approach presented is new, we have gradually proceeded towards the more complete problem of a deformable shaft with a nonlinear action of the journal aerodynamic bearings. Thus, the first part of the analysis consists of a dynamic model of a simple deformable rotor resulting from [14]. The Rayleigh-Ritz method with a three mode modal base is employed.

The dynamic behavior of a rotor mounted on two ball bearings was then compared to existing results for validation. Subsequently, the model was used to study the behavior of a deformable shaft running on two air bearings. The comparison with a linear "traditional" dynamic modeling confirmed once again the unique nonlinear dynamic behavior of the system. Finally, a comparison between a ball bearing and an air bearing points out the importance of the bearings on the overall dynamic behavior.

Rotor Dynamic Study With Foil Bearings

Short Description of the Rayleigh-Ritz Model. The Rayleigh-Ritz model uses a modal base restricted to three simple modes: pumping (or translation), pitching (or swinging), and first bending, Fig. 7. This modeling constitutes a first approach taking into account the two rigid body modes and the first bending mode of the shaft [54].

The symbol R_0 (X,Y,Z) indicates the initial frame (Fig. 8), in which the rotor axis at rest lies along the Y direction. The rotational speed Ω is considered constant. The rotor is considered as a beam and the neutral fiber displacement is studied. Each point on this fiber has two degrees of freedom that are displacements in the X and Z directions.

The expressions of the shaft neutral fiber displacements in the X and Z directions are, respectively, written in the following form:

$$u(y,t) = f_a(y)q_1(t) + f_b(y)q_3(t) + f_c(y)q_5(t)$$
$$= f_a(y)q_1 + f_b(y)q_3 + f_c(y)q_5 \quad (6)$$

$$w(y,t) = f_a(y)q_2(t) + f_b(y)q_4(t) + f_c(y)q_6(t)$$
$$= f_a(y)q_2 + f_b(y)q_4 + f_c(y)q_6 \quad (7)$$

where q_i are the generalized independent coordinates. The displacement functions, f_a, f_b, and f_c are, respectively, selected to represent the geometry of the vibration modes: pumping, pitching, and bending of a beam of constant section supported at its ends,

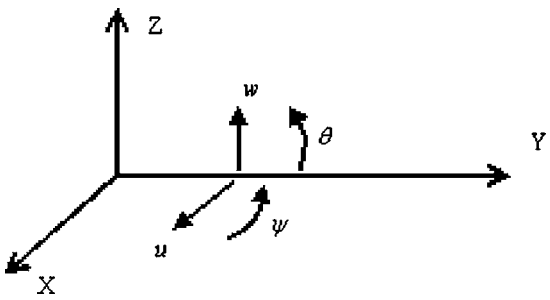

Fig. 8 Coordinate representation

Downloaded 02 Jun 2010 to 171.66.16.107. Redistribution subject to ASME license or copyright; see http://www.asme.org/terms/Terms_Use.cfm

$$f_a(y) = 1 \tag{8}$$

$$f_b(y) = 1 - \frac{2y}{L} \tag{9}$$

$$f_c(y) = \sin\frac{\pi y}{L} \tag{10}$$

The angular displacements ψ and θ of Fig. 8 are small and they can be approximated by

$$\theta = \frac{\partial w}{\partial y} = \frac{df_a(y)}{dy}q_2 + \frac{df_b(y)}{dy}q_4 + \frac{df_c(y)}{dy}q_6$$
$$= g_a(y)q_2 + g_b(y)q_4 + g_c(y)q_6 \tag{11}$$

and

$$\psi = -\frac{\partial u}{\partial y} = -\frac{df_a(y)}{dy}q_1 - \frac{df_b(y)}{dy}q_3 - \frac{df_c(y)}{dy}q_5$$
$$= -g_a(y)q_1 - g_b(y)q_3 - g_c(y)q_5 \tag{12}$$

The second order derivatives for u and w displacements are necessary to express the elastic energy of the shaft,

$$\frac{\partial^2 u}{\partial y^2} = \frac{d^2 f_a(y)}{dy^2}q_1 + \frac{d^2 f_b(y)}{dy^2}q_3 + \frac{d^2 f_c(y)}{dy^2}q_5$$
$$= h_a(y)q_1 + h_b(y)q_3 + h_c(y)q_5 \tag{13}$$

$$\frac{\partial^2 w}{\partial y^2} = \frac{d^2 f_a(y)}{dy^2}q_2 + \frac{d^2 f_b(y)}{dy^2}q_4 + \frac{d^2 f_c(y)}{dy^2}q_6$$
$$= h_a(y)q_2 + h_b(y)q_4 + h_c(y)q_6 \tag{14}$$

One may observe from the above expressions that $g_a(y)=0$ and $h_a(y)=0$ because f_a is of zero order. In the same way, $h_b(y)=0$ because f_b is of order one.

In the calculations below, we will not entirely develop the equations because manipulations are extensive but straightforward. We point out the expressions of various energies which should be calculated to write the Lagrange equations system [53].

Disk Element. The disk is considered as symmetrical. Its kinetic energy T_D can be written in the following way:

$$T_D = \frac{1}{2}M_D(\dot{u}^2 + \dot{w}^2) + \frac{1}{2}I_{Dx}(\dot{\theta}^2 + \dot{\psi}^2) + \frac{1}{2}I_{Dy}(\Omega^2 + 2\Omega\dot{\psi}\theta) \tag{15}$$

The energy of deformation of the disk is nil since it is considered as being rigid.

Rotor Element. The rotor elements are considered to be axisymmetric. The expression of kinetic energy T_S is as follows:

$$T_S = \frac{\rho S}{2}\int_0^L (\dot{u}^2 + \dot{w}^2)dy + \frac{\rho I}{2}\int_0^L (\dot{\theta}^2 + \dot{\psi}^2)dy + \rho IL\Omega^2$$
$$+ 2\rho I\Omega\int_0^L \dot{\psi}\theta dy \tag{16}$$

As the term $\rho IL\Omega^2$ is constant, we do not have to introduce this term in the writing of the Lagrange equations. The energy of deformation of the shaft, U_S is written as

$$U_S = \frac{EI}{2}\int_0^L \left[\left(\frac{\partial^2 u}{\partial y^2}\right)^2 + \left(\frac{\partial^2 v}{\partial y^2}\right)^2\right]dy \tag{17}$$

As the functions h_a and h_b are nil, the expression of the energy of deformation of the shaft is written according to the generalized coordinates,

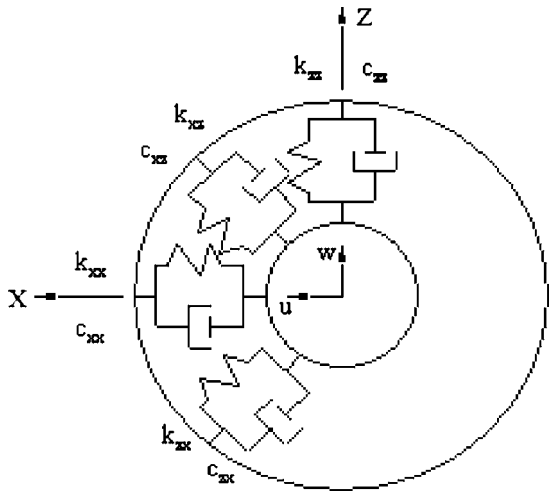

Fig. 9 Stiffness and damping coefficients of a ball bearing

$$U_S = \frac{EI}{2}\int_0^L h_c^2(y)dy(q_5^2 + q_6^2) \tag{18}$$

Unbalance. The shaft can be unbalanced. This unbalance is defined by a mass m_u at a distance d to the geometric center of the shaft. Its kinetic energy is written as

$$T_u = m_u d\Omega(\dot{u}\cos\Omega t - \dot{w}\sin\Omega t) \tag{19}$$

Having presented the energies, it is now appropriate to look at the actions of the ball bearings and/or the air bearings. In addition, to represent the operation of a shaft on air bearings, the influence of gravity must be added to the equations.

Ball Bearings. The shaft can possibly be supported by ball bearings. Their stiffness and damping coefficients are assumed to be known. The influence of the deflection is neglected, Fig. 9. The expression of the forces' virtual work exerted on the shaft is written in the following way:

$$\delta W_{rlt} = -k_{xx}u\,\delta u - k_{xz}w\,\delta u - k_{zz}w\,\delta w - k_{zx}u\,\delta w - c_{xx}\dot{u}\,\delta u - c_{xz}\dot{w}\,\delta u$$
$$- c_{zz}\dot{w}\,\delta w - c_{zx}\dot{u}\,\delta w \tag{20}$$

or

$$\delta W_{rlt} = F_{rltx}\delta u + F_{rltz}\delta w \tag{21}$$

where F_{rltx} and F_{rltz} are the components of the generalized forces of the ball bearing. In matrix form it can be written as

$$\begin{bmatrix} F_{rltx} \\ F_{rltz} \end{bmatrix} = -\begin{bmatrix} k_{xx} & k_{xz} \\ k_{zx} & k_{zz} \end{bmatrix}\begin{bmatrix} u \\ w \end{bmatrix} - \begin{bmatrix} c_{xx} & c_{xz} \\ c_{zx} & c_{zz} \end{bmatrix}\begin{bmatrix} \dot{u} \\ \dot{w} \end{bmatrix} \tag{22}$$

Air Bearings. Taking the air bearings into account in the behavior of a shaft requires the expression of the virtual work due to these bearings. As presented previously, the forces generated by the air bearings on the shaft depend at the same time on the local deflection of the rotor on the level of each bearing as well as the rotational speed. The expression of the virtual work of the forces generated by an air bearing is as follows:

$$\delta W_{pal} = F_{palx}\delta u + F_{palz}\delta w \tag{23}$$

with F_{palx}, F_{palz}, the components of the forces generated by the air bearing on the rotor. The components of the forces generated by the bearing are calculated at each time step, using Reynolds equation expressed in dynamic regime (Eq. (5)).

The Reynolds equation provides the field pressure which leads, upon integration, to the fluid film forces acting in the bearing. This kind of coupling is detailed in [26] in the case of a rigid rotor

Downloaded 02 Jun 2010 to 171.66.16.107. Redistribution subject to ASME license or copyright; see http://www.asme.org/terms/Terms_Use.cfm

symmetrically supported by two air bearings. In order to simplify calculations, we do not consider misalignment of the bearing generated by pitching, bending of the shaft or a difference in value of the magnitude of the static loads applied to the bearings.

Gravity. The action of gravity creates an offset of the rotor in the air bearings. We consider that the total mass of the shaft exerts a force located at the shaft center of gravity. The expression of the virtual work due to gravity is as follows:

$$\delta W_{\text{gravity}} = -M_{\text{total}} g \, \delta w(y_{cdg}) \tag{24}$$

with M_{total} as the total mass of the shaft, g is the acceleration of gravity, and y_{cdg} is the Y-coordinate of the shaft's center of gravity.

We obtain the system of equations by application of the Lagrange formalism,

$$\frac{d}{dt}\left(\frac{\partial T_c}{\partial \dot{q}_i}\right) - \frac{\partial T_c}{\partial q_i} + \frac{\partial U}{\partial q_i} = \delta W_i \tag{25}$$

with $i=1-6$, T_c being the kinetic energy, U the energy deformation of the whole shaft components, δW the total virtual work, and q_i the generalized coordinates of the system. Thus we can obtain the system of equations for the rotor dynamic which can be written in the following matrix form,

$$[M]\{\ddot{q}\} + [C]\{\dot{q}\} + [K]\{q\} = \{F\} \tag{26}$$

with $[M]$ the matrix of mass, $[C]$ the matrix governing the gyroscopic effect and possibly the ball bearing damping, $[K]$ the matrix of the rotor stiffness and possibly the ball bearing stiffness, $\{F\}$ the vector of the external actions (the unbalance, the air bearings forces and gravity).

Dimensionless Equations. The system of equations can be written in the following form:

$$[\bar{M}]\{\bar{\ddot{Q}}\} + \frac{1}{\Omega}[\bar{C}]\{\bar{\dot{Q}}\} + \frac{1}{\rho L^3 \Omega^2}[\bar{K}]\{\bar{Q}\} = \{\bar{F}\} \tag{27}$$

with the following dimensionless variable definitions:

$$\bar{Q}_i = \frac{q_i}{C_0}, \; \bar{\dot{Q}}_i = \frac{\dot{q}_i}{C_0 \Omega}, \; \bar{\ddot{Q}}_i = \frac{\ddot{q}_i}{C_0 \Omega^2}, \; [M], \; \overline{M_{ij}} = \frac{M_{ij}}{\rho L^3},$$

$$\overline{C_{ij}} = \frac{C_{ij}}{\rho L^3}, \; \bar{F}_i = \frac{F_i}{\rho L^3 C_0 \Omega^2} \tag{28}$$

with time $T=t\Omega$, Ω as the rotational speed. The parameter C_0 denotes an arbitrary value of the order of the bearing radial clearance. The symbols ρ and L, respectively, denote the density and the length of the rotor.

This dynamic system must be solved step by step in time to take into account the nonlinear variations of aerodynamic bearing forces in the right hand side member. The numerical integration scheme is the same as that presented in [26].

Validation

The results from the model are compared to those given in [14] for a rotor described in Fig. 10, supported by two ball bearings (Table 3). In the reference, the rotor is modeled by finite element method with a pseudo-modal reduction.

Four critical speeds are given by the Rayleight Ritz model (Table 4). The first two critical speeds are very close to the reference value, Fig. 11. The last two critical speeds are quite different. In this case, modes three and four involve bending modes that are more complex than the first bending mode involved in the Rayleigh-Ritz model. The first two modes are the first bending mode. This study confirms that the simplified Rayleigh-Ritz model gives good results if the rotor bending mode remains simple. Generally, the rotors used in oil-free turbomachinery are quite stiff, thus considering only rigid and first bending modes is a reasonable assumption.

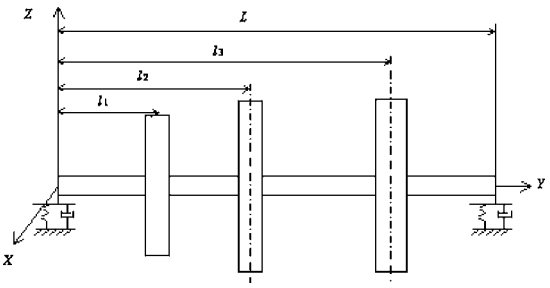

Fig. 10 Configuration of the reference case

Results and Discussion

The Rayleigh-Ritz model will now be used to study the dynamic behavior of a deformable shaft supported by air bearings. Thus we will be able to show the usefulness of this type of analysis while observing, in particular, the influence of the rotor flexibility on the response to an unbalance and the stability threshold of the system. We consider a solid or hollow shaft of external length 300 mm and 50 mm of diameter, as shown in Fig. 12. In the speed range of 2000–18,000 rpm, the dynamic behavior is close to the symmetrical rigid configuration (Fig. 13). This rotor seems too short and thus too stiff to observe deflection phenomena in the considered speed range. Once again this validates the Rayleigh-Ritz model. The influence of the bending mode has not been shown by this example.

To increase the bending mode, a rotor with 900 mm length is chosen for the rest of the study. The air bearings, as in the preceding case, are located at 50 mm from the ends of the rotor. The dynamic calculation of this shaft's behavior with nonlinear action of the air bearings gives an interesting response curve to unbalance. We always observe a peak of amplitude towards 4000 rpm. It is similar to the case of a rigid rotor but a second peak appears towards 9500 rpm. We compare this response curve in Fig. 14 with that obtained from the symmetrical rigid rotor simple model in order to highlight the effect of the rotor's flexibility.

It is interesting to represent the deformation of the rotor for speeds of 4000 and 9500 rpm, Figs. 15 and 16. These figures give the representation of the trajectory of the rotor's center for various Y-coordinates. We took the precaution to remove the static deformation of the shaft due to gravity, so that the observation of the deformation in rotation is easier.

It appears clearly that the mode of vibration at the speed of 4000 rpm is of the "rigid body" type because we obtain a very small twist of the shaft. The amplitude of displacements along the Z-axis is one third of those along the X-axis, Fig. 15.

For the speed of 9500 rpm, the associated mode of vibration introduces the inflection of the rotor whose form is complex. It should be noted that the amplitude of the deformation along the Z-axis (direction of the weight) is approximately four times higher than that in the X-direction, Fig. 16.

One can also plot on the same graph the response curves to unbalance in configuration ball bearings and air bearings, Fig. 17. It appears that the two curves present notable differences. First of all, we note that the air damping of the bearings leads to a decrease of the amplitude of the rotor center trajectory compared that of a "ball bearing" configuration (with identical unbalance). At high speed, the eccentricity is low, film thickness is high, and the air bearing stiffness is less than that of a classical ball bearing. Hence, a part of the second mode energy is in the bearing and not in the rotor, as with ball bearings. In the air bearing configuration, we thus obtain displacements which are due to both the rigid and

Downloaded 02 Jun 2010 to 171.66.16.107. Redistribution subject to ASME license or copyright; see http://www.asme.org/terms/Terms_Use.cfm

Table 3 Data for the reference case

	l_1=0.2 m, l_2=0.5 m, l_3=1 m, L=1.3 m		
Rotor	Plain section, ϕ=0.05 m $E=2\times10^{11}$ N/m^2, ρ=7800 kg/m^3, ν=0.3		
Disk	Thickness, m	Inner diam, m	Outer diam, m
Disk 1 (l_1)	0.05	0.05	0.12
Disk 2 (l_2)	0.05	0.05	0.2
Disk 3 (l_3)	0.06	0.05	0.2
Bearing stiffness and damping	$K_{xx}=5\times10^7$ N/m, $K_{zz}=7\times10^7$ N/m, $K_{xz}=K_{zx}=0$ $C_{xx}=5\times10^2$ N/m/s, $C_{zz}=7\times10^2$ N/m/s, $C_{xz}=C_{zx}=0$		
Unbalance	200 g mm on disk 2		
Velocity	from 0 to 30000 rpm		

bending modes. At low speed, a rigid vibration mode is present with the air bearing configuration and not with that of the ball bearings. This simple case outlines how bearings influence the whole dynamic response of the system.

General Conclusions

This study of aerodynamic journal bearing dynamic characteristics has been conducted because it is crucial to understanding rotor dynamic behavior. Initially, the rotor is considered to be rigid and supported symmetrically by two identical radial bearings. We have shown that the linear modeling, i.e., representing the bearings with stiffness and damping coefficients, has a restricted field of validity. For instance, in the case of a three lobe rigid bearing without geometrical preload, this range is limited to relative eccentricities lower than 0.65.

Thus, the prediction of the bearing stability threshold and the response to dynamic excitations can be erroneous if one uses a linear approach beyond the appropriate limit for this type of aerodynamic bearing. In addition, we illustrated the fact that for high loads the deformable bearing profiles have a lower stability than their rigid counterparts. Since we were fully aware that this observation goes against some physical phenomena observed in experiments, we set up a model which takes into account a structural damping of viscous type in the nonlinear approach. Even with very low coefficient values of the bearing structural damping, the level of stability could be increased, in accordance with the phenomena presented in the literature.

Having clearly highlighted the nonlinear character of aerodynamic bearings dynamic behavior, we considered direct coupling with a deformable shaft. At this point we developed a calculation

Table 4 Critical speeds

	Critical speed, Rayleigh-Ritz rpm	Critical speed, Reference rpm
1	3610	3620
2	3840	3798
3	12850	10018
4	15080	11279
5	···	16785
6	···	24408
7	···	26615

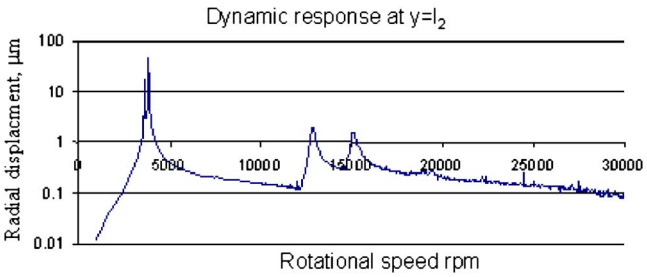

Fig. 11 Dynamic response at $y=l_2$

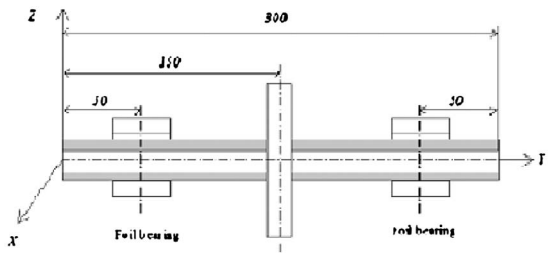

Fig. 12 Scematic of a hollow shaft with a central disk

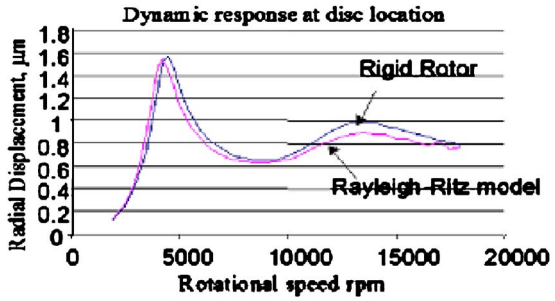

Fig. 13 Comparison between the Rayleigh-Ritz model and rigid rotor model

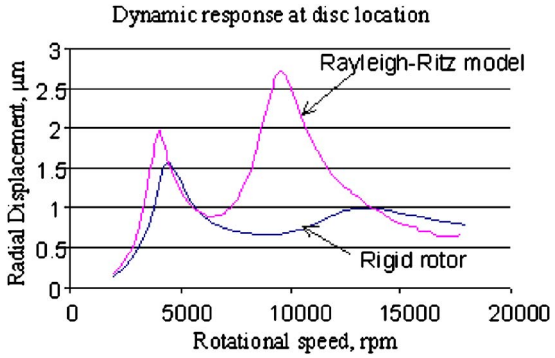

Fig. 14 Response curve to unbalance. Comparison with the rigid case.

Downloaded 02 Jun 2010 to 171.66.16.107. Redistribution subject to ASME license or copyright; see http://www.asme.org/terms/Terms_Use.cfm

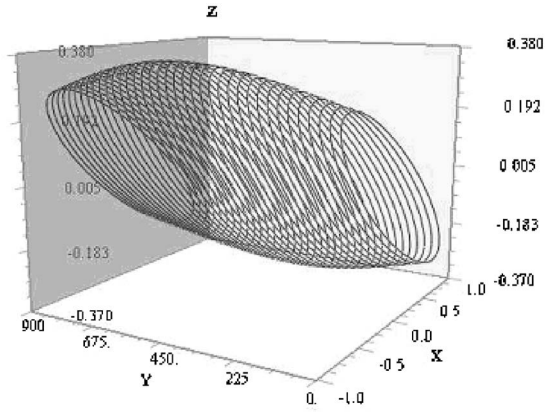

Fig. 15 Deformation of the rotor at 4000 rpm

based on the Rayleigh-Ritz method using a base of three modes (pumping, pitching, and bending). Thus, we were able to confirm the coherence of the obtained results compared to those from the rigid rotor model.

The deformation of the rotor reveals modes of vibrations which cannot be predicted by the rigid model. At low speed, a rigid mode of vibration is present with the air bearing configuration. At high speed we obtain displacements which are due to both rigid and bending modes. This simple case brought into light the influence of the bearing on the dynamic response of the complete system. It appears clearly in the first part of this paper that the addition of damping within the deformable structure leads to the increase of the deformable bearing's stability level.

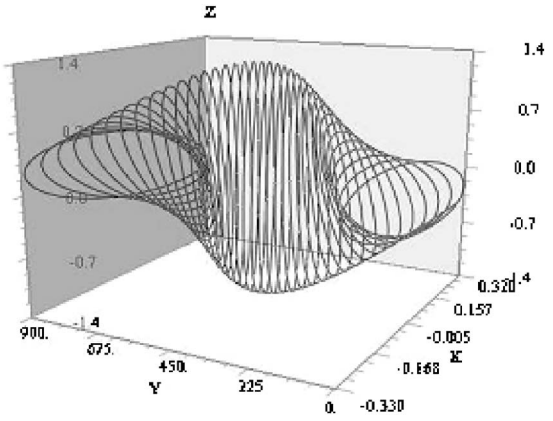

Fig. 16 Deformation of the rotor at 9600 rpm

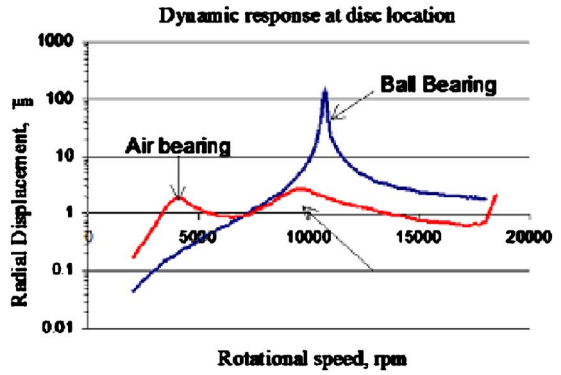

Fig. 17 Response curves to unbalance in configuration ball bearings, air bearings with linear and nonlinear action

As could be expected, the higher the damping coefficient, the higher the critical speed. Furthermore, the critical speed does not decrease further with load increase. The relation between the critical engine failure speed and the static load seems to deviate from linear behavior and approach a higher order polynomial form. It is clear that future work will relate on the one hand to the modeling of dry friction between the foils and the bumps to properly quantify the damping brought by this process, and on the other hand to the development of a more realistic rotor dynamic model so as to properly characterize the dynamic behavior of the whole system.

Nomenclature

C = radial clearance
C_{ij} = damping coefficients
D = bearing diameter
e = bearing eccentricity
E = Young modulus
$f_{a,b,c}$ = displacement functions
F_{rltx}, F_{rltz} = roller bearing forces
F_{palx}, F_{palz} = bearing forces
g = gravity acceleration
h = film thickness
H = dimensionless film thickness, $H=h/C$
I = rotor inertia in the X direction
I_{Dx} = disk inertia in the X direction
I_{Dy} = disk inertia in the Y direction
K_{ij} = bearing stiffness coefficients
K_s = stiffness coefficient of the structure
L = bearing length
M = rotor mass
M_D = disk mass
O = bearing center
O_a = shaft center
p = pressure
p_a = ambient pressure
P = dimensionless pressure, p/p_a
q_i = generalized coordinates
R = bearing radius
R_a = shaft radius
S_c = compliance
S = bearing section
$\bar{S}_c$ = dimensionless compliance $\bar{S}=S(P_a/C)$
t = time
T = dimensionless time, $T=t\omega$
T_S = rotor kinetic energy
T_D = disk kinetic energy
T_C = total kinetic energy
T_u = unbalance kinetic energy
U_1 = speed component in X direction
U_S = rotor energy deformation
$u(y,t)$, v, w = shaft displacement in the X, Y, and Z directions
X, Y, Z = initial frame
x, y, z = local frame
W_o = static load
W = carrying capacity
$\bar{W}$ = dimensionless carrying capacity, $\bar{W}=W/(p_aLD)$
$W_{dx,y}$ = external dynamic forces
δW = virtual work
α = damping coefficient
Ω, ω = rotational speed
Θ, Ψ = shaft angular displacements
Λ = bearing number

Downloaded 02 Jun 2010 to 171.66.16.107. Redistribution subject to ASME license or copyright; see http://www.asme.org/terms/Terms_Use.cfm

References

[1] Cameron, M., 1965, *The Principles of Lubrication*, Longmans Green Editions.
[2] Heshmat, H., Shapiro, W., and Gray, S., 1982 "Development of Foil Journal Bearings for High Load Capacity and High Speed Whirl Stability," J. Lubr. Technol., **104**, pp. 149–156.
[3] Heshmat, H., Walowit, A., and Pinkus, O., 1983, "Analysis of Gas-Lubricated Foil Journal Bearings," J. Lubr. Technol., **105**, pp. 647–655.
[4] Licht, L., and Branger, M., 1975, "Motion of a Small High—Speed Rotor in 3 Types of Foil Bearings," J. Lubr. Technol., **97**(2), pp. 270–282.
[5] Iordanoff, I., 1996, "Paliers Axiaux Aérodynamiques à Structure à Feuilles: Analyse et Optimisation," Ph.D. thesis, Université Paul Sabatier, Toulouse, France.
[6] Flamand, L., 1999, "Lubrification Hydrodynamique," GMD, Institut National des Sciences Appliquées de Lyon, France.
[7] Iordanoff, I., 1999, "Analysis of an Aerodynamic Compliant Foil Thrust Bearing: Method for a Rapid Design," ASME J. Tribol., **121**, pp. 816–822.
[8] Heshmat, H., Ming Chen, H., and Walton, J. F., 2000, "On the Performance of Hybrid Foil-Magnetic Bearings," ASME J. Eng. Gas Turbines Power, **122**, pp. 73–82.
[9] Salehi, M., and Heshmat, H., 2000, "On the Fluid and Thermal Analysis of a Compliant Surface Foil Bearing and Seal," Tribol. Trans., **43**, pp. 318–324.
[10] Yang, B. S., Lee, Y. H., Choi, B. K., and Kim, H. J., 2001, "Optimum Design of Short Journal Bearings by Artificial Life Algorithm," Tribol. Int., **34**, pp. 427–435.
[11] Stephan, P., and Iordanoff, I., 2001, "Butées et Paliers Aérodynamiques," Techniques de l'Ingénieur, B5335.
[12] Dellacorte, C., and Laskowski, A., 1997, "Tribological Evaluation of PS300: A New Chrome Oxide-Based Solid Lubricant Coating Sliding Against Al_2O_3 From 25° to 650°C," Tribol. Trans., **40**, pp. 163–167.
[13] Dellacorte, C., 1998, "A New Foil Air Bearing Test Rig for Use to 700°C and, 70,000 rpm," Tribol. Trans., **41**, pp. 335–340.
[14] Dellacorte, C., Fellenstein, J. A., and Benot, P. A., 1999, "Evaluation of Advanced Solid Lubricant Coatings for Foil Air Bearings Operating at 25 and 500°C," Tribol. Trans., **42**, pp. 338–342.
[15] Suriano, F. J., Keiser, R. J., Woessner, F. G., and Valori, R., 2001, "High-Temperature (649°C/1200°F) Coatings for Gas-Lubricated Foil Bearings of the Navy's Advanced Auxiliary Power Unit Concepts," Garret Turbine Engine Company and Naval Air Propulsion Cente report.
[16] Herbelot, C., 1995, "Comportement Stationnaire ou Dynamique de Paliers Aérodynamiques à Feuilles," Ph.D. thesis, Universite Paul Sabatier, Toulouse, France.
[17] Boedo, S., and Eshkabilov, S. L., 2003, "Optimal Shape Design of Steadily Loaded Journal Bearings using Genetic Algorithms," Tribol. Trans., **46**, pp. 134–143.
[18] Roger KU, C. P., and Heshmat, H., 1993, "Compliant Foil Bearing Structural Stiffness Analysis, Part II: Experimental Investigation," ASME J. Tribol., **115**, pp. 364–369.
[19] Heshmat, H., 1994, "Advancements in the Performance of Aerodynamic Foil Journal Bearings: High Speed and Load Capability," ASME J. Tribol., **116**, pp. 287–295.
[20] Carpino, M., Peng, J. P., and Medvetz, L., 1994, "Misalignment in a Complete Shell Gas Foil Journal Bearing," Tribol. Trans., **37**, pp. 829–835.
[21] Carpino, M., Peng, J. P., and Medvetz, L., 1994, "Effects of Membrane Stresses in the Prediction of Foil Bearing Performance," Tribol. Trans., **37**, pp. 43–50.
[22] Heshmat, H., and Heshmat, C. A., 1995, "An Analysis of Gas-Lubricated, Multileaf Foil Journal Bearings With Backing Springs," ASME J. Tribol., **117**, pp. 437–443.
[23] Czolczynski, K., and Marynowski, K., 1996, "Stability of Symmetrical Rotor Supported in Flexibly Mounted, Self-Acting Gas Journal Bearings," Wear, **194**, pp. 190–197.
[24] Czolczynski, K., 1996, "How to Obtain Stiffness and Damping Coefficients of Gas Bearings," Wear, **201**, pp. 265–275.
[25] Howard, S. A., 1999, "Preliminary Development of Characterization Methods for Compliant Air Bearings," Tribol. Trans., **42**, pp. 789–794.
[26] Heshmat, H., 2000, "Operation of Foil Bearings Beyond the Bending Critical Mode," ASME J. Tribol., **122**, pp. 192–198.
[27] Howard, S. A., Dellacorte, C., Valco, M. J., Prahl, J. M., and Heshmat, H., 2001, "Steady-State Stiffness of Foil Air Journal Bearings at Elevated Temperatures," Tribol. Trans., **44**, pp. 489–493.
[28] Howard, S. A., Dellacorte, C., Valco, M. J., Prahl, J. M., and Heshmat, H., 2001, "Dynamic Stiffness and Damping Characteristics of a High-Temperature Air Foil Journal Bearing," SLTE presentation, preprint No. 01-TC-7.
[29] Lee, N. S., Choi, D. H., Lee, Y. B., Kim, T. H., and Kim, C. H., 2002, "The Influence of the Slip Flow on Steady—State Load Capacity, Stiffness and Damping Coefficients of Elastically Supported Gas Foil Bearings," Tribol. Trans., **45**, pp. 478–484.
[30] Yoshimoto, S., and Nakano, Y., 1983, "Stability of Unsymmetrical Rigid Rotor Supported by Self-Acting Gas-Lubricated Journal Bearings," J. Lubr. Technol., **105**, pp. 656–661.
[31] Abdul Wahed, N., Nicolas, D., and Pascal, M. T., 1982, "Stability and Unbalance Response of Large Turbine Bearings," J. Lubr. Technol., **104**, pp. 66–75.
[32] Klit, P., and Lund, W., 1986, "Calculation of the Dynamic Coefficients of a Journal Bearing, Using a Variational Approach," ASME J. Tribol., **108**, pp. 421–425.
[33] Stephan, P., 1991, "Paliers à Gaz à Alésage Expansible, Comportement Dynamique," Ph.D. thesis, Université Paul Sabatier, Toulouse, France.
[34] Carpino, M., and Peng, J. P., 1993, "Calculation of Stiffness and Damping Coefficients for Elastically Supported Gas Foil Bearings," ASME J. Tribol., **115**, pp. 20–27.
[35] Abdul Wahed, N., 1982, "Comportement Dynamique des Paliers Fluides. Etude Linéaire et Nonlinéaire," Ph.D. thesis, INSA de Lyon, France.
[36] Hsia, Y. T., and Domoto, G. A., 1983, "An Experimental Investigation of Molecular Rarefaction Effects in Gas Lubricated Bearings at Ultra-Low Clearances," J. Lubr. Technol., **105**, pp. 120–130.
[37] Frene, J., Nicolas, D., Berthe, D., and Berthe, D., 1990, *Lubrification Hydrodynamique, Paliers et Butées*, edition Eyrolles.
[38] Tichy, J., and Bou-Saïd, B., 1991, "Hydrodynamic Lubrication and Bearing Behaviour With Impulsive Loads," Tribol. Trans., **34**, pp. 505–512.
[39] Li, D. F., Choy, K. C., and Allaire, P. E., 1980, "Stability and Transient Characteristics of Four Multilobe Journal Bearing Configurations," J. Lubr. Technol., **102**, pp. 291–299.
[40] Li, D. F., Choy, K. C., and Allaire, P. E., 1980, "Transient Unbalance Response of Four Multilobe Journal Bearings," J. Lubr. Technol., **102**, pp. 300–306.
[41] Jai, M., Buscaglia, G., and Iordanoff, I., 2004, "Multi-Constrained Optimization of Running Characteristics of Mechanisms Lubricated With Compressible Fluid," ASME J. Tribol., **126**, pp. 126–132.
[42] Buscaglia, G., and Jai, M., 2001, "A New Numerical Scheme for Nonuniform Homogenized Problems: Application to the Nonlinear Reynolds Compressible Equation," Math. Probl. Eng., **7**(4), pp. 355–377.
[43] Bonneau, O., 1989, "Comportement Statique et Dynamique de Ligne d'Arbre Montée sur Paliers Fluides: Influence des Caractéristiques des Paliers," Ph.D. thesis, Universite de Poitiers, France.
[44] Nrakis, Y., and Cohen, M. J., 1977, "Response of Infinite Journal Gas Bearings to Harmonic Perturbations in the Rotational Speed," J. Lubr. Technol., **99**(4), pp. 428–433.
[45] Braun, M. J., Choy, F. K., Dzodzo, M., and Hsu, J., 1996, "Two-Dimensional Dynamic Simulation of a Continuous Foil Bearing," Tribol. Int., **29**, pp. 61–68.
[46] Howard, S. A., 1999, "Rotordynamics and Design Methods of an Oil-Free Turbocharger," Tribol. Trans., **42**, pp. 174–178.
[47] Carpino, M., and Peng, J. P., 1994, "Coulomb Friction Damping Effects in Elastically Supported Gas Foil Bearings," Tribol. Trans., **37**, pp. 91–98.
[48] Roger, C. P., and Heshmat, H., 1992, "Compliant Foil Bearing Structural Stiffness Analysis, Part I: Theoretical Model Including Strip and Variable Bump Foil Geometry," ASME J. Tribol., **114**, pp. 394–400.
[49] Roger KU, C. P., and Heshmat, H., 1994, "Structural Damping of Self-Acting Compliant Foil Journal Bearings," ASME J. Tribol., **116**, pp. 76–82.
[50] Roger KU, C. P., and Heshmat, H., 1994, "Structural Stiffness and Coulomb Damping in Compliant Foil Journal Bearings: Theoretical Considerations," Tribol. Trans., **37**, pp. 525–533.
[51] Arakere, N., and Nelson, H. D., 1988, "An Interior Collocation Method for Static and Dynamic Analysis of Finite Length Gas Journal Bearings," ASME J. Tribol., **110**, pp. 456–461.
[52] Grau, G., Iordanoff, I., Bou-Saïd, B., and Berthier, Y., 2004, "An Original Definition of the Profile of Compliant Foil Journal Bearings: Static and Dynamic Analysis," Tribol. Trans., **47**, pp. 1–9.
[53] Lalanne, M., and Ferraris, G., 1998, *Rotordynamics Prediction in Engineering*, 2nd ed., Wiley, NY.
[54] Lalanne, M., Berthier, P., and Der Hagopian, J., 2000, *Mechanical Vibrations for Engineers*, Wiley, NY.

Downloaded 02 Jun 2010 to 171.66.16.107. Redistribution subject to ASME license or copyright; see http://www.asme.org/terms/Terms_Use.cfm

Heavily Loaded Gas Foil Bearings: A Model Anchored to Test Data

Tae Ho Kim
Research Assistant

Luis San Andrés
Mast-Childs Professor
Fellow ASME
e-mail: lsanandres@mengr.tamu.edu

Mechanical Engineering Department,
Texas A&M University,
College Station, TX 77843-3123

Widespread usage of gas foil bearings (FBs) into microturbomachinery to midsize gas turbine engines requires accurate performance predictions anchored to reliable test data. This paper presents a simple yet accurate model predicting the static and dynamic force characteristics of gas FBs. The analysis couples the Reynolds equation for a thin gas film to a simple elastic foundation model for the top foil and bump strip layer. An exact flow advection model is adopted to solve the partial differential equations for the zeroth- and first-order pressure fields that render the FB load capacity and frequency-dependent force coefficients. As the static load imposed on the foil bearing increases, predictions show that the journal center displaces to eccentricities exceeding the bearing nominal clearance. A nearly constant FB static stiffness, independent of journal speed, is estimated for operation with large loads, and approaching closely the bearing structural stiffness derived from contact operation without rotor spinning. Predicted minimum film thickness and journal attitude angle demonstrate good agreement with archival test data for a first-generation gas FB. The bump-foil-strip structural loss factor, exemplifying a dry-friction dissipation mechanism, aids to largely enhance the bearing direct damping force coefficients. At high loads, the bump-foil structure influences most the stiffness and damping coefficients. The predictions demonstrate that FBs have greatly different static and dynamic force characteristics when operating at journal eccentricities in excess of the bearing clearance from those obtained for operation at low loads, i.e., small journal eccentricity. [DOI: 10.1115/1.2770494]

Keywords: gas foil bearing, dynamic force coefficients, structural force coefficients, structural loss factor

Introduction

Implementing gas foil bearings in turbomachinery reduces system complexity and maintenance costs, and increases efficiency and operating life [1,2]. Gas foil bearings (FBs) are compliant-surface (self-acting) hydrodynamic bearings that use ambient air or any process gas as the lubricating fluid. A hydrodynamic film pressure builds up within the small gap between the rotating shaft and the smooth foil. Figure 1 shows the configuration of a "first-generation" gas FB [3]. A gas FB consists of a thin (top) foil and a series of bump strip supports. The leading edge of the top foil is free while the foil trailing edge is welded to the bearing housing. Beneath the thin foil, a bump-foil structure is laid on the inner surface of the bearing. The thin foil of smooth surface is supported by a series of bump foils acting as springs, thus making the bearing compliant. High operating speeds, high temperature endurance using solid lubricants (coatings), and superior stability characteristics to rigid gas bearings distinguish gas FBs. Heshmat [4] demonstrated the successful operation of FBs at 132,000 rpm with a 35 mm diameter, 31 mm length journal FB, i.e., 4.61 $\times 10^6$ DN (bearing bore diameter (mm) $\times$ shaft speed (rpm)) value. Advanced multistage bump-foil layouts are adopted to achieve an ultimate load capacity of 728 N corresponding to a projected area pressure of 6.73 bars (98 psi) at a top speed of 59,700 rpm. DellaCorte et al. [5] performed durability tests of foil journal bearings with a PS304 (high temperature solid lubricant) coating for operations between 25°C and 650°C. The same authors also measured the start/stop torque, friction coefficient, and bearing wear rate during 100,000 start/stop cycles, which demonstrated a suitable static performance of gas foil bearings for high temperature applications. A viscoelastic-bump FB introduced by Lee et al. [6,7] improved the damping characteristics of FBs at ambient temperature applications. Test results obtained from a flexible rotor show that the viscoelastic-bump FBs not only aid to attenuate large amplitudes of motion near the rotor bending critical speed but also suppress subsynchronous vibrations at speeds above the bending critical speed. Note that this novel improvement is presently restricted to low and moderate temperature applications.

An accurate prediction of load-carrying capacity is necessary to implement gas FBs into high performance applications. Heshmat et al. [8,9] first presented analyses for bump-foil journal bearings and bump-foil thrust bearings and detailed the bearings' static load performance. The bump-foil strip is treated as an elastic foundation with stiffness per unit area. The investigation revealed that the stiffness for a FB can be tailored and adjusted by a mechanical designer to the demands of a rotordynamic system. Peng and Carpino [10] presented synchronous dynamic stiffness and damping force coefficients for foil journal bearings using a perturbation method. The effects of the elastic foundation, foil membrane/bending stresses, journal misalignment, and subfoil Coulomb friction are accounted for [11,12]. The investigations demonstrate that the structural analysis of the thin foil and structural bumps can be simplified by recognizing that the film thickness is nearly constant across the (axial) width of the bearing due to membrane bending effects. San Andrés [13] analyzed turbulent flow FBs for cryogenic turbopump applications and included hysteretic damping effects in the form of a complex dynamic stiffness coefficient. The bearing compliance is modeled as a simple elastic foundation

Contributed by the International Gas Turbine Institute of ASME for publication in the JOURNAL OF ENGINEERING FOR GAS TURBINES AND POWER. Manuscript received April 14, 2006; final manuscript received December 13, 2006; published online January 9, 2008. Review conducted by Mihai Arghir. Paper presented at the ASME Turbo Expo 2005: Land, Sea and Air (GT2005), Reno, NV, June 6–9, 2005. Paper No. GT2005-68486.

Copyright © 2008 by ASME

Downloaded 02 Jun 2010 to 171.66.16.107. Redistribution subject to ASME license or copyright; see http://www.asme.org/terms/Terms_Use.cfm

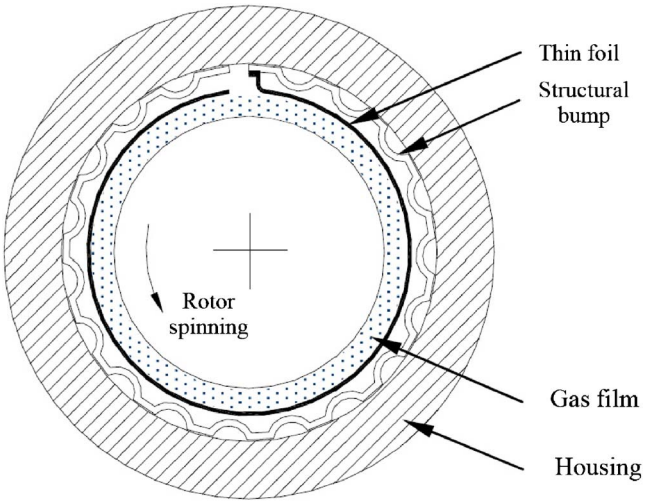

Fig. 1 Schematic view of first-generation FB

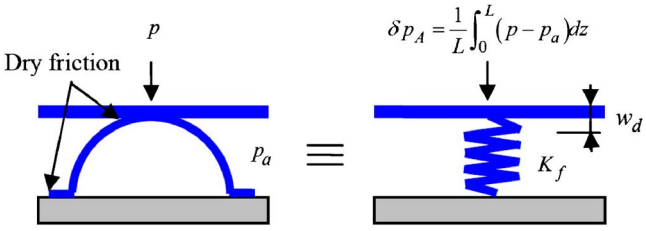

Fig. 2 Geometry of a journal and arcuate foil with arc preload

where an axially averaged pressure couples the pressure field to the structural deflection. The author finds that a liquid oxygen FB has a linear behavior between load and journal displacement.

Iordanoff [14] introduced a simple method enabling the rapid design of gas foil thrust bearings. The model is based on results obtained with rigid bearing profiles and determines an optimum initial compliant profile to produce a maximum load capacity. The method was applied successfully to the design of an 80 mm outer diameter, 40 mm inner diameter thrust bearing with greatly improved load capacity, when compared to previously reported configurations. Khonsari and Peng [15] analyzed the static load characteristics of first-generation air FBs. The authors present a computational analysis with consideration of the compressibility of the lubricant and the bearing compliance, using an arithmetic mean pressure in the axial direction. In Ref. [15], predicted loads for a FB reported in Ref. [16] were obtained at an arbitrary minimum film thickness of 11 μm. Carpino and Talmage [17] recently developed a fully coupled finite element formulation for FBs. The model incorporates both the pressure developed in the lubricant flow and the structural deflections of the top and subfoils into a single finite element. The predictions exhibit irregular shapes of pressure and film thickness due to foil detachment in the exit region of the gas film.

There is lack of reliable experimental evidence on gas FB performance, in particular, for rotordynamic coefficients. Despite continuous improvements in analysis methods, the lack of accurate performance predictions for even the simplest FBs has delayed their ubiquitous usage into high performance turbomachinery systems, such as gas turbine engines, for example, in Ref. [3]. The difficulties in prediction lie in the fact that a FB has an ultimate load capacity at a journal eccentricity well in excess of its nominal bearing clearance [11]. In actual FBs, a nominal clearance may not even exist or be well defined.

This paper presents a simple though efficient model to predict the static and dynamic force characteristics of heavily loaded gas FBs. The model uses an axially averaged pressure coupling the pressure field to the structural deflection, thus enabling a journal to move beyond the nominal bearing clearance when subjected to large loads. The exact advection model given in Ref. [18] is adopted to solve the partial differential equations (PDEs) for the zeroth- and first-order pressure fields. This method, based on the numerical integration of the nonlinear Reynolds equation over a finite control volume, ensures numerically stable and accurate solutions at arbitrary operating conditions.

Comparisons of predictions to limited experimental data available in the open literature [16] validate the computational analysis program. The measured journal radial travel within the FB, as experimentally obtained from a load-deflection test in Ref. [16], is hereby referred as the nominal bearing clearance. Predicted minimum film thickness and journal attitude angle for increasing static loads are in good agreement with the test data. Dynamic force coefficients versus excitation frequency are examined for increasing static loads, considering the effect of a structural loss factor, and compared to the structural force coefficients of the FB resting at zero rotor speed.

2 Description of Model for Foil Journal Bearings

Figure 2 shows a typical geometry of a simple foil journal bearing. Journal center displacements (e_X, e_Y) are referred to the inertial axes, X and Y. A foil arc extends from leading edge (Θ_l) to its trailing edge (Θ_t); hence its circumferential length (l_x) is $R(\Theta_t - \Theta_l)$. An offset angle (Θ_p) between the leading and trailing edges sets the angular location of minimum film thickness when the journal is centered and the local foil arc deflection (w_d) is null. The arc preload is $r_p = c - c_m$, where c and c_m denote the bearing and assembled radial clearances, respectively.

In FBs, the radial clearance (c) is largely unknown. A positive preload $(r_p > 0)$ produces a converging film thickness, which generates hydrodynamic pressure to support a load and produce a direct stiffness, even when the journal is centered $(e_X = e_Y = 0)$ and the foil deflection $w_d = 0$. The preload can be given to a foil journal bearing with a differential bump height [19] or by locating shims under the bump strips [20]. The film thickness for a perfectly aligned journal is

$$h = c - r_p \cos(\Theta - \Theta_p) + e_X \cos(\Theta) + e_Y \sin(\Theta) + w_d \tag{1}$$

Figure 3 shows the equivalent structural model for the elastic foundation (bump strip). The local deflection of a bump (w_d) depends on the bump structural stiffness of the elastic foundation (K_f) and the average pressure (δp_A) across the bearing width [13], i.e.,

$$w_d = \delta p_A / K_f \tag{2}$$

where $\delta p_A = 1/L \int_0^L (p - p_a) dz$, and p_a is the ambient pressure beneath the foil.

When considering the dynamic behavior of a bump strip, a complex stiffness, $K_f' = K_f(1 + i\gamma)$, permits to write Eq. (2) as

$$w_d = \frac{\delta p_A}{K_f} \frac{1}{(1 + i\gamma)} \tag{3}$$

where γ is a bump structure loss factor arising from material hysteresis and dry friction. Although the bump stiffness (K_f) is linear, the overall bearing structure has a nonlinear stiffness that depends on the applied load and assembly preload [21]. The loss factor, γ, in particular, must be determined experimentally. In operation, the top foil could detach from the support bumps, not allowing for a subambient pressure in the gas film; thus, $p \geq p_a$ and structural deflection $w_d \geq 0$ are enforced in the computational model.

Downloaded 02 Jun 2010 to 171.66.16.107. Redistribution subject to ASME license or copyright; see http://www.asme.org/terms/Terms_Use.cfm

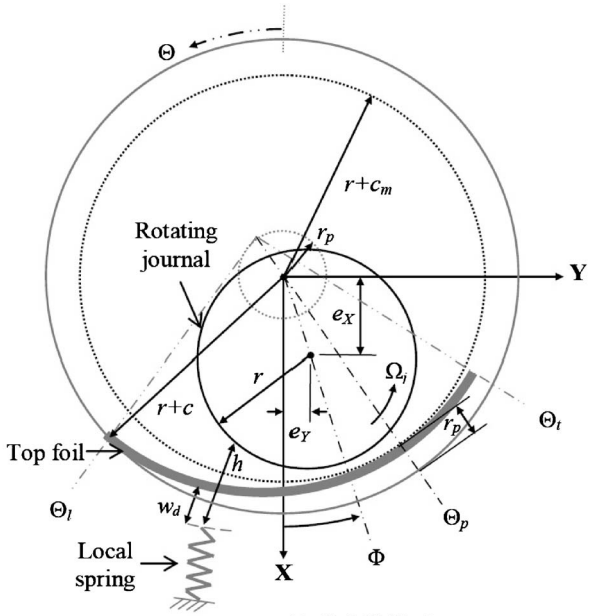

$r_p = c - c_m$ — c: Radial (foil) clearance
$r_p = 0$: Null preload — c_m: Assembled radial clearance
$r_p = c$: Journal – foil contact — h: Local film thickness considering, local top foil deflection, w_d

Fig. 3 Equivalent foil structural model for elastic foundation (bump strip)

Perturbed Film Thickness and Pressure Fields. The general motion of the rotor or journal at frequency (ω) with small amplitude harmonic motions (Δe_X, Δe_Y) about an equilibrium position (e_{X_0}, e_{Y_0}) is

$$e_X = e_{X_0} + \Delta e_X e^{i\omega t} \quad e_Y = e_{Y_0} + \Delta e_Y e^{i\omega t} \tag{4}$$

Corresponding perturbed pressures and film thickness due to the journal dynamic motions follow as

$$p = p_0 + \Delta e_X p_X e^{i\omega t} + \Delta e_Y p_Y e^{i\omega t} \tag{5}$$

and

$$h = c - r_p \cos(\Theta - \Theta_p) + e_{X_0} \cos(\Theta) + e_{Y_0} \sin(\Theta) + \Delta e_X e^{i\omega t} \cos(\Theta) + \Delta e_Y e^{i\omega t} \sin(\Theta) + w_d + \Delta w_d \tag{6}$$

where

$$w_d = \frac{\delta p_{A0}}{K_f} \quad \Delta w_d = \frac{(\delta p_{AX} \Delta e_X e^{i\omega t} + \delta p_{AY} \Delta e_Y e^{i\omega t})}{K_f(1 + i\gamma) + iC_f\omega} \tag{7}$$

and

$$\delta p_{A0} = \frac{1}{L}\int_0^L (p_0 - p_a)dz \quad \delta p_{AX} = \frac{1}{L}\int_0^L p_X dz \quad \delta p_{AY} = \frac{1}{L}\int_0^L p_Y dz \tag{8}$$

Note that for generality, a viscous damping coefficient per unit area (C_f) is added to the dynamic support stiffness $K_f(1+i\gamma)$.

In Eq. (6), separating the steady state terms (zeroth order) and the perturbed terms (first order) gives

$$h = h_0 + \Delta h e^{i\omega t} \tag{9a}$$

where

$$h_0 = c - r_p \cos(\Theta - \Theta_p) + e_{X_0} \cos(\Theta) + e_{Y_0} \sin(\Theta) + \frac{\delta p_{A0}}{K_f} \tag{9b}$$

$$\Delta h = \Delta e_X \left[\cos(\Theta) + \frac{\delta p_{AX}}{K_f(1 + i\gamma) + iC_f\omega} \right] + \Delta e_Y \left[\sin(\Theta) + \frac{\delta p_{AY}}{K_f(1 + i\gamma) + iC_f\omega} \right] \tag{9c}$$

Let $h = Hc$, $r_p = \bar{r}_p c$, $e_X = \varepsilon_X c$, $e_Y = \varepsilon_Y c$, $p = Pp_a$, $t = \tau/\omega$. Dimensionless forms of the perturbed pressures and compliant film thickness follow as

$$P = P_0 + \Delta P e^{i\tau}$$
$$\Delta P = (P_X \Delta\varepsilon_X + P_Y \Delta\varepsilon_Y) \tag{10}$$

and

$$H = H_0 + \Delta H e^{i\tau}$$
$$H_0 = 1 - \bar{r}_p \cos(\Theta - \Theta_p) + \varepsilon_{X_0} \cos(\Theta) + \varepsilon_{Y_0} \sin(\Theta) + \delta P_{A0} S \tag{11}$$

$$\Delta H = \{\Delta\varepsilon_X[\cos(\Theta) + \bar{S}\delta P_{AX}] + \Delta\varepsilon_Y[\sin(\Theta) + \bar{S}\delta P_{AY}]\}$$

where

$$S = \frac{p_a}{cK_f} \quad \bar{S} = \frac{p_a}{c[K_f(1 + i\gamma) + iC_f\omega]}$$

S and $\bar{S}$ denote compliance coefficients, static and dynamic, respectively. C_f represents a generic viscous damping coefficient underneath a foil.

The Reynolds equation for an isothermal, isoviscous ideal gas in the film region is

$$\frac{\partial}{\partial x}\left(ph^3\frac{\partial p}{\partial x}\right) + \frac{\partial}{\partial z}\left(ph^3\frac{\partial p}{\partial z}\right) = 6\mu\Omega R\frac{\partial(ph)}{\partial x} + 12\mu\frac{\partial(ph)}{\partial t} \tag{12}$$

where (x, z) are the circumferential and axial coordinates on the plane of the bearing.

Letting $x = l_x\bar{x}$, $z = l_x\bar{z}$, and $t = \tau/\omega$ leads to the dimensionless form

$$\frac{\partial}{\partial\bar{x}}\left(PH^3\frac{\partial P}{\partial\bar{x}}\right) + \frac{\partial}{\partial\bar{z}}\left(PH^3\frac{\partial P}{\partial\bar{z}}\right) = \Lambda_g\frac{\partial(PH)}{\partial\bar{x}} + \sigma_g\frac{\partial(PH)}{\partial\tau} \tag{13}$$

where $\Lambda_g = 6\mu\Omega R l_x/p_a c^2$ and $\sigma_g = 12\mu\omega l_x^2/p_a c^2$ are known as the bearing speed number (also compressibility number) and squeeze film number, respectively.

Substitution of Eqs. (10) and (11) into the dimensionless Reynolds equation (13) and neglecting higher order terms yield the zeroth- and first-order equations for the equilibrium and perturbed pressure fields, respectively.

Zeroth-order equation,

$$-\left[\frac{\partial}{\partial\bar{x}}\left(P_0H_0^3\frac{\partial P_0}{\partial\bar{x}}\right) + \frac{\partial}{\partial\bar{z}}\left(P_0H_0^3\frac{\partial P_0}{\partial\bar{z}}\right)\right] + \Lambda_g\frac{\partial(P_0H_0)}{\partial\bar{x}} = 0 \tag{14}$$

First-order equations,

$$\begin{aligned}
&\frac{\partial}{\partial\bar{x}}\left(P_0H_0^3\frac{\partial P_\alpha}{\partial\bar{x}} + P_\alpha H_0^3\frac{\partial P_0}{\partial\bar{x}} + 3P_0H_0^2\bar{S}\delta P_{A\alpha}\frac{\partial P_0}{\partial\bar{x}}\right) \\
&\quad + \frac{\partial}{\partial\bar{z}}\left(P_0H_0^3\frac{\partial P_\alpha}{\partial\bar{z}} + P_\alpha H_0^3\frac{\partial P_0}{\partial\bar{z}} + 3P_0H_0^2\bar{S}\delta P_{A\alpha}\frac{\partial P_0}{\partial\bar{z}}\right) \\
&\quad + \left(\Lambda_g\frac{\partial}{\partial\bar{x}} + i\sigma_g\right)(P_0\bar{S}\delta P_{A\alpha} + P_\alpha H_0) \\
&\quad = \frac{\partial}{\partial\bar{x}}\left(-3P_0H_0^2H_\alpha\frac{\partial P_0}{\partial\bar{x}}\right) + \frac{\partial}{\partial\bar{z}}\left(-3P_0H_0^2H_\alpha\frac{\partial P_0}{\partial\bar{z}}\right) \\
&\quad + \left(\Lambda_g\frac{\partial}{\partial\bar{x}} + i\sigma_g\right)P_0H_\alpha
\end{aligned} \tag{15}$$

Downloaded 02 Jun 2010 to 171.66.16.107. Redistribution subject to ASME license or copyright; see http://www.asme.org/terms/Terms_Use.cfm

where $\alpha=X,Y$, and $H_X=\cos(\Theta)$ and $H_Y=\sin(\Theta)$. The boundary conditions for Eqs. (14) and (15) are

$$P(\Theta,b/2)=P(\Theta,-b/2)=P(\Theta_l,\bar{z})=P(\Theta_t,\bar{z})=1$$

$$P_Y(\Theta,b/2)=P_Y(\Theta,-b/2)=P_Y(\Theta_l,\bar{z})=P_Y(\Theta_t,\bar{z})=0 \quad (16)$$

$$P_X(\Theta,b/2)=P_X(\Theta,-b/2)=P_X(\Theta_l,\bar{z})=P_X(\Theta_t,\bar{z})=0$$

where $b=L/l_x$.

For given operating conditions and specified journal eccentricity, numerical solution of the nonlinear PDE (14) with Eqs. (7) and (11) determines the steady state pressure field (P_0), elastic deformation (w_d), and film thickness (h_0). The numerical scheme is an *exact flow advection*, finite difference model [18] that is numerically stable and accurate even for bearing speed numbers (Λ_g) approaching infinity. A Newton–Rhapson procedure finds the equilibrium journal eccentricity for a given load.

The solution of the *linear* first-order equations for perturbed pressures (P_X, P_Y) due to journal motions along the X and Y directions is straightforward. Note that the solution procedure requires of the zeroth-order fields (P_0, h_0).

Fluid Film Forces and Dynamic Force Coefficients. The bearing reaction forces and dynamic force coefficients, stiffness and damping, are found by integration of the zeroth- and first-order pressures pressure field on the bearing surface,

$$F_{\alpha_0}=\int_0^L\int_{\Theta_l}^{\Theta_t}(p_0-p_a)H_\alpha R d\Theta dz$$

$$K_{\alpha\beta}+i\omega C_{\alpha\beta}=-\int_0^L\int_{\Theta_l}^{\Theta_t}p_\beta H_\alpha R d\Theta dz \quad (17)$$

where $\alpha,\beta=X,Y$. The magnitude of the bearing reaction force must equal the applied load, i.e., $W=\sqrt{F_{X_0}^2+F_{Y_0}^2}$.

Equation (17) can be extended to a bearing comprised of multiple foils by adding vectorially the reaction forces and dynamic force coefficients from each foil arc.

Contact Forces and Structural Force Coefficients

Figure 4 depicts a schematic view of a journal and (simple) FB at rest, i.e., without rotor speed and statically loaded with a load angle (Φ_L). For the structural model of the journal in contact with the top foil and pushing on the bump strip layers, the top foil deflection along the axial direction is necessarily unique, and hence membrane forces and bending moments are negligible. As the static load increases, the journal contacts the top foil, pushing on the bumps that deflect in reaction to the applied load. A particular bump deflection (w_d) for journal displacements (e_X, e_Y) is given in Ref. [21] as

$$w_d=e_X\cos(\Theta-\pi)+e_Y\sin(\Theta-\pi)-c>0 \quad (18)$$

The journal eccentricity ($e=\sqrt{e_X^2+e_Y^2}$) follows from $e=c+w_{d_{\max}}$. Note that $w_{d_{\max}}$ is a maximum bump deflection. Reference [21] details the assembly method that renders the bump-foil deflections to support the applied static load. An individual bump-foil reaction force (F_r) along the radial direction and the whole structure elastic reaction forces are

$$F_{r_i}=K_{f_i}s_0Lw_{d_i}$$

$$F_X=\sum_{i=1}^{N_b}F_{r_i}\cos(\Theta_i) \quad F_Y=\sum_{i=1}^{N_b}F_{r_i}\sin(\Theta_i) \quad (19)$$

The bearing elastic reaction load versus journal displacement is piecewise linear, with a pronounced hardening effect as the applied load increases. From the curves generated by Eqs. (19), a bearing structural stiffness coefficient $K_S\sim\Delta F_X/\Delta e_X$ is easily derived. See Ref. [21] for details on the curve-fitting model. In addition, an equivalent viscous damping coefficient ($C_{S\text{-eq}}$) for the FB structure is defined as ($K_S\gamma/\omega$), where (ω) is an excitation frequency.

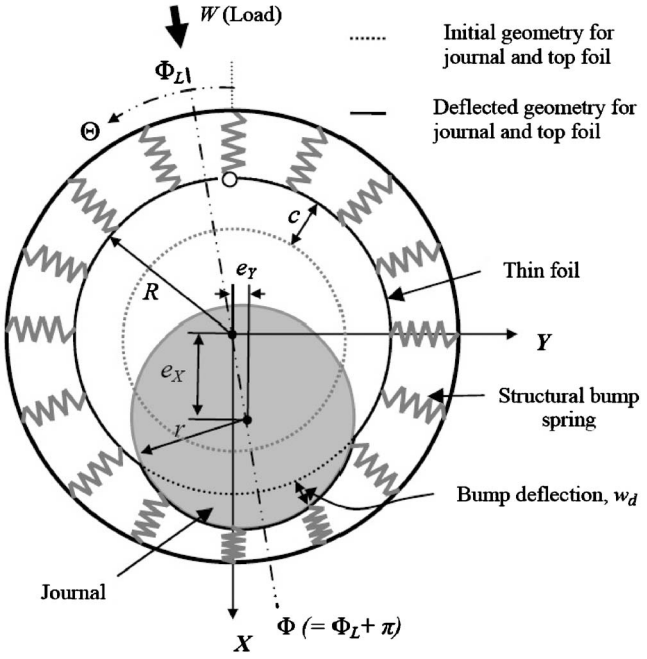

Fig. 4 Schematic view of nonrotating journal and FB in contact

Results and Discussion

Table 1 lists the design parameters of the studied FB and Fig. 5 shows a detailed configuration of the bump-foil strip. Identical FB parameters as given by Ruscitto et al. [16] are used throughout the analysis and to compare the predictions to the experimental data reported.

The FB in Ref. [16] is a first-generation type with one 360 deg top foil and one strip layer with 26 bumps. The top foil and bump layer are made of Inconnel X-750. One end of the top foil and bump layer is spot-welded to the bearing sleeve. The other end of both the foil and bump strip layer is free. The journal rotational direction is from the free end of the top foil toward its fixed end. The test FB does not have a preload ($\bar{r}_p$). All tests were performed

Table 1 Geometry of Ruscitto et al. [16] FB

Parameters	Values
Bearing radius, $R=D/2$	19.05 mm (0.75 in.)
Bearing length, L	38.1 mm (1.5 in.)
Foil arc circumferential length, l_x	120 mm (4.7 in.)
Radial journal travel, c_J	31.8 μm (1.25 mil)
Top foil thickness, t_t	101.6 μm (4 mil)
Bump-foil thickness, t_b	101.6 μm (4 mil)
Bump pitch, s_0	4.572 mm (0.18 in.)
Bump half-length, l_0	1.778 mm (0.07 in.)
Bump height, h_b	0.508 mm (0.02 in.)
Bump height angle, α	63.8 deg
Number of bumps, N_b	26
Number of bump strips, N_s	1
Bump-foil Young's modulus, E	214 GPa (31 Mpsi)
Bump-foil Poisson's ratio, ν	0.29

Downloaded 02 Jun 2010 to 171.66.16.107. Redistribution subject to ASME license or copyright; see http://www.asme.org/terms/Terms_Use.cfm

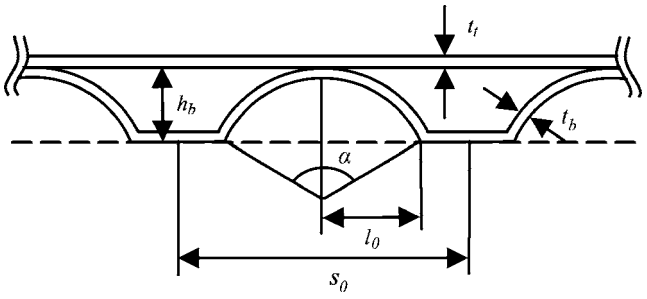

Fig. 5 Configuration of top foil and bump-foil strip

with air at ambient conditions [16]. Ruscitto et al. [16] noted that the bearing clearance in the test bearing is unknown. Thus, the journal radial travel (c_J) was measured by performing a static load-bump deflection test. The journal radial travel refers to the radial displacement where the journal can sway under an arbitrary static load condition. This ad hoc procedure reveals the region where the foil structure is apparently very "soft." Hence, in the referred literature, the radial travel (c_J) is defined as the total motion of the bearing when a 0.9 kg (2 lb.) load was applied first downward, and then upward.

In the predictions, a bump structural stiffness per unit area (K_f) is estimated by using Iordanoff's formulas [14]. This is a simple model for a single bump with either its two ends free or one end free and the other fixed. The bump pitch (s_0) is considered constant and the interaction between adjacent bumps is neglected. Although the formulas include provisions for a dry-friction coefficient, none is presently used. The calculated bump stiffness per unit area for a free-free (K_{f_F}) ends bump and a fixed-free (K_{f_W}) ends bump are

$$K_{f_F} = \frac{N_s E t_b^3 \sin^3(\alpha/2)}{6 l_0^3 s_0 I(\alpha)(1-\nu^2)} = 4.7 \times 10^9 \text{ N/m}^3$$

$$K_{f_W} = \frac{N_s E t_b^3 \sin^3(\alpha/2)}{12 l_0^3 s_0 J(\alpha)(1-\nu^2)} = 1.04 \times 10^{10} \text{ N/m}^3 \quad (20)$$

respectively. See Ref. [14] for the definitions of the I and J geometrical functions.

The free-free ends bump stiffness is used in Eqs. (2) and (3) to calculate the deflection of the bump strip layers. The test FB has only one welded-free end bump located opposite to the direction of the static load. Presently, for prediction of the test FB force performance, the nominal bearing clearance (c_J) is set equal to the measured journal travel (c_J=31.8 μm) reported in Ref. [16]. The dimensionless compliance coefficient (S) equals 0.67 for the tested bearing.

Figure 6 shows the predicted FB journal eccentricity versus static load at rotational speeds of 30 krpm, 40 krpm, and 100 krpm, and also the structural deflection for contact without journal spinning. For the cases with journal rotation, i.e., hydrodynamic operation, the journal static displacement increases rapidly from low to moderate loads (~60 N). The journal eccentricity soon exceeds the nominal clearance (c_J) for larger static loads. Most notably, at larger loads (>200 N), the journal displacement is proportional to the applied load. The same behavior is evident from the maximum bump deflection at contact without journal spinning. The figure depicts the estimated FB static stiffness coefficient (K_G=5.2×10^6 N/m), which is nearly identical to the structural stiffness (K_S=5.3×10^6 N/m) accounting solely for the FB structure without journal spinning. Thus, at high loads the elastic structure (bump strip layer) dominates the forced performance of a FB. Note that by necessity, the elastic structure reaction force must be identical to the gas FB reaction force. Hence, a FB ultimate load depends solely on the strength of its underlying elastic structure.

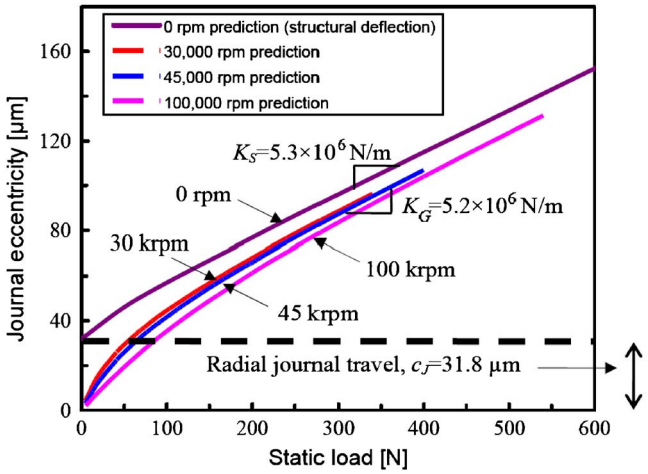

Fig. 6 Predicted journal eccentricity versus static load. Compliance coefficient S=0.67. Bearing configuration given in Ref. [16].

Figures 7 and 8 depict the minimum film thickness and the journal attitude angle versus applied static load, respectively, for operation at 30,000 rpm and 45,000 rpm. The film thicknesses correspond to measurements at the bearing centerline where the maximum hydrodynamic pressure is generated [16]. The tests were conducted to an ultimate load of ~200 N (specific pressure W/LD=1.37 bars or 20 psi) leading to very small film thicknesses, and undoubtedly, journal displacements much larger than the nominal FB clearance. The journal eccentricity exceeds the radial journal travel (c_J) for loads above ~60 N (W/LD =0.41 bar). The predicted minimum film thicknesses are in good agreement with the test results for static loads above 60 N. The predicted journal attitude angles are slightly smaller than those experimentally recorded. Importantly enough, the small attitude angles at high loads demonstrate reduced cross-coupled hydrodynamic effects and reveal the dominant effect of the foil-strip structure.

On the other hand, below 60 N, there is a significant discrepancy between predictions and test results for both minimum film

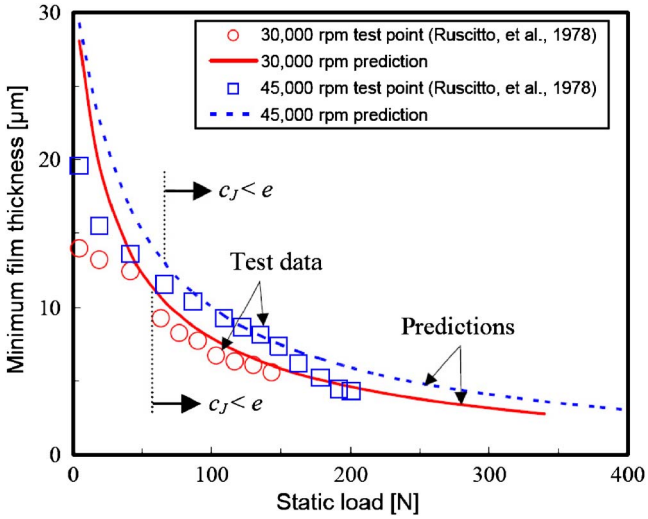

Fig. 7 Minimum film thickness versus static load. Compliance coefficient S=0.67. Comparison to test data in Ref. [16].

Downloaded 02 Jun 2010 to 171.66.16.107. Redistribution subject to ASME license or copyright; see http://www.asme.org/terms/Terms_Use.cfm

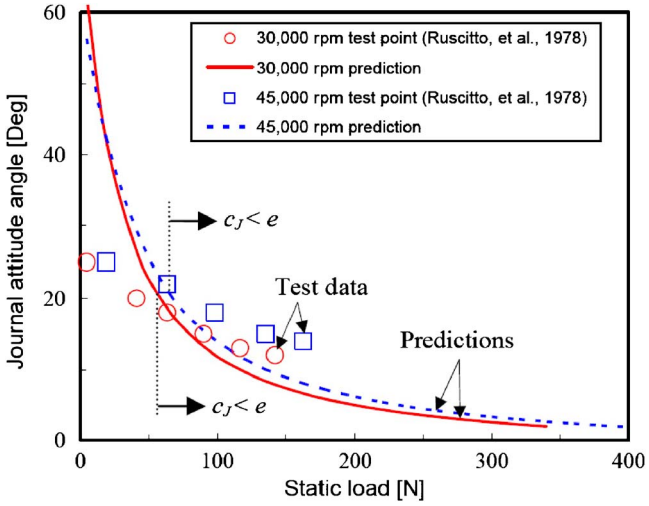

Fig. 8 Journal attitude angle versus static load. Compliance coefficient S=0.67. Comparison to test data in Ref. [16].

thickness and journal attitude angle. The main reason for the difference is attributed to fabrication inaccuracy, i.e., imperfect conformity of the arc radius from both the formed bump layer and top foil to the radius of the shaft. Note that Ruscitto et al. [16] do not report the uncertainty of their measurements, including the nominal clearance.

The experimental program in Ref. [16] did not include investigations on the stability and dynamic forced performance of the test FB. The archival literature shows scant information of FB rotordynamic force coefficients. Hence, only predictions for the bearing geometry given in Table 1 follow. Predictions are obtained for various structural loss factors (γ) and without accounting for a viscous damping parameter (C_f), whose physical value is to date most uncertain.

Figure 9 displays the FB stiffness coefficients versus excitation frequency for various applied static loads at a rotor speed of 30,000 rpm. Synchronous excitation corresponds to a frequency of 500 Hz. The structural damping loss factor has no discernible effect on the stiffness coefficients; thus the results shown correspond to γ=0.0. The direct stiffness coefficients (K_{XX},K_{YY}) increase both with excitation frequency and the static load (applied along X direction). At the largest loads considered, the FB stiffness K_{XX} approaches the structural stiffness $K_S(5.3\times10^6$ N/m) owing to a stiffened hydrodynamic gas film when compared to the elastic FB structure. That is, gas films become "hard" at large loads and high frequencies. Most importantly, K_{XX} cannot ever exceed K_S. Thus, the accurate knowledge of this structural parameter is of great importance in the design of FBs.

Note the different scale for the cross-coupled stiffness coefficients in Fig. 9. In general, K_{XY} decreases as the excitation frequency or static load increases. The other cross-coupled stiffness, K_{YX}, has a complicated trend at frequencies lower than the synchronous frequency (500 Hz). Below this frequency, K_{YX} increases with an increase in static load to ~70 N, but then decreases with larger loads. At high loads, the cross-coupled coefficients K_{YX} and K_{XY} are but a fraction of the direct stiffness coefficients. These predictions favor stable rotor dynamically performance.

Figure 10 shows the predicted direct damping coefficients (C_{XX},C_{YY}) versus excitation frequency for various static loads at 30,000 rpm (synchronous frequency=500 Hz). Damping coefficients for two structural loss factors, γ=0 and γ=0.4, are given for comparison. Ku [22] reports experimental values of γ =0.2–0.6 for bump strips attached at one end and free at the other. The cross coefficients (C_{XY},C_{YX}) are typically one order of magnitude smaller and not shown for brevity. In general, these coefficients decrease as the applied load increases and the excitation frequency increases.

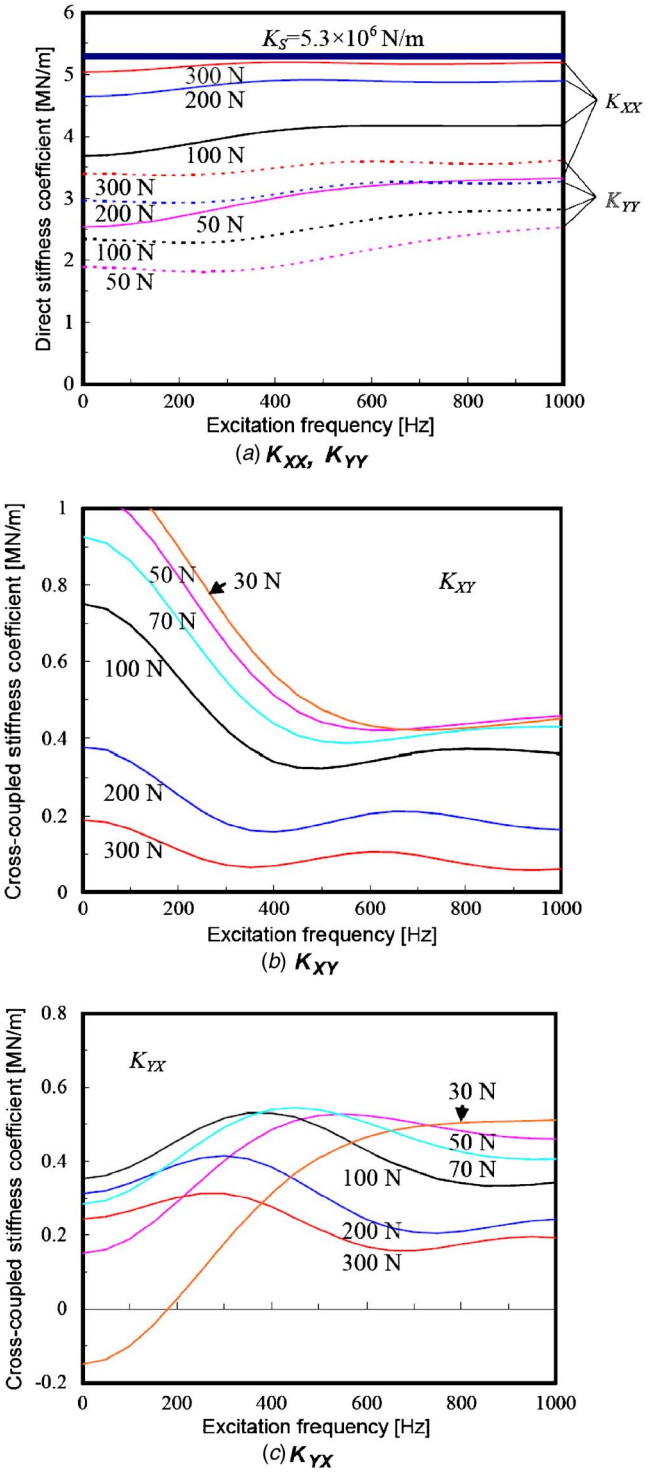

Fig. 9 Predicted FB stiffness coefficients versus excitation frequency for various static loads at 30 krpm. Compliance coefficient S=0.67, loss factor γ=0.0.

Without structural damping (γ=0), the damping coefficients show relatively small magnitudes and dropping rapidly as the excitation frequency increases above the rotor speed (500 Hz), and importantly enough, as the static load increases. The lack of damping is characteristic of gas films since the gas viscosity is

Downloaded 02 Jun 2010 to 171.66.16.107. Redistribution subject to ASME license or copyright; see http://www.asme.org/terms/Terms_Use.cfm

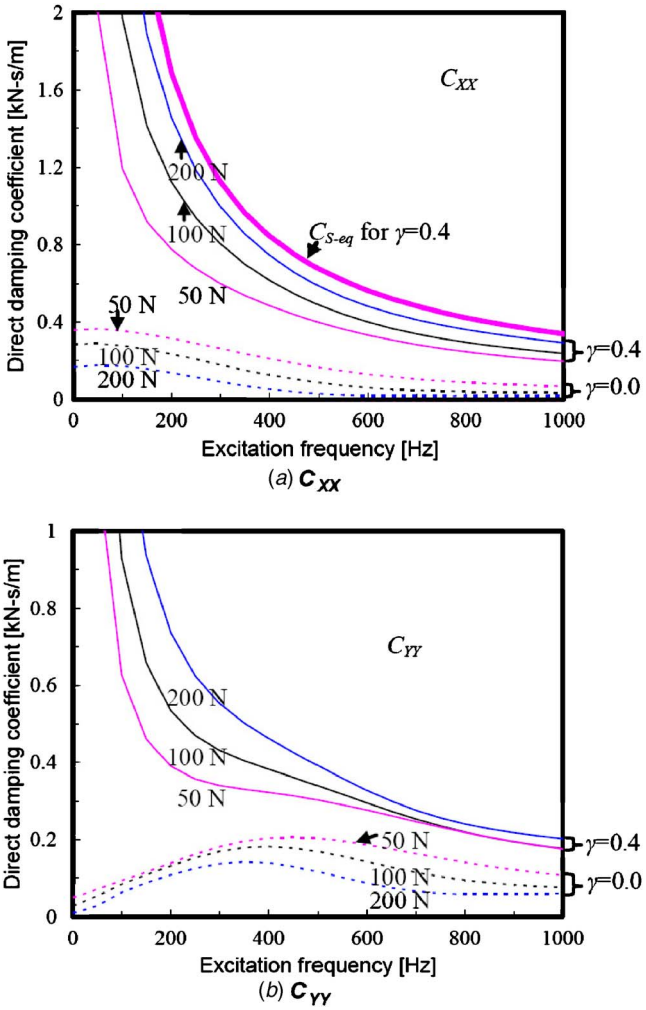

Fig. 10 Predicted damping coefficients versus excitation frequency for various static loads at 30 krpm. Compliance coefficient S=0.67, loss factor γ=0.0 and 0.4.

quite small. The structural loss factor (γ=0.40) represents the effect of material hysteresis and dry-frictional effects between the bumps and top foil and between the bumps and the bearing inner surface [22]. The direct damping coefficients (C_{XX}, C_{YY}) increase as the static load increases. C_{XX} trends toward the structural equivalent damping coefficient ($C_{S\text{-eq}}$) determined for large loads. Thus, the maximum damping in heavily loaded gas FBs depends on the structure material properties and the configuration of the underlying bump-foil structure.

At very low excitation frequencies ($\omega \to 0$), the damping coefficients that include a structural loss factor approach an infinite magnitude. This is physically not correct. The predictions showcase the severe limitation of an equivalent *viscous damping* dissipation model since the derived damping coefficient is inversely proportional to the frequency of excitation, i.e., $C \sim \gamma/\omega$. Thus, the predictions at low frequencies should be taken with caution. The authors merely note that dry-friction effects are dominant at this operating condition.

Conclusions

This paper presents a simple though efficient model to predict the static and dynamic force performance of gas FBs. Predicted journal eccentricities versus static load show a nearly constant static stiffness coefficient (K_G) for heavily loaded conditions and independent of shaft speed. The gas film FB stiffness approaches the structural stiffness (K_S) determined from a simple elastic deformation model of the bump-foil-strip layer for operation without rotor spinning. Predictions of minimum film thickness and journal attitude angle show excellent agreement with experimental data obtained in a "first-generation" FB for two rotor speeds and increasing load conditions. At the highest test load, predicted journal eccentricities exceed by approximately three times the *nominal* clearance of the test gas FB.

Predicated frequency-dependent direct stiffness coefficients (K_{XX}, K_{YY}) increase steadily as the static load augments. The stiffness coefficient, K_{XX}, along the direction of the applied static load, approaches from below to the structural stiffness, K_S. Thus, at high loads the bearing elastic structure influences most the static performance of a FB since the ensuing minute gas film shows a typical *hardening* effect. A structural loss factor (γ), exemplifying the dry-friction damping capacity of the underlying foil-bump strip structure, enhances the damping ability of gas FBs. Frequency-dependent direct damping coefficients (C_{XX}, C_{XX}) increase as the static load increases, while decreasing in a gas FB configuration that does not account for structural energy dissipation effects. The direct damping coefficient (C_{XX}) trends toward the calculated structural equivalent damping coefficient ($C_{S\text{-eq}} = K_S\gamma/\omega$) found for large applied loads.

A comparison of predictions against archival test data results validates the computational model advanced. The analysis of the predictions forwards important design considerations concerning to the operation of gas FBs under heavy loads. Reference [23] details further progress on a more advanced computational model integrating the top foil as a finite element shell and reports predictions showing the local sagging of the top foil in between adjacent bumps, as found experimentally by Ruscitto et al. [16].

Acknowledgment

This material is based upon work supported by the National Science Foundation under Grant No. 0322925. The continued support of the TAMU Turbomachinery Research Consortium is gratefully acknowledged. The original manuscript was prepared as a requirement for a Scientific Writing Course at TAMU. The authors thank the class instructor, Professor K. Ted Hartwig, for his guidance and review of the first draft manuscript.

Nomenclature

$C_{\alpha\beta}$ = bearing damping coefficients, $\alpha\beta = X, Y$ (N s/m)
C_f = bump layer viscous damping per unit area (N s/m^3)
$C_{S\text{-eq}}$ = structure equivalent viscous damping, $K_S\gamma/\omega$ (N s/m)
c = bearing (pad) radial clearance (m)
c_J = measured journal radial travel (m)
c_m = assembled radial clearance (m)
D = bearing diameter, $D = 2 \times R$ (m)
E = Young's modulus (N/m^2)
e_X, e_Y = journal eccentricity components, $e = \sqrt{e_X^2 + e_Y^2}$; $\varepsilon_X = e_X/c$, $\varepsilon_Y = e_Y/c$ (m)
F_X, F_Y = bearing reaction forces (N)
h = film thickness, $H = h/c$ (m)
H_X, H_Y = $\cos(\Theta)$, $\sin(\Theta)$
H_b = bump height (m)
i = imaginary unit, $(-1)^{0.5}$
K_f = bump structural stiffness per unit area, $K_f' = K_f(1 + i\gamma)$ (N/m^3)
K_G = bearing stiffness coefficient at high load (N/m)
K_S = structure stiffness coefficient (N/m)
$K_{\alpha\beta}$ = bearing stiffness coefficients, $\alpha\beta = X, Y$ (N·s/m)
L = bearing axial width, $b = L/l_x$ (m)
l_x = pad circumferential length, (m) $R(\Theta_t - \Theta_l)$

Downloaded 02 Jun 2010 to 171.66.16.107. Redistribution subject to ASME license or copyright; see http://www.asme.org/terms/Terms_Use.cfm

l_o = bump half-length (m)
N_b, N_s = number of bumps, number of bump strips
p = hydrodynamic pressure, $P=p/p_a$ (N/m^2)
p_A = average pressure along axial direction (N/m^2)
p_a = ambient pressure (N/m^2)
R, r = bearing and journal radii (m)
r_p = pad preload, $\bar{r}_p=r_p/c$ (m)
S = compliance coefficient, $S=p_a/(cK_f)$
s_o = bump pitch (m)
t = time, $\tau=\omega t$ (s)
t_b = bump thickness (m)
t_t = top (thin) foil thickness (m)
W = static load (N)
w_d = bump elastic deflection (m)
X, Y = inertial coordinate system (m)
x, z = coordinate system on plane of bearing (m)
α = bump height angle (rad)
ϕ = journal attitude angle, $\tan^{-1}(e_Y/e_X)$ (rad)
γ = bump structure hysteretic loss factor
Λ_g = bearing speed number, $\Lambda_g=6\mu\Omega Rl_x/p_a c^2$
μ = gas absolute viscosity (Pa s)
ν = Poisson's ratio
Θ = pad angular coordinate (rad)
σ_g = squeeze film number, $\Lambda_g=6\mu\Omega Rl_x/p_a c^2$
Ω, ω = rotor angular velocity and whirl frequency (rad/s)

Subscripts

0 = zeroth-order field
α, β = directions of perturbation for first order pressure fields (X, Y)
l, t, p = pad leading and trailing edges, and offset position

References

[1] Heshmat, H., and Hermel, P., 1993, "Compliant Foil Bearings Technology and Their Application to High Speed Turbomachinery," *Thin Films in Tribology*, D. Dowson et al., eds. (Elsevier Tribology Series, Vol. 25), Elsevier, Amsterdam, pp. 559–575.
[2] Agrawal, G. L., 1997, "Foil Air/Gas Bearing Technology: An Overview," ASME Paper No. 97-GT-347.
[3] DellaCorte, C., and Valco, M. J., 2000, "Load Capacity Estimation of Foil Air Journal Bearings for Oil-Free Turbomachinery Applications," NASA/TM, Report No. 2000-209782.
[4] Heshmat, H., 1994, "Advancements in the Performance of Aerodynamic Foil Journal Bearings: High Speed and Load Capacity," ASME J. Tribol., **116**, pp. 287–295.
[5] DellaCorte, C., Lukaszewicz, V., Valco, M. J., Radil, K. C., and Heshmat, H., 2000, "Performance and Durability of High Temperature Foil Air Bearings for Oil-Free Turbomachinery," NASA/TM, Report No. 2000-209187/REV1.
[6] Lee, Y. B., Kim, T. H., Kim, C. H., Lee, N. S., and Choi, D. H., 2003, "Unbalance Response of a Super-Critical Rotor Supported by Foil Bearings: Comparison With Test Results," Tribol. Trans., **47**, pp. 54–60.
[7] Lee, Y. B., Kim, T. H., Kim, C. H., Lee, N. S., and Choi, D. H., 2004, "Dynamic Characteristics of a Flexible Rotor System Supported by a Viscoelastic Foil Bearing (VEFB)," Tribol. Int., **37**, pp. 679–687.
[8] Heshmat, H., Walowit, J. A., and Pinkus, O., 1983, "Analysis of Gas-Lubricated Foil Journal Bearings," ASME J. Lubr. Technol., **105**, pp. 647–655.
[9] Heshmat, H., Walowit, J. A., and Pinkus, O., 1983, "Analysis of Gas Lubricated Compliant Thrust Bearings," ASME J. Lubr. Technol., **105**, pp. 638–646.
[10] Peng, J.-P., and Carpino, M., 1993, "Calculation of Stiffness and Damping Coefficients for Elastically Supported Gas Foil Bearings," ASME J. Tribol., **115**, pp. 20–27.
[11] Carpino, M., Medvetz, L. A., and Peng, J.-P., 1994, "Effects of Membrane Stresses in the Prediction of Foil Bearing Performance," Tribol. Trans., **37**, pp. 43–50.
[12] Peng, J.-P., and Carpino, M., 1997, "Finite Element Approach to the Prediction of Foil Bearing Rotor Dynamic Coefficients," ASME J. Tribol., **119**, pp. 85–90.
[13] San Andrés, L., 1995, "Turbulent Flow Foil Bearings for Cryogenic Applications," ASME J. Tribol., **117**, pp. 185–195.
[14] Iordanoff, I., 1999, "Analysis of an Aerodynamic Compliant Foil Thrust Bearing: Method for a Rapid Design," ASME J. Tribol., **121**, pp. 816–822.
[15] Khonsari, M. M., and Peng, Z.-C., 2004, "Hydrodynamic Analysis of Compliant Foil Bearing With Compressible Air Flow," ASME J. Tribol., **126**, pp. 542–546.
[16] Ruscitto, D., Mc Cormick, J., and Gray, S., 1978, "Hydrodynamic Air Lubricated Compliant Surface Bearing for an Automotive Gas Turbine Engine I-Journal Bearing Performance," NASA, Report No. CR-135368.
[17] Carpino, M., and Talmage, G., 2003, "A Fully Coupled Finite Element Formulation for Elastically Supported Foil Journal Bearings," Tribol. Trans., **46**, pp. 560–565.
[18] Faria, M., and San Andrés, L., 2000, "On the Numerical Modeling of High speed Hydrodynamic Gas Bearing," ASME J. Tribol., **122**, pp. 124–130.
[19] Heshmat, H., Shapiro, W., and Gray, S., 1982, "Development of Foil Journal Bearings for High Load Capacity and High Speed Whirl Stability," ASME J. Lubr. Technol., **104**, pp. 149–156.
[20] Chen, H. M., Howarth, R., Geren, B., Theilacker, J. C., and Soyars, W. M., 2000, "Application of Foil Bearings to Helium Turbocompressor," *Proceedings of the 30th Turbomachinery Symposium*, pp. 103–113.
[21] Rubio, D., and San Andrés, L., 2006, "Bump-Type Foil Bearing Structural Stiffness: Experiments and Predictions," ASME J. Eng. Gas Turbines Power, **128**, pp. 653–660.
[22] Ku, C.-P. R., 1993, "An Experimental and Theoretical Study of the Dynamic Structural Stiffness in Compliant Foil Journal Bearings," *ASME 14th Biennial Conference on Mechanical Vibration and Noise*, Albuquerque, NM, DE-Vol. 63, ASME, New York, pp. 83–88.
[23] Kim, T. H., 2006, "Analysis of Gas Foil Bearings Integrating 1D and 2D Finite Element Structural Models: Predictions Compared to Test Data," ASME Paper No. IMECE2006–16375.

Downloaded 02 Jun 2010 to 171.66.16.107. Redistribution subject to ASME license or copyright; see http://www.asme.org/terms/Terms_Use.cfm

A Design to Improve the Effective Damping Characteristics of Hole-Pattern-Stator Annular Gas Seals

Dara W. Childs
The Leland T. Jordan Professor
of Mechanical Engineering
e-mail: dchilds@tamu.edu

Yoon-Shik Shin
Graduate Research Assistant

Brent Seifert
Graduate Research Assistant

Turbomachinery Laboratory,
Texas A&M University,
College Station, TX 77843

Predictions are presented for hole-pattern-stator seals for which the hole depth is varied axially, showing that various depth patterns can significantly improve damping performance in terms of both increasing the seal's effective damping and reducing its crossover frequency—the frequency at which effective damping changes from positive to negative. Test results are presented for the seal with the best variable hole depth (VHD) pattern showing an increase in peak damping by a factor of 1.6 over a constant hole depth (CHD) design versus predictions of 2.7. The crossover frequency is reduced by approximately 40%. The VHD seal has a significant negative static stiffness that probably arises from a friction-factor-jump phenomenon, not flow path divergence. The VHD seal leaks less than a comparable CHD design. [DOI: 10.1115/1.2771242]

Introduction

Injection compressors require comparatively long annular seals with high-pressure drops that have a significant impact on rotordynamics. The balance-piston seal for straight-through compressor absorbs the full head rise of the machine. The division-wall seal for a back-to-back machine takes about one-half of the machine's head rise but deals with higher density gas. Annular seals using smooth rotors and honeycomb (HC) stators have been used since the 1960s in some petrochemical compressors. Conventional aluminum labyrinths were replaced because of the corrosion resistance of a stainless-steel HC material. To the authors' knowledge, the first intentional application of HC seals for enhancement of rotordynamics arose with the high pressure oxygen turbopump of the space shuttle main engine. A stepped, tooth-on-rotor labyrinth was replaced with a constant-clearance, smooth-rotor, HC-stator seal, eliminating synchronous and subsynchronous vibration problems, Childs and Moyer [1]. Subsequently, numerous case studies in centrifugal compressors and at least one steam turbine have been cited where replacing labyrinth seals with HC seals eliminated rotordynamic instabilities.

HC surfaces are normally made from high temperature stainless steels, developed as abradable surfaces for tooth-on-rotor labyrinths in aircraft gas turbines. This material is unforgiving in a rubbing condition. In addition, long lead times are frequently involved in securing a custom manufactured HC seal for a compressor. In response to these circumstances, Yu and Childs [2] tested three hole-pattern (HP)-stator seals made from aluminum. One of the seals with a hole-area density of 69% performed as well as previously tested HC-stator seals. Moore et al. [3] recently reported test results for a back-to-back centrifugal compressor that used an HP division-wall seal (with a swirl brake) to remarkably good effect—the compressor's stability characteristics improved with increasing differential pressure. One manufacturer of injection compressors uses an electrical discharging manufacturing process to produce a HC pattern in an aluminum stator. Most manufacturers have shifted to aluminum HP stators and away from traditional stainless-steel HC.

Kleynhans and Childs' [4] two-control-volume model predicted that HP seals had strongly frequency-dependent stiffness and damping coefficients, and test results have confirmed these predictions for HP [5] and HC [6] seals. The seal's effective damping C_{eff} (defined below in Eq. (3)) combines the destabilizing influence of the cross-coupled stiffness coefficient k and the stabilizing influence of direct damping C. C_{eff} is negative at low rotor precession frequencies due to k and positive at higher frequencies due to C. The frequency at which it changes sign is called the crossover frequency Ω_{co}. In applications, Ω_{co} needs to be lower than the rotor system's first natural frequency ω_{nl}. Otherwise, the seal will be highly destabilizing instead of highly stabilizing.

From a rotordynamics viewpoint, we would like to decrease Ω_{co} and increase C_{eff}. Kleynhans and Childs showed that the gas compliance provided by HC cells or HP holes causes a reduction in the local effective acoustic velocity. Hence, varying the hole depth axially could be expected to modify the 2D acoustic mode shapes within the seal and might favorably modify the seal's rotordynamic characteristics. A mechanical-vibration analog would be changing from a constant-radius circular rod to a tapered rod. Varying the cell depths of HC seals could be difficult because of their mode of manufacture; however, HP seals are normally created via numerically controlled machining. Hence, varying the hole depth axially is an easily realized outcome. The questions to be answered are (i) How should the hole depth be varied to enhance Ω_{co} and C_{eff}? and (ii) How much benefit would be expected? The present results provide answers to these questions plus supporting test data to confirm predictions.

Seal Reaction Force/Motion Model

For motion about a centered position, Kleynhans and Childs produced the following reaction-force/relative-motion model for HP- and HC-stator seals:

$$-\begin{Bmatrix} \mathbf{f}_{sX}(s) \\ \mathbf{f}_{sY}(s) \end{Bmatrix} = \begin{bmatrix} \mathbf{G} & \mathbf{E} \\ -\mathbf{E} & \mathbf{G} \end{bmatrix} \begin{Bmatrix} X(s) \\ Y(s) \end{Bmatrix} \tag{1}$$

Here, s is the Laplace-domain variable, $\mathbf{f}_s$ the reaction-force vector, and $X(s)$, $Y(s)$ are the Laplace-domain components of the relative displacement vector between the seal's rotor and stator. In

Contributed by the International Gas Turbine Institute of ASME for publication in the JOURNAL OF ENGINEERING FOR GAS TURBINES AND POWER. Manuscript received June 13, 2006; final manuscript received August 16, 2006; published online January 9, 2008. Review conducted by J. Jeffrey Moore. Paper presented at the ASME Turbo Expo 2006: Land, Sea and Air (GT2006), Barcelona, Spain, May 8–11, 2006, Paper No. GT2006-90777.

Copyright © 2008 by ASME

Downloaded 02 Jun 2010 to 171.66.16.107. Redistribution subject to ASME license or copyright; see http://www.asme.org/terms/Terms_Use.cfm

terms of frequency-dependent stiffness and damping coefficients, the seal model looks like

$$-\begin{Bmatrix} \mathbf{f}_{sX} \\ \mathbf{f}_{sY} \end{Bmatrix} = \begin{bmatrix} K(\Omega) & k(\Omega) \\ -k(\Omega) & K(\Omega) \end{bmatrix} \begin{Bmatrix} X \\ Y \end{Bmatrix} + \begin{bmatrix} C(\Omega) & c(\Omega) \\ -c(\Omega) & C(\Omega) \end{bmatrix} \begin{Bmatrix} \dot{X} \\ \dot{Y} \end{Bmatrix} \tag{2}$$

The two models are related by $\mathbf{G}(j\Omega)=K(\Omega)+jC(\Omega)$ and $\mathbf{E}(j\Omega)=k(\Omega)+jc(\Omega)$, where $j=\sqrt{-1}$. In comparing the rotordynamic performance of seals, the effective stiffness and damping coefficients

$$K_{\text{eff}}(\Omega) = K(\Omega) + c(\Omega)\Omega \quad C_{\text{eff}}(\Omega) = C(\Omega) - k(\Omega)/\Omega \tag{3}$$

are helpful. C_{eff} combines C, the stabilizing direct damping coefficient, and k, the destabilizing cross-coupled stiffness coefficient. These definitions apply only for small motion about a centered position.

Optimum Hole Depth Variation

Predictions are obtained by modifying a code based on the two-control-volume model of Ref. [4] to allow for a variable hole depth (VHD) function $H_d(Z)$. The analysis was applied to an existing HP seal with $R=57.37$ mm, $L=86.06$ mm, and $C_r=0.020$ mm at a supply pressure of 70 bars and a pressure ratio of 0.5. Figure 1 shows the existing constant hole depth (CHD) HP geometry.

The following basic hole-depth functions $H_d(Z)$ were examined: (1) linear, (2) quadratic, (3) $\sqrt{Z}$, (4) $\cos(\pi Z/L)$, and (5) $\cos^{-1}(1-2Z/L)$. For each $H_d(Z)$ function, both increasing and decreasing hole depth variations in the direction of flow were considered. Figure 2 shows the resultant effective damping $C_{\text{eff}}(f=\Omega/\omega)$ for the CHD seal with $H_d=3.30$ mm zero preswirl, and $\omega=20{,}000$ rpm plus results for the ten VHD functions. In descending order, the best performers for reducing Ω_{co} are (1) $\cos(\pi Z/L)$ decreasing, (2) $\sqrt{Z}$ decreasing, (3) linear decreasing, (4) $\cos^{-1}(1-2Z/L)$ decreasing, (5) quadratic decreasing, (6) quadratic increasing, and (7) CHD. Generally, decreasing the hole depth axially is productive in reducing Ω_{co}. All of the functions

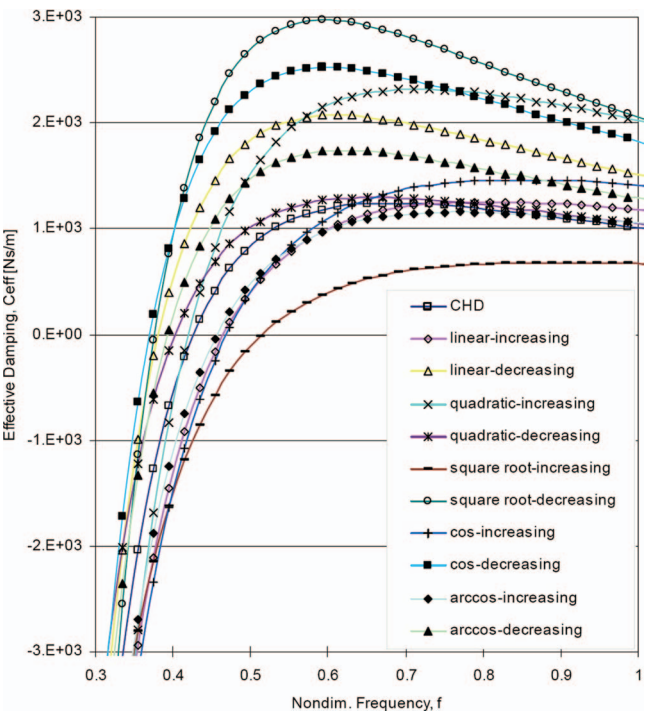

Fig. 2 Effective damping versus *f*

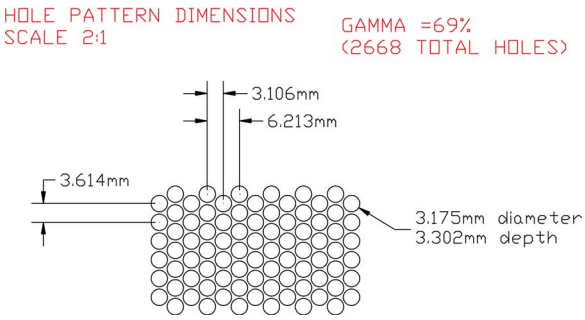

Fig. 1 CHD, HP geometry [5]

that give reduced Ω_{co} also yield marked overall increases in C_{eff}. The $\sqrt{Z}$-decreasing function is predicted to give about 2.7 times greater peak value for C_{eff} than the CHD design.

Figure 3 shows K_{eff} for all VHD designs. In descending order, for $f=0.5$, the highest K_{eff} values were achieved by the following designs: (1) Quadratic increasing, (2) $\sqrt{Z}$ decreasing, (3) cos increasing, (4) linear increasing, and (5) arccos increasing. The static stiffness is constant for all designs. The only design that produces both better damping characteristics and higher K_{eff} is the $\sqrt{Z}$-decreasing function.

Test Seal Geometry

Based on the above predictions, the following $\sqrt{Z}$-decreasing hole-depth function was selected:

$$H_d(Z) = H_{\text{dim}} + (H_{d\ \text{ex}} - H_{d\ \text{in}})\sqrt{\frac{Z}{L}} \tag{4}$$

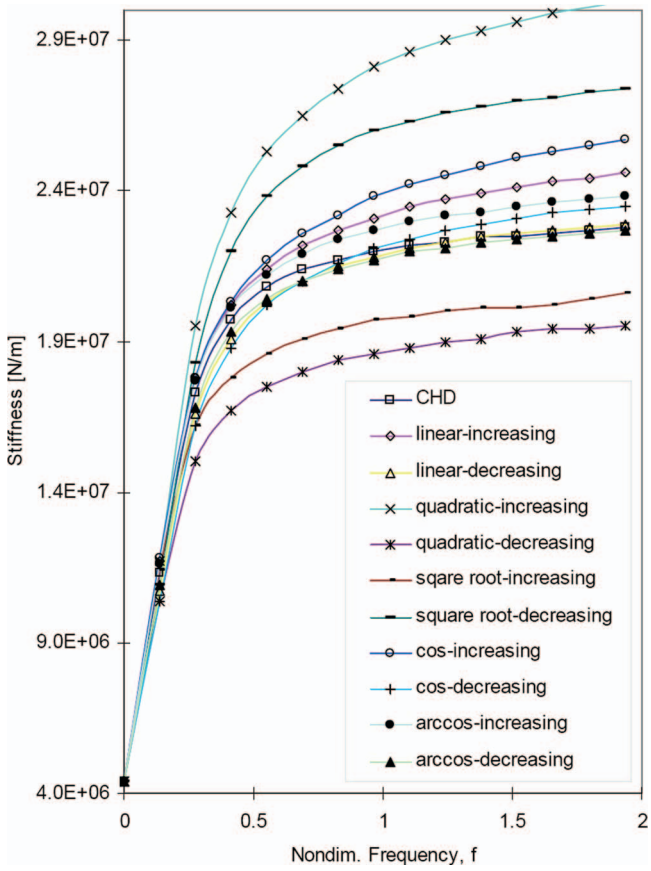

Fig. 3 Effective stiffness versus *f*

Downloaded 02 Jun 2010 to 171.66.16.107. Redistribution subject to ASME license or copyright; see http://www.asme.org/terms/Terms_Use.cfm

The test seal HP function was defined by $H_{d\,\mathrm{in}}=5.067$ mm (0.1995 in.) $H_{d\,\mathrm{ex}}=1.689$ mm (0.0665 in.), and $L=81.610$ mm (3.213 in.). The VHD test seal has a total length of 85.725 mm and a diameter of 72.9 mm. Tests were conducted at the radial clearance $C_r=0.020$ mm.

Test Apparatus and Parameter

Identification. The test apparatus has been described in several prior publications–Dawson et al. [7] and Weatherwax and Childs [8]–and will only be briefly reviewed here. The test apparatus uses external shakers to excite a softly mounted stator that contains two identical seals. The rotor is supported by two stiff hybrid bearings. Transient measurements capture components of the input excitation force, the stator acceleration, and the relative displacement between the stator and rotor. Starting with these measurements and $\Sigma f=m_s\ddot{R}_s$, a frequency-domain parameter identification approach is employed to identify the $\mathbf{H}_{ij}$ complex dynamic-stiffness coefficients for the following model:

$$\begin{Bmatrix} \mathbf{F}_X-\mathbf{m}_s\mathbf{A}_X \\ \mathbf{F}_Y-\mathbf{m}_s\mathbf{A}_Y \end{Bmatrix} = -\begin{bmatrix} \mathbf{H}_{XX}\mathbf{H}_{XY} \\ \mathbf{H}_{YX}\mathbf{H}_{YY} \end{bmatrix}\begin{Bmatrix} \mathbf{D}_Y \\ \mathbf{D}_Y \end{Bmatrix} \tag{5}$$

where **F**, **A**, and **D** are complex fast Fourier transforms (FFTs) of the applied force, stator acceleration, and relative stator-rotor displacement vectors. Rouvas and Childs [9] discussed the identification procedure for the $\mathbf{H}_{ij}$ coefficients. Diagonal $\mathbf{H}_{ij}$ coefficients are "direct" dynamic-stiffness coefficients. Off-diagonal terms are "cross-coupled" dynamic-stiffness coefficients. The test rig uses alternate shakes in orthogonal X and Y directions to obtain all of the coefficients. For motion about the centered position, theory predicts and measurements confirm that $\mathbf{H}_{XX}=\mathbf{H}_{YY}=\mathbf{G}$ and $\mathbf{H}_{XY}=-\mathbf{H}_{YX}=\mathbf{E}$ for **E** and **G** in Eq. (1).

Steady-state measurements in the test rig include rotor speed plus upstream and downstream temperatures and pressures. The available supply pressures reach 70 bars, and (within limits) the seal pressure ratios can be varied independently of supply pressure. Tests were conducted at the following three pressure ratios: 0.3, 0.4, and 0.5. The test VHD seal produced a pronounced negative static stiffness that limited test conditions to a supply pressure of no more than 55 bars. Division-wall or balance-piston seals of compressors normally operate at pressure ratios near 0.5, and the present paper will mainly discuss pressure-ratio data in this range. The VHD was tested with three different preswirl inserts, producing a range of preswirl circumferential velocity ratios. Since all current and proposed compressor applications employ swirl brakes, only zero-preswirl data will be reviewed. Finally, tests were conducted at 10,200 rpm, 15,200 rpm, and 20,200 rpm, but most of the results to be presented will be at 20,200 rpm to get surface velocities that are nearer to compressor applications. Complete data sets are given by Seifert [10].

The dynamic tests obviously aim to measure rotordynamic coefficients of the test seals. However, the test procedure will also measure stiffness and damping arising from the exit seals, hose connections, etc. To account for these additional elements, "base line" tests are conducted with the test seals removed. These tests are conducted at reduced supply pressures to match the "real test" backpressures experienced by the backpressure seals. One set ($\mathbf{H}_{XX}$, $\mathbf{H}_{YY}$, $\mathbf{H}_{XY}$, and $\mathbf{H}_{YX}$) of frequency-dependent dynamic-stiffness coefficients is obtained as the average of 32 separate shake tests, which are averaged in the frequency domain.

To estimate the variability of dynamic data, ten consecutive tests are conducted at 15,200 rpm. During these tests, the operating conditions are held as constant as possible. The dynamic-stiffness data are reduced, and the standard deviations of the dynamic-stiffnesses and rotordynamic coefficients are obtained for discrete frequencies. The standard deviation obtained from these ten sequential tests defines the uncertainty at each frequency for both the base line and seal tests. Uncertainties in the dynamic-stiffness coefficient results vary with frequency. For example, results near the line frequency of 60 Hz or multiples of this frequency are consistently poor. These frequencies are avoided in creating the excitation wave form. Also, data at or near running speed are poor and are discarded. The test uncertainty is calculated at each frequency as the square root of the sum of the squares of base line and seal test uncertainty at each frequency. The average uncertainty is displayed on the plots as error bars for the rotordynamic coefficients. The uncertainty bars reflect $\pm$ one standard deviation.

Test Results

The first issue of interest concerns the accuracy of predictions for a seal with varying hole depth. Figure 4 illustrates measurements and predictions for the VHD test seal at 20,200 rpm for a zero preswirl, for $P_{\mathrm{in}}=41.4$ bars, and for PR=0.5. The zero-preswirl condition is used in calculations and tests for the VHD seal because prior test results [5,6] and field experiences have shown that balance-piston or division-wall seals need swirl brakes (or shunt injection) to minimize the cross-coupled stiffness coefficient k. Starting with $K(\Omega)$, the predicted and measured functions are qualitatively similar. The static stiffness is negative and fairly large versus predictions for small and positive. The relative uncertainties are reasonable. $K_{\mathrm{eff}}(\Omega)$ basically coincides with $K(\Omega)$. For $k(\Omega)$, measurements and predictions are in qualitative agreement, but measured values are consistently higher by an approximate factor of 1.7 at lower frequencies. Relative uncertainties are reasonable.

Moving to the damping coefficients, measured and predicted functions for $C(\Omega)$ are qualitatively similar, but measured damping values are higher by an approximate factor of 2. Relative uncertainties are reasonable. For $c(\Omega)$, again, the measurements and predictions agree qualitatively, but the measured values are higher. The relative uncertainties are higher for $c(\Omega)$, but this reflects the lower magnitudes for this function, more than higher absolute uncertainty. $C_{\mathrm{eff}}(\Omega)$ is qualitatively well predicted. The crossover frequency Ω_{co} is closely predicted. Above Ω_{co}, measured effective damping is higher than predicted by an approximate factor of 2.2.

The following nondimensionalized and normalized stiffness and damping coefficients will be used to compare the present VHD seal to a CHD seal [5]

$$K^*=K\left(\frac{C_r}{DL\Delta P}\right) \quad k^*=k\left(\frac{C_r}{DL\Delta P}\right) \quad C^*=C\left(\frac{C_r}{DL\Delta P}\right) \tag{6}$$

With this approach, normalized damping coefficients have dimensions of seconds. The nondimensionalization of Eq. (6) is generally effective for HP and HC seals.

Figure 5 provides nondimensionalized, measured rotordynamic coefficients for the VHD seal and CHD seal. The two seals are identical except that the CHD seal had $H_d=3.30$ mm [5]. For both seals, $\omega=20{,}200$ rpm, preswirl is zero, and PR=0.5. For the VHD seal, $P_{\mathrm{in}}=55.2$ bars; for the CHD seal, $P_{\mathrm{in}}=70$ bars. The functions $k^*(\Omega)$ and $c^*(\Omega)$ basically coincide for the VHD and CHD seals. For $K^*(\Omega)$, the VHD seal starts with a large negative value versus the CHD seal's low positive value. The VHD seal's $K^*(\Omega)$ increases rapidly and catches up with the CHD seal around 200 Hz. The $K^*_{\mathrm{eff}}(\Omega)$ function closely resembles the $K^*(\Omega)$ function for both seals.

The VHD seal has a much higher low-frequency value for $C^*(\Omega)$ than the CHD seal. The two seals have about the same values at 300 Hz. For $C^*_{\mathrm{eff}}(\Omega)$, the Ω_{co} values for the CHD and VHD seals are, respectively, 50 and 70 Hz, reflecting a reduction of about 40%. The peak values for $C^*_{\mathrm{eff}}(\Omega)$ for the CHD and VHD seals are, respectively, 7.42×10^{-5} at 160 Hz and 10.8×10^{-5} at 100 Hz, reflecting an increase in peak effective damping by a factor of about 1.60.

Downloaded 02 Jun 2010 to 171.66.16.107. Redistribution subject to ASME license or copyright; see http://www.asme.org/terms/Terms_Use.cfm

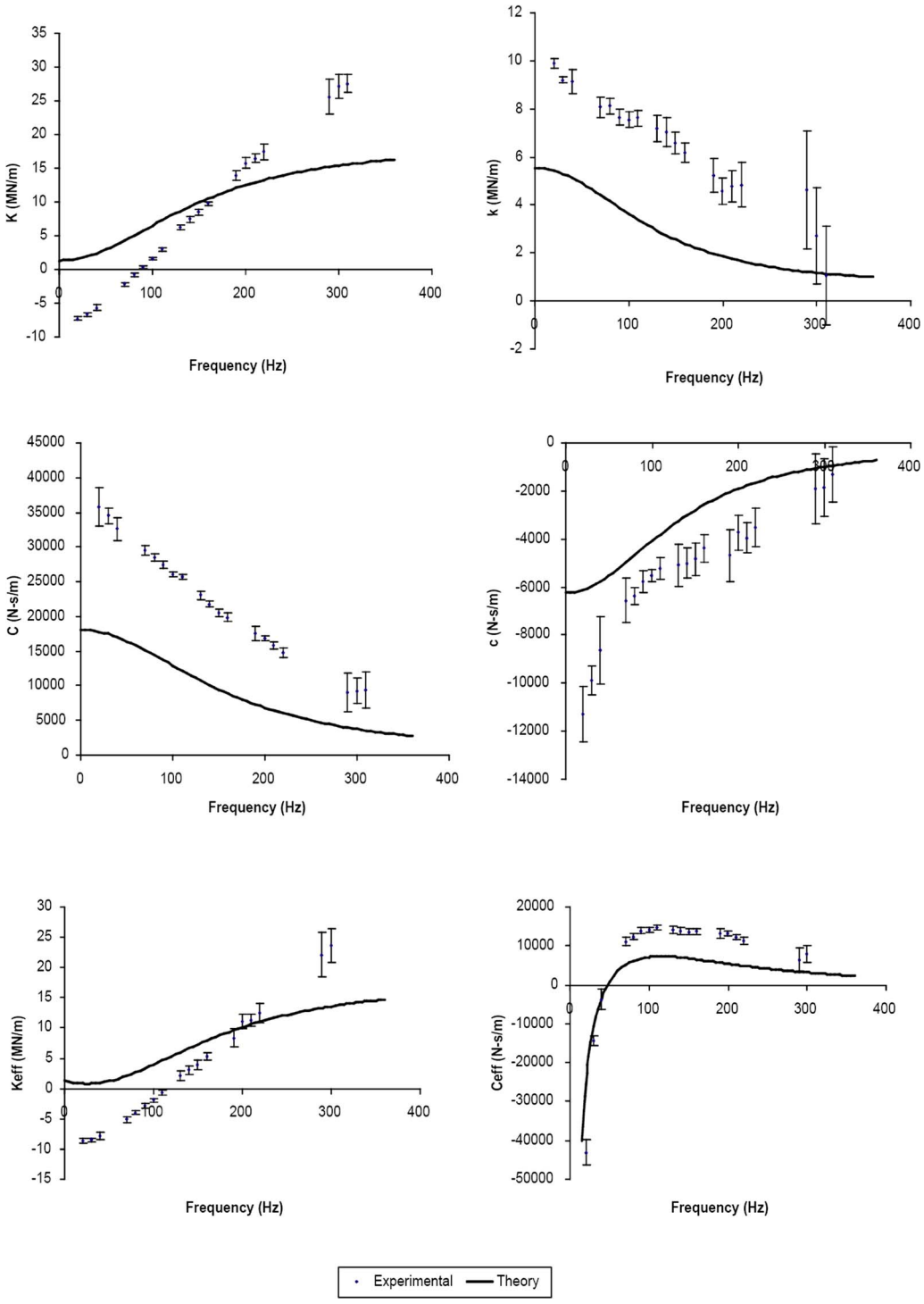

Fig. 4 Measured values versus predictions for the VHD test seal

Figure 6 provides a comparison of the VHD and CHD seal's leakage coefficient, $\phi=(\dot{m}/\pi DC_r)(\sqrt{R_cT_{\text{in}}/2\Delta PP_{\text{in}}})$ versus pressure ratio. In the leakage-coefficient definition, $\dot{m}$ is the mass flow rate, R_c is the gas constant, and T_{ln} is the inlet temperature. The VHD seal leaks less than the CHD seal. The difference decreases with increasing PR (decreasing ΔP).

Conclusions and Discussion

As predicted, the test results show that a properly designed VHD seal can produce improved damping characteristics in terms of a reduced crossover frequency and increased effective damping. However, the improvement is less than that predicted. The measured increase in peak effective damping for the VHD seal was around 1.6 versus predictions of 2.7.

One obvious question in reviewing Figs. 4 and 5 is: If in Fig. 4, the VHD seal has a higher effective damping than that predicted, why is it not comparatively higher than the CHD seal in Fig. 5? The answer is that the model underpredicts the dynamic-stiffness coefficients for both seals by about the same amount for the test conditions shown. Figure 7 provides comparisons between measurements and predictions for the CHD seal for comparable speed,

Downloaded 02 Jun 2010 to 171.66.16.107. Redistribution subject to ASME license or copyright; see http://www.asme.org/terms/Terms_Use.cfm

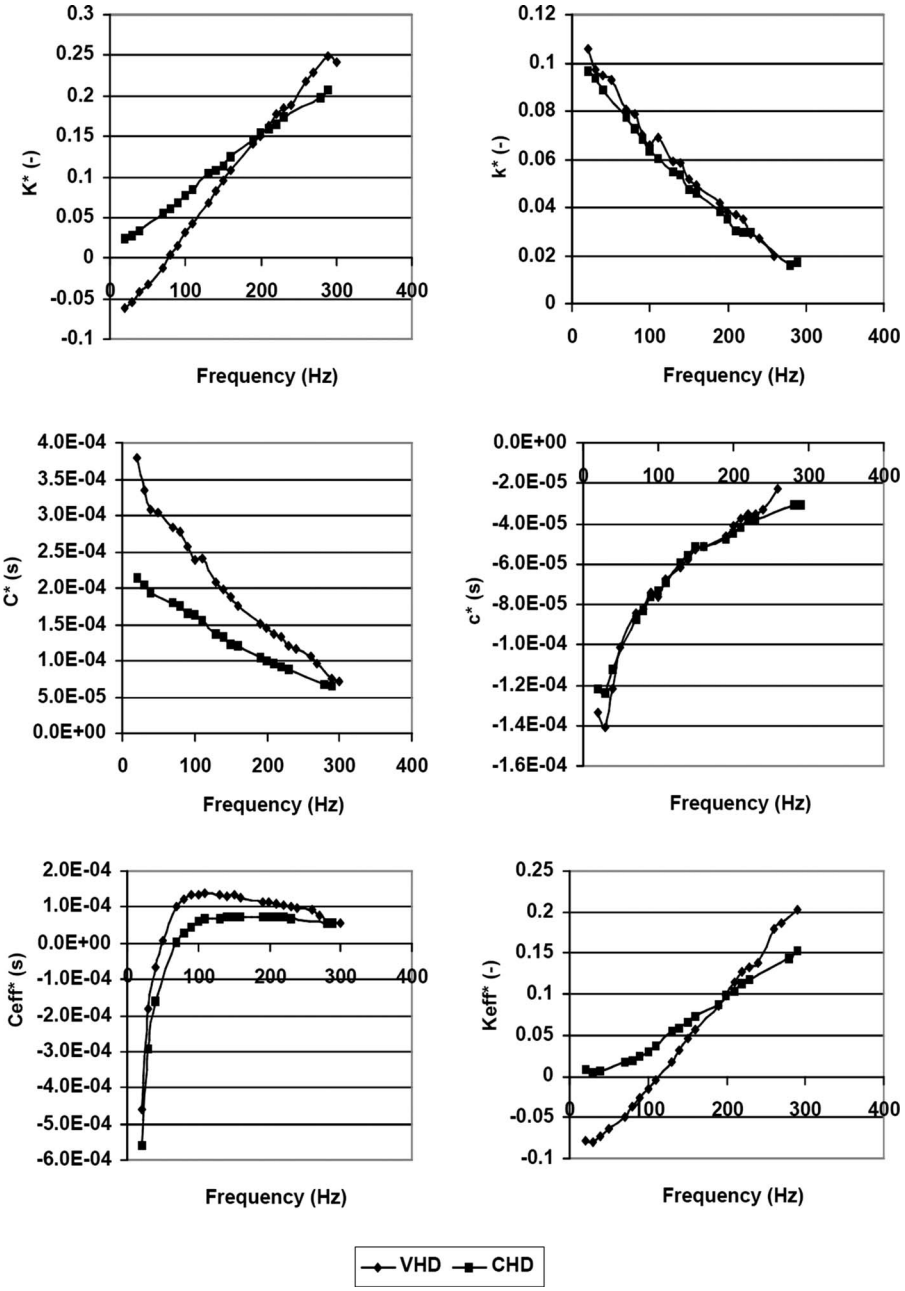

Fig. 5 Nondimensional measured rotordynamic coefficients for the CHD seal with PR =.45 and the VHD seal with and PR=.50 for ω=20,200 rpm, zero preswirl, and C_r =0.20 mm

preswirl, and clearance conditions, showing comparable under predictions for k and C coefficients. The model does a significantly better job with nonzero-preswirl conditions.

The pronounced negative static stiffness shown by the VHD seal was not predicted and limited the feasible test supply pressures, ΔPs, and clearances. Beyond a limiting supply pressure or ΔP, the test rig stator would "stick" to the test rotor and could not be pulled away using the hydraulic shakers. Each shaker has approximately 4400 N static capability. This phenomenon and restriction have appeared previously while testing one HC and several HP seals. The CHD seal of Fig. 2, with H_d=3.30 mm, was tested at full pressure and the two radial clearances of 0.10 and 0.20 mm. An identical seal, except for a smaller H_d=3.18 mm, could not be tested at full pressure at the 0.10 mm radial clearance because of negative stiffness. (Data from this seal are proprietary and cannot be presented.) Because of the negative stiffness, the present VHD seal could not be tested effectively at any reasonable supply pressure for the reduced 0.10 mm radial clearance.

Seal divergence is known to cause negative stiffness. The dimensions of the present seals were measured after being fitted into the test housing, and no measurable divergence could be detected. During tests, the axial pressure distribution tends to create larger clearances at the inlet, leading to a converging flow path rather than a diverging flow path. Also, the gas expansion creates a significant drop in temperature as the gas moves down the seal. Again, this temperature distribution would cause a convergent flow condition with tighter exit clearances.

The "friction-factor jump" phenomenon observed by Ha and Childs [11] and discussed by Ha et al. [12] provides the most reasonable explanation for negative stiffness. Specifically, these

Downloaded 02 Jun 2010 to 171.66.16.107. Redistribution subject to ASME license or copyright; see http://www.asme.org/terms/Terms_Use.cfm

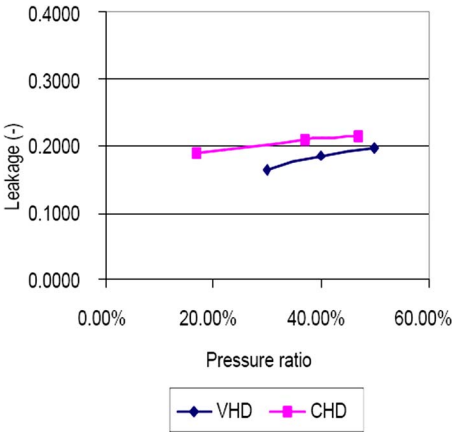

Fig. 6 Leakage coefficient for the VHD seal at P_{in}=41.4 bars and the CHD seal with P_{in}=70 bars for zero preswirl and ω =20,200 rpm

references cite flat-plate test results for which the friction factor increases with increasing Reynolds numbers at elevated Reynolds numbers in the range of 20,000; i.e., $\partial f_f/\partial R_e > 0$. Ha and Childs observed a friction-factor jump behavior in about one-third of their tests. Ha et al. used a miniature pressure transducer to explain the jump behavior as a consequence of an unstable, longitudinal, cavity-flow phenomena within the cells.

The "Lomakin" effect [13] predicts a positive stiffness of annular seals, resulting from the interaction of the inlet loss and friction factor when the friction factor decreases with increasing Reynolds number, $\partial f_f/\partial R_e > 0$, and a reduced or negative stiffness for the opposite behavior. The fact that the present VHD seal leaks appreciably less than the CHD seal supports the idea that the VHD seal has a friction-factor jump behavior. Since the model does not account for friction-factor jump phenomenon, its failure to predict the pronounced negative direct stiffness of Fig. 4 is understandable. Note that no method exists today for predicting the occurrence of friction-factor jumps due to cavity flow phenomena for CHD or VHD geometries.

The negative static stiffness produced by the seal was a problem for this test program because the stator is softly mounted. However, our experience in tests and with predictions suggests that negative stiffness is not a problem in compressors because of the much higher bearing-rotor stiffness. Moreover, a small convergent taper can probably produce sufficient additional stiffness to offset any concerns due to the seal's negative stiffness.

The results produced here with a variable hole depth are not predicted for deeper or shallower CHD geometries. The VHD configurations could readily be realized with HC HPs that are made via electrical discharge machining, rather than standard stainless-steel HC surfaces. Smalley et al. [14] recently presented analyses and supporting test results for a HC pattern HP-stator seal with intentional divergence to enhance effective damping. This approach works, but the predicted negative stiffness and increased leakage present concerns for the design.

Recent papers by Camati et al. [15] and Kocur and Hayles [16] present case studies in which compressor instabilities were caused

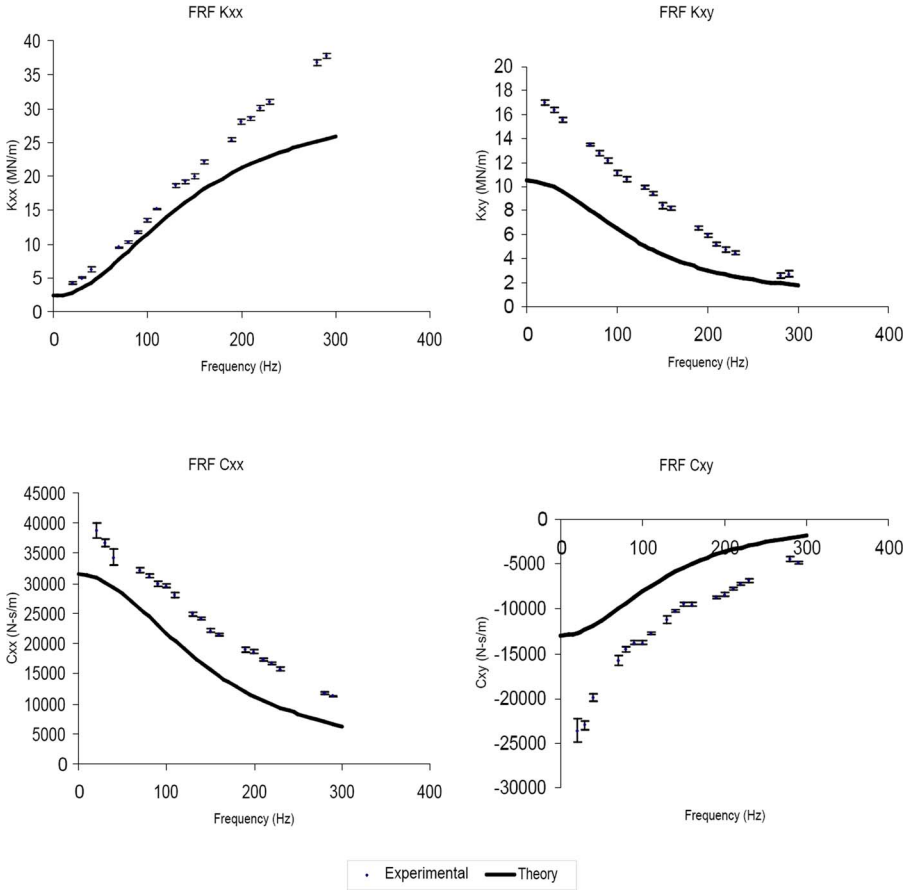

Fig. 7 K_{xx}, K_{xy}, C_{xy}, C_{xy} versus excitation frequency Ω for a CHD seal for C_r=0.20 mm, ω=20,200 rpm, $u_0(0)$=0.028, and PR=0.45 [5].

Downloaded 02 Jun 2010 to 171.66.16.107. Redistribution subject to ASME license or copyright; see http://www.asme.org/terms/Terms_Use.cfm

by HP seals. The division-wall seal in Ref. [15] became destabilizing because the seal flow path became divergent. The negative stiffness dropped the rotor natural frequency precipitously. At this reduced precession frequency, the seal (and other destabilizing elements) within the rotor caused a strong subsynchronous instability. A corrected geometry that prevented divergence worked well. In Kocur and Hayles' case, squeeze-film dampers were used with intentionally soft bearing-support springs, producing a very low first natural frequency. When a HC seal replaced the original labyrinth seal the rotor was strongly unstable. With the soft bearing supports, the rotor-system natural frequency was below the seal crossover frequency, and the seal was destabilizing. The soft bearing supports caused the low system natural frequency, not the negative stiffness from the HC seal. Clearly, the installation of HP or HC seals requires care and analysis. Used properly, they can produce high damping and high stiffness and very good rotordynamic performance. Used improperly, they can produce instability and unanticipated critical-speed locations.

Nomenclature

C_r = radial clearance (L)
C, c = direct and cross-coupled damping coefficient (FT/L)
C_{eff} = effective damping coefficient, Eq. (3) (FT/L)
$f=\Omega/\omega$ = nondimensionalized excitation frequency
f_s = seal reaction force (F)
H_d = hole depth (L)
$\mathbf{H}_{ij}$ = dynamic-stiffness coefficient (F/L)
K, k = direct and cross-coupled stiffness coefficients (F/L)
K_{eff} = effective direct stiffness coefficient (F/L)
L = seal length defined in Eq. (3) (L)
m_s = stator mass (M)
P_{in} = inlet pressure (F/L^2)
P_{ex} = exit pressure (F/L^2)
$\text{PR}=P_{\text{ex}}/P_{\text{in}}$ = pressure ratio
R, D = seal radius and diameter (L)
$U(0)$ = inlet circumferential (swirl) velocity (L/T)
$u(0)_0=U(0)_0/(R\omega)$ = inlet preswirl ratio
Z = axial length along seal (L)
γ = ratio of hole area to surface area
Ω = excitation frequency $(1/T)$
Ω_{co} = crossover frequency for C_{eff} and k_{eff} $(1/T)$
ω = running speed $(1/T)$

References

[1] Childs, D., and Moyer, D., 1985, "Vibration Characteristics of the HPOTP (High Pressure Oxygen Turbopump) of the SSME (Space Shuttle Main Engine)," ASME J. Eng. Gas Turbines Power, **107**, pp. 152–159.
[2] Yu, Z., and Childs, D., 1998, "A Comparison of Experimental Rotordynamic Coefficients and Leakage Characteristics Between Hole-Pattern Gas Damper Seals and a Honeycomb Seal," ASME J. Eng. Gas Turbines Power, **120**(4), pp. 778–783.
[3] Moore, J., Walker, S., and Kuzdal, M., 2002, "Rotordynamic Stability Measurements During Full Load Testing of a 6000 psi Reinjection Centrifugal Compressor," *Proceedings, 31st Texas A&M University Turbomachinery Symposium*, September, pp. 29–38.
[4] Kleynhans, G., and Childs, D., 1997, "The Acoustic Influence of Cell Depth on the Rotardynamic Characteristics of Smooth-Rotor/Honeycomb-Stator Annular Gas Seals," ASME J. Eng. Gas Turbines Power, **119**(4), pp. 949–957.
[5] Childs, D., and Wade, J., 2004, "Rotordynamic-Coefficient and Leakage Characteristics for Hole-Pattern-Stator Annular Gas Seals—Measurements Versus Predictions," ASME J. Tribol., **126**(2), pp. 326–333.
[6] Sprowl, B., and Childs, D., 2004, "A Study of the Effects of Inlet Preswirl on the Dynamic Coefficients of a Straight-Bore Honeycomb Gas Damper Seal," ASME Paper No. GT2004-53328.
[7] Dawson, M., Childs, D., Holt, C., and Phillips, S., 2002, "Theory versus Experiments for the Dynamic Impedances of Annular Gas Seals: Part 1—Test Facility and Apparatus," ASME J. Eng. Gas Turbines Power, **124**, pp. 958–963.
[8] Weatherwax, M., and Childs, D., 2003, "The Influence of Eccentricity on the Leakage and Rotordynamic Coefficients of a High Pressure, Honeycomb, Annular Gas Seal…Measurements Versus Predictions," ASME J. Tribol., **125**, pp. 422–429.
[9] Rouvas, C., and Childs, D., 1993, "A Parameter Identification Method for the Rotordynamic Coefficients of a High Reynolds Number Hydrostatic Bearing," ASME J. Vibr. Acoust., **115**, pp. 264–270.
[10] Seifert, B., 2005, "Measurements Versus Predictions for Rotordynamic Coefficients and Leakage Rates for a Novel Hole-Pattern Gas Seal," M.S. thesis, Mechanical Engineering Department, Texas A&M University.
[11] Ha, T.-W., and Childs, D., 1992, "Friction-Factor Data for Flat-Plate Tests of Smooth and Honeycomb Surfaces," ASME J. Tribol., **114**, pp. 722–730.
[12] Ha, T.-W., Morrison, G., and Childs, D., 1992, "Friction-Factor Characteristics for Narrow-Channels With Honeycomb Surfaces," ASME J. Tribol., **114**, pp. 714–721.
[13] Lomakin, A., 1958, "Calculation of Critical Numbers of Revolutions and the Conditions Necessary for Dynamic Stability of Rotors in High-Pressure Hydraulic Machines When Taking Into Account Forces Originating in Sealings," Power and Mechanical Engineering, **4**, pp. 1–5.
[14] Smalley, A. J., Camatti, M., Childs, D., Hollingsworth, J., Vannini, G., and Carter, J., 2004, "Dynamic Characteristics of the Diverging-Taper Honeycomb-Stator Seal," ASME Paper No. GT2004-53084.
[15] Camati, M., Vanini, G., Fulton, J., and Hopenwasser, F., 2003, "Instability of a High Pressure Compressor Equipped With Honeycomb Seals," *Proceedings of the 32nd Texas A&M University Turbomachinery Symposium*, September, pp. 39–48.
[16] Kocur, J., and Hayles, G., 2004, "Low Frequency Instability in a Process Compressor," *Proceedings of the 33rd Texas A&M University Turbomachinery Symposium*, September, pp. 25–32.

Downloaded 02 Jun 2010 to 171.66.16.107. Redistribution subject to ASME license or copyright; see http://www.asme.org/terms/Terms_Use.cfm

Nonlocal Cyclic Life Prediction for Gas Turbine Components With Sharply Notched Geometries

Roland Mücke

Holger Kiewel

Alstom,
Brown Boveri Strasse 7,
5401 Baden, Switzerland

The safe and efficient operation of modern heavy duty gas turbines requires a reliable prediction of fatigue behavior of turbine components. Fatigue damage is located in areas where cyclic stress and strain amplitudes are highest. Thus, geometrical notches associated with stress/strain concentrations and stress/strain gradients appear to be the most important sites for fatigue crack initiation. The paper addresses a nonlocal concept for cyclic life prediction of notched components. Contrary to various local approaches in the field, the proposed method explicitly accounts for stress and strain gradients associated with notches arising from grooves, cooling holes, fillets, and other design features with stress raising effect. As a result, empirical analytical expressions for considering either strain or stress gradients for cyclic life prediction are obtained. The method has been developed from cyclic test data on smooth and notched specimens made of a ferritic 1.5CrNiMo rotor steel. The analytical formulations obtained have then been applied to test data on the nickel base superalloy MAR-M247 CC showing a good agreement between prediction and measurement. Moreover, the proposed nonlocal lifing concept has been validated by component tests on turbine blade firtrees. The predicted number of cycles to failure correlates well with the experimental results showing the applicability of the proposed method to complex engineering designs. [DOI: 10.1115/1.2747642]

Introduction

Reliable and safe operation of modern heavy duty gas turbines at increasingly higher loads is closely related to improvements in the predictability of a component's lifetime. The following elements contribute to reliable lifetime prediction:

1. robust models for finite element analysis (FEA) with suitable constitutive features and validated thermal and mechanical boundary conditions for evaluating the state of loading in the component;
2. lifetime prediction procedures for predicting the component's lifetime as a function of the load conditions;
3. sensitivity analyses and probabilistic analyses for assessing the robustness of the component's design; and
4. field experience and component tests for validating the applied computational models.

The paper addresses the second item. In particular, a nonlocal concept for cyclic life prediction of notches is proposed. As a result of the investigation, general analytical equations are presented that account for the cyclic life increase of notched components as a function of the (nonlocal) strain or stress gradient. Moreover, the validation of the concept by the results of component tests is shown.

Although the development has been motivated by the fatigue life assessment of firtree designs for rotor-blade connections in gas turbines, the methodology is general and independent of specific design features.

Effect of Stress and Strain Gradients on Fatigue Strength. It is well established that stress and strain gradients increase the fatigue strength. Comparing a notched and a smooth sample with the same maximum strain or stress amplitude, (Fig. 1), the fatigue life in the notched sample is higher and the enhancement of lifetime depends on the magnitude of the notch strain and stress gradients. There are different aspects that explain this effect [1]:

- Fatigue crack initiation is controlled by the average stress that acts over an area of small but finite size (fatigue process zone) rather than by the peak stress on the notch surface;
- Crack initiation requires a combination of high stress and crack initiation sites. In a notched volume the probability of having crack initiation sites at sufficiently high stress levels is smaller than in a smooth volume (weakest link effect);
- Microscopic crack initiation may start early but crack growth to a dominant crack is slower in a region of rapidly decreasing stress; and
- Yielding at notches causes the actual stress amplitude to be lower than the linear-elastic stress.

More details on general aspects of notch gradient effects in fatigue can be found in Refs. [1–4].

Outline of the Nonlocal Cyclic Life Prediction Approach. Most classic procedures of cyclic life prediction of notched components are based on one of the following two approaches: (a) the component's local stress and strain amplitudes—either peak values or average values in the fatigue process zone—are compared to material data solely derived from cyclic tests of smooth samples [5], and (b) the theoretical linear-elastic notch factors of stress and strain are evaluated and a suitable notch sensitivity concept is used [6–8]. Both methods have inherent disadvantages when applied to engineering problems. While the local approach (a) gives too many conservative results for high stress and strain gradients, the notch sensitivity concept (b) requires knowledge on theoretical notch factors and net stress levels and its application is therefore limited to handbook design features.

Therefore in this paper an alternative concept to fatigue life assessment in notches is followed. The proposed approach is referred to as the nonlocal concept since gradients of stress and strain are explicitly taken into account in addition to the local magnitudes of stress, strain, and temperature. As in classic fatigue

Contributed by the International Gas Turbine Institute of ASME for publication in the JOURNAL OF ENGINEERING FOR GAS TURBINES AND POWER. Manuscript received April 27, 2007; final manuscript received May 7, 2007; published online January 9, 2008. Review conducted by Dilip R Ballal. Paper presented at the ASME Turbo Expo 2007: Land, Sea and Air (GT2007), Montreal, Quebec, Canada, May 14–17, 2007, Paper No. GT2007-27448.

Copyright © 2008 by ASME

Downloaded 02 Jun 2010 to 171.66.16.107. Redistribution subject to ASME license or copyright; see http://www.asme.org/terms/Terms_Use.cfm

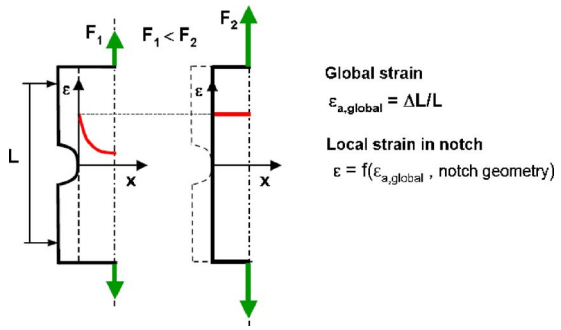

Fig. 1 Strain distribution in notched and smooth specimens

assessment we thereby distinguish between strain and stress approaches, i.e., the number of load cycles to failure N_0 is affected by the temperature (either the maximum temperature of the load cycles or an appropriate damage temperature), the material and either the strain range or the stress range

$$N_0 = N_0(\Delta\varepsilon_{ij}, T, \text{material}) \tag{1}$$

$$N_0 = N_0(\Delta\sigma_{ij}, T, \text{material}) \tag{2}$$

In addition to local strain and stress approaches, the proposed nonlocal concept uses analytical functions to describe the fatigue life enhancement N/N_0, where N_0 denotes the cycles to failure derived by the local concept (i.e., without considering the load gradient), whereas N describes the number of load cycles predicted with the nonlocal concept (i.e., by considering the load gradient).

The life enhancement functions have empirically been derived from comparing test results of smooth and notched samples. In the strain approach the life ratio N/N_0 depends on the strain gradient $\nabla\varepsilon$ ahead of the notch and the local strain amplitude ε_a on the notch surface, whereas in the stress approach the stress gradient $\nabla\sigma$ and the local stress amplitude σ_a are applied, i.e.,

$$\frac{N}{N_0} = f_\varepsilon(\nabla\varepsilon, \varepsilon_a) \tag{3}$$

$$\frac{N}{N_0} = f_\sigma(\nabla\sigma, \sigma_a) \tag{4}$$

The application of the nonlocal concept requires the computation of the peak load (either strain or stress) and the corresponding load gradient. In the case where no FEA results with sufficient mesh density in the critical areas are available, analytical or approximate solutions for simple notch geometries and load conditions might be useful. Solutions for stress gradients for various notch geometries have been investigated by Filippini [9], Xu et al. [10], and Glinka and Newport [11] among others. Stress concentration formulas can be found in the classical textbook of Peterson [6] but also in recent publications as, e.g., in Noda and Takase [12].

The type of approach proposed in this paper, i.e., considering the load gradients in cyclic life assessment, has been used by other authors before. Among them are Siebel and Stieler [13] who suggested a notch sensitivity approach which relates the fatigue notch factor to the notch factor of the linear-elastic solution, the relative stress gradient, and a temperature dependent material parameter. Moreover, Qylafku et al. [14] propose a method to estimate the fatigue notch factor by considering the stress gradient over the fatigue process zone. Naik et al. [15] have applied a critical plane approach using the Findley parameter and they considered the gradient of the Findley parameter over a critical distance at the notch tip. Note that the above mentioned studies address cyclic loading at notches under high-frequency and low-load amplitude leading to high cycle fatigue (HCF). In this case, the load is small enough for an elastic response of the material which exclusively allows stress gradients to be considered. In contrast, the presented paper considers test results of low-frequency and high-load amplitude conditions as typical for low-cycle fatigue (LCF) and thermo-mechanical fatigue (TMF) problems.

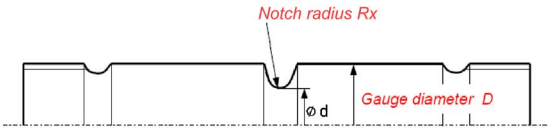

Fig. 2 Example of notched specimen

LCF Tests on Notched Samples

The proposed nonlocal lifetime procedure is based on cyclic tests of notched samples. The scope of the investigation included different ferritic rotor steels as well as nickel base superalloys for turbine blade applications. The testing of the ferritic rotor steel samples was performed under $R_\varepsilon = -1$ strain-controlled conditions as typical for the stabilized load cycle in rotor components. The nickel base superalloys were subjected to $R_\sigma = 0$ stress-controlled load conditions as they occur in turbine blade firtree designs. Isothermal tests at room temperature (RT) as well as at $T = 300°C$ and 400°C were performed.

Figure 2 shows the geometry of a cylindrical specimen with a circumferential notch. In addition, specimens with V notches have been used. To match typical component's stress and strain gradients and different load levels an optimization of the notch geometry and the loading was required. Different stress and strain gradients are produced by suitable combinations of the notch radius Rx, the gauge diameter D, and the axial load, (Fig. 2). In particular, the ratio D/d, together with the axial load, controls the net stress and strain levels in the notch section, whereas the radius Rx influences the peak stress and strain in the notch. The test matrix included specimens with notch geometries in the range of $1.2 \leqslant D/d \leqslant 2.0$ and $2.6 \leqslant d/Rx \leqslant 30.0$ corresponding to stress gradients between 700 MPa/mm and 3500 MPa/mm and mechanical strain gradients between 0.2%/mm and 4%/mm. The respective linear-elastic stress concentration factors in the specimens covered the range of $1.5 \leqslant k_t \leqslant 3.3$.

Development of a Failure Criterion

Testing of notched specimens requires a sophisticated and well-defined failure criterion. A total life criterion, i.e., where the lifetime is exhausted after the rupture of the specimen, considers both fatigue crack initiation and crack growth. For notched samples the phase of crack propagation may dominate the total life and under strain-controlled test conditions the crack might even arrest. As a consequence, the number of load cycles depends on the specimen dimensions when using a total life criterion. Thus a reliable correlation of the specimen's test results to the component's life is difficult. Therefore, in this investigation a *crack initiation criterion* for characterizing the failure was applied.

Measuring crack initiation in notched samples requires sophisticated experimental techniques. On the one hand, crack initiation inside the notch can hardly be monitored by visual or optical methods. On the other hand, a measurable increase of the total specimen elongation (in stress-controlled testing) or a decrease of stiffness (in strain-controlled testing) may already correlate with a significant crack size.

Potential Drop Monitoring. In addition to the above methods, potential drop monitoring of fatigue crack initiation and crack growth was applied. The potential drop method exploits the increase of electric resistance R with progressing damage. To this end, a constant electric current I was fed into the specimen and the voltage U (the potential drop) between two points located on both

Downloaded 02 Jun 2010 to 171.66.16.107. Redistribution subject to ASME license or copyright; see http://www.asme.org/terms/Terms_Use.cfm

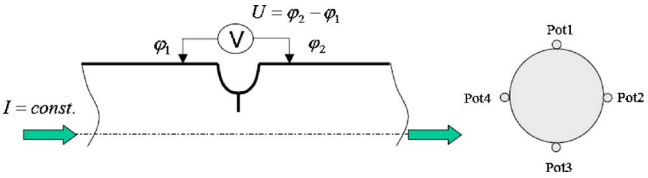

Fig. 3 Principle of potential drop monitoring

Field equations		Boundary conditions	
Potential law	$\nabla^2 U = 0$	1st kind	$U = \bar{U}$
Flow law	$\mathbf{E} = -\nabla U$	2nd kind	$-\mathbf{n}\cdot\nabla U = \bar{E}_n$
Constitutive equation	$\mathbf{j} = \boldsymbol{\kappa}\cdot\mathbf{E}$ (Ohm's law)		$-\mathbf{n}\cdot\boldsymbol{\kappa}\cdot\nabla U = \bar{j}_n$

Fig. 5 The electrostatic field problem

sides of the notch was measured. The change of the normalized electric resistance, $(R-R_0)/R_0$, and the increase of the corresponding normalized potential drop, $(U-U_0)/U_0$, go along with the increase of the normalized cracked area A_{cr}/A_0 in the notch section

$$\frac{R-R_0}{R_0} = \frac{U-U_0}{U_0} = f(A_{cr}/A_0) \tag{5}$$

Thereby, the subscript 0 refers to the undamaged condition, i.e., A_0 is the cross-sectional area before cracking, A_{cr} is the cracked area, and $f(.)$ denotes a calibration function which depends on the geometry of the specimen and the positions of the potential drop probes (Fig. 3).

The low electric resistance of the specimen demands a high-capacity signal amplifier to obtain measurable signals. The use of a direct current of $I=10$ A, for example, produces a potential difference of about 100 μV. Thus a measurement precision of at least ± 0.1 μV is required to monitor the change of the electric potential. For reducing drift effects, a fully reversed (square wave) direct current was used. Moreover, four pairs of potential probes were welded onto each specimen to consider nonsymmetric crack initiation (Fig, 3). The distance between the probes and the notch was minimized as much as possible in order to make the potential drop sufficiently sensitive to the propagation of the crack surface.

Potential drop measurements for monitoring crack initiation and crack growth have been used by many authors before. Examples can be found in Härkegard et al. [16], Coffin [17], and Gangloff [18] among others.

Figure 4 shows a typical example of potential drop measurements. While the first 50–70% of cyclic life can be related to the crack initiation phase, in the remaining part the increased slope of the normalized potential drop indicates the growth of a macroscopic crack surface.

For simple specimen geometries and crack shapes analytical solutions are available for correlating potential drop and crack size, see e.g., Johnson [19]. For more sophisticated notched samples as considered here, the calibration function $f(.)$ in Eq. (5) can be established either experimentally by using artificial eroded cracks of certain length or computationally by solving the electrostatic field problem with finite element analysis (FEA) or boundary element methods. Note that the normalized potential drop $(U-U_0)/U_0$ is independent of the electrical conductivity $\boldsymbol{\kappa}$ of the material as long as the probes are exposed to about the same temperature or the temperature dependence of $\boldsymbol{\kappa}$ can be neglected. Thus, a low–cost material with different electrical conductivity can be used for experimental calibration purpose.

For the study presented the *computational* calibration method was preferred because of the variety of notched samples with significant geometrical variations. Moreover, sensitivity studies for optimizing the potential probe positions have been performed conveniently in a computational manner. Figure 5 summarizes the governing equations of the electrostatic field problem and Fig. 6 shows the boundary conditions of the analyses. Note that the electric current results from integrating the electric current density over the flow through surface, i.e., $I=\int_A \mathbf{j}\cdot d\mathbf{A}$. At a sufficient distance from the notch, however, a constant electric current density of $j=I/A$ can be assumed.

Figure 7 shows potential drop calibration curves produced by FEA with parameterized geometry models. The following procedure can be applied to determine the end of life of the test specimens:

1. Monitor the potential drop and stop the testing when the signals reach an appropriate limit, (Fig. 4).
2. Determine the crack shape by heat tinting and subsequent breaking up of the specimen under HCF loading, (Fig. 8).

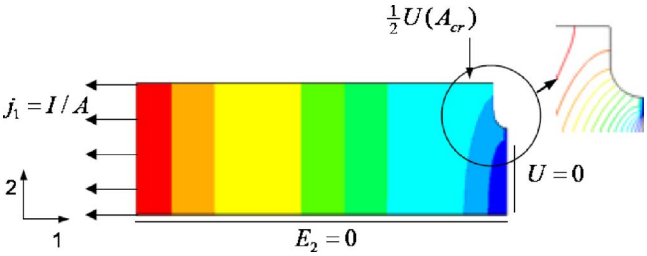

Fig. 6 Boundary conditions for electrostatic field calculations

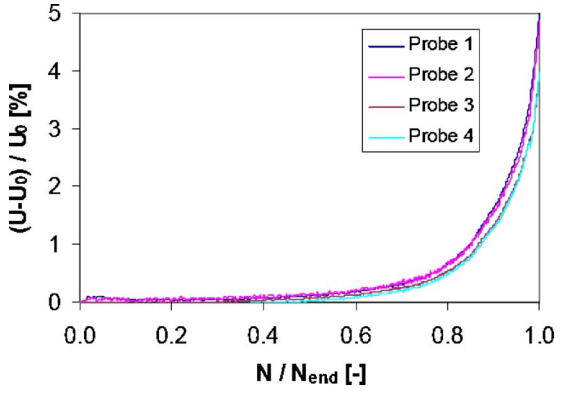

Fig. 4 Example of potential drop measurements

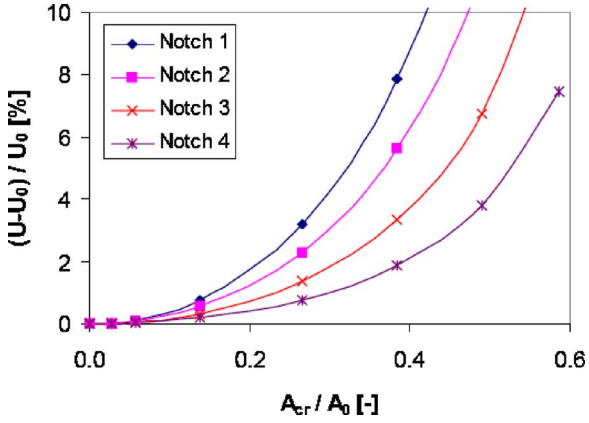

Fig. 7 Example of potential drop calibration curves

Downloaded 02 Jun 2010 to 171.66.16.107. Redistribution subject to ASME license or copyright; see http://www.asme.org/terms/Terms_Use.cfm

Fig. 8 LCF crack shape after heat tinting

3. Define a crack size limit, e.g., 0.5 mm maximum crack depth, and determine the corresponding normalized crack surface A_{cr}/A_0.
4. Obtain the potential drop corresponding to the A_{cr}/A_0 ratio by using the calibration curve for the considered specimen geometry, (Fig. 7).
5. Apply the potential drop level in Fig. 4 to evaluate the corresponding number of load cycles.

Nonlocal Strain Approach for a 1.5CrNiMo Rotor Steel

The flow chart in Fig. 9 shows the procedure for correlating LCF data at notches to those of smooth samples. The proposed method requires three inputs: (1) cyclic test data on smooth samples; (2) cyclic test data on notched samples; and (3) the relations between global and local strain amplitudes, $\varepsilon_{a,\text{global}}$ and ε_a, respectively, as well as between local strain amplitudes and local strain gradients, ε_a and $\nabla\varepsilon$, respectively.

The cyclic tests on smooth samples are required for establishing the baseline of smooth LCF data. If a comprehensive database is already available, a few additional tests are recommended to confirm that the cyclic behavior of the investigated melt is sufficiently represented by the database reference. The cyclic tests on notched samples generate the basic data for the proposed lifing concept. Data from different notch geometries implying different strain gradients are required to identify the effect of the gradient on fatigue lifetime. Finally, in order to keep the method independent of geometry, the global strain amplitudes applied in the cyclic tests have to be related to the local strain amplitudes and the strain gradients in the notch using FEA. Since moderate global strain amplitudes already produce notch loadings above yield, the elastic-plastic constitutive behavior needs to be accounted for. This can be done either by using approximate methods for localized plasticity (for example the Neuber rule) or, as we preferred, by the application of a cyclic elastic-plastic constitutive model. Using the cyclic elastic-plastic model, the computation of ten load cycles was sufficient to evaluate the stabilized stress-strain hysteresis of the material.

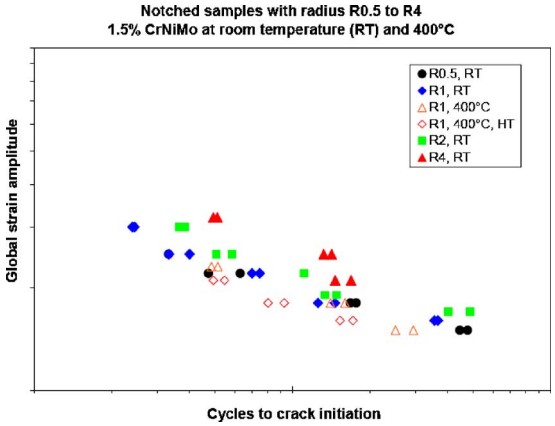

Fig. 10 Cycles to crack initiation versus global strain amplitudes

Figure 10 shows the measured cycles to crack initiation of 1.5CrNiMo rotor steel samples as a function of the global strain amplitude. Using FEA the global strain amplitude can be related to the local strain amplitude in the notch. Thus the cycles to crack initiation in Fig. 10 can be associated to the local strain amplitude in the notch, (Fig. 11). Note that for each notch radius, the relation between the local strain and the fatigue life can be approximated linearly on the log-log scale. Motivated by this observation we applied the Coffin–Manson type relation

$$\frac{N}{N_0} = C(Rx) \cdot \varepsilon_a^{n(Rx)} \tag{6}$$

to express the ratio of cyclic life of notched and smooth samples, N/N_0, as a function of the local strain amplitude ε_a and the Coffin–Manson parameters $C(Rx)$ and $n(Rx)$. Note that, for the time being, the Coffin–Manson parameters depend on the notch radius Rx and thus implicitly on the strain gradient in the notch.

The actual fitting of material data is now performed in three steps: First, the notch radii are related to the strain gradients using FEA. Thereby it was noticed that even for elastic-plastic material

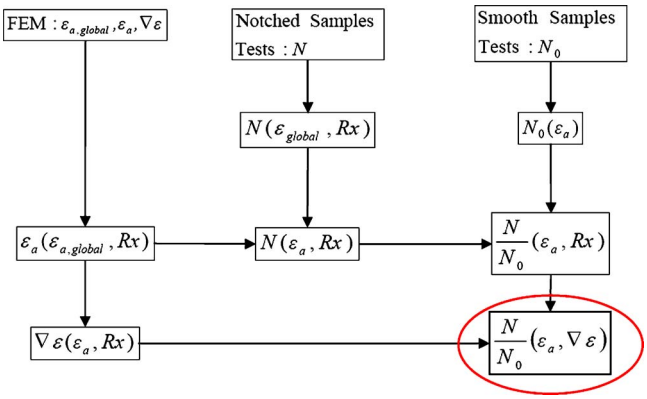

Fig. 9 Strain-based approach for cyclic life assessment at notches

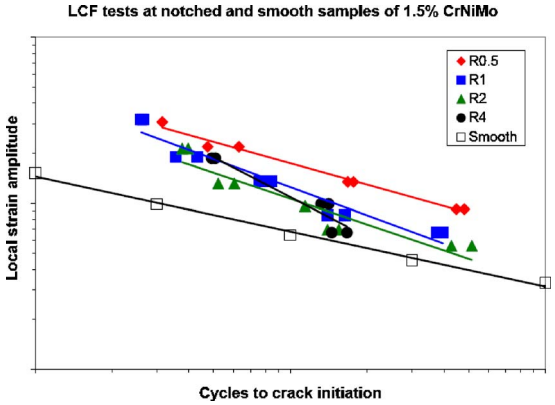

Fig. 11 Cycles to crack initiation versus local strain amplitudes

Downloaded 02 Jun 2010 to 171.66.16.107. Redistribution subject to ASME license or copyright; see http://www.asme.org/terms/Terms_Use.cfm

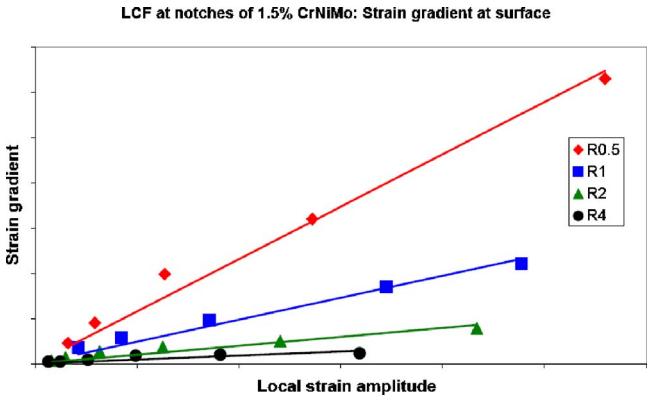

Fig. 12 Linear fit of local strain amplitudes and strain gradients

behavior the relation between the local strain amplitude ε_a and the strain gradient $\nabla\varepsilon$ can be approximated by the linear relation

$$\nabla\varepsilon = a(Rx) \cdot \varepsilon_a \tag{7}$$

where the factor $a(Rx)$ depends on the notch radius (Fig. 12). According to Eq. (7), the radius determines the relative strain gradient $\chi_\varepsilon = \nabla\varepsilon/\varepsilon_a$. Thus, instead of the notch radii Rx, the Coffin–Manson parameters in Eq. (6) can be expressed in terms of χ_ε. In the second step, for each of the notch radii, Eqs. (6) and (7) were determined separately using the test data in Figs. 11 and 12. Finally, the Coffin–Manson parameters for each radius were applied for fitting polynomial functions of the relative strain gradient. Thereby we noticed that for the coefficient C a linear function of the form $g(\chi_\varepsilon) = 1 + d\chi_\varepsilon$ is sufficient, whereas the exponent n, which has a much larger influence on cyclic life, requires a quadratic function of the relative strain gradient to achieve sufficient accuracy. The final expression reads

$$\frac{N}{N_0} = (1 + d\chi_\varepsilon) \cdot \varepsilon_a^{f(\chi_\varepsilon)} \tag{8}$$

with $\chi_\varepsilon = \nabla\varepsilon/\varepsilon_a$ and $f(\chi_\varepsilon) = a\chi_\varepsilon^2 + b\chi_\varepsilon$.

For the rotor steels investigated, the constant d is between 2 and 5. The exponent $f(\chi_\varepsilon)$ approaches zero for zero strain gradients leading to

$$\frac{N}{N_0}(\chi_\varepsilon = 0) = 1 \tag{9}$$

The maximum value of $f(\chi_\varepsilon)$ is approximately 2 for the performed LCF tests at notches with high relative strain gradients.

Figure 13 compares the raw data with the prediction of Eq. (8). Because a conservative fitting approach was used on purpose, the measured lifetime for six samples is significantly higher than the predicted data. Altogether, the theoretical prediction reflects the experimental data within the typical scatter of fatigue.

Nonlocal Stress Approach for the Nickel Base Superalloy MAR-M247 CC

The strain-based approach according to Eq. (8) is transferred to the stress-based approach as follows

$$\frac{N}{N_0} = (1 + d'\chi_\sigma) \cdot \varepsilon_a^{h(\chi_\sigma)} \tag{10}$$

with

$$\varepsilon_a = \frac{\sigma_a^2}{E \cdot R_{p0.2}}, \quad \chi_\sigma = \frac{\nabla\sigma}{\sigma_a} \tag{11}$$

and the polynomial function fit of the exponent

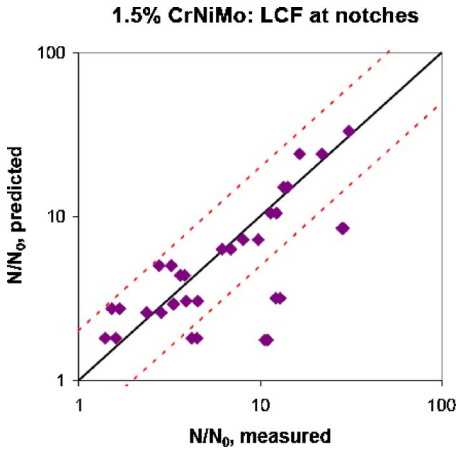

Fig. 13 Comparison of raw data and prediction for the 1.5%CrNiMo rotor steel

$$h(\chi_\sigma) = a'\chi_\sigma^2 + b'\chi_\sigma \tag{12}$$

The substitution of ε_a in Eq. (10) according to Eq. (11) is based on the strain energy balance for ideally plastic material.

The above equations have been used to describe the results of stress-controlled LCF tests of notched samples made of MAR-M247 CC. Similar to for rotor steels, Eq. (10) fits the measured test data well within the typical scatter of a factor of 2 for cyclic life assessment (Fig. 14). Based on the results we concluded that the type of nonlocal strain and stress approach according to Eqs. (8) and (10), respectively, can be applied to fatigue life prediction for both ferritic rotor steels and nickel base superalloys.

Validation of the Method

Apart from field experience the new lifing method was validated by two identical component tests on a rotor-blade firtree design (Fig. 15). This section addresses various aspects of the component tests including the component test setup, the mechanical analysis, the potential drop calibration, as well as a comparison of the predicted lifetime with the measured number of load cycles to failure. Thereby attention is paid to the variety of investigations rather than going into detail on the performed analyses.

Component Test Setup. The component tests were performed on a firtree of a turbine blade made of MAR-M247 CC and a corresponding support piece made of a 1.5CrNiMo rotor steel. The components were subjected to a stress-controlled cyclic load-

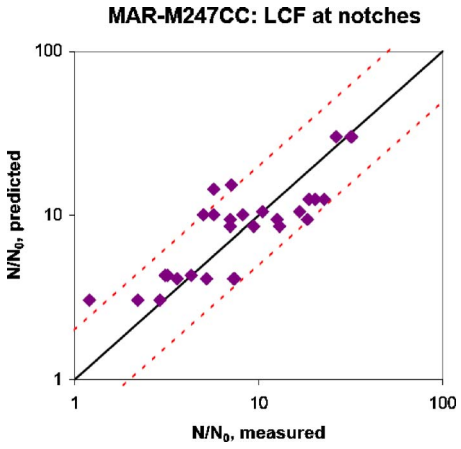

Fig. 14 Comparison of raw data and prediction for MAR-M247 CC

Downloaded 02 Jun 2010 to 171.66.16.107. Redistribution subject to ASME license or copyright; see http://www.asme.org/terms/Terms_Use.cfm

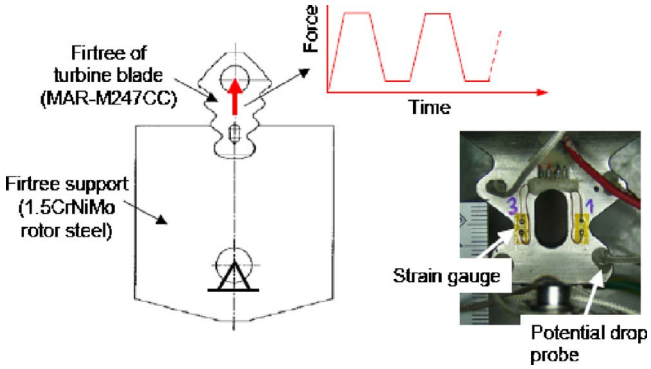

Fig. 15 Component test setup with strain gauges and potential drop probes

ing of constant amplitude (Fig. 15). A load ratio of $R_\sigma=0.05$ was applied to ensure defined contact conditions during the testing. In order to produce first crack initiation in the turbine material, the thickness of the turbine firtree was chosen much smaller than the thickness of the corresponding support piece. Moreover, the cross section of the turbine firtree was reduced by a slot to match peak stress and stress gradient with those in last stage turbine blades.

Strain gauges were applied at the turbine notches for determining the symmetry of loading during the testing. Moreover, four pairs of potential drop probes were welded onto the firtree for monitoring crack initiation and crack growth (Fig. 15).

Mechanical Analyses. Prior to testing, FEA was used to determine the state of loading in the firtree. Nonlinear material constitutive behavior and contact conditions on the blade-support interfaces were applied. Because of symmetry of geometry and loading, the FEA involved only one-quarter of the component test setup together with appropriate symmetry boundary conditions (Fig. 16). A cyclic elastic-plastic material model based on Ziegler's kinematic hardening law together with a recovery term was applied for the analysis (for details see ABAQUS [20]).

Sensitivity studies on contact modeling showed that the friction coefficient significantly influences the stress field around the notch

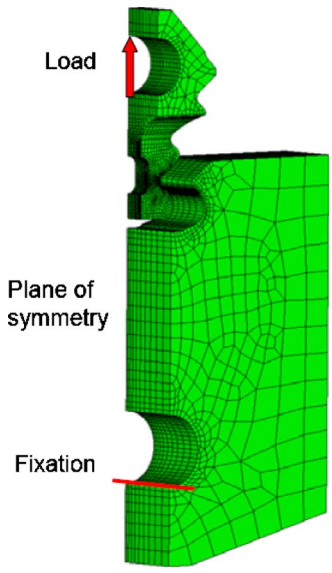

Fig. 16 FEA model of the component test setup

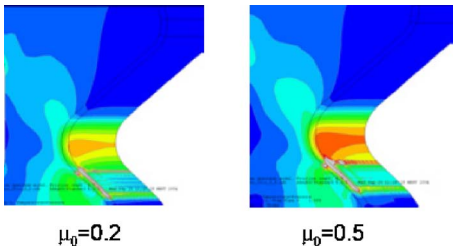

Fig. 17 Effect of friction coefficient on maximum principal stress distribution in the notch

(Fig. 17). Therefore, much attention has been paid to verify the friction coefficient under cyclic stress conditions. In this context, digital image correlation techniques based on speckle pattern shearing interferometry described in Steinchen et al. [21,22] were applied for measuring the strain distribution at the notch. A comparison with FEA results using different contact conditions showed that the friction coefficient of $\mu_0=0.2$ best matches the interferometric strain measurements.

Another study concerning the mechanical analysis addressed the required FEA mesh quality at the notch for evaluating the peak stress and the stress gradient. Of course, a higher mesh density always improves the quality of stress approximation; however, it may exorbitantly increase the size of the FEA model, especially when the complete turbine blade and the corresponding rotor section are considered. The investigation showed that hexagonal elements with quadratic shape functions are preferred for meshing and the mesh size in the direction of the stress gradient should be at least 20% of the notch radius.

Electric Field Analysis. Computational electric field analyses have been used to investigate the sensitivity of the potential drop signals (Fig. 18). Thereby different crack scenarios have been considered. Among them are cases with crack initiation on one lobe of the firtree as well as symmetric crack initiation on opposite firtree lobes (Fig. 19).

Results of the Component Tests. Figure 20 shows the results of the component tests together with the mean data design curves of the classical local concept (without considering the load gradient) and the proposed nonlocal concept (considering the load gradient). The stress gradient in the notch reached 1130 MPa/mm. The number of load cycles is related to an increase of the potential drop signal of 5% corresponding to a crack depth of about 1 mm. Note that a load ratio of $R_\sigma=0.05$ was applied to ensure defined contact conditions. Therefore both the peak stress and the (slightly lower) stress range were put into the diagram. Moreover, the strain gauge measurement of the component test 1 indicated a nonsymmetry of loading by 10%. Therefore, the peak stress of the first component test has been multiplied by a factor of 1.1. After the test, the nonsymmetry of loading could be confirmed by nonsymmetric contact marks (Fig. 21).

The results of the validation component tests shown in Fig. 20 clearly demonstrate the improvement in notch fatigue prediction when using the proposed nonlocal concept.

Conclusions

The presented work addresses a nonlocal concept to fatigue life prediction of notched components. Contrary to most work in the

Downloaded 02 Jun 2010 to 171.66.16.107. Redistribution subject to ASME license or copyright; see http://www.asme.org/terms/Terms_Use.cfm

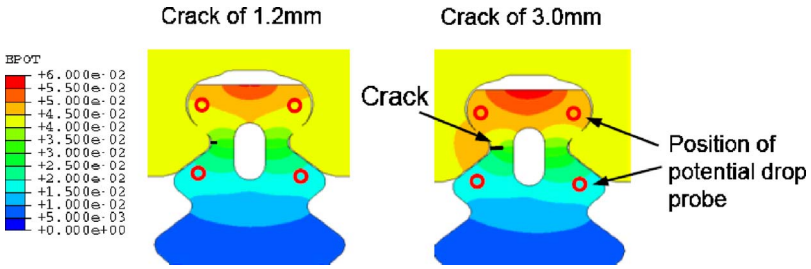

Fig. 18 Examples for the distribution of the electric potential for a crack on one lobe

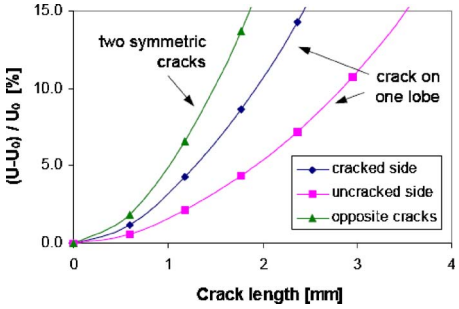

Fig. 19 Examples for potential drop calibration curves

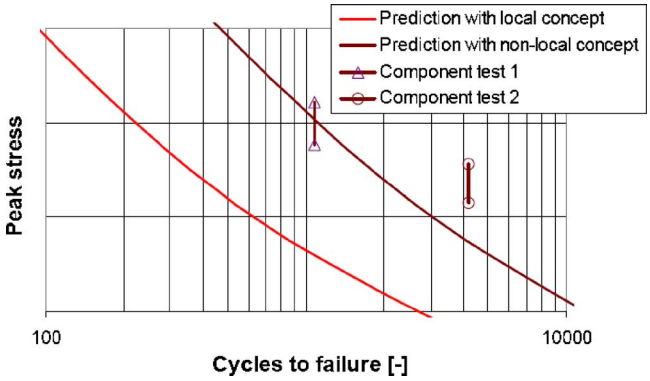

Fig. 20 Results of component test

field, the approach accounts explicitly for the magnitude of stress and strain gradients. The concept is general and independent of specific design features. In regions without stress and strain gradients the approach reproduces the results of the classical local lifing approaches. The investigations allow the following conclusions:

- Stress and strain gradients have a significant influence on the fatigue behavior. The higher the load gradient the larger the increase in cyclic life compared to data on smooth samples;
- The increase of fatigue life due to the load gradient can be described by empirical analytical equations that depend on load and load gradient;
- The same fatigue life enhancement function which was derived from test results on a 1.5CrNiMo rotor steel could be used for predicting the lifetime increase of the Nickel base superalloy MAR-M247 CC due to load gradients;
- Component tests on a blade-rotor firtree design showed the reliable prediction of the test results when using the proposed nonlocal cyclic life prediction concept; and
- The presented approach will be applied to Alstom gas turbines for further improved and even more precise lifetime predictions.

Future investigations should address further classes of metallic materials in order to confirm the general applicability of the method. Moreover, the effect of temperature should be analyzed in more detail.

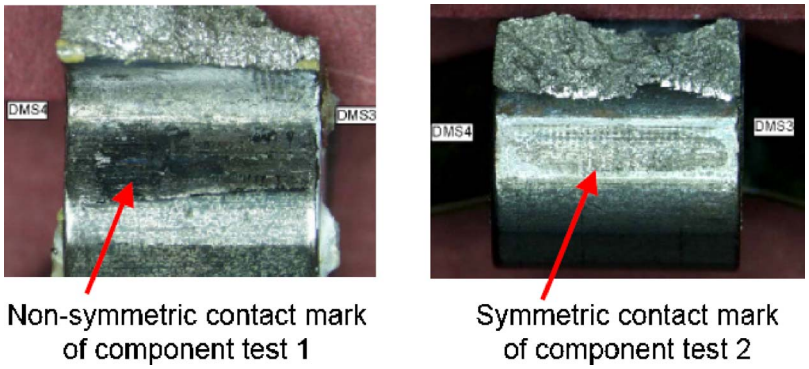

Fig. 21 Contact faces after testing

Downloaded 02 Jun 2010 to 171.66.16.107. Redistribution subject to ASME license or copyright; see http://www.asme.org/terms/Terms_Use.cfm

Acknowledgment

The authors are grateful to Dipl.-Ing. Markus Ernsberger, Dr.-Ing. Ulrich Krasselt, and Dr.-Ing. Klaus Stärk from the Alstom Material Laboratory in Baden, Switzerland for performing the tests. The authors also thank Alstom for permission to publish.

Nomenclature

FEA = finite element analysis
LCF = low cycle fatigue
HCF = high cycle fatigue
TMF = thermo-mechanical fatigue
RT = room temperature
a, b, d = coefficients of the nonlocal strain approach
a', b', d' = coefficients of the nonlocal stress approach
A_{cr} = cracked area the notch section (mm^2)
A_0 = cross-sectional area of notch section (mm^2)
E = Young's modulus (GPa)
$\mathbf{E}$ = vector of electric field strength (V/m)
I = electric current (A)
$\mathbf{j}$ = vector of electric current density (A/m^2)
$\mathbf{n}$ = surface normal vector
N = cycles to crack initiation
N_0 = cycles to crack initiation of smooth samples
R = electric resistance of cracked specimen (Ω)
R_0 = electric resistance of noncracked specimen (Ω)
R_ε = strain ratio; $R_\varepsilon = \varepsilon_{min}/\varepsilon_{max}$
R_σ = stress ratio; $R_\sigma = \sigma_{min}/\sigma_{max}$
$R_{p0.2}$ = yield limit (MPa)
Rx = notch radius of magnitude x (mm)
T = metal temperature (°C)
U = potential drop in the cracked specimen (V)
U_0 = potential drop in the noncracked specimen (V)
ε_a = local strain amplitude at the notch
$\varepsilon_{a,global}$ = global strain amplitude
$\nabla\varepsilon$ = local strain gradient (1/mm)
$\boldsymbol{\kappa}$ = electrical conductivity (A/V)
σ_a = local stress amplitude (MPa)
$\nabla\sigma$ = local stress gradient (MPa/mm)
φ_1, φ_2 = electric potential at position 1 and 2 (V)
χ_ε = relative local strain gradient (1/mm); $\chi_\varepsilon = \nabla\varepsilon/\varepsilon_a$
χ_σ = relative local stress gradient (1/mm); $\chi_\sigma = \nabla\sigma/\sigma_a$
∇ = Nabla operator (1/mm)
∇^2 = Laplacian operator ($1/mm^2$)

Throughout the paper the term "strain" denotes the mechanical strain, i.e., the difference between the total strain and the thermal strain.

References

[1] Dowling, N. E., 1999, *Mechanical Behavior of Materials*, Prentice-Hall, Englewood Cliffs, NJ.
[2] Suresh, S., 1991, *Fatigue of Materials*, Cambridge Solid State Science Series, Cambridge University Press, Cambridge, UK.
[3] Makkonen, M., 2003, "Notch Size Effects in the Fatigue Limit of Steels," Int. J. Fatigue, **25**, pp. 17–26.
[4] Ciavarella, M., and Meneghetti, G., 2004, "On Fatigue Limit in the Presence of Notches: Classical vs. Recent Unified Formulations," Int. J. Fatigue, **26**, pp. 289–298.
[5] Sehitoglu, H., 1983, "Fatigue Life Prediction of Notched Members Based on Local Strain and Elastic-plastic Fracture Mechanics Concepts," Eng. Fract. Mech., **18**, pp. 609–621.
[6] Peterson, R. E., 1974, *Stress Concentration Factors*, Wiley, New York.
[7] Taylor, D., and O'Donnell, M., 1994, "Notch Geometry Effects in Fatigue: A Conservative Design Approach," Eng. Failure Anal., **1**, pp. 275–287.
[8] Bellett, D., Taylor, D., Marco, S., Mazzeo, E., Guillois, J., and Pircher, T., 2005, "The Fatigue Behavior of Three-dimensional Stress Concentrations," Int. J. Fatigue, **27**, pp. 207–221.
[9] Filippini, M., 2000, "Stress Gradient Calculation at Notches," Int. J. Fatigue, **22**, pp. 397–409.
[10] Xu, R. X., Thompson, J. C., and Topper, T. H., 1995, "Practical Stress Expressions for Stress Concentration Regions," Fatigue Fract. Eng. Mater. Struct., **18**, pp. 885–895.
[11] Glinka, G., and Newport, A., 1987, "Universal Features of Elastic Notch-Tip Stress Fields," Int. J. Fatigue, **8**, pp. 235–237.
[12] Noda, N.-A., and Takase, Y., 2006, "Stress Concentration Formula Useful for all Notch Shape in a Round Bar," Int. J. Fatigue, **28**, pp. 151–163.
[13] Siebel, E., and Stieler, M., 1955, "Ungleichförmige Spannungsverteilung bei schwingender Beanspruchung," VDI Z. (1857-1968), **97**(5), pp. 121–126.
[14] Qylafku, G., Azari, Z., Kadi, N., Gjonaj, M., and Pluvinage, G., 1999, "Application of a New Model Proposal for Fatigue Life Prediction on Notches and Key-Seats," Int. J. Fatigue, **21**, pp. 753–760.
[15] Naik, R. A., Lanning, B. D., Nicholas, T., and Kallmeyer, A. R., 2005, "A Critical Plane Gradient Approach for the Prediction of Notched HCF Life," Int. J. Fatigue, **27**, pp. 481–492.
[16] Härkegard, G., Denk, J., and Stärk, K., 2005, "Growth of Naturally Initiated Fatigue Cracks in Ferritic Gas Turbine Rotor Steels," Int. J. Fatigue, **27**, pp. 715–726.
[17] Coffin, L. F., 1987, "Notch Fatigue Crack Initiation Studies in a High Strength Nickel Base Superalloy," Eng. Fract. Mech., **28**, pp. 485–503.
[18] Gangloff, R. P., 1981, "Electrical Potential Monitoring of Crack Formation and Subcritical Crack Growth for Small Defects," Fatigue Fract. Eng. Mater. Struct., **4**, pp. 15–33.
[19] Johnson, H. H., 1965, "Calibrating the Electric Potential Method for Studying Slow Crack Growth," Mater. Res. Stand., **5**, pp. 442–445.
[20] ABAQUS, 2003, *User's Manual*, Version 6.4, Vol. III, Hibbitt, Karlsson, & Sorenson, Inc.
[21] Steinchen, W., Yang, L. X., Kupfer, G., and Mäckel, P., 1998, "Strain Analysis by Digital Shearography: Potentials, Limitations and Demonstrations," J. Strain Anal. Eng. Des., **33**, pp. 171–182.
[22] Steinchen, W., Kupfer, G., Mäckel, P., and Vössing, F., 1999, "Determination of Strain Distributions by Means of Digital Shearography," Measurement, **26**, pp. 79–90.

Downloaded 02 Jun 2010 to 171.66.16.107. Redistribution subject to ASME license or copyright; see http://www.asme.org/terms/Terms_Use.cfm

Yahya Dogu[1]
Department of Mechanical Engineering,
Kirikkale University,
Yahsihan, Kirikkale 71450, Turkey
e-mail: ydogu@kku.edu.tr

Mahmut F. Aksit
Faculty of Engineering and Natural Sciences,
Sabanci University,
Tuzla, Istanbul 34956, Turkey
e-mail: aksit@sabanciuniv.edu

Mehmet Demiroglu
Department of Mechanical Engineering,
Rensselaer Polytechnic Institute,
Troy, NY 12180
e-mail: mehmet@alum.rpi.edu

Osman Saim Dinc
Calik Enerji A.S.,
Ak Plaza, Yasam Cad, No. 7,
Sogutozu, Ankara 06510, Turkey
e-mail: saim.dinc@calikenerji.com

Evaluation of Flow Behavior for Clearance Brush Seals

The industrial applications of brush seals have been increasing due to their superior sealing performance. Advances in the understanding of seal behavior have been pushing the design limits to higher-pressure load, temperature, surface speed, and rotor excursion levels. The highest sealing performance can be achieved when the bristle pack maintains contact with the rotor surface. However, due to many design and operational constraints, most seals operate with some clearance. This operating clearance cannot be avoided due to rotor runouts, transient operating conditions, or excessive bristle wear. In some applications, a minimum initial clearance is required to ensure a certain amount of flow rate for component cooling or purge flow. Typically, brush seal failure occurs in the form of degraded sealing performance due to increasing seal clearance. The seal performance is mainly characterized by the flow field in close vicinity of the bristle pack, through the seal-rotor clearance, and within the bristle pack. This work investigates the flow field for a brush seal operating with some bristle-rotor clearance. A nonlinear form of the momentum transport equation for a porous medium of the bristle pack has been solved by employing the computational fluid dynamics analysis. The results are compared with prior experimental data. The flow field for the clearance seal is observed to have different characteristics compared to that for the contact seal. Outlined as well are the flow features influencing the bristle dynamics. [DOI: 10.1115/1.2770479]

1 Introduction

Sealing in turbomachinery is a crucial technology in order to achieve higher engine efficiency. Large rotor excursions combined with high surface speeds present major challenges in rotor-stator sealing applications. With their inherent flexibility and superior sealing performance over conventional labyrinth and honeycomb seals, the use of brush seals has increased since the 1980s [1–7].

A brush seal consists of three main components: bristle pack, front plate, and backing plate, as illustrated in Fig. 1. Welded at the outer periphery, multiple rows of fine diameter flexible bristles are clamped with a lay angle in the direction of rotor rotation between the front and backing plates. A typical bristle diameter has a range of 0.05–0.18 mm (0.002–0.007 in.).

The inherent flexibility of the bristle pack enables the brush seal to survive during rotor excursions without permanent performance degradation. Brush seal design aims to impede leakage flow through the rotor-backing plate gap by the bristle pack. In order to achieve minimum leakage rates, the bristle pack should maintain the contact with the rotor. In practice, however, bristle-rotor contact cannot be sustained due to high speed contact, which then leads to bristle tip wear. When bristle-rotor interactions are considered, a brush seal has three different operating modes: clearance, line to line, and interference. Since all the flow goes through the bristle pack, line-to-line and interference modes show similar flow characteristics, and will be referred to as the contact case. Therefore, for flow analysis purposes, brush seals can be grouped as contact and clearance seals.

1.1 Reasons for and the Importance of Clearance Operation. Being dynamic contact seals, it is certain for brush seals to experience wear at the bristle tips. Most seals, which are designed to work at interference or line-to-line position, end up with clearance operation conditions due to seal wear during operation. The causes of operational seal clearance can be grouped as bristle wear, bristle hang-up, and initial clearance.

Bristle wear is caused by many dynamical factors: transient rotor excursions [6,7], bristle instability and flutter due to aerodynamic excitation [8], bristle blowdown [9–11], and others, such as rotor runout, eccentricity, etc. Blowdown happens due to radial pressure gradient and inward radial flow within the bristle pack that pushes bristles toward the rotor and reduces the clearance formed by the tip wear. However, excessive wear reaches a point where bristle blowdown is no longer sufficient to maintain the bristle-rotor contact. Eventually, the brush seal starts operating at some clearance.

For an applied pressure load, the frictional forces between the bristles and the backing plate cause them to remain hung up after an excessive rotor excursion. Bristles remain hung up, leaving a clearance at the bristle-rotor interface [9,10,12] until the pressure load is relieved.

Meanwhile, some applications require the brush seal to be designed with some initial clearance. A steady state clearance is needed for cooling purposes and purge flow [7]. Special applications may also require seal clearance only during startup or shutdown. Therefore, a seal has to be designed with some assembly clearance in order to compensate for the transient closure and to reach a line-to-line operating mode when the transient is over. For example, a steam turbine has a typical application where the initial clearance is needed in order to pass the rotor natural frequency at startup [6,7].

Overall, the clearance operation of a brush seal is a fact in practical applications. The flow field is very different for contact and clearance seals. For a contact case, the flow has a smooth shape in front of the bristle pack, with some disturbances at the downstream face at the fence height section. For the clearance case, however, the lack of flow resistance at the seal-rotor clearance directs a main portion of the flow through the opening that leads to bristle disturbance. Bristle flutter caused by aerodynamic forces may result in fatigue failure. Consequently, clearance operation of a brush seal is an inevitable fact, and the flow fields influencing bristle dynamics need careful investigation.

1.2 Literature Review. Despite the importance of clearance operation of brush seals, available literature remains limited. Previous research on brush seal flow modeling can be grouped into

[1]Corresponding author.

Submitted to ASME for publication in the JOURNAL OF ENGINEERING FOR GAS TURBINES AND POWER. Manuscript received March 15, 2004; final manuscript received July 15, 2007; published online January 9, 2008. Review conducted by Nagaraj Arakere.

Copyright © 2008 by ASME

Downloaded 02 Jun 2010 to 171.66.16.107. Redistribution subject to ASME license or copyright; see http://www.asme.org/terms/Terms_Use.cfm

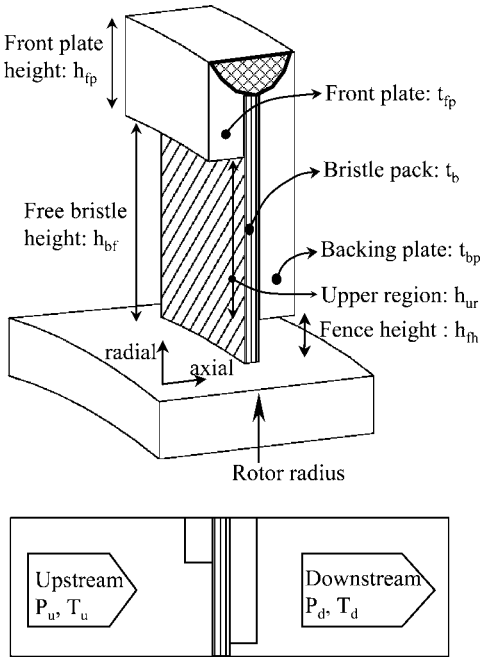

Fig. 1 Schematic of a brush seal

three categories: cross-flow models, bulk flow models, and porous flow models. Brush seal modeling efforts began mainly after the flow visualization studies [13–16]. In order to gain insight into axial flow and pressure fields among the bristles, a two-dimensional cross-flow analysis was conducted for uniformly distributed bristles [17–21]. Meanwhile, several bulk flow models were developed, offering empirical relations to predict the leakage as a function of seal geometry and operating conditions [22–29].

By treating the bristle pack as a porous medium, flow analyses can provide more insight into the flow and pressure fields within the entire seal. The flow in the porous medium is subject to additional resistance forces (frictional forces between fluid and bristle surfaces) compared to flow in a nonporous medium. Depending on their utilization of resistance terms, porous media-based modeling efforts can be categorized into three groups as follows.

The first porous media modeling efforts involved the linear Darcian porous medium relation that considers only viscous resistance terms. This approach was first applied for a brush seal by Bayley and Long in 1993 [30]. Their work was limited to seals operating with interference.

The second group of porous media models involved a non-Darcian transport equation including both the viscous and inertial resistance terms. Ergun's equation [31] for flow in porous media was introduced with modifications for the bristle pack [32]. Chew et al. [33] in 1995 and Chew and Hogg [34] in 1997 were the first to include this modified relation to the right hand side of the Navier–Stokes equation in order to define a porous medium model for brush seals. They were the first studying clearance seals with a 0.75 mm opening at the seal-rotor interface. A follow-up study by Turner et al. [35] included experimental and numerical investigations for the clearance seal. In addition to leakage, they measured pressure distribution over the rotor surface and backing plate. Chen et al. [36] took one step further, placing a video system to visualize seal behavior operating with clearance. They observed that blowdown occurs predominantly in the first few upstream bristle rows. They were the first to compare flow fields for both the interference and clearance seals. The follow-up study by Chen et al. [37] compares this model with some experimental observations using a large-scale brush seal model.

Dogu [38] introduced the third porous medium modeling strategy in 2003. The model also involved a non-Darcian transport relation for the bristle pack. In addition, it was assumed that the bristle pack matrix behaves as a highly flow resistive porous medium. Therefore, flow resistance forces in the Navier–Stokes equation are dominant and other terms are negligible. This assumption is valid for the porous media with high flow resistance, which is the physical case for firmly packed bristles under a pressure load. Instead of dealing with the full Navier–Stokes equation, the simplified form of the transport equation was solved by employing the computational fluid dynamics (CFD) analysis. Using this approach, Dogu [38] studied the flow behavior of contact brush seals in detail.

As a follow-up to this study, the present work deals with the flow behavior of clearance brush seals. Taking the few clearance seal modeling efforts [33,35–37] further, this work investigates the effect of high flow rates through the seal clearance on the flow field and turbulent kinetic energy. The amount of bristle blowdown is calibrated as a function of initial clearance and pressure load. The ratio of the flow rates through the bristle pack and clearance is quantified for various operating conditions. A fine mesh is adapted to capture flow details for high gradient flows that are typically observed for very small clearances. Finer mesh provides better insight to flow fields than the coarse mesh analyses, as stated by prior models [33,35,36].

1.3 Scope of the Work. All of the porous medium CFD models contribute valuable insight to the dynamic behavior of brush seals. Further improvements are needed to develop CFD models in parallel to advanced seal designs. Clearance cases require more emphasis on brush seal design due to its aggressive and harsh flow conditions, which may lead to failure. In this study, flow fields for contact and clearance seals are compared side by side for similar operating conditions. The significant flow features of clearance seals are presented. The discussion for the flow field further explores the brush seal dynamics, such as blowdown, bristle instability, bristle stiffening, and failure. The study also includes results and discussions on leakage performance and flow properties as a function of clearance, pressure load, and blow-down.

2 Governing Equations and the Computational Fluid Dynamics Model

The computational model includes brush seal and the cavities upstream and downstream of the seal, as illustrated in Fig. 1. Rotor and stator surfaces are modeled as lower and upper walls, respectively. The bristle pack is defined as a porous medium with effective flow resistance coefficients. Up-/downstream cavities are axially extended to one and a half of the seal radial height to ensure fully developed flow conditions when approaching and leaving the seal.

The governing equations describing the flow across the brush seal are numerically solved. Details of the applied modeling procedure and the bulk porous medium approach are described in the previous study by Dogu [38] and summarized here for completeness.

The leakage flow that is driven by the pressure difference across the brush seal is assumed turbulent and compressible. The Navier–Stokes equations governing the fluid flow in the up-/downstream cavities can be written in the Cartesian tensor notation as

$$\frac{\partial \rho u_i}{\partial x_i} = 0 \tag{1}$$

$$u_j \frac{\partial \rho u_i}{\partial x_j} = -\frac{\partial P}{\partial x_i} + \mu \frac{\partial^2 u_i}{\partial x_j \partial x_j} \tag{2}$$

The k-ε model is used for the turbulent flow. The ideal gas law is applied for the compressible air flow. Constant air properties are evaluated at cavity temperature and atmospheric pressure conditions. Pressure boundary conditions are imposed at the inlet and exit boundaries.

Downloaded 02 Jun 2010 to 171.66.16.107. Redistribution subject to ASME license or copyright; see http://www.asme.org/terms/Terms_Use.cfm

2.1 Transport Equation for Bulk Porous Medium Approach for Bristle Pack. Flow through a porous bristle pack is subject to additional resistance forces (fluid friction with solid bristle surfaces) compared to flow in nonporous upstream and downstream cavities. Among different porous media resistance models, the following flow resistance relationship has been selected as the best fit for the flow in the bristle pack and has been validated by many researchers [32–38]:

$$-\frac{dP}{dx_i} = (\alpha_i |u_i| + \beta_i) u_i \tag{3}$$

where x_i represents the orthographic flow directions and u_i is the superficial velocity in the x_i direction. The superficial velocity is the velocity that would exist in the absence of a porous medium for the same volumetric flow rate. The coefficients α and β are the effective inertial and viscous flow resistances, respectively. Their values change in each spatial direction for an anisotropic porous bristle pack. This relation defines a non-Darcian porosity model yielding an equation between the pressure gradient and effective resistance terms. These flow resistance terms are calibrated for the porous bristle pack based on experimental leakage and pressure data.

In previous porous brush seal studies [33–37], Eq. (3) is added to the right hand side of the momentum equation, (Eq. (2)). Nevertheless, when the porous medium is highly resistive, the inertial and viscous shear terms in the momentum equation become negligibly small compared to the flow resistance terms. Thus, as stated in Eq. (3), the momentum equation reduces to a balance equation between the pressure gradient and flow resistance forces (viscous and inertial forces).

Under a pressure load, the bristles move and get firmly packed against the backing plate. Thus, the bristle pack forms a highly resistive medium to the flow diffusion. The purpose of the porous medium approach is to match the measured leakage and pressure distribution through the calibration of the flow resistance coefficients in the transport equation. Rather than dealing with many terms in the momentum equation, a simplified form (Eq. (3)) is implemented to investigate flow and pressure fields in the bristle pack. Therefore, the presented bulk porous medium model utilizes Eq. (3) as the transport equation. Experimental data for leakage, axial pressure on the rotor, and radial pressure on the backing plate are used to calibrate the flow resistance coefficients in Eq. (3).

In the porous bristle pack, the flow resistance coefficients are functions of seal geometry, operating conditions, and dynamic behavior of the bristles. The porosity of the bristle pack is a direct function of bristle diameter, packing density, and lay angle. It is also influenced by pressure load and rotor excursion. Dynamic issues, such as bristle flutter, blowdown, and hang-up, affect brush seal stiffness and permeability. In addition to all of these complexities, the portion of the bristles forms two different physical structures: the fence height region near the rotor and the upper region. Bristles under a pressure load compact over the backing plate at the upper region, while they bend/spread at the fence height region. Thus, the upper region has more resistance to the flow diffusion. In order to correlate this compactness effect, the bristle pack is divided into two permeable regions: fence height and upper regions. Different flow resistance coefficients are defined for these two distinct regions. It can be concluded that the bulk porous medium approach for the bristle pack overcomes all of the dynamic issues as long as flow resistance coefficients are precisely calibrated based on the experimental data. In the present model, only one set of resistance coefficients is employed for all pressure ratios. Flow resistance coefficients for the upper region are defined to be 20% higher than those for the fence height region. The calibration of the anisotropic flow resistance coefficient is done for the low-pressure ratio where the blowdown is negligible. Details of the calibration procedure can be found in Ref. [38].

Table 1 Brush seal properties used in the CFD model

Parameter		(mm)	Parameter	
Rotor radius		60.610 and 60.130	Clearance (mm)	0.27 and 0.75
Fence height	h_{fh}	1.400	Bristle diameter (mm)	0.076
Upper region height	h_{ur}	9.280	Cant angle	45 deg
Free bristle height	h_{bf}	10.680	Packing density (bristle/mm circ.)	200
Front plate height	h_{fp}	4.660		
Front plate thickness	t_{fp}	1.600	Working fluid	Air
Bristle pack thickness	t_b	0.750	p_u (kPa)	110–400
Backing plate thickness	t_{bp}	1.600	p_d (kPa)	100
Seal axial thickness	t_{bs}	3.950	Temperature (°C)	20

3 Results and Discussion

The CFD model is built in a two-dimensional axisymmetric coordinate system, as illustrated in Fig. 1. The features of the modeled brush seal are summarized in Table 1. In an attempt to capture high gradients around the clearance region, a fine mesh has been adopted (Fig. 2). The typical element size in this region is in the order of 0.01 mm. In prior CFD models [33,35,36], a coarse mesh was employed.

Navier–Stokes equations are solved using the finite volume method by applying the upwind differencing scheme for velocity and the central differencing scheme for density. Downstream boundary is kept at atmospheric pressure. The pressure ratio $R_p = p_u/p_d$ is varied from 1.1 to 4.0. The air inlet temperature is set constant at 20°C. The rotor is considered as stationary in the present investigation. Flow and pressure fields for the various pressure ratio and clearance cases are calculated. The results are compared to experimental data reported by Turner et al. [35], who experimentally and numerically studied two cases with 0.27 mm and 0.75 mm radial clearance.

3.1 Leakage. Figure 3 compares leakage flow with respect to pressure ratio. Model results are compared with those of Turner et al. [35], who considered two operating modes: full blowdown and no blowdown. They employed different sets of permeability coefficients for both cases to match experimental leakage data. However, as observed by Chen et al. [36], a full blowdown did not happen, especially for low-pressure loads. In practice, the level of the blowdown depends on the pressure difference. Therefore, clearance with partial blowdown cases are also analyzed and compared in the present model.

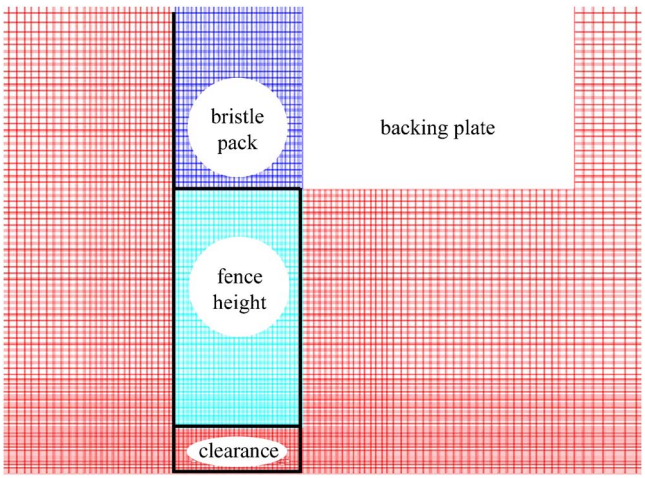

Fig. 2 Sample mesh view

Downloaded 02 Jun 2010 to 171.66.16.107. Redistribution subject to ASME license or copyright; see http://www.asme.org/terms/Terms_Use.cfm

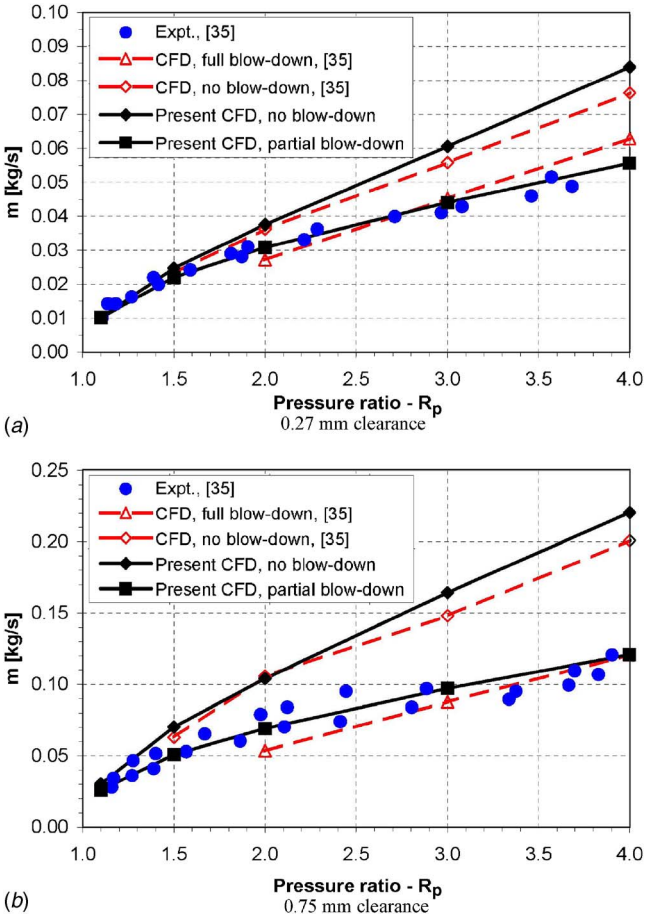

Fig. 3 Leakage versus pressure ratio

As also observed by Turner et al. [35], the presented CFD results (Fig. 3) overestimate the experimental data for high-pressure ratio cases when no blowdown is considered. This indicates existence of partial blow-down at high-pressure ratio cases where clearance gradually reduces. A slight decrease in clearance results in a considerable drop in leakage. To capture this effect, a gradual blowdown is modeled to match experimental leakage rates. For a realistic representation of bristle dynamics, analyses are performed for the entire range of the considered pressure ratios. As illustrated in Fig. 4, the blowdown is calculated as a function of

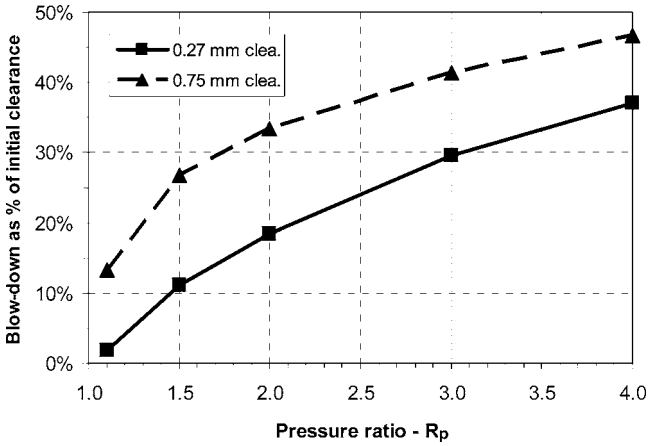

Fig. 4 Variation of bristle blowdown with respect to pressure ratio for initial clearances of 0.27 mm and 0.75 mm

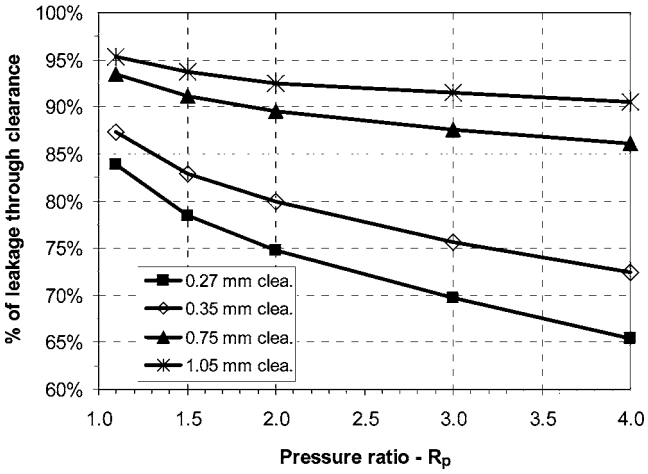

Fig. 5 Leakage percentages through clearance with respect to pressure ratio for various clearances

pressure ratio and initial clearance. The blowdown for the larger clearance is more than that for the lower clearance. This observation also agrees with the experimental data reported by Crudgington and Bowsher [11].

As expected, the clearance seal has a considerably higher leakage than the contact seal as most of the flow occurs through the clearance. The percentage of the leakage through the clearance and bristles at the fence height section is also calculated, and plotted in Fig. 5. The portion of the flow through the clearance range from 65% to 84% of the total leakage for a 0.27 mm clearance and from 86% to 94% for a 0.75 mm clearance. The percentage of flow through the clearance decreases with pressure ratio.

3.2 Axial Pressure. The calculated axial pressure distribution over the rotor surface is shown in Fig. 6. The pressure (p) is normalized with respect to upstream (p_u) and downstream (p_d) pressures as $p^*=(p-p_d)/(p_u-p_d)$. The origin of the axial coordinate is located at the upstream face of the bristle pack. The axial coordinate (z) is also normalized by the thickness of the bristle pack (t_b) as $z^*=z/t_b$. For the contact seal, the pressure drop starts at the upstream face of the bristle pack. Most of the pressure drop occurs at the downstream side of the bristle pack due to compressibility and flow expansion effects. Overall, the axial pressure profile over the rotor surface does not follow a linear drop. These

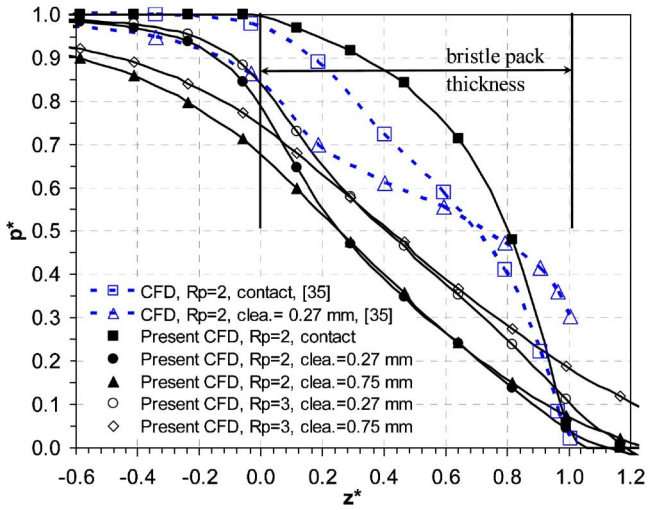

Fig. 6 Axial pressure distribution on the rotor surface

Downloaded 02 Jun 2010 to 171.66.16.107. Redistribution subject to ASME license or copyright; see http://www.asme.org/terms/Terms_Use.cfm

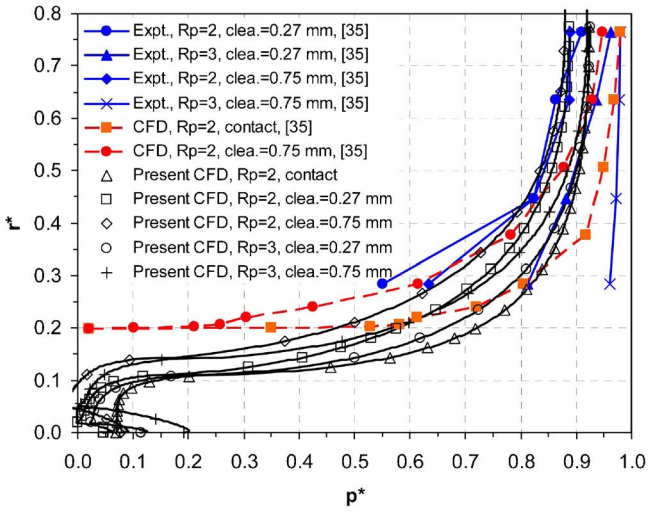

Fig. 7 Radial pressure distribution on the backing plate

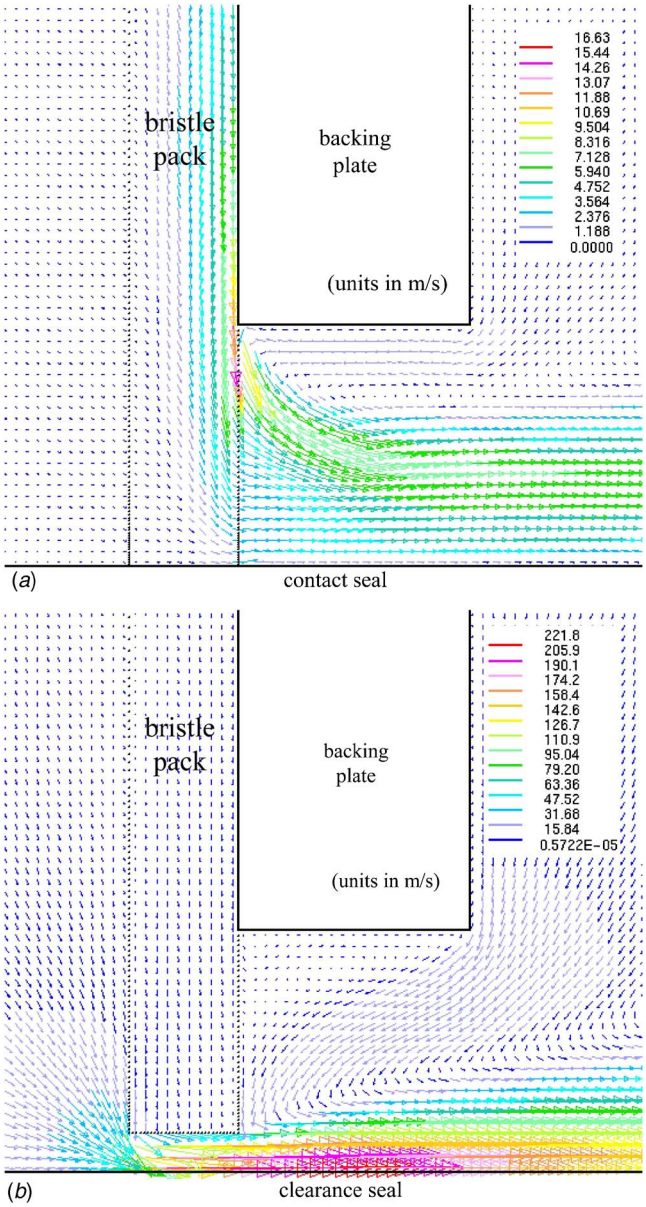

Fig. 8 Velocity vectors around the fence height for contact and clearance (0.27 mm) seals for R_p=1.5

results are in agreement with some of the earlier works [35–38] while conflicting with some others [13–21,30]. The axial pressure drop for the clearance seal shows approximately a linear trend compared to the contact seal. The pressure drop starts in front of the bristle pack due to flow acceleration through the clearance.

3.3 Radial Pressure. The radial pressure distribution over the backing plate is compared in Fig. 7. The normalized pressure p^* is plotted with respect to the normalized radial distance from the rotor surface $r^*=y/h_{bf}$, where y is the radial distance from the rotor surface and h_{bf} is the radial free bristle height. The results show a similar trend with the experimental data with some discrepancies for high-pressure ratio cases. Most of the radial pressure drop occurs in the inner half of the free bristle height near the rotor surface. The pressure in the upper half region approaches the upstream pressure. As the inward radial flow is weaker in the upper region, flow diffusion balances the pressure close to the upstream pressure at the backing plate. The radial flow accelerates toward the rotor as axial diffusion adds more mass flow toward the rotor. This confirms the observed radial pressure gradient. The radial pressure gradient governs the inward radial flow driving the blowdown. For the clearance seal, the pressure approaches the upstream pressure value faster as the clearance relieves the pressure drop closer to the rotor surface.

3.4 Velocity Vectors. Flow properties (velocity, pressure, and turbulent kinetic energy fields) are compared for both contact and clearance seals, as illustrated in Figs. 8–11. All of the comparative analyses for the velocity vectors, contours, and line plots are performed using an average pressure ratio of 1.5 and a clearance of 0.27 mm as the base line case. Figure 8 compares velocity vectors around the fence height region. The fence height region is critical for the brush seal flow and dynamic behavior. The flow diffusion into the bristle pack is observed as the predominant flow behavior for the contact seal. Axial flow diffusion into the bristle pack governs a strong inward radial flow over the backing plate. This radial flow turns axial and discharges to downstream at the fence height region under the backing plate. A maximum velocity is observed mostly in the radial inward direction reaching 16 m/s at the inner corner of the backing plate.

Inward radial flow attains a similar maximum velocity for the clearance seal as well. However, excessive axial flow through the clearance is dominant. Therefore, clearance seals experience higher velocity magnitudes in front of the bristle pack at the upstream face of the clearance region. Discharging flow through the clearance expands to the downstream cavity from higher to lower pressures. The maximum velocity occurs in the axial direction at the clearance discharge, which is about 14 times greater than that of the contact seal. The flow through the clearance gap is similar to an orifice flow. For high-pressure loads, a strong expansion downstream is observed under the bristles tips.

3.5 Contour Plots. Figure 9 extends the comparison of contact and clearance seals by using contour plots for pressure, axial velocity, radial velocity, and turbulent kinetic energy. Pressure contours are plotted in Fig. 9(*a*). The results indicate that most of the pressure drop occurs at the downstream side of the bristle pack for the contact seal. For the clearance seal, however, the pressure drop is distributed over the thickness of the bristle pack, including the clearance. On the other hand, radial velocity contours have a completely different distribution for contact and clearance seals (Fig. 9(*b*)). Negative values of radial velocity indicate an inward radial flow. It is noted that the radial flow at the upstream face of the backing plate has comparable magnitudes for both seals. For the clearance seal, a strong radial flow develops at the clearance

Downloaded 02 Jun 2010 to 171.66.16.107. Redistribution subject to ASME license or copyright; see http://www.asme.org/terms/Terms_Use.cfm

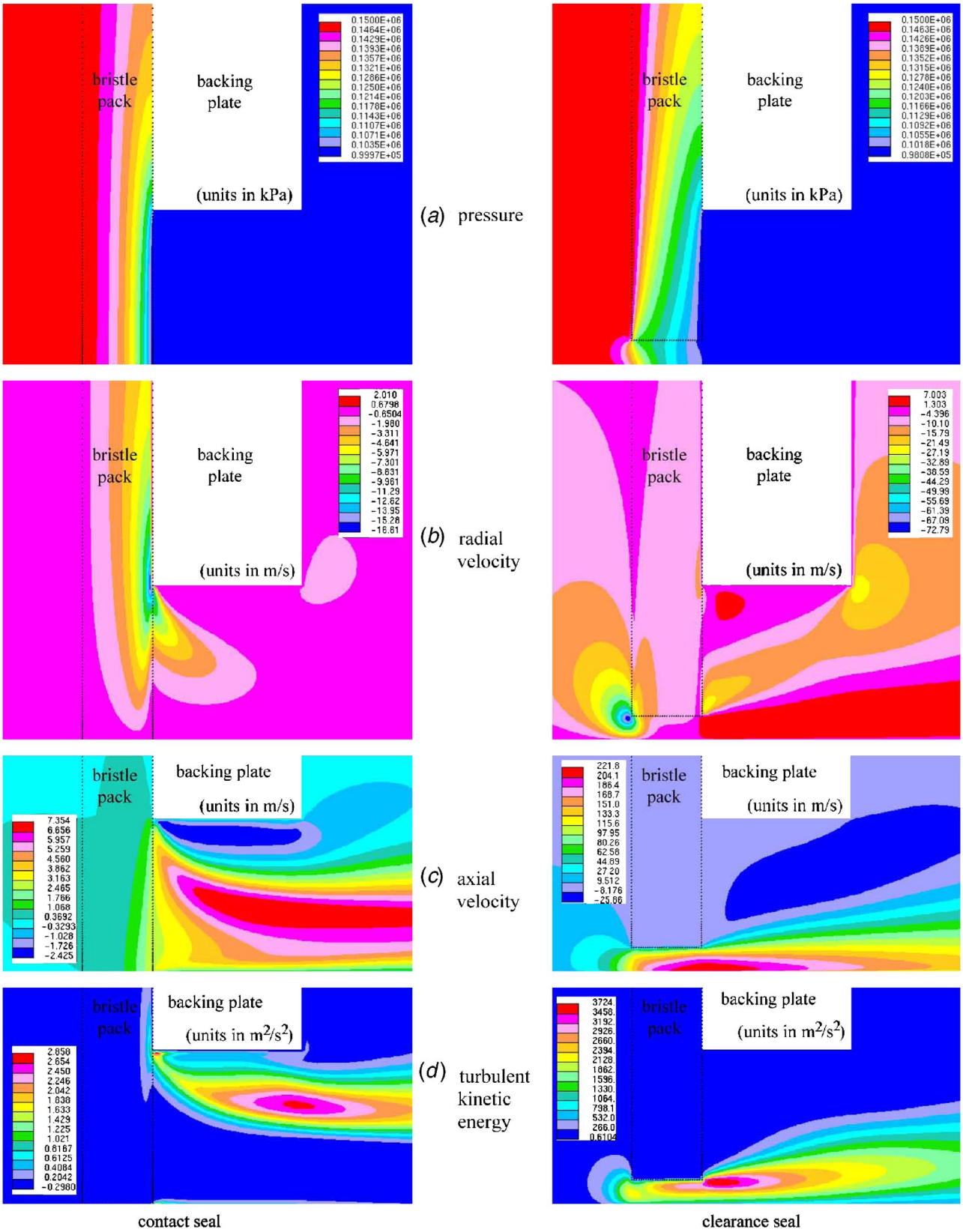

Fig. 9 Contour plots around the fence height for contact and clearance (0.27 mm) seals for R_p=1.5

entrance due to flow acceleration. Similarly, the axial flow is also accelerated (Fig. 9(*c*)). For axial velocity, the positive flow direction is downstream. Contour lines enlarging at the clearance exit indicate the flow expansion. For the contact seal, the axial velocity is generated by the flow through the bristle pack. The turbulent kinetic energy makes its peak at the maximum flow velocity region, as illustrated in Fig. 9(*d*). This energy is very high at the leading edge of the clearance.

Downloaded 02 Jun 2010 to 171.66.16.107. Redistribution subject to ASME license or copyright; see http://www.asme.org/terms/Terms_Use.cfm

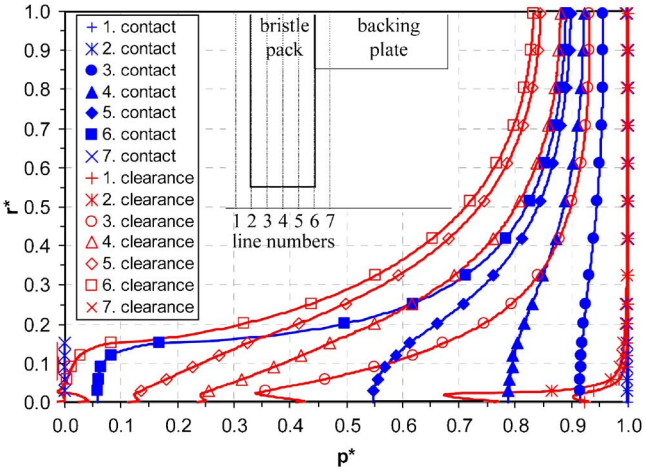

Fig. 10 Pressure in the bristle pack for contact and clearance (0.27 mm) seals for R_p=1.5

3.6 Line Plots. In order to further illustrate different flow configurations for contact and clearance seals, the bristle pack region is scanned in the axial direction by plotting flow properties at the selected sections. As shown in Fig. 10, radial lines are equally spaced at seven locations. The first line is placed at one-fourth of the pack thickness upstream of the bristle pack. Figures 10 and 11 illustrate the radial distribution of pressure, radial and axial velocities, and turbulent kinetic energy for both contact and clearance seals. At the outer perimeter near the bristle root region, the downstream pressure gets closer to the upstream pressure (Fig. 10). Most of the pressure change occurs in the inner half of the bristle height. The main difference between contact and clearance seals is the starting point of the axial pressure drop. For the clearance seal, the pressure drop in the axial direction starts in front of the bristle pack and approaches the downstream pressure faster.

The magnitude of the radial and axial velocities as well as the turbulent kinetic energy shows large differences for contact and clearance seals. Therefore, they are plotted in two separate graphics, as shown in Fig. 11. For the contact seal, the inward radial velocity makes its peak at line 6 over the backing plate (Fig. 11(*a*)). However, in a clearance seal, the maximum radial velocity occurs on line 2 at the upstream face of the bristle pack, with a magnitude larger than that of the contact seal. As confirmed with the experimental observations by Chen et al. [36], bristles at the upstream face of the bristle pack are subject to a high inward radial flow causing more blowdown. Aksit [9] also reported the uneven bristle wear due to more blowdown and flutter at upstream bristles. On the contrary, the maximum inward radial flow for the contact seal is located closer to the downstream of the bristle pack. The calculated minimum/maximum radial velocities are −14/1 m/s and −67/7 m/s for the contact and clearance seals, respectively. The axial velocity is low for the contact seal (Fig. 11(*b*)). On the other hand, bristle tips of the clearance seal are subject to a very high axial flow momentum and drag force that might lead to stronger bristle bending. The turbulent kinetic energy is also high for the clearance seal, especially at the bristle tips through the clearance exit (Fig. 11(*c*)). This exerts more excitation energy on the bristle tips. With minimal support and restraint from adjacent bristle rows, upstream and downstream bristles are especially vulnerable to this excitation, which may lead them into instability and flutter.

4 Conclusions

In the field, the brush seal reaches its nominal working conditions after several engine cycles. After some service hours, the seal starts to operate at clearance due to wear. Therefore, brush seal operation at some clearance is an unavoidable operational fact. The aggressive flow conditions at clearance may activate seal dynamics, such as bristle flutter and excessive blowdown, that speed up bristle wear. Therefore, it is important to understand brush seal flow configuration for the clearance operation.

In this work, the flow behavior of brush seals operating at clearance is investigated by developing a CFD flow model. The model includes the bristle pack as a porous medium. A bulk porous medium approach is employed, incorporating a simple non-Darcian formulation for the porous bristle pack. A fine mesh is adapted to capture details of flow behavior with higher gradients typically observed for small clearances. After the evaluation of the flow fields for various operating conditions and the comparison of contact and clearance seals, the following conclusions were reached:

- Analyses show that the flow field for a brush seal operating at clearance is different compared to that for a contact seal.
- Leakage flow increases drastically with clearance. Leakage through the clearance accounts for 65–94% of the total leakage depending on clearance and pressure difference.
- Blowdown is calibrated as a function of clearance and pressure difference. Higher clearance and pressure difference result in higher bristle blowdown.
- Clearance seal is subject to more aggressive flow fields due to increased mass flow rate. The location of the maximum inward radial flow shifts from downstream rows in the contact seals to upstream rows in the clearance seals. This flow behavior confirms an uneven wear of the bristle tips.
- The excessive axial flow momentum at clearance can transfer a large turbulent kinetic energy to bristles leading to bristle bending, instability, and failure.

Porous medium CFD models have provided a better understanding of brush seal flow. They have been evolving to be more comprehensive as a result of developments in CFD codes and computer power. Further improvements in the presented model may involve the inclusion of rotor rotation, flow resistance coefficients as a function of operating conditions and seal geometry, frictional and viscous heating, and flow-structure coupling.

Nomenclature

h_{bf} = free bristle height
h_{fh} = fence height
h_{ur} = upper region height
p = static pressure
p^* = normalized pressure=$(p-p_d)/(p_u-p_d)$
r^* = normalized radial coordinate=y/h_{bf}
R_p = pressure ratio=p_u/p_d
t_{bp} = thickness of backing plate
t_{fp} = thickness of front plate
t_b = thickness of bristle pack
u = (radial) velocity component
u_i = superficial velocity
w = axial velocity component
x = spatial coordinate direction
y = radial distance from rotor surface
z = axial coordinate direction
z^* = normalized axial coordinate=z/t_b
μ = dynamic viscosity
ρ = density
α, β = inertial and viscous flow resistance coefficients

Subscripts

i = spatial coordinate and radial direction
j = spatial coordinate direction
k = axial direction
u/d = up/down stream

Downloaded 02 Jun 2010 to 171.66.16.107. Redistribution subject to ASME license or copyright; see http://www.asme.org/terms/Terms_Use.cfm

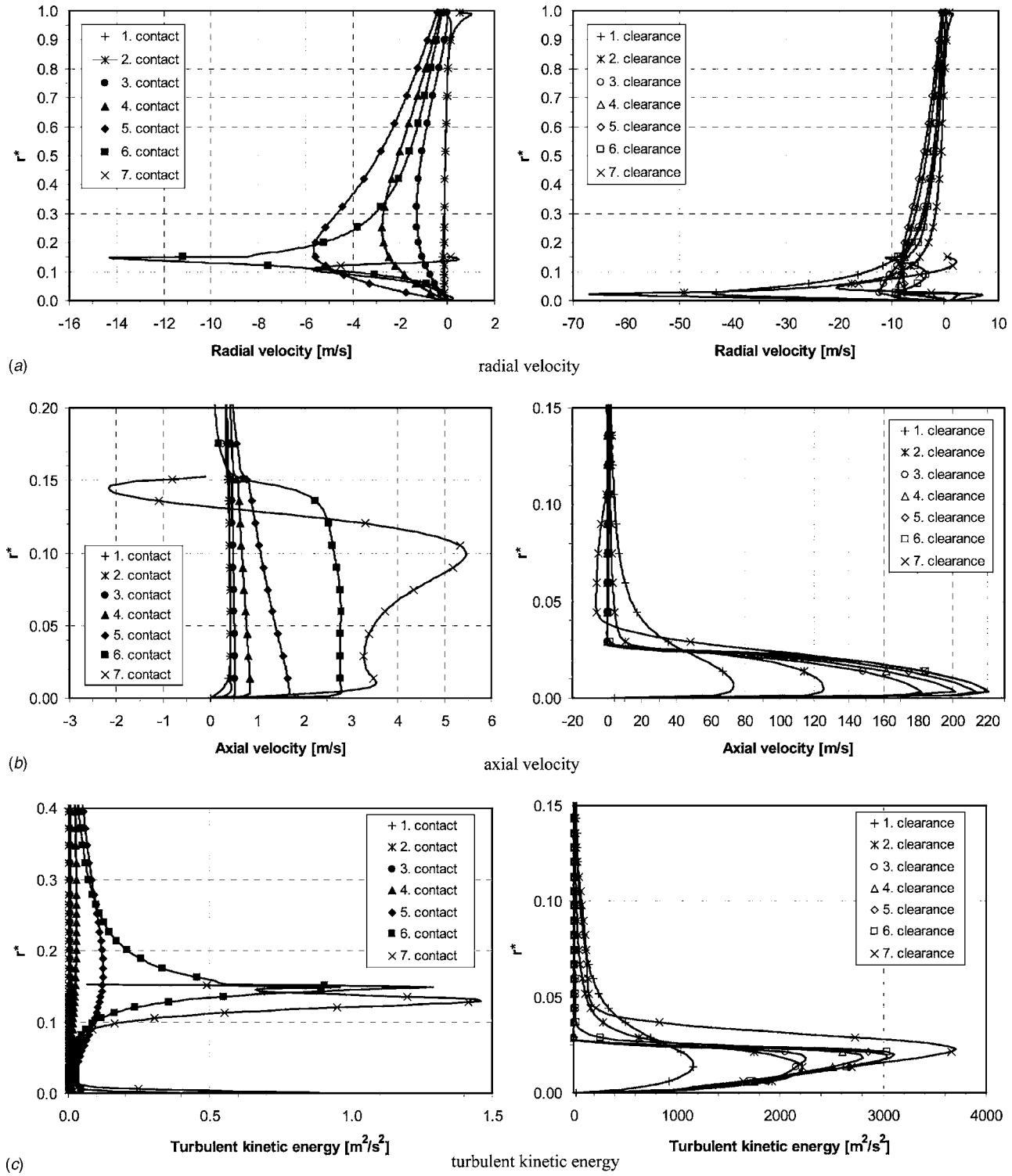

Fig. 11 Flow properties in the bristle pack for contact and clearance (0.27 mm) seals for R_p=1.5

References

[1] Ferguson, J. G., 1988, "Brushes as High Performance Gas Turbine Seals," ASME Paper No. 88-GT-182.

[2] Gorelov, G. M., Reznik, V. E., and Tsibizov, V. I., 1988, "Experimental Study of Brush Seal Flow Characteristics and Comparison With a Labyrinth Seal," Izvestitiya VUZ. Aviatsionnaya Tekhnika, **31**(4), pp. 43–46.

[3] Chupp, R. E., and Nelson, P., 1993, "Evaluation of Brush Seals for Limited-Life Engines," J. Propul. Power, **9**(1), pp. 113–118.

[4] Chupp, R. E., and Dowler, C. A., 1993, "Performance Characteristics of Brush Seals for Limited-Life Engines," ASME J. Eng. Gas Turbines Power, **115**, pp. 390–396.

[5] Carlile, J. A., Hendricks, R. C., and Yoder, D. A., 1993, "Brush Seal Leakage Performance With Gaseous Working Fluids at Static and Low Rotor Speed Conditions," ASME J. Eng. Gas Turbines Power, **115**, pp. 397–403.

[6] Chupp, R. E., Aksit, M. F., Ghasripoor, F., Turnquist, N. A., and Demiroglu, M., 2001, "Advanced Seals for Industrial Turbine Applications," AIAA Paper No. 2001-3626.

[7] Dinc, S., Demiroglu, M., Turnquist, N., Mortzheim, J., Goetze, G., Maupin, J., Hopkins, J., Wolfe, C., and Florin, M., 2002, "Fundamental Design Issues of Brush Seals for Industrial Applications," ASME J. Turbomach., **124**, pp. 293–300.

[8] O'Neill, A. T., Hogg, S. I., Withers, P. A., Turner, M. T., and Jones, T. V.,

Downloaded 02 Jun 2010 to 171.66.16.107. Redistribution subject to ASME license or copyright; see http://www.asme.org/terms/Terms_Use.cfm

1997, "Multiple Brush Seals in Series," ASME Paper No. 97-GT-194.
[9] Aksit, M. F., 1998, "A Computational Study of Brush Seal Contact Loads With Friction," Ph.D. thesis, Rensselaer Polytechnic Institute, Troy, NY.
[10] Crudgington, P. F., and Bowsher, A., 2002, "Brush Seal Pack Hysteresis," AIAA Paper No. 2002-3794.
[11] Crudgington, P. F., and Bowsher, A., 2003, "Brush Seal Blow Down," AIAA Paper No. 2003-4697.
[12] Basu, P., Datta, A., Loewenthal, R., Short, J., and Johnson, R., 1994, "Hsyteresis and Bristle Stiffening Effects in Brush Seals," J. Propul. Power, **10**(4), pp. 569–575.
[13] Braun, M. J., Hendricks, R. C., and Canacci, V., 1990, "Flow Visualization in a Simulated Brush Seal," ASME Paper No. 90-GT-217.
[14] Braun, M. J., Canacci, V. A., and Hendricks, R. C., 1991, "Flow Visualization and Quantitative Velocity and Pressure Measurements in Simulated Single and Double Brush Seals," Tribol. Trans., **34**, pp. 70–80.
[15] Braun, M., Canacci, V., and Hendricks, R., 1990, "Flow Visualization and Motion Analysis for a Series of Four Sequential Brush Seals," AIAA Paper No. 90-2482.
[16] Braun, M., Hendricks, R., and Yang, Y., 1991, "Effects of Brush Seal Morphology on Leakage and Pressure Drops," AIAA Paper No. 91-2106.
[17] Mullen, R., Braun, M., and Hendricks, R., 1990, "Numerical Modeling of Flows in Simulated Brush Seal Configurations," AIAA Paper No. 90-2141.
[18] Braun, M. J., and Kudriavtsev, V. V., 1995, "A Numerical Simulation of a Brush Seal Section and Some Experimental Results," ASME J. Turbomach., **117**, pp. 190–202.
[19] Kudriavtsev, V. V., and Braun, M. J., 1996, "Model Developments for the Brush Seal Numerical Simulation," J. Propul. Power, **12**(1), pp. 193–201.
[20] Sharatchandra, M. C., and Rhode, D. L., 1996, "Computed Effects of Rotor-Induced Swirl on Brush Seal Performance—Part 1: Leakage Analysis," ASME J. Tribol., **118**, pp. 912–919.
[21] Demiroglu, M., Aksit, M. F., and Tichy, J. A., 1998, "A Numerical Study of Brush Seal Leakage Flow," AIAA Paper No. 98-3173.
[22] Braun, M. J., Hendricks, R. C., and Canacci, V. A., 1990, "Non-Intrusive Qualitative and Quantitative Flow Characterization and Bulk Flow Model for Brush Seals," *Proceedings of the Japan International Tribology Conference*, Nagoya, Japan, pp. 1611–1616.
[23] Hendricks, R. C., Braun, M. J., Canacci, V., and Mullen, R. L., 1990, "Brush Seals in Vehicle Tribology," *Presented at 1990 Leeds/Lyon Symposium*, Leeds, England, pp. 231–242.
[24] Hendricks, R. C., Schlumberger, S., Braun, M. J., Choy, F., and Mullen, R. L., 1991, "A Bulk Flow Model of a Brush Seal System," ASME Paper No. 91-GT-325.
[25] Hendricks, R., Proctor, M., Schlumberger, J., Braun, M., and Mullen, R., 1991, "Some Preliminary Results of Brush Seal/Rotor Interference Effects on Leakage at Zero and Low RPM Using a Tapered-Plug Rotor," AIAA Paper No. 91-3390.
[26] Chupp, R. E., Holle, G. F., and Dowler, C. A., 1991, "Simple Leakage Flow Model for Brush Seals," AIAA Paper No. 91-1913.
[27] Holle, G. F., Chupp, R. E., and Dowler, C. A., 1992, "Brush Seal Leakage Correlations Based on Effective Thickness," *Proceedings of the Fourth International Symposium on Transport Phenomena and Dynamics of Rotating Machinery (ISROMAC-4)*, Honolulu, HI, pp. 253–261.
[28] Dowler, C. A., Chupp, R. E., and Holle, G. F., 1992, "Simple Effective Thickness Model for Circular Brush Seals," AIAA Paper No. 92-3192.
[29] Chupp, R. E., and Holle, G. F., 1996, "Generalizing Circular Brush Seal Leakage Through a Randomly Distributed Bristle Bed," ASME J. Turbomach., **118**, pp. 153–161.
[30] Bayley, F. J., and Long, C. A., 1993, "A Combined Experimental and Theoretical Study of Flow and Pressure Distributions in a Brush Seal," ASME J. Eng. Gas Turbines Power, **115**(2), pp. 404–410.
[31] Ergun, S., 1952, "Fluid Flow Through Packed Columns," Chem. Eng. Prog., **48**, pp. 89–94.
[32] Hendricks, R. C., Flower, R., and Howe, H., 1996, "A Brush Seal Program Modeling and Developments," NASA Technical Memorandum No. 107158.
[33] Chew, J. W., Lapworth, B. L., and Millener, P. J., 1995, "Mathematical Modeling of Brush Seals," Int. J. Heat Fluid Flow, **16**(6), pp. 493–500.
[34] Chew, J. W., and Hogg, S. I., 1997, "Porosity Modeling of Brush Seals," ASME J. Tribol., **119**, pp. 769–775.
[35] Turner, M. T., Chew, J. W., and Long, C. A., 1998, "Experimental Investigation and Mathematical Modeling of Clearance Brush Seals," ASME J. Eng. Gas Turbines Power, **120**, pp. 573–579.
[36] Chen, L. H., Wood, P. E., Jones, T. V., and Chew, J. W., 1999, "An Iterative CFD and Mechanical Brush Seal Model and Comparison With Experimental Results," ASME J. Eng. Gas Turbines Power, **121**(4), pp. 656–662.
[37] Chen, L. H., Wood, P. E., Jones, T. V., and Chew, J. W., 2000, "Detailed Experimental Studies of Flow in Large Scale Brush Seal Model and a Comparison With CFD Predictions," ASME J. Eng. Gas Turbines Power, **122**, pp. 672–679.
[38] Dogu, Y., 2003, "Investigation of Brush Seal Flow Characteristics Using Bulk Porous Medium Approach," ASME Paper No. GT-2003-38970.

Downloaded 02 Jun 2010 to 171.66.16.107. Redistribution subject to ASME license or copyright; see http://www.asme.org/terms/Terms_Use.cfm

Girija Parthasarathy[1]
Vehicle Health Management Laboratory,
Honeywell Aerospace,
3660 Technology Drive,
Minneapolis, MN 55418
e-mail: girija.parthasarathy@honeywell.com

Sunil Menon

Kurt Richardson

Ahsan Jameel

Dawn McNamee

Tori Desper

Michael Gorelik

Chris Hickenbottom

Honeywell Aerospace,
111 South,
34th Street,
Phoenix, AZ 85034

Neural Network Models for Usage Based Remaining Life Computation

In engine structural life computations, it is common practice to assign a life of certain number of start-stop cycles based on a standard flight or mission. This is done during design through detailed calculations of stresses and temperatures for a standard flight, and the use of material property and failure models. The limitation of the design phase stress and temperature calculations is that they cannot take into account actual operating temperatures and stresses. This limitation results in either very conservative life estimates and subsequent wastage of good components or in catastrophic damage because of highly aggressive operational conditions, which were not accounted for in design. In order to improve significantly the accuracy of the life prediction, the component temperatures and stresses need to be computed for actual operating conditions. However, thermal and stress models are very detailed and complex, and it could take on the order of a few hours to complete a stress and temperature simulation of critical components for a flight. The objective of this work is to develop dynamic neural network models that would enable us to compute the stresses and temperatures at critical locations, in orders of magnitude less computation time than required by more detailed thermal and stress models. The current paper describes the development of a neural network model and the temperature results achieved in comparison with the original models for Honeywell turbine and compressor components. Given certain inputs such as engine speed and gas temperatures for the flight, the models compute the component critical location temperatures for the same flight in a very small fraction of time it would take the original thermal model to compute. [DOI: 10.1115/1.2771248]

Introduction

Accurate life prediction for turbine engines has become increasingly important in recent years as military and commercial aircraft fleet age, and engine component failures cause unplanned maintenance and repair. Failure modes such as low cycle fatigue (LCF), stress rupture (SR), or creep are caused by operational stresses (either cyclic or constant) to the engine component material. The common industry practice today is to count engine start-stop cycles and decrement it from a precalculated number for life, to arrive at remaining life. This precalculated number is overly conservative for obvious safety reasons. Probabilistically, we throw away 1000 components to remove the unknown one that is theoretically predicted to be in a failed state [1]. Therefore, increasing the life prediction confidence is of utmost importance if we are to increase the service life of aircraft turbomachinery components or if we are to predict imminent failure of an overused engine. Consequently, work is being done to increase our prediction and analysis capability for structural failure. Advances in fatigue prediction material models, damage tolerance life prediction model, modeling crack growth, and assessing strength have been made [2–5]. In all these advances, however, stresses and temperature of a critical component location need to be computed for the operation conditions it sees, before these advanced techniques can yield practical results for health monitoring. Since stresses and temperatures are computed with detailed numerical models, it is impractical to do the same on an every flight basis. In order to be able to capture the important information necessary in a timely manner, a reduced model concept was introduced [6]. The results of using impulse response model for model reduction were demonstrated for a Honeywell engine [6]. The idea of the model reduction (illustrated in Fig. 1) was to be able to build a dynamic model of the temperature or stress at a critical location as a function of changing gas temperature or engine speed. In Ref. [6], the impulse response model was used as the system was close to linear. However, in highly nonlinear systems, the temperature or stress response cannot be predicted accurately by an impulse response model. In this paper, we describe the development and use of dynamic neural networks as a tool for model reduction for near real-time computation of critical location temperatures and stresses.

The objective of model reduction is to take an existing numerical model (thermal, stress, fluid flow) that predicts detailed spatial and temporal quantities, and condense it so that instead of the detailed predictions, only task-specific targeted quantities are predicted, albeit at a fraction of the cost to computational resources. This usage of the knowledge of design phase numerical model in an online system is novel. Another unique aspect of this work is the creation of a dynamic model, as opposed to a static model, since dynamic stresses and temperatures are very important in the calculation of remaining life.

Model reduction, as explained above, can be achieved in various ways such as system identification methods, neural networks, regression techniques, and so on. In the case of finite element models, however, there is literature in the area of *reduced-order* modeling, which is distinct from the approach in this paper. Algorithms have been developed for solving transient thermal problems in a reduced subspace of the original discretization space [7]. Mass and stiffness matrices can be reduced with the Guyan reduction method [8], decreasing the size of the model. However, later literature indicates that it cannot be successfully applied to dynamic thermal problems and that in fact, cruder finite element approximations do better [9]. Model size reduction using compo-

[1]Corresponding author.

Contributed by the International Gas Turbine Institute of ASME for publication in the JOURNAL OF ENGINEERING FOR GAS TURBINES AND POWER. Manuscript received June 28, 2006; final manuscript received July 24, 2006; published online January 11, 2008. Review conducted by Lee Langston. Paper presented at the ASME Turbo Expo 2006: Land, Sea and Air (GT2006), Barcelona, Spain, May, 8–11, 2006, Paper No. GT2006-91099.

Copyright © 2008 by ASME

Downloaded 02 Jun 2010 to 171.66.16.107. Redistribution subject to ASME license or copyright; see http://www.asme.org/terms/Terms_Use.cfm

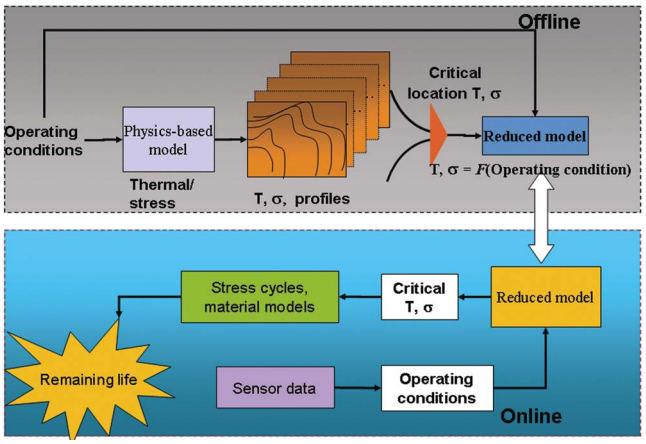

Fig. 1 Model reduction concept

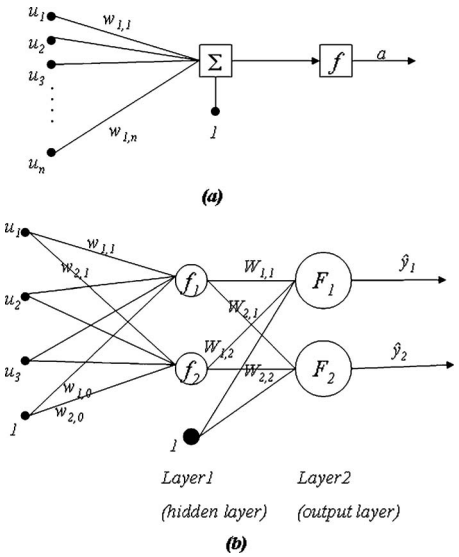

Fig. 2 Neural network schematics (*a*) neuron and (*b*) example network

nent mode synthesis has been applied to turbine engine disk temperature calculation [10]. In this method, nodal degrees of freedom are divided into two sets—active and omitted. Active degrees of freedom are translated into the reduced model, while omitted ones are replaced by the most important modal shapes.

The above model-order reduction techniques require all inputs to the finite element model including nodal boundary conditions, which can be in the hundreds or more, and are applicable when the output required is of the same magnitude as the full numerical model. These reduced-order models are strictly applicable to only the full finite element model part of the process. In other words, we cannot include in the reduced-order model, models that provide the boundary conditions themselves, such as the performance model. These reduced-order modeling techniques have been generally applied for ease of use of complex models or combination of models. In our case, however, the reduced model needs to predict temperature and stress in certain locations, and also reduce the input space as much as possible.

With these considerations in mind, work was done toward developing system identification techniques for the purpose of computing stress and temperature at the life-critical locations Honeywell propulsion engines [6]. The impulse response method was used to compute temperatures and stresses. This technique lends itself well to systems that exhibit linear or close to linear behavior. For components that show nonlinear behavior, however, other methods need to be explored. We present the use of *dynamic neural networks* for computing stresses and temperatures at critical locations of Honeywell turbomachinery components. The following sections provide a brief background of neural networks and describe the approaches taken in developing the current method.

Neural Networks

Neural networks are nonlinear empirical model structures. Neural networks have been used in deriving models for complex and nonlinear systems, where developing physics-based models could be extremely time consuming and not very accurate. Neural networks have been used for diverse fields such as control, insurance, banking, image processing, and medicine. In our case, we wish to derive a reduced dynamic model for computation of critical location temperature and stress of an engine component for application such as health or usage monitoring of aircraft systems. A very brief introduction to neural networks is given below. For more in-depth study, other references should be consulted [11,12].

Figure 2(*a*) illustrates a neuron, the basic processing element for a neural network. A neuron takes a number of inputs (u), multiplies them by a constant (weight), then sums them up, and uses the result as input to a singular valued activation function f as shown. Figure 2(*b*) illustrates a feedforward neural network with two layers, three inputs, two hidden nodes, and two outputs.

Here, the weighted inputs are processed through function f. This is the first layer of the network. The outputs from this layer are in turn processed through the output layer function F, giving us the network outputs, $\hat{y}$. This can be mathematically represented as

$$\hat{y}_i(w,W) = F_i\left[\sum_{j=1}^{q} W_{ij} f_j\left(\sum_{l=1}^{m} w_{jl}u_l + w_{j0}\right) + W_{i0}\right] \tag{1}$$

Common activation functions used for f and F are the sigmoid or hyperbolic tangent (tanh) function, linear transfer function, and the step transfer function.

Training the network is the process of finding the optimum weights w and W that will give the best match with the known target outputs from the data. This is accomplished through methods such as backpropagation and its variations, and quasi-Newton methods such as Levenberg–Marquard all of which differ in speed, memory requirements, etc. The neural network described above, also known as multilayer perceptron network, is directly applicable to static systems. In the next section, we describe the extension to developing models of dynamic systems.

Dynamic Neural Networks

System Identification Background. In general, given a system's input and output data, the science of deriving a dynamic model from the data is called system identification. There are many different methods and model structures in system identification, as applied to linear systems. Dynamic neural networks [1] complement the suite of system identification techniques by extending to nonlinear systems. A general input-output linear model for a single-output system with input u and output y can be written as

$$A(q^{-1})y(t) = \frac{B(q^{-1})}{F(q^{-1})}u(t-nk) + \frac{C(q^{-1})}{D(q^{-1})}e(t) \tag{2}$$

where u denotes the input; $e(t)$ is the disturbance signal; A, B, C, D, and F are polynomials in terms of the time shift operator q; and nk denotes the time delay.

Downloaded 02 Jun 2010 to 171.66.16.107. Redistribution subject to ASME license or copyright; see http://www.asme.org/terms/Terms_Use.cfm

$$A(q^{-1}) = 1 + a_1 q^{-1} + \cdots + a_n q^{-n}$$

$$B(q^{-1}) = b_0 + b_1 q^{-1} + \cdots + b_n q^{-n}$$

$$C(q^{-1}) = 1 + c_1 q^{-1} + \cdots + c_n q^{-n} \tag{3}$$

$$D(q^{-1}) = 1 + d_1 q^{-1} + \cdots + d_n q^{-n}$$

The time shift operator is a notation that works on a function thus

$$q^{-d} x(t) = x(t-d) \tag{4}$$

Some linear model structures are auto regressive, external inputs (ARX), (output error) (OE), ARMA, ARMAX, etc. We describe the ARX and OE linear model structures below, since they are going to be used in the model structure for the dynamic neural network. For a linear ARX model, the above equation simplifies to

$$A(q^{-1}) y(t) = B(q^{-1}) u(t - nk) + e(t) \tag{5}$$

Ignoring the noise term, the above equation can be written as

$$y(t) + a_1 y(t-1) + \cdots + a_{na} y(t - na) = b_1 u(t - nk) + \cdots + b_{nb} u(t - nk - nb + 1) \tag{6}$$

Once the parameters a_1 through a_n and b_1 through b_n are determined, the output y can be predicted in terms of past inputs and past outputs. The number of past inputs and outputs to be used is given by the order of the system $[na\ nb\ nk]$, where na is the number of past outputs, nb the number of past inputs, and nk the time delay. For multiinput systems, nb and nk are vectors with as many entries as the number of input channels. For multiple outputs, na is a vector as many entries as the number of outputs.

For a linear OE model, the above equation simplifies to

$$y(t) = [B(q^{-1})/F(q^{-1})] u(t - nk) + e(t) \tag{7}$$

The parameters of the OE model structure are estimated using a prediction error method. In this case, the prediction $\hat{y}$ can be computed in terms of past inputs and past output predictions.

Dynamic Neural Networks

For dealing with nonlinear system identification, one approach is to use the feedforward network but use input structures similar to the linear system identification model structures, such as ARX, OE, ARMAX, etc. Norgaard [13] has implemented a toolbox for just such an approach and the same approach has been followed in this work. The neural network implementation of ARX model structure is called Neural Network ARX (NNARX), and that for OE model structure is called NNOE, and so on. Nonlinear counterparts to the linear model structures are obtained by

$$\hat{y}(t) = g[\varphi, \theta] \tag{8}$$

where g is the function realized by the neural network, φ is the regression vector, and θ is the vector containing the weights.

For the above representation, the regressors for the NNARX model structure is given by

$$\varphi(t) = [y(t-1), \ldots, y(t-na) u(t-nk), \ldots, u(t - nk - nb + 1)] \tag{9}$$

Similarly, the regressors for the NNOE model structure is given by

$$\varphi(t) = [\hat{y}(t-1), \ldots, \hat{y}(t-na) u(t-nk), \ldots, u(t - nk - nb + 1)] \tag{10}$$

As we can see, the NNOE regressors have the past predictions of the output rather than actual past outputs. These representations are depicted schematically in Fig. 3.

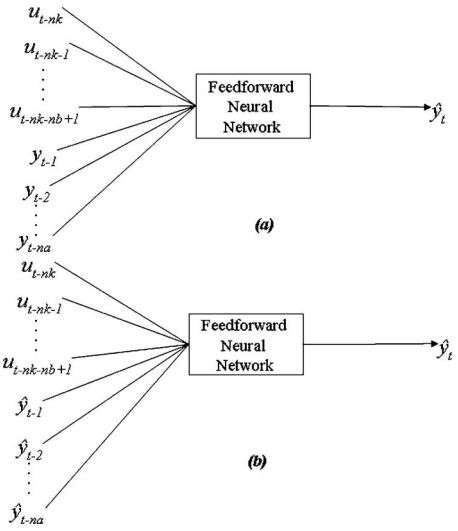

Fig. 3 (*a*) NNARX model structure and (*b*) NNOE model structure

Dynamic Neural Network Development and Implementation

Problem Domain Definition and Selection of Input(s). Before the dynamic neural network model is built, the domain and inputs need to be defined well. Figure 4 shows different domain boundaries that can be considered for this problem, As in the previous work on impulse response model, we choose domain boundary 3 [6]. Selecting boundary 3 implies that various performance model outputs such as engine station parameters (gas temperature, pressure, flow) and engine speed would be used as inputs to the dynamic neural network model.

Model Structure Selection. The next step in the development is selection of the model structure. In our case, the problem is unique from the system identification point of view in that the outputs (critical location metal temperature or stress) are not likely to be measured or computed with the original models during operation. However, we do have the original model outputs from different flight profiles, for training purposes. Therefore, during training, the NNARX model structure is used to get the full benefit of the original model outputs. During validation, the NNOE model structure is used, so that past predictions are used as inputs in place of the past outputs. This ensures that during operation, when no past outputs are likely to be present, the past predictions can be used, and that we validate our approach to real conditions.

We use the two-layer network architecture as shown in the ex-

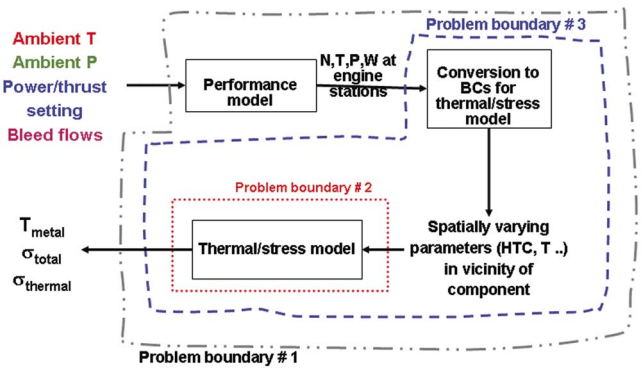

Fig. 4 Problem domain and input selection

Downloaded 02 Jun 2010 to 171.66.16.107. Redistribution subject to ASME license or copyright; see http://www.asme.org/terms/Terms_Use.cfm

ample. The other phases of model structure selection is the selection of number of hidden nodes, selection of model order (number of past inputs and outputs), and time delay. Several experimental runs were conducted to arrive at good combinations of these parameters, with help from physical insights into the system responses. The hyperbolic tangent (tanh) and linear functions were used as the activation functions for the hidden and output layers. All implementation was done in MATLAB. Results are described in the next section. Once the weights are found, the output predictions can be computed by Eq. (1).

Critical Node Temperature Predictions for Engine Component. The dynamic neural network method was applied to predict the temperature at several critical locations of a Honeywell turbomachinery component. The inputs used were rotational speed (N), related gas temperature (T_g), and gas flow (W_g) near the component. A two layer architecture of one hidden layer and one output layer was used. The usual procedure of tweaking the inputs, model structure, the network, and the system order was followed to learn from the interim results and obtain the best model. Finalizing the number of past inputs to be used for each physical input (N, T_g, and W_g) takes some trial and error and physical insight for that particular location. For example, for a location with a slow thermal response, the number of past inputs should be higher. In the following results, eight hidden nodes with three physical inputs were used. The order of the system used for these results were as follows:

(a) number of past outputs (na): 1
(b) number of past inputs (nb): [4 8 2] (for inputs N, T_g, and W_g)
(c) number of time delays (nk): [1 1 1] (for inputs N, T_g, and W_g)

The regressors in this case can be written as (see Eq. (9))

$$\varphi(t) = [T(t-1) \quad N(t-1) \quad N(t-2) \quad N(t-3) \quad N(t-4)$$
$$T_g(t-1) \quad T_g(t-2) \quad T_g(t-3) \quad T_g(t-4) \quad T_g(t-5)$$
$$T_g(t-6) \quad T_g(t-7) \quad T_g(t-8) \quad W_g(t-1) \quad W_g(t-2)]$$

The above regressors serve as inputs (u_i) to the neural network representation in Eq. (1). The actual metal temperature predicted from the original model serves as $\hat{y}$ during training. We use the linear and hyperbolic tangent functions, respectively, for activation functions F and f [14–17].

Once the physical inputs, the number of past inputs, and the number of hidden neurons have been identified, the model structure definition is complete. Norgaard's toolbox is used to train the network and obtain the weights using the training data sets. The toolbox uses the Levenberg–Marquard method for training the network. Once the weights w and W are found, the outputs are calculated by use of Eq. (1). Because of the availability of toolboxes, the bulk of the work is done in experimenting to find the optimum model structure, inputs, and model order. Several realistic flight profiles were used for the training and validation of the neural networks model. Out of the nine flight profiles available, six were used for training and the rest for validation.

Figures 5–8 show the results comparing the temperatures obtained by the dynamic neural network model and the original finite element thermal model. Figure 5 displays the comparison for flight profiles (a), (b), and (c) for critical location 1. The data in these flight profiles were used for training and the maximum error between the original and reduced model is very small. Figure 6 shows the comparison for three flight profile data that the neural network model had not seen (validation data) for the same critical location. These flight profiles are a more rigorous test of the reduced model performance, and as can be seen from the plots, the reduced model results match very well with the original model

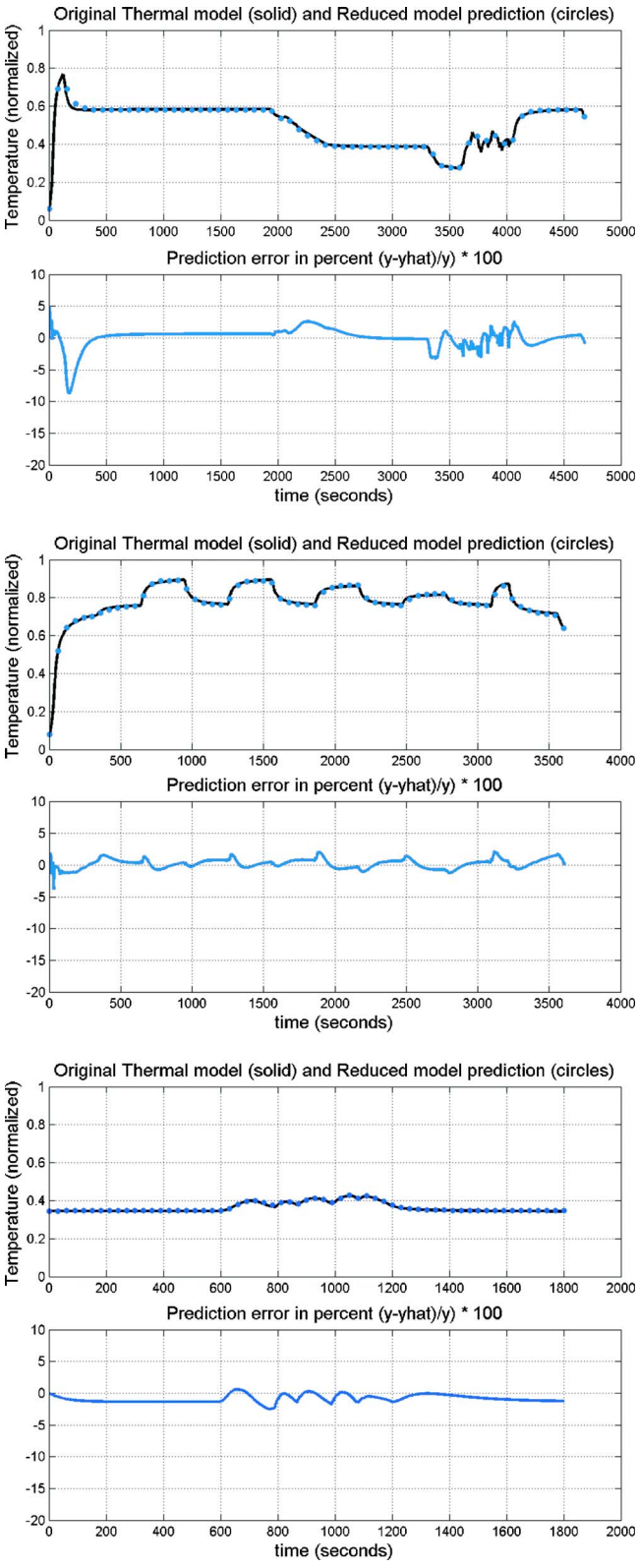

Fig. 5 Critical location 1 temperatures for different flight profiles (training data)

results, with maximum error of 10%.

Figures 7 shows the plots of critical location 2 temperatures against mission time, for flight profiles used for training. While (a) and (b) represent a full flight profile, (c) represents minor fluctuations that could be part of a full flight. In all cases, the error

Downloaded 02 Jun 2010 to 171.66.16.107. Redistribution subject to ASME license or copyright; see http://www.asme.org/terms/Terms_Use.cfm

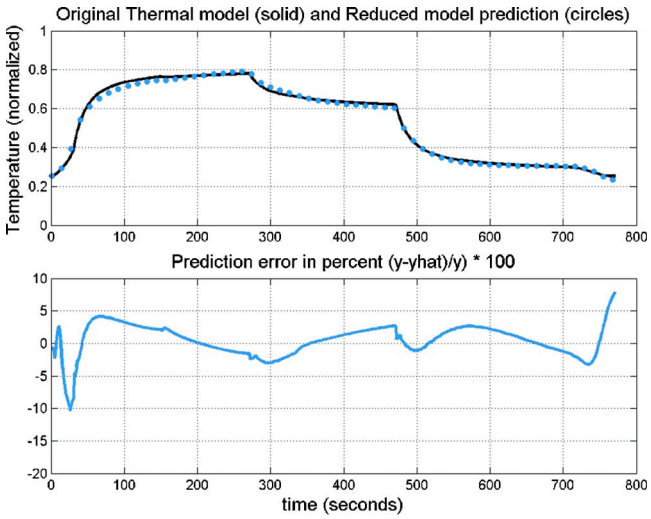

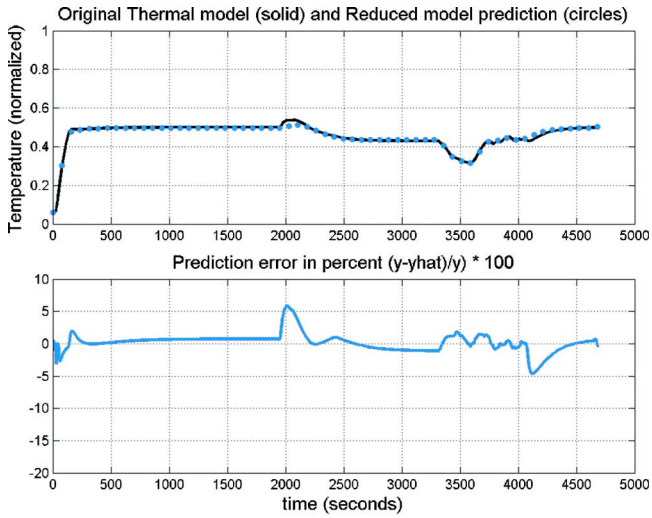

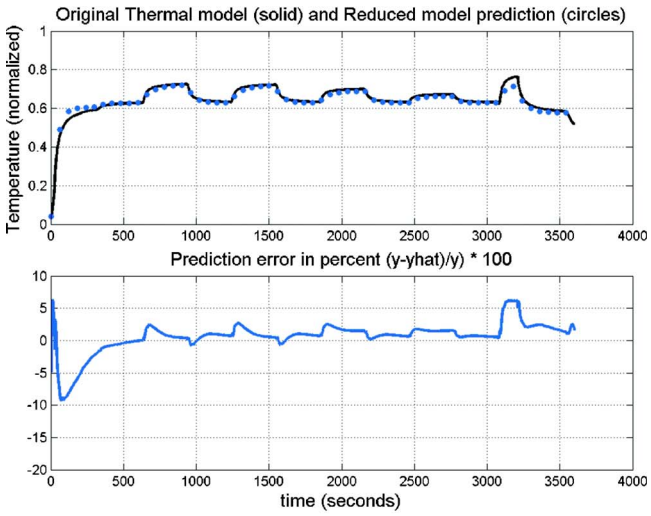

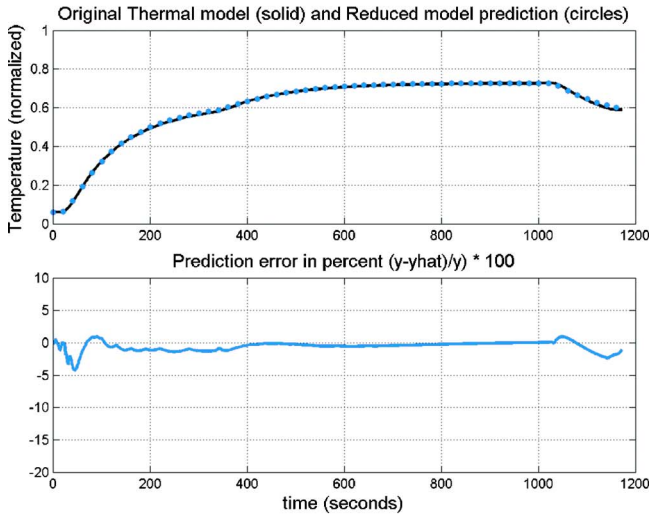

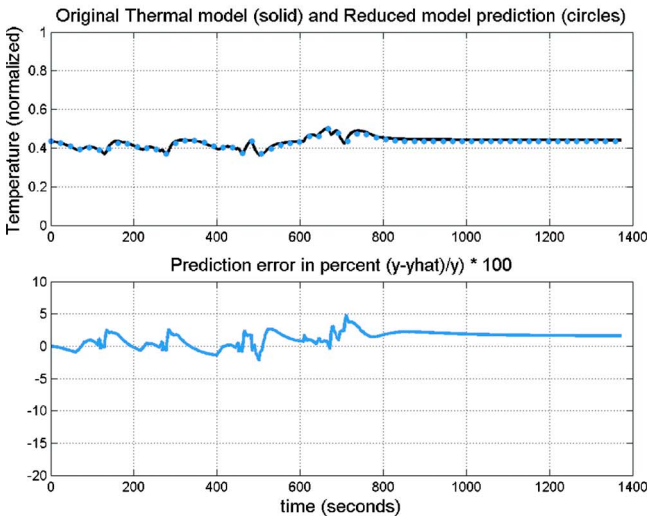

Fig. 6 Critical location 1 temperatures for different flight profiles (validation data)

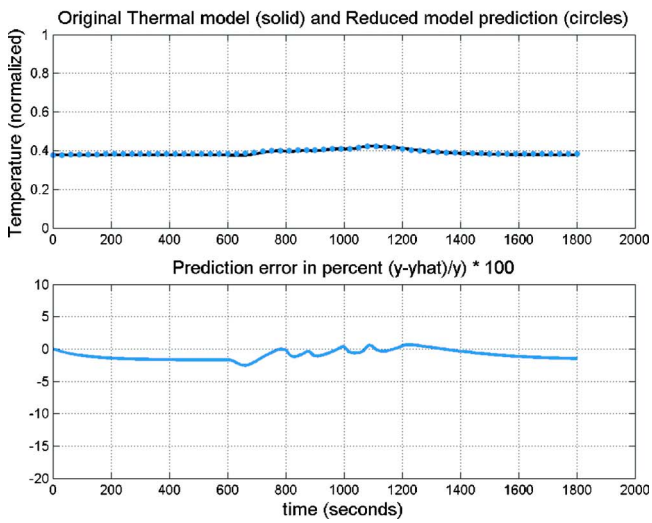

Fig. 7 Critical location 2 temperatures for different flight profiles (training data)

rate is small, within 5%. Figure 8 shows the critical location 2 temperatures, for validation flight profiles that were not used for training. Other than in flight profile (*a*), the error between the original and reduced models show good agreement, within 10%.

Discussion

One of the sources for the errors shown is the difference in the model structure used for validation versus training. As discussed in the section model structure selection, we used the NNARX

Downloaded 02 Jun 2010 to 171.66.16.107. Redistribution subject to ASME license or copyright; see http://www.asme.org/terms/Terms_Use.cfm

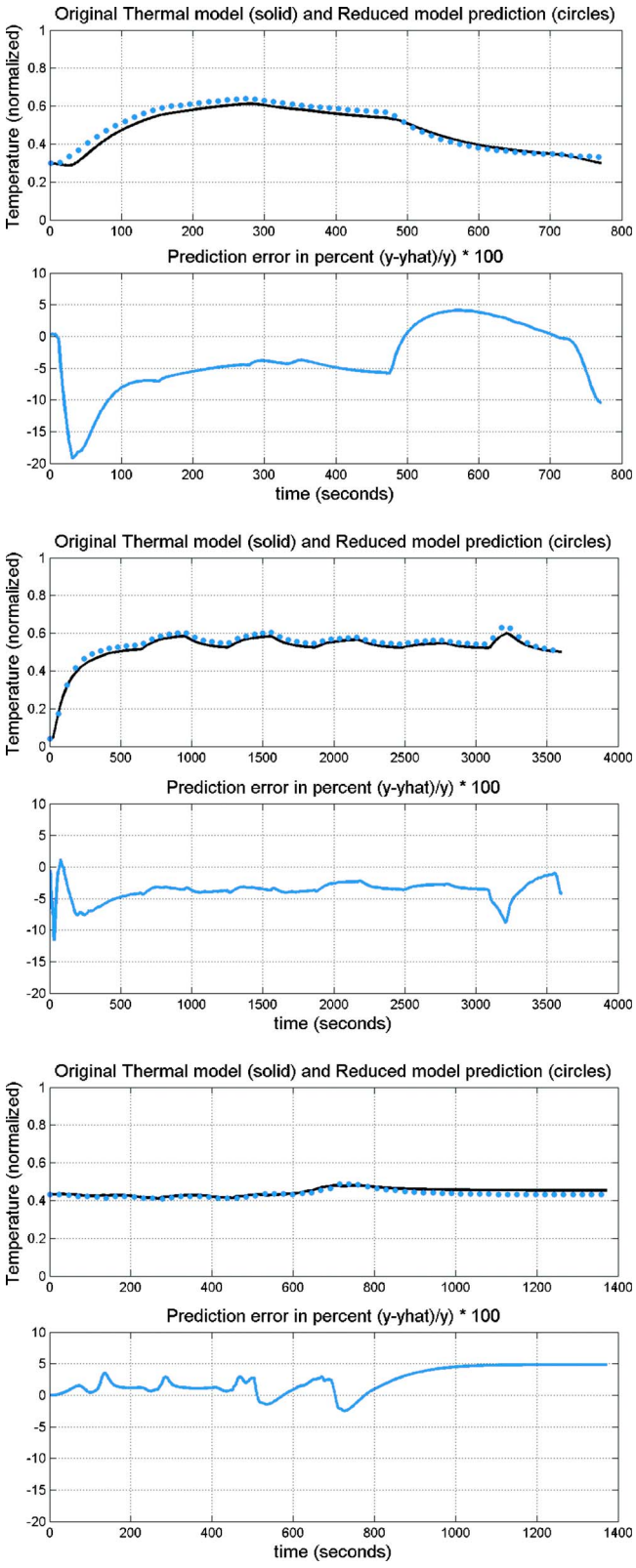

Fig. 8 Critical location 2 temperatures for different flight profiles (validation data)

model structure for training, and the NNOE model structure for validation. This is because actual past outputs (metal temperatures) will not be available during operation of the real system. As a result, the regressor $T(t-1)$ is the actual metal temperature from the original model for training, and the neural network model predicted metal temperature during validation.

Another cause for some of the errors is the "one size fits all" approach for the implementation where the same model structure was used for all critical locations. Structure in this context means the inputs, model order, delays, and number of neurons. During the initial development of this approach, several locations in one component were being evaluated for temperature estimation. Since each location was physically situated differently with the gas path and its fluctuations, each had its own thermal response characteristic. It would have been ideal to fit each with a separate neural net model. However, at the demonstration phase of this work, the question to be resolved was "would this approach be feasible to estimate metal temperature within a certain percentage?" Considering that we were evaluating multiple locations with multiple flight profiles, the additional permutations of varying the model structure (inputs, number of past inputs, delays, number of neurons) would have been very large. It was decided to fix the model inputs and order at an optimum for all locations. By developing a different model structure that fits the temperature response characteristics of each location better, these errors can be minimized. During implementation, different model inputs, order, delays, and neurons were used for different locations and components, to meet the accuracy constraints of temperature prediction.

In neural network modeling, under- and overtraining can be sources of errors. With undertraining, sufficient data are not available to capture all features of the system. Since a model is the source of training data, undertraining is not a serious concern here. Overtraining can happen if the amount of data is very large and the network may be capturing insignificant details (such as those with noise) at the expense of capturing the significant ones. In our case, noise is not a factor because the data are generated by a model. However, some parts of a flight profile such as a long steady state phase (see Fig. 5(*a*)) could contribute to overtraining at the expense of capturing shorter transients. In such a case, the repetitive or redundant data can be removed during training, taking care to keep enough of that feature for training, and added back during testing. This was done for the flight profiles shown in Figs. 5(*a*) and 7(*a*).

Another point to be noted is that the validation flight profiles were chosen to be different from the training flight profiles. The dynamics in each case could be different, although the static conditions enveloped the validation sets. The validation sets illustrate the scenario, wherein a dynamic behavior is being estimated with the model trained on different operating dynamics, and hence possibly different dynamic behaviors.

A concern, or rather a challenge, of the neural network technique is finding the right amount of training data to cover all possible operating conditions and dynamics so that the model generalizes well to new inputs during operation. There may well be a case when the network encounters inputs or dynamics that are out of the data range that it was trained on. The network predictions could then have large errors. The remedy is to train the network on all known limits of operating conditions and dynamics. Periodic retraining and updates of network weights with real operating data would also go a long way to remedy this limitation.

Conclusions

A model reduction technique for computing critical component parameters for remaining life prediction was demonstrated. A dynamic neural network model was developed for the computation of engine critical location metal temperatures. The dynamic neural network model reduces the original thermal model of a turbomachinery component, so that the temperatures can be computed on the fly if needed. Results for two critical locations of a component were presented. The results show that such techniques can be

Downloaded 02 Jun 2010 to 171.66.16.107. Redistribution subject to ASME license or copyright; see http://www.asme.org/terms/Terms_Use.cfm

applied with minimal error for computing remaining life estimates, while taking into account the actual operating conditions of the turbomachinery.

The same approach can also be used for the computation of thermal stress at the critical location. There are several other applications for the model reduction concept, where the potential for detailed models can be exploited for estimating quantities that cannot be measured.

Nomenclature

u = input
y = output
$\hat{y}$ = predicted output
f, F = activation functions
w, W = network weights
A, B, F, C, D = polynomials identifying model structure
q = time shift operator notation
e = disturbance signal
t = time or sample
na = number of past outputs
nb = number of past inputs
nk = time delay
φ = regression vector
θ = vector containing weights
N = rotational speed
T = metal temperature at critical location
T_γ = gas temperature
W_g = gas flow

References

[1] Larsen, J. M., Russ, S. M., Rosenburger, A. H., John, R., Fecke, T., and Rasmussen, B., 2002, "Achieving the Potential of Material Prognosis for Turbine Engines," DARPA Bidders Conference on Materials Prognosis, Washington, DC.

[2] Fujimoto, W. T., 2002, "A Critical Assessment of Fatigue Prediction Methodologies for Rotorcraft Members," Sixth Joint FAA/DoD/NASA Conference on Aging Aircraft, San Francisco, CA.

[3] Forth, S. C., Everett, R. A., and Newman, J. A., 2002, "A Novel Approach to Rotorcraft Damage Tolerance," Sixth Joint FAA/DoD/NASA Conference on Aging Aircraft, San Francisco, CA.

[4] Kwon, Y. S., Fawaz, S. A., and Ingram, J. E., 2002, "3D Finite Element Modeling of MSD-Cracked Structural Joints," Sixth Joint FAA/DoD/NASA Conference on Aging Aircraft, San Francisco, CA.

[5] Cope, D. A., Lacy, T. E., and Luzar, J. J., 2002, "Application of Advanced Fracture Mechanics Methods for KC-135 Fuselage Structural Integrity Evaluation," Sixth Joint FAA/DoD/NASA Conference on Aging Aircraft, San Francisco, CA.

[6] Parthasarathy, G., and Allumallu, S., 2004, "Reduced Models for Rotating Component Lifing," *Proceedings of ASME Turbo Expo 2004*, Vienna, Austria, Jun. 14–17, 2004.

[7] Cardona, A., and Idelsohn, S., 1986, "Solution of Non-linear Thermal Transient Problems by a Reduction Method," Int. J. Numer. Methods Eng., **23**, pp. 1023–1042.

[8] Guyan, R. J., 1965, "Reduction of Stiffness and Mass Matrices," AIAA J., **3**(2), p. 380.

[9] Bushard, L. B., 1981, "On the Value of Guyan Reduction in Dynamic Thermal Problems," Comput. Struct., **13**, pp. 525–531.

[10] Botto, D., Zucca, S., Gola, M. M., and Salvano, S., 2002, "A Method for On-line Temperature Calculation of Aircraft Engine Turbine Discs," *Proceedings of ASME Turbo Expo 2002*, Amsterdam, The Netherlands.

[11] Haykin, S., 1999, *Neural Networks: A Comprehensive Foundation*, 2nd ed., Prentice-Hall, Englewood Cliffs, NJ.

[12] Norgaard, M., Ravn, O., Poulsen, N. K., and Hansen, L. K., 2000, *Neural Networks for Modeling and Control of Dynamic Systems*, Springer-Verlag, London.

[13] Norgaard, M., 2000, "Neural Network Based System Identification Toolbox, Version 2," Technical University of Denmark.

[14] Ogunnaike, B. A., and Ray, W. H., 1994, *Process Dynamics, Modeling, and Control*, Oxford University Press, New York.

[15] Korb, R., Skorjanz, P., and Jorgl, H. P., 1997, "Black Box Modeling of an Industrial Combustion Plant," SYSID'97, 11th IFAC Symposium on System Identification, Kitakyushu, Japan.

[16] Bittani, S., and Lovera, M., 1997, "Identification of Linear Models for a Hovering Helicopter Rotor," 11th IFAC Symposium on System Identification, Kitakyushu, Japan.

[17] L., Ljung, 1987, *System Identification: Theory for the User*, P.T.R. Prentice Hall, Englewood Cliffs, NJ.

Downloaded 02 Jun 2010 to 171.66.16.107. Redistribution subject to ASME license or copyright; see http://www.asme.org/terms/Terms_Use.cfm

Spiral Vibration of a Turbogenerator Set: Case History, Stability Analysis, Measurements and Operational Experience

Lothar Eckert
ALSTOM,
Zentralstrasse 40,
5242 Birr, Switzerland

Joachim Schmied
DELTA JS AG,
Technoparkstrasse 1,
8005 Zurich, Switzerland

A hydrogen-cooled turbogenerator operating at 3600 rpm showed the phenomenon of spiral vibration with a forward rotating unbalance vector. The relative shaft vibration measured at the non-driven end-bearing was close to the trip level. Spiral vibration is observed at various types of rotating machinery with both rotation directions of the unbalance vector, i.e., forward and backward. Spiral vibration is caused by a vibration-induced hot spot on the shaft surface generated by friction. The turbogenerator has three bearings: two main bearings and the brush gear bearing. The carbon brushes sliding on the slip rings were identified as the hot spot location. Potential modifications were studied using hot spot stability analyses with a rotor dynamic model of the generator rotor on three journal bearings. The applied method, introduced by Schmied (1987, "Spiral Vibrations of Rotors" Proc. 11th Biennial ASME Design Engineering Div. Conf., Vib. Noise, DE-Vol. 2, Rotating Machinery Dynamics, Boston, MA, ASME H0400B, pp. 449–456), allows the handling of general systems. The hot spot model is based on the theory of Kellenberger (1978, Ingenieur-Archiv, 47, pp. 223–229; 1980, Journal of Mechanical Design, 102, pp. 177–184) using a thermal equation between the shaft's thermal deflection and the shaft displacement at the hot spot location. Three different relations between the heat input and the shaft vibration were modeled: heat input proportional to the shaft displacement, to the shaft velocity, and to the shaft acceleration. The model, in which the heat input is proportional to the velocity, is the most suitable variant for slip rings. This was confirmed by comparison with the measured vibration behavior. A modification of the shaft line was selected based on the calculation results and was successfully implemented. This generator and other generators with the same modified brush gear unit have been in operation for more than four years. [DOI: 10.1115/1.2747645]

Keywords: Newkirk effect, vector turning, rotating unbalance vector, rub, hot spot phenomenon

Introduction

Spiral vibration is a phenomenon that is observed in various types of rotating machinery, e.g., compressors, water turbines, steam turbines, and turbogenerators. It is caused by a vibration-induced hot spot on the shaft surface generated by friction due to "soft" rubbing of the shaft to stationary (non-rotating) parts, e.g., labyrinth seals, seal rings, oil film of journal bearings, hydrogen seals, or brushes on slip rings. Spiral vibration is characterized by circular loops of the measured unbalance response vector on a polar plot (Fig. 1(*a*)) or by sinusoidal variation in amplitude versus time plots (Fig. 1(*b*)).

The phenomenon is also referred to as Newkirk-effect [1] and rotating vectors or vector turning [2]. The mechanism for the case of a hot spot caused by viscous shearing with the lubricant of a journal bearing is often referred to as the Morton effect [3–7]. Various rub-related phenomena are described in the literature survey of Muszynska [8].

An increasing magnitude of the spiral, which does not end in a limit cycle, leads to an unacceptable high level of vibration and enforces a shutdown of the machine. Spiral vibration on a limit cycle - vector turning - with low amplitude is acceptable if the cause of the heat input is known and is of no concern for any machine component. The rotation of the unbalance vector is slow with periods T for one 360 deg turn of the vector between 20 min and several hours (Table 1). On turbogenerators, both rotation directions were observed: backward and forward rotation of the unbalance response vector. The classic case of a backward rotating vector due to heat input proportional to the shaft displacement is well described in textbooks [2,9]. The forward rotating vector is explained with a simplified two-degrees-of-freedom system in [2] by inertia modulated heat input proportional to the shaft acceleration.

This paper describes the case history of a 450 MVA, 3600 rpm hydrogen-cooled turbogenerator equipped with a brush gear unit, which showed the phenomenon of spiral vibration with a forward rotating unbalance vector. This case could only be described with a model where the heat input was proportional to the shaft velocity. According to the authors' knowledge, this case has not yet been studied in the literature. The root cause analysis, the hot spot stability analyses using three different heat input models, and finally the successful modification, are described further below. The operational experience of other turbogenerators that were delivered with the modification is described.

Case History

Prior to release of turbogenerator up rates, the machine is tested to verify all electrical and performance data. The turbogenerator is

Contributed by the International Gas Turbine Institute of ASME for publication in the JOURNAL OF ENGINEERING FOR GAS TURBINES AND POWER. Manuscript received April 30, 2007; final manuscript received May 6, 2007; published online January 11, 2008. Review conducted by Dilip R Ballal. Paper presented at the ASME Turbo Expo 2007: Land, Sea and Air (GT2007), Montreal, Quebec, Canada, May 14–17, 2007. Paper No. GT2007-27314.

Copyright © 2008 by ALSTOM

Downloaded 02 Jun 2010 to 171.66.16.107. Redistribution subject to ASME license or copyright; see http://www.asme.org/terms/Terms_Use.cfm

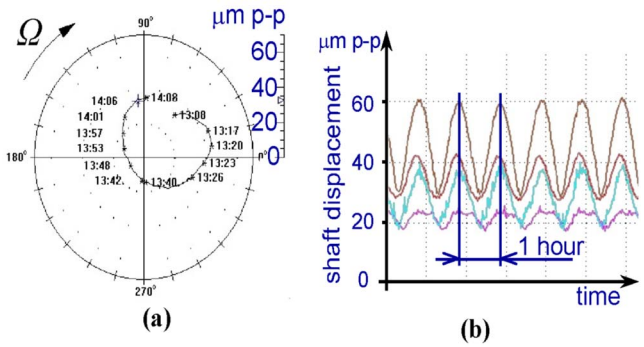

Fig. 1 Measured displacement p-p (peak-to-peak) amplitudes showing spiral vibration: (*a*) polar plot of bearing pedestal vibration; (*b*) amplitude versus time plot of relative shaft vibration

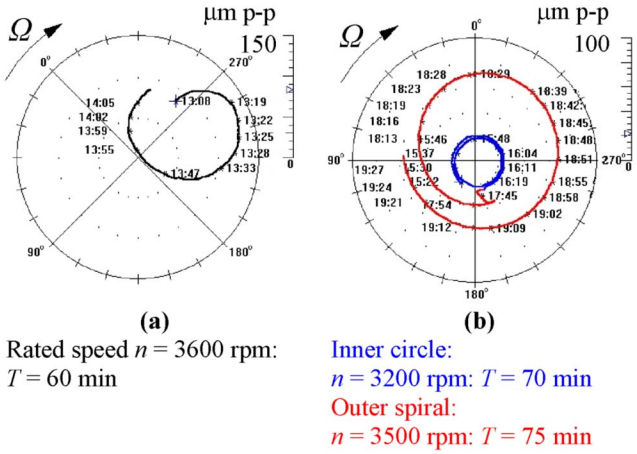

Fig. 3 Polar plots of measured vibration at different rotor speeds *n* and period *T* for one 360 deg turn: (*a*) relative shaft vibration at NDE-bearing; (*b*) horizontal DE-bearing pedestal vibration

mounted on a test stand in the factory and driven by a synchronous motor (Fig. 2). The generator is operated at its rated speed. The drive motor only needs to deliver the losses of the generator (around 1% of the machine's rated power).

During the running test of a hydrogen-cooled turbogenerator with three bearings, spiral vibration with increasing magnitude occurred. In the text below, the three bearings will be referred to as DE- (driven end), NDE- (non-driven end), and end bearings (Fig. 7). The spiral vibration with increasing magnitude would limit the duration of continuous running in the power plant. Immediately, a root cause analysis was started to solve the problem.

Table 1 Cases of spiral vibration, machine types: Compressor (COM), Steam Turbine (ST), Turbogenerator (GEN)

Type	Power	Speed in rpm	Rotation direction of vector *(2)*	Period *T* for 360 deg turn	Ref.
COM	Not given	11,500	(+) Forward	Not given	[6]
		>11,500	(–) Backward		
ST	HP rotor	Rated speed	(–) Backward	0.5 to 2 h	[10]
GEN	100 MW	3000	(–) Backward	20 min	[11]
GEN	650 MW	3600	(–) Backward	3.5 h	[11]
GEN	722 MVA	3600	(–) Backward	3.2 h	[12]
GEN	600 MVA	3000	(–) Backward	Not given	[13]
GEN	760 MW	3600	(+) Forward	3 h	[2]
GEN	450 MVA	3600	(+) Forward	60 to 100 min	[14]
GEN	1180 MVA	3000	(–) Backward	70 to 100 min	[14]
GEN	1180 MVA	2350 *(1)*	(+) Forward		[14]

(1): below rated speed of 3000 rpm

(2): (–): backward (counter-rotational) (+): forward (co-rotational)

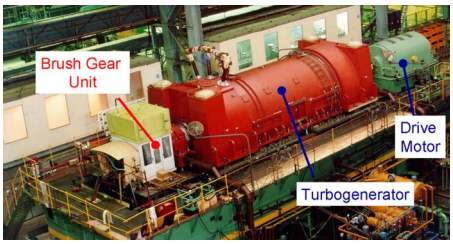

Fig. 2 Turbogenerator during running test in factory

Various tests with the running generator were performed in order to identify the location of the hot spot. In parallel, a hot spot calculation model was set up.

Measured Vibrational Behavior. The generator was run at speeds below rated speed in order to find out the speed range during which the spiral vibration occurs. Figure 3 shows the measured vibrations for 3200, 3500, and 3600 rpm. At 3200 rpm, the magnitude of the spiral was stable and the spiral became a limit circle. Above 3200 rpm, the spiral vibration has increasing magnitude in a wide speed range of more than 400 rpm. At all three speeds, a forward (co-rotational) rotating vector was observed.

Potential Hot Spot Locations

The vibration-induced hot spots may be generated at various locations of hydrogen-cooled turbogenerators, such as:

1. labyrinth seals at the hydrogen seals, bearing pedestals and the brush gear housing
2. oil film in journal bearings
3. seal ring of the hydrogen seals
4. carbon brushes sliding on the two slip rings.

The labyrinth seals were excluded by inspection of the clearances. The journal bearings and the hydrogen seal ring were excluded by variation of the lube oil temperatures and lube oil flows, which did not change the vibrational behavior. A test without carbon brushes revealed that the carbon brushes sliding on the slip rings were the location of the hot spot.

The generator was brought to rated speed without brushes and operated for about 1 h. No spiral vibration occurred. Immediately after insertion of the brushes, which can be done under operational conditions (Fig. 5), spiral vibration appeared with increasing magnitude. After brush removal, the spiral vibration promptly stopped and the vibration vector returned straight to its original position as when the test was started. Figure 4 shows the polar plot of the relative shaft vibration measured at the NDE-bearing during this run.

Brush Gear and Carbon Brushes. The brush gear unit supplies the DC current to the field winding of the generator rotor. The field current of hydrogen-cooled generators is in the range from 3000 A to 7000 A. The slip ring shaft (SR) with two slip rings and a radial fan for cooling is supported by the NDE- and the end-bearing. Carbon brushes sliding on the slip rings transfer the current from the stationary brush holders (Fig. 5) to the rotating slip rings. The slip rings are shrunk on the shaft via soft

Downloaded 02 Jun 2010 to 171.66.16.107. Redistribution subject to ASME license or copyright; see http://www.asme.org/terms/Terms_Use.cfm

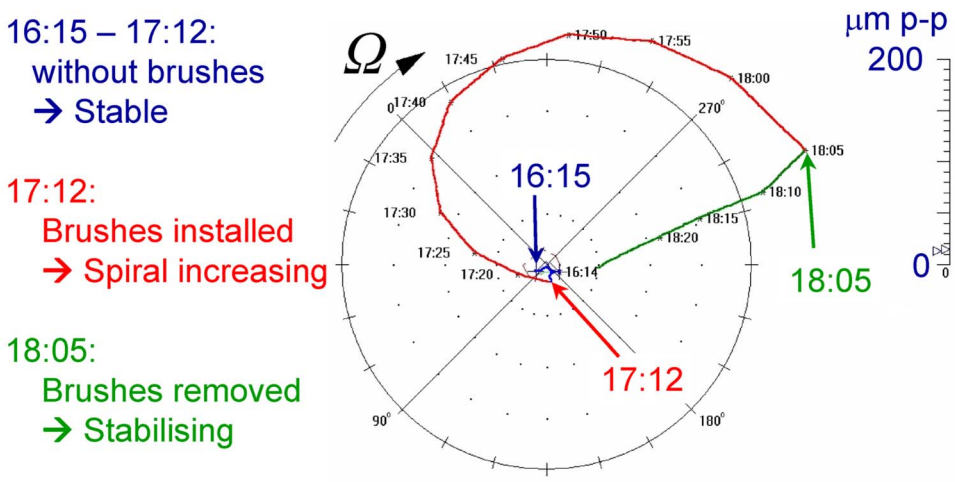

Fig. 4 Measured relative shaft vibration at NDE-bearing. Rotor speed n=3600 rpm.

insulation material for electrical insulation. Nevertheless, the thermal bow of the slip rings is transmitted to the shaft to some extent. Slip ring shafts may be particularly prone to the spiral vibration phenomenon due to the friction heat that is inevitably generated by the brushes. During operation the generated friction heat may increase due to humidity being too low (below 4.5 grams/m^3 H_2O abs.) or current density being too low (below 5.5 to 8 A/cm^2).

Hot Spot Stability Analyses

With a hot spot stability analysis using a rotor dynamic model of the generator rotor, potential modifications were studied. The modeling of the hot spot phenomenon is based on the theory of Kellenberger [11,12] using a thermal equation between the shaft's thermal deflection and the shaft displacement at the location of a hot spot. In case of slip rings, the friction between brushes and shaft causes the hot spot. The contact forces of the brushes around the circumference may vary due to the shaft vibration and cause a thermal bend of the slip ring shaft due to the differential heat input. The stability threshold is determined as a function of the rotor speed and the ratio of the added heat to the dissipated heat at the slip rings. A threshold at low ratio indicates that the shaft is sensitive to hot spots, i.e., little heat input is necessary to destabilize the system.

The calculation method for generalized shaft systems according to Schmied [13] is described in Appendix A.

Three Different Heat Input Models. In the case of slip rings, the friction between the carbon brushes and the slip ring causes the hot spot. The brushes are pressed against the slip ring by roller springs (Fig. 5(*b*)). The pressure around the circumference may vary due to the shaft vibration. In the case of a synchronous vibration, it is always at the same point on the shaft, which is submitted to an increased heat input. The pressure can vary due to the following three mechanisms (Fig. 6, cases a to c). The brush contact force varies:

(a) due to the stiffness of the roller springs
(b) due to the friction in the brush holder, which inhibits the movement of the brush in radial direction
(c) due to the inertia effects of the brushes.

Thus three different relations between the added heat and the shaft vibration were modeled:

(a) heat input proportional to the shaft displacement
(b) heat input proportional to the shaft velocity
(c) heat input proportional to the shaft acceleration.

The calculation method for these three different relations is described in Appendix A (cases a to c).

The most suitable case will be selected by comparison of the analytical results to the practical experience.

Case a: Heat Input Proportional to Shaft Displacement. For a rub with a spring-contact force, this would be the appropriate relation. It is a good approximation for the effect in a journal bearing or labyrinth seals. Kirk's method [5] to estimate the stability is limited to the effect in a journal bearing. A stability criterion is given, although it does not provide a clear stability

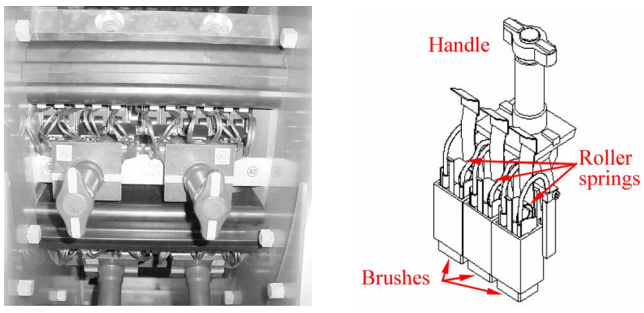

Fig. 5 Brush gear unit: (*a*) view on removable brush carriers; (*b*) brush carrier with three brushes

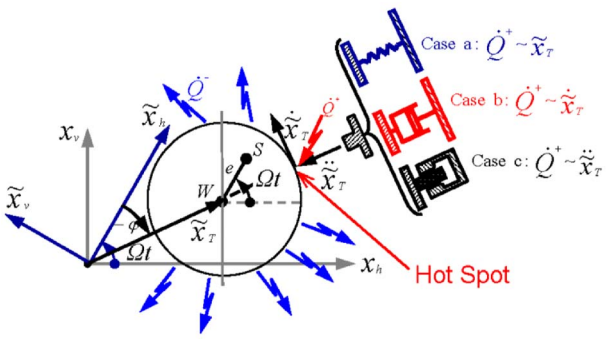

Fig. 6 Three heat input mechanisms of brushes

Downloaded 02 Jun 2010 to 171.66.16.107. Redistribution subject to ASME license or copyright; see http://www.asme.org/terms/Terms_Use.cfm

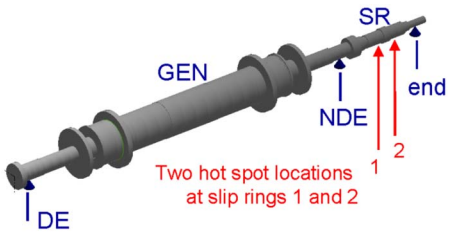

Fig. 7 Rotor model of the turbogenerator with slip ring shaft between the NDE- and the end-bearings

threshold.

However, roller springs (Fig. 5(*b*)) are designed to provide a constant force not dependent on spring displacement or brush wear and thus have very low spring stiffness. Therefore, it is highly likely that one of the other two mechanisms prevails.

Case b: Heat Input Proportional to Shaft Velocity. For a rub with a contact force varying due to Coulomb friction, this would be the appropriate relation. This may be a good approximation for the brushes sliding within the brush holders. It is assumed that the heat input is proportional to the shaft velocity instead of the shaft displacement, since a friction force changes its direction with the direction of the velocity.

Case c: Heat Input Proportional to Shaft Acceleration. For a rub with a contact force varying due to inertia effects, this would be the appropriate relation, e.g., in case the inertia forces of the brush masses themselves would play a role. The heat input is assumed to be proportional to the shaft acceleration.

Rotor Dynamic Model. Figure 7 shows the rotor dynamic model of the turbogenerator.

The model of the turbogenerator with brush gear unit consists of the generator rotor (GEN) and the slip ring shaft (SR), supported on three journal bearings in free-standing pedestals, which are modeled as equivalent mass-spring-damper systems with representative parameters for the horizontal and vertical direction. In Fig. 7, the locations of the slip ring 1 and 2 and the three bearings (DE-, NDE-, and end-bearing) are indicated.

Natural Frequencies and Damping Ratios. Table 2 summarizes the natural frequencies and corresponding damping ratios at rated speed.

The generator rotor has four critical speeds n_k up to a rated speed of 3600 rpm. The first bending modes of the generator (GEN) and the slip ring shaft (SR) have a U-shape. The second bending modes of the GEN rotor have an S-shape.

The natural frequencies of the generator ($k=1$ to 4) are well below rated speed and have a minor influence on the hot spot stability. The modes with largest influence on the hot spot behavior are the two slip ring shaft modes (SR first bending horizontal/vertical) shown in Fig. 8. For these two SR modes the natural frequency and damping ratio as functions of speed are plotted in a Campbell diagram (Fig. 11(a), original design).

Table 2 Natural frequencies and damping ratios at rated speed (six modes)

	Natural frequency		Damping ratio	
k	f_k, Hz	f_k, cpm	D_k, %	Mode shape description, main vibration direction
1	9.99	600	0.5	GEN first-bending, hor.
2	10.75	650	0.3	GEN first-bending, vert.
3	26.57	1590	3.8	GEN second-bending, hor.
4	30.02	1800	0.2	GEN second-bending, vert.
5	55.19	3310	15.4	SR first-bending, hor.
8	82.35	4940	2.5	SR first-bending, vert.

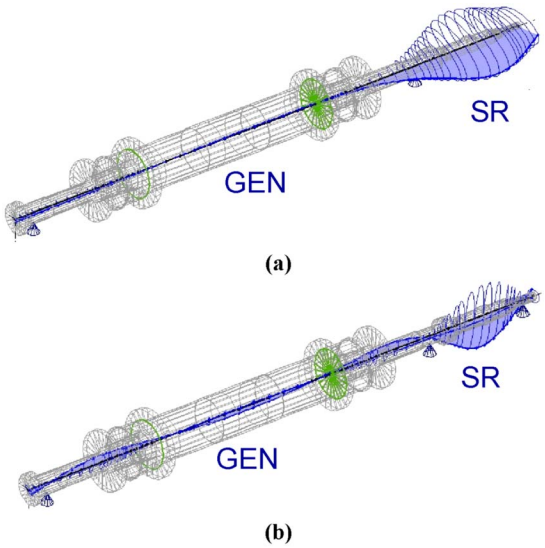

Fig. 8 Slip ring shaft (SR) modes at rated speed: (*a*) horizontal; (*b*) vertical

The rated speed is between the critical speeds of the horizontal and vertical slip ring shaft mode. The natural frequency of the horizontal SR mode (3310 cpm) is close to rated speed. This mode is highly damped, with a damping ratio of 22.5% at its critical speed of 3210 rpm.

Thermal Bow of Shaft. The thermal deformations of the shaft for a temperature difference of 1 K across the section over the seat length of slip ring 1 are shown in Fig. 9. The maximum deflection occurs at slip ring 1 with 2.8 μm/K in horizontal direction and with 2.9 μm/K in vertical direction. For the temperature difference at slip ring 2, the maximum defection are 3.2 μm/K in the horizontal direction and 3.3 μm/K in the vertical direction.

Hot Spot Stability Charts. The hot spot stability analysis as described in Appendix A yields additional natural modes—the so-called hot spot modes. The hot spot modes are the rotor response to the thermal bent shaft, basically an unbalance response.

The assessment of the hot spot stability is carried out in two steps:

1. Determination of the threshold as a ratio of the added to dissipated heat at the slip rings, as a function of the rotor speed. For heat input below the threshold, the vibration am-

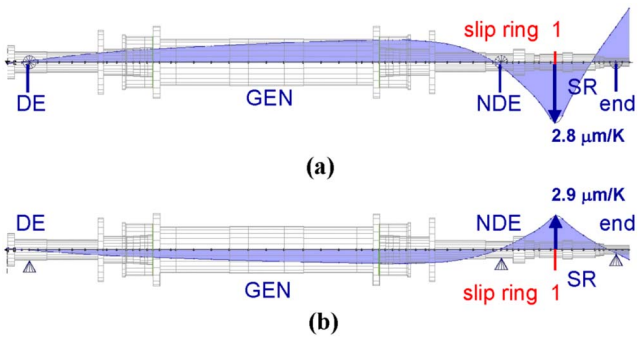

Fig. 9 Thermal deflection due to hot spot at slip ring 1: (*a*) horizontal deflection; (*b*) vertical deflection

Downloaded 02 Jun 2010 to 171.66.16.107. Redistribution subject to ASME license or copyright; see http://www.asme.org/terms/Terms_Use.cfm

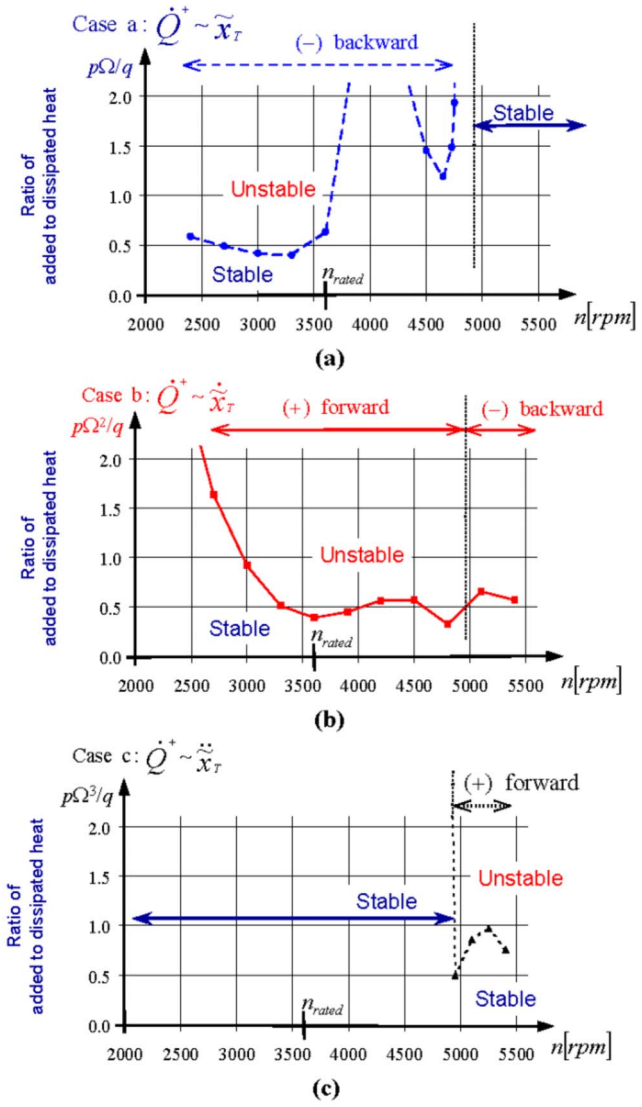

Fig. 10 Stability charts for the three different heat input models: (*a*) case a: heat input ~ shaft displacement; (*b*) case b: heat input ~ shaft velocity; (*c*) case c: heat input ~ shaft acceleration

plitude decays to a value corresponding to the residual unbalance; in the case in which it is above the threshold, the vibration amplitude theoretically increases to infinity. In practice, it will stabilize at a high level due to nonlinearity, which is not considered in the model. The stability threshold primarily is a property of the rotor bearing system and its natural modes.

2. Estimation of the ratio p/q of the added to dissipated heat as done in [13] for heat input proportional to shaft displacement in a journal bearing and heat input proportional to shaft acceleration for brushes on slip rings. In Appendix B, the ratio p/q of the added to dissipated heat as estimated for heat input proportional to shaft velocity.

Figure 10 shows the stability charts for the three different heat input models (Fig. 6). The dimensionless heat ratios for the cases b and c are $p\Omega^2/q$ and $p\Omega^3/q$, respectively. The "±" signs indicate the direction of the unbalance vector turning due to the hot spot: "(+)" for forward (co-rotational) and "(–)" for backward (counter-rotational).

For case b, the ratio $p\Omega^2/q$ for the added to dissipated heat at rated speed is estimated for different radius of the shaft orbit at the slip ring (see Table 3, Appendix B). For small shaft orbits, the estimated $p\Omega^2/q$ ratio lies above the stability threshold in the unstable region. The ratio decreases with increasing vibration level due to nonlinear friction and thus stabilizes at a high vibration level.

Since the model has two hot spot locations, two "thermal" modes appear. One thermal mode is a kind of first bending of the slip ring shaft (temperature differences in phase), and the second mode is a kind of second bending (temperature differences out of phase). The second thermal mode has the higher stability threshold, i.e., the stability is determined by the first mode. In the case of the acceleration heat input model, the second thermal mode is always stable (no threshold exists for this mode). One would have obtained similar results using only one hot spot location for the two slip rings.

The shape of the stability threshold lines are determined mainly by the horizontal and vertical SR resonances:

Case a (Fig. 10(a)). For the displacement heat input model, the threshold is low in the whole speed range below the horizontal SR resonance (3310 rpm). Above this resonance, the threshold increases steeply. Close to the vertical SR resonance, only a small spike with a lower threshold appears. Only backward rotating vectors (–) occur in the whole speed range.

Case b (Fig. 10(b)). For the velocity model, the threshold decreases from low speeds toward the horizontal SR resonance and then remains at a low level for higher speeds. A forward rotating vector (+) occurs below 4950 rpm (vertical SR resonance) and backward (–) above 4950 rpm.

Case c (Fig. 10(c)). The acceleration model is unstable above the vertical SR resonance (4950 rpm) with a forward rotating vector (+) only.

These behaviors can be explained with the simplified two-degrees-of-freedom system used by Adams [2] by the phase angle φ of the response to an unbalance or thermal bending of the slip ring shaft. In case of a small angle φ, i.e., in the subcritical region, the displacement model yields a heat input in the same direction as an unbalance and thus can amplify an initial thermal bending ($\rightarrow$ low threshold). For the velocity model, this situation occurs for a phase angle φ around –90 deg, since the velocity is 90 deg ahead of the displacement. For the acceleration model, this situation occurs only in the supercritical region with phase angles between –90 deg and –180 deg. Thus, the six cases given in Table 3 of [14] may be distinguished.

Selection of the Adequate Heat Input Model. As shown in Figs. 3 and 5, only the forward rotating vector was observed in the speed range from 3200 rpm to 3600 rpm. With the acceleration model (case c), no unstable behavior was calculated at 3600 rpm below the vertical SR resonance. The displacement model (case a) does not show a forward rotating vector at 3600 rpm or at speeds below the vertical SR resonance. This model is also questionable regarding the design of the springs in the brush holder. Roller springs have very low stiffness.

Only the hot spot modes, calculated for case b with the heat input proportional to the shaft velocity, match the observed spiral vibration behavior with forward rotating vector. The stability threshold of case b is low enough at rated speed to explain the increasing magnitude due to the hot spot phenomenon. Therefore, the case b model is used to investigate potential modifications.

The calculated behavior of case b also matches the case of an 1180 MVA, 3000 rpm turbogenerator (Table 1), which showed spiral vibration with a backward rotating vector at 3000 rpm, a forward rotating vector at 2350 rpm and no spiral vibration at 3200 rpm. The slip ring shaft critical speed with 2830 rpm was

Downloaded 02 Jun 2010 to 171.66.16.107. Redistribution subject to ASME license or copyright; see http://www.asme.org/terms/Terms_Use.cfm

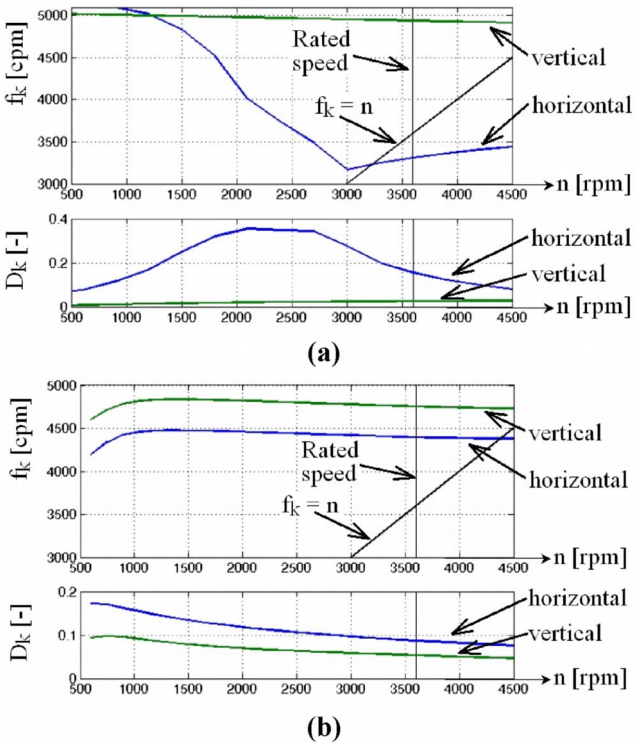

Fig. 11 Campbell diagram of horizontal and vertical slip ring shaft mode: (a) original design; (b) selected modification: five tilting-pad bearings at NDE- and end-bearings

initially too close to rated speed and was shifted to lower speeds by increasing the bearing span of the slip ring shaft to solve the problem.

Potential Modifications and Selected Modification. The following three options were considered:

1. use carbon brushes with low friction coefficient (of 0.14 instead of 0.26 for standard brush);
2. shift the horizontal SR critical speed above rated speed by increased horizontal stiffness of the journal bearings using other journal bearing types;
3. shift both the horizontal and vertical SR-critical speed below rated speed by increasing the bearing span between the NDE- and end-bearing.

The use of low friction brushes (option 1) will reduce the vibration level through the reduction in heat input, however, this will not eliminate the sensitivity of the shaft line to spiral vibration behavior. Option 2 is promising, because the highly damped horizontal SR mode has the main influence on the hot spot behavior. It was studied together with option 3 by calculating Campbell diagrams and hot spot stability charts.

Option 3 would require an increase of the bearing span by more than 1 m and a large effort to implement within the power plant. With option 2, finally an appropriate bearing configuration was found to shift the horizontal SR mode well above rated speed. This bearing modification was selected to overcome the spiral vibration with increasing magnitude. The modification consists of five tilting-pad bearings ("load between pads") at both the NDE- and end-bearings.

Figure 11 compares the natural frequency n_k and damping ratio D_k of the horizontal SR mode for the original and the modified bearing configuration. In Fig. 12 the calculated hot spot stability charts of the original and the modification are shown. The hot spot stability chart of the modified configuration clearly shows that the

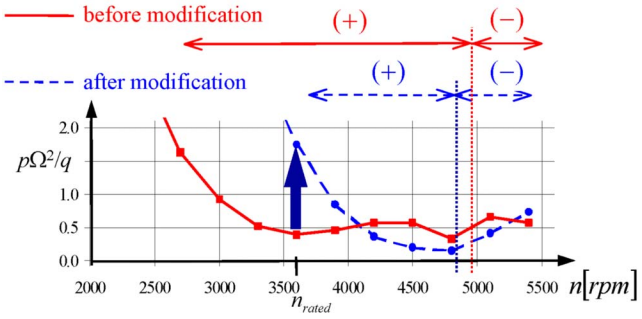

Fig. 12 Hot spot stability chart before and after modification. Heat input proportional to shaft velocity.

unstable region is shifted to higher rotor speeds as the horizontal slip ring shaft mode is shifted to higher frequencies. The heat ratio at the stability threshold at 3600 rpm increases by a factor of 4.5 from 0.39 to 1.75. The vibration level is expected to drop to 22% (=1/4.5) of the original value. This can be estimated using Eq. (B11) and Table 3.

Modification on Site

During the initial commissioning in the power plant, low friction brushes were used to reduce the vibration levels. Standard brushes replaced them when five tilting-pad bearings were installed at the NDE- and end-bearings. With the bearing modification, the spiral vibration is reduced to small magnitude even with higher friction. Figure 13 shows the relative shaft vibration at the NDE-bearing before and after the modification.

Before the modification the unit could be operated with shaft vibration level of up to 250 μm p-p (peak-to-peak amplitude) just below the trip limit. After the modification the relative shaft vibration levels at the DE- and NDE-bearings were well within zone A of ISO 7919-2 for newly commissioned machines. At the NDE-bearing, the shaft vibration level reduced to 16 μm p-p. This large improvement is not only caused by the increased stability threshold, but also to some extent by the increased horizontal stiffness of the five tilting-pad bearings.

Operational Experience

The same brush gear unit is used with two other types of 3600 rpm turbogenerator with higher rating. In total, 13 units are in operation in Mexico, USA, and the Middle East. The first few of them were modified on site during the erection and commissioning phase. Later units were delivered with the modified bearings. These 13 generators accumulated more than 200,000 operating hours.

Stable spiral vibration (vector turning) is observed at measured relative shaft vibration. The maximum levels of shaft vibration at the DE- and NDE-bearings are well within zone A of ISO 7919-2

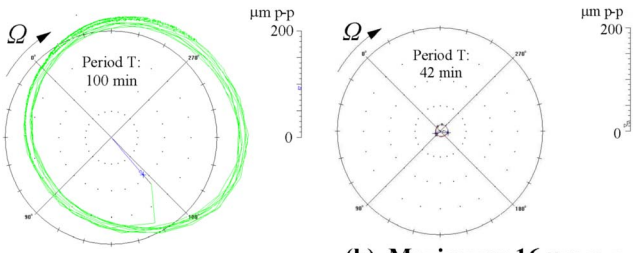

Fig. 13 Polar plot of measured relative shaft vibration at NDE: (*a*) before modification; (*b*) after modification

Downloaded 02 Jun 2010 to 171.66.16.107. Redistribution subject to ASME license or copyright; see http://www.asme.org/terms/Terms_Use.cfm

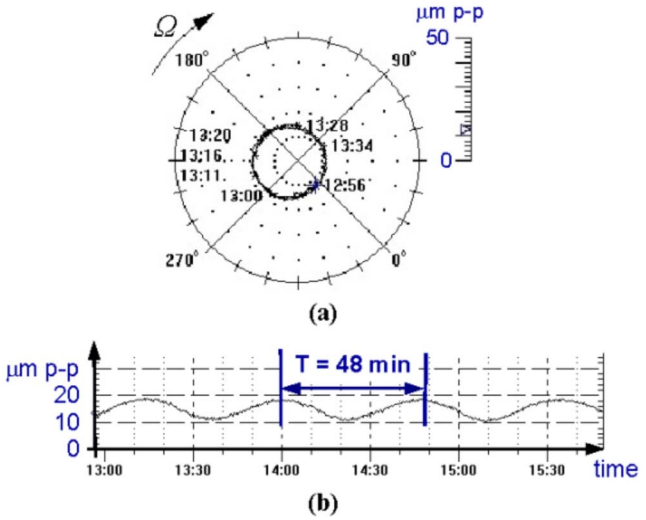

Fig. 14 Typical measured relative shaft vibration at NDE: (*a*) polar plot; (*b*) amplitude versus time plot

(<75 μm p-p for rotational speed of 3600 rpm). Figure 14(*a*) shows a typical polar plot of the shaft vibration at the NDE-bearing recorded during operation at full load. Figure 14(*b*) shows the same time period as amplitude versus time plot. The sinusoidal variation of the shaft displacement between 10 and 20 μm p-p has a period of 48 min.

Increased shaft vibrations levels were observed at one unit. However, the shaft vibration levels at the DE- and NDE-bearings were still within zone A of ISO 7919-2 [15], close to the zone boundary A/B. During an inspection, the vibration levels were reduced by:

- ensuring proper operation of the air humidifier
- more symmetric arrangement of the brushes.

Conclusions

A 450 MVA, 3600 rpm hydrogen-cooled turbogenerator equipped with a brush gear unit showed the phenomenon of spiral vibration with a forward rotating vector. After tests with the running turbogenerator, the carbon brushes sliding on the slip rings were identified as the hot spot location.

With the help of hot spot stability analyses using a rotor dynamic model of the generator rotor on three bearings, potential modifications were studied. In the case of slip rings, the friction between brushes and shaft causes the hot spot. The stability threshold is determined as a function of the rotor speed and the ratio of the added heat to the dissipated heat at the slip rings. A threshold at low ratio indicates that the shaft is sensitive to hot spots, i.e., little heat input is necessary to destabilize the system. Three different relations between the heat input and the shaft vibration were modeled: heat input proportional to the shaft displacement, to the shaft velocity, and to the shaft acceleration. The model, in which the heat input is proportional to the velocity, was found to be the most suitable variant for brushes on slip rings, which was confirmed by comparison with the measured vibration. Finally, a modification of the generator shaft line was selected based on the calculation results: both slip ring shaft critical speeds were shifted well above rated speed by using five tilting-pad bearings at the NDE- and end-bearings. The modification was successfully implemented within the power plant. In total, thirteen 3600 rpm generators with this modified design are in operation and accumulated more than 200,000 operating hours. The shaft vibration levels are within zone A of ISO 7919-2. Stable spiral vibration (vector turning) with low amplitude is acceptable if the cause of the heat input is known and is of no concern for any machine component, as in the case of carbon brushes sliding on slip rings.

Acknowledgment

The authors acknowledge the efforts of Alfred Ziegler, ALSTOM, for leading the additional tests for identification of the hot spot location, and Jean-Claude Pradetto, DELTA JS AG, for the performance of the hot spot stability analysis, and thank ALSTOM for allowing publication of this document.

Nomenclature

R_a = outer radius of the slip ring
R_i = inner radius of the slip ring
γ = R_i/R_a, ratio of inner to outer radius
B = width of the slip ring seat
c = specific heat capacity of the shaft material
ρ = density of the slip ring material
p = proportionality factor for the added heat
q = proportionality factor for the eliminated heat
F = contact force of brushes
μ_s = friction coefficient between brush and shaft
μ_h = friction coefficient between brush and holder
u = circumferential speed of the shaft
Ω = shaft speed in rad/s
Θ = cross-sectional temperature difference
κ = factor for heat dissipation
K = factor for heat input
$\Delta\dot{Q}$ = added heat due to the vibration
ψ = circumferential angle on the shaft surface
α = heat transfer coefficient of the slip ring to ambience
x = shaft displacement
$\hat{x}$ = radius of the circular shaft orbit
x_T = thermal deflection
β = ratio of the thermal deflection at the slip ring to the cross-sectional temperature difference (Fig. 9)

Appendix A: Hot Spot Stability Analysis

Calculation Method

The equation of motion of the finite element model of a multi bearing turbine generator set has the form:

$$\mathbf{M}\ddot{\mathbf{x}} + (\mathbf{D} + \mathbf{G})\dot{\mathbf{x}} + \mathbf{K}\mathbf{x} = \mathbf{f}(t) \tag{A1}$$

with the mass matrix **M**, the damping matrix **D**, the gyroscopic matrix **G**, and the stiffness matrix **K**.

Due to the damping and stiffness coefficients of the journal bearing the matrices **D** and **K** are non-symmetric and dependent on rotor speed.

If the rotor is thermally deformed, the equation of motion for coordinates **x** relative to the static position of the rotor not deformed is

$$\mathbf{M}\ddot{\mathbf{x}} + (\mathbf{D} + \mathbf{G})\dot{\mathbf{x}} + \mathbf{K}\mathbf{x} - \mathbf{K}^{\mathbf{R}}\mathbf{x}_{\mathbf{T}} = \mathbf{f}(t) \tag{A2}$$

where $\mathbf{K}^{\boldsymbol{R}}$ is the stiffness matrix of the rotor alone (without pedestals and journal bearings) and $\mathbf{x}_{\boldsymbol{T}}$ is the vector describing the thermal deformation.

The thermal deformation $\mathbf{x}_{\mathbf{T}}$ is assumed to depend linearly on the thermal deflections $\mathbf{x}_{\mathbf{T,HS}}$ of the shaft at the location of the hot spot (HS):

$$\mathbf{x}_{\mathbf{T}} = \mathbf{T}\mathbf{x}_{\mathbf{T,HS}} \tag{A3}$$

Downloaded 02 Jun 2010 to 171.66.16.107. Redistribution subject to ASME license or copyright; see http://www.asme.org/terms/Terms_Use.cfm

$$\mathbf{x_{T,HS}} = (x_{T,h}, x_{T,v})^T \tag{A4}$$

where $x_{T,h}$ and $x_{T,v}$ are the thermal translatory deflections in horizontal and vertical directions, respectively, at the location of the hot spot. The matrix **T** is derived from the thermal deformation of the rotor (see Fig. 9), which is determined by a static calculation with thermal loads: for the first column of **T** for a temperature gradient in horizontal direction and for the second column for a temperature gradient in vertical direction.

Three Different Heat Input Models

Case a: Heat Input Proportional to Shaft Displacement. The modeling of the hot spot phenomenon according to the theory of Kellenberger is based on the following thermal equation:

$$\dot{\tilde{\mathbf{x}}}_{\mathbf{T,HS}} = \underbrace{p\Omega\tilde{\mathbf{x}}_{\mathbf{HS}}}_{\dot{\mathbf{Q}}^+} - \underbrace{q\tilde{\mathbf{x}}_{\mathbf{T,HS}}}_{\dot{\mathbf{Q}}^-} \tag{A5a}$$

with $\tilde{\mathbf{x}}_{\mathbf{T,HS}}$ as the thermal deflection at the location of a hot spot and $\tilde{\mathbf{x}}_{\mathbf{HS}} = (\tilde{x}_h, \tilde{x}_v)^{\mathbf{T}}$ as the vector of the translatory shaft displacements at the location of the hot spot. $\dot{\mathbf{Q}}^+$ is the added heating efficiency and $\dot{\mathbf{Q}}^-$ is the dissipated heating efficiency.

Equation (A5*a*) was derived in detail by Kellenberger [11,12]. The coordinates in Eq. (A5*a*) are rotating in contrast to the coordinates in Eqs. (A1)–(A3), which are stationary (Fig. 6).

Equation (A5*a*) implies the following:

- The change of cross-sectional temperature difference is proportional to the change of thermal deflection.
- The differential heat input across the shaft cross section is proportional to the shaft displacement and the speed.
- The differential dissipated heat across the shaft cross section is proportional to the thermal deflection.

The proportionality factors for the added and dissipated heat are p and q. Kellenberger has applied the method to simplified shaft models. The method was extended for the use on general shaft systems (see [13]). In Eq. (A5*a*), the heat input is proportional to the displacement of the shaft at the location of the hot spot.

Case b: Heat Input Proportional to Shaft Velocity. It is assumed that the heat input is proportional to the shaft velocity instead of the shaft displacement, since a friction force changes its direction with the direction of the velocity. This yields the following thermal equation:

$$\dot{\tilde{\mathbf{x}}}_{\mathbf{T,HS}} = p\Omega\dot{\tilde{\mathbf{x}}}_{\mathbf{HS}} - q\tilde{\mathbf{x}}_{\mathbf{T,HS}} \tag{A5b}$$

Case c: Heat Input Proportional to Shaft Acceleration. The heat input is assumed to be proportional to the shaft acceleration, i.e., the following thermal equation applies:

$$\dot{\tilde{\mathbf{x}}}_{\mathbf{T,HS}} = p\Omega\ddot{\tilde{\mathbf{x}}}_{\mathbf{HS}} - q\tilde{\mathbf{x}}_{\mathbf{T,HS}} \tag{A5c}$$

Hot Spot Stability. Transforming Eq. (A5*a*) into stationary coordinates $x_{T,h}$, $x_{T,v}$, x_h, x_v yields:

$$\begin{bmatrix} 1 & 0 \\ 0 & 1 \end{bmatrix}\begin{bmatrix} \dot{x}_{T,h} \\ \dot{x}_{T,v} \end{bmatrix} + \begin{bmatrix} -p\Omega & 0 \\ 0 & -p\Omega \end{bmatrix}\begin{bmatrix} x_h \\ x_v \end{bmatrix} + \begin{bmatrix} q & \Omega \\ -\Omega & q \end{bmatrix}\begin{bmatrix} x_{T,h} \\ x_{T,v} \end{bmatrix} = \begin{bmatrix} 0 \\ 0 \end{bmatrix} \tag{A6}$$

or by using matrices and vectors

$$\mathbf{I}\dot{\mathbf{x}}_{\mathbf{T,HS}} + \mathbf{P}\mathbf{x}_{\mathbf{HS}} + \mathbf{Q}\mathbf{x}_{\mathbf{T,HS}} = \mathbf{0} \tag{A7}$$

Substituting (A3) into (A2) and extending (A2) by (A7) yields

$$\underbrace{\begin{bmatrix} \mathbf{M} & \mathbf{0} \\ \mathbf{0} & \mathbf{0} \end{bmatrix}}_{A}\begin{bmatrix} \ddot{\mathbf{x}} \\ \ddot{\mathbf{x}}_{\mathbf{T,HS}} \end{bmatrix} + \underbrace{\begin{bmatrix} (\mathbf{D}+\mathbf{G}) & \mathbf{0} \\ \mathbf{0} & \mathbf{I} \end{bmatrix}}_{B}\begin{bmatrix} \dot{\mathbf{x}} \\ \dot{\mathbf{x}}_{\mathbf{T,HS}} \end{bmatrix} + \underbrace{\begin{bmatrix} \mathbf{K} & -\mathbf{K_R}\mathbf{T} \\ \mathbf{P} & \mathbf{Q} \end{bmatrix}}_{\mathbf{C}}\begin{bmatrix} \mathbf{x} \\ \mathbf{x}_{\mathbf{T,HS}} \end{bmatrix} = \begin{bmatrix} \mathbf{0} \\ \mathbf{0} \end{bmatrix} \tag{A8}$$

where **P** is a $2 \times N$ matrix (with N as the dimension of Eq. (A2)), which has the coefficients of **P** at the columns of the translatory coordinates $\mathbf{x_{HS}}$ of the hot spot. Equation (A8) is valid for the heat input proportional to the shaft displacement according Eq. (A5*a*). For the other two models with heat input proportional to shaft velocity (Eq. (A5*b*)) and shaft acceleration (Eq. (A5*c*)), respectively, the parameter matrix **P** appears in matrix **B** and **A** respectively, instead of **C**.

To receive Eq. (A8), the original finite element model of the rotor represented by Equation (A1) must be extended by introducing the two extra degrees of freedom $x_{T,h}$ and $x_{T,v}$. The additional coefficients must be added to the global matrices. This possibility is provided for the input of the program MADYN [16].

From Eq. (A8), one could calculate the time history of **x** by a time step method. The polar plot of the time history of each coordinate would be a spiral either increasing or decreasing in magnitude. This calculation, however, would require larger computational effort, since the period of a spiral to complete a 360 deg turn is very long for realistic examples (see Table 1). That is why the computation would require the simulation of quite a long period of time until one could judge whether a spiral increases or decreases in magnitude.

As described in [13], this information could be extracted more easily from the complex eigenvalues of Eq. (A8). Their calculation requires little computational effort.

Equation (A8) has $2(N+1)$ eigenvalues. Since realistic values for p and q are very small—p is in the order of magnitude of 10^{-4} and q is in the range of $10^{-3}\omega_0$, where ω_0 is a representative natural frequency of the rotor system [11,13]—a set of $2N$ eigenvalues is practically the same as those of Eq. (A1) representing the rotor system.

Thermal Eigenvalues. The additional two eigenvalues are a conjugate complex pair

$$\lambda_T = \alpha \pm i\nu \tag{A9}$$

and will be called "thermal" eigenvalue in the following. The imaginary part ν of the thermal eigenvalue is almost equal to Ω. The interpretation of the thermal eigenvector (so-called hot spot mode) is derived in [13].

The difference $|\nu - \Omega|$ indicates the circular frequency of the hot spot moving around the circumference of the shaft surface. This is the circular frequency at which the spiral is traced. The period to complete a 360 deg turn of the spiral is

$$T = 2\pi/|\nu - \Omega| \tag{A10}$$

The direction of the revolution of the unbalance response vector is as follows:

$$\nu > \Omega \text{ Forward} \tag{A11a}$$

(co-rotational, same direction as the rotor spin)

$$\nu < \Omega \text{ Backward} \tag{A11b}$$

(counter-rotational, opposite direction of the rotor spin).

The real part of the thermal eigenvalue λ_T indicates whether the spiral increases or decreases in magnitude:

$$\alpha > 0 \text{ Increasing magnitude (unstable behavior)} \tag{A12a}$$

$$\alpha < 0 \text{ Decreasing magnitude (stable behavior)} \tag{A12b}$$

Downloaded 02 Jun 2010 to 171.66.16.107. Redistribution subject to ASME license or copyright; see http://www.asme.org/terms/Terms_Use.cfm

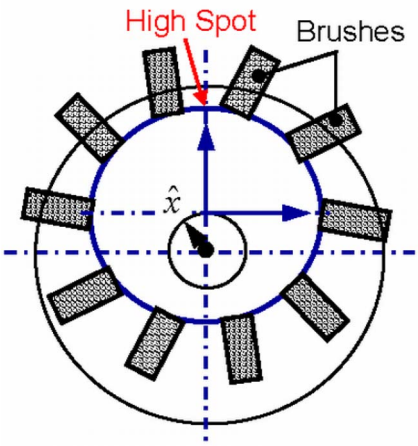

Fig. 15 Circular orbit of the shaft center at the slip rings

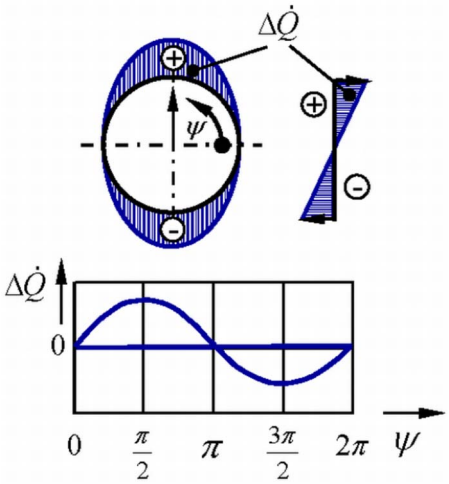

Fig. 16 Circumferential distribution of added and eliminated heating efficiency

Appendix B: Estimation of the Ratio Between Added to Eliminated Heat at the Slip Rings

Assumptions for the Estimation

The analytical estimation is done with the following assumptions:

1. The slip ring orbit is a synchronous circle (Fig. 15). The orbit at the slip rings is circular.
2. The circumferential distribution of the added heat due to the vibration is a sinus shape (Fig. 16). The maximum is at the high spot of the shaft.
3. For the eliminated heat distribution, the same applies as for the added heat.
4. The axial distribution of the temperature in the slip ring is constant.
5. The slip ring is adiabatic.
6. The complete sinusoidal shaped friction power due to the vibration enters the ring.
7. The thermal bow of the slip ring is fully transmitted to the shaft. This assumption is probably too extreme due to the soft insulation material between the slip rings and the shaft.

The thermal equation for the cross-sectional temperature difference Θ in the journal is

$$\dot{\Theta} + \kappa\Theta = K \tag{B1}$$

Table 3 Estimated heat ratio $p\Omega^2/q$ as a function of radius $\hat{x}$ of shaft orbit at the slip ring

$\hat{x}$, μm	10	20	40	80	160
$\hat{x}$, μm p-p	20	40	80	160	320
$p\Omega^2/q$	6.64	3.32	1.66	0.83	0.415

The effective heat capacity of a hollow cylinder and the heat dissipation on the cylinder surface for a temperature distribution according to Fig. 16 with the above assumptions yields:

$$\kappa = \frac{6\alpha}{\rho R_a c(1-\gamma^3)} \tag{B2}$$

$$K = \frac{3}{2\rho B R_a^2 c(1-\gamma^3)}\Delta\dot{Q} \tag{B3}$$

The thermal equation for the thermal bending of the slip ring for the case of a heat input proportional to the vibration velocity (see Eq. (A5*b*) of Appendix A) is:

$$\dot{x}_T = p\Omega\dot{x} - qx_T \tag{B4}$$

The relation between x_T and Θ is:

$$x_T = \beta\Theta \tag{B5}$$

Equation (B5) substituted into (B4) yields:

$$\dot{\Theta} + q\Theta = \frac{p\Omega}{\beta}\dot{x} \tag{B6}$$

Comparing (B6) and (B1) considering (B2) and (B3) yields:

$$q = \frac{6\alpha}{\rho R_a c(1-\gamma^3)} \tag{B7}$$

$$\frac{p\Omega}{\beta}\dot{x} = \frac{3}{2\rho B R_a^2 c(1-\gamma^3)}\Delta\dot{Q} \tag{B8}$$

Equations (B7) and (B8) yield:

$$\frac{p\Omega}{q} = \frac{\Delta\dot{Q}\beta}{4BR_a\alpha\dot{x}} \tag{B9}$$

The heat input $\Delta\dot{Q}$ caused by the variation of the contact force due to the friction in the brush holder can be expressed as follows:

$$\Delta\dot{Q} = F\frac{\dot{x}}{\Omega\hat{x}}\mu_s^2\mu_h u \tag{B10}$$

Substituting (B10) into (B9) with $u = \Omega R_a$ yields

$$\frac{p\Omega^2}{q} = \frac{F\mu_s^2\mu_h\beta\Omega}{4B\alpha\hat{x}} \tag{B11}$$

The resulting contact force for a continuous distribution of the brushes (Fig. 15) is:

$$F = 2BpR_a\int_0^\pi \sin\psi\, d\psi = 4BR_a p \tag{B12}$$

with p as the substitute pressure (sum of contact forces from all carbon brushes homogeneously distributed on the whole slip ring surface).

As can be seen from Eq. (B11), the estimated ratio $p\Omega^2/q$ of added to eliminated heat decreases with increasing radius of the shaft orbit. With realistic parameters for the brush arrangement one gets the estimated ratio of added to eliminated heat according to Table 3.

The data of Table 3 indicate that the magnitude of the spiral vibration ends in a limit cycle when the ratio of added to elimi-

Downloaded 02 Jun 2010 to 171.66.16.107. Redistribution subject to ASME license or copyright; see http://www.asme.org/terms/Terms_Use.cfm

nated heat reduces to a value at the stability threshold. Note that the displacement at the NDE-bearing is significantly smaller than at the location of the slip ring.

Equation (B11) and the numbers in Table 3 explain that in the case of slip rings, the spiral vibration stabilizes at increased amplitude. A slip ring shaft with an increased residual unbalance will show a lower tendency to spiral vibration, because the increased orbit will result in a low heat ratio $p\Omega^2/q$ and thus may already be in the stable region below the stability threshold (Fig. 12).

References

[1] Newkirk, B. L., 1926, "Shaft Rubbing. Relative Freedom of Rotor Shafts From Sensitiveness to Rubbing Contact When Running Above Their Critical Speeds," Mech. Eng. (Am. Soc. Mech. Eng.), **48**(8), pp. 830–832.

[2] Adams, M. L., 2001, "Vector Turning From Synchronously Modulated Rubs," in *Rotating Machinery Vibration from Analysis to Troubleshooting*, Marcel Dekker, Inc., New York, Chap. 12.3, pp. 312–318.

[3] Balbahadur, A. C., 2001, "A Thermoelastohydrodynamic Model of the Morton Effect Operating in Overhung Rotors Supported by Plain or Tilting Pad Journal Bearings," Ph.D. thesis, Faculty of the Virginia Polytechnic Institute and State University, Blacksburg, Virginia.

[4] Balbahadur, A. C., and Kirk, R. G., 2004, "Part I—Theoretical Model for a Synchronous. Thermal Instability Operating in Overhung Rotors," Int. J. Rotating Mach., **10**(6), pp. 469–475.

[5] Kirk, R. G., Guo, Z., and Balbahadur, A. C., "Synchronous Thermal Instability Prediction for Overhung Rotors," *Proceedings of the Thirty-Second Turbomachinery Symposium*, Texas A&M University, Houston, Texas, September 8–11, pp. 121–135.

[6] De Jongh, F. M., and Morton, P. G., 1996, "The Synchronous Instability of a Compressor Rotor Due to Bearing Journal Differential Heating," ASME J. Eng. Gas Turbines Power, **118**, pp. 816–824.

[7] Keogh, P. S., and Morton, P. G., 1993, "Journal Bearing Differential Heating Evaluation With Influence on Rotor Dynamic Behaviour," Proc. R. Soc. London, Ser. A **441**, pp. 527–548.

[8] Muszynska, A., 1989, "Rotor-to-Stationary Element Rub-Related Vibration Phenomena in Rotating Machinery-Literature Survey," Shock Vib. Dig., **21**(3), pp. 3–11.

[9] Gasch, R., Nordmann, R., and Pfützer, H., 2002, "Der sanft anstreifende Rotor," in *Rotordynamik*, 2nd ed., Springer-Verlag, Berlin, Chap. 26, pp. 537–554.

[10] Bastow, P., and Fenner, R., 1993, "The Practical Application of On-Line Systems To the Diagnosis of Machine Problems," CISM Courses and Lecture No. 352, *Proceedings of the CISM/IFToMM Symposium "Diagnostics of Rotating Machines in Power Plants*," October 27-29, Udine, Italy, G. Diana, ed., Springer-Verlag, Berlin, pp. 49–73.

[11] Kellenberger, W., 1978, "Das Streifen einer rotierenden Welle an einem federnden Hindernis—Spiralschwingungen," Ing.-Arch., **47**, pp. 223–229.

[12] Kellenberger, W., 1980, "Spiral Vibrations Due to the Seal Rings in Turbogenerators Thermally Induced Interaction Between Rotor and Stator," ASME J. Mech. Des., **102**, pp. 177–184.

[13] Schmied, J., 1987, "Spiral Vibrations of Rotors," *Proc. 11th Biennial ASME Design Engineering Div. Conf., Vib. Noise, DE-Vol. 2, Rotating Machinery Dynamics*, Boston MA, ASME H0400B, pp. 449–456.

[14] Eckert, L., Schmied, J., and Ziegler, A., 2006, "Case History and Analysis of the Spiral Vibration of a Large Turbogenerator Using Three Different Heat Input Models," *7th IFToMM International Conference on Rotor Dynamics*, Vienna, Austria, September 25–28, Paper-ID 161, pp. 1–10.

[15] ISO 7919-2, 2001, "Mechanical Vibration—Evaluation of Machine Vibration by Measurements on Rotating Shafts. Part2: Land-Based Steam Turbines and Generators in Excess of 50 MW With Normal Operation Speeds of 1500 r/min, 1800 r/min, 3000 r/min, and 3600 r/min," 2nd ed., ISO (International Organization for Standardization), pp. 11–15.

[16] Klement, H. D., 1997, *Manuals of MADYN*, Version 4.2, Program System for Machine Dynamics, Ingenieur-Büro Klement, Troyesstr. 4, Darmstadt, Germany.

Downloaded 02 Jun 2010 to 171.66.16.107. Redistribution subject to ASME license or copyright; see http://www.asme.org/terms/Terms_Use.cfm

Labyrinth Seal Leakage Tests: Tooth Profile, Tooth Thickness, and Eccentricity Effects

Ahmed J. M. Gamal
e-mail: ajmg@aggienetwork.com

John M. Vance
e-mail: jvance@tamu.edu

Turbomachinery Laboratory,
Department of Mechanical Engineering,
Texas A&M University,
College Station, TX 77843

The effects of two seal design parameters, namely blade (tooth) thickness and blade profile, on labyrinth seal leakage, as well as the effect of operating a seal in an off-center position, were examined through a series of nonrotating tests. Two reconfigurable seal designs were used, which enabled testing of two-, four-, and six-bladed see-through labyrinth seals with different geometries using the same sets of seal blades. Leakage and cavity pressure measurements were made on each of 23 seal configurations with a in. (101.6 mm) *diameter journal. Tests were carried out with air as the working fluid at supply pressures of up to* 100 psia *(*6.89 bar*). Experimental results showed that doubling the thickness of the labyrinth blades significantly influenced leakage, reducing the flow rate through the seals by up to 20%. Tests to determine the effect of blade-tip profile produced more equivocal results, with the results of experiments using each of the two test seal designs contradicting each other. Tests on one set of hardware indicated that beveling blades on the downstream side was most effective in limiting leakage, whereas tests on newer hardware with tighter clearances indicated that seals with flat-tipped blades were superior. The test results illustrated that both blade profile and blade thickness could be manipulated so as to reduce seal leakage. However, an examination of the effects of both factors together indicated that the influence of one of these parameters can, to some extent, negate the influence of the other (especially in cases with tighter clearances). finally, for all configurations tested, results showed that leakage through a seal increases with increased eccentricity and that this phenomenon was considerably more pronounced at lower supply pressures.* [DOI: 10.1115/1.2771571]

1 Introduction

In response to the constantly increasing demand for higher levels of productivity, turbomachines are being designed to run at higher speeds, last longer, and operate more efficiently. This has resulted in a need to reach an optimum balance between a turbomachine's leakage characteristics and its rotordynamic performance, while dealing with ever-tightening rotor-to-stator clearances. Research on one particular component used in such machines, the annular gas seal, has been essential in achieving the operating speeds and efficiency levels that are regularly obtained today.

These seals, which include labyrinth seals, pocket damper seals, and hole-pattern seals, limit fluid flow across regions of unequal pressure and have been invaluable in this respect due to their desirable leakage prevention characteristics and their noncontacting nature, which allows rotor speeds to be increased significantly. Due to issues associated with stability and dynamic performance, the rotordynamic characteristics of labyrinth seals continue to be studied in detail. The subject of this paper however, is the labyrinth seal's primary purpose; its ability to reduce leakage.

Empirical results as well as theoretical analyses have shown that several factors affect the flow rate through a labyrinth seal such as the one shown in Fig. 1. The pressure drop across a seal, the blade-to-journal clearances, the blade angle, the cavity depth, the blade shape, and the blade thickness are among the parameters that may impact a seal's leakage. This paper describes the investigation of the effect of the last two of these factors; the blade profile and the blade thickness as well as the effect of eccentricity.

Results of past experiments (described below) suggest that these two design parameters do indeed affect the leakage through the seal. Certain surprising results arising from comparisons of experimental data obtained from different seals were linked to differences in the geometries of the seals that were being compared. While blade profile and blade thickness may usually be of secondary importance to such parameters as clearances and the number of blades, the former two factors seem to have contributed to the unexpected results and were able to explain result trends that the latter factors could not account for. The following section is a summary and discussion of the results of several relevant studies that have led to questions concerning the shape and thickness of seal blades and their effect on leakage.

2 Background Review

A detailed summary of experimental and theoretical analyses of both liquid and gas annular seals for turbomachinery applications was presented in a recent paper by Tiwari, et al. [1]. This paper describes the seal configurations tested and the results obtained through both rotordynamic and leakage analyses. Much of the work on annular gas seals in recent years has concentrated on either the rotordynamic effects of these seals, for example Childs and Vance [2], or on analysis of more complex labyrinth seal configurations, for example Willenborg et al. [3]. However, several papers that examine the leakage and heat transfer of labyrinth seals analytically and experimentally, such as the one by Waschka et al. [4], have also been published. The use of computational fluid dynamics (CFD) methods to analyze labyrinth seal leakage has also become common. While this offers a great deal of insight into seal flow behavior, it is being relied on more and more frequently at the expense of experimental data. A paper by Moore [5] uses CFD to evaluate not only the flow rates through labyrinth seals,

Contributed by the International Gas Turbine Institute of ASME for publication in the JOURNAL OF ENGINEERING FOR GAS TURBINES AND POWER. Manuscript received April 26, 2007; final manuscript received May 7, 2007; published online January 11, 2008. Review conducted by Dilip R. Ballal. Paper presented at the ASME Turbo Expo 2007: Land, Sea and Air (GT2007), Montreal, Quebec, Canada, May 14–17, 2007, Paper No. GT2007-27223.

Copyright © 2008 by ASME

Downloaded 02 Jun 2010 to 171.66.16.107. Redistribution subject to ASME license or copyright; see http://www.asme.org/terms/Terms_Use.cfm

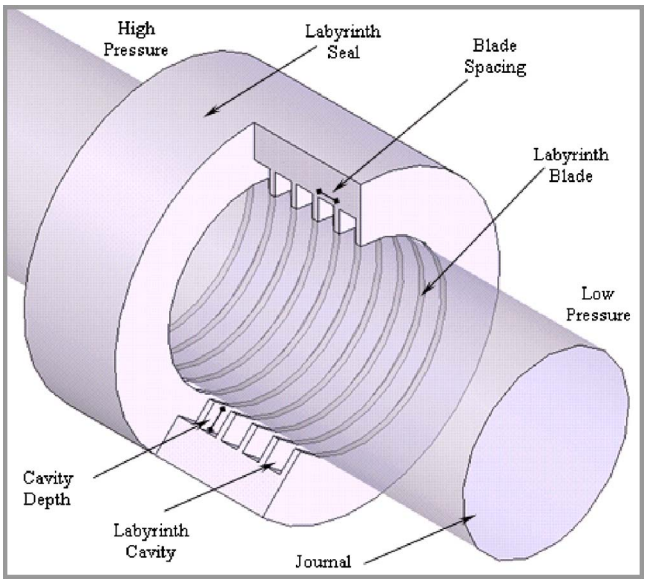

Fig. 1 Ten-bladed labyrinth seal

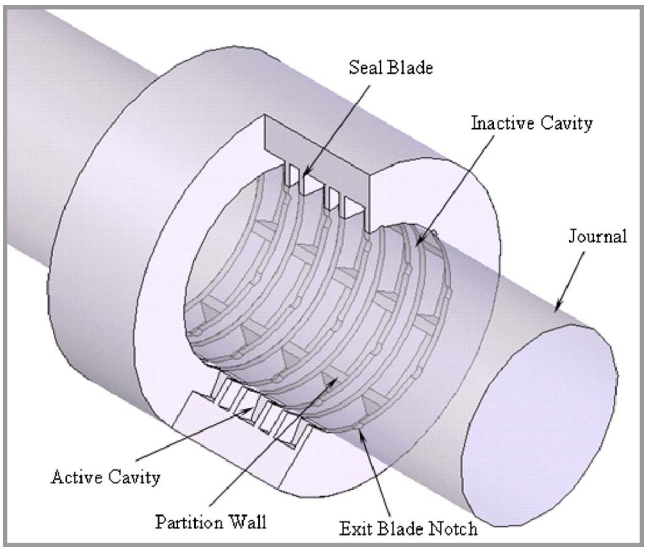

Fig. 3 Ten-bladed pocket damper seal

but also the rotordynamic coefficients. With particular relevance to the topic of this paper, Rhode and Hibbs [6] examined the effect of tooth thickness on leakage through gas labyrinth seals. Contrary to the experimental results presented below, however the results of their simulations did not reveal a significant dependence of leakage rates on blade thickness.

An analytical examination of the impact of different blade profiles on the flow rate through labyrinth seals was included in a 1972 study of the effects of various geometric factors on leakage by Fasheh [7]. This study compared, among other configurations, a labyrinth seal with a rectangular blade profile with one with a tapered profile (Fig. 2). The results of the analysis showed that the seal with the tapered blades had lower leakage values than the flat-tipped seal.

Experimental research on pocket damper seals (see Childs and Vance [2]) also indicated that blade profile can significantly affect leakage rates. Pocket damper seals (also known as TAMSEALs) differ from labyrinth seals primarily in that they are designed with circumferential partition walls separating the cavities of the seal into pockets and with notches on the exit blades of odd-numbered cavities. In the conventional PDS design (Fig. 3), the partition walls are incorporated in only even numbered cavities and in the newer, "fully partitioned" PDS design, these walls are present in all cavities. The partition walls and notches greatly reduce circumferential flow and allow for pressure variations around the seal. These two factors mean that the seal has no destabilizing cross-coupled stiffness and high direct damping, both desirable attributes from a rotordynamic point of view.

Laos [8] tested two four-bladed pocket damper seals (one with four pockets and one with eight pockets) and a six-bladed labyrinth seal. His results showed that the labyrinth seal, although it had more blades, leaked more than either pocket damper seal configuration. Laos attributed the unexpected result to the reduction in circumferential flow in the pocket damper seal due to the seal's circumferential partition walls.

Aside from this characteristic of the pocket damper seal, there were other significant differences between the two seals, as can be seen in Fig. 4 (note that for the seals shown in the figure, the flow enters through the center plenum and exits axially outwards). Both the cavity depth and the pitch length of Laos's labyrinth seal were significantly smaller than those of the pocket damper seal, and (more directly relevant to the topic of this paper) the labyrinth seal blades were beveled in the downstream direction, whereas the pocket damper seal blades were flat tipped. It is likely that the elevated leakage rates through the labyrinth seal resulted from a combination of these factors and if blade profile was indeed a cause, then Laos's results would seem to contradict the predictions made by Fasheh [7].

Laos's conclusion was backed up by the results of leakage tests conducted by Gamal et al. [9] on eight-and 12-bladed pocket damper seals (Fig. 5 (left and center)). These tests were conducted with pressure drops across the seals of up to 900 psia (62 bar) on diverging and straight through (constant clearance) seal configurations. The blades of the eight-bladed seal had a flat profile, whereas the 12-bladed seal had a double-beveled configuration (alternating downstream and upstream beveled blades). Measurements showed that the 12-bladed seal consistently leaked more than the eight-bladed seal for various test pressures, rotor speeds, and clearance ratios. This result was so surprising that the tests were repeated, with confirmation.

Gamal suggested that the unexpectedly high leakage in the case of the 12-bladed seal resulted from the beveled blade profile and from the short cavity pitch (blade spacing) of that seal. Although the inlet clearances of the eight-bladed and 12-bladed seals were

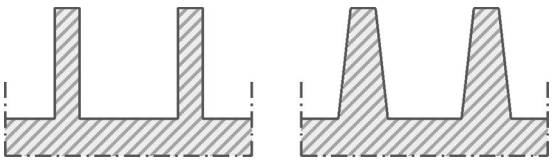

Fig. 2 Labyrinth seals with square and tapered blades

Fig. 4 Four-bladed pocket damper (left) and six-bladed labyrinth (right) test seals

Downloaded 02 Jun 2010 to 171.66.16.107. Redistribution subject to ASME license or copyright; see http://www.asme.org/terms/Terms_Use.cfm

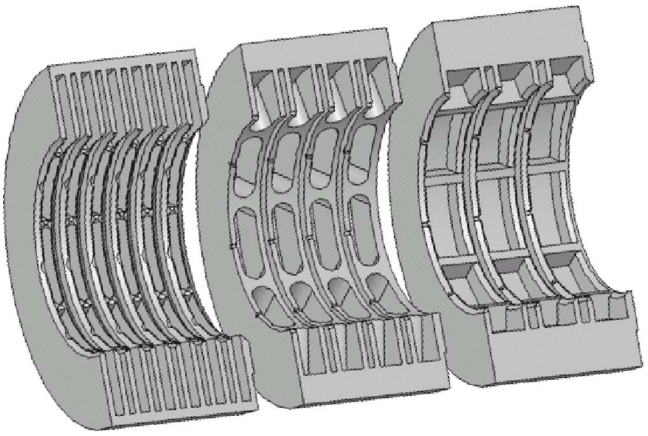

Fig. 5 High-pressure pocket damper tests seals

identical, the clearance ratio (the ratio of a pocket damper seal's active cavity's exit clearance to its inlet clearance) of the diverging 12-bladed seal was larger than that of the diverging eight-bladed seal. Additionally, the shapes of the exit blade notches were not the same for the two seals. Regardless of these factors, however, prediction codes showed that the 12-bladed seal should still have leaked less than the eight-bladed seal.

In order to eliminate such geometric discrepancies, Ertas [10] tested two six-bladed pocket damper seals with a flat blade profile at similarly high pressures. These seals were then machined and retested with beveled blade profiles (Fig. 5 (right)). The tip of each blade was purposely left with a short flat land area to ensure that the beveling process did not alter the blade-to-journal clearance. With all other geometric parameters and external conditions kept constant, Ertas showed that the beveled pocket damper seal leaked more than the seal with flat-tipped blades (supporting the results obtained by Gamal).

The results obtained by Laos [8], Gamal et al. [9], and Ertas [10] indicated that beveling the blades of a labyrinth-type seal, in either the downstream or upstream directions, reduces the seal's ability to limit leakage. While the cases being compared are not exactly identical, they do seem to contradict Fasheh's [7] findings that tapering a labyrinth seal's blades improves its leakage limiting performance

$$\dot{m}_i = C \cdot \frac{P_i \cdot A_i}{\sqrt{\gamma \cdot R \cdot T_i}} \cdot \sqrt{\frac{2 \cdot \gamma^2}{\gamma - 1} \cdot \left[\left(\frac{P_{i+1}}{P_i} \right)^{2/\gamma} - \left(\frac{P_{i+1}}{P_i} \right)^{\gamma+1/\gamma} \right]} \quad (1)$$

A somewhat normalized comparison for the different test cases can be obtained, by examining the discharge coefficients calculated by Shultz [11], Gamal et al. [9], and Ertas [10] for their seals. These coefficients, summarized in Table 1, were computed using prediction codes based on a modified form of the St. Venant equation shown below. Since this equation was derived for flow through an orifice of round cross section, it is to be expected that the predicted flow rate would not match the flow through the annular section formed by the blades and the journal. This discrepancy, along with other factors, gives rise to the need for discharge coefficients as correcting factors. For pocket damper seals, the numerical value of the discharge coefficient C differs based on whether the equation is being written for the inlet blade or the exit

Table 1 Pocket damper seal discharge coefficients

Seal (blade profile)	Inlet C	Exit C
Diverging six blades (flat)	0.710	0.780
Diverging six blades (downstream bevel)	0.965	1.200
Diverging eight blades (flat)	0.866	1.118
Diverging 12 blades (double bevel)	1.517	1.658

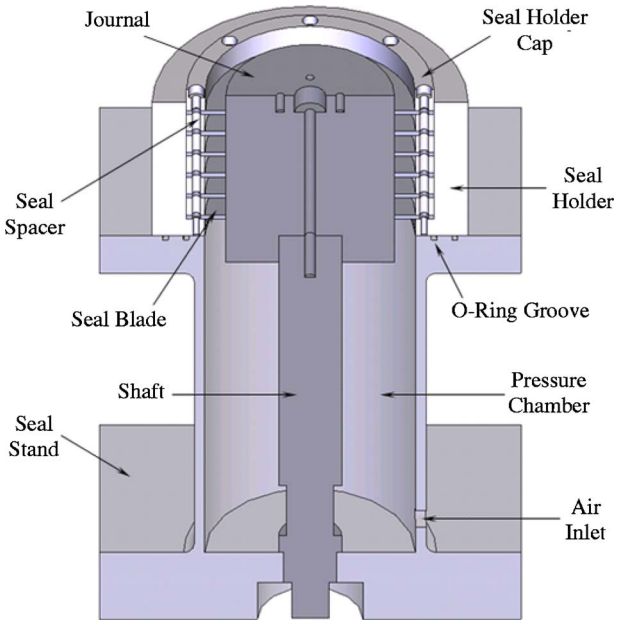

Fig. 6 Nonrotating seal testrig (sectioned model view)

blade of an active cavity. A discharge coefficient value greater than 1 indicates that the flow equation underpredicts the leakage through the seal, whereas a value less than one indicates that the leakage is being overpredicted.

The current discussion of both labyrinth seals and pocket damper seals offers an opportunity to clarify a discrepancy in the terminology used in the literature pertaining to each, of these two seals. The term *discharge coefficient* as it has been used in the literature pertaining to pocket damper seals is not synonymous with that used in the literature pertaining to labyrinth seals. With regard to the latter, the discharge coefficient relates the leakage through a seal to the leakage through an analogous *ideal labyrinth* as was described by Egli [12]. Such an ideal labyrinth is one in which the kinetic energy of the jet is completely depleted once it enters a downstream cavity. Egli stated that the case of an ideal labyrinth is similar to that of flow through a single constriction and presented an equation for the former.

With regard to pocket damper seals, however, the discharge coefficient is a factor that accounts for the difference between the leakages calculated using Eq. (1) (intended for use with round orifices rather than annular cavities) and the experimentally measured leakage. The discharge coefficients described in this section should more correctly be referred to as *empirical correction factors* which can be used to asses the degree to which the leakage model underpredicts or overpredicts the leakage through a seal.

Investigation of the effects of eccentricity, cavity depth, and blade thickness was suggested to provide further understanding of the impact of seal geometry on leakage. Since the above blade-profile tests involved comparisons to pocket damper seals, this paper presents experimental data comparing labyrinth seals with different blade profiles and blade thicknesses to each other. In addition, since such seals normally operate in an off-center position, the effect of eccentricity is examined to see if this too was a contributing factor to the results of the previous experiments.

3 Test-Rig and Testing Procedure

The facility used to test the seals is located at the Turbomachinery Laboratory at Texas A&M University and was first used by Shultz [11] to test a two-bladed pocket damper seal. The test rig, shown in Fig. 6 with a six-bladed labyrinth seal installed, has also been used to test wire-mesh dampers and pocket damper seals.

Downloaded 02 Jun 2010 to 171.66.16.107. Redistribution subject to ASME license or copyright; see http://www.asme.org/terms/Terms_Use.cfm

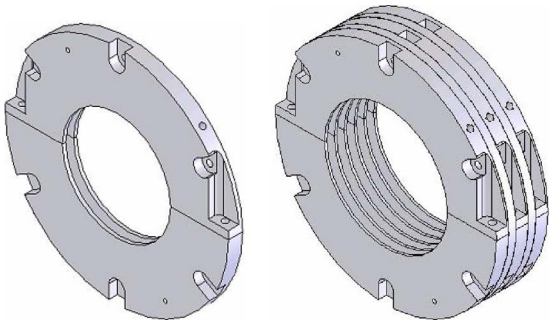

Fig. 7 Seal Set A: Modified two-bladed air-buffer labyrinth seal base unit (left) and six-bladed seal (right)

Fig. 8 New reconfigurable seal components (Seal Set B)

Pressurized air enters the chamber at the bottom and exhausts to the atmosphere through the clearance between the test seal's blades and the journal, which is mounted on a cantilevered shaft. The seal rests on the upper surface of the test stand (an O-ring seals the interface) and is held in place by four adjustable toggle clamps. The seal is clamped down, not bolted, onto the housing so as to allow for lateral movement during the centering process. The rig is supplied with air, remotely controlled using a Masoneilan valve and pressurized at up to 275 psi (18.9 bar), from an Atlas Copco GR 1520 compressor.

3.1 Test Seals. Carrying out the tests on two reconfigurable seals allowed the number of blades, blade spacing (pitch), cavity depth, and blade thickness to be varied while using the same sets of blades. This had the dual advantage of not requiring a large number of different test seals and of eliminating the difficulty involved in ensuring that the blade tip clearances were kept constant for all tests cases.

Two separate sets of seal hardware (described below) were used. The older set of seals was used only for blade profile tests and is referred to below as *Seal Set A*. The newer hardware was used to examine the effect of blade thickness and eccentricity, as well as to reexamine the effect of blade profile, and is referred to below as *Seal Set B*. Table 9 detailing the tested seal configurations can be found in the Appendix of this paper.

3.1.1 Seal Set A. This older set of seal hardware consists of three air-buffer seals which were modified to create three two-bladed labyrinth seals. These two-bladed seal base units were then assembled, along with annular spacers to construct two-, four-, or six-bladed labyrinth seals as shown in Fig. 7. The main geometric features of these test seals are detailed in Table 2.

Leakage and pressure tests were carried out on two-, four-, and six-bladed seals of this type with flat-tipped blades. Once the tests were completed, bevels were machined into the same blades and the seal was tested with upstream-beveled blades, then flipped over and tested with downstream-beveled blades. Seal Set A was made up of a total of nine test configurations.

3.1.2 Seal Set B. This seal design consists of a seal holder, a set of blades, three sets of spacers, a set of cavity inserts, and a seal holder cap (components shown in Fig. 8 The main geometric features of the test seals (made up of either four or six blades) are detailed in Table 3. The blade thickness could be doubled by arranging the blades in back-to-back pairs in the holder. The depths of the cavities could be reduced by 80% by inserting 0.4 in. (10.2 mm) thick annular inserts between the blades.

Leakage and pressure tests were carried out on six four-bladed and five six-bladed seals with flat-tipped blades and two four-bladed seals with beveled blades. Seal Set B was made up of a total of 14 test configurations.

3.2 Instrumentation. The flow rate through the seal was measured using an Omega FTB-938 turbine flow meter. The cavity pressures were measured using a Kulite XT-190M strain gauge type pressure transducer, which was connected to radial holes in the seal using Nylon tubing via a multidirectional valve.

In order to ensure that the seal remained in the centered position throughout testing, two orthogonally mounted proximity probes were used to display and monitor the journal position with respect to the seal on an oscilloscope. Figure 9 is a photograph of the test stand with the toggle clamps raised and the seal removed to reveal the journal.

3.3 Test Procedure. During assembly, a tight fit (0.5 mils or 12.7 μm radial) between the outer diameter of the blades and the inner diameter of the seal holder served to ensure that the blades of Seal Set B would be aligned when they were installed around the journal. The seal holder therefore doubled as an "external mandrel" for the assembly purposes. The seal sections and spacers of Seal Set A were assembled on a separate internal mandrel with a 0.5 mil (12.7 μm) radial clearance with the blades. In order to eliminate any radial leakage at the interfaces between the seal blades and the spacers, the interface surfaces were machined closely and treated with a sealing compound. After several checks it was determined that the sealant was unnecessary for the newer set of blades. Shims were used to center the seal around the journal before it was clamped into place. The seals' inlet pressures were varied using the supply valve and flow rate and cavity pressure readings were recorded. Several of the seal configurations were also tested in an off-center position to determine the effect of

Table 2 Old test seal geometry (Seal Set A)

Design parameter	Configurations tested
No. of blades	2, 4, 6
Cavity depth	0.4 in. (10.16 mm)
Blade spacing	0.245 in. (6.223 mm)
Inner diameter	4.012 in. (101.9 mm)
Radial clearance	6 mils (152.4 mm)
Blade thickness	0.075 in. (1.905 mm)

Table 3 New test seal geometry (Seal Set B)

Design parameter	Configurations tested
No. of blades	4, 6
Cavity depth	0.1 in., 0.5 in. (2.5 mm, 12.7 mm)
Blade spacing	1/8 in., 1/4 in., 1/2 in. (3.2 mm, 6.4 mm, 12.7 mm)
Inner diameter	4.008 in. (101.8 mm)
Radial clearance	4 mils (101.6 mm)
Blade thickness	1/8 in., 1/4 in., (3.2 mm, 6.4 mm)

Downloaded 02 Jun 2010 to 171.66.16.107. Redistribution subject to ASME license or copyright; see http://www.asme.org/terms/Terms_Use.cfm

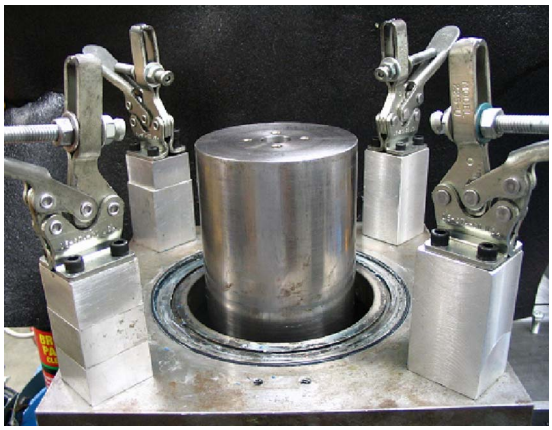

Fig. 9 Nonrotating testrig (seal not installed)

eccentricity. This was achieved by releasing the toggle clamps following a centered test and pushing the seal over until the blades came into contact with the journal and repeating the test.

After the required configurations were tested, the seals were retested with bevels (chamfers) machined into the downstream and upstream sides of the blades. Short segments of land area were left on the blades to ensure that clearances were not altered by the beveling process. The remaining portions of the blade tips were beveled at an angle from the seal's axis as shown in Fig. 10.

Concurrent with the leakage tests, cavity pressure measurements were made in the four- and six-bladed seals of Set A and all the seals of Set B. Due to geometric restrictions in the seals of Set A, pressure measurements could not be made in the first upstream two-bladed seal section or in the cavities formed by the spacers. As a result, cavity pressure data were taken in the third cavity of the four-bladed seal and in the third and fifth cavities of the six-bladed seal. Cavity pressure measurements were made in all cavities of the seals of Set B except for the seals with short pitch lengths.

4 Dimensionless Coefficients

The graphs presented here are displayed in dimensionless form with either flow rate or cavity pressure on the vertical axis and supply pressure on the horizontal axis. The graphs conform to the current customary presentation format for papers on labyrinth seals

$$\phi = \frac{\dot{m}_i \cdot \sqrt{R \cdot T_{\text{in}}}}{A_i \cdot P_{\text{in}}} \tag{2}$$

$$\psi = \frac{P_i - P_{\text{out}}}{P_{\text{in}} - P_{\text{out}}} \tag{3}$$

The flow rates are made dimensionless through the flow-coefficient ϕ defined in Eq. (2) as used by Yucel and Kazakia [13]. The cavity pressures are made dimensionless through the pressure coefficient ψ, defined by Eq. (4) as used by Rhode and Hibbs [6], and the external seal pressure conditions were made dimensionless through the pressure ratio PR defined as the ratio of the absolute seal exit to seal inlet pressures. It is important to note that these dimensionless variables are representative of these test measurements and do not constitute a nondimensional analysis. This paper does not attempt to develop dimensionless Π groups for the purpose of any such analysis. The dimensional flow rates, cavity pressures, and supply pressures are presented in tabular form in the Appendix of this paper.

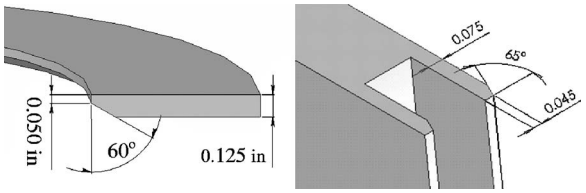

Fig. 10 Beveled blades for new (left) 1.27 mm tip, 3.18 mm base and old (right) 1.14 mm tip, 1.91 mm base seals

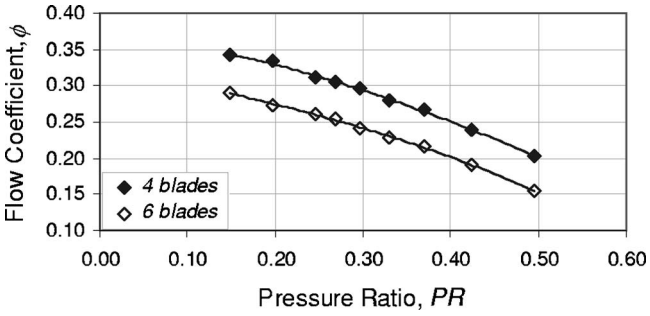

Fig. 11 Seal leakage (four and six blades, long pitch)

5 Experimental Results

Leakage and mean cavity pressure measurements were made to examine blade thickness effects using two-, four-, and six-bladed seals of Set A, and to examine blade thickness, blade profile, and eccentricity effects using four- and six-bladed seals of Set B with long (0.5 in. or 12.7 mm), intermediate (0.25 in. or 6.35 mm), and short (0.125 in. or 3.175 mm) pitch lengths. In all cases, the exit pressure from the seal was atmospheric and the inlet pressure was varied up to 100 psia (6.89 bar). The test conditions were kept as close to constant as possible for each seal. Measurements on the newer hardware were made at seal inlet pressures of 15, 20, 25, 30, 35, 40, 45, 60, and 85 psig (1.03, 1.38, 1.72, 2.07, 2.41, 2.76, 3.10, 4.13, and 5.86 bar). These pressures correspond to the absolute pressure ratios shown in the figures below (see Table 4).

A preliminary indication that the leakage measurements obtained from the tests were reasonable was provided by a comparison of the leakage through the four- and six-bladed seals of Set B. Figure 11 compares leakage through seals with the same blade thickness, cavity depth, and blade spacing, but with a different number of blades. Similar results were obtained from tests on seals with short and intermediate pitch lengths and from the modified air-buffer labyrinth seals of Set A.

5.1 Blade Thickness Effects. Varying the thickness of the blades was found to have a significant impact on the leakage through the test seals of Set B. The blade thickness tests were carried out on four-bladed seals (see Fig. 12) with eight blades arranged in pairs so as to create labyrinth constrictions with double the original thickness (an increase from

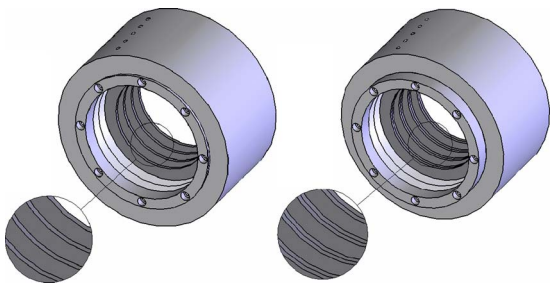

Fig. 12 Four-bladed seals with single—(left) and double—(right) thickness blades (blade spacing maintained constant)

Downloaded 02 Jun 2010 to 171.66.16.107. Redistribution subject to ASME license or copyright; see http://www.asme.org/terms/Terms_Use.cfm

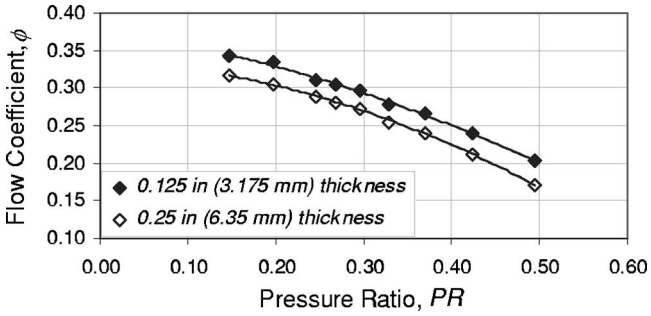

Fig. 13 Blade thickness effect (four blades, long pitch)

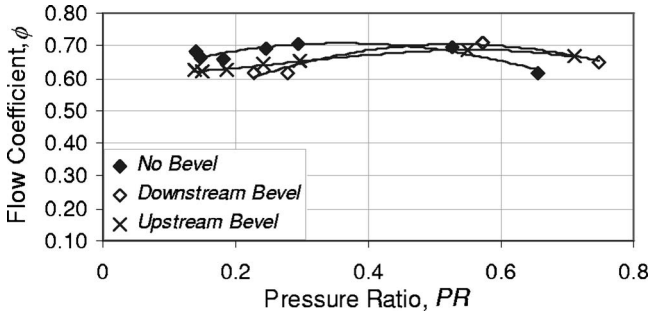

Fig. 16 Effect of blade profile on leakage (two blades)

0.125 in. to 0.25 in. or from 3.175 mm to 6.35 mm).

Four configurations were tested for this part of the experimentation; long pitch and intermediate pitch length seals each with single and double thickness blades. Each of these seal assemblies was measured to ensure that the added blades did not tighten the tip clearances. Figures 13 and 14 compare the leakage rates through four-bladed seals with different blade thicknesses. The percent reduction in leakage resulting from replacing the original 0.125 in. (3.175 mm) thick blades with the 0.25 in. (6.35 mm) thick blades in two different four-bladed seals can be seen in Fig. 15. A reduction in leakage of about to 20% was observed at low supply pressures and a reduction of roughly 10%–15% is observed at higher pressures.

5.2 Blade Profile Effects. Tests were carried out on two separate sets of seal hardware to investigate the effect of blade profile on labyrinth seal leakage. The results of the two sets of tests, presented below, were found to contradict each other. A possible explanation of this contradiction, which is related to blade thickness effects, is presented in Sec. 6 of this paper.

5.2.1 Seal Set A. The dimensionless flow coefficients for the two-bladed seal for the all three blade profiles are shown in Fig. 16. The effect of beveling the blades is insignificant at low pressures. At higher pressures, the different blade profiles still result in close leakage values (see Table 7 in Appendix), but a trend begins to emerge, showing that the seals with the beveled blade profiles leak less than the flat profile seal. The flat-tipped seal was found to leak slightly more than the upstream beveled seal, which in turn leaked more than the downstream beveled seal. At pressures of approximately 60 psia (4.13 bar, PR=0.25), the downstream-beveled seal leaked up to 7.5% less than the flat-tipped seal. The results of tests on the four-bladed seal configurations (Fig. 17) show that beveling the blades has practically no effect on the leakage. The six-bladed seal showed the highest dependency on blade shape (Fig. 18). As in the case of the two-bladed seal, the upstream-beveled configuration leaked less than the flat-tipped profile and the downstream beveled seal leaked less than either of the other configurations. Beveling the seal blades in the downstream direction reduced the leakage by 10%–15% over the range of test pressures.

Figure 19 shows the variation of pressure (in terms of the dimensionless pressure coefficient) in the third cavity of the four-bladed seal for the three blade profiles. Pressure readings from the beveled seals, particularly the downstream-beveled configuration, are clearly lower than those from the flat-tipped configuration. While the leakage results for the configurations of the four-bladed seal were especially close, the pressure data in the third cavity

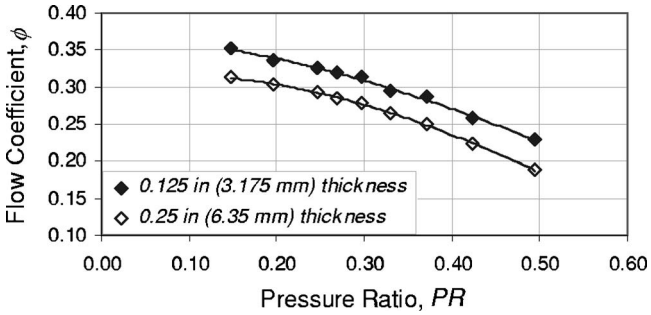

Fig. 14 Blade thickness effect (four blades, short pitch)

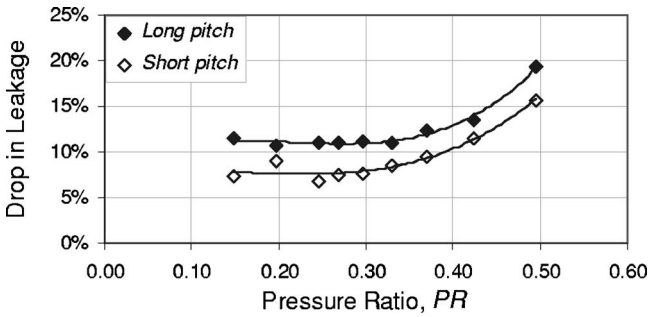

Fig. 15 Effect of doubling blade thickness on leakage through seals with short and long pitch lengths

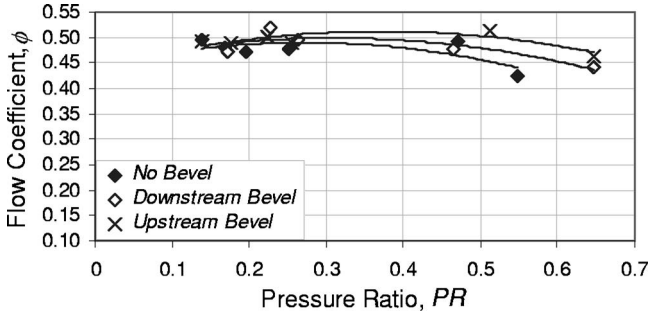

Fig. 17 Effect of blade profile on leakage (four blades)

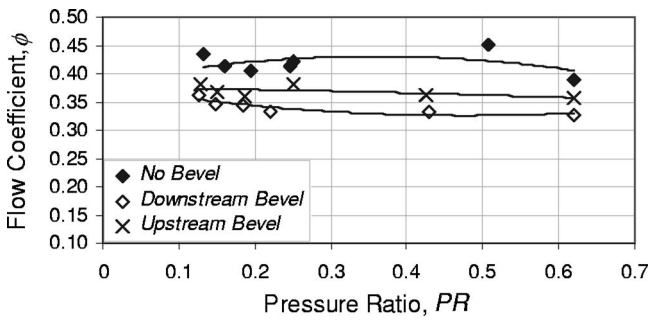

Fig. 18 Effect of blade profile on leakage (six blades)

Downloaded 02 Jun 2010 to 171.66.16.107. Redistribution subject to ASME license or copyright; see http://www.asme.org/terms/Terms_Use.cfm

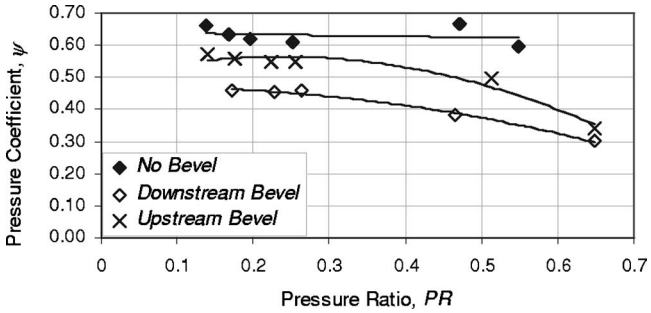

Fig. 19 Pressure in third cavity of four-bladed seal

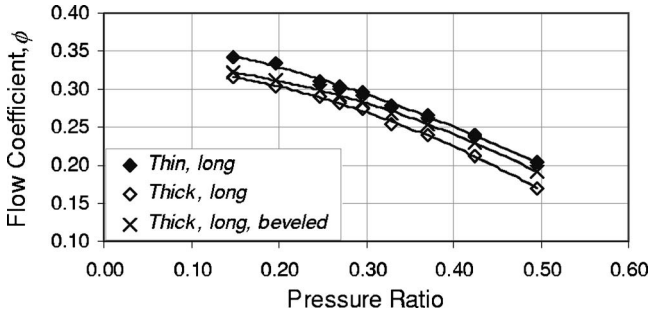

Fig. 22 Effect of blade profile on leakage (four blades, long pitch)

indicate that the first three blades of the beveled seals were more successful in dropping the gas pressure. This indicates that the beveled seals would be more effective in reducing the leakage through the seal.

The cavity pressures in the third and fifth cavities of the six-bladed seal are represented in Figs. 20 and 21 respectively. Both these figures support the results of the cavity pressure measurements in the four-bladed seal and the leakage results presented above.

5.3 Seal Set B. The leakage results for four-bladed seals are shown in Fig. 22 for long pitch and in Fig. 23 for short pitch. Each of these plots compares the leakage through seals with 1/8 in. (3.175 mm) thick flat-tipped blades, 1/4 in. (6.35 mm) thick flat-tipped blades, and 1/4 in. (6.35 mm) thick beveled blades.

Comparing the curves (or the data in the Appendix) for thick flat-tipped and thick beveled blades shows that beveling the blades in the downstream direction increased the leakage through the seal. These results contradict the results obtained from the earlier set of blade profile tests. Furthermore, it appears from the graphs that for these seals, blade thickness was more of a factor than blade profile. This can be concluded from the fact that the thicker the tip of the blade, the lower the leakage regardless of blade profile.

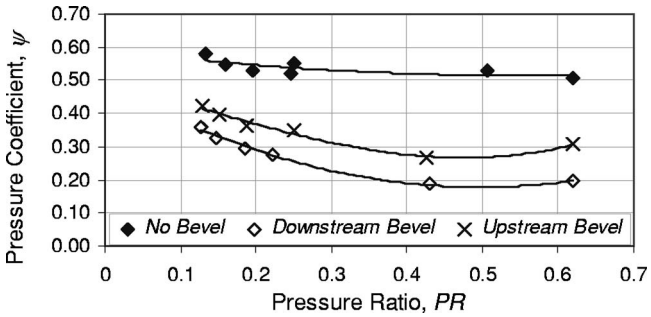

Fig. 20 Pressure in third cavity of six-bladed seal

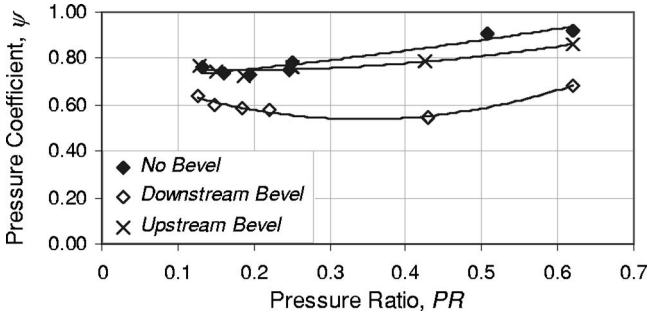

Fig. 21 Pressure in fifth cavity of six-bladed seal

5.4 Eccentricity Effects. Immediately following several of the leakage tests, the seals of Set B were moved to a fully eccentric position and retested to examine the effect of eccentricity on the leakage. As was expected, the seal leakage increased in the off-center position. These tests were initially proposed as an attempt to explain the contradiction between the effect of blade profile on labyrinth seal leakage and that on pocket damper seal leakage. The experimental results presented earlier and discussed in the next section suggest another reason for this contradiction, but the eccentricity results are presented here nonetheless. It is clear from the curves of Fig. 24 that eccentricity significantly increases seal leakage at low supply pressures.

6 Comments on the Results

The results of the leakage and cavity pressure tests were most easily interpreted with respect to the effect of blade thickness. The effect of blade profile is not insignificant, but is less easily interpreted and contradicts some of the earlier results. In cases where the leakage data were ambiguous, such as in the results of the tests on the four-bladed seals of Set A, the cavity pressure data were

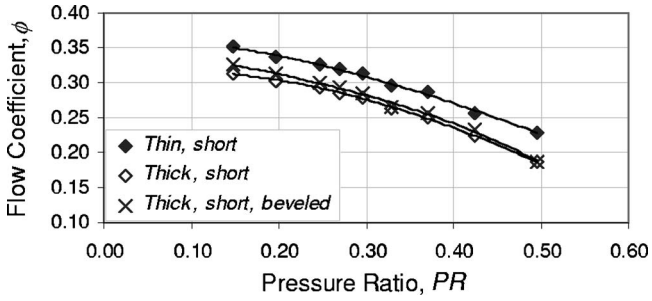

Fig. 23 Effect of blade profile on leakage (four blades, short pitch)

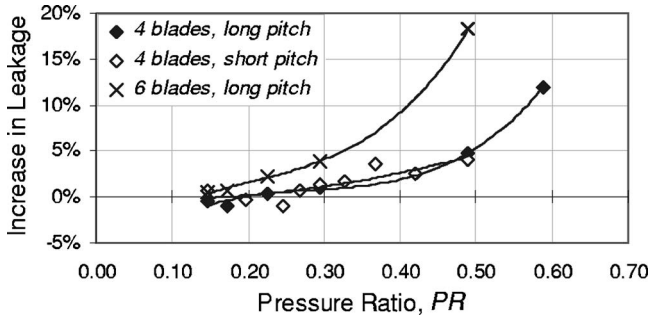

Fig. 24 Increased flow rates due to eccentricity for three seal configurations

Downloaded 02 Jun 2010 to 171.66.16.107. Redistribution subject to ASME license or copyright; see http://www.asme.org/terms/Terms_Use.cfm

Table 4 Sample test repeatability (average of four assemblies)

Supply pressure		Average pressure		Standard deviation		
(psia)	(bar)	(lb/s)	(kg/s)	(lb/s)	(kg/s)	Percentage (%)
30	2.07	0.467	0.212	0.003	0.001	0.68
35	2.41	0.670	0.305	0.011	0.005	1.68
40	2.76	0.868	0.395	0.007	0.003	0.83
45	3.1	1.036	0.471	0.008	0.004	0.79
50	3.45	1.221	0.555	0.017	0.008	1.41
55	3.79	1.413	0.642	0.016	0.007	1.14
60	4.13	1.571	0.714	0.010	0.005	0.63
75	5.17	2.070	0.941	0.014	0.006	0.69
100	6.89	2.929	1.331	0.026	0.012	0.89

used to verify the trends in question. In general, a seal with a lower distribution of total cavity pressures will have better leakage reduction capacity.

6.1 Repeatability. In order to ensure that the seal assembly process did not significantly impact the results, each seal configuration was assembled and tested four times. The data presented in this paper are the averages of the four tests on each seal configuration. The standard deviations in the leakage and pressure measurements were calculated at each point and were found to be less than 2% of the corresponding mean value for all data points in all test cases with the exception of some of the low-pressure data points, which had standard deviations under 5%. A majority of data points actually had a standard deviation under 1%. As an example, Table 4 lists the flow-rate data for the six-bladed seal of Set B with single-thickness blades and long pitch.

6.2 Blade Thickness. Increasing the blade thickness resulted in a 10%–20% drop in leakage for all the configurations tested at all supply pressures. This was possibly the result of increased frictional losses in the longer constrictions of the thick-bladed seals. The blades initially had a thickness of 1/8 in. (3.175 mm) and were thicker than the 0.070 in. (1.778 mm) thick blades of the seals of Set A. Another possible explanation is provided by Bell and Bergelin [14], who state that there is a partial recovery of pressure after the fluid passes through a thin annular constriction and enters the subsequent cavity, but also state that this phenomenon is lessened when the orifice thickness is increased. A comparison with a prediction code based on the modified St. Venant equation described earlier showed that the newer seals leaked considerably less than predicted, whereas the leakage through the older seals was predicted considerably more closely. While correction factors are needed for this equation to accurately predict the leakage through a seal, the amount by which the code overpredicted the leakage (using correction factors of 1) indicated that an additional factor was keeping the leakage levels low. It was assumed that this factor was the increased blade thickness and this hypothesis was supported by the results, which indicate a strong dependency on blade thickness.

As is discussed below, beveling the blades of the test seals increased their leakage rates. This contradicted the results of the tests on the older labyrinth seals and is another indication that the newer seals had a heightened sensitivity to blade thickness. It was further theorized that it was the tighter clearances of the newer seals that were responsible for this sensitivity. As the fluid jet leaves the constriction it expands into the subsequent downstream cavity. The angle of expansion, and therefore the amount of carried over kinetic energy, can be affected by both the clearance and the thickness of the blades Hodkinson [15].

6.3 Blade Profile. The findings summarized by Fasheh [7], which stated that a tapered profile would lead to lower leakage rates than a flat blade profile, were supported by the results of the tests on the two- and six-bladed seals of Seal Set A. The tests conducted by Gamal et al. [9] and Ertas [10] on pocket damper seals showed opposite results, indicating that the flow-rate through a seal increases when the seal blades are beveled. It was initially assumed that the main difference that could explain these conflicting results was the type of seal used. The seemingly contradictory results were attributed to differences in the flow regime through the two different seal types, but differences in the geometries of the pocket damper seals and the labyrinth seals were also considered as possible causes. The partition walls of the pocket damper seals tested by both Gamal and Ertas considerably reduced the flow of air in the circumferential direction and the effect of this on the overall leakage through the seal is not completely understood.

The seal inlet pressures for the pocket damper seal tests were one order of magnitude higher than the current sets of tests, indicating that the effect of blade profile may also be pressure dependent. The cavity depths, clearance ratio, number of blades, and pitch length of Gamal's seals were different, giving rise to several possible causes for the leakage results other than the blade profile. However, all of these factors were kept constant in the tests conducted by Ertas, leaving the effects of the partition walls and the higher pressures as the possible causes for the disagreement with the results presented in the previous section.

It was initially thought that the effect of beveling the blades of a pocket damper seal might be different from the effect of beveling the blades of a labyrinth seal. This is clearly not the case however, since the labyrinth seal test results from Seal Set B presented here show that beveling the blades increased the leakage as was the case with the pocket damper seal tests.

A possible explanation for the contradictions described above is provided by simultaneous examination of the effects of blade thickness and blade profile. When the seals tested by Ertas [10] were beveled, only a short land pitch was left, reducing the blade-tip thickness by 77%. The blade-tip thicknesses of the seals described in this paper were reduced by only 40% for Set A and 60% for Set B. These changes are summarized in Table 5. The seal tests that indicated a detrimental effect of beveling the blades were also the tests in which more than half the blade-tip land pitch was removed in the beveling process.

These results can be explained if it is assumed that both increasing blade thickness and beveling the blades can reduce the leakage. However, these trends work against one another to some extent in that beveling the blades will remove some of the blade-tip land area and therefore reduce the tip thickness. If the seal is more sensitive to thickness effects, as was the case with the test seals of Set B, beveling the blades will increase the leakage. On the other hand if the seal is less sensitive to changes in blade thickness, beveling the blades will reduce the leakage as was the case with the seals of Set A. While these results are not intended to imply that a reduction in blade tip land area through chamfering more than 50% of the tip length will automatically increase the leakage and that a reduction of less than 50% will decrease the leakage, they do illustrate that there are two factors, with opposite effects on leakage, that come into play when the blades are

Downloaded 02 Jun 2010 to 171.66.16.107. Redistribution subject to ASME license or copyright; see http://www.asme.org/terms/Terms_Use.cfm

Table 5 Blade-tip geometries before and after beveling

Seal	Initial tip thickness (in.)	Initial tip thickness (mm)	Final tip thickness (in.)	Final tip thickness (mm)	Percent reduction (%)
Pocket damper seal	0.13	3.302	0.03	0.762	77
Labyrinth seal Set A	0.075	1.905	0.045	1.143	40
Labyrinth seal Set B	0.125	3.175	0.05	1.27	60

beveled.

The sensitivity of the leakage rates through a seal to the thickness of the blades seems to be linked to the seal clearances. This effect may be related to the partial recovery of pressure (described above) once the fluid jet expands from the vena contracta into the subsequent downstream cavity. This phenomenon is discussed by Hodkinson [15] and by Bell and Bergelin [14]. The radial clearances for the pocket damper seals tested by Ertas [10] were 5 mils (127 μm) and 7.5 mils (191 μm) for the inlet and exit of each blade pair, respectively. For the current group of test seals, the radial clearances were 6 mils (152 μm) for Set A and 4 mils (102 μm) for Set B.

6.4 Cavity Depth. The seals tested had a cavity depth of 0.4 in. (10.2 mm) for Set A and 0.5 in. (12.7 mm) for Set B. This relatively large value for the cavity depth was necessitated by the need to use the same spacers for tests comparing labyrinth seal leakage to pocket damper seal leakage (to be presented elsewhere). So as to confirm that the additional cavity depth did not significantly impact the results, four six-bladed seals and two four-bladed seals were tested to examine the effect of this factor. The cavity depth was changed by placing annular inserts between the blades, which served to decrease the cavity depth from 0.5 in. to 0.1 in. (12.7 mm to 2.54 mm). Figure 25 shows one of the seals used for these tests.

If the cavity depth were to be reduced until the cavity is completely filled, the seal would effectively become a smooth, or plain, seal. This indicates that there is a range of values of cavity depth (from zero to a small value) where the cavity depth would have a significant effect on the leakage, but that beyond that value the effect begins to attenuate rapidly. Further investigation of this effect would require using a set of cavity inserts that would provide smaller depths.

Table 6 shows the effect of cavity depth on the leakage through six-bladed seals with 0.5 in. (12.7 mm) blade spacing, and clearly indicates that an 80% reduction in cavity depth had virtually no impact on leakage. Similar results were obtained from tests on four-bladed seals with long and intermediate pitch lengths and a six-bladed seal with intermediate pitch length.

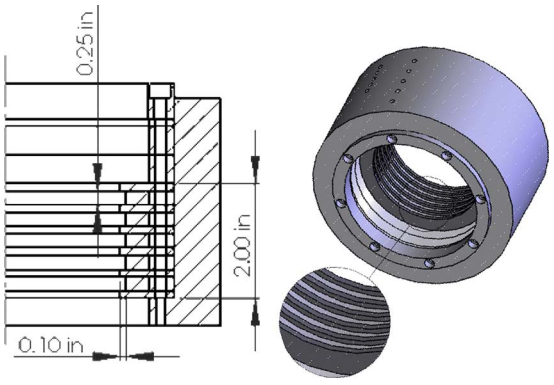

Fig. 25 Six-bladed test seal with shallow cavities (cavity inserts installed) and intermediate pitch

7 Conclusions

The following points summarize the topics covered and the results presented in this paper. The effects of varying blade profile and blade thickness on the leakage through see-through labyrinth seals were examined. This was accomplished through a set of nonrotating tests on two-, four-, and six-bladed seals with supply pressures of up to 100 psia (6.89 bar). The seals were tested both in the centered and off-center positions in order to examine the effect of eccentricity:

- Tests carried out to determine the effect of blade thickness showed that doubling the thickness of the blades reduced leakage rates by up to 20% for certain test configurations;
- Once the flat-tipped seals were tested, bevels were machined into the blades in order to examine the effect of blade profile. One set of tests showed that flat-tipped blades were more effective in limiting leakage, while tests on older hardware showed that downstream-beveled blades were more effective;
- Blade profile results, together with the results of the blade-thickness tests, led to the conclusion that while both factors can be used to improve seal leakage performance, they can also work counter to each other in some cases, especially if the clearances are small; and
- Finally, the tests showed that operating a seal eccentrically had the effect of increasing the leakage-rates. This phenomenon was considerably more pronounced at lower supply pressures.

In an important area of research in turbomachinery that has seen a large number of CFD related papers published in recent years, this paper provides experimental data for seals with practical geometries for high-pressure applications. Such data should prove valuable for validation of analytical models or numerical simulations of seal flow and may offer insight into labyrinth seal performance factors.

Table 6 Ratio of shallow cavity to deep cavity seal leakage (six blades, long pitch, flat tipped)

Seal inlet pressure (psia)	Seal inlet pressure (psia)	Leakage ratio
30	2.05	0.9955
35	2.39	0.9997
40	2.74	1.0009
45	3.08	0.9999
50	3.42	1.0082
55	3.77	0.9840
60	4.11	1.0017
75	5.15	1.0052
100	6.87	0.9953

Downloaded 02 Jun 2010 to 171.66.16.107. Redistribution subject to ASME license or copyright; see http://www.asme.org/terms/Terms_Use.cfm

Table 7 Labyrinth seal leakage results for Set A (see table for seal numbers—back pressure atmospheric for all seals)

Seal No. 15 (Fig. 16)			Seal No. 16 (Fig. 16)			Seal No. 17 (Fig. 16)		
PR (−)	Leakage (lb/s)	Leakage (kg/s)	PR (−)	Leakage (lb/s)	Leakage (kg/s)	PR (−)	Leakage (lb/s)	Leakage (kg/s)
0.65	0.035	0.016	0.70	0.035	0.016	0.74	0.033	0.015
0.52	0.050	0.023	0.54	0.047	0.021	0.56	0.047	0.021
0.29	0.090	0.041	0.29	0.083	0.038	0.28	0.083	0.038
0.24	0.106	0.048	0.24	0.100	0.045	0.22	0.102	0.046
0.18	0.136	0.062	0.18	0.126	0.057	—	—	—
0.15	0.169	0.077	0.15	0.156	0.071	—	—	—
0.14	0.182	0.083	0.14	0.169	0.077	—	—	—
Seal No. 18 (Fig. 17)			Seal No. 19 (Fig. 17)			Seal No. 20 (Fig. 17)		
PR (−)	Leakage (lb/s)	Leakage (kg/s)	PR (−)	Leakage (lb/s)	Leakage (kg/s)	PR (−)	Leakage (lb/s)	Leakage (kg/s)
0.54	0.029	0.013	0.64	0.027	0.012	0.64	0.026	0.012
0.46	0.039	0.018	0.51	0.038	0.017	0.46	0.039	0.018
0.25	0.072	0.033	0.25	0.072	0.033	0.26	0.071	0.032
0.19	0.091	0.041	0.22	0.084	0.038	0.22	0.086	0.039
0.17	0.108	0.049	0.17	0.105	0.048	0.17	0.104	0.047
0.14	0.135	0.061	0.14	0.133	0.060	—	—	—
Seal No. 21 (Fig. 18)			Seal No. 22 (Fig. 18)			Seal No. 23 (Fig. 18)		
PR (−)	Leakage (lb/s)	Leakage (kg/s)	PR (−)	Leakage (lb/s)	Leakage (kg/s)	PR (−)	Leakage (lb/s)	Leakage (kg/s)
0.61	0.024	0.011	0.61	0.022	0.010	0.61	0.020	0.009
0.50	0.033	0.015	0.42	0.032	0.015	0.42	0.029	0.013
0.24	0.063	0.029	0.25	0.057	0.026	0.22	0.057	0.026
0.25	0.063	0.029	—	—	—	—	—	—
0.19	0.078	0.035	0.18	0.072	0.033	0.18	0.070	0.032
0.16	0.097	0.044	0.15	0.091	0.042	0.15	0.088	0.040
0.13	0.123	0.056	0.13	0.112	0.051	0.13	0.107	0.049

Table 8 Labyrinth seal leakage rates for Set B (see table for seal numbers—back pressure atmospheric for all seals)

Pin:	psia / bar	30 / 2.07	35 / 2.41	40 / 2.76	45 / 3.10	50 / 3.45	55 / 3.79	60 / 4.13	75 / 5.17	100 / 6.89	Plotted in Fig.
Seal	lb/min	0.610	0.843	1.069	1.261	1.489	1.686	1.878	2.529	3.453	11, 13, and 15,
No. 1	kg/min	0.277	0.383	0.486	0.573	0.677	0.766	0.854	1.149	1.569	22 and 24
Seal	lb/min	0.680	0.897	1.137	1.327	1.566	1.765	1.975	2.547	3.542	14, 15, and 23,
No.2	kg/min	0.309	0.408	0.517	0.603	0.712	0.802	0.898	1.158	1.610	24
Seal	lb/min	0.514	0.745	0.966	1.155	1.376	1.559	1.749	2.300	3.200	13, 15, and 22
No.3	kg/min	0.234	0.339	0.439	0.525	0.625	0.708	0.795	1.046	1.454	
Seal	lb/min	0.520	0.738	0.964	1.151	1.354	1.526	1.715	2.243	3.121	—
No.4	kg/min	0.236	0.336	0.438	0.523	0.616	0.693	0.779	1.019	1.418	
Seal	lb/min	0.549	0.776	0.996	1.181	1.392	1.570	1.757	2.277	3.137	14, 15, and 23
No.5	kg/min	0.250	0.353	0.453	0.537	0.633	0.714	0.799	1.035	1.426	
Seal	lb/min	0.579	0.809	1.026	1.219	1.436	1.623	1.806	2.364	3.257	22
No.6	kg/min	0.263	0.368	0.467	0.554	0.653	0.738	0.821	1.075	1.480	
Seal	lb/min	0.566	0.815	1.030	1.207	1.440	1.628	1.811	2.370	3.292	23
No.7	kg/min	0.257	0.370	0.468	0.549	0.655	0.740	0.823	1.077	1.497	
Seal	lb/min	0.668	0.905	1.120	1.324	1.556	1.745	1.940	2.551	3.528	—
No.9	kg/min	0.304	0.412	0.509	0.602	0.707	0.793	0.882	1.160	1.604	
Seal	lb/min	0.621	0.844	1.047	1.238	1.467	1.662	1.855	2.451	3.403	—
No.8	kg/min	0.282	0.384	0.476	0.563	0.667	0.756	0.843	1.114	1.547	
Seal	lb/min	0.467	0.670	0.868	1.036	1.221	1.413	1.571	2.070	2.929	11 and 24
No.10	kg/min	0.212	0.305	0.395	0.471	0.555	0.642	0.714	0.941	1.331	
Seal	lb/min	0.529	0.720	0.939	1.124	1.317	1.488	1.670	2.195	3.082	—
No.11	kg/min	0.241	0.327	0.427	0.511	0.598	0.676	0.759	0.998	1.401	
Seal	lb/min	0.555	0.772	0.989	1.177	1.379	1.564	1.744	2.282	3.179	—
No.12	kg/min	0.252	0.351	0.449	0.535	0.627	0.711	0.793	1.037	1.445	
Seal	lb/min	0.464	0.670	0.869	1.036	1.231	1.390	1.574	2.081	2.915	—
No.13	kg/min	0.211	0.304	0.395	0.471	0.559	0.632	0.715	0.946	1.325	
Seal	lb/min	0.499	0.698	0.909	1.086	1.285	1.460	1.641	2.178	3.075	—
No.14	kg/min	0.227	0.317	0.413	0.493	0.584	0.664	0.746	0.990	1.398	

Downloaded 02 Jun 2010 to 171.66.16.107. Redistribution subject to ASME license or copyright; see http://www.asme.org/terms/Terms_Use.cfm

Table 9 Labyrinth seal test matrix (down and up refer to side of the blade that is beveled)

Seal No.	No. of blades	Pitch (in.)	Pitch (mm)	Thickness (in.)	Thickness (mm)	Profile	Depth (in.)	Depth (mm)	Radial clearance (mils)	Radial clearance (μm)	Seal length (in.)	Seal length (mm)	Seal hardware
1	4	0.5	12.7	0.125	3.2	Flat	0.5	12.7	4	102	2.00	50.80	Set B
2	4	0.125	3.2	0.125	3.2	Flat	0.5	12.7	4	102	0.88	22.23	Set B
3	4	0.5	12.7	0.25	6.4	Flat	0.5	12.7	4	102	2.50	63.50	Set B
4	4	0.25	6.4	0.25	6.4	Flat	0.5	12.7	4	102	1.75	44.45	Set B
5	4	0.125	3.2	0.25	6.4	Flat	0.5	12.7	4	102	1.38	34.93	Set B
6	4	0.5	12.7	0.25	6.4	Dwn	0.5	12.7	4	102	2.50	63.50	Set B
7	4	0.125	3.2	0.25	6.4	Dwn	0.5	12.7	4	102	1.38	34.93	Set B
8	4	0.5	12.7	0.125	3.2	Flat	0.1	2.5	4	102	2.00	50.80	Set B
9	4	0.25	6.4	0.125	3.2	Flat	0.1	2.5	4	102	1.25	31.75	Set B
10	6	0.5	12.7	0.125	3.2	Flat	0.5	12.7	4	102	3.25	82.55	Set B
11	6	0.25	6.4	0.125	3.2	Flat	0.5	12.7	4	102	2.00	50.80	Set B
12	6	0.125	3.2	0.125	3.2	Flat	0.5	12.7	4	102	1.38	34.93	Set B
13	6	0.5	12.7	0.125	3.2	Flat	0.1	2.5	4	102	3.25	82.55	Set B
14	6	0.25	6.4	0.125	3.2	Flat	0.1	2.5	4	102	2.00	50.80	Set B
15	2	0.245	6.2	0.075	1.9	Flat	0.4	10.2	6	152	0.40	10.03	Set A
16	2	0.245	6.2	0.075	1.9	Up	0.4	10.2	6	152	0.40	10.03	Set A
17	2	0.245	6.2	0.075	1.9	Dwn	0.4	10.2	6	152	0.40	10.03	Set A
18	4	0.245	6.2	0.075	1.9	Flat	0.4	10.2	6	152	1.04	26.29	Set A
19	4	0.245	6.2	0.075	1.9	Up	0.4	10.2	6	152	1.04	26.29	Set A
20	4	0.245	6.2	0.075	1.9	Dwn	0.4	10.2	6	152	1.04	26.29	Set A
21	6	0.245	6.2	0.075	1.9	Flat	0.4	10.2	6	152	1.68	42.55	Set A
22	6	0.245	6.2	0.075	1.9	Up	0.4	10.2	6	152	1.68	42.55	Set A
23	6	0.245	6.2	0.075	1.9	Dwn	0.4	10.2	6	152	1.68	42.55	Set A

Acknowledgment

The work presented in this paper was conducted at Texas A&M University's Turbomachinery Laboratory and was funded by the Turbomachinery Research Consortium. The authors would like to acknowledge Dr. Fouad Zeidan of Bearings Plus Inc., who provided the seal hardware, Mr. Kiran Toram, now with Bently Nevada, whose help in machining and modifying the seals was greatly, appreciated, and Mr. Rahul Kar, now with Praxair, who assisted with the testing.

Nomenclature

- A_i = annular clearance area for the ith construction (L^2)
- C = empirical leakage correction factor (-)
- g = acceleration due to gravity (L/t^2)
- $\dot{m}_i$ = mass flow-rate through the ith constriction (M/t)
- P_i = pressure in the ith cavity (F/L^2)
- P_{in} = absolute seal supply pressure (F/L^2)
- P_{out} = absolute seal exit pressure (F/L^2)
- PR = pressure ratio (P_{out}/P_{in}) (-)
- ΔP = pressure drop across seal (F/L^2)
- R = gas constant (FL)/(MT)
- T_i = temperature in the ith cavity (T)
- ϕ = dimensionless flow coefficient (-)
- γ = specific heat ratio (-)
- ρ = gas density (M/L^3)
- ψ = dimensionless pressure coefficient (-)

Appendix

Tables 7 and 8 contain the leakage data used to generate the dimensionless plots presented in the body of this paper for seal Sets A and B respectively. The seal numbers referred to in these two tables are explained in Table 9, which lists the major dimensions and features of the test seals.

References

[1] Tiwari, R., Manikandan, S., and Dwivedy, S. K., 2005, "A Review of the Experimental Estimation of the Rotor Dynamic Parameters of Seals," Shock Vib. Dig., **37**(4), pp. 261–284.

[2] Childs, D. W. and Vance, J. M., 1997, "Annular Gas Seals and Rotordynamics of Compressors and Turbines," *Proceedings of 26th Turbomachinery Symposium*, Texas A&M University, College Station, TX, pp. 201–220.

[3] Willenborg, K., Schramm, V., Kim, S., and Wittig, S., 2002, "Influence of a Honeycomb Facing on the Heat Transfer in a Stepped Labyrinth Seal," ASME J. Eng. Gas Turbines Power, **124**(1), pp. 133–139.

[4] Waschka, W., Wittig, S., and Kim, S., 1992, "Influence of high rotational speeds on the heat transfer and discharge coefficients in labyrinth seals," ASME J. Turbomach., **114**(2), pp. 462–468.

[5] Moore, J. J., 2003, "Three Dimensional CFD Rotordynamic Analysis of Gas Labyrinth Seals," J. Vibr. Acoust., **125**, pp. 427–433.

[6] Rhode, D. L., and Hibbs, R. I., 1992, "Tooth Thickness Effect on the Performance of Gas Labyrinth Seals," ASME J. Tribol., **114**(4), pp. 790–795.

[7] Fasheh, J. I., 1972, "Review and Summary of Labyrinth Seal Theory and Design," TMR Report 2115–3351, Rocketdyne, Canoga Park, CA.

[8] Laos, H. E., 1999, "Rotordynamic Effects of Pocket Damper Seals," Ph.D. dissertation, Texas A&M University, College Station, TX.

[9] Gamal, A. M., Ertas, B. H., and Vance, J. M., 2006, "High-Pressure Pocket Damper Seals: Leakage Rates and Cavity Pressures," ASME Paper No. GT2006–90858.

[10] Ertas, B. H., 2005, "Rotordynamic Force Coefficients of Pocket Damper Seals" Ph.D. dissertation, Texas A&M University, College Station, TX.

[11] Shultz, R. R., 1996, "Analytical and Experimental Investigation of a Labyrinth Seal Test Rig and Damper Seals for Turbomachinery," M.S. thesis, Texas A&M University, College Station, TX.

[12] Egli, A., 1935, "The Leakage of Steam through Labyrinth Seals," Trans. ASME, **57**, pp. 115–122.

[13] Yucel, U., and Kazakia, J. Y., 2001, "Analytical Prediction Techniques for Axisymetric Flow in Gas Labyrinth Seals," ASME J. Eng. Gas Turbines Power, **123**, pp. 255–257.

[14] Bell, K. J., and Bergelin, O. P., 1957, "Flow Through Annular Orifices," Trans. ASME, **79**(3), pp. 593–601.

[15] Hodkinson, B., 1939, "Estimation of the Leakage through a Labyrinth Gland," Proc. Inst. Mech. Eng., **141**, pp. 283–288.

Downloaded 02 Jun 2010 to 171.66.16.107. Redistribution subject to ASME license or copyright; see http://www.asme.org/terms/Terms_Use.cfm

The Effect of Engine Exhaust Temperature Modulations on the Performance of Automotive Catalytic Converters

Tariq Shamim
Department of Mechanical Engineering,
The University of Michigan–Dearborn,
Dearborn, MI 48128-2406

This paper presents a computational investigation of the effect of exhaust temperature modulations on an automotive catalytic converter. The objective is to develop a better fundamental understanding of the converter's performance under transient driving conditions. Such an understanding will be beneficial in devising improved emission control methodologies. The study employs a single-channel based, one-dimensional, nonadiabatic model. The transient conditions are imposed by varying the exhaust gas temperature sinusoidally. The results show that temperature modulations cause a significant departure in the catalyst behavior from its steady behavior, and modulations have both favorable and harmful effects on pollutant conversion. The operating conditions and the modulating gas composition and flow rates (space velocity) have substantial influence on catalyst behavior. [DOI: 10.1115/1.2747256]

Keywords: engine emissions, engine exhaust after-treatment, dynamic behavior, numerical simulations

Introduction

Automotive catalytic converters, which are employed to reduce engine exhaust emissions, are subjected to highly transient conditions during a typical driving cycle. These transient conditions arise from changes in driving mode (acceleration and deceleration), and the hysteresis and flow lags of the feedback control system. The transients result in fluctuations of gas flow rates, compositions, and temperatures. These transients make the catalyst behavior differ significantly from that under steady-state conditions [1–5]. Because of its practical significance, the investigation of the catalyst dynamic behavior has been a subject of active research for more than two decades. Most prior studies have been focused on the effects of air-fuel ratio (A/F) and composition modulations. These studies determined that modulations have both beneficial and harmful effects on pollutant conversion, depending on the catalyst type, driving mode, exhaust conditions, and pollutants to be removed [4].

In addition to A/F and composition, temperature also has a large influence on the reaction behavior. Van Neer et al. investigated the effects of a fast periodic change of the reaction temperature on certain heterogeneously catalyzed reactions [6]. In this theoretical study, the influence of fast periodic modulations of the temperature to the preferential oxidation of CO in a hydrogen-rich gas mixture was studied. The effect postulated to arise by fast periodic changes of the temperature was the generation of a residual behavior of adsorbed reactant molecules within temperature ranges where they normally are not adsorbed on the catalyst surface. Therefore, the frequency of the temperature modulations has to be high enough to prevent desorption of the reactants, but low enough to allow adsorption and to avoid quasi-steady state by switching the temperature very rapidly.

The potential benefits of temperature modulations are reported to be higher catalyst yield owing to the improvement of catalyst coverage and higher selectivity of the catalyst [7]. The imposed modulation frequencies are found to play an important role in determining the benefits of temperature modulations [7]. However, little attention has been paid to the investigation of temperature modulation. One potential reason for the limited work in this area is the difficulty associated with the temperature modulation in conventional reactors. This is owing to the large thermal masses and the poor surface-to-volume ratio, which restrict the heat exchange between conventional reactor systems and heating/cooling systems [7,8].

The present study is motivated by realizing the scarcity of extensive investigation of the effects of temperature modulation on catalysts especially on automotive catalysts. It investigates the effects of exhaust gas temperature modulations on a three-way automotive catalyst. The objective is to clearly understand the effect of temperature modulation on the catalyst performance under engine exhaust conditions.

Mathematical Formulation

The governing equations were developed by considering the conservation of mass, energy, and chemical species. Using the assumptions and notations listed elsewhere [9], the governing conservation equations for a typical single channel may be written as follows:

Gas phase energy equation:

$$\rho_g C_{P_g}\left(\varepsilon\frac{\partial T_g}{\partial t}+v_g\frac{\partial T_g}{\partial z}\right)=-h_g G_a(T_g-T_s) \tag{1}$$

Gas phase species equations (for seven species):

$$\left(\varepsilon\frac{\partial C_g^j}{\partial t}+v_g\frac{\partial C_g^j}{\partial z}\right)=-k_m^j G_a(C_g^j-C_s^j) \tag{2}$$

Surface energy equation:

Contributed by the Internal Combustion Engine Division of ASME for publication in the JOURNAL OF ENGINEERING FOR GAS TURBINES AND POWER. Manuscript received March 28, 2006; final manuscript received January 16, 2007; published online December 13, 2007. Review conducted by Margaret Wooldridge. Paper presented at the 2006 Spring Conference of the ASME Internal Combustion Engine Division (ICES2006), May 7–10, 2006, Aachen, Germany.

Copyright © 2008 by ASME

Downloaded 02 Jun 2010 to 171.66.16.107. Redistribution subject to ASME license or copyright; see http://www.asme.org/terms/Terms_Use.cfm

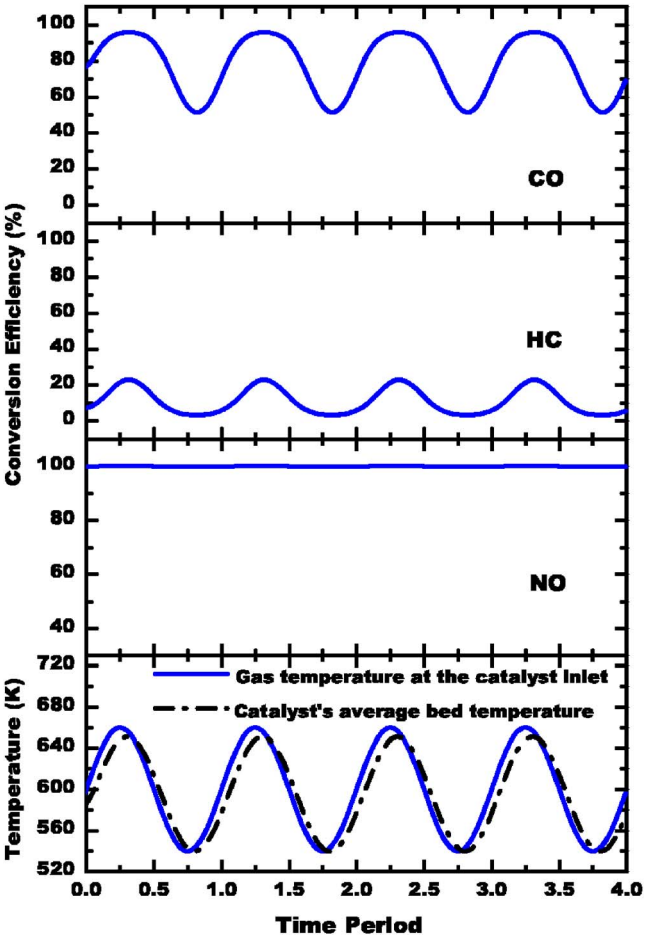

Fig. 1 Catalyst response to sinusoidal modulations in exhaust gas temperature near stoichiometric operating conditions (A/F=14.7, mean exhaust temperature=600 K, frequency =0.01 Hz, amplitude=10%)

$$(1-\varepsilon)\rho_s C_{Ps}\frac{\partial T_s}{\partial t} = (1-\varepsilon)\lambda_s\frac{\partial^2 T_s}{\partial z^2} + h_g G_a(T_g - T_s) - h_\infty S_{\text{ext}}(T_s - T_\infty) + G_a\sum_{k=1}^{n_{reaction}} R^k(T_s, C_s^1, \ldots, C_s^{N_{\text{species}}})\cdot\Delta H^k \quad (3)$$

Surface species equations (for seven species):

$$(1-\varepsilon)\frac{\partial C_s^j}{\partial t} = k_m^j G_a(C_g^j - C_s^j) - G_a R^j(T_s, C_s^1, \ldots, C_s^{N_{\text{species}}}) \quad (4)$$

The superscript j in species equations varies from 1 to 7, representing the following species: CO, NO, NH_3, O_2, C_3H_6, H_2, and C_3H_8. In addition to these species, the kinetic expressions also include CO_2, H_2O, and N_2. The conservation equation for the surface oxygen storage mechanism is represented by Eq. (4), excluding the convective mass transport term. The heat and mass transfer coefficients in the above equations are calculated from the conventional correlations of Nusselt and Sherwood numbers [10]. The chemical reactions and the corresponding kinetic data used in the present study were similar to those used in Ref. [9]. The governing equations were discretized by using a nonuniform grid and employing the control volume approach with the central implicit difference scheme in the spatial direction. A standard tridiagonal matrix algorithm with an iterative successive line under relaxation method was used to solve the finite difference equations. The spatial node size ranging from 0.1693 mm to 19.32 mm and the time step of 0.001 s were employed. The grid insensitivity of

Table 1 Comparison of time-average conversion efficiencies for exhaust gas temperature modulations (mean exhaust gas temperature=600 K, modulation amplitude=10%)

	Frequency (Hz)	CO (%)	NO (%)	HC (%)
Stoichiometric (A/F=14.7)	0.01	78.34	99.94	11.22
	0.05	81.38	99.94	9.23
	0.1	82.59	99.94	9.10
	0.5	82.55	99.95	8.91
	1	82.43	99.95	8.86
	Steady state	82.1	99.90	8.71
Lean (A/F=17.5)	0.01	99.86	5.64	83.82
	0.05	99.90	5.83	89.95
	0.1	99.92	5.22	91.55
	0.5	99.91	4.59	92.03
	1	99.91	4.56	92.03
	Steady state	99.9	4.70	90.55
Rich (A/F=12.5)	0.01	0.02	92.40	5.05
	0.05	0.01	92.41	5.03
	0.1	0.01	92.38	5.03
	0.5	0.01	92.38	5.04
	1	0.01	92.38	5.04
	Steady state	0	92.40	5.04

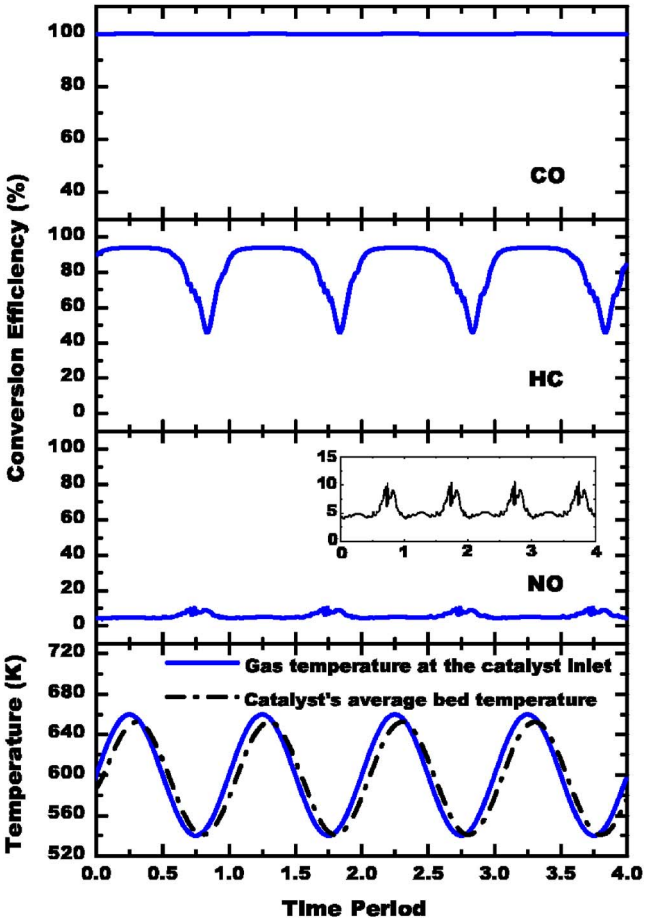

Fig. 2 Catalyst response to sinusoidal modulations in exhaust gas temperature under lean operating conditions (A/F=17.5, mean exhaust temperature=600 K, frequency=0.01 Hz, amplitude=10%)

Downloaded 02 Jun 2010 to 171.66.16.107. Redistribution subject to ASME license or copyright; see http://www.asme.org/terms/Terms_Use.cfm

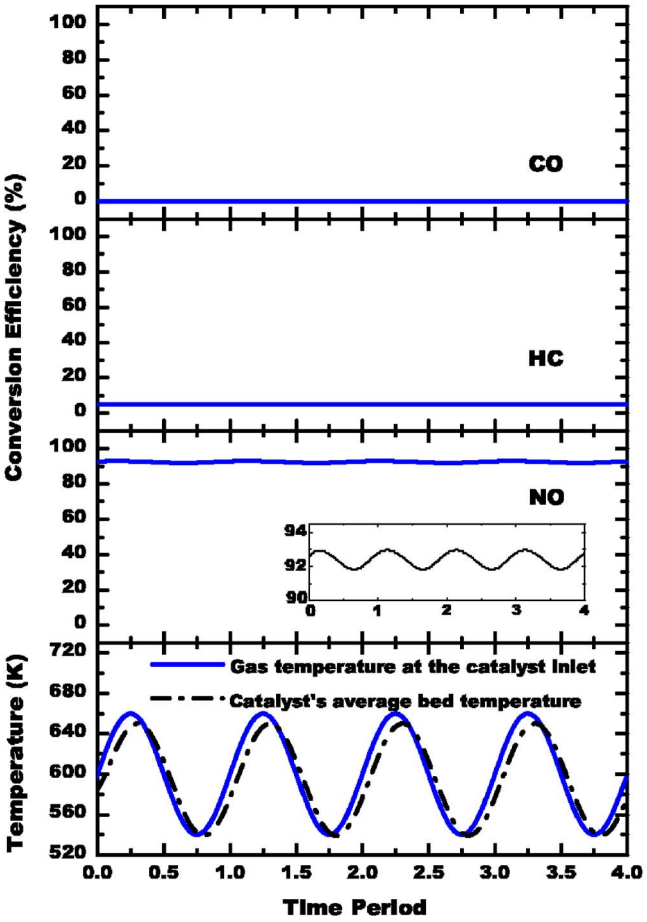

Fig. 3 Catalyst response to sinusoidal modulations in exhaust gas temperature under rich operating conditions (A/F=12.5, mean exhaust temperature=600 K, frequency=0.01 Hz, amplitude=10%)

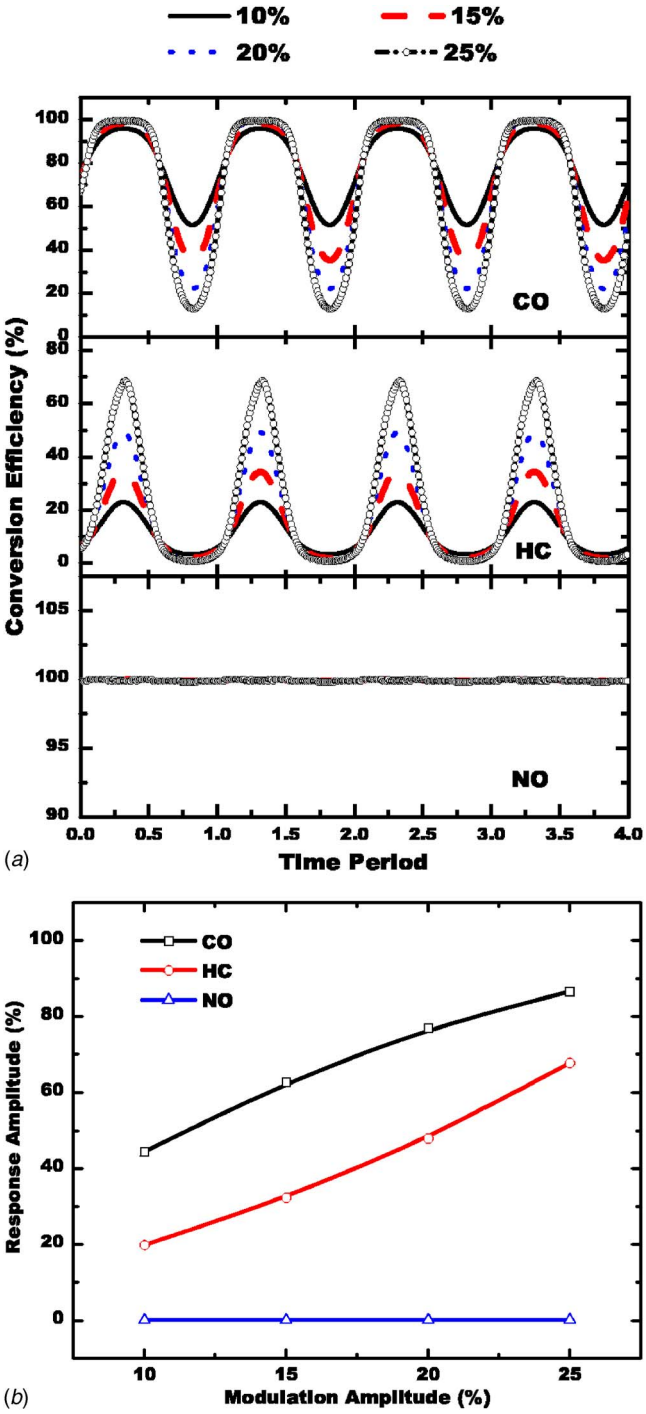

Fig. 4 Catalyst response to sinusoidal modulations in exhaust gas temperature: Effect of modulation amplitudes on conversion efficiencies. (*a*) Conversion efficiencies as a function of oscillation time period and (*b*) catalyst response amplitude as a function of the imposed modulation amplitude (A/F=14.7, mean exhaust temperature=600 K, frequency=0.01 Hz)

results was ensured by performing a sensitivity study. Details of the solution procedure are described elsewhere [9].

Results and Discussion

The numerical model's performance under actual transient driving conditions was assessed by using experimental measurements across the front catalyst brick from a 4.6L 2V Lincoln Town Car as it was driven during the Federal Test Procedure (FTP-72). The model results were compared to experimental measurements elsewhere [9]. The model predictions for the cumulative conversion efficiencies during the FTP cycle were found to be within 5% of the experimental measurements. The model's transient performance was validated by comparing the model's predictions of *instantaneous* conversion to the experimental measurements taken at 1 Hz resolutions. The comparison showed that the average difference between the model results and measurements was around 30%, which is within the experimental uncertainties. These validation results showed the suitability of the model in simulating the transient performance of catalyst.

The catalyst used for the present study was palladium based and had a length of 3 cm, cross-sectional area of 86.0254 cm^2, cell density of 62 cells/cm^2, and wall thickness of 0.1905 mm. The catalyst aging conditions were similar to those of Ref. [10]. The gas mass flow rate was 1.417×10^{-2} kg/s with 4.7184×10^{-5} kg/s CO, 8.0727×10^{-6} kg/s total HC, and 2.0363×10^{-6} kg/s NO, and the stoichiometric value of A/F was 14.51. The mean feed gas temperature was 327°C (600 K). The influence of exhaust gas temperature modulation on the catalyst dynamic behavior was investigated by considering a steady operating catalyst suddenly subjected to transient effects. The transient effects were simulated by sinusoidal modulations of the exhaust gas temperature entering the catalyst. During these oscillations, other inlet conditions remained unchanged.

Figure 1 shows the results of the imposed modulation near stoichiometric conditions at 14.7. During the simulations, the exhaust gas temperature, initially set at 600 K, is varied sinusoidally with

Downloaded 02 Jun 2010 to 171.66.16.107. Redistribution subject to ASME license or copyright; see http://www.asme.org/terms/Terms_Use.cfm

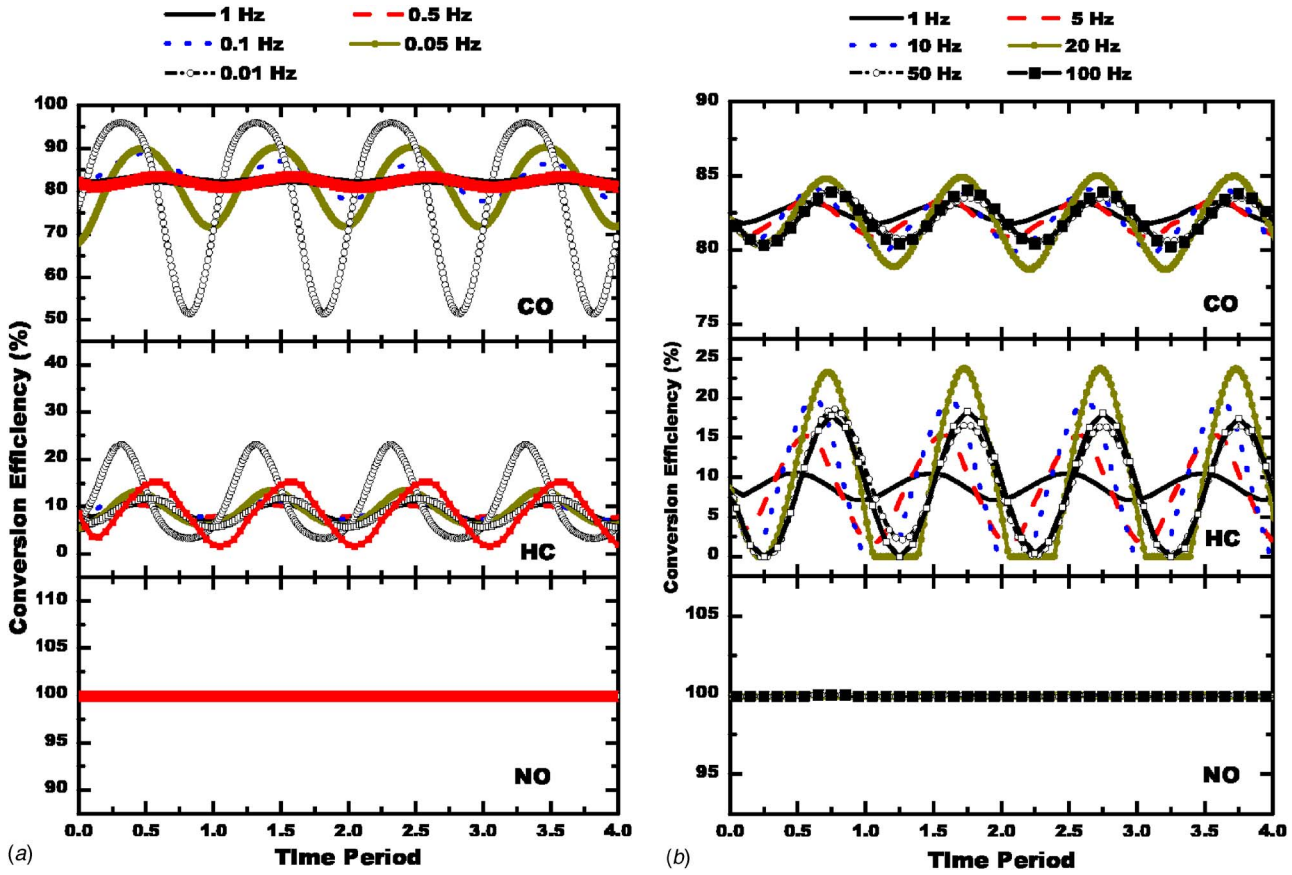

Fig. 5 Catalyst response to sinusoidal modulations in exhaust gas temperature: Effect of modulation frequencies on conversion efficiencies. (*a*) Frequency range=0.01–1 Hz, (*b*) frequency range=1–100 Hz (A/F=14.7, mean exhaust temperature =600 K, amplitude=10%).

a frequency of 0.01 Hz and amplitude of 10%. The low value of modulation frequency is selected in order to emphasize the effect of imposed modulation even though it is lower than that of the typical realistic modulations. The effect of other frequencies, which include more realistic values (such as 0.1–5 Hz), is presented in the following section. With the exhaust gas temperature ranging between 540 K and 660 K, the selected value of amplitude represents a modest level of modulation. The effect of higher modulation amplitudes are also considered in the next section. The imposed temperature modulations cause the catalyst to respond with a time delay.

The results show that CO and HC conversion efficiencies respond sinusoidally to the imposed sinusoidal temperature modulations. The conversion efficiencies increase corresponding to an increase in the exhaust gas temperature at the catalyst inlet. After reaching peak values, the conversion efficiencies decrease corresponding to a decrease in the exhaust gas temperature. The catalyst periodic response continues as long as the modulating temperature field is maintained. For the conditions studied, the catalyst NO conversion is very high (~100%) and is not much influenced by the imposed temperature modulations.

The imposed temperature modulation has a negative effect on the CO conversion. The time-average conversion efficiency, which is obtained by considering the cumulative pollutant species in and out of the catalyst during the first 400 s, exhibits a decrease of 3.8% from its steady-state value of 82.1% (see Table 1). For these operating conditions and the CO/HC ratio, HC conversion is low. It is, however, improved by the imposed modulation. The result listed in Table 1 shows that the HC time-average conversion efficiency exhibits an increase of 2.5% from its steady-state value of 8.71%. The catalyst's response is asymmetric with respect to its initial steady-state value. With a response amplitude, which is defined as the difference of peak and trough values of conversion efficiency, of 44.5%, the modulations have greater influence on CO emission conversion. The effect on HC emission conversion is

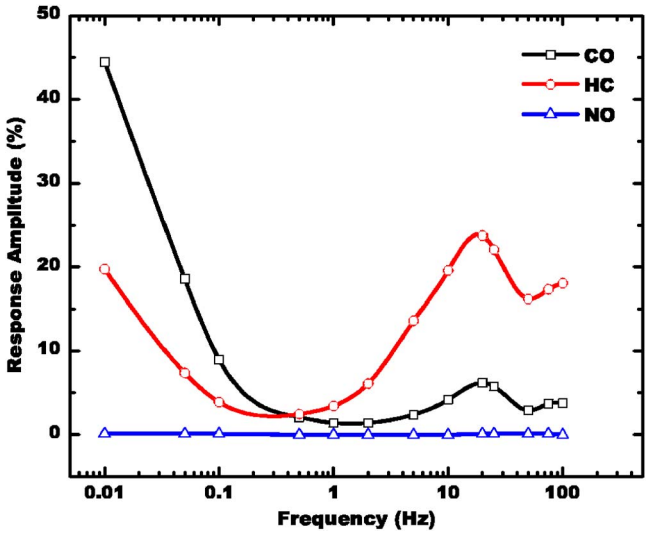

Fig. 6 Catalyst response to sinusoidal modulations in exhaust gas temperature: Effect of modulation frequencies on conversion response amplitudes (A/F=14.7, mean exhaust temperature=600 K, amplitude=10%)

Downloaded 02 Jun 2010 to 171.66.16.107. Redistribution subject to ASME license or copyright; see http://www.asme.org/terms/Terms_Use.cfm

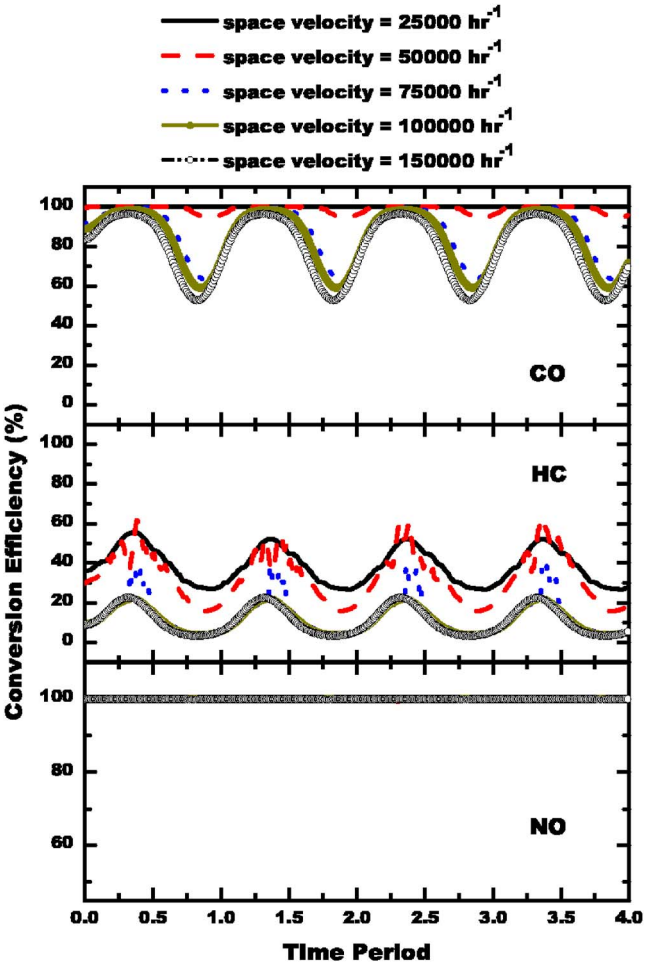

Fig. 7 Catalyst response to sinusoidal modulations in exhaust gas temperature near stoichiometric operating conditions for different space velocities (A/F=14.7, mean exhaust temperature=600 K, frequency=0.01 Hz, amplitude=10%)

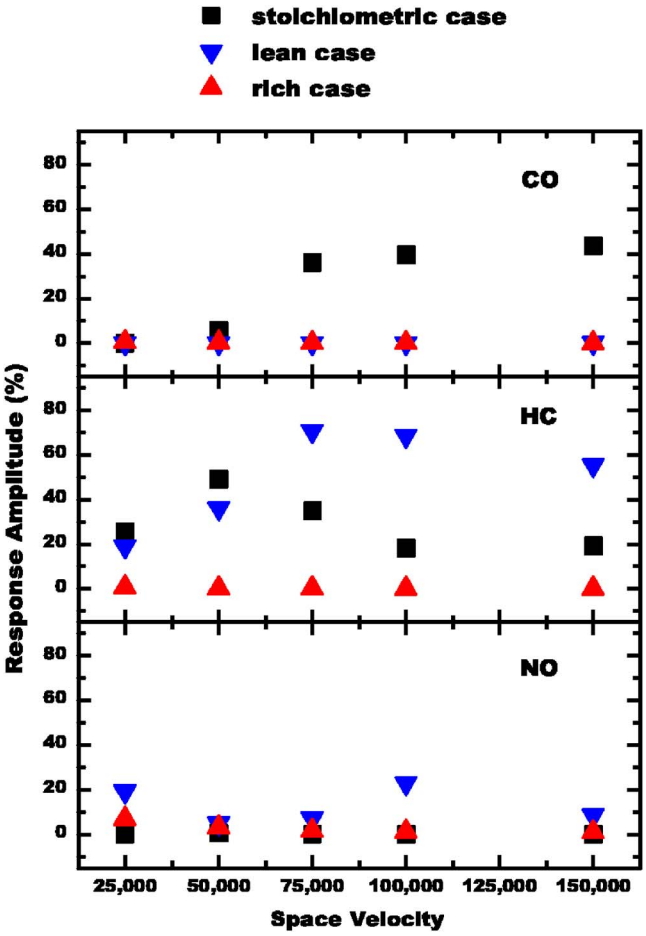

Fig. 8 Catalyst response to sinusoidal modulations in exhaust gas temperature for different space velocities (mean exhaust temperature=600 K, frequency=0.01 Hz, amplitude=10%)

relatively low (response amplitude is 19.8%) and the effect on NO conversion is insignificant (response amplitude is 0.1%).

The effects of temperature modulation in rich and lean regimes are presented next. The lean regime results, as shown in Fig. 2, were obtained by setting the A/F at 17.5. The catalyst is subjected to sinusoidal modulations in the exhaust temperature with a 0.01 Hz frequency and 10% amplitude. Under these conditions, CO conversion is high (~100%) and is not influenced by the imposed modulations. The HC conversion is also high (~90%), but is sensitive to the exhaust gas temperature and responds to the imposed modulations with a large amplitude. The response is periodic, nonsinusoidal, and asymmetric with respect to its initial steady-state value. The modulations result in a decrease in HC conversion performance as the time-average conversion efficiency is decreased by 6.7% from its steady-state value of 90.55%. The imposed modulations bring about a relatively small response from NO conversion, which is initially quite low owing to lean conditions. The response is periodic and nonsmooth, especially near the peak values. Overall, the effect of modulations on NO conversion is positive since the time-average conversion efficiency (5.6%) is higher than the initial steady-state value (4.7%).

The rich regime results, as shown in Fig. 3, were obtained by setting the A/F at 12.5. The catalyst is subjected to sinusoidal modulations in the exhaust temperature with a 0.01 Hz frequency and 10% amplitude. Under rich conditions, the catalyst is less sensitive to the imposed temperature modulations. The conversion performance responds to the modulations with very small amplitudes. Overall, there is no appreciable influence on the catalyst conversion performance.

Effect of Modulation Amplitude

Figures 4(*a*) and 4(*b*) show the effect of imposed modulation amplitude on the catalyst's pollutant conversion performance. These figures depict the catalyst conversion efficiencies as a function of oscillation time period for different amplitudes of exhaust gas temperature modulations and the response amplitude as a function of the imposed modulation amplitude. The results are for catalysts which are operating at A/F of 14.7 and are subjected to sinusoidal fluctuations in exhaust temperature of 0.01 Hz frequency. The results show that the increase of oscillation amplitude increases the catalyst's CO and HC conversion responses. The NO conversion is not affected by any imposed modulation amplitude, and remains high at 100%. For all imposed modulation amplitudes, the response amplitude of CO conversion is the largest. However, the HC conversion is relatively more sensitive to the changes in the imposed modulation amplitude, as indicated by a steeper slope of the HC response amplitude curve in Fig. 4(*b*). For all amplitudes, the catalyst response exhibits steady periodic behavior. For the conditions studied, other than the response amplitude, the fluctuation amplitude has insignificant influence on any other aspect of the catalyst response.

Downloaded 02 Jun 2010 to 171.66.16.107. Redistribution subject to ASME license or copyright; see http://www.asme.org/terms/Terms_Use.cfm

Effect of Modulation Frequency

Figure 5(*a*) presents the CO, HC, and NO conversion efficiencies as a function of imposed modulation time period for different frequencies. All these results are for catalysts initially operating at exhaust gas temperature of 600 K and subjected to sinusoidal modulation in exhaust gas temperature of 10% amplitude. Figure 5(*a*) depicts, as expected, that the catalyst response to imposed oscillation is large at low frequencies and its amplitude decreases with an increase of the imposed frequency.

The decrease in catalyst response at high frequencies is attributed to progressively greater neutralization of high-frequency fluctuations by diffusion processes over the time period required to convect them to the reaction sites. After reaching a minimum value, the influence of frequency on the catalyst response is reversed and the catalyst response to the imposed modulation starts increasing with an increase of frequency, as shown in Fig. 5(*b*). Figure 5(*b*) shows that the trend of increasing catalyst response with increasing frequency continues until 20 Hz. Beyond this value, the trend is again reversed and the response starts decreasing with increasing frequency until 50 Hz, followed by another reversal of trend.

The effect of frequency on the catalyst response can be better understood by plotting the response amplitude as a function of the imposed frequency, as in Fig. 6, which clearly shows that the catalyst response to the imposed temperature modulations is multimodal. This behavior is different from that caused by the imposed A/F and composition modulations. In such cases, the response has been reported to be unimodal [11,12]. This may be explained by considering that the catalyst's response to imposed modulations is mainly determined by diffusion and kinetic processes. Each of these processes has a different resonant frequency and is dominant in different frequency regimes. The diffusion processes are generally dominant in the low frequency regime. With the increase of imposed modulation frequency (the decrease of modulation time scale), the effect of diffusion processes becomes smaller. At higher frequencies, the response is mainly determined by the kinetic effects. Compared to A/F and composition modulations, the temperature modulations have stronger influence on kinetic effects and can invoke several response modes at high-frequency regimes resulting in a multimodal response.

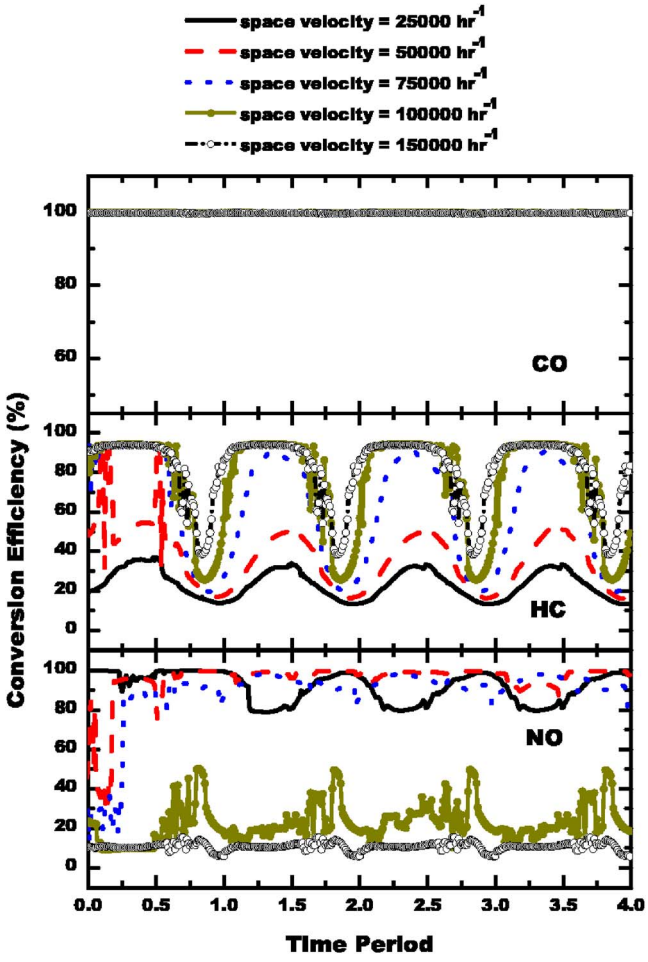

Fig. 9 Catalyst response to sinusoidal modulations in exhaust gas temperature under lean operating conditions for different space velocities (A/F=17.5, mean exhaust temperature=600 K, frequency=0.01 Hz, amplitude=10%)

Effect of Space Velocity

This section presents the effect of space velocity, which is defined as a ratio of the gaseous volumetric flow rate at standard temperature and pressure and the volume of the catalyst, on the catalyst's response to exhaust gas temperature modulation. In this study, the space velocity is varied by changing the inlet total gaseous mass flow rate while keeping the mass flow rates of three major pollutants constant. The study investigates a range of space velocities from 25,000 h^{-1} to 150,000 h^{-1}, which corresponds to a total gaseous mass flow rate range of 2.145×10^{-3} kg/s to 1.289×10^{-2} kg/s. Since the mass flow rates of major pollutant species (CO, HC, and NO) are fixed, the variations in the space velocity and in the corresponding total gaseous mass flow rate affect the molar concentrations of pollutant species, which are different for different space velocity cases. For example, inlet molar concentrations of pollutant species at 150,000 h^{-1} are six times higher than those at 25,000 h^{-1}. Thus, there are two effects of an increase in space velocity on the pollutant conversion performance: (i) a reduction in conversion performance owing to reduction is residence time and (ii) a variation in conversion performance owing to an increase in pollutant inlet molar concentrations. The second effect depends on the catalyst operating condition and generally increases the conversion performance [13]. Hence, the net effect of the variations in space velocity is the result of these opposing effects.

Figure 7 shows the results of the imposed modulation near stoichiometric conditions. During the simulations, the A/F is set at 14.7 and the exhaust temperature (initially set at 600 K) is varied sinusoidally with a frequency of 0.01 Hz and amplitude of 10%. The temperature ranges between 540 K and 660 K during each modulation time period. The catalyst responds to temperature modulation with different amplitudes at different space velocities.

The results show that the temperature modulation has a strong effect on the catalyst CO conversion at high space velocities, where the response amplitude is high and the conversion efficiency fluctuates within a wide range. The response is generally smooth and periodic. The response amplitude decreases with a decrease in space velocity (see Fig. 8). For 25,000–50,000 h^{-1}, the response is negligible and the catalyst becomes insensitive to the imposed modulation due to higher residence time.

The results show a significant effect of space velocity on the catalyst HC conversion response to the imposed temperature modulation. The response amplitude increases with an increase of space velocity up to 50,000 h^{-1} (see Fig. 8). After reaching a maximum value, the response amplitude decreases with increasing space velocity. The response is generally periodic and smooth except at 50,000 h^{-1} and 75,000 h^{-1}, where the response exhibits somewhat unsmooth behavior, which is owing to numerical convergence problem. NO conversion remains insensitive to the imposed temperature modulation for all values of space velocities.

The effects of space velocity on the catalyst's response to temperature modulation in lean and rich regimes are presented next. The lean regime results, as shown in Fig. 9, were obtained by setting the A/F at 17.5. The catalyst is subjected to sinusoidal

Downloaded 02 Jun 2010 to 171.66.16.107. Redistribution subject to ASME license or copyright; see http://www.asme.org/terms/Terms_Use.cfm

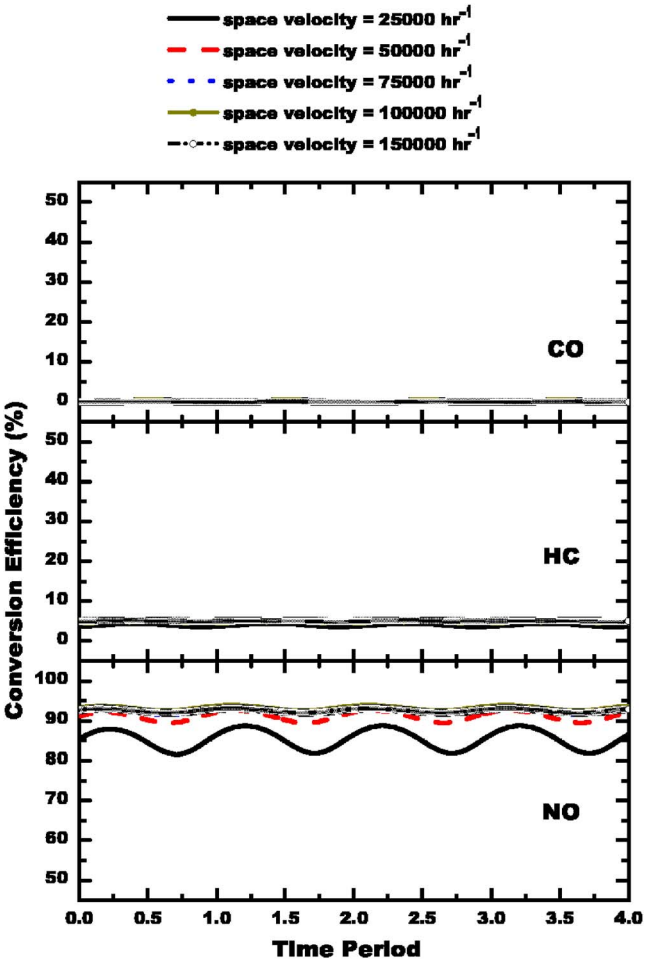

Fig. 10 Catalyst response to sinusoidal modulations in exhaust gas temperature under rich operating conditions for different space velocities (A/F=12.5, mean exhaust temperature =600 K, frequency=0.01 Hz, amplitude=10%)

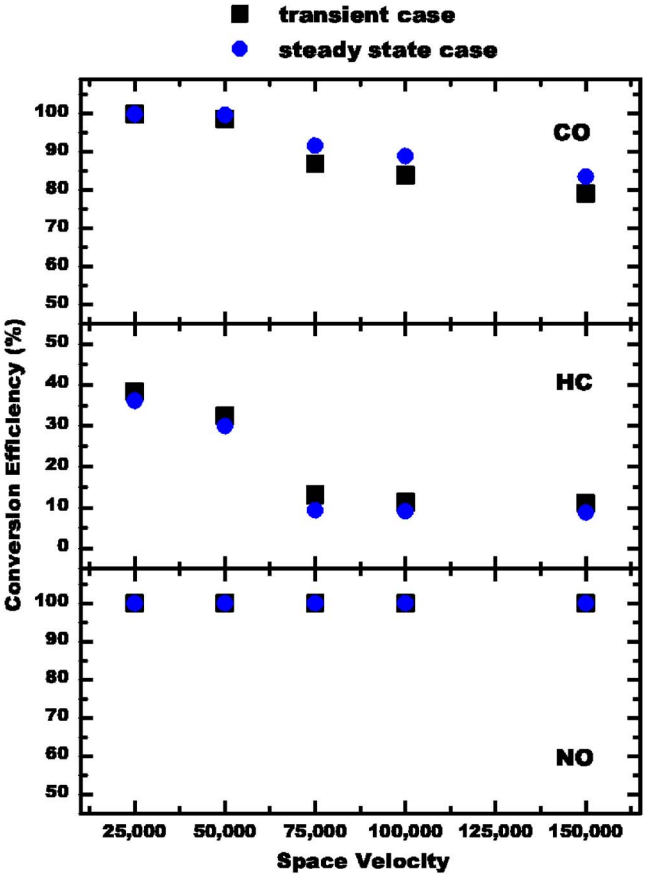

Fig. 11 Catalyst conversion efficiency for different space velocities in steady-state and transient (exhaust gas temperature modulation) conditions: near stoichiometric operating conditions (A/F=14.7, mean exhaust temperature=600 K, frequency=0.01 Hz, amplitude=10%)

modulations in the temperature with a 0.01 Hz frequency and 10% amplitude. Under these conditions, the CO conversion is very high (~100%) for all space velocities. The conversion is not affected by temperature modulation at any value in the range of space velocities investigated. The HC conversion is high at large space velocities. It decreases with a decrease in the space velocity, which is owing to a corresponding decrease in the inlet molar concentration of HC. The response amplitude increases with an increase of space velocity from 25,000 h^{-1} to 75,000 h^{-1} (see Fig. 9). Beyond this range, the response amplitude decreases slightly with an increase of the space velocity. The response is generally smooth and periodic.

Figure 9 shows that the space velocity also affects the NO conversion response to imposed modulation under lean conditions. As expected, the NO conversion is low at high space velocities and increases with a decrease of space velocity. The response amplitude is also affected by the space velocity, but there is no continuous increasing or decreasing trend. For the space velocity range investigated, the catalyst is most sensitive to the imposed modulation at 100,000 h^{-1}. The response is generally unsmooth and nonperiodic at several space velocities.

The rich regime results, as shown in Fig. 10, were obtained by setting the A/F at 12.5. The catalyst is subjected to sinusoidal modulations in the temperature with a 0.01 Hz frequency and 10% amplitude. Under rich conditions, the catalyst conversion performance is relatively less sensitive to the imposed temperature modulation. Particularly, the CO and HC conversions are insensitive and remain at their respective steady-state values for all space velocities. Under rich conditions, the NO conversion is high for all space velocities. The small increase of NO conversion with an increase of space velocity is owing to the corresponding increase of the inlet molar concentration of NO. The NO conversion response is low and decreases further with an increase of space velocity.

Comparison of Steady-State and Transient Results. Figures 11–13 show comparisons of the influence of the space velocity on the catalyst conversion performance under transient and steady-state conditions. For the transient case, the conversion efficiency shown represents the time-average conversion efficiency, which is obtained by considering the cumulative pollutant species in and out of the catalyst during the first 4 cycles.

Figure 11 shows the results near stoichiometric condition. The figure depicts that CO and HC conversion efficiencies decrease with an increase of space velocity for both steady-state and transient cases. The NO conversion remains mostly unchanged at all space velocities. The difference in conversion efficiencies of steady-state and transient cases is negligible at most of the space velocities. The modulations have a slightly negative effect on the CO conversion and a slightly positive effect on the HC conversion.

The results of lean conditions are plotted in Fig. 12. For these conditions, the space velocity does not have much influence on CO conversion, which remains high for both steady-state and transient cases. The effect of temperature modulation on the CO conversion is also negligible for all space velocities. The HC conver-

Downloaded 02 Jun 2010 to 171.66.16.107. Redistribution subject to ASME license or copyright; see http://www.asme.org/terms/Terms_Use.cfm

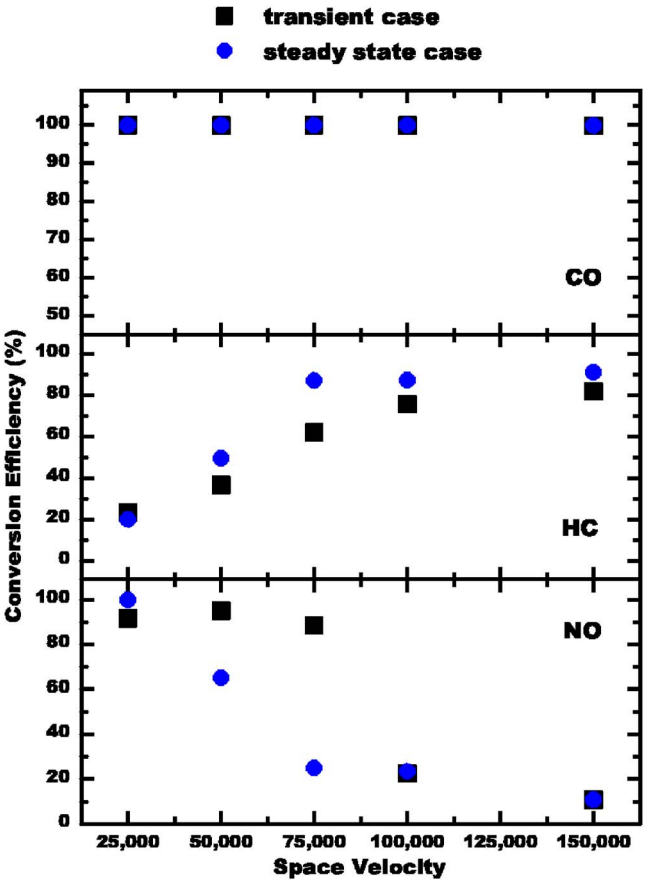

Fig. 12 Catalyst conversion efficiency for different space velocities in steady-state and transient (exhaust gas temperature modulation) conditions: under lean operating conditions (A/F =17.5, mean exhaust temperature=600 K, frequency=0.01 Hz, amplitude=10%)

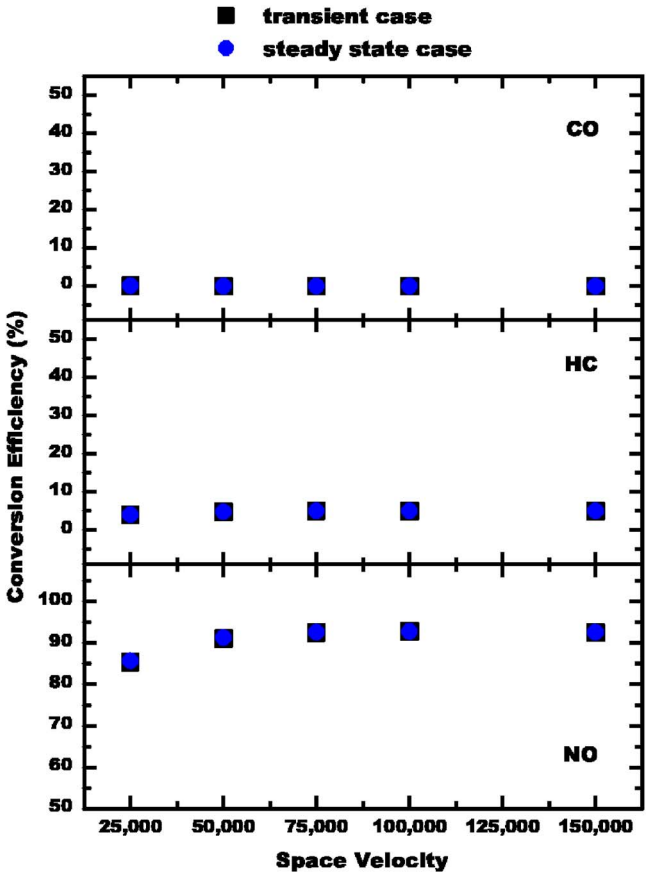

Fig. 13 Catalyst conversion efficiency for different space velocities in steady-state and transient (exhaust gas temperature modulation) conditions: under rich operating conditions (A/F =12.5, mean exhaust temperature=600 K, frequency=0.01 Hz, amplitude=10%)

sion is high at higher space velocities and decreases with a decrease in the space velocity for both steady-state and transient cases. This decrease is due to the corresponding decrease in the inlet molar concentration of HC, which has a more dominant negative effect on HC conversion than the opposing positive effect by an increase in the residence time. The lower HC conversion due to the corresponding increased availability of HC reductants improves the NO conversion at low space velocities. For 50,000–75,000 h^{-1}, the temperature modulation has a strong positive effect on the NO conversion, which becomes negligibly small at higher space velocities.

Figure 13 shows the comparison of the catalyst performance under rich conditions. The results show that the temperature modulation has no appreciable influence on the catalyst conversion performance for the investigated range of space velocities. At low space velocities, NO conversion shows a slight increase with an increase of the space velocity, which is due to corresponding increase of the inlet molar concentration of NO.

Conclusions

In this work, the influence of exhaust gas temperature on the catalyst dynamic behavior was examined. The transient conditions were simulated by considering the catalyst subjected to temporal modulation in exhaust gas temperature. The results led to the following conclusions:

- Under exhaust gas temperature modulations, a three-way catalytic converter exhibits a significant departure from its steady behavior. The departure is relatively significant near stoichiometric conditions and for catalyst CO and HC conversion performance. Near stoichiometric conditions, exhaust gas temperature modulations result in a decrease of CO conversion and improve HC conversion. The effect on NO conversion is insignificant.
- Under lean operating conditions, the temperature modulations result in a decrease of HC conversion and have no significant effect on CO and NO conversions. The modulations also do not have any appreciable effect on conversion performance under rich operating conditions.
- The effect of imposed modulation frequency on the catalyst's behavior is multimodal. At low frequencies, the catalyst's response is large and its amplitude decreases with an increase of the imposed frequency. After reaching a minimum value, the response starts increasing with an increase of frequency. The trend reverses again after reaching a maximum value. This behavior is different from that caused by the imposed air-fuel ratio and composition modulations, which depict unimodal response.
- The space velocity significantly influences the catalyst response to the imposed temperature modulation. The influence is greater at stoichiometric conditions and is different for different pollutant species.

Acknowledgment

The financial support from the Ford Scientific Research Laboratory, Oak Ridge National Laboratory, and the Center for Engineering Education and Practice (CEEP) of the University of Michigan–Dearborn is greatly appreciated.

Downloaded 02 Jun 2010 to 171.66.16.107. Redistribution subject to ASME license or copyright; see http://www.asme.org/terms/Terms_Use.cfm

Nomenclature

A/F = air-fuel ratio
C_g^j = gas phase concentration of species j, $\mathrm{mol/m^3}$
C_s^j = surface concentration of species j, $\mathrm{mol/m^3}$
Cp_g = specific heat of gas, J/(kg K)
Cp_s = specific heat of substrate, J/(kg K)
G_a = geometric surface area, $\mathrm{m^2/m^3}$
ΔH^k = heat of reaction of species k, J/mol
h_g = heat transfer coefficient between flow and substrate, $\mathrm{J/(m^2\ s\ K)}$
h_∞ = heat transfer coefficient between substrate and atmosphere, $\mathrm{J/(m^2\ s\ K)}$
k_m^j = mass transfer coefficient for species j, m/s
$n_{reaction}$ = total number of reactions
$N_{species}$ = total number of species
R^k = reaction rate of kth reaction, $\mathrm{mol/(m^2\ s)}$
S_{ext} = external surface to volume area ratio, $\mathrm{m^2/m^3}$
t = time, s
T_∞ = ambient temperature, K
T_g = gas temperature, K
T_s = substrate temperature, K
v_g = gas flow velocity, m/s
z = coordinate along catalyst axis, m

Greek Symbols

ε = void volume fraction
λ_s = thermal conductivity of substrate, J/(m s K)
ρ_g = gas density, $\mathrm{kg/m^3}$
ρ_s = substrate density, $\mathrm{kg/m^3}$

References

[1] Silveston, P. L., 1995, "Automotive Exhaust Catalysis Under Periodic Operation," Catal. Today, **25**, pp. 175–195.
[2] Herz, R. K., 1987, "Dynamic Behavior of Automotive Three-Way Emission Control System," *Catalysis and Automotive Pollution Control*, Elsevier, Amsterdam, pp. 427–444.
[3] Herz, R. K., 1981, "Dynamic Behavior of Automotive Catalysts: 1. Catalyst Oxidation and Reduction," Ind. Eng. Chem. Prod. Res. Dev., **20**, pp. 451–457.
[4] Silveston, P. L., 1996, "Automotive Exhaust Catalysis: Is Periodic Operation Beneficial?," Chem. Eng. Sci., **51**, pp. 2419–2426.
[5] Koltsakis, G. C., and Stamatelos, A. M., 1999, "Dynamic Behavior Issues in Three-Way Catalyst Modeling," AIChE J., **45**, pp. 603–614.
[6] Van Neer, F. J. R., Kodde, A. J., Den Uil, H., and Bliek, A., 1996, "Understanding of Resonance Phenomena on a Catalyst Under Forced Concentration and Temperature Oscillations," Can. J. Chem. Eng., **74**, pp. 664–673.
[7] Brandner, J. J., Emig, G., Liauw, M. A., and Schubert, K., 2004, "Fast Temperature Cycling in Microstructure Devices," Chem. Eng. J., **101**, pp. 217–224.
[8] Silveston, P. L., and Hudgins, R. R., 2004, "Periodic Temperature Forcing of Catalytic Reactions," Chem. Eng. Sci., **59**, pp. 4043–4053.
[9] Shamim, T., Shen, H., Sengupta, S., Son, S., and Adamczyk, A. A., 2002, "A Comprehensive Model to Predict Three-Way Catalytic Converter Performance," ASME J. Eng. Gas Turbines Power, **124**, pp. 421–428.
[10] Montreuil, C. N., Williams, S. C., and Adamczyk, A. A., 1992, "Modeling Current Generation Catalytic Converters: Laboratory Experiments and Kinetic Parameter Optimization—Steady State Kinetics," SAE Paper No. 920096.
[11] Shamim, T., and Medisetty, V. C., 2003, "Dynamic Response of Automotive Catalytic Converters to Variations in Air-Fuel Ratio," ASME J. Eng. Gas Turbines Power, **125**, pp. 547–554.
[12] Shamim, T., 2005, "Dynamic Behavior of Automotive Catalytic Converters Subjected to Variations in Engine Exhaust Compositions," Int. J. Engine Res., **6**, pp. 557–568.
[13] Shamim, T., 2005, "The Effect of Space Velocity on the Dynamic Characteristics of an Automotive Catalytic Converter," SAE Trans., **114**(4), pp. 974–982.

Downloaded 02 Jun 2010 to 171.66.16.107. Redistribution subject to ASME license or copyright; see http://www.asme.org/terms/Terms_Use.cfm

1D Engine Simulation of a Small HSDI Diesel Engine Applying a Predictive Combustion Model

T. Cerri
e-mail: tarcisio.cerri@polimi.it

A. Onorati
e-mail: angelo.onorati@polimi.it

Department of Energetics,
Politecnico di Milano,
Via La Masa 34, 20158 Milano, Italy

E. Mattarelli
e-mail: mattarelli.enrico@unimore.it
Department of Mechanical and Civil Engineering,
University of Modena and Reggio Emilia,
Via Vignolese 905, 41100 Modena, Italy

The paper analyzes the operations of a small high speed direct injection (HSDI) turbocharged diesel engine by means of a parallel experimental and computational investigation. As far as the numerical approach is concerned, an in-house 1D research code for the simulation of the whole engine system has been enhanced by the introduction of a multizone quasi-dimensional combustion model, tailored for multijet direct injection diesel engines. This model takes into account the most relevant issues of the combustion process: spray development, air-fuel mixing, ignition, and formation of the main pollutant species (nitrogen oxide and particulate). The prediction of the spray basic patterns requires previous knowledge of the fuel injection rate. Since the direct measure of this quantity at each operating condition is not a very practical proceeding, an empirical model has been developed in order to provide reasonably accurate injection laws from a few experimental characteristic curves. The results of the simulation at full load are compared to experiments, showing a good agreement on brake performance and emissions. Furthermore, the combustion model tuned at full load has been applied to the analysis of some operating conditions at partial load, without any change to the calibration parameters. Still, the numerical simulation provided results that qualitatively agree with experiments. [DOI: 10.1115/1.2747258]

Introduction

1D thermofluid dynamic simulation has been demonstrated to be a fundamental tool for engine design, thanks to its capability to provide an accurate prediction of intake and exhaust flows under actual engine operations [1–6]. However, when attention is focused on brake performance and engine-out emissions, a large amount of experimental information is generally required to model the combustion process.

As far as the diesel combustion process is concerned, some researchers [4,5] have recently tried to reduce the dependence of 1D engine simulation on experiments or empirical correlations. In order to have reliable estimations of engine outputs at an earlier design stage, it is necessary to develop multizone thermodynamic models for the most relevant in-cylinder processes.

Although for spark ignition (SI) premixed charge engines a few combustion models have been successfully implemented [6,7], the challenge is more difficult on diesels. Here, the combustion rate is primarily controlled by the interaction between fuel jets and surrounding air; thus, besides in-cylinder turbulence and chemical kinetics, it is necessary to properly model the droplet breakup and atomization process. Such a process is strongly related to fuel injection patterns, so that any accurate diesel combustion model must be integrated by specific information on the injection rate. Unfortunately, an experimental characterization at each operating condition is not a practical proposition, besides the fact that such a characterization would impair the capability of the combustion model as a fast predictive tool.

In the field of 1D thermofluid dynamic simulation of compression ignition engines, most of the combustion models are either based on the user inputs (typically, a heat release law is prescribed by means of a Wiebe function), or predictive (multizone, quasi-dimensional).

The first development of the latter class of models may be awarded to Austen and Lyn [8]. Through the years, many diesel multizone combustion models have been proposed, introducing simple submodels to account for the spray evolution in the chamber. Some models consider only the mixing between fuel vapor and surrounding air [9], generally assuming an instantaneous vaporization of the injected fuel [10]. In other models, the liquid fuel atomization and evaporation are analyzed, but under the hypothesis that they occur more quickly than the fuel vapor-air mixing process. In both the previous cases, the modeling of a liquid phase within the combustion chamber is not considered. Nowadays, most of the recent multizone models are based on the Hiroyasu approach for the description of the fuel spray formation and evolution within the combustion chamber, even though some researchers [11] pointed out that the Hiroyasu correlation may not be fully reliable, when applied to the injection process of modern common-rail diesel engines.

In literature, different approaches are adopted to simulate the diffusive and premixed phases of compression ignition (CI) engines combustion: some researchers [12] assume that the burning rate is a function of the air entrainment into the spray during the premixed phase; others [13] suggest that the chemical reactions between air and fuel take place only under stoichiometric conditions. The present paper reviews the development of a 1D thermofluid dynamic numerical model for the simulation of a modern HSDI diesel engine, including a multizone combustion model for the prediction of heat release and engine-out emissions. This goal has been achieved by enhancing the simulation code developed in house by the authors.

As far as fuel injection patterns are concerned, the authors have also developed, for common-rail injection systems, an empirical model that is able to calculate the instantaneous fuel injection rate as a function of injection pressure and energizing time. Obviously, the model parameters must be tuned for each application, on the basis of a few experimental data.

The diesel engine investigated is a FIAT mass-production automobile unit, 1.25 L of capacity, as shown in Fig. 1; its main features are listed in Table 1. An experimental campaign has been carried out on this engine at the dynamometer bench, at both full

Contributed by the Internal Combustion Engine Division of ASME for publication in the JOURNAL OF ENGINEERING FOR GAS TURBINES AND POWER. Manuscript received May 26, 2006; final manuscript received April 11, 2007; published online December 26, 2007. Reveiw conducted by Margaret Wooldridge. Paper presented at the 2006 Spring Conference of the ASME Internal Combustion Engine Division (ICES2006), May 7–10, 2006, Aachen, Germany.

Copyright © 2008 by ASME

Downloaded 02 Jun 2010 to 171.66.16.107. Redistribution subject to ASME license or copyright; see http://www.asme.org/terms/Terms_Use.cfm

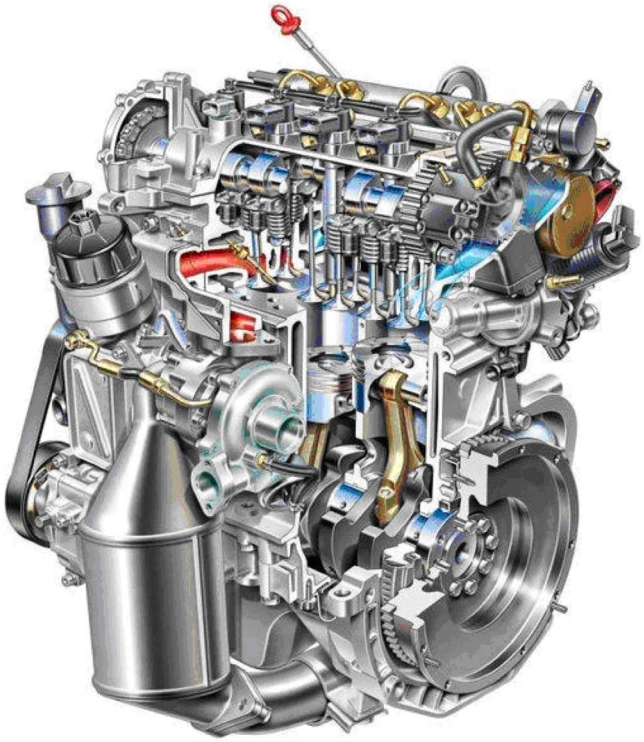

Fig. 1 Picture of the HSDI turbocharged diesel engine investigated (FIAT 1.25 L multijet)

and partial load. The experimental results have been used to calibrate the parameters of the numerical model, as well as to assess the accuracy of simulation.

Fluid Dynamic Simulation

The GASDYN thermofluid dynamic 1D code, developed by the authors at Politecnico di Milano [1,3,7], has been used to predict the engine gas exchange process. The numerical model is based on the conservation equations for one-dimensional, unsteady, compressible, reacting flows in ducts with variable cross section. The mass, momentum, energy conservation equations plus the species continuity equations (introduced to account for transport of chemical species with reactions) are considered. The internal energy of the *n*th species of the mixture can be expressed by means of polynomial relationships; hence, the specific heats depend on both gas temperature and chemical composition. The source terms, which express the production/destruction rate of the *n*th species during transport, are determined on the basis of the species reaction rates in the exhaust manifold (gas-phase reactions) and in the catalytic converters (solid-phase reactions). The system of conservation equations represents a quasi-linear hyperbolic problem that can be solved by means of shock-capturing numerical methods. The simulation code makes use of symmetric finite difference techniques with second-order accuracy, such as the classical MacCormack predictor-corrector method and the two-step Lax-Wendroff method, with the addition of flux-limiting techniques [1–3,7], the conservation element–solution element (CE-SE) method [1–3,7], and the first-order Harten-Lax-Leer contact surface (HLLC) method [1–3,7].

Table 1 Main characteristics of the HSDI turbocharged diesel engine investigated

Engine type	HSDI 4-S diesel
Number of cylinder	4 in-line
Total displacement [cm^3]	1248
Bore [mm]	69.6
Stroke [mm]	82
Compression ratio	17.6:1
Number of valves per cylinder	4
Air metering	VGT turbocharger, intercooler
Injection system	Common rail, multijet
Max. injection pressure [MPa]	160
Injector hole diameter [mm]	0.121
Number of injector holes	6

The turbocharged HSDI diesel engine studied in this work has been modeled considering the whole intake and exhaust systems and the turbocharger. The prediction of the compressor delivery pressure and temperature is essential to provide proper initial conditions for the combustion process. Hence, a detailed simulation of the turbocharger matching to the engine has been carried out for each operating condition, calculating the instantaneous turbocharger energy balance. A quasi-steady approach has been followed to calculate the compressor and the variable geometry turbine boundary conditions, accounting for the transmission and reflection of pressure waves. The steady flow maps provided by the manufacturer have been used to represent the characteristics of the turbocharger, in terms of pressure ratio and efficiency as a function of mass flow rate and revolution speed. The maps allow the code to calculate the instantaneous energy balance of the turbocharger, then the inlet and outlet conditions at each crank angle along the simulation. A standard proportional-integral-derivative (PID) controller has been adopted to regulate the rack of the variable geometry turbine, in order to achieve the required boost pressure.

A critical issue of the simulation is the modeling of the exhaust gas recirculation (EGR) circuit, including the cooling system. The EGR valve has been represented by an orifice, whose effective area is calculated in order to predict the experimental air mass flow rate. The heat transfer coefficients have been calibrated in order to match the measured gas temperatures.

A satisfactory prediction of air mass flow rate, air pressure, and temperature downstream of the compressor, and exhaust gas pressure and temperature upstream and downstream of the turbine, has been achieved at all the operating conditions of interest. However, since the paper is focused on the description and validation of the multizone diesel combustion model, more emphasis will be given to the combustion simulation and to performance and emissions results.

In-Cylinder Spray Model Development and Combustion

The computational time requested by the simulation of a turbocharged diesel engine, including the whole intake and exhaust systems and the turbocharger, is generally high. The modeling of the engine-turbocharger assembly requires, indeed, the calculation of many thermodynamic cycles before convergence (20–50, depending on initial conditions and the setup of the turbine controller). During this transient calculation, compressor boost pressure and air temperature may be far from their final values, as well as the value of the trapped mass. Hence, combustion simulation may provide incorrect values of pressure and temperature of exhaust gases, thus influencing the energy available to the turbine and the convergence speed of the whole fluid dynamic simulation. To reduce this computational effort, it is suitable to adopt a simplified three-zone combustion model, until the convergence of the turbocharger parameters has been reached. Hence, it is assumed that the in-cylinder volume is divided into three different zones: fuel vapor zone, fresh charge zone (air and burnt gas of the previous thermodynamic cycle), and burnt gas zone [14]; furthermore, the injected fuel vaporizes instantaneously [9] and the fuel and air chemical reaction is stoichiometric [15]. All the gases within the cylinder (including fuel vapor) are assumed to be ideal.

After convergence, a more complex quasi-D, multizone, predictive combustion model is applied to determine in-cylinder pres-

Downloaded 02 Jun 2010 to 171.66.16.107. Redistribution subject to ASME license or copyright; see http://www.asme.org/terms/Terms_Use.cfm

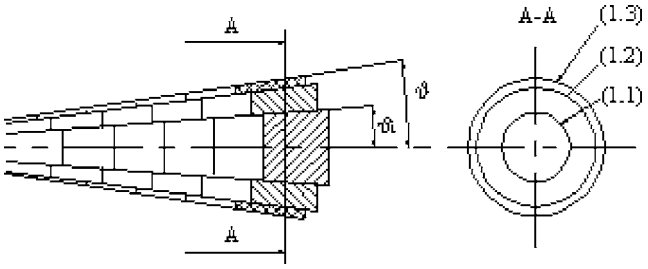

Fig. 2 Schematic of the fuel spray structure

sure and temperature and raw emissions. This model, implemented by the authors, can be described as follows.

First, a spray submodel is introduced to predict the distribution of air-fuel ratio throughout the combustion chamber. During combustion, there are as many fuel jets as the injector holes: for the sake of simplicity, any difference among sprays is neglected. In order to simulate the operations of a modern DI diesel engine, the model may take into account multiple injections, for instance, pilot injection, preinjection, main, and after (post-) injection.

Each fuel spray is divided into a set of zones along its axis, according to the instantaneous injected quantity and the computational time step. Each zone is then subdivided into annular regions, on the plane normal to the penetration axis (Fig. 2). Typically, the total number of zones in the radial direction is three or four. No mass exchange occurs between adjacent zones, but only between spray and surrounding gas, according to the air entrainment model. The fuel flow rate through the nozzle is calculated by means of a specific model that will be described later.

The fuel is injected at the liquid state and is supposed to behave as a "liquid column" along the penetration axis until breakup. Breakup and spray penetration lengths have been calculated using the Levich [16], Hiroyasu and Arai [17], and Hiroyasu et al. [18] correlations, after a proper calibration of the parameters, on the basis of experimental measurements performed on current HSDI diesel injectors [4,5].

The parcel velocity along the jet axis before breakup is obtained from the following relation [19]:

$$v = C_D\left(\frac{2\Delta p}{\rho_l}\right)^{0.5} \tag{1}$$

where Δp is the pressure drop through the nozzle hole, ρ_l is the liquid fuel density, d_n is the nozzle hole diameter, and C_D is the discharge coefficient varying from 0.6 to 0.8 for nozzles of modern HSDI diesel engines.

The breakup time is calculated by means of [5]

$$t_b = 4.351\frac{\rho_l d_n}{C_D(\rho_a \Delta p)^{0.5}} \tag{2}$$

After breakup and before any jet impingement against the combustion chamber walls, the parcel velocity along the jet axis becomes [4]

$$v = \frac{2.95}{2}\left(\frac{\Delta p}{\rho_a}\right)^{0.25}\left(\frac{d_n}{t}\right)^{0.5} \tag{3}$$

where ρ_a is the ambient gas density.

After any wall impingement, the jet velocity is defined by means of the following relation [17]:

$$v = \frac{2.95}{2}\left(\frac{\Delta p}{\rho_a}\right)^{0.25} d_n \frac{t_{\text{hit}}^{0.25}}{t^{0.75}} \tag{4}$$

where t_{hit} is the time instant when the spray parcel touches the wall (Fig. 3). In order to calculate the t_{hit} value, it is necessary to model, at least in a simplified manner, the geometry of the combustion chamber.

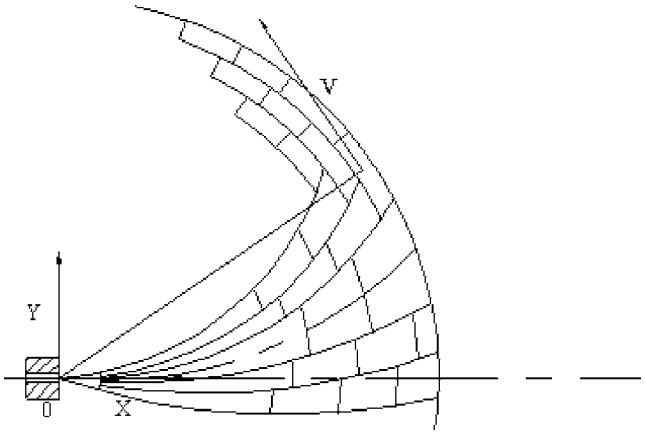

Fig. 3 Schematic of the fuel spray: jet formation after wall collision

During injection, three impingement conditions may occur:

- The piston is far from TDC; the collision is on the cylinder liner (Fig. 4(*a*)).
- The piston is close to TDC; the collision occurs within the bowl (Fig. 4(*b*)).
- The piston is close to TDC; the jet is deflected by the piston crown and then hits the cylinder liner (Fig. 4(*c*)). In this case, any liquid film formation on the piston is neglected.

The effect of air swirling motion on spray is accounted for considering the local components of air velocity in the radial and axial directions, and modifying the air-entrainment rate, which is computed on the basis of the momentum conservation equation [17]. When the breakup time is reached, all the droplets into a zone are assumed to have a diameter equal to the initial SMD. Although droplet size distribution and atomization details are neglected [4,5,17], their dependence on the instantaneous in-cylinder physical and thermodynamic conditions and on the characteristics of the fuel injection system is considered.

Each liquid droplet receives energy from the surrounding gas, increasing its temperature and then evaporating. Heat transfer from gas to liquid droplet is given by

$$m_d \dot{h}_d = \dot{m}_d L + \pi D \kappa \text{Nu}(T - T_d) f \tag{5}$$

where m_d is the droplet mass, h is the enthalpy, T is the temperature, L is the latent heat of evaporation, D is the droplet diameter, k is the thermal conductivity, Nu is the Nusselt number following the correlation proposed by Ranz and Marshall [20], and f is a factor [21] that corrects the heat exchange rate for the presence of mass transfer.

The evaporation rate can be deduced by Eq. (5), setting the left-hand term to zero; then, the following correlation is used:

$$\dot{m}_d = \pi D D_V \text{Sh}\frac{p_{\text{cyl}}}{R_v T_m}\ln\left(\frac{p_{\text{cyl}}}{p_{\text{cyl}} - p_{v,\text{surf}}}\right) \tag{6}$$

where D_V is the mass diffusivity, Sh is the Sherwood number, p_{cyl} is the cylinder pressure, and $p_{v,\text{surf}}$ is equal to the saturation pressure corresponding to the temperature of the droplet [5].

When evaporation occurs, the surrounding air enters the spray zone and mixes with the evaporated fuel. The air entrainment rate can be calculated assuming that the initial momentum imparted to a parcel at the nozzle exit is conserved at any subsequent location [4,5], so that

Downloaded 02 Jun 2010 to 171.66.16.107. Redistribution subject to ASME license or copyright; see http://www.asme.org/terms/Terms_Use.cfm

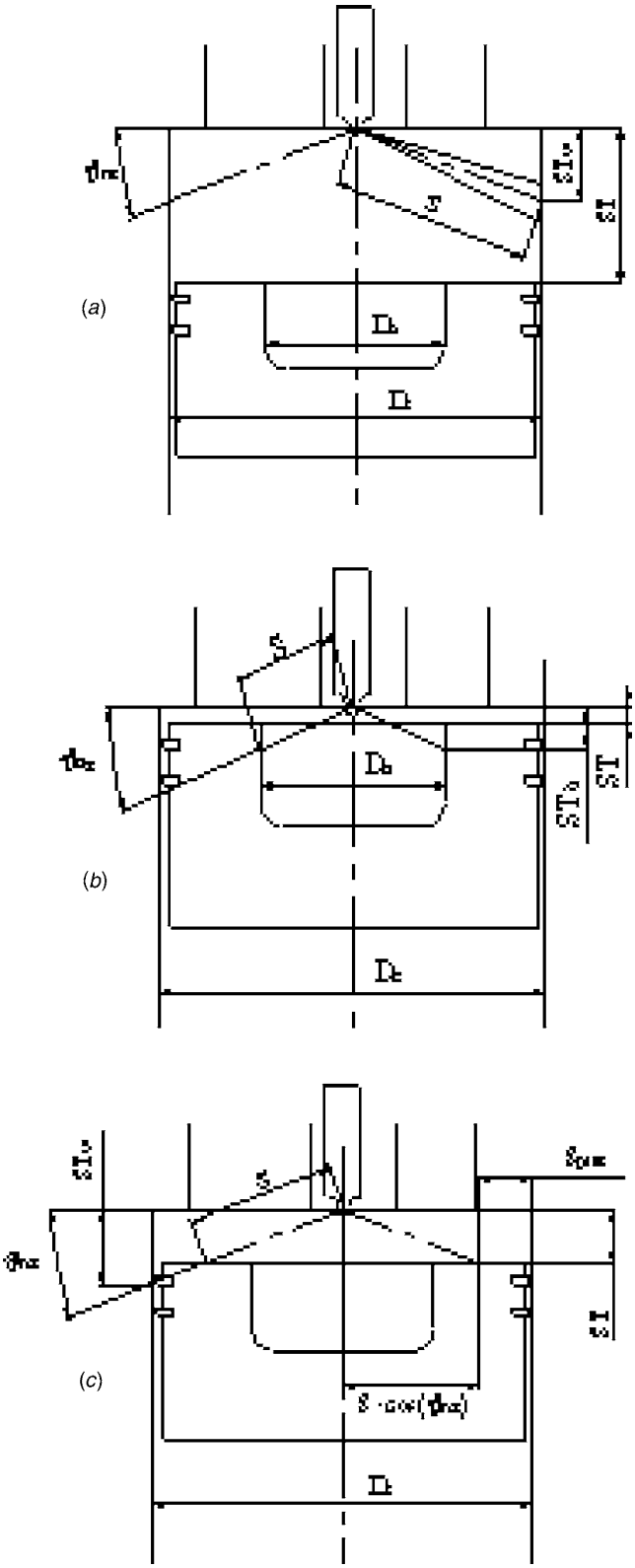

Fig. 4 (*a*) Cylinder wall collision, (*b*) piston bowl wall collision, and (*c*) impact with piston crown

$$m_u = m_f\left(\frac{u_i}{v - v_s} - 1\right)c_f \tag{7}$$

where m_u is the unburned mass entrained into the zone, u_i is the fuel velocity at the nozzle, v_s is the component of swirl velocity along the hole axis, m_f is the liquid fuel mass into the zone at the injection time, and c_f is a calibration factor. It is remarked that the unburned mass is the sum of fresh air and residual gases within the cylinder.

Into each zone, convective heat transfer from hot gases to liquid fuel droplets is determined as [22]

$$q = \pi D N k_m f(T_a - T_l)\mathrm{Nu} \tag{8}$$

where N is the number of droplets within a zone, T_a and T_l are the ambient gas and the liquid temperature, Nu is the Nusselt number, k_m is the mean thermal conductivity, and f is the heat factor previously defined.

Finally, an energy balance is applied to the liquid fuel contained in each zone. Since the evaporation rate and relative heat transfer are already known for all the droplets, it is possible to compute the resulting variation of liquid fuel temperature. The ignition delay of each single zone is computed through a semi-empirical formulation, considering the influence of pressure, temperature, and local equivalence ratio [4]. Then, the fuel reaction rate is calculated according to the following equation:

$$\dot{m}_{fb} = K_b C_f^{af} C_O^{aO} e^{-E_c/RT} \tag{9}$$

where K_b is a constant, E_c is the activation energy, and C_f and C_O are the mass concentration of fuel and oxygen, respectively.

Heat fluxes through the wall boundaries are determined by means of the Woschni correlation [23], considering both convective and radiation terms for each zone into which the combustion chamber has been divided. Once the total heat transfer rate has been calculated, its value is distributed among the parcels, according to a weighting criterion based on the energy content of each zone

$$\dot{Q}_k = \dot{Q}_{ht}\frac{(m_k c_{vk} T_k)}{\sum_{j=1}^{n} m_j c_{vj} T_j} \quad k = 1, \ldots, n \tag{10}$$

where k and j represent the index of each zone defined into the combustion chamber.

After evaluating the global heat transfer through the walls, the thermodynamic properties can be calculated taking into account the heat released by combustion and the work done by the piston sweeping the cylinder. In this way, each burnt zone will feature its own temperature and air-fuel ratio, so that each local contribution to the formation of pollutant emissions can be accounted for. As far as the chemical composition of in-cylinder burnt gases is concerned, the GASDYN code uses the method described in [7,24], based on the evaluation of the equilibrium concentrations of the major species (H_2O, H, H_2, CO, CO_2, O, O_2, OH, N_2, NO). An extended six-reaction Zeldovich model is applied to simulate the kinetically controlled NO formation process [7], while the semi-empirical Hiroyasu model predicts the net soot formation rate [25].

At the end of injection and after the start of combustion, some air (generally mixed with residual gases) has not yet entered the burned zones. As this process takes place, it will influence, significantly, the concentration of pollutant emissions. For this reason, a specific model has been developed in the code, in order to describe the mixing of residual air and burnt gases. The mass flow rate entering this mixing zone is defined by the following expression:

Downloaded 02 Jun 2010 to 171.66.16.107. Redistribution subject to ASME license or copyright; see http://www.asme.org/terms/Terms_Use.cfm

$$\dot{m}_{\mathrm{mix}} = \frac{m_u \sum_{i=1}^{n} m_{b_j}}{m_u + \sum_{j=1}^{n} m_{b_j} + m_{\mathrm{mix}}} \frac{1}{t_t} \tag{11}$$

where m_u is the residual mass not entrained into the burnt zones, m_{bj} is the burnt mass of the jth spray zone, t_t is the turbulent time scale, given by

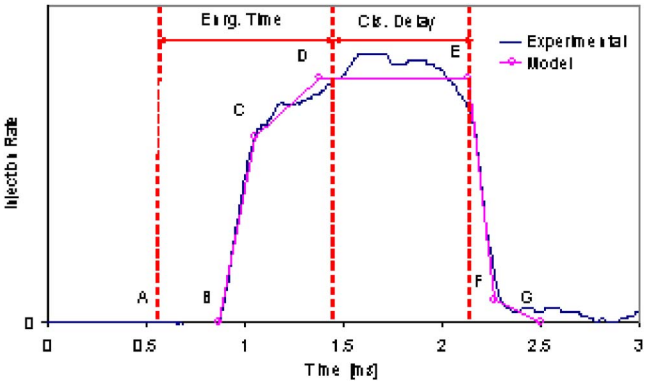

Fig. 5 Comparison of experimental and model results at the rail pressure of 160 MPa and energizing time of 0.8 ms

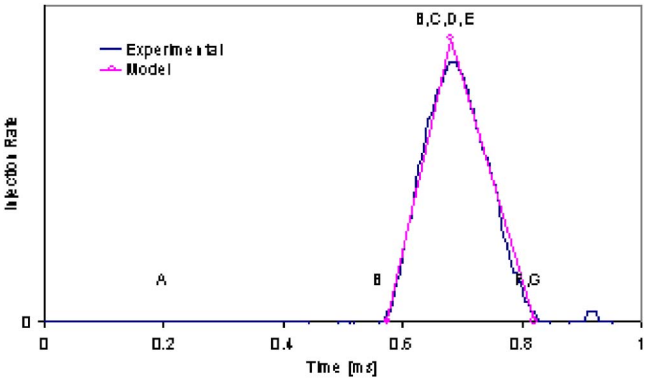

Fig. 6 Comparison of experimental and model results at the rail pressure of 120 MPa and energizing time of 0.24 ms

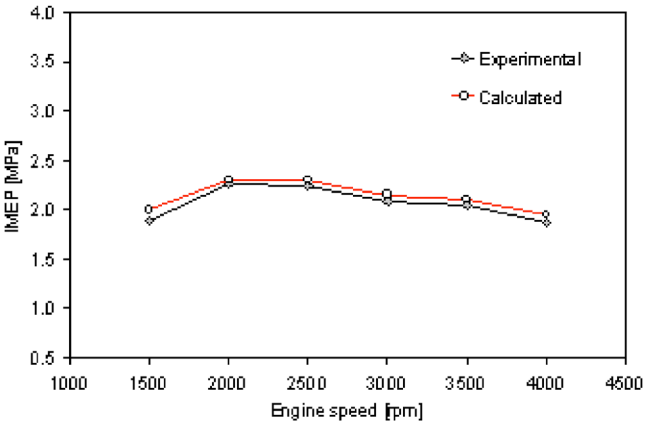

Fig. 7 Comparison between predicted and measured IMEP of the HSDI turbocharged diesel engine, as a function of the engine speed at full load

$$t_t = c_t \frac{L_i}{u'} \tag{12}$$

where L_i (in meters) is the integral length scale and u' (in meters per second) is the mean turbulent intensity (computed by a K-k turbulence model [26]), and c_t is a tuning constant. A full description of this model has been already given in [7].

Finally, the temperature of this mixing zone will be determined assuming an isoenthalpic process,

$$T_{\mathrm{mix}} = \frac{m_{\mathrm{mix},u} c_{p,u} T_u + \sum_{j=1}^{n} m_{\mathrm{mix},b_j} c_{p,b_j} T_{b_j}}{m_{\mathrm{mix}} c_{p,\mathrm{mix}}} \tag{13}$$

where the subscript u refers to the unburned external mass, b to the burnt gas, and "mix" to the mixing zone.

The chemical composition of the mixing zone will depend on the composition of the surrounding zones, which contribute directly to its formation,

$$n_{\mathrm{mix},i} = (n_{\mathrm{mix},i})_p + \frac{n_{u,i}}{\sum_i n_{u,i}} \frac{dm_{\mathrm{mix},u}}{\mathrm{MW}_u} + \frac{n_{b,i}^N}{\sum_i n_{b,i}^N} \frac{dm_{\mathrm{mix},b}}{\mathrm{MW}_b} \tag{14}$$

where the subscript i stands for the ith chemical species and the suffix p is used to indicate the previous time step; the suffix N denotes the last existing burnt zone, while MW is the molecular weight. Hereafter, the composition evolves according to the previously mentioned chemical algorithm, whose importance becomes fundamental for the kinetically controlled species.

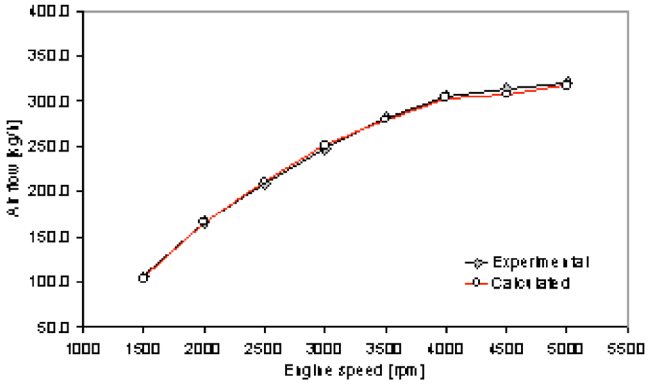

Fig. 8 Comparison between predicted and measured air mass flow rates, as a function of engine speed at full load

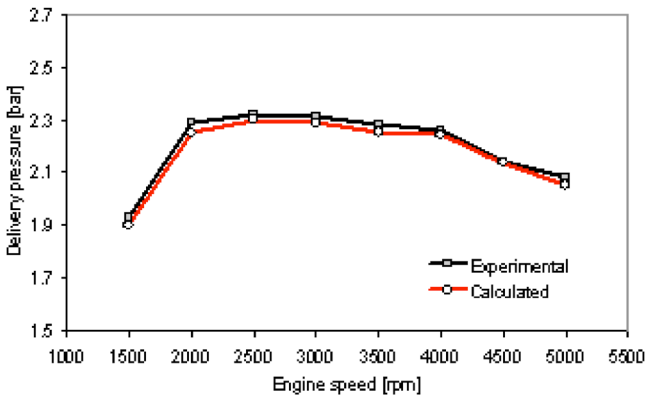

Fig. 9 Comparison between predicted and measured compressor boost pressure as a function of engine speed at full load

Downloaded 02 Jun 2010 to 171.66.16.107. Redistribution subject to ASME license or copyright; see http://www.asme.org/terms/Terms_Use.cfm

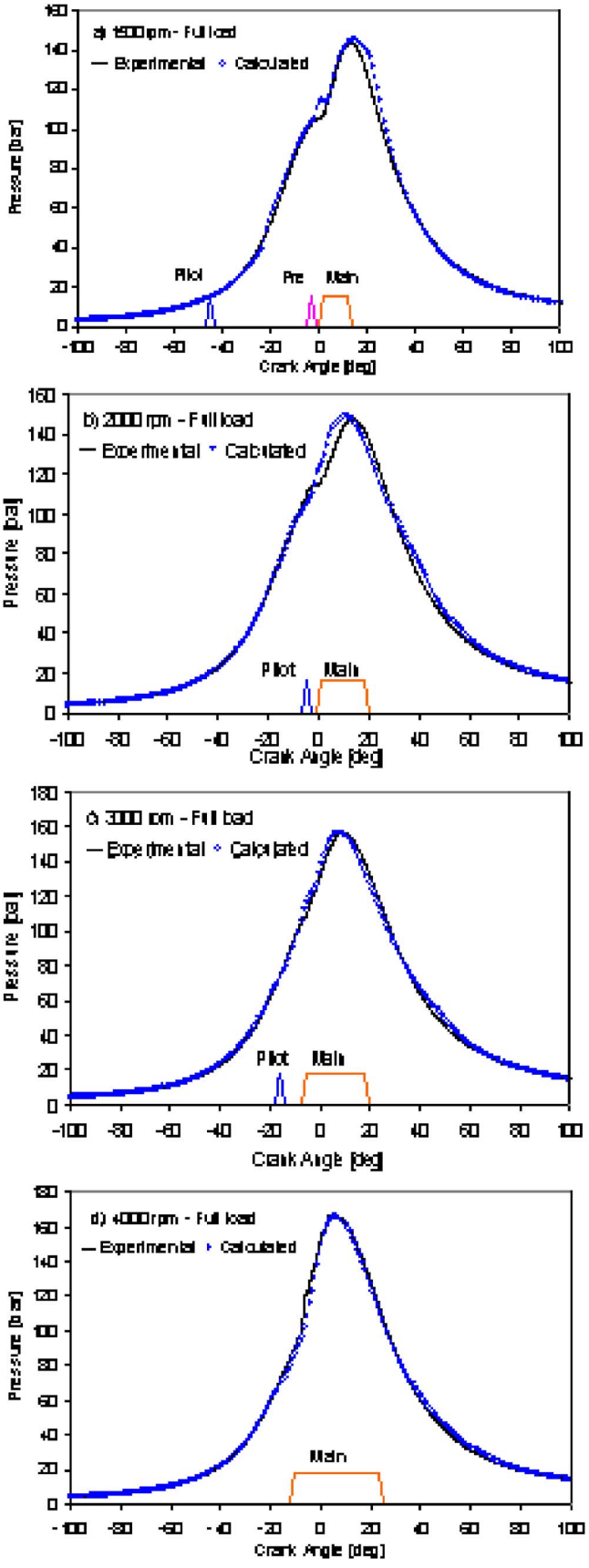

Fig. 10 Comparison between measured and predicted in-cylinder pressure at full load and different speeds: (*a*) 1500 rpm, (*b*) 2000 rpm, (*c*) 3000 rpm, and (*d*) 4000 rpm

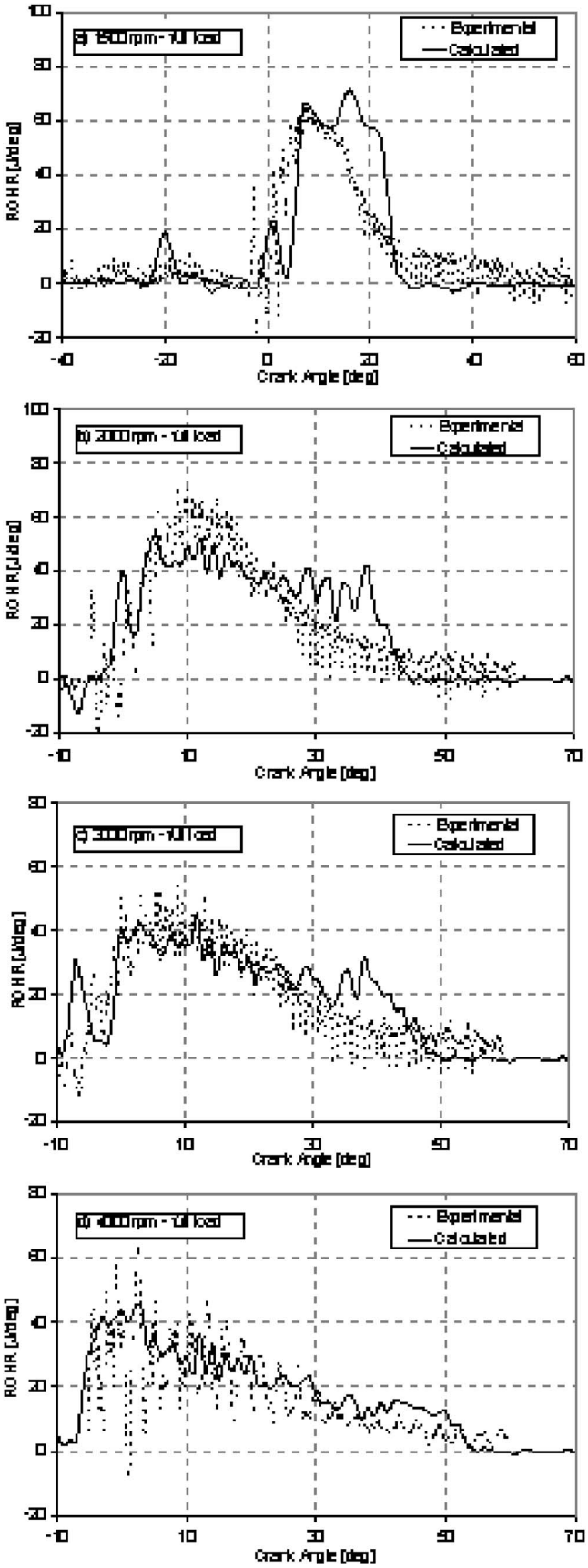

Fig. 11 Comparison between measured and predicted rate of heat release at full load and different speeds: (*a*) 1500 rpm, (*b*) 2000 rpm, (*c*) 3000 rpm, and (*d*) 4000 rpm

Downloaded 02 Jun 2010 to 171.66.16.107. Redistribution subject to ASME license or copyright; see http://www.asme.org/terms/Terms_Use.cfm

Injection Rate Model

The prediction of the spray basic patterns requires previous knowledge of the instantaneous fuel injection rate. This parameter can be measured by means of specific devices [27–29], yielding a proportional electric signal. The correlation factor is obtained by equating the time integral of the signal to the injected mass, which, in turn, must be carefully measured. Since this standard procedure is time consuming, in practice it can be carried out only at a few operating conditions, defined by energizing time and rail pressure. The goal of the empirical model, developed by the authors in conjunction with Bianchi and Falfari [30], is the extrapolation of the injection rate at a generic operating condition from the experimental characterization of a few points. All the hypotheses of the model are based on theoretical and experimental results available on the second generation of the Bosch common rail, and the extension of the model to other injection systems should be made with a lot of care.

For long energizing time, it is assumed that the curve of injection rate as a function of time can be represented by a broken line, as in Fig. 5, where each tract corresponds to an operating stage. Tract AB represents the opening delay, i.e., the elapsed time between the start of energizing and the beginning of needle lift. It is assumed that this time does not depend on operating conditions. Tract BC corresponds to the first opening ramp, where flow rate is controlled by both nozzle area and the growing of pressure within the sac. It is assumed that the slope of this tract is proportional to rail pressure. Tract CD is the second opening ramp. In comparison to the first ramp, the slope is reduced since the nozzle area does not change anymore. Also in this case, the slope is assumed to be proportional to rail pressure. In tract DE, neither sac pressure nor nozzle area change, since injection pressure has reached a value very close to that within the rail (besides flow losses), while the needle is "floating" at the maximum lift, so that the nozzle area corresponds to the cross section of the holes. In this tract, the fuel mass flow rate is given by

$$\dot{m}_f = C_D A_H \sqrt{2\rho_l \Delta p} \tag{15}$$

with being C_D a discharge coefficient, A_H the hole cross-sectional area, ρ_l the fuel density, and Δp the pressure drop across the injector nozzle.

Tract EF is the first closing ramp, where both injection pressure and nozzle area are reducing. It is assumed that the slope is proportional to rail pressure. Finally, tract FG is the second closing ramp, characterized by a lower slope since the needle has reached its seat, and the flow is given only by the residual fuel within the sac. Also in this case, the slope can be assumed proportional to rail pressure.

Further hypotheses made in the model are that the closing delay (i.e., the elapsed time between the end of energizing and the start of needle closing) is proportional to the square root of rail pressure, while the transition from the first to the second ramp, in both opening and closing events, occurs when velocity reaches a given fraction of its maximum value. For short energizing times (typical of pilot, pre-, and post-injections) the shape of the fuel rate curves changes as visible in Fig. 6. This behavior can be explained considering that the energizing time is not long enough to allow the needle to reach the floating condition. Furthermore, the second closing stage is suppressed because of the low value of the residual pressure within the sac. However, all the hypotheses previously made on the first opening and the first closing tract may apply also in this case. It must be remarked that the reliability of this empirical model is directly related to the number and the accuracy of experimental points. According to the authors' experience, a set of five operating conditions, including both long and short energizing times, is the minimum requirement to get reasonable results.

Simulation Results at Full Load

The 1D thermofluid dynamic simulation of the whole engine (including the turbocharger group) provides a prediction of engine performance in terms of torque, power, fuel consumption, and emissions. In Fig. 7, the IMEP values at full load, plotted as a function of engine speed, are compared to experiments. The fuel injection rates and timings have been assigned as input data for all the simulations. A split injection strategy is adopted from 1250 rpm to 3000 rpm, while a single injection is used at higher engine speeds. In the split injection cases, fuel is delivered through two or three pulses.

Figures 8 and 9 show the comparison between experimental and calculated values of air mass flow rate and compressor boost pressure, as a function of engine speed. As visible, the simulation results match very well the experimental values, demonstrating the reliability of the fluid dynamic model. A more detailed experimental-numerical comparison is carried out in terms of instantaneous in-cylinder pressure and rate of heat release. Figures 10 and 11 show this comparison at four different regimes, still at full load. It is remarked that a good agreement has been achieved without any adjustment of injection timing, which strongly affects the shape of the curves.

NO and soot emissions calculated values are compared to the experimental data in Figs. 12 and 13, as a function of engine speed. Both the NO and the soot submodels have been calibrated at one operating point (the regime selected for this purpose is 2500 rpm). Therefore, all the values of engine-out emissions are predicted with the same parameter settings. The calculated amount of nitrogen oxide and soot agrees fairly well with experiments, in terms of both trend and absolute values.

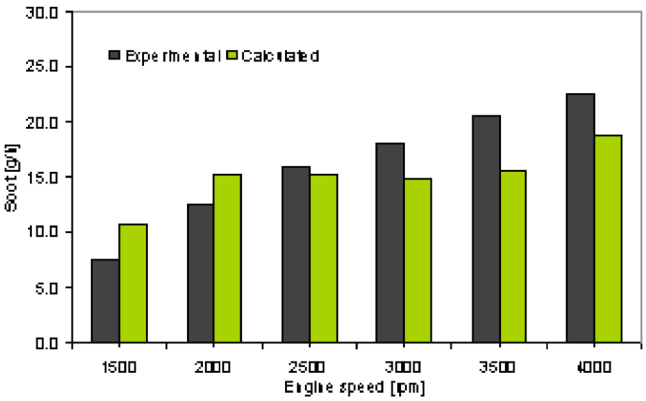

Fig. 13 Comparison between predicted and measured soot emissions as a function of engine speed at full load

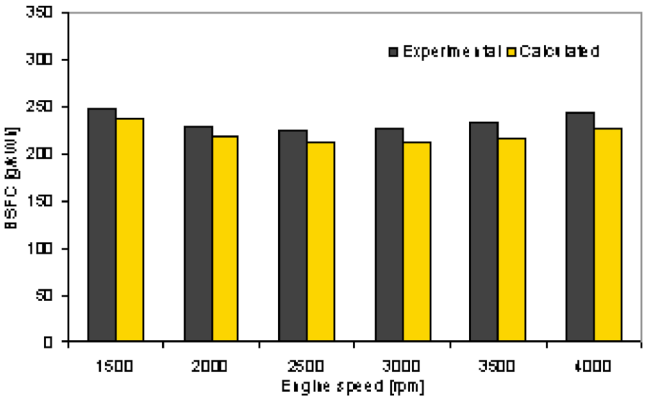

Fig. 14 Comparison between predicted and measured BSFC as a function of engine speed at full load

Downloaded 02 Jun 2010 to 171.66.16.107. Redistribution subject to ASME license or copyright; see http://www.asme.org/terms/Terms_Use.cfm

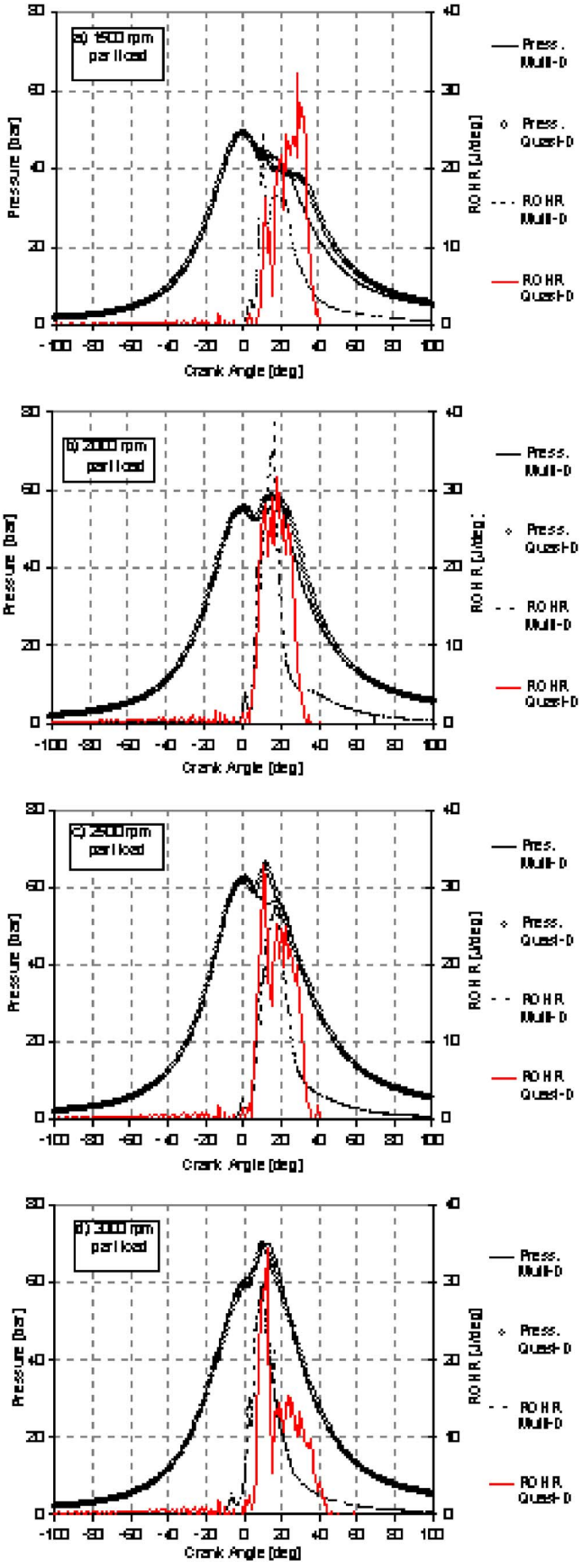

Fig. 15 Comparison between calculated in-cylinder pressure and rate of heat release, at four engine speeds, partial load (BMEP=0.6 MPa). 3D results are obtained by KIVA-3V simulations.

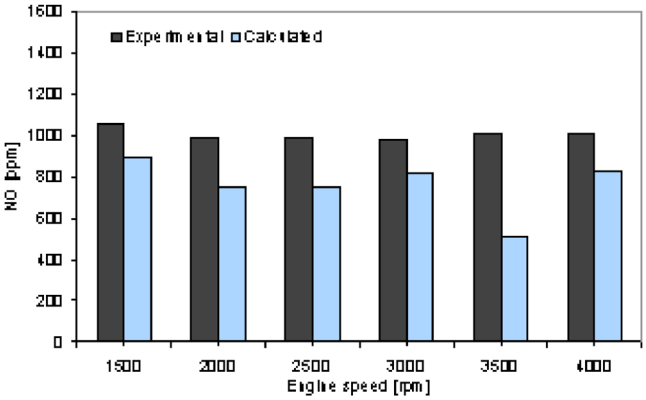

Fig. 12 Comparison between predicted and measured NO emissions as a function of engine speed at full load

Figure 14 shows the comparison between predicted and measured BSFC at full load. The accuracy of the numerical predictions is satisfactory, thanks to the proper modeling of FMEP.

Results at Partial Load

After the model setup at full load, some simulations have been carried out also at partial load, with no specific further calibrations, except for the soot model. The selected operating conditions are representative of points in the New European Driving Cycle for a class B vehicle (BMEP of 0.6 MPa, while speed varies from 1500 rpm to 3000 rpm). It is also remarked that these operations are among the most critical in terms of exhaust emissions in a driving cycle.

At partial load, the task of a predictive multizone model is much more difficult, for many reasons. First, the angular speed of the equivalent in-cylinder swirl vortex can be strongly different from the value calculated on the basis of the steady flow bench characterization (swirl ratio). Second, the system complexity grows up because of the presence of a cooled EGR system, which is active at partial load. It should be pointed out that the EGR rate was not directly measured at the test bench; thus, the in-cylinder gas composition may be affected by some error.

Third, the compressor and turbine generally operate at conditions quite far from the maximum efficiency points, within map regions where experimental information is scarce. In order to reduce the influence of the unknown initial in-cylinder conditions on combustion simulation, it has been chosen to refer to 3D-CFD calculations, performed through a well-established simulation code, instead of experiments. The 3D code is a customized version of the KIVA-3V code, developed by the University of Modena and Reggio Emilia and specifically calibrated on the HSDI diesel engine analyzed in the paper. The description of the KIVA calculations is beyond the scope of this paper. However, a full account on the models used in the program and the calibration process performed on this HSDI diesel engine is given in [31]. Despite the difficulties listed above, the simulation is able to predict, with good accuracy, the engine fluid dynamic parameters, combustion heat release rates, and brake performance.

Figure 15 shows a comparison between the predicted values of pressure and heat release compared to the curves obtained by the KIVA-3V calculations. A split injection strategy is adopted from 1500 rpm to 3000 rpm in this partial-load operating condition. In all these points, the fuel is delivered by two pulses: pilot and main injections. In Fig. 16, the predicted values of BSFC are compared to the experimental values, measured at the test bench.

NO calculated values are compared to the experimental data in Fig. 17 as a function of the engine speed; in this comparison, a

Downloaded 02 Jun 2010 to 171.66.16.107. Redistribution subject to ASME license or copyright; see http://www.asme.org/terms/Terms_Use.cfm

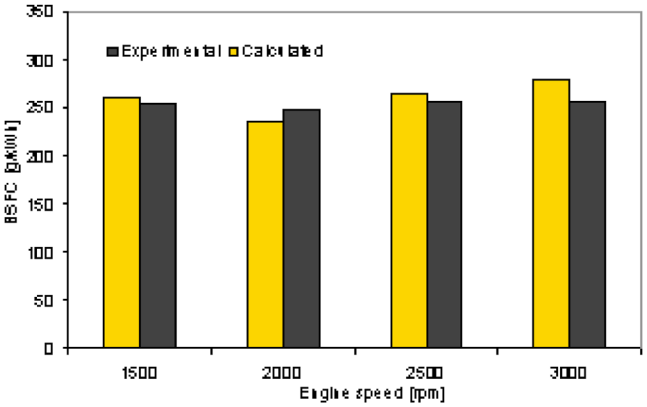

Fig. 16 Comparison between predicted and measured BSFC, as a function of engine speed at partial load (BMEP=0.6 MPa)

good global agreement have been achieved. Because it occurs at full load, the simulation is still able to capture the relative trend, confirming the physical soundness of the model.

About soot (Fig. 18), computational results are satisfactory in terms of trend, a little less as far as the absolute values are concerned. The agreement is good only at 1500 rpm and 2000 rpm, the latter being the operating condition at which the soot model parameters have been tuned. A further case-by-case calibration would be required to match the experiments at the other speeds. A possible explanation of this behavior is the coarse grain modeling

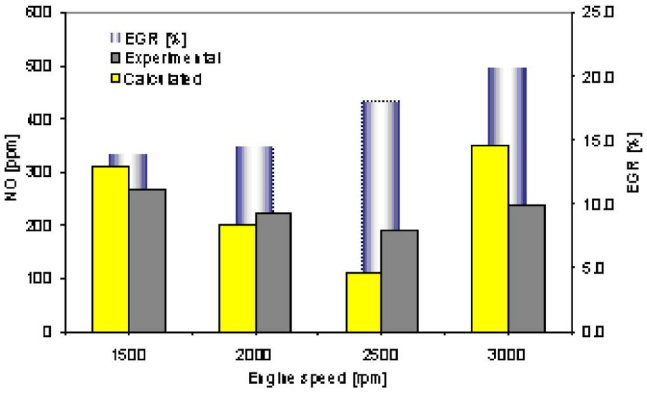

Fig. 17 Comparison between predicted and measured NO emissions, as a function of engine speed at partial load (BMEP=0.6 MPa)

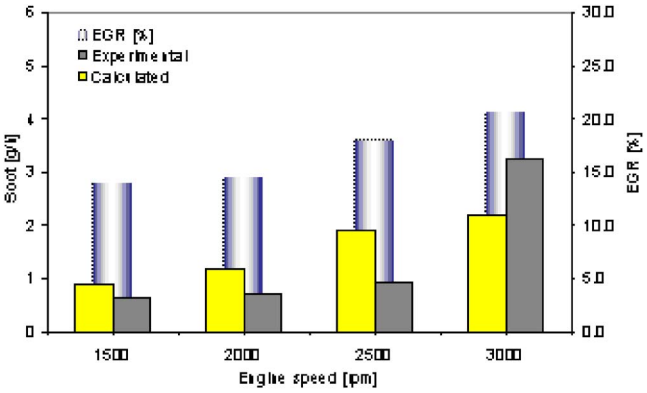

Fig. 18 Comparison between predicted and measured soot emissions, as a function of the engine speed at partial load (BMEP=0.6 MPa)

of in-cylinder mean turbulence, which fails to predict the influence of engine speed. Another critical issue is the presence of exhaust gases in the trapped charge, whose influence is not properly accounted for in the soot model.

Conclusions

A 1D research code for engine simulations has been enhanced by the introduction of a multizone quasi-dimensional combustion model, tailored for multijet direct injection diesel engines. An empirical model has also been developed for the calculation of the instantaneous fuel injection rate. Applying the code to analyze the operations of a small HSDI turbocharged diesel engine, the following conclusions can be drawn:

- Numerical results are in very good agreement with experiments in terms of indicated and brake quantities, as well as in terms of average thermo-fluid-dynamic parameters (pressure, temperature, flow rates, etc.) all over the engine system, at both full and partial load.
- A fairly good agreement between predicted results and experimental data has been found for NO and soot emissions at full load.
- Some further effort is still required to improve the prediction of exhaust emissions at partial load.

Nomenclature

C_D = discharge coefficient
c_f = calibration factor (see air entrainment rate)
C_f = fuel mass concentration
C_O = oxygen mass concentration
c_t = tuning constant
c_p = specific heat under constant pressure
c_v = specific heat under constant volume
D = droplet diameter
d_n = nozzle hole diameter
D_v = mass diffusivity
E_c = activation energy
f = correction factor
h = enthalpy
k = thermal conductivity
K_b = constant
L = latent heat of evaporation
L_i = integral length
m = mass
m_f = liquid fuel mass in the zone
m_u = air unburned entrainment mass
$\dot{m}$ = mass rate
N = number of droplets
Nu = Nusselt number
p = pressure
$p_{v,\mathrm{surf}}$ = saturation pressure
q = convective heat transfer
$\dot{Q}$ = heat transfer rate
R = gas constant
Sh = Sherwood number
T = temperature
t = time
t_b = breakup time
t_{hit} = time instant when the zone of the spray impacts
t_t = turbulent time scale
u' = mean turbulence intensity
u_i = fuel velocity at the nozzle
v = velocity
v_s = swirl velocity component along the axis penetration

Downloaded 02 Jun 2010 to 171.66.16.107. Redistribution subject to ASME license or copyright; see http://www.asme.org/terms/Terms_Use.cfm

Greek Symbol

ρ = density

Subscripts

a = spray surrounding zone
b = burned zone
cyl = cylinder
d = droplet
f = fuel
j = zone index into the combustion chamber
k = zone index into the combustion chamber
l = liquid phase
mix = mixing zone
u = unburned zone

Superscripts

A_f = fuel mass concentration exponent
a_O = fuel mass concentration exponent

Acronyms

BP = brake power
BMEP = brake mean effective pressure
BSFC = brake specific fuel consumption
BT = brake torque
DI = direct injection
EVO = exhaust valve open
FMEP = friction mean effective pressure
IMEP = indicated mean effective pressure
IVC = inlet valve close
SMD = Sauter mean diameter
TDC = top dead center

References

[1] Onorati, A., Ferrari, G., D'Errico, G., and Montenegro, G., 2002, "The Prediction of 1D Unsteady Flows in the Exhaust System of a S.I. Engine Including Chemical Reactions in the Gas and Solid Phase," SAE Paper No. 2002-01-0003.

[2] Winterbone, D. E., and Pearson, R. J., 2000, *Theory of Engine Manifolds Design*, Professional Engineering Publishing, London.

[3] D'Errico, G., Montenegro, G., Onorati, A., Merola, S., and Vaglieco, B. M., 2005, "Thermo-Fluid Dynamic Modeling and Experimental Investigation of a Turbocharged Common Rail DI Diesel Engine," SAE Paper No. 2005-01-0689.

[4] Hountalas, D. T., Kouremenos, D. A., Pariotis, E. G., Schwarz, V., and Binder, K. B., 2002, "Using a Phenomenological Multi-Zone to Investigate the Effect of Injection Rate Shaping on Performance and Pollutants of a DI Heavy Duty Diesel Engine," SAE Paper No. 2002-01-0074.

[5] Jung, D., and Assanis, D. N., 2001, "Multi-Zone DI Diesel Spray Combustion Model for Cycle Simulation Studies of Engine Performance and Emissions," SAE Paper No. 2002-01-1246.

[6] Bozza, F., Gimelli, A., Senatore, A., and Caraceni, A., 2001, "A Theoretical Comparison of Various VVA Systems for Performance and Emission Improvements of SI-Engines," SAE Paper No. 2001-01-0670.

[7] D'Errico, G., Ferrari, G., Onorati, A., and Cerri, T., 2002, "Modeling the Pollutant Emissions From a S.I. Engine," SAE Paper No. 2002-01-0006.

[8] Austen, A. E. W., and Lyn, W. T., 1961, "Some Steps Toward Calculating Diesel Engine Behavior," SAE Paper No. 409A.

[9] Kamimoto, T., Kobayashi, H., and Matsuoka, S., 1981, "A Big Size Rapid Compression Machine for Fundamental Studies of Diesel Combustion," SAE Paper No. 811235.

[10] Lipkea, W. H., and DeJoode, A. D., 1987, "A Model of a Direct Injection Diesel Combustion System for Use in Cycle Simulation and Optimization Studies," SAE Paper No. 870573.

[11] Naber, J. D., and Siebers, D. L., 1996, "Effects of Gas Density and Vaporization on Penetration and Dispersion of Diesel Spray," SAE Paper No. 960034.

[12] Kono, S., Nagao, A., and Motoka, H., 1985, "Prediction of In-Cylinder Flow and Spray Formation Effects on Combustion in Direct Injection Diesel Engines," SAE Paper No. 850108.

[13] Hiroyasu, H., and Kadota, T., 1976, "Models for Combustion and Formation of Nitric Oxide and Soot in Direct Injection Diesel Engines," SAE Paper No. 760129.

[14] Timoney, D. J., McNally, C. P., and Doyle, C. T., 2000, "A Three-Zone Heat Release Model Injection Diesel Engines," THIESEL Conference, Valencia, Spain.

[15] Yoshizaki, T., Nishida, K., and Hiroyasu, H., 1993, "Approach to Low NO_x and Smoke Emission Engines by Using Phenomenological Simulation," SAE Paper No. 930612.

[16] Levich, V. G., 1962, *Physicochemical Hydrodynamics*, Prentice-Hall, Englewood Cliffs, NJ, pp. 639–650.

[17] Hiroyasu, H., and Arai, M., 1980, "Fuel Spray Penetration and Spray Angle of Diesel Engines," Trans. JSAE, **21**, pp. 5–11.

[18] Hiroyasu, H., Arai, M., and Tabata, M., 1989, "Empirical Equations for the Sauter Mean Diameter of a Diesel Spray," SAE Paper No. 890464.

[19] Heywood, J. B., 1998, *Internal Combustion Engine Fundamentals*, McGraw-Hill, New York.

[20] Ranz, W. E., and Marshall, W. R., 1952, "Evaporation From Drops," Chem. Eng. Prog., **48**, No. 4, pp. 173–180.

[21] Wakilli, M. M., Uyeahra, O. A., and Myers, P. S., 1954, "Theoretical Investigation of Heating up Period of Injected Fuel Droplets Vaporizing in Air," NACA TN 3179.

[22] Gosman, A. D., and Johns, R. J. R., 1980, "Computer Analysis of Fuel-Air Mixing in Direct Injection Engines," SAE Paper No. 800091.

[23] Woschni, G., 1967, "Universally Applicable Equation for the Instantaneous Heat Transfer Coefficient in the Internal Combustion Engine," SAE Paper No. 670931.

[24] Ericksonn, W. D., and Probhu, R. K., 1986, "Rapid Computation of Equilibrium Composition: An Application to Hydrocarbon Combustion," AIChE J., **32**(7), pp. 1079–1087.

[25] Hiroyasu, H., Kadota, T., and Arai, M., 1983, "Development and Use of a Spray Combustion Modeling to Predict Diesel Engine Efficiency and Pollutant Emission, Part 1: Combustion Modeling," Bull. JSME, **26**, No. 214, pp. 569–575.

[26] Poulos, S. G., and Heywood, J. B., 1983, "The Effect of Chamber Geometry on Spark-Ignition Engine Combustion," SAE Paper No. 830334.

[27] Bosch, W., 1966, "The Fuel Rate Indicator: A New Measuring Instrument for Display of the Characteristics of Individual Injection," SAE Paper No. 660749.

[28] Bower, G. R., and Foster, D. E., 1991, "A Comparison of the Bosch and Zeuch Rate of Injection Meters," SAE Paper No. 910724.

[29] Takamura, A., Ohta, T., Fukushima, S., and Kamimoto, T., 1992, "A Study on Precise Measurement of Diesel Fuel Injection Rate," SAE Paper No. 920630.

[30] Bianchi, G. M., and Falfari, S., 2004, "The Black Box Model," Internal Report of DIEM, Faculty of Engineering of Bologna.

[31] Montorsi, L., Rinaldini, C. A., and Golovitchev, V. I., 2006, "CFD Combustion and Emission Formation Modeling for a HSDI Diesel Engine Using Detailed Chemistry," *Proc. ASME Fall Technical Conference*, Nov. 5–8, ASME, New York, ASME Paper No. ICE2006-1506.

Downloaded 02 Jun 2010 to 171.66.16.107. Redistribution subject to ASME license or copyright; see http://www.asme.org/terms/Terms_Use.cfm

Validating the Phenomenological Smoke Model at Different Operating Conditions of DI Diesel Engines

Y. V. Aghav
Kirloskar Oil Engines Limited,
Pune, 411 003 India

P. A. Lakshminarayanan
Ashok Leyland Ltd.,
Hosur, Tamilnadu, 635 126 India

M. K. G. Babu
Indian Institute of Technology,
Delhi, 110 016 India

Azeem Uddin
Ashok Leyland Ltd.,
Hosur, Tamilnadu, 635 126 India

A. D. Dani
Kirloskar Oil Engines Limited,
Pune, 411 003 India

A new phenomenological model that was published in Aghav et al. (2005, "Phenomenology of Smoke From Direct Injection Diesel Engines," Proceedings of ICEF2005, ASME Paper No. 1350) encompasses the spray and the wall interaction by a simple geometrical consideration. The current study extends this earlier work with investigations made on 16 different engines from six-engine families of widely varying features, applied to off-highway as well as on-road duty. A dimensionless factor was introduced to take care of the nozzle hole manufactured by hydroerosion, as well as the conical shape of the nozzle hole (k factor) in the case of valve-closed-orifice type of nozzles. The smoke emitted from the wall spray formed after wall impingement is the major contributor to the total smoke at higher loads. As the fuel spray impinges upon the walls of the combustion chamber, its velocity decreases. This low-velocity jet contributes to the higher rate of the smoke production. Therefore, the combustion bowl geometry along with injection parameters play a significant role in the smoke emissions. The new model is one dimensional and based on the recent phenomenological description of spray combustion in a direct injection diesel engine. The satisfactory comparison of the predicted and observed smoke over the wide range of engine operation demonstrated applicability of the model in simulation study of combustion occurring in direct injection (DI) diesel engines.
[DOI: 10.1115/1.2771239]

Keywords: soot, DI diesel, turbulent structure, free jet, wall jet, Kolmogorov scale

Introduction

Direct injection type of diesel engines is becoming popular because of their fuel economy as well as low exhaust emissions. However, they emit higher amount of visible exhaust termed as smoke. The characterization of this smoke has remained a challenge in engine development and modeling work.

Many efforts have been put in experimental and theoretical investigations with the objective of understanding smoke formation. The cause of exhaust smoke and its reduction methods in a small direct injection (DI) diesel engine with a nozzle of small orifice diameter and common rail fuel injection equipment were investigated under high speed and high load conditions using both in-cylinder observations and three-dimensional numerical analysis by Hotta et al. [1]. These studies revealed that fuel sprays were easily pushed away by a strong swirl and that the air-fuel mixture immediately flows out to the squish area by a strong reverse squish. Therefore, the air in the cavity is not effectively used. Suppressing the airflow in a cavity using such ideas as enlarging the piston cavity diameter or reducing the port swirl ratio decreases the excessive outflow of the fuel-air mixture into the squish area and allows the full use of air in the whole cavity. Hence, exhaust smoke reduces.

Lyu and Shin [2] investigated the effect of nozzle characteristics on the performance of a small-bore high-speed DI diesel engine. The volume between needle tip and seat in the nozzle is referred to as the sac. The fuel in this volume contributes to hydrocarbon emissions. Therefore, valve-closed-orifice (VCO) type of nozzles was developed wherein the sac is absent. These VCO nozzles resulted into higher smoke due to poorer fuel atomization than sac type nozzles. They concluded that swirl and spray penetration should be carefully optimized and higher injection pressure is not always advantageous.

Benajas et al. [3] analyzed the effect of swirl on combustion and exhaust emissions. They concluded that there is no single optimum value of swirl ratio for the whole operating range of the engine and that matching the level of swirl with other parameters depends on the combustion chamber geometry and injection characteristics. Nevertheless, the results obtained shed light on the swirl effect on diesel engine combustion and exhaust emissions over a wide range of operating conditions. They observed that NO_x is formed very early in the combustion process and that it depends on the temperature reached during premixed combustion while soot emissions are dependent on oxidation during late combustion phase which is mixing controlled.

Recently, Dec and Tree [4,5] investigated interactions of combusting fuel jet and the wall in a diesel engine using laser diagnostics. They found that the blowoff of soot deposited on the wall is not a major contributor in engine-out soot emissions and that the soot is continuously generated by some other mechanisms. A theoretical investigation on the effect of combustion chamber geometry and the engine speed on the emissions of soot and NO_x was carried out by De Risi et al. [6]. The bowl reentrance, the spray angle, and the injection timing were the critical parameters that had to be optimized. Subsequently, new methodologies for design of the combustion chamber shape and the injection strategy were developed aiming at the reduction in emissions without deteriorating engine performance [7].

Kurtz and Foster [8] identified a critical time for mixing in a direct injection diesel engine through the study of increased in-cylinder mixing and its effect on emissions. The results suggested

Submitted to ASME for publication in the JOURNAL OF ENGINEERING FOR GAS TURBINES AND POWER. Manuscript received June 4, 2006; final manuscript received April 28, 2007; published online January 9, 2008. Review conducted by Margaret Wooldridge. Paper presented at the 2006 Spring Conference of the ASME Internal Combustion Engine Division (ICES2006), Aachen, Germany, May 7–10, 2006.

Copyright © 2008 by ASME

Downloaded 02 Jun 2010 to 171.66.16.107. Redistribution subject to ASME license or copyright; see http://www.asme.org/terms/Terms_Use.cfm

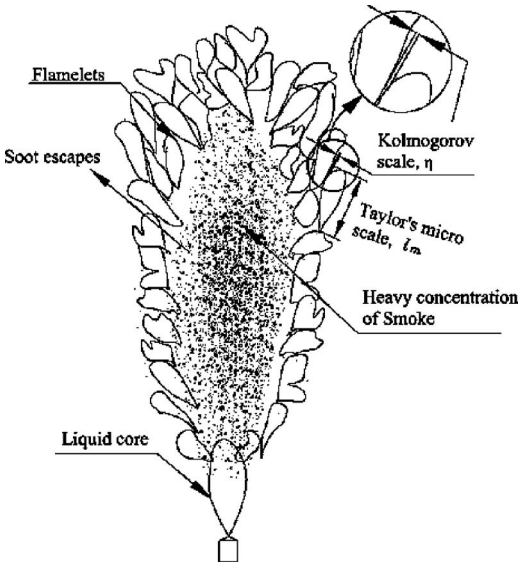

Fig. 1 Conceptual cross section of turbulent flame indicating the soot path

that the fuel injected at the tail end of the fuel injection event had difficulty in mixing and caused large quantities of soot. An innovative method of secondary injection was used to reduce the exhaust emissions by a substantial amount.

Hiroyasu and Kadota [9] proposed a difficult two-step semiempirical model and applied it to the multipacket combustion model. Fusco et al. [10] developed a phenomenological soot model consisting of an eight-step mechanism. Although these models are popular, they require tuning of a number of empirical parameters. Dent [11] identified the importance of turbulent energy dissipation rate and correlated the turbulent mixing rate to the smoke for a quiescent chamber diesel engine. Extending this concept, the authors have proposed a new model in a recent paper [12] for estimation of the soot by describing the wall and the free jet regimes of the engine spray.

In the present paper, experimental investigations and the parametric studies aimed at improving understanding of soot formation in an engine environment are described. Based on this analysis, a smoke model is described without any adjustable factors that are to be tuned for a given engine to obtain good correlation with the experimental data. Finally, the model is validated for a number of diesel engines of widely varying features.

Description of the Model

In a conceptual sketch of a steady open turbulent flame, all the fuel injected go through vaporization process during ignition delay and then is converted into soot, Fig. 1. The simplest description for a burning spray is the model where the products of combustion exist outside a thin mantle of flame and the fuel-rich mixture remains unburned inside it. Many flamelets form at the peripheral mantle of the combusting spray. Most of this soot will be oxidized at the surface of flame depending on the level of turbulence. The average size of a flamelet could be equated to Taylor's microscale, ℓ_m. This scale defines the size of the mixing field. However, some of the soot escapes through the gaps that are scaled by viscosity and the high frequency components of turbulence between these eddies. The Kolmogorov length scale η describes the gap between adjacent flamelets. This description is also applicable to the fuel spray in an engine; however, the wall impingement needs to be considered, as it results in loss of turbulent kinetic energy that is necessary for oxidation. Most of this soot will then be oxidized at the periphery of the spray. The escaping soot can be estimated by calculating flow through the holes scaled by the Kolmogorov length scale during a characteristic time as follows [12].

$$\text{soot} = \left(\frac{u_{\text{inj}} A_h n_h A_s t_{\text{int}} \rho_s}{V_{\text{air}}} \right) \tag{1}$$

where soot is the soot in mg/m^3, A_h is the area of soot hole, function of Kolmogorov scale η, $(=\pi \ell_m \eta)$, n_h is the number of soot holes per unit surface area, A_s is the surface area of the spray, t_{int} is the time scale for integration of smoke passing through holes of size given by Kolmogorov scale, $u_{\text{inj}} = Q/C_d A_o n_o t_{\text{dur}}$ is the average velocity of sprays, $A_o = \pi d_o^2 (1+N_f)/4$ is the effective area of nozzle hole, N_f is the nozzle feature, %HE or KF, e.g., 10%, 15%, etc. The nozzles holes are defined as some base orifice size with %HE. The sample calculation is given in the Appendix. d_o is the diameter of the basic nozzle hole, t_{dur} is the injection duration, V_{air} is the volume of air sucked in per cycle, and ρ_s is the density of soot, 2000 kg/m^3. The nozzle hole features, namely, hydroerosion, (HE) and k factor (KF) used in the above equation, are explained in the Appendix.

Smoke is modeled to form instantaneously, as the chemical reaction rates are too high compared to the physical rate of diffusion of the smoke. The phenomenological model, therefore, neglects chemical reaction and emphasizes the physical phenomenon.

In turbulent sprays, the liquid droplets are not only decelerated and deformed by the gas phase, but an additional dispersion and some diffusion of the liquid phase can be observed that is caused by the turbulent eddies in the gas flow. On an average, the random orientation of the turbulent velocity fluctuations leads to a quicker, more homogenous dispersion of the liquid droplets than in a laminar gas flow. At the same time, the momentum transfer between gas and liquid moderates the turbulent level within the gas phase. In turbulent sprays, typically a particle is assumed to interact with an eddy for a period taken as the eddy lifetime, t_{int} [13]. This period is also considered as the time scale of integration.

$$t_{\text{int}} = \frac{C_u^{3/4}}{\sqrt{2/3}} \frac{k}{\varepsilon} \tag{2}$$

Where C_u is the Steich constant=0.09 [13], ε is the turbulent kinetic energy dissipation rate, and $k=(3u_{\text{inj}}^2/2)$ is the turbulent kinetic energy.

Though the above equation is only true for an isotropic flow, which is not the case at the spray envelope, for brevity, it is assumed to be uniform all over the surface by considering a mean time, t_{int}. The authors hypothesized t_{int} as a mean time scale for the two types of spray, e.g., free and wall sprays and the favorable comparison presented later in the paper validates such a bold assumption.

To derive the concept equation (1), a steady open nongrowing turbulent flame is considered. For simplicity, there is no liquid or wall jet considered, Fig. 1. Therefore, only the time scale of integration t_{int} is considered. However, in the case of the engine sprays, there are a liquid phase, a free growing spray, and a growing wall jet, which are happening one after another, Fig. 2. Initially, the free spray would grow up to wall with a conical shape. Then, the spray penetrates along a flat wall and is modeled equally in all directions. The tip of the spray would form a surface of a right circular cylinder. This model simplifies the complicated combustion cavity wall to a flat plate perpendicular to the spray axis. The liquid phase is not considered to be contributing to soot. The free growing spray is considered to be a frustum of cone up to the wall impingement on the wall. Soot is estimated with integration limits of t_{liq} to t_{imp}. The following equation considers growing surface area of this free spray as time marches until wall impingement occurs.

Downloaded 02 Jun 2010 to 171.66.16.107. Redistribution subject to ASME license or copyright; see http://www.asme.org/terms/Terms_Use.cfm

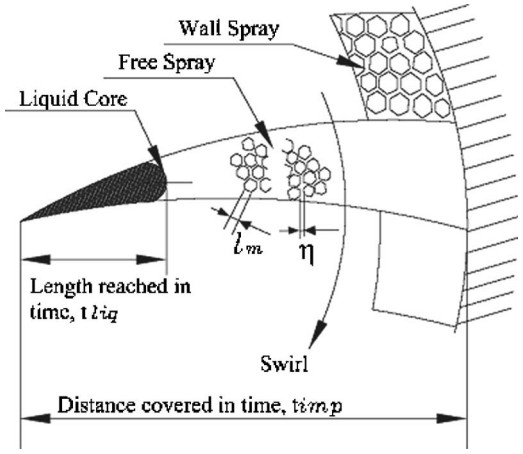

Fig. 2 Free jet fuel spray and subsequent wall jet under engine conditions

$$\text{soot}_{\text{free}} = \int_{t_{\text{liq}}}^{t_{\text{imp}}} u_{\text{inj}} A_h n_{h_{\text{free}}} \rho_s dt \tag{3}$$

If wall impingement occurs, then soot is estimated from the free spray as well as wall jet. During this period, wall jet grows along the wall, while the free portion of the jet remains static as a cone up to the wall. The portion of smoke from the free spray is modeled with a shape of frustum of static cone.

$$\text{soot}_{\text{freestat}} = \int_{t_{\text{imp}}}^{t_{\text{imp}}+t_{\text{int}}} u_{\text{inj}} A_h n_{h_{\text{free}}} \rho_s dt \tag{4}$$

The soot emitted from the growing wall spray can be estimated as below.

$$\text{soot}_{\text{wall}} = \int_{t_{\text{imp}}}^{t_{\text{imp}}+t_{\text{int}}} u_{\text{wall}} A_h n_{h_{\text{wall}}} \rho_s dt \tag{5}$$

The duration of integration t_{int} used in Eqs. (4) and (5), is explained earlier in Eq. (2). After soot escapes from spray boundaries, there is no burnout of soot is considered to take place. Finally, the soot emitted from the free and wall portions of all the sprays are summed up to arrive at total soot in mg/m^3 by using the following equation.

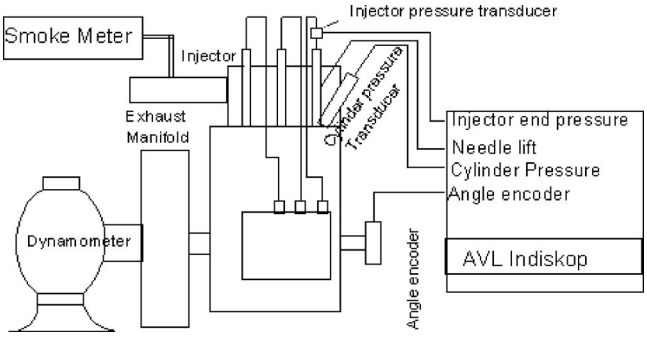

Fig. 3 Experimental set up and instrumentation

$$\text{soot}_{\text{all}} = \frac{(\text{soot}_{\text{free}} + \text{soot}_{\text{freestat}} + \text{soot}_{\text{wall}}) n_o}{V_{\text{air}}} \tag{6}$$

Where A_h is the area of soot hole, $n_{h_{\text{free}}}$ is the number of smoke holes for free portion $(=(A_{s_{\text{con}}}/A_{s_\ell}))$, $A_{s_{\text{con}}}$ is the surface area of spray considering cone, A_{s_ℓ} is the area of Taylor microscale, $n_{h_{\text{wall}}}$ is the number of smoke holes for wall portion $(=(A_{s_{\text{cir}}}/A_{s_\ell}))$, $A_{s_{\text{cir}}}$ is the circular surface area of spray at the wall, t_{liq} is the time for which spray is liquid, t_{free} is the time for which spray is free, t_{imp} is the time at which impingement starts, A_{s_w} is the surface area of wall spray, $u_{\text{wall}} = 0.75\sqrt{u_{\text{inj}} d_e / t_{\text{imp}}}$ is the velocity of wall jet, and d_e is the equivalent diameter of spray hole.

The total soot estimated is converted to bosch smoke unit (BSU) by using the MIRA correlation [14], because BSU of smoke is selected for comparison with the experimental data for validation.

Experimental Validation

Experimental Setup. The schematic diagram of the experimental setup is shown in Fig. 3. The needle lift is measured by a linearly variable differential transformer (LVDT) assembled in the injector. The cylinder pressure is measured using the piezoelectric pressure transducer of type AVL GM12D. The fuel line pressure is measured using the strain gauged pressure transducer of type AVL 31DP2000. The crank angle position is sensed using the AVL angle encoder. The engine is loaded using an eddy current dynamometer. All the signals from different transducers and the encoder are fed into the AVL Indiskop 647. In the Indiskop, there are amplifiers, signal conditioners, and a computer to process the

Table 1 Details of experimental engines; TCIC, turbocharged and after cooled; TC, turbocharged; NA, Naturally aspirated; TCJC, turbocharged and jacket water cooled

Engine	Bore (mm)	Stroke (mm)	Engine speed (rpm)	Aspiration	Boost pr. ratio	Swirl number	Emission norms
A	105.0	120	2700	NA	1.0	2.5	Euro II
B	105.0	120	2500	TCIC	1.9	2.5	Euro II
C	105.0	120	1500	NA	1.0	2.5	Tier I
D	105.0	120	1500	TC	2.0	2.5	Tier I
E	100.0	120	1500	NA	1.0	2.7	Tier II
F	124.0	130	2250	NA	1.0	2.7	Tier II
G	105.0	125	2500	TC	2.0	2.5	Tier I
H	105.0	125	2500	TCJC	2.1	2.5	Tier I
I	105.0	125	2500	TCIC	2.3	2.5	Tier I
J	105.0	120	2200	TC	2.0	2.5	Tier I
K	105.0	120	1500	TCIC	2.3	2.5	Tier I
L	104.0	113	2400	TCIC	2.1	2.3	Euro II
M	104.0	113	2400	TCIC	1.9	2.3	Euro II
N	104.0	113	2400	TCIC	1.9	2.3	Euro II
O	107.3	121	2400	TCIC	2.0	2.5	Euro II
P	107.3	121	2400	TCIC	2.2	2.5	Euro II

Downloaded 02 Jun 2010 to 171.66.16.107. Redistribution subject to ASME license or copyright; see http://www.asme.org/terms/Terms_Use.cfm

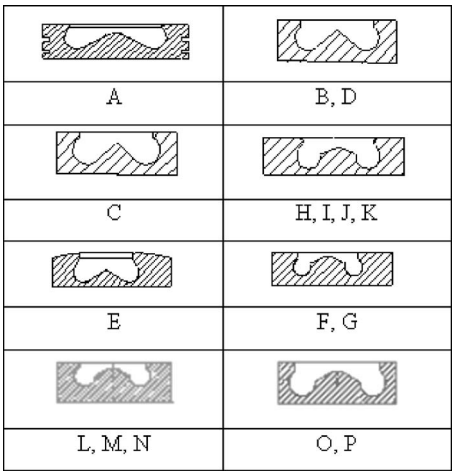

Fig. 4 Combustion chambers

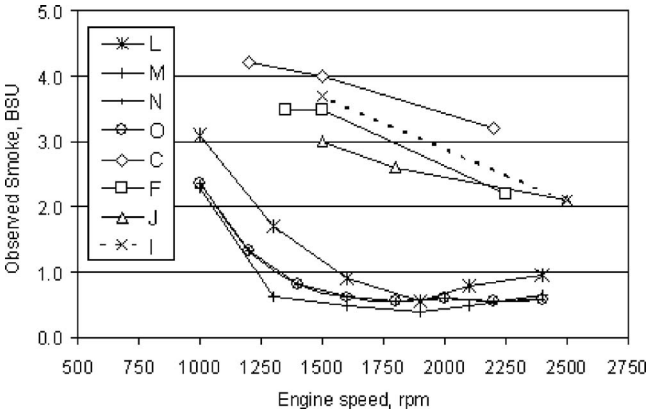

Fig. 5 Experimentally observed smoke along full throttle for different engines

signals.

AVL Opacimeter-439 and Bosch smoke gun are used to collect data of smoke. AVL Opacimeter-439 measures the opacity of a sample of the exhaust gas extracted from the exhaust pipe and passed through a heated measurement chamber of standardized size. Since condensation of hydrocarbon and water is avoided, by heating the exhaust in the smoke chamber, the measured opacity is only by black carbon. Bosch smoke gun, on the other hand, works on filtering principle wherein soot particles are collected on a filter medium from a known volume of the exhaust. The filter is evaluated by comparison with standards using photoelectric reflectance method. Both the methods mentioned above are partial flow systems having a maximum error of 0.2 BSU, which is the uncertainty in the experiments. The average of three readings was acquired for reliable exhaust smoke data.

Experimental Engines. Sixteen engines of widely varying features are selected for conducting parametric studies as well as the model validation. The engines are designed for heavy-duty on-road and off-highway applications requiring high backup torque at lower speeds. The engines feature reentrant combustion chambers, well-optimized fuel injection systems with single injection per cycle and without exhaust gas recirculation. The engines meet the prevailing norms of Euro for on-road applications and US Tier emission norms for off-highway application in India [15]. The important technical specifications of the engines are given in Table 1. The shapes of combustion chambers employed in these engines are given in Fig. 4. Table 2 shows some important data related to the fuel injection systems of the experimental engines.

Experimental Observation. The engines were run at full throttle and part throttle operating conditions. The investigations were limited to operating conditions of the engines with single injection and no exhaust gas recirculation. Different parameters related to the engine performance and fuel injection system were collected simultaneously along with the smoke. In Fig. 5, the observed smoke was plotted against the speed, for engines of variable speed applications. Here, rising trend of smoke is indicated as the speed reduces. These engines are sufficiently fueled at lower speeds to derive higher torque at lower speeds, hence are working at lower air-fuel ratios. Similarly, at a constant engine speed, as the load increases, the smoke increases, Fig. 6. The slope of the curve changes at 50% load approximately. The increase in smoke with increase in load is seen to be less significant when the engine runs at high speed, compared to the drop in smoke at the same load, when the engine runs at a low speed. This can be attributed to the higher air-fuel ratio and turbulence level at higher speeds.

The correlation of smoke with method of aspiration and brake mean effective pressure met with little success. The smoke reduces as the injection pressures and air-fuel ratio increase; however, the correlation is not satisfactory. A correlation of these fundamental factors at microscopic level as explained earlier in the model must be considered to improve the prediction of smoke.

To evaluate the effect of impingement, the observed smoke was plotted against the degree of impingement [12], Fig. 7, where the degree of impingement is defined as the ratio of time after wall impingement to the total duration of injection. There is no im-

Table 2 Fuel injection systems and its parameters; VE, rotary pump; PE-A, inline A type pump; HE, hydro erosion; KF, *k* factor

Engine	Injector	Fuel pump	Hole size	No. of holes	Nozzle feature	Injection pressure (bar)	Fuel timing static, BTDC
A	P type	VE	0.190	5	10% KF	900	15
B	P type	VE	0.190	5	17% HE	1100	12
C	S type	PE-A	0.200	5	—	475	18
D	S type	PE-A	0.240	5	—	650	22
E	P type	PE-A	0.180	5	10% HE	550	10
F	P type	PF	0.226	5	10% HE	675	11
G	S type	PE-A	0.240	5	—	700	22
H	S type	PE-A	0.240	5	—	725	22
I	S type	PE-A	0.250	5	—	750	22
J	S type	PE-A	0.240	5	—	485	13
K	S type	PE-A	0.240	5	—	525	15
L	P type	VE	0.225	5	10% HE	463	12
M	P type	VE	0.228	5	10% HE	775	12
N	P type	VE	0.228	5	10% HE	834	12
O	P type	VE	0.175	6	10% HE	802	11
P	P type	VE	0.190	6	10% HE	812	11

Downloaded 02 Jun 2010 to 171.66.16.107. Redistribution subject to ASME license or copyright; see http://www.asme.org/terms/Terms_Use.cfm

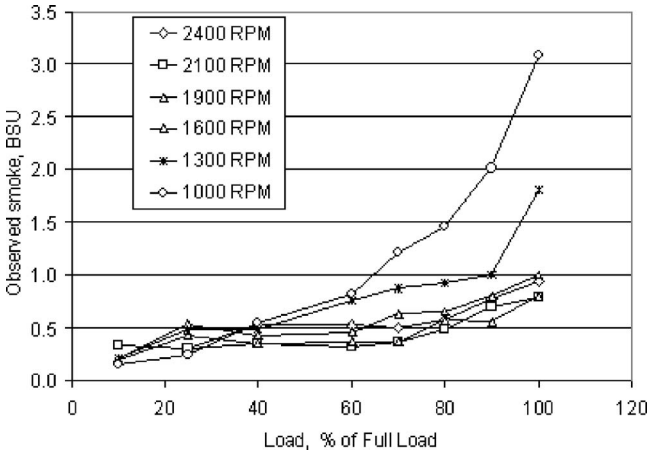

Fig. 6 Experimentally observed smoke along part loads at different speeds for engine L

pingement when this value is negative and there is impingement when this value becomes positive. The smoke increases as the impingement increases. The effect of the wall jet on the smoke emission due to abrupt loss of turbulence at the wall, therefore, seems to be more important than that of injection pressure or air-fuel ratio. The wall effect was given less importance in phenomenological models for smoke, published earlier [11,16]. Beyond 50% load, wall impingement is the important parameter in heavy-duty DI diesel engines. Therefore, the new model presented earlier in this paper, which considers these two effects, namely, wall effect and turbulence effect, has better prediction capability.

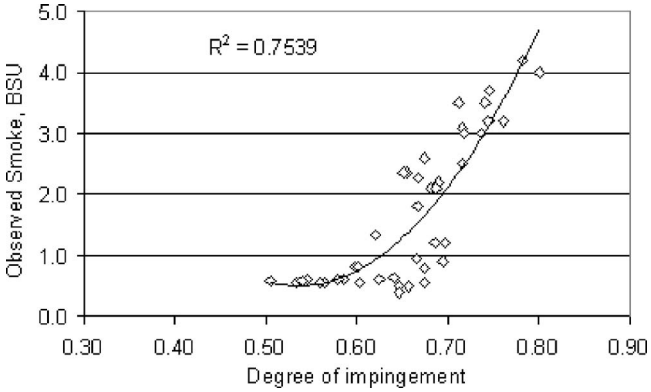

Fig. 7 Degree of impingement and observed smoke

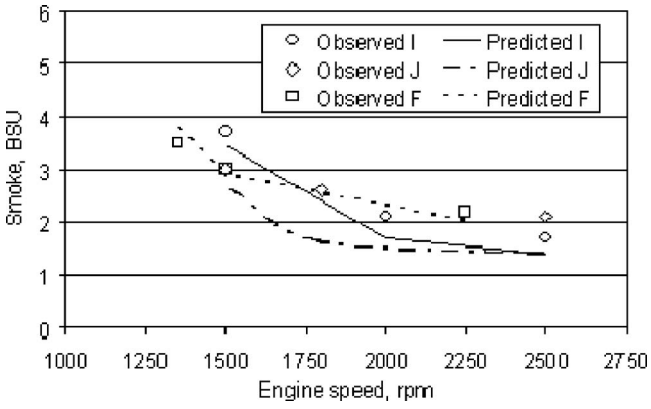

Fig. 8 Predicted and observed smoke, full throttle of engines I, J, and F

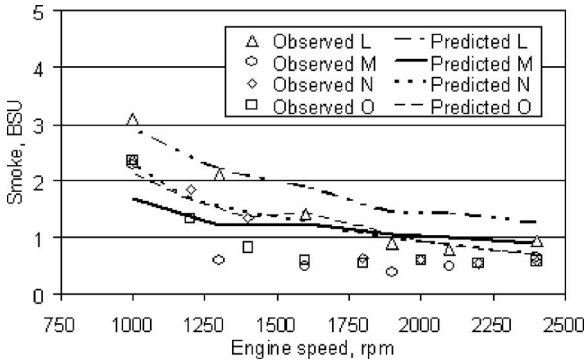

Fig. 9 Predicted and observed smoke, full throttle of engines L, M, N, and O

Application of the Model and Results

At all the experimental data points, the smoke values were predicted using the new model that considers the effective turbulent energy at the spray surface for burning of smoke generated inside the spray. The main inputs are the maximum injection pressure, the engine airflow, the geometry of the nozzle spray, and the cavity shape. The impingement parameters are estimated using the geometry and the equations of spray penetrations [17,18]. Then, the duration of integration is evaluated using the density of turbulent energy supplied by the fuel sprays [12]. The fuel sprays were divided into free and wall jets and the smoke is evaluated from these jets separately and added together to obtain the total smoke in the exhaust, Eq. (6).

Initially, the model was applied at full throttle condition of the engines of variable speed application. The predicted and observed

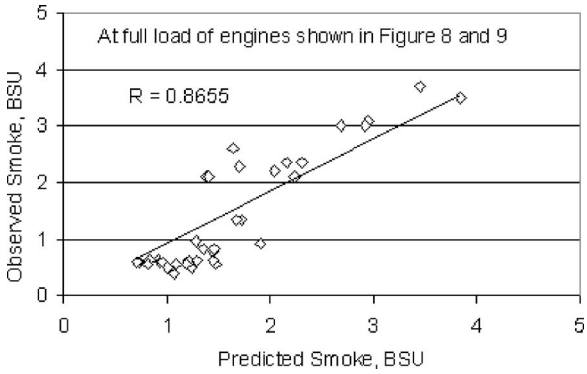

Fig. 10 Comparison of predicted and observed smoke at full load of engines I, J, F, L, M, N, and O

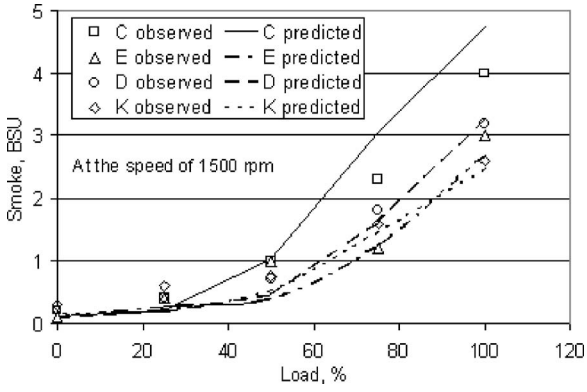

Fig. 11 Predicted and observed smoke, part loads of engines C, E, D, and K at constant speed

Downloaded 02 Jun 2010 to 171.66.16.107. Redistribution subject to ASME license or copyright; see http://www.asme.org/terms/Terms_Use.cfm

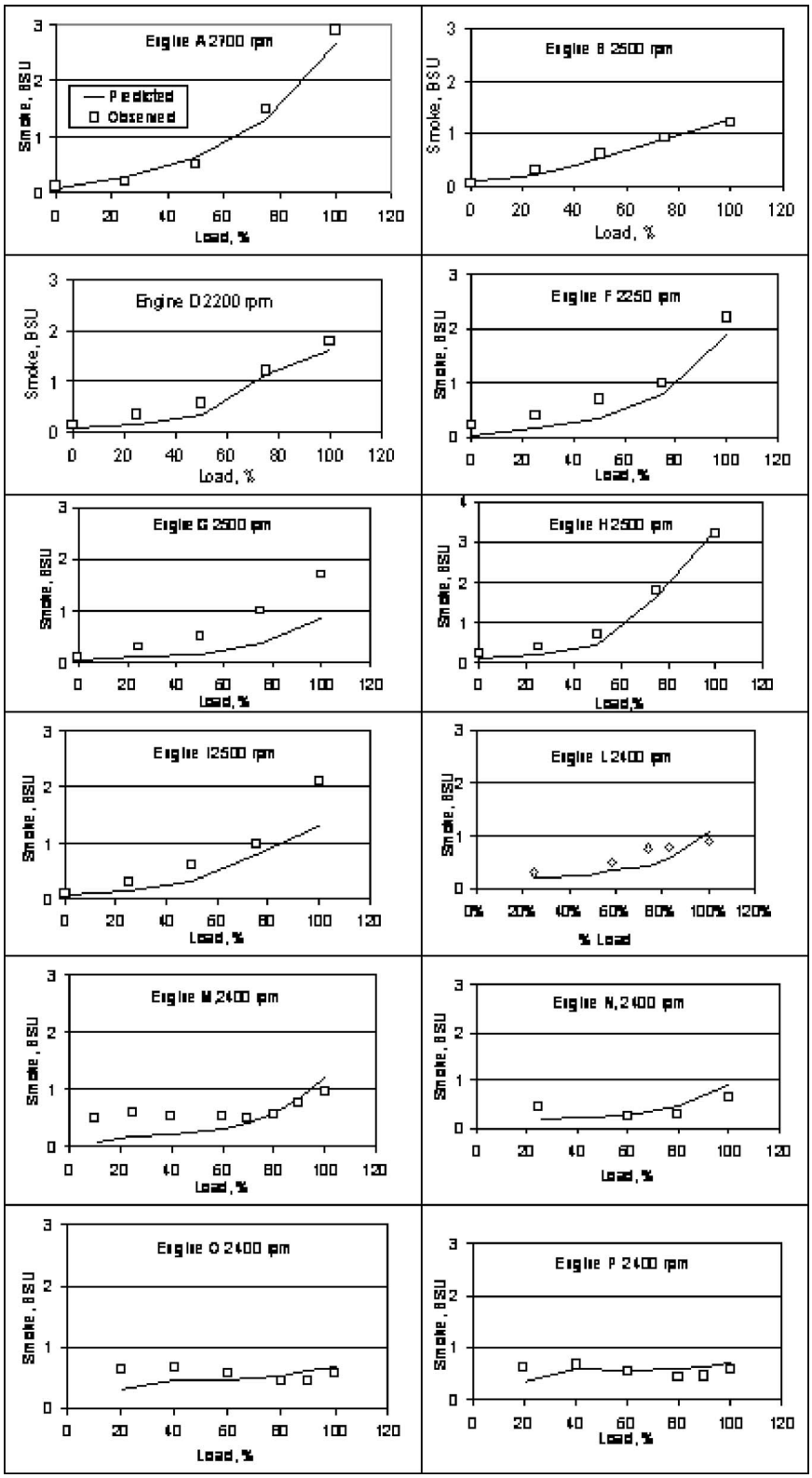

Fig. 12 Comparison of predicted and observed smoke for various engines at part loads at rated speed

smoke values of these engines were plotted against speed, Figs. 8 and 9. For the engine types I, J, F, and L, the predictions at full load follow both the magnitude and trend of the observed values. In the case of engines M, N, and O, the model slightly overpredicts the smoke. The observed smoke was compared with predicted smoke, at all the data points of above engines in Fig. 10. Although there are some deviations, the overall regression coefficient is 0.87 for these points. These slight discrepancies are dealt with later in the Discussion section. With an increase in engine speed, the turbulence increases on the spray boundaries both in free spray and at the wall due to higher injection pressure of mechanical cam-driven injection equipment. This causes more

Downloaded 02 Jun 2010 to 171.66.16.107. Redistribution subject to ASME license or copyright; see http://www.asme.org/terms/Terms_Use.cfm

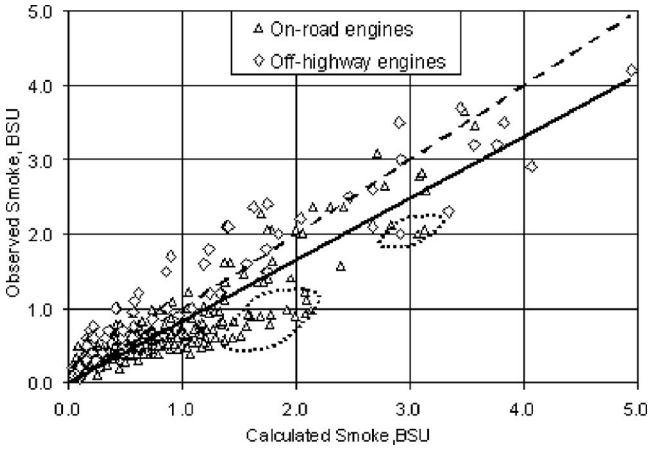

Fig. 13 Predicted observed smoke for all engines in Table 1

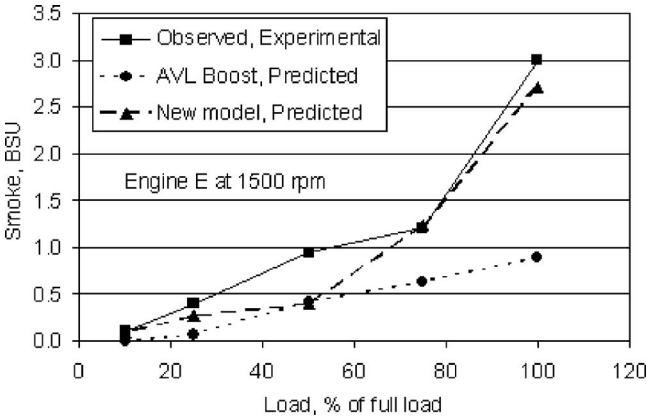

Fig. 14 Comparison of present model with AVL BOOST model texperimental data

complete burnout of smoke and hence the smoke decreases with increase in speed. The comparison of experiment and prediction is encouraging.

Then, the model was applied for typical part load conditions of engines at a constant speed of 1500 rpm. The predicted smoke values plotted against load are in close agreement with observed values, Fig. 11. The departure of the rate of increase in smoke with load at 50% load is correctly predicted. The rate at which the smoke increases with load is very small initially corresponding to when the spray is free and increases at a high rate after the spray impinges on the wall at higher loads. The smoke was also modeled at part throttle i.e., part load conditions for the engines. The predicted values were compared favorably against the observed, Fig. 12. The same trend of smoke at all speeds for different engines could be seen. Finally, the predicted values of smoke were compared with all the observed values at different speeds and loads, Fig. 13. The observed regression coefficient is 0.89 with a slope of 0.88 represented by thick line. This study using the new smoke model indicated satisfactory comparison over a wide range of smoke values.

While the correlation between the observed smoke and the calculated smoke is good for a wide variety of engines, some deviations could be observed at full load for the on-road engines, M, N, and O. These points are enclosed in ellipses. If these specific few points are considered as outliers, then the slope becomes close to 1.0 with a regression coefficient tending to 0.95 represented by the dashed line in Fig. 13. The possible causes for the deviation of computed smoke from the observed smoke values might be the lack of consideration of the reverse squish and the complete profile of the cavity where spray impinges. The injector offset with respect to the cavity is also not considered which might change the degree of impingement and hence, the soot produced at the wall. In addition, the simplified model of a flat wall perpendicular to the spray axis is a reason for the differences observed between the experiment and the model. Thus, better understanding of the Kolmogorov scales at the wall will improve prediction capability of the model. The agreement between the experimental results and the theoretical results without any tuning of model constants that are engine specific makes the model a potentially useful tool for predicting the smoke emissions.

Discussion

The comparison of the experimental data over the entire engine performance map at different loads and speeds is satisfactory, even though for some engines the differences are large. The previous phenomenological models found it difficult to predict (a) the sudden change in the rate of increase in the smoke with increase in load at 50% load and (b) gradual decrease with increase in speed even with many empirical constants adjusted for every given engine. In the present attempt, there is no empirical constant that is to be fine tuned for a given engine. The model rightly predicts the increase in smoke with load, due to the loss of turbulence at the wall and hence higher Kolmogorov scale that allows escape of smoke unburnt through the spray periphery. In addition, it shows the decrease in smoke with speed, due to better turbulence, i.e., lower Kolmogorov scale at higher injection pressure. There are, however, some limitations to the soot model in terms of understanding pulsed injection, effect of squish, and fuel type.

Compared to the extremely complex 3D models or the phenomenological soot model based on mixing-controlled combustion used in advanced software such as AVL-BOOST [19], the present model focuses on the main physical phenomenon at the surface of the spray for a brief period of the life of the eddies. Figure 14 shows the comparison of observed smoke with the predicted smoke using this software and using the model described in this paper. The prediction of the trend of smoke behavior by the present model with respect to load, especially above 50% load, is more favorable than AVL-BOOST. The present model could be extended to multijet and multiple injection common rail system, which enhances the turbulence many times at the surface area of jet at the wall and free portion. By modeling the turbulence scale, it will be possible to predict lower smoke when such a fuel injection system is used.

Conclusion

A comprehensive study was carried out on 16 different engines from six engine families of widely varying features and off-highway as well as on-road heavy-duty applications to investigate the smoke formation. A new phenomenological model [12] was developed based on the turbulence structure of a diesel engine spray in free condition and at the wall and was applied to these 16 engines. This paper reinforces for many types of engines the model reported on one engine in the earlier work [12]. The model identifies the large contributions of the soot production at the wall to the overall engine soot. The wall jet with less turbulence contributes to higher rate of smoke production. Therefore, the combination of the combustion bowl geometry and injection parameters plays a significant role in smoke emissions. The model also gives importance to the slow physical processes at the turbulence Kolmogorov scale at the spray boundaries that enable soot burn out and neglects the fast chemical kinetics of combustion. As the fuel spray impinges upon the walls of the combustion chamber, its velocity decreases. A dimensionless factor was introduced to take care of the effect of nozzle hole manufactured by HE as well as conical shape of the nozzle hole (k factor) in the case of VCO type of nozzles. The correlation of the experimental data with the predicted smoke is satisfactory in magnitude and good at describing the trend for all the engines over a wide range of operating speeds

Downloaded 02 Jun 2010 to 171.66.16.107. Redistribution subject to ASME license or copyright; see http://www.asme.org/terms/Terms_Use.cfm

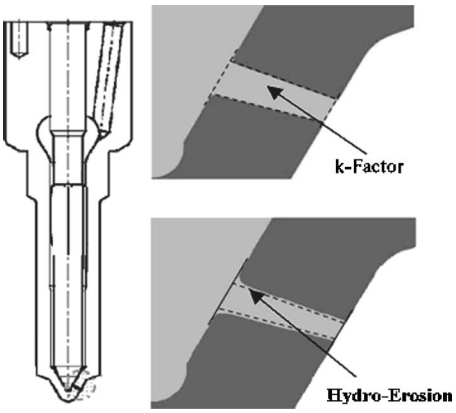

Fig. 15 Explanation of KF and HE nozzles

and loads. The model recognizes the most important contribution of the Kolmogorov scale of dissipation at the wall to the overall soot formation in a DI diesel engine.

Nomenclature

A = area, m^2
A_s = surface area, m^2
C_d = coefficient of discharge
C_u = Steich constant=0.09
d = diameter, m
HE = hydroerosion, % of nozzle hole area
KF = k factor of nozzle hole
k = turbulent kinetic energy, m^2/s^2
ℓ_m = Taylor microscale, m
n = number
N_f = nozzle feature, % HE or k factor
Q = injected quantity per stroke, mm^3/str
soot = soot in mg/m^3
t = time, s
u = average velocity, m/s
V = volume, m^3
ν = kinematic viscosity of air, m^2/s
ε = turbulent kinetic energy dissipation rate, m^2/s^3
ρ_s = density of soot, 2000 kg/m^3
η = Kolmogorov length scale, m

Subscripts

air = cylinder charge air
cir = circular shape of wall spray
con = conical shape of free spray
dur = injection duration
e = equivalent
free = free portion of spray
h = soot hole
h_{free} = soot holes of free portion of spray
h_{wall} = soot holes of wall portion of spray
inj = injection
imp = impingement
int = integral
liq = liquid portion
o = nozzle hole
wall = wall jet

Appendix

The terms "KF" and "HE" used in the paper refer to spray hole-manufacturing signatures of nozzles, Fig. 15. The nozzles with conical spray holes are termed as k-factor (KF) nozzles. Sometimes the spray holes are finished by hydrogrinding process, known as HE [20]. The smoother entry of spray in the holes improves discharge coefficient of the spray holes.

The nozzles hole is defined as base orifice size with %HE or k factor. This effect is considered as enlargement of orifice diameter over base diameter.

$$N_f = \text{HE} \quad \text{or} \quad N_f = \frac{k \text{ factor}}{10} \tag{A1}$$

The HE and k factor are defined below:

$$\%\,\text{HE} = \frac{\text{flow after HE-flow before HE}}{\text{flow before HE}} \tag{A2}$$

$$k \text{ factor} = \frac{d_{\text{inlet}} - d_{\text{outlet}}}{10\ \mu m} \tag{A3}$$

In Example 1, the base hole size is 0.19 mm with a HE of 10.5%. Then, the effective area of nozzle, A_o

$$A_o = \frac{\pi d_o^2(1+N_f)}{4} = \frac{\pi 0.19^2(1+0.105)}{4} \tag{A4}$$

In Example 2, the base hole size is 0.19 mm with a k factor of 1.5. Then, the effective area of nozzle, A_o

$$A_o = \frac{\pi d_o^2(1+N_f)}{4} = \frac{\pi 0.19^2(1+0.15)}{4} \tag{A5}$$

References

[1] Hotta, Y., Nakakita, K., Fuyuto, T., Inayoshi, M., and Sakata, I., 2002, "The Cause of Exhaust Smoke and Its Reduction Methods in an HSDI Diesel Engine Under High Speed and High Load Conditions," SAE Paper No. 2002-01-1160.
[2] Lyu, M. S., and Shin, B. S., 2002, "Study of Nozzle Characteristics on the Performance of a Small Bore High Speed D. I. Engine," Int. J. Engine Res., **3**(2), pp. 69–79.
[3] Benajes, J., Molina, S., Garcia, J. M., and Riesco, J. M., 2004, "The Effect of Swirl on Combustion and Exhaust Emissions," Proc. Inst. Mech. Eng., Part D (J. Automob. Eng.), **218**, pp. 1141–1148.
[4] Dec, John E., and Tree, Dale R., 2001, "Diffusion-Flame/Wall Interactions in a Heavy-Duty DI Diesel Engine," SAE Paper No. 2001-01-1295.
[5] Tree, Dale R., and Dec, John E., 2001, "Extinction Diesel Combustion: An Integrated View Combining Laser Diagnostics, Chemical Kinetics and Empirical Validation," SAE Paper No. 2001-01-1296.
[6] De Risi, A., Manieri, D., and Laforgia, D., 1999, "A Theoretical Investigation on the Effects of Combustion Chamber Geometry and Engine Speed on Soot and NO_x Emissions," ASME-ICE Paper No. 99-ICE-207, Vol. 33–1.
[7] Risi, A., Donateo, T., and Laforgia, D., 2004, "An Innovative Methodology to Improve the Design and the Performance of Direct Injection Diesel Engine," Int. J. Engine Res., **5**(5), pp. 425–441.
[8] Kurtz, E. M., and Foster, D. E., 2004, "Identifying a Critical Time for Mixing in a Direct Injection Diesel Engine Through the Study of Increased In-Cylinder Mixing and Its Effect on Emissions Through Study of Increased In-Cylinder Mixing and Its Effects on Emissions," Int. J. Engine Res., **5**(3), pp. 247–256.
[9] Hiroyasu, H., and Kadota, T., 1976, "Models for Combustion and Formation of Nitric Oxide and Soot in Direct Injection Diesel Engines," SAE Paper No. 760129.
[10] Fusco, A., Knox-Kelecy, A. L., and Foster, D. E., 1994, "Application of a Phenomenological Soot Model to Diesel Engine Combustion," *Third International Symposium COMODIA*.
[11] Dent, J. C., 1980, "Turbulent Mixing Rate—Its Effect on Smoke and Hydrocarbon Emissions From Diesel Engines," SAE Paper No. 800092.
[12] Aghav, Y. V., Lakshminarayanan, P. A., Babu, M. K. G., Nayak, N. S., and Dani, A. D., 2005, "Phenomenology of Smoke From Direct Injection Diesel Engines," *Proceedings of ICEF2005*, ASME Paper No. 1350.
[13] Stiech, G., 2003, *A Textbook on Modelling Engine Spray and Combustion Processes*, Springer, New York, 2003.
[14] "The Measurement of Diesel Exhaust Smoke," 1965, Motor Industry Research Association (MIRA) Report No. 10.
[15] http://www.dieselnet.com/standards/
[16] Kyriakides, S. C., Dent, J. C., and Mehta, P. S., 1986, "Phenomenological Diesel Combustion Model Including Smoke, and No Emission," SAE Paper No. 860330.
[17] Lakshminarayanan, P. A., and Dent, J. C., 1983, "Interferometric Studies of Vapourising and Combusting Sprays," SAE Paper No. 830244.
[18] Heywood, John B., 1988, *A Text Book on Internal Combustion Engine Fundamentals*, McGraw-Hill, New York.
[19] *AVL Boost 4.1 Users Guide*, July 2005.
[20] Kampmann, S., Dittus, B., Mattes, P., and Kirner, M., 1996, "The Influence of Hydrogrinding at VCO Nozzles on the Mixture Preparation in a DI Diesel Engine," SAE Paper No. 960867.

Downloaded 02 Jun 2010 to 171.66.16.107. Redistribution subject to ASME license or copyright; see http://www.asme.org/terms/Terms_Use.cfm

Application of a Spark Ignition Engine Simulation Tool for Alternative Fuels

Nirendra N. Mustafi

Robert R. Raine
e-mail: r.raine@auckland.ac.nz

Department of Mechanical Engineering,
The University of Auckland,
Private Bag 92019,
Auckland, New Zealand

Investigations on alternative fuels for internal combustion engines are regarded as one of the major research areas for the age. Engine simulation tools can play an important role in such investigations without performing the experimental works. It usually saves both time and money and provides better and additional understanding where the experimental facilities are limited. A spark ignition (SI) engine simulation tool (ISIS) is used in this present study to simulate the performance and emissions of SI engines, operated on alternative fuels such as biogas and "Powergas" (a synthesis gaseous fuel mixture of mainly carbon monoxide and hydrogen). An extended investigation is done for the oxides of nitrogen emissions considering multiple burn zones. The results are verified against those obtained for engine torque/brake power, exhaust temperature, and exhaust emissions experimentally and a good agreement is found between them.
[DOI: 10.1115/1.2747264]

Keywords: alternative fuels, spark ignition engine, simulation, performance, emissions

1 Introduction

The consumption of fossil fuels in internal combustion engines and the associated environmental impacts are now the worldwide concerns. These concerns have stimulated researchers into more environmentally friendly alternative fuels that can replace the use of fossil fuels to a greater or lesser extent. Biogas and "Powergas" are examples of these alternative fuels.

Biogas, which is renewable in nature, is obtained by anaerobic digestion of organic waste materials such as animal, human, agricultural, municipal, and industrial wastes. Its composition usually ranges between 30 and 40% carbon dioxide (CO_2), with a balance of methane (CH_4), and other trace gases. The most notable trace gas is hydrogen sulfide (H_2S), which may have no effect on combustion but its acidic products can affect engine parts. However, careful choice and monitoring of lubricant and avoiding the use of copper-based bearing materials can solve the problem [1]. Biogas is used in both SI and diesel engines. However, for the smaller applications, the use of SI engines operated on nonpurified biogas is quite common. In developing nations, biogas utilization without any further treatment for the removal of non-fuel components enables its production costs to be minimized [2].

"Powergas" a synthetic gaseous fuel that has been introduced in this study is another possible alternative fuel for the SI engine. The synthetic gas is originally derived during the processing of Aqua-fuel. The Aqua-fuel process encompasses an electric discharge on carbon rods submerged in water. The discharge decomposes the carbon rods and the water molecules and creates plasma composed of mostly ionized hydrogen, oxygen, and carbon atoms. The atoms combine in various forms, and are cooled down in the water surrounding the discharge. The exact composition of the gas depends on the production site, the time history of the decomposition, and the ambient conditions. The major constituents of the synthetic gas after formation are hydrogen (H_2), carbon monoxide (CO), and CO_2. It may also contain trace amount of hydrocarbons, oxygen (O_2), nitrogen (N_2), and water vapor. The gases are collected above the water surface, after drying, and compressed and stored in a cylinder. The synthetic gas resulting during the Aqua-fuel process was originally identified by the patent owner [3]. The synthetic gas is known by several different names among researchers. "Powergas" is the product and trade name used in New Zealand by Newman [4]. The "Powergas" used in this study was supplied by Newman and the original composition was unknown during the experiment. However, a typical composition can be assumed to be similar to that found by other research organizations for Aqua-fuel. Table 1 shows the composition of Aqua-fuel analyzed by two different organizations: NASA [5] and IBR [6].

Gas composition can have a significant impact on the performance and emission characteristics of the engine by affecting the stoichiometry, charge energy content, flame speed, ignition, and knock characteristics. The overall goal of this study is to predict the performance and emissions of SI engines operated on biogas and "Powergas" by an SI engine simulation tool (ISIS) compared to the baseline fuels, methane/natural gas (NG), and gasoline. The simulated results are then compared with the experimental results obtained by Midkiff et al. [7] for biogas fueling and with those obtained during our previous experimental investigation on "Powergas" fueling [8].

It is always advantageous to predict the effects of fuel quality on engine performances and emissions by computer modeling and simulation, without performing actual engine tests. It provides a higher flexibility in changing parameters, savings in time and money.

2 Simulation Tool

The spark ignition engine model used here is ISIS (Integrated Spark Ignition engine Simulation) and is based on the routines presented by Ferguson [9] and extended to include nitric oxide kinetics and a choice of the number of zones in the burned gas by Raine et al. [10]. The model predicts parameters such as power output, losses in the engine, fuel consumption, efficiency, and emissions. This program allows the user to vary engine parameters to enable the user to tune the model to the particular engine under test. The ISIS model assumes the well established extended Zeldovich mechanism for oxides of nitrogen emissions [10],

$$O + N_2 \rightleftarrows NO + N$$

$$N + O_2 \rightleftarrows NO + O$$

Submitted to ASME for publication in the JOURNAL OF ENGINEERING FOR GAS TURBINES AND POWER. Manuscript received November 9, 2006; final manuscript received April 17, 2007; published online January 9, 2008. Review conducted by Thomas W. Ryan III.

Copyright © 2008 by ASME

Downloaded 02 Jun 2010 to 171.66.16.107. Redistribution subject to ASME license or copyright; see http://www.asme.org/terms/Terms_Use.cfm

Table 1 Compositions of Aqua-fuel [5,6].

	NASA	IBR
Hydrogen (%)	46.48	48
Carbon dioxide (%)	9.33	2
Ethylene (%)	0.05	...
Ethane (%)	0.01	...
Acetylene (%)	0.62	...
Oxygen (%)	1.16	5
Nitrogen (%)	3.82	...
Methane (%)	0.18	...
Carbon monoxide (%)	38.37	44
Misc. structures in ppm (%)	...	1
Total (%)	100.02	100

$$N + OH \rightleftarrows NO + H$$

The first two reactions were identified by Zeldovich and the third was incorporated by Lavoie et al. [11] on the basis of engine spectroscopic measurements. Concentrations of CO_2, H_2O, O_2, and N_2 are computed on the basis of thermodynamic equilibrium. Full details of the method and relevant rate constants for the nitric oxide kinetics are provided in [10]. The emissions of CO and H_2 are computed by freezing the composition of the cylinder contents at a user-specified temperature.

ISIS extends earlier models by incorporating multiple zones for the burnt gas region. Details of the multizone modeling are described in [10]. The combustion of each zone is initiated at a different time, with the first zone formed at the time of ignition, and the last zone as combustion ends. Other zones are formed at equal increments of time between the first and the last zones. The number of zones to be modeled is selected by the user [10]. The model takes as input data: engine geometry, operating conditions (ignition timing, air/fuel ratio, etc.) ambient conditions and in-cylinder conditions at the inlet valve closure. Options exist in the program to select: fuel, in-cylinder heat transfer correlations (and weighting factors), and factors for blowby and friction and gas-exchange losses.

Heat transfer is calculated in the model from the Woschni correlation [12], the Eichelberg correlation [13], the Hohenberg correlation [14], and the user can choose any of them along with weighting factors for both the burnt and unburnt gas regions for fine tuning. In the present work, the Hohenberg heat transfer correlation is used with a unity weighting factor. The frictional losses are computed from the Chen and Flynn correlation [15] with a choice of weighting factor (0 to 1; unity is used in the present work). The gas exchange or pumping losses are determined from the correlation by Bishop [16]. The model considers different options to choose the burn laws appropriate for a particular engine operation. The burn rate is chosen to follow a Wiebe burn-rate equation [17] in this study, with burn duration taken from experimental data (Sec. 3.2).

3 Simulation

3.1 Fuel Data. Although biogas mixtures may vary considerably in composition, a typical composition of 60% CH_4 and 40% CO_2 and no water vapor is used in this simulation study. The model has an option to add diluents such as CO_2 and water vapor in volumetric proportion to the main fuel. In the case of biogas application, the main fuel that remains is methane and the added diluent is CO_2 (40% by volume, for instance). The baseline fuel for simulation is considered as pure methane, whereas that for the experiment is pipeline NG which has a lower heating value of 48.38 MJ/kg [7].

As mentioned, an estimate for "Powergas" composition is made based on the published data for the Aquafuel and also the exhaust gas mole fractions obtained experimentally. The estimated composition for "Powergas" simulation by ISIS is 52% CO, 44% H_2, and 4% N_2. Since the actual composition was unknown, results from the computer simulation must be interpreted with this proviso in mind. The computer simulation is employed mainly to allow a better understanding and interpretation of the experimental results. The simulation model needs an appropriate data file as an input for any specific fuel [9]. Therefore, a data file for "Powergas" is developed using the composition mentioned above and using the thermodynamic properties of the constituents obtained from the National Institute of Standards and Technology (NIST) Chemistry webbook [18].

Table 2 Engine specifications for biogas fuel [7]

Number of cylinders	4
Displaced volume per cylinder	625.0 cm^3
Cylinder bore	101.6 mm
Stroke	76.2 mm
Connecting rod length	153.7 mm
Compression ratio	11:1
Intake valve head diameter	43.7 mm
Exhaust valve head diameter	38.1 mm

3.2 Engine Specifications and Operating Conditions. The engine specifications for this study are given in Tables 2 and 3, to compare the simulated results with the experimental results. Engine operating conditions are kept almost similar in the simulation for both types of fueling except the engine speed. Table 4 provides the engine operating conditions for biogas and "Powergas" fueling. The maximum brake torque (MBT) spark timings and burn duration for biogas fueling are selected (Table 5) according to the experimental data provided by Midkiff et al. [7]. The parameters for "Powergas" fueling are taken from our experimental data [8]. Experimentally the MBT spark timings for "Powergas," NG, and gasoline are found to be 4°btdc (before top dead center), 24–30°btdc and 15–20°btdc, respectively, for the whole operating speed range. For the ISIS simulation, the spark timings for "Pow-

Table 3 Engine specifications for "Powergas" fuel [8]

Number of cylinders	1
Engine Displacement	508 cm^3
Cylinder bore	76.21 mm
Stroke	111.11 mm
Connecting rod length	241.3 mm
Compression ratio (variable)	8:1–11:1
Intake valve diameter	34.6 mm
Exhaust valve diameter	30.1 mm

Table 4 Engine operating conditions considered in ISIS

Biogas fueling [7]		"Powergas" fueling [8]	
Fuel/air equivalence ratio (Φ)	Varied from stoichiometric to lean misfire limit (Φ=0.65)	Fuel/air equivalence ratio (Φ)	Varied from stoichiometric to lean misfire limit
Engine speed	2350 rpm	Engine speed	1500 rpm
Throttle position	Wide open throttle (WOT)	Throttle position	Wide open throttle (WOT)
Spark timing	Maximum brake torque (MBT)	Spark timing	Maximum brake torque (MBT)

Downloaded 02 Jun 2010 to 171.66.16.107. Redistribution subject to ASME license or copyright; see http://www.asme.org/terms/Terms_Use.cfm

Table 5 MBT spark timing and the corresponding burn duration (θ_b) used in ISIS for biogas fueling [7]

	Methane/NG		Biogas	
Fuel/air equivalence ratio, Φ	MBT	Burn duration, θ_b	MBT	Burn duration, θ_b
0.65	55	96	58	118
0.70	49	88	50	100
0.75	44	81	44	90
0.80	39	75	43	88
0.85	36	70	42	86
0.90	34	66	41	84
0.95	31.5	64	40	82
1.00	30	62	40	81

ergas," gasoline, and NG are considered as 4°btdc, 20°btdc, and 30°btdc, respectively, corresponding to the speed of 1500 rpm. The MBT spark timing of "Powergas" clearly indicates a very rapid combustion compared to other fuels mainly due to its composition.

4 Results and Discussion

4.1 Biogas Fueling. The simulated results presented here include brake power and the emissions of oxides of nitrogen (NO_x) and CO. Figures 1(*a*) and 1(*b*) present the brake power output and the exhaust temperature respectively, as a function of fuel/air equivalence ratio (Φ) with a comparison to the baseline fuel methane/NG at MBT timing and 2350 rpm at WOT position. Brake power decreases gradually as the Φ decreases as a lower proportion of fuel is induced into the cylinder with decreasing Φ. A similar trend in power curve is obtained in the case of biogas fueling. But for a fixed Φ, the power output is decreased due to the presence of diluent CO_2 in the biogas mixture. The experimental results for biogas obtained by Midkiff et al. [7], are also plotted in Fig. 1(*a*) for comparison. The simulated results show similar trends to the corresponding experimental results. Although the NG used in the experiment has a very high CH_4 content, measured in excess of 98 mol% in [7], ISIS (pure CH_4) gives slightly higher values compared to the experimental counterparts. The difference between these two types of results is higher for higher equivalence ratios and at Φ=1, ISIS gives about 5% higher power output. A similar behavior is noted in the case of biogas fueling. It indicates, at weaker mixtures, ISIS shows a good agreement with the experimental results. The researchers [7] found a reduction in power output approximately by 13% at Φ=1, when the fuel changes from natural gas to biogas, whereas ISIS predicts about 12% reduction for the same condition.

A good agreement between the simulation and experimental results in the case of exhaust temperatures is observed for the whole operating range of equivalence ratios (Fig. 1(*b*)). At lower values of Φ (0.7–0.85), the exhaust temperatures of biogas are quite similar to methane but at higher Φ, the exhaust temperatures are found to be lower for biogas.

Figures 2 and 3 show the NO_x and CO emissions respectively, as a function of Φ for both fuels at the same engine operating conditions. The peak of the NO_x emissions has shifted slightly to the rich side for the simulation results compared to experimental results. ISIS predicts a slightly higher value of NO_x in the case of NG and slightly lower in the case of biogas fueling. But the trends are quite similar to each other. The presence of inert gas, CO_2, in biogas reduces the combustion temperature and this reduces NO_x formation substantially. The NO_x emissions are always lower for all the operating equivalence ratios for biogas fueling than the methane/NG fueling. ISIS shows about a 50% reduction in NO_x at peak and the experimental value shows about a 40% reduction at peak. Simulated results for CO emissions follow a similar trend to that of experiment, which is measured as around 2.68 g/kW h between Φ≈0.65 and 0.92 [7] for lower equivalence ratios irrespective of fuel quality (Fig. 3). In simulation the freezing equilibrium emissions temperature is considered as 2100 K. A sharp rise in brake specific CO emissions starts due to shortage of O_2, at the slightly lean side of the stoichiometric point (about Φ=0.90) for biogas fueling in the case of experimental observation and that for ISIS simulation starts at closer to the stoichiometric point (about Φ=0.95). In both experiment and simulation, CO emis-

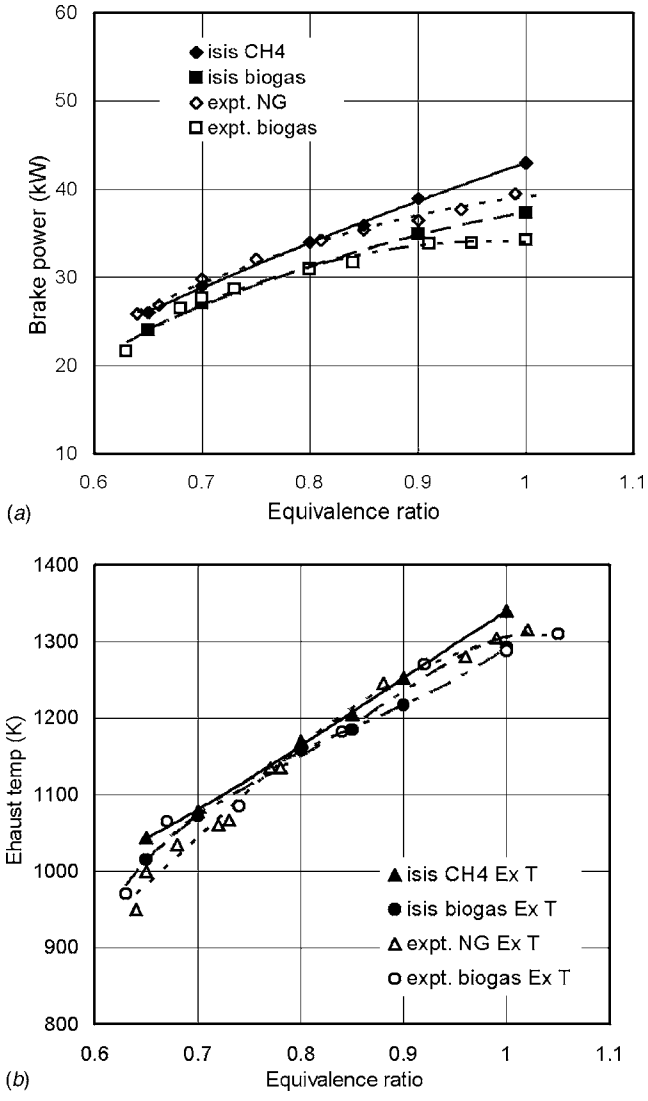

Fig. 1 Experimental and simulation results. (*a*) Brake power, (*b*) exhaust temperature, as a function of Φ for methane/NG and biogas fuels at 2350 rpm, WOT, and MBT spark timing.

Downloaded 02 Jun 2010 to 171.66.16.107. Redistribution subject to ASME license or copyright; see http://www.asme.org/terms/Terms_Use.cfm

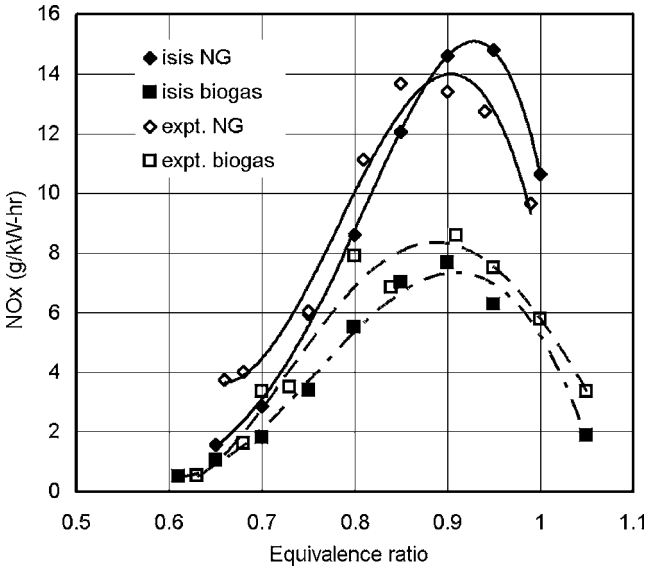

Fig. 2 Experimental and simulation results in NO_x emissions, as a function of Φ for methane/NG and biogas fuels at 2350 rpm, WOT, and MBT spark timing

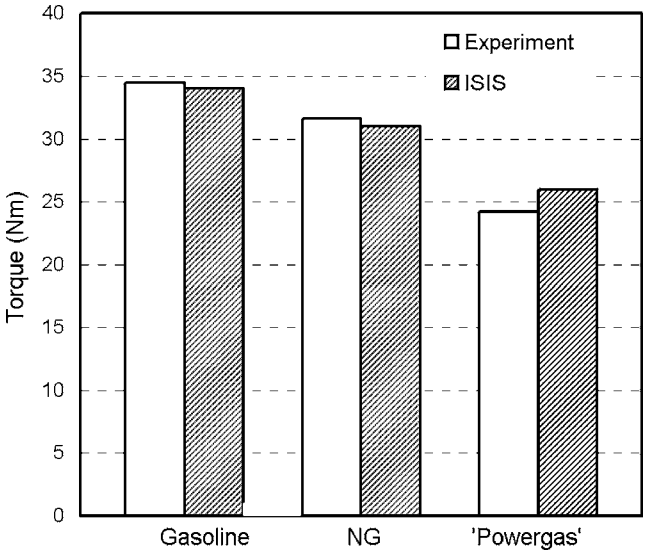

Fig. 4 Comparison of simulation results with experiment for engine brake torque (at 1500 rpm, MBT and WOT and at a CR of 8:1) for different fuels

sions for NG are found to be slightly lower than for biogas. However, the difference increases for rich mixtures. This is primarily due to the decrease in exhaust temperature for biogas operation as it contains diluents [19].

4.2 "Powergas" Fueling. Figure 4 shows the comparative results between the computer simulation and experiment in the case of engine torque output for the fuels: gasoline, NG, and "Powergas." ISIS shows slightly lower torque for gasoline and NG but slightly higher for "Powergas" fueling compared to the experimental values. The "Powergas" fuel may contain some other diluent such as CO_2, which was not considered in the simulation. This may explain the measured result of a lower torque output than modeled.

Figure 5 shows the trends of the exhaust emissions of CO_2, CO, and O_2 as a function of Φ, for the "Powergas" operation. ISIS results show good agreement with the experiments.

Figure 6 shows the comparison between the experimental and simulation results for the behavior of nitrogen oxides emissions for the three different fuels. The continuous curves show the model results for the variation of exhaust NO_x with equivalence ratio. The bars refer to measured results at the equivalence ratios indicated. In every case, simulation results show higher values than those obtained during experiment. However, the simulation results strongly support the NO_x emissions behavior that was measured by experiment. The peaks of NO_x emissions for the conventional fuels occur on the slightly lean side of the stoichiometric point. This is well established for the conventional hydrocarbon fuels [19]. In contrast, the peak for "Powergas" occurs at a very lean operating point (between $\Phi=0.7$ and 0.75). The peak NO_x emission for "Powergas" is found to be the highest among the three fuels. The higher concentration trend for "Powergas" at lower equivalence ratios can be attributed to the availability of

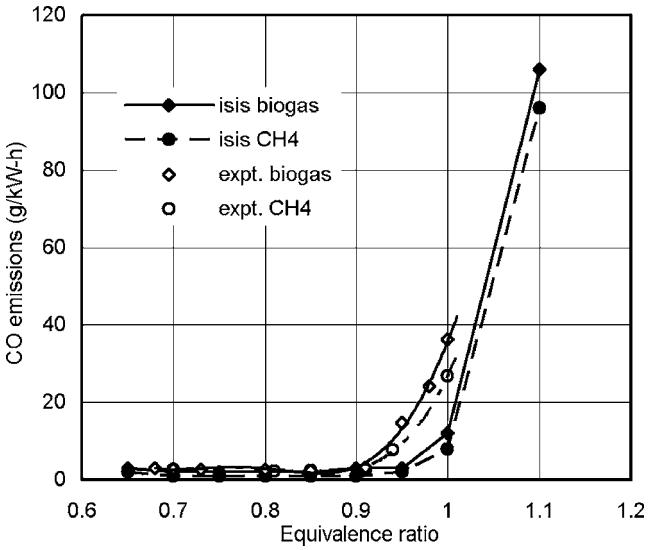

Fig. 3 Experimental and simulation results in CO emissions, as a function of Φ for methane/NG and biogas fuels at 2350 rpm, WOT, and MBT spark timing

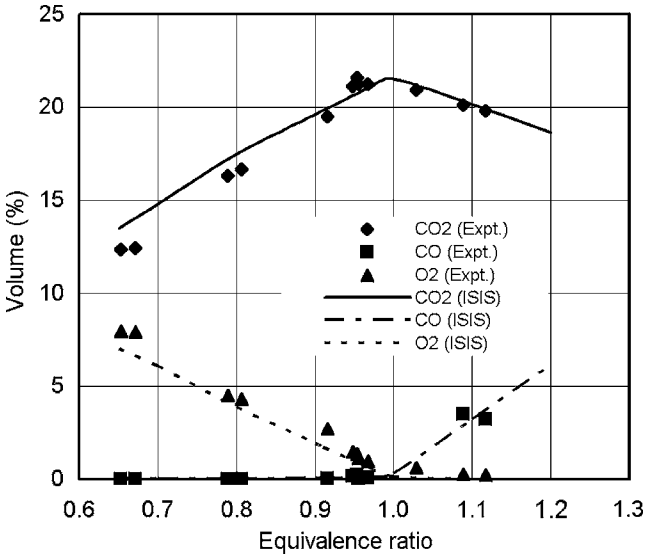

Fig. 5 Exhaust CO_2, CO, and O_2 emissions for "Powergas" as a function of equivalence ratio (at 1500 rpm, MBT, and WOT and at a CR of 8:1)

Downloaded 02 Jun 2010 to 171.66.16.107. Redistribution subject to ASME license or copyright; see http://www.asme.org/terms/Terms_Use.cfm

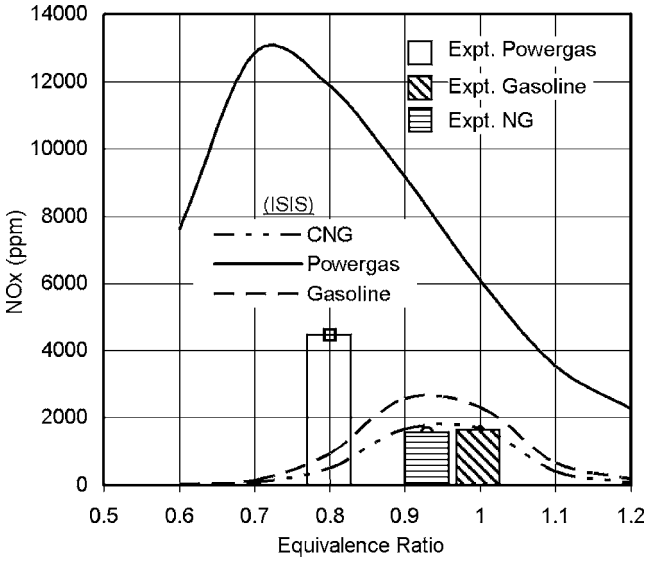

Fig. 6 Exhaust NO_x emissions as a function equivalence ratio (at 1500 rpm, MBT, and WOT and at a CR of 8:1)

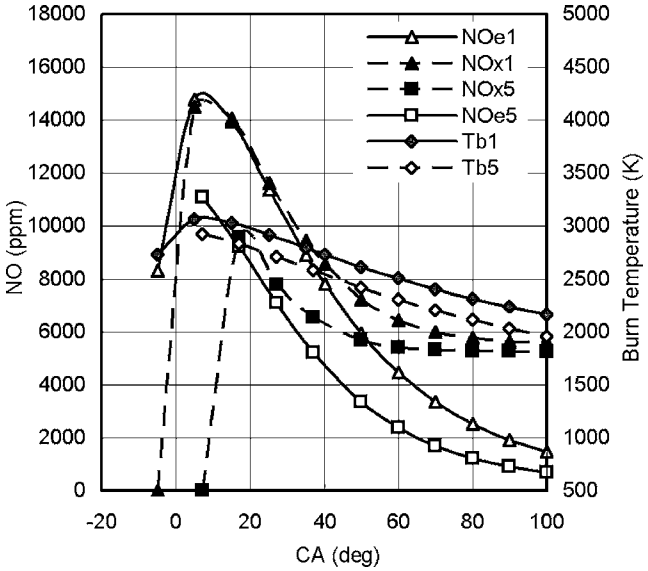

Fig. 8 Results from 5-burned zones model showing: burned gas temperatures (*Tb*), and kinetic NO_x and equilibrium (NO_e) nitric oxide concentrations as a function of crank angle for the first and fifth zones at $\Phi=0.99$; Fuel: "Powergas"

enough N_2 and O_2 at these operating conditions keeping in mind the very low stoichiometric air/fuel ratio of "Powergas" (4.25) compared to NG (~15.5) and gasoline (~14.6). Therefore, the kinetics of NO_x formation is dominated by species availability at these states compared to the states of higher equivalence ratios where the temperature is dominant with the lower availability of oxygen. During simulation the combustion temperatures are also found to be much higher in the case of "Powergas" compared to the conventional fuels, which leads to much higher exhaust NO_x emissions. This is further investigated by the extended simulation with multiple burn zones (5 zones).

Figures 7 and 8 present the simulation results for oxides of nitrogen formation (NO_x is kinetic and NO_e is equilibrium) and burn gas temperatures as a function of crank angle (CA). The figures clarify the process of NO formation during the combustion period. The peak of equilibrium NO concentration is overlapping with the peak of kinetically determined NO_x, which freezes at a value significantly higher than the equilibrium value. At lower equivalence ratio such as $\Phi=0.79$, the peak burned gas temperature is about 100°C lower than that at $\Phi=0.99$ (Fig. 8), but NO_x concentrations are significantly higher. This indicates that the availability of N and O species for the kinetics of NO_x formation is dominant at the lean condition, rather than the combustion temperature. At higher equivalence ratios, the combustion temperature acts as a dominant factor. Compared to the conventional fuels such as NG (Fig. 9), the zone temperatures and NO concentrations are found to be much higher in the case of "Powergas." At $\Phi=0.79$, for "Powergas," NO_x freezes at above 10,000 ppm, whereas at $\Phi=0.99$, it freezes at less than 6000 ppm. As a result, the exhaust NO_x emissions are higher at the leaner operating

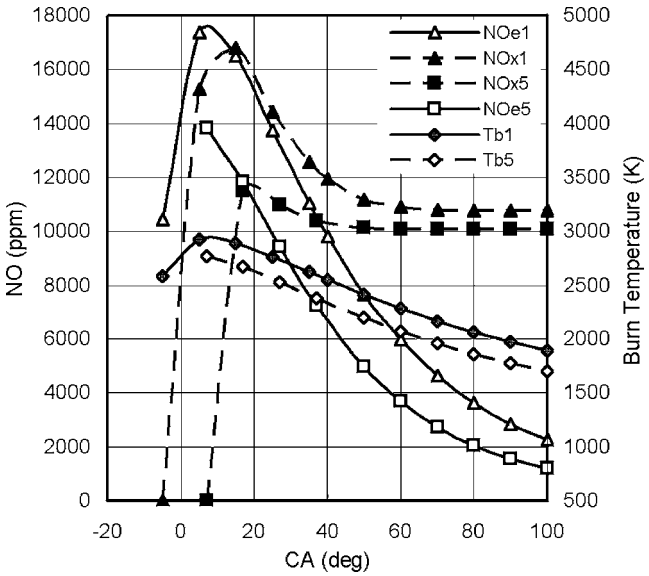

Fig. 7 Results from 5-burned zones model showing: burned gas temperatures (*Tb*), and kinetic NO_x and equilibrium (NO_e) nitric oxide concentrations as a function of crank angle for the first and fifth zones at $\Phi=0.79$; Fuel: "Powergas"

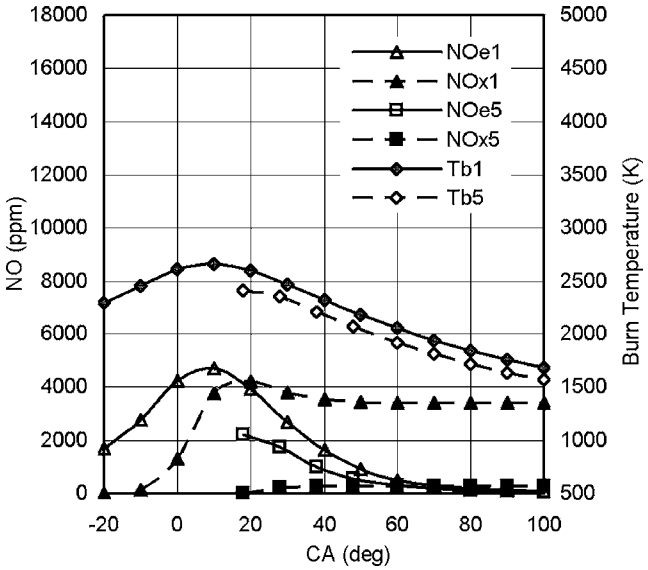

Fig. 9 Results from 5-burned zones model showing: *Tb*, and kinetic and equilibrium (NO_e) nitric oxides concentrations as a function of CA for the first and fifth zones (fuel: natural gas at $\Phi=1.0$)

Downloaded 02 Jun 2010 to 171.66.16.107. Redistribution subject to ASME license or copyright; see http://www.asme.org/terms/Terms_Use.cfm

condition.

Figure 9 shows the temperature and NO profiles for NG at stoichiometric mixture. This shows a clear difference from the profiles of "Powergas" (Figs. 7 and 8). The lower temperature in the case of NG leads to much slower rate of NO formation, and therefore much lowers peak concentrations for both equilibrium and kinetic NO. While the freezing of the NO reactions occur at similar temperatures for both fuels (about 2000–2300 K), the kinetic NO is decreasing from a very high level in the case of "Powergas" compared to the much lower peaks in the case of NG. The end result is much higher concentration of NO in the case of "Powergas" than for the conventional fuels.

5 Conclusions

The SI engine simulation software ISIS has been applied successfully for the alternative fuels such as biogas and "Powergas" to predict their performance and emissions while operated in SI engines. The results from the computer simulation are found to be generally consistent with the experimental data where the engine operating points are optimized for the respective fuels. The results also show some inconsistency with the experimental results and the reasons might be as follows: MBT spark timing and the corresponding burn duration are very important input variables for ISIS simulation and in many cases they have been either assumed or tried to be interpolated to simulate similar operating conditions to the experiment; various factors such as residual fraction, blowby coefficient, pressure and temperature at inlet valve closure, weighting factors, etc. are assumed and can have significant effects on output results. For the "Powergas" fueling, the limitation was the unknown actual fuel composition. Multiple burn zone modeling helps to interpret the reasons for higher NO_x emissions in the case of "Powergas" fueling compared to NG. "Powergas" operation produces very high NO_x at lean operations and the peak NO_x is found at a very lean operating condition compared with the conventional hydrocarbon fuels. Though it is very unusual for conventional hydrocarbon fuels, it can happen for the fuel gas which contains mainly CO and H_2 (that has very high flame temperature and flame speed). The simulation results interpret and confirm that the availability of species to form NO_x is dominant instead of temperature at such a lean operating condition in the case of "Powergas." In conclusion, ISIS has been shown to be regarded as a useful simulation tool not only for the conventional hydrocarbon fuels, but also for nonhydrocarbon alternative fuels for SI engines.

References

[1] Picken, D. J., Fox, M. F., and Bush, G. P., 1991, "An Investigation of Piston Ring Blowby and a Discussion of Its Impact on Biogas Engines," *Proceedings of the IMechE, Conference on Internal Combustion Engine Research in Universities, Polytechnics and Colleges*, IMechE, London, pp. 177–184.

[2] Crookes, R. J., 2006, "Comparative Bio-fuel Performance in Internal Combustion Engines," Biomass Bioenergy, **30**(5), pp. 461–467.

[3] Richardson, Jr., W. H., "Electrical Power Generation Without Harmful Emissions." U.S.Patent No. 5,435,274.

[4] Newman, C., 2004, Managing Director, Four Rings Enterprises Ltd. (personal communication).

[5] Santilli, R. M., 1998, "AquaFuel, An Example of the Emerging New Energies and the New Methods for, Their Scientific Study," Institute for Basic Research, available http://arxiv.org/PS_cache/physics/pdf/9805/9805031.pdf, accessed August 29, 2006.

[6] Santilli, R. M., 1998b, "Application of Hadronic Mechanics to New, Clean, Over-Unity, Fuels and Energies (Cont'd), Part 3," Institute for Basic Research, available at http://www.usmagnegas-.com/science/ir00020b.htm, accessed August 29, 2006.

[7] Midkiff, K. C., Bell, S. R., Rathnam, S., and Bhargava, S., 2001, "Fuel Composition Effects on Emissions from a Spark-Ignited Engine Operated on Simulated Biogases," ASME J. Eng. Gas Turbines Power, **123**, pp. 132–138.

[8] Mustafi, N. N., Miraglia, Y. C., Raine, R. R., Bansal, P. K., and Elder, S., 2006, "Spark-Ignition Engine Performance with 'Powergas' Fuel (Mixture of CO/H_2): A Comparison with Gasoline and Natural Gas," Fuel, **85**(12–13), pp. 1605–1612.

[9] Ferguson, C. R., 1986, *Internal Combustion Engines*, Wiley, New York.

[10] Raine, R. R., Stone, C. R., and Gould, J., 1995 "Modelling of Nitric Oxide Formation in Spark Ignition Engines with a Multi-Zone Burned Gas," Combust. Flame, **102**(3), pp. 241–255.

[11] Lavoie, G. A., Heywood, J. B., and Keck, J. C., 1970, "Experimental and Theoretical Investigation of Nitric Oxide Formation in Internal Combustion Engines," Combust. Sci. Technol., **1**, pp. 313–326.

[12] Woschni, G., 1967, "Universally Applicable Equation for Instantaneous Heat Transfer Coefficient in the Internal Combustion Engine," SAE Paper 670931.

[13] Eichelberg, G., 1939, "Some New Investigations on Old Combustion-Engine Problems," Engineering, **148**, pp. 463 and 547.

[14] Hohenberg, G. F., 1979, "Advances Approaches for Heat Transfer Calculations," SAE Paper 790825.

[15] Chen, S. K, and Flynn, P., 1965, "Development of a Compression Ignition Research Engine," SAE Paper 650733.

[16] Bishop, I. N., 1964, "Effect of Design Variables on Friction and Economy," SAE Paper 640807.

[17] Stone, R., 1992, *Introduction to Internal Combustion Engines*, 2nd ed., McMillan, London.

[18] "National Institute of Standards and Technology (NIST) Chemistry WebBook, NIST Standard Reference Database Number 69, March 2001 Release," available at http://webbook.nist.gov/chemistry/, accessed August 20, 2006.

[19] Heywood, J. B., 1988, *Internal Combustion Engine Fundamentals*, McGraw-Hill, New York.

Downloaded 02 Jun 2010 to 171.66.16.107. Redistribution subject to ASME license or copyright; see http://www.asme.org/terms/Terms_Use.cfm

Instantaneous Engine Speed Time-Frequency Analysis for Onboard Misfire Detection and Cylinder Isolation in a V12 High-Performance Engine

Fabrizio Ponti
DIEM,
University of Bologna,
Bologna 40136, Italy

The diagnosis of a misfire event and the isolation of the cylinder in which the misfire took place is enforced by the onboard diagnostics (OBD) requirements over the whole operating range for all the vehicles, whatever the configuration of the engine they mount. This task is particularly challenging for engines with a high number of cylinders and for engine operating conditions that are characterized by high engine speed and low load. This is why much research has been devoted to this topic in recent years, developing different detection methodologies based on signals such as instantaneous engine speed, exhaust pressure, etc., both in time and frequency domains. This paper presents the development and the validation of a methodology for misfire detection based on the time-frequency analysis of the instantaneous engine speed signal. This signal contains information related to the misfire event, since a misfire occurrence is characterized by a sudden engine speed decrease and a subsequent damped torsional vibration. The identification of a specific pattern in the instantaneous engine speed frequency content, characteristic of the system under study, allows performing the desired misfire detection and cylinder isolation. Particular attention has been devoted to designing the methodology in order to avoid the possibility of false alarms caused by the excitation of this frequency pattern independently from a misfire occurrence. Although the time-frequency analysis is usually considered a time-consuming operation and not associated to onboard application, the methodology proposed here has been properly modified and simplified in order to obtain the quickness required for its use directly onboard a vehicle. Experimental tests have been performed on a 5.7 l V12 spark-ignited engine run onboard a vehicle. The frequency characteristic of the engine-vehicle system is not the same that could be observed when running the engine on a test bench, because of the different inertia and stiffness that the connection between the engine and the load presents in the two cases. This makes it impossible to test and validate the methodology proposed here only on a test bench, without running tests on the vehicle. Nevertheless, the knowledge of the mechanical design of the engine and driveline gives the possibility of determining the resonance frequencies of the system (the lowest one is always the most important for this work) before running tests on the vehicle. This allows saving time and reducing costs in developing the proposed approach. [DOI: 10.1115/1.2436563]

Introduction

Misfire detection strategies are today integrated in every engine diagnostic system designed for automotive applications, due to onboard diagnostic (OBD) regulations requirements [1]. Although numerous approaches have been attempted in these last decades [2–5], most of the strategies that have been successfully implemented are based on the crankshaft speed signal analysis [6–10]. One positive aspect is the availability of such information to the electronic control unit (i.e., no need for additional sensors), but the main reason is the existence of a strong physical correlation between the presence (or absence) of combustion—in one or more cylinders—and the engine speed trend. In fact, the misfire event implies a lack of positive torque on the crankshaft during the corresponding expansion stroke and, therefore, a sudden decrease of engine speed. The objective of most diagnostic strategies is the detection of such speed variation and the isolation of the event that caused it—the missing combustion(s) of the misfiring cylinder(s). An example is given by a methodology developed by Bosch research [11–13] based on the evaluation of the time periods spent by the crankshaft to perform the rotation of predefined angular sectors.

The novel approach presented here is based on the observation that the misfire causes an impulsive lack of torque acting on the engine crankshaft, and thus, it causes not only a sudden decrease of engine speed, but also the excitation of damped torsional vibrations at frequencies characteristic of the system (engine and load) under study. In order to enlighten the presence of this torsional vibration (and therefore detect the misfire event), the instantaneous crankshaft speed signal is processed in the time-frequency domain. The objective is to detect the appearance of such torsional vibration (whose natural frequency can be determined knowing

Contributed by the Internal Combustion Engine Division of ASME for publication in the JOURNAL OF ENGINEERING FOR GAS TURBINES AND POWER. Manuscript received June 19, 2006; final manuscript received August 11, 2006; published online January 9, 2008. Review conducted by Lee Langston. Paper presented at the 2002 Fall Technical Conference of the ASME Internal Combustion Engine Division (ICEF2002), September 8–11, 2002, New Orleans, Louisiana, USA.

Copyright © 2008 by ASME

Downloaded 02 Jun 2010 to 171.66.16.107. Redistribution subject to ASME license or copyright; see http://www.asme.org/terms/Terms_Use.cfm

the system geometry and, eventually, experimentally verified) and to isolate the event that originated it—the missing combustion(s) of the misfiring cylinder(s).

The applicability of this methodology onboard the vehicle is discussed in detail in the last section of the paper. In terms of computational resources, the implementation of the strategy in the ECU seems feasible, because the time-frequency content of the engine speed signal can be partially extracted without the considerable computational effort usually required by classical time-frequency analysis. A comparison between the detection capability of this approach and that obtained with the time based approach described in [14] is also discussed.

Methodology Background

As it is well known, the absence of combustion in one of the cylinders of an internal combustion engine corresponds to a lack of positive torque acting on the crankshaft during the expansion stroke of the misfiring cylinder. Considering for example a four-cylinder engine with uniformly spaced combustions (one every 180 deg of crankshaft rotation), the mean overall indicated torque produced during one single stroke results as the sum of the torques produced by the four cylinders during that angular interval. Under normal operating conditions (no misfires), only one of these four terms is positive (the one corresponding to the cylinder that has undergone an expansion stroke), while one is definitely negative (compression stroke contribution) and the sum of the last two (intake and exhaust strokes contribution) is essentially negligible. The overall sum is usually positive (greater or smaller than the sum of load, friction and auxiliary torques, respectively, implying acceleration or deceleration of the crankshaft) under normal operating conditions, except when cutoff strategies are active. When a misfire occurs, such a sum is obviously negative, since the only positive contribution (corresponding to the expansion stroke of the misfiring cylinder) is smaller than the one corresponding to the compression phase that has taken place in another cylinder [15]. These considerations lead to describe the effect of a missing combustion as a negative torque step superimposed on the overall indicated torque trend that would have been produced in case of a regular combustion. The application of this negative step lasts for the expansion stroke of the misfiring cylinder even if its intensity is not uniformly distributed over this 180 deg interval.

Similar considerations can be made for engines with a higher number of cylinders; the misfire event still corresponds to a lack of positive torque, but since the expansion strokes of the various cylinders partially overlap, the resultant indicated torque acting on the crankshaft could still be positive even during the expansion stroke of the misfiring cylinder. This is due to the positive contribution of the other cylinders that are undergoing an expansion stroke within the angular interval considered.

For this reason, traditional approaches based on the recognition of a sudden engine speed decrease are critical for engines having more than four cylinders: The higher the number of cylinders, the smaller the torque lack during the expansion stroke of the misfiring cylinder, the smaller the effect on engine speed [16]. In addition, since the expansion strokes partially overlap, the torque lack will show its effects over more than one angular sector considered for misfire detection. This makes the identification of the cylinder where the misfire took place more difficult.

Figures 1 and 2 help to clarify this point of view, showing data acquired on a V12 SI engine. Figure 1 shows both the overall instantaneous indicated torque produced by the 12 cylinders during normal operating conditions and in case of misfire in cylinder 1. The mean values obtained by integrating the indicated torque over angular sectors of 720 deg/12=60 deg of crankshaft rotation are also shown in Fig. 1. Figure 2 shows the difference between the indicated torques reported in Fig. 1, together with the difference mean values over the 60 deg angular sectors taken into account.

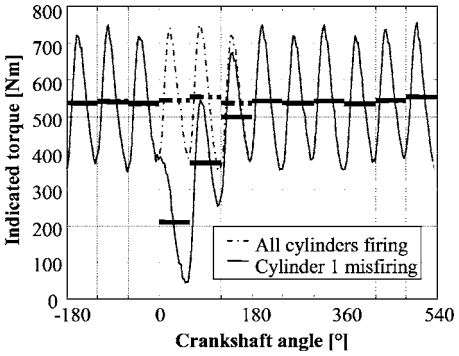

Fig. 1 Indicated torque mean value evaluation over 60 deg intervals, for a V12 engine with cylinder 1 misfiring at the beginning of the engine cycle

As it can be seen, the effect of the misfire is equivalent to a negative torque step superimposed on the regular indicated torque value, whose duration is equal to 180 deg of crankshaft rotation, starting at 0 deg (corresponding to cylinder 1 combustion TDC). This corresponds in terms of indicated torque mean values to a decrease for three consecutive angular sectors with respect to the normal torque production, with the decrease highest for the first sector of the sequence.

Looking at the corresponding engine speed trend, shown in Fig. 3, two aspects are particularly interesting: one is the well-known sudden and localized speed decrease, and the other one is the appearance of a damped torsional vibration. Both start around 0 deg crankshaft angle (CA), but while the first one is a very short phenomenon, the crankshaft is still oscillating ten cycles later. The reason is very simple: the absence of combustion in cylinder 1 causes the average indicated torque produced in the interval 0–180 deg CA to be smaller than the corresponding resistant torque (sum of load, friction, auxiliaries and reciprocating masses effects), thus causing a negative angular acceleration of the engine-load rotating inertias. Even a simple one-inertia engine-load model, as follows, clearly describes this phenomenon [17,18]:

$$J\dot{\omega} = T_i(\theta) - [T_f(\theta) + T_L + T_r(\theta)] \tag{1}$$

But this model does not explain why the engine speed increases subsequently (reaching values even higher than the ones attained before the misfire), nor why a damped oscillation should arise. What makes the model described by Eq. (1) inappropriate for this type of dynamics is the assumption of infinite stiffness of the system, which leads to a single inertia (one degree-of-freedom (DOF)) model. This behavior can be understood by simply adopting a two (or more) DOF model, assuming a certain elasticity and

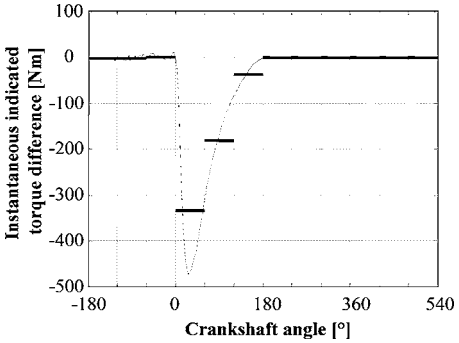

Fig. 2 Difference between the indicated torque production in case of misfire in cylinder 1 and during normal operating conditions

Downloaded 02 Jun 2010 to 171.66.16.107. Redistribution subject to ASME license or copyright; see http://www.asme.org/terms/Terms_Use.cfm

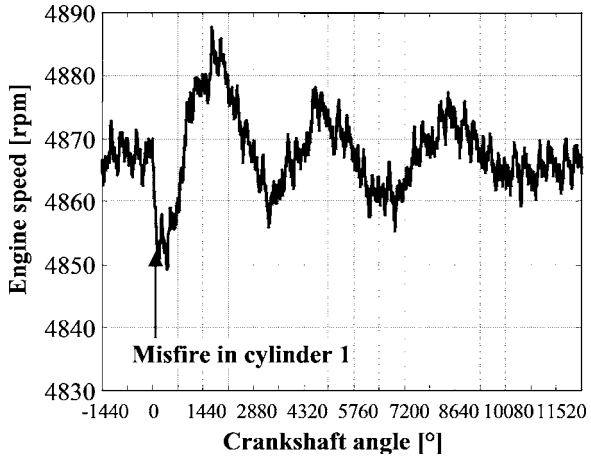

Fig. 3 Engine speed trend for a V12 engine with cylinder 1 misfiring at 0 deg crankshaft angle in fifth gear at 230 km/hr

a certain degree of damping are present between the two (or more) rotating inertias [19]. Such models reveal the presence of one (or more) natural frequency, characteristic of the system under study (and therefore different if the engine is on board the vehicle or on the test cell), at which the system starts vibrating when excited by a torque impulse (or step), such as the one due to a missing combustion.

For example, a two DOF model can be used to describe the observed behavior

$$J_{\text{eng}}\ddot{\theta}_{\text{eng}} = T_i(\theta) - T_f(\theta) - T_r(\theta) - k(\theta_{\text{eng}} - \theta_{\text{load}}) - c(\dot{\theta}_{\text{eng}} - \dot{\theta}_{\text{load}})$$

$$J_{\text{load}}\ddot{\theta}_{\text{load}} = T_L + k(\theta_{\text{eng}} - \theta_{\text{load}}) + c(\dot{\theta}_{\text{eng}} - \dot{\theta}_{\text{load}}) \quad (2)$$

Equation (2) obviously contains equivalent inertias, stiffness, and damping, all evaluated with respect to the engine speed, since a gearbox is present onboard the vehicle. From Eq. (2) the natural frequency of the system can be derived

$$f_n = \frac{1}{2\pi}\sqrt{\frac{k(J_{\text{eng}} + J_{\text{load}})}{J_{\text{eng}}J_{\text{load}}}} \quad (3)$$

Changing the inserted gear, the equivalent inertias and stiffness will change, thus modifying the natural frequency of the system. Simply knowing the engine, driveline and vehicle design it is possible to evaluate the lower natural frequency of the system under study for all the gears, using Eq. (3), and evaluating equivalent inertia and stiffness of the system for all the inserted gears. The values in Table 1 have been obtained for the V12 SI engine onboard the vehicle used for this study.

The main objective of this work therefore consisted of verifying the presence of a certain frequency (characteristic of the system under study and inserted gear dependent) that is excited by a misfire and developing the most appropriate tools to detect its occurrence, and to subsequently isolate the misfiring cylinder(s).

The procedure has been setup and validated using a V12 SI engine mounted onboard a vehicle. The results are compared to those obtained using the approach based on the observation of the time periods spent by the crankshaft to perform the rotation of predefined angular sectors, described in [12–14], and briefly discussed in the following.

Table 1 Frequencies for gears employed in this work

Inserted gear	Frequency (Hz)
1	3
2	5
3	6
4	8
5	10

Mathematical Tools: Time-Frequency Approach. The appearance of the torsional vibration excited by the misfire(s) can be detected by continuously monitoring the frequency content of the engine speed signal. Such a spectrum presents various frequencies at which the energy is concentrated; they usually are multiples of the engine cycle frequency, and the harmonic of maximum amplitude is normally the one corresponding to the combustion frequency (i.e., Z times the cycle frequency, or Zth harmonic order, if Z is the number of cylinders of the given engine and the combustions are evenly spaced) [20]. The frequencies associated to such harmonics are therefore dependent on the engine speed. As it has been previously clarified, a particular frequency f^* is excited when a missing combustion takes place; the value of such frequency only depends on the engine-load system setup (i.e., stiffness and inertia of the various shafts, flywheels, inserted gear,…), and is therefore constant for a given system, once the inserted gear is known.

Once the frequency f^*, characteristic of the system under study, is known, a diagnostic algorithm can be developed to detect its appearance. When a missing combustion takes place, the frequency f^* is excited and its amplitude increases, determining a variation of the signal spectrum that is to be detected by the designed algorithm.

The information of interest is the engine speed spectrum variation over time, and the best approach is therefore the use of joint time-frequency analysis. There exist several techniques to perform this kind of analysis, such as Wigner distribution, etc. [21]. The short-time Fourier transform (STFT), defined by Eq. (4), has been chosen for this work because it is the simplest and most intuitive, even if it usually guarantees lower resolution with respect to other more complex techniques [22]

$$S_t(2\pi f) = \frac{1}{\sqrt{2\pi}}\int e^{-j2\pi f\tau}\omega(\tau)h(\tau - t)d\tau \quad (4)$$

The reason for such a choice is related to the limited computational resources usually available in the ECU: The simplest tool has been used, to verify its capability of detecting the malfunctioning condition. It should however be noted that even the STFT requires a large amount of computational resources, but once the frequency f^* is known, it is possible to extract the STFT only around that frequency and dramatically reduce the computational effort [17]. Finally, the main design parameters when developing STFT algorithms are the type of window function $h(\tau - t)$ and its duration, since they both strongly influence the degree of resolution that can be attained in the time and frequency axes.

Mathematical Tools: Time-Based Approach. The time-based approach considered in the following as an alternative to the proposed frequency-based approach uses the information coming from a magnetic pickup to evaluate the so-called combustion periods, which are time periods spent by the crankshaft to perform the rotation of a predefined angular sector, related to the combustion phase of each cylinder [11–13]. Knowledge of the combustion periods allows evaluation of the parameter LU_i, defined as

$$LU_i = \frac{\tau_{i+1} - \tau_i}{\tau_i^3} \quad (5)$$

where τ_i and τ_{i+1} are the combustion periods related to two consecutive combustion events. It can be demonstrated that LU_i is related to the crankshaft kinetic energy variation caused by each combustion event, as it is reported in the following equation [12,13]:

Downloaded 02 Jun 2010 to 171.66.16.107. Redistribution subject to ASME license or copyright; see http://www.asme.org/terms/Terms_Use.cfm

$$LU_i = \frac{\tau_{i+1} - \tau_i}{\tau_i^3} \cong \frac{\tau_{i+1} - \tau_i^2}{2\tau_i^2 \tau_{i+1}^2} = \frac{\frac{1}{2\tau_i^2} - \frac{1}{2\tau_{i+1}^2}}{\Delta\theta^2} = \frac{\frac{\dot{\theta}_i^2}{2} - \frac{\dot{\theta}_{i+1}^2}{2}}{\Delta\theta^2} \quad (6)$$

It can be seen, in addition, that the crankshaft kinetic energy variation evaluated over a well defined angular period $\Delta\theta$ is related to the mean net torque acting on the crankshaft over the same angular period [18]. Integrating Eq. (1) over the angular period $\Delta\theta$ it is possible, in fact, to obtain

$$\frac{1}{\Delta\theta}\int_0^{\Delta\theta} J\dot{\omega}d\theta = \frac{1}{\Delta\theta}\int_0^{\Delta\theta} [T_i(\theta) - T_f(\theta) - T_r(\theta) - T_L(\theta)]d\theta$$

$$\frac{1}{\Delta\theta}\int_0^{\tau} J\dot{\omega}\omega dt = \overline{T_i(\theta)} - \overline{T_f(\theta)} - \overline{T_r(\theta)} - \overline{T_L(\theta)}$$

$$\frac{J[\dot{\theta}^2]_0^{\tau}}{2} \cong [\overline{T_i(\theta)} - \overline{T_f(\theta)} - \overline{T_L(\theta)}]\Delta\theta \quad (7)$$

Therefore, it has been demonstrated that LU_i is related to the mean net torque acting on the crankshaft over the considered angular period $\Delta\theta$,

$$LU_i \cong \frac{-[\overline{T_i(\theta)} - \overline{T_f(\theta)} - \overline{T_L(\theta)}]}{J\Delta\theta} \quad (8)$$

If the engine is running steadystate, the value of LU_i is supposed to be near to 0. If a misfire occurs, the right-hand side of Eq. (8) assumes values different from 0, and the same happens for LU_i. The presence of LU_i values far from 0 and positive can be used to detect the absence of combustion.

As reported in previous works [12–14], misfire diagnosis procedures based on the comparison of LU_i with a threshold value can generate false alarms during transient engine operating conditions characterized by relevant crankshaft speed variations, such as gear shifts, cutoffs, etc., since the net torque acting on the crankshaft (and, therefore, LU_i) assumes relevant values different from 0 also during such engine operating conditions. For this reason, the following studies [14] developed a methodology based on the recognition of a particular pattern of LU_i that allows detecting the misfire without also generating false alarms during cutoffs and gear shifts.

But the main limitation with an LU_i based approach is that it tends to fail at higher engine speed. Let us consider, for example, two different engine-vehicle operating conditions characterized by approximately the same value of the net torque acting on the crankshaft but different engine speed values. If a misfire occurs, LU_i is supposed to assume for the two tests taken into account approximately the same value, due to the fact that, as already mentioned, LU_i is related to the mean net torque acting on the crankshaft in the angular portion taken into account. Since the engine speed for the two tests is different (and, therefore, the value of τ_i^3 is very much different), it can be seen from Eq. (5) that also the values of $\tau_{i+1} - \tau_i$ should be different, being lower for the higher engine speed test. If the engine speed is very high (and, but not necessarily, the load is low), $\tau_{i+1} - \tau_i$ could assume values that are of the same order of magnitude of disturbances on the magnetic pickup signal. This consideration leads to the conclusion that if the engine speed is very high, the values of LU_i associated to misfire events may be not distinguished and therefore isolated.

Experimental Tests

The experimental data shown in this paper have been recorded during tests carried out on a racetrack with a Lamborghini Diablo prototype. The vehicle was equipped with a 5.7 l 12-cylinder engine, having a 60 deg V, firing order 1-7-4-10-2-8-6-12-3-9-5-11, and developing 362 kW at 6800 rpm.

Table 2 Frequencies for gears tested

Inserted gear	Frequency (Hz)
1	3.0
2	5.2
3	6.3
4	7.8
5	10.3

During the road tests, two signals coming from two magnetic pickups were recorded, the first sensor facing the flywheel teeth in order to detect the crankshaft instantaneous speed, while the other one facing the camshaft in order to obtain a cycle reference signal. The instantaneous crankshaft analog signal was obtained by a frequency to voltage converter, fed by the flywheel signal, and then both speed and phase signals were sampled at constant angular interval using the flywheel teeth in order to have a constant number of samples for each engine cycle (210 samples per cycle with a 105 teeth flywheel).

Methodology Definition

The first step is the verification of the frequencies characteristic of the engine-load system that have been previously determined for each gear employed on the vehicle. Figure 3 allows determining that in fifth gear this frequency is equal to ~10 Hz. In fact, the damped oscillation presented a period of ≈4 engine cycle, while the engine was running at 5000 rpm, yielding

$$f^* = \frac{5000}{4 \times 120} \approx 10 \text{ Hz} \quad (9)$$

Table 2 contains the engine-load system frequencies for different inserted gears, that have been experimentally evaluated: The comparison with the calculated ones (reported in Table 1) is very good. As an example, the engine speed STFT analysis for a test conducted at 5000 rpm in fifth gear is reported in Fig. 4. Since the engine speed has been sampled at a constant angular interval the STFT related information is obtained in the crankshaft angle (engine cycles), and the angular frequency domains. Figure 4 shows the amplitude of the angular frequency harmonic components at each crankshaft angle position. It can be observed that when a misfire occurs a higher amplitude appears at an engine cycle frequency order equal to ~0.25. This corresponds at 5000 rpm to a relevant harmonic component at a frequency of ~10 Hz.

Figure 5 shows the speed variation over a number of engine cycles for a transient test conducted in third gear with a misfire induced in cylinder 1 every 50 cycles. The STFT analysis of the instantaneous engine speed signal for the test considered is reported in Fig. 6. Still the misfire presence appears as a higher amplitude value on the STFT representation, meaning that a particular frequency has been excited by the misfire event. It can be observed that the higher amplitudes appear at engine cycle frequency orders varying along the test approximately from 0.45 to 0.16. This is due to the fact that the excited frequency assumes constant values in the time-frequency domain (the third gear is inserted corresponding to $f^* = 6.3$ Hz), and therefore, as the engine speed increases, it assumes decreasing values in the angular-frequency domain. The relationship between the time-frequency and the angular frequency representation can in fact, be, expressed as

$$\Phi^* = \frac{f^*}{f_{\text{cyc}}}$$

$$f_{\text{cyc}} = \frac{1}{2}\frac{\omega}{2\pi} \text{ Hz} \quad (10)$$

Downloaded 02 Jun 2010 to 171.66.16.107. Redistribution subject to ASME license or copyright; see http://www.asme.org/terms/Terms_Use.cfm

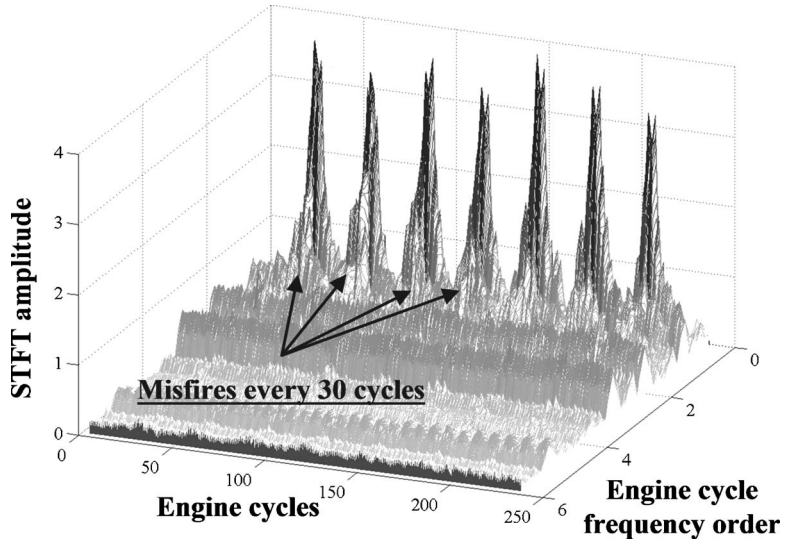

Fig. 4 Waterfall representation of the engine speed STFT analysis at 5000 rpm in fifth gear at 230 km/hr (one induced misfire in cylinder 10 every 30 cycles)

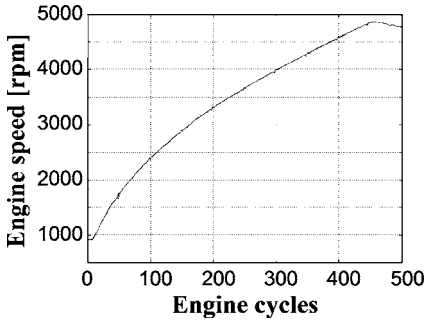

Fig. 5 Engine speed variation for the transient test in third gear (one induced misfire every 50 cycles in cylinder 1)

The decaying peak heights that can be observed in Fig. 6 are related to the result obtained in Eq. (8), as it will be explained in the following. It has to be underlined now that it is possible to detect the misfire occurrence by simply isolating the presence of a strong component, in the engine speed waveform, at a frequency f^*. From this point of view, STFT gives much more information than that required; in fact, it evaluates the amplitude variation over time for the harmonic components of the whole spectrum and not just for the one corresponding to the frequency f^*. For this reason, the STFT algorithm has been customized for the evaluation of only the frequency component of interest.

Equation (4) states that in order to evaluate the amplitude of only the frequency component at f^* (i.e., to determine $S_t(2\pi f^*)$), the windowed engine speed $\omega(\tau)h(\tau-t)$ has to be multiplied by the term $e^{-j2\pi f^*\tau}=\cos(2\pi f^*\tau)-j\sin(2\pi f^*\tau)$ and then integrated (summated when dealing with sampled signals). The result of these operations is a complex number whose modulus is the de-

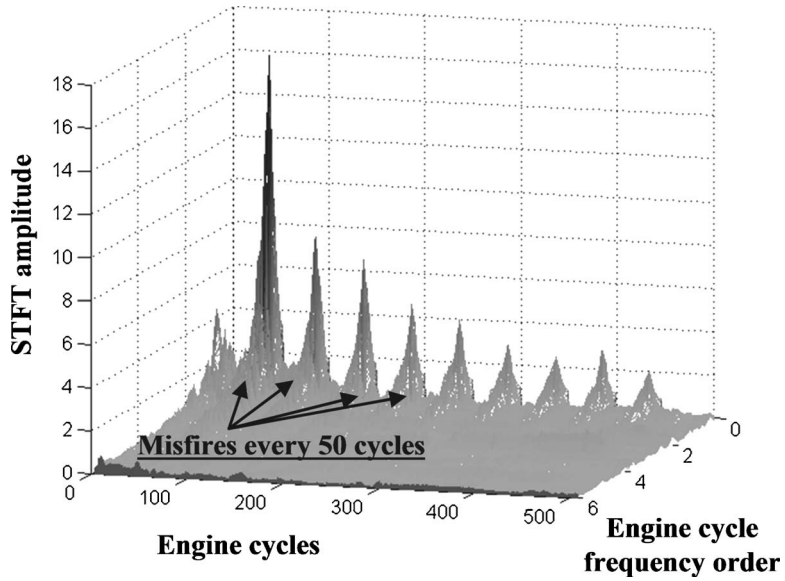

Fig. 6 Engine speed STFT analysis for the transient test in third gear (one induced misfire every 50 cycles in cylinder 1)

Downloaded 02 Jun 2010 to 171.66.16.107. Redistribution subject to ASME license or copyright; see http://www.asme.org/terms/Terms_Use.cfm

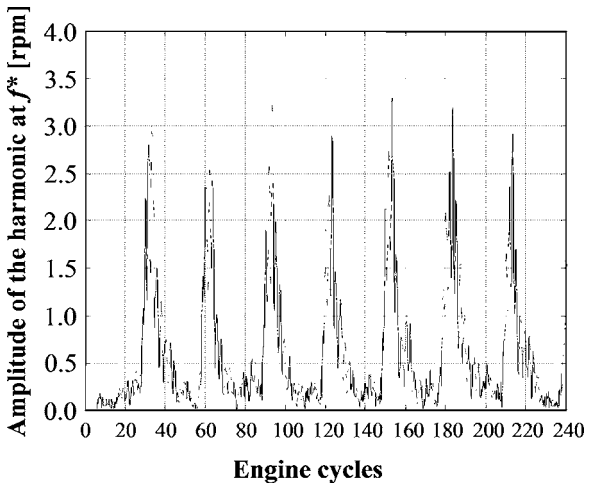

Fig. 7 Amplitude of the harmonic at f^* for the steady-state test at 5000 rpm in fifth gear at 230 km/hr (one induced misfire every 30 cycles in cylinder 10)

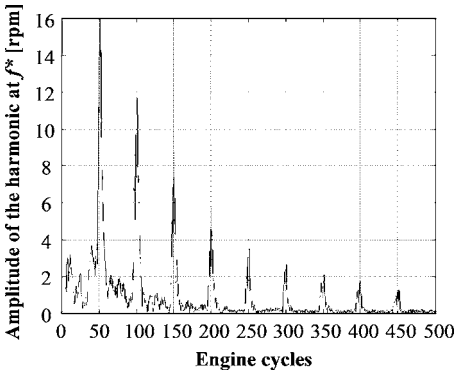

Fig. 8 Amplitude of the harmonic at f^* for the transient test in third gear (one induced misfire every 50 cycles in cylinder 1)

sired frequency component amplitude. The real and complex components of $S_t(2\pi f^*)$ can therefore be evaluated by computing the summations of the products between the windowed engine speed and the sinusoidal functions $\cos(2\pi f^* \tau)$ and $\sin(2\pi f^* \tau)$, respectively.

In order to get information about all the combustions in the various cylinders, $S_t(2\pi f^*)$ has to be evaluated once for each combustion event and, therefore, every 60 deg of crankshaft rotation. The length of the window over which the calculation takes place should be at least long enough to contain a whole period of the sinusoidal functions at frequency f^*, if a good resolution is required. If, for example, the engine is running at 5000 rpm and the fifth gear is inserted, the minimum window width to be used should be 4.2 cycles, whereas if the inserted gear is the third, the minimum width should become 6.6 cycles.

These considerations also lead to the conclusion that the proposed methodology can detect the misfire event only after a defined angular delay. In fact, at least one period of the damped oscillation caused by the absent combustion has to take place in order to be sensed. The delay entity is affected by the width of the chosen window, higher delays corresponding to wider windows. In order to have a good compromise between the resolution and the delay value, an observation window length of eight cycles has been chosen. The window shape is composed by a four-engine-cycles-long Hanning function with two null appendixes two cycles long at the beginning and at the end.

In order to analyze both steady-state and transient tests using the same algorithm, the engine speed has been previously high pass filtered at a cutoff frequency of 1 Hz. The application of the developed methodology on the tests presented in Figs. 4 and 6 yields the results presented in Figs. 7 and 8. The jagged peaks that can be observed in Fig. 7 are due to the methodology used to fast compute the amplitude of the f^* frequency component, since the signal duration is not always a multiple of the period $1/f^*$.

It can be seen from the preceding figures how it would be possible to detect the misfire presence by simply setting a variable threshold over the engine operating range. The need for a variable threshold arises from Eq. (8), as already mentioned. In fact, the engine speed decrease after a misfire event, and the subsequent engine speed oscillation present an amplitude proportional to $\dot{\theta}_{i+1} - \dot{\theta}_i$, that, using Eqs. (6) and (8), can be written as

$$\dot{\theta}_{i+1} - \dot{\theta}_i \cong \frac{[\overline{T_i(\theta)} - \overline{T_f(\theta)} - \overline{T_L(\theta)}]\Delta\theta}{J\dot{\theta}_i} \tag{11}$$

The amplitude of the expected oscillation is therefore inversely proportional to the engine speed value. This explains why the peak heights in Fig. 8 are decaying as the engine speed increases and why a variable threshold should be chosen for misfire detection.

As already mentioned, the methodology can detect the absence of combustion only after a certain delay because the damped oscillation needs time in order to be visible. Setting a threshold value of 1.5 for the test of Fig. 7, the delay between the misfire event and the overcoming of the threshold is approximately 0.5–1.0 engine cycles.

Once the amplitude of the harmonic at f^*, $S_t(2\pi f^*)$, has overcome the threshold, it remains over the threshold value for a crankshaft rotation of approximately four engine cycles. This makes the methodology insensitive to eventual misfire events within this angular portion. For this reason, the methodology seems not capable of detecting multiple misfires.

The length of the crankshaft rotation during which $S_t(2\pi f^*)$ overcomes the threshold could be a problem also for cylinder isolation since an apparent uncertainty between 48 different combustion events seems to be present. To solve this problem, it can be observed that the angular distance between the misfire event and the maximum value of $S_t(2\pi f^*)$ is approximately constant for all the tests investigated (four engine cycles). Taking this angular distance as a reference, the misfiring cylinder can be isolated as the combustion taking place four cycles before the maximum value of $S_t(2\pi f^*)$. This will give a correct cylinder isolation in the 73% of the cases for the steady-state test and in the 33% for the transient test, even if the misfire event occurrence is correctly diagnosed. In order to improve cylinder isolation performance, a different approach has been developed: Five engine speed values have been considered around the position taking place four cycles before the maximum of $S_t(2\pi f^*)$, each corresponding to the combustion phase of one cylinder. The misfiring cylinder has been then isolated among the five selected as the one that undergoes the higher engine speed decrease. Following this second approach, it has been possible to increase the correct cylinder isolation to, respectively, the 98% and 100% of the total misfire events. The methodology is therefore capable of detecting the absence of combustion with an angular delay of approximately 0.5–1.0 engine cycles, while for the correct cylinder isolation the delay increases to approximately four engine cycles.

Results

The methodology previously developed has been applied to different engine-vehicle operating conditions and then compared to the results obtained with a time-based approach as the one briefly discussed in the preceding sections. Figures 9–11 report respectively the engine speed waveform, the value of $S_t(2\pi f^*)$, and the value of *LU*, for a transient test conducted in second gear from

Downloaded 02 Jun 2010 to 171.66.16.107. Redistribution subject to ASME license or copyright; see http://www.asme.org/terms/Terms_Use.cfm

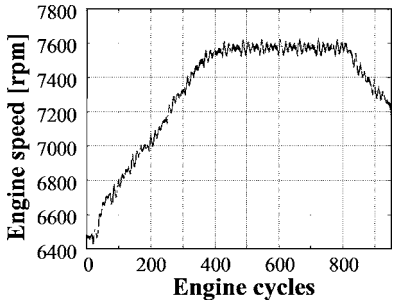

Fig. 9 Engine speed waveform for a test conducted in second gear from 6400 rpm to 7600 rpm (from 135 km/hr to 160 km/hr)

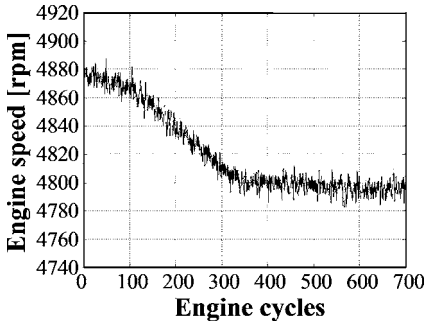

Fig. 12 Engine speed waveform for a test conducted in third gear at 4850 rpm (140 km/hr)

6400 rpm to 7600 rpm (from 135 km/hr to 160 km/hr), with a misfire induced in cylinder 1 approximately every 60 cycles.

As can be seen, the proposed methodology allows detecting the misfire events by simply defining a threshold value, since there exists a threshold value that enables misfire detection without generating false alarms. The LU_i approach for the same test does not give a clear misfire identification, even if the pattern recognition previously discussed is applied, with a probability of correct diagnosis around 25%. The proposed methodology therefore seems to give better results when the engine speed is particularly high, as in the case of the test taken into account, and the diagnosis becomes critical with other approaches.

The reason why the *LU* approach tends to fail at higher engine speed is related to the decreased signal-to-noise ratio that this approach presents for these operating conditions, as already explained in a preceding section. It is worth recalling that at higher engine speed $\tau_{i+1}-\tau_i$ decreases and can assume the same order of magnitude of the engine speed noise, thus causing a signal-to-noise ratio decay for *LU* evaluation. On the contrary the value of the oscillation amplitude shows still a good signal-to-noise ratio since this evaluation is made using a high number of samples and, thus, reducing the noise effects. This allows diagnosing the misfire occurrence for all the investigated conditions.

Figures 12–14 respectively report the engine speed waveform, the value of $S_t(2\pi f^*)$, and the value of *LU*, for a test conducted in third gear at 4850 rpm (140 km/hr), with a misfire induced in cylinder 1 approximately every 30 cycles.

Also in this case, the methodology based on the amplitude evaluation of the harmonic at frequency f^* guarantees better results than the LU_i based approach, due to the high speed at which the test has been conducted. Again there exists a threshold value that enables misfire detection without generating false alarms, while the LU_i approach is successful without false alarms only in the 60% of the induced misfires.

For a test at lower engine speed (2500 rpm) and fifth gear, during which one misfire every 30 cycles in cylinder 9 has been induced, the detection capabilities are, as expected, similar for the

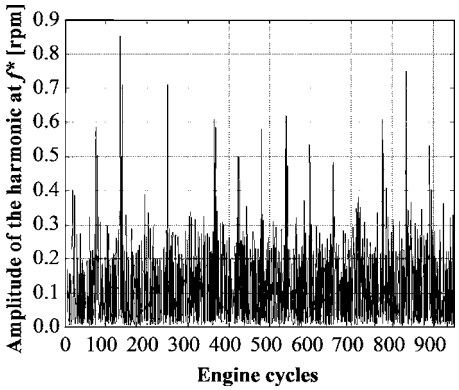

Fig. 10 $S_t(2\pi f^*)$ evaluation for the test shown in Fig. 9

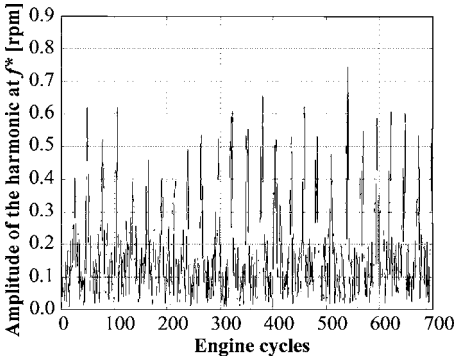

Fig. 13 $S_t(2\pi f^*)$ evaluation for the test shown in Fig. 12

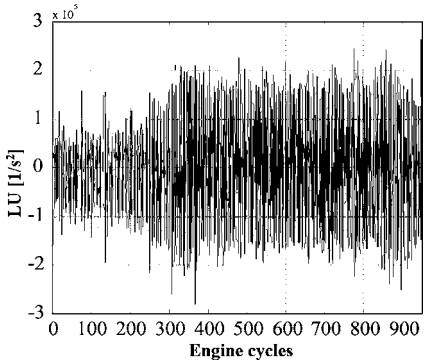

Fig. 11 LU_i evaluation for the test shown in Fig. 9

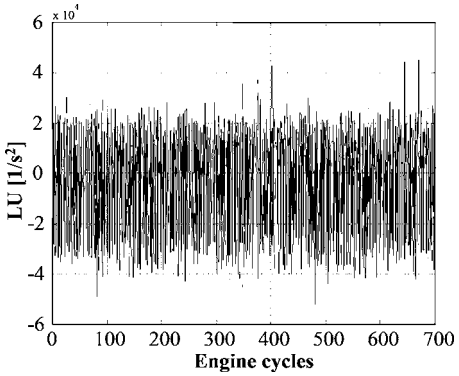

Fig. 14 LU_i evaluation for the test shown in Fig. 12

Downloaded 02 Jun 2010 to 171.66.16.107. Redistribution subject to ASME license or copyright; see http://www.asme.org/terms/Terms_Use.cfm

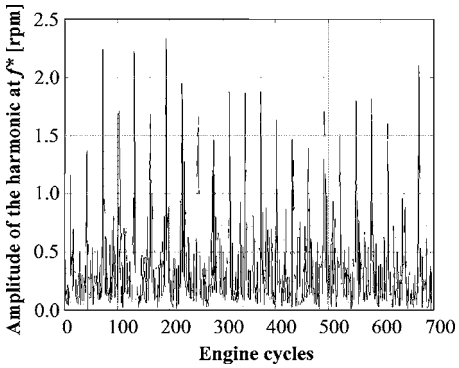

Fig. 15 $S_t(2\pi f^*)$ **evaluation for a test conducted at 2500 rpm in fifth gear**

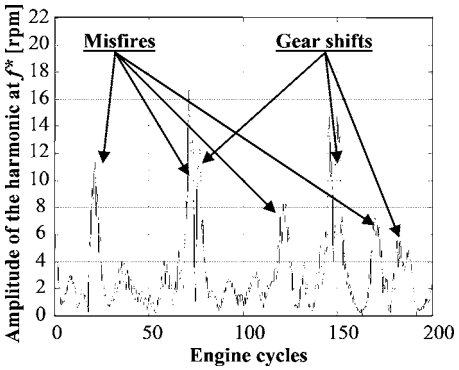

Fig. 18 LU_i **evaluation for a test conducted at 2500 rpm in fifth gear**

two considered approaches, both enabling the detection of all the induced misfires. The results are reported in the following Figs. 15 and 16.

Frequency-analysis-based misfire detection seems to be very robust, giving good results for all the engine operating conditions taken into account. The possibility of false alarms using this approach is related to a strong excitation of the investigated frequency that is independent from a misfire event. Phenomena that can cause such excitations on the driveline are, for example, clutch insertions after a gear shift or very strong road disturbances acting on the wheels. The first phenomenon has been investigated in Figs. 17 and 18, where the engine speed waveform during three consecutive gear shifts, from second to fifth during an urban test in which one misfire has been induced in cylinder 1 every 50 cycles, and the relative $S_t(2\pi f^*)$ evaluation has been respectively reported. As it can be seen when the clutch is inserted, a strong excitation of the investigated frequency takes place. For this reason, misfire detection should be inhibited during gear shifts, when using this frequency-based approach. The second phenomenon did not cause false alarms for the tests conducted in this study.

The comparison between the proposed frequency-based approach and the time-based one leads to the conclusion that, when the engine speed is high, only the first one can be used. For the engine operating condition in which they give similar results (i.e., at lower engine speed), the time-based one is obviously preferable, since it detects the absence of combustion faster (without the four cycles delay), and requires less computational resources. The best solution in terms of detection capability should therefore be a combined use of the two methodologies, using the frequency analysis based one when the engine is running under the operating conditions in which the LU_i-based one fails (high speed).

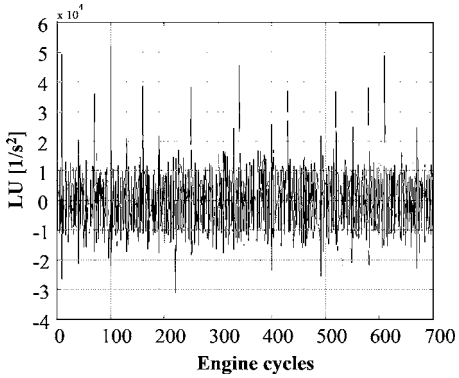

Fig. 16 LU_i **evaluation for a test conducted at 2500 rpm in fifth gear**

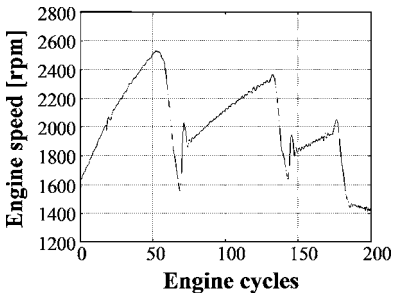

Fig. 17 $S_t(2\pi f^*)$ **evaluation for a test conducted at 2500 rpm in fifth gear**

Conclusions

The presence of a damped oscillation in the engine speed waveform that follows a missing combustion allowed designing a misfire detection methodology based on the observation of the amplitude of one specific frequency. This frequency is characteristic of the engine-load system under study, depending on the actual inserted gear. The evaluation of the investigated frequency component amplitude has been conducted using a proper simplification of the well known STFT time-frequency-analysis approach. This allowed reducing both computational time and ECU resources required by the methodology, making feasible its implementation onboard a vehicle.

The methodology readiness has been evaluated, being capable of detecting the misfire event only with a delay of approximately 0.5–1.0 cycles, and isolating the cylinder where the misfire occurred with a delay of ~4.0 cycles. These delays occur because the damped oscillation needs time in order to be fully developed and therefore sensed by the frequency observation methodology. This delay would likely compromise the possibility of detecting multiple misfires.

A comparison between the proposed approach and the time-based one has been finally conducted, showing that the new frequency-based methodology works better in the high engine speed range, where the time-based one tends to fail. For this reason, the best solution in terms of detection capability, readiness, computational time, and the ECU resources requirement seems to be the combined use of the two methodologies, the time-based one in the low engine speed range, the frequency-based one in the high engine speed range.

Acknowledgment

The author would like to thank Lamborghini Spa, Italy, for the support and contribution in the development of the experimental tests.

Downloaded 02 Jun 2010 to 171.66.16.107. Redistribution subject to ASME license or copyright; see http://www.asme.org/terms/Terms_Use.cfm

Nomenclature

- OBD = onboard diagnostics
- ECU = electronic control unit
- DOF = degree of freedom
- STFT = short-time Fourier transform
- A_p = piston surface (m^2)
- r = crank-slider mechanism radius (m)
- l = connecting rod length (m)
- θ = crank angle (rad)
- θ_{eng} = engine crank angle (rad)
- θ_{load} = load angular position (rad)
- $p_m(\theta)$ = relative pressure inside m-th cylinder (Pa)
- $\lambda = r/l$ = crank-slider radius/connecting rod ratio
- $f_m(\theta)$ = $\sin[\theta+m(\pi/3)]+\{\lambda \sin[2(\theta+m\pi/3)]/2\sqrt{1-\lambda^2 \sin^2(\theta+m\pi/3)}\}$=crank slider mechanism function for mth cylinder
- $T_i(\theta)$ = indicated torque of the engine (Nm)
- $T_L(\theta)$ = load torque (Nm)
- $T_f(\theta)$ = friction and auxiliaries torque (Nm)
- $T_r(\theta)$ = reciprocating torque (Nm)
- Z = number of cylinders
- ω = engine angular velocity (rad/s)
- J = inertia of the engine-load system ($kg\,m^2$)
- J_{eng} = engine inertia ($kg\,m^2$)
- J_{load} = load inertia ($kg\,m^2$)
- k = stiffness of the connection between engine and load ($N\,m/rad$)
- c = damping of the connection between engine and load ($N\,m\,s/rad$)
- f = frequency (Hz)
- f^* = natural frequency (Hz)
- f_{cyc} = engine cycle frequency (Hz)
- Φ = engine cycle frequency order
- t = time (s)
- $h(\tau-t)$ = window function
- S_t = STFT evaluated at time t
- j = imaginary unit
- τ_i = combustion periods (s)
- $\Delta\theta$ = angular period (rad)
- LU_i = misfire detection parameter evaluated for the ith combustion ($1/s^2$)

References

[1] California Air Resources Board, 1991, "Technical Status Update and Proposed Revisions to Malfunction and Diagnostic System Requirements Applicable to 1994 and Subsequent California Passenger Cars, Light-Duty Trucks, and Medium-Duty Vehicles—(OBD II)," CARB Staff Report.

[2] Ceccarani, M., Rebottini, C., and Bettini, R., 1998, "Engine Misfire Monitoring for a V12 Engine by Exhaust Gas Pressure Analysis," SAE Technical Paper No. 980518.

[3] Willimowski, M., and Isermann, R., 2000, "A Time Domain Based Diagnostic System for Misfire Detection in Spark-Ignition Engines by Exhaust Gas Pressure Analysis," SAE Technical Paper No. 2000-01-0366.

[4] Lee, A., and Pyko, J. S., 1995, "Engine Misfire Detection by Ionization Current Monitoring," SAE Technical Paper No. 950003.

[5] Chung, Y., Bae, C., Choi, S., and Yoon, K., 1999, "Application of a Wide Range Oxygen Sensor for the Misfire Detection," SAE Technical Paper No. 1999-01-1485.

[6] Azzoni, P. M., Cantoni, G., Ceccarani, M., Mazzetti, S., Minelli, G., Moro, D., and Rizzoni, G., 1995, "Measurement of Engine Misfire in a Lamborghini 533 V-12 Engine Using Crankshaft Speed Fluctuations," SAE Technical Paper No. 950837.

[7] Ribbens, W. W., and Park, J., 1994, "Road Tests of a Misfire Detection System," SAE Technical Paper No. 940975.

[8] Iida, K., Akishino, K., and Kido, K., 1990, "IMEP Estimation From Instantaneous Crankshaft Torque Variation," SAE Technical Paper No. 900617.

[9] Williams, J., 1996, "An Overview of Misfiring Cylinder Engine Diagnostic Techniques Based on Crankshaft Angular Velocity Measurements," SAE Technical Paper No. 960039.

[10] Moskwa, J. J., Wang, W., and Bucheger, D. J., 1998, "A New Methodology for Engine Diagnostics and Control Utilizing "Synthetic" Engine Variables: Theoretical and Experimental Results," *Proc. of ASME, Dynamic Systems and Control Division*, ASME, New York, DSC-Vol. 64.

[11] Forster, J., Lohmann, A., Mezger, M., and Ries-Muller, K., 1997, "Advanced Engine Misfire Detection for SI-Engines," SAE Technical Paper No. 970855.

[12] Klenk, M., Moser, W., Muller, W., and Wimmer, W., 1993, "Misfire Detection by Evaluating Crankshaft Speed—A Means to Comply With OBD II," SAE Paper No. 930399.

[13] Plapp, G., Klenk, M., and Moser, W., 1998, "Methods of On-Board Misfire Detection," SAE Technical Paper No. 900232.

[14] Moro, D., Azzoni, P., and Minelli, G., 1994, "Misfire Pattern Recognition in High Performance SI 12 Cylinder Engine," SAE Paper No. 980521.

[15] Heywood, J. B., 1989, *Internal Combustion Engine Fundamentals*, McGraw Hill, New York.

[16] Shiao, Y., and Moskwa, J. J., 1994, "Misfire Detection and Cylinder Pressure Reconstruction for SI Engines, SAE Technical Paper No. 940144.

[17] Cavina, N., Ponti, F., and Rizzoni, G., 1999, "Fast Algorithm for On-Board Torque Estimation," SAE Technical Paper No. 1999-01-0541.

[18] Cavina, N., and Ponti, F., 2001, "Engine Torque Non-Uniformity Evaluation Using Instantaneous Crankshaft Speed Signal," ASME ICED Fall Conference, Chicago.

[19] Pan, C. H., and Moskwa, J. J., 1995, "Dynamic Modeling and Simulation of the Ford AOD Automotive Transmission," SAE Technical Paper No. 950899.

[20] Prakash, V., Vadiraj, M. R., Venkatesh, D. N., and Shrinivasa, U., 1994, "Parametric Study of Crankshaft Natural Frequencies," SAE Technical Paper No. 940698.

[21] Cohen, L., and Posch, T. H., 1985, "Positive Time-Frequency Distribution Functions," IEEE Trans. Acoust., Speech, Signal Process., **33**(1), pp. 383–389.

[22] Cohen, L., 1995, *Time-Frequency Analysis*, Prentice-Hall, Englewood Cliffs, NJ.

Downloaded 02 Jun 2010 to 171.66.16.107. Redistribution subject to ASME license or copyright; see http://www.asme.org/terms/Terms_Use.cfm

Thermomechanical Fatigue Life Prediction of Cylinder Heads in Combustion Engines

Stefan Trampert
Dr.
FEV Motorentechnik GmbH,
Neuenhofstraße 181,
52078 Aachen, Germany

Taner Gocmez

Stefan Pischinger
Professor Dr.

RWTH Aachen,
Institute for Internal Combustion Engines (VKA),
Schinkelstraße 8,
D-52062 Aachen, Germany

While the deformation and damage behavior of aluminum cylinder heads under complex thermal mechanical loading has been the subject of numerous studies in the past, cast iron cylinder heads have been in the focus of thermomechanical fatigue (TMF) only to a minor extent. In this paper, a feasible procedure is presented to set up material models and estimate service life of cast iron cylinder heads under variable thermomechanical loading conditions by the use of computer-aided engineering tools. In addition, the influence of thermal load and mechanical constraints on TMF life span is shown. A specimen model is used for parameter identification in material model setup and a cylinder head model is used for correlation with cracking phenomena. Investigation of different thermomechanical load influences is conducted on the cylinder head model. The principal strain and energy based fatigue criteria are used in assessment of TMF lifetime for the cast iron family and material specific evaluation procedures are pointed out. The results highlight the importance of exact definitions of the boundary conditions and underline the sensitivity of TMF lifespan of cast iron cylinder heads with respect to the defined boundary conditions. Considering this sensitivity, an approach conforming to the engine development requirements is proposed. It is shown that both the crack location and fatigue lifetime are predicted with high accuracy. [DOI: 10.1115/1.2771251]

Introduction

Due to today's demands to reduce cost and product time to market, engineering procedures are increasingly using more sophisticated simulation techniques, instead of validation testing. In particular, the rapidly increasing specific loads of diesel engines require advanced calculation methods. One of the most challenging simulations is the thermomechanical fatigue prediction of cylinder heads. The relatively new and more pronounced challenge in engine design, thermomechanical fatigue (TMF) analysis, as the demand for high torque, high specific power, and low emissions continues to grow, is necessitated due to the increasing operating temperatures.

In TMF, the stress-strain behavior is associated with mechanical cycles as well as thermal ones. The induced severe temperature gradients due to operational loads do not occur in all components in the automotive industry but in the ones related to the engine such as cylinder heads and exhaust manifolds. It is important to notice that the TMF problems, caused due to the heating up and cooling down of the engine material, in cylinder heads are related to the start-operate-stop cycles and basically not with the combustion cycles [1]. Also, strong engine load changes (e.g., from full load to coasting or idle operation mode) contribute to the TMF of the relevant components. The large temperature changes in flame deck result in thermal expansion and contraction and accompany high amplitude low frequency plastic strains, primarily in valve bridges. Therefore, linear finite element analysis (FEA) is a degree of oversimplification to simulate the material behavior.

It has always been a question to decide on necessary and sufficient level of details to model cylinder head behavior in computer-aided engineering (CAE) environment. This decision is influenced by the boundary conditions of engine development: increasing complexity of cylinder head geometries (four-valve designs, intermediate deck, added ribbings, port design), short development times, and also the production process. In addition, the design engineer should also consider the limitations of finite element software tools and workstations, multiaxial stresses and strains on flame deck, and the testing programs required to calibrate material parameters. Figure 1 shows the details/complexity of material models generally considered in engine development process as a function of time.

As the number of material parameters increases exponentially with the use of complex models, reproducibility of simulations and material parameter calibration becomes more difficult, if not infeasible. Therefore, substantial testing programs are necessary considering the fact that the effect of simultaneously varying temperature and mechanical strain is quite sensitive to material composition, maximum and minimum temperatures, temperature range, strain rate, strain range, cycle times, etc. On the other hand, simulation of the cyclic loading until a stabilized state is obtained may lead to a transient analysis where the number of loading cycles required is intolerable. From this standpoint, an uncoupled thermal, mechanical, and fatigue analysis and a simple elasto(visco)plastic constitutive law to represent material behavior under anisothermal loading, where the number of material parameters are of order 2^2-2^3, is the favorable choice in an efficient engine development program.

In the first section of this paper, an overview of the TMF life prediction approach is presented. The materials of interest are described in the next section. The first modeling step of the approach—material model setup—is discussed in the third section, which is followed by the results comparison of materials investigated in this study. Then we present the second modeling step of the approach: lifetime prediction. Finally, application of this approach on a heavy duty cylinder head is presented and several thermal, mechanical, and material influencing factors are discussed.

Approach

TMF analysis of a cast iron cylinder head includes stress-strain determination and lifetime prediction, succeeding the thermal

Contributed by the Internal Combustion Engine Division of ASME for publication in the JOURNAL OF ENGINEERING FOR GAS TURBINES AND POWER. Manuscript received July 19, 2006; final manuscript received May 16, 2007; published online January 11, 2008. Review conducted by Christopher J. Rutland. Paper presented at the 2006 Spring Conference of the ASME Internal Combustion Engine Division (ICES2006), Aachen, Germany, May 7–10, 2006.

Copyright © 2008 by ASME

Downloaded 02 Jun 2010 to 171.66.16.107. Redistribution subject to ASME license or copyright; see http://www.asme.org/terms/Terms_Use.cfm

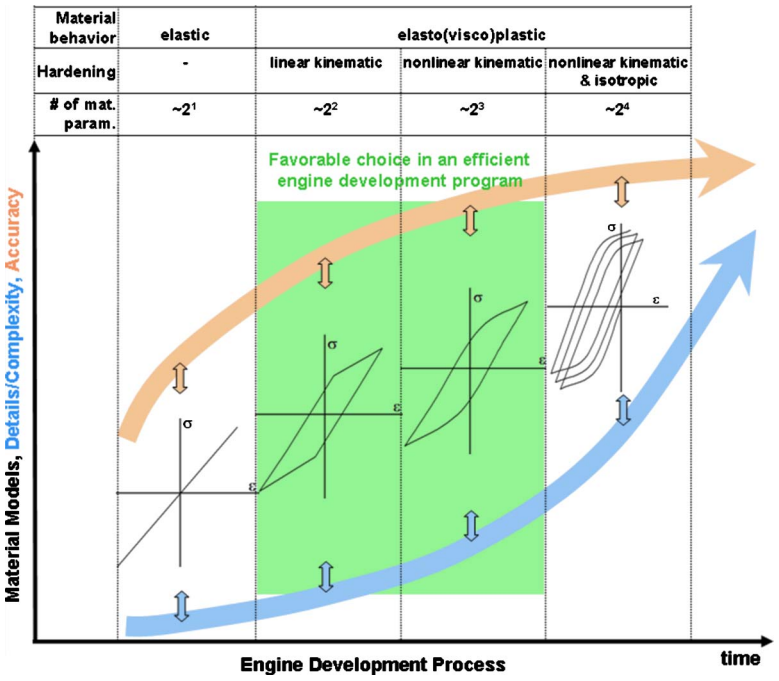

Fig. 1 Standpoint for material modeling in TMF analysis

analysis. In order to consider the boundary conditions of the engine development process, stabilized cyclic behavior (plastic shakedown) is assumed in representing the elasto(visco)plastic response of the material. Uncoupling of thermal and mechanical analysis assumption is justified by the negligible contribution of inelastic dissipation to heating. Finally, damage independent constitutive law allows time saving in calibration of fatigue parameters and lifetime evaluation.

The stress-strain and lifetime prediction modeling are crucial, and independent models allow the design engineer to evaluate the dependencies in a relatively short period of time. The thermal loading and the material behavior together with the restraining of the model are the main inputs for the mechanical analysis. As per the damage independent constitutive law, lifetime prediction can be conducted using the output of mechanical analysis and the fatigue parameters of the material. These two primary steps in a TMF analysis conducted for the specimen model are shown in Fig. 2. The global structural FEA methodology for cylinder heads is demonstrated in Fig. 14, and these analyses are carried out for cast irons in the following.

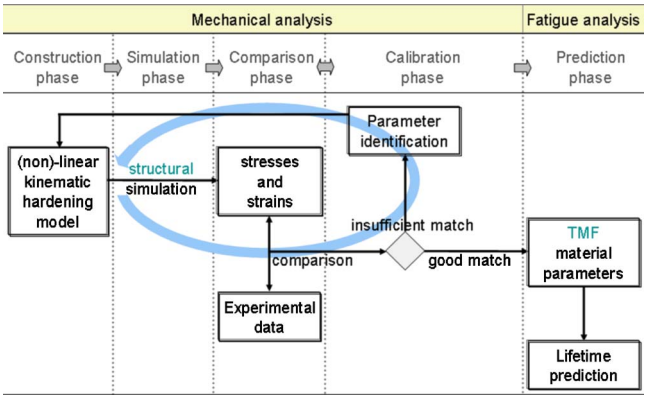

Fig. 2 TMF analysis approach for specimen model

Materials

The specific materials considered in this study belong to the cast iron family. Three main classifications describing general graphite shape in graphitic cast irons are in common use: flake, compacted, and spheroidal. The cast irons with these graphite morphologies are called gray cast iron (CI-GJL according to DIN EN), compacted graphite iron (CGI-GJV), and spheroidal or

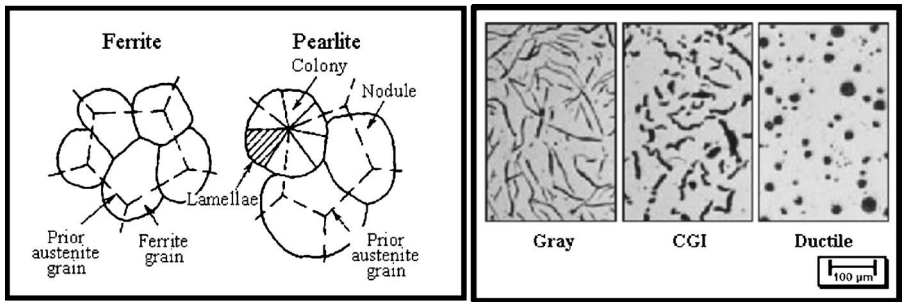

Fig. 3 The two most common matrix structures; ferrite and pearlite on the left [2] and graphite shapes on the right

Downloaded 02 Jun 2010 to 171.66.16.107. Redistribution subject to ASME license or copyright; see http://www.asme.org/terms/Terms_Use.cfm

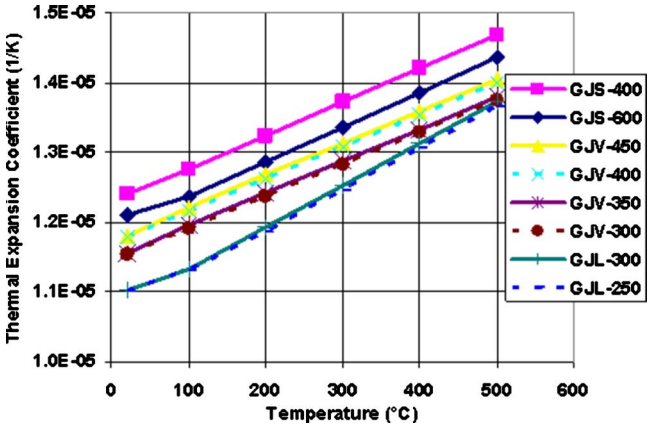

Fig. 4 Thermal expansion coefficient as a function of temperature

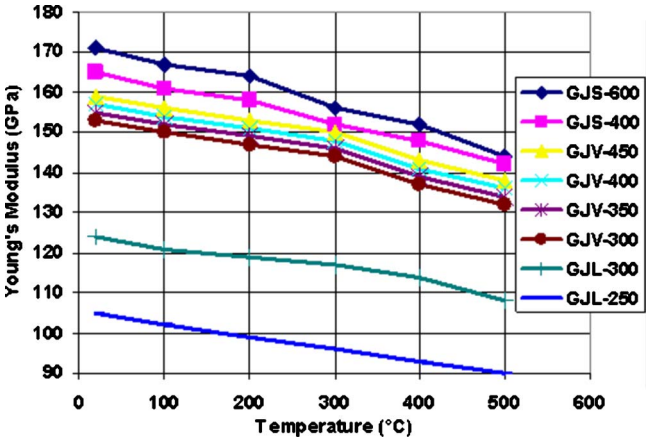

Fig. 6 Young's modulus as a function of temperature

nodular or ductile cast iron (SGI-GJS), respectively. Differences in these three main classes are in chemical composition, graphite shape, and material matrix, which lead to different material properties [2]. The most common material matrix structures and the graphite morphologies are demonstrated in Fig. 3.

The coefficient of linear thermal expansion of cast irons depends primarily on graphite structure and temperature, although it is influenced to a certain extent by microstructure. The thermal expansion coefficient curves in the temperature range of 100–500°C are presented in Fig. 4.

The thermal conductivity of cast irons is influenced strongly by graphite morphology. The conductivity is higher in gray iron because of the semicontinuous nature of the graphite flakes. The rounded edges of graphite inside CGI work together to boost thermal conductivity to that of ductile iron (see Fig. 5). In addition to graphite shape, microstructure, composition, and temperature also influence the thermal conductivity.

The tensile strength and yield strength of cast irons increase with increasing nodularity. The variation in elastic modulus as a function of graphite nodularity is similar to that observed for tensile strength (see Fig. 6).

Among the main classes mentioned and depicted above, emphasis is given to GJL-300 with flake (CI-conventional heavy duty cylinder head material), GJV-300 and GJV-450 with compacted (CGI-becoming popular with increasing demands for lightweight design and peak firing pressure increase/emissions reduction), GJS-400 and GJS-600 with spheroidal (SGI) graphite shapes. GJL-300, GJV-450, and GJS-600 have pearlitic matrix structure while GJV-300 and GJS-400 have ferritic matrix structure.

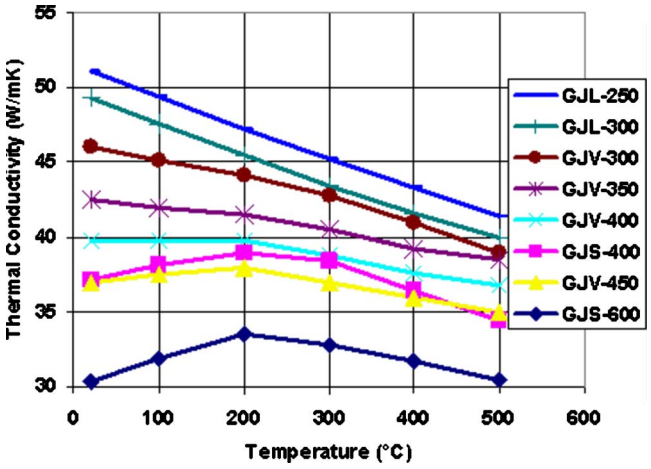

Fig. 5 Thermal conductivity as a function of temperature

Material Modeling

Material behavior is affected by loading conditions, which results in mechanical fatigue, by time, which is also known as creep, and by oxidation, which is caused by environmental effects. When time effects and oxidation are neglected, yielding depends only on instantaneous increments of stress or strain and on the previous history of the material. This kind of material behavior, which is independent of time, is known as elastoplastic behavior [3].

For modeling purposes, it is important to know how the material behaves under the investigated loading conditions. The damaging cycle of a cast iron cylinder head corresponds to a heat-up and cool-down cycle. The operational temperature range of cast iron cylinder heads could be specified up to approximately 420°C, 450°C, and 480°C for gray cast iron, compacted graphite iron, and spheroidal graphite iron, respectively. Above these temperatures, grain growth and matrix decomposition (pearlite to ferrite transformation) are responsible for reduction in material strength of pearlitic cast irons [4]. When these temperatures are set as a predefined upper limit, creep and oxidation effects are negligible, if existing. In addition, cylinder head is subjected to out-of-phase loading (maximum strain occurs at minimum temperature). Nevertheless, creep damage is dominant under in-phase loading conditions. Hence, considering the upper temperature limits that should not be exceeded and the loading conditions of the cylinder head, the assumption of elastoplastic material behavior for modeling is justified.

It should be noted that, for exhaust manifolds where the maximum temperature is up to 900°C (for gasoline turbocharged engines temperatures may even exceed 1100°C), elastoviscoplastic behavior of the material has to be considered in order to model the material behavior properly. Therefore, creep must be taken into account for exhaust manifolds and to represent the viscous behavior of the material at high temperatures elastoviscoplastic constitutive laws should be utilized [5].

For the analysis of strain and stress distributions in a material loaded beyond the elastic limit (elastoplastic material behavior), a constitutive theory of plasticity must specify the yield condition under multiaxial states of stress. The uniaxial condition $I\sigma I = \sigma_y$ (yield stress) is inadequate if there is more than one stress component. The constitutive theory must define the postyield behavior, answering the following questions:

(1) Yield Criterion. What stress combinations cause plastic deformation?

Downloaded 02 Jun 2010 to 171.66.16.107. Redistribution subject to ASME license or copyright; see http://www.asme.org/terms/Terms_Use.cfm

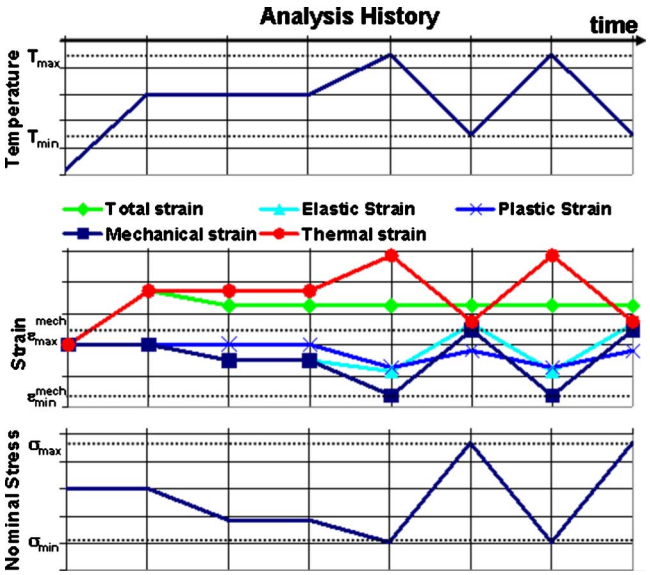

Fig. 7 Analysis history for parameter identification, temperatures, and stresses and strains over time

(2) Postyield Behavior. How are the plastic deformation increments related to the stress components? How does the yield condition change with work hardening?

Based on the previous standpoint, linear kinematic hardening model with von Mises yield criterion and an associated flow rule is selected as the base model to be used for simulating cast iron response under anisothermal cyclic loading. In addition, nonlinear kinematic hardening model is also utilized so as to compare the uniaxial and multiaxial influences on material response.

In order to calibrate the material parameters, a specimen model is used for temperature varied strain controlled simulations to have comparable results with the experimental results at hand. The output of the analysis after conducting several iteration cycles is the validated material model on the one hand and the stresses and strains to be used in fatigue life prediction on the other hand.

Simulation history for material parameter identification is constructed to be consistent with the experiments from Hallstein [6]. The specimen tests were done with a fixed minimum temperature and variable temperature amplitude for the cast irons. As the specimen is fixed at both ends (100% restraining), heating up to maximum temperature results in compressive stresses (material tends to expand but it is not allowed because of fixation) and cooling down to minimum temperature leads to tensile stresses (material tends to shrink but it is not allowed because of fixation). Temperature variation over time and the induced strains and stresses for GJL-300 are depicted in Fig. 7 as an example.

Material Models, Results, and Comparison

Maximum and minimum stress versus temperature amplitude is provided in Fig. 8 for the fixed minimum temperature of 150°C. Displayed simulation results are from the stabilized cycle (third cycle). The results of temperature amplitude of 75°C and 100°C do not exist for GJL-300, as plasticity does not occur under these circumstances. Also for gray cast iron, temperature amplitude effects on maximum and minimum stress are negligible. For the pearlitic spheroidal graphite iron (GJS-600), a different behavior is observable, which means that not only the microstructure but also the chemical composition and graphite morphology have significant effects on material behavior.

In order to achieve a fine match between the experimental and simulation results, parameter identification is carried out in the calibration phase based on the experimental results and other data

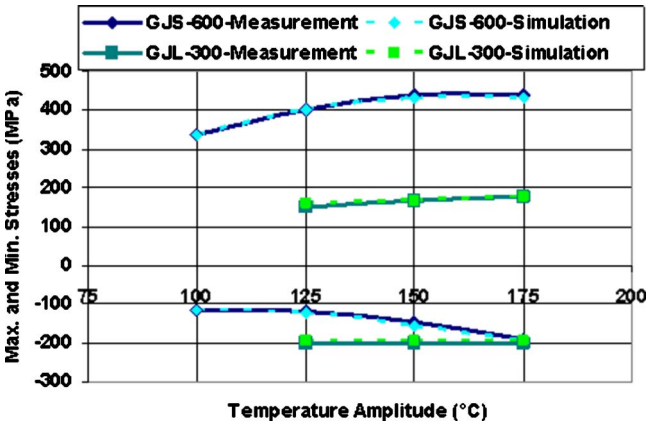

Fig. 8 Maximum and minimum stresses as a function of temperature amplitude: $T_{min}=150°C=\text{const}$, $\varepsilon_{m,t}^{GJS-600}=4‰$, $\varepsilon_{m,t}^{GJL-300}=-1‰$

found in literature [7–11]. Parameter identification using temperature dependent material data only, to define material plasticity, did not lead to a good match for materials other than GJL-300. The reason for this is that material behavior changes as the maximum temperature, the material is subject to in his history, is different. Therefore, the material model developed using local temperatures does not represent the exact material at wide temperature ranges.

In order to represent the exact material behavior, which after a few hundred hours of engine operation shows different values of yield strengths in different areas of the material according to the temperature in that area, a material model, with different proportional limit and kinematic hardening modulus values corresponding to an additional field variable (here equal to the maximum temperature at a particular area of the material), is built.

In Fig. 9, mean stress as a function of mean strain at half number of cycles to failure for temperature amplitude of 150°C when the minimum temperature is also 150°C is shown. Fine match of measurement and simulation results is primarily achieved by fine-tuning of kinematic hardening modulus. Note that this mean strain is the externally applied mean strain as the experiments are mean total strain controlled experiments together with temperature control. The induced mean stresses because of the cyclic plastic com-

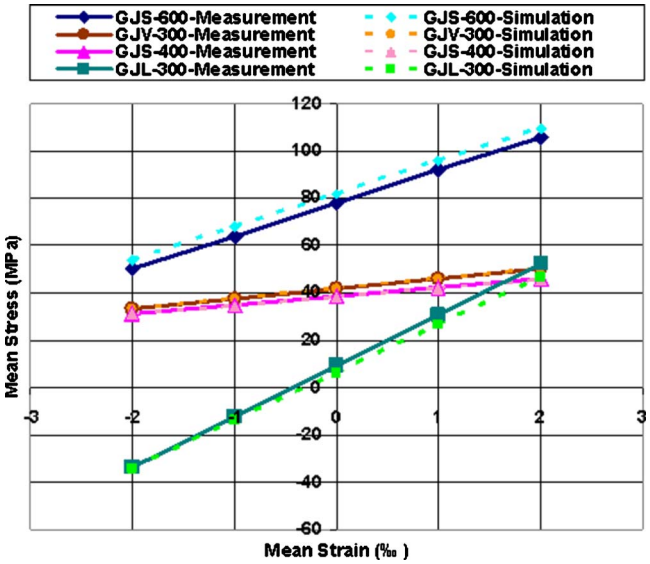

Fig. 9 Mean stress as a function of mean strain for GJL-300, GJV-300, GJS-400, and GJS-600. $T_{min}=150°C$, $T_{amplitude}=150°C$.

Downloaded 02 Jun 2010 to 171.66.16.107. Redistribution subject to ASME license or copyright; see http://www.asme.org/terms/Terms_Use.cfm

Table 1 TMF life prediction approaches [12–16]

Manson–Coffin	$\varepsilon_{pl,amp}=\varepsilon_f'\ (2N)^c$
Total strain approach	$\varepsilon_{mech,amp}=\sigma_f'/E\ (2N)^b+\varepsilon_f'\ (2N)^e$
Morrow equation	$\varepsilon_{mech,amp}=(\sigma_f'-\sigma_m)/E\ (2N)^b+e_f'\ (2N)^c$
SWT parameter	$\sigma_{max}\ \varepsilon_{mech,amp}\ E=(\sigma_f')^2\ (2N)^{2b}+\sigma_f'\ \varepsilon_f'\ E\ (2N)^{b+c}$
Energetic approach	$\Delta W\ N^\beta=C$

pression strains can be read where the mean total strain equals zero. For GJL-300, this induced mean stress is tensile (positive).

Mean stress dependency on mean strain is more pronounced for the pearlitic irons. An important and interesting concern is the examination of mean stress effects on fatigue life on the thermal cyclically loaded materials. According to Fig. 9, almost no effects are present for the ferritic materials. However, this is not the case for pearlitic irons, and with increasing tensile stress fatigue life decreases significantly. Additionally, for the pearlitic materials, with increasing compressive stresses or decreasing tensile stresses, matrix structure becomes dominant in determination of the lifetime. In the next section, lifetime prediction is handled considering these facts.

Lifetime Prediction, Methods, and Application

Increase in operating temperatures was the main driving force for the efforts to predict TMF of cylinder heads in the near past. Many high temperature material relations and TMF theories have been published over years. TMF life assessment approaches could be classified as strain based, energy based, damage parameters, fracture mechanics, cumulative, and microstructural approaches. Independent of the theory used, the life prediction is based on functions of the induced strains and stresses due to thermomechanical loading and the material parameters.

Strain based approaches are highly utilized in automotive industry due to their simplicity and reliability. The damage parameter proposed by Smith, Watson, and Topper (SWT) considers the mean stress effects and has proven its reliability especially for components with tensile mean stresses. On the other hand, energy based approaches gained respect in the last decade especially for their conformability to multiaxial loading conditions.

In the following, strain based approaches (Manson–Coffin criterion, total strain approach, and Morrow equation), SWT damage parameter, and energy based approach are applied to the specimen and cylinder head models. These approaches are shown in Table 1. The aim is to find material specific evaluation strategy.

Among the class of strain life (ε-N) approaches, Manson–Coffin criterion, which describes the relation between plastic strain amplitude and life, stands for simplicity and robustness. Total strain approach and Morrow equation (total strain approach with mean stress correction) are based on total mechanical strain amplitude. It is clear that the Manson–Coffin criterion is independent of mean stress. However, for some materials, such as GJL-300, mean stress effects are also important in the low cycle fatigue region. In order to correlate only the plastic strain with lifetime, the mean stress effects have to be incorporated to the Manson–Coffin criterion; in practice, fatigue parameters have to be modified. Regression analysis is carried out to find the dependencies and to construct the function for the fatigue parameters with mean stress effects.

Strain based approaches and SWT parameter are corresponding to isothermal uniaxial loading conditions. Therefore, we calculate equivalent strain amplitudes and the mean stress using critical cutting plane approach [17] and calibrate the material parameters with consideration of the operational temperature range to apply these criteria for cylinder heads subjected to multiaxial anisothermal loading. In contrast, energy based approach, which correlates

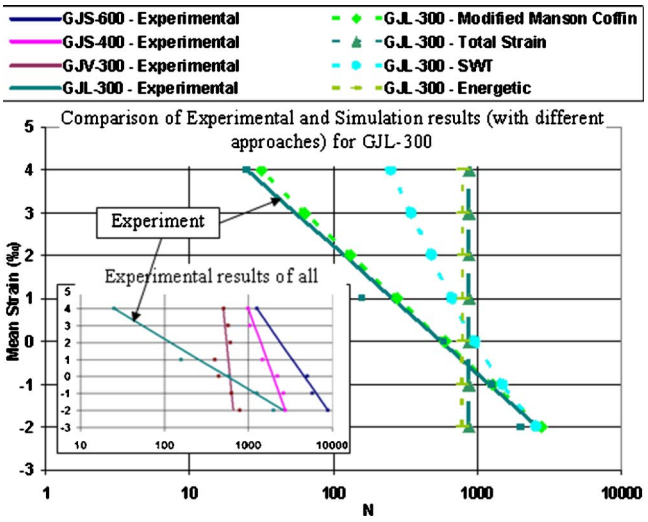

Fig. 10 Number of cycles to failure as a function of mean total strain. $T_{min}=150°C$, $T_{max}=450°C$.

lifetime with dissipated energy per cycle, is a multiaxial fatigue criterion and does not require additional calculations but lacks the mean stress effects.

In Fig. 10, the number of cycles to failure is depicted as a function of externally applied mean strain. GJL-300 has highest dependency on externally applied mean strain (which in turn results in mean stress). Negative mean strains result in higher number of cycles for both the pearlitic cast irons. Note that lifetime of the pearlitic cast irons does not differ much from each other with negative mean strains applied and is even the same for a mean strain of −3‰. So we can state that, when compressive stresses are applied, material matrix becomes more dominant than the graphite shape in influencing the lifetime of the specimen made of pearlitic cast irons.

The calculation results, which are mean stress independent, are straight lines parallel to the vertical axis as expected. Consideration of mean stress influence is vital for the calculations and a good match for GJL-300 is achieved with modified Manson–Coffin criterion as can be seen from the figure. For the other pearlitic cast irons, SWT damage parameter provided the best fit to the experimental results.

When mean stress effects are negligible—the case for ferritic irons—energetic approach came out to be the best method covering a wide temperature range with a very narrow deviation band. The comparison of approaches for temperature amplitude variation at constant mean strain is depicted below in Fig. 11 for GJV-300.

Considering all experiments and calculations done with different parameter variations and material specific approaches (see Table 2), fair agreement between measured and computed results for lifetime is observed as all data points lie inside $2N$ and $0.5N$ lines (see Fig. 12). In the second part of the study, the validated TMF life analysis approach is safely applied to a cylinder head example.

Application of TMF Assessment Approach to a Heavy Duty Diesel Cylinder Head

Heavy duty engines developed for future requirements of higher power density and low emission are subject to high thermal load and peak firing pressure. The problem of cracks in-cylinder heads due to thermal fatigue is well known for these engines with high specific power output (see Fig. 13 for an example—cast iron cylinder head). However, it is still difficult to predict the lifetime of a new cylinder head due to the number of influencing parameters and the complexity of the material behavior [18]. Material

Downloaded 02 Jun 2010 to 171.66.16.107. Redistribution subject to ASME license or copyright; see http://www.asme.org/terms/Terms_Use.cfm

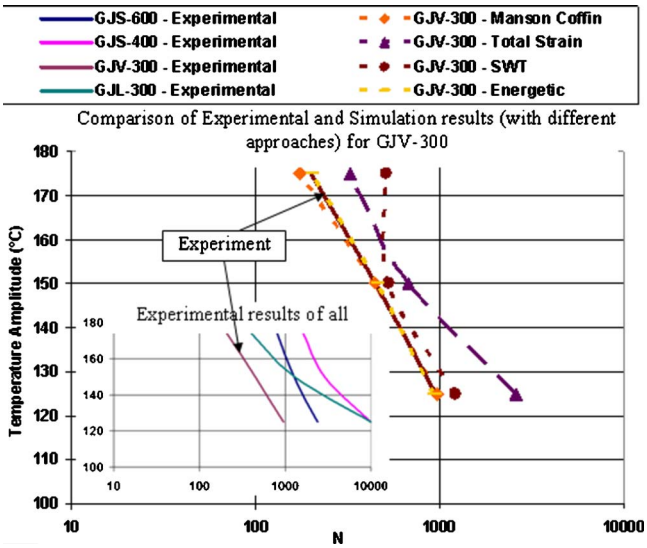

Fig. 11 Number of cycles to failure as a function of temperature amplitude. $\varepsilon_{m,t}^{GJS\text{-}600}=4‰$, $\varepsilon_{m,t}^{GJS\text{-}400}=0‰$, $\varepsilon_{m,t}^{GJV\text{-}300}=0‰$, $\varepsilon_{m,t}^{GJL\text{-}300}=-1‰$.

data describing the properties under complex thermal and mechanical loading conditions do generally not exist, and if at all, exist only for specific temperature ranges. Also, there is no standardized TMF testing method established yet. Therefore, validated material parameters under uniaxial loading in the previous section are used in the analysis of cylinder head, which is subject to multiaxial loading.

In order to simulate the thermal cycles, thermal and mechanical analyses are necessary assuming that the 3D computational fluid

Table 2 Material specific approaches and fatigue ductility exponent (FDE)—for strain based evaluation—or dissipated energy exponent (DEE)—for energy based evaluation—of cast irons

Material	Lifetime prediction approach	FDE/DEE
GJL-300	Modified Manson-Coffin	–0.587
GJV-300	Energetic approach	–0.925
GJV-450	SWT parameter	–0.800
GJS-400	Energetic approach	–0.920
GJS-600	SWT parameter	–0.770

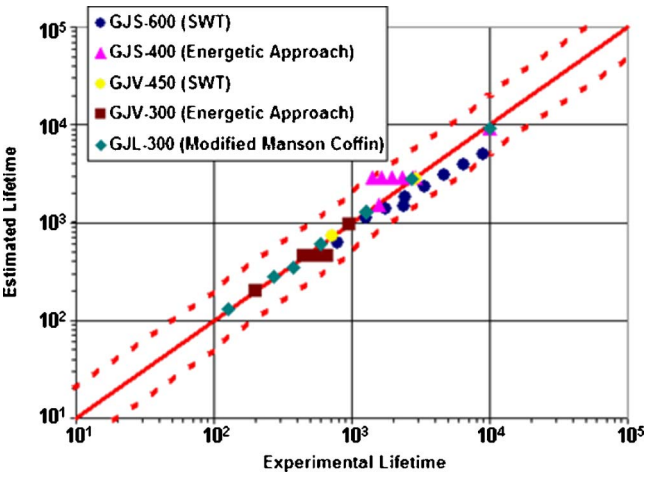

Fig. 12 Correlation of experimental and simulation results

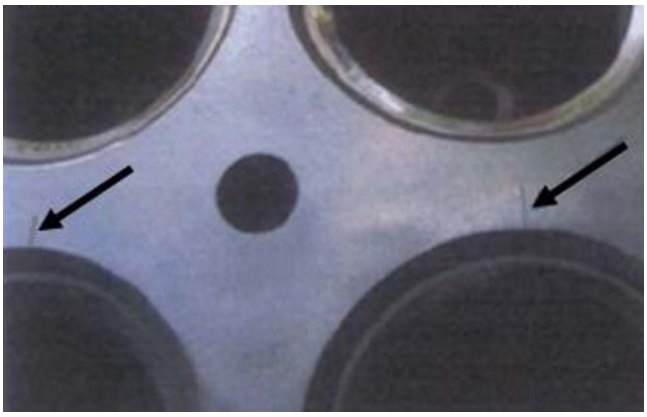

Fig. 13 TMF cracks on a heavy duty diesel cast iron-GJV-450-CH

dynamics (CFD) analysis results for coolant and gas side heat transfer are available. In particular, (a) thermal computation simulating heating of the part and (b) a mechanical computation, which includes the assembly of the model (bolt preloading, seat-ring and valve guide press fits) and the thermal cycles (heating up to max. temperature and cooling down) are carried out and the mechanical fields are an input to the next step, which is the lifetime prediction using a fatigue criterion.

Together with these steps, the whole analysis loop is sketched in Fig. 14.

Several factors affect the TMF life span while some are given (parameters) and direct influencing is not possible and some are changeable (variables) with direct influence:

- influence of thermal load
  - (a) cylinder power (variation of engine load)
  - (b) cooling (coolant temperatures, system pressure, global/local flow rates)
- influence of mechanical loads/constraints
  - (a) friction between gasket and cylinder head (mainly material dependent)
  - (b) interference fit of valve seat rings (variation of interference)
- influence of structural design
  - (a) cylinder head stiffness (e.g., fire deck thickness)
  - (b) valve arrangement (parallel, twisted, tandem)
  - (c) length (single, block cylinder head)
  - (d) water jacket design (cast design, cooling bores)
- influence of material
  - (a) CI, CGI, SGI (thermal conductivity, Young's modulus, coefficient of thermal expansion, etc.)

In the following, some analysis examples of the above listed parameters are depicted for the heavy duty diesel cylinder head. Results presented below belong to the stabilized cycle (third cycle).

Influence of Thermal Load. A significant influence on the TMF life span is due to the temperature loading. Various engine parameters are influencing the temperature of the cylinder head. The main drivers are the engine power and the cooling system, but also extreme ambient conditions may impact the thermal load cycle. Depending on the engine application, the critical TMF load cases have to be specified. Being aware of the importance of a correct temperature field on the lifetime, 3D-CFD coolant and

Downloaded 02 Jun 2010 to 171.66.16.107. Redistribution subject to ASME license or copyright; see http://www.asme.org/terms/Terms_Use.cfm

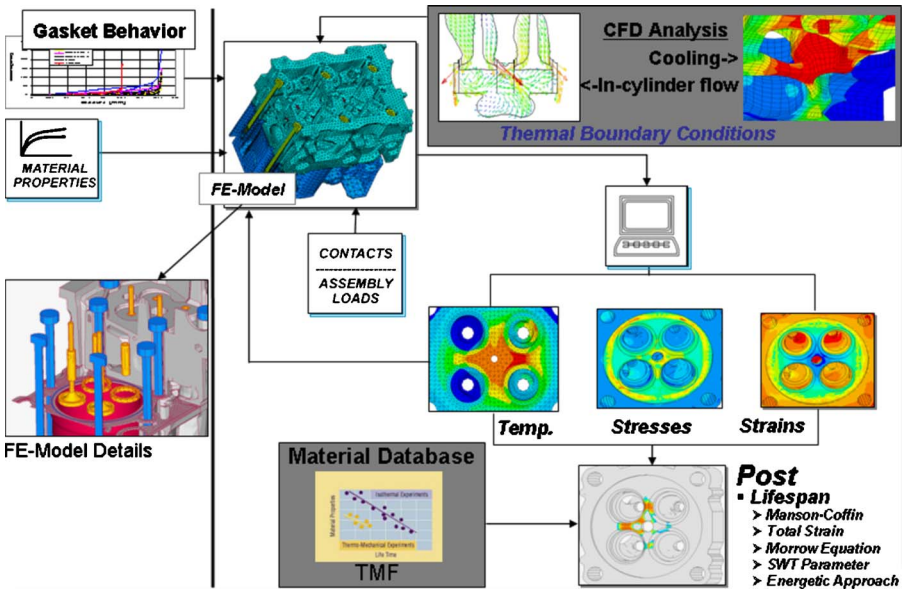

Fig. 14 TMF analysis approach for CH

in-cylinder flow analysis results are prerequisite simulations to derive most accurate boundary conditions for the thermal analysis. Alternatively conjugated heat transfer simulations can be conducted to determine the temperature distribution within the cylinder head, while these results have to be mapped onto the structure of FEA model.

Temperature field not only determines the critical locations but also it is decisive in limiting the number of cycles to failure. In addition, consideration of mean stress effects does not change the critical locations but negative mean stresses on flame deck surface lead to increased lifetime in critical locations for cast iron.

The influence of power increase on lifetime is investigated in order to distinguish the temperature amplitude effects from the effects of temperature distribution. It is assumed that the distribution of temperature and heat transfer coefficients does not change and only scaling up is necessary. An increase of 16% in power leads to a 50% decrease in lifetime of the cylinder head made of gray cast iron. The temperature and lifetime plots are depicted below in Fig. 15. The critical locations are marked as N1 and N2, lifetimes corresponding to these locations at nominal power are set as reference (100%).

Influence of Mechanical Constraints. Combination of thermal and mechanical loads results in complex stress states, which in turn decrease the lifetime of the structures. The friction between cylinder head gasket (CHG) and cylinder head (CH) is one of the mechanical constraints that deteriorates the lifetime in combination with the thermal load. Two extreme cases are investigated below one without friction and the other with a high friction coefficient. The outcome of the analysis highlights a 10–35% decrease in number of cycles to failure in the most critical area with the introduction of friction between gasket and CH (see Fig. 16). In this case, the more deteriorative effect of friction is on intake side. The lifetime corresponding to critical locations without friction are set as reference (100%) for both materials. Compacted graphite iron is affected more severely than gray cast iron with its higher Young's modulus. It is clear that friction is a given parameter; nevertheless, the results point out the sensitivity of the radial constraining.

Influence of Material. The temperature field corresponding to nominal power condition is plotted in Fig. 17 for different types of cast irons. Application of thermal boundary conditions from 3D-process simulation for the flame deck surface and water jacket (including nucleate boiling) results in a temperature distribution with a significant difference between intake and exhaust valve

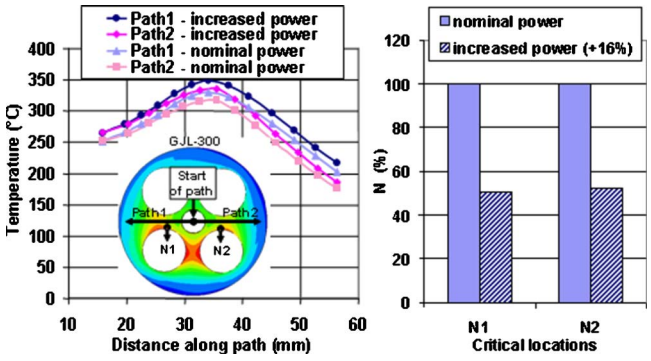

Fig. 15 Temperature comparison (left) and life span comparison with respect to Modified Manson–Coffin (right) of nominal rated and increased power for GJL-300

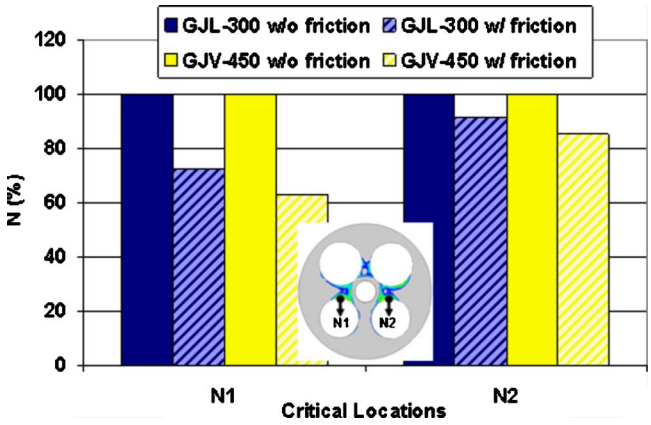

Fig. 16 Influence of friction between CH and CHG on lifetime with respect to Modified Manson–Coffin and SWT parameter for GJL-300 and GJV-450, respectively, at increased power

Downloaded 02 Jun 2010 to 171.66.16.107. Redistribution subject to ASME license or copyright; see http://www.asme.org/terms/Terms_Use.cfm

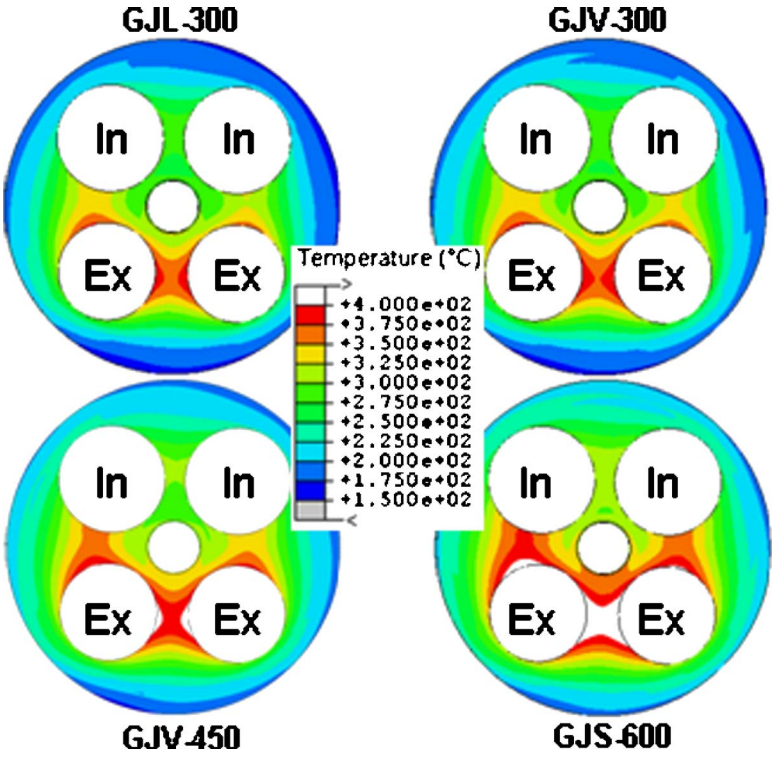

Fig. 17 Temperature distribution at nominal rated power for different types of cast irons

bridges. Highest temperatures in exhaust valve bridge occur at a distance of 35 mm from the center, which is due to the impact of high local heat flux at piston bowl rim.

Lifetime comparison for the cylinder head with respect to material specific evaluation approaches is depicted in Fig. 18.

Note that critical locations are the same as crack locations in Fig. 13. In addition, the computed number of cycles to failure agrees very well with the running time of the test engine up to the macroscopic crack observation.

Some calculation results do not match the trends of the uniaxial experimental results in terms of material thermal fatigue resistance and here, some important remarks should be stated:

- Experimental conditions are the same for all material specimens. Temperature is varied between the minimum and maximum temperatures, which are the same for the investigated materials [6]. However, in a 3D analysis of cylinder head, thermal conductivity plays an important role in temperature field and different materials have different maximum temperatures (see Fig. 17)
- The increasing lifetime with increasing tensile strength of material in experimental results is based on 0% mean total strain in the specimen for all materials. On the contrary, nonlinear temperature dependent material properties result in different mean stress distributions on the flame deck surface for investigated materials. In the current design, resulting mean stress distributions favors the lifetime of GJL-300 (negative mean stresses on flame deck surface) and deteriorates the lifetime of GJS-600 (positive mean stresses on flame deck surface)
- The fatigue parameters are calibrated according to the uniaxial experimental results (see Figs. 8–11). The use of the same parameters in multiaxial case is unavoidable but one should be aware of the importance of norm calculations. This fact underlines an important design criterion: the evaluation of lifetime according to the design variations using the same material and fatigue parameters is more reliable than material comparison for the same design.
- Assuming that the transfer from the uniaxial validation to multiaxial calculations is achieved correctly, under the applied boundary conditions and in the case of GJL-300 as the material for the cylinder head (see Fig. 18), one should try to optimize the structural design in a way that compressive mean stresses occur on the flame deck surface.
- Finally, before concluding it is important to note that the best interpretation could be achieved by calibrating the material models with experiments, which have exactly the same conditions of the real application (e.g., cylinder head component test bench capable of testing thermal cycles). FEV currently investigates the possibilities of efficient component testing. Only then the sensitivity of the TMF behavior with respect to the loading conditions could be accurately determined.

Conclusion

A complete TMF prediction methodology is presented in the case of cast iron cylinder heads. In order to avoid on the one hand the prolonged experimental programs to determine required material parameters and on the other hand significant calculation times, simple constitutive law uncoupled from damage is proposed.

Material models for different types of cast irons are validated for large temperature ranges. Different fatigue criteria are efficiently applied in finite element code so as to allow comparison for uniaxial and multiaxial loading. The outcome of the analysis is material specific evaluation approaches, which lead to a good correlation with experimental results.

Several influencing factors are investigated. Material comparison in diesel cylinder head yields contradictory results compared to uniaxially loaded specimen. For the same thermal load applied to the specimen, the number of cycles to failure increases with increasing material strength. However, when a cylinder head is of

Downloaded 02 Jun 2010 to 171.66.16.107. Redistribution subject to ASME license or copyright; see http://www.asme.org/terms/Terms_Use.cfm

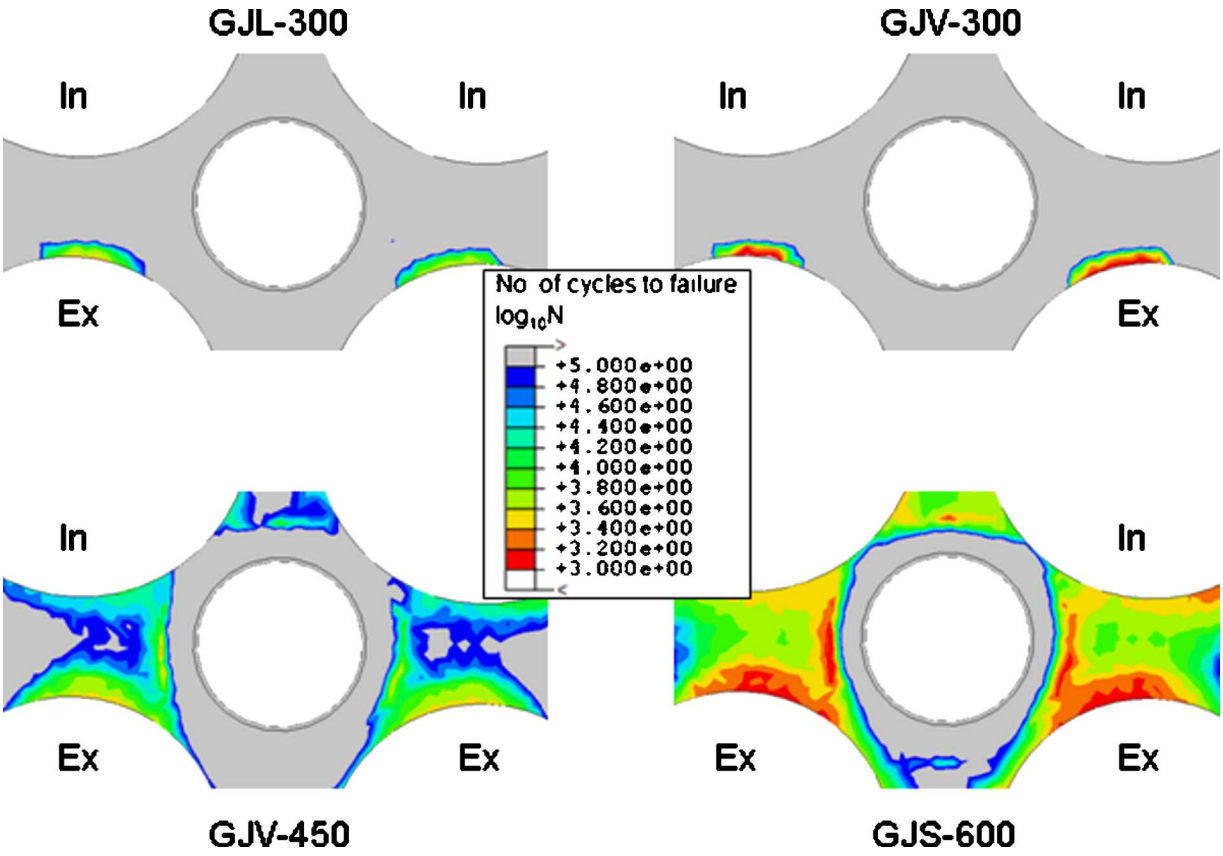

Fig. 18 Lifetime distribution at increased power (+16%) for different types of cast irons, flame deck surface injector-valve bridge area

interest instead of a specimen, temperatures on flame deck surface resulting from the same applied thermal load differs due to the different thermal conductivities, of the cast irons.

A central question is if and where a break point in comparison of two different cast irons in terms of thermal fatigue resistance exists. Depending on the application field of the engine, different requirements (maximum power, durability, emissions/peak firing pressure, weight, production costs, etc.) lead to different design measures. Rough guidelines could be constructed but each design should be investigated in its own to end up with accurate results.

Nomenclature

b = fatigue strength exponent
β = accumulated energy to fracture exponent
c = fatigue ductility exponent
C = accumulated energy to fracture parameter
E = Young's modulus
ε_f' = fatigue ductility coefficient
$\varepsilon_{\text{mech,amp}}$ = mechanical strain amplitude
$\varepsilon_{m,t}$ = mean total strain
$\varepsilon_{\text{pl,amp}}$ = plastic strain amplitude
N = number of cycles
σ_f' = fatigue strength coefficient
σ_m = mean stress
$\sigma_{\max}$ = maximum stress
ΔW = energy dissipated per cycle

International Material Cross Reference:

DIN EN		ASTM
1561, EN-GJL-250*	=	A48, Class 40 B
1561, EN-GJL-300	=	A48, Class 45 B
1560, EN-GJV-300	=	A842, Grade 300
1560, EN-GJV-350	=	A842, Grade 350
1560, EN-GJV-400	=	A842, Grade 400
1560, EN-GJV-450	=	A842, Grade 450
1563, EN-GJS-400-15	=	A536, Grade 60-40-18
1563, EN-GJS-600-3	=	A536, Grade 80-55-06

*The three digit numbers in cast iron classification represents the ultimate tensile strengh value of the material.

References

[1] Thomas, J. J., Verger, L., Bignonnet, A., and Borret, S. M., 2002, "Thermo-mechanical Design on the Automotive Industry," SAE Technical Report 2002–01–0659.
[2] Hertzberg, R. W., 1996, *Deformation and Fracture Mechanics of Engineering Materials*, 4th ed., Wiley, New York.
[3] Dieter, G. E., 1986, *Mechanical Metallurgy*, 3rd ed., McGraw Hill, New York.
[4] Buni, S. Y., Raman, N., and Seshan, S., 2004, "The Role of Graphite Morphology and Matrix Structure on Low Frequency Thermal Cycling of Cast Irons," Sadhana: Proc., Indian Acad. Sci., **29**, Part I, pp. 117–127.
[5] Constantinescu, A., Charkaluk, E., Lederer, G., and Verger, L., 2004, "A Computational Approach to Thermomechanical Fatigue," Int. J. Fatigue **26**, pp. 805–818.
[6] Hallstein, R., 1991, "Das Verhalten von Gusseisenwerkstoffen unter isothermer, thermischer und thermisch-mechanischer Wechselbeanspruchung," Dissertation, University of Karlsruhe, Juli.
[7] Gusseisenwekstoff, V., 1982, "Untersuchungen zum ein- und wechselsinnigen Verformungsverhalten verschiedener Gusseisensorten im Temperaturbereich $20°C \leqslant = T < = 500°C$," *Forschungsberichte Verbrennungs-kraftmaschinen*, FVV, Bericht.
[8] Nechtelberger, E., 1980, *The Properties of Cast Iron up to 500°C*, Technicopy Ltd., England.
[9] Blackmore, P. A., and Morton, K., 1982, "Structure-Property Relationships in Graphitic Cast Irons," Int. J. Fatigue, **4**, pp. 149–155.
[10] Dawson, S., 1999, "Compacted Graphite Iron: Mechanical and Physical Properties for Engine Design," *Werkstoff und Automobilantrieb Materials in Powertrain VDI (Verein Deutscher Ingenieure)*, Dresden Germany, Oct. 28–29.
[11] Tartaglia, J. M., Ritter, P. E., Gundlach, R. B., 2000, "Monotonic and Cyclic

Downloaded 02 Jun 2010 to 171.66.16.107. Redistribution subject to ASME license or copyright; see http://www.asme.org/terms/Terms_Use.cfm

Design Data for Ductile Iron Castings," Research Project No. 30.
[12] Manson, S. S., 1953, "Behaviour of Materials Under Conditions of Thermal Stresses," NACA TN 2933.
[13] Coffin, L. F., 1953, "A Study of the Effects of Cyclic Thermal Stresses on a Ductile Metal," Trans. ASME 53-A76.
[14] *SAE Fatigue Design Handbook*, 1997, R. C. Rice, ed., 3rd ed., Society of Automotive Engineers, Warrendale, PA.
[15] Smith, K. N., Watson, P., and Topper, T. H., 1970, "A Stress-Strain Function for the Fatigue of Metals," J. Mater., **5**(4), pp. 767–778.
[16] Charkaluk, E., and Constantinescu, A., 2000, "An Energetic Approach in Thermomechanical Fatigue for Silicon Molybdenum Cast Iron," Mater. High. Temp., **17**(3), pp. 373–380.
[17] Steyr-Daimler-Puch Engineering Center Steyr, FEMFAT Theory Manual, Version 3.2.
[18] Koch, F., Maassen, F., Deuster, U., Loeprecht, M., and Marckwardt, H., 1999, "Low Cycle Fatigue of Aluminium Cylinder Heads—Calculation and Measurement of Strain Under Fired Operation," SAE Technical Paper Series No. 1999-01-0645.

Downloaded 02 Jun 2010 to 171.66.16.107. Redistribution subject to ASME license or copyright; see http://www.asme.org/terms/Terms_Use.cfm

Measurement and Simulation of Instantaneous Emissions of a Heavy Truck Diesel Engine During Transients

Xavier Tauzia
e-mail: xavier.tauzia@ec-nantes.fr

Pascal Chesse

Jean-François Hetet

Nicolas Thouvenel

Ecole Centrale de Nantes,
LMF/EMCI,
UMR CNRS 6598, BP 92101,
44321 Nantes Cedex3, France

During the last decades, pollutant emissions from internal combustion engines used for transportation have become a major concern. Today, not only steady state emissions but also emissions during transients are regulated and have to be studied in order to be reduced. In this paper, we describe a new methodology developed to measure the instantaneous level of gaseous emissions from a internal combustion engine during transients, using an analyzer initially designed for steady state operation. Moreover, a new phenomenological thermodynamical combustion model is proposed in order to compute emissions during transients. The results of these two methods are compared on various transients. The measurement method seems to give good results (except for hydrocarbon (HC) measurements), as long as the speed and load variations are not too fast. Otherwise, the frequency of the analyzer which was used becomes the limiting factor. The new combustion heat release developed to simulate transients, coupled with an existing two-zone model for emission calculations, leads to satisfactory results for CO_2 *and* O_2 *concentrations and* NO_x *emissions. The agreement with measurements is good for smooth transients and seems promising for faster dynamics. The initial goal was reached, although some improvements are still necessary concerning HC measurements and the fastest transients. These results could be helpful when trying to reduce the amount of pollutant emissions at the exhaust during transients, directly or with after treatment devices.*
[DOI: 10.1115/1.2771254]

Keywords: diesel engine, pollutant emissions, transients, measurements, modeling

1 Introduction

Pollutant emissions produced by internal combustion engines used for transportation (automotive, trucks, etc.) have been investigated for more than 40 years. Progressively, they have become of a major concern, the regulations being more and more stringent. This has led to major improvements in the understanding and the control of emission formation, thanks to highly sophisticated injection system, engine control, and post-treatment devices introduced in the last decade. Pollution was first studied during steady state operations, then transients were introduced in the regulated measurement cycles. But until now, only the total amount of pollutant is regulated. Anyway, it seems interesting to investigate the instantaneous level of emissions during transient for various reasons:

- This would lead to a better understanding of how and when the total amount of pollutant is formed, thus indicating ways of reduction of emissions.
- If a post-treatment has to be installed, it is important to know not only the mean level of emissions but also the instantaneous and peak level of emissions to dimension and control the after-treatment device.

The objective of this paper is to present an experimental method as well as a simulation code, which were developed to study instantaneous emissions of heavy truck diesel engines and to compare and discuss their performances.

2 Experimental Study: Emission Measurements During Transients

The first attempts to experimentally evaluate the instantaneous levels of pollutant emissions during transients were made in the late 1980s. The authors generally use measurement devices designed for steady state measurements and apply mathematical models to correct the rough results. McClure [1] pioneered a numerical approach constituting a first alternative to evaluating the cumulative global emission levels during the transient cycle. His objective was to extrapolate real-time pollutant concentrations from experimental measurements. The sampling process and instrumentation were characterized to develop procedures aimed at reducing their inherent limitations. Gas was briefly blown at the exhaust to collect the resulting concentration peaks. The degree of distortion in the concentrations was described by a time delay as well as distortion parameters characterizing the shape of the response. After defining the system response, he established a numerical technique to reconstruct the concentration levels at the exhaust. The technique was applied to an 8 min long transient cycle for nitrogen oxides and led to concentration peaks larger than measured. Then, Beaumont et al. [2] and Arcoumanis and Jou [3] proposed new methods using standard exhaust gas analyzers and signal processing techniques to reconstruct emission levels from distorted measured signals. These techniques were based, respectively, on the generalized predictive control theory and on a phenomenological modeling of gas sample transport and diffusion. Both methods led to encouraging results when applied to NO_x instantaneous measurements.

Contributed by the Internal Combustion Engine Division of ASME for publication in the JOURNAL OF ENGINEERING FOR GAS TURBINES AND POWER. Manuscript received August 28, 2006; final manuscript received May 21, 2007; published online January 11, 2008. Review conducted by Christopher J. Rutland. Paper presented at the 2002 Spring Technical Conference of the ASME Internal Combustion Engine Division (ICES2002), Rockford, IL, April 14–17, 2002.

Copyright © 2008 by ASME

Downloaded 02 Jun 2010 to 171.66.16.107. Redistribution subject to ASME license or copyright; see http://www.asme.org/terms/Terms_Use.cfm

Table 1 Gas analyzer main characteristics

Emission	Analyzer type	Calibration range	Accuracy	Relative error
CO	COSMA Beryl 102	0–500 to 0–5000 ppm	±5 ppm	1%
CO_2	COSMA Beryl 102	0–16%	±0.1%	1%
NO_x	COSMA Topaze 2020	0–10 to 0–10,000 ppm	±5 ppm	1%
HC	COSMA Graphite 655	0–10 to 0–1000 ppm	±5 ppm	1%
O_2	COSMA Beryl 100	0–25%	±0.1%	1%

More recently, Weilenmann et al. [4] proposed a mathematical model whose objective was to reduce the distortions of pollutant emission measurements. The gas that was investigated was the dioxygen and the results showed a satisfactory agreement with those obtained with a lambda sensor. Manchur and Checkel [5] have made a very detailed study on real-time NO_x measurements, showing the need and the difficulty to correct rough measurements. They made onboard measurements on a gasoline vehicle. Such onboard real-time measurements were performed on a diesel engine by Kihara and Tsukamato [6] for NO_x and HC. The comparison with CVS bag analysis on several transient test cycles showed good agreement.

Alternative methods have been developed [7], using a solenoid valve in order to get gas samples at particular instants of a given transient. But, these techniques are limited to short and simple transients and require to repeat several times the transient to get the complete emission signal.

Today, there are fast response analyzers which may be used to determine instantaneous emissions directly and few studies have been published. Broatch et al. [8] use analyzers which are fast enough to measure emissions during transients (according to ISO16183:2002). They propose a testing protocol to improve measurement repeatability and an interesting automatic procedure to correct the misalignment of real-time measurements. Kang and Farrell [9] use fast response analyzers to investigate start of injection (SOI) and exhaust gas recirculation (EGR) effects on NO_x and HC transient emissions on a high speed diesel engine. Darlington [10], Alimin et al. [11], and Campbell et al. [12] use the same kind of device to validate a model or to study the efficiency of after-treatment devices. In the future, these analyzers should generalize for transient emission measurements. However, when this study was performed, such devices were not available and the choice was made to use an existing setup, initially designed for stationary measurements in order to obtain experimental results to confront with simulation. Moreover, as this kind of analyzer is available in most laboratories, it can be interesting to evaluate their potential for instantaneous emission measurement.

The pollutants examined at steady state are carbon monoxide (CO), unburnt HCs and nitrogen oxides (NO_x). The five gas COSMA analyzer uses nondispersive infrared (NDIR) method for CO_2 and CO, a flame ionization detector (FID) for HC, chemiluminescence for NO_x, and a paramagnetic sensor for O_2. Detailed characteristics can be found in Table 1.

Preliminary tests have been made to evaluate the capabilities of the analysis device to directly measure gaseous pollutants during transients. A three-way fast electrovalve is located ahead of the sample line (A), as shown in Fig. 1 to switch the sampling between a nitrogen tank (neutral gas) and the engine exhaust (the engine operates at steady state). A concentration step is thus created for each gas being investigated. The analyzer results are shown in Fig. 2.

The measured output is delayed and distorted. The time delay between the measured signal and the applied step is called reaction time and the time required to stabilize the signal is called response time, as shown in Fig. 3. Both the reaction and response times are too long to allow the direct use of the analyzer in transient response tests. In addition, these times vary from one gas to another. It can be reasonably assumed that the reaction time is due to the common 20 m long sample line as well as each apparatus. Given that each apparatus reacts in the order that they receive the gas to be analyzed (they are placed in series), it can be presumed that the delay incurred by each apparatus is related to the time required by the gas to reach them. The different response times can be explained by the variety of the analysis techniques being used.

Complementary tests made with a shorter sample line led to shorter reaction time, as expected. Then, various engine-operating conditions were also tested, which showed that the exhaust gas temperature and pressure had no influence on the analyzer response [13]. Finally, Fig. 2 shows that the experimental measurements include various steps. They are due to the analysis device sampling frequency, which is too small (and impossible to increase). A smoothing process is performed on the experimental measurements to clean up the results and make them easier to use.

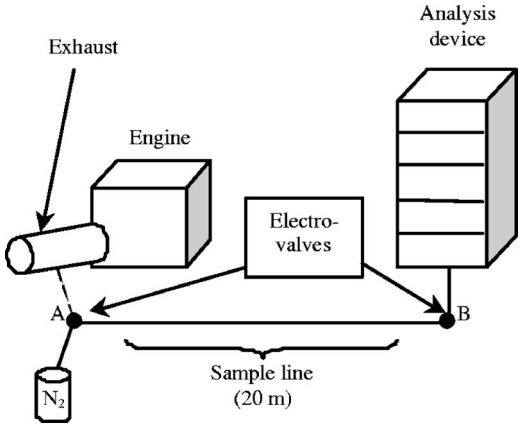

Fig. 1 Test configuration

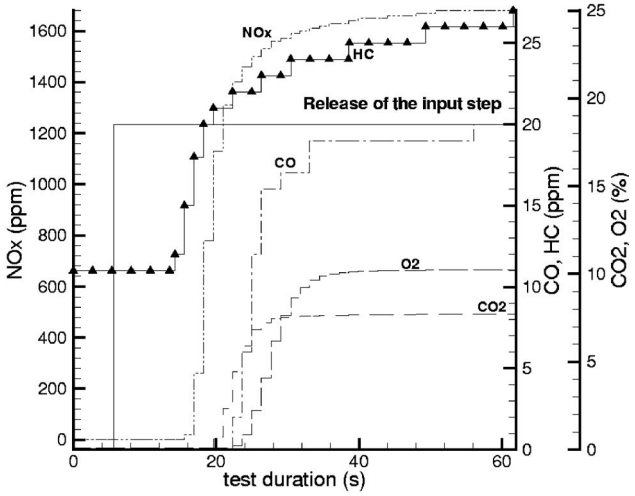

Fig. 2 Steady state pollution measurements at 1500 rpm and 82% throttle

Downloaded 02 Jun 2010 to 171.66.16.107. Redistribution subject to ASME license or copyright; see http://www.asme.org/terms/Terms_Use.cfm

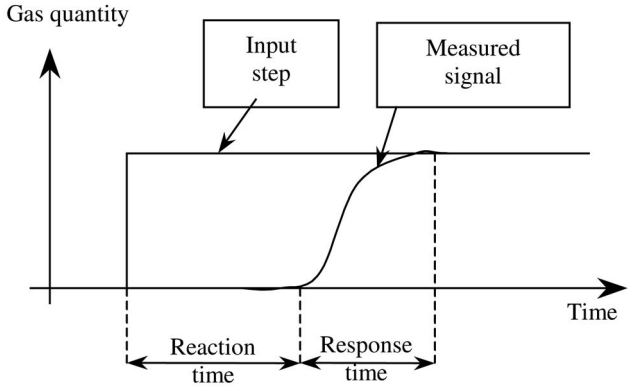

Fig. 3 Characteristics of the measurement system

The underlying concept of the reconstruction technique is to numerically process the signals obtained from the analysis device to reconstruct the initial signal. Consequently, the objective is to determine a transfer function [14–16] that transforms a given actual signal into an output signal measured with the analysis device (Fig. 4).

The transfer function H is defined as follows:

$$H = \frac{B}{F} = \frac{\sum_{i=0}^{n_b} b_i z^{-i}}{\sum_{i=0}^{n_f} f_i z^{-i}} \tag{1}$$

The order of B and F depends on the shape of the signal received from the analysis device. Determining H requires two major steps (performed with MATLAB functions [17]): first, the function coefficients are identified, then the signal computed with H is compared with the measured signal. The order of the coefficients of B and F is determined to optimize the agreement between measured and computed signals. H is then reversed to reconstruct the actual signal $\mathbf{u}$, as shown in Fig. 5.

Two cases must then be considered; either the complex poles of the polynomial terms of B are within the unit circle (module smaller than 1) and the measured signal is directly filtered with H^{-1} or these poles are outside the unit circle and the measured signal is filtered in reverse order for stability reasons. In the second case, the following equations are used:

$$H^{-1} = \frac{\hat{\mathbf{u}}}{\mathbf{y}} = \frac{F}{B} = \frac{\sum_{i=0}^{n_f} f_i z^{-i}}{\sum_{i=0}^{n_b} b_i z^{-i}} = \frac{z^{-n_f}}{z^{-n_b}} \frac{\sum_{i=0}^{n_f} f_i z^{n_f-i}}{\sum_{i=0}^{n_b} b_i z^{n_b-i}} = z^{n_b-n_f} \frac{\sum_{i=0}^{n_f} f_i z^{n_f-i}}{\sum_{i=0}^{n_b} b_i z^{n_b-i}} \tag{2}$$

where $n_b - n_f = d$, known as the integer delay between $\mathbf{y}$ and $\mathbf{u}$. z is called the advance operator. The $\mathbf{u}$ signal is d in advance of $\mathbf{y}$. The vectors $\mathbf{u}^r$ and $\mathbf{y}^r$ ($\mathbf{u}$ and $\mathbf{y}$ in reverse order) are then used. z is replaced with z^{-1} (delay operator). There is now a delay of d

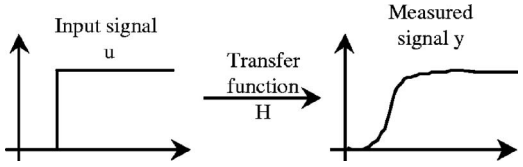

Fig. 4 Basis of the reconstruction technique

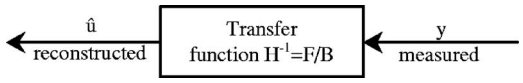

Fig. 5 Reconstruction scheme

between $\mathbf{u}^r$ and $\mathbf{y}^r$. The following equation is obtained:

$$\frac{\mathbf{u}^r}{\mathbf{y}^r} = z^{-d} \frac{\sum_{i=0}^{n_f} f_i z^{-(n_f-i)}}{\sum_{i=0}^{n_b} b_i z^{-(n_b-i)}} \tag{3}$$

The resulting denominator includes poles whose module is less than 1. The signal $\mathbf{y}^r$ can then be directly filtered to reconstruct the signal $\mathbf{u}^r$. Finally, the signal $\mathbf{u}^r$ is again put in reverse order to obtain the instantaneous exhaust signal $\mathbf{u}$.

The step used to identify H is obtained by switching from the nitrogen tank to the exhaust system while the engine remains at steady state at 1500 rpm and 82% throttle. The measured signal is then filtered using the transfer function.

The reconstruction technique is then applied to other steps obtained for various engine-operating conditions. Figure 6 shows that the least satisfactory results for CO_2 remain acceptable with a maximum oscillation amplitude equal to 13% of the final quantity. A few numerical oscillations are observed at the bottom and top of the step. They can be explained by two main factors.

- Determining the transfer function on a specific test and then applying it to other experiments can generate oscillations. Indeed, the transfer functions are slightly different from one test to another. Consequently, the best results are obtained for the test used in the definition of H.
- In addition, the characteristics inherent to the measurement method, i.e., the presence of steps as previously explained, can result in oscillations.

The same reconstruction process was repeated for the other gases after determination of the corresponding transfer functions. The results obtained for O_2, NO_x, and CO are similar to the results obtained for CO_2, with maximum variations that do not exceed 15% of the final quantities. On the other hand, HC measurements are harder to reconstruct due to the shape of the signal provided by the analysis device. As a result, identifying a transfer

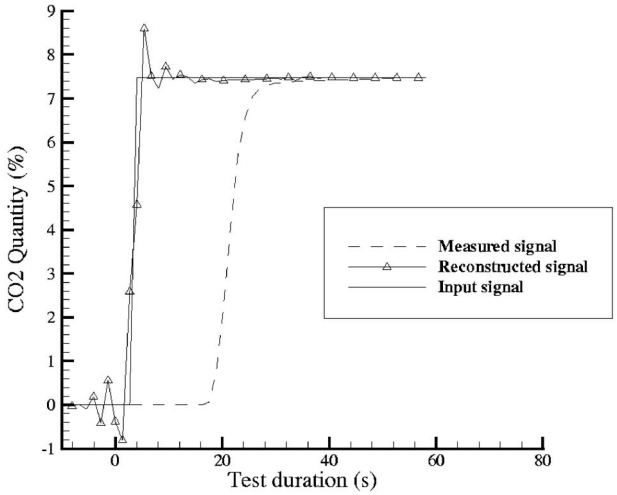

Fig. 6 Reconstruction of a step different from the step used for identification-comparison of the signals

Downloaded 02 Jun 2010 to 171.66.16.107. Redistribution subject to ASME license or copyright; see http://www.asme.org/terms/Terms_Use.cfm

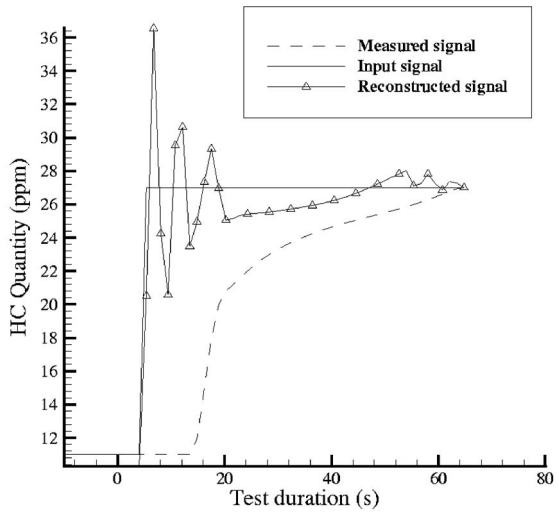

Fig. 7 Reconstruction of a HC step

function capable of reconstructing HC measurements can hardly be achieved. Oscillations whose amplitude reaches 30% of the final quantity are observed, as shown in Fig. 7.

Since particulate emissions are a major challenge for diesel engines, particularly during transients, a method was developed in order to quantify the instantaneous level of particulate at the exhaust. The classical measurement method for steady state is tunnel dilution, filtration, and measurement of particulate mass collected on a filter. Since particulate emissions are generally low, the measurement period must be rather long to get enough mass to perform an accurate measurement. Thus, this method cannot be applied to evaluate the instantaneous level of particulate at the exhaust. So, a correlation was established to link particulate concentrations with CO concentration and smoke opacity. It is based on steady state measurements at various engine-operating points. This correlation is the following second order polynomial equation whose coefficients are determined using multilinear regression:

$$\mathrm{PM} = (1.98e^{-3}) - (5.97e\mathrm{O}_P) + (1.36e^{-5}\mathrm{CO}) + (3.77e^{-4}\mathrm{O}_P{}^2) - (3.74e^{-10}\mathrm{CO}^2) \quad (4)$$

where PM is the particulate concentration in g/nm^3, O_p is the opacity in %, and CO is the CO concentration in ppm. Although unburnt HCs are generally involved (see Ref. [18] for an alternative correlation and a comparison of various existing correlations), they are intentionally omitted in this correlation due to the poor quality of their reconstruction during transients.

The correlation was validated for 13 different transient tests comprising several increasing and decreasing ramps between two operating conditions. Test Nos. 1 and 2 correspond to road load simulation (including gear changes), Test Nos. 3–9 correspond to conjugate variations of engine speed and load, Test Nos. 10 and 11 were conducted at constant load, and Test Nos. 12 and 13 at constant speed. The instantaneous opacity level was directly measured with an optical opacimeter, whereas CO concentrations were reconstructed as previously described. The mass of particulate computed with the correlation was integrated and compared with the mass of particulate collected on the filter throughout the duration of the test. The results show (Fig. 8) a satisfactory agreement with a difference of less than 15%.

However, this comparison does not mean that the correlation is fully validated. It would be interesting to compare its results to recent techniques which aim to perform particulate real-time measurements (such as laser induced incandescence or tapered element oscillating microbalance, see, for instance, Ref. [19,20], or [21]).

3 Engine Modeling and Emission Calculation

Diesel combustion is a particularly complex phenomenon and is the result of various processes such as atomization and evaporation of the fuel, mixing of fuel with surrounding gases (fresh air and EGR), interactions between the fuel jet and the walls, thermal transfers, etc. [22,23]. Computational fluid dynamics (CFD) is the most detailed way to model diesel combustion, but it is not fast enough to be used for transient calculations when hundreds of cycles are involved. On the contrary, simplified models (for instance, Ref. [24] or [25]) use maps generated from data measured on stationary test bench, corrected to take into account the transients. They are very useful for specific applications, including real-time emission evaluation. But, they are dedicated to a given

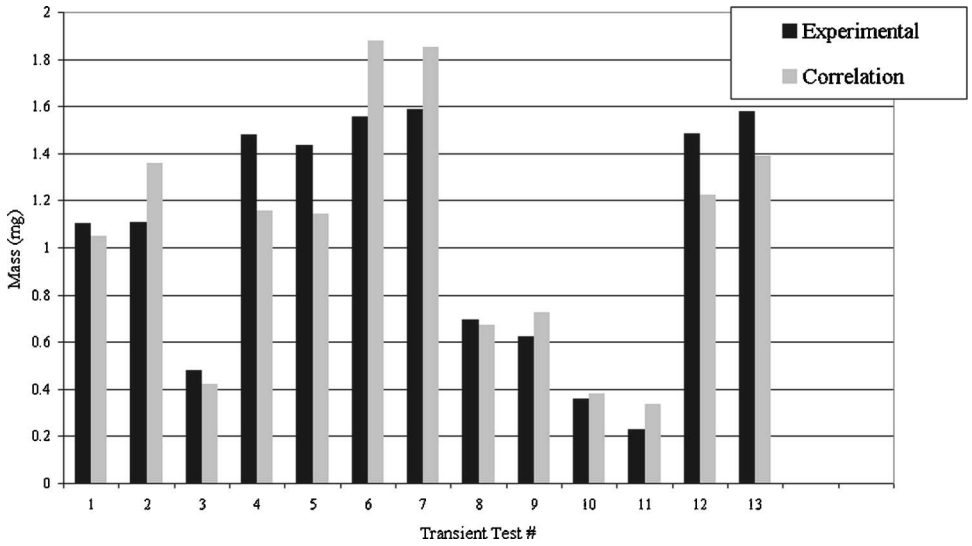

Fig. 8 Comparison between total particulate emissions measured and calculated by integration of correlation (4)

Downloaded 02 Jun 2010 to 171.66.16.107. Redistribution subject to ASME license or copyright; see http://www.asme.org/terms/Terms_Use.cfm

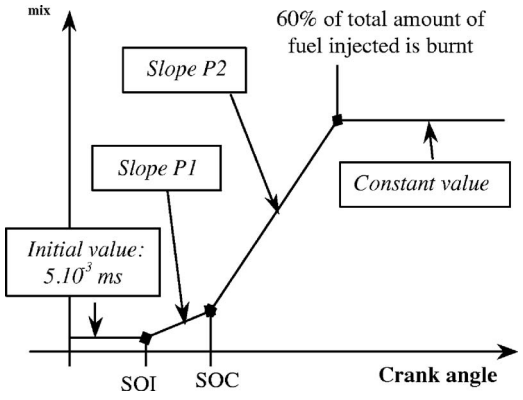

Fig. 9 Evolution of characteristic time of preparation τ_{mix}

engine or type of engine, and the lack of physical models makes them inappropriate to study the influence of combustion parameters such as injection timing or EGR on transient emissions. Thus, a thermodynamical 0D/1D approach with phenomenological models for combustion heat release and pollutant formation must be used. Several models of combustion heat release have been developed since the 1970s. The most famous may be the model created by Vibe [26]. It is a purely mathematical model, the coefficients of which must be adjusted for every operating point so that its use for transients seems hazardous.

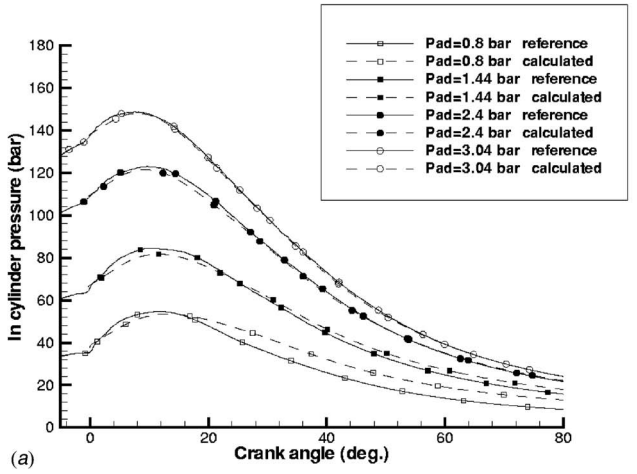

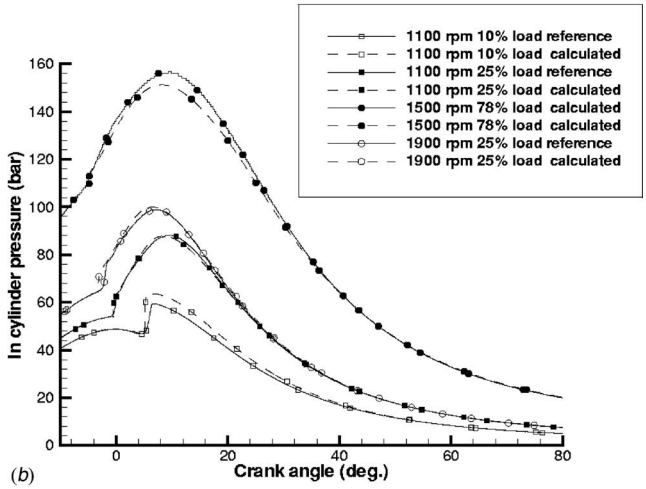

Fig. 10 Comparison between calculated and reference in-cylinder pressures: Engine A, influence of engine boost pressure (*a*) and speed and load (*b*)

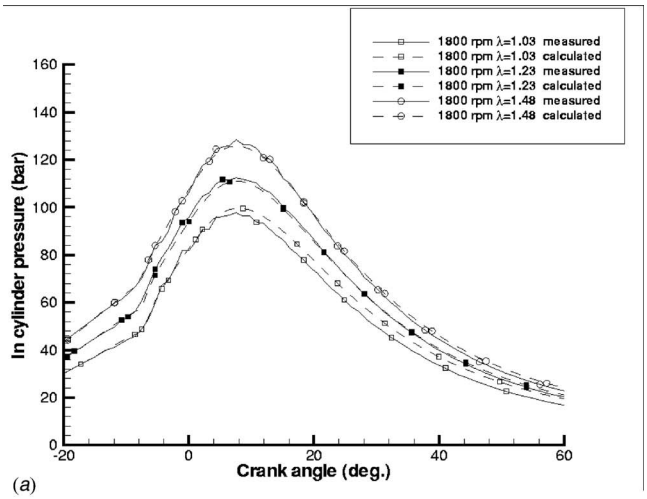

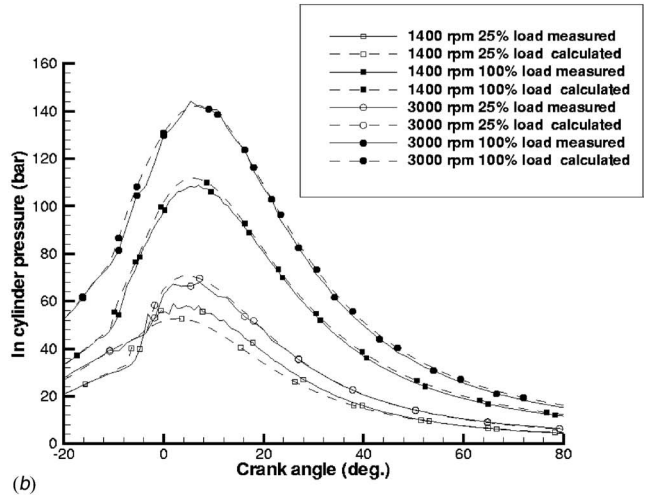

Fig. 11 Comparison between calculated and measured in-cylinder pressures: Engine B, influence of air/fuel ratio (*a*) and speed and load (*b*)

During the last decade, several phenomenological models have been proposed. The most complex are quasidimensionnal multizone models. The first multizone model was developed by Hiroyasu et al. in the early 1980s [27], and ever since several authors have proposed some evolutions and improvements (see, for instance Refs. [28–30] for the recent publications). The basic concept is to divide the combustion chamber into various zones, each one having its own temperature and air/fuel ratio. Generally, this is done by discretizing the fuel jet axially and radially. The results obtained for combustion heat release and pollutant emission formation are rather good, although some tuning is generally necessary because semiempirical equations are used to describe the various phenomena occurring during combustion. By the way, the number of zones used (typically from 30 to 60) considerably increases the computation time, which remains low for steady state study but becomes an important drawback for transients which may include thousands of cycles. That is why this option was not considered in this paper. Some other authors have developed phenomenological combustion model with a monozone approach (see, for instance, Refs. [31–35]). They use physical-based submodels and empirical formulas to describe the physical and

Downloaded 02 Jun 2010 to 171.66.16.107. Redistribution subject to ASME license or copyright; see http://www.asme.org/terms/Terms_Use.cfm

Table 2 Engine main characteristics

	Engine A	Engine B
Bore	123.8 mm	115 mm
Stroke	165.1 mm	105 mm
Unitary displacement	1.99 l	1.090 l
Total displacement	11.9 l	6.54 l
Volumetric compression ratio	16.1	15.25
Number of cylinders	6 in line	90 deg V6
Injection	Electronic unit pump	Distributor pump
Turbocharging	Single stage	Single stage
Maximum power	360 kW at 1900 rpm	206 kW at 3000 rpm
Maximum torque	2200 N m at 1300 rpm	820 N m at 2000 rpm

chemical phenomena governing combustion and to evaluate the heat release. They lead to a good agreement with experimental measurements when engine parameters such as speed, load, or rate of injection are modified. Nevertheless, they are rarely tested on transients, although diesel transients involve specific conditions such as potentially very low air/fuel ratios.

The section briefly presents a new heat release model that was developed to describe direct injection (DI) diesel engine behavior during steady state and transients. This model is not intended to be perfect for all operating points, but tries to find the principal tendencies, while varying, for example, the load, the engine speed, the injection profile, the injection timing, the inlet temperature, or the air-fuel ratio.

Diesel combustion is mainly a diffusion combustion controlled by fuel-air mixing process, with a premixed phase occurring first. The relative importance of this premixed phase is very variable depending on the engine speed and load, and is strongly influenced by the injection process, mainly by the quantity of fuel injected during the ignition delay. The diffusion phase is governed by the turbulent mixing between air and fuel, the in-cylinder turbulence resulting from air motion, and fuel jet induced turbulence, which is predominant on modern high pressure injection engines. These now well established observations lead to the basic concept of the model. The fuel present in the cylinder can be under three states.

- "1" is injected fuel, which is not ″prepared″ yet.
- "2" is fuel, which is prepared (that is to say, it is vaporized and mixed with air but has not undergone chemical oxidation).
- "3" is burnt fuel, which is supposed to be completely oxidized.

In order to simplify the model, the "preparation" of fuel is considered as a global process including vaporization and mixing with air. The preparation rate is calculated by introducing a characteristic time of preparation τ_{mix}:

$$R_{prep} = \frac{\min(m_{fuel\ 1}; m_{air}/C_{st})}{\tau_{mix}} \quad (5)$$

If the mass of air available is less than stoichiometric, then it becomes a limiting factor.

The burn rate as it is defined below is, in fact, the chemical reaction rate, since it does not include mixture formation rate. The choice is made to neglect the influence of temperature on chemical reaction rate. Indeed, in most cases, when temperatures are "sufficient," chemical reactions are much faster than the mixing process, so that the whole combustion process is not limited by chemical reaction rates but by preparation rate, in other words, by the availability of fuel ready to undergo chemical reactions [23]:

$$R_b = K_{C1} m_{fuel\ 2} \quad (6)$$

Mass conservation for various states of fuel in the cylinder is written as

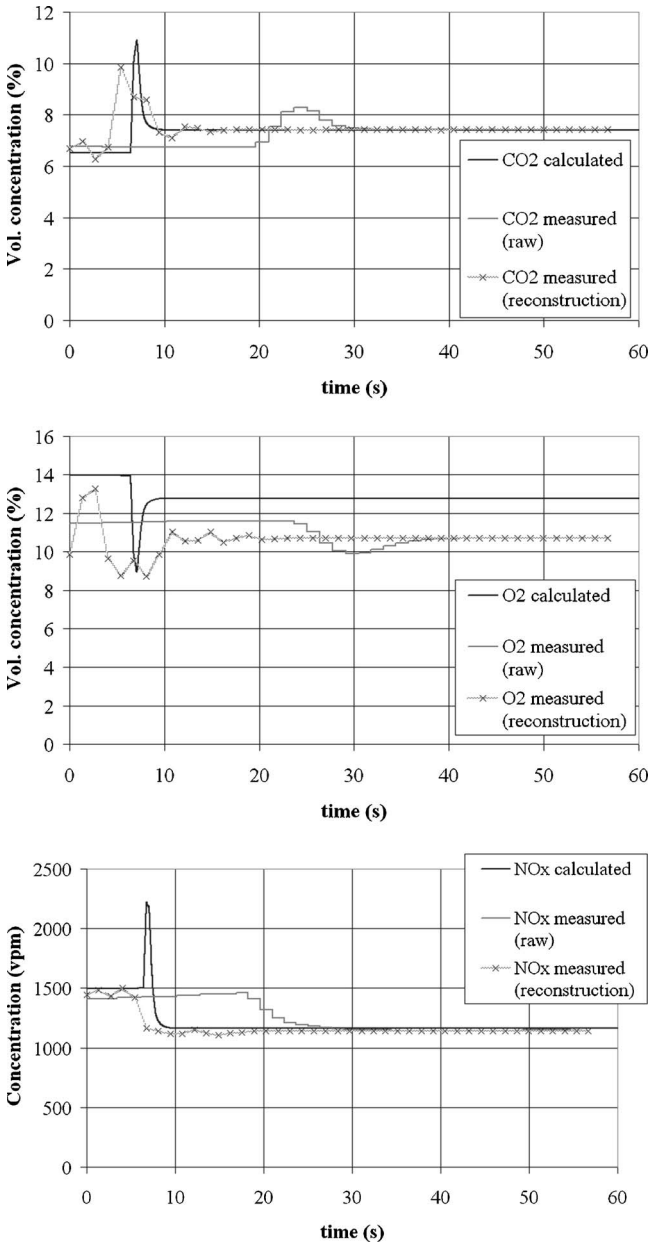

Fig. 12 Comparison of measured and calculated emissions for a 1 s long increasing ramp (Test 1)

Downloaded 02 Jun 2010 to 171.66.16.107. Redistribution subject to ASME license or copyright; see http://www.asme.org/terms/Terms_Use.cfm

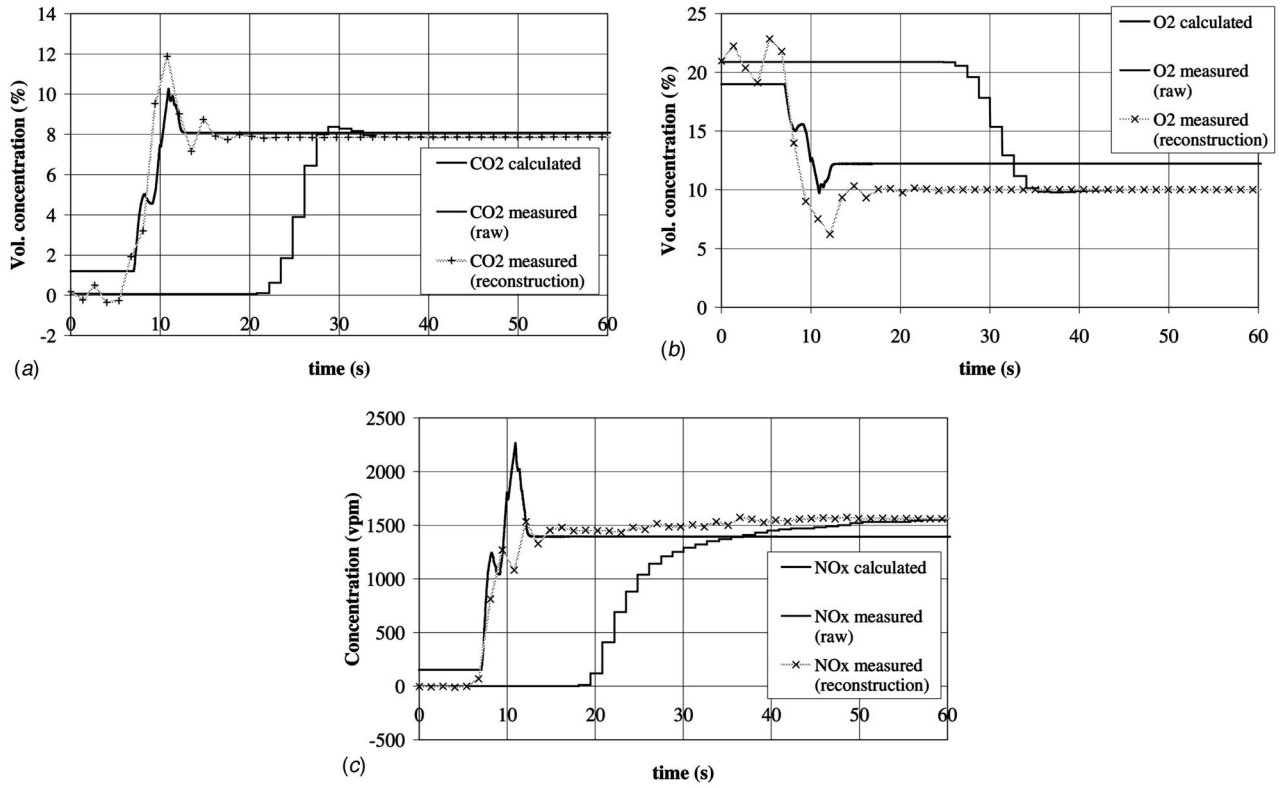

Fig. 13 Comparison of measured and calculated emissions for a 5 s long increasing ramp (Test 2)

$$\frac{dm_{\text{fuel 1}}}{dt} = R_{\text{inj}} - R_{\text{prep}} \tag{7}$$

$$\frac{dm_{\text{fuel 2}}}{dt} = R_{\text{prep}} - R_b \tag{8}$$

Finally, the combustion heat release is given by

$$\frac{dQ_c}{dt} = R_b \text{LHV} \tag{9}$$

The characteristic time of preparation is not constant during the whole combustion process. An initial value of 5×10^{-3} ms and a linear increase with a slope P_1 are chosen to describe τ_{mix} during ignition delay. After ignition, τ_{mix} increases linearly with a slope P_2 until 60% of fuel is burnt and then is constant (Fig. 9).

If the evolution of τ_{mix} during combustion seems to be qualitatively similar for the various operating conditions studied, the quantitative values of the slopes P_1 and P_2 undergo significant variations. Intensive testing has led to propose the following equations:

$$\tau_i = C P_{\text{vt}}^{-Z} P_{\text{inj}}^{-X} \left(\frac{N_{\text{rot}}}{N_{\text{rotn}}}\right)^{-Y} \exp\left(\frac{K}{T_{\text{inj}}}\right) (\text{fracO}_2)^{-W} \left(\frac{S_{\text{noz}}}{D^2}\right)^{-V} \tag{10}$$

$$P_1 = C P_{\text{vt}}^{-X} P_{\text{inj}}^{Y} T_{\text{inj}}^{-Z} \left(\frac{N_{\text{rot}}}{N_{\text{rotn}}}\right)^{-K} \text{FracO}_2^{-U} \left(\frac{S_{\text{noz}}}{D^2}\right)^{V} \text{Swirl}^{W} \tag{11}$$

$$P_2 = C P_{\text{max inj}}^{-X} P_{\text{inj}}^{Y} T_{\text{inj}}^{-Z} \left(\frac{N_{\text{rot}}}{N_{\text{rotn}}}\right)^{K} \text{FracO}_2^{-U} \left(\frac{S_{\text{noz}}}{D^2}\right)^{V} \text{Swirl}^{W} \tag{12}$$

The numerical values of the various coefficients are determined by a multilinear regression. Full justifications, including the various tests carried out to establish this model, can be found in Refs. [36,37]. Figure 10 shows some examples of results obtained with the model on Engine A (see Table 1). The reference data were obtained with the CFD code KIVA 3V. Indeed, various parametric studies were conducted on test bench. But, some others are more difficult to perform or require important modifications on the engine (i.e., turbocharger, injector nozzle, or cylinder head changes). So the choice was made to use CFD to generate reference data corresponding to a great amount of parameter variations, including inlet air pressure, temperature and O_2 fraction, swirl, injection shape and pressure, and nozzle diameter. Details can be found in Ref. [37] about the CFD calculations (code description, validation, and calculation conditions). The model leads to a good agreement with reference in-cylinder pressure when the boost pressure is modified, for a given operating point, or when engine rotation speed and load vary.

In Fig. 11, a comparison is shown between calculated and measured in-cylinder pressures for Engine B when the air/fuel ratio (AFR) is modified, and for various speeds and loads. Again, the agreement is good so that a good accuracy can be expected when using the model during transients, which involves large fluctuations of speed, load, and AFR.

The method to evaluate pollutant emissions remains classical: a two-zone combustion model proposed by Heider et al. [38] is used to compute temperature in the burnt gases where NO_x are produced. The NO concentrations are then calculated with Zeldowitch extended mechanism [23]. A HC formation model is also implemented but the results are not presented here, since the HC

Downloaded 02 Jun 2010 to 171.66.16.107. Redistribution subject to ASME license or copyright; see http://www.asme.org/terms/Terms_Use.cfm

instantaneous levels during transients could not be measured correctly. Attempts were made to evaluate soot emissions with simplified models with two empirical equations to describe soot formation and oxidation. The qualitative increase of soot production during engine accelerations and loadup was captured, but the quantitative agreement of the model with measured data is not satisfying yet. So, no results are shown in this paper. CO calculation is somewhat difficult for diesel engines where levels are generally very low, and no model was found to give satisfactory results. A full description of emission calculation can be found in Refs. [37,39]. Finally, the new combustion model is implemented in the SELENDIA code. Based on 0D thermodynamical approach, it has been developed and validated for more than ten years and describes diesel engine behavior during steady state and transient operations (see Ref. [40] for a general description of the code, Ref. [41] for aspects relative to turbocharging and inlet and exhaust modeling, and Ref. [39] for transients).

4 Comparison and Results

The aim of this section is to compare experimental measurements (made according to the method presented in Sec. 2) and calculations made with the models presented in Sec. 3. The results presented here are instantaneous emissions during transients. They concern a modern heavy-duty diesel engine, the characteristics of which are gathered in Table 2 (Engine A).

Figures 12–14 show a comparison between measured and calculated emissions for three transients.

Test 1: 1 s long increasing ramp from 50% throttle and 1200 rpm to 90% throttle and 1700 rpm

Test 2: 5 s long increasing ramp from 0% throttle and 615 rpm (idle condition) to 82% throttle and 1500 rpm

Test 3: 30 s long increasing ramp from 0% throttle and 615 rpm (idle condition) to 82% throttle and 1500 rpm

For the three tests, the resistive torque was regulated by the high dynamic dynamometer.

First of all, the only difference between the tests shown in Figs. 13 and 14 is the transient duration since the start and end conditions are the same in both tests. A direct comparison of their reconstruction is thus possible. The shorter the transient phase is, the more the slope and peak are amplified, as confirmed by previous publications [2,3]. This result is expected since the faster the transient is, the more the response time distorts the actual signal. On the other hand, slow transients (quasisteady) could result in quasinull differences between measured and reconstructed signals, except for a time delay.

The CO_2 peaks shown by the reconstructed signals correspond to a decrease of the excess air during the transient phase (acceleration and loading). The fuel mass flow in the combustion chamber increases faster than the air flow due to the turbocharger response time. Figures 13 and 14 show that the faster the transient phase is, the higher the peak is. This is due to the fact that the increase of the fuel mass flow is more sudden and results in a larger decrease of the excess air. Of course, O_2 variations are opposite.

The nitrogen oxide variations are linked to temperature and excess-air effects. A temperature increase leads to an increase of the NO_x concentration whereas a decrease of the local excess air results in a decrease of the NO_x concentration. The contribution of the temperature factor, which increases due to the decrease of the global excess air, seems to be predominant since variations similar to those of the CO_2 are observed, i.e., the NO_x concentration increases during the transient phase and presents a peak.

Similar results were found for CO and HC emissions [37] but they are not presented here since they were not confronted to calculations. The agreement between measured and calculated emissions is rather good, but the calculated peaks are narrower and sometimes higher than the measured ones. For CO_2, the calculation, based on complete oxidation of fuel, is very simple. It might not lead to important errors as long as fuel and air mass

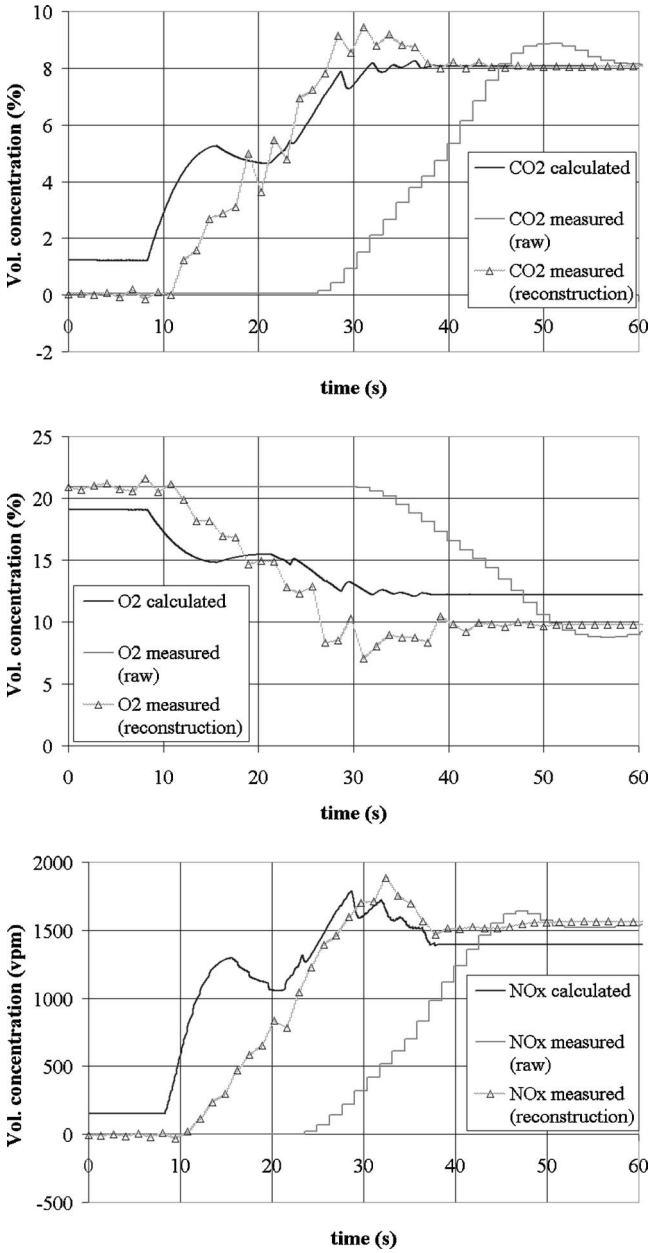

Fig. 14 Comparison of measured and calculated emissions for a 30 s long increasing ramp (Test 3)

flow are correct. So, the discrepancies could be explained by gas diffusion phenomenon along the sample line. For NO_x emissions, the calculation can be criticized as well. Indeed, the change in global air/fuel ratio is taken into account when calculating the in-cylinder temperature, but the local air/fuel ratio in the combustion zone, which is used for NO_x production calculations, is kept constant. This might not be true when the global air/fuel ratio reaches very low values, which is briefly the case during the transients studied here.

Finally, Fig. 15 shows a test corresponding to a 1000 m dash from zero to full throttle with a load simulating the complete vehicle cinematic (clutch, gear box, transmission, vehicle inertia) called road load simulation. Here, the limits of the measurement method are reached. The variations in emissions are too fast to be captured by the analyzer. This result was anticipated due to the low frequency of acquisition. The calculation, on the other hand, shows concentration peaks corresponding to gear changes with zero to full load variations.

Downloaded 02 Jun 2010 to 171.66.16.107. Redistribution subject to ASME license or copyright; see http://www.asme.org/terms/Terms_Use.cfm

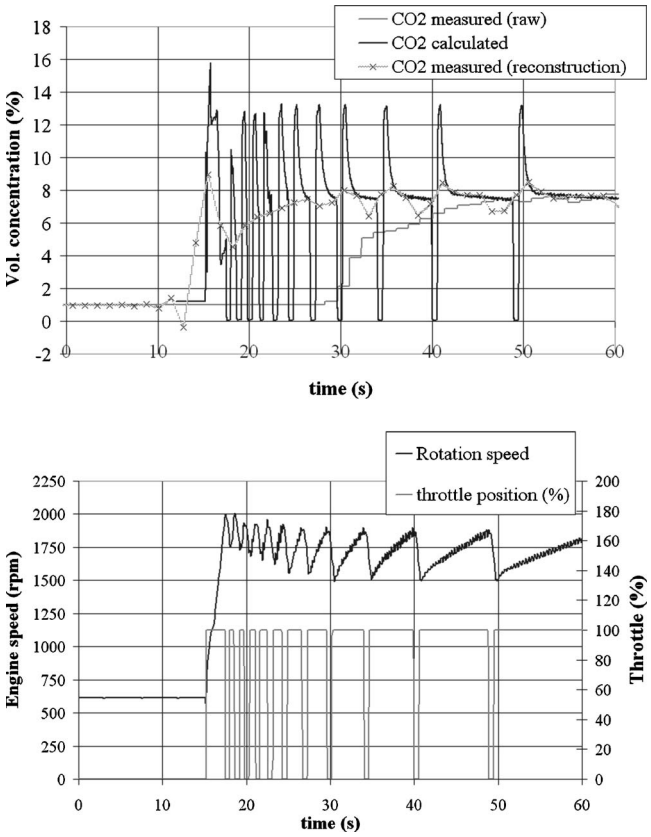

Fig. 15 Comparison of measured and calculated emissions for a 1000 m dash from zero to full throttle (road load simulation)

5 Conclusion

The measurement method presented here is able to evaluate instantaneous gaseous emissions of a heavy-duty diesel engine during transients, as long as the variations are not too fast. Otherwise, the frequency of the analyzer, which is originally designed for steady state measurements, becomes the limiting factor. Moreover, gas diffusion may occur in the sample line and smooth the actual concentration variations. In the future, fast response analyzers will help to characterize the exact potential of the method.

The new combustion heat release developed to simulate transients, coupled with an existing two-zone model for emission calculations, leads to satisfactory results for CO_2 and O_2 concentrations and NO_x emissions. The agreement with measurements is good for smooth transients and seems promising for faster dynamics.

Additional development must be done in order to model CO, HC, and particulate emissions which undergo significant variations during transients. A more detailed description of fuel-air mixing modifications under very low air/fuel ratio could also improve the NO_x emission prediction.

Acknowledgment

The authors want to thank X. Perdriau and Etas d'Angers (DGA) where the experimental measurements have been realized.

Nomenclature

B = polynomial term defining the transfer function H
b_i = coefficients of term of degree i of polynomial B
C_{st} = stoichiometric air/fuel ratio
D = bore (m)
F = polynomial term defining the transfer function H
f_i = coefficient of term of degree i of polynomial F
fracO_2 = O_2 fraction (kg/kg)
H = transfer function
K_{Cl} = empirical constant (set to 10^5 s^{-1}) (s^{-1})
LHV = lower heating value of the fuel (J/kg)
m_{air} = mass of air (kg)
m_{fuel1} = mass of fuel not yet prepared (kg)
m_{fuel2} = mass of fuel prepared (kg)
n_b, n_f = degree (order) of polynomials B and F
N_{rot} = engine rotation speed (rpm)
N_{rotn} = engine nominal rotation speed at maximum power (rpm)
P = pressure (Pa)
P_1 = first slope for τ_{mix}
P_2 = second slope for τ_{mix}
P_{vt} = injection velocity variation (see details in the text) (m/s)
Q_c = heat release (J)
R_b = fuel burn rate (kg/s)
R_{inj} = injection mass flow rate (kg/s)
R_{prep} = fuel preparation rate(kg/s)
S_{noz} = injection nozzle area (m^2)
T = temperature (K)
$\mathbf{u}$ = input signal vector
$\hat{\mathbf{u}}$ = reconstructed actual signal
$\mathbf{u}_r$, $\mathbf{y}_r$ = u and y in reverse order
$\mathbf{y}$ = signal vector measured by the analysis device

Greek Symbols

ρ_f = fuel density (kg/m^3)
τ_{mix} = characteristic time of preparation (s)
τ_i = ignition delay (s)

Subscripts

i = index of polynomial terms
inj = at the start of injection

Abbreviations

CA = crank angle
CFD = computational fluid dynamics
DI = direct injection
EGR = exhaust gas recirculation
SOC = start of combustion
SOI = start of injection

References

[1] McClure, B. T., 1988, "Characterization of the Transient Response of a Diesel Exhaust-Gas Measurement System," SAE Technical Paper No. 881320, pp. 1680–1689.
[2] Beaumont, A. J., Noble, A. D., and Pilley, A. D., 1990, "Signal Reconstruction Techniques for Improved Measurement of Transient Emissions," SAE Technical Paper No. 900233, pp. 95–101.
[3] Arcoumanis, C., and Jou, C. S., 1992, "Measurement and Prediction of Transient NO_x Emissions in DI Diesel Engines," ImechE Paper No. C448/039, pp. 97–105.
[4] Weilenmann, M., Bach, C., and Rüdy, C., 2000, "Aspects of Instantaneous Emission Measurement," *Proceedings of Ninth International Symposium on Transport and Air Pollution*, I. Avignon, ed., pp. 119–126.
[5] Manchur, T. B., and Checkel, M. D., 2005, "Time Resolution Effects on Accuracy of Real-Time NO_x Emission Measurements," SAE World Congress and Exhibition, Detroit, MI, Apr. 2005, SAE Paper No. 2005-01-0674.
[6] Kihara, N., and Tsukamoto, T., 2001, "Real-Time On-Board Measurement of Mass Emissions of NO_x, THC and Particulate Matters From Diesel Vehicles," *Fifth International Symposium on Diagnostic and Modeling of Combustion in Internal Combustion Engines, COMODIA*, Nagoya, Japan, July 2001, pp. 71–76.
[7] Myamoto, N., Ogawa, H., Shibuya, M., Fuwa, and N., 1993, "Time Series Analysis of Diesel Exhaust Gas Emissions Under Transient Operation," SAE Technical Paper No. 930976, pp. 724–731.
[8] Broatch, A., Lujàn, J. M., Serrano, J. R., and Pla, B., 2006, "Pollutants Instan-

Downloaded 02 Jun 2010 to 171.66.16.107. Redistribution subject to ASME license or copyright; see http://www.asme.org/terms/Terms_Use.cfm

taneous Measurements and Data Analysis of Engine in the Loop Tests," Thiesel 2006 Conference, Valencia, Spain, Sep. 2006.
[9] Kang, H., and Farrell, P. V., 2005, "Experimental Investigations of Transient Emissions (HC and NO_x) in a High Speed Direct Injection (HSDI) Diesel Engine," SAE Powertrain and Fluid Systems Conference and Exhibition, San Antonio, TX, Oct. 2005, SAE Technical Paper No. 2005–01-3883.
[10] Darlington, A., 2006, "A Simple Diesel Engine Air-Path Model to Predict the Cylinder Charge During Transients: Strategies for Reducing Transient Emissions Spikes," Powertrain and Fluid Systems Conference and Exhibition, Toronto, Ontario, Canada, Oct. 2006, SAE Paper No. 2006-01-3373.
[11] Alimin, A., Roberts, C. A., and Benjamin, S., 2006, "A NO_x Trap Study Using Fast Response Emission Analysers for Model Validation," SAE 2006 World Congress and Exhibition, Detroit, MI, Apr. 2006, SAE Paper NO. 2006-01-0685.
[12] Campbell, B., Peckham, M., Symonds, J., Parkinson, J., and Finch, A., 2006, "Transient Gaseous and Particulate Emission Measurements on a Diesel Passenger Car Including a DPF Regeneration Event," SAE 2006 World Congress and Exhibition, Detroit, MI, Apr. 2006, SAE Paper No. 2006-01-1079.
[13] Thouvenel, N., Tauzia, X., Chessé, P., and Hétet, J.-F., 2002, "Experimental Method for Determination of Instantaneous Diesel Engine Pollutant Emissions During Transient," *ASME ICE Division Spring Technical Conference Proceedings*, Vol. 38, pp. 207–214.
[14] Delarminat, P., 1993, *Automatique, Commandes des Systèmes Linéaires*, Hermes Ed., Paris, France.
[15] Dieulesaint, E., and Royer, D., 1990, *Automatique Appliquée: Systèmes Linéaires de Commande à Signaux Échantillonés* Masson Ed., Paris, France.
[16] Rivoire, M., and Ferrier, J. L., 1991, *Cours d'Automatique: Signaux et Systèmes* Eyrolles ed., Paris France.
[17] The Math Works Inc., 1995, MATLAB, Version 4, User's Guide.
[18] Arregle, J., Bermúdez, V., Serrano, J. R., and Fuentes, E., 2006 "Procedure for Engine Transient Cycle Emissions Testing in Real Time," *Experimental Thermal and Fluid Science*, Elsevier, New York, pp. 485–496.
[19] Moosmüller, H., Arnott, W. P., Rogers, C. F., Bowen, J. L., Gillies, J., Pierson, W. R., Collins, J. F., Durbin, T. D., and Norbeck, J. M., 2000, "Evaluation of Five Instruments for the Real-Time Measurement of Diesel Particulate Mass Emissions," *Proceedings of the Tenth CRC On-Road Vehicle Emissions Work Shop*, Atlanta, GA.
[20] Gupta, S., Hillman, G., andRaj Sekar, R., 2003, "Transient Particulate Emission Measurements in Diesel Engine Exhausts," SAE Powertrain and Fluid Systems Conference and Exhibition, Pittsburgh, PA, Oct. 2003, SAE Paper No. 2003-01-3155.
[21] Xu, S., 2005, "Comparison of Heavy-Duty Truck Diesel Particulate Matter Measurement: Teom and Traditional Filter," 2005 SAE Brasil Fuels and Lubricants Meeting, Rio De Janiero, Brazil, May 2005, SAE Paper No. 2005-01-2153.
[22] Dec, J. E., 1997, "A Conceptual Model of DI Diesel Combustion Based on Laser-Sheet Imaging," International Congress and Exposition, Detroit, MI, Feb. 1997, SAE Paper No. 970873, pp. 1319–1348.
[23] Heywood, J. B., 1988, *Internal Combustion Engine Fundamentals*, McGraw-Hill, New York.
[24] Urano, Y., Nakano, Y., Takada, H., and Sugita, M., 2005, "Optimization Technique for Transient Emission Reduction of Heavy Duty Diesel Engine," SAE 2005 World Congress and Exhibition, Detroit, MI, Apr. 2005, SAE Paper No. 2005-01-1099.
[25] Ericson, C., Westerberg, B., and Egnell, R., 2005, "Transient Emission Predictions With Quasi Stationary Models," SAE Powertrain and Fluid Systems Conference and Exhibition, San Antonio, TX, Oct. 2005, SAE Paper No. 2005-01-3852.
[26] Vibe, I. I., 1970, *Brennverlauf und Kreisprozess von Verbrennungsmotoren*, VEB Verlag Technik, Berlin.
[27] Hiroyasu, H., Kadota, T., and Arai, M., 1983, "Development and Use of a Spray Combustion Modeling to Predict Diesel Engine Efficiency and Pollutant Emissions," Bull. JSME, **26**(214), pp. 569–575.
[28] Hountalas, D. T., Kouremenos, D. A., Pariotis, E. G., Schwarz, V., and Binder, K. B., 2002, "Investigation Concerning the Effect of Post Fuel Injection on the Performance and Pollutants of Heavy Duty Diesel Engines Using a Multi-Zone Combustion Model," *Thiesel Conference on Thermo-and Fluid Dynamic Processes in Diesel Engines*, Valencia, Spain, pp. 292–2309.
[29] Jung, D., and Assanis, D. N., 2001, "Multi-Zone DI Diesel Spray Combustion Model for Cycle Simulation Studies of Engine Performance and Emissions," SAE Paper no. 2001-01-1246, pp. 1–23.
[30] Zhou, P., Zhou, S., and Clelland, D., 2006, "A Modified Quasi-Dimensional Multi-Zone Combustion Model for Direct Injection Diesels," Int. J. Eng. Res., **7**(4), pp. 335–345.
[31] Arregle, J., Lopez, J. J., Garca, J. M., and Fenollosa, C., 2003, "Development of a Zero-Dimensional Diesel Combustion Model, Part 1: Analysis of the Quasi-Steady Diffusion Combustion Phase and Part 2: Analysis of the Transient Initial and Final Diffusion Combustion Phases," Appl. Therm. Eng., **23**, pp. 1301–1331.
[32] Arsie, I., Di Genova, F., Pianese, C., Sorrentino, M., Rizzo, G., Caraceni, A., Cioffi, P., and Flauti, G., 2004, "Development and Identification of Phenomenological Models for Combustion and Emissions of Common-Rail Multi-Jet Diesel Engines," Fuels and Lubricants Meeting and Exhibition, Toulouse, France, Jun. 2004, SAE Paper No. 2004-01-1877, pp. 37–47.
[33] Chmela, F. G., and Orthaber, G. C., 1999, "Rate of Heat Release Prediction for Direct Injection Diesel Engines Based on Purely Mixing Controlled Combustion," International Congress and Exposition, Detroit, MI, Mar. 1999, SAE Paper No. 1999-01-0186.
[34] Chmela, F. G., Engelmayer, M., Pirker, G., and Wimmer, A., 2004, "Prediction of Turbulence Controlled Combustion in Diesel Engines," THIESEL 2004 Conference on Thermo- and Fluid Dynamic Processes in Diesel Engines.
[35] Barba, C., Burkhardt, C., Boulouchos, K., and Bargende, M., 2000, "A Phenomenological Combustion Model for Heat Release Prediction in High-Speed DI Diesel Engines With Common-Rail Injection," International Fuels and Lubricants Meeting and Exposition, Baltimore, MD, Oct. 2000, SAE Paper No. 2000-01-2933.
[36] Tauzia, X., Maiboom, A., Chessé, P., and Thouvenel, N., 2006, "A New Phenomenological Heat Release Model for Thermodynamical Simulation of Modern Heavy Duty Diesel Engines," Appl. Therm. Eng., **26**(16), pp. 1851–1857.
[37] Thouvenel, N., 2004, "Contribution à l'Étude des Émissions Polluantes et des Moyens de Dépollution dans un Moteur Diesel Suralimenté en Fonctionnement Transitoire," Ph.D. thesis, Ecole Centrale de Nantes, France.
[38] Heider, G., Zeilinger, K., and Woschni, G., 1995, "Two Zone Calculation Model for the Prediction of NO Emissions From Diesel Engines," *Proceedings of 21st Cimac Conference*, Interlaken, Switzerland, Jun. 1995.
[39] Tauzia, X., Chessé, P., Hétet, J.-F., and Bonin, A., 2002, "MERIMEE: A Simulation Software to Study Diesel Engines Used for Military Propulsion," ASME ICE Division Fall Technical Conference, New Orleans, LA, Sep. 8–11.
[40] Hétet, J.-F., Inozu, B., Roy, P., Tauzia, X., and Chessé, P., 1999, "Performance Simulation of Marine Diesel Engines With SELENDIA," J. Ship Res., **43**(4), pp. 201–217.
[41] Chesse, P., Hetet, J.-F., Tauzia, X., Roy, P., and Inozu, B., 2000, "Performance Simulation of Sequentially Turbocharged Marine Diesel Engines With Applications to Compressor Surge," J. Eng. Gas Turbines Power, **122**(4), pp. 562–569.

Downloaded 02 Jun 2010 to 171.66.16.107. Redistribution subject to ASME license or copyright; see http://www.asme.org/terms/Terms_Use.cfm

MotoGP 2007: Criteria for Engine Optimization

Enrico Mattarelli
Assoc. Professor
DIMeC,
University of Modena and Reggio E.,
Via Vignolese 905,
41100 Modena, Italy
e-mail: mattarelli.enrico@unimore.it

The paper proposes some design criteria for the MotoGP engines, complying with the FIM 2007 Technical Regulations. Five configurations have been considered: engines with three cylinders in line and four cylinders in line, and three V engines with four, five, and six cylinders. All the analyzed solutions have been optimized from a fluid-dynamic point of view by means of one dimensional engine cycle simulations. Then, the engines are compared in terms of full load performance at steady conditions. Finally, the influence of engine performance, along with operation regularity and motorbike weight, is assessed by means of a lap time simulator, developed by the author on the base of real data. The best configurations turned out to be the four-cylinder engines, while three-cylinder and five-cylinder engines are quite penalizing. The key of the four-cylinder engines success is their good breathing capability and mechanical efficiency at high speed, yielding an optimum power-to-weight ratio, associated with a good engine regularity, i.e., a smooth response to throttle angle variations.
[DOI: 10.1115/1.2771238]

Introduction

The regulations, issued by the Federation Internationale de Motocyclisme (FIM) for the 2002 World Championship, opened a new era in motorbike road racing. Four-stroke prototypes, with a maximum engine capacity of 990 cm^3, were allowed to race in the former 500 cm^3 two-stroke class, now called MotoGP. Since the first year, the bikes powered by the new engines outclassed the two-stroke competitors, and the involvement in this race series on the part of motorbike manufacturers has grown steadily, thanks to the enhanced synergies between racing prototypes and production bikes. However, some concern about riders' safety has emerged due to the escalation of bikes' top speed, currently exceeding 340 km/h. As a consequence, on August 30, 2005, the Grand Prix Commission issued some modifications to the technical regulations for the next championships [1].

From January 1, 2007, the maximum engine capacity for the MotoGP class racers will be reduced from 990 cm^3 to 800 cm^3. This new rule will have a strong impact on engine design. With a capacity of 990 cm^3, it was relatively easy to get a peak brake power of 230–250 HP, which is generally considered the upper limit of usable power for a MotoGP bike. Therefore, the attention of designers up to now has been more focused on other issues, such as regularity of power delivery and engine-bodywork matching [2,3]. These issues will remain fundamental, but it will also be important to recover the 20% reduction of engine power, resulting in the limitation of displacement.

It is predictable that most manufacturers will keep their current engine architecture in order to take the maximum advantage from their own experience on engine-bike matching. Under this point of view, it should be easier to fit a smaller engine in the bodywork and to find a proper position for optimum bike dynamics.

A further implication of the new technical rules is the increase of minimum weight: a three-cylinder engine shifts from 135 kg to 140.5 kg, a four-cylinder one changes from 145 kg to 148 kg, and a five-cylinder one varies from 145 kg to 155.5 kg. On the one hand, the pursuit of lightness will be less stringent, particularly for a five-cylinder engine; on the other hand, the power requirement will be even greater. As a consequence, it should be convenient to design relatively heavier but stronger engines, in order to endure higher specific powers.

The pursuit of higher specific power, without variations on engine architecture, will require higher bore-to-stroke ratios. This trend, steadily followed in the Formula 1 (F1) history, may be easily justified considering that a larger total piston area will yield more brake power, provided that brake mean effective pressure (BMEP) and mean piston speed can remain constant. However, engine design must be completely reviewed, and new challenges will emerge. For instance, the combustion chamber will be less compact. Therefore, it will be much more difficult to get high compression ratios, and the combustion process may be less regular. The last occurrence is particularly critical for a MotoGP bike. At the corner exit, when the bike is still listing and the rider starts to accelerate, it is paramount that the engine runs smoothly since the balance of the bike can be spoiled by any abrupt or delayed output of the engine. Only at the end of the corner, when the bike is almost straight, can the rider open the throttle wide for a full acceleration. Therefore, a bike powered by a nonregular engine will clock higher lap times since the rider will be slower at each corner, and in the following straight he will start the acceleration from a lower speed.

In the author's opinion, a full recovery of the power lost in the displacement reduction enforced by the new regulations is possible, at the cost of a further step of technical sophistication and, in some cases, with a deep change in the previous design criteria. A critical issue is the number of cylinders: As this parameter increases, it is easier to get higher specific power, but the bike must be heavier. Furthermore, the number of cylinders affects engine dimensions, weight, operations regularity, and vibrations [2–4], so that it is far from trivial to predict which will be the best configuration.

General Design Criteria

In order to achieve a specific power of about 300 HP/l it is necessary to refer to F1 technology, where, in the 2005 championship, 3.0 l, ten-cylinder engines' peak power was in excess of 900 hp [5]. Such an impressive performance was obtained by adopting bore-to-stroke ratios of about 2.5 and maximum mean piston speeds over 25 m/s, as well as by an optimization of the thermo-fluid-dynamic processes and a reduction of friction and pumping losses [6]. As in F1 [7], it is assumed that 800 cm^3 MotoGP engines will have an aluminum alloy structure, with block, heads, cam covers, and lower crankcase cast in that material, while connecting rod and valves will be made of titanium. The piston will be of aluminum alloy, with a short skirt and two small, light rings. Cylinders will have four valves and a pent-roof combustion chamber with a central spark plug. Pneumatic valves, actuated by means of a finger follower device, will be adopted. The intake manifold will be as straight as possible and shaped in order to minimize flow losses, i.e., with elliptic cross sections. The throttle plate will be placed just out of the engine head, while the fuel injector will be over the duct bell mouth. The length of the intake pipe may be continuously varied by means of a telescopic trumpet device. Both intake duct length and throttle position will be controlled by the electronic control unit. Finally, a dry sump will be adopted for the reduction of mechanical friction losses.

As far as the number of cylinders is concerned, the configurations of interest goes from three to six-cylinder engines, while the

Submitted to ASME for publication in the JOURNAL OF ENGINEERING FOR GAS TURBINES AND POWER. Manuscript received May 26, 2006; final manuscript received May 11, 2007; published online January 16, 2008. Review conducted by Jim Cowart. Paper presented at the 2006 Spring Conference of the ASME Internal Combustion Engine Division (ICES2006) Aachen, Germany, May 7–10, 2006.

Copyright © 2008 by ASME

Downloaded 02 Jun 2010 to 171.66.16.107. Redistribution subject to ASME license or copyright; see http://www.asme.org/terms/Terms_Use.cfm

Table 1 Fundamental design parameters of the analyzed engines

	L3	L4/V4	V5	V6
Bore (mm)	94.2	85.6	79.5	74.8
Stroke (mm)	38.2	34.7	32.3	30.4
Compression ratio	12.5	12.5	12.5	12.5
D_{v_int} (mm)	36.7	33.4	31.0	29.2
D_{v_exh} (mm)	30.1	27.4	25.4	23.9
L_{max_int} (mm)	16.2	14.7	13.6	12.8
L_{max_exh} (mm)	13.0	11.8	11.0	10.3
IVO CA BTDC (deg)	80	80	80	80
IVC CA ABDC (deg)	90	90	90	90
EVO CA BBDC (deg)	110	110	110	110
EVC CA ATDC (deg)	85	85	85	85
N_{max} (rpm)	19,500	20,000	20,000	20,000
$U_{p_{max}}$ (m/s)	24.8	23.1	21.5	20.3

two-cylinder engine must be discarded because of the relatively poor specific power. Three-cylinders will be in line (in the following it will be referred to as L3), while the four-cylinders will be both in line and with two banks of cylinders at 90 deg (referred to as L4 and V4, respectively). Finally, five- and six-cylinder engines will have two banks of cylinders at 75.5 deg and 90 deg, respectively. They will be referred to as V5 and V6. As far as the choice of the V angle is concerned, depending on crankshaft balance and engine-bodywork matching, it has been already discussed by the author in a previous paper [4], and these issues will not be repeated here for the sake of brevity.

Adopting a bore-to-stroke ratio of 2.46 and a maximum mean piston speed of 25 m/s, the top revving speed of four, five, and six-cylinder engines would be higher than 20,000 rpm. This value is assumed as a limit since a further increase of speed would produce small benefits in the face of several complications. Therefore, the different engine configurations will not have the same maximum mean piston speed: As the number of cylinder increases, this parameter is reduced, with ensuing advantages in terms of mechanical stress and breathing capability at high speed.

A database on F1 engines and a few empirical rules are used to define the valve features. Valve dimensions are proportional to bore: The ratio of the valve seat inner diameter to bore is 0.39 for intake and 0.32 for exhaust. Also, valve lift profiles are proportional to bore in order to guarantee a good packaging of the valve train within the head, as well as to design a compact combustion chamber, without deep pockets on the piston crown. Due to the geometric similarity, it is assumed that the curve of valve discharge coefficients versus nondimensional lift does not change among the different engines. Finally, valve timings are kept constant. This choice is due the constraints related to valve phasing, particularly, to the interference between the valves and the piston crown.

It should be observed that under the hypotheses listed above, the ratio of piston area to the mean effective intake valve area is constant for all the engines and equal to the value of a typical F1 engine. It is well known that engine "permeability" depends on this ratio, as well as on the maximum mean piston speed [8]: Since on MotoGP engines the last parameter is equal to or lower than that in F1, all the analyzed power plants will have good breathing capabilities at high speed. As far as the combustion chamber is concerned, reference is made again to F1, where compression ratios are typically between 12 and 13. The general features of the analyzed engines are reviewed in Table 1.

One Dimensional Gasdynamic Models

All the 1D models for engine cycle simulation employed in this study have been derived from a baseline, corresponding to a three-cylinder MotoGP prototype, having a capacity of 990 cm^3. The features of this reference engine are confidential, and only a few fundamentals can be disclosed in the paper. The bore-to-stroke ratio is higher than 2, the combustion chamber is a traditional four valve, pent-roof type, with a central spark plug. Valves are pneumatic and actuated by means of a finger follower. A dry sump is adopted. Fuel metering is electronically controlled, with one injector per cylinder located over the manifold bell mouth. The length of the duct can be modulated by means of a telescopic device. For the full load operating conditions, spark advance, fuel to air ratio, and taper stroke have been set up for a maximum brake torque. It should be observed that the features of this engine are remarkably similar to those of a F1 engine. Calculations have been performed by using the WAVE software (Ricardo Software, [9]).

Full Load Operations. The setup of the simulation model at a wide open throttle (WOT) presented some critical issues. Since the intake duct is quite short (less than 200 mm), end effects must be carefully modeled in order to properly capture the manifold dynamics. It is also important to include the airbox and the air scoops into the model. Furthermore, particular care must be devoted to the modeling of the exhaust primary pipe junction, which has been described as a net of volumes, ducts, and orifices, with discharge coefficients properly calibrated. In particular, a discharge coefficient equal to 0.3 has been enforced on the flow going from the exhaust junction toward each primary pipe in order to account for the effect of the junction geometry specifically designed to reduce the interference among cylinders. It was also found that the influence of fuel evaporation on engine performance is relevant: Once injection parameters have been properly tuned at the dynamometer bench, fuel vaporization helps to cool the charge and increase the total amount of delivered mass, specially at medium and low speeds. Finally, the influence of piston shrouding on the intake flow [10] is taken into account by using a modified valve actuation law.

As far as combustion is concerned, the burn rate has been determined by processing in-cylinder pressure data at a few engine speeds. Information has been used to tune the parameters of the Wiebe function, modeling the rate of heat release [8]. The duration of turbulent combustion (i.e., the angle during which the burnt fuel fraction varies from 0.1 to 0.9) was included between 50 deg and 60 deg, while the angle at which the burnt fuel fraction is 0.5 was found between 5 deg and 15 deg. Finally, combustion resulted almost complete, with an efficiency higher than 95%.

For the available in-cylinder pressure traces, friction mean effective pressure (FMEP) has been determined as the difference between indicated mean effective pressure (IMEP) and BMEP. The measured values are used for tuning the parameters of the Chen–Flynn function [9],

$$\text{FMEP} = C_1 + C_2 P_{\max} + C_3 U_p + C_4 U_p^{\,2} \tag{1}$$

The values of the constants are $C_1 = 15{,}000$ Pa, $C_2 = 0.06$, $C_3 = 1125$ Pa s/m, and $C_4 = 540$ Pa.s^2/m^2

The numerical model of the engine proved to be very accurate at full load, as shown in Fig. 1, where the percentage error on the brake torque is plotted against a nondimensional engine speed. It should be observed that the absolute error at high speed is less than 0.5% and never exceeds 2%.

Partial Load Operations. Since for a MotoGP engine partial load conditions are fundamental, the accuracy of the numerical model should be assessed also for throttled operations. Modeling a throttled flow in these engines is not trivial since the butterfly plate is very close to the intake valves (about 100 mm) and the flow through the port may be influenced by upstream throttling.

In order to address the 1D engine modeling, some 3D CFD analyses have been performed using the VECTIS code (Ricardo Software, [11]). This software has been extensively used by the author in several analyses on engine flows, as reported in Refs. [10,12,13]. The comparison with experiments presented in previous studies demonstrated the good accuracy of the code, allowing

Downloaded 02 Jun 2010 to 171.66.16.107. Redistribution subject to ASME license or copyright; see http://www.asme.org/terms/Terms_Use.cfm

Fig. 1 Percentage error on brake torque prediction at full load versus nondimensional engine speed

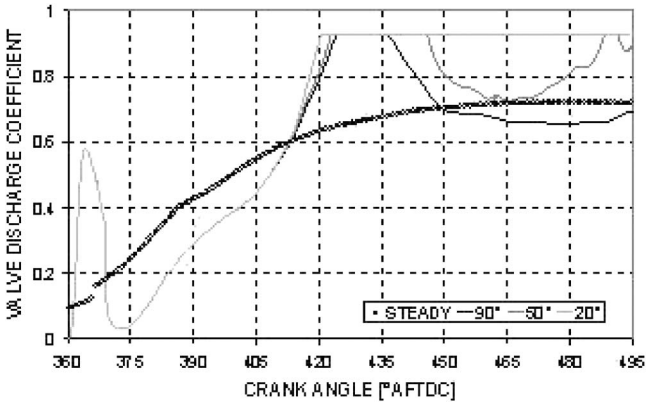

Fig. 2 Valve discharge coefficient, i.e., valve effective area divided by seat area at top engine speed, for three throttle positions (90 deg, 50 deg, and 20 deg). The values calculated by CFD intake simulations are compared to their experimental steady counterparts.

the author to rely on the physical soundness of results.

The inlet flow during the intake process has been investigated at six operating conditions, corresponding to three throttle plate angles (90 deg, i.e., WOT, 50 deg, and 20 deg) and two engine speeds (top speed and medium speed).

The computational domain is made up of the cylinder, the intake valve port, the intake manifold, and a large volume, modeling the induction ambient. Only one-half of the geometry has been meshed because of the symmetry plane bisecting the intake valve pair. The total number of cells changes during the simulation, reaching a maximum of about 500,000 units.

All the simulations start at the top dead center (TDC), with the intake valve slightly open and the ambient condition (zero velocity) imposed all over the computational domain. For the sake of simplicity, the exhaust valve is kept closed, so that the meshing of the exhaust port is not required. After intake value closing (IVC), the flow field is calculated only in the intake manifold and the simulation stops just before intake value opening (IVO). It is observed that the calculations do not correspond to actual operating conditions for two reasons.

- The influence of the exhaust system is neglected;
- The actual flow field within the intake manifold at the beginning of the calculation is far from still.

Nonetheless, this "pseudo intake" stroke simulation is able to reproduce very realistic flow conditions.

The simulation results have been processed in order to get information on the dynamic flow patterns, particularly through the throttle plate and the valves. A key parameter is the instantaneous effective area of the valves, assumed as the throat area of an equivalent 1D steady isentropic flow,

$$A_{\text{eff}} = \frac{\dot{m}}{\rho_0 a_0 \Phi\left(\frac{p_{s1}}{p_0}\right)} \tag{2}$$

where $\dot{m}$ is the mass flow rate; ρ_0, a_0, p_0 are the total quantities (density, speed of sound, and pressure, respectively) at the upstream section; p_{s1} is the static pressure at the throat section. Finally,

$$\Phi\left(\frac{p_{s1}}{p_0}\right) = \sqrt{\frac{2}{\gamma-1}\left[\left(\frac{p_{s1}}{p_0}\right)^{2/\gamma} - \left(\frac{p_{s1}}{p_0}\right)^{\gamma+1/\gamma}\right]} \tag{3}$$

The rigorous application of the above equation requires several conditions, which are never verified under engine operations. Particularly, the ramming effect occurring when the intake valve closes cannot be accounted for in a steady approach. Therefore, the results presented in Figs. 2 and 3 are referred only to a portion of the intake process, from TDC to an angle just after the maximum lift. As a comparison, the effective areas calculated through the intake stroke simulations are compared to the steady values, measured at a conventional flow bench.

The following observations are made.

- Close to TDC, the clearance between valves and piston is very small, so that the flow entering the cylinder undergoes a shrouding effect. Such an effect does not occur at the steady flow bench; thus the calculated effective area is lower than its steady counterpart.
- Dynamic effects are far from negligible: At 410 deg AFTDC, the calculated values of effective area would be higher than the throat area, clearly demonstrating the limits of a simple steady approach to study pulsating phenomena.
- The pressure ratio trace, depicted in Fig. 3, is the key to understand the fluctuations of effective area around the steady value. As this parameter decreases, the effective area falls, and vice versa.
- The difference among the three cases (90 deg, 50 deg, and 20 deg) can be totally ascribed to the fluctuation of pressure ratio, while the position of the throttle plate has not a visible influence. This means that the flow patterns through the valves are not coupled to the ones of the throttle.

The flow field within the intake manifold predicted by the CFD-3D calculations has been carefully analyzed in order to build

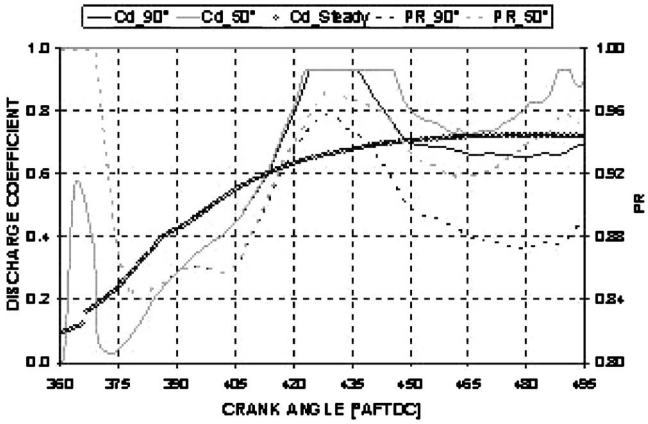

Fig. 3 Valve discharge coefficient and pressure ratio across the valve at top engine speed for two throttle positions (90 deg and 50 deg). The steady discharge coefficient is also plotted as a reference.

Downloaded 02 Jun 2010 to 171.66.16.107. Redistribution subject to ASME license or copyright; see http://www.asme.org/terms/Terms_Use.cfm

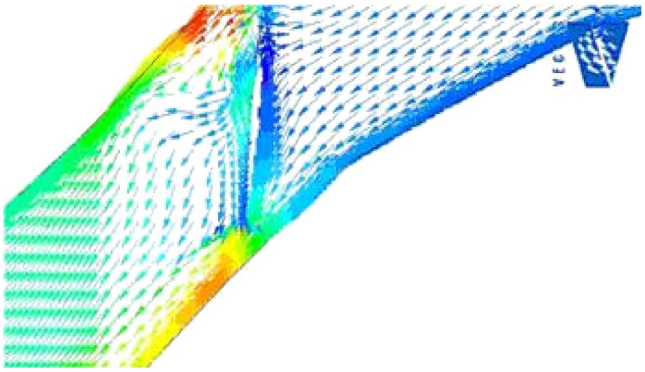

Fig. 4 Flow field through the throttle body depicted on a cross section passing through the valve axis at 100 deg after TDC (intake stroke), throttle angle of 50 deg, and top engine speed. Results of a CFD-3D intake stroke simulation.

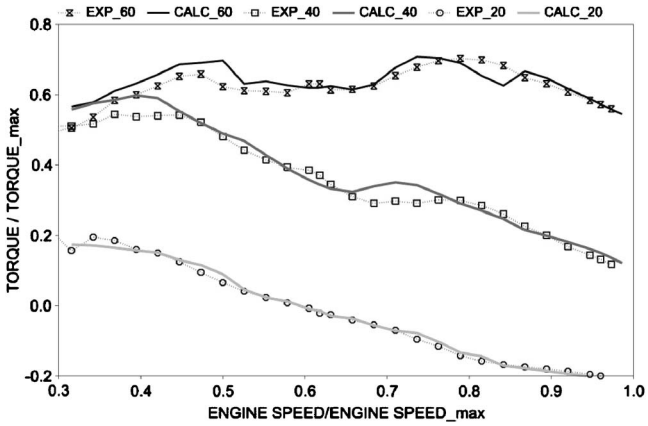

Fig. 6 Experimental versus computational results of the reference engine (torque at partial load)

a throttle model for 1D engine simulations.

It was observed that for a throttle angle included between 90 deg and 40 deg, the throttle plate splits the flow neatly into two main streams, one above and the other below the dish. A picture of the flow field through the throttle is shown in Fig. 4. It can be observed that the shape of the channels is complementary: Whether the former is convergent, the latter is divergent, and vice versa. In the convergent stream the flow is uniformly accelerated, while in the divergent duct strong velocity gradients occur. After the throttle plate, the flow field is strongly turbulent and nonuniform. Such nonuniformity is observed also in the flow entering the pair of circular ducts connected to the valves. Streamlines become regular again close to the valve seats. When the airflow is strongly throttled (plate angles lower than 40 deg), the flow patterns change, as visible in Fig. 5. The throttle plate does not drive the flow anymore, but it behaves as a wall: The airflow spills through the clearance between throttle and duct walls.

On the base of the qualitative analysis presented above, the throttle valve can be modeled as an orifice adjoining a volume. Such a volume is the high turbulence region extending from the throttle axis up to the junction of the valve ports, while the orifice diameter corresponds to the average area of the clearance between duct and throttle plates. It is also necessary to introduce a discharge coefficient for the flow entering the valve ports in order to account for the "wake" effect of the throttle plate. Finally, it is assumed that the throttle position does not affect the flow through the valves, so that valve discharge coefficients determined at WOT can be applied also at partial load.

The accuracy of the throttle model has been assessed, comparing simulation results with experiments, carried out at the dynamometer bench for different throttle angles (Fig. 6). It should be observed that the agreement is slightly less good than that found at full load; the main reason for this behavior is that the setup of combustion and fuel evaporation parameters has not been changed from the WOT operations due to the lack of data.

MotoGP 2007 Models. The WAVE models of the 800 cm^3 engines are strictly derived from the baseline. In particular, it is supposed that friction losses do not change from the 990 cm^3 engine; i.e., the parameters in Eq. (1) are the same. As far as combustion is concerned, at each engine speed and load, the angular duration of turbulent combustion is assumed to be proportional to the bore-to-stroke ratio (since the time of the process is proportional to the ratio of bore to turbulence intensity, the latter being proportional to the mean piston speed). Thus, the 800 cm^3 engines, featuring a bore-to-stroke ratio of 2.46, will have a slightly slower combustion in comparison to the present MotoGP engines. Finally, the flow-dynamic features of the airbox and the silencers are identical to those of the reference engine.

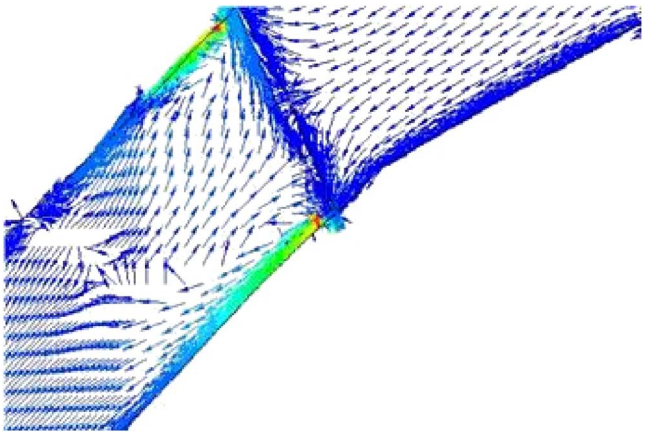

Fig. 5 Flow field through the throttle body depicted on a cross section passing through the valve axis at 120 deg after TDC (intake stroke), throttle angle of 20 deg, and top engine speed. Results of a CFD-3D intake stroke simulation.

Gas Exchange Optimization

It is well known that the amount of mixture trapped within the cylinder depends on valve permeability and the proper tuning of both intake and exhaust system. Tuning consists in finding the best compromise out of several geometrical configurations in order to reach some given targets. Obviously, the final result of the whole optimization process is related to these targets, and multiple solutions are generally possible. In this study, the main goal is the achievement of a peak brake power value of about 175 kW, associated with a torque curve as flat as possible between 8000 rpm and 20,000 rpm.

Volumetric efficiency at full load reaches a maximum when the following conditions occur concurrently [14,15].

1. The instantaneous intake total pressure (upstream of the valve) presents a strong pulse just before IVC and another one just after IVO.
2. Between the two pulses mentioned above, there is a smooth trough, phased with in-cylinder maximum suction.
3. The instantaneous exhaust pressure (downstream the valve) presents a deep trough during the overlap period.

For a nonvariable geometry, these conditions occur at a few engine speeds, basically when the intake pressure trace is made up

Downloaded 02 Jun 2010 to 171.66.16.107. Redistribution subject to ASME license or copyright; see http://www.asme.org/terms/Terms_Use.cfm

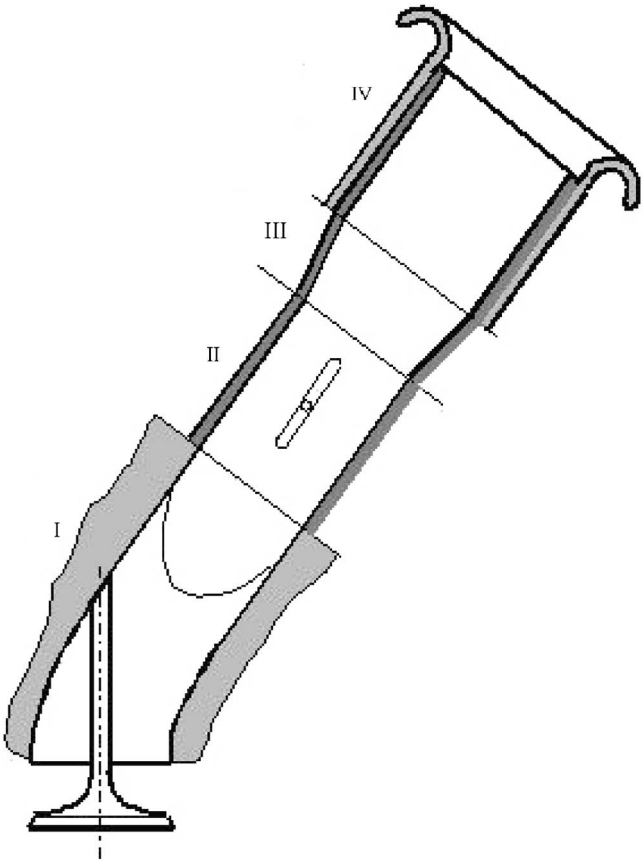

Fig. 7 Sketch of an intake manifold featuring telescopic trumpet

of a well timed series of "neat" pulses and troughs, whose number can vary between 3 and 5. Below a given engine speed, the exhaust system is no longer able to produce a suction during the overlap, while the intake pulses become very weak and out of phase as regards valve events. As a consequence, a large amount of a fresh mixture is rejected from the cylinder between bottom dead center (BDC) and the IVC, and engine operations become more difficult since a significant amount of residual gases remains trapped within the cylinder.

Intake System. In order to keep the intake system tuned from high to medium speeds (i.e., to have the proper conditions previously described), it is necessary to optimize the length and the geometrical shape of the manifold.

As far as length is concerned, a telescopic trumpet device is the most suitable solution. In order to avoid complex design issues for the actuation system, the sliding stroke of the duct must be limited: The maximum value assumed in this study is 40 mm.

The optimization of the manifold shape is more complicated. The duct of a four valve racing engine with telescopic trumpet can be divided into four parts, as shown in the sketch of Fig. 7. The first one, within the engine head, is made up of twin ducts merging at the head outlet. The second part of the pipe begins outside the head and presents an almost constant cross section area. The throttle body is placed here. The third part, a convergent taper, is used to induce a smooth flow from the airbox to the duct, as well as to condition the pressure waves traveling along the manifold. Finally, the last part is a sliding straight pipe, ending with a bell mouth.

The most important geometric parameters of the intake system that can be optimized by means of 1D engine cycle simulations are the length of the sliding duct, the cross section area of the throttle, and the cross section area of the taper. Other fundamental design issues concern the geometry of valve ports and the airbox: Since these subjects require painstaking analyses (by means of experiments at the steady flow bench and 3D-CFD simulations) and are related to a number of specific constraints, only a few general guidelines are given here for the sake of brevity.

As far as intake valve ports are concerned, the attention of the designer must be focused on the reduction of flow losses, particularly at high lift. This goal may be achieved by designing ducts as straight and smooth as possible, with a narrow angle between valve and duct axis (about 10 deg).

For the airbox, the designer must leave the maximum clearance between the intake manifold ends and the surrounding walls, creating a large volume over the ducts (10–15 l) able to dump flow-dynamic pulsations. Air scoops may be designed to recover the kinetic energy of the entering airflow, especially when the bike is running at high speed.

In the calculations that will be shown in the following, it is supposed that valve ports (both intake and exhaust), bell mouths, and airbox are already optimized, as they were in the reference engine.

Exhaust System. The layout of the exhaust system depends on the engine architecture (number of cylinders and angle between banks), as well as from specific design targets and constraints. In this study, it is assumed that all the engines will be mounted in transverse position, i.e., with the crankshaft orthogonal to the direction of march, and the length of the primary pipes is the same for all the cylinders.

In-line engines will have the exhaust system at the front, and the pipes will be routed under the crankcase toward the bike rear. In this case, no critical constraint is imposed for the exhaust geometry. V engines are more complex: It is assumed that the exhaust ducts are external to the "V," and each bank has its own terminal pipe and silencer. Since the front pipes are routed under the engine block, the length of the rear cylinder terminal pipe will be 500 mm shorter than that of the front cylinders. The terminals may be connected by a compensator tube, placed just downstream the junction among the primary pipes.

General design guidelines can be given only for primary pipes. In order to reduce flow losses, within the engine head the exhaust manifold must be shaped as a diffuser. Thus, the exhaust cross sections must be always larger than the valve areas. The primary pipe, out of the head, presents two "steps." These steps are abrupt variations of the cross section area, which enhance exhaust suction during the overlap period.

1D simulation has been used in this study to optimize the length and the cross sections of primary pipes, the cross section of the compensator (if present), and the geometry of secondary pipes and terminals. The junctions between primary and secondary pipes have a strong influence on the fluid-dynamic efficiency of the exhaust system and must be carefully designed. Basically, it is necessary to merge the pipes with a smooth junction (a typical length is about 100 mm), taking care of minimizing the interference among cylinders. For the optimization of these components, the most suitable investigation tool would be a coupled 1D-3D CFD simulation. In the calculation presented in the paper, the exhaust junctions will be considered optimized, as in the reference engine.

Finally, it is observed that the geometry of terminals and silencers is not critical. Thus, the features of the last part of the exhaust system can be adjusted according to the specific requirements of each layout.

Similarity Rules and Results. Once the optimization process has been carried out on one engine, similarity rules can be applied in extending the results to the others, with just a few further adjustments for a finer tuning. Basically, it can be assumed that for a

Downloaded 02 Jun 2010 to 171.66.16.107. Redistribution subject to ASME license or copyright; see http://www.asme.org/terms/Terms_Use.cfm

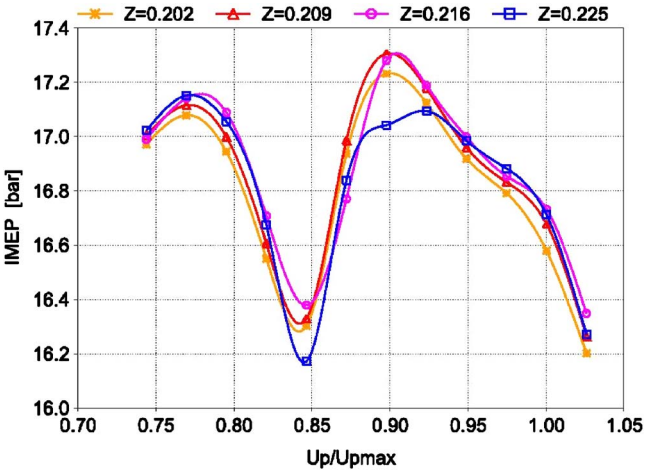

Fig. 8 Influence of the intake manifold Mach index on IMEP

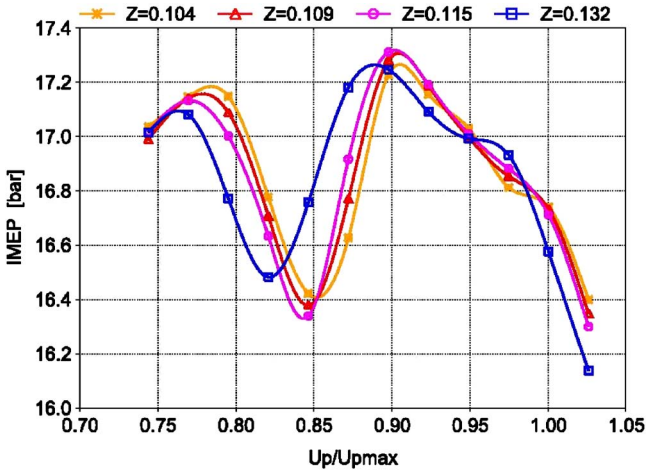

Fig. 9 Influence of the intake taper Mach index on IMEP

given mean piston speed, the mean fluid-dynamic parameters at each section of the intake (or exhaust) system depend mainly on the Mach index Z defined as follows [14]:

$$Z = (A_p U_p)/(Aa) \tag{4}$$

From a practical point of view, the acknowledgement of this index as the main factor controlling the manifold fluid dynamics implies that wherever there is a given Mach, similar flow patterns can be found. Thus, a set of optimum Mach indices can be used to calculate the manifold cross section areas of each engine, just applying Eq. (4). Conversely, the length of the ducts has been calibrated case by case, according to the specific requirements.

Figures 8–10 present the influence of some Mach parameters calculated by means of 1D engine simulations carried out on the three-cylinder engine. It must be mentioned that the length of the intake pipe is adjusted at each speed, assuming the use of telescopic trumpets with a stroke of 40 mm.

Figure 8 shows that the intake manifold cross section modifies engine performance at full load, expressed in terms of IMEP. The optimum value of Mach that can be deduced from the graph is 0.216. The criterion used in chosing the best configuration is that of maximum IMEP all over the speed range of interest. If the curves are intersecting, the preferred solution is the best one at high engine speed (to get the maximum power).

The optimum dimension of the taper can be determined from Fig. 9, where four configurations characterized by Mach parameters varying from 0.104 to 0.132 are compared. The Mach index in the constant cross section part of the manifold is kept at 0.216. As shown, the best configurations are those corresponding to Mach indices of 0.109 and 0.115.

Finally, Fig. 10 reviews the influence of the cross section of the exhaust primary pipe. The shape of the intake manifold corresponds to the optimum values of the Mach index obtained from previous analyses. It can be observed that as the Mach index is

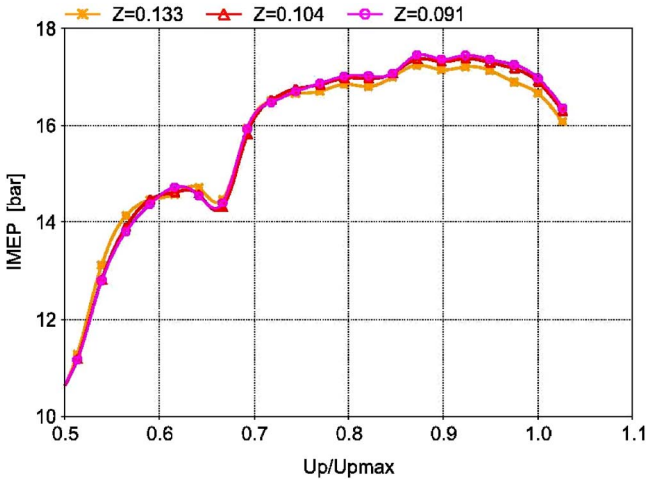

Fig. 10 Influence of the exhaust primary pipe Mach index on IMEP

reduced, IMEP increases at high mean piston speed, and it is slightly depressed at medium-low. Due to the necessity of having a very high power density, the configuration with $Z=0.091$ is assumed as the best one. The Mach index cannot be too small since the corresponding dimension of pipe cross section would become too large, with ensuing difficulties to bend the ducts (at least in the three-cylinder engine). In Table 2, the main geometric features of the intake and exhaust systems are reviewed.

Full Load Performance

Some results of 1D engine simulations at full load are presented in Figs. 11 and 12. It is reminded that all the analyzed

Table 2 Fundamental dimensions of the intake and exhaust system

	L3	L4	V4	V5	V6
Throttle diameter (mm)	54.7	48	48	43	39.2
Intake taper diameter (mm)	77	67.5	67.5	60.5	55.2
Intake duct maximum length (mm)	216			191	
Exhaust prmry pipe diameter (mm)	63	55.2	55.2	49.5	45.2
Exhaust prmry pipe length (mm)			600		
Exhaust sec. pipe diameter (mm)	—	75	—	—	—
Exhaust sec. pipe length (mm)	—	200	—	—	—
Compensator diameter (mm)	—	—	50	50	—
Compensator length (mm)	—	—	300	300	—

Downloaded 02 Jun 2010 to 171.66.16.107. Redistribution subject to ASME license or copyright; see http://www.asme.org/terms/Terms_Use.cfm

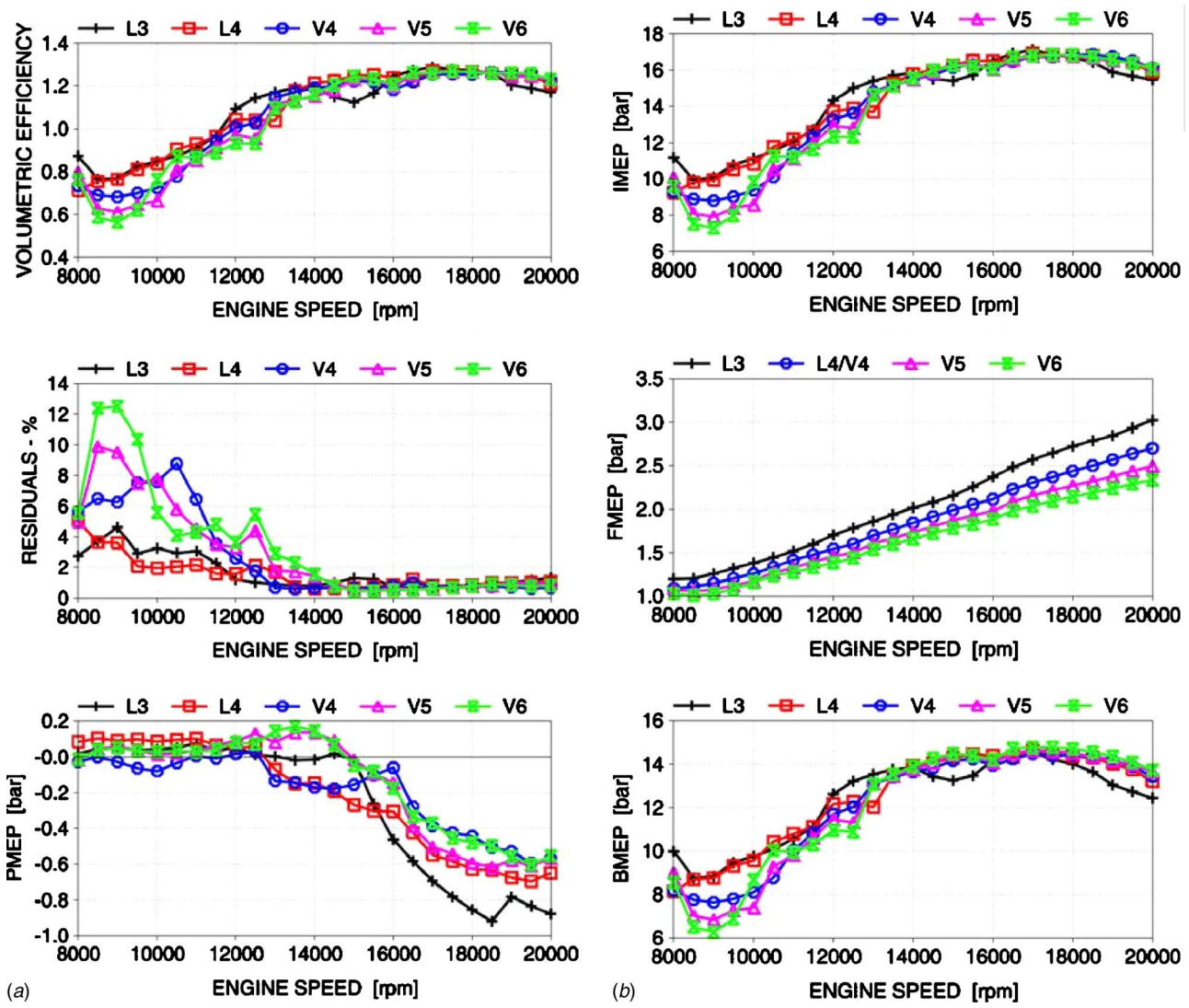

Fig. 11 (*a*) **Comparison among the engines at WOT in terms of volumetric efficiency, residual fraction, and PMEP.** (*b*) **Comparison among the engines at WOT in terms of IMEP, FMEP, and BMEP.**

engines are optimized from a fluid-dynamic point of view, according to the criteria presented in the previous section. In Fig. 11(*a*), it can be observed that all the engines, except L3, have a flat distribution of volumetric efficiency at high engine speed (from 14,000 rpm to 20,000 rpm), with quite high maximum values (up to 1.25). This is the evidence of the tuning effectiveness, thanks to the use of telescopic trumpets.

For L3, the shape of the curve is less regular for two reasons.

- Permeability at top revving speed is lower than in the other engines since the mean piston speed is higher;
- A perfect tuning of the intake system would require a taper stroke longer than 40 mm, which is the maximum allowed value; this limitation is particularly penalizing for L3.

L3 has the best breathing performance at medium engine speed (8000–14,000 rpm). In these operating conditions, volumetric efficiency decreases as the number of cylinders increases. This behavior can be explained considering that at a given engine speed, mean piston speed decreases as the number of cylinders increases. Thus, the engines with a high number of cylinders will have weaker dynamic effects, with an ensuing poorer tuning. Among the other engines, L4 is the closest to L3 at medium speed, thanks to the specific layout of the exhaust system (4 in 2 in 1).

All the engines present a minimum of volumetric efficiency at about 9000 rpm. This is due to a bad tuning of the exhaust system. It can be observed that the minimum volumetric efficiency corresponds to a maximum in the residual fraction: values of residuals higher than 10% (V6) suggest that engine operations may be difficult, with strong cycle-by-cycle variations, particularly at partial load.

As far as PMEPs are concerned, all the engines are equivalent, except L3, which has more losses due to the lower permeability at the top engine speed. It may be also observed that pumping losses at medium speed are very low (even positive in some conditions) since the engines have neither air cleaners nor catalysts (only a nonobtrusive silencer is used, more for the rider comfort than for technical requirements).

As expected, the shape of IMEP curves (Fig. 11(*b*)) is almost identical to that of volumetric efficiency graphs. Only for L3, it can be observed that the penalization at high speed is larger since the reduction of volumetric efficiency is associated with higher pumping losses.

Friction mean effective pressure (FMEP) depends on mean piston speed. Thus, the higher the number of cylinders are, the lower are the mechanical losses at a given speed. Also under this point of view, L3 is penalized at high speed.

Downloaded 02 Jun 2010 to 171.66.16.107. Redistribution subject to ASME license or copyright; see http://www.asme.org/terms/Terms_Use.cfm

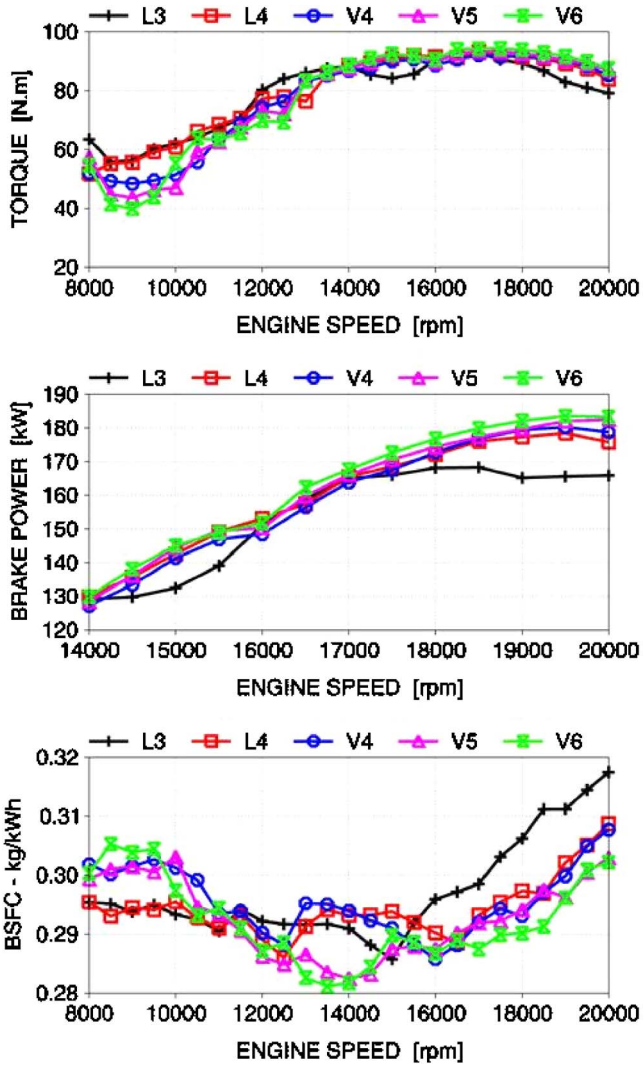

Fig. 12 Comparison among the engines at WOT in terms of brake performance

Analyzing the BMEP curves, it can be observed that the maximum values (14.5–14.8 bars) lay between 16,500 rpm and 17,500 rpm. At high speed, all the curves are very flat, except for L3, which presents two peaks at 14,000 rpm and 17,000 rpm. As the number of cylinder increases, the values of BMEP at high speed grow because of the lower friction and pumping losses. At medium speed, L3 exhibits the best performance.

In terms of maximum brake torque (Fig. 12), the performance of the analyzed engines is about 20% lower than that of current 990 MotoGP racers. Therefore, it will be possible to design lighter clutches, flywheels, and gear trains.

As far as brake power is concerned, no penalization is found, in comparison to 990 cm^3 engines. The peak power values are related to the number of cylinders: V6 is the most powerful, with 183.5 kW at 19,500 rpm, followed at close distance by V5 (182.5 kW at 20,000 rpm), V4 (180.2 kW at 19,500 rpm), and L4 (178.4 kW at 19,500 rpm). L3 falls behind, with just 168.3 kW at 18,500 rpm. However, L3 presents an almost flat distribution of brake power, so that the average power available at high speed is only 7% lower than that of the most powerful engine.

Finally, BSFC does not change very much among the engines because of the thermo-fluid-dynamic similarity. It can be observed that L3 has higher fuel consumption at high speed due to higher pumping and friction losses. However, between 8000 and 11,000 rpm, the situation is reversed, and L3 is the most fuel efficient power unit, thanks to a better pumping and mechanical efficiency, that is matched only by L4.

Lap Time Simulation

A simple simulator has been developed by the author in order to assess the engine influence on lap time. Reference has been made to the Mugello circuit in Italy. Five motorbikes, each one mounting a different engine among L3, L4, V4, V5, and V6, are compared.

The simulator is based on the hypothesis that a circuit is made up of a sequence of corners and straights. Each corner can be divided into two parts: the entrance, where the listing bike slows down reaching for the cord, and the exit, from the cord up to the point where the bike is straight again. In the second part of the corner, the rider starts to accelerate, without opening the throttle wide, because of the adherence limit. Also a straight is divided into two portions: the acceleration part and the braking part.

During the acceleration, the variation of engine speed may be calculated by solving the following equation:

$$P_{\text{eng}} = \frac{P_d}{\eta_{\text{drv}}} + (J_l + J_d + J_{\text{eng}})\omega\frac{d\omega}{dt} \tag{5}$$

P_{eng} is the engine brake effective power, corresponding to the value calculated at a given speed and full load, under steady conditions, P_d is the power loss due to aerodynamic drag and tire resistance. Due to the lack of experimental data, driveline efficiency is assumed to be constant and equal to 0.9, while driveline and engine moment of inertia are neglected in comparison with load inertia (i.e., the inertia associated with the bike and rider weight).

Several empirical assumptions are made.

- Engine design does not affect bike aerodynamics. Thus, all the bikes in the confrontation undergo the same drag force, derived from the data of a current MotoGP bike.
- The bike weight is the minimum one defined by the technical rules, while the rider weight is 70 kg.
- The engine type or the bike weight does not affect the bike speed at the corner entrance. Thus, all the bikes enter a corner at the same speed, determined on the base of data from a current MotoGP bike.
- In the straights, all the engine power can be discharged for the acceleration.
- No time is lost for gear shifting.
- At the end of the straight, the rider brakes at the maximum deceleration rate, supposed to be 20 m/s^2 for all the bikes.
- Gear ratios are optimized for each bike in order to minimize the time spent in the straights.
- The bike acceleration at the corner exit is constant and depends on engine regularity, assessed through some rules defined by the author.

For the calculation of the cornering time, reference is made to an "ideal maneuver," deduced from real data: Whenever engine operations are regular, the cornering time corresponds to the value obtained in these ideal conditions; otherwise, the bike acceleration at the corner exit is reduced by multiplying it to a penalization factor (PF).

Engine operations are considered to be regular when, varying rotational speed, it is possible to keep brake torque constant by applying a smooth variation of throttle angle. Conversely, any abrupt adjustment of throttle makes engine control more difficult.

For each corner exit and for each bike, the average engine torque required to perform the ideal maneuver mentioned above has been calculated. Then, 1D engine calculations have been carried out in order to simulate engine operations at the corner exit. For the sake of simplicity, it is supposed that the rider applies a constant brake torque by controlling engine throttling.

Downloaded 02 Jun 2010 to 171.66.16.107. Redistribution subject to ASME license or copyright; see http://www.asme.org/terms/Terms_Use.cfm

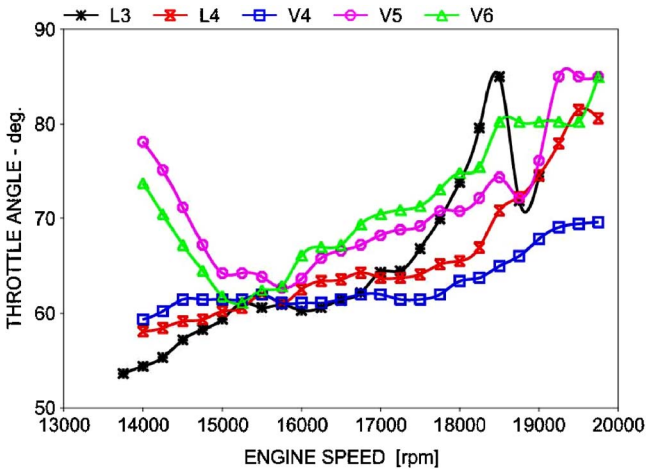

Fig. 13 Throttle angle calculated by engine simulations at the exit of the Bucine turn

The PF is determined on the base of the maximum throttle angle variation required to keep torque within a narrow band, with a tolerance of 0.5%. Whenever the throttle adjustment overcomes a threshold value, the following equation applies:

$$\mathrm{PF} = 1 - C_1 \left(\frac{\partial^2 \alpha}{\partial N^2} \right)_{\max} \tag{6}$$

where C_1 is an empirical constant, α is the percentage of throttle opening (i.e., the percentage ratio of actual throttle angle to wide opening angle).

1D calculations demonstrate that the most critical corners are the fast ones, where the engine is less throttled and its revving speed approaches the maximum value. Conversely, in slow turns, all the engines considered in the confrontation run smoothly since the volumetric efficiency fluctuations are almost canceled by throttling, while the amount of residual gas is always lower than 10%. Therefore, the most important corners of the Mugello circuit [16] are Materassi (second gear, from 130 km/h to 185 km/h), Savelli (third gear, from 145 km/h to 200 km/h), Palagio (second gear, from 125 km/h to 180 km/h), and Bucine (second and third gears from 120 km/h to 210 km/h). The last turn is particularly important for the lap time since it precedes the main straight (1145 m long), where the bikes reach the maximum speed (330–340 km/h).

Some results of the 1D engine simulations in the corner exit are presented in Fig. 13: Here, reference is made to the Bucine turn, and the calculated throttle angle is plotted against the engine speed. It can be observed that the most regular engine is V4, followed by L4 and V6. Conversely, the rider of L3 must apply abrupt variations of throttle angle in order to keep torque constant. Thus, L3 is the less regular engine. Finally, V5 and V6 present an abrupt power output from 14,000 rpm to 15,000 rpm, so that the rider is forced to throttle the engine in order to control the bike acceleration.

Table 3 reviews the results of the lap time simulation. The fastest bike is the one powered by V4, while L4 is very close (+130 ms). V5 and V6 are penalized by weight and engine regularity, so that they fall behind the four-cylinder engines. Finally, L3 has less power and is less regular. Therefore, its performance is the worst of the group, with a delay of 600 ms from the leader.

Table 3 Lap time simulation results

	Total time	Straights time	Corners time	Delay (ms)
V4	1′49″780‴	34″780‴	1′15″000‴	
L4	1′49″911‴	34″850‴	1′15″061‴	131‴
V6	1′50″006‴	34″940‴	1′15″066‴	226‴
V5	1′50″161‴	35″000‴	1′15″161‴	381‴
L3	1′50″380‴	35″170‴	1′15″210‴	600‴

Final Comments

*L*3. This configuration, characterized by the smallest total piston area, must be pushed to the limit in order to get a peak power of about 225 HP (167 kW). In spite of this, its power output at high speed remains lower than that of the other virtual competitors analyzed in this paper. Furthermore, at high speed, L3 requires a more sophisticated throttle control to compensate for the poor regularity of the engine. L3 yields an advantage at medium speed (8000–14,000 rpm), where it has the higher torque curve. Such an advantage is very slight on a fast circuitlike Mugello, but may be important on slower tracks not considered in this analysis. In terms of engine-bodywork matching, L3 is not an ideal power plant, being quite large and transmitting strong vibrations. Finally, the weight lower limit of 140.5 kg for the bike does not necessarily represent an advantage as regards four cylinders (148 kg) since it is really difficult to make a bike this light.

*L*4. The most traditional engine configuration yields very good performance at medium and high speeds, associated with a satisfactory regularity. It may be observed that L4 can reach the same peak power of L3 at 17,500 rpm, instead of 18,500, with an ensuing advantage in terms of fuel efficiency and mechanical reliability. The only limit of this configuration is the length of the crankshaft that makes the engine a little bit cumbersome (nonetheless, Yamaha won two championships, in 2004 and 2005, with this configuration applied to a 990 cm^3 engine).

*V*4. It is considered the best configuration under almost every point of view: performance at high speed, regularity, and easy matching with the bodywork. The only drawback, in comparison with L3 and L4, is the torque curve at medium speed, which is a little depressed basically because of the less favorable firing order.

*V*5. This quite unusual configuration is very similar to V4 in terms of performance at high and medium speeds, as well as in terms of easy fitting within the bodywork. However, the bike must be 7.5 kg heavier and the engine is less regular.

*V*6. This configuration is characterized by the larger total piston area. Thus, it has the higher potential in terms of performance. Instead of pursuing the maximum specific power, this potential may be exploited in order to reduce the maximum engine speed and thus, the mechanical stress and the costs related to sophisticated technologies, such as pneumatic valves, dry sump, and telescopic tapers. To follow this approach, a new and different optimization process is obviously required.

At the time of completing the last review of this paper (April 2007), the new rules have already taken effect, and some technical data of the new engines and bikes have been disclosed. All the 800 cm^3 engines are four-cylinder ones (even Honda, the world champion in 2006, passed from a V5 to a V4) and, despite the displacement reduction, the 2007 bikes are clocking faster times than in 2006. Even if the emerging trend seems to confirm the design guidelines proposed in this paper, the author believes that also different approaches may be successfully attempted. For instance, assuming as a primary goal the reduction of the costs related to engine development, it may be interesting to derive a MotoGP engine from a current four-cylinder SuperBike 1000 cm^3 unit through a 20% reduction of stroke and a specific optimization of the intake and exhaust systems.

Conclusions

The paper proposes some design criteria for the MotoGP engines, complying with the FIM 2007 Technical Regulations. Five configurations have been considered: engines with three cylinders in line and four cylinders in line, and three V engines with four,

Downloaded 02 Jun 2010 to 171.66.16.107. Redistribution subject to ASME license or copyright; see http://www.asme.org/terms/Terms_Use.cfm

five, and six cylinders. Reference is made to the current F1 technology. Therefore, all the analyzed engines present an extreme bore-to-stroke ratio (2.46) in order to reach a very high top rotational speed (20,000 rpm); pneumatic valves, telescopic trumpets, and a dry sump are adopted. 1D engine simulation and similarity criteria have been used to optimize gas exchange processes at full load, from high to medium rotational speed. Information on combustion and friction losses is derived from experiments on a 990 cm^3, three-cylinder MotoGP prototype. The calculations demonstrated that despite the displacement reduction, in 2007 it will be possible to equate the top brake power value of current 990 cm^3 MotoGP engines.

For the comparison among the five configurations, attention has been focused on three issues: the distribution of brake power from medium to high speed, bike weight, and engine regularity. It was found that as the number of cylinder increases, the value of top brake power goes up; the difference between V6 and L3 is relevant (15 kW), while the gap among V6 and the four and five-cylinder engines is limited (less than 5 kW). The best power-to-weight ratio belongs to V4, and the worse to L3. In terms of operation regularity (defined on the base of the rate of throttle angle variation required to keep a given constant value of torque), the best engine turned out to be V4, and the worse is L3.

Finally, a simple simulator and some empiricism have been used in order to assess the differences among the analyzed engines in terms of lap time on the Mugello circuit. The best configurations turned out to be the four-cylinder engines (V4 first, then L4); L3 and V5 fall behind, with a delay from V4 of 600 ms and 381 ms, respectively, while V6 lies in the middle (+226 ms).

Acknowledgment

The authors wish to acknowledge Ricardo Software, Burr Ridge, IL for the use of the WAVE and VECTIS codes granted to the University of Modena and Reggio E.

Nomenclature

a = speed of sound
A = cross section area of a duct
A_{eff} = valve effective area
A_p = area of the piston
AFTDC = after firing top dead center
$C_1 \cdots C_4$ = constant parameters
CA = crank angle
CFD = computational fluid dynamics
D_v = valve seat inner diameter
EVC = exhaust valve closing
EVO = exhaust valve opening
Exh. = exhaust
J_d = driveline moment of inertia
J_{eng} = engine moment of inertia
J_l = load moment of inertia
L = valve lift
L3 = three-cylinders in line
L4 = four-cylinders in line
$\dot{m}$ = mass flow rate
N = engine rotational speed
P_d = power loss of the bike (drag, tyres)
P_{eng} = engine brake power
p_0 = total pressure
p_s = static pressure
Prmry = primary (pipe)
Sec. = secondary (pipe)
V4 = four-cylinder engine, V engine
V5 = five-cylinder engine, V engine
V6 = six-cylinder engine, V engine
Z = mach index
α = percent of throttle opening
γ = ratio of gas specific heats
ρ = density
ω = engine angular speed

References

[1] Federation Internationale de Motocyclisme (FIM), 2005, *Road Racing World Championship Grand Prix Regulations* (www.fim. ch/EN/rules/Sportifs/ccrGP/2005).
[2] Domenicali, C., 2002, "From SuperBike to MotoGP: Evolution of Design and Experimental Methodologies for the Development of a Racing Motorbike," Proceedings of the Seminar held at the Faculty of Engineering of Modena, October 30 (in Italian).
[3] Yamaha Motor, http://www.yamaha-motor.co.jp/global/profile/sports/race/motogp/review/003
[4] Mattarelli, E., and Cantore, G., 2005, "Comparison of Four Stroke MotoGP Engines," SAE Paper No. 2004-01-3559.
[5] Toyota Motor, 2005, http://www.toyota-f1.com/public/en/technologies/tf105.html
[6] Ferrari, P., 2002, "Ferrari Formula 1 Engines, From 1947 Up Today," Proceedings of the Seminar held at the Faculty of Engineering of Modena, October 16 (in Italian).
[7] Wright, P. G., 2004, *Ferrari Formula 1: Under the Skin of the Championship-Winning F1-2000*, SAE Publications, Warrendale, PA.
[8] Heywood, J. B., 2001, *Internal Combustion Engine Fundamentals*, McGraw-Hill, New York.
[9] Ricardo Software, 2004, WAVE Documentation/User's Manual, Version 5.2.
[10] Ricardo Software, 2004, VECTIS Documentation/User's Manual, Version 3.8.
[11] Cantore, G., Fontanesi, S., Mattarelli, E., and Bianchi, G. M., 2002, "A Methodology for In-Cylinder Flow Field Evaluation in a Low Stroke-to-Bore SI Engine," SAE Paper No. 2002-01-1119.
[12] Mattarelli, E., 2000, "Comparison Between Two Combustion Chambers for a Motorcycle Racing Engine," SAE Paper No. 2000-01-1894.
[13] Balestrazzi, D., Borghi, M., Fontanesi, S., and Mattarelli, E., 2004, "The Influence of Swirl Control Strategies on the Intake Flow in Four Valve HSDI Diesel Engines," SAE Paper No. 2004-01-0112.
[14] Pignone, G. A., and Vercelli, U. R., 1995, *Motori ad Alta Potenza Specifica*, Giorgio Nada Editore, Milano.
[15] Blair, G. P., 1999, *Design and Simulation of Four-Sroke Engines*, SAE Publications, Warrendale, PA.
[16] Mugello circuit website: www.mugellocircuit.it

Downloaded 02 Jun 2010 to 171.66.16.107. Redistribution subject to ASME license or copyright; see http://www.asme.org/terms/Terms_Use.cfm